# The Assessment of Using High Nitrogen Austenitic Stainless Steels in Core Structural Materials of Pressurized Water Reactors

by

Abdullah Saeed Sinjlawi

A dissertation submitted in partial fulfillment
of the requirements for the degree of
Doctor of Philosophy
(Nuclear Engineering and Radiological Sciences)
in the University of Michigan
2025

Doctoral Committee:

Professor Emeritus Gary S. Was, Chair
Associate Professor Liang Qi
Assistant Professor Stephen Raiman
Research Scientist Peng Wang

Abdullah S. Sinjlawi

sinjlawi@umich.edu

ORCID iD: 0009-0007-3753-833X

© Abdullah S. Sinjlawi 2025

**Acknowledgements**

I am deeply grateful to my advisor, Dr. Gary Was, for his invaluable guidance, support, and the resources provided, which made the completion of this work possible. As his last Ph.D. student, being part of his research group has been an especially meaningful and enriching experience. I also extend my sincere thanks to my dissertation committee members, Dr. Liang Qi, Dr. Stephen Raiman, and Dr. Peng Wang, for their insightful feedback and assistance.

I sincerely thank everyone who contributed to my work, even with a single word of support. I thank my esteemed colleagues in the Was research group for our fruitful discussions over the past years. My deep appreciation goes to Connor Shamperger for his valuable assistance in the lab, where he spared no effort in providing hands-on help and ensuring the equipment ran smoothly. I am also grateful to the Michigan Ion Beam Laboratory (MIBL) staff, represented by Zhijie Jiao (George), Fabian Naab, Prashant Niraula, and Alex Flick, for their support in my extended proton irradiation experiments at MIBL. A special thanks goes to Kai Sun for his significant contributions, whether by helping me obtain results from electron microscopes or offering essential guidance to streamline my work on these instruments. Also, I express my heartfelt thanks to the Rolls-Royce Small Modular Reactor (SMR) project team for their support and valuable advice, which was instrumental in bringing this work to fruition.

I would like also to express my gratitude to all the members of the Nuclear Engineering and Radiological Sciences (NERS) department at the University of Michigan who supported me in various ways throughout my Ph.D. journey.

Finally, none of this would have been possible without the patience and support of my beloved wife, Haneen Obeidat, and my beloved kids (Abdalrahman, Ibrahim, and Elyas). My family: my father (Saeed), mother (Fatima), siblings (Rania, Ashraf, Reema, Mohammad, Bilal, and Dua), and their families. Their constant emotional support and encouragement through this process was constant and that kept me going through the difficult times. Support for this project was provided by funding from the Rolls-Royce Small Modular Reactor project (contract number 5005318489) and the United States Department of Energy Light Water Reactor Sustainability Program (contract number 4000136608).

## Table of Contents

Acknowledgements ..... ii

List of Tables ..... viii

List of Figures ..... xv

List of Appendices ..... xxxi

Abstract ..... xxxii

Chapter 1 Introduction ..... 1

Chapter 2 Background ..... 5

2.1 Austenitic stainless-steel applications in nuclear power plants ..... 7

2.1.1 Degradation modes of stainless steels in LWRs ..... 7

2.2 Metallurgy of austenitic stainless steels ..... 8

2.2.1 Structure and composition ..... 8

2.2.2 Physical and mechanical properties of austenitic stainless steels ..... 11

2.2.3 Solid solution strengthening of austenitic stainless steel ..... 12

2.2.4 Irradiation effects on austenitic stainless steel in PWRs ..... 19

2.2.5 Corrosion behavior in PWR environments ..... 54

2.3 Irradiated assisted stress corrosion cracking in LWRs ..... 58

Chapter 3 Objectives ..... 70

Chapter 4 Experimental Conditions ..... 72

4.1 Alloys ..... 72

4.1.1 Grains morphology and size ..... 73

4.1.2 Mechanical properties ..... 74

4.2 Sample preparation ..... 79
4.2.1 Four-point bend samples ..... 79
4.2.2 Tensile bars preparation ..... 81
4.3 Tensile test for mechanical properties measurements ..... 84
4.4 Samples designations ..... 86
4.4.1 Test samples ..... 86
4.4.2 Microscopy analysis samples ..... 86
4.5 Proton irradiation ..... 87
4.5.1 Proton irradiation ..... 87
4.6 Irradiation-assisted stress corrosion cracking test ..... 109
4.6.1 Autoclave system ..... 109
4.6.2 Water chemistry ..... 114
4.6.3 Sample loading ..... 114
4.6.4 Incremental four-point bend test ..... 115
4.7 Incremental constant extension rate tensile ..... 116
4.7.1 Quantification of dislocation channels density ..... 117
4.7.2 Dislocation channel height ..... 118
4.7.3 Number of dislocations in a dislocation channel ..... 119
4.8 Microscopy analysis ..... 120
Chapter 5 Finite Element Analysis ..... 123
5.1 FEA with ANSYS ..... 124
5.1.1 Nonlinear analysis with ANSYS ..... 125
5.2 FEA Model ..... 127
5.3 Model setup ..... 128
5.4 Input data ..... 134

5.4.1 Yield strength of the irradiated layer at high temperature ..... 135
5.4.2 Yield strength of the unirradiated bulk at high temperature ..... 138
5.4.3 Other material properties from literature ..... 138
5.5 FE model validation ..... 140
5.5.1 FEA model validation tests at room temperature ..... 140
5.5.2 High temperature validation test ..... 141
5.5.3 Data comparison ..... 143
5.5.4 FEA output ..... 146
5.6 Uncertainty Analysis for mechanical testing and FEA ..... 159
5.6.1 Error sources ..... 159
5.6.2 DPA calculation ..... 164
5.6.3 Sensitivity analysis ..... 165
5.6.4 Uncertainty application on the failure stress ..... 174
Chapter 6 Results ..... 176
6.1 Irradiated-induced microstructure ..... 176
6.1.1 Dislocation loops ..... 177
6.1.2 Cavities ..... 179
6.1.3 Precipitates ..... 181
6.1.4 Radiation-induced segregation ..... 183
6.2 Four-point bend tests ..... 187
6.2.1 Load profiles ..... 187
6.2.2 Water chemistry profiles ..... 190
6.2.3 IASCC initiation and cracking statistics ..... 197
6.2.4 Surface and grain boundary oxidation ..... 203
6.2.5 Cracking morphology and crack tip analysis ..... 212

6.3 Dislocation channels ..... 244
6.3.1 CERT tests ..... 244
6.3.2 Dislocation channels quantification ..... 246
6.3.3 Step height measurement ..... 248
6.3.4 Microscopic strains within the dislocation channel ..... 252
6.3.5 Spacing between dislocation channels ..... 253
Chapter 7 Discussion ..... 256
7.1 Proton irradiation-induced microstructure ..... 257
7.1.1 Irradiation-induced defect evolution ..... 258
7.1.2 Radiation hardening ..... 271
7.1.3 The deformation mechanism: dislocation channels characteristics ..... 280
7.2 IASCC susceptibility ..... 282
7.2.1 IASCC initiation stress ..... 282
7.2.2 Crack morphology ..... 291
7.3 The role of solute nitrogen on the IASCC susceptibility ..... 303
7.4 Evaluation of the hypothesis ..... 310
Chapter 8 Conclusion ..... 313
Appendices ..... 315
Bibliography ..... 495

## List of Tables

Table 2-1 IASCC service experience [163, 164]. ..... 59

Table 4-1 Chemical composition of alloys used in this study in wt.% obtained from materials vendor and from the chemical analysis performed by Luvak Inc (USA). ..... 73

Table 4-2 Mechanical properties of both alloys from the vendor's certificate ..... 73

Table 4-3 Samples designations. ..... 86

Table 4-4 Microscopy samples designations. ..... 87

Table 4-5 Summary of proton-irradiation parameters. ..... 93

Table 4-6 Proton irradiation experiments parameters for 4PB samples. ..... 99

Table 4-7 Proton irradiation experiments parameters for tensile bars. ..... 99

Table 5-1 Mesh settings used in the FEA. ..... 130

Table 5-2 FEA results dependent on element size. ..... 132

Table 5-3 Irradiated yield strength at high temperature from literature. ..... 136

Table 5-4 Comparison of the irradiated YS at 25 ºC and 340 ºC. ..... 137

Table 5-5 Irradiated YS at 25 ºC and 340 ºC. ..... 137

Table 5-6 Other material's properties used in the FEA. ..... 139

Table 5-7 Elastic of Modulus of austenitic stainless steels. ..... 140

Table 5-8 Testing parameters used in the 4PB test for the FEA model validation. ..... 141

Table 5-9 Sample deflection for the 4PB test at RT and 340 ºC. ..... 145

Table 5-10 Fitting equations created from curves in Figure 5-7. ..... 147

Table 5-11 Load and maximum surface stress used in 4PB test. ..... 148

Table 5-12 Hardness measurements of the standards block. ..... 162

Table 5-13 Post-irradiation hardness measurement ..... 163

Table 5-14 Hardness to $YS_{Irradiated}$ conversion. ..... 163

Table 5-15 Damage rate uncertainty calculation from SRIM analysis. ..... 165

Table 5-16 Summary of the key input parameters that used for the FEA. ..... 167

Table 5-17 Reference points outputs. ..... 168

Table 5-18 The percent change of the input parameter value that used to estimate the sensitivity of the FEA model. ..... 168

Table 5-19 Sensitivity coefficients for each input parameter for SS 304LN and SS 304L-R, and the total uncertainty from FEA based on the sensitivity analysis. ..... 170

Table 5-20 Influence factor (NCS) of each input parameter and the contribution of the NCS in the total uncertainty. ..... 173

Table 5-21 The uncertainty in the FEA-calculated surface tensile stress at the last loading step that initiates a crack. ..... 175

Table 6-1 Summary of nickel and silicon compositions showing the effect of RIS after irradiation to 5 dpa. ..... 187

Table 6-2 Water chemistry parameters calculated during each loading step. ..... 190

Table 6-3 4PB tests results for the six samples including the uncertainty results showing the range of the expected failure. ..... 198

Table 6-4 Cracking statistics of SS 304LN and SS 304L-R samples after straining in high temperature water containing $H_3BO_3$ and LiOH at 340 $^oC$. ..... 200

Table 6-5 Total number of cracks observed in both alloys and the contribution of microstructural features initiating cracking. ..... 201

Table 6-6 Summary of inner oxide layer thickness taken from different locations. ..... 209

Table 6-7 Chemical compositions of key RIS elements (Si, Ni, and Cr) across different GBs and different depth from the crack tip. ..... 244

Table 6-8 AFM measurement check against well-calibrated OM. ..... 249

Table 7-1 Summary of calculated YS from the microstructural features in SS 304LN and SS 304L-R. ..... 278

Table B-1 Surface deflection profiles for sample N3, step 39%YS. ..... 320

Table B-2 Surface deflection profiles for sample N3, step 47%YS. ..... 321

Table B-3 Surface deflection profiles for sample N3, step 51%YS. ..... 323

Table B-4 Surface deflection profiles for sample N3, step 62%YS. ..... 324

Table B-5 Surface deflection profiles for sample N3, step 70%YS. ..... 325

Table B-6 Surface deflection profiles for sample N7, step 44%YS. ..... 327

Table B-7 Surface deflection profiles for sample N7, step 52%YS. ..... 328

Table B-8 Surface deflection profiles for sample N7, step 59%YS. ..... 329

Table B-9 Surface deflection profiles for sample N7, step 66%YS. ..... 331

Table B-10 Surface deflection profiles for sample N7, step 74%YS. ..... 332

Table B-11 Surface deflection profiles for sample N7, step 89%YS. ..... 333

Table B-12 Surface deflection profiles for sample N10, step 50%YS. ..... 335

Table B-13 Surface deflection profiles for sample N10, step 60%YS. ..... 336

Table B-14 Surface deflection profiles for sample N10, step 70%YS. ..... 337

Table B-15 Surface deflection profiles for sample L-R-1, step 50%YS. ..... 339

Table B-16 Surface deflection profiles for sample L-R-1, step 60%YS. ..... 340

Table B-17 Surface deflection profiles for sample L-R-1, step 70%YS. ..... 341

Table B-18 Surface deflection profiles for sample L-R-1, step 80%YS. ..... 343

Table B-19 Surface deflection profiles for sample L-R-3, step 50%YS. ..... 344

Table B-20 Surface deflection profiles for sample L-R-3, step 60%YS. ..... 345

Table B-21 Surface deflection profiles for sample L-R-3, step 70%YS. ..... 347

Table B-22 Surface deflection profiles for sample L-R-3, step 80%YS. ..... 348

Table B-23 Surface deflection profiles for sample L-R-6, step 60%YS. ..... 349

Table B-24 Surface deflection profiles for sample L-R-6, step 70%YS. ..... 351

Table B-25 Surface tensile stress profiles for sample N3, step 39%YS..... 352

Table B-26 Surface tensile stress profiles for sample N3, step 47%YS..... 353

Table B-27 Surface tensile stress profiles for sample N3, step 51%YS..... 355

Table B-28 Surface tensile stress profiles for sample N3, step 62%YS. ..... 356

Table B-29 Surface tensile stress profiles for sample N3, step 70%YS. ..... 358

Table B-30 Surface tensile stress and strain profiles for sample N7, step 44%YS. ..... 359

Table B-31 Surface tensile stress and strain profiles for sample N7, step 52%YS. ..... 360

Table B-32 Surface tensile stress and strain profiles for sample N7, step 59%YS. ..... 362

Table B-33 Surface tensile stress and strain profiles for sample N7, step 66%YS. ..... 363

Table B-34 Surface tensile stress and strain profiles for sample N7, step 74%YS. ..... 364

Table B-35 Surface tensile stress and strain profiles for sample N7, step 89%YS. ..... 366

Table B-36 Surface tensile stress and strain profiles for sample N10, step 50%YS. ..... 367

Table B-37 Surface tensile stress and strain profiles for sample N10, step 60%YS. ..... 369

Table B-38 Surface tensile stress and strain profiles for sample N10, step 70%YS. ..... 370

Table B-39 Surface tensile stress and strain profiles for sample L-R-1, step 50%YS. ..... 371

Table B-40 Surface tensile stress and strain profiles for sample L-R-1, step 60%YS. ..... 373

Table B-41 Surface tensile stress and strain profiles for sample L-R-1, step 70%YS. ..... 374

Table B-42 Surface tensile stress and strain profiles for sample L-R-1, step 80%YS. ..... 376

Table B-43 Surface tensile stress and strain profiles for sample L-R-3, step 50%YS. ..... 377

Table B-44 Surface tensile stress and strain profiles for sample L-R-3, step 60%YS ..... 378

Table B-45 Surface tensile stress and strain profiles for sample L-R-3, step 70%YS. ..... 380

Table B-46 Surface tensile stress and strain profiles for sample L-R-3, step 80%YS. ..... 381

Table B-47 Surface tensile stress and strain profiles for sample L-R-6, step 60%YS. ..... 383

Table B-48 Surface tensile stress and strain profiles for sample L-R-6, step 70%YS. ..... 384

Table B-49 Surface tensile strain profiles for sample N3, step 39%YS. ..... 385

Table B-50 Surface tensile strain profiles for sample N3, step 47%YS. ..... 387

Table B-51 Surface tensile strain profiles for sample N3, step 51%YS. ..... 388

Table B-52 Surface tensile strain profiles for sample N3, step 62%YS. ..... 389

Table B-53 Surface tensile strain profiles for sample N3, step 70%YS. ..... 391

Table B-54 Surface tensile strain profiles for sample N7, step 44%YS. ..... 392

Table B-55 Surface tensile strain profiles for sample N7, step 52%YS. ..... 393

Table B-56 Surface tensile strain profiles for sample N7, step 59%YS. ..... 395

Table B-57 Surface tensile strain profiles for sample N7, step 66%YS. ..... 396

Table B-58 Surface tensile strain profiles for sample N7, step 74%YS. ..... 397

Table B-59 Surface tensile strain profiles for sample N7, step 89%YS. ..... 399

Table B-60 Surface tensile strain profiles for sample L-R-1, step 50%YS. ..... 400

Table B-61 Surface tensile strain profiles for sample L-R-1, step 60%YS. ..... 401

Table B-62 Surface tensile strain profiles for sample L-R-1, step 70%YS. ..... 403

Table B-63 Surface tensile strain profiles for sample L-R-1, step 80%YS. ..... 404

Table B-64 Surface tensile strain profiles for sample L-R-3, step 50%YS. ..... 405

Table B-65 Surface tensile strain profiles for sample L-R-3, step 60%YS. ..... 407

Table B-66 Surface tensile strain profiles for sample L-R-3, step 70%YS. ..... 408

Table B-67 Surface tensile strain profiles for sample L-R-3, step 80%YS. ..... 409

Table B-68 Surface tensile strain profiles for sample L-R-6, step 60%YS. ..... 411

Table B-69 Surface tensile strain profiles for sample L-R-6, step 70%YS. ..... 412

Table B-70 Stress and strain profiles across sample thickness for sample N3, step 39%YS. .... 413

Table B-71 Stress and strain profiles across sample thickness for sample N3, step 47%YS. .... 415

Table B-72 Stress and strain profiles across sample thickness for sample N3, step 51%YS. .... 417

Table B-73 Stress and strain profiles across sample thickness for sample N3, step 62%YS. .... 419

Table B-74 Stress and strain profiles across sample thickness for sample N3, step 70%YS. .... 421

Table B-75 Stress and strain profiles across sample thickness for sample N7, step 44%YS. .... 423

Table B-76 Stress and strain profiles across sample thickness for sample N7, step 52%YS. .... 425

Table B-77 Stress and strain profiles across sample thickness for sample N7, step 59%YS. .... 427

Table B-78 Stress and strain profiles across sample thickness for sample N7, step 66%YS. .... 429

Table B-79 Stress and strain profiles across sample thickness for sample N7, step 74%YS. .... 431

Table B-80 Stress and strain profiles across sample thickness for sample N7, step 89%YS. .... 433

Table B-81 Stress and strain profiles across sample thickness for sample N10, step 50%YS. .. 435

Table B-82 Stress and strain profiles across sample thickness for sample N10, step 60%YS. .. 436

Table B-83 Stress and strain profiles across sample thickness for sample N10, step 70%YS. .. 438

Table B-84 Stress and strain profiles across sample thickness for sample L-R-1, step 50%YS. ..... 440

Table B-85 Stress and strain profiles across sample thickness for sample L-R-1, step 60%YS. 442

Table B-86 Stress and strain profiles across sample thickness for sample L-R-1, step 70%YS. 444

Table B-87 Stress and strain profiles across sample thickness for sample L-R-1, step 80%YS. 446

Table B-88 Stress and strain profiles across sample thickness for sample L-R-3, step 50%YS. 447

Table B-89 Stress and strain profiles across sample thickness for sample L-R-3, step 60%YS. 449

Table B-90 Stress and strain profiles across sample thickness for sample L-R-3, step 70%YS. 451

Table B-91 Stress and strain profiles across sample thickness for sample L-R-3, step 80%YS. 453

Table B-92 Stress and strain profiles across sample thickness for sample L-R-6, step 60%YS. 455

Table B-93 Stress and strain profiles across sample thickness for sample L-R-6, step 70%YS. 457

Table B-94 Surface stress profiles for reference. ..... 459

Table B-95 Surface stress profiles for applied loading sensitivity. ..... 460

Table B-96 Surface stress profiles for unirradiated bulk yield strength sensitivity. ..... 462

Table B-97 Surface stress profiles for irradiated layer yield strength sensitivity. ..... 463

Table B-98 Surface stress profiles for the sample thickness sensitivity. ..... 464

Table B-99 Surface stress profiles for reference. ..... 466

Table B-100 Surface stress profiles for applied loading sensitivity. ..... 467

Table B-101 Surface stress profiles for unirradiated bulk yield strength sensitivity. ..... 468

Table B-102 Surface stress profiles for irradiated layer yield strength sensitivity. ..... 470

Table B-103 Surface stress profiles for the sample thickness sensitivity. ..... 471

## List of Figures

Figure 1-1 Interacting degradation mechanism structural materials leading to IASCC in LWRs environment. ..... 3

Figure 2-1 Iron-nickel-chromium diagram at 1100 ºC [22]..... 10

Figure 2-2 Schaeffler diagram for stainless steel [23]. ..... 11

Figure 2-3 The impact of interstitial atoms on the stainless-steel strengthening [27]. ..... 12

Figure 2-4 The role of nitrogen on the yield strength of SS 316L. The YS is increasing with nitrogen content [37] and (b) in Fe-17Cr-10Mn-5Ni Alloys and SS 304 alloy [38]. ..... 16

Figure 2-5 Influence of nitrogen on the temperature sensitivity of the yield stress in austenitic stainless steels [43]. ..... 18

Figure 2-6 The dependence of mechanical and chemical phenomena on the irradiation-induced damage in dpa [14]..... 20

Figure 2-7 Evolution of the Frank loop density and size in various austenitic stainless steels following irradiation to doses of up to 13 dpa at a temperature near 300°C [54]..... 22

Figure 2-8 Effect of irradiation temperature in the range of 50–400 °C on the components of the dislocation density in neutron-irradiated austenitic stainless steel [57] and (b) from 400 – 600 °C [58]..... 23

Figure 2-9 Void swelling as a function of (a) internals materials, irradiation temperature, and neutron dose, and (b) as a function of dose in PWR internals [68]. ..... 26

Figure 2-10 Schematic showing the role of (a) cold working on the swelling behavior of PWR core internals observed either in fast reactor or under charged particle irradiation showing the early swelling of SS 304 compared to SS 316 [68] and (b) the role of alloying modification to SS 316 on the swelling behavior showing suppressive role to void swelling at temperature ranges of 400 – 500 ºC [67]. ..... 27

Figure 2-11 Cavities in CW SS 316 BFB irradiated in Tihange 1 from different locations across bolt head and shank at dpa range between 7.5 - 19.5 dpa and temperature ranges of 320 - 340 ºC [67]. ..... 27

Figure 2-12 (a) Swelling of annealed SS 304 in the temperature range of 373 - 388 ºC measured by density changes in the lower halves of four EBR-II reflector subassemblies

showing the dependence of swelling on the dose rate [71], (b) results of void swelling prediction model developed by F.A. Garner showing the strong dependence on dose rates [68].28

Figure 2-13 Sensitivity of RIS to temperature and dose rate in austenitic stainless steels [76]. .. 30

Figure 2-14 Dose dependence of grain boundary chromium concentration for several 300-series austenitic stainless steels irradiated at a temperature of about 300°C [55]. ..... 31

Figure 2-15 The segregation of Si at the GB of various austenitic stainless steels irradiated with neutrons or protons to 13 dpa (after [83]). ..... 32

Figure 2-16 A comparison between the elemental composition at the GB and dislocation loops in SS 304 irradiated with 2 MeV protons to 5 dpa to 360 ºC showing depletion of Fe, Cr, Mn, and Cu and segregation of Ni, Si, P, and B [85]. ..... 33

Figure 2-17 (a) A Si loop shaped cluster observed by Etienne et al. in a Type 316 austenitic steel irradiated at 350 °C by $Fe5^{+}$ ions to a dose of 10 dpa. The height of the bounding box is 34 nm [87] and (b) A dislocation loop with Ni, Si, Cu, and P segregation at its periphery in proton irradiated SS 304 to 10 dpa [89]. ..... 34

Figure 2-18 Variations in the composition of Ni and Si ($C_{Ni/Si}$) around a dislocation loop in a CP Type 304 austenitic stainless steel irradiated by 2 MeV protons to a dose of 5 dpa at 360 °C [85]. The diameter of the loop is 12–14 nm and the measured concentrations were taken in a clockwise direction around the loop. ..... 34

Figure 2-19 Concentration of the indicated elements at GBs in a tip of neutron irradiated Type 304 stainless steel, neutron-irradiated to a dose of 24 dpa at 300 °C; results of Toyama et al. [88]. The box inset in the image for Si represents the region used to trace the elemental concentrations across the GB; the box is ∼20 nm long. ..... 36

Figure 2-20 The effect of alloying with interstitial C and N atoms on RIS in an austenitic steel irradiated by 12 MeV Ni3+ ions at 300 °C. All units of concentration are in wt.%. The abscissa represents the changes in concentration of the specified solute atom (Cr, Ni, Si) measured at the half-widths of the concentration profiles at the GBs, referred to the concentrations far from the boundaries. Data of Kano et al [99]. ..... 37

Figure 2-21 Precipitates phased observed in neutron irradiated SS 316 a range of dpa levels and temperatures. The plot is originally found in Ref. [101] and modified by [102] through adding the low temperature data (red dots). The plot shows the formation of γ′ phase in the shaded area and G phase in the black dots with some unidentified phases as well. ..... 39

Figure 2-22 (a) Strengthening of various annealed austenitic stainless steels with neutron dose in LWRs at temperatures of range 280 - 330 ºC and up to 10 dpa [119] (modified by [120]) and (b) experimental data plotted against the change in the yield strength in hardness for austenitic stainless steels [118] ..... 42

Figure 2-23 Calculated radiation hardening compared with measured results of type 304 and 316 variants at room temperature and 330 °C. The enclosed letters denote the corresponding alloy samples [125]. ..... 46

Figure 2-24 TEM image of dislocation channel in an Fe-18Cr-12Ni alloy irradiated with protons to 5 dpa at 360 °C and strained to 7% at 288 °C showing a region of defects-free after being cleared out by many dislocations [134]. ..... 47

Figure 2-25 Example of (a) continuous dislocation channels crossing a GB towards the adjacent grain and (b) example of discontinuous dislocation channels arrested at the GB causing [135]. ..... 48

Figure 2-26 Conceptual diagram showing the measurement of DC width, spacing, and height following its intersection with the surface, and converting the measured values into real one using crystallographic analysis [83, 136]. ..... 48

Figure 2-27 Grain boundary normal stress at the discontinuous DC-GB intersection and several micrometers away. Dashed red lines denote the upper and lower bounds for calculated stresses from HR-EBSD over the 75 analyzed sites [140]. ..... 50

Figure 2-28 Direct comparison of grain boundary normal stress profiles near (a) discontinuous dislocation channel-grain boundary intersection, and (b) near a continuous dislocation channel-grain boundary intersection and cracking fraction of HR-EBSD analyzed grain boundaries as a function of the total stress acting normal to the grain boundary [140]. ..... 51

Figure 2-29 Two examples (a) and (b) of the percentage of IG cracking rises with increased nitrogen content in SS 304L and SS 316L when strained by SSRT at rate of 1.65 × 10-7 $s^{-1}$ at 240–300 °C [141]. ..... 52

Figure 2-30 SCC occurrence in austenitic alloys as a function of nickel content in both pure water and sodium chloride environments [151]. ..... 56

Figure 2-31 Plot of the percent of the irradiated yield stress (%YS) at which cracking occurs as a function of damage level, in dpa, for irradiated austenitic stainless steel alloys strained in simulated PWR primary water [20]. The curve represents a threshold at which no cracking observed below it. ..... 62

Figure 2-32 Effect of Si on SCC in 304L at 30 MPa/m in 288°C pure water [181]. ..... 64

Figure 2-33 High resolution TEM image and STEM-EDS maps of a crack tip in 347 SS irradiated to 26.4 and strained to 60 % of the irradiated yield stress in KOH at 320 ºC showing amorphous silicon oxide (a-$SiO_x$) extending over 50 nm ahead of the crack tip and down the GB [20]. ..... 65

Figure 2-34 Schematic illustration of the IASCC process: (a) radiation produces defect clusters and drives solute segregation to grain boundaries, initiating oxidation at low doses; (b) applied stress combined with irradiation accelerates oxidation and promotes dislocation channel formation; (c) dislocation channels intersect grain boundaries near the surface, fracturing the

oxidized and weakened regions; (d) exposure of Si-enriched boundaries to water leads to amorphous $SiO_x$ formation/dissolution, enabling continued oxidation and crack initiation [20]. 69

Figure 4-1 Grains morphology of (a) SS 304L and (b) SS 304LN. ..... 75

Figure 4-2 Average grain size for SS 304L-R and SS 304LN for planes L-T and L-ST. ..... 75

Figure 4-3 Indentation profile along the L-ST direction to identify the homogenous properties along the thickness. ..... 77

Figure 4-4 Hardness measurement distribution for SS 304L-R along (a) L-T plane and (b) L-ST plane and for SS 304LN along (c) L-T plane and (d) L-ST plane ..... 77

Figure 4-5 Hardness profile along L-ST plane for SS 304L-R and SS 304LN. ..... 79

Figure 4-6 Morphology of L-ST plane showing the δ-ferrite stringers distribution along the thickness in (a) SS 304L-R and (b) SS 304LN. ..... 79

Figure 4-7 Four-point bend samples grinding and polishing procedure as preparation for proton irradiation and subsequent IASCC testing. ..... 81

Figure 4-8 Conceptual design of the four-point bend samples including the proton irradiation layer and the unirradiated bulk. ..... 82

Figure 4-9 Conceptual design of the tensile sample used for the dislocation channels quantification. ..... 83

Figure 4-10 Hardness profile within the irradiated area (red box) and unirradiated region (blue box). ..... 84

Figure 4-11 Conceptual design of the SS-3 tensile sample used for the tensile test. ..... 85

Figure 4-12 An example of indents profile at the edge of tensile sample 1 (SS 304L) which was tested at 340 $^{o}$C in argon for (a) pre-loading and (b) post-loading conditions. ..... 85

Figure 4-13 Damage profile caused by proton irradiation on the surface of stainless steel. The calculation used for 4PB samples and tensile bars. ..... 89

Figure 4-14 Schematic diagram of the irradiation area covering (a) the position of beam and stage area and (b) the dimensions of the beam, stage, and aperture used to calculate the irradiation parameters. ..... 94

Figure 4-15 (a) Python code results calculating the current density distribution io the stage and apertures based on locations defined in Figure 14 (a) and (b) the total current density on the stage area. ..... 95

Figure 4-16 Schematic diagram of the irradiation area covering of the tensile bars, the dimensions of the beam, stage, and aperture used to calculate the irradiation parameter. ..... 96

Figure 4-17 (a) Python code results calculating the current density distribution in the stage and apertures based on locations defined in Figure 4-16 (a) and (b) the total current density..... 97

Figure 4-18 MBIL facilities showing the TORIVS ions source, 3MV Pelletron Accelerator, BL2, and its chamber. ..... 99

Figure 4-19 Copper Irradiation stage showing the setup of samples, guide bars, and thermocouples for pre- and post- irradiation experiments. For SS 304LN; (a) pre-irradiation, (b) post-irradiation, SS 304L-R; (c) pre-irradiation, (d) post-irradiation, and tensile bars; (e) pre-irradiation, and (f) post-irradiation. ..... 101

Figure 4-20 Pressure values in the accelerator, beamline, and chamber for (a) first irradiation (4PB: SS 304LN), (b) second irradiation (4PB: SS 304L-R), and (c) third irradiation experiments (tensile bars). ..... 104

Figure 4-21 Ion beam alignment using a laser beam, the alignment ensures that the aperture opening follows the calculated data in 4PB samples in (a) and (b) and tensile bars in (c)..... 105

Figure 4-22 FLIR camera output showing AOIs used to track the temperature history on AOIs for (a) first irradiation (4PB: SS 304LN), (b) second irradiation (4PB: SS 304L-R), and (c) third irradiation experiments (tensile bars). ..... 105

Figure 4-23 Temperature of AOIs recorded from (a) first irradiation, (b) second irradiation, and (c) third irradiation. ..... 106

Figure 4-24 Current density at the stage, slits, and the total current recorded from (a) first irradiation (4PB: SS 304LN), (b) second irradiation (4PB: SS 304L-R), and (c) third irradiation experiments (tensile bars). ..... 107

Figure 4-25 Beta counts per minute per sample after the (a) first irradiation (4PB: SS 304LN), (b) second irradiation (4PB: SS 304L-R), and (c) third irradiation experiments (tensile bars).. 108

Figure 4-26 IM3 system used to simulate testing environments for this study. ..... 110

Figure 4-27 Process flow diagram for the IM3 testing system used for IASCC tests. ..... 111

Figure 4-28 Loading fixture used in this study, the magnified image within the red box showing the 4PB sample and the loading applicator (punch). ..... 113

Figure 4-29 An example of pH measurement of the main water column ahead of the 60%YS step for sample L-6 loading step. ..... 114

Figure 5-1 (a) FEA model used to calculate the applied load, the model with mesh is on the right and (b) mesh settings for the unirradiated bulk and the irradiated layer. ..... 129

Figure 5-2 Conceptual diagrams showing (a) Degree of freedom components for inner supports, outer supports, and 4PB sample, and (b) the element type and node configuration

used in the ANSYS simulation showing a second order quadratic element type of 20 nodes per each element (in 3D). ..... 131

Figure 5-3 FEA results showing the effect of element size in the irradiated layer and unirradiated bulk: (a) one element layer, (b) two element layers, (c) three element layers, and (d) four element layers. Panels (e)–(g) present the corresponding equivalent stress, total strain, and deflection profiles, demonstrating that the FEA results are independent of element size. .. 133

Figure 5-4 A flow chart explaining the process of using FEA for calculating the applied load required for 4PB test. ..... 135

Figure 5-5 Irradiated yield strength extrapolation at high temperature. ..... 138

Figure 5-6 BSE images for the deflection measurement for sample N1 which strained at room temperature in air for (a) pre-loading, (b) post-loading, and sample N4 which strained at 340 °C in water for (c) pre-loading and (d) post-loading. ..... 142

Figure 5-7 FEA calculations of (a) surface stress-strain and (b) surface deflection profiles for samples N1 strained in air and N4 strained in high temperature water. ..... 144

Figure 5-8 Measured strain by indents spacing in (a) and the comparison with the FEA in (b). 145

Figure 5-9 Applied load determination from FEA for 4PB tests. ..... 147

Figure 5-10 FEA results of sample N3 for surface profiles of longitudinal (a) stress, (b) strain, (c) deflection, and transverse (d) stress, (e) strain, and (f) deflection ..... 151

Figure 5-11 FEA results of sample N7 for surface profiles of longitudinal (a) stress, (b) strain, (c) deflection, and transverse (d) stress, (e) strain, and (f) deflection ..... 152

Figure 5-12 FEA results of sample N10 for surface profiles of longitudinal (a) stress, (b) strain, (c) deflection, and transverse (d) stress, (e) strain, and (f) deflection ..... 153

Figure 5-13 FEA results of sample L-R-1 for surface profiles of longitudinal (a) stress, (b) strain, (c) deflection, and transverse (d) stress, (e) strain, and (f) deflection. ..... 154

Figure 5-14 FEA results of sample L-R-3 for surface profiles of longitudinal (a) stress, (b) strain, (c) deflection, and transverse (d) stress, (e) strain, and (f) deflection. ..... 155

Figure 5-15 FEA results of sample L-R-6 for surface profiles of longitudinal (a) stress, (b) strain, (c) deflection, and transverse (d) stress, (e) strain, and (f) deflection. ..... 156

Figure 5-16 FEA results of the total equivalent stress profiles across thickness for (a) sample N3, (b) sample N7, and c) sample N10, and normal stresses profiles across thickness for (d) sample N3, (e) sample N7, and (f) sample N10. ..... 157

Figure 5-17 FEA results of the total equivalent stress profiles across thickness for (a) sample L-R-1, (b) sample L-R-3, and (c) sample L-R-6, and normal stresses profiles across thickness for (d) sample L-R-1, (e) sample L-R-3, and (f) sample L-R-6. ..... 158

Figure 5-18 Flow chart of the error sources contributed to the final result of the IASCC initiation stress. ..... 160

Figure 5-19 Sensitivity analysis for SS 304LN and SS 304L-R, (a) the sensitivity coefficients for all input parameters, indicating that variations in sample thickness have a strong influence on the calculated surface tensile stress ($\sigma_{surfaces}$), whereas the irradiated yield strength has negligible impact. (b) Measurement errors for $YS_{Bulk}$, $YS_{Irradiated}$, applied load and sample thickness, along with the corresponding sensitivity-amplified errors that reflect the impact of each parameter on $\sigma_{surfaces}$. ..... 171

Figure 5-20 Summary of the percent change in the FEA-calculated surface stress as a function of the percent change in the inputs showing strong impact from the applied load and sample thickness while no impact from the $YS_{irradiated}$. The solid line represents the sensitivity of input parameters on the FEA outputs from SS 304L-R and SS 304LN in the dashed lines. ..... 172

Figure 5-21 The influence of input parameters on the total uncertainty of each alloy. Note: 100% in this figure means total uncertainty calculated from Eqn. 5.15. ..... 174

Figure 6-1 TEM DF images of dislocation loops in (a) SS 304L-R (L-R-1) and (b) SS 304LN (N3) after 5 dpa proton irradiation at 360 °C. Loops were imaged at 12 µm depth under g = ½{311} condition. SS 304LN shows higher loop density with smaller average size. ..... 178

Figure 6-2 Dislocation loop size distribution in SS 304L-R and SS 304LN after 5 dpa proton irradiation. SS 304L-R exhibits a slightly larger average loop size (9.9 nm) and lower density ($2.69 \times 10^{22}$ $m^{-3}$), while SS 304LN shows a higher density ($3.96 \times 10^{22}$ $m^{-3}$) and lower size (8.2 nm). Dashed vertical lines are the median which are included in the table. ..... 179

Figure 6-3 TEM BF images of cavities in (a) SS 304L (L-R-1) and (b) SS 304LN (N3) after 5 dpa proton irradiation at 360 °C. Images were acquired at ~12–12.5 µm depth. L-R-1 shows a significantly higher cavity density compared to N3. ..... 180

Figure 6-4 Cavity size distribution and density comparison between L-R-1 and N3 after 5 dpa proton irradiation. L-R-1 exhibits higher cavity density ($7.40 \times 10^{21}$ $m^{-3}$) with smaller size (4.73 nm), while N2 shows lower density ($7.45 \times 10^{20}$ $m^{-3}$) and larger cavities (8.08 nm). ..... 181

Figure 6-5 TEM-HAADF, DF, and EDS elemental mapping for matrix in (a) SS 304LN and (b) SS 304L showing the precipitates exist following proton irradiation. ..... 183

Figure 6-6 (a) TEM-HAADF, -DF, and -EDS elemental mapping of a high angle grain boundary in SS 304LN showing RIS of Si and Ni while depletion of Fe and Cr, (b) the location where the profile taken from, (c) the composition of elements at the GB, (d) the composition of Si and Ni at the GB. ..... 185

Figure 6-7 (a) TEM-HAADF, -DF, and -EDS elemental mapping of a high angle grain boundary in SS 304L-R showing RIS of Si and Ni while depletion of Fe and Cr, (b) the location where the profile taken from, (c) the composition of elements at the GB, (d) the composition of Si and Ni at the GB. ..... 186

Figure 6-8 Loads vs displacement for all loading steps of samples (a) L-R-1, (b) L-R-3, (c) L-R-6, (d) N3, (e) N7, and (f) N10. ..... 189

Figure 6-9 Time-dependent measurements of water chemistry and autoclave conditions for sample N3 during loading steps at (a) 39%YS, (b) 47%YS, (c) 52%YS, (d) 62%YS, and (e) 70%YS. The dashed vertical lines indicate the periods during which the sample was exposed to high temperature and applied loading. ..... 192

Figure 6-10 Time-dependent measurements of water chemistry and autoclave conditions for sample N7 during loading steps at (a) 44%YS, (b) 52%YS, (c) 59%YS, (d) 66%YS, (e) 74%YS, and (f) 89%YS. ..... 193

Figure 6-11 Time-dependent measurements of water chemistry and autoclave conditions for sample N10 during loading steps at (a) 50%YS, (b) 60%YS, and (c) 70%YS. ..... 194

Figure 6-12 Time-dependent measurements of water chemistry and autoclave conditions for sample L-R-1 during loading steps at (a) 50%YS, (b) 60%YS, (c) 70%YS, and (d) 80%YS. .. 195

Figure 6-13 Time-dependent measurements of water chemistry and autoclave conditions for sample L-R-3 during loading steps at (a) 50%YS, (b) 70%YS, and (c) 80%YS. ..... 196

Figure 6-14 Time-dependent measurements of water chemistry and autoclave conditions for sample L-R-6 during loading steps at (a) 60%YS and (b) 70%YS. ..... 196

Figure 6-15 Total exposure time to the high-temperature water at 340 $^{o}$C containing $H_3BO_3$ and LiOH in the autoclave for SS 304LN and SS 304L-R samples. ..... 197

Figure 6-16 Summary of 4PB test results for proton-irradiated samples to 5.0 dpa, showing percent of yield strength (%YS) at failure or non-failure. Solid symbols indicate failure; open symbols indicate non-failure. Error bars represent FEA estimation error, and arrows represent 4PB uncertainty ranges. ..... 198

Figure 6-17 Cracking statistics for proton irradiated SS 304LN and SS 304L-R after straining in high temperature water containing $H_3BO_3$ and LiOH at 340 $^{o}$C. (a) Number of cracks and number of cracks initiator, (b) the distribution of cracks lengths per alloy, and (c) crack density and crack length per unit area. ..... 202

Figure 6-18 Inclination angle of the cracked GB with the respect of the applied load axis in SS 304L-R and SS 304LN showing a mean value of 89$^{o}$ for SS 304L-R and 96$^{o}$ for SS 304LN. .. 203

Figure 6-19 SEM images of surface oxides formed within the constant strain region of samples (a) N3 and (b) L-R-1. Oxide particles appear unevenly distributed across the surface, with variations in morphology and size. ..... 205

Figure 6-20 Dissolution of surface oxide particles with increasing applied load (and exposure time to the water solution), as observed in sample N3. (a) BSE image showing a high density of surface oxide particles after the initial applied load step. (b)–(e) BSE images illustrating the progressive decrease in surface oxide particles with each successive load step, highlighting significant degradation of the outer surface oxide particles. (f) SEM image from a randomly selected surface location showing a mix of partially dissolved and intact surface oxide particles. (Note: The orange box marks a tracking feature in each image, confirming that all images were captured from the same location but at different applied load steps). ..... 206

Figure 6-21 Dissolution of surface oxide particles with increasing applied load (and exposure time to the water solution), as observed in sample L-R-1. (a)-(d) BSE image showing progressive decrease in surface oxide particles with each successive load step, highlighting a less extent degradation of the outer surface oxide particles compared to sample N3. ..... 207

Figure 6-22 Examples of the two oxide rupture mechanisms observed in this study, based on images from sample N3. (a)–(c) BSE and SEI images showing continuous dislocation channels and a magnified view of one channel with oxide rupture occurring above it. (d)–(f) STEM-HAADF, DF, and EDS images from a different location illustrating a similar mechanism, where the step-up at the dislocation channel ruptures the inner surface oxide layer, leading to localized corrosion. (g) and (h) Another example of partial surface oxide rupture caused by a dislocation channel with a relatively lower step height compared to the first example. ..... 210

Figure 6-23 STEM-HAADF images and corresponding EDS elemental maps showing the surface oxide morphology and composition in (a–c) sample N3 and (d–e) sample L-R-1. Oxidation penetration along the grain boundary is evident in sample N3, while sample L-R-1 shows a more uniform oxide layer without localized penetration. ..... 211

Figure 6-24 SEM cross-sectional images of FIB-milled surfaces showing the inner oxide layer thickness and grain boundary oxidation for (a) SS 304LN (sample N3) and (b) SS 304L (sample L-R-1). The measured oxide thicknesses near the grain boundary are indicated, showing localized oxide thickening in both samples. A Pt layer was deposited to protect the surface during FIB milling. The dashed line represents the average inner oxide thickness across the examined region. ..... 212

Figure 6-25 Cracking maps showing the distribution of cracks within the constant strain region for samples (a) N3 (70% YS), (b) N7 (89% YS), and (c) N10 (70% YS). Cracks are marked in red overlaid on the constant strain region. ..... 214

Figure 6-26 Cracking maps showing the distribution of cracks within the constant strain region for samples (a) L-R-1 (80% YS), (b) L-R-3 (80% YS), and (c) L-R-6 (70% YS). Cracks are marked in red overlaid on the constant strain region. ..... 215

Figure 6-27 Crack N-3-1 in sample N3 after staining to 70%YS, (a) BSE and high magnification SEI images of the IG crack that initiated from TJ sites, and (b) BSE images of the history of the location over all loading steps showing the evolution of microstructural features. ..... 217

Figure 6-28 Crack N-3-3 in sample N3 after staining to 70%YS, (a) BSE and high magnification SEI images of the IG crack that initiated from TJ and DC, and (b) BSE images of the history of the location over all loading steps showing the evolution of microstructural features. ..... 218

Figure 6-29 Crack N-3-5 in sample N3 after staining to 70%YS, (a) BSE and high magnification SEI images of the IG crack that initiated from DDC and TJ, and (b) BSE images of the history of the location over all loading steps showing the evolution of microstructural features. ..... 219

Figure 6-30 Crack N-3-12 in sample N3 after staining to 70%YS, (a) BSE and high magnification SEI images of the IG crack that initiated from CDC and TJ, and (b) BSE images of the history of the location over all loading steps showing the evolution of microstructural features. ..... 220

Figure 6-31 Crack N-3-14 in sample N3 after staining to 70%YS, (a) BSE and high magnification SEI images of the IG crack that initiated from TJ and DC, and (b) BSE images of the history of the location over all loading steps showing the evolution of microstructural features. ..... 221

Figure 6-32 Crack N-7-1 in sample N7 after staining to 89%YS, (a) BSE and high magnification SEI images of the IG crack that initiated from a TJ, and (b) BSE images of the history of the location over all loading steps showing the evolution of microstructural features. ..... 223

Figure 6-33 Crack N-10-1 in sample N10 after staining to 70%YS, (a) BSE and high magnification SEI images of the IG crack that initiated from a TJ, and (b) BSE images of the history of the location over all loading steps showing the evolution of microstructural features. ..... 224

Figure 6-34 Crack L-R-1-3 in sample L-R-1 after staining to 80%YS, (a) BSE and high magnification SEI images of the IG crack that initiated at the TJ, and (b) BSE images of the history of the location over all loading steps showing the evolution of microstructural features. ..... 226

Figure 6-35 Crack L-R-1-5 in sample L-R-1 after staining to 80%YS, (a) BSE and high magnification SEI images of the IG crack that initiated at the DC-GB intersection, and (b) BSE images of the history of the location over all loading steps showing the evolution of microstructural features. ..... 227

Figure 6-36 Crack L-R-1-13 in sample L-R-1 after staining to 80%YS, (a) BSE and high magnification SEI images of the IG crack that initiated from a GB-DC intersection, and (b) BSE images of the history of the location over all loading steps showing the evolution of microstructural features. ..... 228

Figure 6-37 Crack L-R-3-2 in sample L-R-3 after staining to 80%YS, (a) BSE and high magnification SEI images of the IG crack that initiated at the TJ, and (b) BSE images of the

history of the location over all loading steps showing the evolution of microstructural features. ..... 230

Figure 6-38 Crack L-R-3-3 in sample L-R-3 after staining to 80%YS, (a) BSE and high magnification SEI images ofn the IG crack that is initiated at the GB-DC intersection, and (b) BSE images of the history of the location over all loading steps showing the evolution of microstructural features. ..... 231

Figure 6-39 Crack L-R-6-4 in sample L-R-6 after staining to 70%YS, (a) BSE and high magnification SEI images of the IG crack that initiated at the GB-DC intersection, and (b) BSE images of the history of the location over all loading steps showing the evolution of microstructural features. ..... 233

Figure 6-40 Crack L-R-6-6 in sample L-R-6 after staining to 70%YS, (a) BSE and high magnification SEI images of the IG crack that initiated at the TJ, and (b) BSE images of the history of the location over all loading steps showing the evolution of microstructural features ..... 234

Figure 6-41 STEM-EDS of crack N-3-1, sample N3. (a–e) HAADF and elemental maps at increasing magnifications show Cr-rich oxidation along a GB, Ni segregation at the oxide–metal interface, and slight Si enrichment near the tip. (f) EDS line profiles (regions 1–6) reveal a compositional transition from the unoxidized GB to the oxidized crack tip. Oxidation initiates with Si, followed by Fe and Cr, while Ni remains excluded. ..... 238

Figure 6-42 STEM-EDS of L-R-1-8 in SS 304L-R, sample L-R-1. (a–d) HAADF and elemental maps at increasing magnifications show Cr-rich oxidation along a GB, Ni segregation at the oxide–metal interface, and slight Si enrichment near the tip. (e) EDS line profiles (regions 1–6) reveal a compositional transition from the unoxidized GB to the oxidized crack tip. Oxidation initiates with Si, followed by Fe and Cr, while Ni remains excluded..... 243

Figure 6-43 Stress-strain curves from CERT for both alloys showing the straining to 2.3% (After correcting the strain by removing the system's compliance) for both alloys in an ultra-high purity Argon at 340 ºC. ..... 245

Figure 6-44 (a) Dislocation channels quantification, three types where characterized; DDC, NDC, and CDC for both samples at all loading steps and (b) the percentage of DDC, NDC, and CDC to the total quantified DCs per each alloy. ..... 247

Figure 6-45 Dislocation channels characterization showing how the steps look like after straining, (a), (b), and (c) for SS 304L-R, and (d), (e), and (f) for SS 304LN..... 248

Figure 6-46 AFM measurement precision compared with OM. ..... 249

Figure 6-47 Examples of step height characterization by AFM and processing using NanoScope Analysis 2.0 software from (a) SS 304LN and (b) SS 304L showing the 3D view of steps. ..... 250

Figure 6-48 Step height measurements for dislocation channels in proton-irradiated Alloy 304L (T-B-L) and Alloy 304LN (T-B-N) after straining to 2.3% at 340 °C in an argon environment. Bars represent the highest, lowest, average, and weighted average step heights based on AFM analysis. Error bars show standard deviation of the average values. All samples were irradiated to 3.0 dpa. ..... 251

Figure 6-49 (a) Step height distribution in proton-irradiated T-B-L and T-B-N after straining to 2.3%, (b) the distribution of step height categorized into defined height intervals. ..... 252

Figure 6-50 (a) The distribution of the number of dislocations per dislocation channel and (b) the distribution of Schmid factors for slip systems in SS 304LN (T-B-N) and SS 304L-R (T-B-L) alloys, after proton irradiation to 3.0 dpa and tensile strain of 2.3% at 340 °C. ..... 253

Figure 6-51 Distribution of spacing between dislocation channels in SS 304L-R and SS 304LN following 3.0 dpa proton irradiation and 2.3% tensile strain at 340°C in argon atmosphere. SS 304LN shows a narrower spacing distribution and smaller average spacing compared to SS 304L-R, indicating a higher density of DCs and more uniform plastic deformation, consistent with nitrogen's effect on dislocation channeling. ..... 255

Figure 7-1 The comparison between the dislocation loops obtained from this study and the literature on neutron irradiated austenitic stainless steels irradiated over a range of temperatures of 300 - 400 °C, for loops density (a) wide range of doses, (b) low regime doses, for loop size (c) wide range of doses, and (d) low regime doses 54, 56, 61, 70, 87, 105, 106, 107, 111, 137, 162, 225, 227 – 229, 231]. Note: the legend in (a) applies to all plots. ..... 262

Figure 7-2 The comparison between the cavities obtained from this study and the literature on austenitic stainless steels irradiated over a range of temperatures of 300 - 375 °C, for (a) cavities density (b) and cavities size [54, 56, 61, 70, 106, 107, 225, 227, 233]. Note: the legend in (a) applies to all plots. ..... 265

Figure 7-3 A comparison between the this study RIS data and literature values on neutron irradiated austenitic stainless steels [227] for the percent of GB (a) depletion in Cr, (b) enrichment in Ni, (c) enrichment in Si, and (d) comparison at low dpa regime for Cr, Ni, and Si [54, 106, 108, 169, 227, 229, 235 - 237]. A simulated data using Grain Boundary-Interstitial-Modified Inverse Kirkendall (GiMIK) model by F. Kevin et. al. [237] is presented in black dashed line and L. Tan et. al. [227] in green dashed line. Both experimental and simulation data show saturation in RIS at 5 dpa. Note: the legend in (a) applies to all plots. ..... 270

Figure 7-4 A comparison between the hardness measurement from proton-irradiated 4PB samples with experiment-based literature data for neutron-irradiated austenitic stainless steel [118]. ..... 273

Figure 7-5 Effect of irradiation dose on measured tensile yield strength for neutron-irradiated austenitic stainless steel of types SS 316, SS 304, SS 304L, and SS 347 irradiated in LWRs and BOR-60 fast reactor at irradiation temperatures ranging from 275 to 380 °C. (b) Only SS 304 and SS 304L were considered for more specific comparison, and (c) at low dpa regime of the data from SS 304 and SS 304L. The data were replotted from Ref. [113]. ..... 274

Figure 7-6 The contribution of microstructural features, in percent, to the hardening of materials based on the calculated YS from S-RSS superimposed equation covering the contribution of lattice friction stress, solid solution strengthening, GB strengthening, and irradiation hardening on the yield strength of SS 304L-R and SS 304LN. ..... 277

Figure 7-7 The sensitivity of hardening coefficient ($\alpha_{Loop}$) to the change in dislocation loops size and density in (a) 3D surface plot and (b) contour plot for better view showing a high sensitivity for loops size..... 280

Figure 7-8 A comparison of results from proton-irradiated 304L and 304LN in LiOH to that in the literature for PWR primary water [70, 162, 170, 171, 176, 245 - 252], (a) and the same comparison focusing on the low dpa regime (b). Results from this project are shown in half-colored symbols. The data is offset slightly along the damage axis to eliminate points, therefore results from this study were all performed at 5 dpa..... 289

Figure 7-9 Comparison of results from proton-irradiated 304L and 304LN in LiOH to that in the literature from (a) SS 304 for PWR primary water [20], and (b) from the 4PB testing method only. Results from this project are shown in half-colored symbols. The data is offset slightly along the damage axis to eliminate points. ..... 290

Figure 7-10 Comparison of total exposure time at failure between proton-irradiated 304L and 304LN in LiOH to that in the literature from austenitic stainless-steel alloys for PWR primary water [162, 194, 245 – 247, 251]. The plot is updated with data from Du [194] and Swaminathan [171]. ..... 291

Figure 7-11 Examples of crack initiation sites observed in this study: (a) a crack initiated from a DC, (b) a crack initiated from a TJ without DC interference, and (c) a crack initiated from a TJ with DC interference..... 293

Figure 7-12 Examples of surface cracking and initiators from neutron-irradiated SS 304L in BOR-60 to 5.4 dpa. The contribution of DC as initiator is clear through the history of the region where the evolution of DC and then cracking (a) from Ref. [171], (b) from Ref. [170]. The intersection of cracking with the oxidized GB and the jagged morphology in (c) from Ref. [170] was also observed in this study. ..... 295

Figure 7-13 Examples of DC appearance at the surface, categorized by the extent of surface oxide rupture: (a) minimal rupture corresponding to low step height, (b) moderate rupture corresponding to intermediate step height, and (c) extensive rupture corresponding to large step height. All examples are from sample N3 (SS 304LN) after straining to 70%YS in PWR environment at 340 ºC, sample L-R-1 exhibited similar behavior as well. ..... 298

Figure 7-14 Examples of intergranular cracks in proton-irradiated (a) SS 304LN and (b) SS 304L-R, compared with IG fracture morphology in neutron-irradiated (c) SS 304L [171] and (d) SS 347 [70]. All specimens in (a–d) were strained using 4PB testing and exhibit oxide-through fracture, and (e) shows a neutron-irradiated SS 316 CW specimen strained with an O-ring test [166], showing an oxide–metal interface fracture. ..... 299

Figure 7-15 STEM-EDS elemental mapping for crack tip of examples from proton-irradiated stainless steel (a) 304, (b) 304L irradiated to 5 dpa, and neutron-irradiated stainless steel of types (c) 304L irradiated to 5.4 dpa [142], (d) 347 irradiated to 7.8 dpa [70], (e) SS 316 CW irradiated to 3 dpa [257] and (f) SS 316 CW irradiated to 60 dpa showing a consistent features of Fe and Cr depletion and Ni enrichment, while Si enrichment varies from condition to another [169]. ..... 302

Figure 7-16 The evolution of dislocation loops (a) density and (b) size as a function of nitrogen content in austenitic stainless steel irradiated to a range of damage levels of 0.3 - 46 dpa and a range of temperature of 275 – 400 ºC, the data from SS 304, 304L, and 304LN only are shown in (c) for the density and (d) for the size [54, 61, 63, 137, 228] . ..... 305

Figure 7-17 Dislocation loops as a function of irradiation damage (dpa) for austenitic stainless steel alloys with different nitrogen contents for (a) density and (b) size while (c) shows the data from SS 304L and SS 304 only. The dashed orange box represents the data obtained from XRD while the purple box represents the data obtained from the TEM characterization showing the role of characterization technique on quantifying the dislocation loops [54, 61, 111, 112, 137, 228]. Data from Pokor [61] is shown in red, from Edwards [54] in blue, and from Stephenson [137] in green. ..... 307

Figure 7-18 IASCC susceptibility of various SS 304 and SS 316 alloys in LWRs as a function of nitrogen content. The dashed lines represent the bottom and top thresholds. Data from CW heats are bound by a gray dashed box [141, 142, 258-261]. ..... 309

Figure 7-19 Summary of evaluating the hypothesis through scaling its components on an arbitrary scale of similarity. SS 304LN was taken as a reference such that similarity means that SS 304L-R is close in response to SS304LN or not. ..... 312

Figure C-1 Surface morphology of crack N-3-2 ..... 473

Figure C-2 Surface morphology of crack N-3-4 ..... 474

Figure C-3 Surface morphology of crack N-3-6. ..... 474

Figure C-4 Surface morphology of crack N-3-7. ..... 475

Figure C-5 Surface morphology of crack N-3-8. ..... 475

Figure C-6 Surface morphology of crack N-3-9. ..... 476

Figure C-7 Surface morphology of crack N-3-10. ..... 476

Figure C-8 Surface morphology of crack N-3-11. ..... 477

Figure C-9 Surface morphology of crack N-3-13. ..... 477

Figure C-10 Surface morphology of crack N-3-15. ..... 478

Figure C-11 Surface morphology of crack N-3-16. 478
Figure C-12 Surface morphology of crack N-3-17. 479
Figure C-13 Surface morphology of crack N-3-18. 479
Figure C-14 Surface morphology of crack N-3-19 480
Figure C-15 Surface morphology of crack N-3-20. 480
Figure C-16 Surface morphology of crack N-3-21. 481
Figure C-17 Surface morphology of crack N-3-22. 481
Figure C-18 Surface morphology of crack N-3-23. 482
Figure C-19 Surface morphology of crack N-3-24. 482
Figure C-20 Surface morphology of crack N-7-2. 483
Figure C-21 Surface morphology of crack N-10-2. 483
Figure C-22 Surface morphology of crack N-10-3. 484
Figure C-23 Surface morphology of crack L-R-1-1. 484
Figure C-24 Surface morphology of crack L-R-1-2. 485
Figure C-25 Surface morphology of crack L-R-1-4. 485
Figure C-26 Surface morphology of crack L-R-1-6. 486
Figure C-27 Surface morphology of crack L-R-1-7. 486
Figure C-28 Surface morphology of crack L-R-1-8. 487
Figure C-29 Surface morphology of crack L-R-1-9. 487
Figure C-30 Surface morphology of crack L-R-1-10. 488
Figure C-31 Surface morphology of crack L-R-1-11. 488
Figure C-32 Surface morphology of crack L-R-1-12. 489
Figure C-33 Surface morphology of crack L-R-1-14. 489
Figure C-34 Surface morphology of crack L-R-1-15. 490
Figure C-35 Surface morphology of crack L-R-1-16. 490

Figure C-36 Surface morphology of crack L-R-1-17. ..... 491

Figure C-37 Surface morphology of crack L-R-1-18. ..... 491

Figure C-38 Surface morphology of crack L-R-3-1. ..... 492

Figure C-39 Surface morphology of crack L-R-6-1. ..... 492

Figure C-40 Surface morphology of crack L-R-6-2. ..... 493

Figure C-41 Surface morphology of crack L-R-6-3. ..... 493

Figure C-42 Surface morphology of crack L-R-6-5. ..... 494

Figure C-43 Surface morphology of crack L-R-6-7. ..... 494

## List of Appendices

Appendix A: Python codes used to calculate currents on stage and slits .....315

A.1 Four-point bend samples irradiation ..... 315

A.2 Tensile bars irradiation..... 317

Appendix B: Appendix B: FEA outputs .....320

B.1 Surface deflection profiles ..... 320

B.2 B.2 Surface tensile stresses profiles ..... 352

B.3 Surface tensile strain profiles ..... 385

B.4 Stress and strain profiles across the sample thickness ..... 413

B.5 FEA sensitivity analysis ..... 459

Appendix C: Surface cracks morphology .....473

C.1 Surface cracks ..... 473

**Abstract**

The aim of this work is to determine the influence of nitrogen in 304L stainless steel on the initiation of irradiation-assisted stress corrosion cracking (IASCC) in high-temperature water under proton irradiation. To bridge the gap between proton- and neutron-irradiation studies, proton-irradiated four-point-bend (4PB) specimens were employed as surrogates for neutron irradiation, with finite element analysis used to determine applied loads and surface tensile stresses. 4PB method was selected because its ability to restrain crack growth allowing for better initiation analysis.

4PB experiments were conducted in simulated pressurized water reactor (PWR) coolant chemistry (2 ± 0.1 ppm LiOH, 1000 ± 50 ppm $H_3BO_3$) at 340 ± 0.5 °C, yielding a water conductivity of 23 ±1 μS/cm and pH 6.55 ± 0.2 at room temperature. Two alloys differing only in nitrogen content were studied: SS 304L (0.068 wt.% N) and SS 304LN (0.14 wt.% N). 4PB specimens were irradiated to 5 dpa for IASCC initiation testing. Finite element analysis (FEA) was employed to determine the applied loads and the corresponding surface stresses. The FEA results were validated against 4PB tests, and a sensitivity analysis was conducted to quantify the uncertainty in the FEA calculations, which was then incorporated into the reported 4PB initiation stresses. An incremental loading of samples in 4PB mode was used to identify the minimum IASCC initiation stress. Tensile specimens were irradiated to 3 dpa under the same conditions and strained to 2.3% at 340 ± 0.5 °C in ultra-high-purity argon using constant extension rate

tensile (CERT) to analyze dislocation channel type, density, spacing, and height through various microscopy techniques to correlate cracking behavior with microstructural evolution.

The study was structured in three parts. First, proton-irradiated specimens were benchmarked against literature on neutron-irradiated austenitic stainless steels, confirming that proton irradiation reproduces key microstructural features such as dislocation loops, cavities, and radiation-induced segregation (RIS), as well as IASCC initiation behavior at low dpa levels. Second, the role of nitrogen was assessed by comparing the two irradiated alloys.

Second IASCC initiation behavior was confirmed to be consistent with literature, with cracking stress falling within the high-stress range typically observed for austenitic stainless steels at low doses.

Finally, nitrogen was found to have no measurable effect on microstructure, mechanical properties, or IASCC initiation behavior. Both alloys exhibited similar dislocation loop densities, dislocation channel characteristics, initiation thresholds, and cracking morphologies, indicating that nitrogen up to 0.14 wt.% does not significantly alter IASCC initiation under PWR-relevant conditions.

In conclusion, the results validate proton-irradiated 4PB testing as a surrogate for neutron irradiation and demonstrate that nitrogen-alloyed stainless steels (≤0.14 wt.% N) retain IASCC resistance comparable to conventional SS 304L. These high N-alloys combine this resistance with enhanced mechanical and corrosion properties, supporting their use as reliable long-term candidates for PWR core internals and compelling alternatives to conventional SS 304L.

# Chapter 1 Introduction

Global efforts to achieve net-zero greenhouse gas emissions have been ongoing for decades, with energy production responsible for about three-quarters of global $CO_2$ emissions, nearly 40% of which originate from electricity and coal plants. Transitioning to low-carbon electricity generation is essential for reducing emissions and mitigating climate change [1].

Nuclear energy, one of the key solutions, contributes 20% (805 billion kWh in 2017) of U.S. electricity and 10% globally [2]. Expanding nuclear capacity is critical for achieving the target of net-zero emissions by 2050, delivering clean, reliable power, driving economic growth through high-paying jobs and local investments, strengthening national security, and positioning the U.S. as a leader in the global transition to sustainable energy [3]. To achieve this target, the US strategy focus is now centered on expanding nuclear energy production through building new large nuclear power plant (NPP), small modular reactor (SMR), and microreactors, along with extending and expanding existing reactors through license renewals, power upgrades, and restarting recently retired reactors [3].

Extending the lifetime of existing NPP presents serious challenges due to the extensive degradation of core structures caused by irradiation, especially as these structures have already exceeded their original lifespan. One of the major concerns is irradiated-assisted stress corrosion cracking (IASCC), which affects the core structures of light water reactor (LWR) under both hydrogenated conditions in pressurized water reactor (PWR) and oxygenated conditions in boiling water reactor (BWR) [4]. As IASCC is not yet considered a safety issue in the US, it is

still a real concern to the energy sector as losses can exceed around 1.2M$ per day when the affected reactor undergoes unscheduled maintenance outages [5, 6]. The challenge with IASCC stems from its multi-precursor nature, involving a complex interplay of factors that collectively create the conditions for crack initiation, therefore, understanding the mechanisms behind IASCC initiation is crucial for establishing effective mitigation strategies for existing reactors and guiding material selection processes for next-generation NPP, SMR, and microreactors.

IASCC is a specific form of stress corrosion cracking (SCC). In SCC, there are primary combined factors that should be interplayed in high-temperature water, leading to premature component failure such as an aggressive environment, susceptible material, and high stress. In IASCC, neutron irradiation exacerbates the issue by inducing high damage to the microstructure of the material, reducing its ductility, and significantly increasing its susceptibility to intergranular (IG) cracking. Moreover, microchemistry at sink sites is expected to undergo significant changes, which will contribute to the initiation of IASCC. Figure 1-1 conceptually shows the combination of factors leading to IASCC in LWRs environment.

In LWRs, austenitic stainless steels are widely used as core structural components due to their excellent mechanical properties and high corrosion resistance relative to cost. However, prolonged exposure to high radiation levels significantly reduces their ductility properties, leading to material degradation over time.

A key factor is the alteration of the mode of deformation from homogeneous to heterogeneous deformation in the form of narrow, highly localized slip bands known as dislocation channels (DC). These channels emerge as dislocations traverse the microstructure, eliminating irradiation-induced defects along their path and leaving behind defect-free regions

that facilitate subsequent dislocation movement. Discontinuous dislocation channels that terminate at a grain boundary are likely sites for the initiation of an IASCC crack [7, 8, 9].

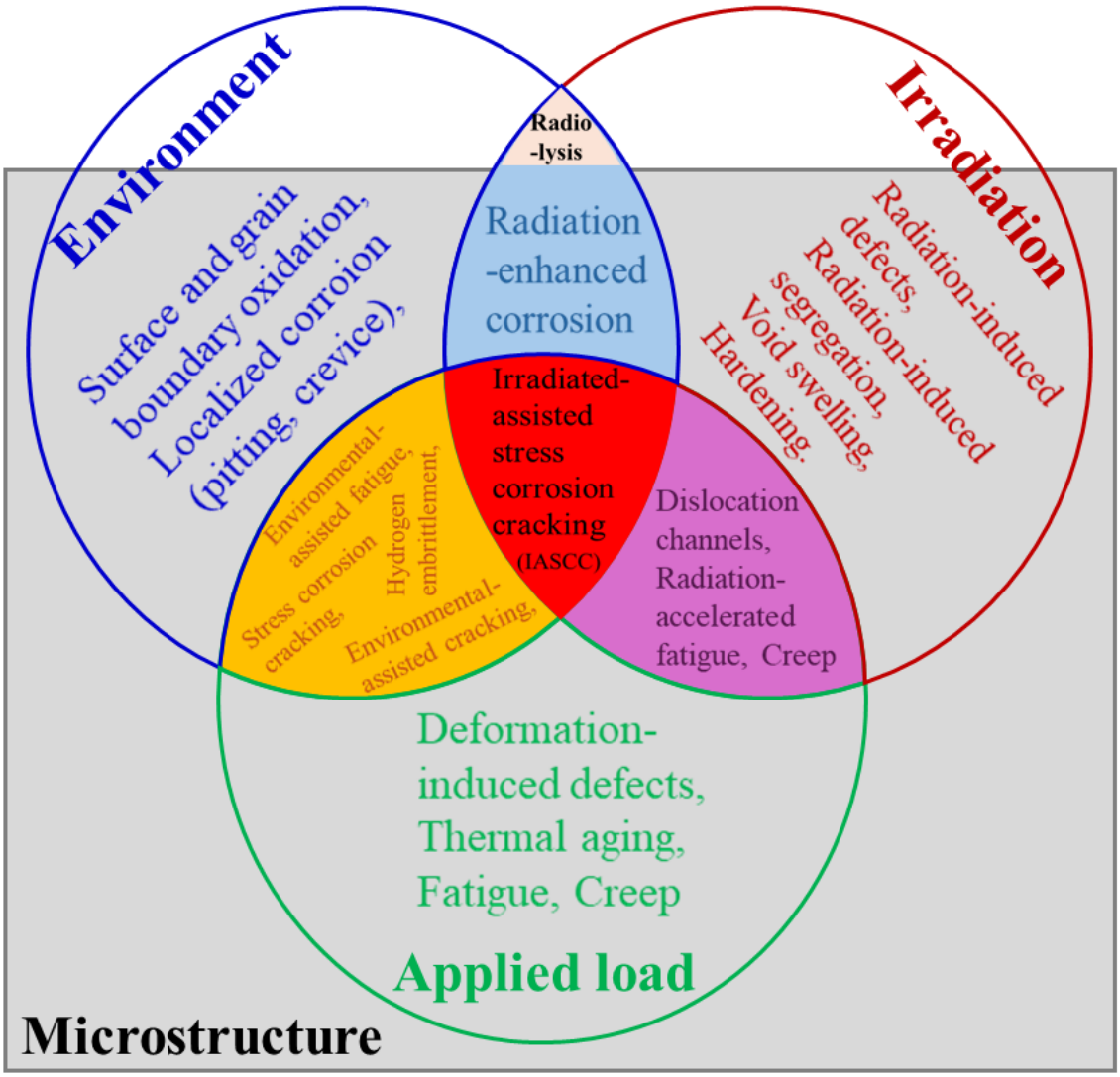


Figure 1-1 Interacting degradation mechanism structural materials leading to IASCC in LWRs environment.

A specific area of interest is the role of alloying elements in IASCC initiation. Stainless steel of type 304LN, which contains increased nitrogen content, offers superior corrosion resistance and mechanical properties but has not been widely used in the core structure of light water reactors due to its higher fabrication cost compared to alternatives like SS 304, SS 304L, and SS 316.

With advancements in manufacturing, the production of austenitic stainless steels has become more cost-effective compared to the 1950s through the 1990s, making the incorporation of SS 304LN into nuclear reactor core structures a viable and economical option. As a result, leveraging the advantages of this alloy is now both practical and feasible, positioning SS 304LN as a strong candidate for future generations of nuclear reactors. However, due to its limited use in nuclear power plant structures, assessing the susceptibility of high-nitrogen austenitic stainless-steel alloys to IASCC in these environments is crucial to ensuring their integrity. Such evaluations could lead to the development of new alloys or the refinement of existing ones, offering potential solutions to IASCC challenges in NPPs.

This study explores the potential of replacing core structural materials made of SS 304 and SS 316 with SS 304LN, due to its superior mechanical strength and corrosion resistance, making it a strong candidate for current and next-generation reactor cores. Since IASCC is the primary degradation mode affecting austenitic stainless steels within PWR cores, assessing the susceptibility of SS 304LN to this mechanism is critical. Demonstrating comparable or improved resistance would support the adoption of SS 304LN in core structural applications.

# Chapter 2 Background

Nuclear power plants are considered as an important source of energy both in the US and globally. This is due to the ability of this technology to produce sustainable carbon-free energy. The confidence in the extended operations of these reactors arises from their structural durability under reactor operational conditions.

In general, all designs of nuclear reactors including current and future generations present a real challenge for materials performance. Operating nuclear reactors endure harsh environments that progressively degrade material performance over extended service periods. However, the major issue lies in the potential for structures made from these degraded materials to experience premature failure, which in turn could impact the reactor's safety systems or even other systems. If these systems fail, the reactor will undergo an unscheduled shutdown, resulting in significant economic losses. Although surveillance and maintenance strategies mitigate the degradation effects, the demands of extended operating lifetimes beyond 60 years and power uprates exacerbate material stress, increasing susceptibility to degradation and introducing new failure modes.

Material degradation in nuclear reactor environments arises from the combined effects of high-temperature water environments, mechanical loading conditions, and irradiation. These factors lead to complex interactions that significantly degrade mechanical performance of structural materials under reactor operating conditions.

During the service, premature failure of core components has often been reported in nuclear power plants (NPPs) across the US. Specifically, Irradiated-assisted stress corrosion cracking (IASCC) has been identified and studied in both boiling water reactors (BWRs) and pressurized water reactors (PWRs) types since the early sixties of the past century [10]. Despite decades of research, the fundamental mechanisms of crack initiation in austenitic stainless steels are still not well understood. Since austenitic stainless steels are prime candidates in current reactor designs and also for next-generation reactors [11], there is a need to continue investigating IASCC to gain a deeper understanding and develop potential solutions.

Furthermore, investigating IASCC behavior at early damage levels, roughly less than 10 displacements per atom (dpa), remains limited in the literature. This is because the early failure at low dpa levels of structural components in the reactor core is relatively rare. However, understanding the susceptibility of stainless steels to IASCC across a broad range of irradiation doses remains essential. Additionally, achieving these levels of dpa through experimental fast reactors requires significant time and comes with high costs.

IASCC susceptibility, particularly in terms of stress required for crack initiation, decreases with increasing dpa, and at low damage levels, the initiation stress may approach the irradiated yield strength (YS) of the alloy or even beyond it. However, experimental data at these lower dpa levels remain sparse and warrant further investigation, particularly for future generations of nuclear power plants, where historical IASCC data at early damage levels are unavailable.

This chapter begins by introducing the application of austenitic stainless steels to understand the reasons for using these materials in reactor core structures. The various degradation modes that austenitic stainless steel may experience during reactor operation will

then be explored, highlighting the challenges associated with using these steels in such environments. Additionally, the benefits of high-nitrogen alloys in reactor applications will be examined, emphasizing their superior properties compared to low-nitrogen alloys. The discussion will also address the role of solute nitrogen in influencing microstructural behavior under irradiation. Finally, the chapter will provide a detailed analysis of the IASCC degradation mode and the impact of solute nitrogen on the material's response to IASCC.

## 2.1 Austenitic stainless-steel applications in nuclear power plants

Structural materials such as low alloy steel (LAS), nickel-based alloys, and austenitic stainless steels are widely used in today's nuclear power plants. The favorable combination of strength, ductility, and corrosion performance under high-temperature water environments made them an attractive option for core structural materials. However, they have demonstrated that they are susceptible to IASCC. Since IASCC occurs exclusively in reactor core structural components, understanding its behavior in austenitic stainless steels is essential for maintaining the safety, reliability, and longevity of nuclear reactors.

### *2.1.1 Degradation modes of stainless steels in LWRs*

LWRs experience material degradation across various components due to extreme operational conditions, including high temperatures, neutron irradiation, mechanical stress, and corrosive coolant environments. Core internals, such as baffle bolts, core shrouds, and control blades, suffer from IASCC due to neutron exposure and water chemistry interactions.

The degradation mechanisms in LWRs can be classified into three broad categories: radiation-induced damage, corrosion-related degradation, and mechanical or thermal aging effects. Radiation-induced damage includes radiation embrittlement, which increases material

strength but reduces ductility and toughness in reactor pressure vessels. Void swelling, primarily affecting austenitic stainless steels, leads to volumetric expansion and dimensional instability, while irradiation creeps cause slow deformation under stress, which is particularly problematic for structural components [12, 13, 14, 15, 16]. Corrosion-related degradation affecting various reactor components includes general corrosion, crevice corrosion, galvanic corrosion, flow-accelerated corrosion, and environmentally assisted cracking (EAC), such as SCC [17, 18, 19, 20]. Although IASCC is a specific form of SCC that primarily affects reactor core structures, it remains a significant concern for stainless steels and nickel-based alloys used in these structures due to the harsh operating environment.

## 2.2 Metallurgy of austenitic stainless steels

### *2.2.1 Structure and composition*

Austenitic stainless steels are iron-based alloys that have a face-centered cubic (fcc) crystal structure, achieved by alloying with chromium (Cr) and nickel (Ni). Typically containing 15–26% Cr and 8–35% Ni, these steels exhibit excellent mechanical properties and resistance to corrosion. Also, austenitic stainless steels exhibit high ductility and formability, attributed to their fcc crystal structure, which contains four distinct {111} slip planes and three ⟨110⟩ slip directions per plane, resulting in a total of 12 slip systems.

Among these alloys, the most common classifications in PWRs are the 200-series, containing nitrogen, 4–15.5% manganese (Mn), and up to 7% Ni, and the 300-series steels with higher nickel content and typically up to 2% Mn. Additionally, molybdenum (Mo), copper (Cu), silicon (Si), aluminum (Al), titanium (Ti), and niobium (Nb) are introduced to enhance specific

properties such as resistance to halide-induced pitting corrosion and oxidation. Small amounts of sulfur (S) or selenium (Se) are sometimes added to improve machinability [21].

In addition to enhancing corrosion resistance and mechanical properties, alloying elements play an important role in maintaining the microstructural stability and phase composition of austenitic stainless steels. Chromium is the primary ferrite-promoting element, while molybdenum, niobium, titanium, aluminum, tungsten, and vanadium also contribute to ferrite formation. In contrast, nickel is the dominant austenite-stabilizing element, assisted by carbon, nitrogen, and copper, which facilitate ferrite-to-austenite transformations at elevated temperatures. While manganese has a limited effect on high-temperature phase stability, it plays a significant role in stabilizing austenite against martensitic transformations at lower temperatures and enhances nitrogen solubility in the alloy, facilitating the production of high-manganese, nitrogen-rich, low-nickel stainless steels [21].

The phase stability of these steels is well-understood through the iron-chromium-nickel ternary alloy system, which primarily dictates the austenite-ferrite phase balance. The equilibrium phase diagram at around 1100 °C shown in Figure 2-1, represents maximum austenite stability, commonly employed for annealing 18-8 stainless steels. Nickel notably expands the austenite phase field compared to the binary Fe-Cr system [22]. As chromium content surpasses approximately 18%, higher nickel additions are necessary to prevent excessive ferrite formation, particularly above 1150 °C, where δ-ferrite may form.

Moreover, nickel significantly lowers the martensitic start temperature ($M_s$) during cooling from solution annealing. All common alloying elements, including chromium and molybdenum, contribute to lowering $M_s$ temperature despite their ferrite-promoting effects at higher temperatures. The Schaeffler diagram shown in Figure 2-2 [23], illustrates these alloying

interactions, providing insight into the expected phase composition and relative strengths of ferrite and austenite stabilizers, originally developed for predicting weld metal microstructures but widely applicable to analyzing general alloy compositions [22, 24].

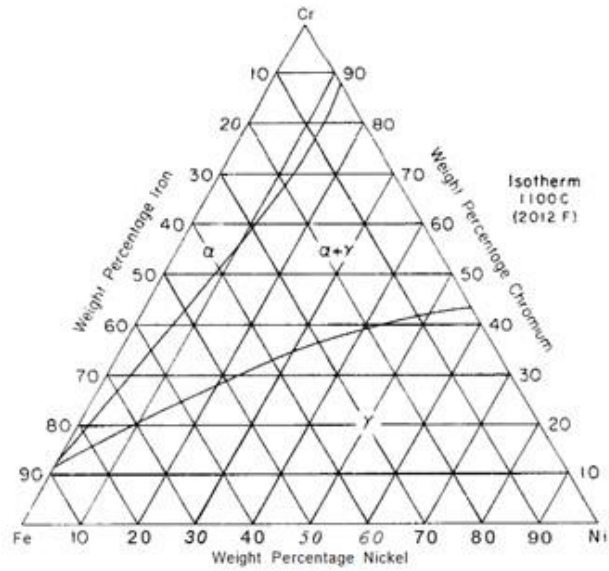


Figure 2-1 Iron-nickel-chromium diagram at 1100 ºC [22].

Nickel and chromium equivalents are used to quantify the influence of alloying elements on the balance between austenite and ferrite in stainless steels. The nickel equivalent accounts for austenite-stabilizing elements such as:

$$Ni_{Equivalent}(wt.\%) = \%Ni + \%Co + 0.5\%Mn + 30\%C + 0.3\%C + 0.3\%Cu + 25\%N \quad (2.1)$$

Meanwhile, the chromium equivalent represents ferrite-stabilizing elements such as:

$$Cr_{Equivalent}(wt.\%) = \%Cr + 2\%Si + 1.5\%Mo + 5\%V + 5.5\%Al + 1.75\%Nb + 1.5\%Ti + 0.75\%W \quad (2.2)$$

These equivalents help predict the microstructure and mechanical properties of stainless steels.

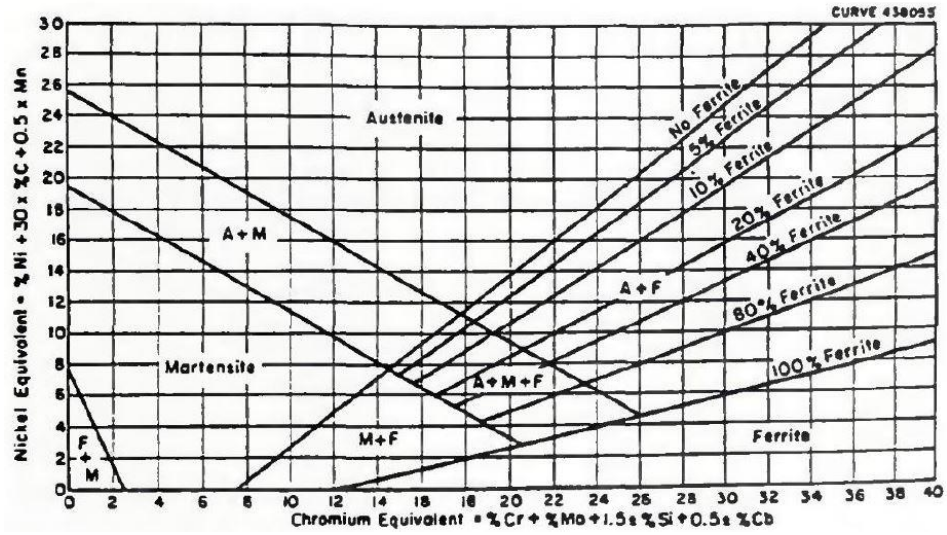


Figure 2-2 Schaeffler diagram for stainless steel [23].

### *2.2.2 Physical and mechanical properties of austenitic stainless steels*

The physical properties of 300-series austenitic stainless steels are generally consistent across the group and varies slightly across other grades, with the focus on 304 stainless steels properties as it is the alloy used in this study. Its density at room temperature varies between 7.5 – 8.0 g/cm$^3$, similar to type 316, and its melting point in the range of 1400 – 1450 ºC. Although density slightly decreases with temperature, within the operational temperature range of this study, the density remains approximately 7.8 g/cm$^3$ [25, 26].

The mean coefficient of linear expansion of austenitic stainless steels of type 304 is significantly high of order of 18 × 10$^{-6}$ /ºC for the temperature range of 20 – 400 ºC, which increases the concerns of material expansion and shrinkage during the system's heating and cooling down.

Austenitic stainless steels possess high elastic moduli. For type 304 stainless steel, the elastic modulus at room temperature is around 193 GPa, while for type 316, it reaches 196 GPa. The shear modulus typically measures approximately 79 GPa at room temperature. Both elastic

and shear moduli decrease with increasing temperature. Specifically, for type 304, the elastic modulus decreases from 193 GPa at room temperature to approximately 139 GPa at 800 ºC [26, 27], while the shear modulus decreases from 79 GPa at room temperature to about 50 GPa at 800 °C [26, 27]. These temperature-dependent variations in moduli are critical considerations in the design and structural analysis of reactor components.

### *2.2.3 Solid solution strengthening of austenitic stainless steel*

Interstitial alloying elements such as nitrogen, carbon, and boron significantly strengthen stainless steels. Solid solution hardening occurs due to the lattice distortion introduced by solute atoms, which restricts dislocation movement, thereby enhancing yield strength. Figure 2-3 shows the impact of solid solution hardening in austenitic stainless steels. Among interstitial elements, nitrogen is the most effective strengthener; even small additions substantially increase yield strength, with a 0.1% nitrogen addition typically resulting in an approximate 50 MPa increase in yield strength [27].

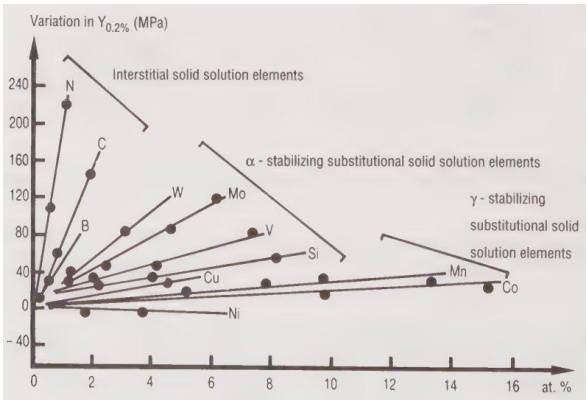


Figure 2-3 The impact of interstitial atoms on the stainless-steel strengthening [27].

Substitutional solid solution elements also enhance yield strength, though the effects are generally moderate compared to interstitial solutes, particularly for elements stabilizing austenite. Additionally, grain refinement provides another effective strengthening method

applicable to both austenitic and ferritic stainless steels. However, grain refinement effects differ due to variations in slip system availability, influencing the ease of transferring plastic deformation across grain boundaries.

Empirical models have been developed to quantify relationships among chemical composition, microstructure, and room-temperature yield strength, providing valuable predictive capabilities to guide alloy design and processing strategies [27]:

$$\begin{aligned} YS(\mathrm{MPa}) = 15.4\big[&4.4 + 23(C) + 32(N) + 1.3(Si) + 0.24(Cr) + 0.94(Mo) \\ &+1.2(V) + 0.29(W) + 2.6(Nb) + 1.7(Ti) + 0.82(Al) + 0.16(\%ferrite) \\ &+0.46d^{-1/2}\big] \end{aligned} \tag{2.3}$$

Where $d$ is the mean grain diameter in $mm$. As evident from equation 2.3, carbon and nitrogen have the strongest hardening effect compared to other alloying elements.

*Solute nitrogen solid solution hardening in austenitic stainless steels*

Nitrogen occupies the interstitial site within the fcc lattice and introduces strong elastic distortions into the crystal lattice, giving rise to strong solid solution hardening. Nitrogen in solid solutions modifies the stacking fault energy (SFE) of austenitic stainless steels, although its effect is non-monotonic and depends on the base alloy composition. Reports on how nitrogen affects SFE in austenitic stainless steels are debatable, some of these studies find a decrease at higher N contents [28, 29], others an increase (especially at low N additions) [30], and still others little net change depending on alloy chemistry, temperature, and method [31, 32]. Nonetheless, nitrogen is widely associated with promoting planar slip in these steels, commonly attributed to interstitial–substitutional short-range ordering that inhibits cross-slip.

The role of nitrogen on the SFE is linked to the composition of stainless steels due to the differences in the free electron state resulting from different reactions between nitrogen and other alloying elements [33].

Nitrogen modifies the SFE in stainless steel through both electronic mechanisms as modification of electron density and bonding character, and structural mechanism such as lattice distortion and interaction with partial dislocations.

Near the stacking fault plane, nitrogen introduces local lattice distortions and alters the electronic structure, which contributes to the stabilization of faulted configurations and a reduction in the energy required for partial dislocation motion. First-principles ab initio calculations and thermodynamic studies have shown that nitrogen lowers the Gibbs free energy difference between the fcc and hexagonal close pack (hcp) configurations, favoring stacking fault formation and reducing SFE [32, 34]. Moreover, nitrogen has been found to preferentially segregate to stacking faults, where it modifies the local bonding environment, further decreasing the fault energy [33]. Experimental observations also support these findings, demonstrating that increased nitrogen content from 0.39 to 0.69 wt.% in Fe-18Cr-10Mn austenitic stainless-steel results in a systematic increase in the SFE from 10.4 to 22.8 $mJ/m^2$ [35]. This increase in SFE correlates with a clear transition in deformation mechanisms, from strain-induced martensitic transformation (SIMT) in low-N alloys to deformation twinning (DT) in high-N alloys [35].

Solute nitrogen interacts more physically (elastic interaction) with dislocations and pins them, resulting in the formation of a Cottrell atmosphere [36], where solute atoms segregate around dislocations, specifically at the expanded region below a positive edge dislocation in the iron lattice. The binding of nitrogen atoms with dislocations is higher compared to carbon, forming stronger obstacles for dislocation movement and contributing significantly to strain

hardening in nitrogen-alloyed steels. The binding energy ($V$) between a dislocation and a solute atom (such as nitrogen) is govern by [36]:

$$V = -\frac{GErh}{4\pi(1-\nu)}\left(\frac{1+\nu\sin^2\alpha}{r^2}\right) \tag{2.4}$$

Where $G$ is the shear modulus, $E$ is the solute-dislocation binding energy, $r$ is the distance from the dislocation core, $h$ is the Burgers vector, $v$ is Poisson's ratio, and $\alpha$ is the angle between the Burgers vector and the vector from the dislocation to the solute atom. The enthalpy of binding ($H_b$) for nitrogen atoms with dislocations is higher than for carbon, indicating a stronger pinning effect. The binding enthalpy values are approximately 0.65 to 1.25 eV. Eqn. 2.3 indicates that the binding energy depends on the position of the solute and the distance between the solute atom and the dislocation. This means that the closer the solute atom is to the dislocation, the higher the binding energy, leading to a stronger interaction between the solute and the dislocation, resulting in a more stable structure. This interaction becomes particularly important under irradiation conditions, where the dislocation density is high and free nitrogen atoms are sufficiently available, provided they are not immobilized by competing irradiation-induced features such as cavities, precipitates, or radiation-induced segregation. Under these conditions, the likelihood and effectiveness of nitrogen-dislocation binding is significantly enhanced.

This pinning of dislocations increases the yield strength and results in strain aging as shown in Figure 2-4 for SS 316L [37, 38]. Therefore, the force required to pull a dislocation from its Cottrell atmosphere is govern by (solute drag):

$$F(x) = \frac{2Apx}{\left(x^2+p^2\right)^2} \tag{2.5}$$

Where $A$ is a material-dependent constant, $p$ is the perpendicular distance from the dislocation line to the point of application of force, and $x$ is the displacement of the dislocation. As the

dislocation moves away from its original position, the force F(x) initially increases, reaches a maximum, and then decreases, with the peak force representing the critical stress required to overcome the solute drag and detach the dislocation from the solute atmosphere, contributing to solute strengthening mechanism.

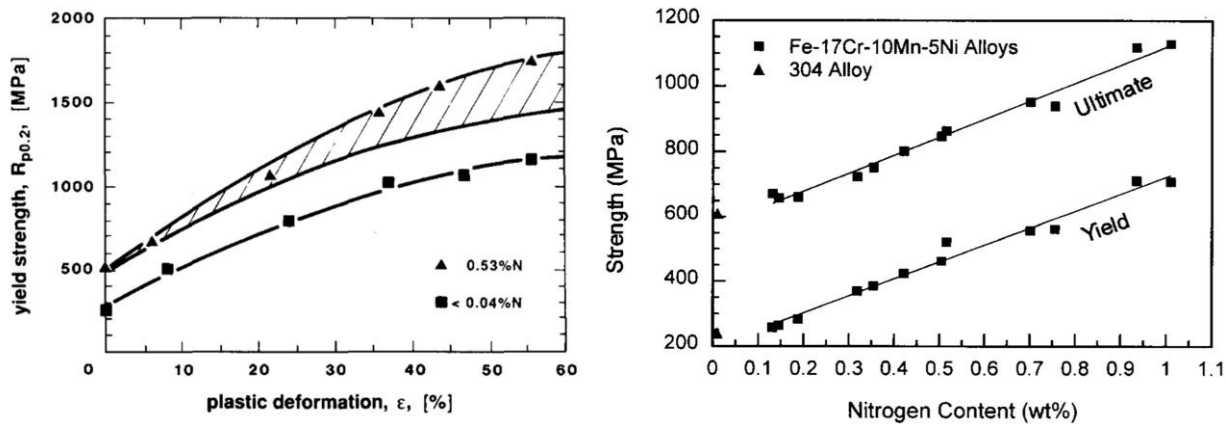


(a) (b)

Figure 2-4 The role of nitrogen on the yield strength of SS 316L. The YS is increasing with nitrogen content [37] and (b) in Fe-17Cr-10Mn-5Ni Alloys and SS 304 alloy [38].

The influence of nitrogen on the flow stress of austenitic stainless steels comprises two main components. The first is temperature dependent component, primarily due to solid solution strengthening, and is proportional to square root of the nitrogen concentration. The second is a temperature independent component, attributed to nitrogen's effect on grain size strengthening, and is proportional to the nitrogen content. The temperature dependent effect is minimal at temperatures above 200 °C but becomes significantly stronger at temperatures below room temperature [38, 39, 40].

Nitrogen plays a significant role in grain size hardening, as described by the Hall–Petch relationship. The Hall–Petch slope, which represents the strengthening contribution from grain boundaries, increases linearly with nitrogen concentration [41, 42, 43], meaning nitrogen enhances the resistance of grain boundaries to dislocation motion. As a solid solution strengthening element, nitrogen is also relatively efficient and thermally stable. High-nitrogen

austenitic stainless steels show only modest reductions in flow stress across the temperature range of 250 – 600 °C, as shown in Figure 2-5. The total flow stress ($\sigma_{0.2}$) caused by nitrogen strengthening can be expressed as [42]:

$$\sigma_{0.2} = \sigma_A + \sigma_T \tag{2.6}$$

Where $\sigma_A$ is the athermal component (dominant) and $\sigma_T$ is the thermally activated component. At elevated temperatures, particularly above 227 °C, the thermal component $\sigma_T$ becomes negligible, and the flow stress is dominated by $\sigma_A$. This athermal contribution arises from short-range ordering between nitrogen and chromium atoms, which impedes dislocation motion in a temperature-independent manner. This effect is quantitatively described by a linear relationship between the reduced athermal flow stress and nitrogen concentration [41, 42]:

$$\frac{\sigma_A}{\mu} = 1.816 + 1.245 X_N \tag{2.7}$$

Where $\mu$ is the shear modulus and $X_N$ is the atomic fraction of nitrogen. Since $\sigma_A$ shows only minimal temperature dependence, the overall strengthening from nitrogen remains stable at high temperatures. This makes nitrogen a highly effective alloying addition for enhancing the high-temperature strength retention of austenitic stainless steels, particularly in demanding environments such as those encountered in nuclear power applications.

Nitrogen also enhances strength through short-range ordering (SRO) mechanisms [41, 42, 43]. Which dominates at high temperatures (above 500 °C) due to increased atomic mobility, nitrogen promotes SRO with chromium atoms chemically ordered clusters, further hindering dislocation glide by increasing the athermal flow stress linearly with nitrogen content. This dual contribution results in a marked increase in yield strength, the direct chemical strengthening effect of nitrogen dominates, contributing approximately 20% to the overall increase, while grain refinement provides a smaller enhancement of about 8%.

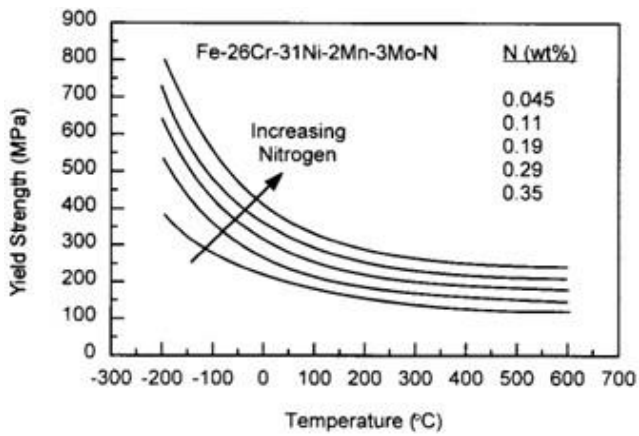


Figure 2-5 Influence of nitrogen on the temperature sensitivity of the yield stress in austenitic stainless steels [43].

As mentioned earlier, nitrogen offers significant advantages over substitutional elements for high-temperature structural applications. Based on experimental results, Kozlov et al. [44] proposed a strengthening factor of approximately 1500 MPa per atomic percent of nitrogen. This value reflects the high efficiency of nitrogen as a strengthener, even in small amounts. Their data show a 12.5 MPa increase in yield strength when nitrogen content increased by just 0.143 wt.%, supporting a linear relationship between nitrogen concentration and yield stress. Although modest in absolute terms, this increase is substantial for solid-solution hardening in fcc steels, where such mechanisms typically provide limited strengthening compared to precipitation or irradiation effects. Nitrogen hardening is even more pronounced than carbon strengthening has a strengthening constant that found at 1000 MPa/at.% by K. Ishio [45], who reported a simplified correlation based on regression analysis that estimates the contribution of adding nitrogen to austenitic stainless steel as follow:

$$\sigma_{0.2\%} = C1 + C2[N] \tag{2.8}$$

Where $\sigma_{0.2\%}$ is the yield strength at temperature $T$ in kelvin, $C1$ and $C2$ are temperature-dependent regression coefficients. The values of C1 and C2 at room temperature are 214 and 532. Given that this correlation has more confidence at cryogenic temperatures (4 and 77 K) with

R = 0.95, this confidence dropped to 0.84 to 300 K however, it still indicated a moderate to strong positive correlation. This also supports the fact that nitrogen's strengthening effect is more dominant at cryogenic temperatures and less isolated at room temperature where other mechanisms influence yield strength more.

Also, nitrogen increases Young's and shear moduli, retards dynamic strain aging (DSA), and suppresses carbide precipitation and cavity formation at grain boundaries, all of which contribute to improved creep resistance and mechanical stability during prolonged high-temperature service. J. Rawers et. al. [40] quantified nitrogen hardening behavior using a statistical model at temperature range of 73 – 900 K, showing that yield strength can be expressed as $\sigma_y = \sigma_0 + \alpha[N] + \beta[N]^{1/2}$, where α and β are temperature-dependent coefficients, [N] is nitrogen concentration in wt.%, and $\sigma_0$ represents the base matrix strength. The thermal term $\beta[N]^{1/2}$ becomes negligible at temperature above 600 K reducing the equation to a form comparable to equation 2.8.

### *2.2.4 Irradiation effects on austenitic stainless steel in PWRs*

Irradiation is another source of hardening once the stainless steels exposed to neutron flux in the reactor core. The mechanical properties of these materials are substantially altered due to the formation and evolution of irradiation-induced defects. The types of defects that develop depend on both the initial microstructure and the irradiation parameters, including temperature, dose, dose rate, and the type of irradiating species. These defects include point defects, defect clusters, dislocation loops and networks, as well as radiation-induced segregation [46, 47, 48, 49]. The evolution of these microstructural features occurs rapidly at early stages of irradiation and tends to stabilize near an equilibrium state around 5 dpa [50]. However, as shown in Figure 2-6 (a), IASCC does not directly correlate with the evolution of these defects. The irradiation-

induced defects cause pronounced hardening at low and intermediate irradiation temperatures by impeding dislocation motion [49], eventually reduce the tensile elongation and fracture toughness, and modifying the deformation mode in the microstructure [48, 50].

The main irradiation degradation modes in austenitic stainless steel in PWRs are low temperature radiation hardening and embrittlement, radiation-induced solute segregation, radiation-induced phase stability, irradiation creep, void-swelling, and high temperature helium embrittlement [49, 51, 14].

The discrepancy between the evolution of defects with dpa indicates that IASCC is influenced by factors beyond only the irradiation-induced defects in the material microstructure as previously shown in Figure 1-1.

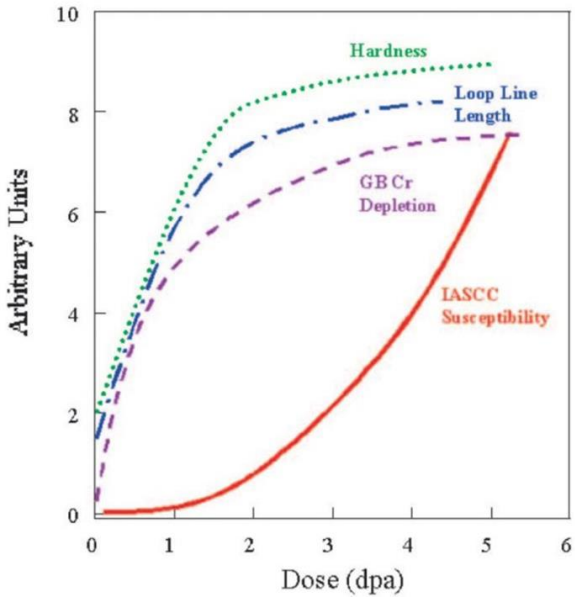


Figure 2-6 The dependence of mechanical and chemical phenomena on the irradiation-induced damage in dpa [14].

*Dislocation loops*

In PWRs core, austenitic stainless steels are subjected to low to intermediate irradiation temperatures (275 ºC – 350 ºC). At this temperatures range, the damage in the microstructure is attributed to the presence of small defect clusters (black dots), faulted loops and network

dislocation. Dislocation loops can form during the recombination phase immediately following the initial damage cascade [52]. These loops act as sinks for point defects, nucleating and growing primarily due to the high mobility of interstitials compared to vacancies. Their growth in austenitic stainless steels continues until they reach equilibrium with the surrounding vacancy and interstitial populations, thus, the evolution of dislocation loops occurs rapidly before stabilizing at an equilibrium around 3 dpa [53]. Figure 2-7 shows the evolution of loop density and size with irradiation dose for an austenitic stainless steel during LWR irradiation reactor relevant temperature near 300 $^{\circ}$C. The figure reveals that the saturation of loop number density occurs rapidly at around 1 dpa while loop size continues to evolve up to 5 dpa. The specific number density and size are dependent on irradiation conditions and alloying elements, but the loop size rarely exceeds 15 nm, and densities are of the order of $1\times10^{24}$ m$^{-3}$ [54]. Variables such has those from irradiation temperature, dose rate, and initial microstructure are known to affect dislocation loops evolution, however, their impact is minor under the PWR relevant environment such that the loop evolution has been reported to be relatively insensitive to temperature within the 300–375 °C range [55], and while dose rate can have an effect [56], it becomes negligible beyond loop saturation.

Figure 2-8 shows the evolution of dislocation loops with irradiation temperature ranging from 50 – 400 ºC [57] and 100 – 500 ºC [58]. At temperatures below 300 °C, loop size is insensitive to neutron fluence. At these low temperatures regime, loop sizes and densities population become dynamically stable when a balance is reached between new loop formation and the destruction of existing loops. Moreover, the microstructure is dominated by a high density of black dots and network dislocations, with relatively few Frank loops. Only a minor fraction of the small loops in stainless steels are identified as stacking fault tetrahedra (SFT),

significantly fewer than 50% typically observed in irradiated copper or nickel [59]. Horiki et. al. [60] found similar SFT in high purity low dose neutron irradiated FeCrNi alloys suggesting that the vacancy aggregation during cascade formation is the reason for SFT formation in fcc. Around 300 °C, the dislocation structure evolves to include larger faulted loops along with pre-existing network dislocations formed by loop unfaulting. As the temperature exceeds 300 °C, the population of Frank loops begins to diminish, and the microstructure transitions into one consisting predominantly of Frank loops and network dislocations. Although loop density reaches a saturation point after a few dpa, it remains relatively stable at higher doses. The density of the dislocation network increases with rising temperature in relation to the faulted loop population, although the total dislocation density is expected to remain relatively constant within the 300–370 °C range.

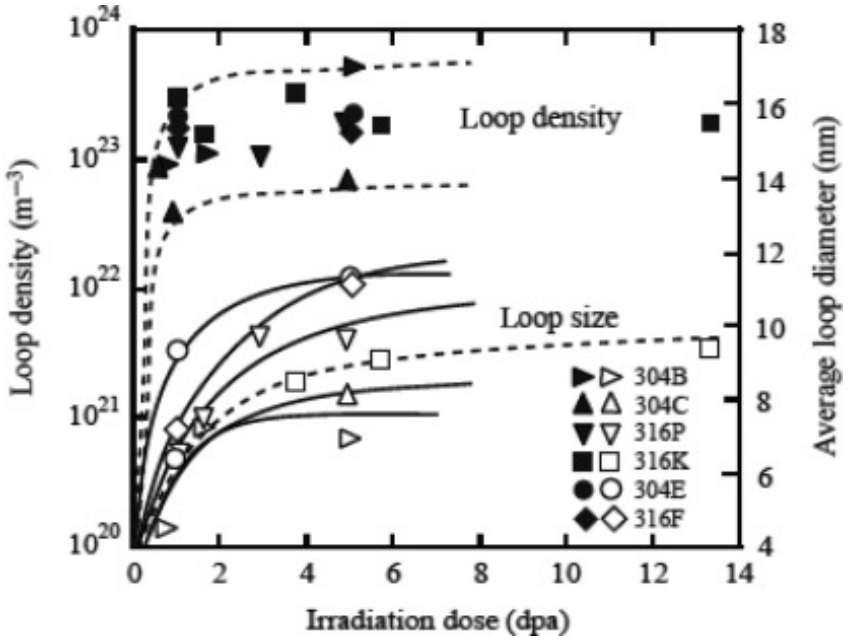


Figure 2-7 Evolution of the Frank loop density and size in various austenitic stainless steels following irradiation to doses of up to 13 dpa at a temperature near 300°C [54].

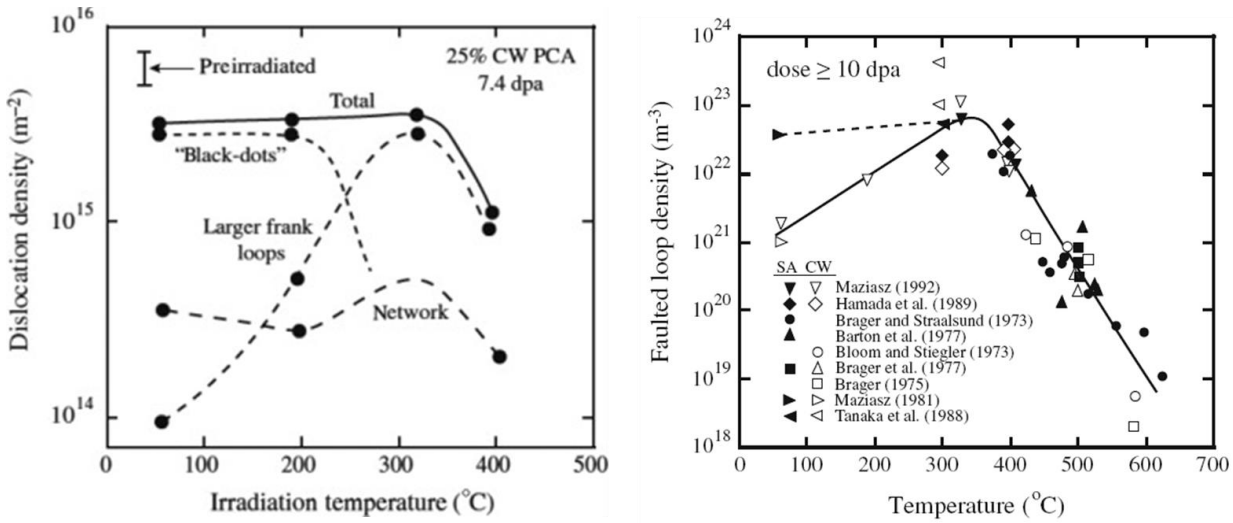


(a) (b)

Figure 2-8 Effect of irradiation temperature in the range of 50–400 °C on the components of the dislocation density in neutron-irradiated austenitic stainless steel [57] and (b) from 400 – 600 °C [58].

Cluster dynamic model was also used to understand the evolution of Frank loop density and size in austenitic stainless steels. Pokor et. al. [61] models three neutron irradiated austenitic stainless steel alloys (CW 316, SA 304, CW 316Ti) and compares the model results with the experimental data at 330 and 375 ºC. Frank loop at different damage levels ranging from 0.8 – 40 dpa were analyzed. The result of the model shows good agreement with the experimental data and confirmed that the sensitive parameters controlling the irradiation microstructure are the temperature, dose, the materials constants and the pre-existing dislocation density prior to the irradiation. A. Etienne et. al. [56] models similar alloys (SA SS 304 and CW SS 316) under 160 keV Fe+ irradiation and to damage level ranging from 0.36 to 5 dpa at 350 ºC. The results demonstrated a high number density of Frank loops that increased with dose and reached saturation around 1.25 dpa. A comparable trend was observed for loop size, although the model slightly underestimated the diameters. Despite this minor discrepancy, the simulation results showed excellent agreement with experimental data from the literature and revealed some distinctions between CW 316 and SA 304. Specifically, SA 304 exhibited larger loop diameters and a slower saturation trend compared to CW 316. While experimental observations did not

clearly reveal this difference, it can be attributed to the high dislocation density introduced by cold working in CW 316 SS.

Pre-existing dislocation substructures (high dislocation density) are typically introduced during fabrication, for example by cold working (up to ~20% in LWR components) or warm rolling. These loops act as additional sinks for point defects, thereby modifying loop nucleation and growth under irradiation. They also influence RIS: solutes such as Si and Ni can interact with and segregate to loop peripheries, and under proton irradiation at 360 °C the segregation at pre-existing loops has been reported to exceed that at irradiation-induced loops [62]. Similar behavior has been observed for cavities [63], ultimately affecting irradiation-induced hardening. By biasing defect fluxes, pre-existing loops tend to suppress the growth of irradiation-induced loops, producing smaller sizes but higher number densities, which reduces overall irradiation-induced hardening [64]. Edwards et. al. [54] reported dislocations loop-free zones adjacent to GBs in SS 304 and SS 316, with 20 to 50 nm wide at doses of 1 to 6 dpa; these zones disappeared at higher doses (> 5 dpa). Bruemmer et. al. [65] observed similar zones in commercial purity SS 304 but not in high-purity SS 304, attributing their presence to pre-existing GB enrichment of Cr and Mo. In the high-purity alloy, where no prior Cr segregation was reported, the loop-free zones were absent. The presence of pre-existing dislocation loops can have a mitigating effect, which is considered beneficial and is one of the reasons cold-worked austenitic stainless steels are selected for use in PWR core internals.

*Cavities*

At typical PWR operating temperatures, cavity formation does occur, but at relatively low densities. This is because the conditions fall outside the optimal temperature range 0.3 – 0.6 of the melting temperature of the material ($T_M$) and high irradiation doses (> 10 dpa) required for

cavity evolution dominance [66, 67]. As a result, the associated void swelling is generally minimal, often below 0.05% [68] as shown in Figure 2-9 (a). Consequently, the risk of void swelling induced embrittlement and intergranular fracture under PWR conditions remains relatively low. Among austenitic stainless steels used for PWR core internals, SS 304 is known to exhibit swelling earlier than SS 316, as shown in Figure 2-10 (a). Cold working has been shown to further delay the onset of swelling in CW SS 316 [68]. Additionally, the introduction of alloying elements can enhance swelling resistance, for instance, Ti additions in SS 316 significantly reduce swelling, as demonstrated in Figure 2-10 (b). Even at higher doses in PWR environment, void swelling does not produce a risk of embrittlement of IG cracking that would significantly impact IASCC susceptibility.

Moreover, cavities have been observed in cold-worked SS 316 baffle bolts (both head and shank regions) exposed to the Tihange 1 environment [69], at doses ranging from 7.5 to 19.5 dpa and temperatures between 320 – 340 ºC as shown in Figure 2-11. Head was close to the core and received the highest dose simultaneously it was exposed to the coolant that maintained its temperature within the range of 320 ºC. Gamma heating increased the temperature in the shank and thread (within the same bolt) to up to +20 ºC from the coolant temperature indicating the high sensitivity of void formation to irradiation temperature. Similar observations were reported in cold-worked SS 347 baffle bolts from the DC Cook 2 and Salem 1 power plants [70], at doses ranging from 7.5 – 26.5 dpa with void swelling in the range of 0.003% at 7.5 dpa to 0.035% at 26.5 dpa.

Void swelling exhibits a strong dependence on dose rate, with lower dpa rates leading to increased swelling. This behavior is attributed to the shortened in the transient swelling regime. Y. Chen [71] reported a high sensitivity of void swelling to dose rate in solution annealed SS 304

irradiated in EBR-II sodium fast reactor at temperatures between 373 – 388 ºC, even with small changes in dose rate, as shown in Figure 2-12 (a). Using similar experimental data, Garner and co-workers [72] developed a model to predict the void swelling across the full range of PWR-relevant dpa rates. However, the model carries significant uncertainty at temperatures below 370 °C. These models and studies are particularly valuable for selecting appropriate dpa/s values in charged particle irradiation experiments, helping to avoid premature exit from the transient swelling regime. Nonetheless, the results of void swelling extent in PWR environment were always minimal and unlikely to influence IASCC behavior.

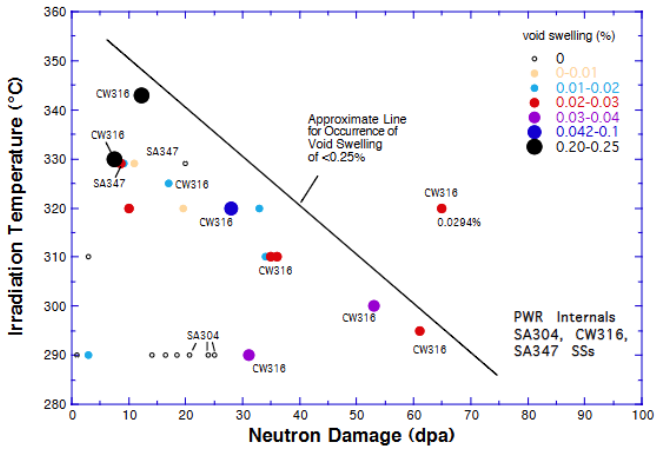


(a)

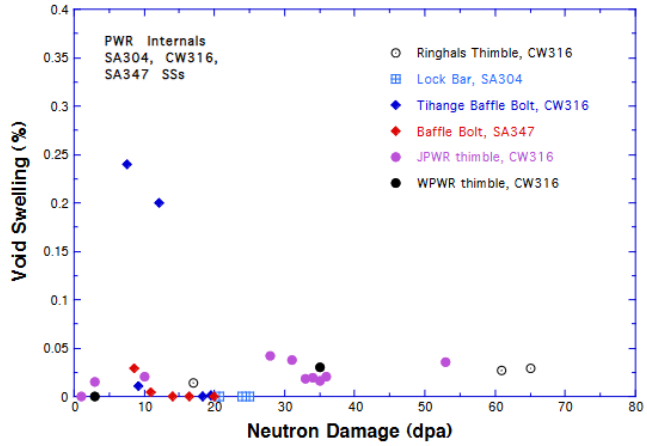


(b)

Figure 2-9 Void swelling as a function of (a) internals materials, irradiation temperature, and neutron dose, and (b) as a function of dose in PWR internals [68].

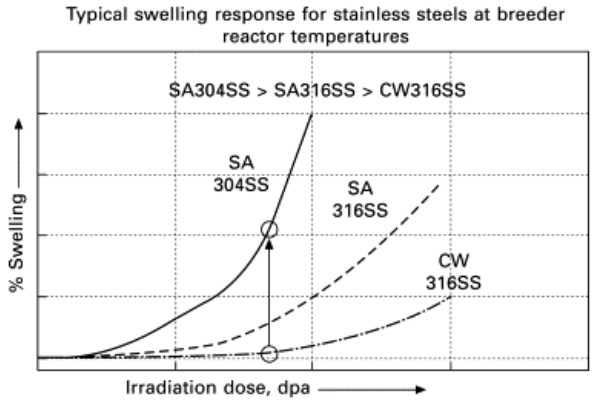


(a)

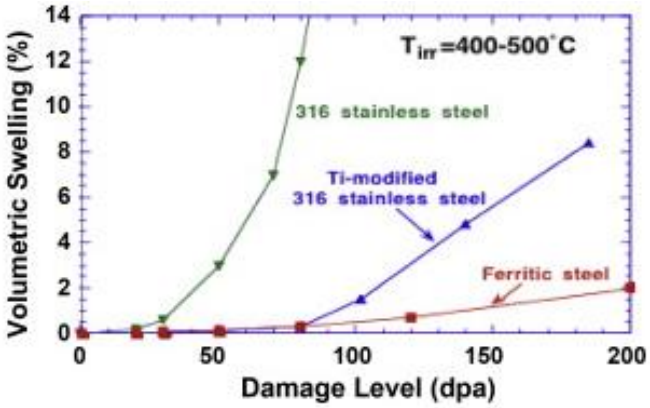


(b)

Figure 2-10 Schematic showing the role of (a) cold working on the swelling behavior of PWR core internals observed either in fast reactor or under charged particle irradiation showing the early swelling of SS 304 compared to SS 316 [68] and (b) the role of alloying modification to SS 316 on the swelling behavior showing suppressive role to void swelling at temperature ranges of 400 – 500 ºC [67].

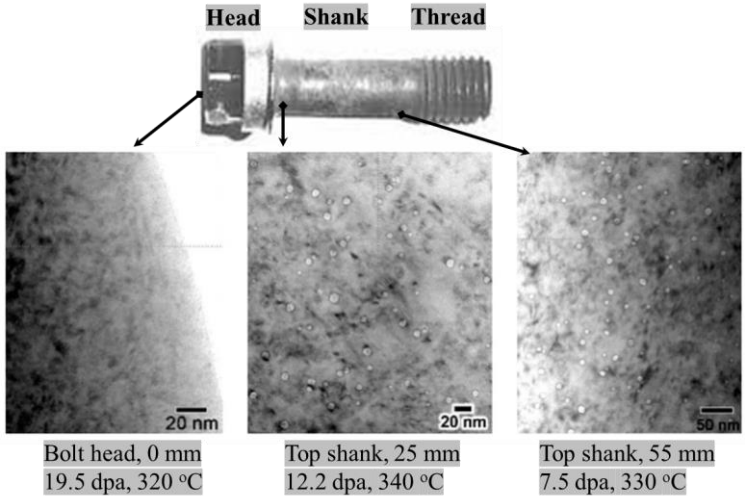


Figure 2-11 Cavities in CW SS 316 BFB irradiated in Tihange 1 from different locations across bolt head and shank at dpa range between 7.5 - 19.5 dpa and temperature ranges of 320 - 340 ºC [67].

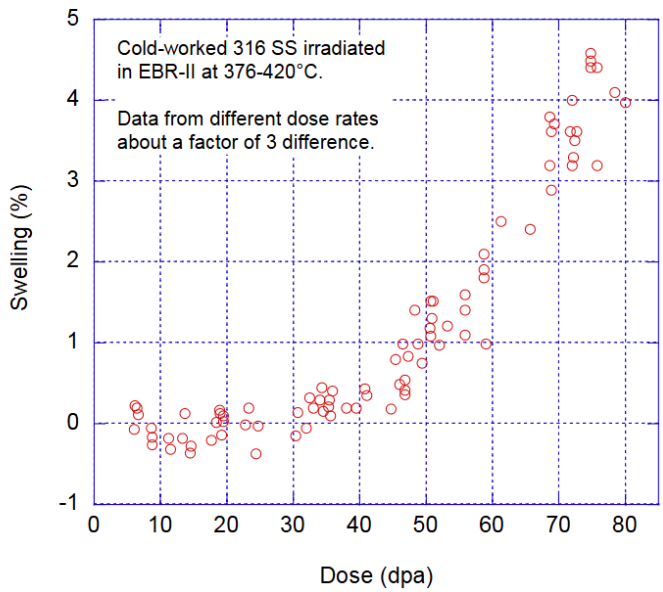


(a)

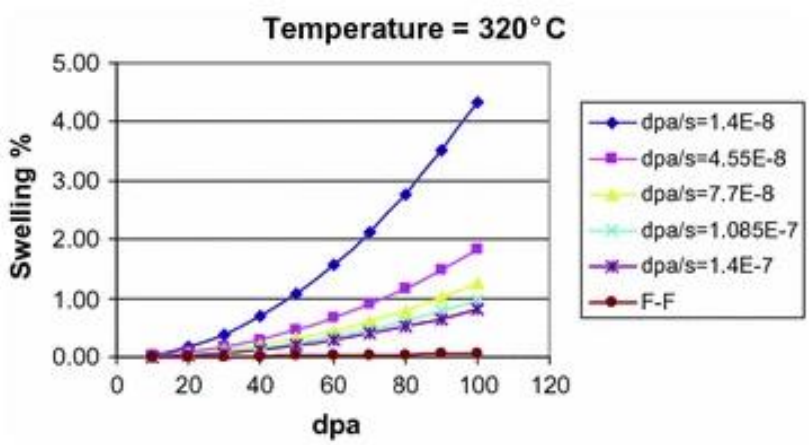


(b)

Figure 2-12 (a) Swelling of annealed SS 304 in the temperature range of 373 - 388 ºC measured by density changes in the lower halves of four EBR-II reflector subassemblies showing the dependence of swelling on the dose rate [71], (b) results of void swelling prediction model developed by F.A. Garner showing the strong dependence on dose rates [68].

The influence of cavities, and thus void swelling, in PWR-relevant environments is complex. Jiao [73] reported that, in SS 304 irradiated to 1–5.5 dpa, alloys with higher void density exhibited a reduced dislocation channel density and, consequently, lower susceptibility to intergranular cracking, although the study attributed this effect to differences SFE. A more recent study by Vo et al. [74] reported significant hardening, measured by microtensile and nanoindentation tests, in neutron-irradiated SS 304 with low-level void swelling (2% and 3.7%)

at doses up to 33 dpa. Notably, despite the observed hardening, ductility was still maintained. This behavior was attributed to the presence of a high density of voids near grain boundaries, which act as barriers to dislocation channels, preventing them from reaching the boundaries and instead terminating at the voids, thereby reducing intergranular cracking. A. Ustrzycka et. al. [75], through atomistic analysis, recently confirmed the role of voids in hardening, showing that nanoscale voids act as stronger barriers to dislocation motion than dislocation loops of comparable size. In irradiated materials, dislocations glide preferentially and interact with radiation-induced voids and loops, resulting in competing mechanisms: hardening through void cutting and softening through loop or void annihilation. These opposing processes coexist and are governed by the size, density, and interactions of radiation-induced defects and dislocations. Further investigation is needed to clarify the role of cavities in hardening and in the evolution of dislocation channels in austenitic stainless steels under LWR conditions, as this could further improve the understanding of IASCC initiation.

*Radiation-induced precipitation and radiation-induced segregation*

*Radiation-induced segregation*

Radiation-induced segregation (RIS) is a nonequilibrium phenomenon that develops at defect sinks in alloys subjected to high-energy particles irradiation at intermediate temperature, typically (0.3–0.5 $T_M$) as shown in Figure 2-13 [76]. The sensitivity of RIS to irradiation temperature and dose rate is high such that at lower dose rates lead to increased segregation, while higher dose rates generate more defects, increasing recombination and consequently limiting defect migration to the grain boundary. Segregation is most pronounced at intermediate

temperatures, as low temperatures restrict atomic mobility, while high temperatures promote solute back-diffusion and reduce defect concentrations toward thermal equilibrium.

RIS is controlled by inverse Kirkendall diffusion mechanism [77], smaller atoms diffuse with interstitial flux while the large one diffuses with vacancy flux. Therefore, in austenitic stainless steels under PWR operating temperature, Fe and Cr depletes at the GB while Ni segregates. In type 304 and 316 stainless steels, the enrichment of Ni compensates for the loss of both chromium and iron and can reach values approaching 30 wt.%.

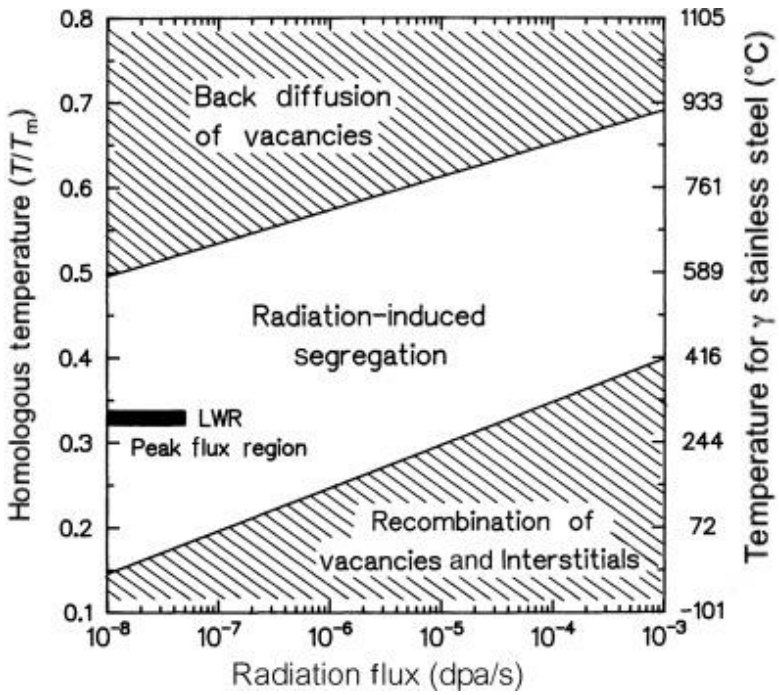


Figure 2-13 Sensitivity of RIS to temperature and dose rate in austenitic stainless steels [76].

RIS is considered as one of the critical problems in the structural materials in PWR environments because it has a significant effect on the chemistry of GB. In PWR, neutron irradiation causes chromium to deplete and light elements (P, Si) and nickel to enrich at GBs. For example, a GB in 304 SS irradiated to a few dpa may see Cr drop from 18% in the matrix to <12% at the boundary, with Ni and Si correspondingly higher. This chromium depletion can prevent formation of intergranular stable chromia ($Cr_2O_3$) [78]. Figure 2-14 shows the Cr

depletion at the GB in austenitic stainless steels as a function of irradiation dose, revealing a clear trend of increasing Cr depletion with higher dose levels [55]. Over the past decades, the initiation of IASCC has been closely associated with GB oxidation, primarily attributed to chromium depletion at the GB because of RIS [79, 80, 81], when RIS continues to deplete chromium at the GB, the susceptibility to oxidation penetration increases [82]. However, chromium depletion at the GB remains a critical factor for crack initiation, particularly when the Cr content drops the threshold for forming a stable and protective layer.

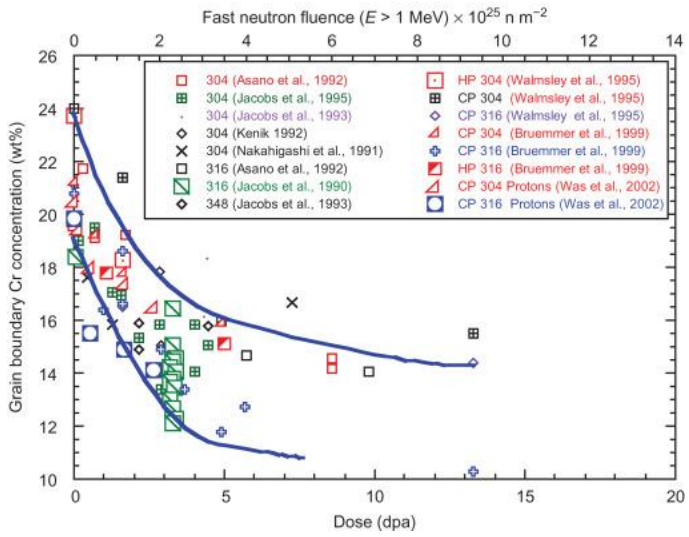


Figure 2-14 Dose dependence of grain boundary chromium concentration for several 300-series austenitic stainless steels irradiated at a temperature of about 300°C [55].

Silicon is also observed to segregate at the GB with strong dependence on dose rate. For austenitic stainless steels irradiated at 288 ºC, measurements from STEM-EDS shows high levels of Silicon at the GB as shown in Figure 2-15 [83]. The spatial resolution limit of TEM has been always a problem in underestimating the actual Si concentration at the GB by a factor of 3 – 5. However, studies show that Si concentration at GB can reach 20% at GB giving rise to its significant role in the GB oxidation thus IG cracking [83].

In irradiation testing laboratories, simulated RIS has been demonstrated over the years; however, RIS is highly sensitive to temperature and dose rate, requiring careful control during irradiation to ensure that the RIS-dominant regime is achieved.

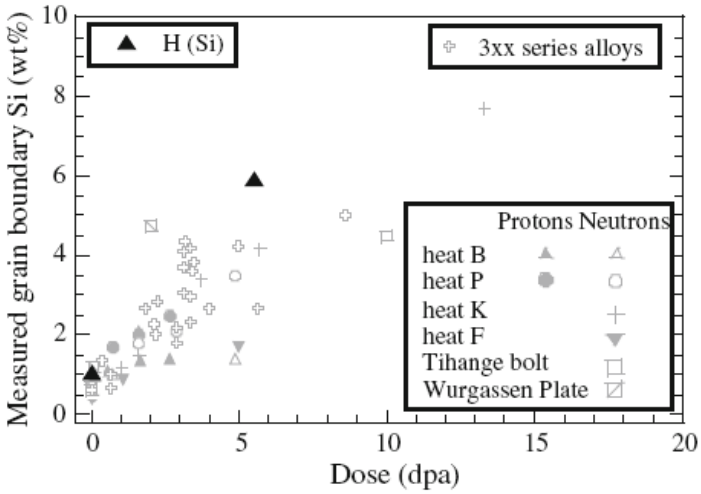


Figure 2-15 The segregation of Si at the GB of various austenitic stainless steels irradiated with neutrons or protons to 13 dpa (after [83]).

For a given irradiation dose, the extent of RIS is typically greater under light particle irradiation (e.g., electrons or light ions) than under heavy particle irradiation (e.g., neutrons or heavy ions). This contrast arises from differences in defect production mechanisms. Heavy particles generate dense displacement cascades, causing many vacancies and interstitials to recombine or cluster within localized regions, thereby reducing the number of freely migrating defects that contribute to RIS. In contrast, light particles produce Frenkel pairs more uniformly across the material, allowing a higher fraction of defects to escape recombination and migrate over longer distances, enhancing RIS development [84].

Under proton irradiation, Jiao and Was [85] investigated RIS in commercial purity SS 304 irradiated with 2 MeV protons to 5 dpa at 360 $^{o}$C as shown in Figure 2-16. Similar observations of Cr and Mn depletion at the GB to the neutron-irradiated steels was observed which is attributed to the large size of these elements. Conversely, Si and Ni found to segregate at the GB

with early enrichment in Ni while Si enriched after reaching a dose of 13 dpa. Other elements with low mass exhibits RIS as well such as B, C, and P but requires high resolution technique such APT. Figure 2-16 compares between the elemental condition at the GB of the APT analysis performed by Jiao and Was showing depletion of Fe, Cr, Mn, and Cu and segregation of Ni, Si, P, and B. Further confirmed that RIS preferentially occurs at dislocation loops.

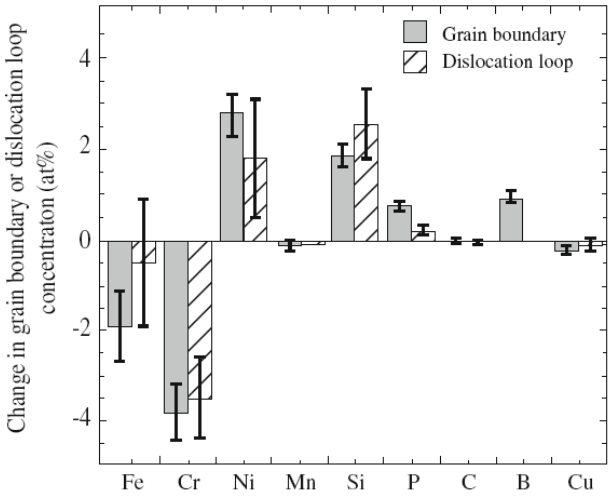


Figure 2-16 A comparison between the elemental composition at the GB and dislocation loops in SS 304 irradiated with 2 MeV protons to 5 dpa to 360 ºC showing depletion of Fe, Cr, Mn, and Cu and segregation of Ni, Si, P, and B [85].

RIS also reported at faulted dislocation loops in neutron-irradiated austenitic stainless steel and was first reported by Kenik [86]. Etienne et. al. [87] demonstrated significant Si segregation at the torus-shaped clusters using APT in SS 316 irradiated with $Fe^{+}$ at 350 ºC as shown in Figure 2-17. Later, A. Etienne [56] observed the formation of Frank loops and solute clusters enriched in Si and Ni and depleted in Cr at doses between 0.5 and 5 dpa. These findings established a strong correlation between the densities of dislocation loops and solute clusters. However, Toyama et al. [88] further proposed that solute clusters nucleate heterogeneously on dislocation loops and that Si atoms are transported to defect sinks via an interstitial-mediated mechanism in neutron-irradiated SS 304 at temperatures between 300 – 400 ºC.

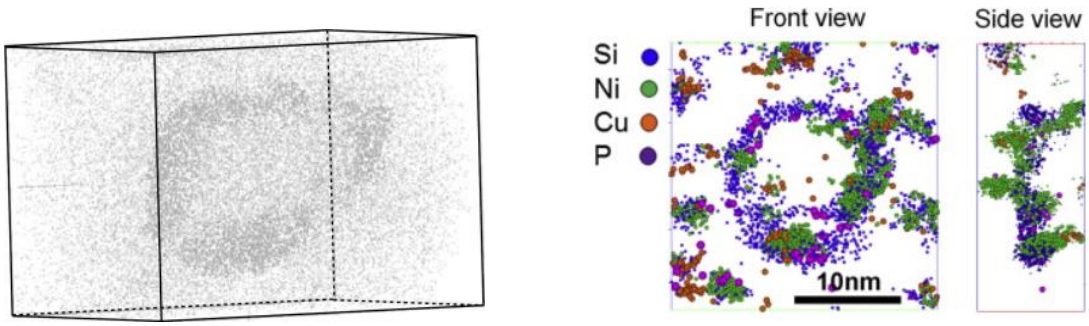


(a) (b)

Figure 2-17 (a) A Si loop shaped cluster observed by Etienne et al. in a Type 316 austenitic steel irradiated at 350 °C by $Fe5^{+}$ ions to a dose of 10 dpa. The height of the bounding box is 34 nm [87] and (b) A dislocation loop with Ni, Si, Cu, and P segregation at its periphery in proton irradiated SS 304 to 10 dpa [89].

Both substitutional and interstitial solute atoms were found to segregate to the loops. Interestingly, in contrast to most previous observations, the solute concentrations varied spatially around the loop, particularly for Ni and Si atoms, as shown in Figure 2-18.

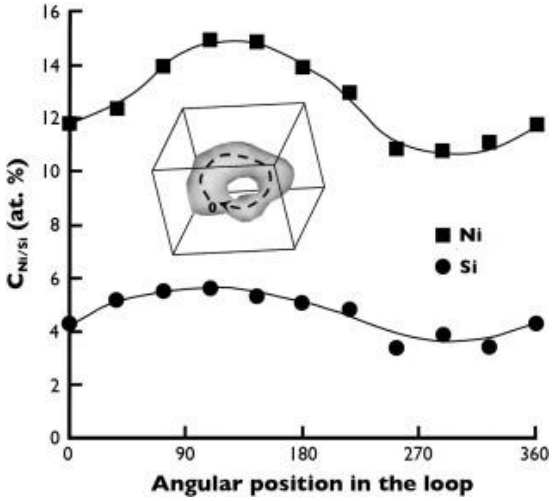


Figure 2-18 Variations in the composition of Ni and Si ($C_{Ni/Si}$) around a dislocation loop in a CP Type 304 austenitic stainless steel irradiated by 2 MeV protons to a dose of 5 dpa at 360 °C [85]. The diameter of the loop is 12–14 nm and the measured concentrations were taken in a clockwise direction around the loop.

Moreover, the segregation of Si, Ni, and P and the depletion of Fe, Cr, Mn, and Mo were reported to form at pure screw dislocations in a solution annealed SS 316 irradiated by fast neutrons to 56 dpa at 589 $^{o}$C by Hatakeyama et. al. [90] following analysis with 3D APT. This observation was particularly surprising, as screw dislocations are not typically considered strong

point defect sinks due to the absence of a dilatational strain component. The attraction of undersized Si atoms to screw dislocations, therefore, was unexpected. In a separate study, Hatakeyama et. al. [91] also observed RIS at stacking faults in the same alloy, despite stacking faults, like screw dislocations, being biased but relatively weak point-defect sinks.

RIS has been also reported to be active at the GB. The segregation of solute atoms at GBs is inherently inhomogeneous in both irradiated and unirradiated conditions [92]. This implies that pre-irradiation segregation plays a critical role in determining not only the concentrations of enriched or depleted elements at the GB, but also their spatial distribution along the boundary [93]. Following irradiation, solute concentration profiles at GBs often exhibit a characteristic W-shaped distribution at low doses (~1 dpa), which tends to evolve into a more monotonic profile with increasing dose, particularly evident in the progressive depletion of Cr near the GB [94, 95]. The inhomogeneity of segregation can be attributed to the complex structure of GBs, which can be described as networks of misfit dislocations. The segregation energy that drives solute atoms to accumulate at these boundaries is not uniform; rather, it varies locally along the GB, even in unirradiated conditions [96]. This further underscores the importance of pre-existing segregation, which can significantly influence both the magnitude and spatial characteristics of irradiation-induced segregation at grain boundaries [93].

Laser-assisted APT technique has revealed the enrichment of Ni, Si, and P along with the depletion of Cr and Fe at the GB of SS 304 irradiated with neutrons to 24 dpa at 300 $^{o}$C [92]. As shown in Figure 2-19, the full width at half-maximum (FWHM) of the RIS region was approximately 3 nm for the concentration peaks of Ni and Si. The atomic concentrations measured at the grain boundary were 19% Ni, 7% Si, and 14% Cr, consistent with previously reported values for neutron-irradiated austenitic stainless steels.

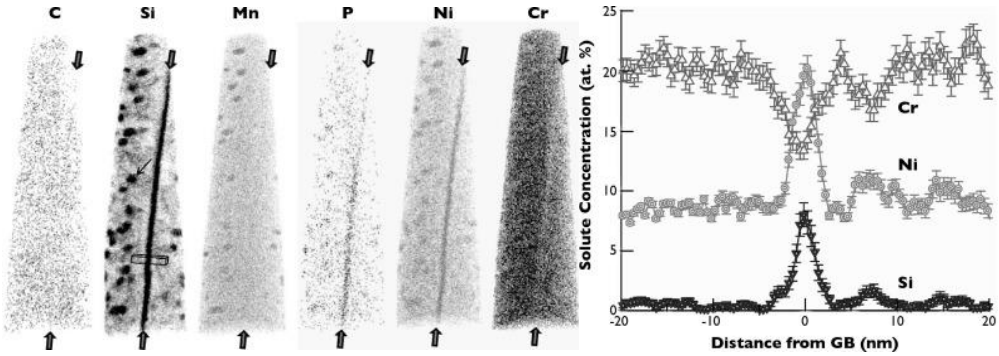


(a) (b)

Figure 2-19 Concentration of the indicated elements at GBs in a tip of neutron irradiated Type 304 stainless steel, neutron-irradiated to a dose of 24 dpa at 300 °C; results of Toyama et al. [88]. The box inset in the image for Si represents the region used to trace the elemental concentrations across the GB; the box is ~20 nm long.

Similar inhomogeneous segregation behavior has also been observed under proton irradiation. Jiao and Was [85] reported that the Cr concentration varied between 7.8 and 19.1 at.%, while Si ranged from 3.5 to 9.1 at.% in steel with nominal bulk compositions of 19.2% Cr and 2.05% Si. The Cr depletion and Si enrichment observed in that study align with earlier findings by Toyama et al. [88].

Moreover, a comparison between proton irradiation and neutron irradiation on the RIS behavior of SS 304 and SS 316 performed by T. Allen [97]. The comparison was made with low dose specimen irradiated in EBR-II reactor. Despite certain experimental limitations, the results indicated that lower dose rates tend to enhance radiation-induced segregation. Specifically, increasing the dose rate was associated with reduced Cr depletion, higher Si enrichment, and lower Ni enrichment at point defect sinks. While the interpretation is somewhat constrained by the inability to fully control all experimental parameters, such as the differences in knock-on damage between proton and neutron irradiation, additional supporting evidence has since been provided later by Allen et. al. [98].

Kano et al. [99] investigated the influence of interstitial atoms such as carbon and nitrogen on RIS in austenitic stainless steels. The study examined SS 316 alloys with varying carbon concentrations (0.004, 0.019, and 0.052 wt.%) and SS 304 alloys with different nitrogen levels

(0.003, 0.032, and 0.095 wt.%). Although the changes in solute concentrations at the grain boundaries relative to their bulk values were modest, the trends appeared systematic, particularly for Ni and the impurity element Si, both of which tend to segregate to grain boundaries under irradiation. As shown in Figure 2-20, the effects of carbon and nitrogen were most notable in modifying the RIS behavior of Ni, with comparatively smaller influences on chromium (Cr) and Si segregation. However, the underlying mechanisms driving these trends were not discussed in detail by F. Kano. These findings highlight that the role of interstitial atoms, particularly nitrogen, in IASCC remains poorly understood. Since the study by Kano et al., no further investigations have been conducted to systematically evaluate the effect of nitrogen on IASCC susceptibility. This knowledge gap underscores the importance of exploring whether interstitial elements influence IASCC behavior, especially given their known interactions with irradiation-induced defects and their potential to enhance irradiation hardening.

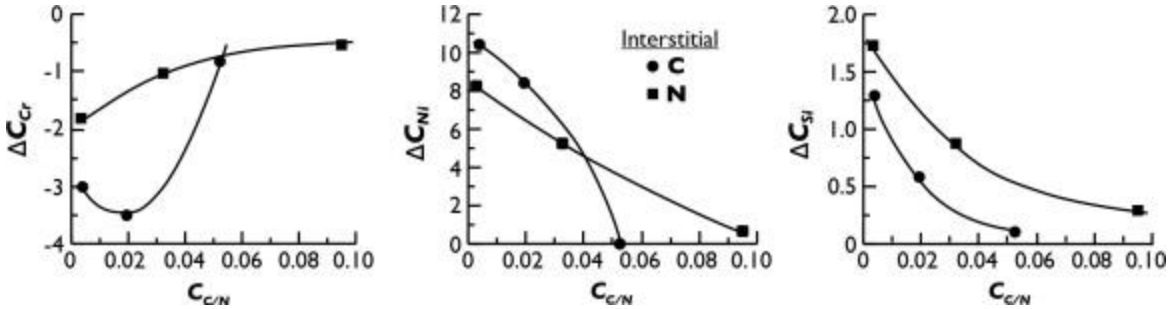


Figure 2-20 The effect of alloying with interstitial C and N atoms on RIS in an austenitic steel irradiated by 12 MeV Ni3+ ions at 300 °C. All units of concentration are in wt.%. The abscissa represents the changes in concentration of the specified solute atom (Cr, Ni, Si) measured at the half-widths of the concentration profiles at the GBs, referred to the concentrations far from the boundaries. Data of Kano et al [99].

*Radiation-induced precipitation*

Another important class of irradiation-induced defects in austenitic stainless steels under PWR conditions is precipitates, which can significantly alter the material's microstructure and microchemistry. The formation of radiation-induced precipitates (RIP) is strongly influenced by

factors such as alloy composition, minor alloying elements, impurities, irradiation temperature, dose, and dose rate. RIP can be classified into four types as per Lee et. al. [100]: radiation-induced (form only under irradiation), radiation-modified (thermally formed but altered by irradiation), radiation-enhanced (thermally possible but more extensive under irradiation), and thermally induced (form without irradiation). Moreover, irradiation can also promote the dissolution of otherwise stable phases through mechanisms such as ballistic recoil, disordering and/or amorphization, or the formation of antisite defects, where displaced atoms occupy lattice sites of different elements, disrupting chemical order and destabilizing precipitates [55].

The extent of RIS at a defect sink may increase by accumulating dose until the solubility limit is reached, beyond which the available driving force promotes the nucleation of a precipitate phase. RIP can continue to act as point defect sinks, with RIS supplying the necessary solute atoms to sustain their growth. Once the matrix becomes depleted of these solutes, a steady state may be established in which RIS-driven enrichment is balanced by the back diffusion of solute atoms, leading to cessation of precipitate growth. Figure 2-21 shows the temperature- and dose-dependent formation of precipitates in neutron-irradiated SS 316 [101]. The $Ni_3Si$ phase (known as $\gamma'$ phase), in particular, forms more readily in cold-worked material compared to solution-annealed counterparts due to high dislocation density, with most of these precipitates decorating dislocations as small, isolated particles [102]. The $\gamma'$ phase can be considered in some cases as a precursor to formation G-phase ($M_6Ni_{16}Si_7$), which is another type of Ni-, Si-rich phase.

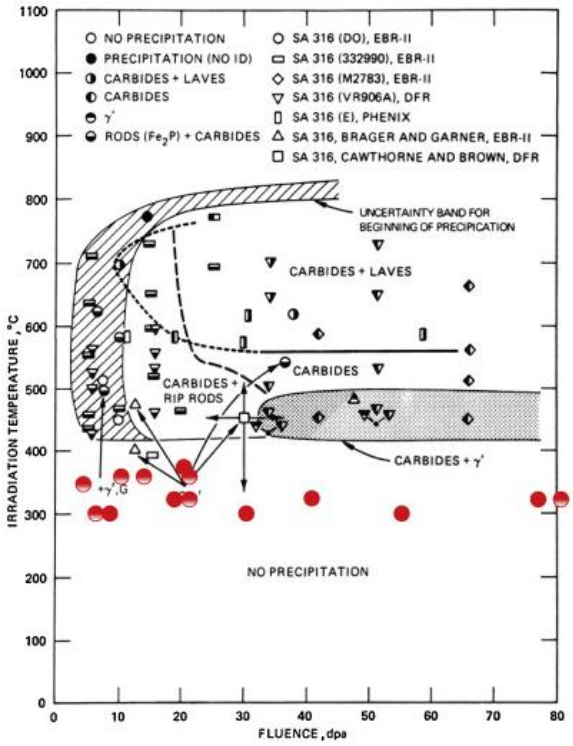


Figure 2-21 Precipitates phased observed in neutron irradiated SS 316 a range of dpa levels and temperatures. The plot is originally found in Ref. [101] and modified by [102] through adding the low temperature data (red dots). The plot shows the formation of γ′ phase in the shaded area and G phase in the black dots with some unidentified phases as well.

A high-purity stainless steel containing 1.0 wt.% Si was irradiated with 3.2 MeV protons to 5.5 dpa at 360 °C [102], resulting in the formation of γ′ phase in the matrix but not along the GB. Although the concentrations of Ni and Si are sufficiently high to form such phases, neither γ′ phase nor other RIS-affected precipitates have been reported at the GB of austenitic stainless steels under PWR-relevant conditions. Fuji et al. [103] reported high density Ni–Si and Ni–Si–Mn enriched clusters in CW 316 stainless steel irradiated to 74 dpa at 305 °C in a PWR by through APT analysis, clusters such as small Ni–Si (with a diameter of 3–4 nm) and larger Ni–Si or Ni–Si–Mn (with a diameter of 8–10 nm) were reported with a total density was $7.7 \times 10^{23}$ $m^{-3}$ and large clusters comprising about 10% of the whole population. Tan et al. [4,5] reported high density of Frank loops, various precipitates including G-phase, $M_{23}C6$, α-ferrite, γ′ phase,

unidentified particles, and RIS but limited cavities in CP 304 SS and 316 SS irradiated to 47 dpa at 320 °C and a dose rate of $8 \times 10^{-7}$ dpa/s in BOR-60 fast reactor [104].

$Ni_3Si$ phase has been reported widely in in austenitic stainless steels in PWR environment has been observed in baffle-to-former bolt (BFB) made of CW SS 316 irradiated to doses ranging from 8.5 – 19.2 dpa [105], SS 347 BFB irradiated to doses ranging from 7.8 – 26.5 dpa [70], and CW SS 316 at lower dose of 4 dpa [106]. High density of the order of $10^{23}$ $m^{-3}$ of γ′ phase reported in SS 304 specimens removed from fuel wrapper plates irradiated in the Chooz A PWR to 24 dpa at 300 ºC [88]. However, formation of these phases does not necessarily occur in PWR environment. D.J. Edwards et. al. [107] reported insignificant γ′ phase in SS 316 FFT irradiated to 70 dpa in PWR-relevant environment while K. Fujimoto [108] reported the absent of γ′ phase.

Under laboratory conditions, γ′ phase has been also identified following proton irradiation at 360 ºC. Recently, irradiation-induced phases stability in austenitic stainless steels has been investigated under both charged particles and neutron irradiation [109, 110]. Cu-rich and Ni-Si-Mn nanoclusters were found to be stable after irradiation with fast neutron in BOR-60 at 318 ºC to a dose of 5.4 dpa. To further assess phase stability, the neutron-irradiated samples were subjected to self-ion irradiation at elevated temperatures (380–420 °C), adding additional ion doses of 4.7 and 42 dpa, resulting in total doses of 10.1 and 47.4 dpa, respectively. Following ion irradiation, Cu-rich clusters were completely dissolved, whereas Ni-Si-Mn-rich clusters showed resistance to ballistic dissolution. At 47.5 dpa, these clusters coarsened into G-phase precipitates. In contrast, ion irradiation at 380 °C preserved the clusters without further growth, while irradiation at 400–420 °C led to the formation of a low density of large G-phase precipitates, with minimal evidence of dissolution. The γ′ phase has consistently been associated with low-

dose conditions. Notably, the number density of these clusters has been reported to exceed that of dislocation loops in SS 304 [111]; however, in CW SS 316, their number density can be up to two orders of magnitude lower than that of dislocation loops [112].

*Radiation hardening*

Radiation hardening occurs due to irradiation-induced defects impeding dislocation motion. The rapid evolution of point defects, dislocation loops, cavities, and precipitates significantly distort the crystal lattice, each defect type creating barriers for dislocation evolution. Radiation-induced hardening, along with reductions in elongation and fracture toughness, tends to occur once the irradiation dose exceeds approximately 0.1 dpa [55, 113]. These effects are most significant at lower homologous irradiation temperatures, specifically below $0.35T_M$ [49].

At higher damage levels (5–10 dpa), the yield stress increases significantly, by approximately 4 to 5 times compared to unirradiated materials [114, 115]. Figure 2-22 shows the yield strength of various solution-annealed austenitic stainless-steel alloys increases with neutron dose, exhibiting saturation at relatively low exposure levels (<10 dpa), which reflects a corresponding saturation in the density of radiation-induced microstructural features. Since the concentration of these features generally decreases with increasing irradiation temperature above 300 °C, the saturation strength is also expected to decline at higher temperatures. Similarly, cold-worked stainless steels exhibit convergence to a common saturation strength when irradiated to the same dose and at the same temperature [116].

Figure 2-22 (a) shows the yield strength can increase to as much as five times its unirradiated value at 5 dpa, with the overall trend exhibiting a square root dependence on irradiation dose [117]. Busby et al. [118] proposed a correlation between the change in hardness and the change in yield strength for irradiated austenitic stainless steels, as shown in Figure 2-22

(b). The relationship is nearly linear, where low levels of hardening correspond to a modest increase in YS, attributed to dislocation shearing of small defects. As hardening increases, the behavior shifts, resulting in a more pronounced rise in YS due to the presence of stronger, more obstructive defects.

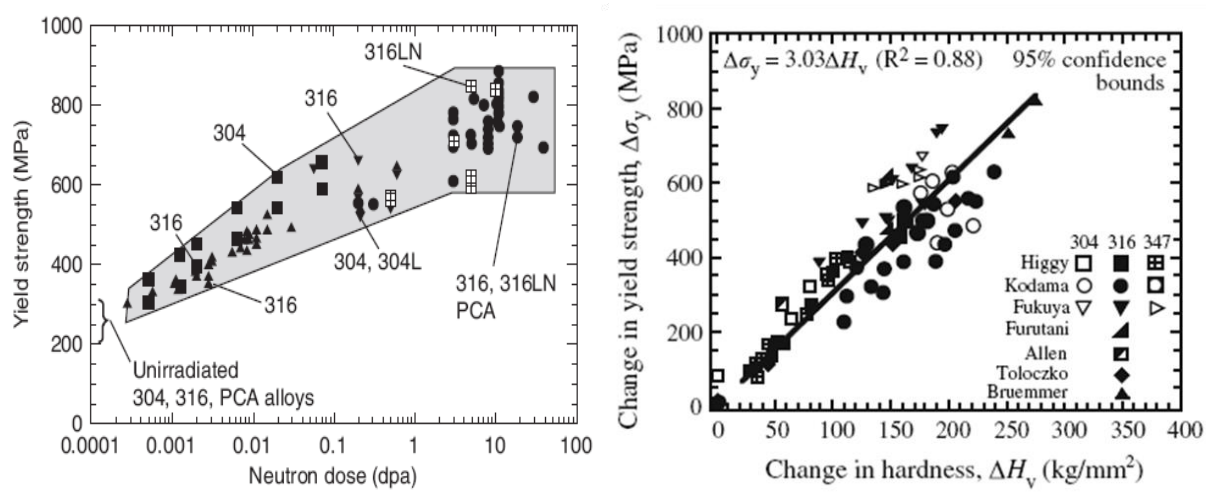


(a) (b)

Figure 2-22 (a) Strengthening of various annealed austenitic stainless steels with neutron dose in LWRs at temperatures of range 280 - 330 $^{o}$C and up to 10 dpa [119] (modified by [120]) and (b) experimental data plotted against the change in the yield strength in hardness for austenitic stainless steels [118]

The increase in yield strength observed in irradiated materials is primarily attributed to irradiation-induced defects, as previously described in this section. These defects act as barriers to dislocation motion, thereby increasing the material hardness. To quantify the hardening contribution from such obstacles, dispersed barrier hardening (DBH) model was proposed, predicting that yield stress is proportional to the square root of defect density, reflecting the complex interactions among dislocations and obstacles [121, 122, 123]. DBH model describes the increase in yield stress due to obstacles, such as irradiation-induced defects, which impede dislocation motion. According to this model, dislocations require additional stress to overcome these barriers and activate slip systems. While such defects significantly hinder dislocation glide, once the applied stress exceeds a critical threshold, as defined by the Schmid criterion, localized

plastic deformation can still occur. According to this model, the change in yield stress is proportional to the size and density of the defects, as expressed by the following equation:

$$\Delta\sigma_y = \alpha\mu b\sqrt{Nd} \tag{2.9}$$

Where $\Delta\sigma_y$ is the yield stress increment, $\alpha$ is the obstacle strength factor, $\mu$ is the shear modulus, $b$ is the Burgers vector, $N$ is the obstacles density, and $d$ is the size of the obstacle. This base formula can be expanded to include the influence of multiple defect populations by linear superposition.

However, because nearly all microstructural defects contribute to the increase in yield strength, the DBH model was later modified to incorporate the effects of all strengthening mechanisms. P. Zhu et al. [124] introduced a significant refinement to the DBH model by quantifying the individual contribution of each type of defect to overall hardening. In their approach, the different strengthening sources were classified into two main categories: strong obstacles, which have a substantial impact on yield strength, and weak obstacles, which contribute to strengthening but with minimal influence, sometimes as little as a few MPa.

In this framework, contributions from pure Fe matrix strength ($\sigma_{Fe}$), solid solution strengthening ($\sigma_{ss}$), and small cavities less than 2 nm in diameter ($\sigma_{c<2}$) were categorized as weak obstacles. These were combined using a root-sum-square (RSS) method under the assumption that each type of obstacle acts independently to resist dislocation motion. The rationale behind using RSS superposition lies in the fact that different mechanisms impede dislocations through distinct interactions, and thus no synergistic effects were assumed.

Strong obstacles, such as carbides ($\sigma_{carbides}$), dislocation lines ($\sigma_{line}$), GB ($\sigma_{GB}$), pure Ni strength ($\sigma_{Ni}$), specific dislocation loop types or orientations ($\sigma_{<100>}$ *and* $\sigma_{1/2<111>}$), and larger cavities over 2 nm in size ($\sigma_{c>2}$) were grouped separately and also combined using RSS. The final

yield strength was then calculated by summing the weak and strong RSS contributions, providing an overall estimate of strengthening in units of MPa. The equation summarizing these contributions is shown below [124].

$$\sigma_y = \sqrt{\sigma_{\mathrm{Fe}}^2 + \sigma_{\mathrm{ss}}^2 + \sigma_{c<2}^2} + \sqrt{\sigma_{\mathrm{carbides}}^2 + \sigma_{\mathrm{line}}^2 + \sigma_{\mathrm{gb}}^2 + \sigma_{\mathrm{Ni}}^2 + \sigma_{(100)}^2 + \sigma_{1/2\langle 111\rangle}^2 + \sigma_{c>2}^2} \quad (2.10)$$

This modified DBH model was developed based on studies of neutron-irradiated T91 and HT9 ferritic-martensitic steels (BCC structure), irradiated at temperatures between 369 °C and 520 °C to dose levels ranging from 16 to 72 dpa. The model was supported by experimental data from TEM imaging and nanoindentation measurements. Although this model was developed for BCC alloys, its fundamental principles are applicable to FCC materials such as austenitic stainless steels. However, adjustments are necessary, particularly in the crystallographic planes and directions (e.g., loop types), strengthening coefficients ($\alpha$, $\mu$), and Burgers vector ($b$), to ensure compatibility with the FCC crystal structure.

Tan and Busby [125] proposed analytical equations to calculate the strength factors ($\alpha$) of individual irradiation-induced defects in SS 304 and SS 316 to obtain reliable estimations that are comparable to experimental data. These equations are valid for austenitic stainless steel in the range of dpa of 0.6 – 120 dpa and irradiation temperature of 275 – 375 $^{o}$C. The Strength factors were found to be strongly dependent on barrier type, size, geometry, and density, as well as temperature.

The hardening coefficient (α) in the DBH equation is defect-dependent and reflects the effectiveness of each defect type in impeding dislocation motion. It is given by [125]:

For dislocation loops,

$$\alpha_{Loop} = \frac{0.271A}{(1-\nu)^{\frac{1}{2}}\sqrt{Nd}(16-\pi tA)} \ln\left(\frac{0.637d}{r_0}\right) \tag{2.11}$$

Where $A$ is given by [125]:

$$A = \sqrt{16\pi Nd + 4Nd^2} - \pi^2 Ndt \tag{2.12}$$

For cavities, the hardening coefficient is given by [125]:

$$\alpha_{Cavities} = \frac{0.333}{(1-\nu)^{\frac{1}{2}}\left(1-0.816d\sqrt{Nd}\right)} \ln\left[\frac{0.247d}{r_0}\left(1-0.816d\sqrt{Nd}\right)\right] \tag{2.13}$$

Where, $N$ represents the number density of dislocation loops or cavities, $d$ is the diameter of the defect, and $r_0$ denotes the dislocation core radius that equals the Burgers vector ($b$ = 0.252 nm) for fcc structure [126]. The parameter $t$ corresponds to the thin plate thickness (or interspacing of {111} planes), which varies depending on the type of the loop and is taken as 0.207 for fcc [125], and $v$ is the poisson's ratio and equals 0.29 [127]. In Equation 2.9, the Taylor factor is 3.06, and the shear modulus ($\mu$) is 78.45 GPa for austenitic stainless steels [128] for FCC.

Figure 2-23 a comparison between the calculated and experimentally measured hardening values at room temperature and 330 °C [125]. Among the microstructural features, Frank loops were found to contribute most significantly to the hardening. The derived ($\alpha$) values can provide a reliable basis for estimating and predicting irradiation-induced hardening. Nevertheless, further investigations are needed to confirm the applicability of these findings to other alloy systems under different irradiation conditions.

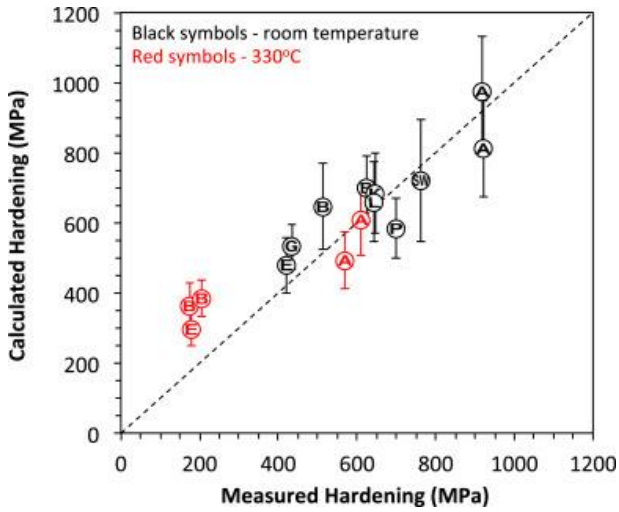


Figure 2-23 Calculated radiation hardening compared with measured results of type 304 and 316 variants at room temperature and 330 °C. The enclosed letters denote the corresponding alloy samples [125].

*Localized deformation*

The models of strengthening provided in the previous section is that austenitic stainless steels undergo a change in their primary deformation mechanism, from uniform slip to localized dislocation channeling. The deformation concentrates within specific narrow regions, while much of the surrounding material experiences minimal strain. The intensity of this localized deformation is often described by the ratio of the strain within these channels to the overall axial plastic strain. Evidence from atomic force microscopy (AFM) [129] and in situ transmission electron microscopy (TEM) studies [130, 131, 132] indicates that this ratio can surpass 10. These concentrated deformation zones form in areas with reduced defect densities, known as dislocation channels [133]. This results in significant hardening drop within the channel.

Dislocation channels pose three main features: width that characterized by TEM, spacing that characterized by SEM, and height that characterized by AFM or TEM.

A dislocation channel is essentially a defect-free narrow band in which the material is plastically deformed and largely cleared of irradiation defects as shown in the TEM image in Figure 2-24 [134] from Fe-18Cr-12Ni alloy irradiated with protons to 5 dpa at 360 ºC and

strained to 7% in BWR environment. DCs typically initiate at one grain boundary and traverse to the opposite grain boundary, because a GB often acts as both a source and sink for dislocation. When a channel interacts with a grain boundary, one of two scenarios occurs: (a) Continuous dislocation channel (CDC), the slip is transmitted across the boundary into the adjacent grain, activating a new channel on the other side as shown in Figure 2-25 (a). This requires a compatible slip system in the neighboring grain and sufficient local resolved shear stress to drive dislocations through the boundary, (b) discontinuous dislocation channel (DDC), the slip does not transmit; the channel terminates at the grain boundary without activating a corresponding slip in the next grain as shown in Figure 2-25 (b) [135]. In this case, a pile-up of dislocations forms at the boundary. These two cases have quite different implications for IASCC. A continuous channel effectively relieves stress by allowing slip to continue, whereas a discontinuous channel creates stress concentration at the blocked boundary site.

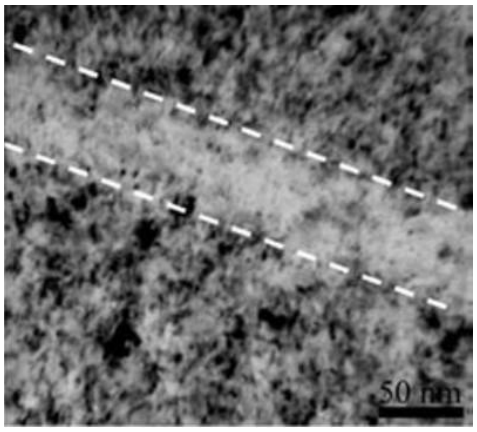


Figure 2-24 TEM image of dislocation channel in an Fe-18Cr-12Ni alloy irradiated with protons to 5 dpa at 360 $^{o}$C and strained to 7% at 288 $^{o}$C showing a region of defects-free after being cleared out by many dislocations [134].

Channel width is generally on order of 100 nm with typical spacing of 1000 – 3000 nm, The height of the channel usually depends on the applied strain level. Figure 2-26 shows the method of measuring channels spacing, width, and height using microscopy techniques such as

SEM, AFM, EBSD, and TEM and converting the measured values into real ones that consider the real projection of the channel on the surface.

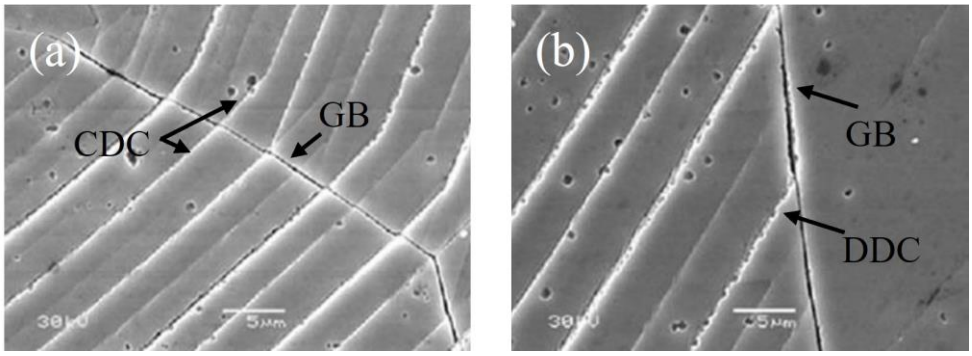


Figure 2-25 Example of (a) continuous dislocation channels crossing a GB towards the adjacent grain and (b) example of discontinuous dislocation channels arrested at the GB causing [135].

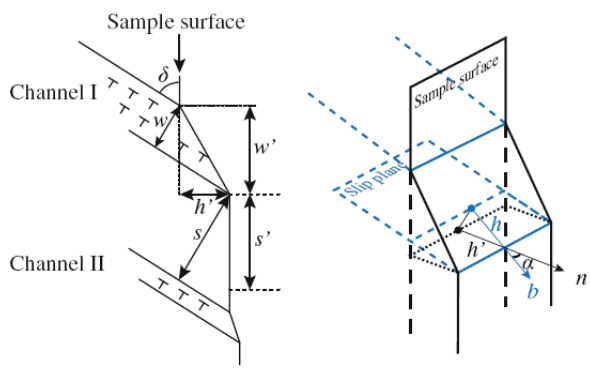


Figure 2-26 Conceptual diagram showing the measurement of DC width, spacing, and height following its intersection with the surface, and converting the measured values into real one using crystallographic analysis [83, 136].

From Figure 2-26, values of $w$`, $h$`, and $s$` must be converted to real values following these equations [83]:

$$w = w' \sin(\delta) - h' \cos(\delta) \tag{2.14}$$

$$h = \frac{h'}{\cos(\alpha)} \tag{2.15}$$

Where $\delta$ is the angle between the dislocation slip plane and the sample surface and $\alpha$ is the angle between the dislocation slip direction and the surface normal.

The number of dislocations in the DC can then be calculated from real step height and the rotated burger vector ($b$) as follows [83]:

$$n = \frac{h}{b} \tag{2.16}$$

Finally, the localized strain ($\gamma$) within the channel can be also estimated as follows [83] :

$$\gamma = \frac{h}{w} \tag{2.17}$$

It should be noted that identifying the activated slip system requires first determining the Euler angles of the grain in which the DC has formed, using EBSD. These Euler angles are essential for transforming the crystallographic frame into the laboratory frame through a rotation matrix. This analysis is critical, as it enables the evaluation of dislocation density at the surface step, typically representing the combined effects of irradiation and applied mechanical load.

Was et. al. [136] estimated a high localized strain of 100% caused by a DC that hold over 1000 dislocations in a SS 316L irradiated with protons to 5.5 dpa at 360 $^{o}$C and strained in argon to 7%. It is important to note that the number of dislocations within DC does not directly correlate with IASCC initiation, although it can sometimes be indicative of localized stress. Dislocation pile-up at the grain boundary intersection significantly increases the local stress. This localization creates intense strain gradients and stress concentrations at grain boundaries [8, 9, 135, 137, 138, 139] as shown in Figure 2-27. If the adjacent grain has a compatible activated slip system, it can accommodate the strain, allowing dislocations to transfer into the next grain and partially relieve the stress at the intersection. However, not all dislocations may be released. If no alternative path exists for dislocation movement, a step will form at the surface, and cracking is likely to initiate at the oxidized grain boundary, as the localized stress must be released under the applied load.

D. Johnson et. al. [140] used HR-EBSD to evaluate the GB normal stress profiles near an intersection between CDC-GB compared to DDC-GB as shown in Figure 2-28. The GB normal stress is quite high at discontinuous channel–grain boundary sites, while those at continuous channel–grain boundary sites exhibit no increase in stress above the ambient. Therefore, the cracking frequency of sites as a function of the GB normal stress found that there is a minimum stress below which cracking does not occur, and above this value, the cracking frequency increases with the magnitude of the stress.

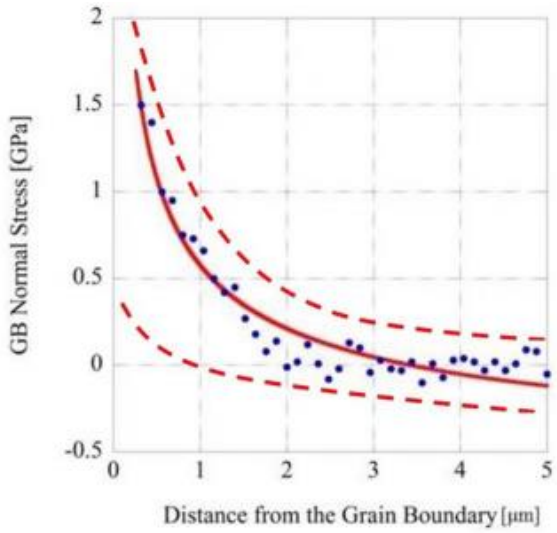


Figure 2-27 Grain boundary normal stress at the discontinuous DC-GB intersection and several micrometers away. Dashed red lines denote the upper and lower bounds for calculated stresses from HR-EBSD over the 75 analyzed sites [140].

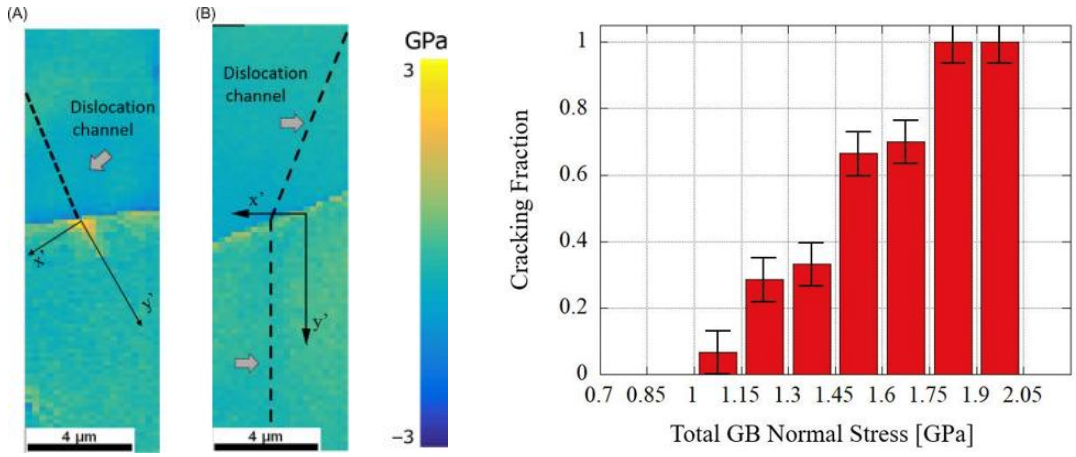


(a) (b)

Figure 2-28 Direct comparison of grain boundary normal stress profiles near (a) discontinuous dislocation channel-grain boundary intersection, and (b) near a continuous dislocation channel-grain boundary intersection and cracking fraction of HR-EBSD analyzed grain boundaries as a function of the total stress acting normal to the grain boundary [140].

*Solute nitrogen role in the irradiated microstructure of austenitic stainless steels*

Irradiation is known to increase the densities of microstructural defects. As previously mentioned, defect production rises with increasing damage levels. Since dislocation loops saturate at around 3 dpa [55] and assuming a low level of irradiation in LWR environments where other defects do not significantly contribute to the IASCC mechanism, this has two implications: first, the mechanical properties of the material will change immediately upon exposure to irradiation, altering the deformation mechanism. Second, after reaching the saturation point, further changes in the deformation mechanism will be limited, meaning the influence of irradiation will diminish, and the effect of stress will become dominant.

In SS 304LN that irradiated with 12 MeV $Ni^{3+}$ ions at 573 K, a high density of dislocation loops with smaller sizes was observed, with no precipitates (such as nitrides) detected within the grains or at GBs [41]. Furthermore, Cr-depletion was observed in high nitrogen sheets, though to a lesser extent than in low nitrogen sheets of the same alloy. The stabilization of defect clusters and small dislocation loops resulted in a higher loop density. With higher

nitrogen content, the sink strength in the alloys increased, thereby restraining GB segregation during irradiation. This suggests that nitrogen could have a suppressive effect on RIS at GBs. However, nitrogen also found to increase intergranular cracking in a BWR environment, likely due to the increased hardness within the grains, which leads to the formation of dislocation channels [141]. Figure 2-29 shows that the percentage of IG cracking rises with increased nitrogen content in SS 304L and SS 316L when strained by slow strain rate tensile (SSRT) at rate of $1.65 \times 10^{-7}$ $s^{-1}$ at 240–300 °C. The data were replotted from ref. [141]. In contrast, SS 316NG irradiated at 50 ºC has been reported to be resistant to IG cracking at 288 ºC in water containing 32 ppm DO [142] as no silicon or phosphorus were found at the GB, although it remains unclear whether this resistance is associated with the presence of nitrogen or just due to the low irradiation temperature. These results also indicate that the irradiation-induced defects have a greater impact than the environment, as a high DO environment typically has a higher corrosion potential.

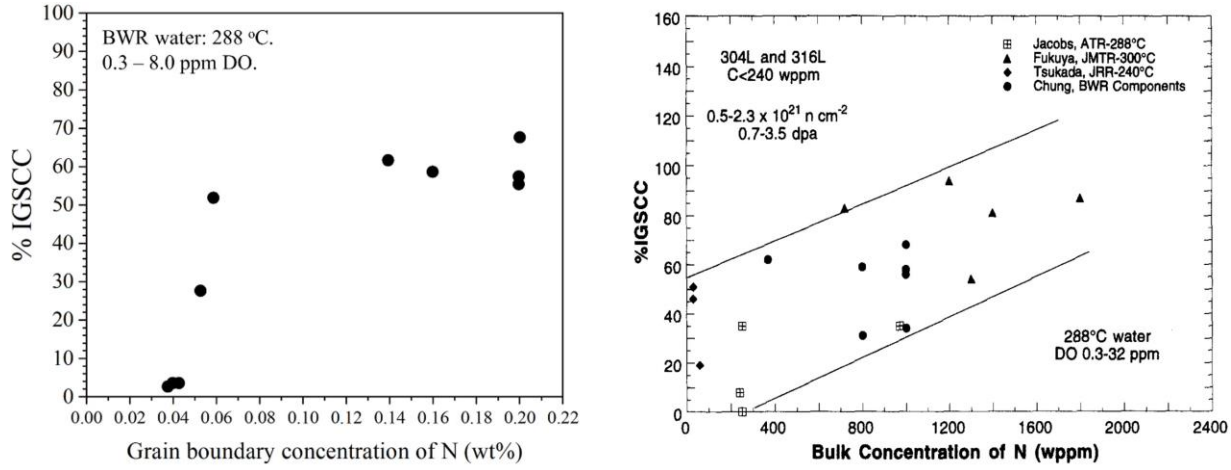


(a) (b)

Figure 2-29 Two examples (a) and (b) of the percentage of IG cracking rises with increased nitrogen content in SS 304L and SS 316L when strained by SSRT at rate of 1.65 × 10-7 $s^{-1}$ at 240–300 °C [141].

Nitrogen has a strong chemical affinity for chromium atoms over iron and tends to be repelled by nickel. This preferential bonding results in the formation of nitrogen-chromium (N–

Cr) complexes within the steel matrix. These complexes act as localized barriers that impede the movement of dislocation defects in the crystal structure that accommodate plastic deformation. As a result, dislocation motion becomes more confined to specific crystallographic planes, leading to more pronounced planar slip behavior [83]. This restricted movement contributes to increased strength and alters the material overall mechanical response.

At moderate temperatures, typically in the range of 400°C to 800°C, nitrogen atoms have sufficient mobility to diffuse through the steel lattice and form these N–Cr complexes. However, at higher temperatures (above 800°C), thermal agitation may disrupt these complexes and reduce local atomic ordering.

Furthermore, as dislocations move through the lattice, they attract interstitial nitrogen atoms, which become anchored to their cores. These nitrogen atoms are dragged along with the dislocation, increasing resistance to its motion. Importantly, the energy required for this process increases linearly with nitrogen concentration and remains independent of temperature [40], making nitrogen an effective strengthening element even under elevated thermal conditions.

P. Zhu et. al. [143] reported that, under irradiation temperatures of 300, 350 and 450 °C and dose levels of 0.37 and 3.7 dpa using dose rates ranging from $10^{-5}$ to $10^{-3}$ dpa/s, one of the most prominent microstructural changes was the decoration of dislocation networks with irradiation-induced black dots. This decoration effect has also been observed in neutron-irradiated α-iron at reactor-relevant temperatures, 300 °C [144]. The likely mechanism behind this phenomenon involves the elastic strain fields surrounding dislocations, which serve as effective sinks for irradiation-generated point defects and small mobile clusters. The role of interstitial solutes, such as nitrogen, is critical in enhancing this behavior. Nitrogen can form Cottrell atmospheres around dislocations, which further intensify the local strain field, increasing

the trapping of interstitials near dislocation lines. This enhanced trapping encourages the formation of defect clusters at an early stage. These black dots are often regarded as precursors to larger dislocation loops, especially at moderate dose rates (~$10^{-4}$ dpa/s) and irradiation temperatures between 300 °C and 450 °C, where loops have been observed to preferentially form along pre-existing dislocations [140].

### *2.2.5 Corrosion behavior in PWR environments*

The corrosion resistance of stainless steels depends on the protective properties of their passive layers, which are influenced by their physical and chemical characteristics closely linked to the film composition. In high-temperature water environments, stainless steel demonstrates excellent corrosion resistance due to the formation of chromium-rich oxide layers, which serve as effective diffusion barriers significantly reducing further surface oxidation. According to Pourbaix diagrams [145, 146], under typical PWR operating conditions (high-temperature water, neutral pH), chromium oxides ($Cr_2O_3$) and spinel-type oxides ($FeCr_2O_4$, $NiCr_2O_4$) are thermodynamically stable, enhancing the long-term integrity of the passive layer.

The oxide morphology typically consists of an outer porous layer mainly composed of magnetite ($Fe_3O_4$) and spinel-type iron-chromium oxides ($FeCr_2O_4$), with a compact, protective chromium-rich inner oxide layer predominantly composed of $Cr_2O_3$. The outer oxide layer generally forms via the re-deposition of dissolved iron and chromium resulting from corrosion process, whereas the inner layer develops through inward diffusion of oxygen and subsequent reactions with iron and chromium atoms at the metal-oxide interface, leading to a stable oxide structure.

Mechanical processing can influence oxide stability rather than stoichiometry; for instance, differences in the microstructure of the inner oxide scale are observed between cold-

worked (CW) and annealed stainless steels (304 and 316L). Specifically, the Cr-rich inner oxide forms a continuous layer in annealed materials but appears discontinuous in CW materials [147].

*Stress corrosion cracking in LWRs*

Austenitic stainless steels are susceptible to SCC in LWRs, influenced by alloy metallurgy, environmental conditions, and stress. Electrochemical potential (ECP) is a key factor, with higher corrosion potential and conductivity accelerating crack propagation [148, 149, 150]. The normal water chemistry (NWC) in BWRs, elevated dissolved oxygen (DO) increases corrosion potential, but hydrogen water chemistry (HWC) helps mitigate cracking. Water purity also plays a crucial role, as high ion concentrations and metal oxide deposits promote localized corrosion. Improved coolant purity in modern BWRs has minimized these effects. IGSCC is linked to grain boundary chromium depletion, often caused by welding or heat treatment, which prevents local passivation. Using low-carbon stainless steels and controlling weld residual stresses reduces susceptibility.

SCC in PWRs primarily affects nickel-based alloys in steam generators, vessel penetrations, and stainless steels in the reactor core [49]. SCC in nickel-based alloys typically occurs without irradiation but is strongly influenced by composition and water chemistry, as shown in Figure 2-30. This figure presents SCC occurrence in austenitic alloys as a function of nickel content in both pure water and sodium chloride environments. In pure water, alloys with high nickel content (above 70%) exhibit significant susceptibility, as shown in Figure 2-30 [151].

Austenitic stainless steels, like Type 304, have low stacking fault energies and are initially deformed by planar dislocation arrays [152]. Planar dislocation structures reduce cross-slips, leading to increased strain hardening and slip-band formation because nitrogen pins dislocations once they interact with them. Increasing nitrogen concentration in austenitic

stainless steels enhances the formation of these structures and deformation twins, but the effect of nitrogen on SFE is debated. While nitrogen is known to improve strain hardening and yield strength, its impact on SFE remains unclear, with reports both for and against nitrogen's role in increasing or decreasing SFE [153]. Cold-working significantly strengthens high-nitrogen austenitic stainless steels, achieving high yield strengths.

Eckenrod et. al. [154] conducted a study on 304 SS to assess the impact of nitrogen content on stress corrosion cracking. They found that nitrogen levels up to 0.16wt.% had insignificant effect on SCC susceptibility, but at 0.25wt.% nitrogen, the susceptibility increased. The study involved exposing U-bend and bent-beam specimens to boiling $MgCl_2$ at 154 °C for 1 hour, then analyzing cross-sections for cracking. They observed that higher nitrogen content led to more frequent and deeper cracks, though the average crack depth was reduced. These findings are consistent with Eckel's research [155, 156], which showed that adding nitrogen to 304 SS increased the rate of crack initiation but decreased the rate of crack propagation.

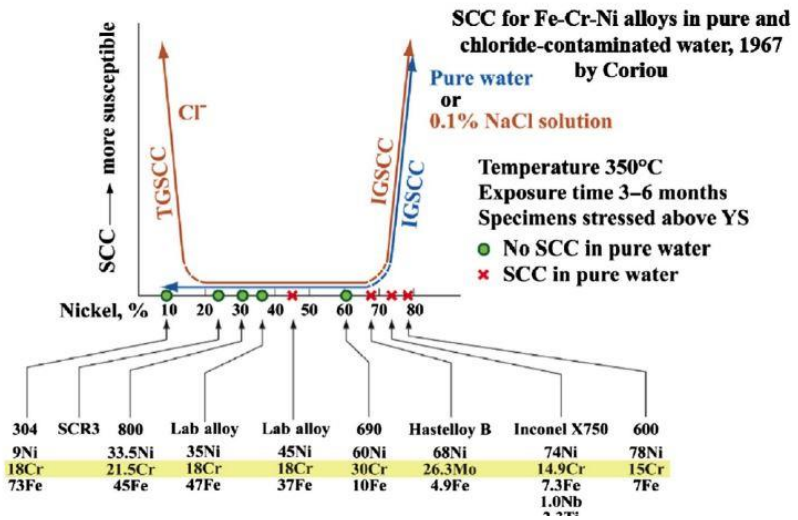


Figure 2-30 SCC occurrence in austenitic alloys as a function of nickel content in both pure water and sodium chloride environments [151].

Z. Lu et. al [157] reported that SS 316NG exhibited a lower crack growth rate in pure water at 288 $^{o}$C compared to sensitized SS 304 and solution-annealed low-carbon stainless steel,

which was attributed to the higher nitrogen content in SS 316NG that alters deformation behavior by affecting strain localization. A similar trend was observed by S.C. Bali et al. [158], who found that sensitized SS 304LN containing up to 0.16 wt.% nitrogen showed improved resistance to IGSCC in BWRs. This beneficial influence of nitrogen in reducing grain boundary sensitization, and thus indirectly lowering IGSCC susceptibility, was also noted in sensitized SS 316NG used in BWR components [159]. On the other hand, nitrogen has been shown to increase the crack growth rate in SS 316LN [160] and SS 304LN [161] due to its role in enhancing strain hardening during warm rolling, which raises crack tip strain rates. Despite nitrogen's contribution to improved passive film stability, its mechanical influence appears to be the dominant factor in governing SCC behavior. Given that SCC mechanisms are closely tied to deformation behavior and SFE, it can be concluded that nitrogen predominantly affects SCC susceptibility through its mechanical impact rather than its chemical properties. This reasoning may be extended to IASCC, as IASCC shares fundamental similarities with SCC, although it includes additional effects due to irradiation-induced changes in mechanical properties. However, there is currently a lack of data on the IASCC susceptibility of high-nitrogen stainless steels, as such alloys were not commonly employed in core structural components of earlier generations of LWRs.

In conclusion, the addition of nitrogen promotes planar dislocation motion, due to factors such as altered SFE. Although the exact cause of this planar dislocation behavior remains unclear, it is widely recognized that increased nitrogen content increases such motion. In austenitic stainless steels, planar dislocation movement is linked to higher susceptibility to SCC in high-temperature pure water. This occurs because dislocations tend to move along specific slip planes without significant cross-slips, causing them to pile up at grain boundaries where these

planes intersect. The resulting localized strain concentration at grain boundaries increases the risk of intergranular SCC.

### 2.3 Irradiated assisted stress corrosion cracking in LWRs

Irradiation-assisted stress corrosion cracking (IASCC) is an intergranular cracking type that occurs in irradiated austenitic alloys exposed to high-temperature water and stress. It was first observed over six decades ago in the 1960s, when stainless steel nuclear fuel cladding began cracking under irradiation [79], subsequent incidents showed IASCC affecting various core internals in BWRs, including 304 SS control rod tubes, fuel assembly bolts, control blade components, and instrument guide tube [80]. In the 1980s–1990s, welded core shrouds in BWRs experienced intergranular cracking at relatively low stress, highlighting IASCC as a pervasive issue in aging reactors. Cracking in hydrogenated water is typically observed at roughly four times higher fluence than in oxidizing water, with IASCC enhanced at elevated temperature [55]. In PWRs, IASCC has been reported in core internals such as baffle-former bolts, those are made of austenitic stainless steels of types 316 and 347, have been found in several PWRs after decades of operation stress [70, 162]. Other components such as guide thimble flux tube made of CW SS 316 reported to experience IASCC. Several other components reported to have suffered from IASCC in both PWR and BWR environments are listed in Table 2-1, highlighting its occurrence across a wide range of components, particularly those made of austenitic stainless steel [163, 164].

These observations established IASCC as a unique degradation phenomenon in LWR core components, driven by the synergistic effect of neutron irradiation, corrosive reactor water, and tensile stress. Unlike thermal sensitization-induced cracking, IASCC requires irradiation damage and can occur even in low corrosion potential PWR water and at stresses way below the

yield strength of the material. This behavior characterized IASCC as an unconventional phenomenon that complicated early efforts to develop a clear mechanistic understanding [20, 55]. Over time, research shifted from viewing IASCC as an isolated phenomenon to identifying key radiation-induced material changes responsible for this cracking mode.

Table 2-1 IASCC service experience [163, 164].

| Component | Material | Reactor type | Source of stress |
|---|---|---|---|
| Fuel cladding | SS 304 | BWR | Fuel swelling |
| Fuel cladding | SS 304 | PWR | Fuel swelling |
| Neutron source holders | SS 304 | BWR | Welding & Be swelling |
| Instrument dry tubes | SS 304 | BWR | Fabrication |
| Control rod absorber tubes | SS 304/ 304L/ 316L | BWR | $B_4C$ swelling |
| Fuel bundle cap screws | SS 304 | BWR | Fabrication |
| Control rod follower rivets | SS 304 | BWR | Fabrication |
| Control blade handle | SS 304 | BWR | Low stress |
| Control blade sheath | SS 304 | BWR | Low stress |
| Control blades | SS 304 | PWR | Low stress |
| Plate type control blade | SS 304 | BWR | Low stress |
| Baffle former bolts | SS 316 CW, SS 347 | PWR | Torque, swelling |
| Core shroud | SS 304, 316, 347 | BWR | Weld residual stress |
| Top guide | SS 304 | BWR | Low bending stress |
| ***Note:*** *Cracking of core internal occurs away from high neutron and gamma fluxes.* | | | |

In PWR cores, the most susceptible components to IASCC are the stainless steel structural internals that receive high neutron fluence such as fuel cladding made of type 304, control rod blades made of type 304, various bolts and springs made of alloy X-750, and Baffle-former bolts made of types 316L or 347 and thimble flux tubes made of CW SS 316 [164]. BFBs which secure the core baffle plates, are particularly prone to IASCC and have been widely

reported to experience it in PWR environments, especially those made of SS 316L [79, 147, 162, 164, 165] or SS 347 [70, 165]. Other PWR internals exposed to high fluence, and stress have also shown susceptibility. Flux thimble tubes (in-core instrumentation tubes) and guide tubes [166, 167, 168, 169], which are often made of stainless steel and sit in the core, have exhibited IASCC in both service and testing.

Historically, neutron-irradiated samples, whether cut from retired PWR components [70, 166, 167, 168, 169] or exposed in fast reactors like BOR-60 [170, 171], have formed the basis of IASCC testing. Numerous studies on IASCC initiation have relied on irradiated segments extracted from decommissioned reactor components, such as flux thimble tubes (often in O-ring configuration) and baffle-to-former bolts, to assess cracking susceptibility. Figure 2-31 shows the IASCC initiation susceptibility of austenitic stainless-steel alloys in a PWR environment, illustrating a threshold of approximately 50–60% of the irradiated yield stress at low to intermediate dose levels (<10 dpa) and around 40% YS at higher doses. While this plot serves as a foundational reference in IASCC initiation studies, it lacks consideration of exposure time, an important influencing factor. Additionally, it excludes data from proton-irradiated specimens, as existing studies have exclusively focused on neutron-irradiated samples derived from retired PWR core internals.

Despite offering valuable insights into the susceptibility of austenitic stainless steels to IASCC in PWR conditions, the dataset is largely constrained to CW SS 316, with limited data available for SS 304 and few data points from SS 347. As a result, the behavior of other austenitic stainless-steel candidates for light water reactors remains underexplored. Moreover, the effects of mechanical processing, heat treatments, and compositional variations have yet to be systematically incorporated. Given the logistical and regulatory challenges associated with

obtaining neutron-irradiated materials, often restricted to components removed from operating reactors, there is a critical need for alternative methods, such as proton irradiation, to expand the existing database and improve our mechanistic understanding of IASCC initiation.

Moreover, the plot underscores one of the key challenges in studying IASCC: the inherently stochastic nature of crack initiation. Although statistical models [172] have been developed to more precisely determine the IASCC initiation threshold, their reliability remains limited by the current scarcity of data and the lack of comprehensive coverage across different experimental conditions and material variables, as previously discussed. A conservative approach is used here and defines the threshold as the lower-bound curve that connects the minimum observed initiation stresses across all neutron irradiation levels, serving as a cautious estimate below which no cracking has been observed. Accordingly, the threshold dashed line presented in Figure 2-31 suggests that the minimum stress required to initiate IASCC in a PWR-relevant environment is approximately 40% of the irradiated yield stress. Later in this study, experimental uncertainty will be incorporated into the determination of initiation stress, which will further lower the threshold to enhance conservatism in assessing IASCC susceptibility.

The development of IASCC is linked to several irradiation-induced changes in austenitic stainless steels. These events are interconnected, sequential, and complex. The process begins with irradiation, which induces radiation hardening through the formation of defect clusters, primarily dislocation loops, within the material. Neutron irradiation at LWR temperatures (280–340 °C) produces a high density of faulted dislocation loops, which act as obstacles to slip and significantly increase the yield strength (often by a factor of about 4 - 5 compared to the unirradiated state [173, 174, 175]. The increase in the yield strength itself has been correlated with SCC susceptibility, when the yield strength exceeded 600 MPa (due to irradiation),

intergranular cracking became inevitable in high-temperature water [176]. Similarly, crack growth rates were found to increase with yield strength in irradiated steels [177, 178].

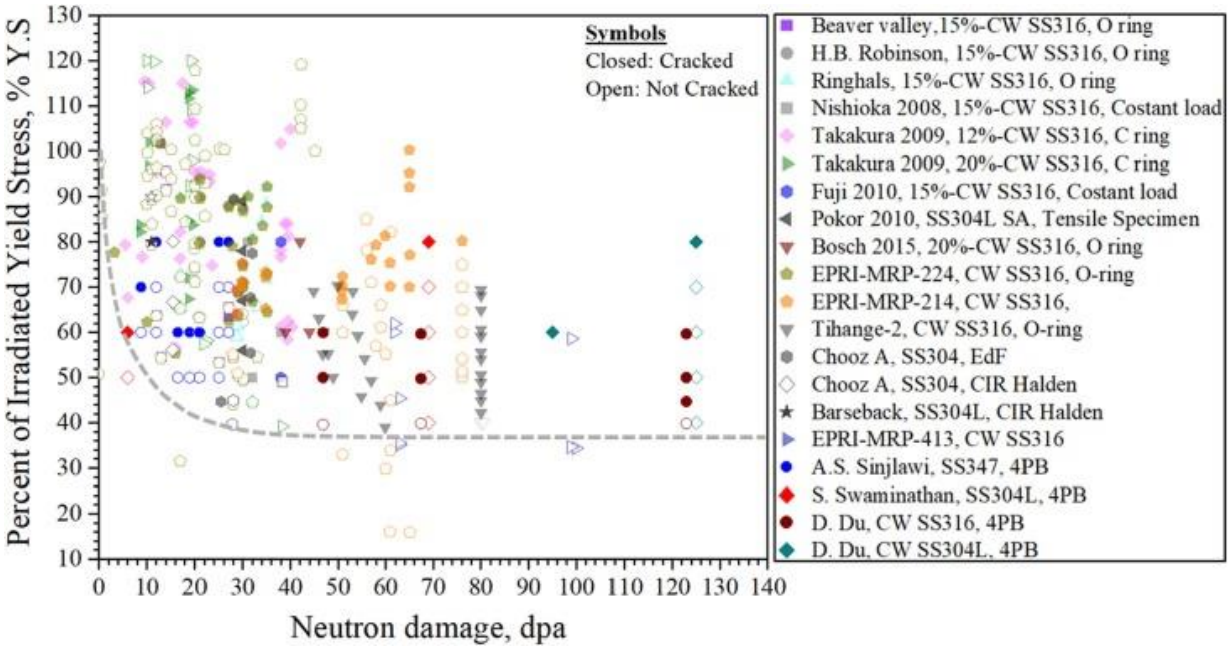


Figure 2-31 Plot of the percent of the irradiated yield stress (%YS) at which cracking occurs as a function of damage level, in dpa, for irradiated austenitic stainless steel alloys strained in simulated PWR primary water [20]. The curve represents a threshold at which no cracking observed below it.

RIS, on the other hand, significantly modifies the grain boundary chemistry. Neutron irradiation causes chromium to deplete and light elements (P, Si) and nickel to enrich at grain boundaries to form precipitates such as Ni–Si rich G-phase or γ' precipitates. For example, a grain boundary in 304 SS irradiated to a few dpa may see Cr drop from 18% in the matrix to <12% at the boundary, with Ni and Si correspondingly higher. This chromium depletion can prevent formation of the stable chromia ($Cr_2O_3$) film at the boundary [78], especially in oxygenated water, rendering the boundary prone to oxidation and corrosion. The Cr depletion at the GB in austenitic stainless steels as a function of irradiation dose, revealing a trend of increasing Cr depletion with higher dose levels. Over the past decades, the initiation of IASCC has been closely associated with GB oxidation, primarily attributed to chromium depletion at the

grain boundaries because of RIS [79, 81, 80], when RIS continues to deplete chromium at the GB, the susceptibility to oxidation penetration increases [179]. However, chromium depletion at the GB remains a critical factor for crack initiation, particularly when the Cr content drops the threshold for forming a stable and protective layer.

The Si segregation at the GB has been also investigated and suspected over the years in the IASCC initiation and propagation. Si is observed to segregate to high levels at the GB and can reach more than five times its content in the matrix. Busby et. al. [180] investigated the role of Si in high-purity SS 316 irradiated with protons to 5.5 dpa at 360 $^{o}$C and doped with 1.0 wt.% Si, the results showed a severe IASCC in normal water condition and the concentration of Si at the GB following the tests measured at 6 wt.%. Andresen et. al. [181] reported a significant increase in the growth rates in SS 304L with silicon content of 1 – 5 wt.% in both reducing and oxidizing environments as shown in Figure 2-32. The issue with silicon that it oxidizes to form $SiO_x$ when interact with oxygen, this oxide is brittle and not stable in LWR-relevant environment, thus its presence at the crack tip has been reported to drive the crack growth [70, 181, 182, 183].

Silicon has lower partial oxygen potential compared to Cr, Ni, and Fe; therefore, oxygen preferentially oxidizes silicon when penetrating several nanometers ahead of the crack tip. The resulting $SiO_x$ oxide exhibits inferior mechanical stability relative to Cr-rich oxides, fracturing more readily under external mechanical loading, dissolving quickly in the high temperature water and thereby facilitating crack advancement. That's concluded mechanism shown in Figure 2-33. Recent studies [20, 70] have highlighted a notable mechanism involving silicon, demonstrating its direct role in crack growth via early oxidation at the crack tip, forming a brittle and unstable $SiO_x$ oxide in PWR environments. In These works, $SiO_x$ was observed for the first time at the crack tip through HR-TEM which was not yet dissolved in the PWR water as shown

in Figure 2-33. However, it is still unknown whether Si plays a comparable role at the crack initiation surface or if its influence is restricted to the crack tip. Further analysis, including measurements of crack growth rates, is necessary to determine whether Si actively accelerates crack propagation or if its primary contribution is limited to the initiation stage.

Finally, the combined effect of Cr depletion and impurity enrichment accelerates GB oxidation in PWR-simulated water. With a weakened $Cr_2O_3$ film and $SiO_x$ nucleation sites, RIS-modified GBs corrode at electrochemical potentials that would be protective on the unirradiated matrix. Radiolysis-driven anodic shifts at irradiated crack tips further exacerbate local oxidation, paving the way for intergranular crack initiation and growth under operational PWR conditions [141, 180, 184, 185].

Grain boundary oxidation is recognized as a primary precursor for cracking in irradiated austenitic stainless steels exposed to PWR environments. Upon exposure, the surface of the material undergoes oxidation, forming a protective oxide layer.

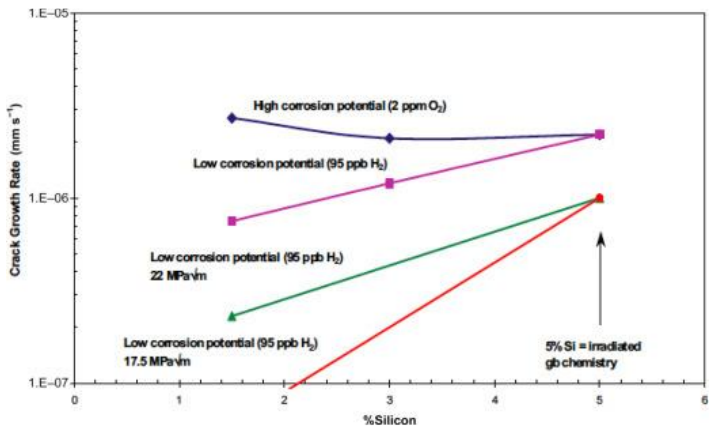


Figure 2-32 Effect of Si on SCC in 304L at 30 MPa/m in 288°C pure water [181].

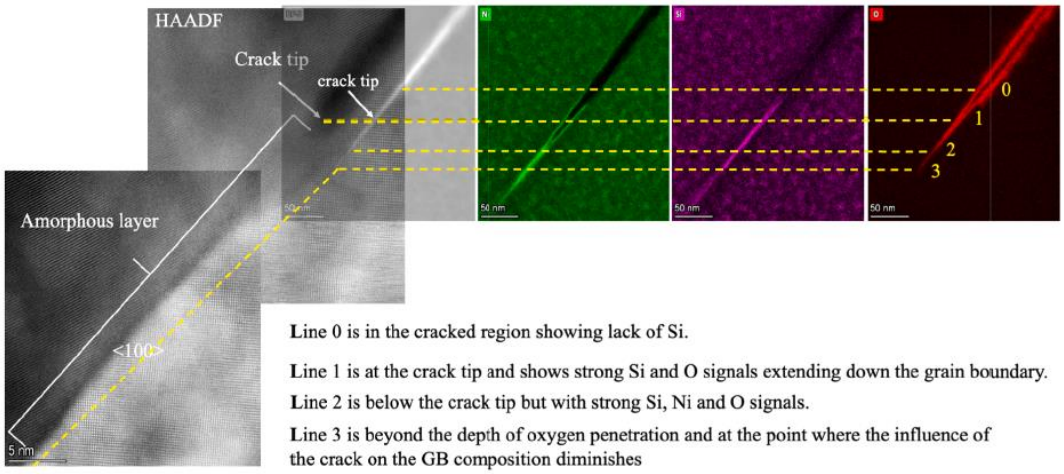


Figure 2-33 High resolution TEM image and STEM-EDS maps of a crack tip in 347 SS irradiated to 26.4 and strained to 60 % of the irradiated yield stress in KOH at 320 ºC showing amorphous silicon oxide (a-$SiO_x$) extending over 50 nm ahead of the crack tip and down the GB [20].

This layer is typically enriched with Cr and oxide structures such as Chromia ($Cr_2O_3$) and spinel ($Cr_xFe_{1-x}O_4$) [186, 187, 188]. Regardless of its exact stoichiometry, the protective oxide generally exhibits sufficient integrity to inhibit further oxidation, particularly along the grain boundaries. However, in unirradiated austenitic stainless steels, GB oxidation is rarely observed. In contrast, under irradiation in the PWR environment, GB oxidation becomes prominent and typically exhibits a multilayered structure. This structure consists of a nickel-rich interfacial layer between the metal matrix and the oxide, along with distinct iron-rich and chromium-rich oxide layers. These features have been consistently observed in PWR environment in various irradiated austenitic stainless steel alloys along IG crack flanks [179, 183, 189].

K. Fujii et. al. [190] linked the degradation of the GB to its microchemistry where phosphorus segregation (RIS effect) at the GB reduced its strength by 50% when its mass percent was almost doubled. Another study by K. Fuji et al [191] reported a substantial reduction (up to -70%) in GB strength in oxidized Alloy 600 in PWR environment compared to its unoxidized counterpart, leading to earlier crack initiation in PWR environments. This weakening was attributed to the weak bonds at oxide-metal interface at the GB [192]. Furthermore, GB

oxidation in PWR environments has been directly correlated with the neutron irradiation damage [193], such that the extent of oxidation increases with increasing dpa levels. First, RIS-driven Cr depletion occurs via inverse-Kirkendall diffusion [77] under irradiation, faster-diffusing Fe and Cr vacancies migrate toward GBs while slower-diffusing Ni segregates, leaving narrow (3–4 nm) Cr-depleted zones (<12 at.% Cr) that no longer support a protective $Cr_2O_3$ film [184]. Such depletion correlates with active intergranular corrosion in constant-extension-rate tests at 288 °C, but direct annealing studies show that IASCC susceptibility can vanish before GB Cr levels recover, implying that Cr depletion is necessary but not alone sufficient to trigger cracking [180].

GB oxidation alone is not sufficient to induce IG cracking, studies have shown that oxidized grain boundary intersections with discontinuous channels are far more likely to crack initiation sites than those with continuous channels [8, 9, 137, 138, 139]. In other words, a channel that "dead-ends" at a boundary imparts a severe local strain incompatibility. Atomistic and finite-element analyses have quantified the stress enhancement: the normal stress on a grain boundary at a DDC intersection can be on the order of 4–8 times the applied stress. For example, one TEM in situ study on 0.16 dpa 304L SS found that for a channel with a typical aspect ratio, a global stress of around 320 MPa translated to an impinging stress of 1.3–2.6 GPa at the blocked boundary. Similarly, large-scale molecular dynamics simulations have calculated 1.5–3.5 GPa stress at a DDC–GB impact site. These extreme local stresses can exceed the fracture strength of the grain boundary, especially given that the boundary may be embrittled by RIS or oxide penetration. The oxidized grain boundaries act as preferential fracture paths under loading because of their weakened cohesion and reduced fracture resistance [70, 171, 170, 194]. The crack path if it grows along the oxide looks tortuous, following oxidized GBs, and is often filled

with oxide debris, indicating an oxide rupture by stress concentrators after the GB oxidation [70, 171].

The mechanism of the IASCC initiation in the PWR environment of austenitic stainless steels can be summarized as the proposal presented by Was et al. [20] that IASCC initiation is essentially caused by grain boundary oxidation that takes place first followed by the presence of stress concentrator at the oxidized GB once the dislocation channels are formed. Evidence for this comes from detailed microscopy: intergranular cracks in irradiated stainless steels often exhibit oxides along their crack faces and even ahead of the crack tip [70, 171]. For example, in a neutron-irradiated SS 347 (7.8–26.4 dpa) tested in PWR water, STEM analysis showed a double-layer oxide (inner Cr-rich spinel, outer Fe-rich oxide) on the crack surface, and oxygen penetration about 40 nm ahead of the crack tip into the grain boundary, precisely where Si was segregated. The crack tip region was depleted in Fe and Cr, due to RIS effect, and an oxide had formed in that depleted region. This suggests that before a crack propagates, the grain boundary is chemically attacked (oxidized) at the weak point created by the dislocation channel. Importantly, experiments have found that cracking can initiate well below the macroscopic yield strength because of this mechanism because the mechanical properties of the oxidized GB reduce significantly upon oxidation compared to pristine boundaries. An analysis of cracked GBs showed that cracks nucleate at DC–GB intersection sites where the local stress is amplified and oxidation has occurred, even though the bulk stress is modest.

S. Swaminathan et al. [171] reported that grain boundary oxidation plays a critical role in initiating IASCC. This conclusion was based on observations made on neutron-irradiated SS 304L specimens exposed to a PWR water environment without applied strain. Subsequent mechanical straining conducted in an ultra-high-purity argon environment revealed GB crack

initiation at stress levels as low as 50–60% of the alloy's irradiated yield strength, strongly suggesting that prior GB oxidation was a primary contributing factor to crack initiation.

The dislocation channel provides a localized mechanical driving force (i.e. a microscopic stress riser), and the environment provides a chemical driving force (i.e. corrosive attack of the GB). Together, they produce intergranular cracks. Grain boundary oxidation alone (from RIS) is not sufficient in low-stress areas, and mechanical factors alone (DCs pile up) rarely crack a boundary in inert gas environments [168, 171]. This is why IASCC initiation is often described as a DC–GB synergy: the dislocation channel creates conditions (strain and bare metal exposure) that allow rapid GB oxidation, resulting in a brittle boundary ready to crack. Once a small intergranular crack initiates, it can then propagate along the GB under the applied stress. In summary, grain boundary oxidation at sites of dislocation channel intersection is now considered a primary mechanism for crack nucleation in IASCC. It explains how cracks initiate stress far below the macroscopic yield and why only irradiated (damage-altered) boundaries suffer cracking in otherwise benign environments. The process of IASCC initiation is concluded in Figure 2-34.

Finally, the role of IASCC in SS 304LN was not reported for the reason that this alloy was not considered as a core internal material. A lack of IASCC information on this alloy requires further studies that can provide the susceptibility of this alloy to IASCC initiation in PWR environment and how this compares with other stainless-steel counterparts.

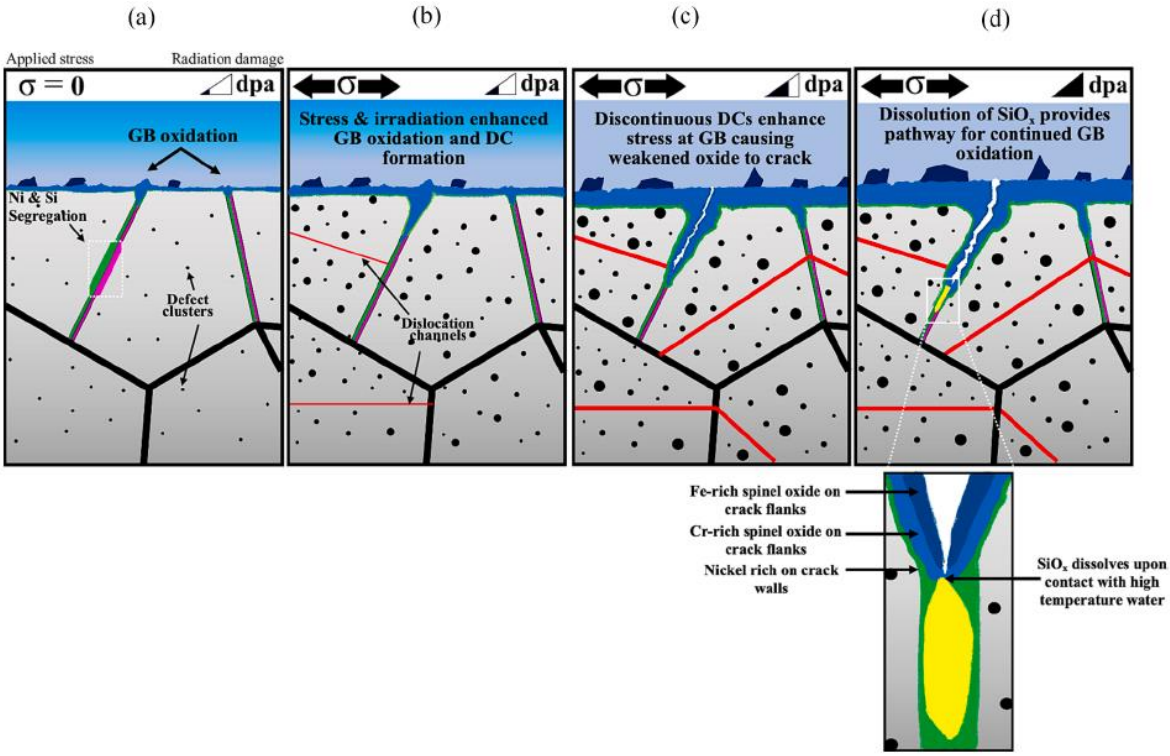


Figure 2-34 Schematic illustration of the IASCC process: (a) radiation produces defect clusters and drives solute segregation to grain boundaries, initiating oxidation at low doses; (b) applied stress combined with irradiation accelerates oxidation and promotes dislocation channel formation; (c) dislocation channels intersect grain boundaries near the surface, fracturing the oxidized and weakened regions; (d) exposure of Si-enriched boundaries to water leads to amorphous $SiO_x$ formation/dissolution, enabling continued oxidation and crack initiation [20].

## Chapter 3 Objectives

The objective of this work is to determine the role of solute nitrogen in the initiation of irradiation-assisted stress corrosion cracking (IASCC) in austenitic stainless steels exposed to high-temperature water environments. A proposed hypothesis on the role of solute nitrogen in promoting IASCC is as follows:

***Solute nitrogen will stabilize dislocation loops, leading to a higher density and smaller size, thus impeding the motion of dislocations within the matrix which eventually increases the matrix hardness. As a result, localized deformation in the form of dislocation channels is enhanced, which leads to increased IASCC susceptibility***.

Four sub-objectives were introduced to evaluate the hypothesis against experimental data. The first sub-objective investigates the nitrogen-induced stabilization of dislocation loops. By comparing dislocation loop characteristics between low-nitrogen and high-nitrogen alloys. Transmission electron microscopy (TEM) will be used to characterize the density, size, and distribution of dislocation loops, cavities, precipitates, or other defects. In addition, interactions between dislocation loops and solute nitrogen, as well as other nitrogen-related complexities, will be examined. The observed differences in these characteristics between the low- and high-nitrogen alloys will be systematically reported.

The second sub-objective is to determine the extent of irradiation-induced hardening with the presence of nitrogen following the interaction of nitrogen with the irradiation-induced defects. This will be done using microhardness indentation. Evaluating the nitrogen interaction with dislocation loops (in the first sub-objective) will be reflected on the materials hardening

since nitrogen stabilizes dislocation loops thus increasing their density, which in turn enhances matrix hardening, as these loops act as obstacles to dislocation motion. This mechanism is expected to contribute to the increased hardness observed in high-nitrogen alloys under irradiation.

The third sub-objective is to determine the dislocation channels behavior, as the hardness of the steel is expected to increase with higher nitrogen content and under external loads, a localized deformation occurs in the matrix allowing dislocation to move through it forming the dislocation channel. It is expected to see more dislocation channels in the high nitrogen alloys compared to the low nitrogen one. Constant extension rate (CERT) testing in an argon environment at 340 $^{o}$C will be conducted to analyze dislocation channel characteristics, such as density and spacing, using scanning electron microscopy (SEM) and electron backscatter diffraction (EBSD), as well as measuring step heights with atomic force microscopy (AFM).

The fourth subobjective is to determine how solute nitrogen eventually affects the IASCC initiation susceptibility. As the dislocation channels are expected to increase, the intersections with grain boundaries will increase as well. Once the GB is oxidized, its strength will drop significantly, therefore, once DC intersects with the oxidized GB, a localized stress becomes high enough to cause GB separation and then crack initiation. The higher DCs density will increase the IASCC initiation susceptibility. The 4-point bend test in PWR primary water will be used to assess the IASCC initiation susceptibility and to analyze the crack tip microstructure using high-resolution TEM and assessing elemental composition through energy-dispersive X-ray spectroscopy (EDS).

# Chapter 4 Experimental Conditions

The primary objective of this study is to quantitatively evaluate the influence of solute nitrogen on irradiation-assisted stress corrosion cracking (IASCC) initiation in austenitic stainless steels subjected to high-temperature water environments. This objective was addressed through investigations on two austenitic stainless-steel alloys: one with a high nitrogen content (SS 304LN) and another with relatively low nitrogen content (SS 304L-R).

To achieve this, the investigation was structured at two distinct levels: macroscopic and microscopic. At the macroscopic level, the study compared two proton-irradiated austenitic stainless-steel alloys, one with a high nitrogen content (SS 304LN) and another with a relatively low nitrogen content (SS 304L-R), using four-point bend (4PB) and constant extension rate tensile (CERT) tests. The 4PB tests were employed to determine the minimum stress required to initiate cracking, thereby capturing the combined effects of irradiation, environment, and applied stress on IASCC susceptibility. In parallel, CERT tests conducted in high-temperature argon provided insights into dislocation channel characteristics, isolating the effects of irradiation and mechanical loading. At the microscopic level, transmission electron microscopy (TEM) was utilized to analyze proton-induced defects, including dislocation loops, cavities, precipitates, and radiation-induced segregation, and to perform crack tip analyses, thereby elucidating the mechanisms underlying cracking in both irradiated alloys.

## 4.1 Alloys

In this study, two austenitic stainless-steel alloys were investigated: AISI SS 304L (grade EN 1.4307) and AISI SS 304LN (grade EN 1.4311). Both alloys were supplied by Outokumpu, a

high-performance stainless-steel manufacturer based in Sweden. The alloys underwent identical heat treatment, consisting of solution annealing at 1070° C (1958 °F) followed by rapid cooling in water and air. Chemical compositions of these alloys are provided in Table 4-1, and the details of the mechanical properties provided by the vendor are summarized in Table 4-2.

Table 4-1 Chemical composition of alloys used in this study in wt.% obtained from materials vendor and from the chemical analysis performed by Luvak Inc (USA).

| Alloy | Fe | Cr | Ni | C | N | Si | Mn | P | S | Mo |
|---|---|---|---|---|---|---|---|---|---|---|
| Vendor data | | | | | | | | | | |
| SS 304L-R | Bal. | 18.1 | 8.1 | 0.017 | 0.068 | 0.33 | 1.24 | 0.034 | 0.001 | NR |
| Luvak Inc. chemical analysis data | | | | | | | | | | |
| SS 304L-R | 71.6 | 17.6 | 7.95 | 0.016 | 0.064 | 0.33 | 1.24 | 0.041 | 0.0005 | 0.44 |
| | | | | | | | | | | |
| Vendor data | | | | | | | | | | |
| SS 304LN | Bal. | 18.2 | 8.6 | 0.025 | 0.140 | 0.43 | 1.55 | 0.034 | 0.001 | NR |
| Luvak Inc. chemical analysis data | | | | | | | | | | |
| SS 304LN | 70.1 | 18.2 | 8.62 | 0.031 | 0.146 | 0.44 | 1.55 | 0.027 | 0.0005 | 0.37 |

*NR: not reported.*

Table 4-2 Mechanical properties of both alloys from the vendor's certificate

| Alloy | Yield strength (MPa) | Ultimate tensile strength (MPa) | Elongation (%) |
|---|---|---|---|
| SS 304L-R | 337 | 633 | 56 |
| SS 304LN | 357 | 672 | 51 |

After receiving the material sheets, the chemical compositions, microstructure, and mechanical properties were analyzed to verify the vendor's data. Chemical analysis was conducted by Luvak Inc. (USA) using multiple methods: carbon and sulfur were measured via combustion infrared detection (ASTM E1019-18 [195]), nitrogen via inert gas fusion (ASTM E1019-11), and other elements via direct current plasma emission spectroscopy (ASTM E1097-12 [196]). Table 4-1 lists the results of the chemical analysis provided by Luvak for both alloys.

### *4.1.1 Grains morphology and size*

The microstructure of each alloy was examined to determine grain morphology and size across all planes and identify the presence of any phases other than austenite. To reveal the grains, electrochemical etching with a 70% Nital solution was used since it selectively attacks GBs and ferrite precipitates, as shown in Figure 4-1 (a) for both planes of SS 304L-R and Figure 4-2 (b) for both planes of SS 304LN. Grains along the longitudinal-transverse (L-T) plane appear equiaxed while along the longitudinal-short-transverse (L-ST) plane, elongated grains located near the δ-ferrite regions were observed. Continuous networks of δ-ferrite stringers were observed along the rolling direction in the L-ST plane, with the density of these ferrite pools increasing closer to the mid-thickness of the bulk.

Grain size measurements were performed using the intercept method in accordance with ASTM E112-13 [197]. The microstructure was examined using scanning electron microscopy (SEM) images at 100x magnification and multiple vertical, horizontal, and diagonal lines overlaid the SEM image to count the line-GBs and line-triple junction intersections, this process was repeated on at least two additional surface locations. The intersections at GBs and triple junctions (TJ) were recorded, and the average grain size along with the standard deviation was determined.

The grain size measurement for both alloys and planes (L-T and L-ST) are plotted in Figure 4-2. For SS 304L, the average grain size along the L-T plane was 22.6 ± 3.9 μm while along the L-ST plane, it was 21.35 ± 6.2 μm. In contrast, SS 304LN exhibited relatively smaller grain sizes, with 19.93 ± 1.1 μm along L-T plane and 19.75 ± 4.0 μm along the L-ST plane.

### *4.1.2 Mechanical properties*

Hardness and yield strength of the alloys were determined at 25 $^{o}$C and additionally, yield strength was determined at 340 $^{o}$C.

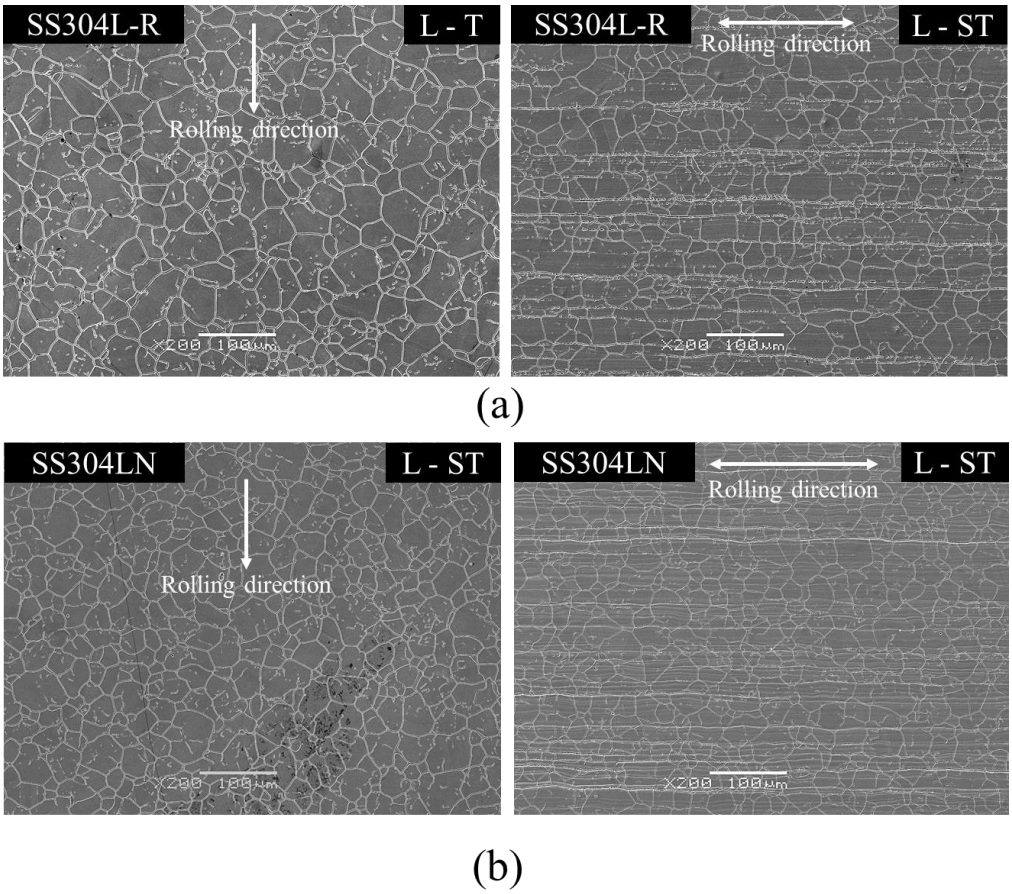


Figure 4-1 Grains morphology of (a) SS 304L and (b) SS 304LN.

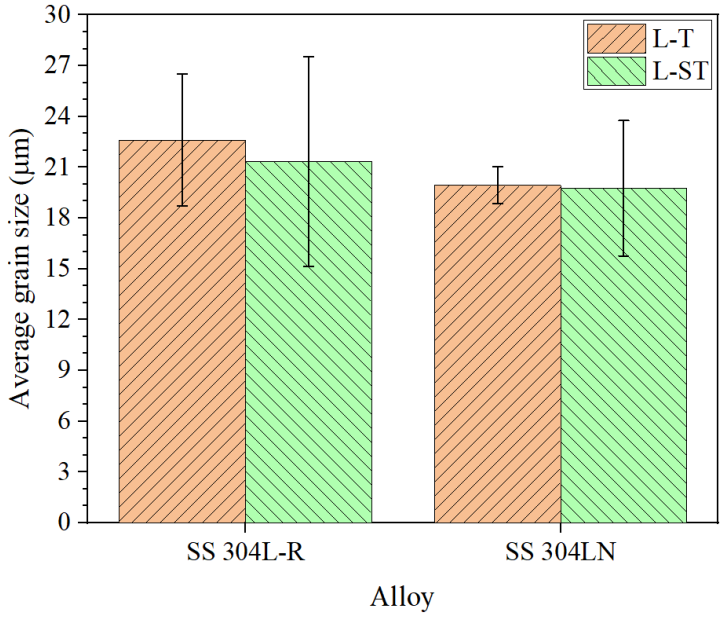


Figure 4-2 Average grain size for SS 304L-R and SS 304LN for planes L-T and L-ST.

#### *4.1.2.1 Room temperature hardness*

Hardness measurements were performed using Vickers microhardness ($H_V$) indentation on the L-T and L-ST planes. The hardness measurement was performed for multiple purposes; (1) verify the room temperature mechanical properties against the vendor's specifications, (2) identify the rolled surface condition using data from the L-T plane, (3) identify the depth of the rolled surface layer along the L-ST plane to ensure the non-uniform properties caused by the damage during the rolling process are excluded, and (4) identify the depth with the lowest density δ-ferrite pools to machine samples from these regions.

Two samples from each alloy, each measuring 1 cm × 1 cm × the steel plate thickness (mm), were cut from the plates using a bandsaw. The as-received surface (L-T) was unsuitable for Vickers indentation due to its high roughness, and the L-ST plane had burrs from the bandsaw cut. Therefore, both surfaces were mechanically polished to a P4000 grit finish, followed by abrasive polishing to 1 µm. The Vickers hardness test followed ASTM E384 [198], utilizing a pyramidal diamond indenter with face angles of 136°. An applied load of 100 gf was used, with measurements conducted at room temperature. For the L-T measurement, three indentation profiles were analyzed, each consisting of 20 indents along the rolling direction. While for the L-ST measurement, a matrix of 7 by 10 indents was used, the profile started around 50 µm from the surface down to about 2000 µm with 200 µm a distance between indents as shown in Figure 4-3. The final hardness value was determined as the average of these measurements. The statistical distribution of the hardness values for the L-T and L-ST planes of both alloys is shown in Figure 4-4. This figure highlights the non-homogeneous surface properties caused by microstructural damage from the rolling process.

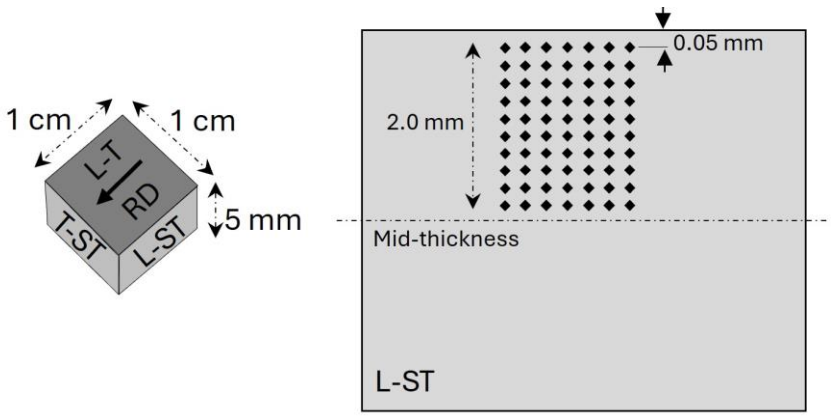


Figure 4-3 Indentation profile along the L-ST direction to identify the homogenous properties along the thickness.

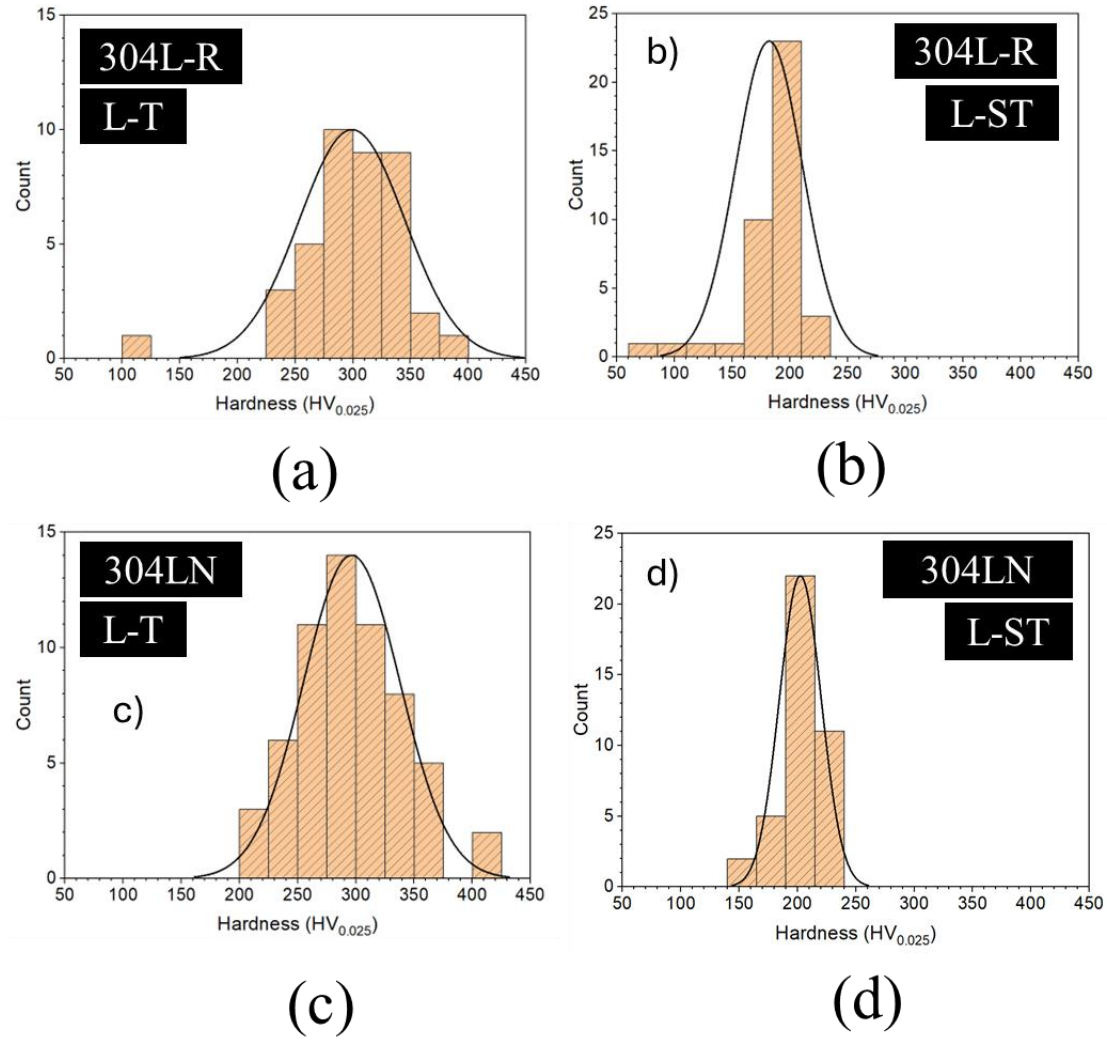


Figure 4-4 Hardness measurement distribution for SS 304L-R along (a) L-T plane and (b) L-ST plane and for SS 304LN along (c) L-T plane and (d) L-ST plane

Figure 4-5 shows the hardness profile across the samples thickness, noting that the seven horizontal lines from each row in the matrix mentioned above were averaged into a single point, resulting in a vertical line consisting of 10 averaged measurements. This profile was important for determining the regions where four-point bend (4PB) samples and tensile bars would be machined. For SS 304LN, the results suggest that machining should start at a minimum of 200 µm from the surface to avoid the damaged layer, while for SS 304L, a distance of 50 µm was sufficient.

Another important feature was the presence of δ-ferrite network, which were concentrated at the mid-thickness of the plates as a result of rolling. To reveal the morphology of grains and precipitates along the L-ST plane, Nital 70% electrochemical etching was used. Figure 4-6 shows the L-ST plane morphology, highlighting the distribution of δ-ferrite stringers across the sample thickness. It was observed that the region around 300 µm depth from the surface had the least δ-ferrite stringers in SS 304LN, while in SS 304L, the least stringers were found deeper at 500 µm.

As a result, 4PB and tensile sample machining by EDM was performed by removing a surface layer of 100 µm in depth. The new surface was designated as the to-be-irradiated surface. This approach effectively avoided both the damaged surface layer and the regions with the highest concentration of δ-ferrite stringers, which could potentially influence the IASCC initiation mechanism.

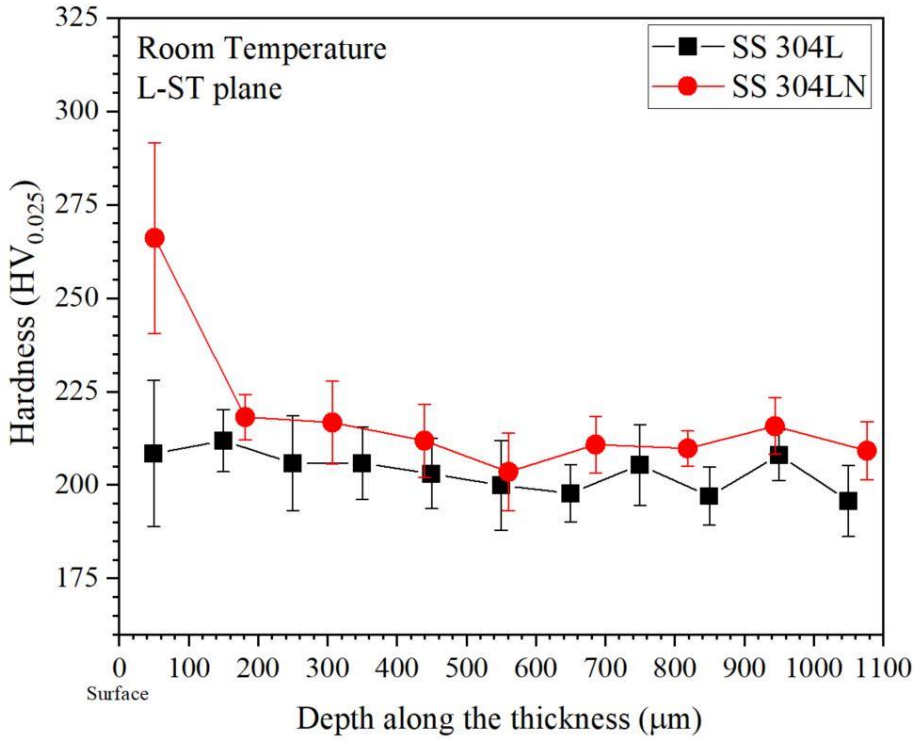


Figure 4-5 Hardness profile along L-ST plane for SS 304L-R and SS 304LN.

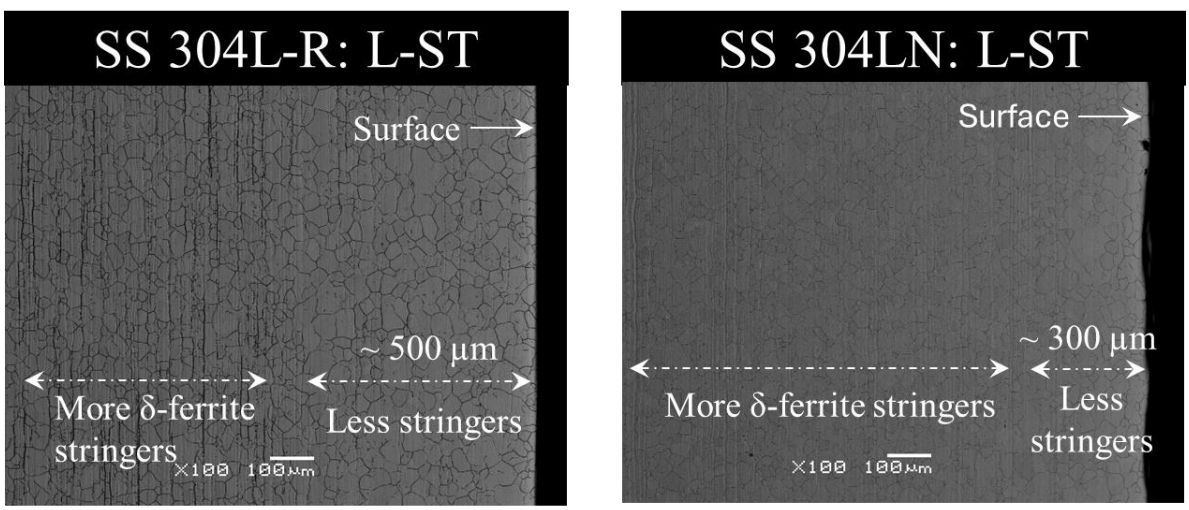


(a) (b)

Figure 4-6 Morphology of L-ST plane showing the δ-ferrite stringers distribution along the thickness in (a) SS 304L-R and (b) SS 304LN.

## 4.2 Sample preparation

### *4.2.1 Four-point bend samples*

The preparation of 4PB samples involved various procedures to ensure their suitability for IASCC testing. Key factors, including surface finish quality, sample thickness, thickness uniformity, burr-free edges, and δ-ferrite free surface, were meticulously addressed to eliminate any factors that could adversely affect the 4PB test results. EDM was employed to machine 4PB blanks from the material plates, considering three main conditions: if cutting burrs from the electric spark were unavoidable, they were confined to the blank's short edge; the opposite edges were ensured to be parallel for a near-perfect prism shape; and the cutting was performed along the rolling direction.

The cutting procedure was performed as follows: rectangles measuring 5.0 ± 0.1 mm by 3.5 ± 0.04 mm were machined from the plate by EDM, these small pieces were then inspected by SEM and a calibrated digital caliper to ensure their dimensions comply with the specified tolerances. Subsequently, grinding and polishing were performed according to the process shown in Figure 4-7. Approximately 100 - 200 µm of material was removed from the designated surface to be irradiated to remove the EDM damage, which was then polished mechanically using sandpapers of grades P1200, P2400, and P4000 and then abrasive polishing to a finish of 0.25 µm to achieve scratches-free surface. The remaining material was then removed from the back surface using sandpapers of grades P1200 to P4000 until the total blank thickness reached 0.90 ± 0.03 mm. Samples were then electropolished in a 9:1 solution of methanol and perchloric acid at -45 $^{o}$C for 20 seconds using a voltage of 33 V.

Finally, the sample ID was engraved on the back surface to ensure accurate tracking, keep the to-be-irradiated surfaces distinct, and prevent the irradiation of the incorrect side.

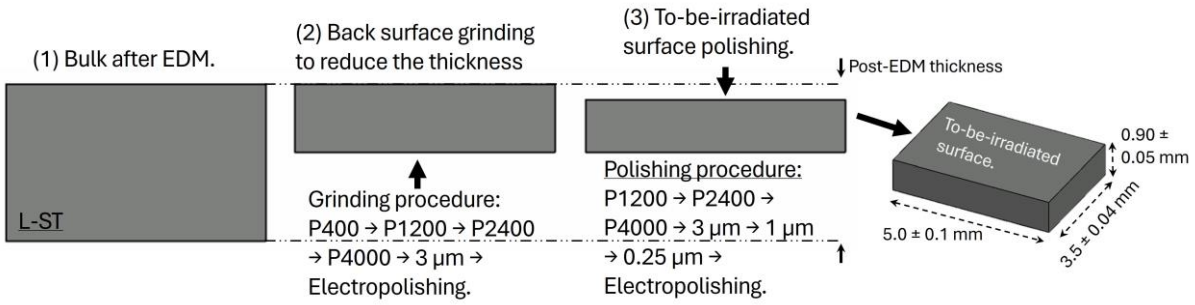


Figure 4-7 Four-point bend samples grinding and polishing procedure as preparation for proton irradiation and subsequent IASCC testing.

Hardness measurements were conducted on the L-T plane of the 4PB bulk prior to proton irradiation. The pre-irradiation data was used to compare against the post-irradiation measurements from the same surface to evaluate hardness changes due to proton irradiation and then the yield strength. A 2.5 mm profile was created parallel to the short edge as shown in the red-dotted line in Figure 4-8, maintaining a 0.5 mm distance from each edge to minimize edge effects on the measurements and a load of 25 gf was applied during the test. This low load was chosen because the proton-irradiated layer is not expected to exceed 25 µm. A higher load could cause the indenter to penetrate the unirradiated bulk, creating a plastic zone and leading to inaccurate $H_V$ measurements.

### *4.2.2 Tensile bars preparation*

The preparation of tensile bars was more complex than that of the 4PB samples. Similar to 4PB initial procedure, a 200 µm layer was removed from the pre-identified surface. Square bars of dimensions 39.0 ± 0.1 mm by 3.9 ± 0.1 mm were then machined from the plates.

The threaded sections of the bars were created using a thread-cutting lathe, which coordinated the rotation of the workpiece with the linear movement of a cutting tool along its axis. The tool, shaped to match the thread profile, progressively cut into the material in multiple passes to achieve the desired thread depth and pitch. Subsequently, EDM was employed to shape

the square gauge section to dimensions of 2.0 ± 0.05 mm by 2.0 ± 0.05 mm, leaving a small margin for further polishing. The conceptual design of these bars is shown in Figure 4-9.

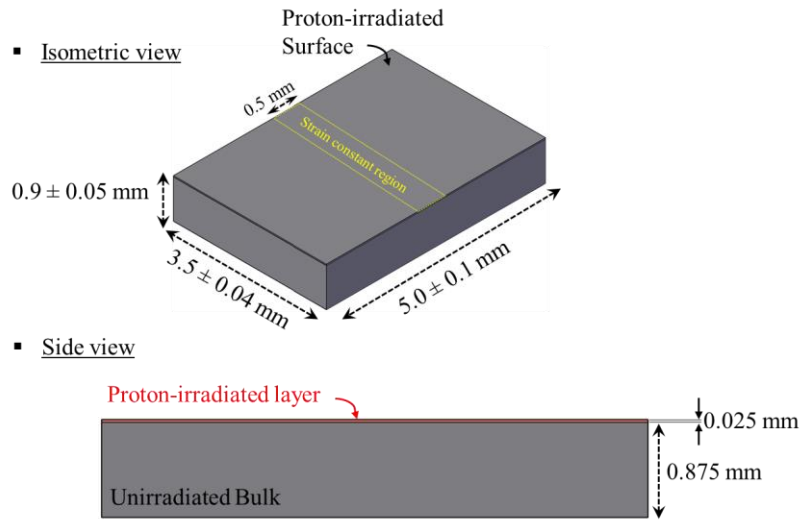


Figure 4-8 Conceptual design of the four-point bend samples including the proton irradiation layer and the unirradiated bulk.

Once these bars were received from the EDM shop, their dimensions were measured by a calibrated digital caliper to ensure they adhered to the specified tolerances. Approximately 50 µm of material was removed from each side of the square gauge, and the designated surface for irradiation was marked and identified. The surfaces were then mechanically polished using sandpapers of grades P1200, P2400, and P4000. Only the to-be-irradiated face was polished to a finish of 0.25 µm using abrasive solutions.

Stainless steel electrical wires were spot-welded to the top of the head of one threaded section using low energy pulse to avoid damaging the threaded section. Threads were then entirely covered with a red licquer to protect them from edge-selective attack during electropolishing. The gauge section of the tensile bars was electropolished in a 9:1 solution of ethanol and perchloric acid at -45 $^{o}$C for 20 seconds using a voltage of 33 V. The selection of ethanol in this polishing was due to the fact that the licquer is solvable in methanol solutions

which will affect the surface finish quality. Following the electropolishing, the red licquer was ultrasonically removed in the acetone bath and samples were cleaned using acetone, methanol, ethanol, and demineralized water.

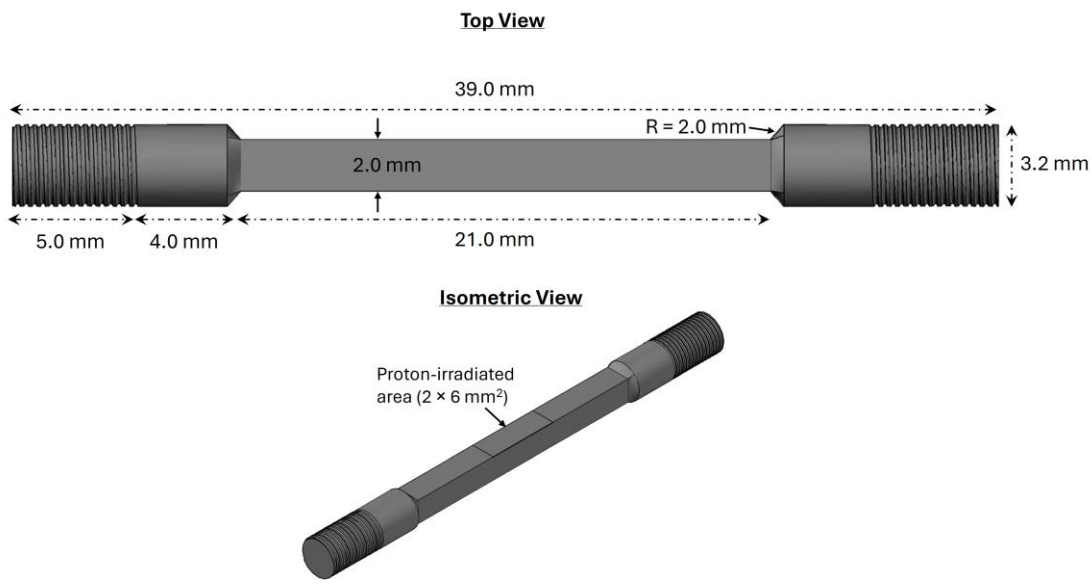


Figure 4-9 Conceptual design of the tensile sample used for the dislocation channels quantification.

Finally, the tensile and guide bars were labeled using an electrical engraver for accurate tracking throughout the experiment. This preparation step ensured that the bars were ready for proton irradiation.

A 3.0 mm profile was created parallel to the short edge as shown in the red box in Figure 4-10, maintaining a 0.1 mm distance between indents a load of 25 gf was applied during the test.

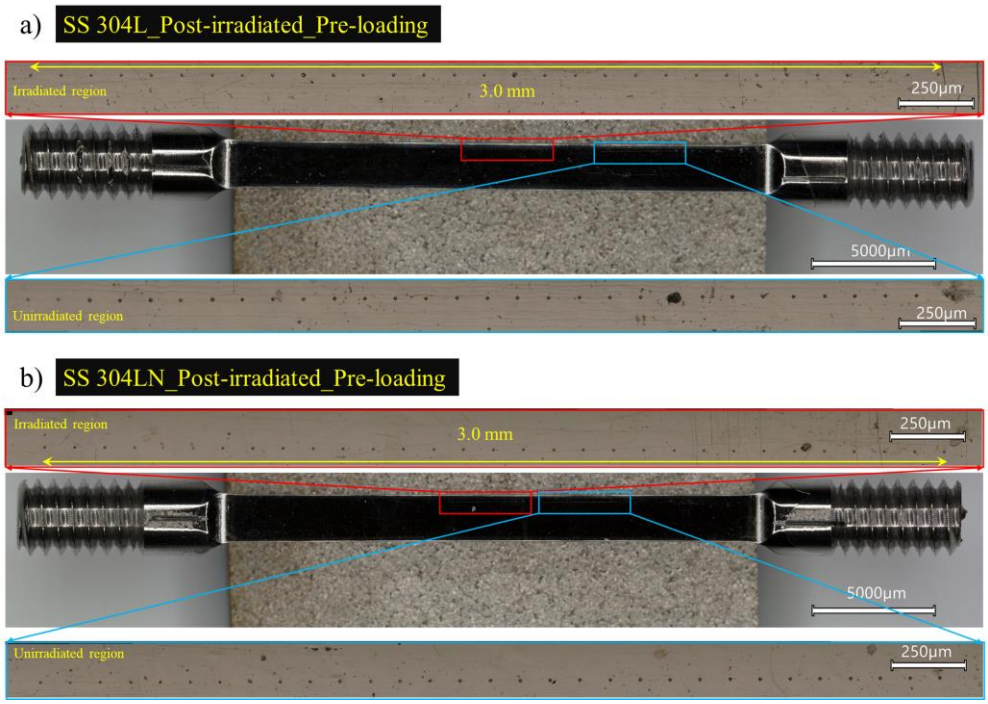


Figure 4-10 Hardness profile within the irradiated area (red box) and unirradiated region (blue box).

### 4.3 Tensile test for mechanical properties measurements

Tensile tests for both alloys were conducted at the irradiated materials testing laboratory (IMTL) at the University of Michigan. The tests were carried out at room temperature in air and at 340 $^{o}$C in an ultra-high-purity (UHP) argon environment. Figure 4-11 shows the conceptual design of the small scale (SS-3) tensile sample used for this analysis. The tensile samples were machined 100 μm below the rolled surface and aligned with the rolling direction using EDM. Following EDM, samples were mechanically polished up to P4000 grit to eliminate any EDM-induced damage. The thickness of the samples was verified using Mitutoyo® thickness gauge and Keyence VHX-7000® optical microscope (OM) after mechanical polishing to ensure it met the required specifications at 0.76 ± 0.02 mm.

Prior to the test, a profile of 30 indents was created along the sample length near the edge as shown in Figure 4-12 to measure the total strain at the end of the test through comparing the

length of the indents profile before and after straining. The indents were spaced 100 µm apart, forming a total profile length of 3.0 mm.

The load was applied by a servo motor to the loading fixture at a strain rate of $4 \times 10^{-4}$ $s^{-1}$. During the test, the onset of yielding was identified as the point where the curve began to plateau. To prevent sample fracture, the test was terminated at around 50% higher than the load at which sample started to yield.

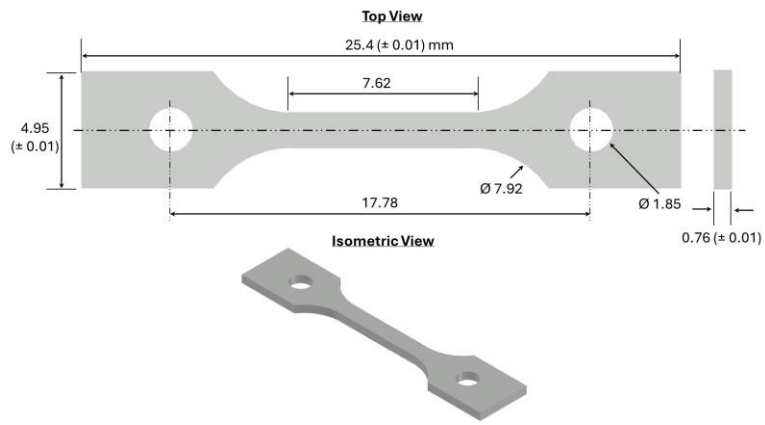


Figure 4-11 Conceptual design of the SS-3 tensile sample used for the tensile test.

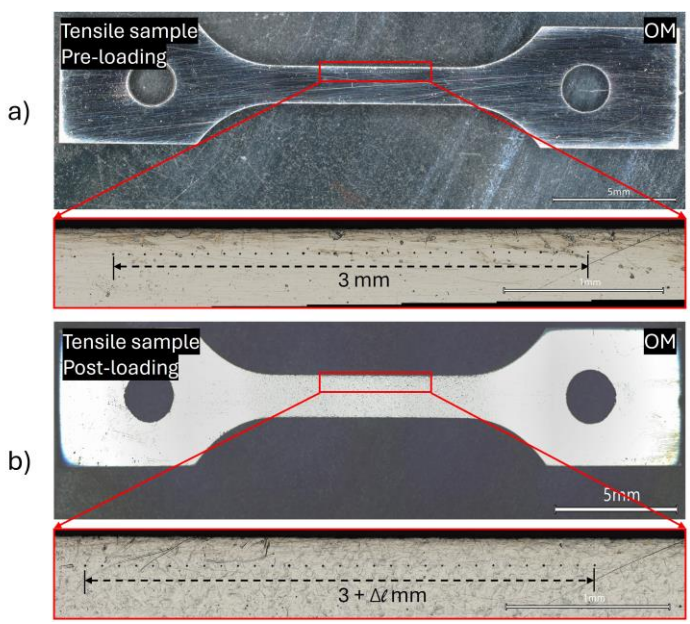


Figure 4-12 An example of indents profile at the edge of tensile sample 1 (SS 304L) which was tested at 340 °C in argon for (a) pre-loading and (b) post-loading conditions.

## 4.4 Samples designations

### *4.4.1 Test samples*

For this study, approximately 12 4PB samples, 2 tensile bars, and 9 SS-3 bars were prepared for 4PB tests, CERT tests, and tensile tests. Of these 4PB samples, only three SS 304LN samples and three SS 304L samples were used. To ensure precise tracking, each sample was assigned a designation, as shown in Table 4-3.

The naming conventions are as follows:

**4PB samples**: Named as *Alloy-Sample Number*. Here, "L" indicates SS 304L, and "N" indicates SS 304LN.

**Tensile bars**: Named as *Test_type-Alloy*. In this case, "T-B" refers to tensile bars, while "L" and "N" represent SS 304L and SS 304LN, respectively.

**SS-3 tensile bars**: Named as *Test_type-Alloy*. Here, "S-B" refers to SS-3 bars, with "L" and "N" denoting SS 304L and SS 304LN.

### *4.4.2 Microscopy analysis samples*

Several liftouts were machined from 4PB samples for microscopy analysis. FIB was used to machine liftouts from the samples and prepare TEM grids. To ensure proper samples tracking, all liftouts were given designations as listed in Table 4-4. The naming conventions are as follows:

Named as *Alloy-defects_sample-number*. Here, "L" indicates SS 304L, and "N" indicates SS 304LN, the second "L" indicated dislocation loops, and "C" indicates the crack.

Table 4-3 Samples designations.

| Alloy | Sample ID | Type | Application |
|---|---|---|---|
| **SS 304L-R** | L-R-1 | 4PB | IASCC test |

| | | | |
|---|---|---|---|
| | L-R-3 | 4PB | |
| | L-R-6 | 4PB | |
| | T-B-L | Tensile, CERT | Tensile test for DCs analysis. |
| | S-B-L-1 | SS-3 | Tensile test for YS measurement at 25 $^{o}$C |
| | S-B-L-2 | SS-3 | Tensile test for YS measurement at 340 $^{o}$C |
| | S-B-L-3 | SS-3 | Tensile test for YS measurement at 340 $^{o}$C |
| **SS 304LN** | N1 | 4PB | FE model validation at 25 $^{o}$C |
| | N4 | 4PB | FE model validation at 340 $^{o}$C |
| | N3 | 4PB | IASCC test |
| | N7 | 4PB | |
| | N10 | 4PB | |
| | T-B-N | Tensile, CERT | Tensile test for DCs analysis. |
| | S-B-N-1 | SS-3 | Tensile test for YS measurement at 25 $^{o}$C |
| | S-B-N-2 | SS-3 | |
| | S-B-N-3 | SS-3 | |
| | S-B-N-4 | SS-3 | Tensile test for YS measurement at 340 $^{o}$C |
| | S-B-N-5 | SS-3 | |
| | S-B-N-6 | SS-3 | |

Table 4-4 Microscopy samples designations.

| Alloy | Sample ID | Application |
|---|---|---|
| **SS 304L-R** | L-R-1-8 | Irradiation-induced defects and crack tip analysis (liftout taken from crack L-R-1) |
| | L-R-1-8 | Irradiation-induced defects and crack tip analysis (liftout taken from crack L-R-1) |
| | L-R-1-8 | Irradiation-induced defects and crack tip analysis (liftout taken from crack L-R-1) |
| **SS 304LN** | N3-4 | Irradiation-induced defects and crack tip analysis (liftout taken from crack N3-4) |
| | N3-4 | Irradiation-induced defects and crack tip analysis (liftout taken from crack N3-4) |
| | N3-4 | Irradiation-induced defects and crack tip analysis (liftout taken from crack N3-4) |

## 4.5 Proton irradiation

### *4.5.1 Proton irradiation*

Proton irradiation was selected to induce microstructure damage on the surface to simulate the damage from the neutrons in the PWR core environment. Following the sample preparation and pre-irradiation hardness, the samples were ready for irradiation.

Proton irradiation experiments were performed at Michigan Ion Beam Laboratory (MIBL) at the University of Michigan. The irradiation was performed using 2 MeV protons at an average temperature 360 ±10 $^{o}$C to a damage level of 5.0 dpa for the 4PB samples and 3.0 dpa for the tensile bars. The dpa damage rate was calculated by Stopping and Range of Ions in Matter (SRIM) computer program [199], and the dpa calculation was done using the following equation:

$$\mathrm{DPA} = \int_0^t \phi_{\mathrm{tot}}(t) \int_0^\infty \sigma_d(E)\phi(E,t)\, dE\, dt \tag{4.1}$$

Where $\phi_{tot}\ (t)$ is the time-dependent fluence rate intensity, $\sigma_d(E)$ is the displacement cross section for an incident particle at energy $E$, $t$ is the irradiation time, $\phi(E,\ t)$ is the fluence rate spectrum. Solving Eqn.1 results in:

$$\mathrm{DPA} = \frac{\text{SRIM damage rate} \times \text{Charge}}{\text{Number density} \times \text{Irradiation area}} \tag{4.2}$$

SRIM damage rate is the value that was calculated from SRIM 2013. SRIM simulation was performed using 'Quick' Kinchin Pease method using $1 \times 10^6$ ions of hydrogen. The displacement threshold energy ($E_d$) for iron-based alloys was obtained from ASTM E521 [200] at 40 eV. The ion current on the samples was measured continuously using a charge integrator, that then integrates the current over time to obtain the total charge delivered to the samples. The charge is then multiplied by the damage rate (Eq. 4.2) as determined by SRIM in Figure 4-13, and divided by the charge on the ion and the atom number density in the target and the irradiation area. In Figure 4-13, the uniform irradiation occurs at 60% of the depth which equals 12.1 µm as shown in the figure.

The current density striking the aperture and stage depends on beam intensity and the rastering area. The proton beam intensity ($I_{Beam}$) follows Gaussian distribution, therefore the beam profile at a point (x, y) for a beam center ($x_0$, $y_0$) is governed by:

$$I_{Beam} = \exp\left(-\frac{(x-x_0)^2+(y-y_0)^2}{2\sigma^2}\right) \tag{4.3}$$

The standard deviation of the Gaussian beam (σ) is related to full width half maximum (FWHM) of the beam by:

$$\sigma = \frac{\text{FWHM}}{2\sqrt{2\ln(2)}} \tag{4.4}$$

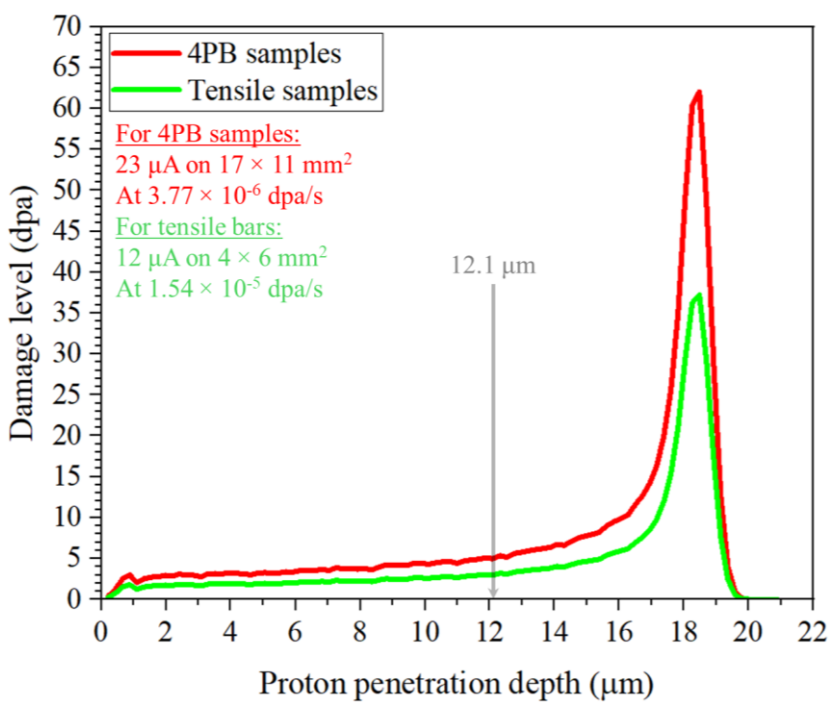


Figure 4-13 Damage profile caused by proton irradiation on the surface of stainless steel. The calculation used for 4PB samples and tensile bars.

To define how far the beam goes beyond the edge of the target stage area, a scaling factor (*F*) is used. Specifically, *F* represents the fraction of beam's radius (FWHM/2) by which the beam center goes beyond the edge of the stage area. For F=1.0 and FWHM = 3.0 mm, the beam center goes 1.5 mm beyond the edge of the samples area on each side which is typical for the off-

sample to off-sample rastering case. The distance the beam center travels beyond the edge of the stage area is given as D:

$$D = \frac{F \cdot \mathrm{FWHM}}{2} \tag{4.5}$$

The beam rastering process was carried out from one off-sample edge to the other, ensuring complete irradiation of the sample area. The beam's FWHM value was approximately 3.0 mm, which was also considered the beam diameter. To minimize beam scattering at the aperture edge, which reduces the number of protons reaching the target, the aperture was widened. Consequently, the beam was shifted 1.05 mm away from the stage. Figure 4.14 (a) shows the schematic diagram of the stage with the 4PB samples showing the beam shift that resulted in a portion of the stage also being irradiated (indicated by the blue area). This adjustment effectively mitigated the reduction in current density at the aperture edge. It was then necessary to calculate the currents at stage and aperture required for 4PB and the constant extension rate test (CERT) tests.

The total irradiation area that covers the entire rastering area in the stage and aperture is defined as:

$$Area_{Raster} = (\mathrm{L_x} + 2\mathrm{D_x})(\mathrm{L_y} + 2\mathrm{D_y}) \tag{4.6}$$

The full beam intensity across a grid point (x, y) for different raster positions ($x_0$, $y_0$):

$$J(x, y) = \sum_{x_0, y_0} I_{Beam}(x, y, x_0, y_0) \tag{4.7}$$

The peak current density value was then normalized to unity by:

$$J_{\mathrm{normalized}}(x, y) = \frac{J(x, y)}{\max(J(x, y))} \tag{4.8}$$

Therefore, the current density striking the stage was calculated by:

$$J_{\text{stage}} = \int_{-\frac{L_y}{2}}^{\frac{L_y}{2}} \int_{-\frac{L_x}{2}}^{\frac{L_x}{2}} J_{\text{normalized}}(x, y)\, dx\, dy \tag{4.9}$$

Integration of Eqn. 4.8 resulted in the total current density across the entire irradiation area:

$$J_{\text{Total}} = \iint J_{\text{normalized}}(x, y)\, dx\, dy \tag{4.10}$$

The current density at the aperture was then calculated as:

$$J_{\text{Aperture}} = J_{\text{Total}} - J_{\text{Stage}} \tag{4.11}$$

And the ratio of the current density at stage and aperture is represented by:

$$Ratio_{Current} = \frac{J_{\text{Stage}}}{J_{\text{Aperture}}} \tag{4.12}$$

This ratio was used to identify the current density at the aperture and the stage. Proton irradiation with 2 MeV usually results in the range of 30 - 33 µA as a total current on the aperture and stage assuming that the source (filament) was just replaced prior to the experiment and was stable over the experiment time. Once the ratio is calculated, the current densities at both the stage and aperture will be determined.

#### *4.5.1.1 Irradiation parameters*

To calculate the current at the aperture and stage in experiments 1 and 2, a python script simulating equations 4.2 through 4.12 was used. The 4PB samples covered a stage area of 14 × 10 $mm^2$. To ensure complete coverage of the sample area during irradiation, the stage area was set to 17 × 11 $mm^2$, providing an additional 1.5 mm on each horizontal side and 0.5 mm on each vertical side, as the remaining stage area could not accommodate a larger adjustment. The areas of the samples, stage, and aperture are shown in Figure 4-14 (a).

As mentioned in the previous section, the beam intensity follows a Gaussian distribution, meaning that the beam does not deliver full intensity on the at the edges of the samples area. This results in reduced damage in these regions, as only a fraction of the beam impacts these areas. Python script is used to calculate the current densities at aperture and stage. Figure 4-14 (b) shows the positions of the stage, beam center, and aperture, along with the distance the beam travels beyond the sample edges. The center of the stage was defined as the origin ($x_0$, $y_0$), for simplicity, and all other points were referenced relative to this origin. In the figure, $L_{A\text{-}x}$ and $L_{S\text{-}x}$ refer to the horizontal lengths of the aperture and stage, $L_{A\text{-}y}$ and $L_{S\text{-}x}$ refer to their vertical lengths. The Python code that is attached to Appendix A-1 was used to calculate the current density resulting from beam rastering over the target area. The output of this script is presented in the heat map in Figure 4-15 (a) and the normalized current density over the irradiated area in Figure 4-15(b).

According to the Python simulation, the configuration shown in Figure 4-15(a) resulted in F = 0.7, indicating that the beam center travels a distance of 1.05 mm beyond the stage area edge. This configuration results in a stage to aperture (*S/A*) ratio of 2.33. Given that the average total current is 32 ± 1.0 μA and applying *S/A* ratio to Eqns. 4.10 and 4.12 yields an average current at the stage of 23.1 ± 1.0 μA and an average current at the aperture of 9.9 ± 1.0 μA. These are the currents values that were used in the 4PB irradiation experiments. This means that the current at the samples edges was approximately 97% of the beam's maximum, corresponding to a damage level of about 4.9 dpa, which is a loss of 2% of the damage and it was considered acceptable. This analysis was conducted for both 4PB irradiation experiments.

The same Python simulation was performed on the tensile bars, which had an area of 7 × 5 $mm^2$. By adding the beam size to each direction (x and y), the total irradiation area was

expanded to 13 × 11 $mm^2$. For F = 1.0, the beam center traveled 1.50 mm beyond the edge of the stage area, as depicted in Figure 17. The current density distribution following proton beam rastering is shown in Figure 18, indicating a similar beam loss at the edges as observed with the 4PB samples. This resulted in an (*S/A*) ratio of 0.74, with an average current at the stage of 14.1 ± 0.5 μA and an average current at the aperture of 19.1 ± 0.5 μA. The Python script used for this analysis is included in Appendix A-2. The summary of irradiation parameters for all irradiation experiments is listed in Table 4-5.

Table 4-5 Summary of proton-irradiation parameters.

| **Parameter** | **Sample type** | |
|---|---|---|
| | **4PB** | **Tensile bars** |
| Dose (dpa) | 5.00 | 3.00 |
| Stage area ($mm^2$) | 187.00 | 46.75 |
| Aperture area ($mm^2$) | 240.00 | 155.25 |
| Stage-to-aperture ratio | 2.33 | 0.87 |
| Stage current (μA) | 23.10 | 14.00 |
| Aperture current (μA) | 9.90 | 16.00 |
| Total current (μA) | 33.00 | 30.00 |
| Irradiation time (h) | 370.00 | 90.00 |

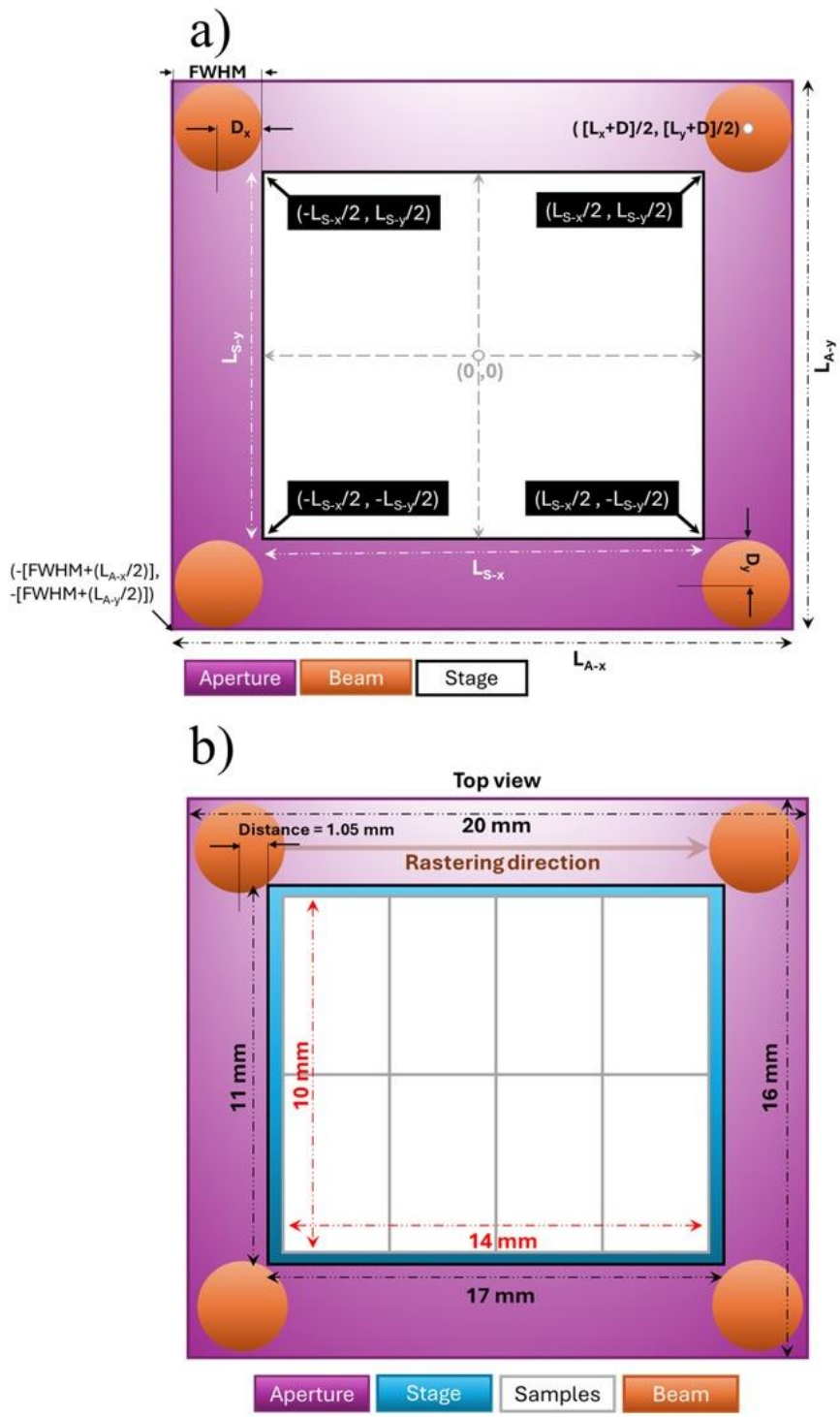


Figure 4-14 Schematic diagram of the irradiation area covering (a) the position of beam and stage area and (b) the dimensions of the beam, stage, and aperture used to calculate the irradiation parameters.

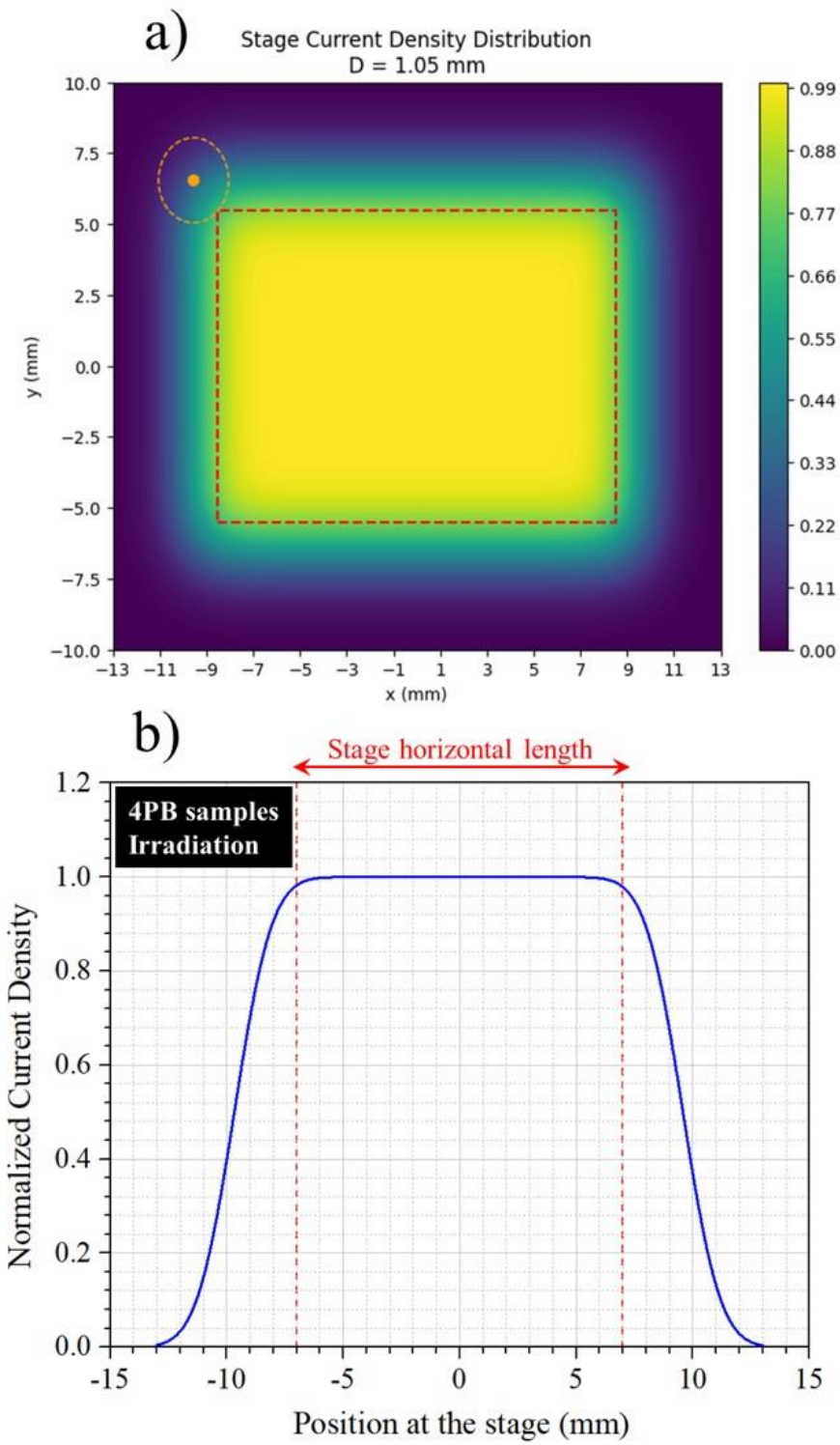


Figure 4-15 (a) Python code results calculating the current density distribution io the stage and apertures based on locations defined in Figure 14 (a) and (b) the total current density on the stage area.

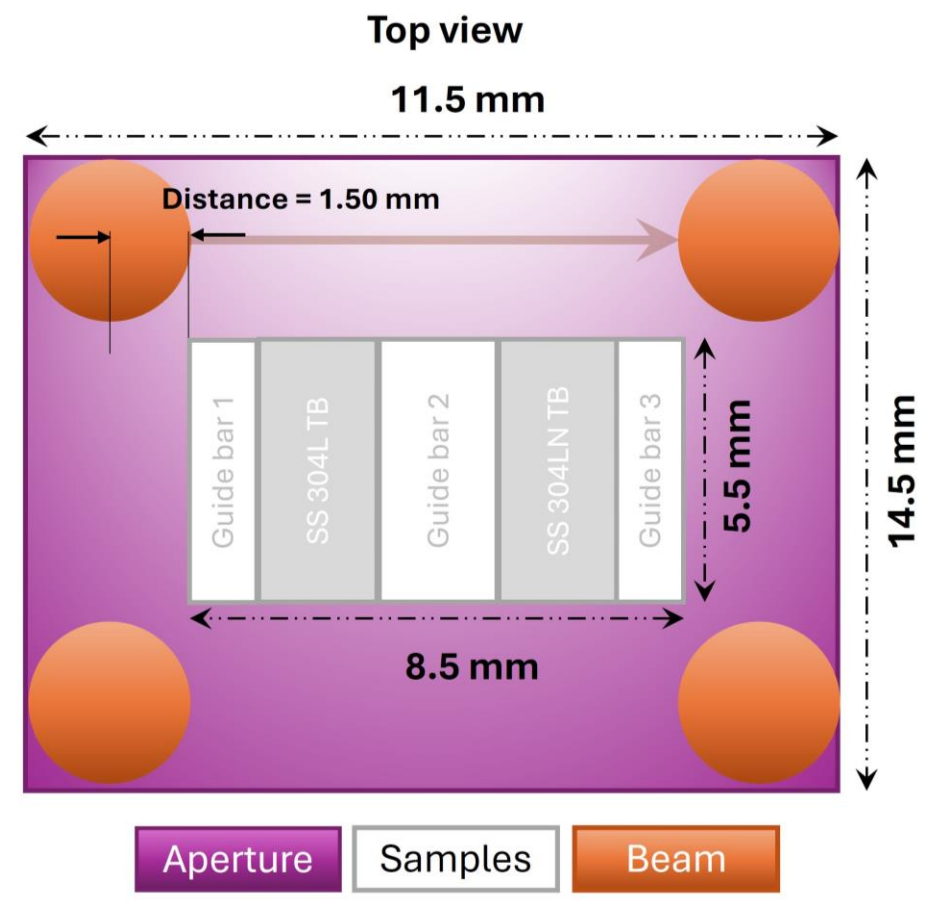


Figure 4-16 Schematic diagram of the irradiation area covering of the tensile bars, the dimensions of the beam, stage, and aperture used to calculate the irradiation parameter.

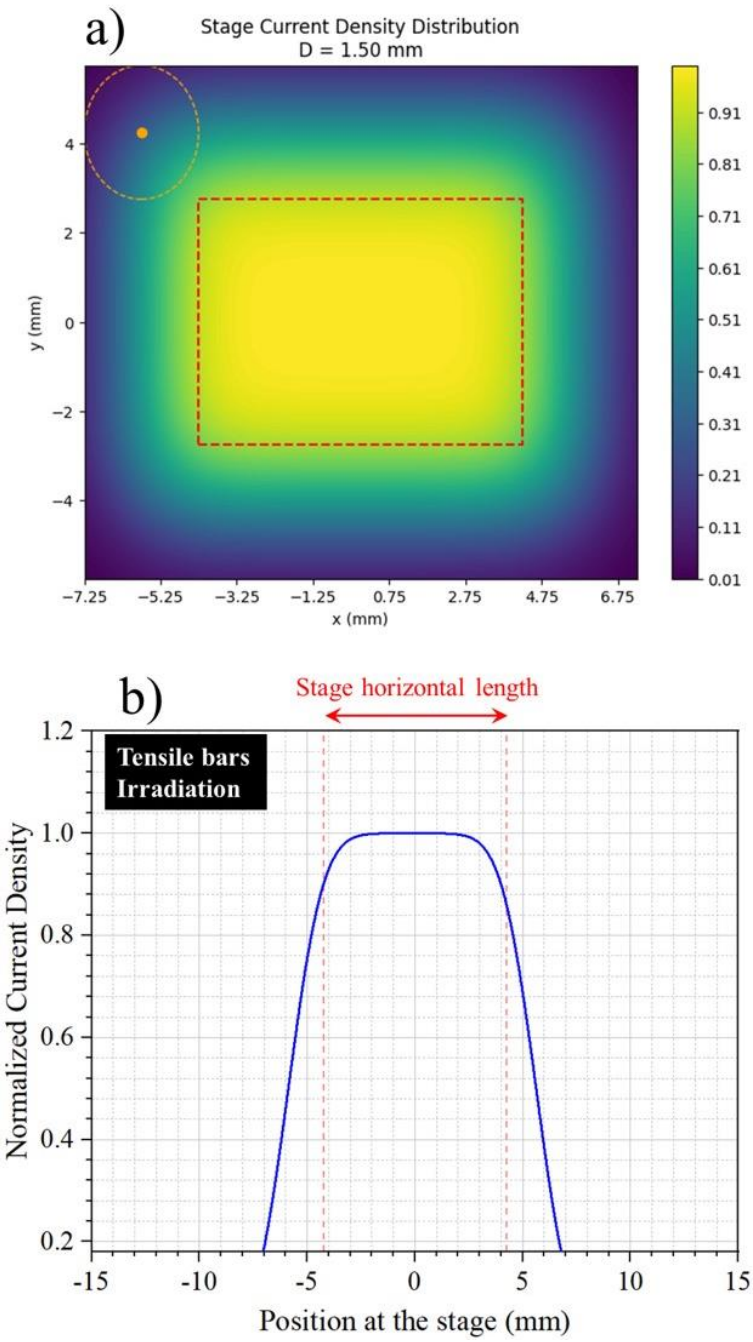


Figure 4-17 (a) Python code results calculating the current density distribution in the stage and apertures based on locations defined in Figure 4-16 (a) and (b) the total current density.

### *4.5.1.2 Proton irradiation experiments*

The Michigan ion beam laboratory contains several ions sources, accelerators, and beamlines. Figure 4-18 shows the bird-view of MIBL and its facilities. For this study, a NEC

Toroidal Volume Ion source (TORVIS) capable of delivering up to 100 μA at the low energy end and with currents of about 25-30 μA on targets (40 μA total) usually generates $H^-$ ions that moves toward the NEC 3MV Tandem Pelletron particle accelerator (Wolverine) which includes quadrupole focusing unit, the high energy magnet that could deliver beams to 5 separate beamlines. Wolverine is capable of delivering a focused beam with 3 mm FWHM; this beam could be raster-scanned, over a max area of 10 mm (Vertical) by 17 mm (Horizontal). When the $H^-$ ions reach the accelerator, an electron is stripped off using nitrogen gas, converting the ion into $H^+$. The $H^+$ ions are then accelerated toward the target in the beamline chamber due to repulsive forces from the positively charged magnets within the accelerator. The proton beam is rastered across the target irradiation area.

Three proton irradiation experiments were conducted based on the calculations: irradiation experiments 1 and 2 two performed using 4PB samples and irradiation experiment 3 performed using tensile bars. For the 4PB samples, experiment 1 involved 8 samples of alloy 304LN, while experiment 2 involved 4 samples of alloy 304L. The stage in experiment 2 was basically loaded with 8 samples, with the remaining 4 allocated to another research group. While experiment 3 involved 2 tensile bars, one from each alloy. The selection of samples for irradiation was primarily determined by the quality of the surface finish following electrochemical polishing. Figure 4-19 shows images of the copper irradiation stage used for holding samples during the irradiation, for experiment 1 the pre- and post-irradiation conditions is shown in Figure 4-19 (a) and (b) while for the experiment 2, the pre- and post-irradiation conditions are shown in Figure 4-19 (c) and (d) while for the tensile bars, Figure 4-19 (e) and (f) show the pre- and post-irradiation conditions of the samples on the stage. The irradiation parameters for the 4PB experiments are provided in Table 4-6, while those for the tensile bars

are listed in Table 4-7. Irradiation experiments performed in beamline 2 in MIBL as indicated by the yellow track in Figure 4-18.

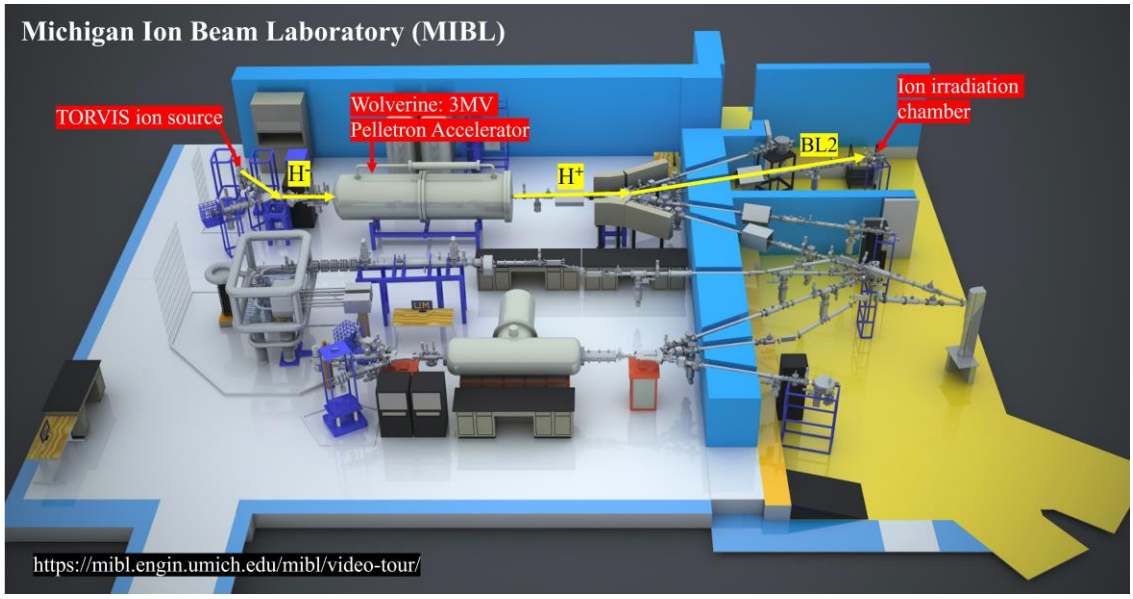


Figure 4-18 MBIL facilities showing the TORIVS ions source, 3MV Pelletron Accelerator, BL2, and its chamber.

Table 4-6 Proton irradiation experiments parameters for 4PB samples.

| Parameter | SS 304L-R | | SS 304LN | |
|---|---|---|---|---|
| | Target | Achieved | Target | Achieved |
| Dose (dpa) | 5.00 | 5.00 | 5.00 | 5.00 |
| Dose rate (dpa/s) | $3.8 \times 10^{-6}$ | $4.0 \times 10^{-6}$ | $3.8 \times 10^{-6}$ | $3.9 \times 10^{-6}$ |
| Average irradiation temperature (°C) | 360.0 ± 10 | 360.6 ± 5.2 | 360.0 ± 10 | 360.4 ± 1.8 |
| Pressure (torr) | $< 1 \times 10^{-7}$ | $< 3 \times 10^{-8}$ | $< 1 \times 10^{-7}$ | $< 3 \times 10^{-8}$ |
| Experiment duration (h) | 380 | 340 | 380 | 360 |

Table 4-7 Proton irradiation experiments parameters for tensile bars.

| Parameter | Tensile bars | |
|---|---|---|
| | Target | Achieved |
| Dose (dpa) | 3.00 | 3.00 |
| Dose rate (dpa/s) | $1.5 \times 10^{-5}$ | $1.1 \times 10^{-5}$ |
| Average irradiation temperature (°C) | 360.0 ± 10 | 358.1 ± 4.3 |
| Pressure (torr) | $< 1 \times 10^{-7}$ | $< 5 \times 10^{-8}$ |
| Experiment duration (h) | 100 | 80 |

The samples were mounted onto the stage using high-performance silver paste from PELCO®, this paste can serve to up to 927 $^{o}$C making it an ideal choice for the experiment. This paste also has excellent thermal conductivity, ensuring effective heat transfer during the irradiation process and enabling better temperature control. However, applying the paste presented challenges, as only a thin layer was required beneath the samples, but the paste dries quickly, complicating its adherence to the samples. An improper application of the silver paste could result in poor thermal conductivity, leading to an overshoot in the surface temperature of the sample during proton irradiation. This could render the samples unsuitable for subsequent 4PB testing. Guide bars made of stainless steel were used to support the samples on the stage and equipped with thermocouples (TCs). The TCs continuously provided real-time temperature readings at the samples height, as the bars were of the same thickness as the 4PB samples. Before loading the stage into the beamline chamber, the TCs were first tested in air at temperatures up to 130 $^{o}$C ahead of loading the stage to the chamber.

Afterwards, the stage was loaded into the beamline chamber which was sealed with a copper seal. Two pumps were used, a roughing pump first to initially evacuate a vacuum system and then a cryopump was used to achieve high vacuum of greater than $1 \times 10^{-7}$ torr through leaving the pump running overnight. High vacuum is necessary to prevent surface oxidation of the samples at the testing temperature. Pressure gauges attached to different locations along the beamline are used to read the pressure at the accelerator, the beamline and the chamber. It is important to note that the beamline is defined as the region between the chamber and the switching magnets that are located at the outlet of the accelerator. Figure 4-20 (a) through (c)

show the pressure values of the accelerator, beamline, and chamber during the experiment for each of the three irradiation experiments showing a stable vacuum during the irradiation.

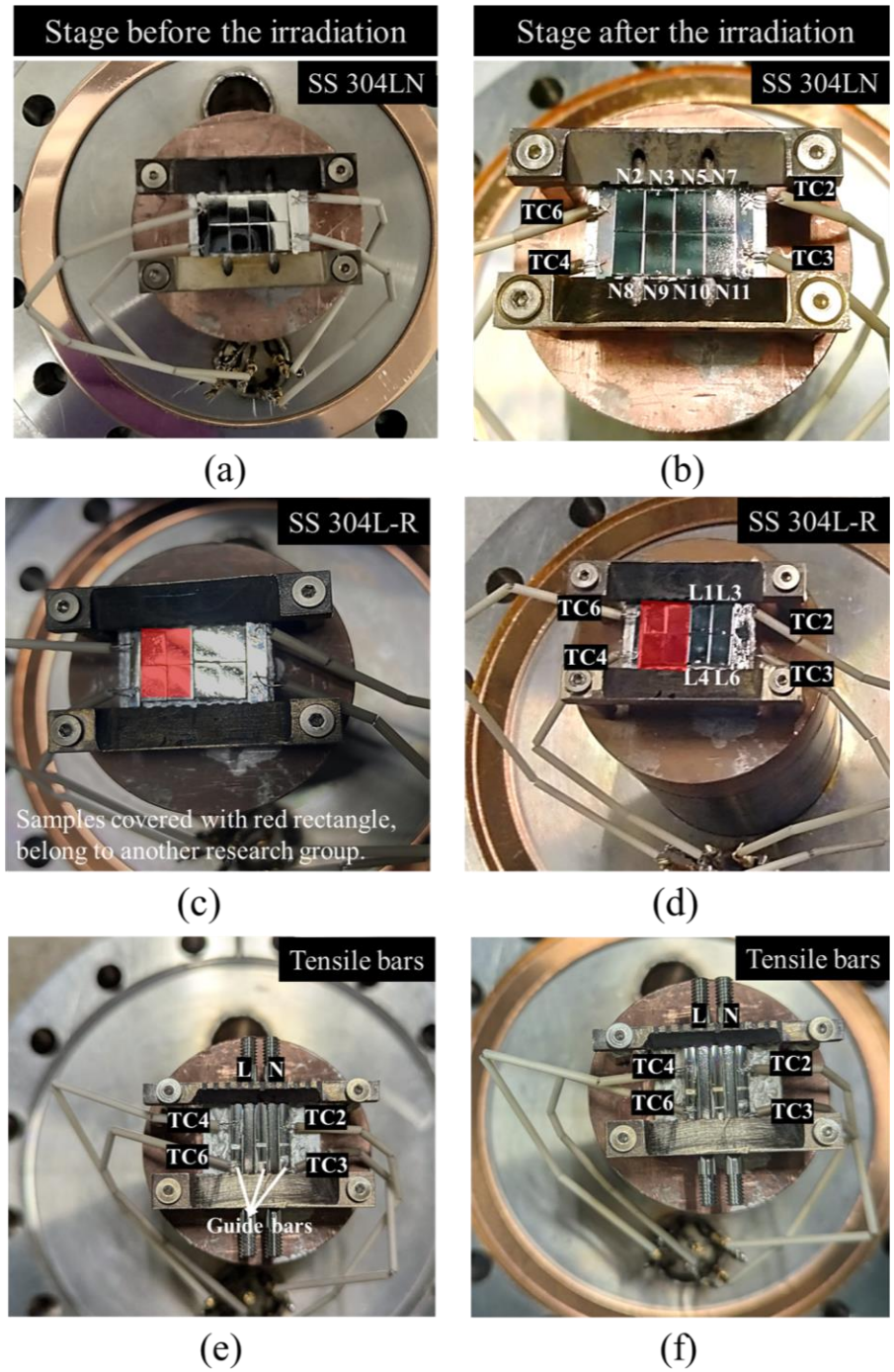


Figure 4-19 Copper Irradiation stage showing the setup of samples, guide bars, and thermocouples for pre- and post-irradiation experiments. For SS 304LN; (a) pre-irradiation, (b) post-irradiation, SS 304L-R; (c) pre-irradiation, (d) post-irradiation, and tensile bars; (e) pre-irradiation, and (f) post-irradiation.

Once pressure inside the chamber and along the beam line are similar, the stage was carefully aligned with the beam direction using a laser source positioned at the beam switching magnets. This alignment was critical to ensure that the aperture matched the previously calculated position as can be seen in Figure 4-21 (a) for first, (b) second, and (c) third irradiation experiments. The laser alignment was challenging since samples used in all irradiation experiments were too shiny as a result of electropolishing.

Once all setups are finalized, irradiation begins by retracting the Faraday cups (FC) positioned before the chamber, allowing the proton beam to hit the stage. During irradiation, a LabView® program monitors key testing parameters, such as the stage temperature.

A Teledyne® forward-looking infrared (FLIR) thermal camera used to capture the samples temperature during the irradiation inside the chamber. FLIR camera was calibrated at 360 $^{o}$C using thermocouple readings from the guide bars. Examples of FLIR camera output are presented in Figure 4-22. The software connected to the camera enables monitoring of specific regions, referred to as areas of interest (AOIs), which can be defined using geometric and graphic elements such as rectangles and circles. These shapes can be created and positioned within the AOI, allowing the software to display temperature data for those regions. The temperature histories of the AOIs for each experiment are shown in Figure 4-23, with (a) representing experiment 1, (b) experiment 2, and (c) experiment 3. The distribution of data is also plotted along with the average temperature and standard deviation. The distribution of the temperature data is plotted alongside the average temperature and standard deviation. The temperature measurements at the AOIs indicate that the irradiation was uniform across the sample surfaces, as temperature variations between AOIs were within 2 $^{o}$C.

Stage and aperture current densities are measured using a current integrator, which detects charge and converts it to current. Figure 4-24 (a), (b), and (c) show the current densities at stage, aperture, and the total one for the three experiments. The current at the stage depends on the total current resulted from the ions hitting the stage. The figure shows stability of current during the experiments; samples area experienced a current of 21 ± 1 μA for 4PB samples while 14 ± 1 μA in case of tensile bars. The stability of current ensures that the charge acquisition is also stable, meaning that the displacement per atom calculation will be within the target values.

Once the target dpa is reached, the experiment is stopped by inserting all three FCs, which effectively block the beam from reaching the stage. The stage cooling air is then increased to its maximum flow to ensure rapid and safe cooling. Once the stage temperature drops to 25 $^{o}$C, the stage is removed from the chamber.

After the irradiation experiment, beta and gamma counts were measured using Ludlum's® Model 2929 Dual Channel Scaler scintillation Geiger radiation detector. Each sample was counted three times, and the average counts, along with their standard deviations, were calculated. The overall average of all sample counts was then determined, and the counts from individual samples were compared and plotted against the overall average. This counting procedure was essential for assessing the irradiation uniformity across the entire sample area. The average counts per minute per sample were plotted for each sample and compared with those of other samples on the stage as shown in Figure 4-25. A closer alignment of these averages, both with each other and with the overall average of all samples, indicates uniform irradiation for each experiment.

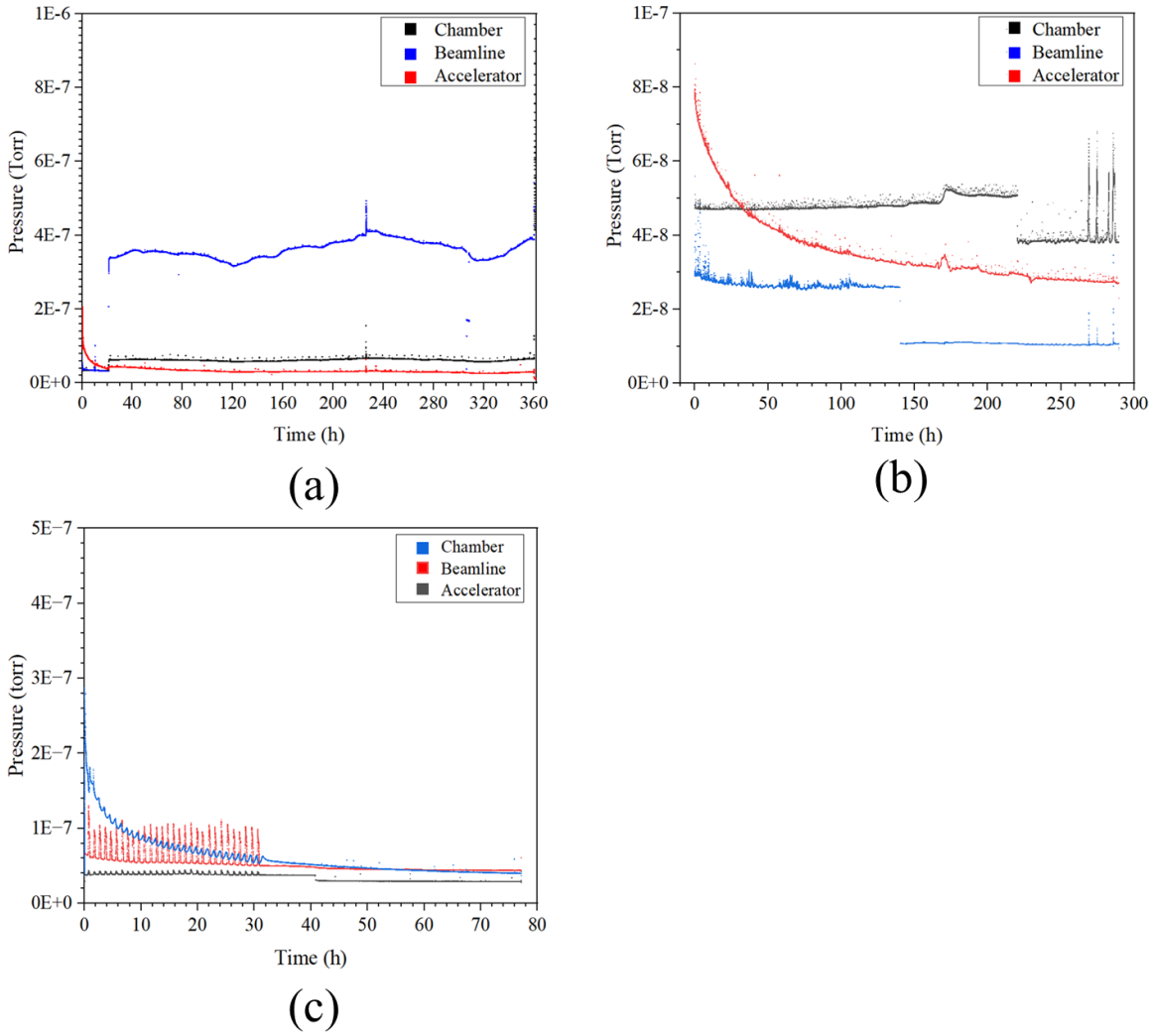


Figure 4-20 Pressure values in the accelerator, beamline, and chamber for (a) first irradiation (4PB: SS 304LN), (b) second irradiation (4PB: SS 304L-R), and (c) third irradiation experiments (tensile bars).

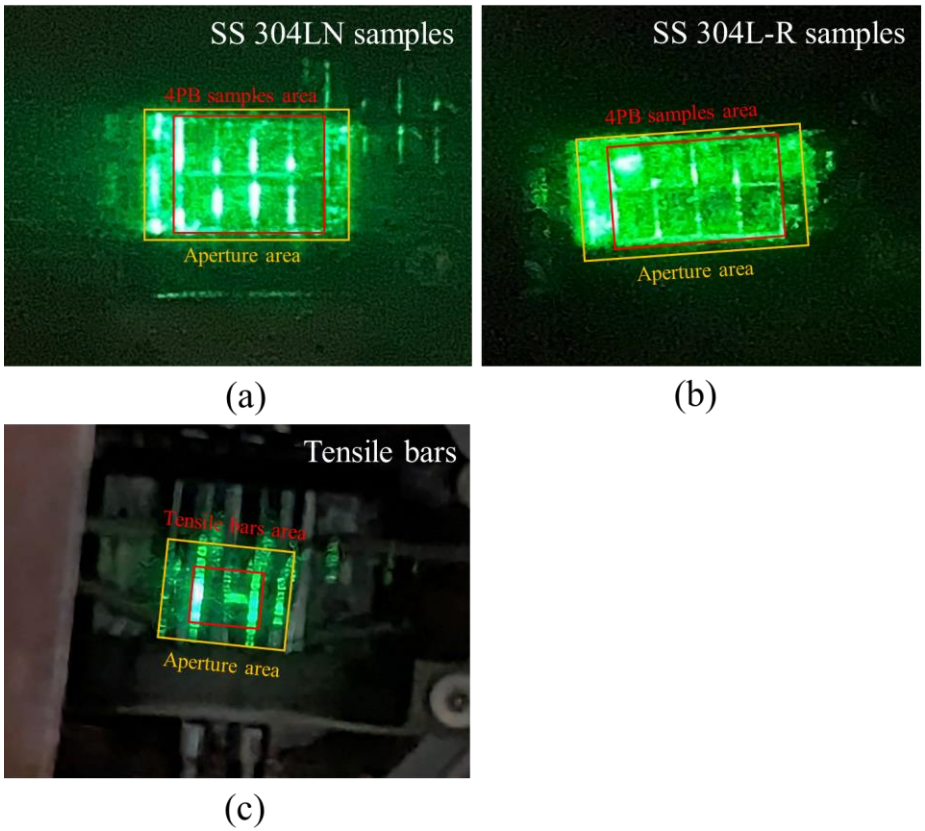


Figure 4-21 Ion beam alignment using a laser beam, the alignment ensures that the aperture opening follows the calculated data in 4PB samples in (a) and (b) and tensile bars in (c).

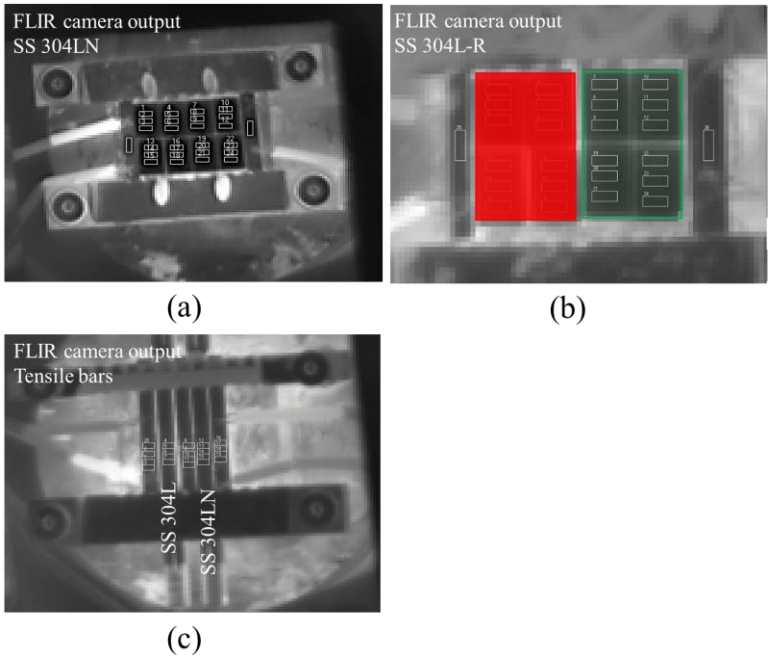


Figure 4-22 FLIR camera output showing AOIs used to track the temperature history on AOIs for (a) first irradiation (4PB: SS 304LN), (b) second irradiation (4PB: SS 304L-R), and (c) third irradiation experiments (tensile bars).

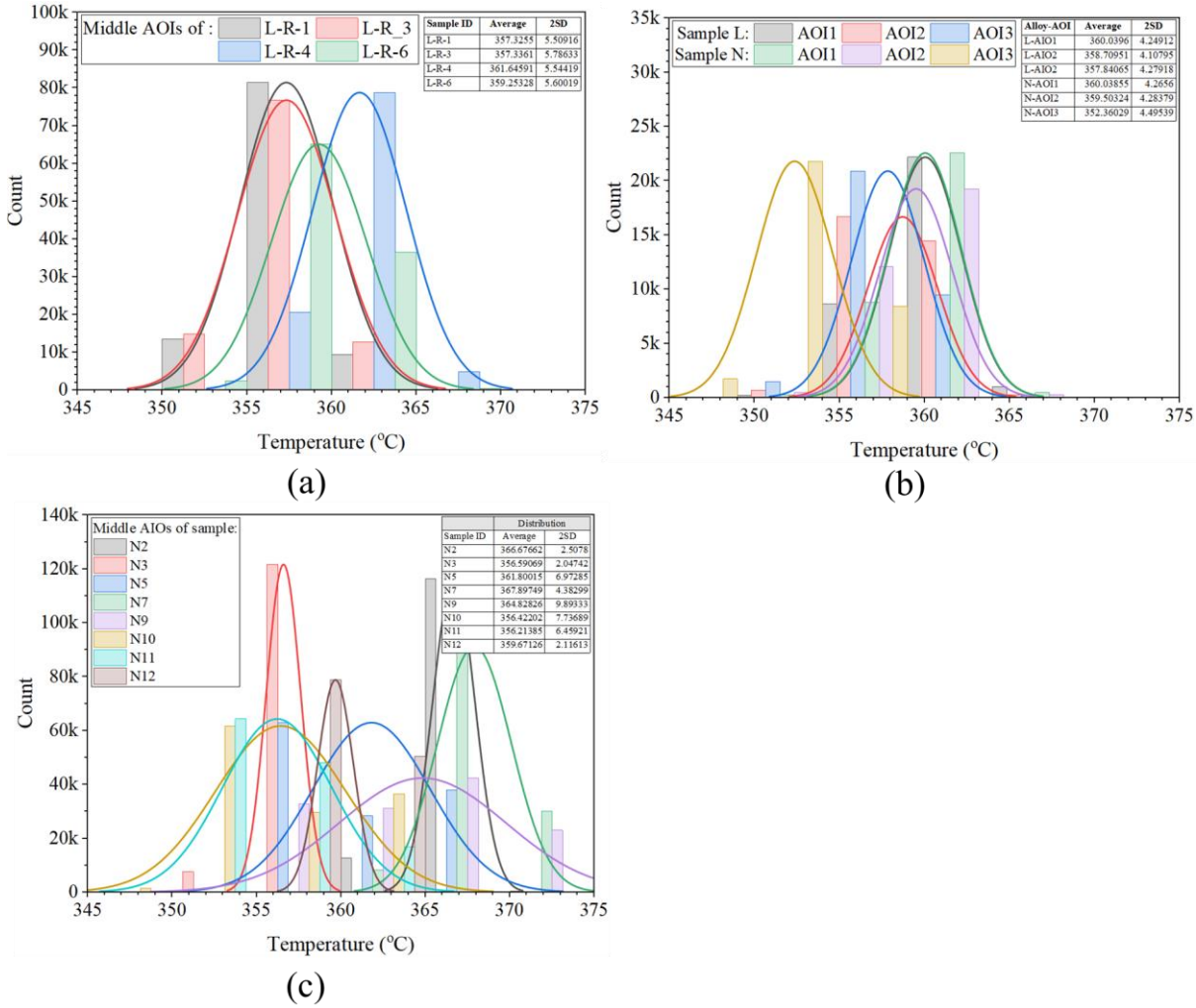


Figure 4-23 Temperature of AOIs recorded from (a) first irradiation, (b) second irradiation, and (c) third irradiation.

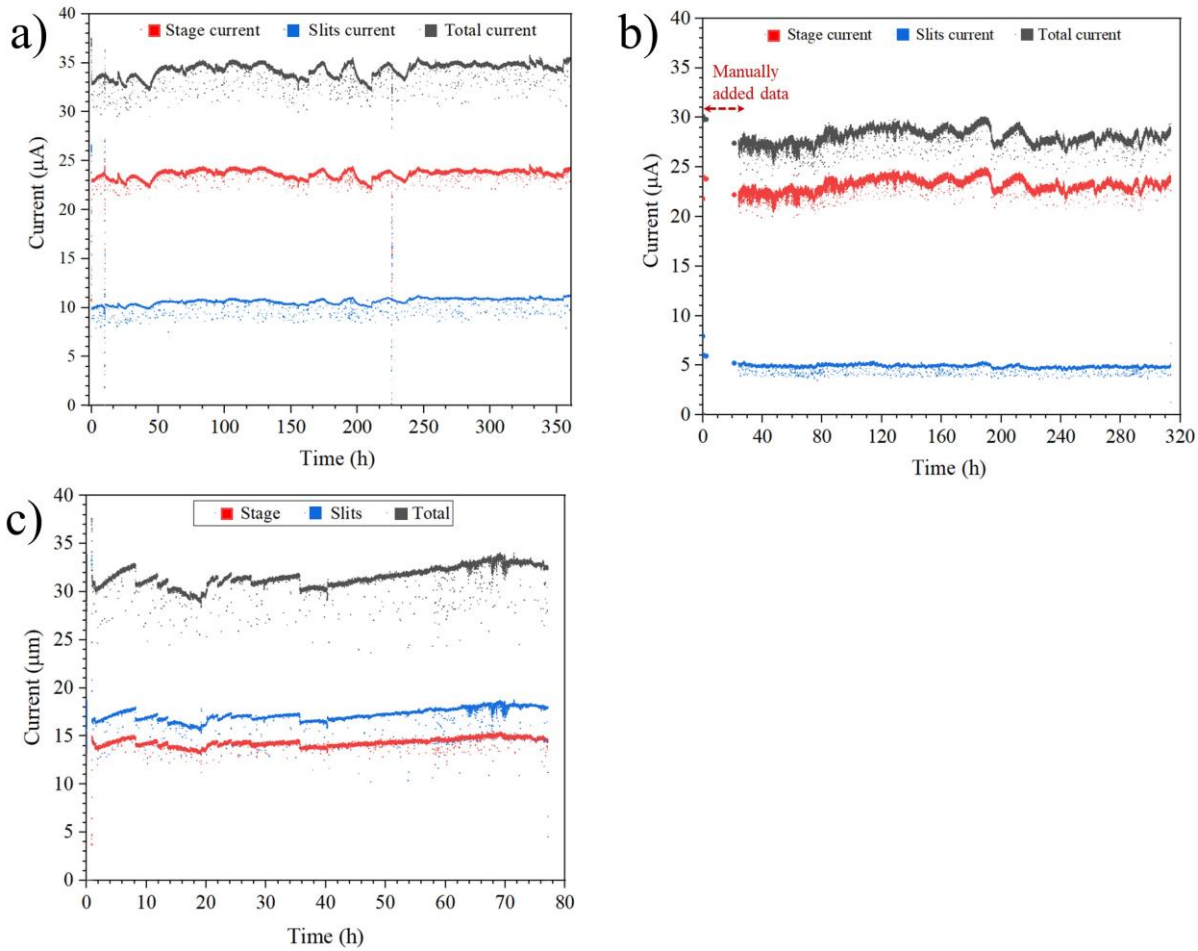


Figure 4-24 Current density at the stage, slits, and the total current recorded from (a) first irradiation (4PB: SS 304LN), (b) second irradiation (4PB: SS 304L-R), and (c) third irradiation experiments (tensile bars).

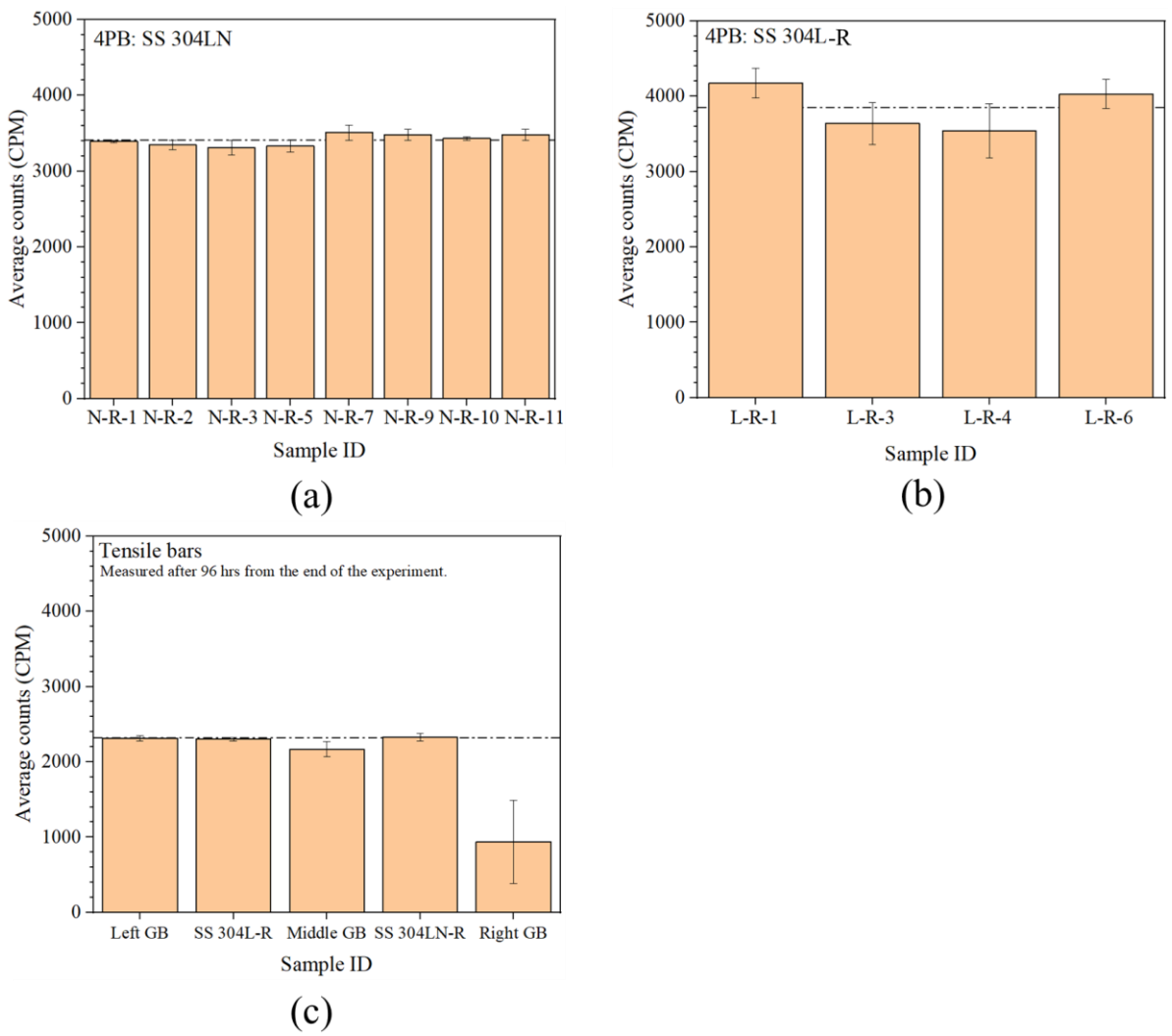


Figure 4-25 Beta counts per minute per sample after the (a) first irradiation (4PB: SS 304LN), (b) second irradiation (4PB: SS 304L-R), and (c) third irradiation experiments (tensile bars).

#### *4.5.1.3 Post-irradiation hardness measurement*

Hardness measurements were conducted on the L-T plane of the 4PB bulk after proton irradiation. The post-irradiation data was used to compare against pre-irradiation measurements from the same surface to evaluate hardness changes due to proton irradiation. To minimize edge effects on the measurements, a profile was created parallel to the short edge, as shown by the red-dotted line in Figure 4-8, maintaining a 0.5 mm distance from each edge. The profile measured 2.5 mm in length, and a 25-gf load was applied during the test. This low load was

chosen because the proton-irradiated layer is expected to remain below 25 μm. Using a higher load could cause the indenter to penetrate the unirradiated bulk, creating a plastic zone and leading to inaccurate $H_V$ measurements.

The yield strength of the irradiated layer was calculated based on the difference in hardness measurements taken before and after irradiation at room temperature. These hardness values were then converted into yield strength by averaging the results from two conversion equations: Equation 4.13 by Busby et. al. [118] and Equation 4.14 by Bruemmer et. al. [201].

$$\Delta\sigma_y = 3.03\Delta H_v, \tag{4.13}$$

$$\sigma_y = 2.5(H_v - 68) \tag{4.14}$$

There was a slight variation in the calculated hardness between the two equations, as both were derived by fitting experimental data from the literature, assuming a linear relationship between hardness and irradiated yield strength. However, Busby et al. [177] incorporated a larger dataset in his fitting curve, resulting in a slightly different slope. To maintain conservatism, the average of the two equations was taken as the irradiated yield strength at room temperature.

## 4.6 Irradiation-assisted stress corrosion cracking test

### *4.6.1 Autoclave system*

Four-point bend tests for IASCC initiation were performed in IM3 testing system in IMTL at the University of Michigan. This system is designed to test LWR environments and is shown in Figure 4-26, while the diagram showing the system design is shown Figure 4-27. Each system consists of two sub-loops: the primary water loop and the backup loop. The primary loop includes the testing solution, inlet and outlet water conductivity sensors, inlet and outlet dissolved oxygen sensors, a back pressure regulator, a heat exchanger, an ion exchanger, and a

high-pressure pump. The backup loop features a water column with pure water, serving as an emergency in case of a loss of water issues with the primary loop. All 4PB samples were strained at slow strain rate of $4.3 \times 10^{-8}$ $s^{-1}$ to provide sufficient time for corrosion process to take place to ensure an adequate surface and grain boundaries oxidation.

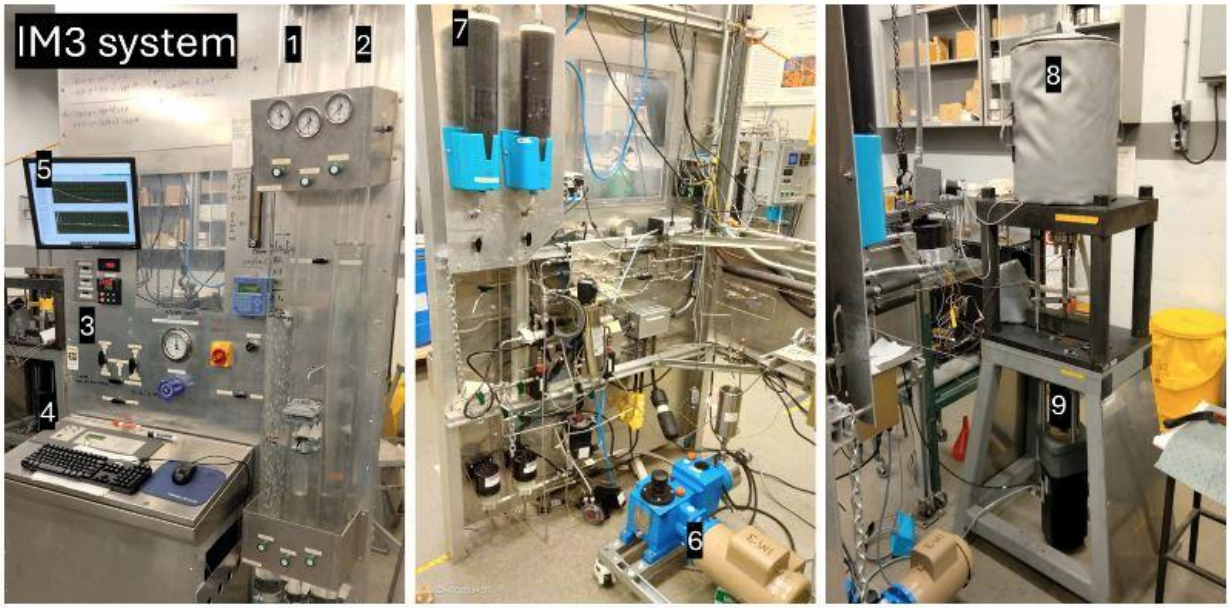


| | | | | | |
|---|---|---|---|---|---|
| 1 | Main water column | 2 | Backup water column | 3 | Water loop control panel |
| 4 | Servo-motor controller | 5 | LabView system | 6 | High pressure pump |
| 7 | Ion exchangers | 8 | Vessel | 9 | Servo-motor |

Figure 4-26 IM3 system used to simulate testing environments for this study.

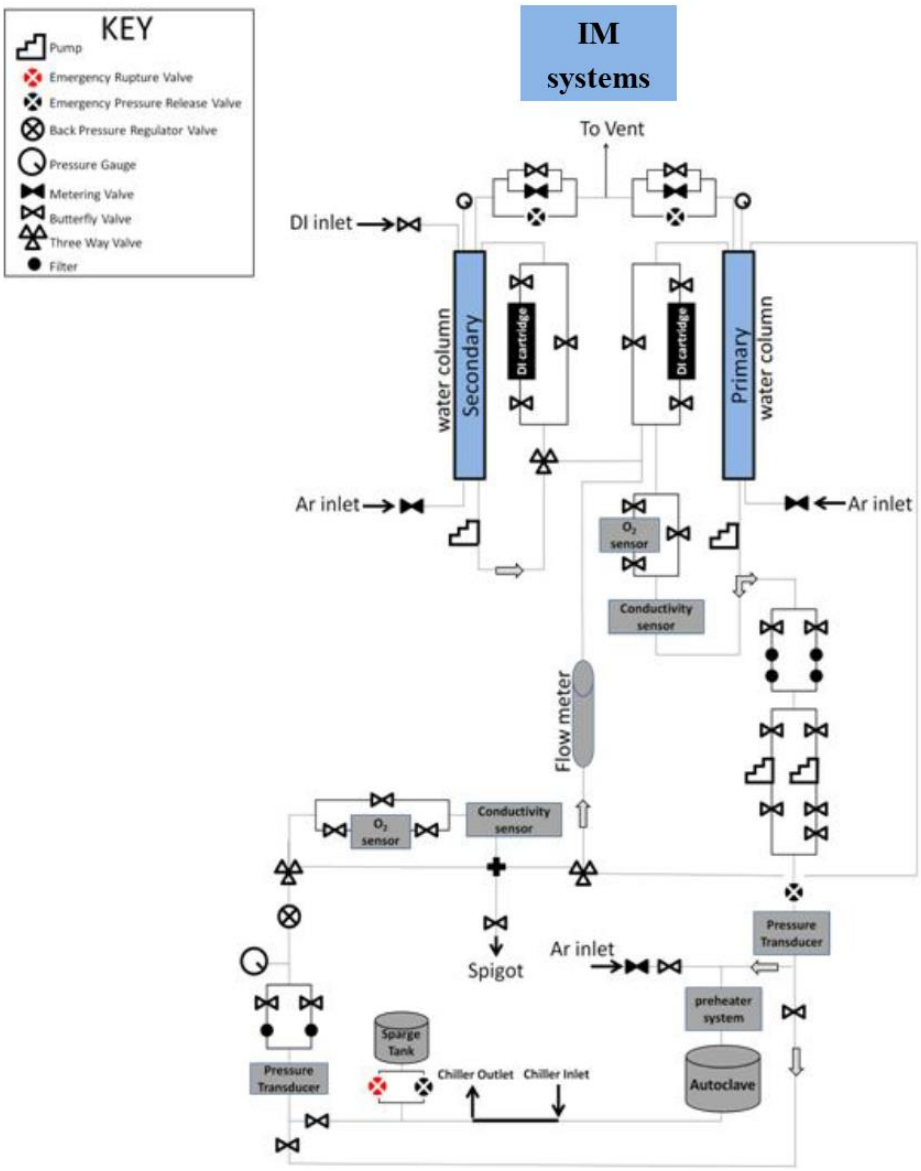


Figure 4-27 Process flow diagram for the IM3 testing system used for IASCC tests.

The loading fixture used in this study is designed to induce pure bending through a four-point bend setup as shown in Figure 4-28. the loading fixture used in this study is constructed from a combination of hardened Inconel 718 alloy and SS 316. Specifically, the base fixture, sample support, punch support, and hanger plate are made of hardened Inconel 718, while the remaining components are fabricated from SS 316. The machining of this fixture was performed by Vacuum Technology Inc. in the US, and the heat treatment was performed in IMTL.

The high-pressure autoclave is made of SS 316. Water flows from the main water column where the chemical solution is added manually from the top of the column (solution mixing was being made outside the loop in a plastic water jug of a 5 gallons capacity). The autoclave is pressurized to 2300 ± 20 pound per square inch (psi) or 15.8 MPa with a LEWA ecoflow® high-pressure pump at flow of 150 mL/min through the autoclave. The pressure inside the autoclave induces a tare load on the sample, this load was determined using the diameter of the pull-rod diameter (3.175 mm) and the autoclave pressure which resulted in a value of 125 N (28 lb). The pressure in the autoclave is maintained by Tescom® back pressure regulator before returning to atmospheric pressure and flowing back to the main water column. Once pressurized and stabilized, the autoclave is heated to 340 $^{o}$C by an 1800 Watt Watlow® heating bands attached to the outer surface of the autoclave. The autoclave temperature was continuously monitored during the test using a K-type thermocouple that is connected to a Watlow EZ-zone® heat controller. The out of autoclave water is initially cooled using a tube-to-tube heat exchanger and is further cooled by a second tube-to-tube heat exchanger connected to a chiller system. Inlet and outlet water conductivities are also monitored during the test using Thoronton 770 MAX® reading panel. Also, inlet and outlet dissolved oxygen are monitored during the test using Orbisphere® 31110 oxygen sensors with a precision of 1.0 parts per billion.

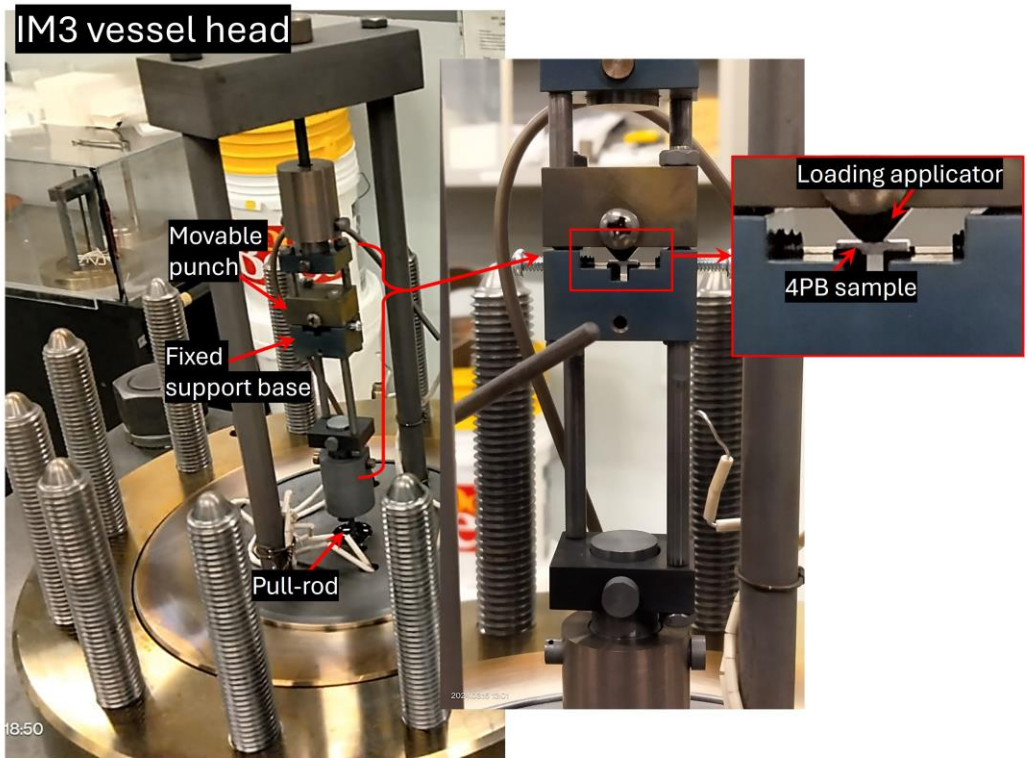


Figure 4-28 Loading fixture used in this study, the magnified image within the red box showing the 4PB sample and the loading applicator (punch).

The main column is pressurized to 8.3 psi which is equivalent to a total of 30 cc/Kg hydrogen concentration during the test to ensure that the water supplied to the autoclave is hydrogenated. Achieving this concentration was through calculating the gas content in the water following Henry's Law and controlled using column overhead pressure using:

$$C_{\text{gas}} = M_{\text{gas}} P_{\text{c}} k_H^{\circ} \exp\left(\frac{\mathrm{d}\ln k_H}{\mathrm{d}(1/T)}\left[\frac{1}{T} - \frac{1}{298.15\,\mathrm{K}}\right]\right) \tag{4.15}$$

Where $M$ is the molecular wight, $P_c$ is absolute partial pressure of the gas in the column overhead which was 15 psi in total, $k_H^{\circ}$ is Henry's constant. The derivative term is the temperature dependent of Henry's constant. For molecular hydrogen, Henry's constant is 0.00078 mol/(kg. bar), the derivative is 500 K [202]. The ambient pressure was assumed to be 0.95 bar, and the column temperature was 293 K.

### *4.6.2 Water chemistry*

IASCC experiments were performed in a high temperature water at 340 ± 0.5 $^{o}$C in water solution containing 1000 ± 50 ppm of boron in the form of $H_3BO_3$ and 2.1 ± 0.1 ppm of lithium in the form of LiOH. To prepare this solution, 0.0725 g of LiOH was dissolved in 10 Liters of demineralized water, and 57.25 g of $H_3BO_3$ was also dissolved in the same water. The solution was mixed in until $H_3BO_3$ crystals dissolved completely in the water. A water sample was then taken from the mixing jug, and pH was measured using SevenExcellence Multiparameter® pH that is equipped with a hand pH probe of a precision of 0.001. A room temperature pH of 6.55 ± 3 was used in this study, Figure 4-29 shows an example of the pH measurement from sample L-R-6 before the start of the 60%YS load step. The water conductivity in the column was around 23 ± 2 µS/cm. Once the water chemistry was confirmed, the water was added to the main column from the top, and the water was recirculated in the loop for at least one hour until all readings from system sensors were stabilized. This process preceded each 4PB test.

Figure 4-29 An example of pH measurement of the main water column ahead of the 60%YS step for sample L-6 loading step.

### *4.6.3 Sample loading*

The load is applied by an Interactive Instruments® 5K servomotor which displaces the system crosshead. The crosshead displacement is measured with a Solartron® LVDT. A pull rod

made of Inconel 718 is connected to the crosshead, and the load is applied to the sample. This rod is sealed at the inlet to the autoclave with self-energizing graphite bal seals. The load at the pull rod was measured with Transducer Techniques® 100 lbf load cell.

During the IASCC test, data from a load cell, LVDT, inlet and outlet water conductivities, inlet and outlet dissolved oxygen, hydrogen overpressure, and autoclave temperature were recorded once per 30 seconds using a LabView® program.

### *4.6.4 Incremental four-point bend test*

An incremental 4PB test was performed to determine the IASCC initiation stress, the tests were conducted in the IMTL at the University of Michigan. This method produces a decreasing tensile stress profile through the specimen thickness, limiting the growth of the crack and preventing the specimen from through-thickness cracking.

4PB tests were conducted in an incremental straining mode in which the specimen was strained at a nominal rate of $4.3 \times 10^{-8}$ $s^{-1}$ to an initially applied stress of 40 – 50% of the irradiated YS. The load was then reversed, and the specimen was removed for SEM analysis of the uniform strain region. If no cracks were observed, the specimen was reloaded, and the test was resumed from the previous load at the same strain rate and adding a stress increment of 10%YS to that of the previous test. The process was repeated until cracking occurred.

The stress level at which IASCC initiates was determined by the stress to create an observable crack at a magnification of 5000x in the SEI mode of the SEM. However, since the stress is incremented in units of 10%YS, the crack may have formed at any stress above the last increment at which no crack was observed, and up to the stress at which it was observed. Therefore, the crack initiation stress is reported as the stress at which the crack was observed, with an error bar of minus 10%YS.

Tracking the oxidized GBs was complicated because of the thick surface oxide film. In most cases, cracks appeared after the last stress increment step but the difference between the crack and the oxidized GB was indistinguishable using secondary electron imaging (SEI) mode (GB separation was unclear). Therefore, our criterion for the cracking was established as any straight and bold line that can be seen clearly in both BSE and SEI modes (at 5000x) will be considered a crack, otherwise, it is an oxidized GB. It was noted that many oxidized GBs were clearly observed in backscattered electrons (BSE) mode of the SEM, but switching to the SEM-SEI revealed little, as only an oxide film was observed at the same position.

### 4.7 Incremental constant extension rate tensile

An incremental CERT test was performed to determine the DCs density for both alloys. Tests were conducted using the IM3 system in the IMTL at the University of Michigan. The tests were conducted in autoclaves, allowing precise control and monitoring of the environment. Tests were performed in UHP argon environment to prevent surface and GB oxidation and then cracking. Initial argon purity was 99.999% and was purified further using a 27601-U Supelco® purifier up to 99.99999% purity. This step was performed to ensure the removal of any trace water and oxygen from the system which could potentially oxidize the samples during straining. Two proton-irradiated tensile samples were used in this test; one from SS 304L and the other from SS 304LN. Figure 4-9 shows the conceptual design of the tensile bars and the dimensions. The tests were performed at 340 $^{o}$C in UHP argon, samples were first strained to 80%YS at a strain rate of $3.5 \times 10^{-7}$ $s^{-1}$, the test was then interrupted, and the sample was removed from the system for microscopy analyses. Similar to the 4PB case, a hardness profile of 3.0 mm was created at the longitudinal edge of each sample to measure the real strain ($\varepsilon_{Total}$) after loading. Two indent profiles, one within the irradiated region and the second created outside it, in the

unirradiated region. Figure 4-10 shows the indents profiles created within the irradiated region and outside it for (a) SS 304L and (b) SS 304LN. The spacing between indents was recorded for the pre-loading condition, and the indents were imaged at a high magnification of 1000x to ensure accurate measurements. After loading the sample in the autoclave, the same indents profile was captured by the OM and the difference in the spacing between indents was measured. The spacing between two indents was measured using the ImageJ® program, with calibration performed using the scale bar of the OM image. These measurements were averaged for all the rows to obtain representative value. The total strain was calculated using the following equation:

$$\varepsilon_{\text{Total}} = \frac{d_{\text{post-loading}} - d_{\text{pre-loading}}}{d_{\text{pre-loading}}} \tag{4.16}$$

Where *d* refers to the distance between two indents.

Both samples were strained to 2.3%. The irradiated area was 2 × 5 $mm^2$, however, only region within the 2 × 3 $mm^2$ area was analyzed region was analyzed, as it was assumed to have been exposed to uniform irradiation. The analysis included quantifying the number of grains, categorizing the type of DCs (continuous, discontinuous, or nascent), determining their distributions and spacings, identifying the activated slip systems, and estimating the number of dislocations per channel.

### *4.7.1 Quantification of dislocation channels density*

Dislocation channels analysis was performed using different microscopy techniques. Initially, the surface of each sample at the pre-loading condition was examined using optical microscope (OM) using partial coaxial lighting (PCA) mode at a magnification of 1000x. Only uniformly irradiated areas were scanned (2 by 3 $mm^2$). The number of DCs formed following samples straining was counted and tracked using OM and grains were identified from inverse

pole figure (IPF) image obtained from EBSD to accurately locate the terminations of the DCs at the GBs.

Post to each loading step, the uniformly irradiated area was scanned by both SEM and OM to quantify the dislocations density ($\rho_{DC}$) at the specified load. Three types of DCs were analyzed: the continuous DC (CDC), the discontinuous DC (DDC) and the Nacent DC (NDC). All DCs types were counted after each load step.

In this analysis, the classification of DCs was based on the behavior at the DC-GB intersection. A DC that passes the GB and extends into the adjacent grain was classified as a CDC. If the DC terminates at the GB without crossing, it was classified as a DDC. An additional category, termed the NDC, was introduced based on experimental observations: this type crossed the GB by several tens of nanometers into the adjacent grain but then faded and disappeared.

Functionally, CDCs allow dislocations to transfer between grains, thereby reducing stress localization at the DC–GB intersection. In contrast, DDCs cause dislocations to pile-up at the GB, significantly increasing local stress. NDCs, while sharing some similarities with CDCs in allowing dislocation transfer across the GB, appear to do so less effectively, as the exact mechanisms of dislocation transfer in these cases are not yet fully understood.

### *4.7.2 Dislocation channel height*

The uniformly irradiated area was imaged using Bruker's Dimension Icon® high resolution atomic force microscopy (AFM) at $MC^2$ at the University of Michigan. This AFM offers a resolution of 0.1 nm in the Z-axis and approximately 1.0 nm in the X and Y axes, with a scanning range of 90 µm. The analysis utilized a SCANASYST-AIR-HPI® probe, the standard probe with a nominal tip radius of 2 nm, frequency of 55 KHz, Length of 100 µm, a width of 40 µm, and spring constant of 0.25 N/m.

A hundred different regions (each measured 10 μm × 10 μm) were scanned by AFM within the uniform irradiated region with a scan rate of 0.512 Hz and 512 scan lines to increase the quality of surface scanning. These settings resulted in 20 nm in lateral resolution. This region was identified based on the indentation profile formed after proton irradiation. Pre-loading data served as a reference for assessing the post-loading dislocation height.

### *4.7.3 Number of dislocations in a dislocation channel*

The number of dislocations per a DC was calculated based on the combination of parameters acquired from EBSD and AFM. First, the activated slip system was identified using slip trace analysis, and the corresponding slip direction was determined in the crystal frame (e.g., ⟨110⟩ for FCC). This slip direction was normalized and multiplied by the magnitude of the Burgers vector ($b$) to obtain the Burgers vector in the crystal frame. To project this vector into the sample frame, it was rotated using the orientation matrix (g-matrix transpose), yielding the slip direction vector ($b_{sample}$) in the sample coordinate system. The vertical component of this vector ($b_{sample,z}$) represents the effective Burgers vector component that contributes to the AFM step height. Next, the AFM was used to measure the vertical slip step height, which represents the component of the slip offset normal to the specimen surface. To obtain the true slip displacement along the slip plane, the measured step height was corrected by dividing it by the cosine of the angle (θ) between the slip plane normal and the surface normal. Finally, the number of dislocations per channel ($N_c$) was calculated as the ratio of the corrected AFM step height to the effective Burgers vector component. This approach ensures an accurate correlation between AFM measurements and the underlying slip activity, accounting for the local orientation of the slip system.

### 4.8 Microscopy analysis

A JOEL JSM 6480 SEM at IMTL was used to identify and quantify cracks in the proton irradiated specimens after each straining increment. SEM was performed first at low magnification (1000x) in BSE imaging mode covering the whole uniform strain region and generating about 300 images of 5.04 × 3.78 $\mu m^2$ size. These images were analyzed carefully and if a cracked GB was suspected by virtue of a difference in contrast with the matrix, higher magnification images up to 30,000x were taken from the same location in SEI mode to confirm the existence of the crack. The TESCAN RISE SEM was occasionally utilized to verify regions where cracks were small and not widely opened. This SEM system offers high magnification (up to 200,000x) and resolution, enabling the detection of fine features in these areas.

FIB lift-outs from the proton irradiated and strained materials were used to characterize the starting condition of the alloy, as well as the crack tips following straining. Lift-outs were first cut and transferred to copper grids with a thickness of 1.5 µm at 30 keV the Michigan Center for Materials Characterization $(MC)^2$ using FEI Helios Nanolab 650 Dual Beam SEM/FIB, TFS Helios G4 Plasma FIB Xue, and TFS Nova 200 Nanolab SEM/FIB. The lift-outs were further thinned down to about 150 nm and were finally thinned at 5 keV to reduce FIB damage induced at high beam energy.

A FEI Tecnai TF 30 TEM and TFS Talos F200X G2 EM operated in a conventional TEM (CTEM) mode at 300 keV was used for imaging Frank loops using a rel-rod dark-field (rdDF) technique with g =1/3{311} and more details is provided in reference [162]. The number of loops from such a DF image of size 1024 × 1024 pixels was counted using Gatan® DigitalMicrograph software from which the total loop number was obtained by multiplying the counted number by a factor of 2. The sizes of the loops were measured from a DF image. Loop

sizes smaller than 4 nm were excluded as it was difficult to separate them from the precipitates or FIB damages/re-depositions, and they constituted no more than 10% of the total loop population.

A Talos F200X at $(MC)^2$ operated in Scanning TEM (STEM) mode at 200 keV was used for imaging the precipitates and radiation-induced segregation (RIS) at GBs. The Talos F200X is equipped with four 30 mm2 silicon drift detectors (SDD) for energy-dispersive X-ray spectroscopy (EDS) that can give strong X-ray signals for STEM spectrum imaging (STEM-SI EDS). The thickness of the lift-out foils was measured using electron energy loss spectroscopy (EELS) performed in STEM mode in the Talos F200X. Atom-resolved high-angle annular dark-field (HAADF), low-angle annular dark-field (LAADF), and STEM bright-field (STEM-BF) images and EDS chemical maps taken from crack tip regions were performed in a Thermo-Fisher Spectra 300 probe-corrected S/TEM at (MC)2 with two 60 mm2 SDD EDS detectors equipped in STEM mode at 300 keV using a probe size of about 0.8 Angstrom.

The uncertainties associated with the irradiation-induced defects sizes were measured by the standard deviation of dislocation loops, precipitates, and cavities. Errors in density numbers of these defects were calculated from the TEM specimen thickness error resulting from the TEM imaging resolution ±10%.

For this analysis, EBSD imaging was performed using a TESCAN system equipped with an EBSD detector. The binning parameter was set to 5×5 (128×96), to enhance the signal-to-noise ratio by averaging the intensities of neighboring pixels by combining the 25 adjacent pixels in the raw image into a super-pixel during the acquisition, thereby improving pattern quality in regions with weak diffraction signals. Gain was adjusted between 120 and 180 to amplify the weak EBSD signal and optimize contrast and exposure times varied from 10 to 18 milliseconds,

depending on the scanning area, to ensure that sufficient signal was collected without saturating the detector. The standard image processing mode was selected to apply baseline corrections and histogram normalization to the captured patterns, which produces consistent, high-quality Kikuchi patterns by suppressing uneven illumination and background noise. For background capture filtering, both "SMART" and "SEM Area" modes were used. The SMART filter adapts to local pattern variations to optimize background subtraction, while the SEM Area filter captures background from the entire scanning region, ensuring uniform background correction across larger scan areas. These settings collectively ensured that the acquired EBSD patterns were of sufficient quality with an acquisition time of 20 – 25 mins per each area of interest.

Crystallographic orientation of grains was acquired from EBSD through identifying Euler angles (φ1, Φ, and φ2) corresponding to rotations which convert the laboratory (or sample) axes $\hat{x}$, $\hat{y}$, and $\hat{z}$ to the crystalline $\hat{a}$, $\hat{b}$, and $\hat{c}$, axes, respectively. Angle φ1 is the first rotation about the laboratory axis $\hat{z}$ in the range of -180 to 180 degrees, Φ is the second rotation about the rotated laboratory $\hat{x}$, in the range of 0 – 180 degrees, and φ2 is the third rotation about the rotated $\hat{z}$, in the range of -180 to 180 degrees.

# Chapter 5 Finite Element Analysis

As mentioned earlier, conducting laboratory experiments on neutron-irradiated 4PB samples is entirely different from those irradiated with protons. This is because neutron-irradiated samples (which are made from structural components that have been removed from service in nuclear reactors) typically exhibit microstructural damage uniformly across the entire sample thickness. This means that the mechanical properties are homogeneous, making it straightforward to conduct IASCC testing at loads below the irradiated YS of the material by following ASTM E855, as the load-displacement relationship remains linear. However, in the case of proton-irradiated samples, the situation is entirely different. This is due to the fact that the 2 MeV protons used in this experiment induce microstructural damage to a depth of 25 μm from the sample surface, leaving the remaining thickness unirradiated and thus free of irradiation-induced microstructural damage. As a result, the sample consists of two layers with different mechanical properties: the irradiated surface layer, which exhibits hardening due to irradiation-induced hardening defect clusters, and the unirradiated bulk, which retains the as-received mechanical properties.

The load to the sample is that which results in a specified fraction of the YS of the irradiated layer, which is approximately four times higher than the YS of the unirradiated bulk. Consequently, during IASCC testing, the bulk material undergoes plastic deformation almost immediately, making the material response to the applied load inhomogeneous. This deviation invalidates the assumptions of ASTM E855 for 4PB testing, as the applied load no longer correlates linearly with the surface stress. To address this, FEA analysis was conducted to

determine the relationship between the applied load (in Newton) and the surface stress (in MPa). The FEA simulation was performed using ANSYS Workbench® 2024 under a license provided by the University of Michigan's Information and Technology Services (ITS).

Since this analysis had not been performed previously, the FEA model required validation which was achieved by conducting an IASCC test on an unirradiated sample at 340 $^{o}$C. The deflection and total strain measured during the test were compared to the model's outputs. Additionally, a sensitivity analysis was performed to confirm that the model output aligned with expected results, ensuring its reliability. The details will be thoroughly discussed in the subsequent sections.

### 5.1 FEA with ANSYS

ANSYS Workbench® is a widely recognized and powerful finite element analysis (FEA) software suite utilized for simulating the mechanical behavior of engineering structures under various loading conditions. It offers a comprehensive platform for both linear and nonlinear analyses, enabling engineers to model complex geometries, apply realistic boundary conditions, and investigate material responses that go beyond the assumptions of linear elasticity. In the context of nonlinear analysis, ANSYS is particularly valuable due to its ability to account for large deformations, plasticity, contact interactions, and other phenomena that arise in real-world engineering problems. The software achieves this by solving the nonlinear equilibrium equations iteratively using advanced algorithms, such as the Newton-Raphson method, which updates the solution based on the current deformation state and material behavior. The accurate application of boundary conditions, including supports and applied loads, is critical in ensuring that the simulation replicates the physical test or operational environment. Additionally, convergence criteria, based on residual forces, displacement norms, or energy balance, are implemented to

monitor and ensure the accuracy and stability of the solution process at each load increment. As a result, ANSYS provides a robust framework for performing high-fidelity simulations of mechanical components, such as specimens subjected to four-point bending, where capturing nonlinear behavior is essential for understanding material performance under complex stress states.

### *5.1.1 Nonlinear analysis with ANSYS*

In nonlinear finite element analysis (FEA), ANSYS solves the nonlinear equilibrium equations that govern the static mechanical response of a structure subjected to external loads. The general equation of equilibrium in incremental form is expressed as [203, 204]:

$$\mathbf{R}(\mathbf{u}) = \mathbf{F}_{ext} - \mathbf{F}_{int}(\mathbf{u}) = 0 \tag{5.1}$$

Where $R(u)$ is the residual force vector (unbalanced force vector), $F_{ext}$ is the vector of externally applied nodal forces which equals $\sum_{i=1}^{n} P_i$ where $P_i$ is the applied load at each loading point, $F_{int}(u)$ is the internal force vector, representing the internal stresses developed in the structure under the current deformation state.

In a nonlinear analysis, the internal force vector depends on the current displacement field and the material constitutive model, and hence the equilibrium equations are inherently nonlinear. To solve this system, ANSYS uses an iterative method, typically the Newton-Raphson method, in which the displacements are updated incrementally [203]:

$$\mathbf{K}(\mathbf{u}^{(i)})\Delta\mathbf{u}^{(i)} = \mathbf{R}(\mathbf{u}^{(i)}) \tag{5.2}$$

Where $K(u^{(i)})$ is the tangent stiffness matrix evaluated at the current configuration, $\Delta u^{(i)}$ is the incremental correction to the displacement field at iteration $i$. Then the solution will be

iterated until the convergence criteria is achieved (such as displacement change or target applied load in Newton).

Once the displacement field is determined at a converged load step, ANSYS proceeds to calculate the strains and stresses at each integration (Gauss) point within the elements. The strain tensor $\varepsilon$ is derived from the displacement field $u$ using the strain-displacement matrix $B$ at:

$$\boldsymbol{\varepsilon} = \mathbf{Bu} \tag{5.3}$$

In nonlinear analysis, ANSYS usually uses either total LaGrangian formulation where strains are measured with respect to the original configuration, or updated LaGrangian formulation where strains are measured with respect to the last known configuration. For small strains as in the case of linear analysis, strain is given by [203]:

$$\varepsilon_{ij} = \frac{1}{2}\left(\frac{\partial u_i}{\partial x_j} + \frac{\partial u_j}{\partial x_i}\right) \tag{5.4}$$

However, for large strain values as in nonlinear cases, a green-LaGrange strain tensor equation is used such as [203]:

$$E_{ij} = \frac{1}{2}\left(\frac{\partial u_i}{\partial X_j} + \frac{\partial u_j}{\partial X_i} + \frac{\partial u_k}{\partial X_i}\frac{\partial u_k}{\partial X_j}\right) \tag{5.5}$$

Where $u_i$ is the displacement components and $X_i$ is the material coordinates.

The stress tensor (σ) is then calculated from the strain tensor in Eqn 5.5 using a constitutive model appropriate for the material. For elastoplastic materials, ANSYS often uses multilinear isotropic hardening, which can be expressed in incremental form:

$$\Delta\boldsymbol{\sigma} = \mathbf{D}\left(\Delta\varepsilon - \Delta\varepsilon^{pl}\right) \tag{5.6}$$

Where $\Delta\varepsilon^{pl}$ is the increment of plastic strain, calculated using the yield criterion such as Von Mises and the flow rule and $D$ is the elastic stiffness tensor for isotropic elasticity which is given by:

$$D_{ijkl} = \lambda\delta_{ij}\delta_{kl} + \mu\left(\delta_{ik}\delta_{jl} + \delta_{il}\delta_{jk}\right) \tag{5.7}$$

Where $\lambda$ and $\mu$ are Lame's constants.

At each load increment, ANSYS usually uses return mapping algorithms to integrate the plastic flow and update the stress tensor, ensuring that the stress state satisfies the desired yield criterion. Once the stress tensor is computed at each integration point, ANSYS then calculates the Von Mises equivalent stress from the distortion energy theory [205] that defined as:

$$\sigma_{VM} = \sqrt{\frac{1}{2}\left[(\sigma_{xx} - \sigma_{yy})^2 + (\sigma_{yy} - \sigma_{zz})^2 + (\sigma_{zz} - \sigma_{xx})^2\right] + 3\left(\tau_{xy}^2 + \tau_{yz}^2 + \tau_{zx}^2\right)} \tag{5.8}$$

Where $\sigma_{xx}$, $\sigma_{yy}$, $\sigma_{zz}$ are the normal stress components, $\tau_{xx}$, $\tau_{yy}$, and $\tau_{zz}$ are the shear stress components. $\sigma_{VM}$ represents the scalar measure of the stress state than can be compared to the yield strength of the material. In nonlinear analysis, the stress components ($\sigma_{ij}$) include both elastic and plastic contributions. The Von Mises stress is evaluated at each integration point and then extrapolated to the nodes or averaged over the element for output visualization.

In a nonlinear 4PB analysis, ANSYS does not explicitly compute the bending moment using classical beam theory equations. Instead, the bending moment effect emerges naturally within the finite element stress field as a result of solving the nonlinear equilibrium equations across the entire geometry. The stress distribution inherently captures the combined effects of loading, geometry, material behavior, and deformation, thereby reflecting the bending moment's influence without needing a separate moment calculation.

### 5.2 FEA Model

An FEA model was built to mimic the actual loading fixture used for IASCC testing in IMTL explained earlier in section 4.6.1. The design incorporated the punch, which serves as the load applicator, and the base, which simulates the fixed support. This configuration has been

previously reported as suitable for simulating the four-point bend method, with further details available in Ref. [137]. Figure 4-8 shows the conceptual design of the 4PB sample used in this study including the proton irradiated layer. Figure 5-1 shows the model design used in the simulation and the mesh settings. The 3D model was initially designed in AutoCAD® 2024, licensed to ITS, and subsequently imported into ANSYS Workbench® 2024 for simulation. The dimensions of the punch and 4PB samples are identical to the actual components, whereas only a small section of the base (support) is included, as the rest is irrelevant to the simulation. The punch and base are modeled as rigid bodies, and the calculations account solely for the unirradiated bulk and the irradiated layer (4PB sample).

The model outputs included profiles of surface stress, strain, and deflection. The maximum surface stress, located in the constant strain region, was used for comparison with the fraction of the yield strength of the irradiated layer. Moreover, since the 4PB test setup is dependent on the sample thickness, individual FEA computation is required for each sample.

### 5.3 Model setup

After defining the material properties, model setup was conducted. In this 4PB test, the sample interacts with other components at four contact points: two where the back surface of the 4PB sample contacts the punch indents, and two where the proton-irradiated surface contacts the support indents. In ANSYS, accurately defining the contact types between bodies is crucial to ensure simulation fidelity. Based on the experimental design, the degrees of freedom (DOF) of the 4PB sample are governed by boundary conditions at the supports and loading points as explained the conceptual drawing in Figure 5-2 (a). At the outer supports, all DOF are restricted (UX, UY, UZ, RX, RY, RZ = 0) to ensure the sample remains fixed in position without translation or rotation. At the inner loading points, forces are applied to the sample and only UY

are allowed while other DOF are restricted (UX, UZ, RX, RY, RZ = 0) to prevent the sample from falling or shifting. Rotations at the loading points are also constrained to preserve the position of the constant strain region.

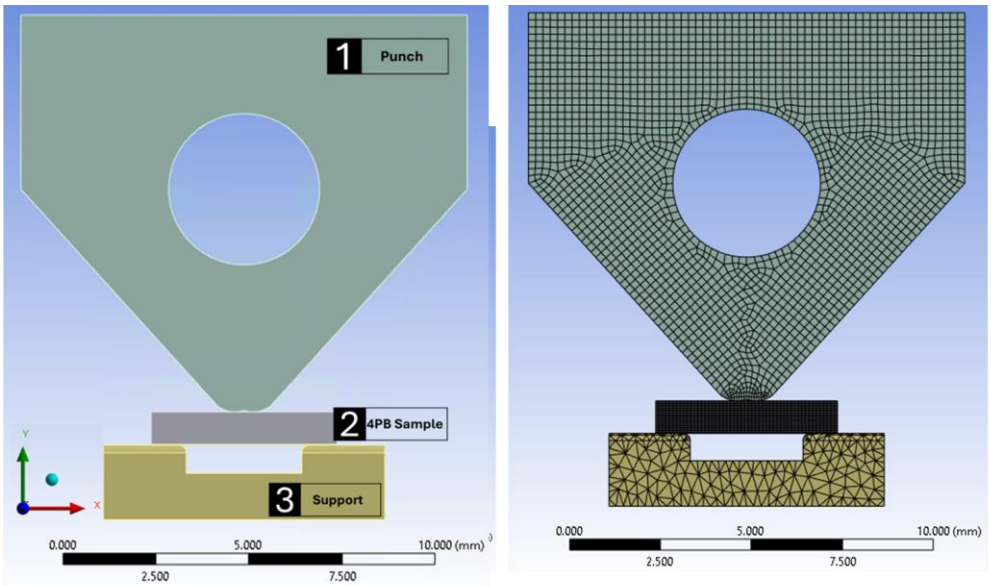


(a)

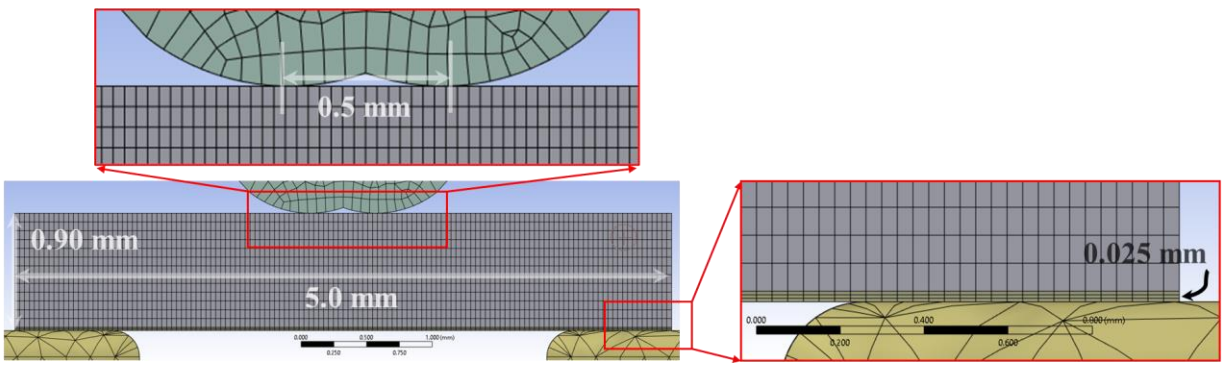


(b)

Figure 5-1 (a) FEA model used to calculate the applied load, the model with mesh is on the right and (b) mesh settings for the unirradiated bulk and the irradiated layer.

The sample is free to deform naturally under the applied loads between the supports and loading points, with translations (UX, UY, UZ) and rotations (RX, RY, RZ) permitted, however, it is constrained between the inner and outer supports making its translations and rotations constrained. In the constant strain region, the sample deforms under bending stresses, with no

additional motion constraints. This configuration ensures that the simulation accurately reflects the mechanical behavior of the 4PB test. Friction forces at the contact points were considered, assuming no separation or sliding occurred during the test.

The coefficient of friction was identified as a critical parameter and was carefully defined. However, accurately determining its value in water at 340 $^{o}$C posed challenges. Consequently, an iterative approach was used to adjust the COF based on the results of the real 4PB test. Other boundary conditions were defined as follows: the support structure was treated as a fixed body, with all translations (UX = UY = UZ) constrained to zero. The applied load was introduced through the punch (load applicator), which was assumed to move exclusively in the negative Y direction, with horizontal translations (UX = UZ) constrained to zero as shown in Figure 5-1.

Mesh element type selected for the sample and the punch was a second-order hexahedral element (Figure 5-2 (b)) while the selection for the base was determined and controlled by ANSYS, as it was not incorporated in the calculations. A hexahedral mesh was chosen for the sample to ensure efficient energy transfer and stress distribution during deformation from the bulk material to the irradiated layer. Also, this type usually minimizes distortion during the deformation. The node-to-node matching, as shown in in Figure 5-2 (b), was considered the most accurate representation for simulating conditions in IASCC testing as it ensures that deformation and energy transfer are accurately captured at the interface. Table 5-1 lists the mesh sizes used in the FEA.

Table 5-1 Mesh settings used in the FEA.

| Component | Contact | Value (mm) | Element type | Number of elements | Number of nodes |
|---|---|---|---|---|---|
| Punch | - | 2.00 | Hexahedral | 127,426 | 802,586 |
| Punch indents | Between the punch and the back surface of the 4PB sample. | 0.07 | Hexahedral | | |

| | | | | | |
|---|---|---|---|---|---|
| Unirradiated bulk | - | 0.07 | Hexahedral | 46,800 | |
| Irradiated bulk | - | 0.01 | Hexahedral | 10,800 | |
| Outer supports | Between the base and the 4PB sample proton-irradiated surface | 0.07 | Tetrahedral | 8,603 | |
| Base (Support) | - | 2.00 | Tetrahedral | | |

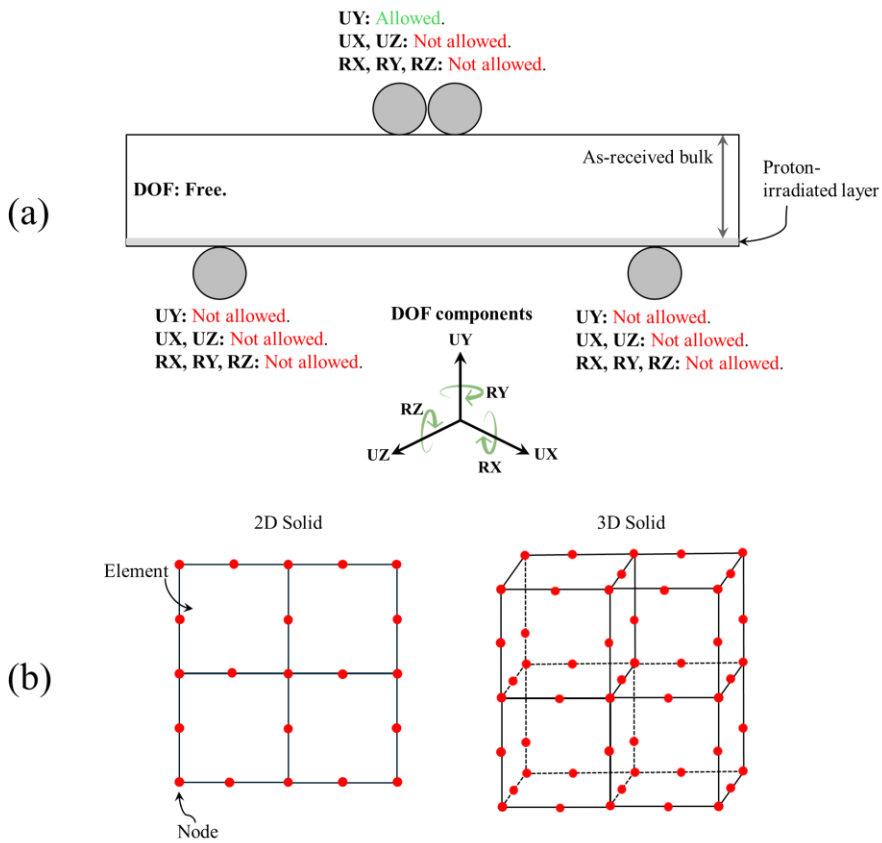


Figure 5-2 Conceptual diagrams showing (a) Degree of freedom components for inner supports, outer supports, and 4PB sample, and (b) the element type and node configuration used in the ANSYS simulation showing a second order quadratic element type of 20 nodes per each element (in 3D).

In this study, the interface between the unirradiated bulk and the irradiated layer was defined using a shared topology tool. This configuration allowed ANSYS to treat both layers as a single body with distinct mechanical properties. Enabling this feature in ANSYS significantly reduced simulation time, as the number of elements decreased from thousands to just a few hundreds, resulting in substantial savings in computational cost.

Shared topology used is not a contact type, but a meshing technique used within ANSYS to ensure mesh continuity across interfaces. When a shared topology is defined between two bodies, ANSYS generates a single, conformal mesh across these bodies, which can be particularly useful for ensuring accurate stress and strain distribution at interfaces without artificially introduced stiffness or stress concentrations that sometimes occur with contact elements.

To verify that the number of elements across the irradiated layer was sufficient, a series of FE experiments were conducted with different element sizes as summarized in Table 5-2: 0.07, 0.02, 0.01, and 0.008 mm. These corresponded to one, two, three, and four layers of elements through the irradiated thickness, respectively, while the unirradiated bulk was kept at 0.07 mm in all cases as shown in Figure 5-3 (a) to (c). An additional run was performed using 0.008 mm in the irradiated layer and 0.05 mm in the bulk to check for sensitivity to bulk refinement as shown in Figure 5-3 (d).

The results showed no significant differences across these conditions in equivalent stress, total strain, and deflection profiles. Only the single-layer case (0.07 mm) produced slightly lower values, indicating that the FE solutions were independent of element size once at least two layers were used. Based on this analysis, an element size of 0.01 mm was selected for the irradiated layer and 0.07 mm for the unirradiated bulk, balancing accuracy with computational efficiency.

Table 5-2 FEA results dependent on element size.

| **Number of elements layers in the irradiated layer.** | **Element size (mm)** | |
|---|---|---|
| | **Irradiated** | **Unirradiated** |
| 1 | 0.07 | 0.07 |
| 2 | 0.02 | 0.07 |
| 3 | 0.01 | 0.07 |
| 4 | 0.008 | 0.07 |
| 4* | 0.008 | 0.05 |
| ** Check the FEA results depending on unirradiated bulk element size.* | | |

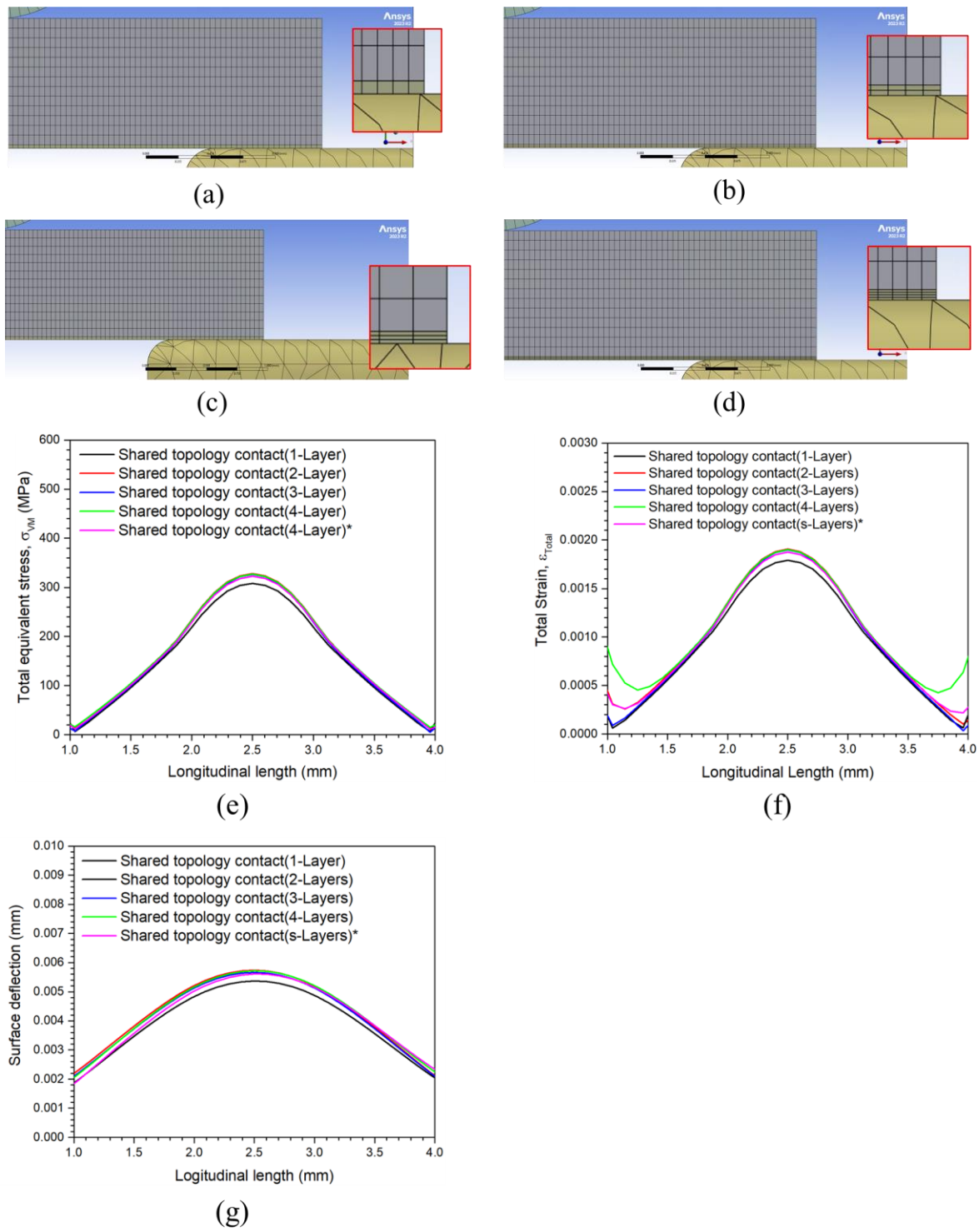


Figure 5-3 FEA results showing the effect of element size in the irradiated layer and unirradiated bulk: (a) one element layer, (b) two element layers, (c) three element layers, and (d) four element layers. Panels (e)–(g) present the corresponding equivalent stress, total strain, and deflection profiles, demonstrating that the FEA results are independent of element size.

## 5.4 Input data

As is well known, input data plays a crucial role in simulation programs. Therefore, maximum effort was made to ensure the accuracy of the input data, either through mechanical testing or through a deep investigation from the literature. Figure 5-4 shows the diagram outlining the FEA procedure used to ensure consistent and accurate results. The primary inputs for the FE model are the IM testing system sensors, 3D model design (sample geometry), materials properties, and contact settings.

The yield strengths of both the unirradiated bulk material and the irradiated surface layer were key inputs. The yield strength of the unirradiated bulk material was determined through tensile testing, as outlined in Section 4.1.2, SS-3 tensile specimens were used to measure the yield strength of the unirradiated bulk at both room temperature and 340 ºC. Tensile tests were only performed on unirradiated conditions because FEA showed that the significant thickness difference between the unirradiated bulk (97% of the sample thickness) and the proton irradiated surface layer (3% of the sample thickness) makes the design sensitive to change in the unirradiated bulk but not the irradiated layer.

The yield strength of the irradiated layer was calculated based on the difference in hardness measurements taken before and after irradiation at room temperature as explained in Section 4.5.1.3 using Eqns. 4.13 and 4.14.

Other properties such as elastic moduli, material density, Poisson's ratio, and coefficient of friction were obtained from the literature at elevated temperatures.

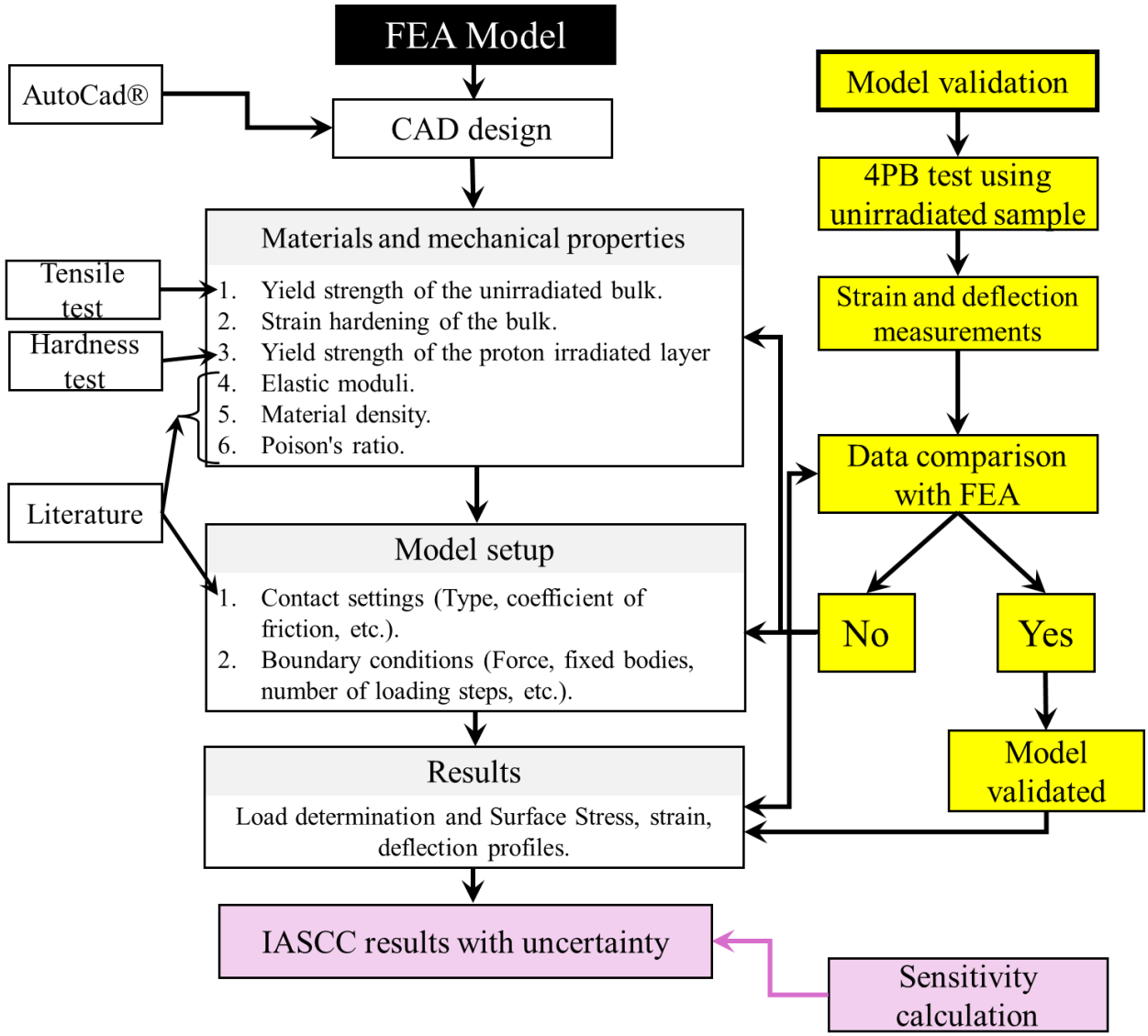


Figure 5-4 A flow chart explaining the process of using FEA for calculating the applied load required for 4PB test.

### *5.4.1 Yield strength of the irradiated layer at high temperature*

Data on the irradiated YS at 340 ºC is not readily available in the literature, likely because this temperature slightly exceeds the operating condition of the primary water system of PWRs. Additionally, determining the irradiated YS of a 25 µm layer at 340 ºC in IMTL was not possible due to the lack of a suitable technique. The only available method for assessing mechanical properties was hardness indentation, which could only be performed at room temperature.

Therefore, the approach taken to determine the irradiated YS at 340 ºC was to gather all relevant data at 320 ºC and extrapolate it to 340 ºC. Table 5-3 summarizes the data obtained from the literature for the irradiated YS at elevated temperatures.

Table 5-3 Irradiated yield strength at high temperature from literature.

| Alloy | Treatment | Irradiation, dpa | Temperature (ºC) | Irradiated YS (MPa) | Reference |
|---|---|---|---|---|---|
| SS 304 | Solution Annealed (SA) | Neutrons, 5.5 dpa | 330 | 783 | [206] |
| SS 304 | SA | Neutrons, 5.0 dpa | 25 | 875 | [207] |
| SS 304 | SA | Protons, 5.0 dpa | 320 | 800 | [207] |
| SS 304 | SA | Neutrons, 4.8 dpa | 320 | 750 | [208] |
| SS 304 | SA | Neutrons, 10.2 dpa | 320 | 740 | [209] |
| SS 304/SS 316L | - | Neutrons, 5.0 dpa | 25 | 875 | [210] |
| SS 304/SS 316L | - | Neutrons, 5.0 dpa | 164 | 725 | [210] |
| SS 304 | - | Neutrons, 12 dpa | 330 | 765 | [211] |
| SS 304 | - | Neutrons, 5.4 dpa | 320 | 794 | [212] |
| SS 304 High Purity | - | Neutrons, 5.5 dpa | 320 | 783 | [213] |

To extrapolate the irradiated YS at 340 ºC, two approaches were employed. The first involves averaging the yield strength values at room temperature and high temperatures. The average YS at room temperature was taken as 875 MPa (from Table 5-3), excluding the 800 MPa value from proton irradiation and the data at 164 ºC, which were considered as outliers. At high temperatures, an average of 758 MPa was calculated from 783, 750, and 740 MPa values (from Table 5-3). Therefore, using the fitting equation in Table 5-4 resulted in an irradiated YS at 340 ºC equals 754.2 MPa.

Table 5-4 Comparison of the irradiated YS at 25 $^{o}$C and 340 $^{o}$C.

| Approach | Irradiated YS at 25 $^{o}$C (MPa) | Irradiated YS at 340 $^{o}$C (MPa) | Difference in the irradiated YS (MPa) | Percentage of the Difference in the $YS_{irradiated}$ |
|---|---|---|---|---|
| 1 | 875 | 754.16 | 120.84 | 13.81% |
| 2 | 875 | 736.27 | 138.73 | 15.85% |
| Average change in the irradiated YS (MPa): 129.79 | | | | |
| Standard deviation (MPa): 12.65 | | | | |

In the second approach, the outlier data (proton-irradiated values and those at 164 ºC were excluded, however, the remaining data points were not averaged. Applying the fitting equation from Figure 5-5 resulted in an irradiated YS at 340 ºC of 736.3 MPa.

To quantify the reduction in irradiated YS at 340 ºC, the extrapolated values were compared to room temperature YS values, and the differences were averaged at 129.79 MPa. The standard deviation was calculated at 12.65 MPa as shown in Table 5-4. The average reduction in irradiated YS at 340 ºC (129.79 ± 12.65 MPa) was then applied to the room-temperature YS data obtained from hardness tests to estimate the irradiated YS at 340 ºC from the data obtained from the hardness tests at room temperature. The resulted irradiated YS at 340 ºC estimated at 746 MPa for SS 304L and 777 MPa for SS 304LN, a summary of the irradiated YS values used in this study is provided in Table 5-5.

Table 5-5 Irradiated YS at 25 $^{o}$C and 340 $^{o}$C.

| Alloy | Irradiated YS at 25 $^{o}$C (MPa)* | Irradiated YS at 340 $^{o}$C (MPa) |
|---|---|---|
| SS 304L-R | 876 | 746 |
| SS 304LN | 908 | 777 |
| ** Measured by hardness test.* | | |

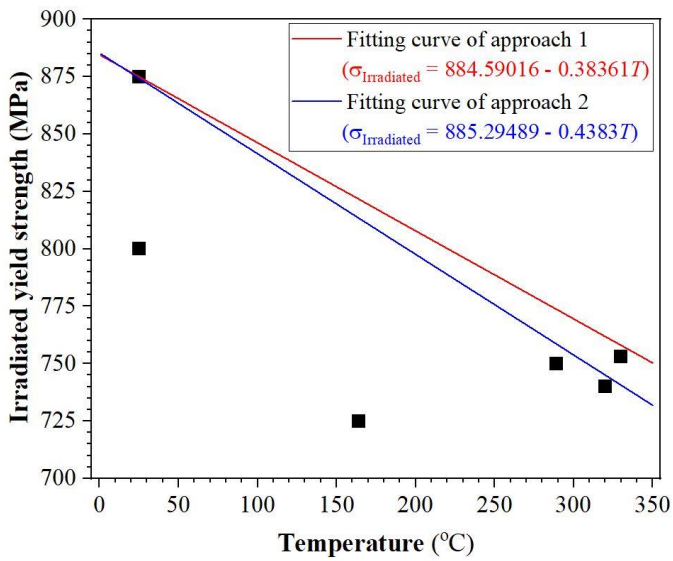


Figure 5-5 Irradiated yield strength extrapolation at high temperature.

### *5.4.2 Yield strength of the unirradiated bulk at high temperature*

Another essential input is the YS of the unirradiated bulk material. As mentioned earlier, the unirradiated bulk accounts for approximately 97% of the sample's thickness, making its YS an influential factor in the FEA because the sample deformation is controlled by the unirradiated bulk. YS at 25 ºC and 340 ºC were measured by tensile test as explained in section 4.1.2. Three samples per each condition were tested for SS 304LN while two sample tested at 340 ºC and one at 25 ºC for SS 304L.

For SS 304L, the average YS at 340 ºC was determined from the two tests measurements, resulting in a value of 197.5 MPa. Similarly, for SS 304LN, the similar procedure resulted in a $YS_{Bulk}$ 340 ºC of 194 MPa. These YS values were used in the FEA on the samples to determine the loads required for IASCC tests.

### *5.4.3 Other material properties from literature*

Other important parameters were also considered in the FEA. Elastic modulus in (GPa), density in (g/cm$^3$), Poisson's ratio, and coefficient of friction were obtained from the literature. A

summary of the values used in the FEA is listed in Table 5-6 at both 25 ºC and 340 ºC. Values of parameters at 340 ºC that were not available in the literature were extrapolated from their values at 320 ºC following the same approach explained as in the previous section. In this study, the value of Posson's ratio at 340 ºC was set at 0.31 [25, 26], the material density was considered at 7.8 g/cm$^3$ [25, 26].

Table 5-6 Other material's properties used in the FEA.

| Parameter | Value at 25 ºC | Value at 340 ºC | Reference |
|---|---|---|---|
| Possion's ratio | 0.29 | 0.31 | [214] |
| Material density (g/cm$^3$) | 7.8 | 7.8 | [25, 26] |
| Friction of coefficient | 0.64 – 0.70 | 0.45 – 0.55 | [215, 216, 217] |

The coefficient of friction (COF) was an influential factor as it defines the interaction between contacting surfaces at the contact points. Since COF data for water at 340 ºC was unavailable in the literature, the results of FEA validation tests, which will be detailed in the following sections, were used as a reference to determine and correct the COF at 340 ºC. In this study, a COF of 0.55 was used at 340 ºC. Although published COF values for metal contacts in high-temperature pressurized water environments are limited, dry and lubricated metal-to-metal contacts at temperatures up to approximately 350 °C typically exhibit COF values in the range of 0.3 to 0.6 [214, 215, 216, 217].

Young's modulus of elasticity (E) for austenitic stainless steels was obtained from various literature sources [214, 218, 219, 220, 221]. Outliers were excluded, and the remaining data points were averaged. Table 5-7 summarizes the literature values for the modulus of elasticity of different austenitic stainless steels at both 25 ºC and 340 ºC. For this study, the value of 172 GPa was used for both alloys.

Table 5-7 Elastic of Modulus of austenitic stainless steels.

| Alloy | Elastic of Modulus at 25 ºC (GPa) | Elastic of Modulus at 340 ºC (GPa) | Reference |
|---|---|---|---|
| SSs 304, 310, 316, 321, 347 | 195 | 173 | [218] |
| SSs 304, 316, 316LN | 185 | 174 | [219] |
| SSs 304, 316 | 200 | 176 | [220] |
| Austenitic SS | 192 | 173 | [214] |
| Austenitic SS | 188 | 173 | [214] |
| SS 304 | 196 | 167 | [221] |
| **Average** | 193 | 172 | - |
| **Standard Deviation** | 5.5 | 3.0 | - |

## 5.5 FE model validation

Since this model was used for the first time for proton-irradiated 4PB samples, the validity of the FEA code output needed to be checked against laboratory measurements. The two values that can be measured are the deflection of the 4PB sample and the surface total strain. The measurements were done at both 25 ºC and 340 ºC. A bend test was performed at 25 ºC using the unirradiated sample N1, the resulting deflection was measured by SEM, LVDT and modeled with FEA. At 340 ºC, the deflection of the unirradiated sample N4 was measured using LVDT and subsequently verified with an optical microscope after testing, while the strain was measured from the surface indents using SEM. These measurements were then modeled using FEA.

### *5.5.1 FEA model validation tests at room temperature*

The first test was performed at 25 ºC in air using the unirradiated sample N1. The testing parameters for this test are listed in Table 5-8. During the test, sample N1 was strained using a load of 444 N (122 lb) at a strain rate of $4.3 \times 10^{-6}$ $s^{-1}$. The sample deflection was measured by calculating the edges curvatures using the SEM before and after the test. Following the test, the sample deflection was measured by LVDT and BSE.

The sample deflection of sample N1 for pre- and post-loading conditions is shown in Figure 5-6 (a) and (b). The curvature of the sample surfaces was measured using Image® software. The deflection from LVDT measured at 0.0211 mm while the curvature of the N1 sample was measured by the SEM-BSE as shown in Figure 5-6. The curvature for the pre-loading sample was unavoidable during the sample preparation where grinding and polishing were performed using a Gatan disc grinder® as the disc surface was not perfectly flat and no other options were available. The curvature after the loading was measured and compared with the pre-loading curvature resulting in 0.0191 mm as shown in the Figure 5-6.

Table 5-8 Testing parameters used in the 4PB test for the FEA model validation.

| Parameter | Test 1 | Test 2 |
|---|---|---|
| Sample ID | N1 | N4 |
| Environment | Air | Water |
| Temperature (°C) | 25 | 340 |
| Pressure (psi) | 14.7 | 2300 |
| Sample thickness (mm) | 1.04 | 0.99 |
| Applied load (N) | 444 | 600 |

### *5.5.2 High temperature validation test*

Prior to loading, a profile of 5 × 21 indents was created at the center of the sample using a Vickers hardness indenter. The spacing between indents was recorded for pre-loading condition, and the indents were imaged at a high magnification of 330x to 420x to ensure accurate measurements. After loading the sample in the autoclave, the same indents profile was captured by the SEM and the difference in the spacing between indents was measured. The spacing between two indents was measured using the ImageJ® program, with calibration performed using the scale bar of the SEM image. These measurements were averaged for all the rows to obtain representative value. The total strain was calculated using the equation 4.16.

This test was performed in simulated water environment explained earlier in section 4.6.2. Following the test, the sample deflection was measured by LVDT and BSE.

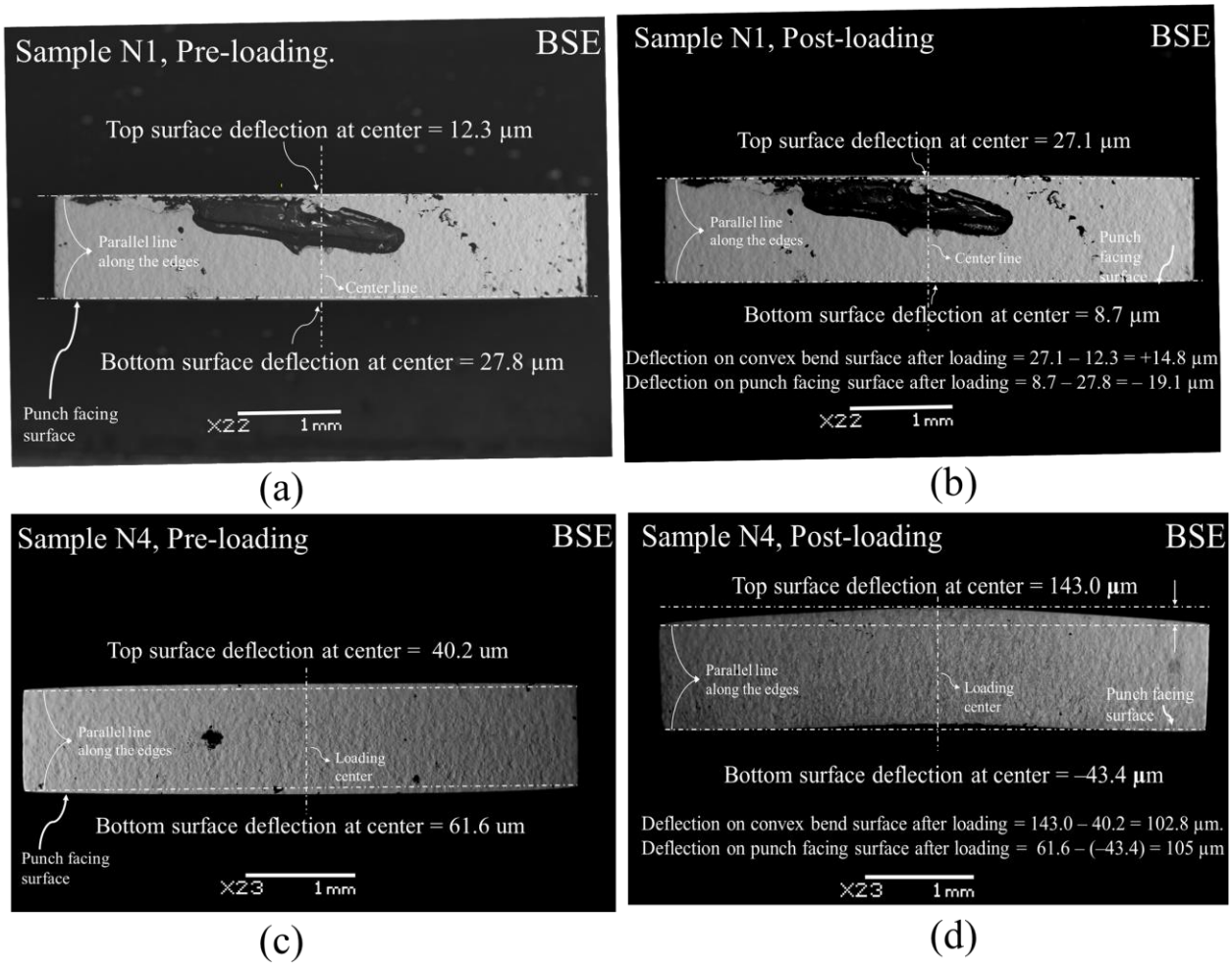


Figure 5-6 BSE images for the deflection measurement for sample N1 which strained at room temperature in air for (a) pre-loading, (b) post-loading, and sample N4 which strained at 340 °C in water for (c) pre-loading and (d) post-loading.

After the test, the surface deflection was measured by the LVDT as 0.1034 mm. This measurement reflects the difference between the initial loading point, near zero, and the endpoint of unloading, marked by the dashed vertical line. Additionally, the deflection was clearly observed in the SEM and measured as 0.1030 mm, determined from the net difference in curvatures before and after loading, as shown in Figure 5-6 (c) and (d).

### *5.5.3 Data comparison*

Following the autoclave tests, FEA simulations performed to simulate 4PB test on samples N1 and N4. the simulation results are plotted in Figure 5-7 (a) shows the surface stress and strain profiles of sample N-1 (black curves), while Figure 5-7 (b) shows the surface deflection profiles of the samples showing a deflection of 0.0214 mm for sample N-1 and 0.1016 mm for sample N-4. Therefore, the average of measured values from LVDT and SEM and the calculated value from the FEA for sample N-1 is 0.0205 mm compared to 0.1027 mm for sample N-4 as listed in Table 5-9. This means that for sample N-1, the FEA calculation differs by 4.2% from the average data, LVDT measurement differs by 7.0, and the SEM measurement differs by 2.8% indicating a good agreement between the FEA calculation and the measurement at 340 ºC.

While in case of sample N-4, the FEA calculation, shown in Figure 5-7 (b), estimated the calculated surface deflection at 0.1016 mm. The average of these values is 0.1027 mm. FEA calculation differs from the average by 1.04%, LVDT measurement by 0.58%, and the SEM measurement by 0.2% showing a good agreement between the FEA calculation and the experimental measurements at 340 ºC. The high-temperature results show better agreement because the sample experienced greater deflection under the applied load in high-temperature water. This increased deflection was more easily captured by the SEM thus reducing errors in the imaging resolution and improving measurement accuracy. A summary of the deflection results for both tests is listed in Table 5-9.

Total strain ($\varepsilon_{total}$) measurement performed only on sample N4 due to its higher deflection. The indents profile, shown in Figure 5-8 (a), was measured after the 4PB test. The total strain, calculated using equation 5.10, was plotted in Figure 5-8 (b) along with the calculated total strain from the FEA performed on sample N4. The blue band around the measured curve represents the

measurement error. The figure demonstrates strong agreement between the measured and calculated strain profiles, confirming the reliability of the FEA model for this type of test.

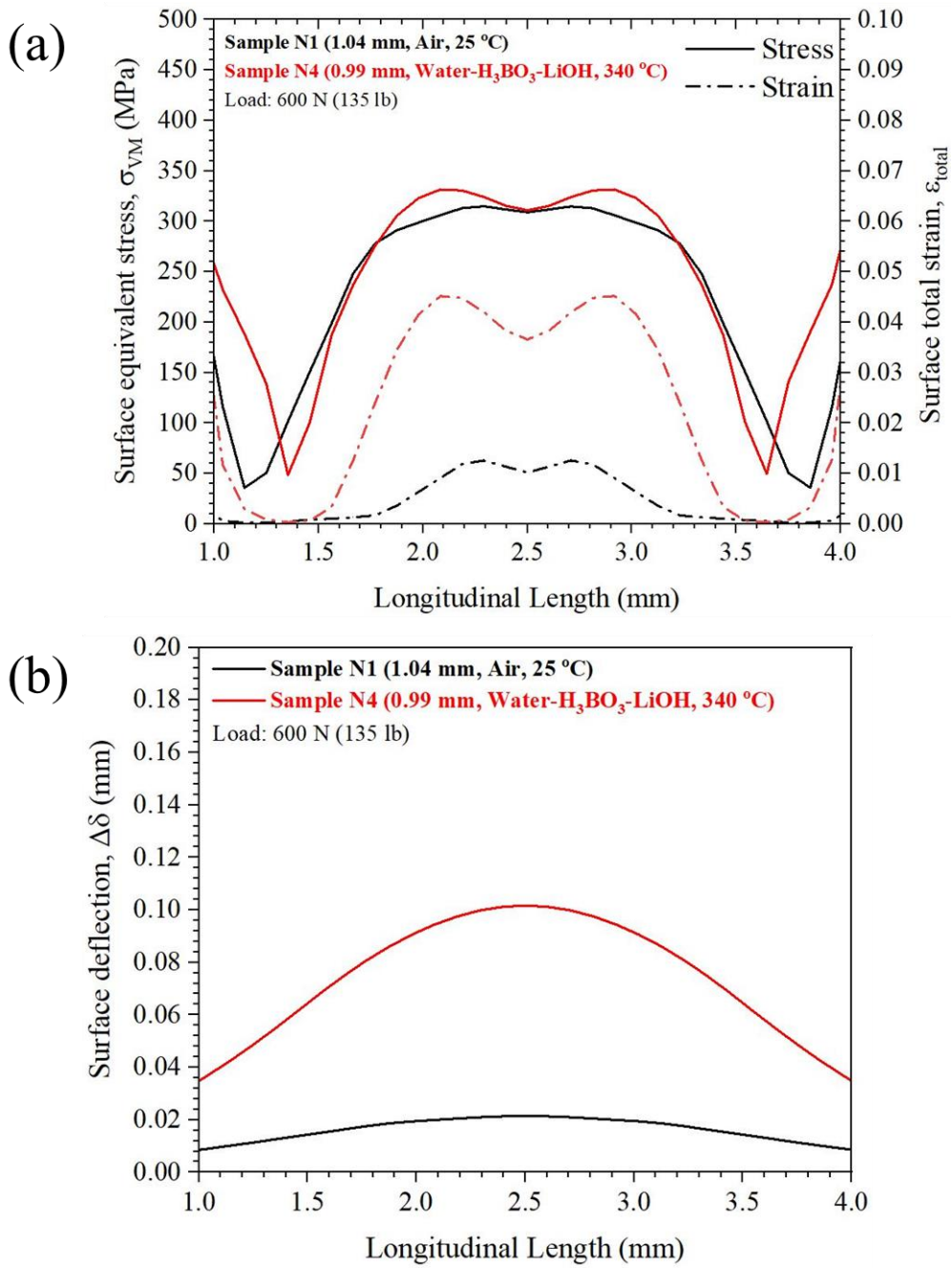


Figure 5-7 FEA calculations of (a) surface stress-strain and (b) surface deflection profiles for samples N1 strained in air and N4 strained in high temperature water.

Table 5-9 Sample deflection for the 4PB test at RT and 340 ºC.

| Method | Sample N1 (RT) | % Difference from Average | Sample N4 (340 ºC) | % Difference from Average |
|---|---|---|---|---|
| FEA | 0.0214 mm | 4.2 | 0.1016 mm | 1.04 |
| SEM | 0.0191 mm | 7.0 | 0.1030 mm | 0.20 |
| LVDT | 0.0211 mm | 2.8 | 0.1034 mm | 0.58 |
| Average | 0.0205 mm | - | 0.1027 mm | - |

Due to the limited irradiated sample availability, it was not feasible to use one of these samples for validation tests. However, as explained in the previous sections, the sample's deflection is predominantly controlled by the unirradiated bulk, making this validation test relevant and applicable.

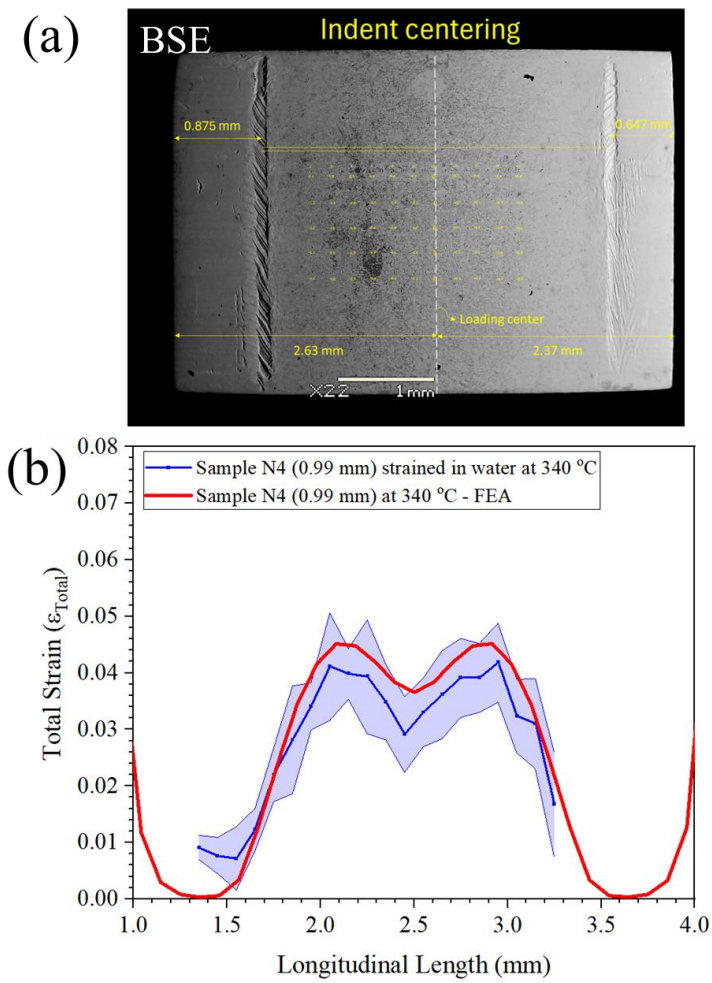


Figure 5-8 Measured strain by indents spacing in (a) and the comparison with the FEA in (b).

### *5.5.4 FEA output*

FEA was primarily employed to calculate the surface stresses as a function of the applied load. The FEA results provided the necessary load values for the 4PB tests, enabling the estimation of surface stress and its correlation with the percentage of the irradiated yield strength. Additionally, the FEA outputs included the distribution profiles of surface stress, strain, and deflection in both the longitudinal and transverse directions at the surface.

#### *5.5.4.1 Load determination for 4PB testing*

This study involved six samples (three samples from each alloy) and FEA calculations were performed for each sample prior to conducting 4PB tests. Since the 4P tests followed the incremental procedure outlined in Section 4.6.4, it was essential to calculate the load for each step until sample failure occurred.

Determining the appropriate load for the first loading step in the FE model was a challenging process that required several iterations to achieve the first target stress level. Sample N3 was the very first sample that underwent 4PB testing. The first planned step was to reach the 40% of YS, but since no record about this alloy at 0.900 mm thickness was available, several FE iterations was required at the beginning to reach the appropriate load that induce a surface stress equal to 40%YS. After performing the initial trials and reaching the target %YS as planned (40%YS in the N3 example), these values were then used to estimate the loads for the subsequent steps using the extrapolation method, thereby reducing the number of FEA simulations required.

The load (N) versus maximum surface stress (MPa) was then plotted, and a fitting equation was established for each sample, serving as a reference for that specific thickness and YS. Figure 5-9 shows the applied load calculations from FEA required for 4PB tests.

Each curve reflects the dependence on sample thickness and bulk YS, explaining the variation in load and surface stress between samples. Additionally, because of the immediate plastic deformation the sample experiences upon loading, the growth rate of the second-order polynomial curve decreases with higher loads.

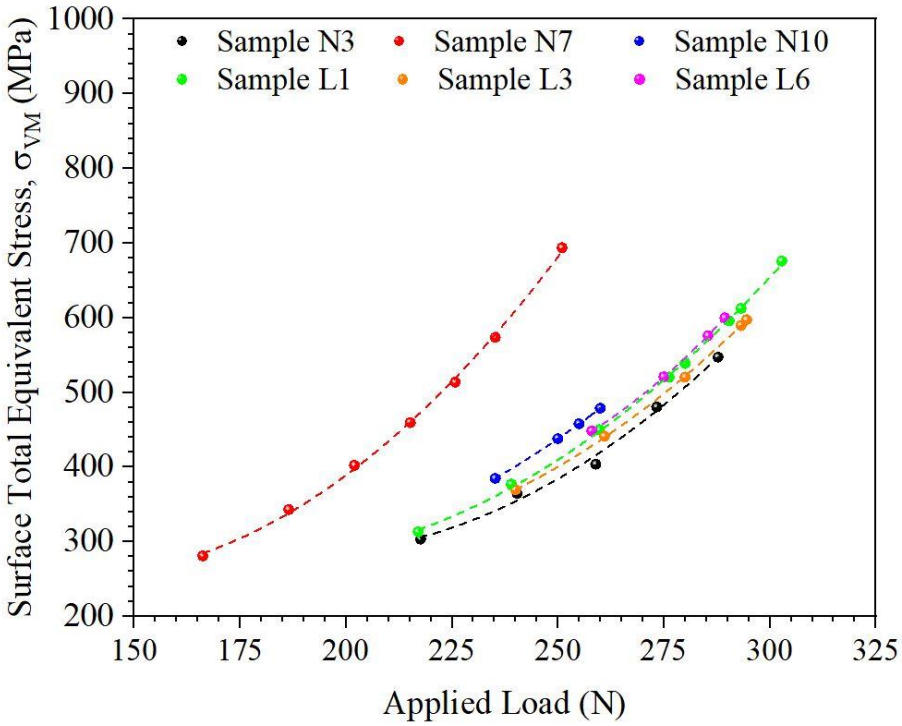


Figure 5-9 Applied load determination from FEA for 4PB tests.

Table 5-10 Fitting equations created from curves in Figure 5-7.

| Alloy | Sample ID | Thickness (mm) | Fitting equation (σ) |
|---|---|---|---|
| SS 304LN | N3 | 0.900 | $0.02693x^2 – 10.1734x + 260.31$ |
| | N7 | 0.808 | $0.03287x^2 – 8.94066x + 127.29$ |
| | N10 | 0.880 | $0.01952x^2 – 5.87174x + 686.03$ |
| SS 304L-R | L-R-1 | 0.887 | $0.02459x^2 – 8.63566x + 1031.76$ |
| | L-R-3 | 0.893 | $0.02481x^2 – 9.09737x + 1124.14$ |
| | L-R-6 | 0.884 | $0.03865x^2 – 16.33357x + 2089.79$ |

Table 5-10 provides the polynomial fitting equations for each curve shown in Figure 5-9. The table shows the importance of sample thickness in the relation between applied load and surface stress, as highlighted by sample N7 with a thickness of 0.808 mm.

Table 5-11 summarizes the load in (N) and the corresponding surface stress in (MPa) for each step that used to achieve 40%, 50%, 60%, 70%, and 80% or higher in some cases. The fractions of tens of the %YS in samples N3 and N7 are due FE analysis initially performed using the YS data from the literature.

Finally, establishing a general equation that encompasses all thickness and $YS_{Bulk}$ cases proved to be difficult. Despite several attempts using various statistical models to identify a general equation that replaces the six fitting equations in Table 5-10, an R-square value exceeding 0.4 could not be achieved.

Table 5-11 Load and maximum surface stress used in 4PB test.

| Sample ID | Loading step | Load (N) | Max. Stress (MPa) | %YS[1] |
|---|---|---|---|---|
| N3[2] | 1 | 217.6 | 308.2 | 39 |
| | 2 | 240.4 | 364.5 | 47 |
| | 3 | 258.9 | 403.9 | 52 |
| | 4 | 273.3 | 480.6 | 62 |
| | 5 | 287.8 | 547.2 | 70 |
| N7 | 1 | 186.5 | 343.1 | 44 |
| | 2 | 202.0 | 402.2 | 52 |
| | 3 | 215.2 | 459.6 | 59 |
| | 4 | 225.8 | 513.7 | 66 |
| | 5 | 235.2 | 573.6 | 74 |
| | 6 | 251.0 | 693.7 | 89 |
| N10 | 1 | 235.2 | 384.7 | 50 |
| | 2 | 257.4 | 468.0 | 60 |
| | 3 | 273.4 | 543.6 | 70 |
| | 4 | 287.3 | 623.1 | 80 |
| L-R-1 | 1 | 239.0 | 377.0 | 50 |
| | 2 | 257.4 | 450.2 | 60 |
| | 3 | 276.2 | 520.3 | 70 |

| | | | | |
|---|---|---|---|---|
| | 4 | 290.4 | 596.0 | 80 |
| L-R-3 | 1 | 240.0 | 369.4 | 60 |
| | 2 | 280.0 | 520.3 | 70[3] |
| | 3 | 294.5 | 597.3 | 80 |
| L-R-6 | 1 | 258.0 | 448.2 | 60 |
| | 2 | 275.0 | 520.8 | 70 |

*[1] Maximum stress with respect to yield strength. The last step is the one that cracks initiation observed.*
*[2] The load was recalculated using the new YS obtained from a tensile test, whereas the initial calculation was based on literature data.*
*[3] Due to a communication issue between the servomotor and LabView, the load, which was intended to stop at 60%YS, exceeded the target and reached 70%YS.*

#### *5.5.4.2 Stress, strain, and deflection profiles*

For each sample, profiles of surface stress, strain and deflections in either longitudinal or transverse directions across the sample's surface were determined. These profiles are valuable for understanding the behavior of the irradiated layer and the unirradiated bulk under the applied load in the testing environment. The equivalent stress at the surface was necessary to compare against the irradiated YS to determine the stress in units of %YS, because the IASCC initiation stress is representative of the $\%YS_{irradiated}$.

For SS 304LN, Figures 5-10 to 5-12 show the longitudinal surface profiles of stress in (a), strain (b), and deflection (c), while the transverse surface profiles of the stress is shown in the same figure in (d), strain in (e), and deflection in (f) for samples N3, N7, and N10. While for S 304L, similar plots for stress, strain, and deflection profiles across both longitudinal and transverse directions for samples L-R-1, L-R-3, and L-R-6 are plotted in Figures 5-13 to 5-15 respectively.

The figures show the surface profiles of both unirradiated bulk in the dashed lines and the irradiated layer in the solid lines. It is clear that the plastic deformation in the bulk starts immediately after applying the load since plastic deformation was observed at all loading steps.

The flat curve suggests plastic deformation, with stress exceeding the unirradiated yield strength, while the hump-shaped curve indicates stresses below the yield strength of the irradiated layer. To further explain this, total equivalent stress and normal stress profiles across the sample thickness were plotted for SS 304LN in Figure 5-16 and SS 304L in Figure 5-17. These plots show a typical behavior in a 4PB method such as the transition of the stress from the compressive stresses to the tensile stress after passing the neutral axis lies roughly at the center of the sample's thickness, where the bending stress transitions from compression to tension. The total equivalent stress decreases significantly because both the normal and shear stresses are minimal at the neutral axis. However, in the proton-irradiated 4PB design, the interface between irradiated and unirradiated layers could introduce stress discontinuities or gradients due to their contrasting mechanical properties, but the profile appears continuous in our design, suggesting effective load transfer and compatibility between the layers. The thin proton-irradiated layer significantly affects the overall stress distribution by bearing higher stress due to its higher yield strength. It is important to note that the actual response to the applied load at the interface between the irradiated layer and the unirradiated bulk is not perfectly linear. This is because microstructural damage decreases with depth from the surface, becoming more attenuated. Additionally, the damage is not strictly confined to 25 μm, as its depth may vary by several microns. However, this design remains well-suited for our study.

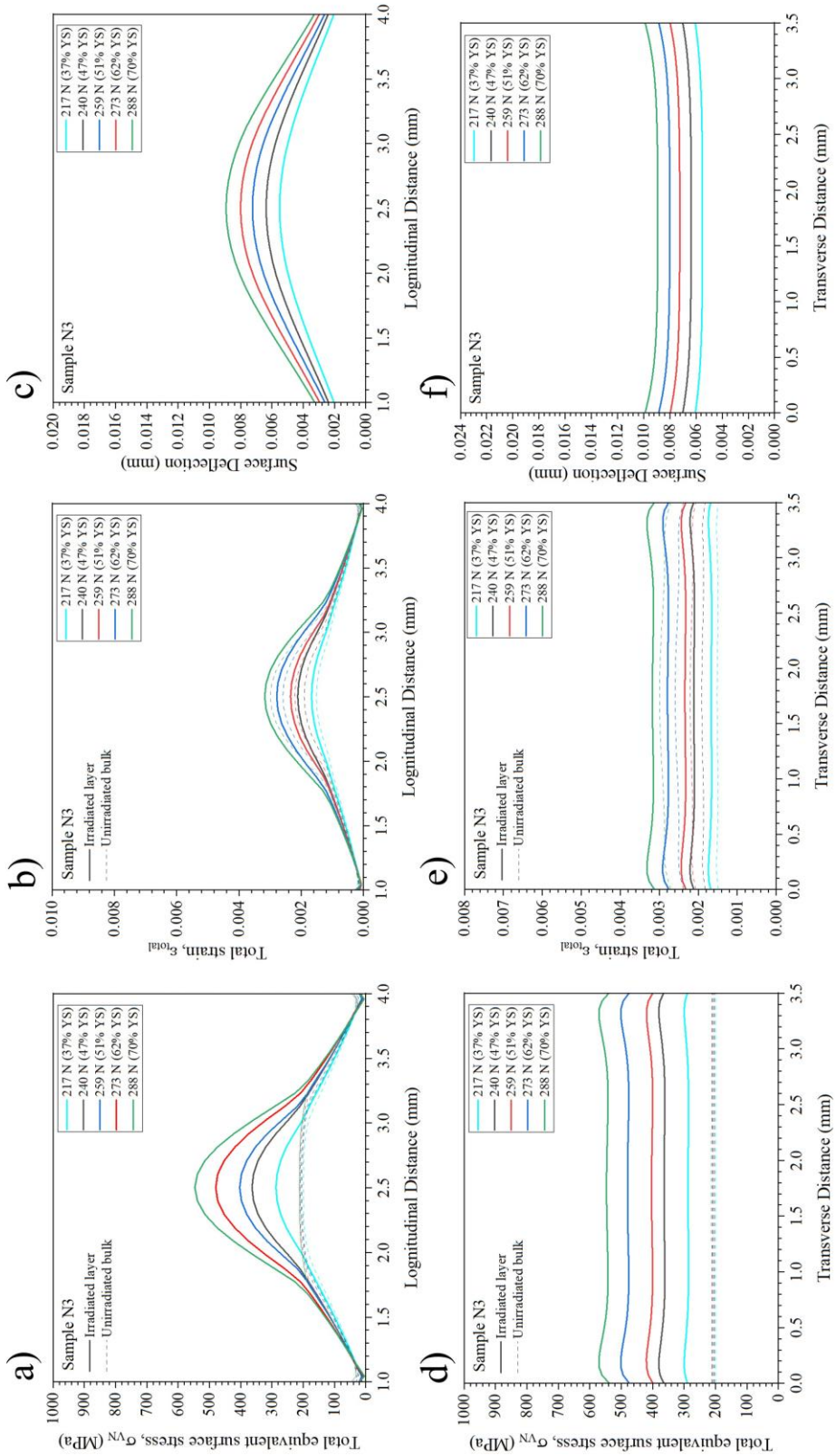


Figure 5-10 FEA results of sample N3 for surface profiles of longitudinal (a) stress, (b) strain, (c) deflection, and transverse (d) stress, (e) strain, and (f) deflection

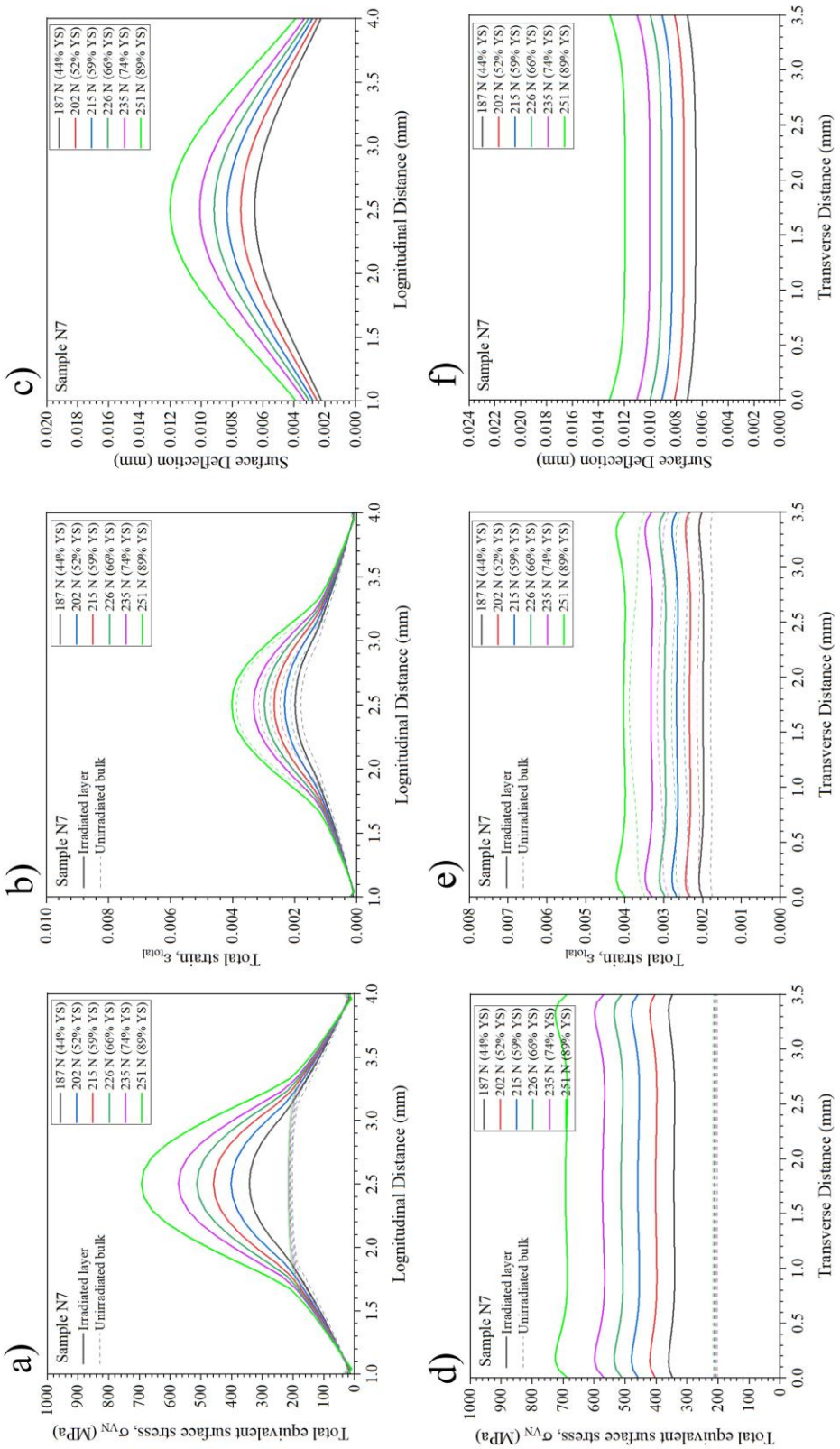


Figure 5-11 FEA results of sample N7 for surface profiles of longitudinal (a) stress, (b) strain, (c) deflection, and transverse (d) stress, (e) strain, and (f) deflection

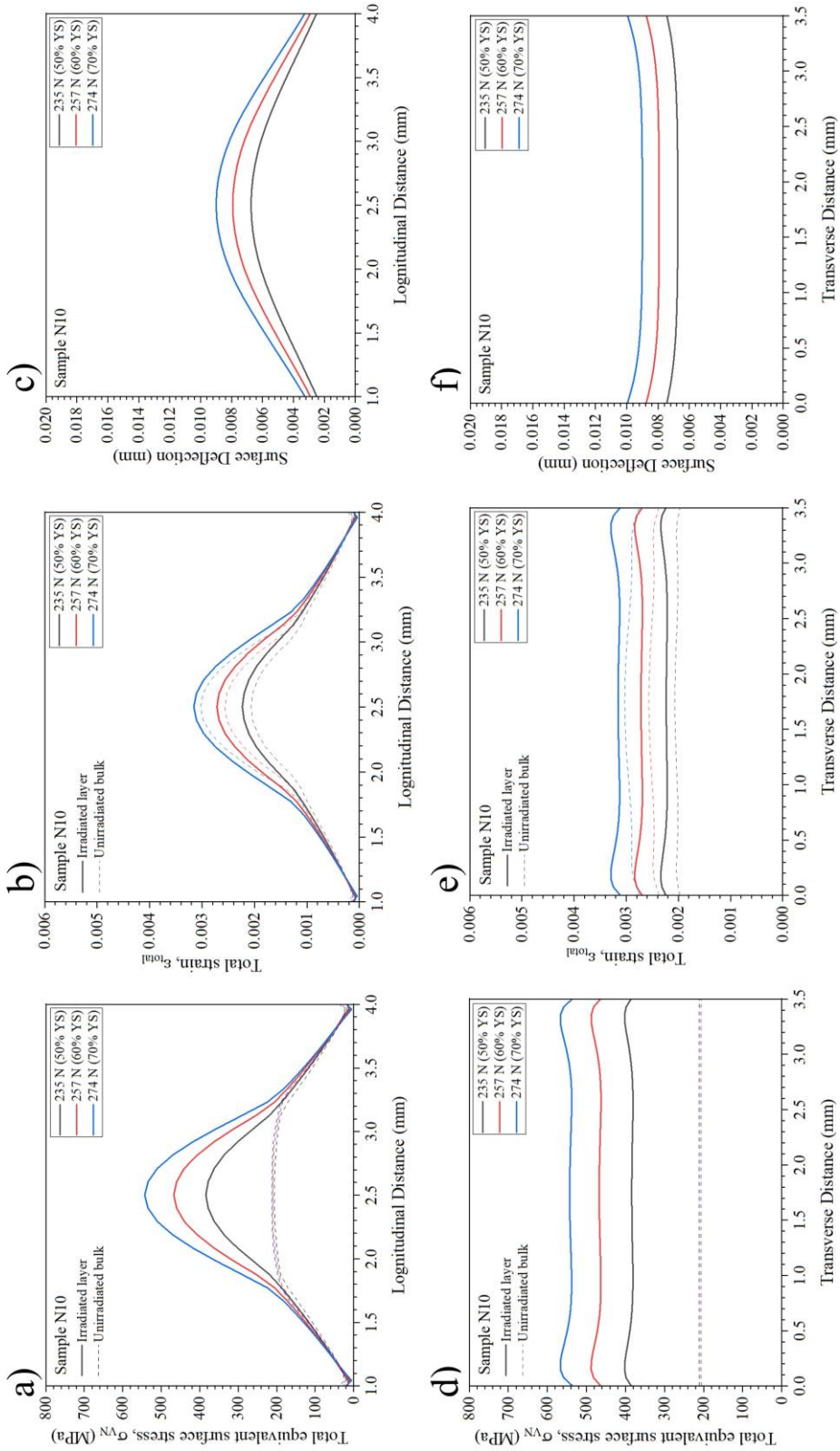


Figure 5-12 FEA results of sample N10 for surface profiles of longitudinal (a) stress, (b) strain, (c) deflection, and transverse (d) stress, (e) strain, and (f) deflection

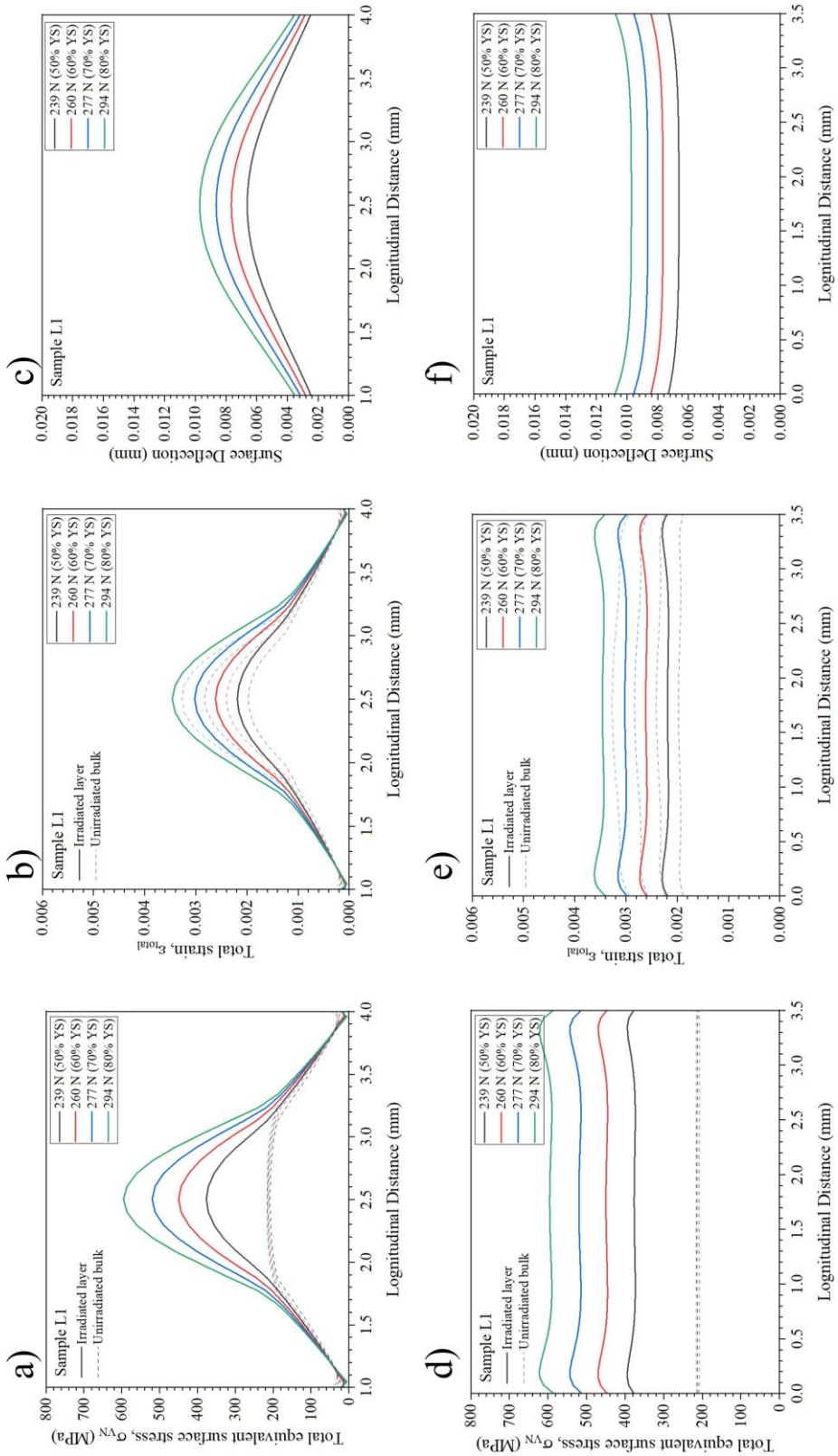


Figure 5-13 FEA results of sample L-R-1 for surface profiles of longitudinal (a) stress, (b) strain, (c) deflection, and transverse (d) stress, (e) strain, and (f) deflection.

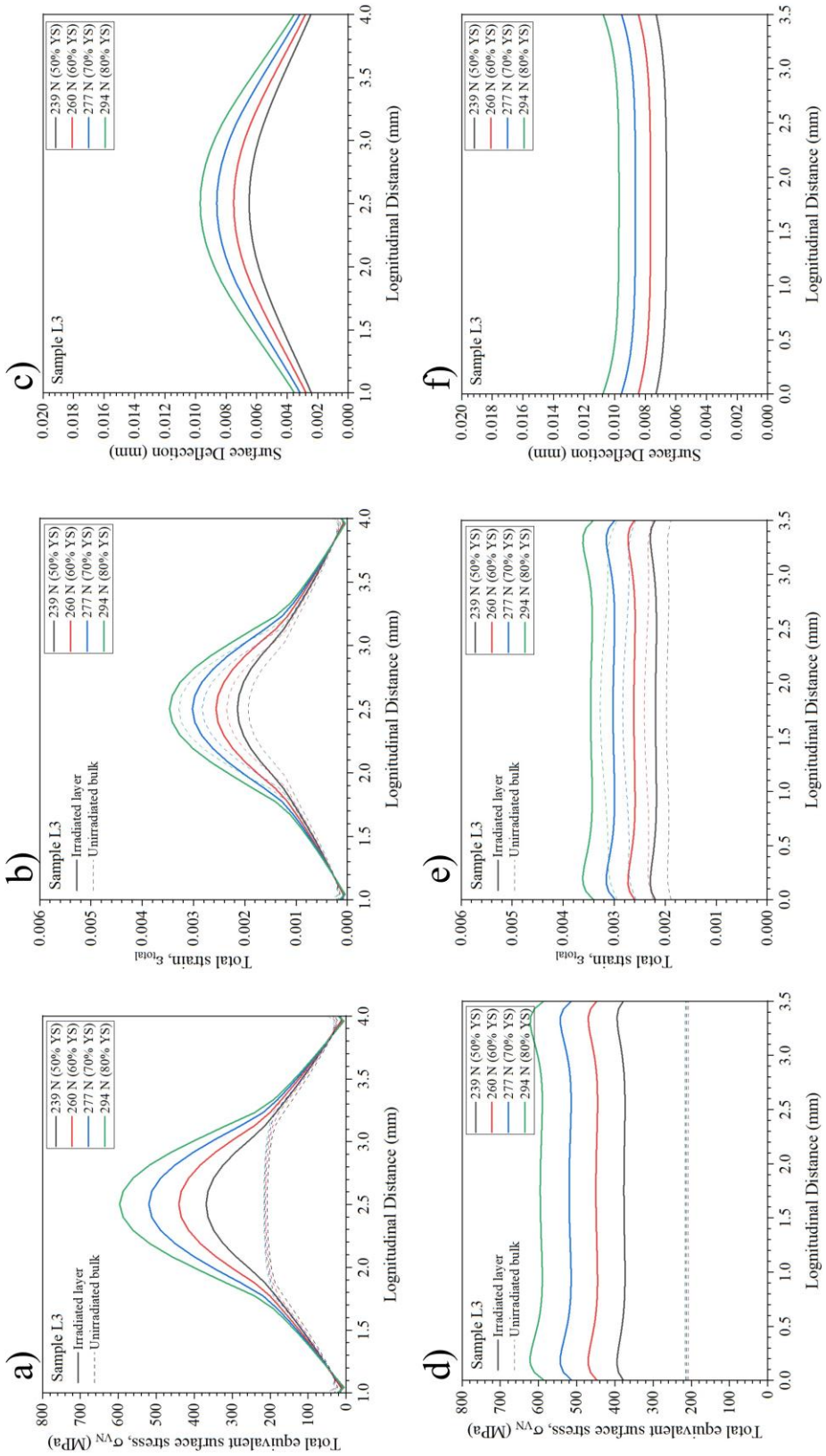


Figure 5-14 FEA results of sample L-R-3 for surface profiles of longitudinal (a) stress, (b) strain, (c) deflection, and transverse (d) stress, (e) strain, and (f) deflection.

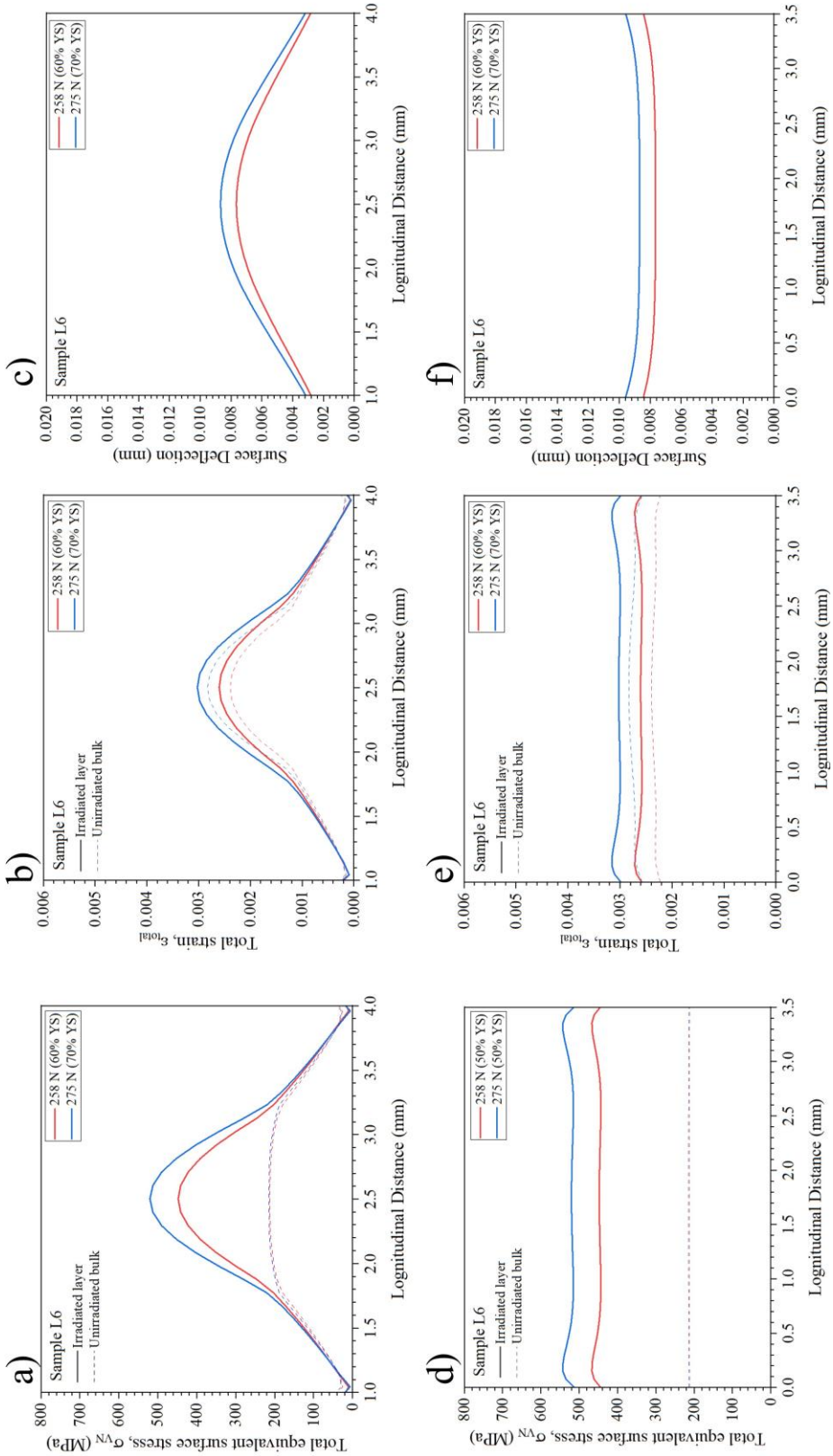


Figure 5-15 FEA results of sample L-R-6 for surface profiles of longitudinal (a) stress, (b) strain, (c) deflection, and transverse (d) stress, (e) strain, and (f) deflection.

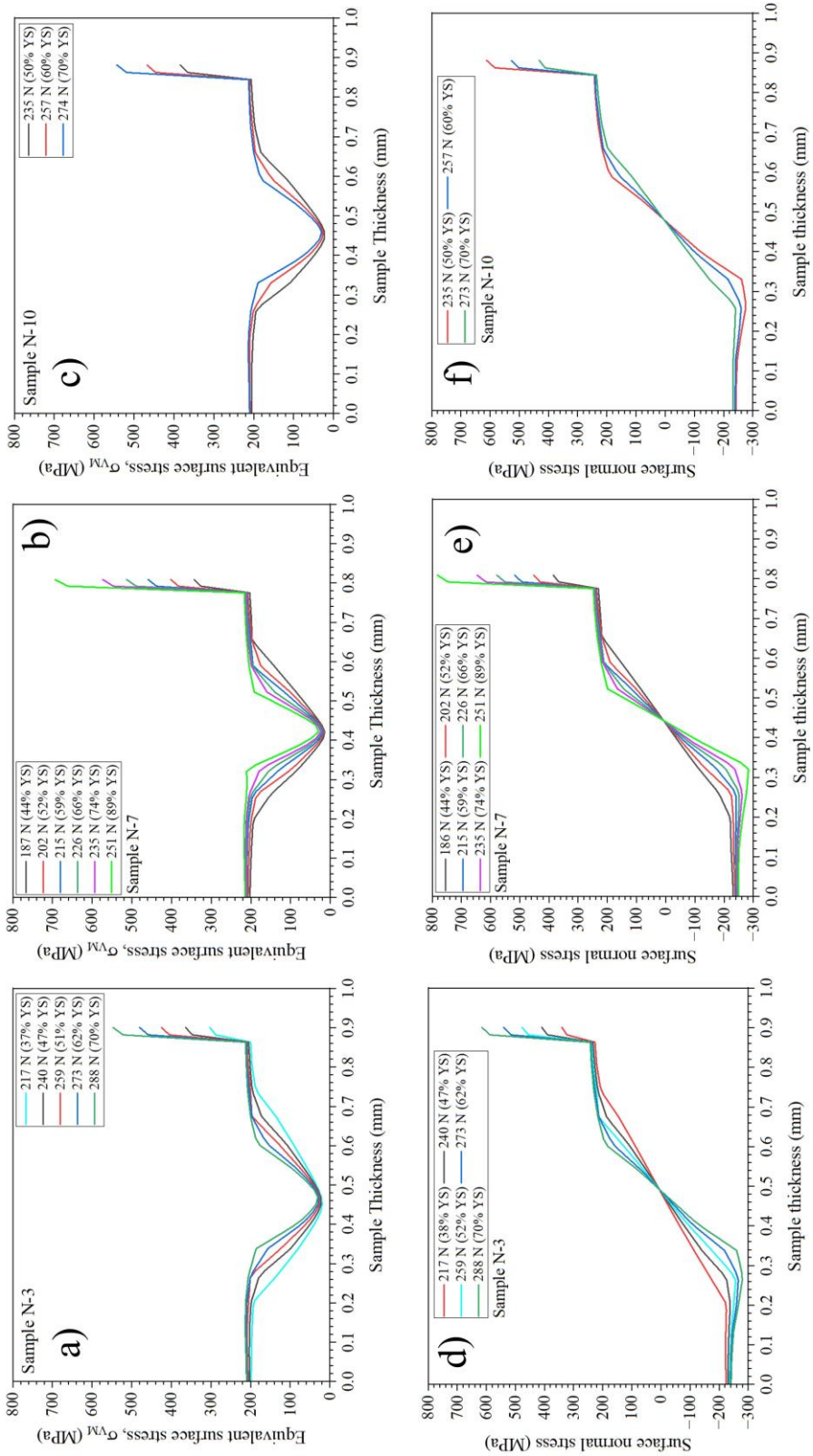


Figure 5-16 FEA results of the total equivalent stress profiles across thickness for (a) sample N3, (b) sample N7, and c) sample N10, and normal stresses profiles across thickness for (d) sample N3, (e) sample N7, and (f) sample N10.

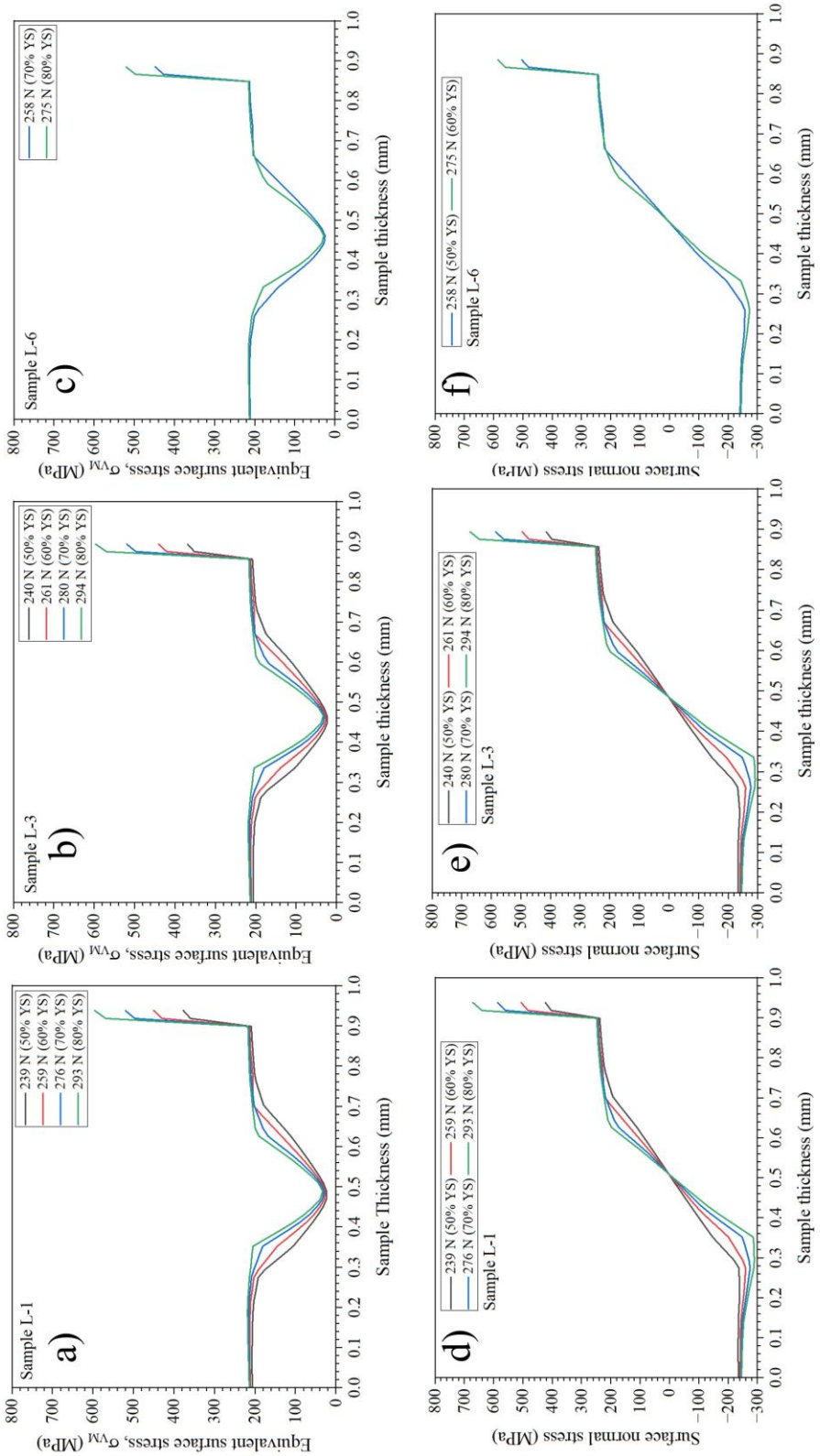


Figure 5-17 FEA results of the total equivalent stress profiles across thickness for (a) sample L-R-1, (b) sample L-R-3, and (c) sample L-R-6, and normal stresses profiles across thickness for (d) sample L-R-1, (e) sample L-R-3, and (f) sample L-R-6.

## 5.6 Uncertainty Analysis for mechanical testing and FEA

The main goal of this analysis was to ensure that the outcome of this study is conservative and could be utilized in reactor design once the application of proton irradiation as a surrogate for neutron irradiation has been approved for licensing purposes, particularly in selecting materials for reactor core internals. Moreover, IASCC is a probabilistic phenomenon that depends on many factors as explained in **Error! Reference source not found.**. Therefore, avoiding more probabilistic factors coming from experimental errors is essential. Also, it is the first time that a proton-irradiated 4PB samples used to determine the IASCC initiation susceptibility meaning that providing a procedure for accurate testing will help to validate the method as well.

In laboratory testing, various sources of error can impact the test results. These sources range from device limitations, sensor precision, and microscope resolution to uncertainties in literature-based data and FEA sensitivity. Therefore, it is essential to identify all potential error sources and filter them based on their influence on the study's final results.

In this section, all possible error sources will be determined and their influence on the FEA results will be identified and reflected on the minimum stress to initiate a crack as an uncertainty factor.

### *5.6.1 Error sources*

In 4PB experiments, there will be uncertainty or error in sample thickness, the yield strength of the bulk, the yield strength of the proton-irradiated layer, testing devices and sensors, microscope resolution, and FEA model inputs. Each factor introduces a degree of variability,

affecting the cumulative error. To ensure accurate analysis, it is crucial not only to identify these error sources but also to quantify the influence of each on the experimental results.

Figure 5-18Figure 5-18 Flow chart of the error sources contributed to the final result of the IASCC initiation stress. shows a flow chart illustrating the contributions of various error sources to the IASCC initiation tress. The primary sources of error highlighted in the figure include the IM3 system sensors, the optical microscope resolution used for measuring sample thickness, and the literature-derived inputs employed to determine the mechanical and material properties for the FEA inputs.

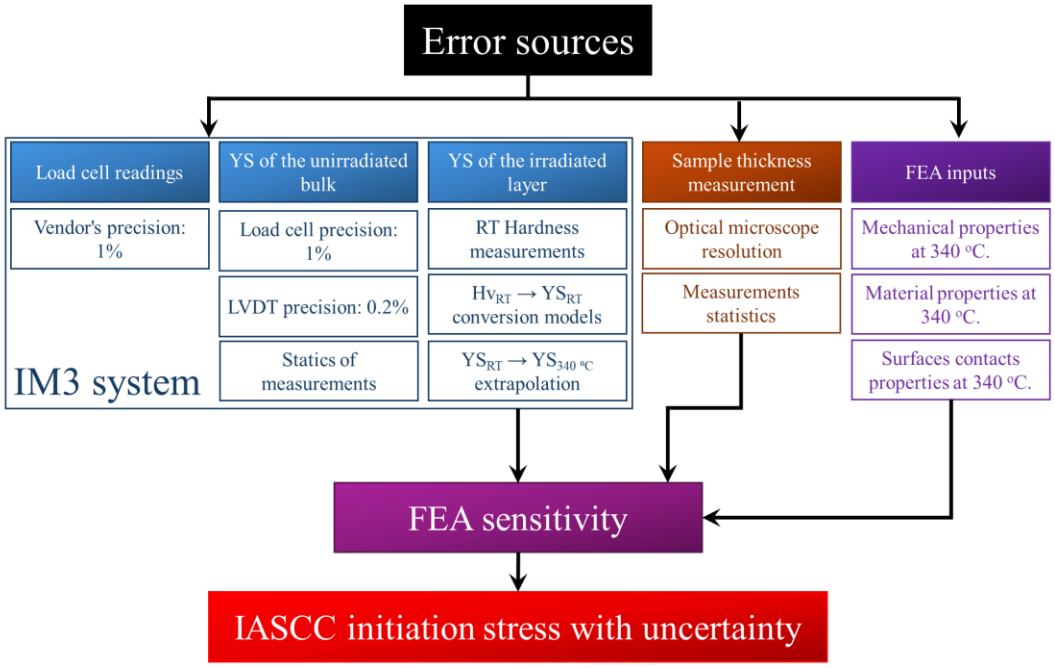


Figure 5-18 Flow chart of the error sources contributed to the final result of the IASCC initiation stress.

*IM systems sensors*

IM systems in IMTL use multiple sensors for the measurement of water conductivity, dissolved oxygen, LVDT, and the load cell. Each of them has a precision in the measurement that either provided by the vendor such as in the case of conductivities and dissolved oxygen sensors or through the calibration of the sensor following NIST. However, the initiation stress is

not directly related to the pH, water conductivity, and dissolved oxygen sensors meaning that these were not considered among the error sources.

The LVDT measurement was not directly related to the IASCC result since the surface deflection was very small (couple of microns) compared to the displacement of the crosshead which is typically couple hundreds of microns. The use of LVDT was then limited to construct the load vs crosshead displacement that was used to track the maximum load applied to the sample during the 4PB test. Therefore, the LVDT measurement was not considered as a source of error.

The load is applied to the sample through the pull-rod that is connected to the servomotor. A load cell of type Transducer Techniques® 1000 lbf is attached in between and reads the applied load, this cell has a precision of 1% as provided in the vendor's certificate. Since the load is directly related to the final results, it was necessary to determine the reading precision. Therefore, the total error in applied load can be calculated from the various error sources of the load cell as listed in the vendor's specifications:

- Nonlinearity (NL): 0.25% of the rated output.
- Hysteresis (H): 0.25% of the rated output.
- Non-repeatability (NR): 0.1% of the rated output.
- Zero balance (Z): 1.0% of the rated output.

Since these errors are independent, the total uncertainty equation is used to obtain the total uncertainty as:

$$\text{Total uncertainty} = \sqrt{NL^2 + H^2 + NR^2 + Z^2} \tag{5.10}$$

The result shows total uncertainty in the load cell readings of 1.06% and it will be used in the uncertainty analysis.

*Yield strength measurement procedures*

Measurement of the YS of both the unirradiated bulk and the irradiated layer considered as error sources. The $YS_{Bulk}$ has a main role in the sample's deformation as it constitutes around 97% of the sample's thickness meaning that the surface deflection is directly related to this value. As already mentioned in 0, the $YS_{Bulk}$ for both alloys were determined from tensile tests. Again, these tests were performed in IM2 which is very similar to IM3 and has exactly same design and sensors. Therefore, error sources apply on this system as well.

*Pre-irradiation hardness test*

The error in hardness measurements was checked by comparison with standard hardness blocks. Two different standard hardness blocks with known hardness values of 212 $H_V$ and 363 $H_V$, which are close to the hardness ranges of the pre- and post-irradiation hardness of the test materials were used. The measured average hardness values for the standard blocks are shown in Table 5-12. It was observed that the measured average hardnesses were very close to the known hardness of the standard blocks.

Table 5-12 Hardness measurements of the standards block.

| **Standard block hardness ($H_V$)** | **Measured average hardness ($H_V$)** | **% deviation from the standards** |
|---|---|---|
| 212 | 209.6 ± 4.6 | 1.13 |
| 363 | 360.4 ± 7.9 | 0.72 |

*Post-irradiation hardness test*

The second round of hardness measurement was done after the irradiation to estimate the irradiated YS of both alloys. As explained in the previous section, hardness measurement comes

with statistical analysis. The hardness performed three times, and the average and the standard deviation were calculated. Table 5-13 lists the average and standard deviation values of both alloys for the pre- and the post- irradiation hardness measurement.

Table 5-13 Post-irradiation hardness measurement

| Alloy | Pre-irradiation hardness ($H_V$) | Post-irradiation hardness ($H_V$) | $YS_{Bulk}$ (MPa) |
|---|---|---|---|
| SS 304L-R | 223.9 ± 17.4 | 412.9 ± 17.3 | 316.1 ± 17.4 |
| SS 304LN | 213.4 ± 12.2 | 425.0 ± 20.8 | 279.1 |

*Hardness to yield strength conversion*

The conversion of hardness values to irradiated YS requires the propagation of the error from the hardness through the conversion equations (Eqns. 4.13 and 4.14). The data from Table 5-13 was used to calculate the $YS_{Irradiated}$ as follows:

For SS304L, using Eqn. 4.13 and Table 5-13, $\Delta H_V = 190$, and $\Delta H_{V\text{-}Error} = 24.6$ MPa. Therefore, the error using Busby equation $YS_{irradiated\text{-}Error} = 71.8$ MPa. Similar calculation using Eqn. 4.14, the error using Bruemmer equation $YS_{irradiated\text{-}error} = 43.38$ MPa. The average error from both equations is given by:

$$(YS_{avg})_{Uncertainty} = \frac{\sqrt{(YS_{Busby})^2_{error} + (YS_{Bruemmer})^2_{error}}}{2} \tag{5.11}$$

Which results in 42.0 MPa as an error.

For SS 304LN, similar calculations using both equations results in an error of 44.8 MPa. The summary of the $YS_{irradiated}$ calculations at 25 ºC is listed in Table 5-14.

Table 5-14 Hardness to $YS_{Irradiated}$ conversion.

| Condition | SS 304L-R | SS 304LN |
|---|---|---|
| $YS_{RT}$ | 876 ± 42.0 | 907 ± 44.8 |
| $YS_{340\ ºC}$ | 746 ± 43.9 | 772 ± 46.5 |

*High temperature $YS_{Irradiated}$ extrapolation from the literature*

As mentioned in Section 5.4.1, the $YS_{Irradiated}$ at 340 ºC is not available in the literature, therefore, data from 320 ºC were used and then extrapolated to 340 ºC. Since the extrapolation process relied on averaging the literature data, the standard deviation calculated and used as an uncertainty value. Table 5-4 shows the average change in the $YS_{Irradiated}$ ($\Delta YS_{Irradiated}$) at 129.8 MPa with a standard deviation ($\sigma_{\Delta YS\text{-irradiated}}$) of 12.7 MPa. Therefore, the uncertainty can be propagated using the following formula:

$$\text{Uncertainty YS}_{Irrad.} = \sqrt{\sigma^2_{YS_{Irrad.}} + \sigma^2_{\Delta_{YS_{Irrad.}}}} \tag{5.12}$$

For SS 304L-R, the uncertainty found at 43.9 MPa while it was 46.5 MPa for SS 304LN. The summary of $YS_{Irradiated}$ at 320 ºC is listed in Table 5-14.

### *5.6.2 DPA calculation*

SRIM calculation was used to determine the irradiation time required to achieve 5 dpa on the 304 SS samples with 2 MeV protons at an average current of 23 µA. From the first calculation, 368.86 h was required to achieve 5 dpa at 12.1 µm (60% of the irradiated depth). To determine the error associated with this calculation, 6 additional calculations were performed, and the corresponding SRIM damage range is given in Table 5-15.

The dpa calculated from 4.10, while the ion beam current was measured by the current integrator with an error of 0.02%. Therefore, error propagation was used to determine the total error in the dpa calculation as follows:

$$\mathrm{DPA}_{Error} = \sqrt{\left(\frac{\Delta\text{SRIM damage rate}}{\text{SRIM damage rate}}\right)^2 + \left(\frac{\Delta\text{current}}{\text{current}}\right)^2} \tag{5.13}$$

Where ΔSRIM damage rate is the standard deviation, and (SRIM damage rate) is the average damage rate in Table 5-15. Plugging in the values into Eqn. 5.14 results in an error of 0.0176 dpa. This means that the calculated displacement per atom from SRIM was 5.12 ± 0.09 dpa for SS 304LN and 5.01 ± 0.09 dpa for SS 304L. However, this error was not directly related to the minimum initiation stress, but it is important to report it when %YS vs dpa is plotted.

Table 5-15 Damage rate uncertainty calculation from SRIM analysis.

| **SRIM run** | **SRIM damage rate (displacement/A*ion)** |
|---|---|
| 1 | $4.27 \times 10^{-5}$ |
| 2 | $4.43 \times 10^{-5}$ |
| 3 | $4.45 \times 10^{-5}$ |
| 4 | $4.36 \times 10^{-5}$ |
| 5 | $4.41 \times 10^{-5}$ |
| 6 | $4.25 \times 10^{-5}$ |
| 7 | $4.39 \times 10^{-5}$ |
| Average | $4.37 \times 10^{-5}$ |
| Standard deviation | $7.68 \times 10^{-7}$ |

### *5.6.3 Sensitivity analysis*

Sensitivity analysis helps clarify the influence of each input uncertainty (or error) on the calculated surface stress, which is the key parameter for determining the minimum stress level at which cracking initiates. The sensitivity analysis therefore explains how variations in key input parameters affect the outputs of the FE model. In the 4PB model, it quantifies the uncertainties in input parameters such as yield strength, sample thickness, and applied load and their impact on key outputs like surface stress, strain, and deflection.

The sensitivity coefficient (S) for each input parameter serves as a multiplier scaling factor, indicating how strongly a small change in that input propagates to the output showing the extent to which the output responds to small changes in that input. In this context, any error in the input is effectively amplified by its corresponding sensitivity coefficient, S. The overall uncertainty in the FE model will be calculated as the quadrature sum of the independent error sources with sensitivity coefficients values. Therefore, S can be read as follows:

For S > 1, the output is highly sensitive to the input parameters, meaning a small change in the input leads to large output change by FEA.

S ~ 1, the output changes at about the same rate as the input, meaning that 1% a change of input lead similar percent change in the output.

S < 1, the output is less sensitive to that input, system is more stable against variations.

S = 0, the output does not depend on the input, it is completely insensitive.

Sensitivity coefficient can be determined from calculating the change in the outputs relative to the change in the inputs following below equation:

$$S_P = \frac{\partial \sigma}{\partial \sigma_P} \times \frac{\sigma_P}{\sigma}, \text{or } S = \frac{\frac{\Delta \text{Output}}{\text{Output}}}{\frac{\Delta \text{Input}}{\text{Input}}} \tag{5.14}$$

Where $P$ indicates the input parameter such as YS, applied load, and sample thickness. The total uncertainty from the FEA calculation can be described as:

$$\Delta\sigma_{Total} = \sqrt{\begin{aligned}(S_{\text{YS-Bulk}} \times \Delta\sigma_{\text{YS-Bulk}})^2 + (S_{\text{YS-Irrad.}} \times \Delta\sigma_{\text{YS-Irrad.}})^2 \\ + (S_{\text{Thickness}} \times \Delta t)^2 + (S_{\text{Load}} \times \Delta F)^2\end{aligned}} \tag{5.15}$$

Where $S$ is the sensitivity coefficient of the parameter, and $\Delta\sigma_{YS}$ is the uncertainty in the $YS$, $\Delta\sigma_{YS}$, $\Delta t$ is the uncertainty in the sample thickness, and $\Delta F$ is the uncertainty in the applied load reading from the load cell.

*Reference point*

A reference was required in which the input parameters were assumed to have no error. The output from this run was used as a reference for comparing the outputs obtained during uncertainty analysis. Table 5-16 lists the input parameters used for the reference FEA run.

Table 5-16 Summary of the key input parameters that used for the FEA.

| **Parameter** | **Reference L (SS 304L-R)** | **Reference N (SS 304LN)** |
|---|---|---|
| $YS_{Bulk\text{-}340\ ^{o}C}$ (MPa) | 198 | 194 |
| $YS_{Irradiated\text{-}340\ ^{o}C}$ (MPa) | 746 | 777 |
| Applied load (N) | 250* | |
| Sample thickness (mm) | 0.900 | |
| ** The measured tare load is 125 N, however, this value is less than 30%$YS_{irradiated}$ which is low so we doubled it to 250 N to ensure an IASCC representative value.* | | |

In this study, the $YS_{Bulk}$ measured from the tensile tests at 340 ºC was assumed as a reference value. The $YS_{Irradiated}$ that was converted from the hardness measurement was also assumed as a reference value. Moreover, the tare load that is induced on the sample due to the pressure inside the vessel is 125 N, however, this value is very small and constitutes less than 25%$YS_{Irradiated}$, therefore, we used double the value at 250 N as a reference value. Finally, the thickness of 0.900 mm was assumed as a reference value.

Two FE tests were performed, one on SS 304L and another on SS 304LN to calculate the reference data as summarized in Table 5-17. The first FE run showed that the maximum surface tensile stress using the reference values for SS 304LN listed in Table 5-16 was 395.06 MPa which equals 50.84%$YS_{Irradiated}$ and 387.65 in case of SS 304L-R which equals 51.96%$YS_{Irradiated}$.

Therefore, the sensitivity analysis in the coming sections will use these two surface stresses values as reference points.

Table 5-17 Reference points outputs.

| Alloy | Surface stress (MPa) | %YS |
|---|---|---|
| SS 304LN | 395.06 | 50.84 |
| SS 304L-R | 387.65 | 51.96 |

*Sensitivity calculations*

The sensitivity coefficient for each input parameter was determined by evaluating the impact of a 0.1% change on its original value. Table 5-18 summarizes the values used for calculating the sensitivity.

The sensitivity analysis was conducted by varying one parameter at a time while keeping all others constant. For instance, in condition L-R-1, the $YS_{Bulk}$ value increased by 0.1% leading to a difference change in the parameter value of 0.198 MPa, while all other inputs were kept constant. The resulting surface stress was then compared to the reference stress. This procedure was repeated for all other conditions.

Table 5-18 The percent change of the input parameter value that used to estimate the sensitivity of the FEA model.

| Input parameter | Value | %Change in its value | Change in the parameter value |
|---|---|---|---|
| SS 304L-R | | | |
| $YS_{Bulk\text{-}340\ ^{o}C}$ (MPa) | 198 | 0.1 | 0.198 |
| $YS_{Irradiated\text{-}340\ ^{o}C}$ (MPa) | 746 | 0.1 | 0.746 |
| Applied load (N) | 250 | 0.1 | 0.250 |
| Sample thickness (mm) | 0.90 | 0.1 | 0.0009 |
| SS 304LN | | | |
| $YS_{Bulk\text{-}340\ ^{o}C}$ (MPa) | 194 | 0.1 | 0.194 |
| $YS_{Irradiated\text{-}340\ ^{o}C}$ (MPa) | 777 | 0.1 | 0.777 |
| Applied load (N) | 250 | 0.1 | 0.250 |
| Sample thickness (mm) | 0.90 | 0.1 | 0.0009 |

The results of the sensitivity calculations are summarized in Table 5-19. The sensitivity coefficient (S) was calculated from Eqn. 5.14.

The $\Delta\sigma_{Total}$ for each alloy was then calculated using Eqn. 5.15 and input parameters from Tables 5-17 and 5-18 and found to be 5.12% for SS 304L-R and at 5.57% for SS 304LN as listed in Table 5-19. The total uncertainty in the FEA for both alloys is less than 6% of the surface results, which accounts for the %YS used as an indicator of IASCC failure. This value can be propagated to the %YS at which the sample fails.

The resulting *S* can be used as a multiplier to outline the change in the output for every 0.1% change in the input as shown in Figure 5-19 (a). This figure demonstrates the sensitivity of the surface stress to individual input parameters, meaning that a 0.1% change in a given input will result in an output change scaled by the corresponding S value. Figure 5-19 (b) further presents the amplified errors, where the measured errors listed in Table 5-19 are multiplied by their respective sensitivity coefficients to reflect their impact on the surface stress. This highlights how S magnifies the effect of input uncertainties.

To further evaluate the influence of these amplified errors, especially in the context of minimizing uncertainties prior to IASCC testing on proton-irradiated 4PB samples, Figure 5-20 shows the relationship between the percent change in FEA-calculated surface tensile stress ($\sigma_{surface}$) and the percent change in input parameters. The figure reveals a clear linear relationship, where increases in the amplified errors ($S\times\%Error_{Measured}$), namely the amplified measured error), correspond to proportional increases in $\sigma_{Surface}$.

The comparison between SS 304L-R and SS 304LN shows minimal difference in most parameters, except for sample thickness. SS 304L-R exhibits slightly lower sensitivity to thickness variations, which can be attributed to its higher yield strength. This underscores the

importance of precise control over sample preparation (e.g., thickness), load calibration, and accurate yield strength measurements. Any inaccuracy in these factors can significantly alter the calculated surface stress, potentially leading to misleading interpretations of the failure stress and IASCC susceptibility.

Table 5-19 Sensitivity coefficients for each input parameter for SS 304LN and SS 304L-R, and the total uncertainty from FEA based on the sensitivity analysis.

| **Sensitivity factor** | **SS 304LN** | | **SS 304L-R** | |
|---|---|---|---|---|
| | New $\sigma_{Surface}$ | $S_P$ (%Error) | New $\sigma_{Surface}$ | $S_P$ (%Error) |
| $YS_{Bulk}$ | 394.66 | 1.0125 (3.90) | 387.25 | 1.0318 (0.70) |
| $YS_{Irradiated}$ | 395.06 | 0.0000 (5.03) | 387.65 | 0.0000 (5.97) |
| Applied Load | 395.86 | 2.0250 (1.00) | 388.45 | 2.0637 (1.00) |
| Sample Thickness | 393.73 | 3.3666 (1.00) | 388.58 | 2.3991 (1.00) |
| $\Delta\sigma_{Total}$ | - | 5.57% | - | 5.12% |

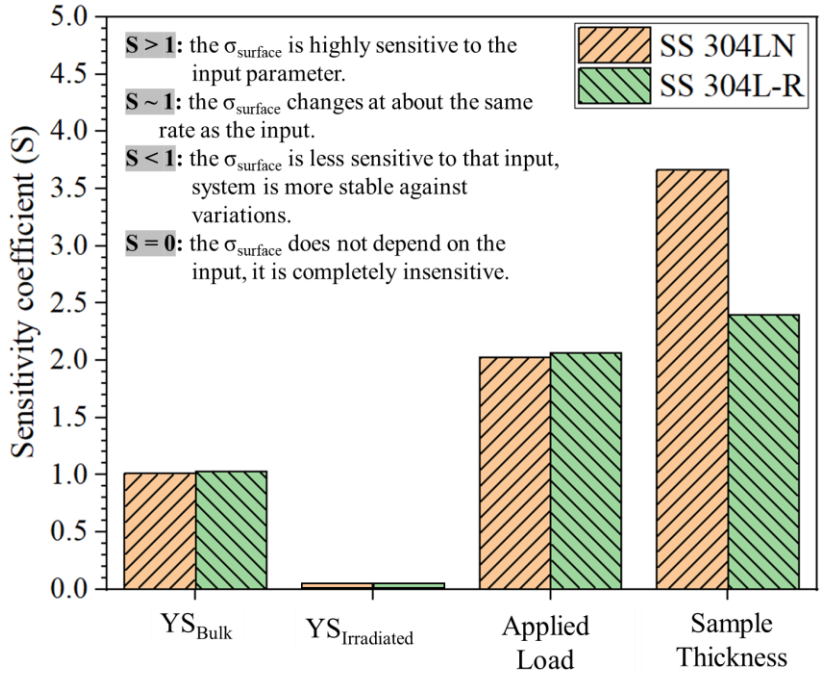


(a)

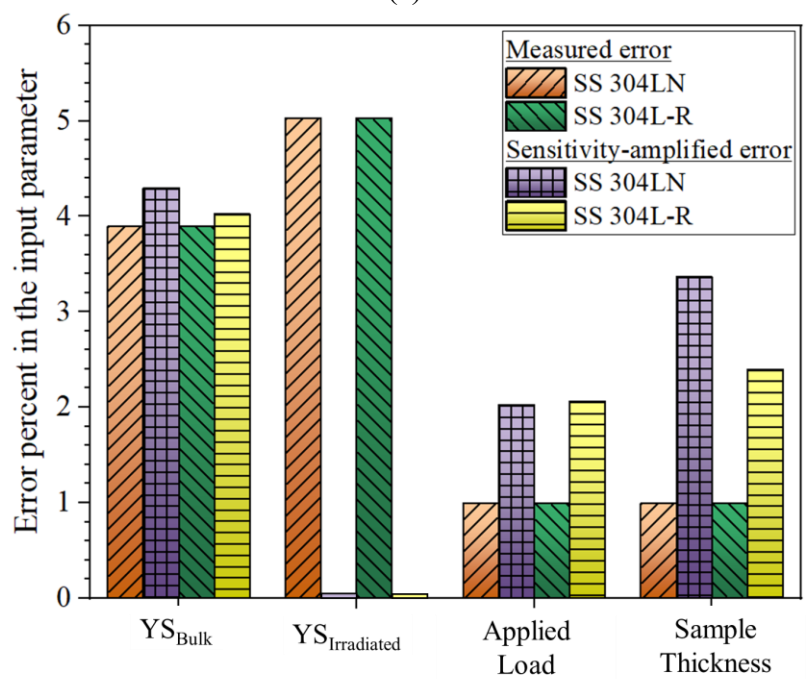


(b)

Figure 5-19 Sensitivity analysis for SS 304LN and SS 304L-R, (a) the sensitivity coefficients for all input parameters, indicating that variations in sample thickness have a strong influence on the calculated surface tensile stress ($\sigma_{surfaces}$), whereas the irradiated yield strength has negligible impact. (b) Measurement errors for $YS_{Bulk}$, $YS_{Irradiated}$, applied load and sample thickness, along with the corresponding sensitivity-amplified errors that reflect the impact of each parameter on $\sigma_{surfaces}$.

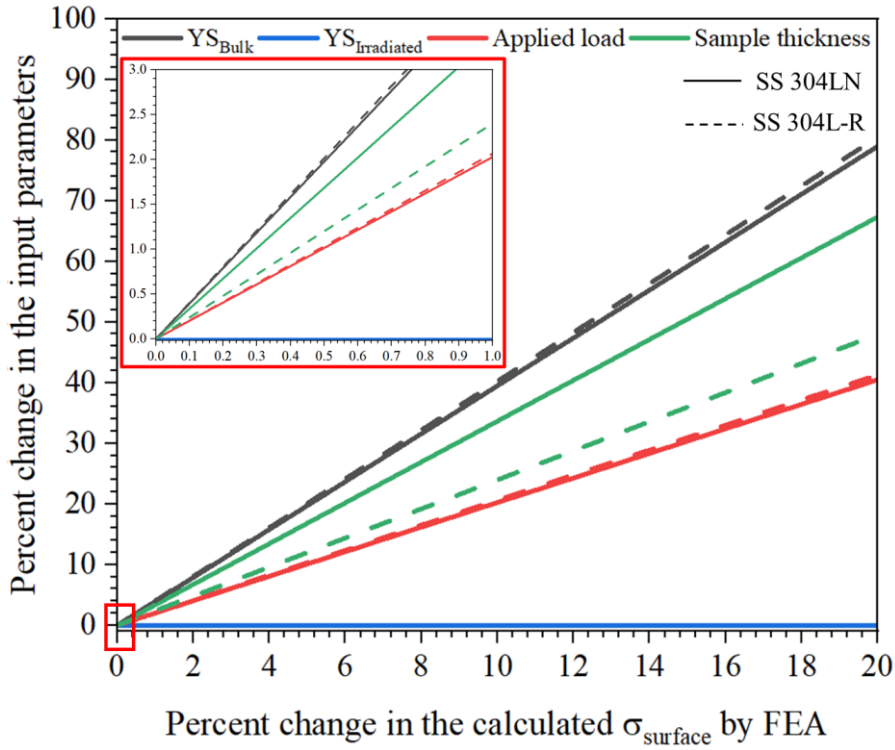


Figure 5-20 Summary of the percent change in the FEA-calculated surface stress as a function of the percent change in the inputs showing strong impact from the applied load and sample thickness while no impact from the $YS_{irradiated}$. The solid line represents the sensitivity of input parameters on the FEA outputs from SS 304L-R and SS 304LN in the dashed lines.

*Input parameters influence*

One additional data point to consider is estimating the influence of each input parameter on the output data. This helps prioritize efforts to reduce errors in the high-impact factors during the 4PB test, ensuring more reliable results. To achieve this, Normalize Sensitivity Coefficient (NSC) was used by calculating sensitivity coefficients and normalizing these values by the sum of all sensitivity coefficients, providing a relative measure of each parameter's contribution to total variability.

$$NSC_{\text{Parameter}} = \frac{|S_{\text{Parameter}} \times \Delta X_{\text{Parameter}}|}{\sum |S_i \times \Delta X_i|}, \tag{5.16}$$

Where $X_i$ is the uncertainty of the parameter. This gives each parameter a percentage contribution to the total error, making it easy to compare their relative importance.

The calculations for SS 304L-R in Table 5-20 show that the $YS_{Bulk}$ has the largest impact on the surface tensile stress, contributing about 47.41% of the total uncertainty (5.12%) on surface stress. Thickness is the next most influential parameter, contributing to 28.27%, Load has an influence of 24.32% while $YS_{Irradiated}$ has no influence on surface stress. While for SS 304LN, $YS_{Bulk}$ has the largest impact on the analysis since its original error was relatively high, contributing about 42.28% of the total influence (5.57%) on surface stress. Sample thickness is the next most influential parameter, contributing 36.05%, Load has a moderate influence at 21.69% while the irradiated yield strength has the minimal to no impact on the FE results.

Table 5-20 Influence factor (NCS) of each input parameter and the contribution of the NCS in the total uncertainty.

| **Parameter** | **%NCS** | | **%(NCS×$\Delta\sigma_{Total}$) *** | |
|---|---|---|---|---|
| Alloy | L-R | LN | L-R | LN |
| $YS_{Bulk}$ | 47.41 | 42.28 | 2.43 | 2.35 |
| $YS_{Irradiated}$ | 0.00 | 0.00 | 0.00 | 0.00 |
| Applied Load | 24.32 | 21.68 | 1.25 | 1.21 |
| Sample Thickness | 28.27 | 36.04 | 1.45 | 2.01 |
| ** $\Delta\sigma_{Total}$ for SS 304L-R is 5.12% and for SS 304LN is 5.57%* | | | | |

This analysis showed that the irradiated yield strength is not an influential factor meaning that the value itself has almost no effect on the surface stress while its importance is limited to the calculation of the percent of the yield stress as a presentation of the minimum stress to initiate IASCC in the particular alloy. Figure 5-21 shows the contribution of each input parameter to the total uncertainty for each alloy, with the 100% reference in the plot corresponding to 5.12% for L and 5.57% for LN.

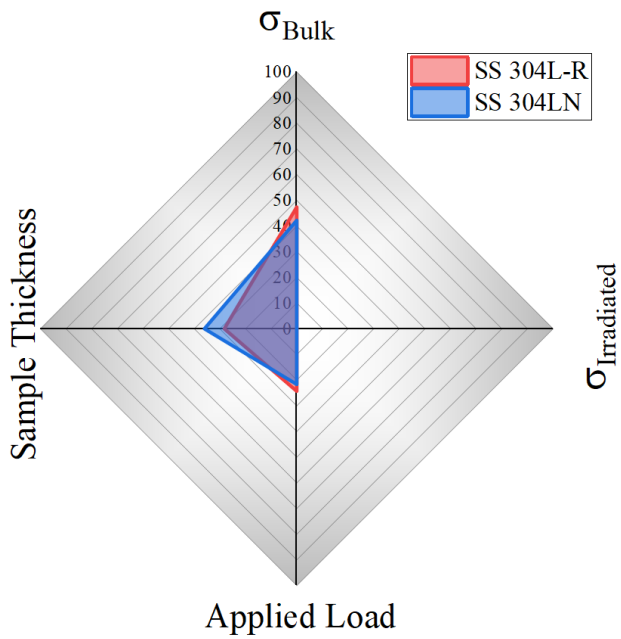


Figure 5-21 The influence of input parameters on the total uncertainty of each alloy. Note: 100% in this figure means total uncertainty calculated from Eqn. 5.15.

### *5.6.4 Uncertainty application on the failure stress*

The last step incorporates the calculated uncertainty into the FEA on the $\%YS_{Irradiated}$, a material property used to locate the minimum stress required to initiate IASCC in the given alloy. Table 5-21 shows the incorporation of the error from FEA into the %YS.

In Table 5-21, the failure stress ($\sigma_{Failure}$) had been previously determined in Table 5-11. The total uncertainty percent (5.12% for SS 304L-R and 5.57% for SS LN) was then applied to the FEA-calculated surface stress at which the samples failed (the minimum stress required to initiate a crack, with further discussion on its uncertainty will be discussed Chapter 6). For example, in sample N3, failure occurred at 72%YS, corresponding to 562 MPa. Applying the 5.57% uncertainty to this value resulted in a stress uncertainty of 31.30 MPa, equivalent to approximately 4.0%YS. Thus, the reported failure stress for sample N3 is 72 ±4%YS or 562 ±31 MPa. This same approach was applied to all other samples, resulting in the values listed in Table 5-21. Specifically, samples N7 and N10 exhibited uncertainties of 5%YS and 3.9%YS,

respectively, while samples L-R-1, L-R-3, and L-R-6 had uncertainties of 4.1%YS, 4.1%YS, and 3.6%YS, respectively after applying the uncertainty percent of 5.12%. The results in Table 5.20 will later be reflected in the %YS vs. Sample plots discussed in Section 6.3.2.

Table 5-21 The uncertainty in the FEA-calculated surface tensile stress at the last loading step that initiates a crack.

| Sample ID | $\sigma_{Failure}$ (MPa) | $\Delta\sigma_{Failure}$ (MPa) | $\%YS_{Failure}$ | %Uncertainty |
|---|---|---|---|---|
| **N3** | 547 | ± 30.47 | 70.1 | 3.9 |
| **N7** | 694 | ± 38.66 | 89.0 | 5.0 |
| **N10** | 544 | ± 30.30 | 69.7 | 3.9 |
| **L-R-1** | 596 | ± 30.52 | 80.0 | 4.1 |
| **L-R-3** | 597 | ± 30.57 | 80.0 | 4.1 |
| **L-R-6** | 521 | ± 26.68 | 70.0 | 3.6 |

# Chapter 6 Results

This chapter summarizes the results obtained from microstructural characterization following proton irradiation, four-point bending (4PB) experiments, constant extension rate tensile (CERT) tests, and associated microscopy analyses. The chapter is organized into four main sections. The first section presents the TEM analysis of irradiation-induced microstructural damage after proton irradiation to 5 dpa at 360 ºC, focusing on dislocation loops, voids, and precipitates. The second section covers the 4PB experiment results, including water chemistry, loading profiles, cracking statistics, and fracture surface morphology, with a comparative analysis between SS 304L and SS 304LN. The third section discusses the CERT experiment results, highlighting EBSD and AFM analyses of dislocation channels evolution after proton irradiation to 3 dpa at 360 °C. The final section presents TEM analysis of crack tips from 4PB samples to investigate the cracking mechanisms in both alloys. These analyses aim to isolate the effect of nitrogen on IASCC initiation by comparing the behavior of low-nitrogen (SS 304L-R) and high-nitrogen (SS 304LN) alloys in both 4PB and CERT tests.

## 6.1 Irradiated-induced microstructure

TEM analysis was performed using one sample per alloy because all samples from each alloy share similar microstructural features, irradiation conditions, sample preparation procedures, and testing environments. The two selected samples were N3 from SS 304LN and L-R-1 from SS 304L-R. Moreover, the characterization of irradiation-induced microstructure was performed at similar depth at around 12.0 – 12.5 µm from the irradiated surface representing the

damage at 5 dpa. This damage is considered as a uniform irradiation damage at around 60% of the irradiation depth based on the damage profile in Figure 4-13.

The analysis involved characterizing dislocation loops using the Rel-rod technique for quantification and TEM DF and BF for characterizing cavities. STEM-EDS mapping was employed to identify element segregation at the periphery of the loops. Furthermore, STEM-EDS mapping was used to analyze radiation-induced segregation (RIS) at the grain boundaries.

### *6.1.1 Dislocation loops*

Dislocation loops were characterized in both SS 304L-R and SS 304LN alloys using dark-field TEM imaging in a TF30 microscope at MIBL at the University of Michigan. The characterization utilized the two-beam condition with a g-vector of g =1/2[311] [137]. The selected depth (2 - 3 µm) corresponds near surface profile, as previously shown in Figure 4-13, and represents a region with relatively uniform microstructural evolution under proton irradiation to 5 dpa at 360 °C. This depth was chosen to ensure consistent comparison of irradiation-induced features such as dislocation loops, cavities, and precipitates between both alloys.

Figure 6-1 (a) and (b) show dark-field TEM images from three different locations in SS 304L (L-R-1) and SS 304LN (N3), respectively, along with selected area electron diffraction (SAED) patterns confirming the zone axis orientation. While the loop contrast in both alloys is consistent with dislocation loops lying on {111} habit plane, a visual comparison reveals noticeable differences. SS 304LN displays a denser population of smaller loops, whereas SS 304L shows fewer loops with slightly larger diameters across all locations.

These qualitative trends are further quantified in Figure 6-2 which presents the loop size distributions for both alloys. The fitted histograms show that the average loop size in SS 304L-R is slightly larger at 9.9 nm with a SD of 5.10 nm, while SS 304LN exhibits a slightly smaller

average loop size of 8.20 nm with a SD of 4.6 nm. Despite this difference in size (19%), the more significant observation lies in the loop density. As summarized in the table within Figure 6-2, SS 304LN shows a higher average loop density of $3.96 \times 10^{22}$ loops/m$^3$ after characterizing 1337 loops compared to $2.69 \times 10^{22}$ loops/m$^3$ in SS 304L-R after characterizing 1674 loops, indicating a 38% increase in loop density in the high nitrogen alloy. However, this difference remains insufficient statistically to cause a significant impact on material susceptibility to IASCC.

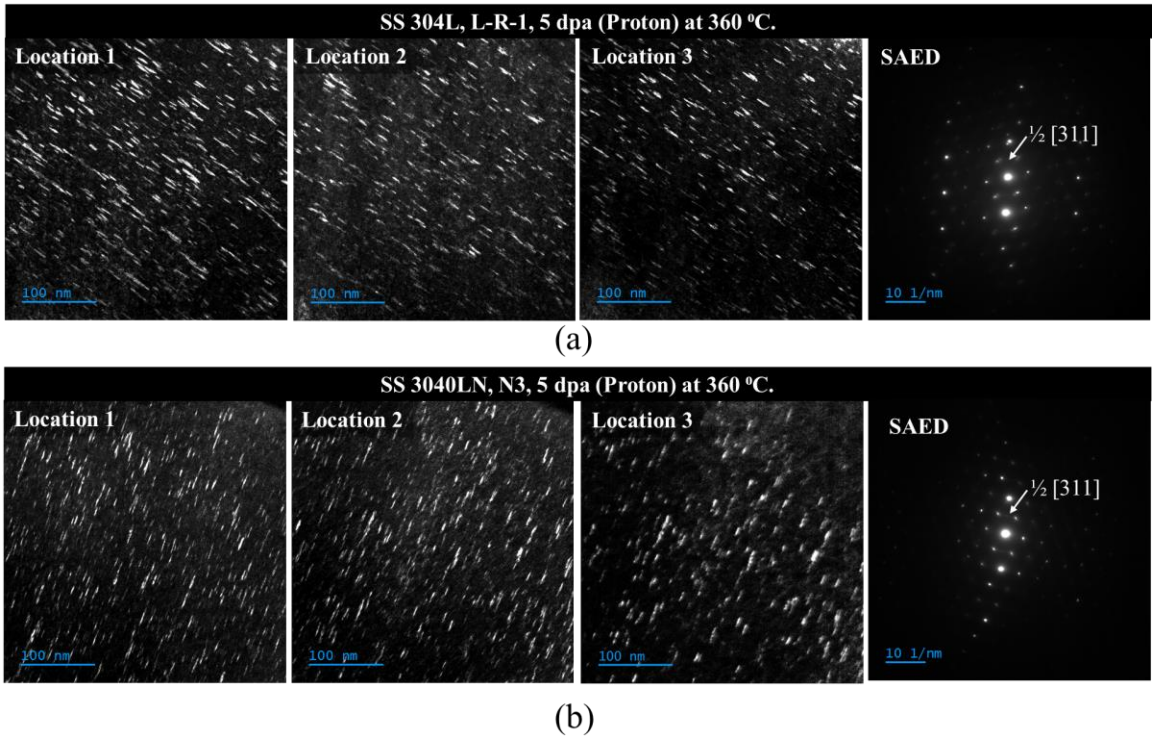


Figure 6-1 TEM DF images of dislocation loops in (a) SS 304L-R (L-R-1) and (b) SS 304LN (N3) after 5 dpa proton irradiation at 360 °C. Loops were imaged at 12 µm depth under g = ½{311} condition. SS 304LN shows higher loop density with smaller average size.

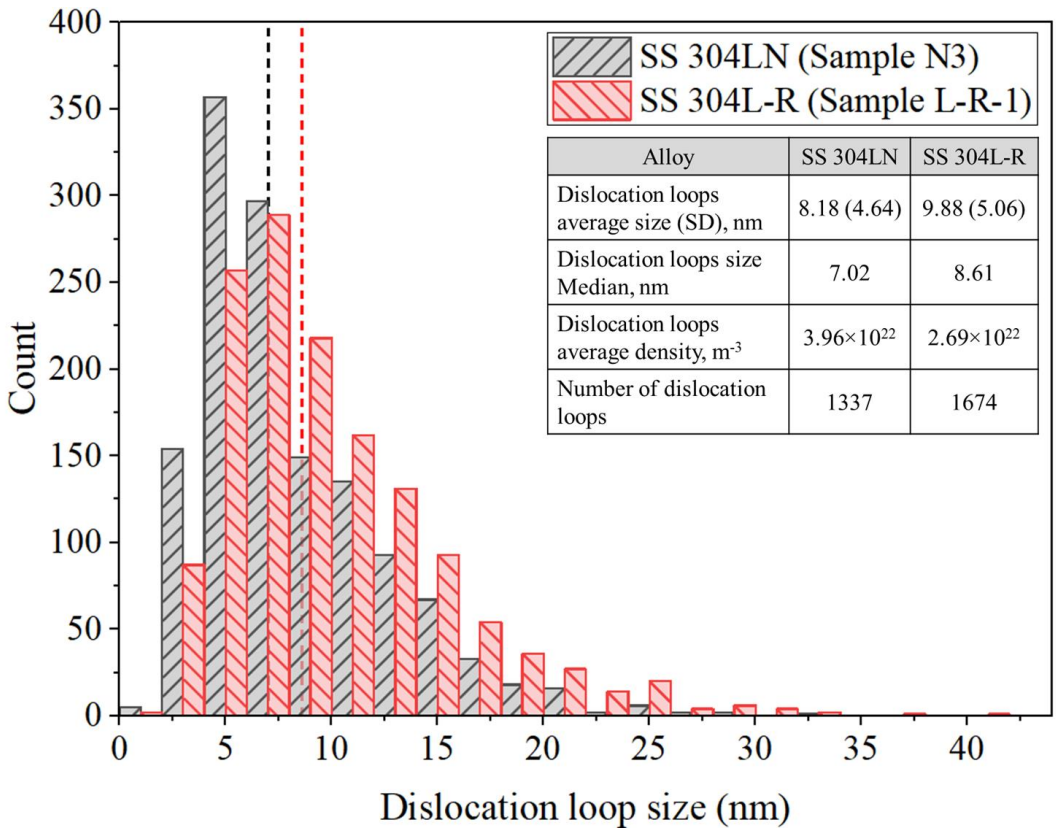


| Alloy | SS 304LN | SS 304L-R |
|---|---|---|
| Dislocation loops average size (SD), nm | 8.18 (4.64) | 9.88 (5.06) |
| Dislocation loops size Median, nm | 7.02 | 8.61 |
| Dislocation loops average density, $m^{-3}$ | $3.96\times10^{22}$ | $2.69\times10^{22}$ |
| Number of dislocation loops | 1337 | 1674 |

Figure 6-2 Dislocation loop size distribution in SS 304L-R and SS 304LN after 5 dpa proton irradiation. SS 304L-R exhibits a slightly larger average loop size (9.9 nm) and lower density ($2.69 \times 10^{22}$ $m^{-3}$), while SS 304LN shows a higher density ($3.96 \times 10^{22}$ $m^{-3}$) and lower size (8.2 nm). Dashed vertical lines are the median which are included in the table.

### *6.1.2 Cavities*

Figure 6-3 shows TEM bright field (BF) images highlighting cavity formation in SS 304L-R and SS 304LN alloys after proton irradiation to 5 dpa at 360 °C. Overfocus imaging was employed to enhance cavity visibility. Figure 6-3 (a) and (b) correspond to SS 304L-R sample L-R-1 and SS 304LN sample N3, respectively. For each alloy, three distinct locations were characterized at a depth of approximately 3 - 4 (±1) µm from the irradiated surface, coinciding with the uniform irradiation region. A qualitative comparison of the plots clearly reveals a substantial difference in cavity density between the two samples. Sample L-R-1 (Figure 6-3 (a)) shows a noticeably higher number of cavities compared to sample N3 (Figure 6-3 (b)), where the cavity density appears significantly lower and cavities are more sparsely distributed across all

three locations. This observation indicates a material-dependent difference in cavity nucleation and growth under identical irradiation conditions.

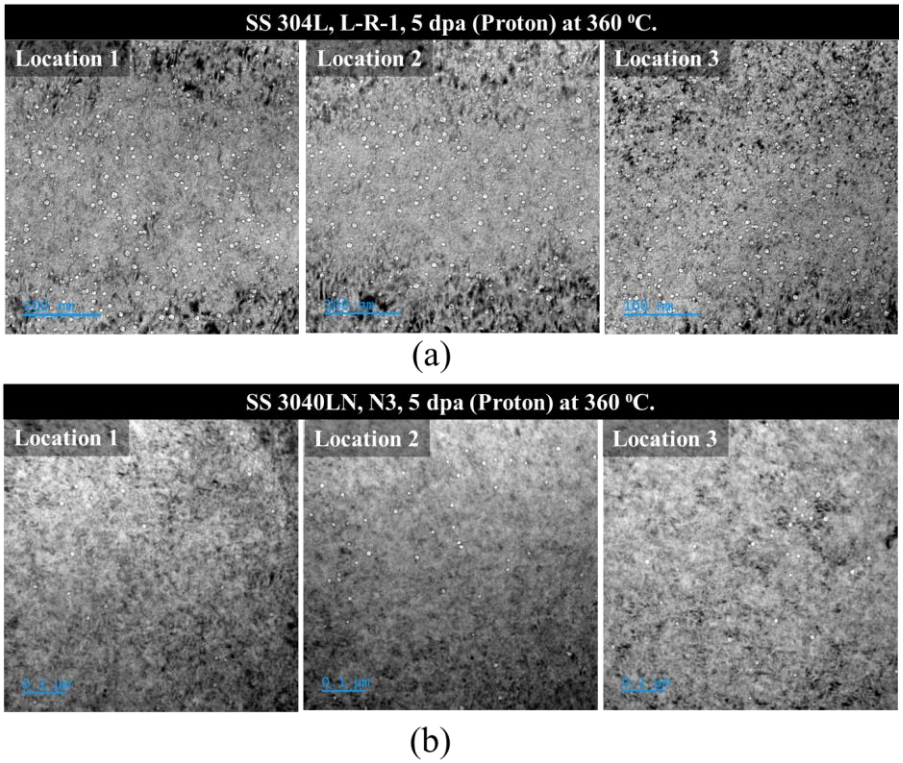


Figure 6-3 TEM BF images of cavities in (a) SS 304L (L-R-1) and (b) SS 304LN (N3) after 5 dpa proton irradiation at 360 °C. Images were acquired at ~12–12.5 µm depth. L-R-1 shows a significantly higher cavity density compared to N3.

A more quantitative assessment is provided in Figure 6-4, which shows the cavity size distribution and corresponding density for both alloys. The main plot on the left compares the overall cavity size distributions, where L-R-1 is represented in red and N3 in grey. The inset plots further detail the individual histograms for each alloy. It is evident that L-R-1 exhibits a much sharper and higher distribution peak, reflecting its higher cavity density. According to the summary table in Figure 6-4, L-R-1 exhibits an average cavity density $7.40 \times 10^{21}$ cavities/m$^3$ after characterizing 904 cavities, which is nearly two orders of magnitude higher than that of N2, measured at $7.45 \times 10^{20}$ cavities/m$^3$ after characterizing 104 cavities. This significant difference

aligns with the qualitative observations from Figure 6-3 and underscores the pronounced susceptibility of L-R-1 to cavity formation under irradiation even at relatively low dpa values.

In terms of cavity size, SS 304LN shows a larger average cavity diameter of 8.08 nm with a relatively broad size distribution (standard deviation of 1.95 nm). Conversely, SS 304L-R cavities are smaller on average (4.94 nm) with a narrower size distribution (standard deviation of 1.30 nm).

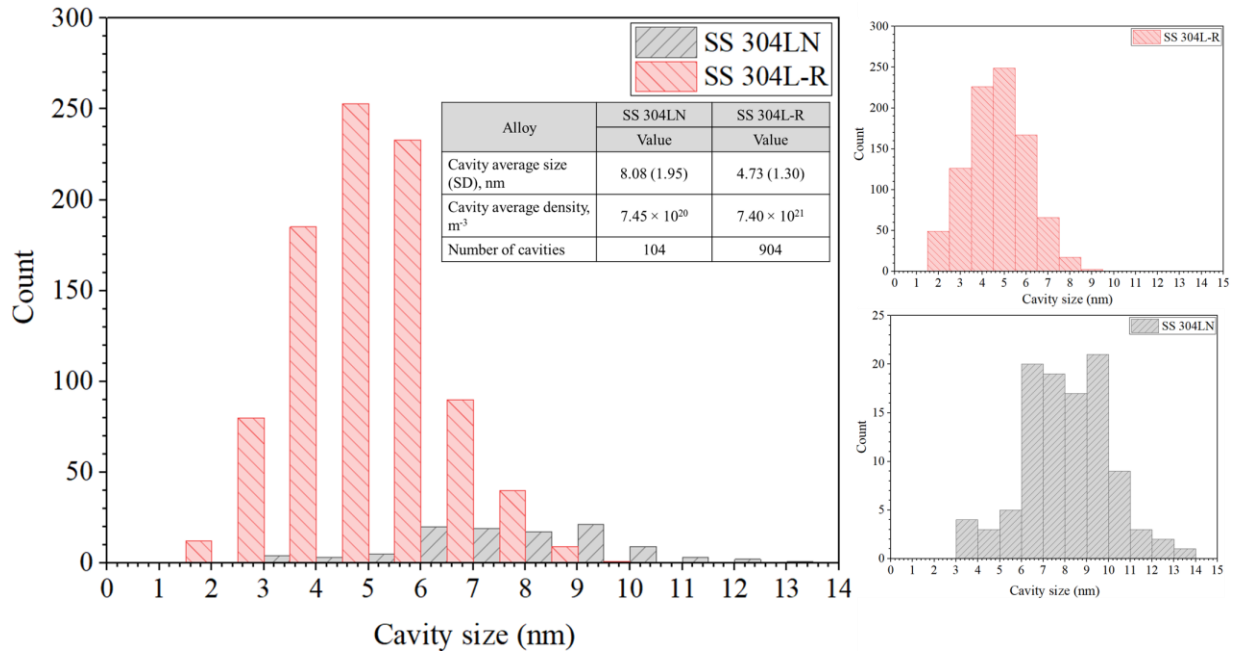


| Alloy | SS 304LN | SS 304L-R |
|---|---|---|
| | Value | Value |
| Cavity average size (SD), nm | 8.08 (1.95) | 4.73 (1.30) |
| Cavity average density, $m^{-3}$ | $7.45 \times 10^{20}$ | $7.40 \times 10^{21}$ |
| Number of cavities | 104 | 904 |

Figure 6-4 Cavity size distribution and density comparison between L-R-1 and N3 after 5 dpa proton irradiation. L-R-1 exhibits higher cavity density ($7.40 \times 10^{21}$ $m^{-3}$) with smaller size (4.73 nm), while N2 shows lower density ($7.45 \times 10^{20}$ $m^{-3}$) and larger cavities (8.08 nm).

### *6.1.3 Precipitates*

After 5 dpa proton irradiation, SS 304LN exhibits fine, uniformly distributed nanoscale features enriched in Ni and Si, as seen in the STEM-EDS maps in Figure 6-5 (a). While the co-location of Ni and Si suggests the formation of Ni-Si rich clusters, the exact phase, such as γ′-$Ni_3Si$, cannot be confirmed solely from the current data. The relatively weak EDS signal and absence of clear precipitate boundaries prevented accurate quantification of their size and

number density. Nonetheless, the elongated morphology of these features, evident in the dark Si and Ni maps, implies that segregation is likely occurring at or near dislocation loops.

By comparison, SS 304L-R (Figure 6-5 (b)) shows a qualitatively similar but less pronounced response, with weaker co-location of Ni and Si signals and a noticeably lower apparent density of enriched features. Due to limited acquisition time and the need for additional TEM sample thinning to improve signal-to-noise ratio, characterization and quantification of these precipitates were not possible due to time constraints and limited access to TEM systems, which were unavailable at times because of ongoing maintenance and high user demand.

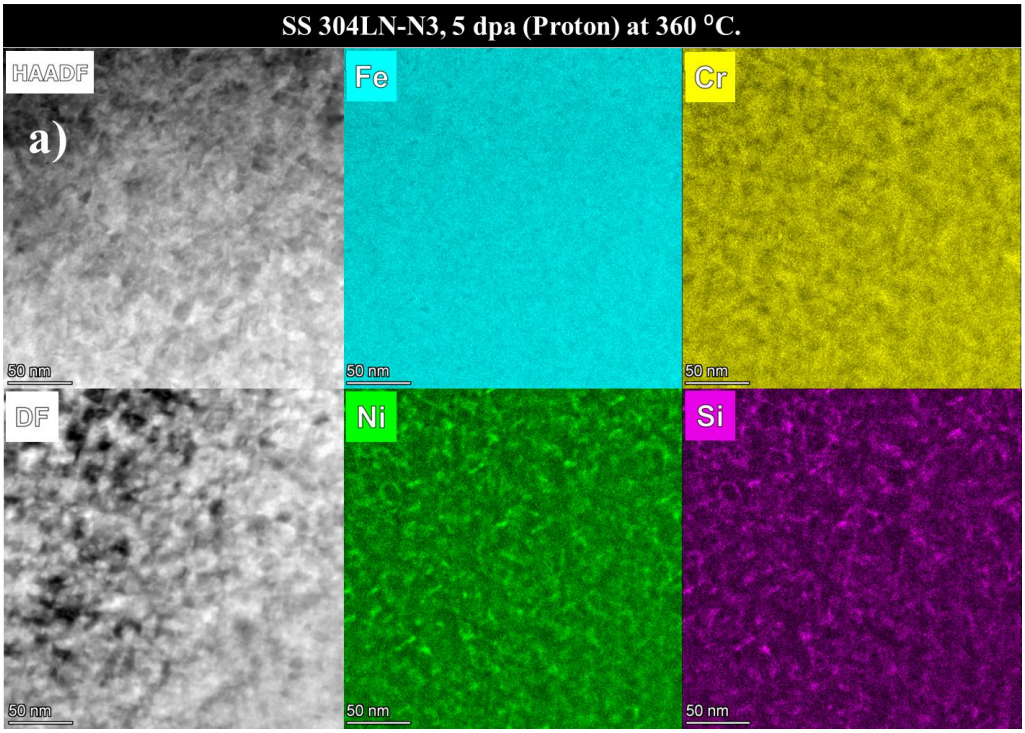

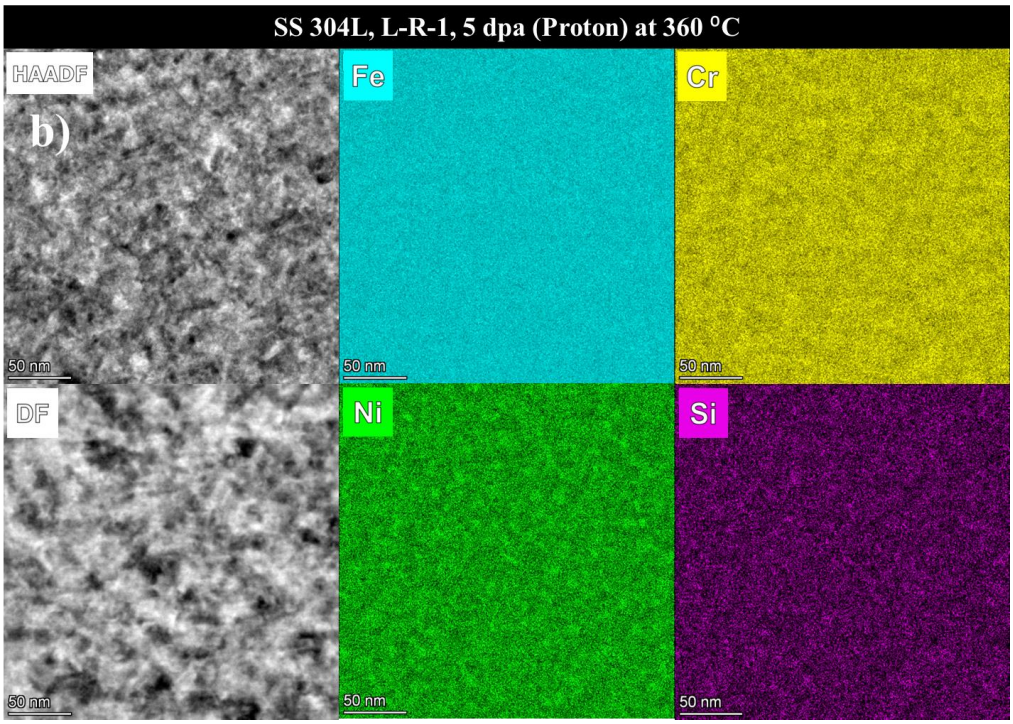


Figure 6-5 TEM-HAADF, DF, and EDS elemental mapping for matrix in (a) SS 304LN and (b) SS 304L showing the precipitates exist following proton irradiation.

### *6.1.4 Radiation-induced segregation*

Radiation-induced segregation (RIS) is another phenomenon that occurs during irradiation, driven by elemental diffusion, particularly of Fe, Cr, Ni, and Si. As discussed in Section 2.2.4, RIS causes elemental redistribution during irradiation due to defect-mediated diffusion. Figure 6-6 (a) shows the TEM-EDS elemental mapping at the GB, showing the RIS effect at the GB. The higher contrast of Si and Ni reveal significant segregation, while Cr and Fe are notably depleted at the boundary through the dark contrast at the GB indicating lower concentration that the neighboring grains. Figure 6-6 (b) shows the profile location where the analysis was performed which is roughly 100 nm away from the oxidation tip to avoid any oxidation effect that might affected the concentrations. Figure 6-6 (c) shows the chemical composition profiles across the GB of Fe, Cr, Ni, and Si, indicating a reduction in Fe and Cr concentrations and an increase in Ni. The magnified profile is shown in Figure 6-6 (d) showing a

significant increase in Ni compared to its original (pre-irradiation) composition which was at 8.6 wt.%. The corresponding atomic fraction is approximately 8.08 at.% in bulk. Following proton irradiation to 5.0 dpa, GB analysis revealed Ni segregation of 19 at.%, indicating a significant enrichment, nearly 2.4x increase in atomic concentration. For Si, the bulk silicon concentration of 0.43 wt.% corresponds to approximately 0.86 at.%. After irradiation to 5.0 dpa, Si enrichment at the GB jumped to 6.5 at.% as shown in Figure 6-6 (d), representing an increase of 7.6x compared to the bulk. While the absolute values may not be precise due to the GB thickness being smaller than the electron beam diameter, the data clearly demonstrates compositional changes at the GB attributed to RIS.

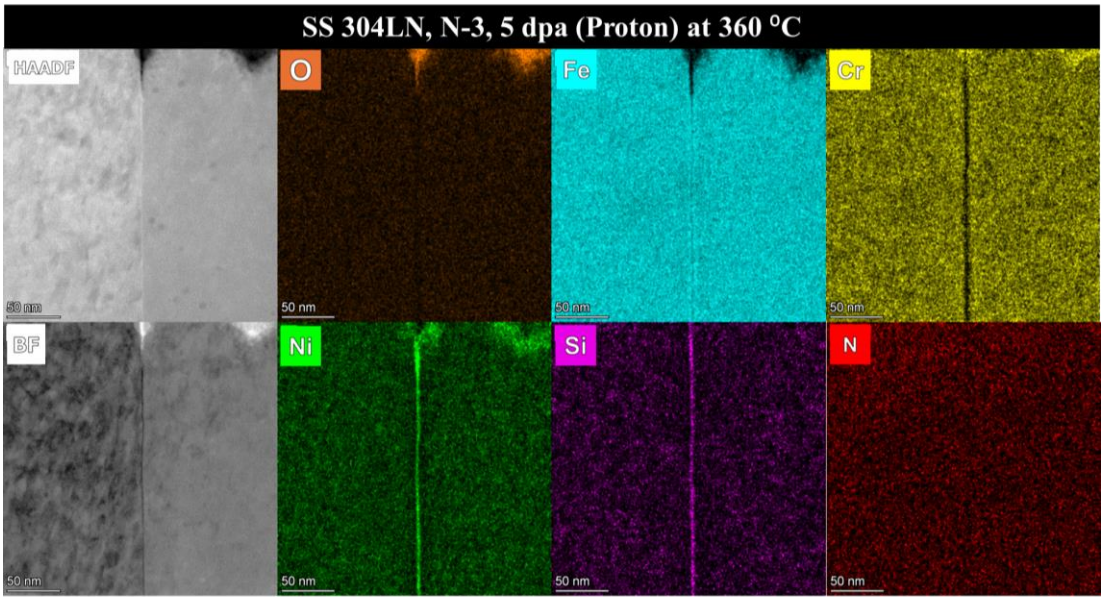


**(a)**

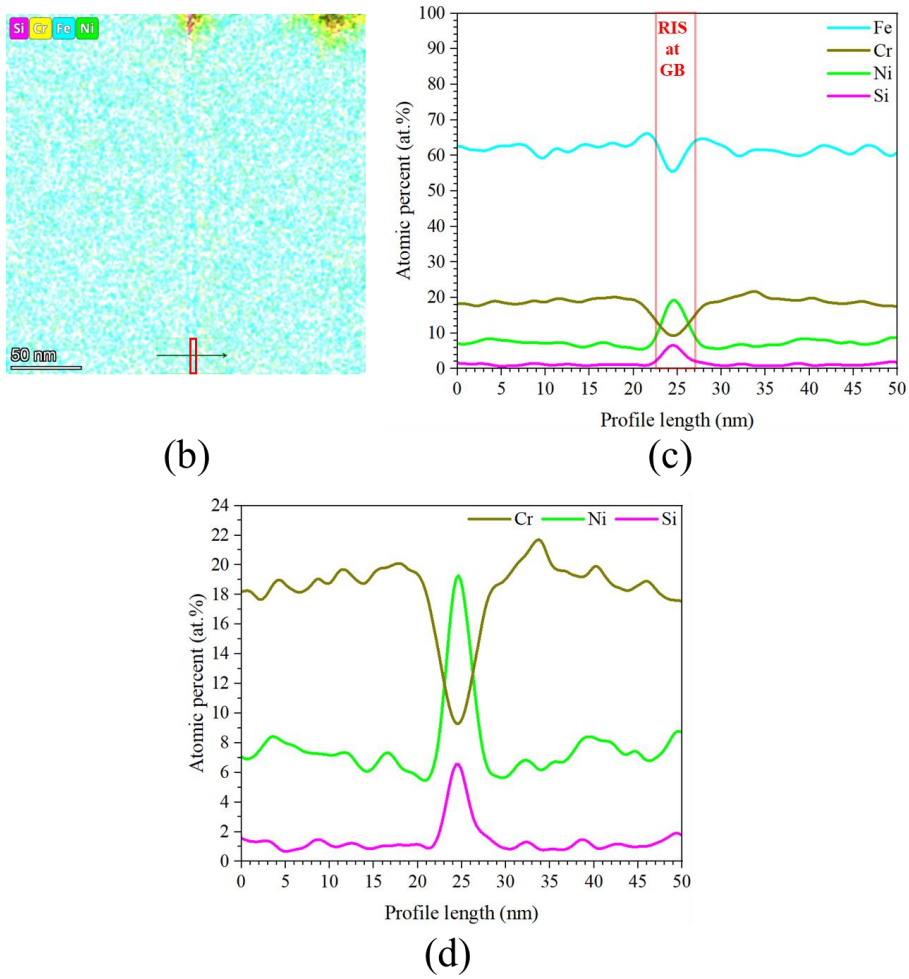


Figure 6-6 (a) TEM-HAADF, -DF, and -EDS elemental mapping of a high angle grain boundary in SS 304LN showing RIS of Si and Ni while depletion of Fe and Cr, (b) the location where the profile taken from, (c) the composition of elements at the GB, (d) the composition of Si and Ni at the GB.

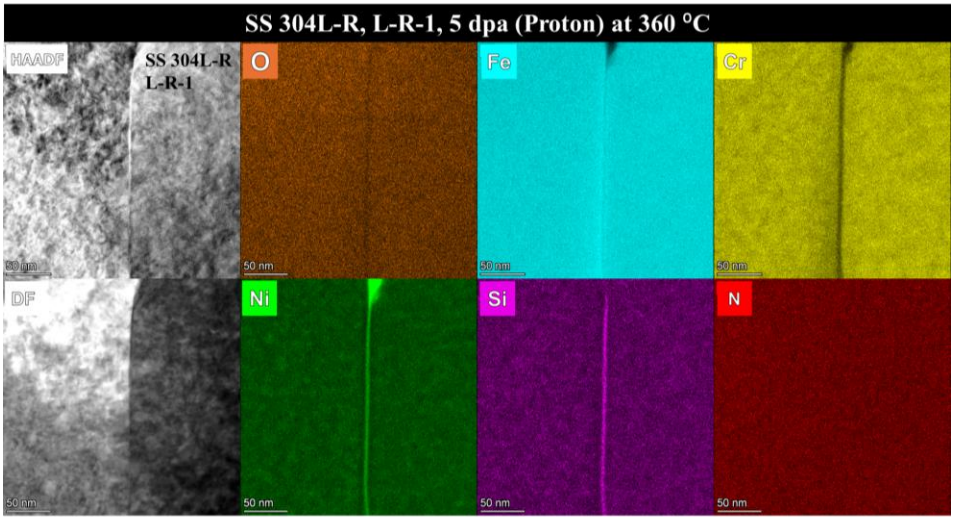


**(a)**

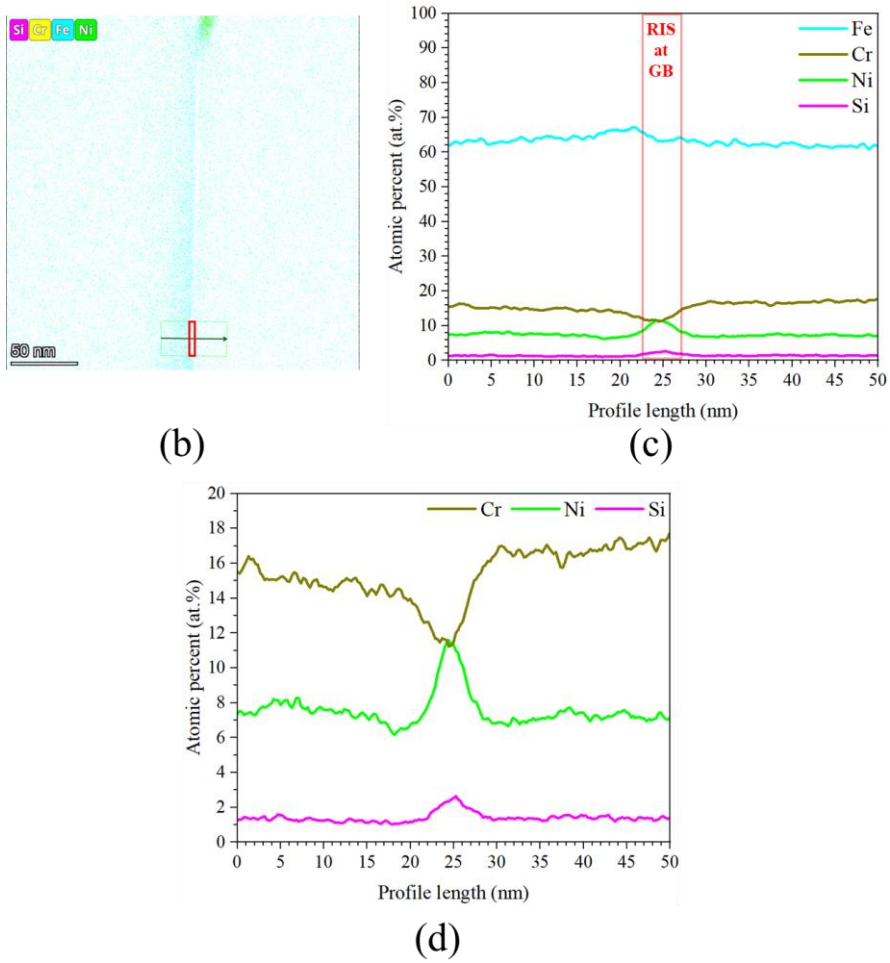


Figure 6-7 (a) TEM-HAADF, -DF, and -EDS elemental mapping of a high angle grain boundary in SS 304L-R showing RIS of Si and Ni while depletion of Fe and Cr, (b) the location where the profile taken from, (c) the composition of elements at the GB, (d) the composition of Si and Ni at the GB.

Figure 6-7 (a) shows the TEM-EDS elemental mapping and Figure 6-7 (b) shows the chemical composition across the GB and around 200 – 300 nm away from the oxide tip of SS 304L-R showing relatively similar behavior with SS 304LN. In SS 304L-R, the bulk nickel concentration of 7.95 wt.% corresponds to approximately 7.49 at.%, while the bulk silicon concentration of 0.33 wt.% corresponds to 0.65 at.%. After proton irradiation to 5.0 dpa, grain boundary concentrations increased to 11.6 at.% for Ni and 2.6 at.% for Si, representing enrichments by factors of approximately 1.5x and 3.9x, respectively. These results further

confirm the segregation tendency of both Ni and Si under irradiation, with Si showing particularly strong enrichment relative to its bulk level.

A comparison between SS 304LN and SS 304L-R revealed that both Ni and Si undergo significant RIS to GB following 5.0 dpa proton irradiation. Ni enrichment was more pronounced in SS 304LN (2.4x) compared to SS 304L-R (1.5x), likely due to the higher bulk Ni content in SS 304LN (6% difference as shown in Table 4-1). Si exhibited strong segregation in both samples, with twofold higher enrichment in SS 304LN (7.6x) compared to SS 304L-R (3.9x). Summary of the chemical compositions of RIS elements at the GB following 5 dpa of proton irradiation is listed in Table 6-1.

Table 6-1 Summary of nickel and silicon compositions showing the effect of RIS after irradiation to 5 dpa.

| **Alloy (sample)** | **Pre-irradiation (at.%)** | | | **Post-irradiation (at.%)** | | |
|---|---|---|---|---|---|---|
| | Silicon | Nickel | Chromium | Silicon | Nickel | Chromium |
| SS 304L (L-R-1) | 0.65 | 7.49 | 18.7 | 2.6 (+ 4x) | 11.6 (+1.6x) | 11.3 (-0.6x) |
| SS 304LN (N3) | 0.86 | 8.08 | 19.2 | 6.5 (+ 6.6x) | 19.0 (+ 2.4x) | 9.3 (- 0.5x) |

## 6.2 Four-point bend tests

### *6.2.1 Load profiles*

A total of six 4PB samples were tested, with three per alloy to ensure reliability and reproducibility. In this study, the criterion was to obtain similar results for at least two samples is considered acceptable.

For SS 304LN, sample N3 was the first ever proton-irradiated 4PB to be tested in the autoclave. Initially, it was decided to start with 36%YS due to the lack of prior data on this alloy in this testing environment so as to avoid missing IASCC initiation at early loading stage as shown in Figure 6-8 (a). No cracks were observed by SEM analysis; testing was continued until the sample failed at 72%YS. The first repeat was sample N7, which strained first to 44%YS as

shown in Figure 6-8 (b) and no cracks were observed by the SEM until the sample was strained to 89%YS. The minimum stress to initiate IASCC was the highest among all other samples, as second repeat was sample N10 (Figure 6-8 (c)) exhibited cracking at 70%YS.

Sample L-R-1 was strained initially to 50% of the irradiated YS of SS 304L. Figure 6-8 (d) shows the load vs displacement profile for this sample. As no cracks observed, the tests were proceeded in an incremental procedure explained in section 4.6.4 until the cracks were observed after straining the sample to 80%YS. For sample L-R-3, that was the first repeat, the straining started again from 50%YS to ensure no cracking will start early as shown in Figure 6-8 (e), no cracks were found. The next step was intended to be 60%YS, however, due to an unexpected issue with the servomotor controller that did not communicate properly with the LabView® to stop the test once the load reached the target, the loading continued until the test was forcefully terminated at a load of around 160 N. FEA was used to calculate the corresponding stress at 70%YS. No cracks were observed after scanning the surface in SEM. The test resumed again, and the sample strained to 80%YS produced cracks. For the sample L-R-6, the second repeat, the first test was started after straining the sample to 60%YS as shown inf Figure 6-8 (f) because no cracks were found earlier than 80%YS of the first two samples. The sample failed at 70%YS.

.

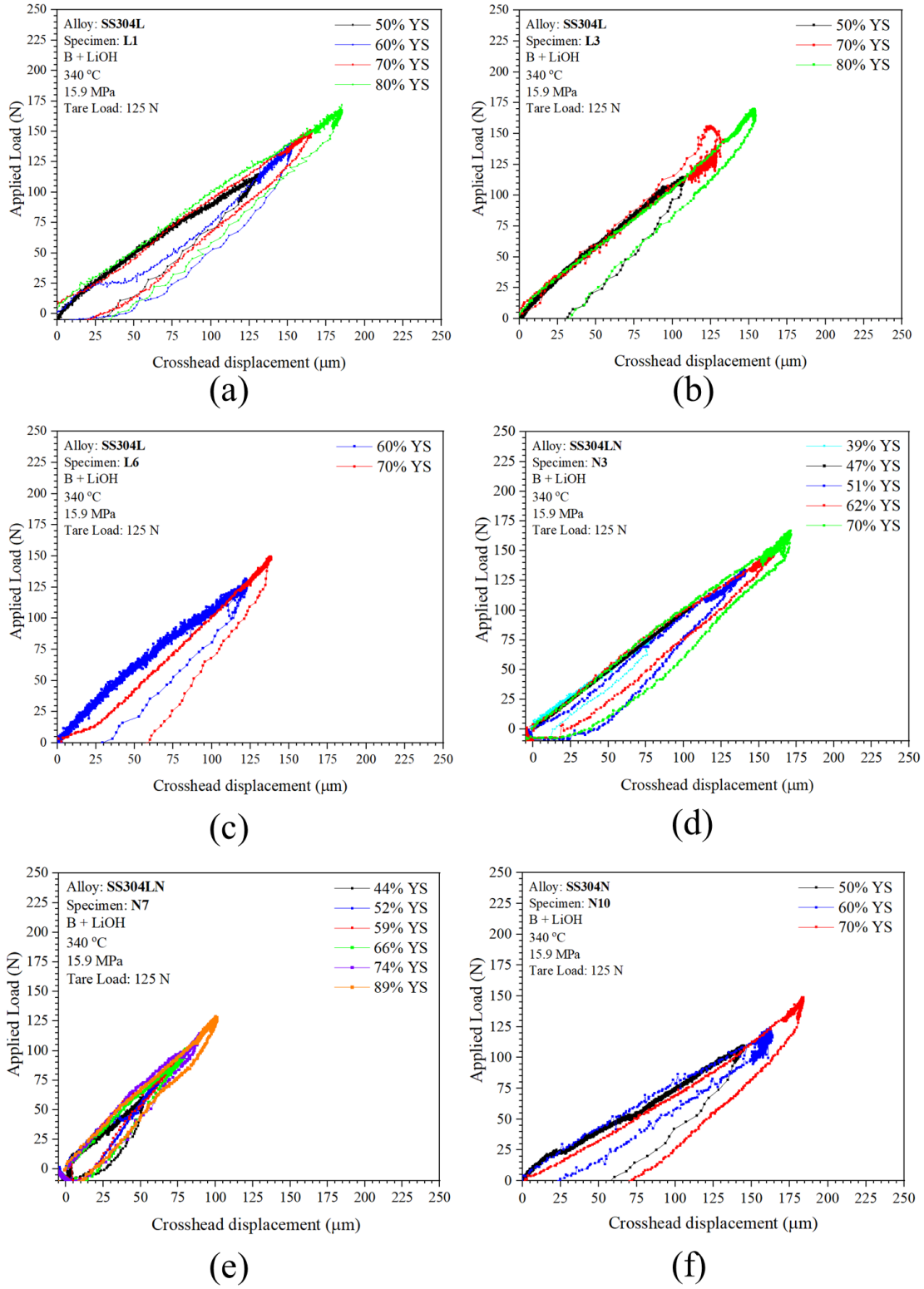


Figure 6-8 Loads vs displacement for all loading steps of samples (a) L-R-1, (b) L-R-3, (c) L-R-6, (d) N3, (e) N7, and (f) N10.

### *6.2.2 Water chemistry profiles*

Table 6-2 summarizes the water chemistry parameters for each loading step as determined using Andresen's software. The table shows a consistent concentration of LiOH and $H_3BO_3$, with the PWR water environment. aligning well with typical PWR water chemistry. The pH ranged from 6.50 to 6.57, remaining within the expected alkaline regime, while water conductivity values ranged from 21.9 to 25.2 µS/cm, meeting the established requirements for PWR environments.

Table 6-2 Water chemistry parameters calculated during each loading step.

| Sample ID | Loading step | Water conductivity (µS/cm) | Boric acid (ppm) | LiOH (ppm) | $pH_{@RT}$ |
|---|---|---|---|---|---|
| N3 | 1 | 22.7 | 1038 | 2.132 | 6.50 |
| | 2 | 22.3 | 988 | 2.088 | 6.53 |
| | 3 | 23.1 | 1048 | 2.170 | 6.50 |
| | 4 | 22.8 | 1039 | 2.136 | 6.50 |
| | 5 | 22.9 | 1001 | 2.236 | 6.55 |
| N7 | 1 | 24.3 | 1010 | 2.272 | 6.55 |
| | 2 | 23.4 | 989 | 2.189 | 6.55 |
| | 3 | 23.6 | 994 | 2.207 | 6.55 |
| | 4 | 24.5 | 1015 | 2.294 | 6.55 |
| | 5 | 25.2 | 1032 | 2.363 | 6.55 |
| | 6 | 23.7 | 995 | 2.213 | 6.55 |
| N10 | 1 | 23.5 | 1005 | 2.201 | 6.54 |
| | 2 | 23.2 | 983.4 | 2.166 | 6.55 |
| | 3 | 23.4 | 977 | 2.190 | 6.56 |
| L-R-1 | 1 | 22.9 | 998 | 2.139 | 6.53 |
| | 2 | 23.2 | 955 | 2.166 | 6.57 |
| | 3 | 23.3 | 1043 | 2.190 | 6.51 |
| | 4 | 23.4 | 1001 | 2.188 | 6.54 |
| L-R-3 | 1 | 23.6 | 978.5 | 2.201 | 6.56 |
| | 2 | 24.0 | 989 | 2.247 | 6.56 |
| | 3 | 23.2 | 1013 | 2.174 | 6.53 |
| L-R-6 | 1 | 23.5 | 979 | 2.197 | 6.56 |
| | 2 | 21.9 | 952 | 2.042 | 6.55 |

Testing environment was continuously monitored during the test. Data collected were water conductivity in μS/cm, dissolved oxygen in ppm, temperature in $^{o}$C, autoclave pressure in psi, and hydrogen overpressure in psi. This data was recorded every 30 seconds during the testing time. After each test, all of these data were plotted as shown in Figure 6-9 through Figure 6-14 for samples N3, N7, N10, L-R-1, L-R-3, and L-R-6. All steps are also included in the figure. All figures show that the environment inside the autoclave was controlled and simulates the PWR properly. It should be noted that the 90%YS step test in Figure 6-10 (e), there is a large discontinuities in hydrogen concentration and small discontinuities in all other parameters due to a miscommunication issue between the LabView and all sensors through the communications ports (COM).

The exposure time was calculated based on the time the sample exposed to high temperature water which is the beginning of the flat red curve in the water chemistry figures until it ends for each curve, the total exposure time was the summation of all exposure times at high temperature for each step that is summarized in Figure 6-15. Overall, the SS 304LN samples experienced slightly longer exposure times compared to the SS 304L-R samples. This difference is primarily attributed to the higher mechanical strength of the 304LN alloy, which required longer durations to reach the target load during slow strain rate testing. For instance, sample N3, which underwent a full loading sequence from 40% to 80% YS, required noticeably more time than sample L-R-1, which followed a similar loading path. Additionally, variations in the loading strategy influenced the exposure time. For example, sample L-R-6 was initially strained to 60% YS and then failed at 70% YS, resulting in a shorter overall test duration and explaining its position as the lowest exposure time among all samples.

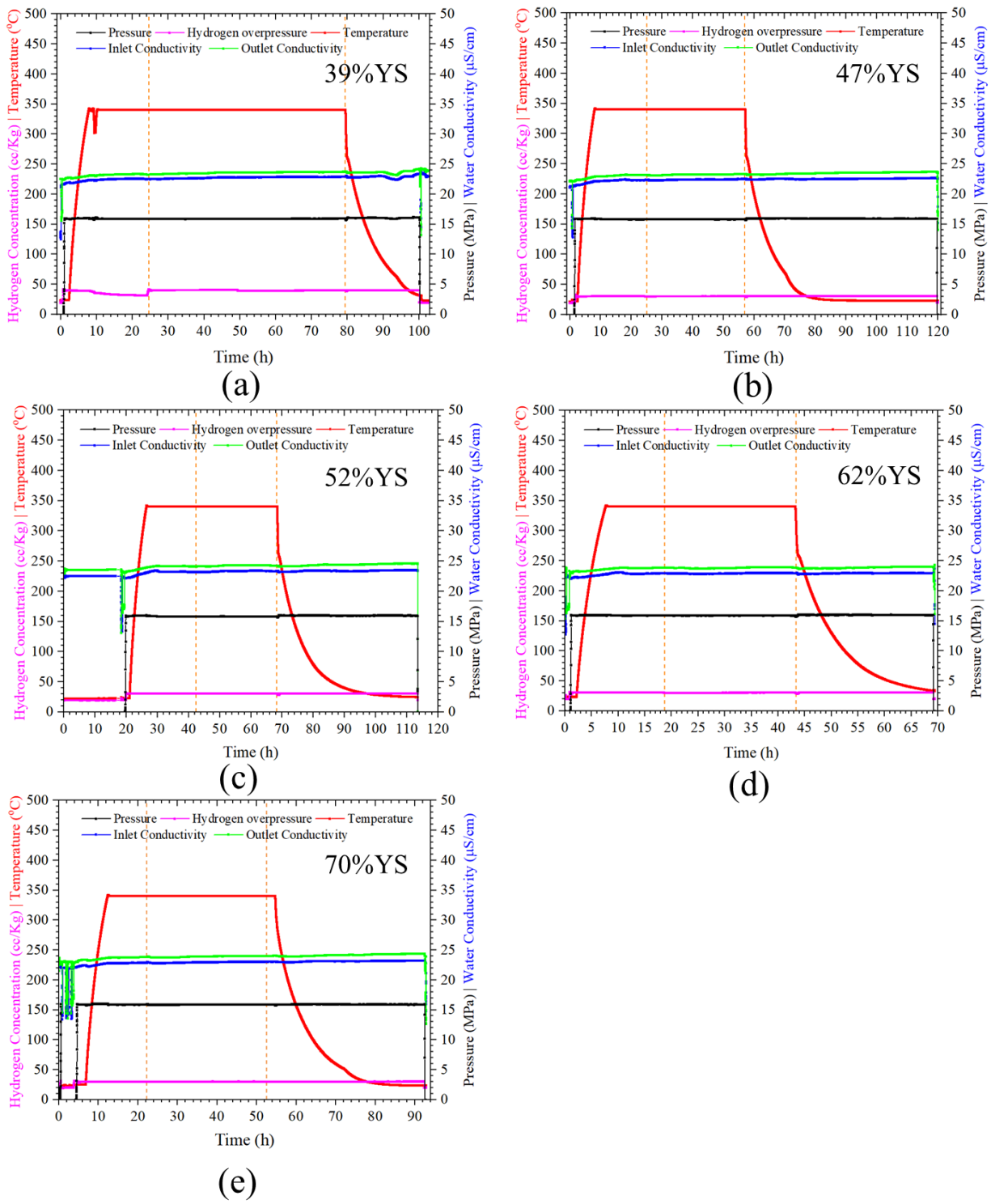


Figure 6-9 Time-dependent measurements of water chemistry and autoclave conditions for sample N3 during loading steps at (a) 39%YS, (b) 47%YS, (c) 52%YS, (d) 62%YS, and (e) 70%YS. The dashed vertical lines indicate the periods during which the sample was exposed to high temperature and applied loading.

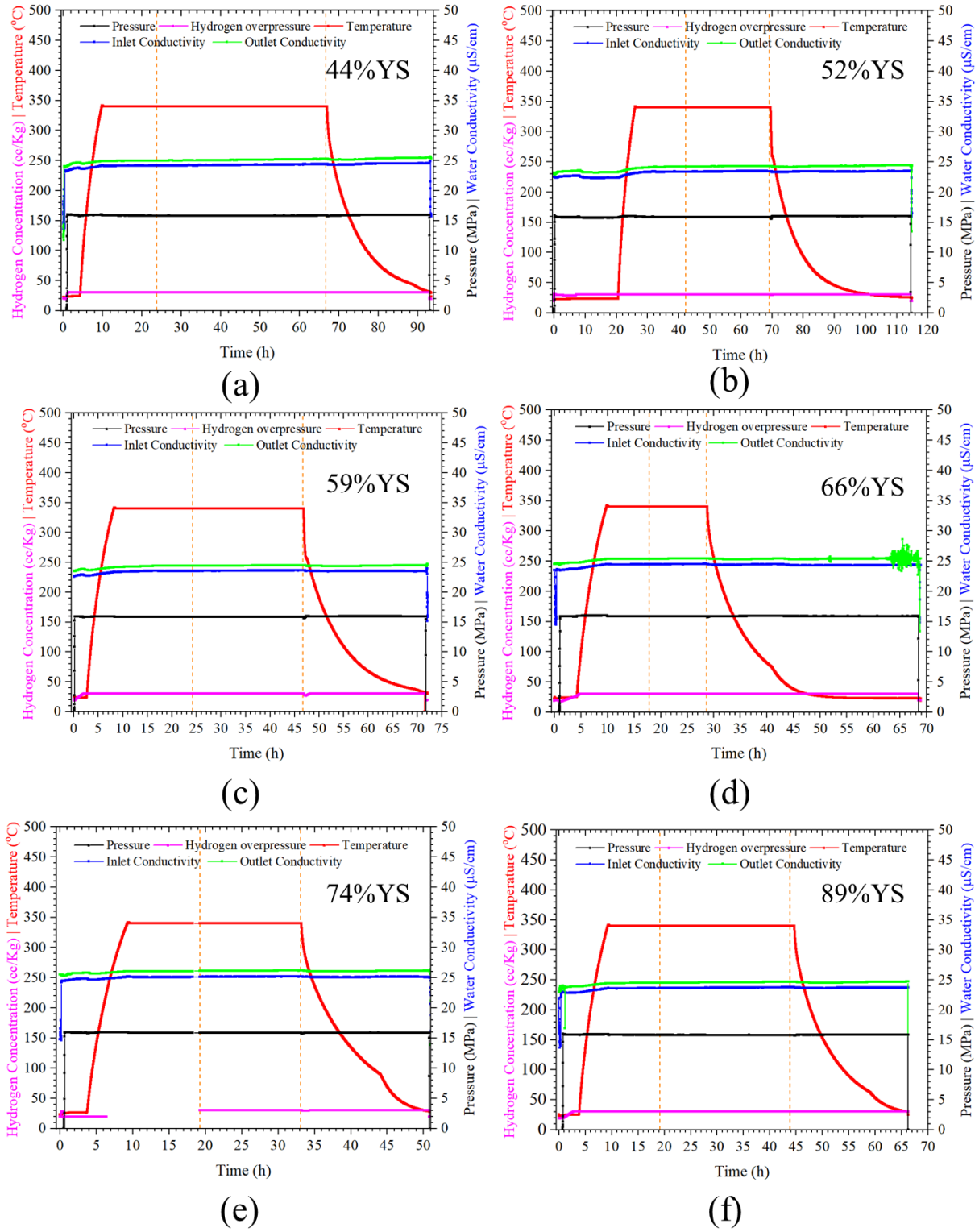


Figure 6-10 Time-dependent measurements of water chemistry and autoclave conditions for sample N7 during loading steps at (a) 44%YS, (b) 52%YS, (c) 59%YS, (d) 66%YS, (e) 74%YS, and (f) 89%YS.

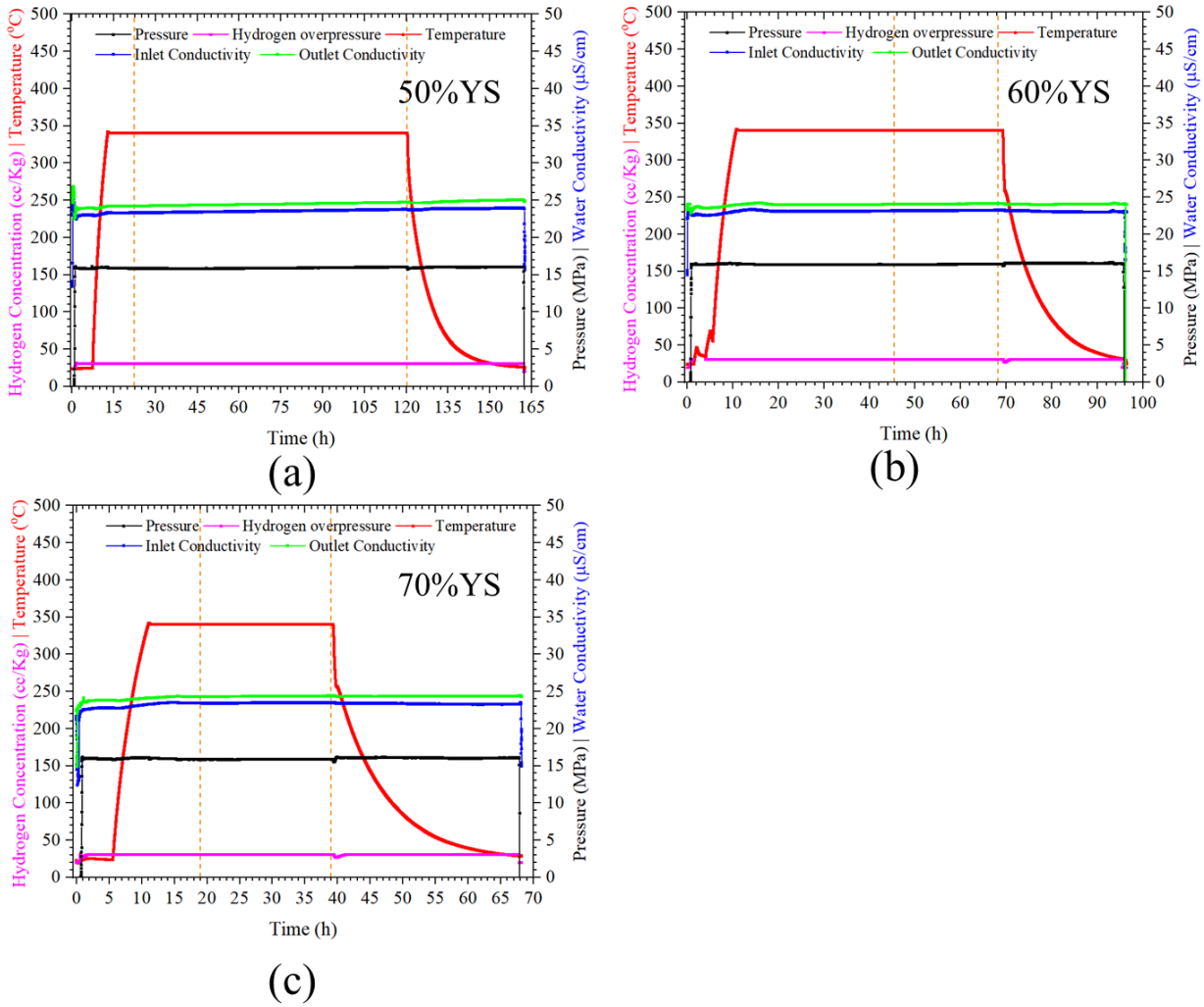


Figure 6-11 Time-dependent measurements of water chemistry and autoclave conditions for sample N10 during loading steps at (a) 50%YS, (b) 60%YS, and (c) 70%YS.

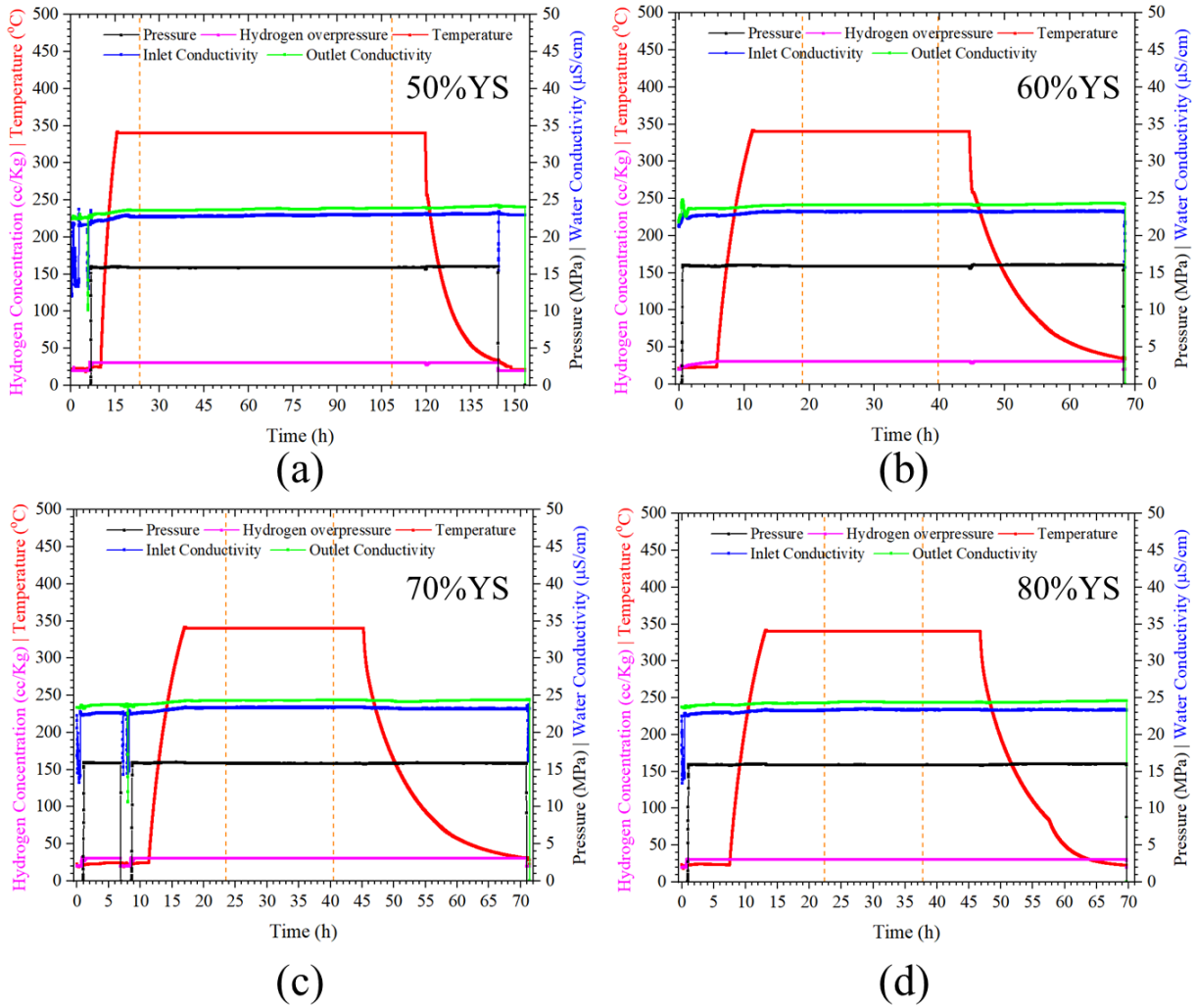


Figure 6-12 Time-dependent measurements of water chemistry and autoclave conditions for sample L-R-1 during loading steps at (a) 50%YS, (b) 60%YS, (c) 70%YS, and (d) 80%YS.

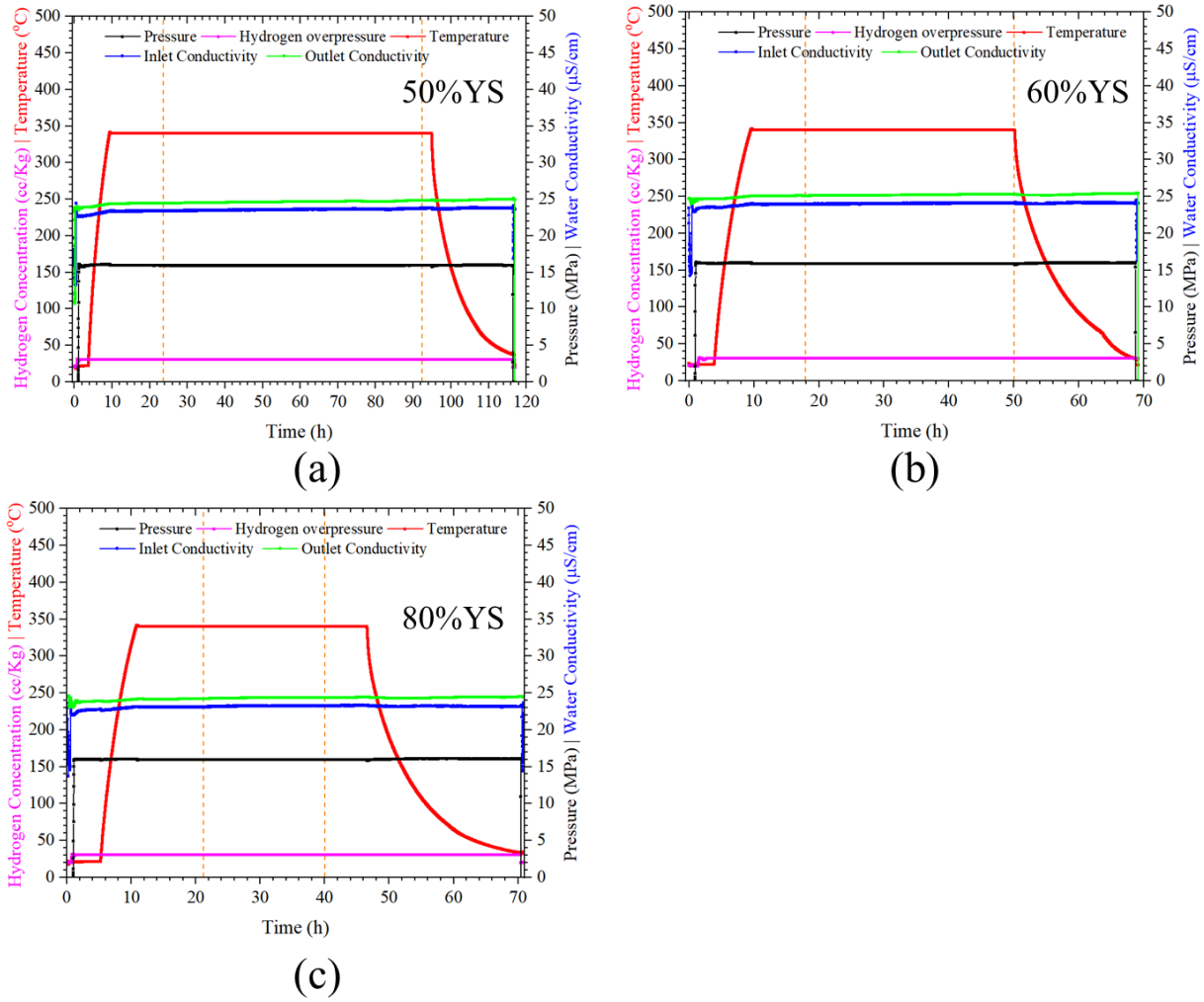


Figure 6-13 Time-dependent measurements of water chemistry and autoclave conditions for sample L-R-3 during loading steps at (a) 50%YS, (b) 70%YS, and (c) 80%YS.

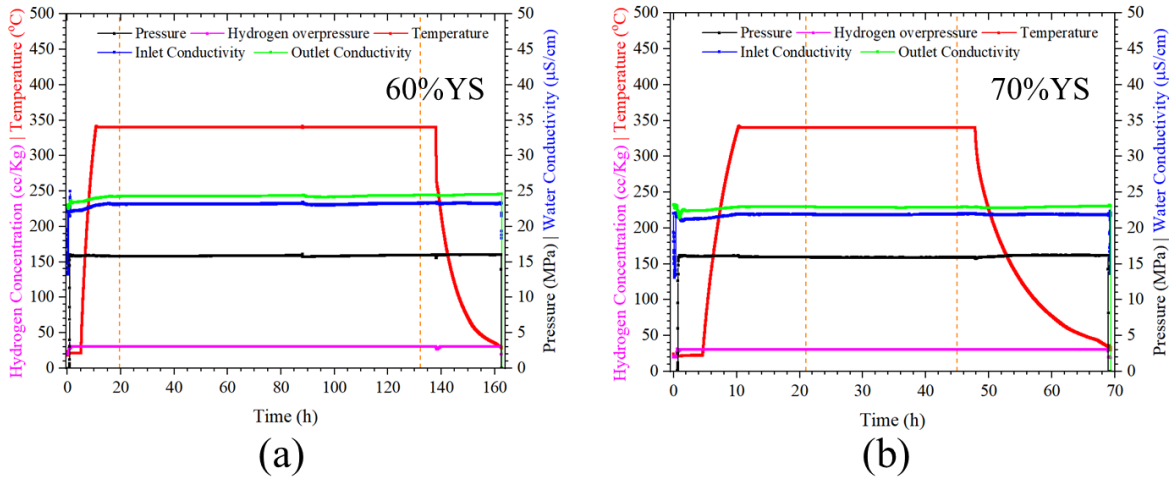


Figure 6-14 Time-dependent measurements of water chemistry and autoclave conditions for sample L-R-6 during loading steps at (a) 60%YS and (b) 70%YS.

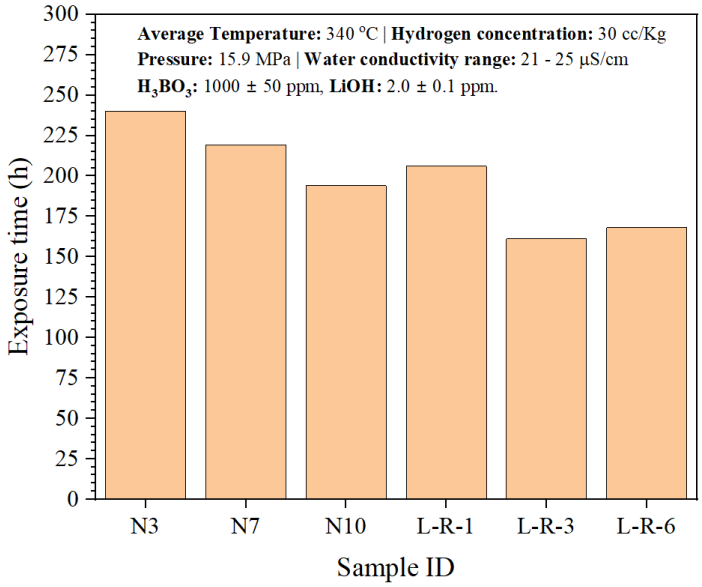


Figure 6-15 Total exposure time to the high-temperature water at 340 °C containing $H_3BO_3$ and LiOH in the autoclave for SS 304LN and SS 304L-R samples.

### *6.2.3 IASCC initiation and cracking statistics*

#### *6.2.3.1 IASCC initiation*

The minimum stress required to initiate IASCC in both alloys was determined using 4PB tests, as previously described. A summary of these tests is shown in Figure 6-16 and Table 6-3, which also incorporates the uncertainty analysis from Table 5-21. This uncertainty is visually represented by faint up and down error bars around the initiation points. Additionally, due to the incremental nature of the test and the load step size of approximately 10% YS, crack initiation may have occurred at any stress level between the observed initiation point and the preceding step. To account for this, a conservative error bar of -10% YS was added to the initiation point.

Sample N3 underwent five load steps, starting at 39%YS, with no cracks observed. The loading sequence continued as outlined in section 4.6.4, and failure occurred at 70%YS, where cracks were observed after scanning the constant strain region with the SEM. Since sample N3

failed at 70%YS, sample N7 tested initially at 44%YS. As no cracking observation, the loading steps continued until 89%YS where two cracks observed at the surface.

Table 6-3 4PB tests results for the six samples including the uncertainty results showing the range of the expected failure.

| Sample ID | $\sigma_{Failure}$ (MPa) | $\%YS_{Failure}$ | 4PB %uncertainty | %FEA uncertainty |
|---|---|---|---|---|
| **N3** | 547 | 70.0 | 8 | 3.9 |
| **N7** | 694 | 89.0 | 15 | 5.0 |
| **N10** | 544 | 70.0 | 10 | 3.9 |
| **L-R-1** | 596 | 80.0 | 10 | 4.1 |
| **L-R-3** | 597 | 80.0 | 10 | 4.1 |
| **L-R-6** | 521 | 70.0 | 10 | 3.6 |

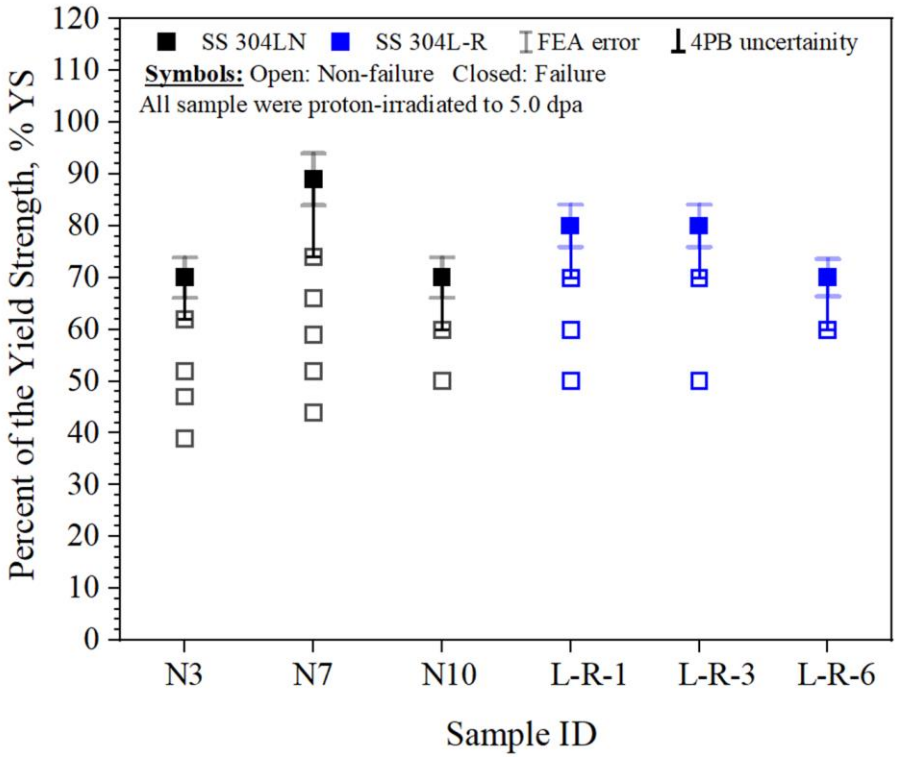


Figure 6-16 Summary of 4PB test results for proton-irradiated samples to 5.0 dpa, showing percent of yield strength (%YS) at failure or non-failure. Solid symbols indicate failure; open symbols indicate non-failure. Error bars represent FEA estimation error, and arrows represent 4PB uncertainty ranges.

Sample N10 was initially tested at 50%YS with no observed cracks, but after straining to 70%YS, three cracks were observed. In conclusion, two samples (N3 and N10) exhibited similar failure stresses (72%YS and 70%YS), whereas sample N7 failed at higher failure stress

(89%YS). However, the average percent of the irradiated yield strength at which cracks observed in all SS 304LN is 76.3%YS with a standard deviation of 9.7%YS.

The SS 304L-R samples demonstrated more consistent behavior. Sample L-R-1 was initially tested at 50%YS, with no cracks detected on the surface. The test continued up to 80%YS, where cracks were observed within the constant strain region. Similarly, Sample L-R-3, a first repeat, was also initially loaded to 50%YS, and cracks did not appear until the sample was strained to 80%YS. Based on these results, Sample L-R-6 was tested at an initial stress of 60%YS, as failure was not expected below this level. No cracks were observed until the sample was strained to 70%YS, which remains consistent with the results from the first two samples. The average percentage of the irradiated yield strength at which cracks were observed in all SS 304LN samples was 76.7% YS, with a standard deviation of 5.1% YS.

In summary, both SS 304L-R and SS 304LN demonstrated comparable IASCC initiation behavior under the tested conditions, with average failure stresses of 76.7% YS and 77.0% YS, respectively. However, if sample N7 is considered an outlier, the average failure stress for SS 304LN drops to approximately 71% YS. Even with this adjustment, the difference remains small and within the ±10% YS range typically within the conservative error bar. These results suggest that while both alloys exhibit similar behavior, SS 304L-R may offer a marginally improved cracking resistance under the applied test conditions.

#### *6.2.3.2 Cracking statistics*

Table 6-4 lists the summary of the crack statistics for all samples. The number of cracks, average crack length in μm, average crack length per unit area in μm/mm$^2$, and the crack density per unit area (number of cracks/mm$^2$) are all listed in the table for each sample. Sample N3 contained at least 24 cracks with an average length of 11.5 ± 8.6 μm, average crack length per

unit area of 6.6 ± 4.9 μm/mm$^2$, and a crack density per unit area of 13.7 cracks/mm$^2$. Sample N7 contained at least two cracks with an average length of 11.9 ± 4.5 μm, average crack length per unit area of 6.8 ± 2.6 μm/mm$^2$, and a crack density per unit area of 1.1 cracks/mm$^2$. Sample N10 showed at least three cracks with an average length of 9.4 ± 7.4 μm, average crack length per unit area of 5.4 ± 4.2 μm/mm$^2$, and a crack density per unit area of 1.7 cracks/mm$^2$. Therefore, the total number of cracks in all SS 304LN samples was 30 with an average crack length of 10.7 μm with a SD of 9.5 μm and crack length per unit area of 183 (± 7.3) μm/mm$^2$ and a crack density of 17.1 mm$^{-2}$.

Table 6-4 Cracking statistics of SS 304LN and SS 304L-R samples after straining in high temperature water containing $H_3BO_3$ and LiOH at 340 ºC.

| **Sample ID / Alloy** | **Number of cracks** | **Average crack length (μm)** | **Crack length per unit area (μm/mm$^2$)** | **Crack density per unit area (#/mm$^2$)** |
|---|---|---|---|---|
| N3 | 24 | 11.5 ± 8.6 | 157.6 ± 6.3 | 13.7 |
| N7 | 2 | 11.9 ± 4.5 | 13.1 ± 0.5 | 1.1 |
| N10 | 3 | 9.4 ± 7.4 | 16.0 ± 0.6 | 1.7 |
| **SS 304LN** | Total: **29** | **10.7 ± 9.11** | **183.0 ± 7.3** | **16.6** |
| L-R-1 | 18 | 12.5 ± 6.4 | 128.8 ± 5.2 | 10.3 |
| L-R-3 | 3 | 8.2 ± 5.2 | 13.9 ± 0.6 | 1.7 |
| L-R-6 | 7 | 13.0 ± 4.5 | 52.0 ± 2.1 | 4.0 |
| **SS 304L-R** | Total: **28** | **11.9 ± 5.9** | **190.4 ± 7.6** | **16.0** |

Sample L-R-1 showed at least 18 cracks within the constant strain region with an average length of 12.5 ± 6.4 μm, average crack length per unit area of 7.2 ± 3.7 μm/mm$^2$, and a crack density per unit area of 10.3 cracks/mm$^2$. Sample L-R-3 showed at least three samples with an average length of 8.2 ± 5.2 μm, average crack length per unit area of 4.7 ± 3.0 μm/mm$^2$, and a crack density per unit area of 1.7 cracks/mm$^2$. Finally, sample L-R-6 showed at least seven cracks with an average length of 13.0 ± 4.5 μm, average crack length per unit area of 7.4 ± 2.6 μm/mm$^2$, and a crack density per unit area of 4.0 cracks/mm$^2$. Therefore, the total number of

cracks in all SS 304LN samples was 30 with an average crack length of 11.9 μm with a SD of 5.9 μm and crack length per unit area of 190.4 (± 7.6) μm/mm$^2$ and a crack density of 16 mm$^{-2}$.

Table 6-5 Total number of cracks observed in both alloys and the contribution of microstructural features initiating cracking.

| Alloy | Number of cracks | Cracks initiated from DCs | Cracks initiated from TJs | Cracks initiated from TJs with DCs |
|---|---|---|---|---|
| SS 304LN | 29 | 9 | 12 | 8 |
| SS 304L-R | 28 | 13 | 10 | 5 |

For better visualization, the data in Table 6-4 and Table 6-5 are plotted in Figure 6-17. The total number of cracks in both alloys (light orange bars) are shown in Figure 6-17(a), along with crack initiators, including DCs (light green with diagonal pattern), TJs (the light purple diagonal pattern), and regions where both DCs and TJs are observed (the light yellow with mesh pattern). Counting these initiators (or precursors) was challenging. Nevertheless, the presented data represents the best effort in identifying these initiators using SEM. Figure 6-17(b) the distribution of crack lengths in both alloys, while Figure 6-17(c) shows the crack density per unit area and crack length per unit area of cracks in both alloys.

In SS 304L-R, a total of 18 cracks were observed, with 14 of them clearly initiated by DCs, accounting for 78% of the cracks. The remaining 22% initiated from TJs locations. In SS 304LN, among the 24 cracks observed in sample N3, 16 were initiated at DC intersections with GBs, representing 67%, while the remaining 33% initiated from TJ locations.

Another critical factor that could influence IASCC initiation is the inclination of the cracked grain boundary relative to the applied loading axis. Figure 6-18 shows the measured GB inclination angles for all samples aggregated for each alloy for easier comparison. Grain boundaries inclined between 40° and 150° were more prone to intergranular cracking. The mean

GB inclination angle with the respect of loading axis is 89º for SS 304L-R with a standard deviation of 23º and 96º with a standard deviation of 20º for SS 304LN.

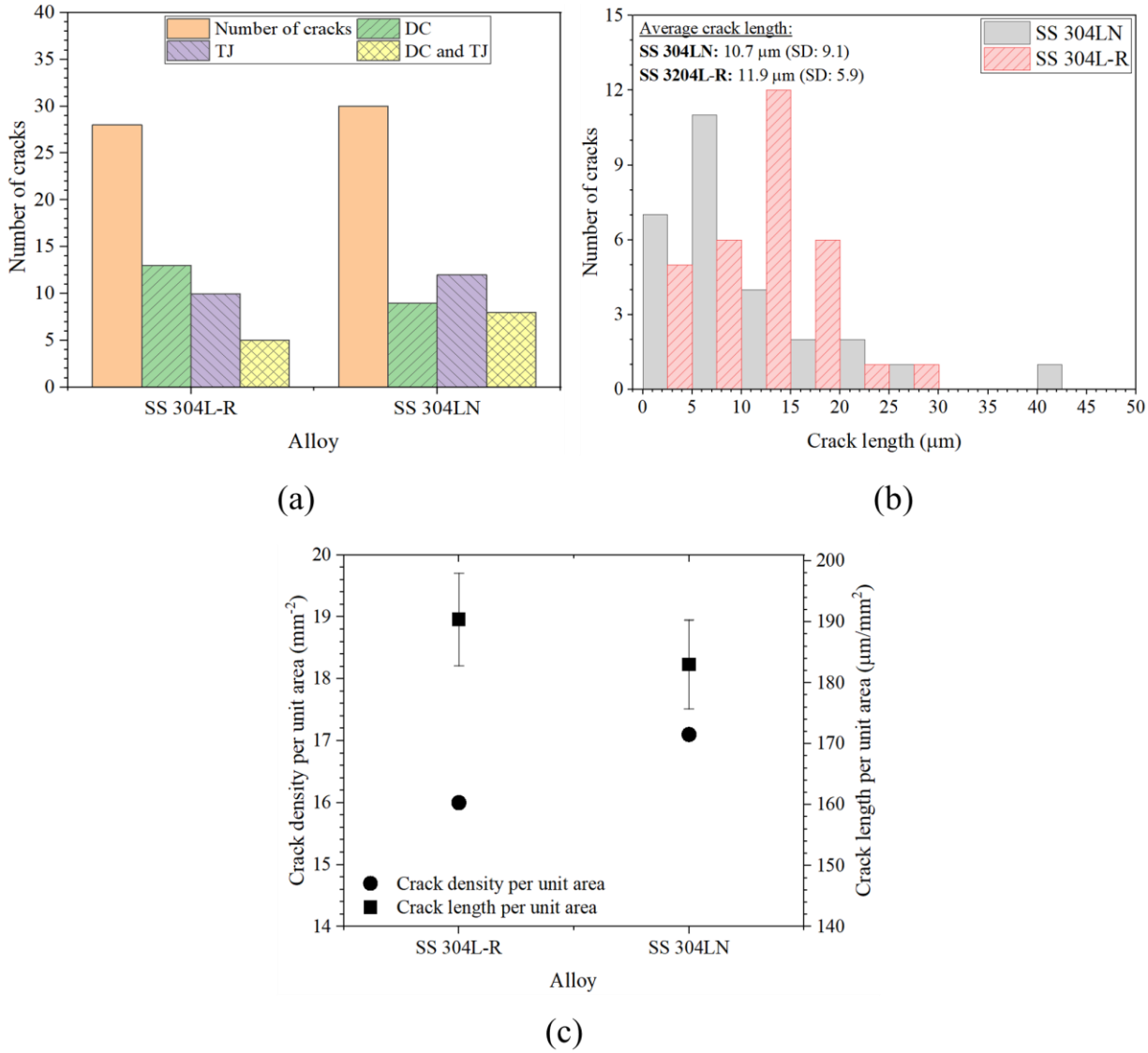


Figure 6-17 Cracking statistics for proton irradiated SS 304LN and SS 304L-R after straining in high temperature water containing $H_3BO_3$ and LiOH at 340 ºC. (a) Number of cracks and number of cracks initiator, (b) the distribution of cracks lengths per alloy, and (c) crack density and crack length per unit area.

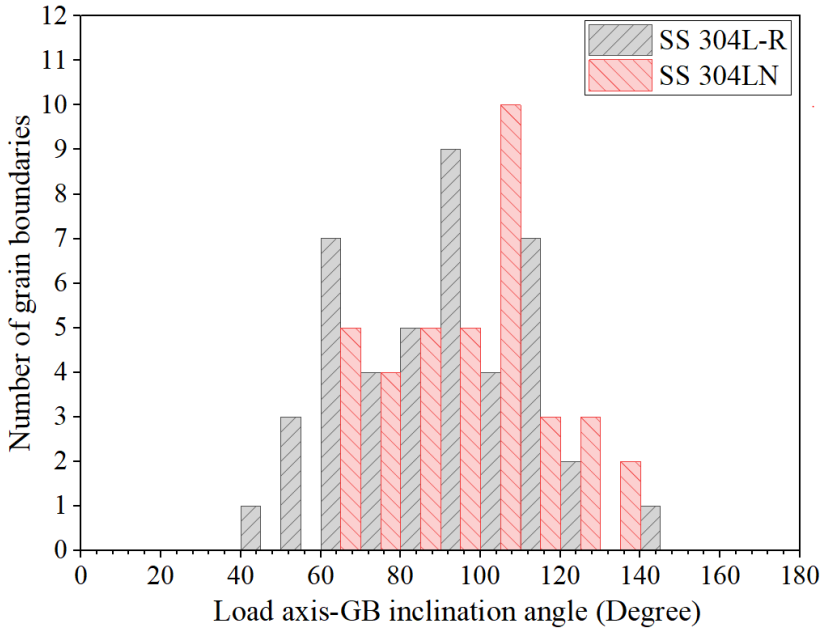


Figure 6-18 Inclination angle of the cracked GB with the respect of the applied load axis in SS 304L-R and SS 304LN showing a mean value of 89º for SS 304L-R and 96º for SS 304LN.

### *6.2.4 Surface and grain boundary oxidation*

#### *6.2.4.1 Surface oxidation*

Surface oxide was analyzed to examine potential differences in morphology between the two alloys in the test environment. Since the surface oxide morphology was consistent within each alloy, a single sample from each alloy was selected for analysis. Sample L-R-1 was exposed to high-temperature water for 206 h, a relatively long exposure time. SEM imaging captured the surface oxide from a randomly chosen region within the constant strain area, as shown in Figure 6-19 (a). The oxide consists of randomly distributed large particles with an irregular, faceted appearance. While the oxide distribution is influenced by grain orientation, no significant differences were observed aside from the density of oxide particles. These particles are deposited on an internal nanoparticle oxide layer, visible in the high-magnification image (100Kx) in Image 4 of Figure 6-19.

Similarly, the surface oxide in sample N3 was characterized, as shown in Figure 6-19 (b). This sample was exposed to high-temperature water for 240 h. Like sample L-R-1, it exhibits randomly distributed oxide particles, whose distribution is also grain orientation dependent.

However, dissolution of oxide particles was observed in both SS 304LN and SS 304L-R samples but with different extents. Sample N3 exhibited the highest surface oxide particles dissolution, as shown from BSE images in Figure 6-20 (a) through (e) and the example obtained from random location across the surface showing the dissolution of oxide particles partially as shown in Figure 6-20 (f). A similar phenomenon was noted in the L-R samples, although to a lesser extent as seen in Figure 6-21 (a) through (d), suggesting that the environment may contribute to the instability of the outer oxide layer.

The inner surface oxide remained chemically stable, showing no signs of degradation. However, oxide rupture was observed in all samples from both alloys at locations coincided with dislocation channel propagating towards the grain boundaries, as shown in Figure 6-22 (a) through (h). Two distinct modes of inner layer oxide rupture were identified. In the first mode, when the dislocation channel exhibited a large step height, a complete rupture of the oxide layer occurred above the channel, as can be seen in Figure 6-22 (a) to (c).

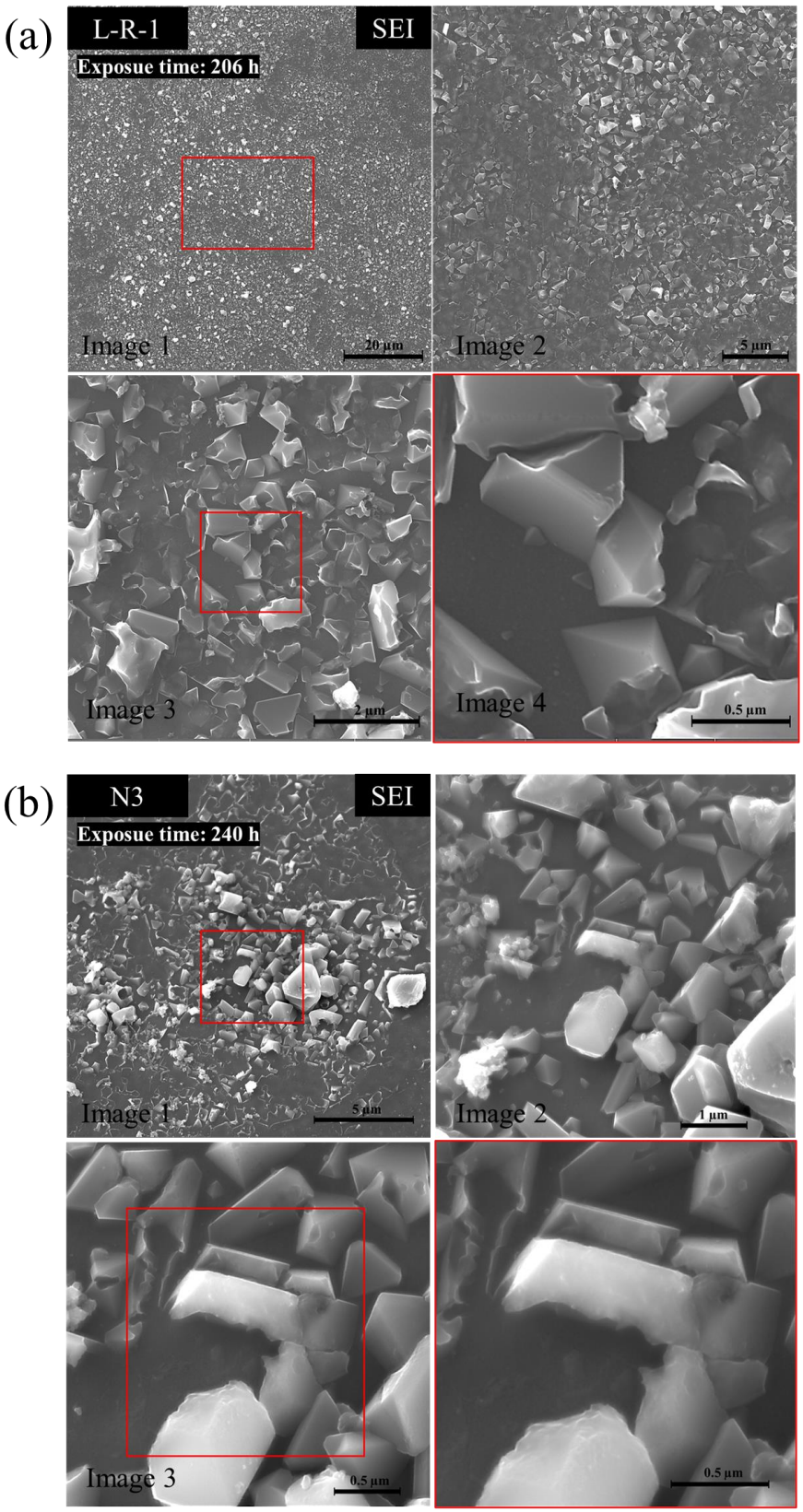


Figure 6-19 SEM images of surface oxides formed within the constant strain region of samples (a) N3 and (b) L-R-1. Oxide particles appear unevenly distributed across the surface, with variations in morphology and size.

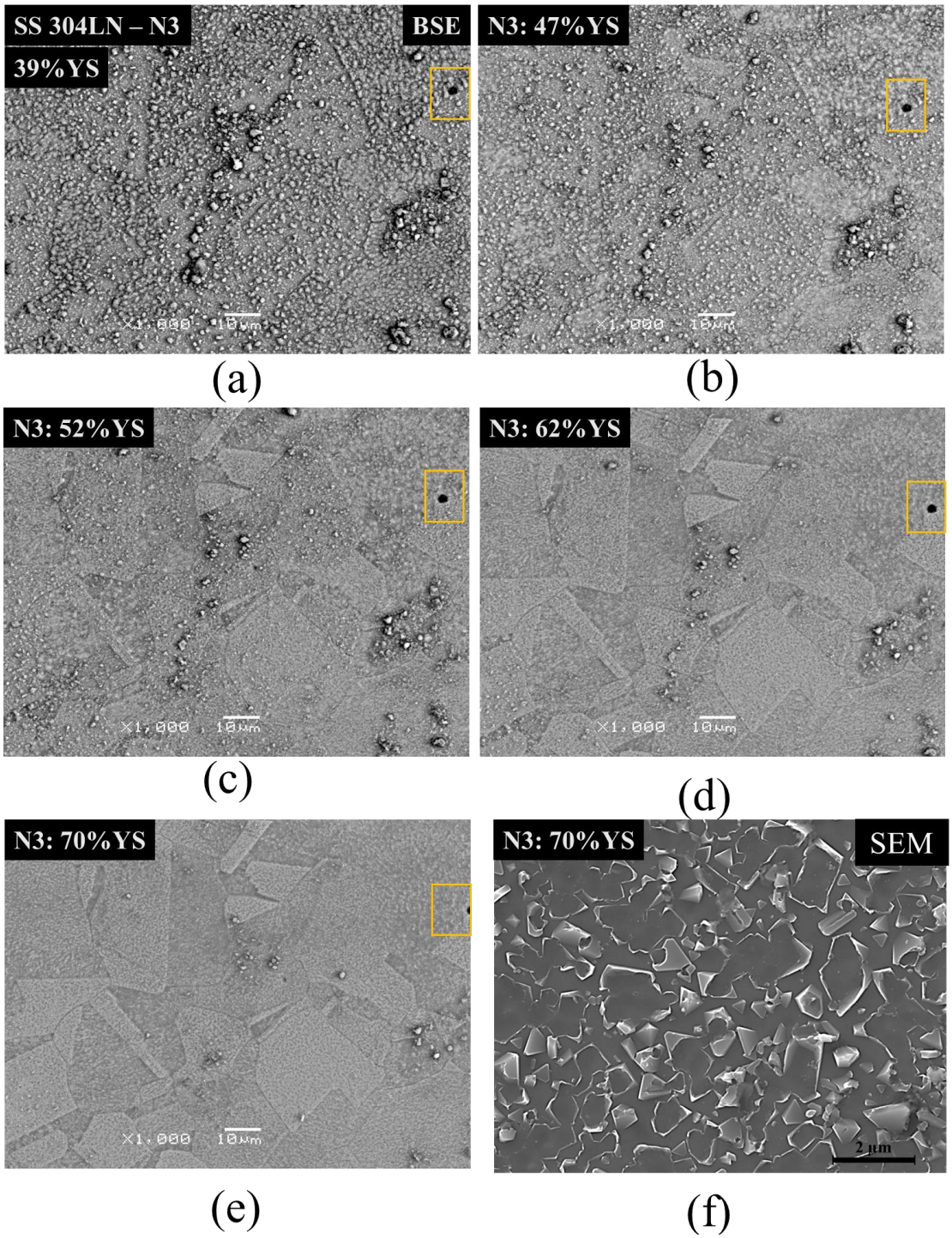


Figure 6-20 Dissolution of surface oxide particles with increasing applied load (and exposure time to the water solution), as observed in sample N3. (a) BSE image showing a high density of surface oxide particles after the initial applied load step. (b)–(e) BSE images illustrating the progressive decrease in surface oxide particles with each successive load step, highlighting significant degradation of the outer surface oxide particles. (f) SEM image from a randomly selected surface location showing a mix of partially dissolved and intact surface oxide particles. (Note: The orange box marks a tracking feature in each image, confirming that all images were captured from the same location but at different applied load steps).

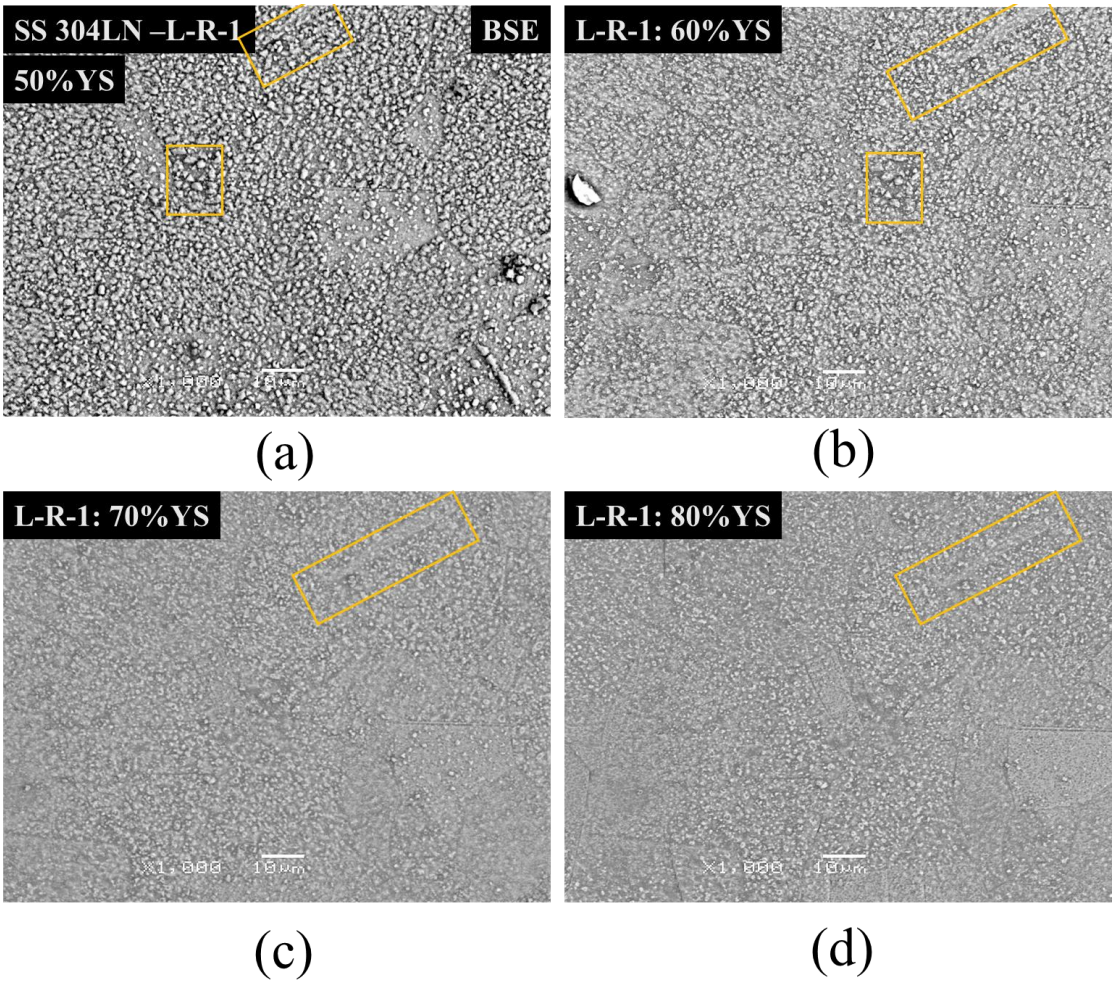


Figure 6-21 Dissolution of surface oxide particles with increasing applied load (and exposure time to the water solution), as observed in sample L-R-1. (a)-(d) BSE image showing progressive decrease in surface oxide particles with each successive load step, highlighting a less extent degradation of the outer surface oxide particles compared to sample N3.

Another example, from a different location on the surface but still representing the same rupture mode, was characterized by STEM-HAADF, DF, and EDS images as shown in Figure 6-22 (d) to (f) showing how dislocation channel disrupted the oxide layer and confirmed the oxygen-rich composition of the oxide. This complemented the SEM observations shown earlier. The oxide thickness on both sides of the dislocation channel appears uniform, indicating that the surface was originally at the same level. The second mode of oxide rupture was associated with dislocation channels exhibiting lower step heights that were insufficient to cause complete

rupture. Instead, these channels induced partial rupture of the oxide layer, resulting in a jagged appearance. This phenomenon was consistently observed in all samples from both alloys.

The inner layer of the surface oxide was analyzed using TEM, with HAADF, DF, and BF detectors employed to identify the oxide layer and assess its penetration into the surface as shown in Figure 6-23 (a) through (c) for sample N3 and (d) and (e) for sample L-R-1. Additionally, other samples were analyzed using SEM following FIB cross-sectioning, as seen in Figure 6-24 (a) and (b) for both alloys. The images revealed a grain-orientation-dependent variation in oxide thickness. STEM-EDS analyses of both samples showed a Cr-rich inner oxide that was depleted of Fe, with nickel segregating at the interface between the oxide layer and the metal surface. Early-stage grain boundary oxidation was also observed in Figure 6-23 (a), where the oxide tip extended a few tens of nanometers toward the GB without any crack initiation. Cracks were only observed within the oxide film itself. It remains unclear whether a dislocation channel contributed to the oxide fracture, as suggested previously in Figure 6-22 (d), because the oxide surfaces are not perfectly level (even slightly). Nevertheless, no solid evidence of the presence of a dislocation channel was found.

The average thickness of the inner oxide layer was obtained by measuring the oxide film at four locations within the uniform strain region. As shown in Figure 6-24, approximately 10 measurements were taken across the oxide film at each location, and the results are summarized in Table 6-6. The standard deviation is also provided, where lower values indicate a smoother interface between the oxide and the metal surface, while higher values suggest greater interface roughness and a higher degree of localized corrosion. The average inner oxide thicknesses in sample N3 were 277 nm and 217 nm, and in sample L-R-1, 274 nm and 306 nm, respectively. Although this dataset is too limited for definitive conclusions regarding the oxide film thickness,

these measurements contribute to understanding why the inner oxide film sometimes exhibits partial rupture and at other times complete rupture, an aspect that will be discussed further in the Discussion chapter. Table 6-6 lists the measured thicknesses of the inner oxide layer at various locations.

Table 6-6 Summary of inner oxide layer thickness taken from different locations.

| **Alloy** | **Average oxide thickness in Grain 1 (nm), (σ)** | **Average oxide thickness in Grain 2 (nm), (σ)** |
|---|---|---|
| SS 304LN | 322 (36) | 248 (40) |
| | 285 (66) | 224 (21) |
| | 221 (28) | 195 (54) |
| | 277 (36) | 202 (21) |
| Average | 277 | 217 |
| SS 304L-R | 254 (53) | 344 (62) |
| | 304 (37) | 320 (48) |
| | 289 (39) | 294 (79) |
| | 247 (33) | 265 (51) |
| Average | 274 | 306 |

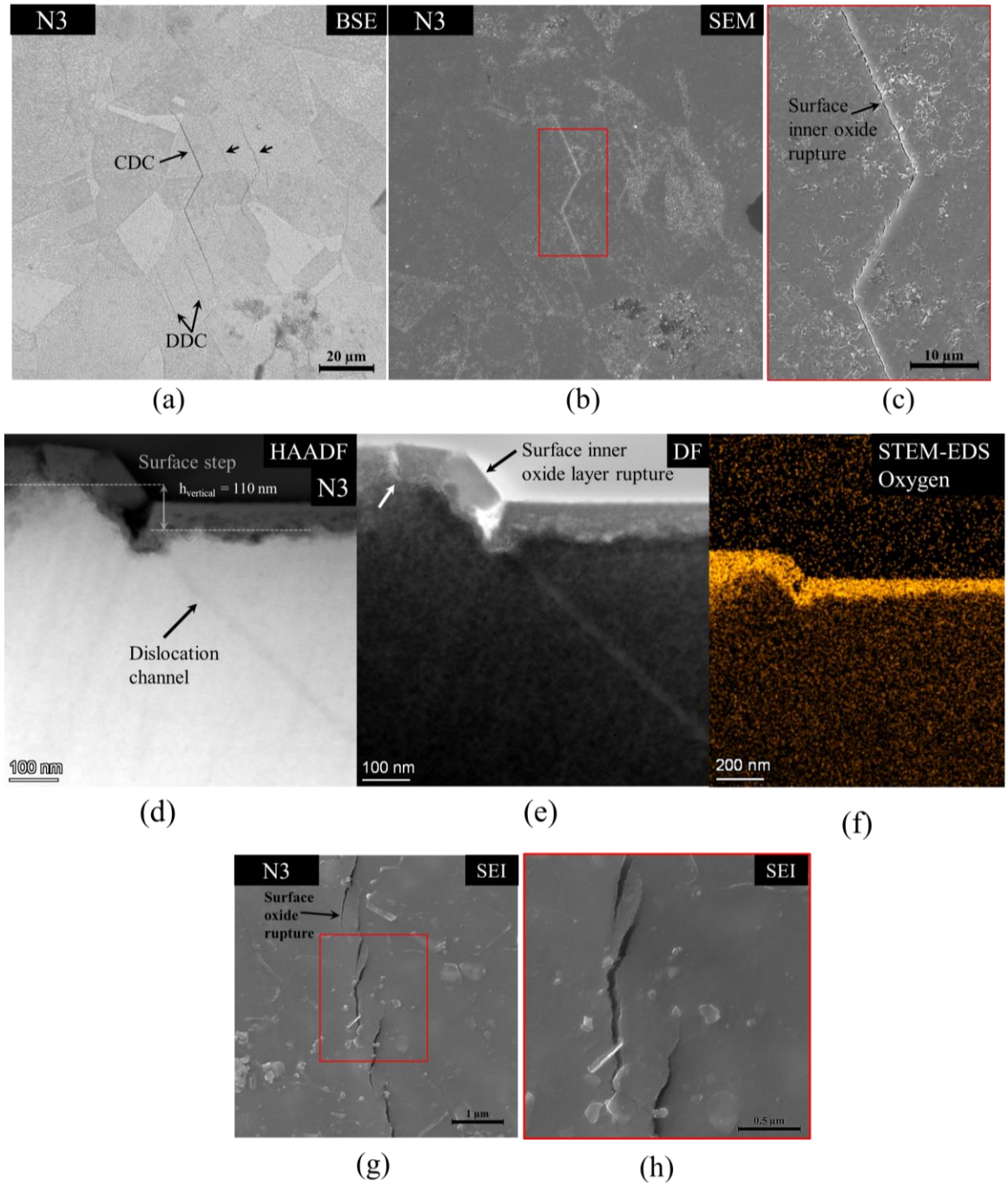


Figure 6-22 Examples of the two oxide rupture mechanisms observed in this study, based on images from sample N3. (a)–(c) BSE and SEI images showing continuous dislocation channels and a magnified view of one channel with oxide rupture occurring above it. (d)–(f) STEM-HAADF, DF, and EDS images from a different location illustrating a similar mechanism, where the step-up at the dislocation channel ruptures the inner surface oxide layer, leading to localized corrosion. (g) and (h) Another example of partial surface oxide rupture caused by a dislocation channel with a relatively lower step height compared to the first example.

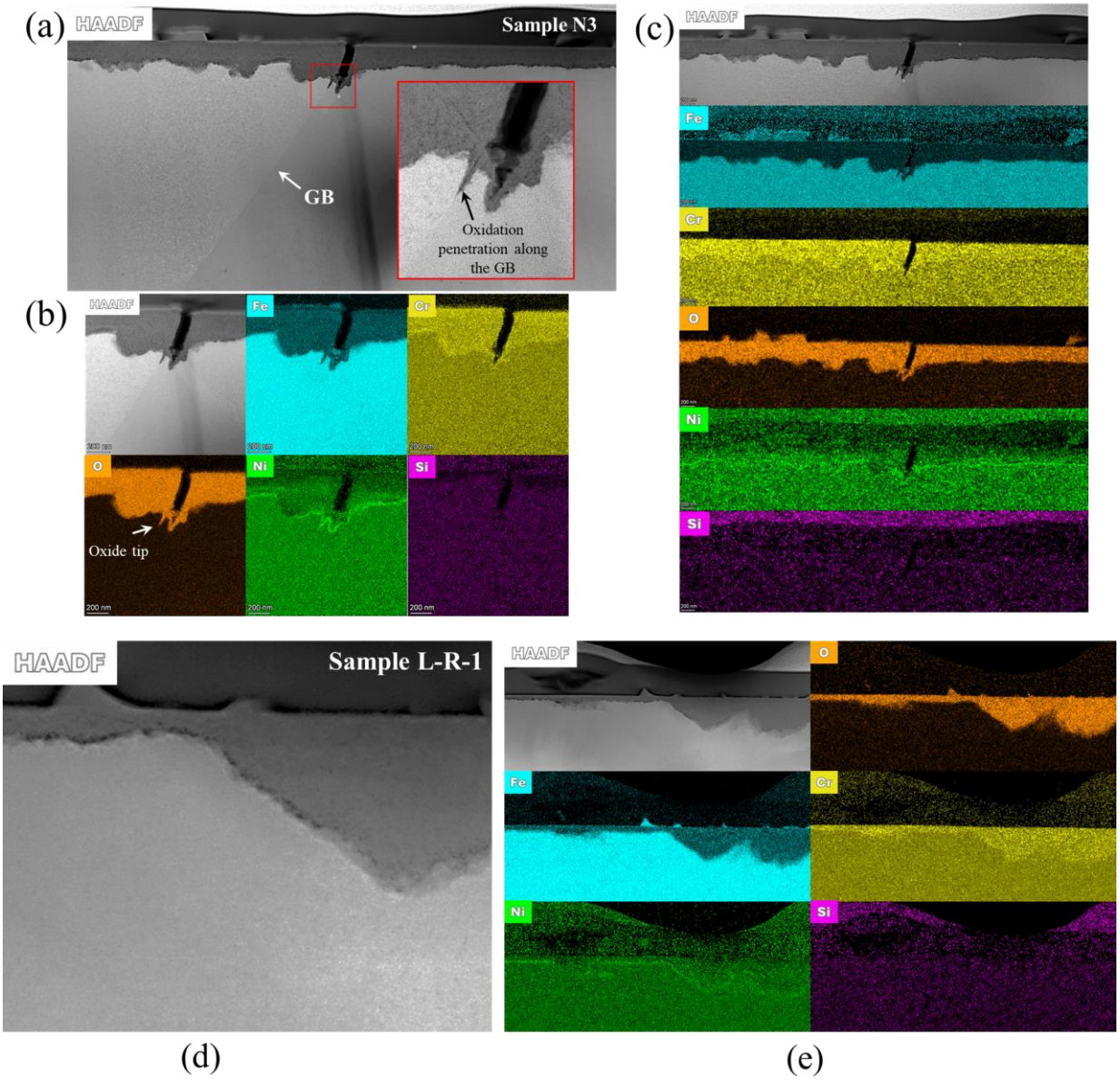


Figure 6-23 STEM-HAADF images and corresponding EDS elemental maps showing the surface oxide morphology and composition in (a–c) sample N3 and (d–e) sample L-R-1. Oxidation penetration along the grain boundary is evident in sample N3, while sample L-R-1 shows a more uniform oxide layer without localized penetration.

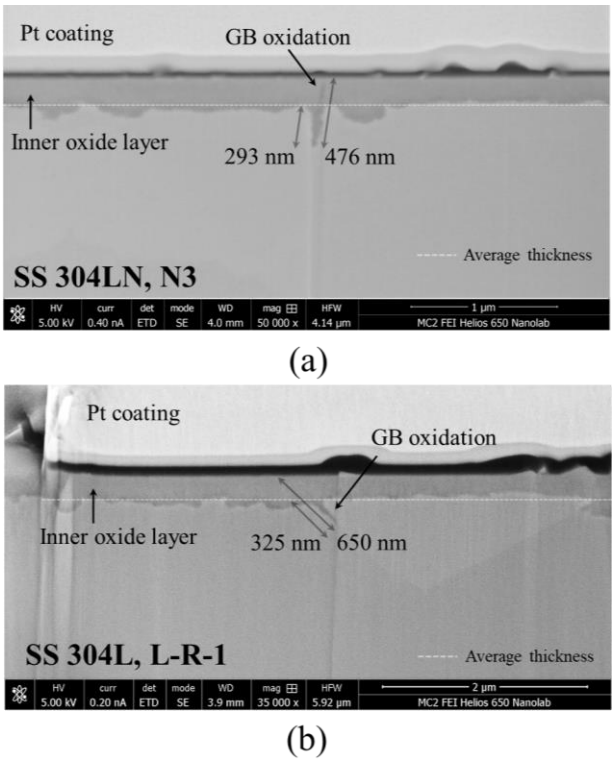


Figure 6-24 SEM cross-sectional images of FIB-milled surfaces showing the inner oxide layer thickness and grain boundary oxidation for (a) SS 304LN (sample N3) and (b) SS 304L (sample L-R-1). The measured oxide thicknesses near the grain boundary are indicated, showing localized oxide thickening in both samples. A Pt layer was deposited to protect the surface during FIB milling. The dashed line represents the average inner oxide thickness across the examined region.

### *6.2.5 Cracking morphology and crack tip analysis*

The surface morphology of the cracks in the samples was analyzed using SEM. Crack length and inclination angle relative to the applied loading axis were measured from the SEM images. Additionally, features contributing to crack initiation, such as DCs or TJs, were identified and documented.

The following subsections provide a detailed microscopy result of the cracking behavior of each sample. However, if a sample contained more than two cracks, only those with distinctive features are discussed, while the remaining cracks, which share similar microstructural characteristics, are documented in Appendix C to avoid redundancy.

After characterizing the surface cracks, selected cracks were examined using TEM to analyze their crack tips. Due to instrument availability constraints, TEM analysis was focused on samples N3 and L-R-1, which exhibited a high crack density. Additionally, these samples contained diverse crack morphologies and initiation features, making them well-suited for TEM investigation. Since cracks in other samples shared similar characteristics, prioritizing N3 and L-R-1 for FIB lift-outs and TEM analysis was an efficient approach to save time.

#### *6.2.5.1 Cracking morphology*

*Sample N3*

Sample N3 was the first sample tested in the series. After each loading step, SEM was used to detect crack initiation. Figure 6-25 (a) shows the distribution of cracks within the constant strain region, where tensile stresses are at their maximum. Cracks are distributed across the whole region except near the top edge. A total of 24 cracks were identified, primarily concentrated in the lower half of the region, with the highest density observed in the bottom half. It is important to note that each red block in the figure does not necessarily represent a single crack, as some regions may contain multiple cracks. The following figures show comprehensive information about the crack, including BSE images that illustrate the initial detection, followed by SEI images confirming the suspected region as a crack. Annotation definitions are also provided for clarity. Additionally, the microstructural history of the region prior to crack initiation is included to help in understanding the evolution of features leading up to cracking.

First example of cracking is crack N-3-1 that is shown in Figure 6-27, this example reveals the initiation of cracks without contribution of DCs. The cracks as seen in the figure initiated between TJ locations. The crack looks in early stage of initiation and can be distinguished from

an oxidized GB from the separate at of the GB as observed in the high-magnification image (Image 3, red rectangle) in Figure 6-27 (a).

The crack measures 14.8 µm in length and is nearly perpendicular (91°) to the applied loading plane. The evolution of this region was tracked from the first loading step when the sample was initially strained to 39%YS. Figure 6-27 (b) did not reveal distinct features such as oxidized GBs or DCs prior to the initiation stress at 70%YS.

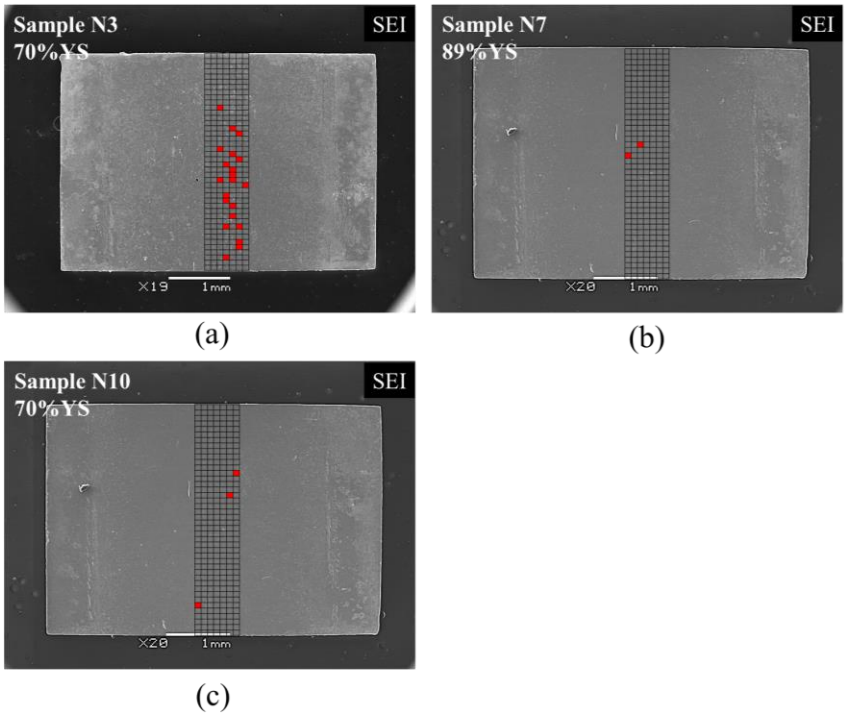


Figure 6-25 Cracking maps showing the distribution of cracks within the constant strain region for samples (a) N3 (70% YS), (b) N7 (89% YS), and (c) N10 (70% YS). Cracks are marked in red overlaid on the constant strain region.

Another example of cracks in sample N3 is crack N-3-3 that is shown in Figure 6-28. The crack initiated from the intersection of DC-GB as shown in Figure 6-28. in Image 1, a continuous DC extends from the upper grain into the lower grain, intersecting a GB at the TJ site, leading to crack initiation (Image 2). This crack measures 9.7 µm in length and has an inclination angle of 73° relative to the loading axis. The history of the region prior to cracking event shows no DCs were observed in earlier loading steps shown in Figure 6-28 (b).

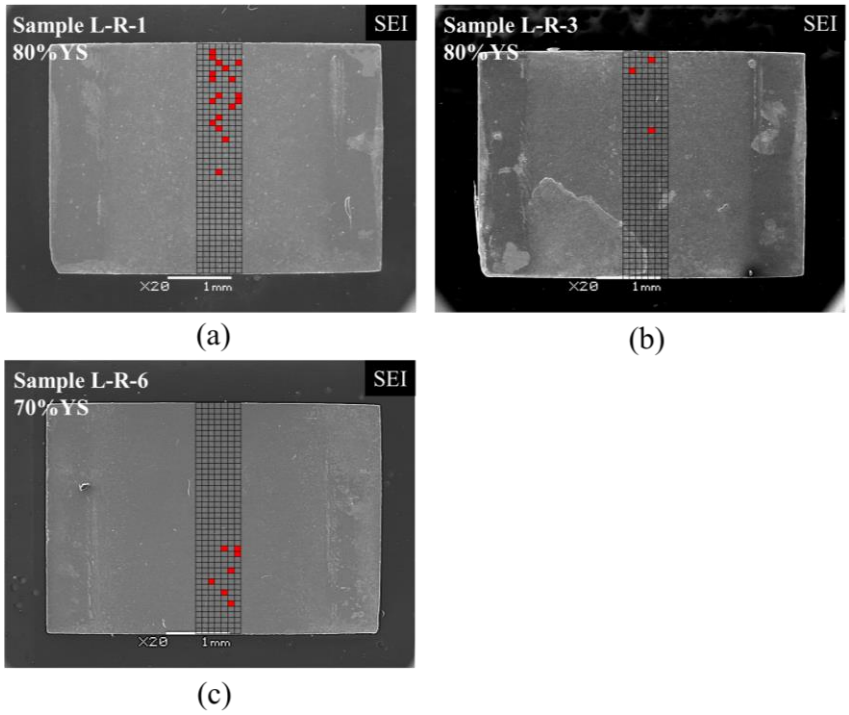


Figure 6-26 Cracking maps showing the distribution of cracks within the constant strain region for samples (a) L-R-1 (80% YS), (b) L-R-3 (80% YS), and (c) L-R-6 (70% YS). Cracks are marked in red overlaid on the constant strain region.

Figure 6-29 shows crack N-3-5, one of the largest cracks observed in this study. Image 1 in Figure 6-29 (a) shows a BSE image of a region with high DC activity. Three neighboring grains, labeled G1, G2, and G3, exhibit a mix of CDC and DDC. Grain G1 contains at least three CDCs (annotated with a double-headed arrow) that extend into G2, terminating at the GB between G2 and G3. One of these DCs (likely DC #4, as identified in the high-magnification BSE image 2) intersects the cracked TJ, making it a probable contributor to crack A initiation. Additionally, another DC intersects the lower TJ of G3 (Image 1) and may have also played a role in IG crack initiation. G2 likely experienced higher local stress than neighboring grains due to its near-perpendicular alignment with the applied load and the presence of two DC-TJ intersections within the same grain, which may explain the relatively wide crack. Other cracks, B and C, also initiated in this region. Crack B appears to have formed either due to the TJ or from the twin boundary intersection with the GB, as evidenced by the increased crack width at that region.

Crack A has a length of 14 µm and its upper leg is inclined by 93° while its lower leg by 80°, this crack has a width of 300 nm. Crack B has a length of 8.3 µm and an inclination angle of 101°, while crack C has a length of 2.1 µm and an inclination angle of 52°. Crack history analysis in Figure 6-29 (b) did not reveal notable GB oxidation or DCs in previous loading steps before the crack was observed at 70% YS.

Another crack is shown in Figure 6-30, crack N-3-12 in an early stage of initiation. High-magnification images (Images 3 and 4) show that this crack, although only 3 µm long, is relatively wide compared to longer cracks, indicating high localized stress at the DC-TJ intersection. The inclination angle of this crack is 111° and tracking history of the region in Figure 6-30 (b) did not reveal any oxidized GBs or DC formation.

The last crack of interest in sample N-3 is crack N-3-14 that is shown in Figure 6-31, the largest crack observed in this study, with the crack growing through four grains. Similar to crack N-3-5, this crack is relatively wide. A CDC between G1 and G2 (Figure 6-31 (a)) exists. Grain G7 contains at least five DDCs and two CDCs, one of which intersects the lower leg of the crack between G4 and G6. This crack has a total length of 40 µm and inclination angles of 124° for the top leg, 63° the middle leg, and 101° at the lower leg. The history of this crack in Figure 6-31 (b) did not reveal any early oxidized GBs or DC formation in earlier loading steps.

The remaining cracks, which exhibit similar characteristics to those discussed in this section, are provided in Appendix C to avoid redundancy.

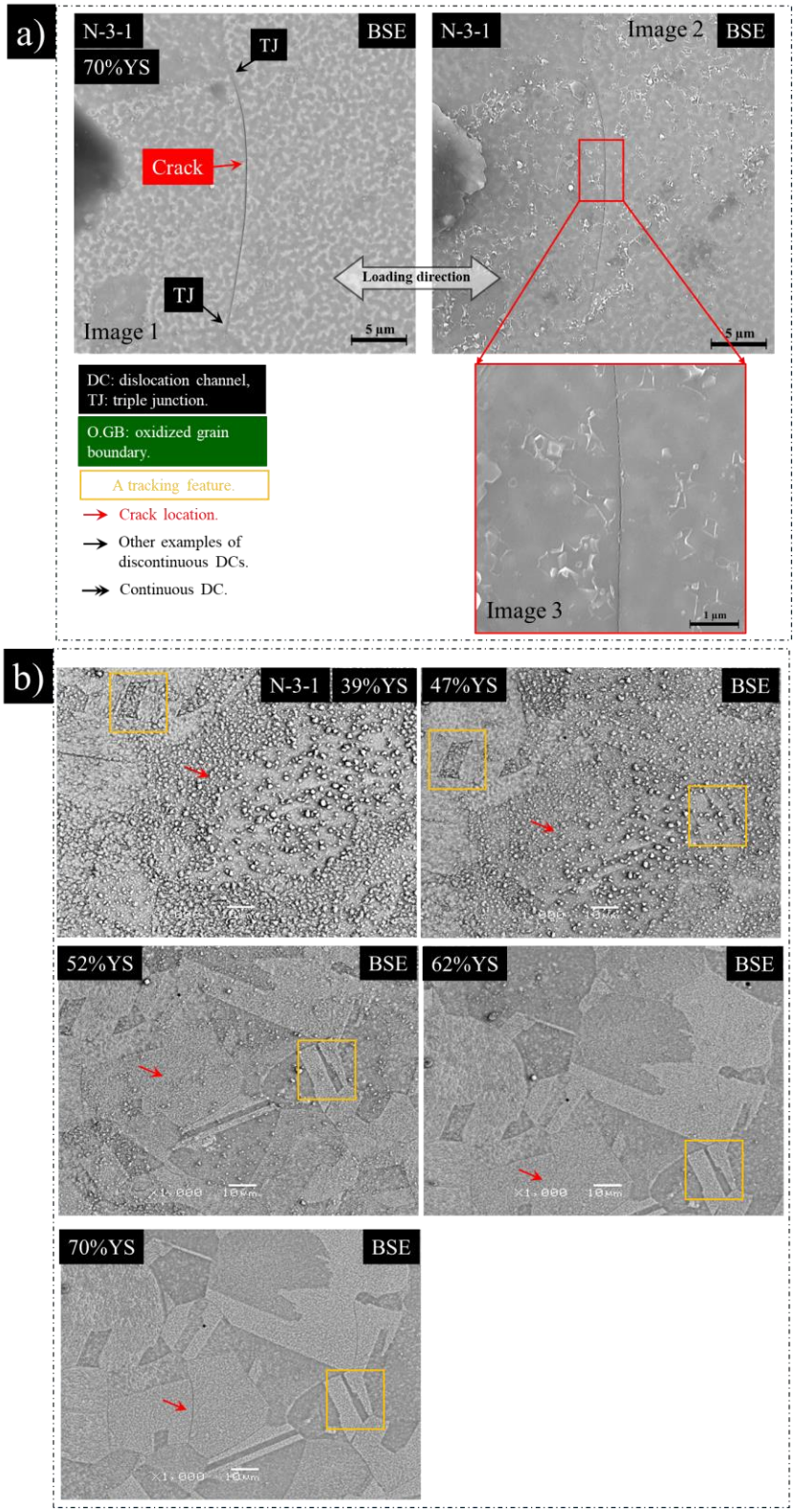


Figure 6-27 Crack N-3-1 in sample N3 after staining to 70%YS, (a) BSE and high magnification SEI images of the IG crack that initiated from TJ sites, and (b) BSE images of the history of the location over all loading steps showing the evolution of microstructural features.

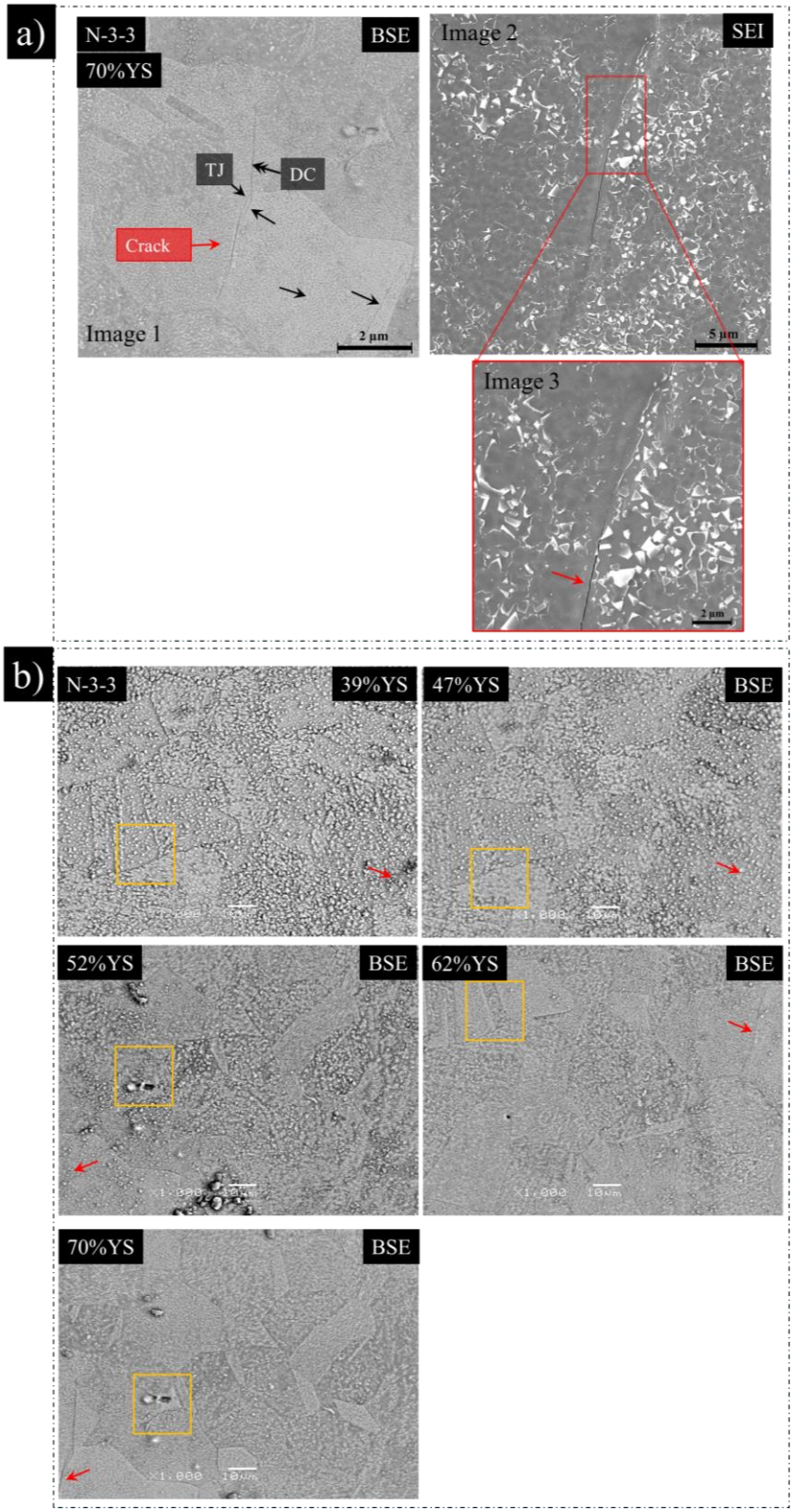


Figure 6-28 Crack N-3-3 in sample N3 after staining to 70%YS, (a) BSE and high magnification SEI images of the IG crack that initiated from TJ and DC, and (b) BSE images of the history of the location over all loading steps showing the evolution of microstructural features.

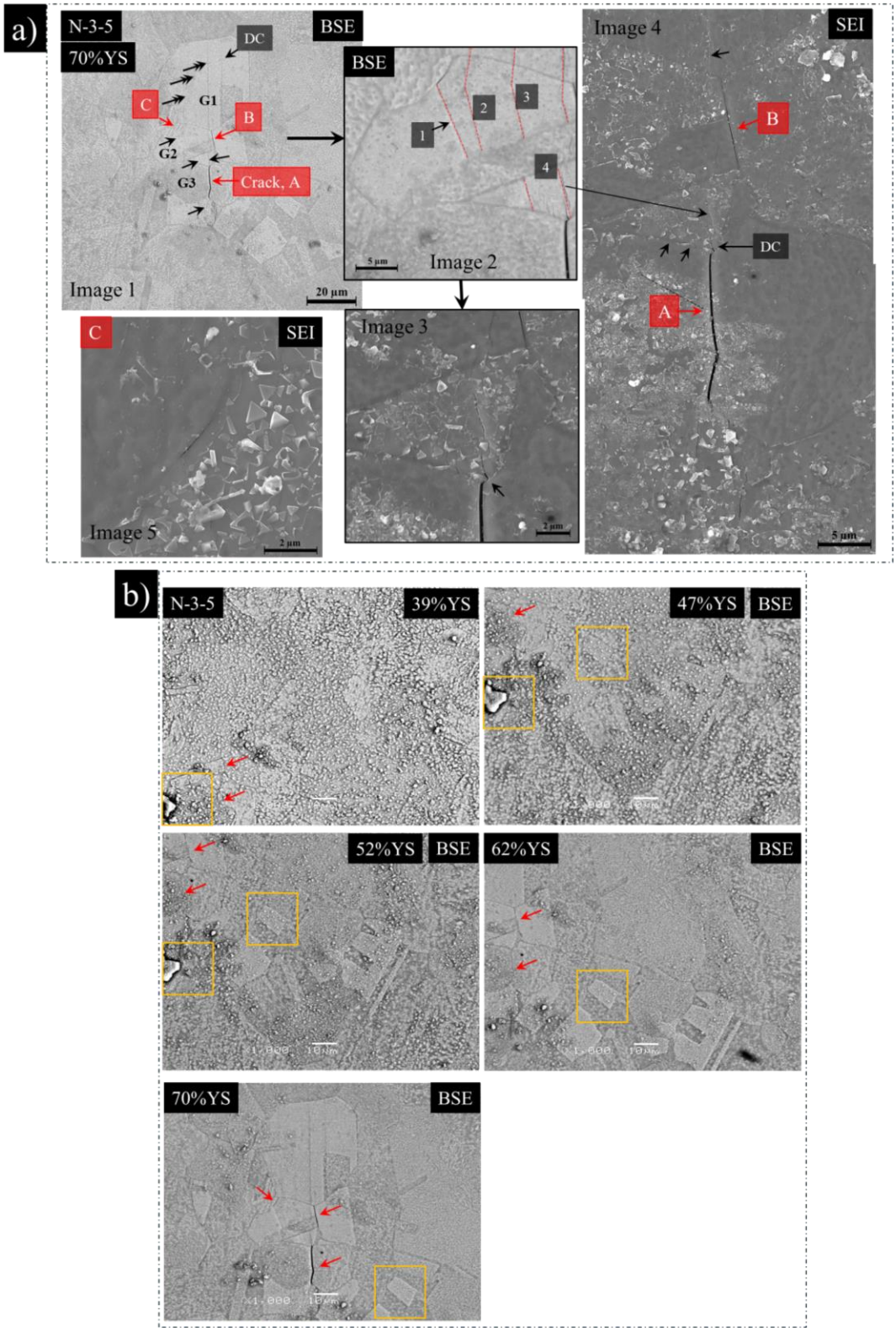


Figure 6-29 Crack N-3-5 in sample N3 after staining to 70%YS, (a) BSE and high magnification SEI images of the IG crack that initiated from DDC and TJ, and (b) BSE images of the history of the location over all loading steps showing the evolution of microstructural features.

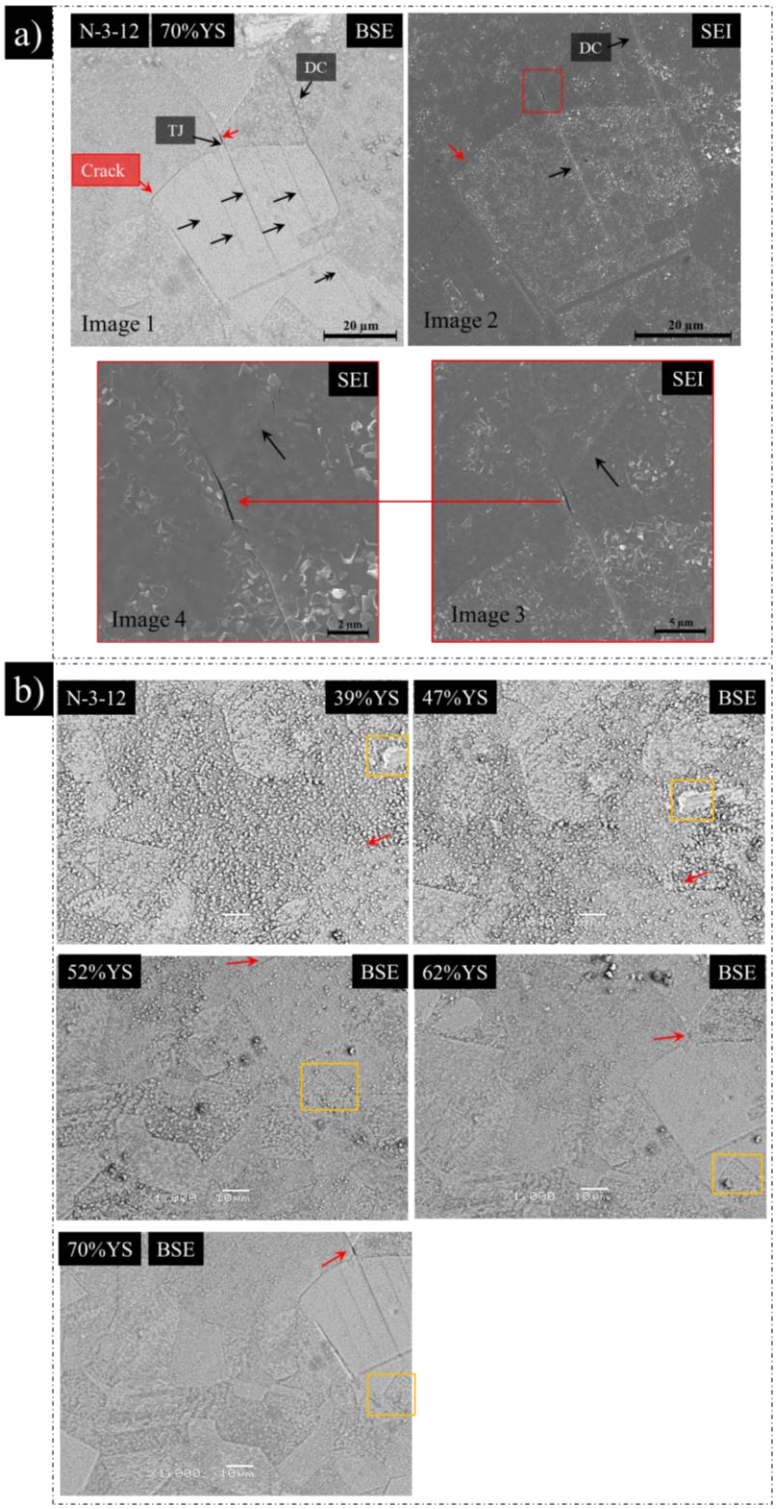


Figure 6-30 Crack N-3-12 in sample N3 after staining to 70%YS, (a) BSE and high magnification SEI images of the IG crack that initiated from CDC and TJ, and (b) BSE images of the history of the location over all loading steps showing the evolution of microstructural features.

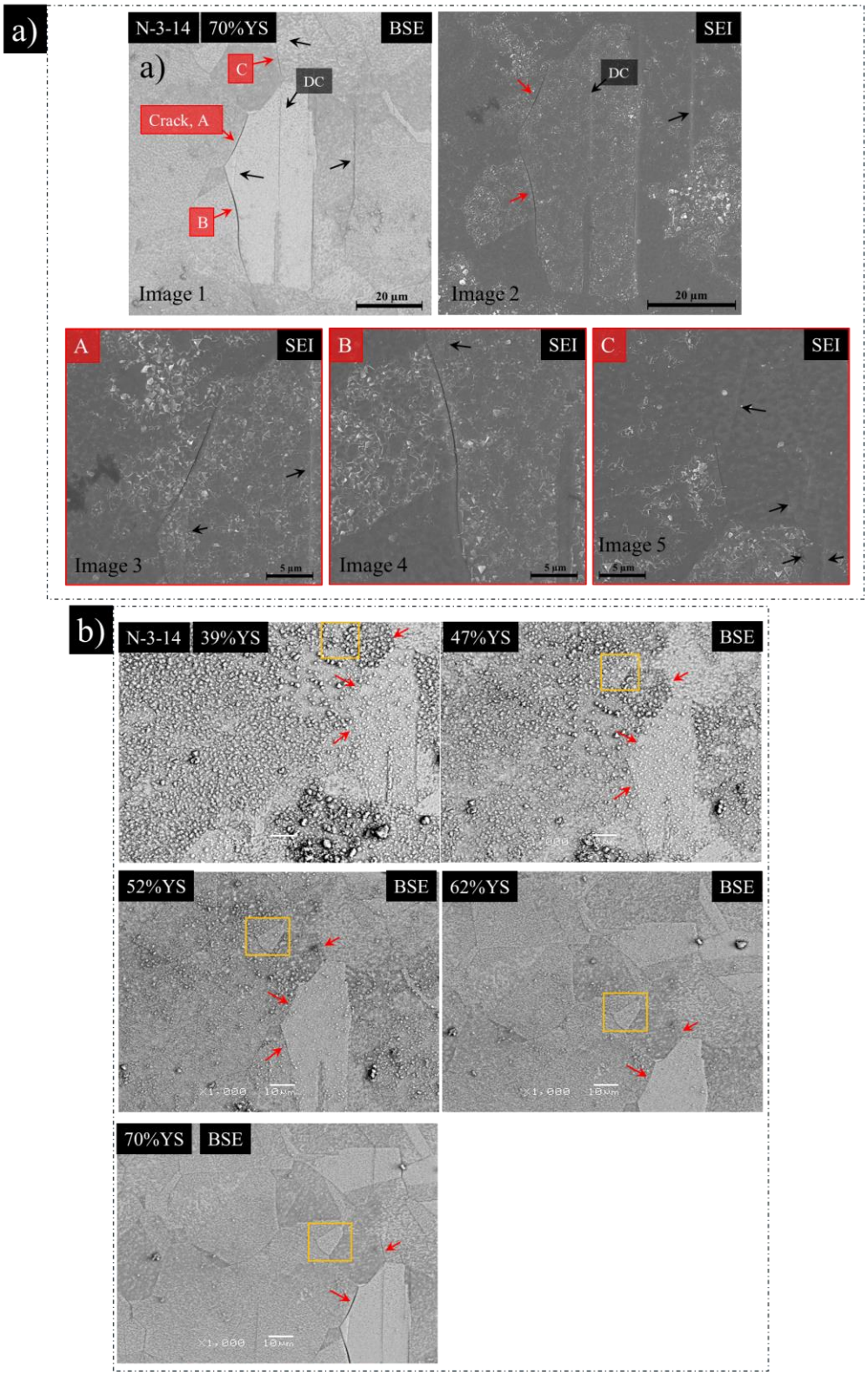


Figure 6-31 Crack N-3-14 in sample N3 after staining to 70%YS, (a) BSE and high magnification SEI images of the IG crack that initiated from TJ and DC, and (b) BSE images of the history of the location over all loading steps showing the evolution of microstructural features.

*Sample N7*

Figure 6-25 (b) shows the distribution of cracks within the constant strain region. A total of 2 detected cracks are distributed in the middle of the region. The first repeat (sample N7) showed no cracks initiation until the sample was strained to 89%YS where cracks observed. Moreover, the number of cracks in this sample was smaller than what observed in N3 at three cracks.

Figure 6-32 (a) shows crack N-7-1, which initiated at the TJ location. This crack opening is small to those observed in sample N3, measuring 24.1 µm in length with an inclination angle of 104°. No DCs were detected in the surrounding area, suggesting that the crack may have initiated from the TJ due to its orientation relative to the applied load. The loading history of this region, depicted in Figure 6-32 (b), reveals no features such as oxidized GBs or DCs preceding crack initiation. The remaining cracks are listed in Appendix C.

*Sample N10*

Figure 6-25 (c) the distribution of cracks across the constant strain region. A total of 3 detected cracks are distributed in the middle of the region and one crack at the bottom.
The second repeat (sample N10) showed cracking initiation after it had strained to 70%YS which was similar to the first sample.

Figure 6-33 shows crack N-10-1, the smallest detected crack in this study. This crack initiated at the TJ location. The crack length is 0.83 µm with an inclination angle of 111°. As can be seen in images 3 and 4 which were taken at 75,000x the crack was in an early initiation stage from the TJ. No DCs were detected in the surrounding area, suggesting that the crack may have initiated from the TJ due to its orientation relative to the applied load. The loading history of this region, depicted in Figure 6-33 (b), reveals no notable features preceding crack initiation.

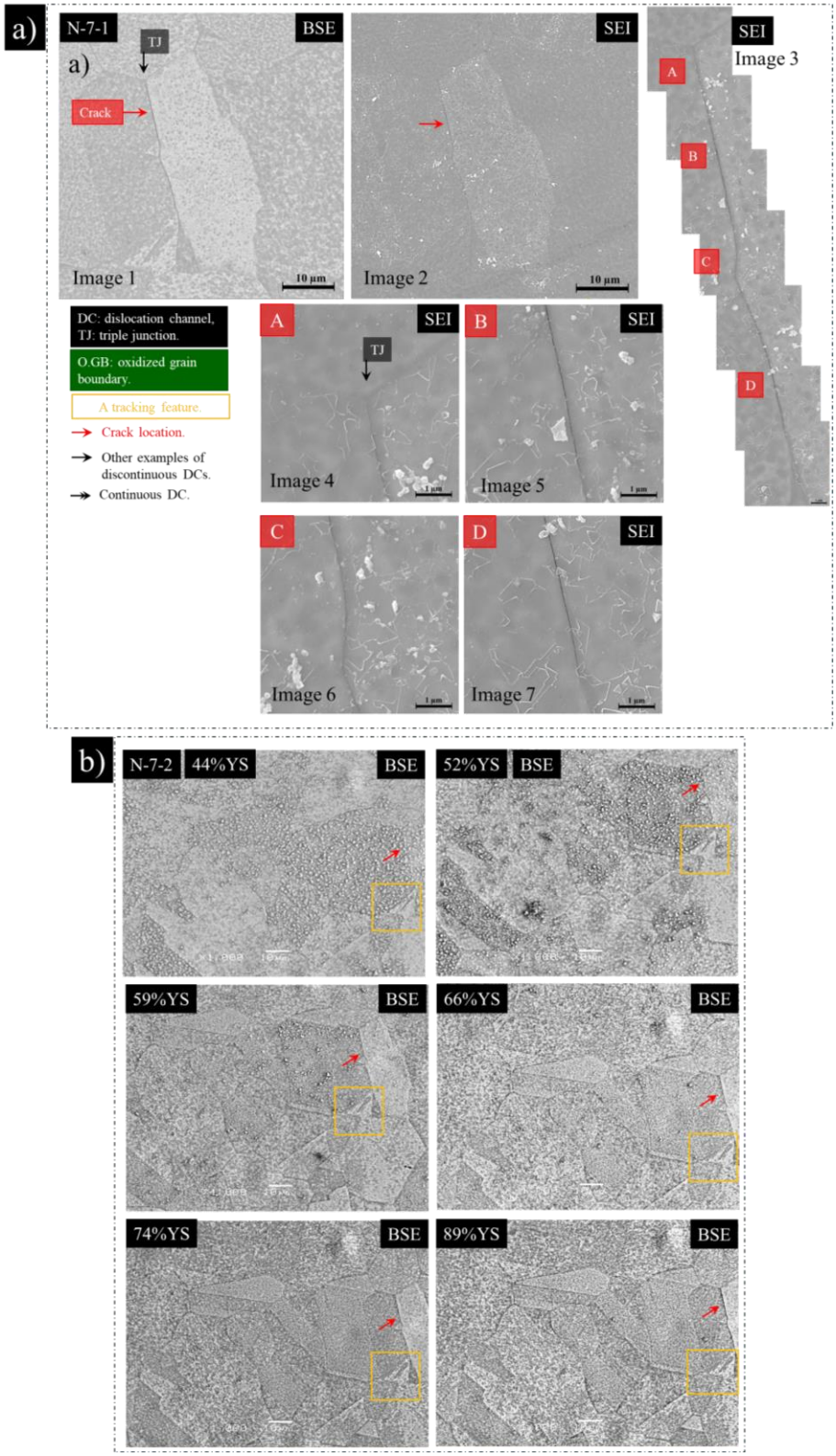


Figure 6-32 Crack N-7-1 in sample N7 after staining to 89%YS, (a) BSE and high magnification SEI images of the IG crack that initiated from a TJ, and (b) BSE images of the history of the location over all loading steps showing the evolution of microstructural features.

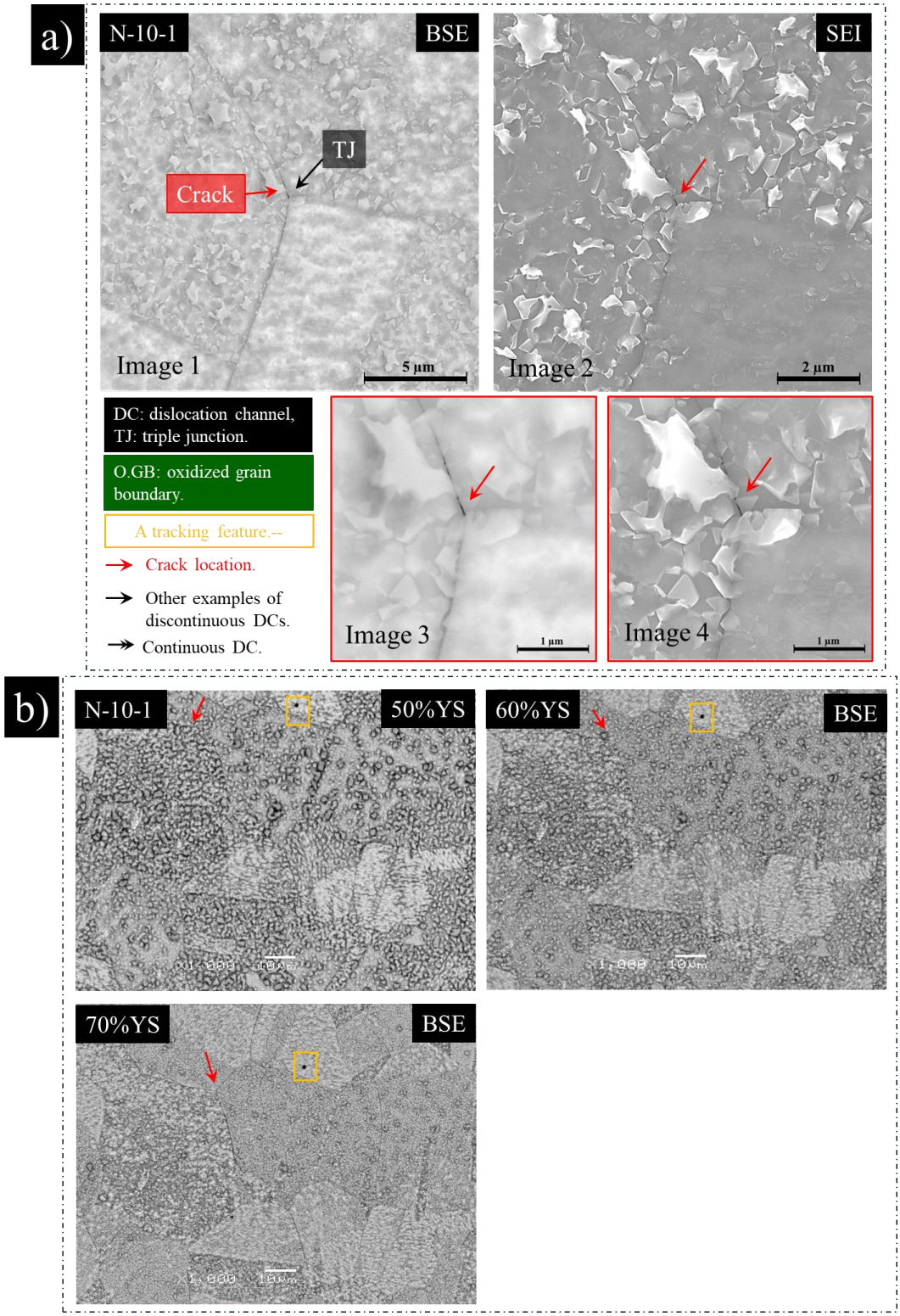


Figure 6-33 Crack N-10-1 in sample N10 after staining to 70%YS, (a) BSE and high magnification SEI images of the IG crack that initiated from a TJ, and (b) BSE images of the history of the location over all loading steps showing the evolution of microstructural features.

*Sample L-R-1*

Figure 6-26 (a) shows the distribution of cracks across the constant strain region of sample L-R-1. A total of 18 detected cracks are distributed at the top half of the region.

A high crack density observed in L-R-1 was similar to what was observed in N3. Samples L-R-1 and N3 showed longest crack among their counterparts.

Six examples of the cracks in sample L-R-1 sample are included in this section while the remaining are included in Appendix C. Figure 6-34 (a) shows crack L-R-1-3, in this crack a DDC transmitted from one grain to another a terminated at the GB of the second grain cause a crack initiation. The CDC terminated at the TJ as shown in Image 4 and it is believed that it is caused the crack initiation. This crack has a total length of 10.2 µm, and an inclination angle of 145$^{o}$ of the top portion and 88$^{o}$ for the bottom one. Figure 6-34 (b) shows the history of the region over all loading steps showing where no specific features preceded the crack initiation was observed.

Figure 6-35 (a) shows crack L-R-1-5, this crack initiated from the intersection of a DDC with the GB from the top and another DDC intersection with the TJ from the bottom. The role of DDC is obvious as the crack is clearly open regardless the fact that it is still a small crack of a length of 9.2 µm. The inclination angle of the GB with the respect of the applied load is 112$^{o}$. The history of the region over the loading steps is shown in Figure 6-35 (b) showing no specific features preceded the crack initiation.

Figure 6-36 (a) shows crack L-R-1-13 that is the longest crack in sample L-R-1. Crack A initiated from the intersection of a CDC with the TJ on the top of the GB, this crack has a length of 21.5 µm with inclination angles of 112$^{o}$ for the top leg, 65$^{o}$ for the leg in between the TJ points, and 115$^{o}$ with the bottom leg as seen on Image 4. Crack B seems to be initiated from the

TJ point; the crack length measures 27.7 µm with inclination angles of 89° from its top portion and 120° on the bottom portion of the cracked GB. Figure 6-36 (b) reveals no signs of specific features when the loading history of the region is considered.

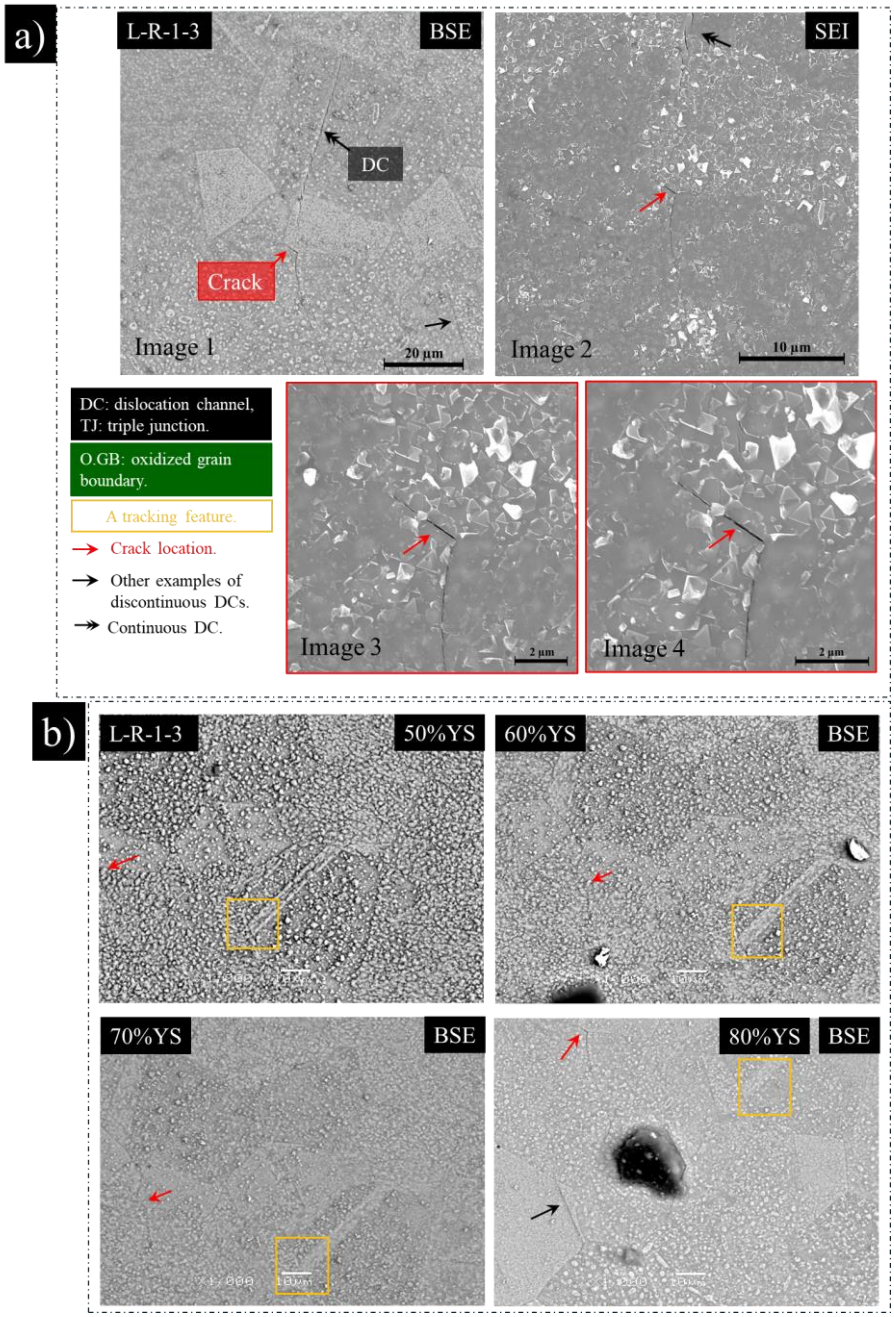


Figure 6-34 Crack L-R-1-3 in sample L-R-1 after staining to 80%YS, (a) BSE and high magnification SEI images of the IG crack that initiated at the TJ, and (b) BSE images of the history of the location over all loading steps showing the evolution of microstructural features.

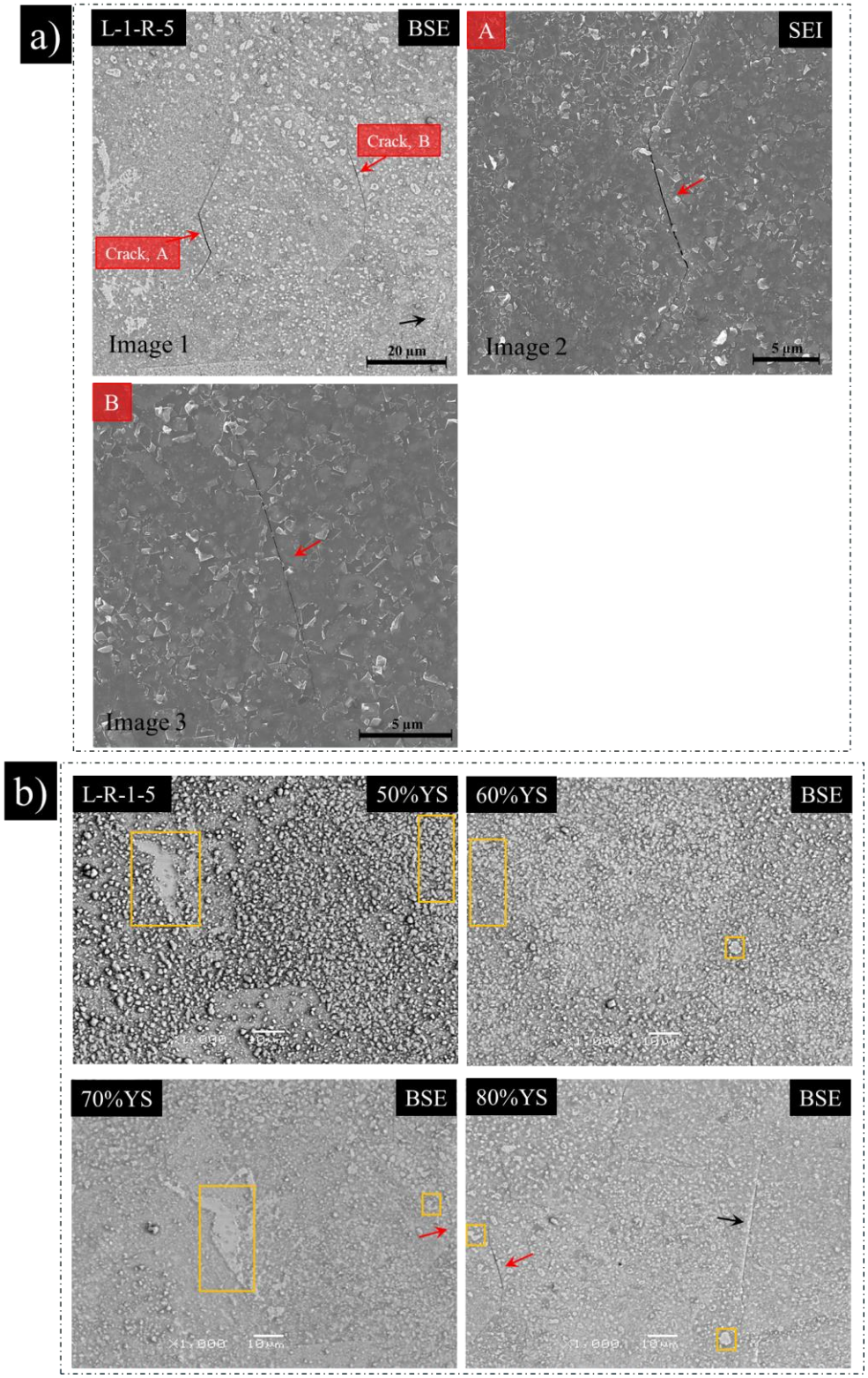


Figure 6-35 Crack L-R-1-5 in sample L-R-1 after staining to 80%YS, (a) BSE and high magnification SEI images of the IG crack that initiated at the DC-GB intersection, and (b) BSE images of the history of the location over all loading steps showing the evolution of microstructural features.

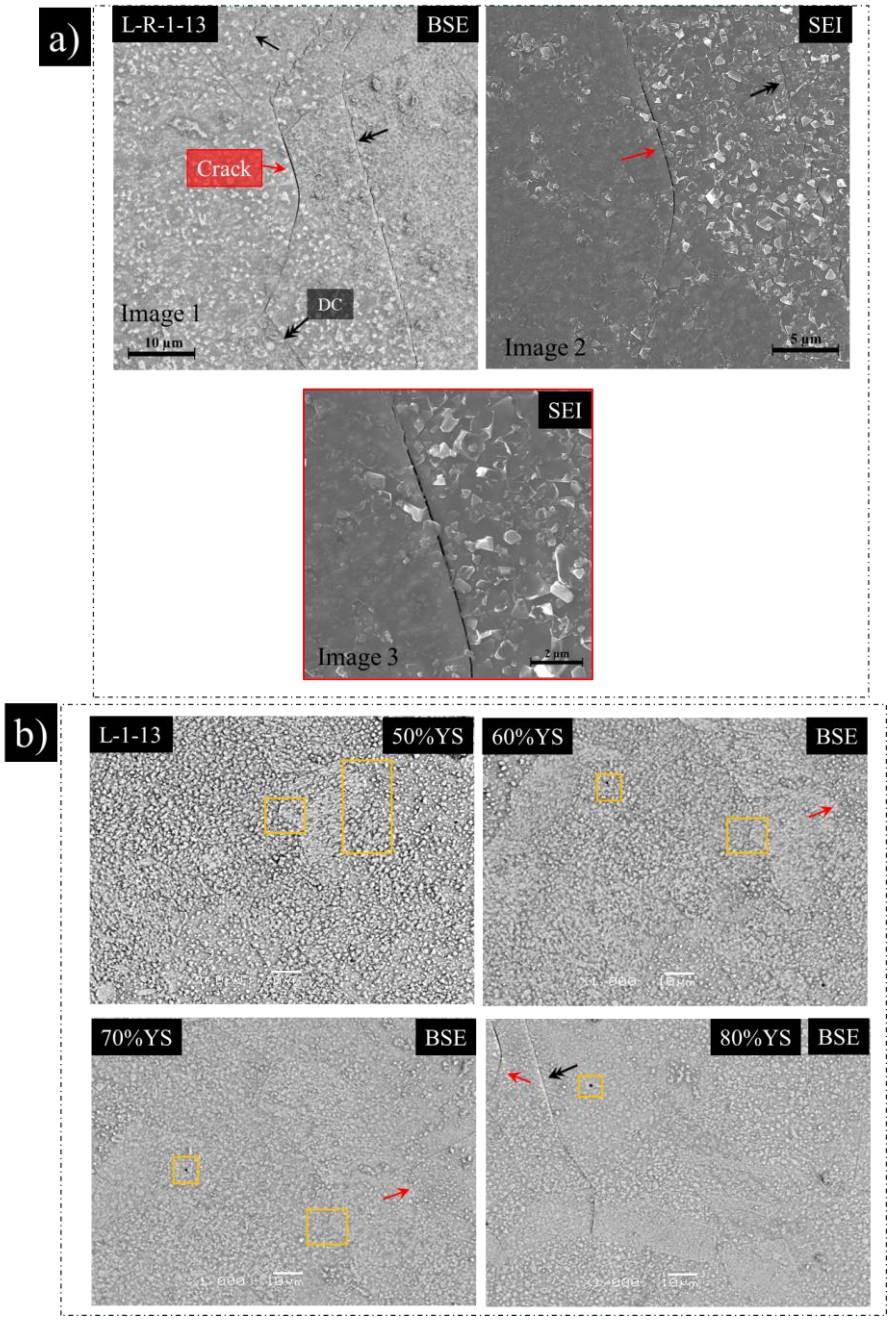


Figure 6-36 Crack L-R-1-13 in sample L-R-1 after staining to 80%YS, (a) BSE and high magnification SEI images of the IG crack that initiated from a GB-DC intersection, and (b) BSE images of the history of the location over all loading steps showing the evolution of microstructural features.

*Sample L-R-3*

Three cracks were identified in sample L-R-3 as shown in Figure 6-26 (b). Figure 6-37 (a), which initiated from a TJ point, with no other features such as DC observed near the cracked

GB. Crack L-R-3-2, also initiated from a TJ point, is shown in Figure 6-38. High-magnification Images 3 and 4 confirm GB separation. This crack has a total length of 14.8 μm, with inclination angles of 113° for the main crack between the TJs and 55° for the bottom leg. The loading history of the region, as shown Figure 6-37 (b), does not indicate any distinct features preceding crack initiation.

Crack L-R-3-3, which initiated at the GB-DC intersection, is shown in Figure 6-38. High-magnification Images 3 and 4 confirm GB separation. This crack has a total length of 10 μm, with inclination angle of 70°. The loading history of the region, as shown Figure 6-38 (b), does not indicate any distinct features preceding crack initiation.

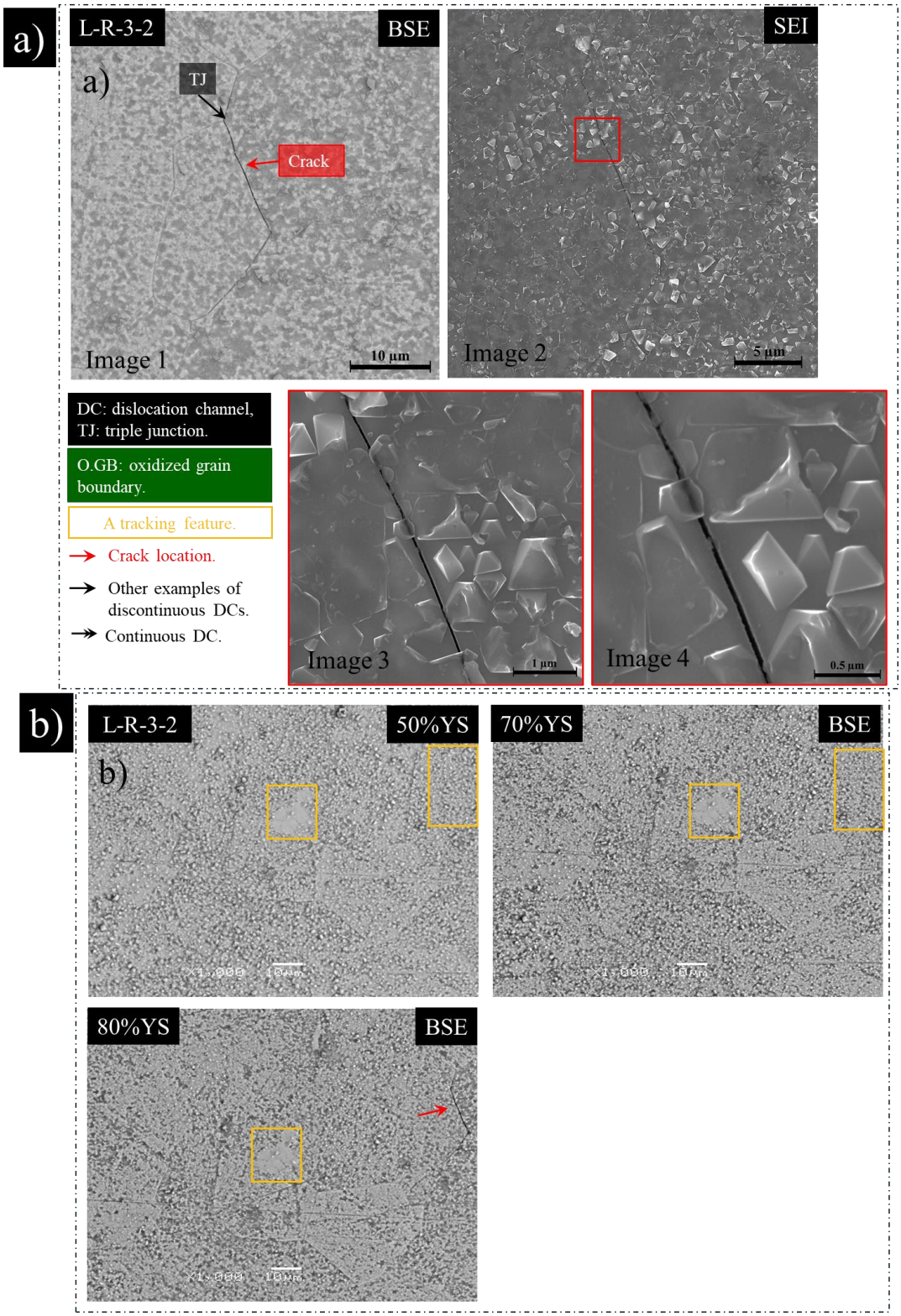


Figure 6-37 Crack L-R-3-2 in sample L-R-3 after staining to 80%YS, (a) BSE and high magnification SEI images of the IG crack that initiated at the TJ, and (b) BSE images of the history of the location over all loading steps showing the evolution of microstructural features.

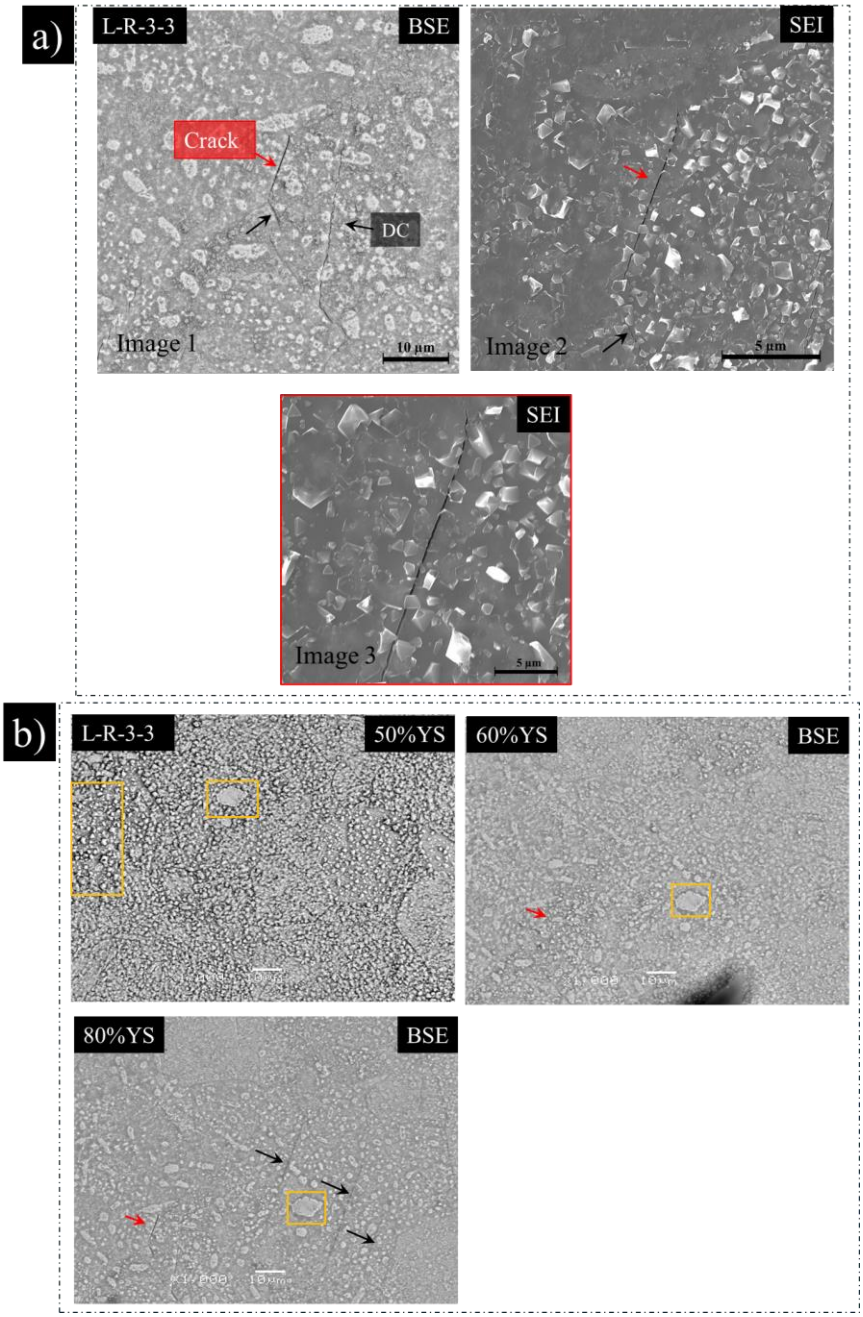


Figure 6-38 Crack L-R-3-3 in sample L-R-3 after staining to 80%YS, (a) BSE and high magnification SEI images ofn the IG crack that is initiated at the GB-DC intersection, and (b) BSE images of the history of the location over all loading steps showing the evolution of microstructural features.

*Sample L-R-6*

Seven cracks were identified in sample L-R-6 as shown in Figure 6-26 (c). Crack L-6-4 is shown in Figure 6-39 (a). It is believed that both that both CDC and TJ played roles in its

initiation. The CDC terminates near the bottom portion of the GB, just a few micrometers from the bottom TJ. Notably, the IG crack does not extend to that TJ, suggesting the influence of the CDC in this region. This crack has a total length of 10.3 µm, with inclination angles of 92º at the top and 117º at the bottom. The loading history of the region, shown in Figure 6-39 (b), does not reveal any significant features preceding crack initiation.

Crack L-R-6-6, also found in sample L-R-6, serves as an example of a grain boundary perfectly perpendicular to the loading axis, with an inclination angle of precisely 90º as shown in Figure 6-40 (a). This crack is relatively short, measuring 6.6 µm and initiates exclusively from TJ points, with no evidence DC contribution. Both ends of the crack at TJ points exhibit clear separation, confirming the role of TJs in its initiation. The previous loading history of the region, as shown in Figure 6-40 (b), does not indicate any distinct precursory features.

A complete list of all other cracks from all samples can be found in Appendix B-2 for further details.

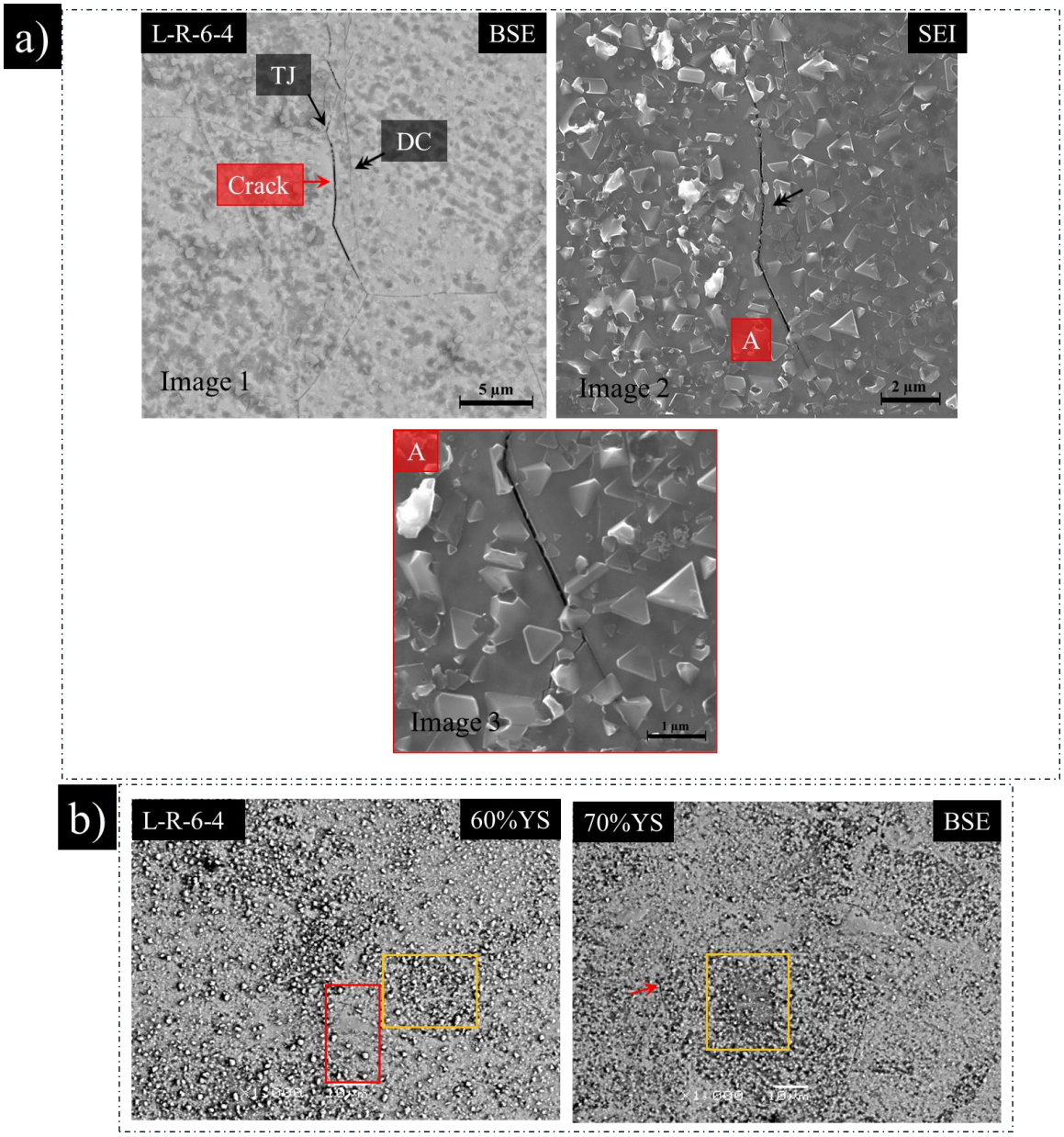


Figure 6-39 Crack L-R-6-4 in sample L-R-6 after staining to 70%YS, (a) BSE and high magnification SEI images of the IG crack that initiated at the GB-DC intersection, and (b) BSE images of the history of the location over all loading steps showing the evolution of microstructural features.

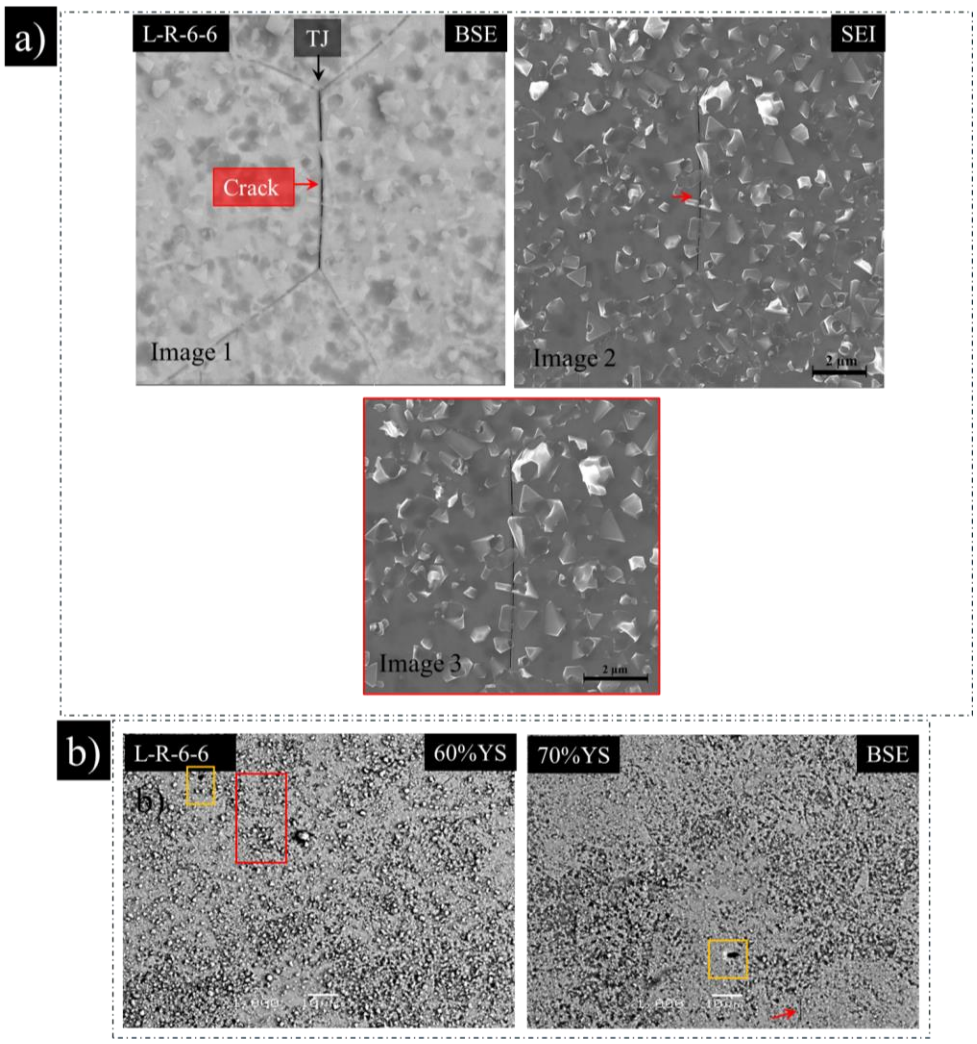


Figure 6-40 Crack L-R-6-6 in sample L-R-6 after staining to 70%YS, (a) BSE and high magnification SEI images of the IG crack that initiated at the TJ, and (b) BSE images of the history of the location over all loading steps showing the evolution of microstructural features

### *6.2.5.2 Crack tip analysis*

Several cracks from samples N-3 and L-R-1 were selected for TEM analysis. The selection criteria were primarily based on crack length, with a preference for shorter cracks to ensure the crack tip was captured. Additionally, cracks initiated by features such as DC were prioritized, and those with an inclination angle close to perpendicular were favored. The criteria for selecting cracks for TEM analysis included the following: cracks with moderately opened mouths were chosen, as widely opened cracks (such as in Crack N-3-5-A) are likely to have deep penetration

beyond the typical FIB lift-out depth, potentially missing the crack tip. Conversely, narrowly opened cracks may indicate limited penetration (such as in Crack N-3-1), possibly only a few nanometers along the GB, or that the GB oxide has not yet been fractured. In addition, cracks associated with DCs were prioritized, as DCs are considered key contributors to crack initiation in this study.

*Alloy 304LN*

In sample N3, three cracks were selected for TEM analysis. Crack N-3-1 (In appendix C), which has a moderately opened mouth and initiated from a TJ, was selected for TEM analysis. This crack is 4.8 µm in length and is inclined at an angle of 135º with the respect of loading axis, the second crack, N-3-5-C, initiated from the intersection of the GB with DC#1 (as shown in Image 2 of Figure 6-29 (a)), and was also selected for analysis. The crack length and inclination angle are 8.5 µm and 111º, respectively.

Figure 6-41 shows TEM analysis on crack N-3-1. Panel (a) shows the HAADF, DF, and BF and HAADF images at high magnifications, (b) a digitally magnified HAADF image from (a), (c) a low magnification image of elemental maps, while (d) and (e) show high magnification images of regions A-1 and A-1-1, respectively, as annotated in (a). Images reveal typical oxidation behavior along both the surface and the crack path, where the oxide layer is enriched in Cr and depleted in Ni and Fe. A distinct Ni-rich interface was observed between the oxide and the underlying metal, extending along the crack flanks. The oxidation depth, as inferred from the oxygen distribution, reaches approximately 1.8 µm from the oxide surface. Additionally, co-segregation of Ni and Si is detected in the region just ahead of the oxide tip.

Identifying the crack tip was challenging due to the oxide fully occupying the grain boundary, preventing clear opening of the crack. Figure 6-41 (b) digitally magnified and cropped

HAADF image highlighting the presence of pores, interpreted as localized damage, within the crack oxide. The crack tip was inferred to be the final dark region at the lower end of the oxide, which likely corresponds to a vacuum or a low-density zone. Given that the oxide is inherently less dense than the surrounding metal, it appears darker in HAADF imaging. Therefore, the darkest regions along the grey oxide path are interpreted as the least dense, possibly voids, and the terminal dark region is reasonably assumed to represent the crack tip.

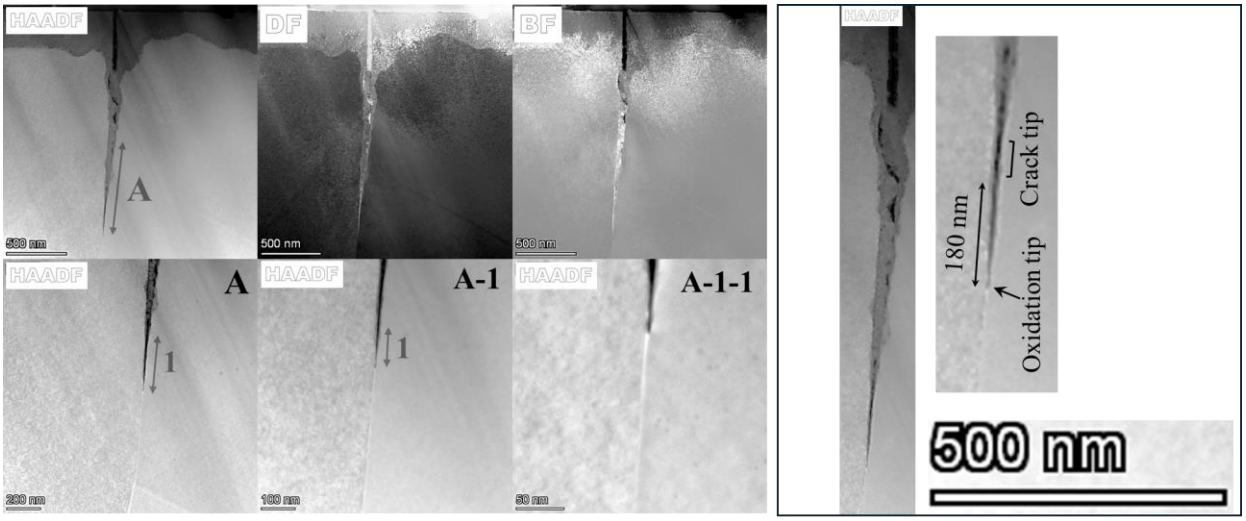


(a) (b)

(c)

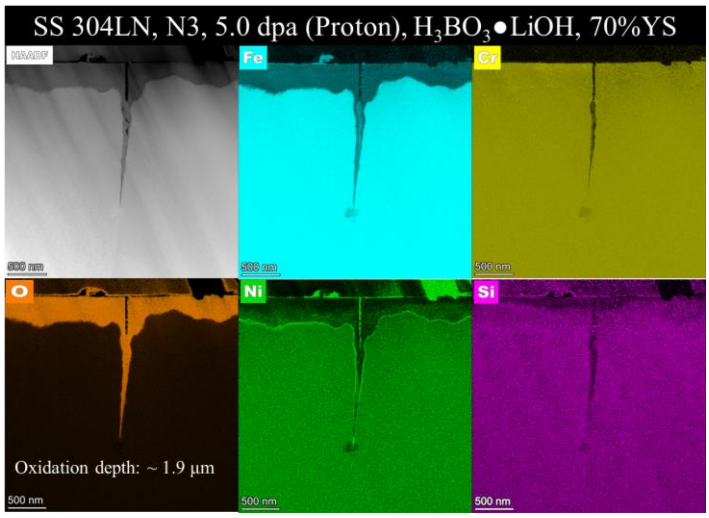

(d)

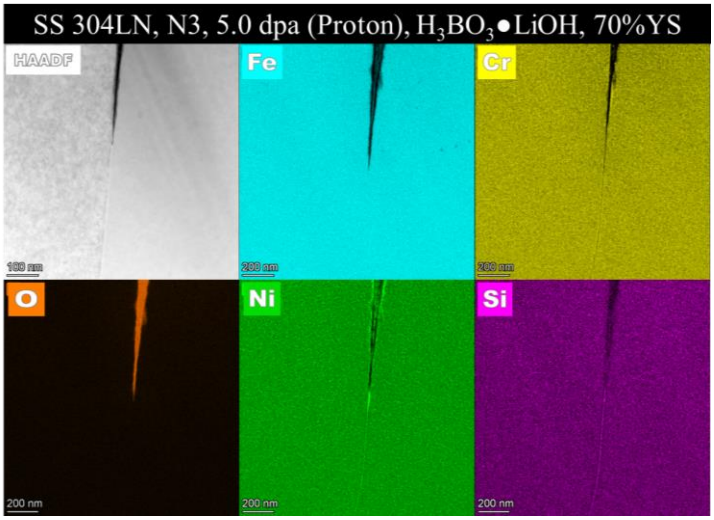
SS 304LN, N3, 5.0 dpa (Proton), $H_3BO_3$●LiOH, 70%YS
HAADF
Fe
Cr
O
Ni
Si
200 nm

(e)

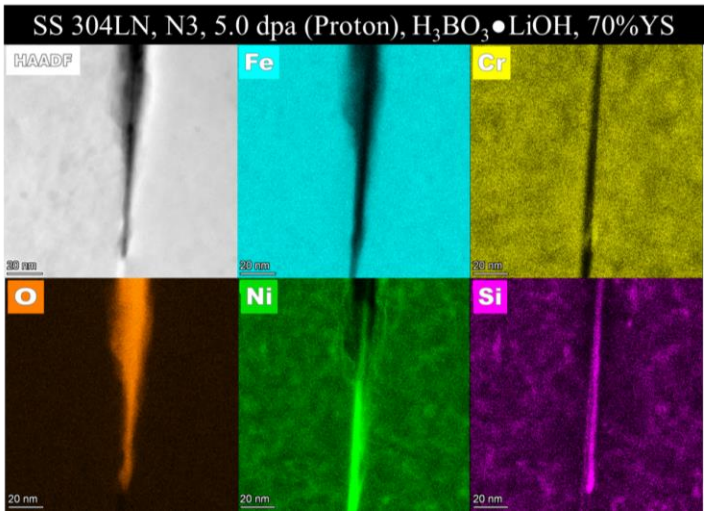
SS 304LN, N3, 5.0 dpa (Proton), $H_3BO_3$●LiOH, 70%YS
HAADF
Fe
Cr
O
Ni
Si
20 nm

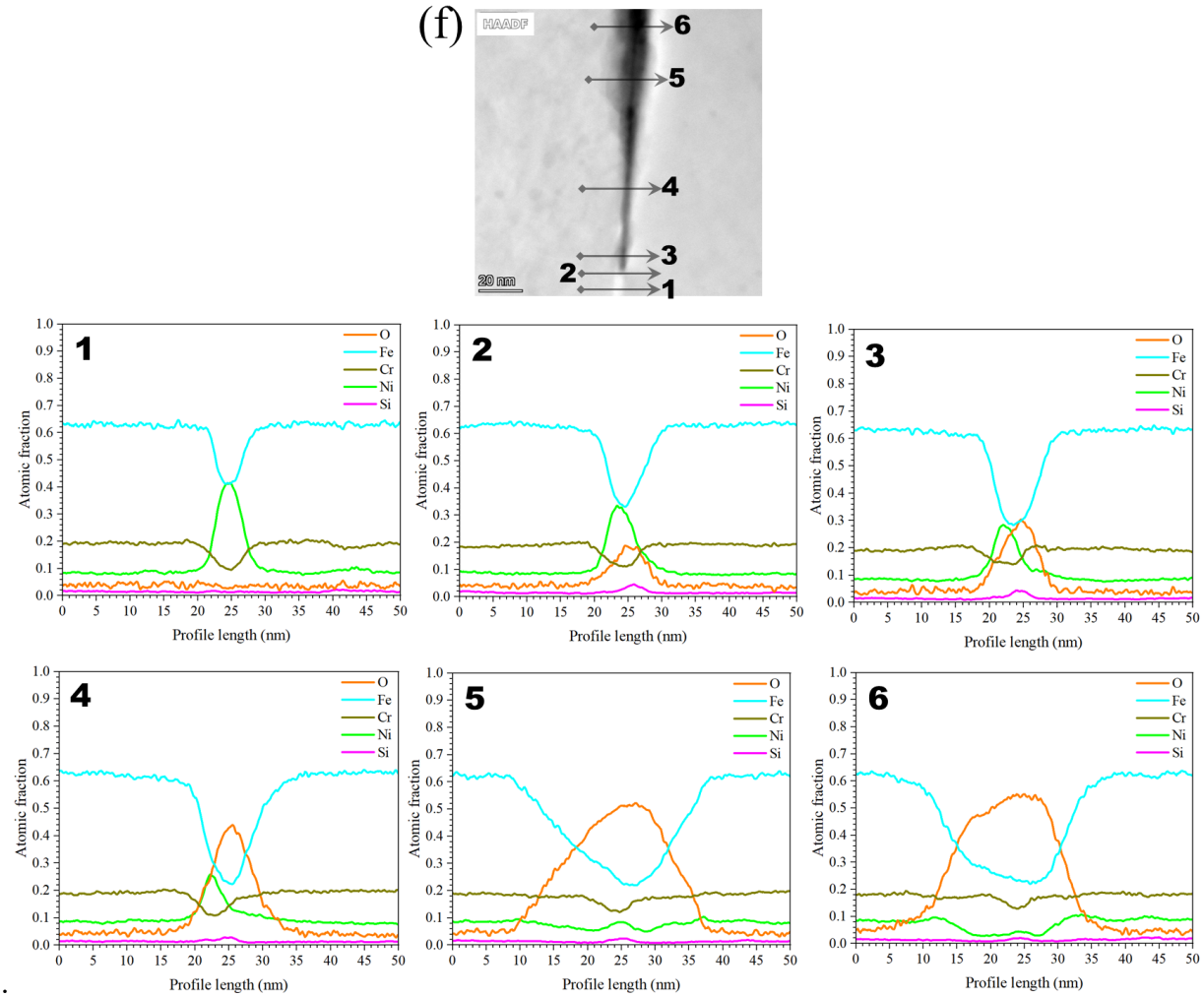


Figure 6-41 STEM-EDS of crack N-3-1, sample N3. (a–e) HAADF and elemental maps at increasing magnifications show Cr-rich oxidation along a GB, Ni segregation at the oxide–metal interface, and slight Si enrichment near the tip. (f) EDS line profiles (regions 1–6) reveal a compositional transition from the unoxidized GB to the oxidized crack tip. Oxidation initiates with Si, followed by Fe and Cr, while Ni remains excluded.

Figure 6-41 (f) shows STEM-EDS line profiles acquired across six distinct regions along the crack path, beginning from the unoxidized grain boundary and extending toward the crack tip. In region 1, representing a pristine grain boundary unaffected by oxidation, no oxygen is detected. The grain boundary is Cr-depleted, with notable segregation of Ni and Si, features consistent with RIS. In region 2, located at the transition between the RIS-affected region and the onset of oxidation, Ni shows a strong segregation peak (~39 at.%), indicating it was expelled from the oxidation front and accumulated at the interface. Oxygen begins to emerge in this

region, though Cr remains depleted. Region 3 corresponds to the oxidation tip, where a significant increase in oxygen is observed, coinciding with a sharp peak in Si, suggesting that Si is among the first elements to oxidize. Cr still shows no substantial enrichment, and Fe begins to deplete, indicating its participation in oxidation. Ni concentration decreases from its peak in region 2 indicating that this region is most likely the oxidation tip.

Progressing into the crack path, region 4 reflects early-stage crack oxidation, where oxygen concentration increases markedly. Cr continues to exhibit relatively low concentrations, suggesting delayed or limited involvement in this phase. Ni and Si levels drop significantly, indicating they have either been consumed (such as in case of Si) or displaced by the growing oxide (such as in case of Ni). Regions 5 and 6 represent the fully developed crack tip, where oxygen reaches its maximum atomic fraction (~0.55), and both Fe and Cr are substantially depleted, confirming their eventual participation in the oxidation process. In contrast, Ni is almost entirely absent, reinforcing its exclusion from the oxide and its earlier segregation at the interface. Si is also depleted in these regions, consistent with early-stage oxidation and consumption near the front.

*Alloy 304L-R*

In sample L-R-1, Crack L-1-8 was selected for the same reason as Crack N-3-12, as it was short and intersected both a DC feature and a TJ. Additionally, Crack L-1-16 was chosen due to the presence of clearly oxidized GBs along with a DC intersecting the TJ, which initiated the crack. This region provides an opportunity to analyze GB oxidation alongside key cracking initiators such as DCs and TJs.

Identifying the crack tip was challenging as well in this alloy due to the oxide fully occupying the grain boundary, preventing clear opening of the crack. Figure 6-42 (a) digitally

magnified and cropped HAADF image highlighting the presence of pores, interpreted as localized damage, within the crack oxide. The crack tip was inferred to be the final dark region at the lower end of the oxide, which likely corresponds to a vacuum or a low-density zone. Given that the oxide is inherently less dense than the surrounding metal, it appears darker in HAADF imaging. Therefore, the darkest regions along the grey oxide path are interpreted as the least dense, possibly voids, and the terminal dark region is reasonably assumed to represent the crack tip.

Figure 6-42 (b)-(d) shows STEM-EDS elemental maps across different magnifications of an intergranular crack and its surrounding oxidation in sample L-R-1. At low magnification (Figure 6-42 (b)), the grain boundary crack propagates from a triple junction and is filled with oxide, with an overall oxidation depth of 1 μm. The maps show the oxide is enriched in Cr and O, with significant depletion of Fe and near-complete absence of Ni, except at the oxide–metal interface. Higher magnification images (Figure 6-42 (c)) resolve the oxide tip and crack tip. The oxygen map reveals continuous oxidation along the crack flanks, while a Ni-rich band forms sharply at the oxide/matrix interface, confirming Ni exclusion from the oxide. Cr shows relatively uniform enrichment throughout the oxide, while Si appears along the segregated interface. At the highest magnification (Figure 6-42 (d)), elemental maps further confirm the localization of Ni at the oxide boundary and depletion within the oxide core, whereas Fe and Cr are strongly depleted and enriched, respectively, in the oxidized region. Si, though generally present at low levels, appears enriched slightly near the crack tip interface.

The corresponding line profiles from Figure 6-42 (e) (regions 1 through 6) further clarify the chemical evolution from the unoxidized grain boundary to the fully developed crack tip. Regions 1 and 2 represents a pristine grain boundary showing Cr depletion and RIS-type

segregation of Ni and Si, with no oxygen present. Region 3 marks the transition from RIS to early oxidation, where Ni begins to segregate at the interface showing highest peak at 0.41 at.%, but no oxidation is detected.

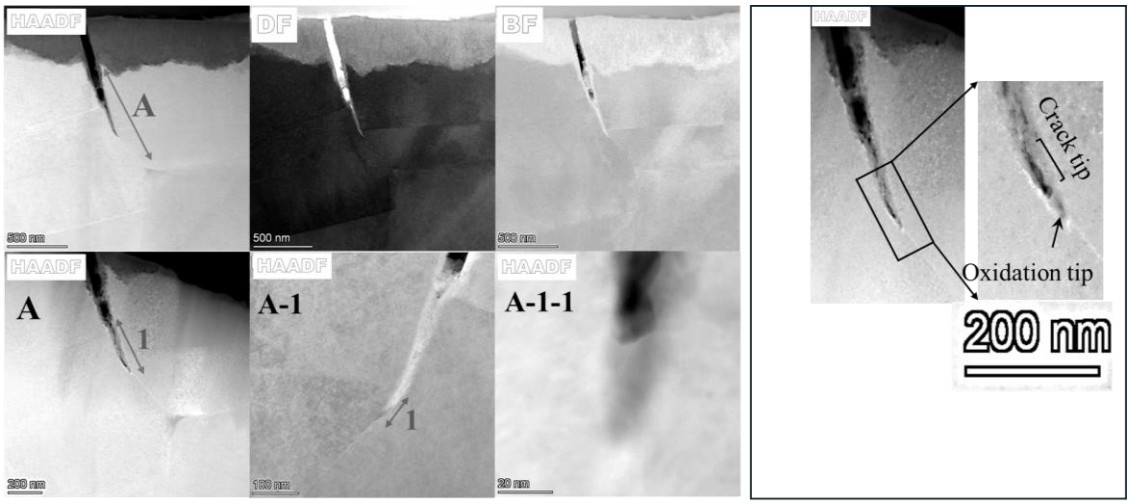


(a) (b)

(b)

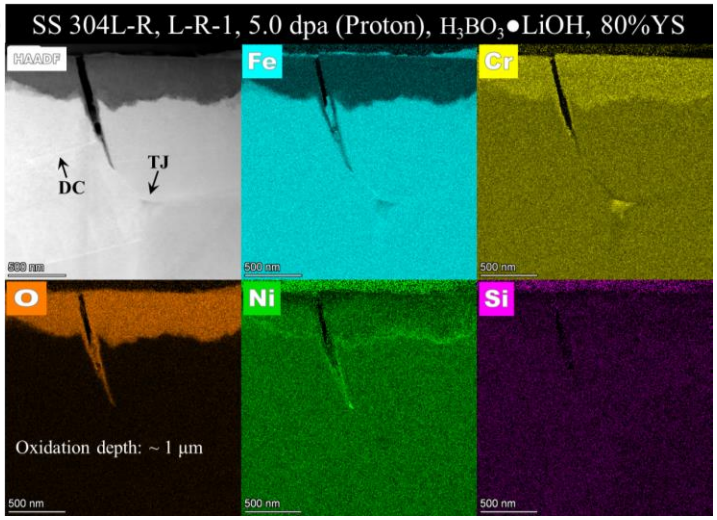

(c)

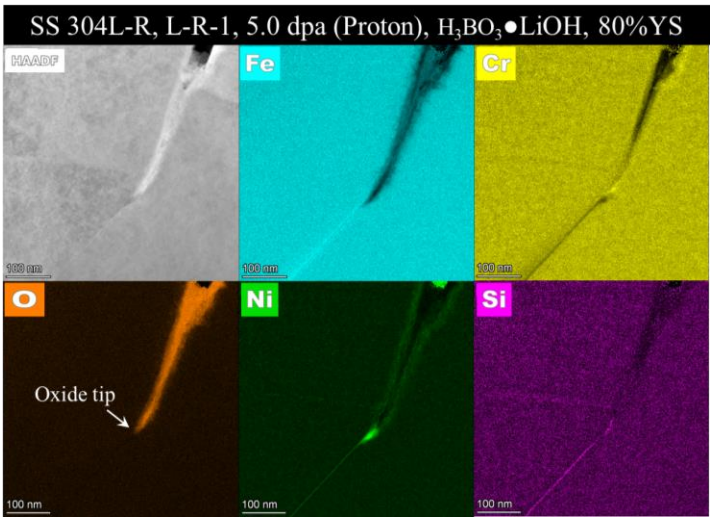
SS 304L-R, L-R-1, 5.0 dpa (Proton), $H_3BO_3$●LiOH, 80%YS
HAADF
Fe
Cr
O
Ni
Si
Oxide tip
100 nm

(d)

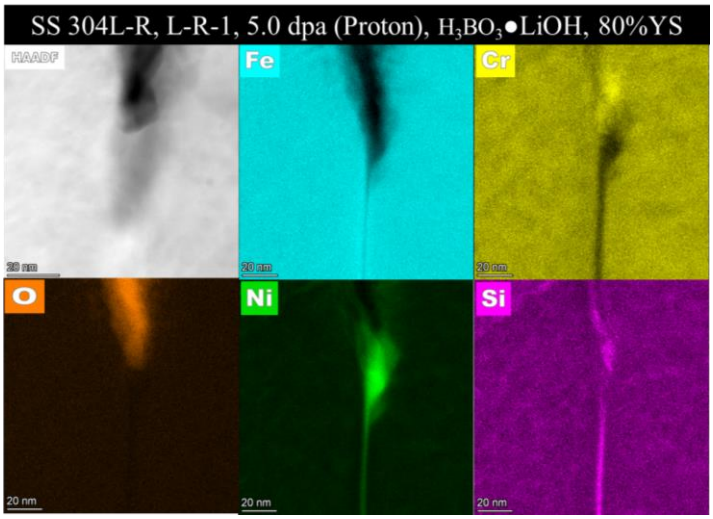
SS 304L-R, L-R-1, 5.0 dpa (Proton), $H_3BO_3$●LiOH, 80%YS
HAADF
Fe
Cr
O
Ni
Si
20 nm

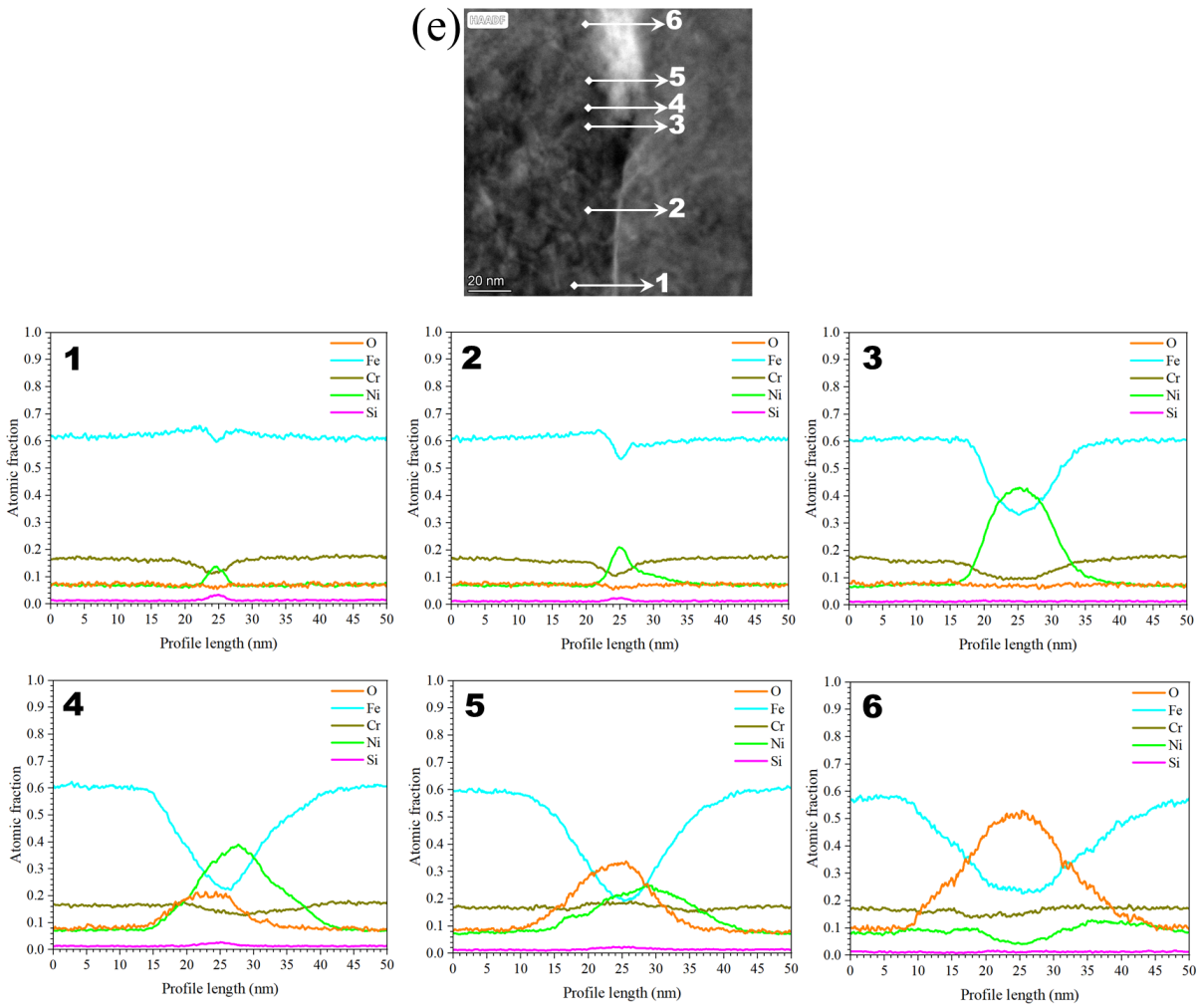


Figure 6-42 STEM-EDS of L-R-1-8 in SS 304L-R, sample L-R-1. (a–d) HAADF and elemental maps at increasing magnifications show Cr-rich oxidation along a GB, Ni segregation at the oxide–metal interface, and slight Si enrichment near the tip. (e) EDS line profiles (regions 1–6) reveal a compositional transition from the unoxidized GB to the oxidized crack tip. Oxidation initiates with Si, followed by Fe and Cr, while Ni remains excluded.

In region 4, the oxidation front is established as oxygen concentration increases, and Si exhibits a concurrent peak, implying early oxidation of Si. Cr remains depleted here, suggesting delayed oxidation involvement. By region 5, oxygen levels increase markedly, while Fe begins to drop, indicating active participation in oxidation. Cr starts to show a more notable decline. Region 6, closer to the crack tip, exhibit maximum oxygen content with strong Fe and Cr depletion, confirming their consumption in the mature oxide. Ni is nearly absent in these regions, consistent with its segregation at earlier interfaces and exclusion from the oxide. These

observations again affirm a sequential oxidation process: Si oxidizes first, followed by Fe and finally Cr, while Ni segregates at the oxide front but does not oxidize, forming a persistent interface layer. The chemical compositions at the GBs are listed in Table 6-7.

Table 6-7 Chemical compositions of key RIS elements (Si, Ni, and Cr) across different GBs and different depth from the crack tip.

| GB | Depth* (nm) | Si | | Ni | | Cr | |
|---|---|---|---|---|---|---|---|
| | | Original** | %Change*** | Original | %Change | Original | %Change |
| L-R-1-1 | 180 | 0.33 | +2.95% | 8.1 | +3.75% | 18.1 | -3.20% |
| L-R-1-2 | 250 | | +2.44% | | +3.29% | | -6.34% |
| L-R-1-3 | 100 | | +3.50% | | +7.37% | | -5.75% |
| L-R-1-4 | 250 | | +2.39% | | +4.09% | | -5.41% |
| N3-1 | 680 | 0.43 | 2.88% | 8.2 | +3.45% | 18.2 | -3.75% |
| N3-2 | 210 | | 7.07% | | +13.61% | | -8.32% |
| N3-3 | 175 | | 2.73% | | +3.34% | | -1.17% |
| N3-4 | 200 | | 3.67% | | +4.39% | | -4.41% |

** The depth from the oxide tip at which the data was collected.*
*** Original composition in the matrix (in wt.%).*
**** The percent change in the composition at GB compared with the matrix.*

## 6.3 Dislocation channels

The final set of experiments involved constant extension rate tensile (CERT) testing to evaluate the density of dislocation channels, along with other characteristics such as step height and channel separation. This study hypothesizes that solute nitrogen plays a role in stabilizing dislocation loops, thereby altering the deformation mechanism by increasing the density of dislocation channels. CERT tests were conducted in an ultra-high purity argon environment at 340 °C. Subsequent characterization using SEM, EBSD, and AFM was carried out to quantify the dislocation channels, determine the orientation of active slip planes, and measure the step heights associated with channel formation.

### *6.3.1 CERT tests*

Two tests were conducted at the IMTL at the University of Michigan, in accordance with the procedure described in Section 4.7. For the T-B-N (SS 304LN) sample, a load of

approximately 1015 N was applied, resulting in a total strain of 2.3%, as shown by the blue curve in Figure 6-43. However, 985 N was applied to the T-B-L (SS 304L-R) sample, which resulted in a total strain of 2.3% (red curve), closely matching the deformation experienced by the sample T-B-N. The two curves show a bow at the beginning of the loading representing a non-linear behavior in the elastic region which is not typical. However, this response reflects system compliance and the relaxation of the loading fixture when the load is applied. Therefore, the strain values from the curves were determined by analyzing the slopes of the loading and unloading segments, which differ due to compliance influences at the early stage of loading. These slopes were used to establish the best-fit linear approximations (shown as gray dashed lines) representing the elastic portion of each curve. The intersection points of these lines with the x-axis were then identified. The horizontal distance between the loading and unloading lines was measured and considered as plastic strain, as seen in Figure 6-43.

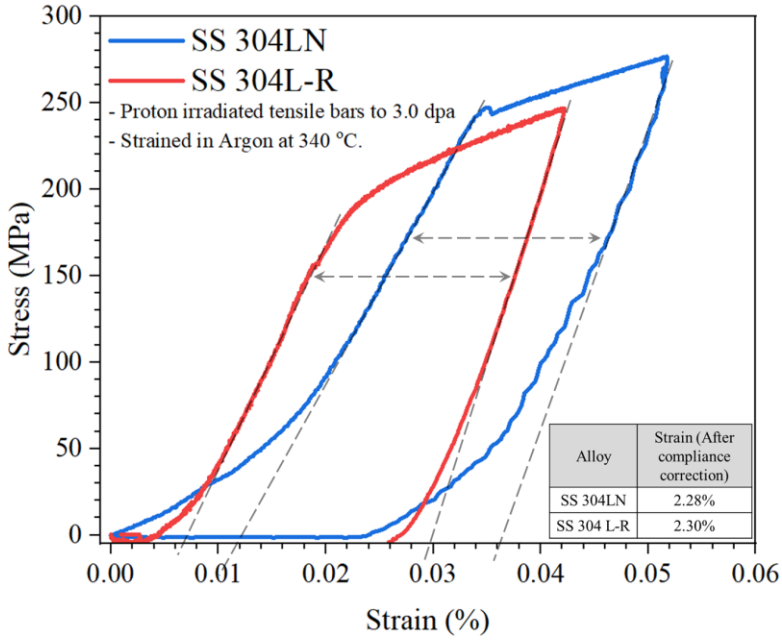


Figure 6-43 Stress-strain curves from CERT for both alloys showing the straining to 2.3% (After correcting the strain by removing the system's compliance) for both alloys in an ultra-high purity Argon at 340 ºC.

The plastic region of each curve was corrected by applying the ratio between the LVDT and indentation measurements. Finally, the plastic strain for both samples was determined to be 2.3%.

### *6.3.2 Dislocation channels quantification*

The dislocation channels quantification was carried out using both SEM and EBSD. In this study, only the dislocation channels that intersected with sample surface were analyzed as IASCC is a surface phenomenon, meaning that only DC-GB intersection may cause IASCC initiation. This implies that dislocation channels intersecting the GB in the bulk (unirradiated) are unlikely to initiate cracks, which is also supported by testing in an argon environment, to be discussed later in this chapter. As a result, the quantification was performed on the dislocations emergent on the surface.

Seven to nine regions were characterized by SEM and EBSD (that employed for the purpose of identifying the grains thus DDCs from CDCs). The DCs density were then averaged for each condition. In this study, the classification of DCs was slightly modified, both CDC and DDC types were already reported in the literature, however, we added nascent DCs (NDC) to this study. An NDC is a dislocation channel that does not transmit slip along a slip plane in the adjacent grain as do CDCs, rather they create a plastic region that extends a few nm, thus, failing in between a DDC and a CDC in terms of transmission of plastic deformation. Although their role at the GBs was not identified whether they help to relief the stress at the DC-GB intersection or intensify it. The reason for adding this qualification is that some of DDCs channels observed to initiate cracks when they terminate at the GB while NDCs do not cause any cracks since they relieve stress at the DC-GB and do not terminate the at the GB.

Figure 6-44 (a) shows the distribution of the characterized dislocation channels in T-B-L and T-B-N after straining to 2.3%. Dislocation channels density was the highest in T-B-N after straining to 2.3% compared to T-B-L. There were 27,375 total DCs counted in T-B-L and 31,723 in T-B-N, therefore, the increased DDC count in T-B-N (2,134 DDC intersections) represents a substantial increment (around 18.7% increase) in the absolute density of potential crack-initiation sites compared to T-B-L. Figure 6-44 (b) shows the pie charts illustrating similar proportions of DDC, CDC, and NDC in T-B-L and T-B-N after straining to 2.3%. DDCs constitute 53 – 54% in both alloys while CDCs constitute 42 – 43% from the total number of detected DCs from each alloy and NDCs constitute 4% in both conditions as well. This chart compares how each alloy behaves under plastic deformation with both exhibited more harmful DDCs. The comparable distributions of DDC and CDC types between the two alloys support the conclusion that both alloys experience similar deformation mechanisms, consistent with their classification as austenitic stainless steels.

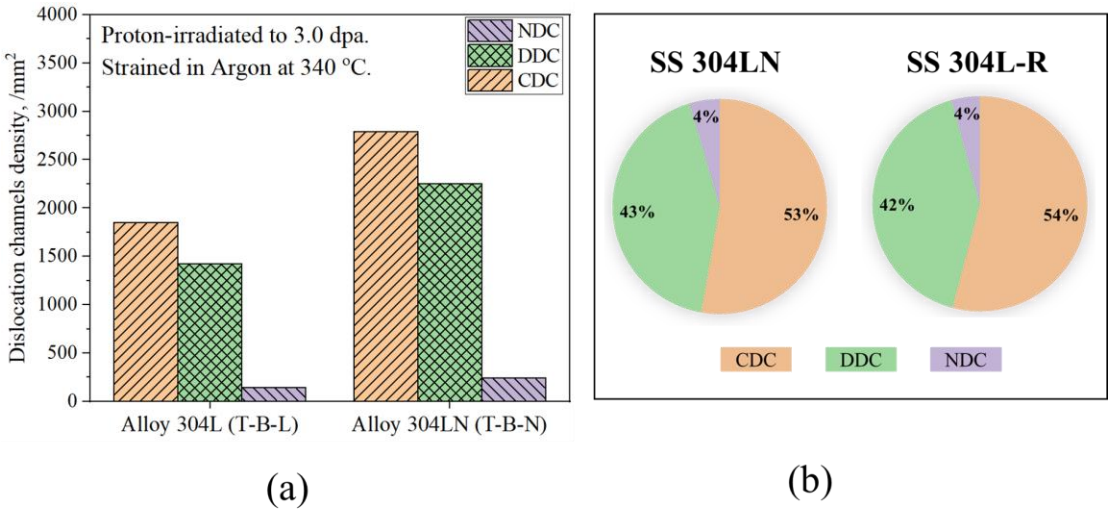


Figure 6-44 (a) Dislocation channels quantification, three types where characterized; DDC, NDC, and CDC for both samples at all loading steps and (b) the percentage of DDC, NDC, and CDC to the total quantified DCs per each alloy.

Figure 6-45 shows examples of the physical appearance of dislocation channels at the surface after straining to 2.3% in SS 304L-R and SS 304LN respectively. These images were captured when the SEM stage titled 70°. A step-up appearance can be clearly observed, and multiple slip systems are shown as well in the scanned area (Figure 6-45 (a) and (d)). GBs were also revealed in T-B-L images as the sample was slightly oxidized even in the Argon environment (which possibly due to some leaks as the systems are old). The oxidation did not affect the test. However, it was useful to reveal the GB and investigate the DDCs and CDCs.

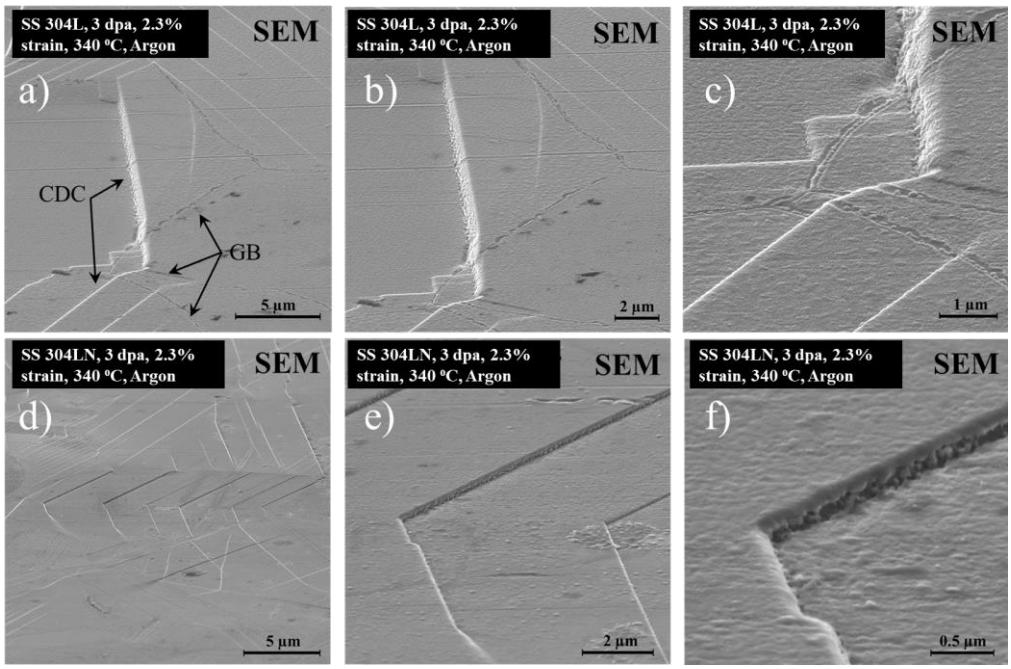


Figure 6-45 Dislocation channels characterization showing how the steps look like after straining, (a), (b), and (c) for SS 304L-R, and (d), (e), and (f) for SS 304LN.

### *6.3.3 Step height measurement*

Dislocation height was measured using AFM techniques as indicated in section 4.7.2. Before DCs height measurement, AFM measurement was checked using optical microscope that was well-calibrated. One of the indents on the surface of T-B-L was characterized by AFM, and three measurement profiles were obtained as shown in Figure 6-46 (a). The indent was then characterized by Keyence VHX-7000® OM, and similar three distance profiles were measured

and shown in Figure 6-46 (b) and the measurements were compared as listed in Table 6-8. The results show a good agreement between AFM and OM with less than 5% difference confirming the validity of the AFM measurement. Raw data from AFM were processed using both NanoScope Analysis 2.0® and Gwyddion (64bit) 2.67® and first order polynomial degree fitting was used to adjust the surface levels and remove noise background.

Table 6-8 AFM measurement check against well-calibrated OM.

| Profile No. | AFM (µm) | OM (µm) | Percent change |
|---|---|---|---|
| **1** | 7.0 | 7.274 | 3.90% |
| **2** | 7.9 | 7.981 | 1.03% |
| **3** | 10.6 | 10.495 | 1.00% |

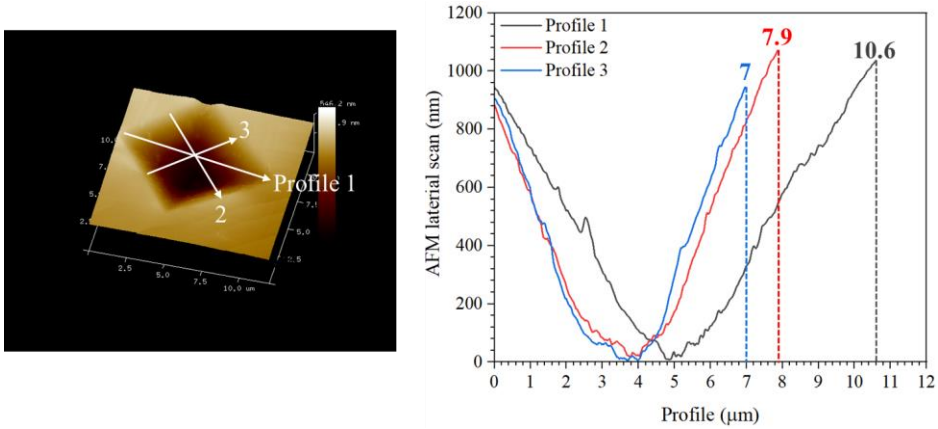


Figure 6-46 AFM measurement precision compared with OM.

More than a hundred locations were investigated on each sample representing areas from the uniform irradiation region. Each AFM scanned area was 10 by 10 µm$^2$ and 512 points per line was selected that resulted in a lateral resolution of 20 nm. Examples of scanned regions are shown in Figure 6-47 (a) and (b) for T-B-N and T-B-L respectively.

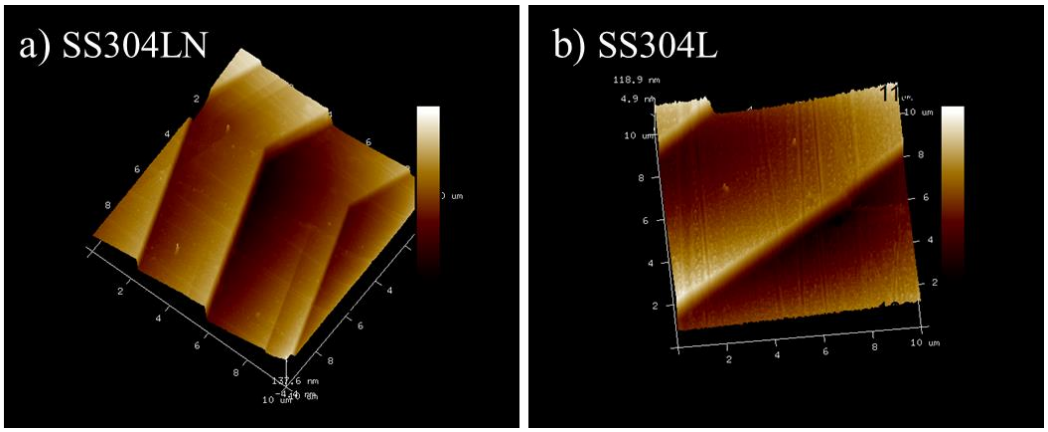


Figure 6-47 Examples of step height characterization by AFM and processing using NanoScope Analysis 2.0 software from (a) SS 304LN and (b) SS 304L showing the 3D view of steps.

The average weight factor ($w_i$) is defined as the relative contribution of each dislocation channel height to the total sum of all channel heights in the dataset. It represents the proportion of each channel's height compared to the collective sum of all heights, thereby giving greater importance to larger channels in calculating the weighted average:

$$w_i = \frac{h_i}{\sum_{j=1}^{n} h_j} \tag{6.1}$$

Where $h_i$ represents the height of the $i^{th}$ dislocation channel and $n$ is the total number of channels considered. This weight factor assigns a proportional significance to each channel height in calculating the weighted average channel height, emphasizing larger channels that are more likely to initiate cracks. In T-B-L after straining to 2.3% was, the average weight factor 125 nm while it was 137 nm in T-B-N. Similar behavior was observed in terms of average height as it was 113.1 nm with a standard deviation of 36.9 nm for T-B-L and 123.9 nm with a standard deviation of 40.6 nm for T-B-N after straining to 2.3% as shown in Figure 6-48. The results show slightly higher dislocation height in T-B-N compared to T-B-L at similar straining level.

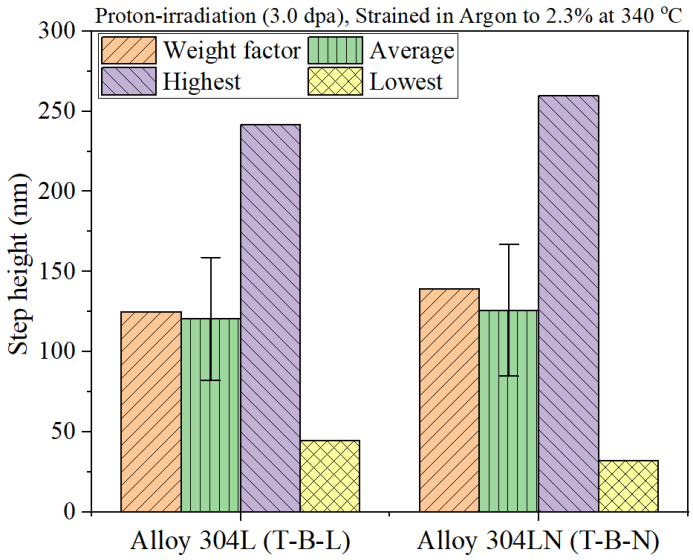


Figure 6-48 Step height measurements for dislocation channels in proton-irradiated Alloy 304L (T-B-L) and Alloy 304LN (T-B-N) after straining to 2.3% at 340 °C in an argon environment. Bars represent the highest, lowest, average, and weighted average step heights based on AFM analysis. Error bars show standard deviation of the average values. All samples were irradiated to 3.0 dpa.

The distribution of DC step height for both alloys is plotted in Figure 6-49 (a), showing slightly higher average channel height in T-B-N compared to T-B-L. Unlike single average values or weighted factors, the plotted distributions provide a more comprehensive representation of the channel heights, particularly when these measurements are acquired using AFM. The observed channel heights predominantly fall within the range of 50–200 nm, with a few instances approaching 250 nm. The step height distributions for both alloys were quantified and categorized into defined height intervals as shown in Figure 6-49 (b). For T-B-N, approximately 3% of the dislocation channels exhibit heights between 1–49.999 nm, while 24% fall within 50–99.999 nm. The majority, about 50%, are within the range of 100–149.999 nm, followed by 20% between 150–199.999 nm. Channels with heights between 200–249.999 nm account for 2%, and only 1% exceed 250 nm. In comparison shown in Figure 6-49 (b), T-B-L shows a slightly different distribution: 2% of channels fall within 1–49.999 nm, 38% within 50–99.999 nm, and 43% within 100–149.999 nm. The proportion decreases to 15% in the 150–

199.999 nm range, with only 1% reaching 200–249.999 nm, and no channels exceeding 250 nm. Although the majority of dislocation channels in both alloys fall within the 100–149.999 nm interval, the proportion is notably lower in T-B-L. This difference arises because a large percentage of channels in T-B-L are concentrated within the 50–99.999 nm range as well. This trend indicates that T-B-N is generally more prone to forming higher channel steps compared to T-B-L, reflecting a shift toward larger step heights in the nitrogen-alloyed material. Approximately 120 channels were characterized by AFM for each alloy. Although the absolute numbers may vary with additional measurements, the average channel height is not expected to change significantly, as imaging 120 channels across a uniformly irradiated region offers a representative sampling of the material response.

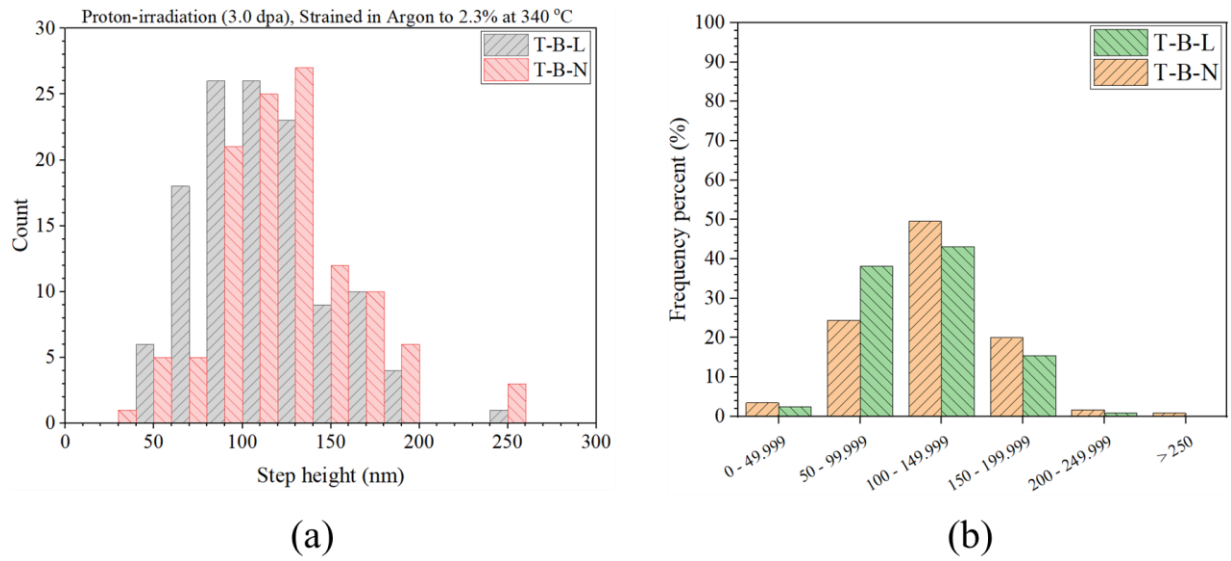


Figure 6-49 (a) Step height distribution in proton-irradiated T-B-L and T-B-N after straining to 2.3%, (b) the distribution of step height categorized into defined height intervals.

### *6.3.4 Microscopic strains within the dislocation channel*

The localized plasticity within individual grains is characterized by the properties of the dislocation channels (DCs) themselves. Key factors include the number of dislocations within each channel, the channel's orientation relative to the applied load and the EBSD scan plane,

quantified by the Schmid factor, as well as the Burgers vector length and its alignment with the DC plane. These parameters were determined through a combination of EBSD and AFM analyses, as described in section 6.3.3. As previously mentioned, the activated slip systems were identified from EBSD analysis and DC height. However, to calculate the number of dislocations per dislocation channel (*Nc*), the true channel height was used. Specifically, the step height measured from AFM (vertical height) was corrected by dividing by the cosine of the angle (ɵ) between the slip plane normal and the specimen surface normal, resulting in the true channel height ($h_{true}$).

Figure 6-50 (a) shows the distribution of the number of dislocations per channel in both samples. T-B-L average Nc around 484 dislocations with a standard deviation of 166 dislocations, while T-B-N peaks slightly higher, around 472 dislocations per channel with a SD of 156. T-B-N also shows a wider spread, with some channels reaching values near 1000 dislocations, whereas T-B-L is more confined to below 800 dislocations.

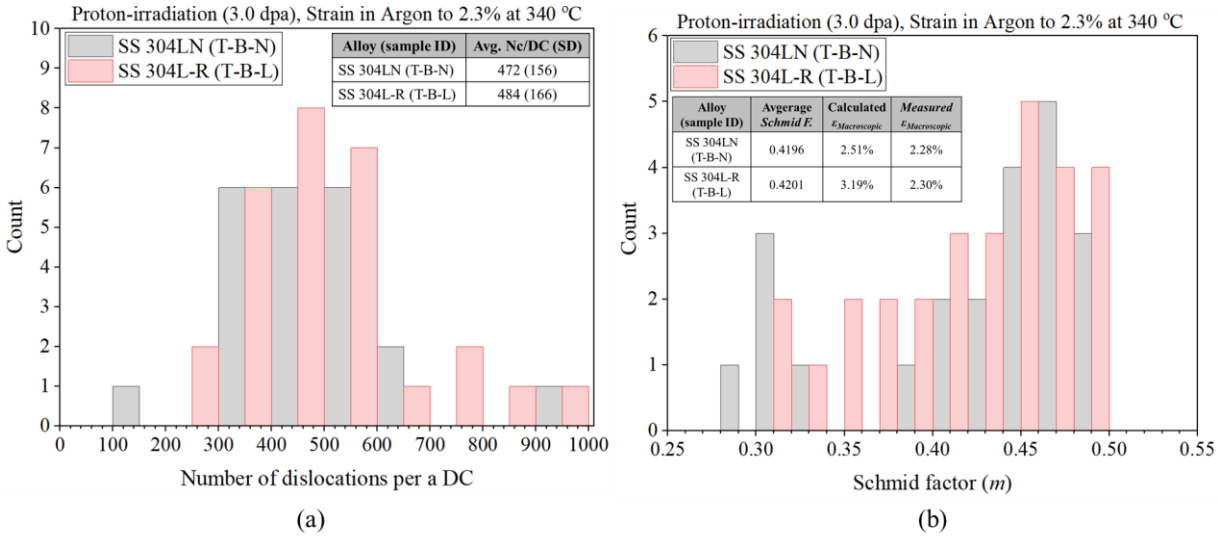


Figure 6-50 (a) The distribution of the number of dislocations per dislocation channel and (b) the distribution of Schmid factors for slip systems in SS 304LN (T-B-N) and SS 304L-R (T-B-L) alloys, after proton irradiation to 3.0 dpa and tensile strain of 2.3% at 340 °C.

### *6.3.5 Spacing between dislocation channels*

Another factor of comparison was the spacing between the dislocation channels as it is another indication of the density of DCs. The spacing was measured using OM at a magnification of 500x. Seven regions from various locations across the uniform irradiated region were characterized each region has an area of 300 by 225 $\mu m^2$. All spacing values were then analyzed and mean, and standard deviation was calculated representing the whole scanned region. Figure 6-51 shows the distribution of spacing between DCs for T-B-L and T-B-N after proton irradiation to 3.0 dpa, followed by tensile straining to 2.3% at 340°C. The measurements were conducted under identical conditions to ensure direct comparison.

The distributions show that T-B-L exhibited wider spacing between the dislocation channels with an average spacing per region of 4.50 µm and a standard deviation of 2.24 µm. T-B-N exhibits a narrower distribution of DC spacing, with a peak between 2–3 µm, and an average spacing of 3.88 µm. The results support the dislocation channels density reported in section 6.3.2 since higher density of DCs results in a shorter spacing between the DCs within the same slip system within the grain.

the smaller and more uniform spacing in SS 304LN suggests a higher density of dislocation channels forming throughout the material, which aligns with its previously observed higher number of dislocations per channel and larger step heights. SS 304L-R shows wider and more dispersed channel spacing, indicating fewer active slip systems or limited channel nucleation in some grains. This reflects the higher fraction of grains with low Schmid factors, as discussed earlier, which resist channel formation and contribute to a more heterogeneous plastic response.

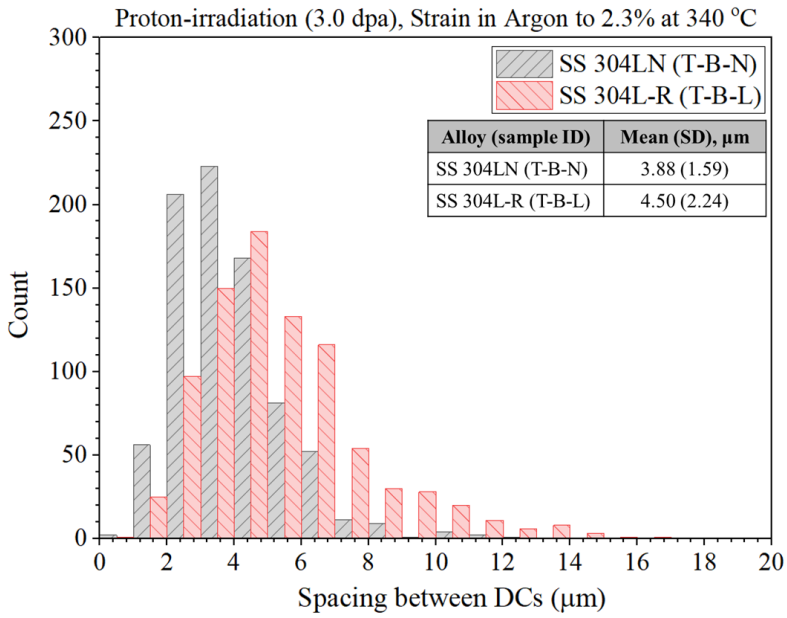


Figure 6-51 Distribution of spacing between dislocation channels in SS 304L-R and SS 304LN following 3.0 dpa proton irradiation and 2.3% tensile strain at 340°C in argon atmosphere. SS 304LN shows a narrower spacing distribution and smaller average spacing compared to SS 304L-R, indicating a higher density of DCs and more uniform plastic deformation, consistent with nitrogen's effect on dislocation channeling.

# Chapter 7 Discussion

This chapter investigates the impact of solute nitrogen on the susceptibility of austenitic stainless steels to irradiation-assisted stress corrosion cracking (IASCC) initiation in pressurized water reactor (PWR) environments. To achieve this, a methodological strategy is proposed: replacing neutron-irradiated four-point bend (4PB) samples with proton-irradiated samples as surrogates. The discussion is therefore organized into three main subtopics.

The first subtopic addresses the validity of using proton-irradiated samples as surrogates for neutron irradiation by comparing the resulting irradiation-induced microstructural features with those reported in the literature for neutron-irradiated materials. The central argument is that an acceptable agreement in microstructural evolution, such as dislocation loops, cavities, precipitates, irradiation-induced hardening, and dislocation channel behavior, supports the validity of the irradiation method and the suitability of the samples for IASCC testing of the samples.

The second subtopic compares the IASCC initiation behavior of the proton irradiated samples tested in 4-point bend geometry with that of various samples irradiated in the reactor. Here, IASCC initiation stress, expressed as a fraction of the irradiation yield strength measured using the 4-point bend test geometry, is evaluated as a function of displacement per atom (dpa) and exposure time. In addition, surface cracking characteristics and crack morphology are compared to neutron-irradiated samples to assess similarities in cracking mechanisms and identify key initiation features such as dislocation channels and oxidized grain boundaries.

Having established the validity of the proton irradiation to produce a microstructure and IASCC behavior consistent with that in reactor, the final section explores the specific influence of solute nitrogen on the irradiated microstructure and its role in IASCC susceptibility. This analysis is conducted by comparing two austenitic stainless-steel alloys, one with high nitrogen content and the other with low nitrogen content to isolate the role of nitrogen. The investigation integrates results from multiple experimental techniques, including four-point bend (4PB) tests to assess IASCC initiation, constant extension rate tensile (CERT) tests to evaluate the influence of dislocation channels and the effect of nitrogen, and crack tip characterization to examine radiation-induced segregation and its relationship to nitrogen content.

To evaluate the main hypothesis of this thesis. Any divergence between the initial hypothesis and final conclusions is examined and explained. The chapter concludes with a statement on how this work advances understanding of IASCC mechanisms and its practical relevance to material selection and performance in nuclear power plants.

### 7.1 Proton irradiation-induced microstructure

The irradiation-induced microstructure serves as the initial basis for validating the testing strategies employed in this study. Establishing the fidelity of these strategies requires a careful comparison between the microstructural features observed in the current proton-irradiated samples and those reported in the literature for materials irradiated with neutrons PWR-relevant conditions or in controlled testing environments. This validation is particularly important given the differences in geometry, irradiation temperature and dose rate between proton irradiation and more traditional neutron irradiation methods.

This section focuses on comparing key irradiation-induced defects, including dislocation loops, cavities, precipitates, and radiation-induced segregation (RIS). In addition, irradiation

hardening is evaluated through hardness measurements, yield strength calculations and measurements, as well as yield strength estimations based on the irradiated microstructure. All features were characterized following 2 MeV proton irradiation to a damage level of 5 dpa at temperatures representative of PWR operating conditions. Their presence and morphology are discussed in detail and compared with microstructural data from the literature on neutron- and ion-irradiated austenitic stainless steels. Emphasis is placed on assessing whether the types and densities of these defects are consistent with those produced by neutron irradiation, as this underpins the suitability of proton irradiation as a surrogate approach.

### *7.1.1 Irradiation-induced defect evolution*

It is important to begin with irradiation-induced defects because they are directly linked to the IASCC mechanism in PWR environments. Faulted dislocation loops are among the earliest and most influential defects formed under irradiation, contributing significantly to irradiation-induced hardening as they act as obstacles to dislocation motion. This hardening increases material strength but also alters its deformation behavior, leading to localized deformation. The resulting formation of dislocation channels is a critical step in the IASCC process, as these channels act as preferential sites for crack initiation in PWR environments.

Therefore, while the analysis of irradiation-induced defects primarily focused on dislocation loops due to their relevance to IASCC, it remains important to account for other defect types as well. This broader assessment serves as an essential first step to verify that the irradiation conditions were appropriate and that the resulting microstructural damage resembles that typically produced by neutron irradiation, given that the variation in dose rates between PWR exposure and laboratory-based accelerated irradiation remains an important factor influencing defect evolution.

Proton irradiation at 360 ºC is not expected to retain a high concentration of hydrogen in the microstructure and at the GB. Hunn et. al. [222] reported a very little retained hydrogen at implantation temperatures above 100 ºC, therefore, it is unlikely to be significant at 360 ºC. J. Cookson et. al. [223] reported no effect of hydrogen on intergranular cracking through series of experiments conducted in both argon at 288°C and in water. The cracks did not appear in argon tests indicating that the presence of implanted hydrogen from 3.4 MeV proton irradiation does not appear to contribute to the cracking observed in identical samples in water.

In the present study, CERT testing also showed no evidence of cracking after straining samples to 2.3% in argon at 340 °C. If hydrogen were a contributing factor, cracking would most likely have been observed in the threaded bars examined here. Furthermore, proton irradiation has been widely employed for decades in various experiments, including CERT, to investigate IASCC susceptibility. No reports have linked hydrogen embrittlement to proton irradiation under the irradiation conditions used in this study.

*Dislocation loops*

The measured dislocation loop number densities in the proton-irradiated 4PB specimens (SS 304L and SS 304LN) were both on the order of $10^{22}$ $m^{-3}$. These values are consistent with the well-established saturation regime typically observed beyond 3 dpa. Literature data for neutron irradiated austenitic stainless steels is shown in Figure 7-1. The plot includes approximately 96 data points obtained under neutron irradiations, alongside two proton-irradiated data points from this study. The majority of the data (~ 74%), including the proton-irradiated samples, fall within the range of $10^{22}$ and $10^{23}$ $m^{-3}$ ($3.96 \times 10^{22}$ $m^{-3}$ for SS 304LN and $2.26 \times 10^{22}$ $m^{-3}$ for SS 304L-R). Approximately 22% of the data points lie above this range, while only about 4% fall below it. The neutron-irradiated data originates from various sources,

including samples extracted from retired PWR internal components as well as specimens irradiated in fast neutron reactors such as BOR-60.

To make the comparison more specific, Figure 7-1 (b), shows data limited to the low-dose regime (≤ 10 dpa), which more closely matches the irradiation conditions used in this study. Both SS 304L-R and SS 304LN fall well within the central band of reported dislocation loop densities. This band includes 12 data points from SS 304, SS 304L, and SS 304LN [54, 61, 224, 225, 226, 227, 228], one from SS 347 [70], one from SS 316LN [228], and the remaining from SS 316 in either cold-worked (CW) or solution-annealed (SA) conditions [105, 106, 107, 162, 226, 227, 229, 230, 231, 232]. It is generally accepted that when dislocation loops of similar size and densities that fall within the same order of magnitude, their mechanical behavior, particularly in terms of hardening, is expected to be comparable. The proton-irradiated samples in this study clearly fall within the accepted range. Moreover, all data considered here are from austenitic stainless steels irradiated under low-dose, low-temperature conditions, beyond the loop saturation point. This implies that the fundamental mechanisms governing dislocation loop formation and evolution are similar across these datasets.

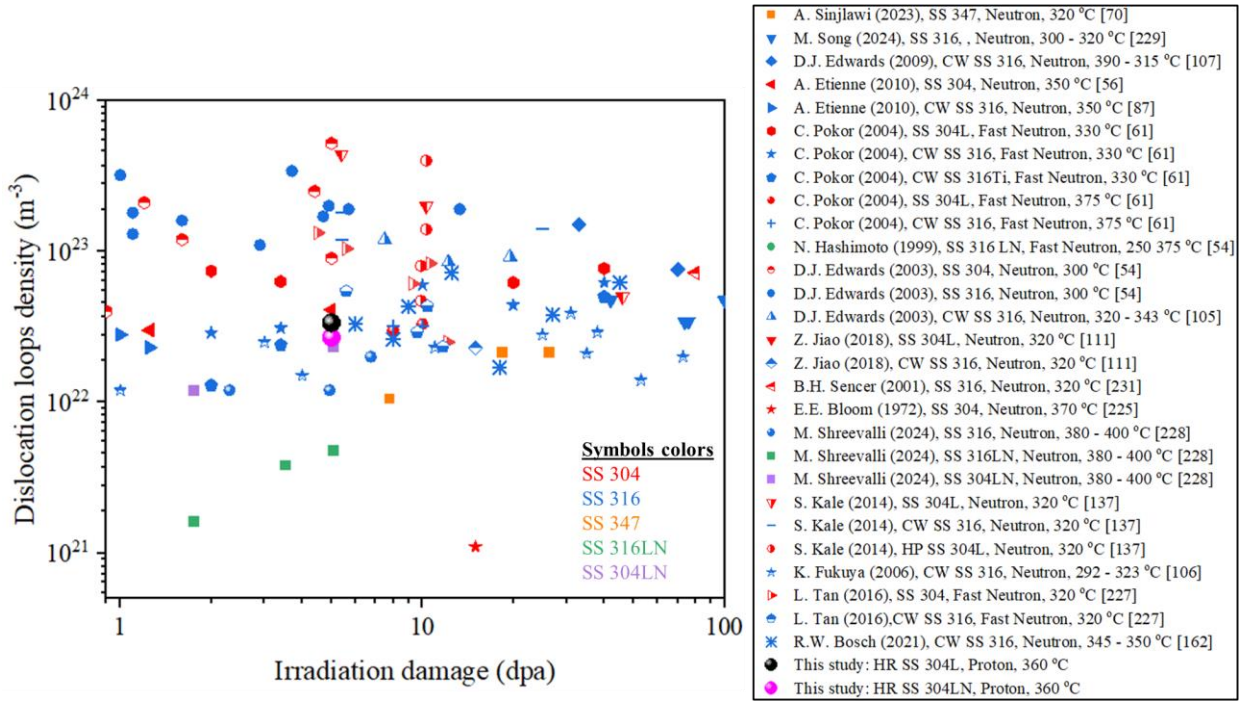
Dislocation loops density (m-3)
Irradiation damage (dpa)
Symbols colors
SS 304
SS 316
SS 347
SS 316LN
SS 304LN
A. Sinjlawi (2023), SS 347, Neutron, 320 °C [70]
M. Song (2024), SS 316, , Neutron, 300 - 320 °C [229]
D.J. Edwards (2009), CW SS 316, Neutron, 390 - 315 °C [107]
A. Etienne (2010), SS 304, Neutron, 350 °C [56]
A. Etienne (2010), CW SS 316, Neutron, 350 °C [87]
C. Pokor (2004), SS 304L, Fast Neutron, 330 °C [61]
C. Pokor (2004), CW SS 316, Fast Neutron, 330 °C [61]
C. Pokor (2004), CW SS 316Ti, Fast Neutron, 330 °C [61]
C. Pokor (2004), SS 304L, Fast Neutron, 375 °C [61]
C. Pokor (2004), CW SS 316, Fast Neutron, 375 °C [61]
N. Hashimoto (1999), SS 316 LN, Fast Neutron, 250 375 °C [54]
D.J. Edwards (2003), SS 304, Neutron, 300 °C [54]
D.J. Edwards (2003), SS 316, Neutron, 300 °C [54]
D.J. Edwards (2003), CW SS 316, Neutron, 320 - 343 °C [105]
Z. Jiao (2018), SS 304L, Neutron, 320 °C [111]
Z. Jiao (2018), CW SS 316, Neutron, 320 °C [111]
B.H. Sencer (2001), SS 316, Neutron, 320 °C [231]
E.E. Bloom (1972), SS 304, Neutron, 370 °C [225]
M. Shreevalli (2024), SS 316, Neutron, 380 - 400 °C [228]
M. Shreevalli (2024), SS 316LN, Neutron, 380 - 400 °C [228]
M. Shreevalli (2024), SS 304LN, Neutron, 380 - 400 °C [228]
S. Kale (2014), SS 304L, Neutron, 320 °C [137]
S. Kale (2014), CW SS 316, Neutron, 320 °C [137]
S. Kale (2014), HP SS 304L, Neutron, 320 °C [137]
K. Fukuya (2006), CW SS 316, Neutron, 292 - 323 °C [106]
L. Tan (2016), SS 304, Fast Neutron, 320 °C [227]
L. Tan (2016),CW SS 316, Fast Neutron, 320 °C [227]
R.W. Bosch (2021), CW SS 316, Neutron, 345 - 350 °C [162]
This study: HR SS 304L, Proton, 360 °C
This study: HR SS 304LN, Proton, 360 °C

(a)

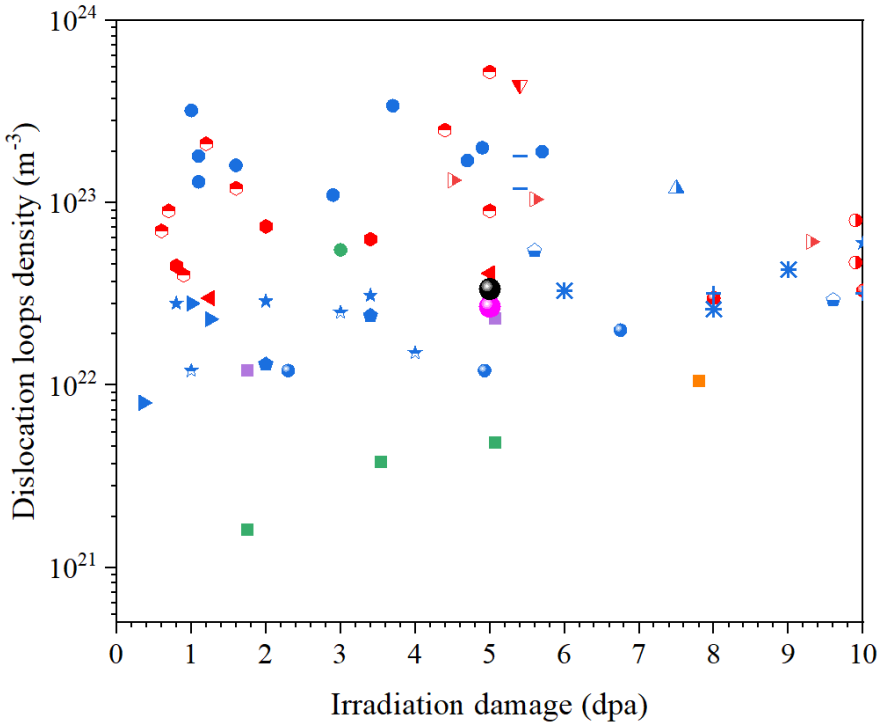
Dislocation loops density (m-3)
Irradiation damage (dpa)

(b)

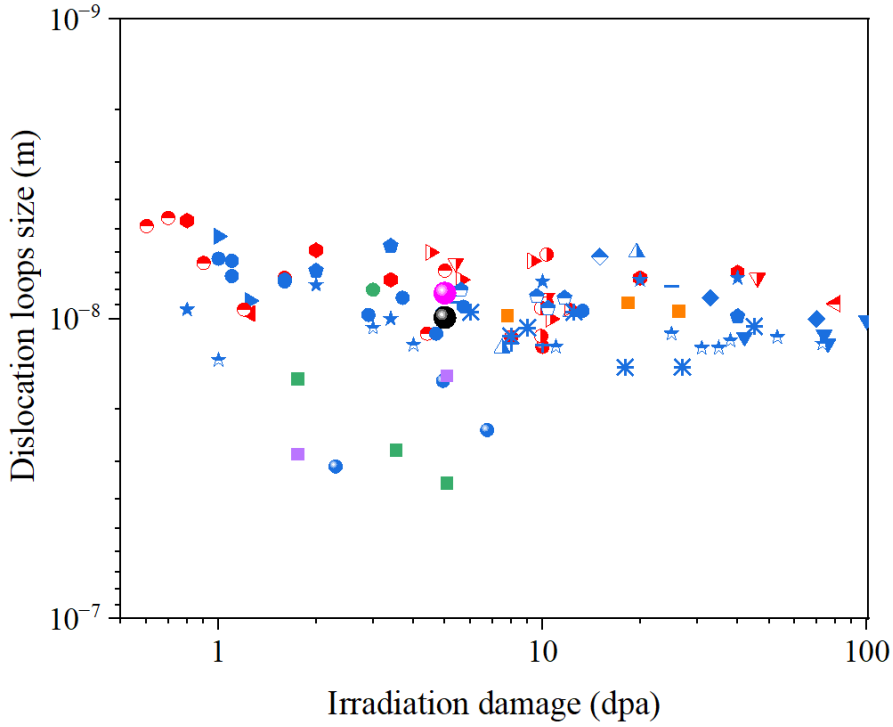


(c)

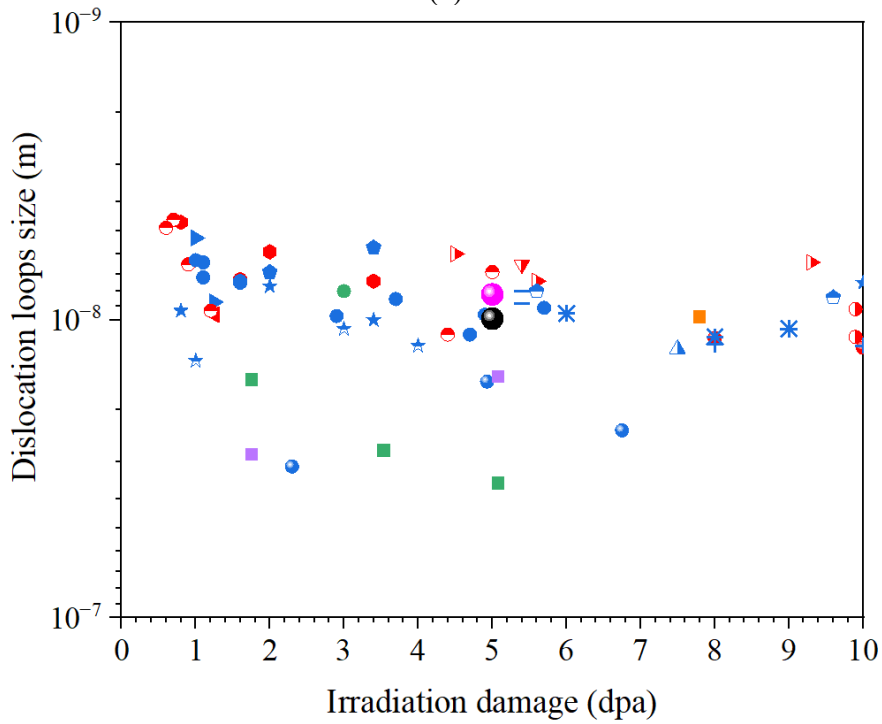


(d)

Figure 7-1 The comparison between the dislocation loops obtained from this study and the literature on neutron irradiated austenitic stainless steels irradiated over a range of temperatures of 300 - 400 °C, for loops density (a)

wide range of doses, (b) low regime doses, for loop size (c) wide range of doses, and (d) low regime doses 54, 56, 61, 70, 87, 105, 106, 107, 111, 137, 162, 225, 227 – 229, 231]. Note: the legend in (a) applies to all plots.

Although variables such as irradiation temperature, dose rate, and initial microstructure can influence defect evolution, their impact is modest under the present conditions. For instance, loop evolution has been reported to be relatively insensitive to temperature within the 300–375 °C range [55], and while dose rate can have an effect [56], it becomes negligible beyond loop saturation. Therefore, the agreement observed here strongly supports the conclusion that the dislocation loop characteristics in proton-irradiated 4PB samples made of SS 304L and SS 304LN are consistent with those from neutron-irradiated counterparts. This provides a solid foundation for using proton-irradiated materials in IASCC initiation studies.

The size of dislocation loops is another important factor to consider, as larger loops trap more interstitial atoms both within their cores and along their peripheries. Dislocation loops serve as preferential segregation sites for larger solute atoms such as Ni and Si, which tend to accumulate at the loop boundaries. Therefore, the loop size directly influences the capacity of these defects to host segregating atoms, potentially affecting the local chemistry, and contributing to radiation-induced segregation phenomena. Figure 7-1 (c) uses similar dataset from Figure 7-1 (a) but on the dislocation loops size. Given the reciprocal relationship between loop density and size, the dislocation loop diameters in this study range from 6 to 60 nm (spanning approximately one order of magnitude). The data from this study (blank and pink circles) show good agreement with literature values for neutron-irradiated conditions, for the same reasons outlined in the discussion of dislocation loop density.

*Cavities*

Cavities were characterized in the same regions where dislocation loops were examined representing similar damage conditions. Following a similar approach to that used for dislocation loops, literature data on cavity formation in neutron irradiated austenitic stainless steels exposed to PWR-relevant irradiation, were reviewed. As seen in Figure 7-2, the available data on cavities at temperatures ranging from 300 to 375 °C are relatively limited compared to those for dislocation loops. This is because cavity formation is generally suppressed at PWR-relevant irradiation temperatures. In this study, cavities were observed at low densities, on the order of $7.47 \times 10^{20}$ $m^{-3}$ in SS 304LN, while SS 304L-R exhibited a higher density of $7.45 \times 10^{21}$ $m^{-3}$. Although cavity formation can lead to swelling and microstructural degradation, it is not typically a concern at low irradiation temperatures (< 0.3 $T_M$). The swelling resulting from cavities was relatively low 0.04% for SS 304L-R and 0.02% for SS 304LN rendering little concern to dimensionality.

As shown in Figure 7-2 (a), literature data on cavity densities at PWR-relevant conditions generally span from $10^{20}$ to $10^{24}$ $m^{-3}$, that is a wider range compared to dislocation loops, in the low-temperature regime (≤ 10 dpa). The figure shows three regimes when compared with dpa levels, the one with high density for those data beyond 10 dpa, almost no presence for those data below 3 dpa, and the intermediate for the region of 3 – 10 dpa where most of SS 304L fall including the proton-irradiated samples of this study. Mostly all SS 304L exhibited cavities densities in the order of $10^{21}$ except from two points just above the $10^{22}$ those are coming from fast neutron exposure [227].

However, a good agreement between the proton-irradiated samples with other SS 304 and SS 304L counterparts in the plot provides confidence about the validity of proton-irradiated results. The results shows also a good agreement in general with the dataset and specifically with

those irradiated by fast neutrons [227, 233] as the irradiation with fast neutrons usually occur at dose rate ranging from $10^{-7}$ to $10^{-6}$ dpa/s that is between 4 and 40 times lower than those used in the proton irradiation in this study ($3.8 \times 10^{-6}$ dpa/s).

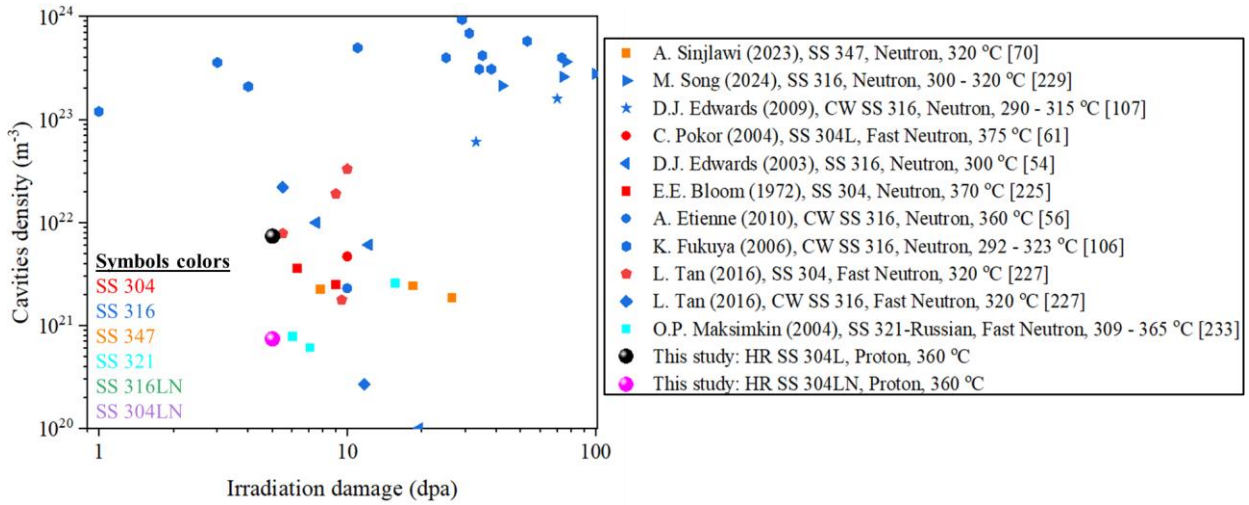


(a)

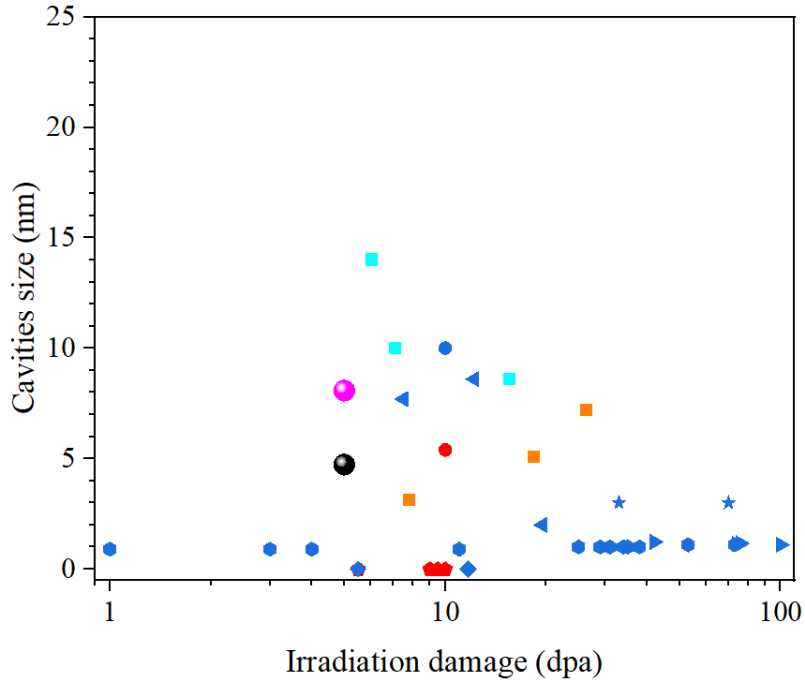


(b)

Figure 7-2 The comparison between the cavities obtained from this study and the literature on austenitic stainless steels irradiated over a range of temperatures of 300 - 375 °C, for (a) cavities density (b) and cavities size [54, 56, 61, 70, 106, 107, 225, 227, 233]. Note: the legend in (a) applies to all plots.

The cavities size shows almost reverse relation, those with high density exhibit low cavity size that is lower than a nm as seen in Figure 7-2 (b). Similar to the cavity density number, the size also follows the same trend along with other SS 304 and SS 304L that is the range of size are varies between 1 – 10 nm and the proton-irradiated samples reside well among the literature data on SS 304.

*Radiation-induced segregation and precipitation*

Radiation-induced segregation (RIS) profoundly alters GB chemistry in austenitic stainless steels, creating a local environment that promotes intergranular attack under PWR conditions. The contribution of RIS to IASCC initiation is attributed to various processes such as irradiated-induced Cr depletion at the GB which occurs via inverse-Kirkendall diffusion [77]. This leads to the formation of narrow Cr-depleted zones, only a few nanometers wide, which may be insufficient to sustain GB oxidation and thereby reduce strength under PWR conditions [184]. In austenitic stainless steels, Cr depletion typically can drop below the critical threshold (believed to be ~ 12 at.%) for formation of a protective film. Moreover, RIS is responsible of segregation of minor impurities such Si at the GB.

RIS profiles in this study were characterized at multiple GBs at depths ranging between 180 and 250 nm from the surface, with the exception of one GB in SS 304L-R, where segregation was detected at approximately 680 nm (this deeper measurement was retained as a reference for RIS measurements at shallower distances from the crack tip, since such regions may lie outside the oxygen diffusion zone but may still be affected by diffusion around the oxidized region). The changes in Cr, Ni, and Si concentrations were quantified and compared with published data for neutron-irradiated austenitic stainless steels under PWR-relevant

conditions. The percent change in composition was defined as the difference between the peak GB concentration and the matrix (or pre-irradiation) composition.

In this study, Cr depletion at the grain boundaries reached approximately -5.5% in SS 304L-R and around -4% in SS 304LN. Ni enrichment ranged from 3.4% to 7.5% in SS 304L-R and from 3.7% to 4.6% in SS 304LN, with one GB showing a notably higher value of 13.8% (the one from sample N at a distance of 210 nm from the GB oxide tip). Similarly, Si exhibited enrichment levels between 2.4% and 3.5% in SS 304L-R and between 2.7% and 3.7% in SS 304LN, with a corresponding increase to 7.1% at the same GB where Ni enrichment was elevated. Such variation in RIS concentrations across different GB is known and typically arises from a combination of factors. However, under otherwise identical irradiation conditions, microstructural features, particularly GB morphology and roughness, are likely the dominant contributors to the non-uniform segregation behavior observed along the GB planes [85].

To assess RIS behavior in proton-irradiated 4PB specimens, the results were compared with literature data as a function of displacement damage, in (dpa), as shown in Figure 7-3. Specifically, Figure 7-3 (a) shows Cr depletion at GBs in various neutron-irradiated austenitic stainless steels, including CW SS 316 and SA SS 304, irradiated at temperatures between 288 and 320 °C [54, 106, 108, 169, 227, 229, 234, 235, 236]. These data are plotted alongside simulation results modeling RIS evolution in PWR environments [227, 237]. Similarly, Figure 7-3 (b) and (c) present Ni and Si segregation trends as a function of dpa. Both experimental and simulated datasets suggest that RIS reaches a threshold near 5 dpa. The measurements from this study, represented by black dots for SS 304L-R and pink dots for SS 304LN, closely follow the established trends from both experimental and modeled literature results. A closer inspection of the low-dose regime, shown in Figure 7-3 (d), confirms that the RIS trends observed in proton-

irradiated 4PB samples align well with simulation predictions (dashed black and green lines). It is worth noting that the Grain Boundary-Interstitial-Modified Inverse Kirkendall (GiMIK) model tends to predict steady-state RIS more rapidly than is observed experimentally, likely due to its use of constant sink strength and dislocation sink density parameters [237].

Another observation is that RIS behavior typically exhibits some scatter in the data, specifically in Ni (Figure 7-3 (b)), due to RIS sensitivity to various analytical and microstructural factors, including GB type and character (e.g., tilt), TEM foil thickness, and the EDS signal acquisition method, particularly at doses below the saturation level. Given that RIS is strongly influenced by irradiation temperature, dose rate, and microstructure, the similarity between the RIS behavior in the 4PB proton-irradiated samples and that observed under neutron irradiation supports the validity of the current irradiation methodology. Noting that irradiation temperature at 360 ±10 °C was selected to simulate neutron damage in proton irradiation studies as previously proposed in Ref. [238].

Ni and Si also form clusters and precipitates such as Ni-Si clusters and precipitates such as $Ni_3Si$ and G-phase under neutron irradiation. However, the situation is different under proton irradiation where the observation of precipitate is more challenging. This does not mean they don't form under proton-irradiation, however, they may not or may form with sizes very small to be captured with TEM. In this study, we observed Ni-Si clusters as presented in Chapter 6 but no evidences of precipitates were observed.

Even though neutron irradiation occurs at 280–340 °C, $Ni_3Si$ precipitates still form because the low flux and long exposure times allow radiation-enhanced diffusion to reach the critical conditions for precipitation. In contrast, proton irradiation at 360 °C, despite being slightly hotter, produces a non-equilibrium environment with insufficient time and solute transport for

Ni3Si to grow into observable precipitates. This highlights the key role of dose rate and irradiation time, not just temperature.

Given the agreement between the irradiation-induced microstructure and corresponding hardening behavior observed in this study with literature data, it can be concluded that the irradiation conditions employed here were appropriate. This, in turn, provides a high degree of confidence to move forward with assessing whether proton-irradiated 4PB specimens can reliably serve as surrogates for neutron-irradiated samples in IASCC investigations, a question that will be addressed in the following section.

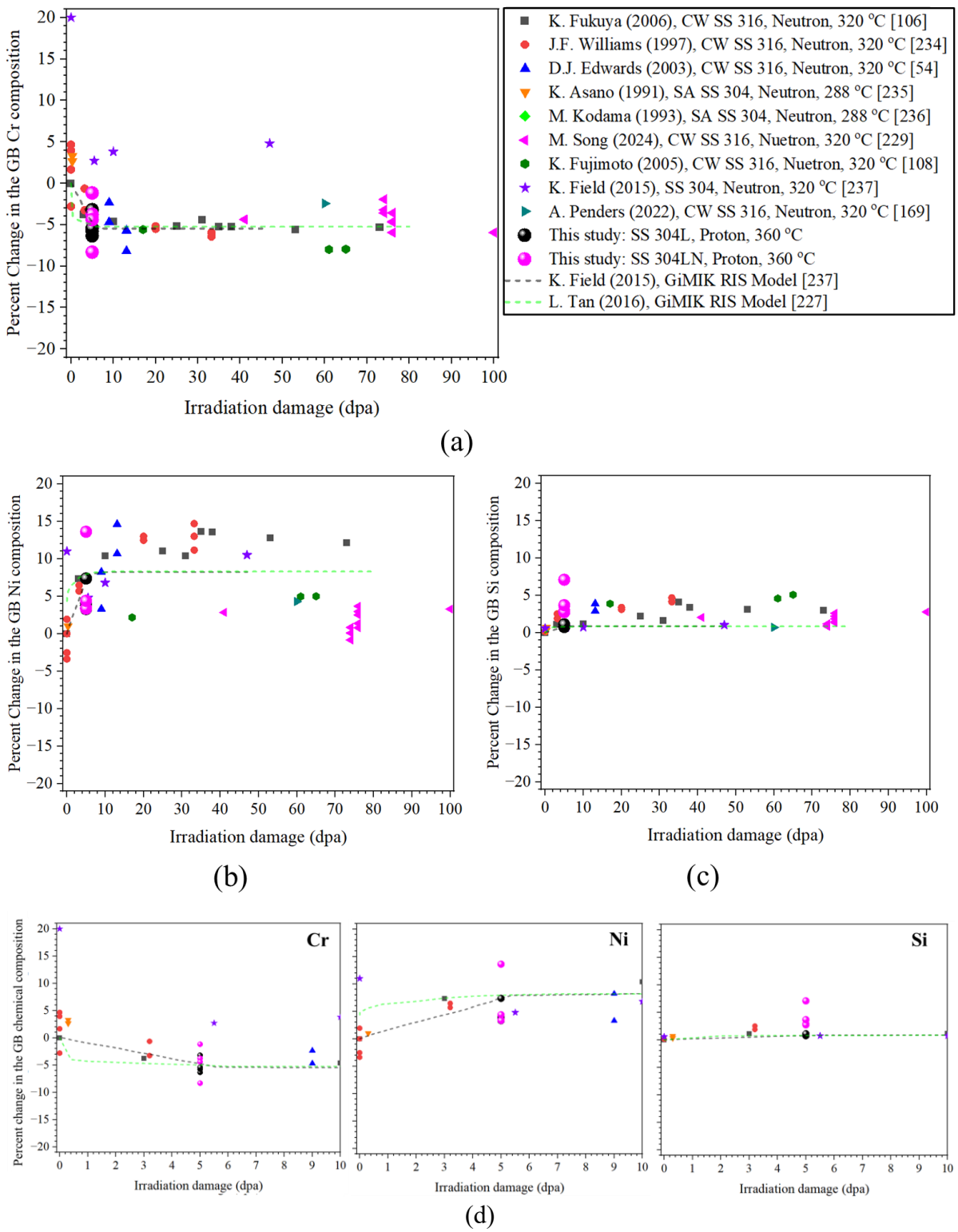


Figure 7-3 A comparison between the this study RIS data and literature values on neutron irradiated austenitic stainless steels [227] for the percent of GB (a) depletion in Cr, (b) enrichment in Ni, (c) enrichment in Si, and (d) comparison at low dpa regime for Cr, Ni, and Si [54, 106, 108, 169, 227, 229, 235 - 237]. A simulated data using Grain Boundary-Interstitial-Modified Inverse Kirkendall (GiMIK) model by F. Kevin et. al. [237] is presented in black dashed line and L. Tan et. al. [227] in green dashed line. Both experimental and simulation data show saturation in RIS at 5 dpa. Note: the legend in (a) applies to all plots.

### *7.1.2 Radiation hardening*

Irradiation hardening is another critical parameter for comparison, as it reflects how the defect evolution discussed in the previous section contributes to the increase in hardness and yield strength of the material. While an increase in hardness is generally considered beneficial, this is not the case for core internals in PWRs. In such components, irradiation-induced hardening promotes heterogeneous rather than homogeneous deformation, which can degrade oxidized grain boundaries and ultimately lead to crack initiation.

As previously outlined, a specific procedure was employed to estimate the irradiated yield strength of SS 304L-R and SS 304LN at the 4PB test temperature of 340°C. This involved measuring room temperature hardness values from the irradiated surfaces, converting these values to YS using the Busby equation (Eq. 4.13) as detailed in Chapter 4 [118], and then applying literature data to estimate the YS at 320°C. Subsequently, an extrapolation technique was used to predict the irradiated YS at 340 °C. Uncertainties associated with these measurements and calculations were systematically evaluated, resulting in estimated YS values of $846 \pm 42$ MPa and $907 \pm 45$ MPa at room temperature for SS 304L-R and SS 304LN, respectively.

To validate the room temperature irradiated YS derived from hardness measurements, these values were compared with literature data on neutron-irradiated austenitic stainless steels, as shown in Figure 7-4. This figure plots the change in YS (before and after irradiation) as a function of the change in hardness, with the current study's results overlaid as red dots (SS 304L-R) and green boxes (SS 304LN). The data points from proton-irradiated 4PB samples fall within the 95% confidence bounds of the literature dataset, indicating strong consistency with previously reported trends.

Building upon this validation, the extrapolated YS values at 340 °C were compared with a broader set of literature data for neutron-irradiated austenitic stainless steels, including SS 316, SS 304, SS 304L, and SS 347, as shown in Figure 7-5 (a). The inclusion of cold-worked SS 316 is justified by the fact that the alloys examined in this study were initially hot-rolled, resulting in mechanical properties between cold-worked and solution-annealed conditions. This explains the slightly higher irradiated YS observed for SS 304L-R and SS 304LN compared to SS 304, SS 304L, and the Materials Reliability Program (MRP) curve [239] for SS 304 (black dashed line). Nevertheless, the irradiated YS remains below that of CW SS 316, likely due to differences in microstructure and chemical composition.

A more focused comparison with only SS 304 and SS 304L is shown in Figure 7-5 (b), while Figure 7-5 (c) highlights data at low irradiation doses of SS 304 and SS 304L only. Most of the literature data for SS 304 and SS 304L were obtained from solution-annealed heats prior to irradiation. Despite this, the agreement with the present proton-irradiated 4PB samples remains strong. Notably, the data show a saturation trend beyond ~15 dpa, indicating that YS values below this threshold are more sensitive to variations arising from microstructural evolution and irradiation conditions. For example, data from a decommissioned PWR (golden diamond) show variations in YS from ~800 MPa to nearly 850–900 MPa as the irradiation dose increased from 5 to 11 dpa.

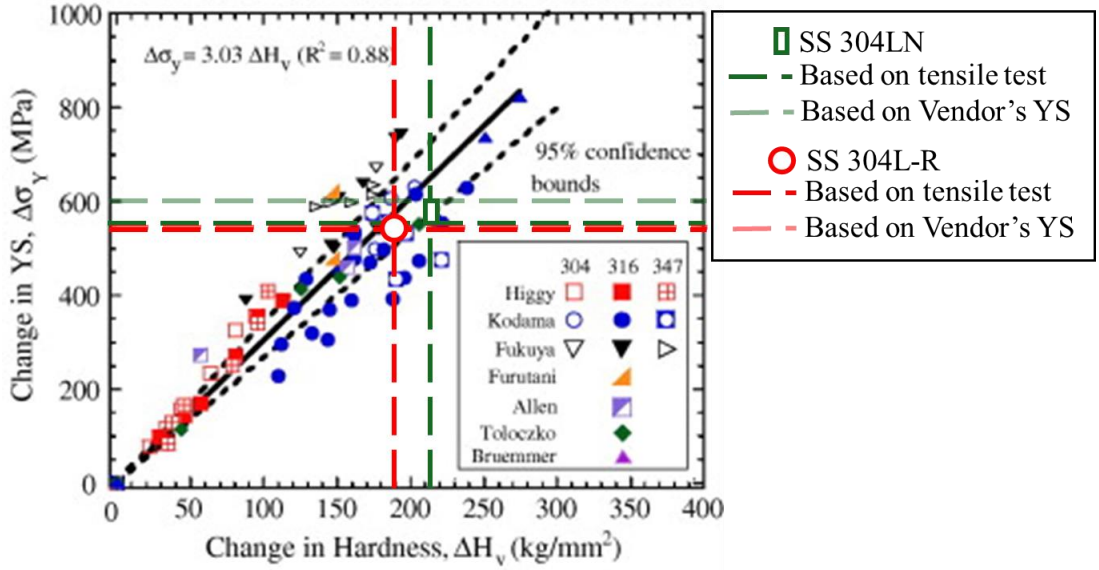


Figure 7-4 A comparison between the hardness measurement from proton-irradiated 4PB samples with experiment-based literature data for neutron-irradiated austenitic stainless steel [118].

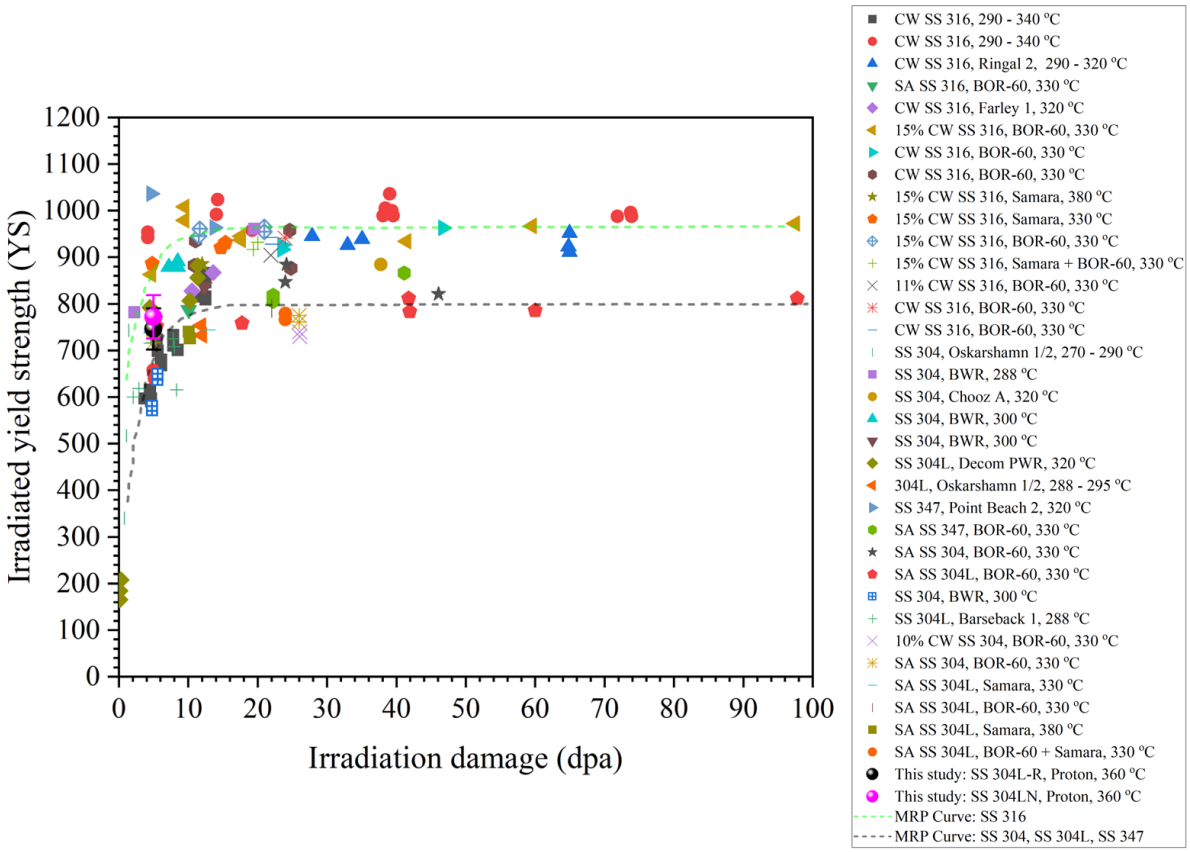


(a)

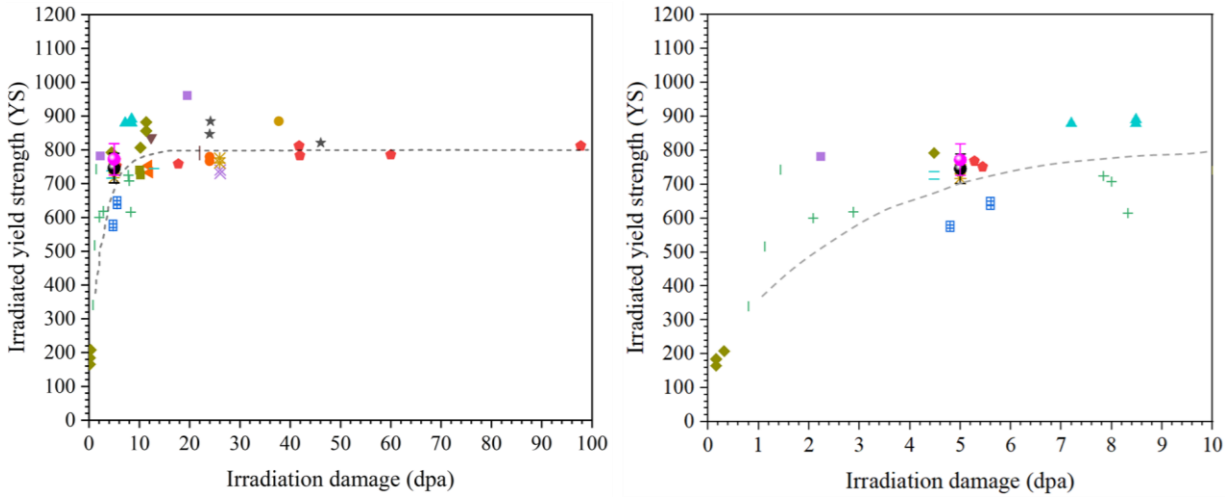


(b) (c)

Figure 7-5 Effect of irradiation dose on measured tensile yield strength for neutron-irradiated austenitic stainless steel of types SS 316, SS 304, SS 304L, and SS 347 irradiated in LWRs and BOR-60 fast reactor at irradiation temperatures ranging from 275 to 380 °C. (b) Only SS 304 and SS 304L were considered for more specific comparison, and (c) at low dpa regime of the data from SS 304 and SS 304L. The data were replotted from Ref. [113].

The proton-irradiated YS values from this study are in excellent agreement with various fast-neutron-irradiated SS 304L datasets, including SS 304L irradiated in BOR-60 (red pentagon), SS 304L from a decommissioned PWR (golden diamond), solution-annealed SS 304L irradiated in BOR-60 (golden star), and SS 304L irradiated in the Samara PWR (cyan dash). These neutron-irradiated alloys exhibited YS values ranging from 700 to 800 MPa at 320–330 °C, aligning closely with the results from this study.

The observed agreement can be attributed to several key factors. First, the hardness measurements from the proton-irradiated surfaces aligned well with literature data (Figure 7-4), establishing a reliable foundation for further analysis. Second, the conversion from hardness to YS using the Busby equation was carefully implemented, with error propagation analyses (Chapter 5) ensuring the robustness and accuracy of the reported values. This treatment of uncertainties lends high confidence to the converted YS data. Finally, the subsequent estimation of YS at 320 °C and extrapolation to 340 °C incorporated these uncertainties, yielding results that are both internally consistent and well-supported by literature comparisons.

Together, these comparisons suggest two key conclusions: (1) the irradiation-induced hardening observed in this study is comparable to that reported for neutron-irradiated austenitic stainless steels; and (2) the methodology used to derive the irradiated YS at 340 °C, from hardness measurements through to extrapolation, is valid and reliable.

*Yield strength estimation from the microstructure*

The yield strength (YS) of materials can also be estimated based on their microstructural state and chemical composition. Superposition yield strength approach accounts for the combined contributions from lattice friction stress ($\sigma_{Fe}$), solid solution strengthening ($\sigma_{ss}$), and GB strengthening ($\sigma_{gb}$), as well as irradiation-induced strengthening from dislocation loops ($\sigma_{loops}$) and cavities ($\sigma_{cavities}$). Additional contributions from features such as precipitates, dislocation networks, and clusters may also be considered; however, these were not observed in this study. A superposition equation ($\sigma_{R\text{-}SSR}$) proposed by P. Zhu et. al. [124] is used to estimate the YS from the microstructure, the equation is divided into two components, the weak hardening contributor such includes lattice stress and solid solution strengthening and given by:

$$\sigma_y = \sqrt{\sigma_{\text{Fe}}^2 + \sigma_{ss}^2} + \sqrt{\sigma_{\text{cavities}}^2 + \sigma_{\text{Loops}}^2 + \sigma_{gb}^2} \tag{7.1}$$

Where $\sigma_{Fe}$ is the lattice friction stress that is typically 50 MPa [240] for austenitic stainless steels, $\sigma_{gb}$ is the GB strengthening, $\sigma_{ss}$ is the solid solution strengthening, $\sigma_{cavities}$ and $\sigma_{Loops}$ are the hardening induced by the irradiation defects. In this equation, the cavities and loops contributions were considered strong while others were weak.

For the Hall–Petch relationship, the equation is given by:

$$\sigma_{\text{gb}} = K_y D^{-0.5} \tag{7.2}$$

Where $K_y$ is Hall–Petch coefficient, a material-dependent constant, and $D$ is the grain size. Since the present study focuses on the effect of nitrogen, a nitrogen-dependent correlation is particularly relevant. S.V. Astafurov et al. [241] developed the following empirical equation for nitrogen-dependent GB strengthening is given by:

$$K_N\,(\mathrm{MPa}\cdot\mu\mathrm{m}^{-0.5}) = 9484\,N^2 + 1256\,N + 366 \tag{7.3}$$

Where $N$ is the nitrogen concentration in wt.%. Using equations 7.2 and 7.3, the $\sigma_{gb}$ was calculated as 106 MPa for SS 304L-R and 163 MPa for SS 304LN. The solid solution strengthening was calculated using:

$$\sigma_{\mathrm{ss}} = \left(\beta_C^2 x_C + \beta_N^2 x_N\right)^{\frac{1}{2}} \tag{7.4}$$

Where $\beta_i$ is the strengthening coefficient for the solute element (1000 MPa/at.% for C [242] and 1500 MPa/at.% for N [243]) and $x_i$ is the atomic fraction of the element in solid solution. The results yield $\sigma_{ss}$ values of 234 MPa for SS 304L-R and 253 MPa for SS 304LN.

The $\sigma_{cavities}$ and $\sigma_{Loops}$ were calculated using equations 2.9 ($\Delta\sigma_y = \alpha\mu b\sqrt{Nd}$), 2.11 for hardening coefficient (α). The calculations yield $\alpha_{Loops}$ of 0.4672 and $\sigma_{Loops}$ of 513 MPa in SS 304LN, and $\alpha_{Loops}$ of 0.4994 and $\sigma_{Loops}$ of 497 MPa in SS 304L-R. Similar calculations were used to estimate the hardening from cavities, equation 2.13 used to calculate α from cavities that results in 0.9449 and 0.6991 for SS 304LN and SS 304L-R respectively. These calculations yield a $\sigma_{Cavities}$ of 141.4 MPa and 252 MPa for SS 304LN and SS 304L-R, respectively.

A comparison between the superimposed YS from microstructural contributions ($YS_{S\text{-}RSS}$) and the hardness-derived yield strength ($YS_{Hv}$) reveals some discrepancies. For SS 304L-R, $YS_{S\text{-}RSS}$ (Equation 7.1) was calculated at 685 MPa, while the $YS_{Hv}$ was estimated at 846 ± 42 MPa, resulting in a difference of 161 MPa, corresponding to an increase of approximately 21%.

Conversely, for SS 304LN, $YS_{S\text{-}RSS}$ was calculated at 711 MPa whereas the $YS_{Hv}$ was of 907 ± 45 MPa, indicating the difference of 196 MPa which constitutes in decrease of 24%.

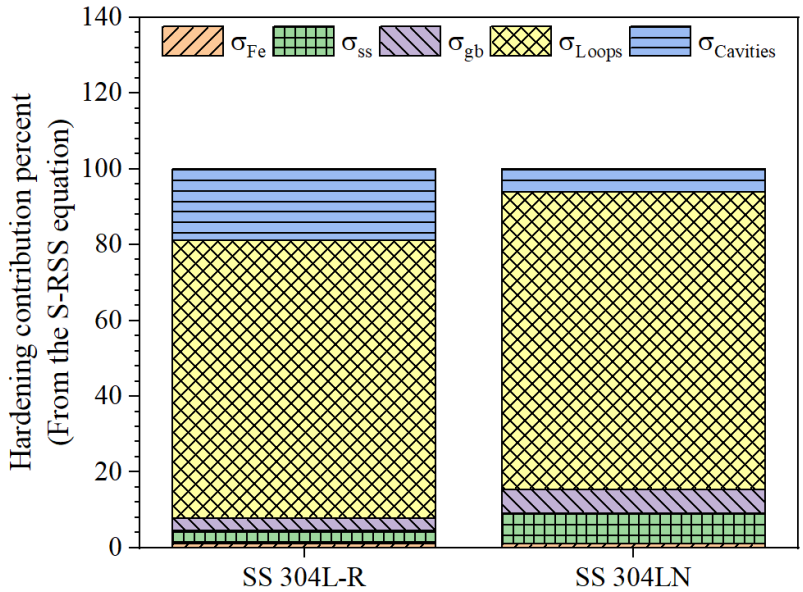


Figure 7-6 The contribution of microstructural features, in percent, to the hardening of materials based on the calculated YS from S-RSS superimposed equation covering the contribution of lattice friction stress, solid solution strengthening, GB strengthening, and irradiation hardening on the yield strength of SS 304L-R and SS 304LN.

The percent of contributions of various microstructural features to the total hardening are shown in Figure 7-6 and the summary of the calculated contributions are listed in Table 7-1. The majority of the hardening arises from irradiation-induced defects, particularly dislocation loops, which account for ~ 79% from the $YS_{S\text{-}RSS}$ and 57% from $YS_{Hv}$ in SS 304LN, and ~ 73% of the sum of all contributors $\Sigma(\sigma_i)$ and 59% of $YS_{Hv}$ in SS 304L-R. It is well established that irradiation can increase YS by approximately 3–5 times, mainly due to irradiation-induced microstructural changes. These include not only dislocation loops and lines but also large cavities, nanocavities, precipitates, and RIS clusters. While dislocation loops are recognized as a dominant contributor to hardening, reported values exceeding 50% are likely overestimates. Such overestimations are often attributed to Rel-rod imaging artifacts, which produce wide variations in contrast, making accurate loop quantification challenging. Therefore, although $YS_{S\text{-}RSS}$ and $\Sigma(\sigma_i)$ values are in

reasonable agreement with $YS_{Hv}$, these calculations carry significant uncertainty. Reliable application of this method as a comparison tool between macroscopic YS (measured or calculated) and microstructurally derived YS requires detailed TEM characterization and rigorous statistical analysis.

Table 7-1 Summary of calculated YS from the microstructural features in SS 304LN and SS 304L-R.

| **Hardening contributor** | **SS 304LN (MPa)** | **SS 304L-R (MPa)** |
|---|---|---|
| $\sigma_{Fe}$ **[240]** | 50 | 50 |
| $\sigma_{gb}$ | 163 | 106 |
| $\sigma_{ss}$ | 145 | 107 |
| $\sigma_{Loops}$ | 513 | 497 |
| $\sigma_{cavities}$ | 141 | 252 |
| $\sigma_{R\text{-}RSS}$ at 25 °C (Eqn 7.1) | 710 | 685 |
| $\Sigma(\sigma_i)$ at 25 °C* | 1012 | 1012 |
| $\sigma_{Hv}$ at 25 °C | 907±46 | 846±43 |
| $\%(\sigma_{Hv} - \sigma_{R\text{-}RSS})$ | -10.9% | -17.9% |
| $\%(\sigma_{Hv} - \Sigma\sigma_i)$ | +27.9% | +22.5% |
| ** The sum of hardening contributors (i; refers to contributor type)* | | |

Several other factors contribute to the observed differences. The coefficients used in the $YS_{S\text{-}RSS}$ calculations, such as those in the Hall–Petch relationship and solid solution strengthening, are not universally fixed and often vary across references, even for materials with similar fcc structures. These constants may be derived from experimental measurements or regression-based models, introducing variability.

Figure 7-7 presents a sensitivity analysis conducted to investigate the influence of dislocation loop size and density on the hardening coefficient (α), which reflects the resistance to dislocation motion imposed by irradiation-induced obstacles within the matrix. A higher α value indicates greater resistance to dislocation movement, resulting in a harder matrix and an increased macroscopic yield strength. The analysis reveals that α is highly sensitive to variations

in dislocation loop size. This sensitivity arises because, in Equations 2.11 and 2.12, α is directly related to the D as follows:

$$\alpha \propto \frac{A(D,N)}{\sqrt{ND}} \ln\left(\frac{D}{r_0}\right) \tag{7.5}$$

The analysis in Figure 7-7 indicates that varying N while keeping the D constant, represented by movement along the x-axis in Figure 7-7 (a) and (b), results in minimal change in the hardening coefficient. In contrast, increasing D while holding N constant, corresponding to movement along the y-axis, produces a significant increase in α. This suggests that when the loop density is comparable, the influence of loop size becomes more dominant. In the case of SS 304L-R, this enhanced contribution from D could explain why the overall hardening remains comparable between the two alloys.

It is important to note that the measurement of loop size using the Rel-rod technique carries relatively high uncertainty. This is primarily due to pixel contrast variations, which hinder the precise determination of loop length using image analysis tools such as ImageJ®. However, the quantification of loop density is subject to lower uncertainty, as the contrast more clearly differentiates between dark regions (indicating the absence of loops) and bright short lines (signifying loop presence).

In this study, dislocation loop density and size were quantified manually using ImageJ® across the entire TEM image field rather than using the conventional approach of sampling a quarter of the image and multiplying by four, a method known to risk underestimation or overestimation. While counting all loops does not eliminate the potential for error entirely, it minimizes systemic bias in quantification. Based on this rigorous methodology, the observed differences in both loop density and size are considered notable and likely attributable to

compositional differences, primarily the higher nitrogen content and, to a lesser extent, silicon, in SS 304LN compared to SS 304L-R.

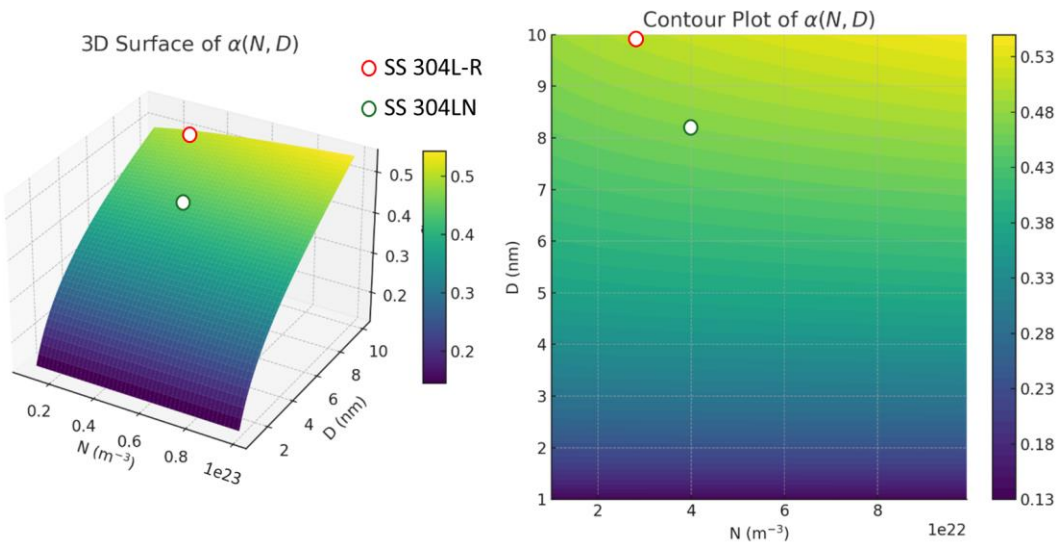


(a) (b)

Figure 7-7 The sensitivity of hardening coefficient ($\alpha_{Loop}$) to the change in dislocation loops size and density in (a) 3D surface plot and (b) contour plot for better view showing a high sensitivity for loops size.

### *7.1.3 The deformation mechanism: dislocation channels characteristics*

As discussed previously in Section 7.1.2, the difference in irradiation-induced hardening between SS 304LN and SS 304L-R was not substantial. Since no significant hardening differences were observed from dislocation loops evolution, the cavities contributed little due to their low swelling values, and the SFE calculations showed no difference, a corresponding similarity in the deformation mode is expected, specifically, in the behavior of dislocation channels.

The characteristics of DCs, including their density, spacing, and height, were outlined in Section 6.3. Consistent with the trends observed for irradiation-induced defects, the difference between SS 304LN and SS 304L-R in DC features is minimal. The percent difference in average DC spacing was negative, indicating that SS 304LN had narrower spacing (15% lower),

consistent with its higher channel density. On the other hand, the channel height, a key parameter influencing the number of dislocations in each channel, showed only a modest difference (10%). Although this corresponds to differences of 12 nm in weighted height and 11 nm in average height, such values are not considered significant given the sample size, which is sufficient to support the conclusion that the difference in height is minimal. Similarly, the 22% difference in the number of dislocations per channel is not considered substantial due to the large uncertainty associated with its estimation, which depends on both channel height and crystallographic orientation.

An estimation of the average strain within the channel was calculated from equation 2.17 ($\gamma = h/w$). The strain per channel was then calculated under the assumption of a single grain containing one active channel that accommodates the entire macroscopic strain. Based on this approach, the calculated strains were 2.51% for SS 304L-R and 3.19% for SS 304LN, corresponding to about 9% and 33% higher than the measured strains of 2.28% and 2.30%, respectively. Overall, the calculated channel strains from the average DCs height, number of dislocations, and spacing, do not differ substantially from the measured values. The observed discrepancies are mainly attributed to uncertainties in calculating dislocation channel characteristics, as well as the simplifying assumption used in the calculation. An accurate comparison between macroscopic and localized strain requires characterizing a defined surface area and extracting the relevant channel features. The channel height and number of dislocations per channel obtained from AFM and EBSD, while the spacing is measured from TEM, and the channel density is determined within the specified area. Using the Schmid factor for each activated slip system, the localized strain can then be correlated with the corresponding macroscopic strain. This methodology further requires hardness indentations to quantify the

macroscopic strain within the examined region. In irradiated stainless steels, more than 90% of the macroscopic strain is accommodated by dislocation channels [83]. Was et al. [244] further reported that a single channel may sustain localized strain exceeding 100%; however, this value represents the strain confined within the channel of a hardened grain and is governed by the extent of stress relaxation that occurs in the grain through the channel.

Examples of surface DC morphology, along with comparisons to neutron-irradiated samples, are presented in Section 7.2.2 through surface cracking morphology observations. Overall, the difference in DC evolution between the two alloys was minimal, consistent with the observations of their irradiation microstructures.

## 7.2 IASCC susceptibility

The evaluation of IASCC susceptibility requires that testing be conducted under conditions that simulate the PWR environment. Many such tests have been developed to achieve this goal as reviewed in Chapter 2. One metric used to evaluate the IASCC susceptibility is the stress to initiate cracking as a function of damage level (dpa). Over the years, a significant database has been created to identify a threshold stress below which IASCC does not occur.

This section will analyze the proton irradiated 4PB results for the IASCC initiation against literature data. Beyond this metric, the cracking behavior and crack morphology, crack tip chemistry and the association of cracks with dislocation channels will be compared to that in the literature for neutron irradiated samples to establish the validity of the 4PB test results.

### *7.2.1 IASCC initiation stress*

To compare the IASCC initiations behavior in the 4PB experiments to that from specimens irradiated in reactor, the database from literature 4PB tests [70, 170, 171], other testing methods such as O-ring, C-ring, constant load, and SSRT [245, 246, 247, 248, 249, 176, 250, 251, 252]

has been plotted as initiation stress (in terms of the %YS) as a function of damage level, as shown in Figure 7-8. This figure represents a highly valuable database for studying IASCC initiation in PWR environments, containing over 300 data points that reflect extensive efforts spanning many years. These data were collected either during the service life of reactor components or later after their decommissioning and re-fabrication into laboratory specimens. To date, the 4PB approach has been validated almost exclusively on neutron-irradiated materials [70, 137, 170, 171, 194], yielding initiation stresses in line with literature as presented in the plot with red symbols.

As shown in Figure 7-8, despite the significant scatter resulting from variations in testing methods (O-ring, C-ring, SSRT, constant load, 4PB), alloy compositions (304, 304L, CW 316, 347), mechanical or thermal processing histories, and exposure durations, the results of this study generally align well with the broader IASCC database. The underlying causes of such variations and their implications on the IASCC response were thoroughly discussed in Chapter 2. This behavior is largely attributed to the stochastic nature of IASCC, observed not only in laboratory tests but also in service conditions, where failures have been reported in certain components, particularly baffle-former bolts (BFBs), while adjacent ones remained unaffected. Nevertheless, current efforts are directed toward identifying the minimum stress necessary for IASCC initiation, which represents the key parameter in the %YS versus dpa relationship.

To overcome the issue of data scatter, particularly that arising from O-ring and C-ring testing methods, 4PB testing offers a superiority due to its relatively short duration and interrupted nature. While some variation still exists, it is considerably less pronounced. This allows for repeated testing at each %YS level, enabling verification of results and the acquisition of replicate data, which enhances confidence in the reported outcomes. As a result, our samples

and their corresponding replicas show good agreement with other data points in the database as shown in Figure 7-8 (b).

Current understanding of IASCC in austenitic stainless steels under PWR-relevant, low-dpa conditions holds that a relatively high stress is required to initiate cracking [20, 49]. Our results match this: both alloys began to crack at 70 % YS. The greater resistance of sample N7 (failure at 89 % YS) reflects the inherently stochastic nature of IASCC and falls in line with Tanguy's observations on CW SS 316 (orange triangle), where failures occurred at 90–100 % YS at 4 dpa. Takakura's data on CW SS 316 (soft-gold diamond) likewise show failures between 70–80 % YS at around 6 dpa (Figure 7-8 (b)). Sinjlawi's data on SS 347 irradiated to 7.8 dpa show failure at 80%YS (Figure 7-9). By comparison, Swaminathan's 4PB specimen (red rectangle), a SA SS 304L irradiated to 5.4 dpa in BOR-60, exhibited the lowest IASCC initiation stress in the low-dose regime, failing at 60% YS [171], as shown in Figure 7-9. The specimen was exposed to 160 h during the first two testing steps, which may have been an additional factor contributing to such early initiation at 5 dpa. Overall, at damage levels below 10 dpa, there are 19 recorded failure points: one occurred at 60%YS, five at 70% YS (including three from proton-irradiated samples), seven at 80% YS (two from proton-irradiated samples), and the remaining six at higher stress levels (with one from proton irradiation). Despite variations in test type and alloy, the results of this study show good overall agreement with the neutron-irradiated data, supporting the observation that austenitic stainless steels exhibit similar IASCC susceptibility when subjected to comparable environmental and irradiation conditions.

In the plot of Figure 7-8, only 51 data initiation points are from 4PB experiments, constituting a small fraction of the total, and these points were accumulated through several research projects conducted over many years. In contrast, this study alone contributed 23 data

points or nearly half the number of data points available from neutron-irradiated 4PB. To date, the experimental data presented plot suggests that the threshold stress for IASCC initiation in austenitic stainless-steel components within PWR core internals is dose dependent. In the low irradiation regime (below 10 dpa), IASCC is generally not observed at applied stresses below 60%YS. Considering the previously defined uncertainty associated with IASCC initiation stress measurements, the findings of this study support the conclusion that the threshold stress for IASCC initiation in the low dpa regime lies within the range of 60–70%YS. However, as the irradiation increases, this threshold progressively decreases, reaching as low as 40% of the yield strength at doses of 24 dpa and higher as shown in the plot. From the available data the 4PB results align well with those from O-ring, C-ring and SSRT tests and display a similar stochastic scatter, as clearly shown in Figure 7-8. The validation of 4PB testing in this study therefore followed a "comparison approach" with literature results obtained using other testing methods. Ideally, a 4PB test conducted on a proton irradiated 304L sample and compared with a 4PB test (same environment and testing method) a neutron irradiated sample from the same block of 304L would provide the best verification of the capability of proton irradiation to produce the same IASCC behavior as neutron irradiation.

Figure 7-9 (a) shows failure stress for SS 304, SS 304L, and SS 304LN, restricting the comparison to alloys of nearly identical chemistry. Two plots are shown: one spanning a wide range of damage levels (left) and the other focusing on a narrower range. Among neutron-irradiated specimens, an SS 304L sample irradiated to 5.4 dpa [171] exhibited cracking at 60% YS. At while at 15 dpa, BFB SS 304 data indicated no failure up to 80% YS. Overall, most SS 304 grades failed within the 70–90% YS range, consistent with the trend observed in this study.

Figure 7-9 (b) shows the failure stress obtained only from 4PB testing, isolating the influence of the testing method by excluding data from alternative methods that impose different loading conditions. Among the neutron-irradiated specimens, one data point for SS 304L irradiated to 5.4 dpa [171] exhibited cracking at 60%YS. Additional data from Stephenson et al. [137] show two SS 304L samples irradiated to 5.5 and 10.2 dpa, failing at 80% and 70% YS, respectively. Another specimen irradiated to 47.5 dpa from the same study failed at 60% YS. Similarly, neutron-irradiated SS 347 samples (removed from BFBs [70]) at 7–11 dpa failed between 70–80% YS, within the failure range observed in the proton-irradiated samples of this study.

Unexpected results are often reported in IASCC testing. For instance, in the same SS 347 study, two samples irradiated to 26 dpa failed at 80% YS, which contradicts the general trend of increased IASCC susceptibility with higher irradiation dose. This discrepancy was attributed to different irradiation, loading, and operational history as these samples were removed from a different reactor than the others [70]. Moreover, field experience with BFBs from inspection and replacement campaigns [253] reveals that cracking does not always exhibit a clear dependence on dose or temperature. Some BFBs cracked at low dpa and temperature, while neighboring BFBs under nearly identical conditions remained uncracked.

An additional key factor in evaluating the reliability of the proton-based testing approach is the effect of high-temperature exposure time in the autoclave on IASCC initiation stress, as shown in Figure 7-10. This factor is especially important because the data in Figure 7-8 do not account for total exposure duration under elevated temperature and sustained loading. Prolonged exposure influences the extent of grain boundary oxidation, a process well-known to play a critical role in IASCC initiation. Only failure points were included in Figure 7-10, as 4PB testing

is known to produce failure consistently below the irradiated yield strength of the alloy. Therefore, the comparison is intentionally limited to failure points alone.

The exposure times for the specimens in this study ranged between approximately 160 and 240 hours, which places them within the same range as several datasets reported in the literature, as shown in Figure 7-10. More specifically, the proton-irradiated 4PB samples failed after exposure durations comparable to those reported for neutron-irradiated 4PB samples. Since exposure time is closely associated with grain boundary oxidation, the slight variations observed can be attributed to differences in microstructure and irradiation damage, yet they remain within an acceptable range.

A noticeable trend in the figure is the decrease in IASCC resistance with increasing exposure time, particularly beyond the 100-hour mark. The proton-irradiated 4PB specimens in this study (red and blue symbols) exhibit this declining trend, aligning well with existing literature data. This minimum failure stress indicates that, regardless of irradiation dose, no failure occurred below 40 %YS. At such a low stress level, resistance to cracking maybe due to the absence of DCs. Consequently, oxidized GBs are unlikely to fail without the involvement of DCs. Experience with 4PB samples irradiated in argon at high temperature suggests that DC formation typically develops above ~60 %YS [171]. However, further investigation is needed to determine the onset and evolution of DCs across the full range of stresses below the irradiated YS. Results from CERT testing provide valuable insight into the role of DCs at GBs, yet they do not clarify the contribution of low-stress DC activity to IASCC at stress levels well below the YS.

The initiation time to failure in this study was consistent with neutron-irradiated data, regardless of the testing method used (i.e., O-ring vs. 4PB), with the closest agreement observed

for neutron-irradiated 4PB specimens. The initiation time is governed by the period required for dislocation channels to form and intersect oxidized grain boundaries, where sufficient oxidation reduces the GB strength below the fracture threshold. Since both neutron- and proton-irradiated specimens exhibited similar time-to-failure trends, this suggests that the resulting microstructures were comparable, and straining in the same environment led to similar cracking behavior.

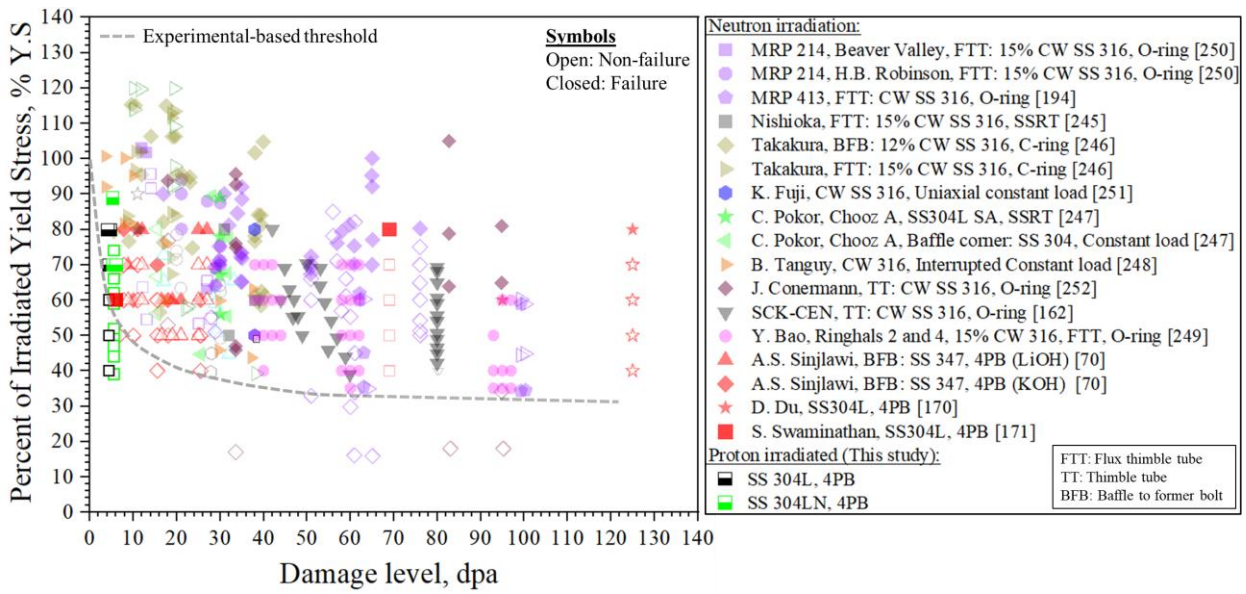


(a)

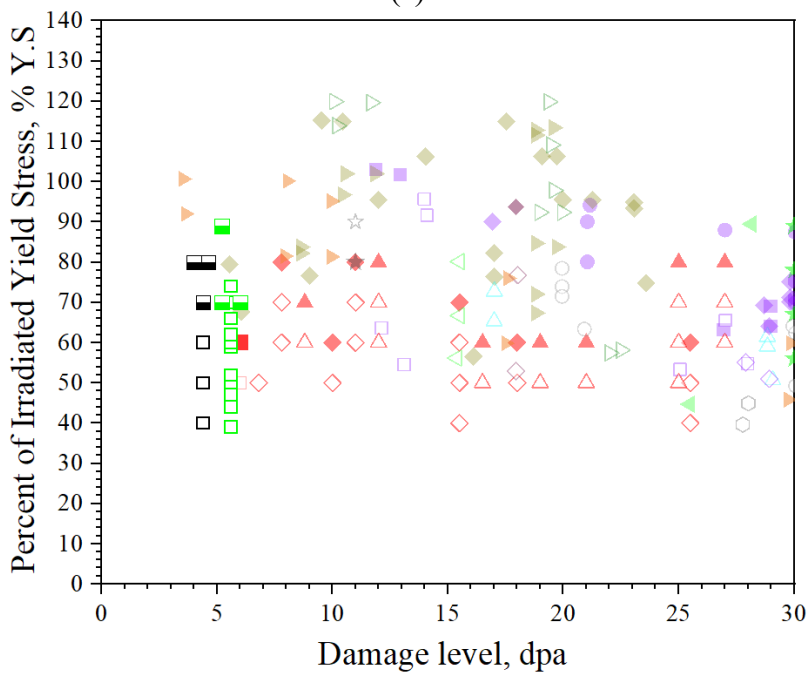


(b)

Figure 7-8 A comparison of results from proton-irradiated 304L and 304LN in LiOH to that in the literature for PWR primary water [70, 162, 170, 171, 176, 245 - 252], (a) and the same comparison focusing on the low dpa regime (b). Results from this project are shown in half-colored symbols. The data is offset slightly along the damage axis to eliminate points, therefore results from this study were all performed at 5 dpa.

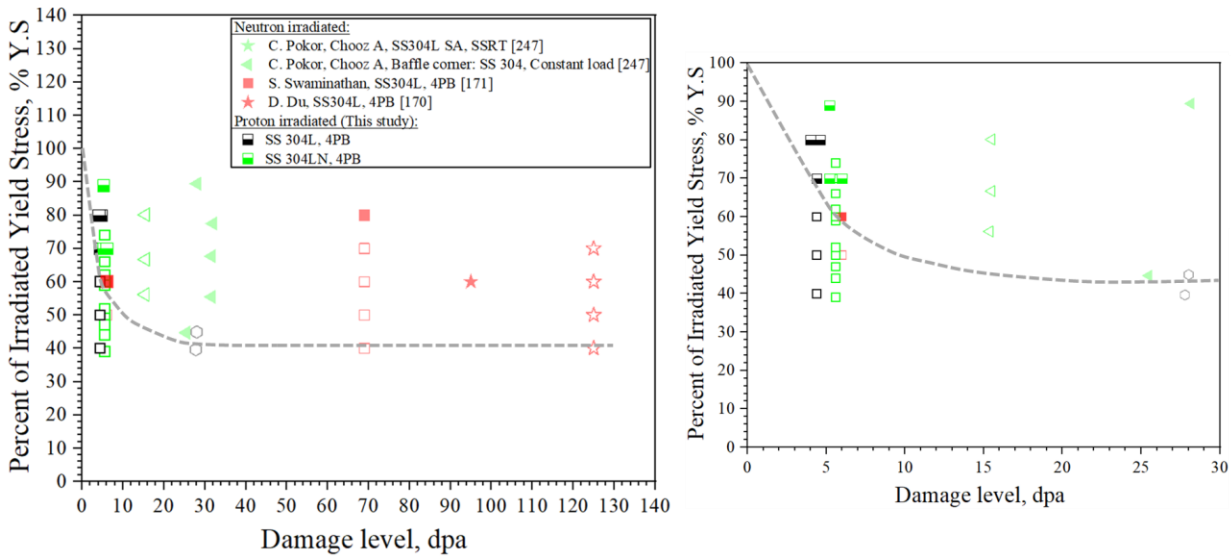


(a)

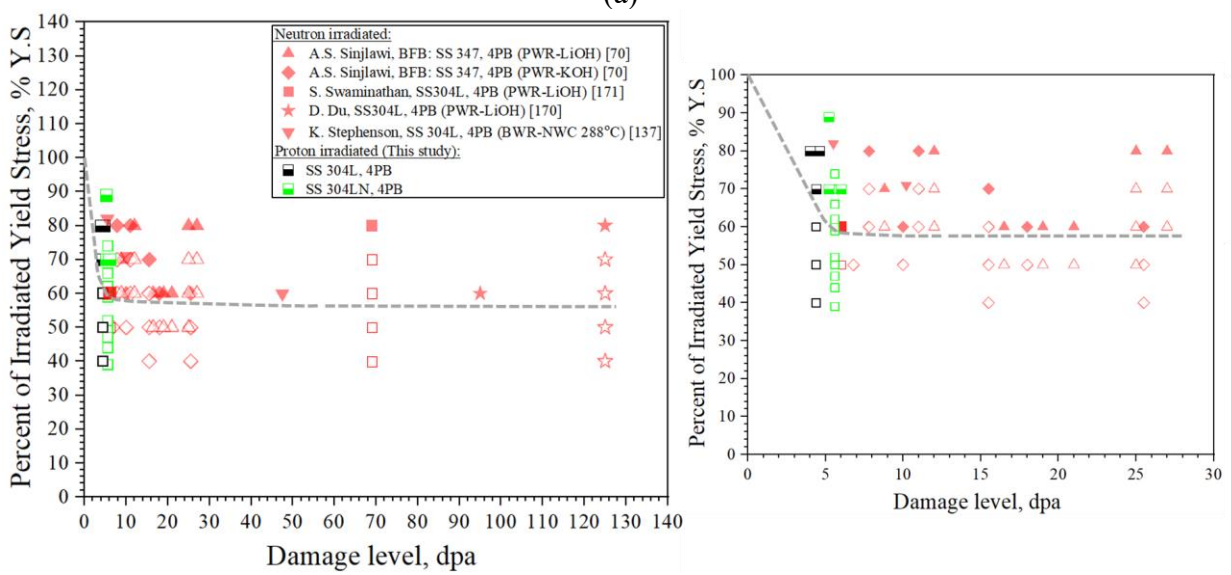


(b)

Figure 7-9 Comparison of results from proton-irradiated 304L and 304LN in LiOH to that in the literature from (a) SS 304 for PWR primary water [20], and (b) from the 4PB testing method only. Results from this project are shown in half-colored symbols. The data is offset slightly along the damage axis to eliminate points.

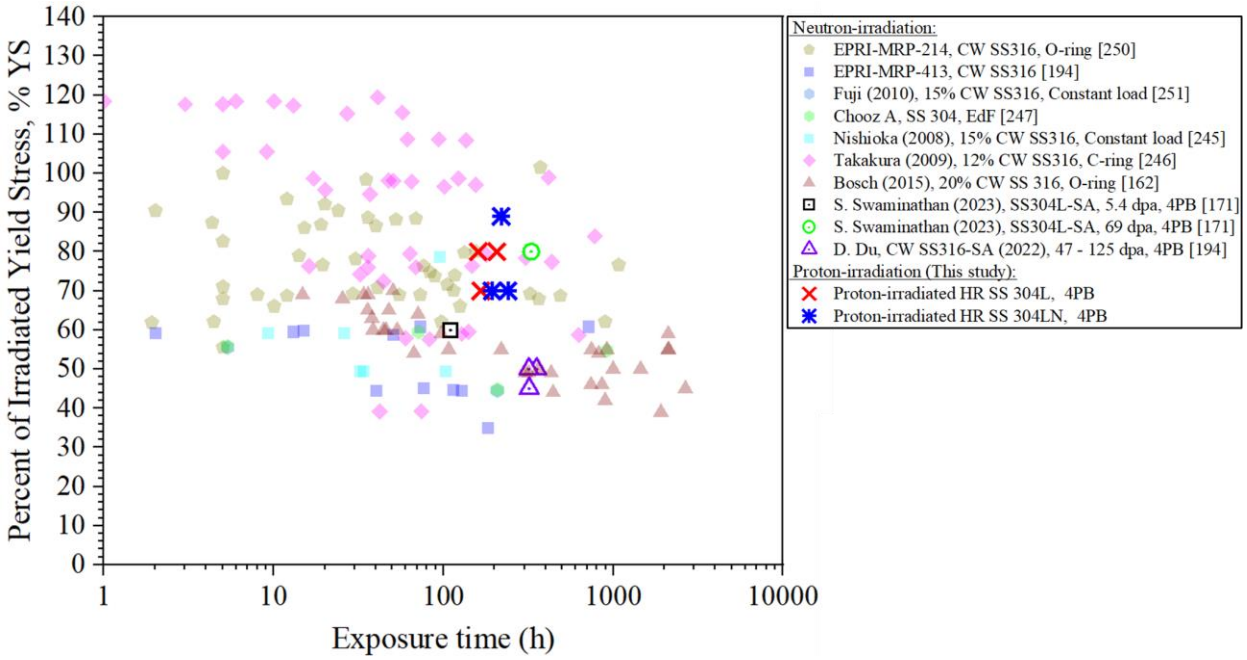


Figure 7-10 Comparison of total exposure time at failure between proton-irradiated 304L and 304LN in LiOH to that in the literature from austenitic stainless-steel alloys for PWR primary water [162, 194, 245 – 247, 251]. The plot is updated with data from Du [194] and Swaminathan [171].

### *7.2.2 Crack morphology*

The final aspect of the comparison involves examining cracking morphology to support the use of proton-irradiated 4PB samples as a surrogate for neutron-irradiated samples. This section compares the surface cracks and crack tip features observed in this study with those reported in the literature to assess their similarity.

*Surface cracking and initiation contributors*

The oxide layers observed at the surface of samples look similar to the well-known oxide form in PWR environment. An outer layer with large, faceted particles observed on all surfaces. This layer is typically Fe-enriched of type magnetite ($Fe_3O_4$). The inner layer is typically enriched with Cr and oxide structures such as Chromia ($Cr_2O_3$) when Cr level is high and spinel ($Cr_xFe_{1-x}O_4$) in most cases [186, 187, 188]. Regardless of its exact stoichiometry, the protective

oxide generally exhibits further oxidation, particularly along the GBs. However, in unirradiated austenitic stainless steels, GB oxidation is observed but with less extent. In contrast, under irradiation in the PWR environment, GB oxidation becomes prominent and typically exhibits a multilayered structure consisting of a nickel-rich interfacial layer between the metal matrix and the oxide, along with iron-rich and chromium-rich oxide layers. These features have been consistently observed in the irradiated austenitic stainless steel along IG crack flanks [183, 254, 255] and observed as well in the results of this study.

In this study, all observed cracks exhibited intergranular characteristics, with the affected GBs predominantly being high angle GB inclining perpendicular to the applied load axis. In irradiated austenitic stainless steels, both DDCs and TJs are known to promote crack initiation once the prerequisite of sufficient GB oxidation is met. The role of DDCs as key initiators of IASCC has been reported widely in recent years in neutron irradiated sample [20, 70, 135, 137, 140, 170, 171]. Similarly, the constraint on the deformation in grains about a TJ also causes an increase in the local stress which can initiate a crack. Figure 7-11, shows examples of the three primary contributors to crack initiation. The overall distribution of these initiator types is summarized in Figure 6-17 (c). In this study, crack initiation was observed at: (1) the intersection of a DDC terminating at a GB oriented nearly perpendicular to the applied load, as shown in Figure 7-11 (a); (2) triple junctions, as shown in Figure 7-11 (b); and (3) locations where both a DDC-GB intersection and a TJ were present, making it difficult to isolate the dominant feature, as seen in Figure 7-11 (c).

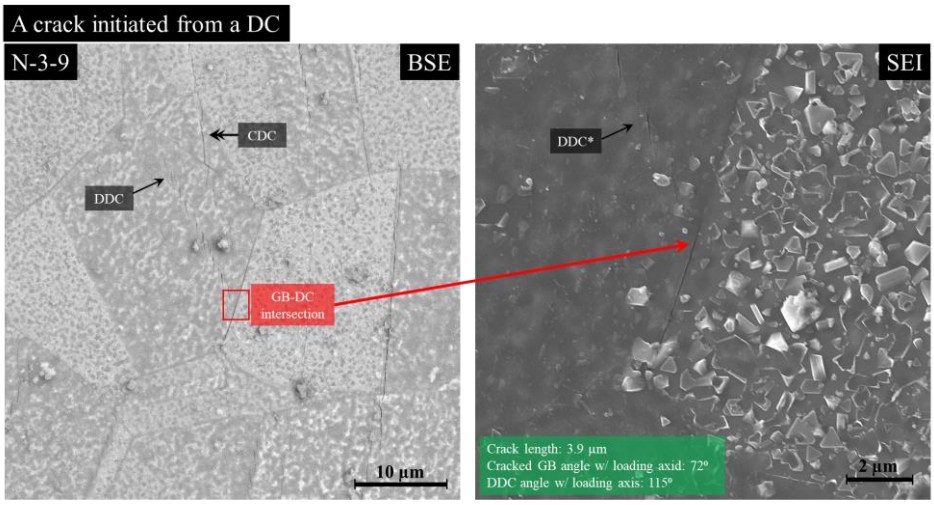


(a)

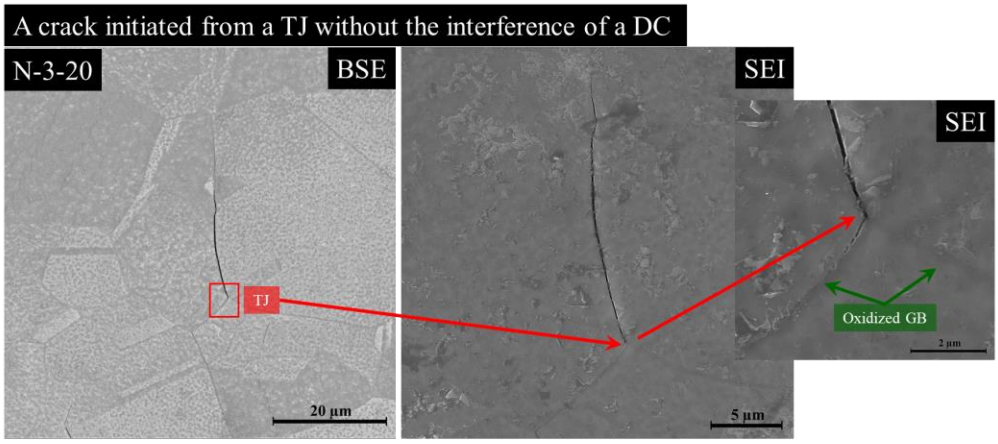


(b)

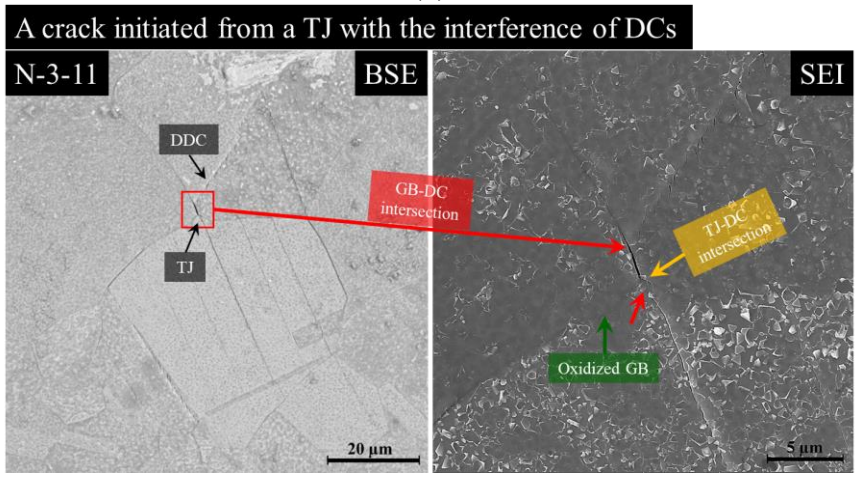


(c)

Figure 7-11 Examples of crack initiation sites observed in this study: (a) a crack initiated from a DC, (b) a crack initiated from a TJ without DC interference, and (c) a crack initiated from a TJ with DC interference.

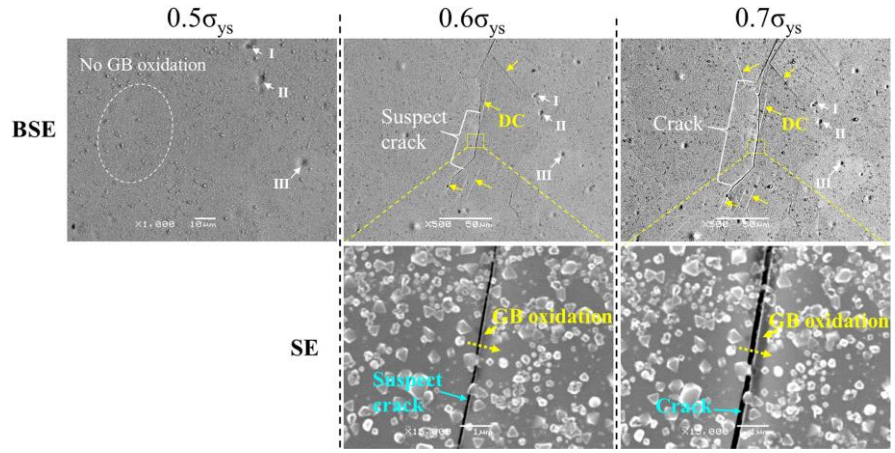
0.5σys
0.6σys
0.7σys
BSE
SE
No GB oxidation
I
II
III
Suspect crack
DC
Crack
GB oxidation
Suspect crack
Crack

(a)

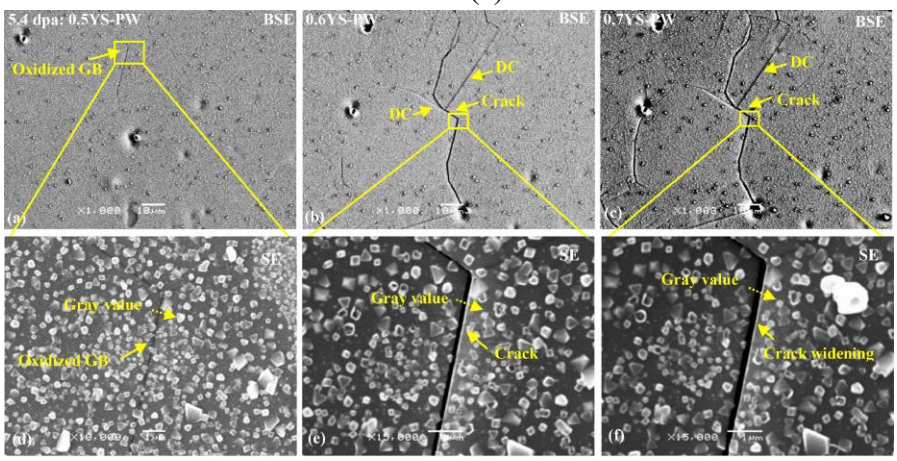
5.4 dpa: 0.5YS-PW
0.6YS-PW
0.7YS-PW
BSE
SE
Oxidized GB
DC
Crack
Gray value
Crack widening

(b)

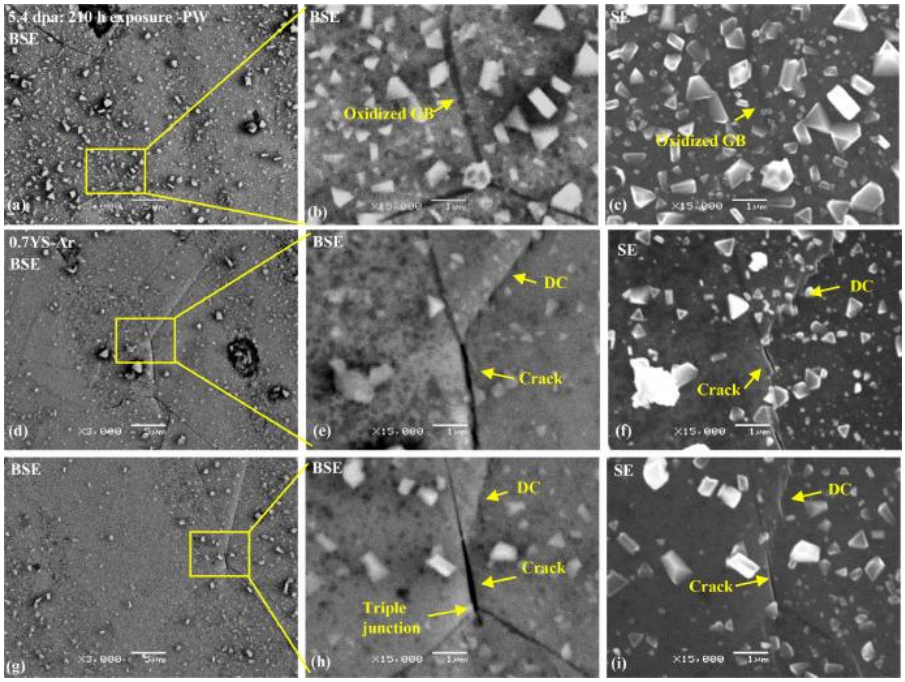
5.4 dpa: 210 h exposure -PW
0.7YS-Ar
BSE
SE
Oxidized GB
DC
Crack
Triple junction

(c)

Figure 7-12 Examples of surface cracking and initiators from neutron-irradiated SS 304L in BOR-60 to 5.4 dpa. The contribution of DC as initiator is clear through the history of the region where the evolution of DC and then cracking (a) from Ref. [171], (b) from Ref. [170]. The intersection of cracking with the oxidized GB and the jagged morphology in (c) from Ref. [170] was also observed in this study.

Note that the initiators of cracks are spread across all three categories with DCs having a somewhat higher frequency than TJs. Also, TJs cracks were easily visible, but those initiated from DCs were difficult to observe due to the coverage of a thick surface oxide, which may be one reason why more DC-GB initiated cracks were not observed. Nevertheless, the results of 4PB show that indeed, these regions of high stress are often the sites of crack initiation which matches with the literature about the role of DCs and TJ in the IASCC initiation.

Figure 7-12 shows three examples from Ref. [170, 171] showing the surfaces of neutron-irradiated SS 304L specimens irradiated in BOR-60 to 5.4 dpa. These examples were selected for comparison because their irradiation dose rate (comparable to that of proton irradiation), irradiation temperature, total dose, 4PB testing method, and exposure to a PWR environment closely match the conditions of this study.

Figure 7-12 (a) DCs appear at approximately 60 %YS, with crack initiation observed at 70 %YS, and GB separation is evident in the secondary electron images. Another case, shown Figure 7-12 (b) shows a clear sequence of IASCC initiation precursors: GB oxidation occurs first, followed by DC formation, and finally crack initiation. This image also reveals a step at the GB, where the adjacent grains exhibit different heights. This is most likely a DC-induced step rather than an orientation-related oxidation effect, as both grains show similar oxidation levels, and the GB edge on the right displays a white contrast in BSE imaging, indicating a higher topographic level compared to the darker GB edge on the left.

A notable difference between 4PB testing of neutron-irradiated and proton-irradiated samples is that, in the latter, observing GB oxidation prior to cracking was challenging, as it

appeared faint at best (as indicated by the green annotation in Figure 7-11), and DCs rarely appeared in the loading step preceding cracking (as introduced in cracking examples in Chapter 6). In the present study, the average oxide thickness for both alloys were ~250 nm that is about 160 % thicker than the example in Figure 7-12, explaining why these features were not apparent here. The importance of this discussion lies in the fact that the interrupted nature of 4PB testing (increments of 10 % YS) enables tracking of GB oxidation and DC formation from their earliest stages, thereby allowing a clearer understanding of their evolution and their link to crack initiation. However, no changes in surface oxidation, including particle size and shape, were observed, indicating that proton and neutron irradiation produced similar surface characteristics in this study.

Another notable observation is the jagged morphology of DCs in the SEM image shown in Figure 7-12 (c) from Ref. [171], which is similar to that in Figure 7-11 (a) from the proton-irradiated specimens in this study. This jagged appearance, visible in both BSE and SE images, is indicative of surface oxide rupture caused by the formation of an underlying step. Once the step height becomes sufficient to protrude through the surface, the surface oxide ruptures, as presented in Figure 6-22, with the extent of rupture depending on the protrusion length. For low step heights, the surface oxide fracture shows a jagged appearance (Figure 7-13 (a)); at intermediate step heights, the fracture remains jagged but appears more linear (Figure 7-13 (b)); and at large step heights, it exhibits a crack-like morphology (Figure 7-13 (c)).

The surface oxide and cracking morphologies shown in Figure 7-12 for the proton-irradiated specimens closely resemble those of neutron-irradiated samples. This similarity is expected, as both sets of tests were conducted under comparable environmental conditions simulating a PWR environment. Comparable oxidation behavior is therefore attributed to the

response of the irradiation-modified microstructure to the environment. To enable a direct and meaningful comparison, cross-sectional imaging of the crack flanks and tips is essential.

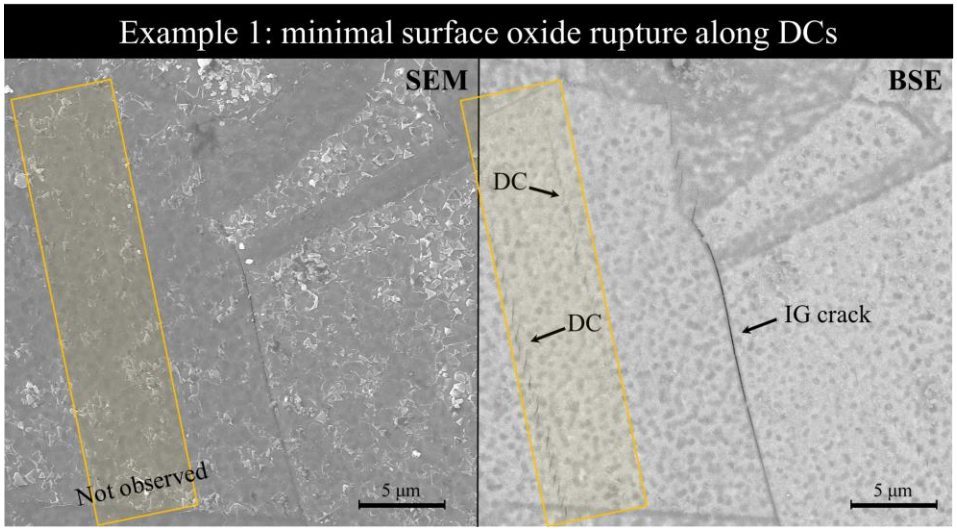


(a)

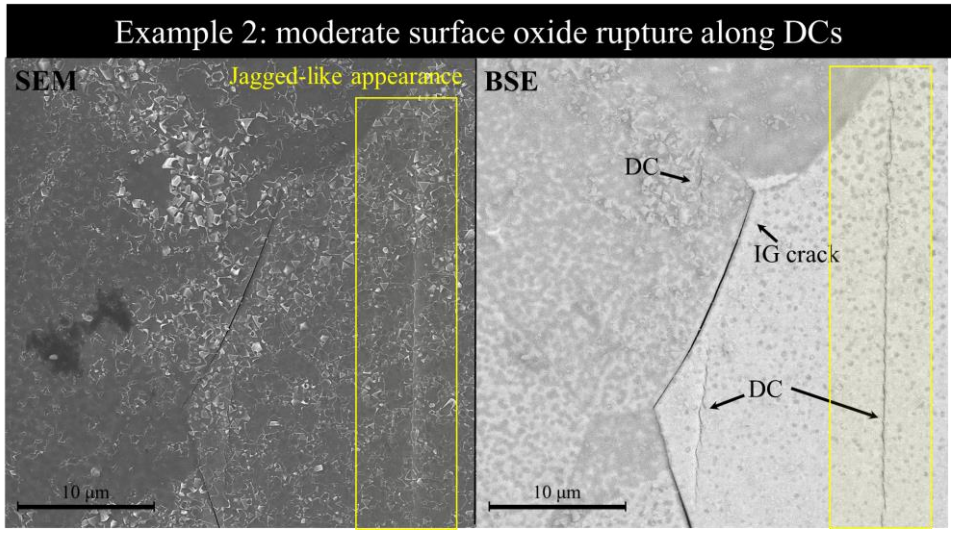


(b)

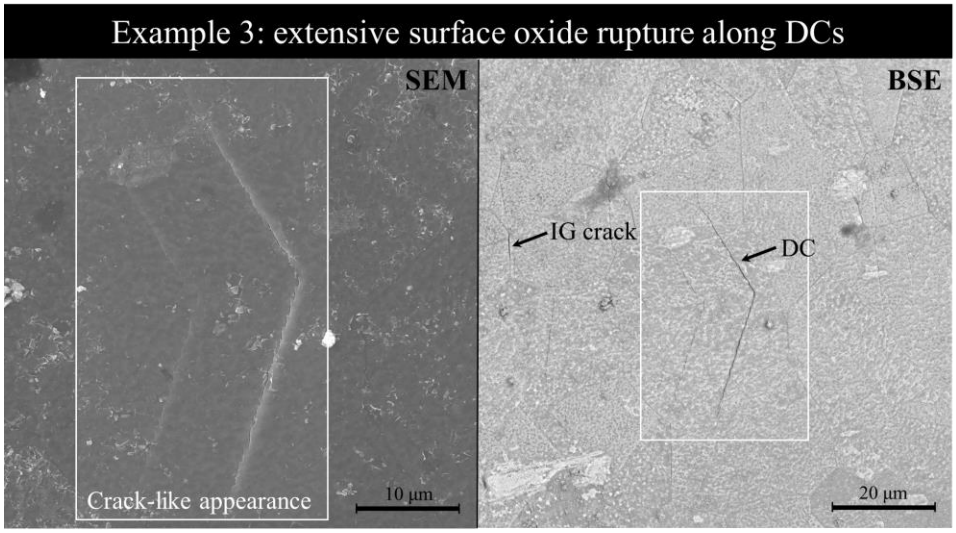


(c)

Figure 7-13 Examples of DC appearance at the surface, categorized by the extent of surface oxide rupture: (a) minimal rupture corresponding to low step height, (b) moderate rupture corresponding to intermediate step height, and (c) extensive rupture corresponding to large step height. All examples are from sample N3 (SS 304LN) after straining to 70%YS in PWR environment at 340 ºC, sample L-R-1 exhibited similar behavior as well.

A similar explanation applies to the early appearance of DCs in some cases, such as in SS 304L from neutron-irradiated conditions shown in Figure 7-12, where DCs occasionally appeared two loading steps prior to fracture. In contrast, in the proton-irradiated condition of the present study, DCs most often appeared at the same step in which failure occurred. This difference is again attributed to the surface oxide layer, as the underlying mechanism of DC formation is similar for both irradiation conditions. Since DC formation primarily depends on irradiation-induced microstructural defects, such as dislocation loops, which were observed in similar number density and size in both conditions, the distinguishing factor is the surface oxide. Oxide thickness plays a key role: the thicker the oxide film, the less visible features such as DCs, oxidized GBs, and small cracks become. Removal of the surface oxide typically reveals a higher density of such features. For example, K. Stephenson [137] reported a higher density of discontinuous DCs at crack sites (previously unobserved) after oxide removal. Similarly, in neutron-irradiated SS 347 strained in PWR relevant environment [256], surface oxide removal revealed a higher quantified crack density. Although the increase was not substantial, it

reinforces the conclusion that a thick surface oxide can obscure these features in SEM observations.

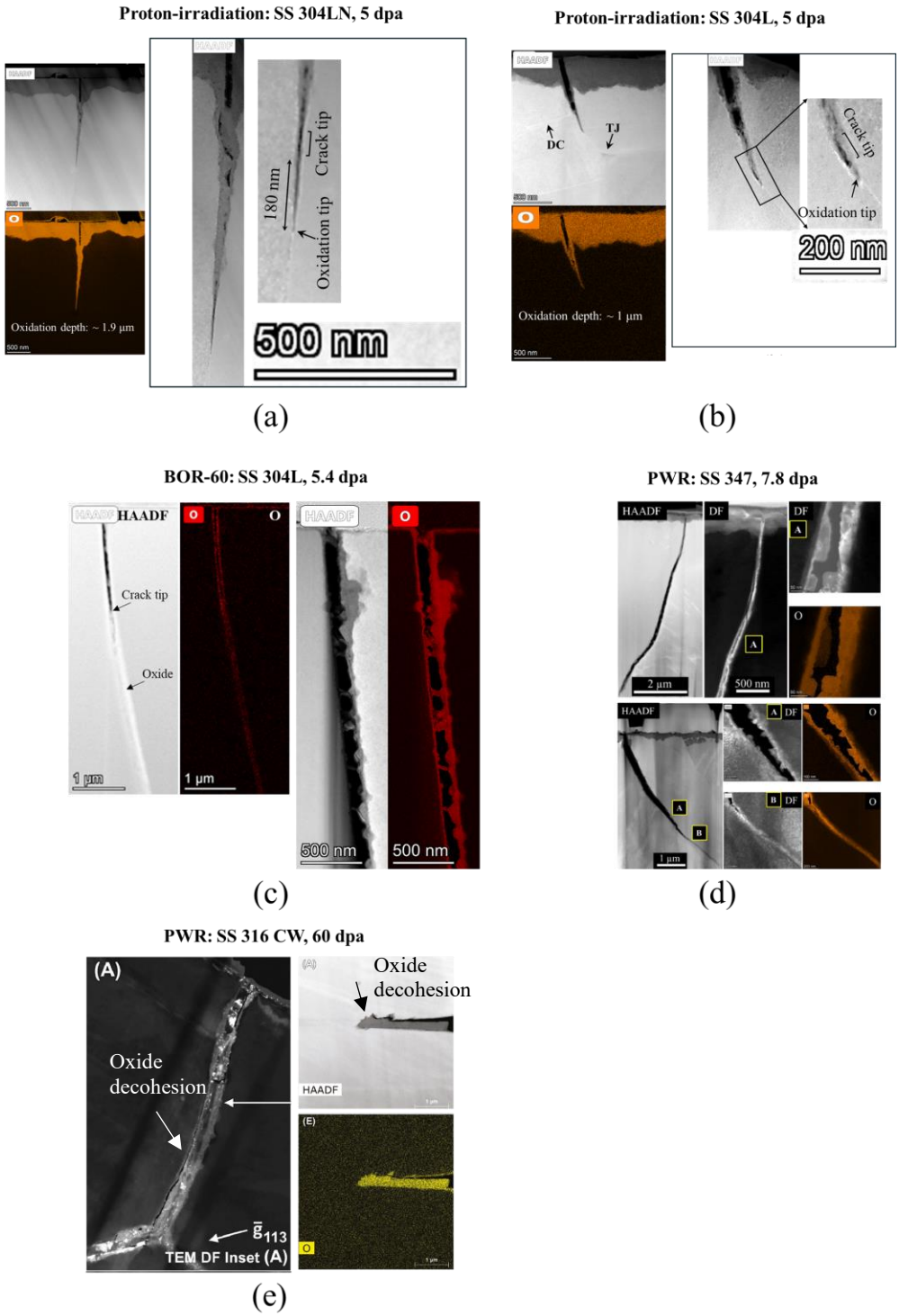


Figure 7-14 Examples of intergranular cracks in proton-irradiated (a) SS 304LN and (b) SS 304L-R, compared with IG fracture morphology in neutron-irradiated (c) SS 304L [171] and (d) SS 347 [70]. All specimens in (a–d) were

strained using 4PB testing and exhibit oxide-through fracture, and (e) shows a neutron-irradiated SS 316 CW specimen strained with an O-ring test [166], showing an oxide–metal interface fracture.

*Crack morphology*

One final comparison to validate the proton-irradiation results against literature on neutron-irradiation concerns the crack morphology. The crack tip is critical for understanding crack initiation once the conditions for GB oxidation are met, since the subsequent growth stage is most likely governed by process at the crack tip. Cracking along oxidized GBs in neutron-irradiated conditions generally follows one of two mechanisms. The first, oxide-through fracture, is characterized by jagged crack flanks and is consistent with the mechanism proposed by Was and co-workers [20, 70, 171], as shown in Figure 7-14 (a-d). The second involves decohesion of the GB oxide at the oxide–metal interface, an example of such cracks is shown in Figure 7-14 (e) [166] from neutron irradiated CW SS 316. Both mechanisms are accepted explanations for IASCC in PWR environments.

The nature of the oxide in the crack and at the crack tip are shown in Figure 7-15. Examples from proton-irradiated SS 304LN and SS 304L are shown in Figure 7-15 (a) and (b) and compared with neutron-irradiated SS 304L irradiated in BOR-60 to 5.4 dpa (Figure 7-15 (c)) [171], SS 347 irradiated in PWR to 7.5 dpa (Figure 7-15 (d)) [70], SS 316 CW irradiated in PWR to 3 dpa (Figure 7-15 (e)) [257], and SS 316 CW irradiated in PWR to 60 dpa (Figure 7-15 (f)) [169]. The STEM-EDS elemental maps are compared to reveal the distribution of key elements, Cr, Ni, and Si, at the crack tip or oxide tip. In all conditions, Fe and Cr depletion accompanied by Ni segregation is consistently observed at the crack tip, oxide tip, and ahead of the crack tip front. However, Si enrichment is not observed uniformly across all conditions. This variability arises from differences in the RIS effect between irradiation environments, as well as from local variations in GB roughness, which can cause spatial fluctuations in RIS along the GB plane.

The crack tip morphology also varies, with a “needle-head” shape predominating, typical of IASCC, reflecting the combined influence of corrosion processes and applied stress. An additional observation in this study is the enrichment of Si at the crack tip and in the region ahead of it. In Figure 7-15 (a), the Si and O signals from STEM-EDS elemental mapping overlap closely, suggesting a role of Si in the cracking mechanism. Similar behavior was recently reported for neutron-irradiated SS 347 [20, 70], as shown in Figure 7-15 (d), where amorphous $SiO_x$ was observed ahead of the crack tip and fractured earlier than the spinel oxide under applied stress, resulting in oxide-through fracture. In the proton-irradiated specimens, the same Si enrichment at the crack tip, as well as along the flanks, likely explains the observed oxide-through fracture in these regions.

Overall, there is a good agreement between the cracking morphology and elemental distributions at the tip in the proton-irradiated samples and those reported in the literature for neutron-irradiated materials. This agreement complements the consistency already observed in the irradiation-induced microstructure and associated hardening (Section 7.1) and in the IASCC initiation stress results (Section 7.2.1).

The agreement between the results of this study and literature data, both from different alloys and various testing methods, as well as from 4PB testing specifically, provides strong support for the proposed approach. The use of proton-irradiated 4PB specimens, combined with FEA, proves to be a viable surrogate for neutron-irradiated samples. This is particularly significant given that proton-irradiated specimens are non-radioactive, more cost-effective, require significantly shorter irradiation times, and enable the production of many samples. This flexibility allows testing under diverse conditions, facilitating the isolation of key factors contributing to IASCC initiation in LWR environments. Moreover, this method holds great

potential for supporting mechanical testing in the development of the next-generation nuclear power plant.

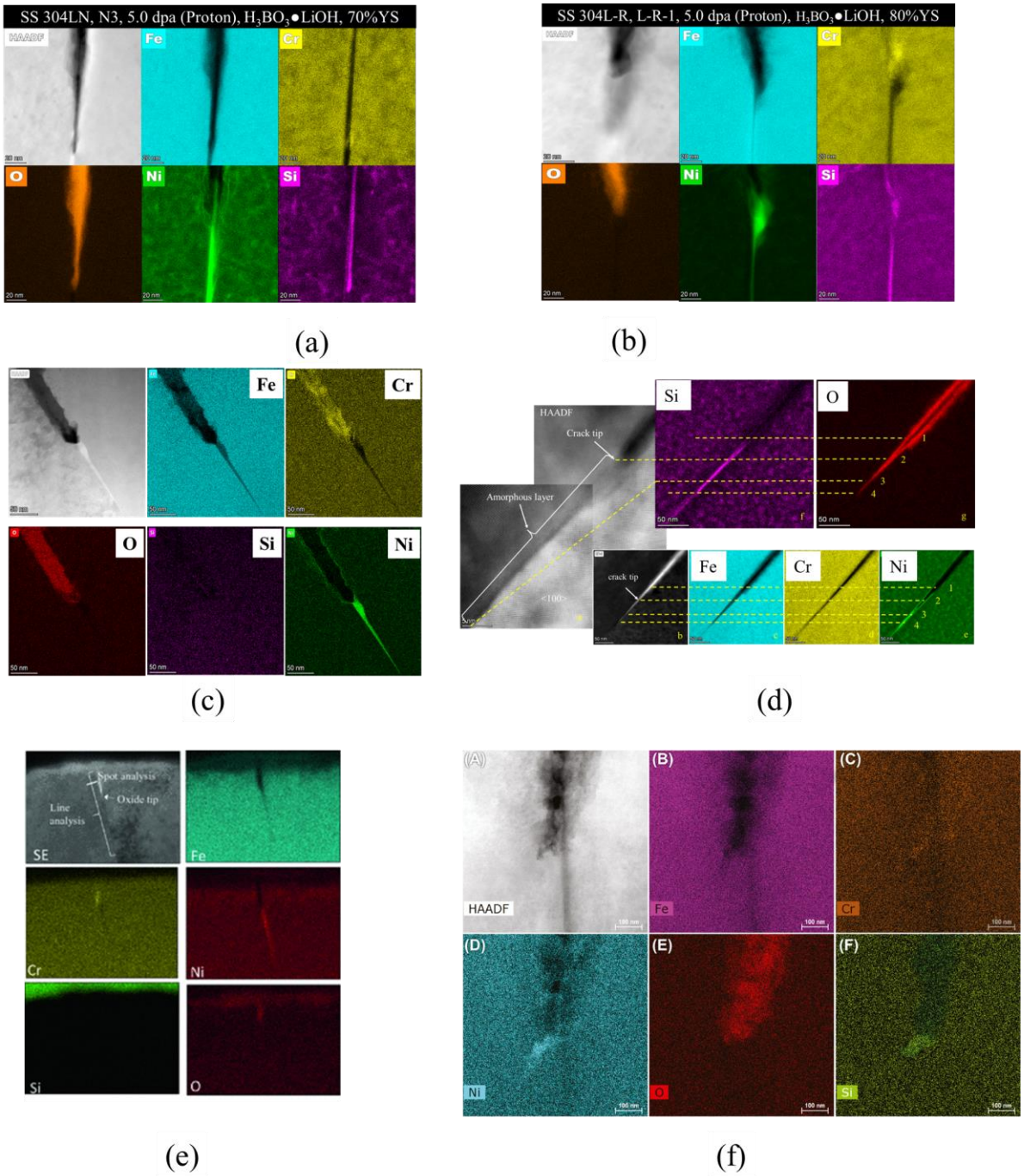


Figure 7-15 STEM-EDS elemental mapping for crack tip of examples from proton-irradiated stainless steel (a) 304, (b) 304L irradiated to 5 dpa, and neutron-irradiated stainless steel of types (c) 304L irradiated to 5.4 dpa [142], (d) 347 irradiated to 7.8 dpa [70], (e) SS 316 CW irradiated to 3 dpa [257] and (f) SS 316 CW irradiated to 60 dpa showing a consistent features of Fe and Cr depletion and Ni enrichment, while Si enrichment varies from condition to another [169].

### 7.3 The role of solute nitrogen on the IASCC susceptibility

Sections 7.1 and 7.2 have established the validity of the four-point bend testing on proton-irradiated samples by showing that both the proton irradiated microstructure (section 7.1) and the IASCC response (section 7.2) are similar to that of samples irradiated in reactor. Specifically, this was done by comparing the results of this study with literature data on neutron-irradiated materials, demonstrating strong agreement in terms of irradiation effects, IASCC susceptibility, crack and crack tip morphology. These consistent findings increase confidence in the reliability of the proposed method for investigating IASCC using proton-irradiated specimens. The discussion also showed that the microstructure, hardening, and IASCC response of SS 304L-R and SS304 LN are very similar and there is no significant difference in these metrics between the two.

This section presents a focused comparison between SS 304LN and SS 304L-R to address the issue of why the higher nitrogen content of SS 304LN did not follow the hypothesis that nitrogen atoms interact with dislocation loops to form nitrogen–loop (N–L) complexes, which act as strong barriers to dislocation motion and thus contribute significantly to matrix hardening, thus increasing the dislocation channel heterogeneity and the susceptibility to IASCC.

Irradiation hardening in stainless steels irradiated in the 320 - 375°C range is controlled largely by the dislocation loop structure. As previously discussed in section 7.1.1, there was no notable difference between the dislocation size and number density observed in sample N3 compared to sample L-R-1 and thus with the literature, indicating no measurable effect of nitrogen on the dislocation loops after irradiation by 2 MeV protons to 5 dpa at 360 $^{o}$C. Dislocation loops usually saturate at around 3 dpa, meaning that both alloys have passed this "nucleation-dominated" regime and lie squarely on the plateau of saturated loop density. This

suggests that, at these nitrogen levels (0.068 wt.% vs. 0.140 wt.%), nitrogen may not significantly change the irradiation response of the material, prompting the question of whether a Δwt.% of 0.072 between two alloys is sufficient to produce a measurable effect. Or by 0.068 wt.%, the effect of N has already saturated.

To understand the role of nitrogen in the evolution of dislocation loops, a wide range of austenitic stainless steels with varying nitrogen content are considered. The dataset presented in Figure 7-16 includes results from multiple studies spanning a broad spectrum of nitrogen levels, from as low as 0.003 wt.% up to 0.15 wt.% [8, 54, 61, 105, 137], and encompasses various irradiation conditions, alloy chemistries, and microstructural states. Although these studies were not conducted specifically to investigate the role of nitrogen in irradiation-induced microstructure, linking their dislocation loop results to the nitrogen content of the tested alloys can still provide useful insights for the purposes of this study.

Despite the differences in irradiation conditions and temperatures, no clear trend was observed in either the dislocation loop number density (Figure 7-16 (a)), or size (Figure 7-16 (b)) as a function of N concentration. The only notable exception is that data from SS 316LN obtained from Shreevalli et. al. [228] deviated by an order of magnitude lower from others, which was attributed to the relatively increased SFE. To enable clearer comparison, data from SS 304 grades only were replotted in Figure 7-16 (c) and (d). The results from this study fall within the same order of magnitude in loop density, while loop sizes Figure 7-16 (d) fall within a range of 4 – 13 nm, with both SS 304L-R and SS 304LN consistent with this band. however, no trend can be observed all across the N concentration ranging from 0 – 0.15 wt.%. This suggests that if there is no discernible effect of N on loop size, or number density then its influence is clearly too weak to overcome variations in other irradiation parameters.

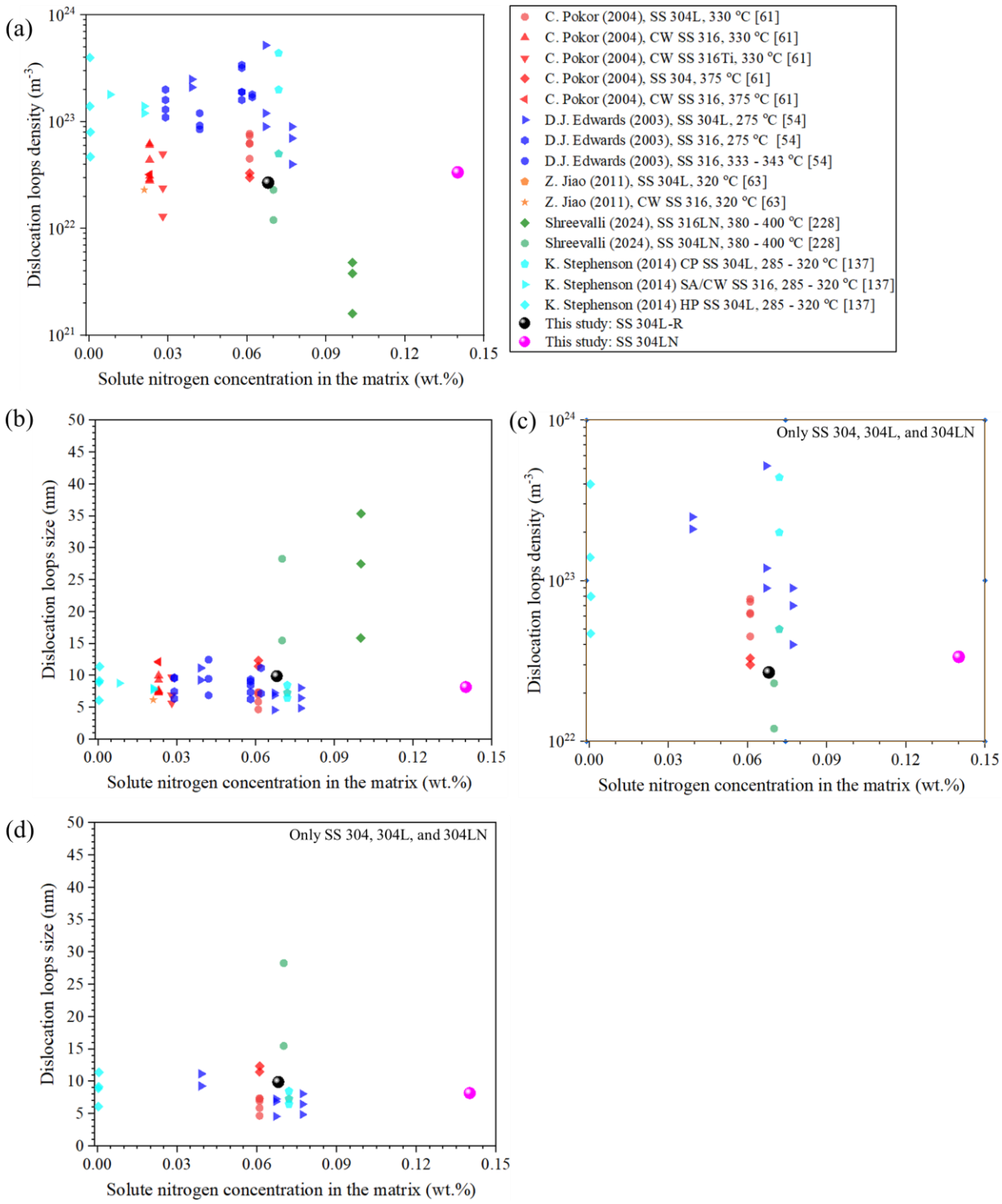


Figure 7-16 The evolution of dislocation loops (a) density and (b) size as a function of nitrogen content in austenitic stainless steel irradiated to a range of damage levels of 0.3 - 46 dpa and a range of temperature of 275 – 400 ºC, the data from SS 304, 304L, and 304LN only are shown in (c) for the density and (d) for the size [54, 61, 63, 137, 228] .

Figure 7-17 shows the dislocation loop number density and size for austenitic stainless steels irradiated with neutrons in either PWR-relevant environments or in fast reactors using fast neutrons. The nitrogen content of each alloy, highlighted in the legend with a shaded red box, is shown for clarity. For simplicity, datasets from the same reference are plotted using a unified color. Similar to the trend in Figure 7-16, the loop size (Figure 7-17 (b)) shows no clear correlation with nitrogen content with the only notable exception is that data from SS 316LN obtained from Shreevalli et. al. [228] as explained earlier.

Figure 7-17 (a) shows that the loop size varies in a narrow window between 4 and 13 nm and is independent of dpa. For the loop density in Figure 7-17 (b), there is also no trend with dpa as the data fall within factor of 10. Given that dpa is not a factor, Therefore, isolating SS 304L is necessary to properly assess the presence of a trend. Figure 7-17 (c) shows only the data from SS 304 grades from Figure 7-17 (a), with nitrogen concentrations from Edwards et al. [54] added for reference. Edwards' data at 300 $^{o}$C show almost no trend, which may be explained by the irradiation regime being in the non-saturated loop region. Pokor's results [61] at 0.061 wt.% N and 330 $^{o}$C indicate a nearly constant loop density over a wide range of irradiation damage, and his data on the same alloy at a higher temperature (375 °C) show similarly minimal variation with irradiation damage when nitrogen is fixed at 0.061 wt.%.

These results suggest that increasing temperature alters vacancy and interstitial kinetics, thereby reducing loop density, but has little influence from irradiation damage itself. Stephenson et al. [137] data suggests a decreasing loop density trend with dpa at 0.072 wt.% N and 320 $^{o}$C, and an increasing trend when dpa is fixed but nitrogen is very low (0.0005 wt.%), though at such a low level, N is believed to have little to no influence. Finally, Shreevali's [228] data at 380 –

400 ºC showing an increase in loop density with dpa at a constant nitrogen content of 0.1 wt.%, from 1 dpa, where loops had not yet saturated, to 3 dpa, where saturation began, explaining the observed increase. In addition, one data point from Z. Jiao [111], located just beneath Stephenson's at 46 dpa (both irradiated to the same damage at 320 °C and 0.072 wt.% N), is in good agreement with Stephenson's loop density data.

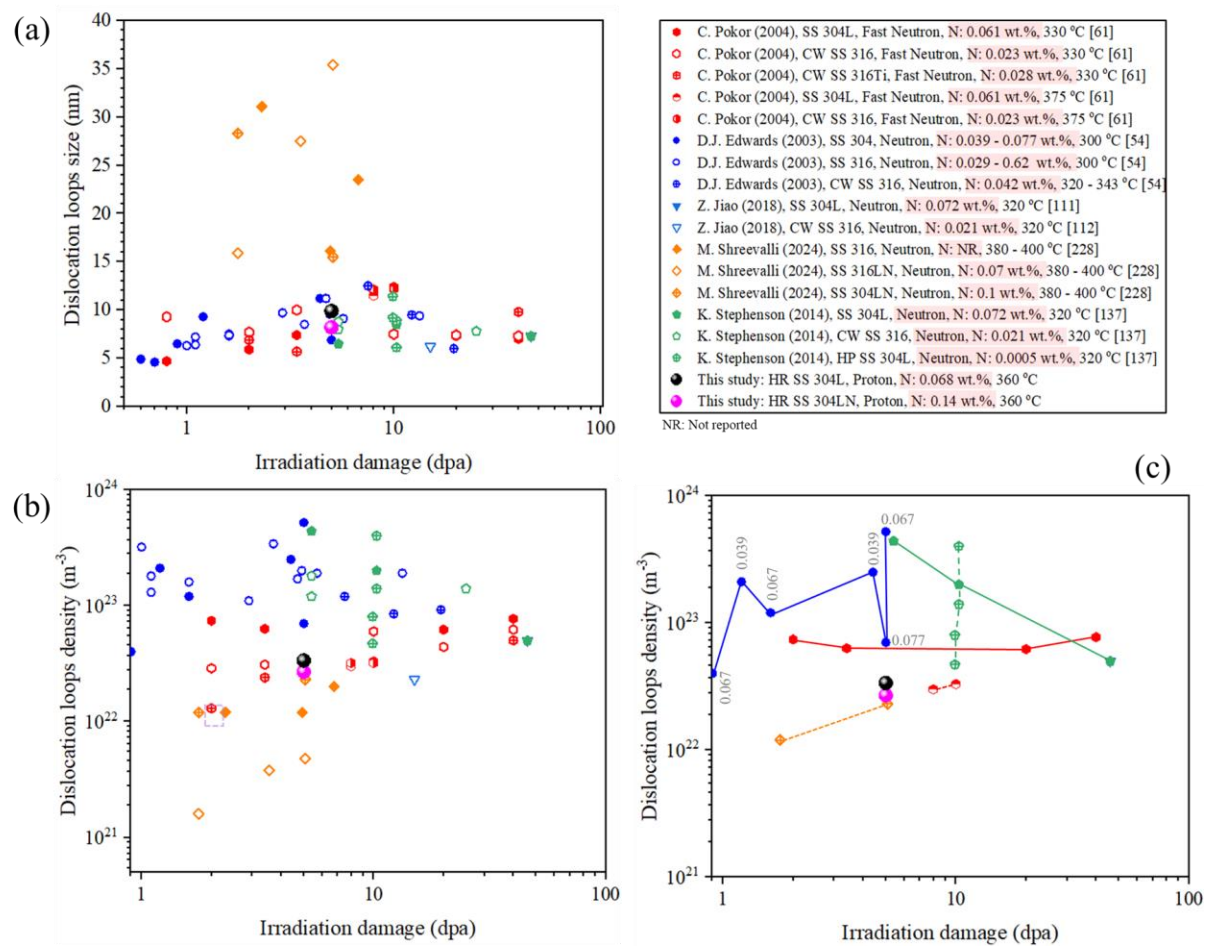


Figure 7-17 Dislocation loops as a function of irradiation damage (dpa) for austenitic stainless steel alloys with different nitrogen contents for (a) density and (b) size while (c) shows the data from SS 304L and SS 304 only. The dashed orange box represents the data obtained from XRD while the purple box represents the data obtained from the TEM characterization showing the role of characterization technique on quantifying the dislocation loops [54, 61, 111, 112, 137, 228]. Data from Pokor [61] is shown in red, from Edwards [54] in blue, and from Stephenson [137] in green.

If nitrogen has little effect on dislocation loop evolution, then IASCC would be expected to follow the same trend. Chung et. al. [141] reported that the percent of IGSCC remains near zero

up to about 0.05 wt.% N, then rises sharply and reaches a plateau almost immediately above that threshold. In contrast, Chung and Shack [258] later found no well-defined correlation between IASCC and impurities, including nitrogen, in neutron-irradiated austenitic stainless steels exposed to BWR environments at doses of 0.5 – 3 dpa. This highlights the need for investigation across a broader range of nitrogen concentrations.

IASCC data, expressed as the fraction of intergranular cracks observed in SSRT/CERT specimens tested in LWR environments, are plotted in Figure 7-18 against nitrogen content in austenitic stainless steels. Most of the data come from solution-annealed SS 304, with additional points from SA SS 316, SS 348, and a few cold-worked alloys. The results suggest no discernible effect of nitrogen on IASCC susceptibility in BWR environments. Fukuya et. al. [259] likewise reported no influence of nitrogen on IASCC in BWR conditions. At higher damage levels (~5 dpa), Nakano et. al. [260] observed high IASCC susceptibility in HP austenitic stainless steels with very low nitrogen content (~0.0014–0.002 wt.%), though this was attributed to other impurities in the bulk. Even at low irradiation temperatures (~50 °C), Kodama et. al. [142] reported no effect of nitrogen on IASCC under BWR conditions, even at contents up to 0.1 wt.%. Also, no role of nitrogen on IASCC was observed in BWR and PWR environment as reported by K. Stephenson et. al. [261].

Together, these results indicate that a threshold value may not exist, and that IASCC is essentially independent of nitrogen content at concentrations below 0.2 wt.%. The wide scatter in the data suggests that other microstructural or environmental factors play a dominant role. However, because data in the high-nitrogen regime are limited, further investigation is needed to clarify the potential influence of nitrogen at higher concentrations.

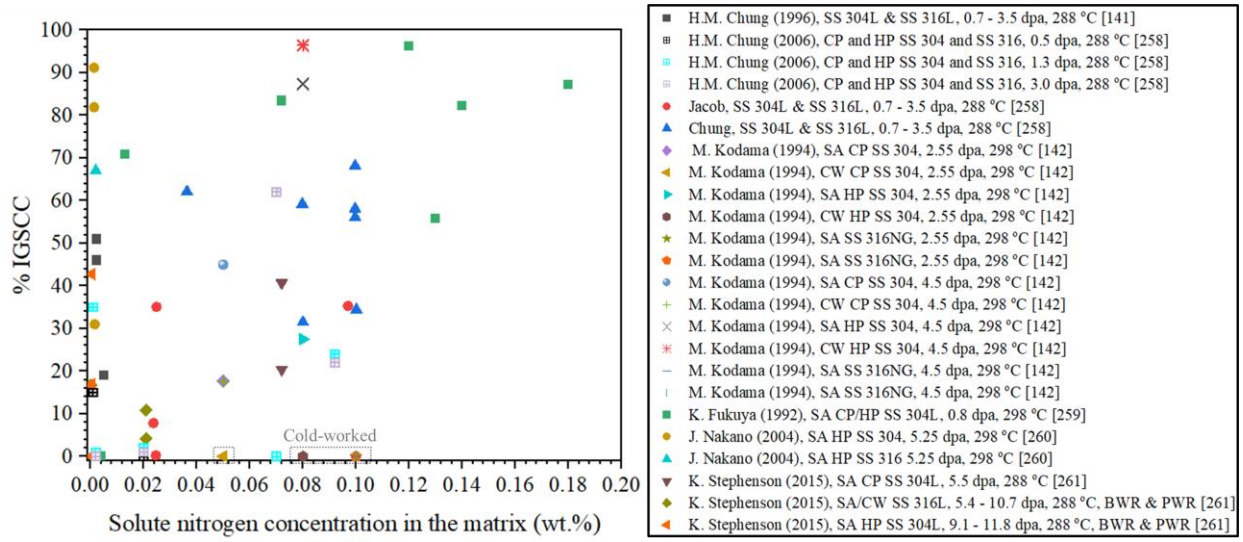


Figure 7-18 IASCC susceptibility of various SS 304 and SS 316 alloys in LWRs as a function of nitrogen content. The dashed lines represent the bottom and top thresholds. Data from CW heats are bound by a gray dashed box [141, 142, 258-261].

Another important observation is that cold-worked alloys exhibit a weaker response; even at higher nitrogen concentrations, the fraction of intergranular cracking generally remains lower, suggesting that cold work mitigates or delays the nitrogen effect, with the microstructure playing the dominant role. In this study, however, the materials were hot-rolled, which may have acted similarly to cold working by altering or delaying the threshold point, leading to no significant difference in IASCC susceptibility between SS 304L-R and SS 304LN. Furthermore, the plot in Figure 7-18.

shows data from early irradiation damage levels, which are below the threshold for dislocation loop evolution. More importantly, the reducing environment of a PWR differs from the oxidizing environment of a BWR, where the elevated corrosion potential in BWRs accelerates SCC. As a result, IASCC susceptibility is expected to be lower under SSRT/CERT testing in PWR conditions.

Overall, Figures 7-16 through 7-18 suggest that nitrogen plays a neutral role in the evolution of dislocation loops and their size and threshold value was not observed. Also, IASCC

is essentially independent of nitrogen content at concentrations below 0.2 wt.%. The wide scatter in the data in this regime suggests that other microstructural or environmental factors play a dominant role. This suggests that if there is no discernible effect of N on IASCC then its influence is clearly too weak to overcome variations in other irradiation and corrosion parameters. The findings of this study are consistent with the literature as no role of N was observed on IASCC initiation in PWR environment.

### 7.4 Evaluation of the hypothesis

At the outset of this study, it was hypothesized that nitrogen plays a role in the initiation of IASCC through the following proposed mechanism:

1. 304LN has a higher concentration of N atoms that form stable nitrogen-loop (N–L) complexes, resulting in a higher density of smaller loops than in 304L.
2. The N–L complexes hinder dislocation motion, contributing to increased matrix hardening.
3. The increased hardness results in the formation and evolution of dislocation channels.
4. In high-temperature pressurized water reactor (PWR) environments, oxidized grain boundaries become vulnerable to cracking, particularly when dislocation channels terminate at GBs without transmitting into neighboring grains.
5. Therefore, nitrogen's potential influence on IASCC is primarily attributed to its role in stabilizing dislocation loops and enhancing the strain in the channels.

Figure 7-19 summarizes the components of this hypothesis developed at the beginning of the study and comparing with two alloys.

Two austenitic stainless-steel alloys were selected for this investigation: SS 304LN, with a high nitrogen content of 0.14 wt.%, and SS 304L-R, with an intermediate nitrogen content of

0.068 wt.%. To ensure a valid comparison, efforts were made to minimize variability between the alloys by applying identical post-fabrication processing. Although differences in chemical composition led to slight variations in mechanical behavior (as shown in Figure 7-19), these differences were not considered significant enough to impact the overall conclusions. Therefore, the comparable irradiation-induced microstructural observed between the alloys were insufficient to influence hardening or dislocation channel formation and consequently led to similar IASCC behavior in both alloys.

Thus, the magnitude of nitrogen effect was less than expected, as its influence on the material did not follow a simple linear correlation as previously assumed. In contrast, comparisons with the literature suggest that the relationship is more complex and not well-defined, beginning with the irradiation microstructure, which appeared independent of nitrogen content. It became more complicated in IASCC susceptibility that showed no dependence on nitrogen content to up to 0.2 wt.%.

To more clearly resolve nitrogen role in IASCC, future studies should examine a wider range of nitrogen concentrations, from near-zero to very high levels. Dividing this range into discrete categories (e.g., near-zero, low, intermediate, high, and very high) would allow more precise identification of threshold regions: where the effect of nitrogen is negligible, neutral, or detrimental. In addition, careful consideration of post-fabrication processing is necessary, particularly the roles of solution annealing, cold working, and hot rolling. This framework would not only build on the findings of the present study but also provide clearer guidance for future research.

Since both alloys showed similar IASCC susceptibility in high-temperature water environments containing boric acid and lithium hydroxide, hot-rolled SS 304LN can be

considered a suitable alternative to SS 304L for core internal structures, offering superior mechanical and corrosion properties.

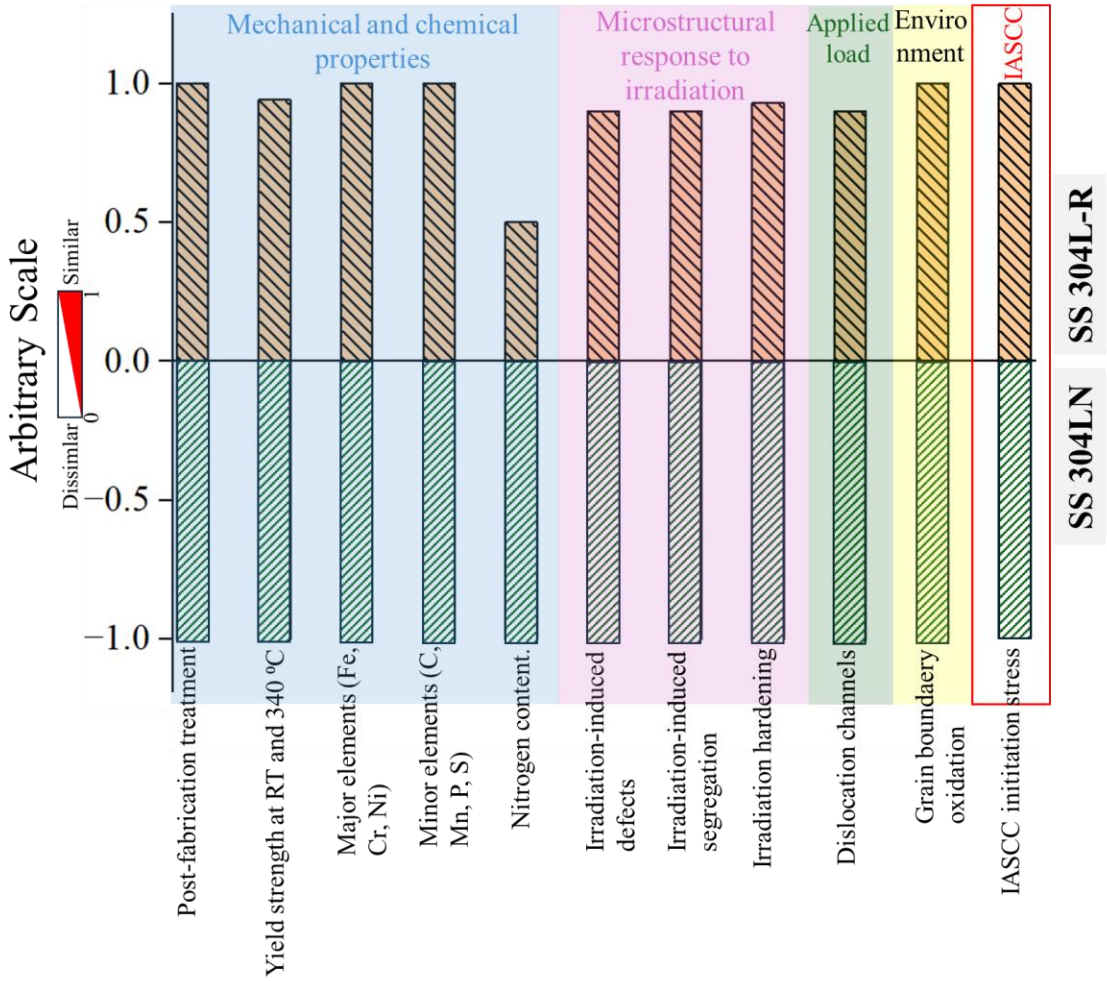


Figure 7-19 Summary of evaluating the hypothesis through scaling its components on an arbitrary scale of similarity. SS 304LN was taken as a reference such that similarity means that SS 304L-R is close in response to SS304LN or not.

# Chapter 8 Conclusion

Four-point bend (4PB) tests were performed to assess the influence of nitrogen on irradiation-assisted stress corrosion cracking (IASCC) of austenitic stainless steels in high-temperature water. The specimens were irradiated with 2 MeV protons at 360 °C and then strained in a pressurized water reactor (PWR) environment at 340 °C. Two alloys were studied: SS 304L-R with 0.068 wt.% nitrogen and SS 304LN with a higher nitrogen content of 0.140 wt.%. Tensile specimens were also proton-irradiated to 3 dpa to investigate the characteristics of dislocation channels.

The following are the major outputs of this study:

1. Dislocation loop microstructure and resulting radiation hardening agree well with that from neutron irradiation, indicating that proton irradiation can replicate the critical features of irradiation in reactor.
2. Crack initiation stress and crack morphology of proton-irradiated 4PB samples agreed with that from neutron-irradiated stainless steels tested in different loading modes. Therefore, proton-irradiated 4PB samples, combined with nonlinear FEA, are suggested as effective surrogates for neutron-irradiated specimens. This approach enables greater experimental flexibility, allowing studies across wider damage levels, environments, and alloy chemistry.
3. Nitrogen in the range of 0.068 – 0.14 wt.% had no clear effect on dislocation density or size, or on the dislocation channel characteristics or IASCC susceptibility contrary to the expected effect.

4. If there is no discernible effect of N on IASCC then its influence is clearly too weak to overcome variations in other irradiation and corrosion parameters.

# Appendices

## Appendix A: Python Codes Used to Calculate Currents on Stage And Slits

### A.1 Four-point bend samples irradiation

This code was used to calculate the current density at the stage for 4PB samples (irradiation experiment # 1).

```
import numpy as np
import matplotlib.pyplot as plt
import pandas as pd
import tabulate

def gaussian_beam_intensity(x, y, x0, y0, sigma):
   return np.exp(-((x - x0)**2 + (y - y0)**2) / (2 * sigma**2))

def raster_beam(FWHM, F, Lsx, Lsy, Lax, Lay):
   # Calculate parameters
   D = (FWHM * F) / 2
   sigma = FWHM / (2 * np.sqrt(2 * np.log(2)))
   # Raster starting point
   x_start = -(Lsx / 2) - D
   y_start = (Lsy / 2) + D
   # Step size for rastering
   step_size = 0.25
   # Create a grid for the stage area
   x = np.linspace(-Lax / 2, Lax / 2, 500)
   y = np.linspace(-Lay / 2, Lay / 2, 500)
   x_grid, y_grid = np.meshgrid(x, y)
   # Rastering and summing beam intensities
   total_intensity = np.zeros_like(x_grid)
   x_positions = np.arange(x_start, (Lsx / 2) + D, step_size)
   y_positions = np.arange(y_start, -(Lsy / 2) - D, -step_size)
   for y0 in y_positions:
   for x0 in x_positions:
   total_intensity += gaussian_beam_intensity(x_grid, y_grid, x0, y0, sigma)
   # Normalize intensity
   normalized_intensity = total_intensity / total_intensity.max()
   # Plotting
   plt.figure(figsize=(8, 6))
   plt.contourf(x, y, normalized_intensity, levels=100, cmap='viridis')
   plt.colorbar()
```

```
    # Add target area
    plt.plot(
    [-Lsx / 2, Lsx / 2, Lsx / 2, -Lsx / 2, -Lsx / 2],
    [-Lsy / 2, -Lsy / 2, Lsy / 2, Lsy / 2, -Lsy / 2],
    linestyle='--', color='red'
    )
    # Add first beam location as a circle
    beam_circle = plt.Circle((x_start, y_start), FWHM/2, color='orange', linestyle='--
', f
    plt.gca().add_patch(beam_circle)
    # Add center of the beam
    plt.scatter([x_start], [y_start], color='orange', )
    plt.title(f'Stage Current Density Distribution\nD = {D:.2f} mm')
    plt.xlabel('x (mm)')
    plt.xticks(np.arange(-Lax / 2, Lax / 2 + 1, 2))
    plt.ylabel('y (mm)')
    plt.show()
    # Plot normalized intensity vs x (at the center y = 0)
    center_idx = len(y) // 2
    plt.figure(figsize=(8, 6))
    plt.plot(x, normalized_intensity[center_idx, :], )
    plt.xticks(np.arange(-Lax / 2, Lax / 2 + 0.2, 2))
    plt.yticks(np.arange(0, 1.1, 0.1))
    plt.title('Normalized Current Density vs x (mm)')
    plt.xlabel('x (mm)')
    plt.ylabel('Normalized Current Density')
    plt.grid(True)
    plt.show()
    # Display data as a table
    data = {
    'x (mm)': x,
    'Normalized Current Density': normalized_intensity[center_idx, :]
    }
    df = pd.DataFrame(data)
    print("\nNormalized Current Density Table:\n")
    print(df.to_string(index=False))

    return normalized_intensity

def calculate_stage_current_density(Lsx, Lsy, x, y, normalized_intensity):
    # Determine indices for the stage area
    x_stage = (x >= -Lsx / 2) & (x <= Lsx / 2)
    y_stage = (y >= -Lsy / 2) & (y <= Lsy / 2)
    # Calculate current density in the stage area
    stage_density = np.trapz(
    np.trapz(normalized_intensity[np.ix_(y_stage, x_stage)], x[x_stage], axis=1),
    y[y_stage]
    )
    return stage_density

def calculate_total_current_density(x, y, normalized_intensity):
    # Calculate total current density across the entire simulation area
    total_density = np.trapz(np.trapz(normalized_intensity, x, axis=1), y)
    return total_density
```

```
# Example parameters
FWHM = 3 # Full Width at Half Maximum
F = 0.7 # Fraction of beam's radius
Lsx, Lsy = 17, 11 # Stage dimensions
Lax, Lay = 26, 20 # Aperture dimensions

# Raster the beam and calculate total intensity
normalized_intensity = raster_beam(FWHM, F, Lsx, Lsy, Lax, Lay)

# Create grid for x and y coordinates
x = np.linspace(-Lax / 2, Lax / 2, 500)
y = np.linspace(-Lay / 2, Lay / 2, 500)

# Calculate stage current density
stage_density = calculate_stage_current_density(Lsx, Lsy, x, y, normalized_intensity)
print(f"Stage current density: {stage_density}")

# Calculate total current density
total_density = calculate_total_current_density(x, y, normalized_intensity)
print(f"Total current density: {total_density}")
```

### A.2 Tensile bars irradiation

This code was used to calculate the current density at the stage for tensile bars (irradiation experiment # 3).

```
import numpy as np
import matplotlib.pyplot as plt
import pandas as pd
import tabulate

def gaussian_beam_intensity(x, y, x0, y0, sigma):
   return np.exp(-((x - x0)**2 + (y - y0)**2) / (2 * sigma**2))

def raster_beam(FWHM, F, Lsx, Lsy, Lax, Lay):
   # Calculate parameters
   D = (FWHM * F) / 2
   sigma = FWHM / (2 * np.sqrt(2 * np.log(2)))
   # Raster starting point
   x_start = -(Lsx / 2) - D
   y_start = (Lsy / 2) + D
   # Step size for rastering
   step_size = 0.25
   # Create a grid for the stage area
   x = np.linspace(-Lax / 2, Lax / 2, 500)
   y = np.linspace(-Lay / 2, Lay / 2, 500)
   x_grid, y_grid = np.meshgrid(x, y)
   # Rastering and summing beam intensities
   total_intensity = np.zeros_like(x_grid)
   x_positions = np.arange(x_start, (Lsx / 2) + D, step_size)
   y_positions = np.arange(y_start, -(Lsy / 2) - D, -step_size)
```

```
    for y0 in y_positions:
    for x0 in x_positions:
    total_intensity += gaussian_beam_intensity(x_grid, y_grid, x0, y0, sigma)
    # Normalize intensity
    normalized_intensity = total_intensity / total_intensity.max()
    # Plotting
    plt.figure(figsize=(8, 6))
    plt.contourf(x, y, normalized_intensity, levels=100, cmap='viridis')
    plt.colorbar()
    # Add target area
    plt.plot(
    [-Lsx / 2, Lsx / 2, Lsx / 2, -Lsx / 2, -Lsx / 2],
    [-Lsy / 2, -Lsy / 2, Lsy / 2, Lsy / 2, -Lsy / 2],
    linestyle='--', color='red'
    )
    # Add first beam location as a circle
    beam_circle = plt.Circle((x_start, y_start), FWHM/2, color='orange', linestyle='--
', f
    plt.gca().add_patch(beam_circle)
    # Add center of the beam
    plt.scatter([x_start], [y_start], color='orange', )
    plt.title(f'Stage Current Density Distribution\nD = {D:.2f} mm')
    plt.xlabel('x (mm)')
    plt.xticks(np.arange(-Lax / 2, Lax / 2 + 1, 2))
    plt.ylabel('y (mm)')
    plt.show()
    # Plot normalized intensity vs x (at the center y = 0)
    center_idx = len(y) // 2
    plt.figure(figsize=(8, 6))
    plt.plot(x, normalized_intensity[center_idx, :], )
    plt.xticks(np.arange(-Lax / 2, Lax / 2 + 0.2, 2))
    plt.yticks(np.arange(0, 1.1, 0.1))
    plt.title('Normalized Current Density vs x (mm)')
    plt.xlabel('x (mm)')
    plt.ylabel('Normalized Current Density')
    plt.grid(True)
    plt.show()
    # Display data as a table
    data = {
    'x (mm)': x,
    'Normalized Current Density': normalized_intensity[center_idx, :]
    }
    df = pd.DataFrame(data)
    print("\nNormalized Current Density Table:\n")
    print(df.to_string(index=False))

    return normalized_intensity

def calculate_stage_current_density(Lsx, Lsy, x, y, normalized_intensity):
    # Determine indices for the stage area
    x_stage = (x >= -Lsx / 2) & (x <= Lsx / 2)
    y_stage = (y >= -Lsy / 2) & (y <= Lsy / 2)
    # Calculate current density in the stage area
    stage_density = np.trapz(
    np.trapz(normalized_intensity[np.ix_(y_stage, x_stage)], x[x_stage], axis=1),
```

```
    y[y_stage]
    )
    return stage_density

def calculate_total_current_density(x, y, normalized_intensity):
    # Calculate total current density across the entire simulation area
    total_density = np.trapz(np.trapz(normalized_intensity, x, axis=1), y)

    return total_density

# Example parameters
FWHM = 3 # Full Width at Half Maximum
F = 1 # Fraction of beam's radius
Lsx, Lsy = 6, 4 # Stage dimensions
Lax, Lay = 15, 12 # Aperture dimensions

# Raster the beam and calculate total intensity
normalized_intensity = raster_beam(FWHM, F, Lsx, Lsy, Lax, Lay)

# Create grid for x and y coordinates
x = np.linspace(-Lax / 2, Lax / 2, 500)
y = np.linspace(-Lay / 2, Lay / 2, 500)

# Calculate stage current density
stage_density = calculate_stage_current_density(Lsx, Lsy, x, y, normalized_intensity)
print(f"Stage current density: {stage_density}")

# Calculate total current density
total_density = calculate_total_current_density(x, y, normalized_intensity)
print(f"Total current density: {total_density}")
```

## Appendix B: FEA Output

### B.1 Surface deflection profiles

In the following tables, length refers to the profile measured along the specimen surface, while longitudinal designates the profile taken in the longitudinal direction, extending from short-edge to short-edge. By contrast, transverse corresponds to the profile measured in the transverse direction, spanning from long-edge to long-edge.

It should be noted that the units in following tables are as follows: lengths are in mm, stresses are in MPa, and strains are percents.

Sample N3

Table B-1 Surface deflection profiles for sample N3, step 39%YS.

| **Hardened Layer** | | | | **Soft Bulk** | | | |
|---|---|---|---|---|---|---|---|
| Longitudinal | | Transverse | | Longitudinal | | Transverse | |
| Length | Stress | Length | Stress | Length | Stress | Length | Stress |
| 0.00E+00 | 2.54E-03 | 0.00E+00 | 6.06E-03 | 0.00E+00 | 2.45E-03 | 0.00E+00 | 6.08E-03 |
| 1.04E-01 | 2.25E-03 | 7.29E-02 | 5.98E-03 | 1.04E-01 | 2.15E-03 | 7.29E-02 | 6.00E-03 |
| 2.08E-01 | 1.98E-03 | 1.46E-01 | 5.90E-03 | 2.08E-01 | 1.87E-03 | 1.46E-01 | 5.92E-03 |
| 3.13E-01 | 1.74E-03 | 2.19E-01 | 5.83E-03 | 3.13E-01 | 1.61E-03 | 2.19E-01 | 5.86E-03 |
| 4.17E-01 | 1.55E-03 | 2.92E-01 | 5.78E-03 | 4.17E-01 | 1.41E-03 | 2.92E-01 | 5.80E-03 |
| 5.21E-01 | 1.42E-03 | 3.65E-01 | 5.73E-03 | 5.21E-01 | 1.28E-03 | 3.65E-01 | 5.76E-03 |
| 6.25E-01 | 1.35E-03 | 4.38E-01 | 5.69E-03 | 6.25E-01 | 1.23E-03 | 4.38E-01 | 5.72E-03 |
| 7.29E-01 | 1.33E-03 | 5.10E-01 | 5.66E-03 | 7.29E-01 | 1.25E-03 | 5.10E-01 | 5.69E-03 |
| 8.33E-01 | 1.63E-03 | 5.83E-01 | 5.63E-03 | 8.33E-01 | 1.46E-03 | 5.83E-01 | 5.66E-03 |
| 9.38E-01 | 1.92E-03 | 6.56E-01 | 5.60E-03 | 9.38E-01 | 1.78E-03 | 6.56E-01 | 5.64E-03 |
| 1.04E+00 | 2.22E-03 | 7.29E-01 | 5.58E-03 | 1.04E+00 | 2.11E-03 | 7.29E-01 | 5.62E-03 |
| 1.15E+00 | 2.55E-03 | 8.02E-01 | 5.57E-03 | 1.15E+00 | 2.45E-03 | 8.02E-01 | 5.60E-03 |
| 1.25E+00 | 2.88E-03 | 8.75E-01 | 5.55E-03 | 1.25E+00 | 2.80E-03 | 8.75E-01 | 5.59E-03 |
| 1.35E+00 | 3.21E-03 | 9.48E-01 | 5.54E-03 | 1.35E+00 | 3.15E-03 | 9.48E-01 | 5.58E-03 |
| 1.46E+00 | 3.54E-03 | 1.02E+00 | 5.54E-03 | 1.46E+00 | 3.50E-03 | 1.02E+00 | 5.57E-03 |
| 1.56E+00 | 3.86E-03 | 1.09E+00 | 5.53E-03 | 1.56E+00 | 3.83E-03 | 1.09E+00 | 5.56E-03 |

| | | | | | | | |
|---|---|---|---|---|---|---|---|
| 1.67E+00 | 4.17E-03 | 1.17E+00 | 5.52E-03 | 1.67E+00 | 4.14E-03 | 1.17E+00 | 5.56E-03 |
| 1.77E+00 | 4.45E-03 | 1.24E+00 | 5.52E-03 | 1.77E+00 | 4.44E-03 | 1.24E+00 | 5.55E-03 |
| 1.88E+00 | 4.72E-03 | 1.31E+00 | 5.51E-03 | 1.88E+00 | 4.71E-03 | 1.31E+00 | 5.55E-03 |
| 1.98E+00 | 4.95E-03 | 1.39E+00 | 5.51E-03 | 1.98E+00 | 4.96E-03 | 1.39E+00 | 5.55E-03 |
| 2.08E+00 | 5.15E-03 | 1.46E+00 | 5.51E-03 | 2.08E+00 | 5.17E-03 | 1.46E+00 | 5.55E-03 |
| 2.19E+00 | 5.30E-03 | 1.53E+00 | 5.51E-03 | 2.19E+00 | 5.33E-03 | 1.53E+00 | 5.55E-03 |
| 2.29E+00 | 5.42E-03 | 1.60E+00 | 5.51E-03 | 2.29E+00 | 5.45E-03 | 1.60E+00 | 5.55E-03 |
| 2.40E+00 | 5.48E-03 | 1.68E+00 | 5.51E-03 | 2.40E+00 | 5.52E-03 | 1.68E+00 | 5.54E-03 |
| 2.50E+00 | 5.51E-03 | 1.75E+00 | 5.51E-03 | 2.50E+00 | 5.54E-03 | 1.75E+00 | 5.54E-03 |
| 2.60E+00 | 5.48E-03 | 1.82E+00 | 5.51E-03 | 2.60E+00 | 5.52E-03 | 1.82E+00 | 5.54E-03 |
| 2.71E+00 | 5.42E-03 | 1.90E+00 | 5.51E-03 | 2.71E+00 | 5.45E-03 | 1.90E+00 | 5.55E-03 |
| 2.81E+00 | 5.31E-03 | 1.97E+00 | 5.51E-03 | 2.81E+00 | 5.33E-03 | 1.97E+00 | 5.55E-03 |
| 2.92E+00 | 5.15E-03 | 2.04E+00 | 5.51E-03 | 2.92E+00 | 5.17E-03 | 2.04E+00 | 5.55E-03 |
| 3.02E+00 | 4.95E-03 | 2.11E+00 | 5.51E-03 | 3.02E+00 | 4.96E-03 | 2.11E+00 | 5.55E-03 |
| 3.13E+00 | 4.72E-03 | 2.19E+00 | 5.51E-03 | 3.13E+00 | 4.72E-03 | 2.19E+00 | 5.55E-03 |
| 3.23E+00 | 4.46E-03 | 2.26E+00 | 5.52E-03 | 3.23E+00 | 4.44E-03 | 2.26E+00 | 5.55E-03 |
| 3.33E+00 | 4.17E-03 | 2.33E+00 | 5.52E-03 | 3.33E+00 | 4.15E-03 | 2.33E+00 | 5.56E-03 |
| 3.44E+00 | 3.87E-03 | 2.41E+00 | 5.53E-03 | 3.44E+00 | 3.83E-03 | 2.41E+00 | 5.56E-03 |
| 3.54E+00 | 3.55E-03 | 2.48E+00 | 5.54E-03 | 3.54E+00 | 3.50E-03 | 2.48E+00 | 5.57E-03 |
| 3.65E+00 | 3.22E-03 | 2.55E+00 | 5.54E-03 | 3.65E+00 | 3.16E-03 | 2.55E+00 | 5.58E-03 |
| 3.75E+00 | 2.88E-03 | 2.63E+00 | 5.56E-03 | 3.75E+00 | 2.81E-03 | 2.63E+00 | 5.59E-03 |
| 3.85E+00 | 2.55E-03 | 2.70E+00 | 5.57E-03 | 3.85E+00 | 2.46E-03 | 2.70E+00 | 5.60E-03 |
| 3.96E+00 | 2.23E-03 | 2.77E+00 | 5.59E-03 | 3.96E+00 | 2.12E-03 | 2.77E+00 | 5.62E-03 |
| 4.06E+00 | 1.92E-03 | 2.84E+00 | 5.60E-03 | 4.06E+00 | 1.78E-03 | 2.84E+00 | 5.64E-03 |
| 4.1667 | 1.64E-03 | 2.9167 | 5.63E-03 | 4.17E+00 | 1.47E-03 | 2.92E+00 | 5.66E-03 |
| 4.2708 | 1.38E-03 | 2.9896 | 5.66E-03 | 4.27E+00 | 1.26E-03 | 2.99E+00 | 5.69E-03 |
| 4.375 | 1.36E-03 | 3.0625 | 5.69E-03 | 4.38E+00 | 1.24E-03 | 3.06E+00 | 5.72E-03 |
| 4.4792 | 1.43E-03 | 3.1354 | 5.73E-03 | 4.48E+00 | 1.28E-03 | 3.14E+00 | 5.76E-03 |
| 4.5833 | 1.55E-03 | 3.2083 | 5.78E-03 | 4.58E+00 | 1.42E-03 | 3.21E+00 | 5.81E-03 |
| 4.6875 | 1.74E-03 | 3.2813 | 5.84E-03 | 4.69E+00 | 1.62E-03 | 3.28E+00 | 5.86E-03 |
| 4.7917 | 1.98E-03 | 3.3542 | 5.90E-03 | 4.79E+00 | 1.87E-03 | 3.35E+00 | 5.93E-03 |
| 4.8958 | 2.25E-03 | 3.4271 | 5.98E-03 | 4.90E+00 | 2.15E-03 | 3.43E+00 | 6.00E-03 |
| 5 | 2.54E-03 | 3.5 | 6.06E-03 | 5.00E+00 | 2.45E-03 | 3.50E+00 | 6.09E-03 |

Table B-2 Surface deflection profiles for sample N3, step 47%YS.

| **Hardened Layer** | | | | **Soft Bulk** | | | |
|---|---|---|---|---|---|---|---|
| Longitudinal | | Transverse | | Longitudinal | | Transverse | |
| Length | Stress | Length | Stress | Length | Stress | Length | Stress |
| 0.00E+00 | 2.95E-03 | 0.00E+00 | 7.03E-03 | 0.00E+00 | 2.85E-03 | 0.00E+00 | 7.06E-03 |
| 1.04E-01 | 2.61E-03 | 7.29E-02 | 6.93E-03 | 1.04E-01 | 2.50E-03 | 7.29E-02 | 6.96E-03 |
| 2.08E-01 | 2.29E-03 | 1.46E-01 | 6.84E-03 | 2.08E-01 | 2.17E-03 | 1.46E-01 | 6.87E-03 |

| | | | | | | | |
|---|---|---|---|---|---|---|---|
| 3.13E-01 | 2.01E-03 | 2.19E-01 | 6.76E-03 | 3.13E-01 | 1.87E-03 | 2.19E-01 | 6.79E-03 |
| 4.17E-01 | 1.79E-03 | 2.92E-01 | 6.69E-03 | 4.17E-01 | 1.63E-03 | 2.92E-01 | 6.72E-03 |
| 5.21E-01 | 1.63E-03 | 3.65E-01 | 6.63E-03 | 5.21E-01 | 1.47E-03 | 3.65E-01 | 6.67E-03 |
| 6.25E-01 | 1.55E-03 | 4.38E-01 | 6.59E-03 | 6.25E-01 | 1.41E-03 | 4.38E-01 | 6.62E-03 |
| 7.29E-01 | 1.51E-03 | 5.10E-01 | 6.55E-03 | 7.29E-01 | 1.43E-03 | 5.10E-01 | 6.59E-03 |
| 8.33E-01 | 1.86E-03 | 5.83E-01 | 6.52E-03 | 8.33E-01 | 1.67E-03 | 5.83E-01 | 6.56E-03 |
| 9.38E-01 | 2.19E-03 | 6.56E-01 | 6.49E-03 | 9.38E-01 | 2.03E-03 | 6.56E-01 | 6.53E-03 |
| 1.04E+00 | 2.55E-03 | 7.29E-01 | 6.47E-03 | 1.04E+00 | 2.42E-03 | 7.29E-01 | 6.51E-03 |
| 1.15E+00 | 2.92E-03 | 8.02E-01 | 6.45E-03 | 1.15E+00 | 2.82E-03 | 8.02E-01 | 6.49E-03 |
| 1.25E+00 | 3.31E-03 | 8.75E-01 | 6.43E-03 | 1.25E+00 | 3.22E-03 | 8.75E-01 | 6.48E-03 |
| 1.35E+00 | 3.70E-03 | 9.48E-01 | 6.42E-03 | 1.35E+00 | 3.63E-03 | 9.48E-01 | 6.47E-03 |
| 1.46E+00 | 4.08E-03 | 1.02E+00 | 6.41E-03 | 1.46E+00 | 4.03E-03 | 1.02E+00 | 6.46E-03 |
| 1.56E+00 | 4.45E-03 | 1.09E+00 | 6.41E-03 | 1.56E+00 | 4.41E-03 | 1.09E+00 | 6.45E-03 |
| 1.67E+00 | 4.81E-03 | 1.17E+00 | 6.40E-03 | 1.67E+00 | 4.79E-03 | 1.17E+00 | 6.45E-03 |
| 1.77E+00 | 5.15E-03 | 1.24E+00 | 6.40E-03 | 1.77E+00 | 5.14E-03 | 1.24E+00 | 6.44E-03 |
| 1.88E+00 | 5.46E-03 | 1.31E+00 | 6.39E-03 | 1.88E+00 | 5.46E-03 | 1.31E+00 | 6.44E-03 |
| 1.98E+00 | 5.74E-03 | 1.39E+00 | 6.39E-03 | 1.98E+00 | 5.75E-03 | 1.39E+00 | 6.44E-03 |
| 2.08E+00 | 5.97E-03 | 1.46E+00 | 6.39E-03 | 2.08E+00 | 5.99E-03 | 1.46E+00 | 6.43E-03 |
| 2.19E+00 | 6.15E-03 | 1.53E+00 | 6.39E-03 | 2.19E+00 | 6.18E-03 | 1.53E+00 | 6.43E-03 |
| 2.29E+00 | 6.28E-03 | 1.60E+00 | 6.38E-03 | 2.29E+00 | 6.32E-03 | 1.60E+00 | 6.43E-03 |
| 2.40E+00 | 6.36E-03 | 1.68E+00 | 6.38E-03 | 2.40E+00 | 6.40E-03 | 1.68E+00 | 6.43E-03 |
| 2.50E+00 | 6.38E-03 | 1.75E+00 | 6.38E-03 | 2.50E+00 | 6.43E-03 | 1.75E+00 | 6.43E-03 |
| 2.60E+00 | 6.36E-03 | 1.82E+00 | 6.38E-03 | 2.60E+00 | 6.40E-03 | 1.82E+00 | 6.43E-03 |
| 2.71E+00 | 6.28E-03 | 1.90E+00 | 6.38E-03 | 2.71E+00 | 6.32E-03 | 1.90E+00 | 6.43E-03 |
| 2.81E+00 | 6.15E-03 | 1.97E+00 | 6.39E-03 | 2.81E+00 | 6.18E-03 | 1.97E+00 | 6.43E-03 |
| 2.92E+00 | 5.97E-03 | 2.04E+00 | 6.39E-03 | 2.92E+00 | 5.99E-03 | 2.04E+00 | 6.43E-03 |
| 3.02E+00 | 5.74E-03 | 2.11E+00 | 6.39E-03 | 3.02E+00 | 5.75E-03 | 2.11E+00 | 6.44E-03 |
| 3.13E+00 | 5.47E-03 | 2.19E+00 | 6.39E-03 | 3.13E+00 | 5.46E-03 | 2.19E+00 | 6.44E-03 |
| 3.23E+00 | 5.16E-03 | 2.26E+00 | 6.40E-03 | 3.23E+00 | 5.14E-03 | 2.26E+00 | 6.44E-03 |
| 3.33E+00 | 4.82E-03 | 2.33E+00 | 6.40E-03 | 3.33E+00 | 4.79E-03 | 2.33E+00 | 6.45E-03 |
| 3.44E+00 | 4.46E-03 | 2.41E+00 | 6.41E-03 | 3.44E+00 | 4.42E-03 | 2.41E+00 | 6.45E-03 |
| 3.54E+00 | 4.09E-03 | 2.48E+00 | 6.41E-03 | 3.54E+00 | 4.03E-03 | 2.48E+00 | 6.46E-03 |
| 3.65E+00 | 3.71E-03 | 2.55E+00 | 6.42E-03 | 3.65E+00 | 3.64E-03 | 2.55E+00 | 6.47E-03 |
| 3.75E+00 | 3.32E-03 | 2.63E+00 | 6.44E-03 | 3.75E+00 | 3.23E-03 | 2.63E+00 | 6.48E-03 |
| 3.85E+00 | 2.93E-03 | 2.70E+00 | 6.45E-03 | 3.85E+00 | 2.83E-03 | 2.70E+00 | 6.49E-03 |
| 3.96E+00 | 2.56E-03 | 2.77E+00 | 6.47E-03 | 3.96E+00 | 2.43E-03 | 2.77E+00 | 6.51E-03 |
| 4.06E+00 | 2.21E-03 | 2.84E+00 | 6.49E-03 | 4.06E+00 | 2.05E-03 | 2.84E+00 | 6.53E-03 |
| 4.1667 | 1.88E-03 | 2.9167 | 6.52E-03 | 4.17E+00 | 1.69E-03 | 2.92E+00 | 6.56E-03 |
| 4.2708 | 1.59E-03 | 2.9896 | 6.55E-03 | 4.27E+00 | 1.45E-03 | 2.99E+00 | 6.59E-03 |
| 4.375 | 1.56E-03 | 3.0625 | 6.59E-03 | 4.38E+00 | 1.43E-03 | 3.06E+00 | 6.63E-03 |
| 4.4792 | 1.65E-03 | 3.1354 | 6.64E-03 | 4.48E+00 | 1.48E-03 | 3.14E+00 | 6.67E-03 |

| | | | | | | | |
|---|---|---|---|---|---|---|---|
| 4.5833 | 1.80E-03 | 3.2083 | 6.69E-03 | 4.58E+00 | 1.64E-03 | 3.21E+00 | 6.72E-03 |
| 4.6875 | 2.02E-03 | 3.2813 | 6.76E-03 | 4.69E+00 | 1.88E-03 | 3.28E+00 | 6.79E-03 |
| 4.7917 | 2.30E-03 | 3.3542 | 6.84E-03 | 4.79E+00 | 2.17E-03 | 3.35E+00 | 6.87E-03 |
| 4.8958 | 2.61E-03 | 3.4271 | 6.93E-03 | 4.90E+00 | 2.50E-03 | 3.43E+00 | 6.96E-03 |
| 5 | 2.95E-03 | 3.5 | 7.03E-03 | 5.00E+00 | 2.85E-03 | 3.50E+00 | 7.06E-03 |

Table B-3 Surface deflection profiles for sample N3, step 51%YS.

| **Hardened Layer** | | | | **Soft Bulk** | | | |
|---|---|---|---|---|---|---|---|
| Longitudinal | | Transverse | | Longitudinal | | Transverse | |
| Length | Stress | Length | Stress | Length | Stress | Length | Stress |
| 0.00E+00 | 3.36E-36 | 0.00E+00 | 9.06E-03 | 0.00E+00 | 3.93E-03 | 0.00E+00 | 9.08E-03 |
| 1.04E-01 | 9.91E-37 | 7.29E-02 | 8.90E-03 | 1.04E-01 | 3.47E-03 | 7.29E-02 | 8.92E-03 |
| 2.08E-01 | 3.08E-37 | 1.46E-01 | 8.75E-03 | 2.08E-01 | 3.03E-03 | 1.46E-01 | 8.77E-03 |
| 3.13E-01 | 2.15E-36 | 2.19E-01 | 8.63E-03 | 3.13E-01 | 2.63E-03 | 2.19E-01 | 8.65E-03 |
| 4.17E-01 | 5.14E-37 | 2.92E-01 | 8.52E-03 | 4.17E-01 | 2.30E-03 | 2.92E-01 | 8.54E-03 |
| 5.21E-01 | 1.62E-37 | 3.65E-01 | 8.43E-03 | 5.21E-01 | 2.05E-03 | 3.65E-01 | 8.45E-03 |
| 6.25E-01 | 5.66E-36 | 4.38E-01 | 8.35E-03 | 6.25E-01 | 1.91E-03 | 4.38E-01 | 8.38E-03 |
| 7.29E-01 | 7.16E-36 | 5.10E-01 | 8.29E-03 | 7.29E-01 | 1.75E-03 | 5.10E-01 | 8.31E-03 |
| 8.33E-01 | 2.23E-03 | 5.83E-01 | 8.24E-03 | 8.33E-01 | 2.13E-03 | 5.83E-01 | 8.26E-03 |
| 9.38E-01 | 2.60E-03 | 6.56E-01 | 8.19E-03 | 9.38E-01 | 2.53E-03 | 6.56E-01 | 8.22E-03 |
| 1.04E+00 | 3.04E-03 | 7.29E-01 | 8.15E-03 | 1.04E+00 | 2.98E-03 | 7.29E-01 | 8.18E-03 |
| 1.15E+00 | 3.51E-03 | 8.02E-01 | 8.12E-03 | 1.15E+00 | 3.46E-03 | 8.02E-01 | 8.15E-03 |
| 1.25E+00 | 4.00E-03 | 8.75E-01 | 8.10E-03 | 1.25E+00 | 3.96E-03 | 8.75E-01 | 8.12E-03 |
| 1.35E+00 | 4.50E-03 | 9.48E-01 | 8.07E-03 | 1.35E+00 | 4.46E-03 | 9.48E-01 | 8.10E-03 |
| 1.46E+00 | 5.00E-03 | 1.02E+00 | 8.06E-03 | 1.46E+00 | 4.97E-03 | 1.02E+00 | 8.08E-03 |
| 1.56E+00 | 5.48E-03 | 1.09E+00 | 8.04E-03 | 1.56E+00 | 5.47E-03 | 1.09E+00 | 8.07E-03 |
| 1.67E+00 | 5.95E-03 | 1.17E+00 | 8.03E-03 | 1.67E+00 | 5.95E-03 | 1.17E+00 | 8.06E-03 |
| 1.77E+00 | 6.40E-03 | 1.24E+00 | 8.02E-03 | 1.77E+00 | 6.40E-03 | 1.24E+00 | 8.05E-03 |
| 1.88E+00 | 6.81E-03 | 1.31E+00 | 8.02E-03 | 1.88E+00 | 6.82E-03 | 1.31E+00 | 8.04E-03 |
| 1.98E+00 | 7.16E-03 | 1.39E+00 | 8.01E-03 | 1.98E+00 | 7.18E-03 | 1.39E+00 | 8.04E-03 |
| 2.08E+00 | 7.46E-03 | 1.46E+00 | 8.01E-03 | 2.08E+00 | 7.48E-03 | 1.46E+00 | 8.04E-03 |
| 2.19E+00 | 7.69E-03 | 1.53E+00 | 8.00E-03 | 2.19E+00 | 7.72E-03 | 1.53E+00 | 8.03E-03 |
| 2.29E+00 | 7.86E-03 | 1.60E+00 | 8.00E-03 | 2.29E+00 | 7.89E-03 | 1.60E+00 | 8.03E-03 |
| 2.40E+00 | 7.96E-03 | 1.68E+00 | 8.00E-03 | 2.40E+00 | 7.99E-03 | 1.68E+00 | 8.03E-03 |
| 2.50E+00 | 8.00E-03 | 1.75E+00 | 8.00E-03 | 2.50E+00 | 8.03E-03 | 1.75E+00 | 8.03E-03 |
| 2.60E+00 | 7.96E-03 | 1.82E+00 | 8.00E-03 | 2.60E+00 | 7.99E-03 | 1.82E+00 | 8.03E-03 |
| 2.71E+00 | 7.86E-03 | 1.90E+00 | 8.00E-03 | 2.71E+00 | 7.89E-03 | 1.90E+00 | 8.03E-03 |
| 2.81E+00 | 7.69E-03 | 1.97E+00 | 8.00E-03 | 2.81E+00 | 7.72E-03 | 1.97E+00 | 8.03E-03 |
| 2.92E+00 | 7.46E-03 | 2.04E+00 | 8.01E-03 | 2.92E+00 | 7.48E-03 | 2.04E+00 | 8.04E-03 |
| 3.02E+00 | 7.16E-03 | 2.11E+00 | 8.01E-03 | 3.02E+00 | 7.18E-03 | 2.11E+00 | 8.04E-03 |

| | | | | | | | |
|---|---|---|---|---|---|---|---|
| 3.13E+00 | 6.81E-03 | 2.19E+00 | 8.02E-03 | 3.13E+00 | 6.82E-03 | 2.19E+00 | 8.04E-03 |
| 3.23E+00 | 6.40E-03 | 2.26E+00 | 8.02E-03 | 3.23E+00 | 6.40E-03 | 2.26E+00 | 8.05E-03 |
| 3.33E+00 | 5.95E-03 | 2.33E+00 | 8.03E-03 | 3.33E+00 | 5.94E-03 | 2.33E+00 | 8.06E-03 |
| 3.44E+00 | 5.48E-03 | 2.41E+00 | 8.04E-03 | 3.44E+00 | 5.46E-03 | 2.41E+00 | 8.07E-03 |
| 3.54E+00 | 4.99E-03 | 2.48E+00 | 8.06E-03 | 3.54E+00 | 4.96E-03 | 2.48E+00 | 8.08E-03 |
| 3.65E+00 | 4.49E-03 | 2.55E+00 | 8.07E-03 | 3.65E+00 | 4.46E-03 | 2.55E+00 | 8.10E-03 |
| 3.75E+00 | 3.99E-03 | 2.63E+00 | 8.10E-03 | 3.75E+00 | 3.95E-03 | 2.63E+00 | 8.12E-03 |
| 3.85E+00 | 3.50E-03 | 2.70E+00 | 8.12E-03 | 3.85E+00 | 3.45E-03 | 2.70E+00 | 8.15E-03 |
| 3.96E+00 | 3.02E-03 | 2.77E+00 | 8.15E-03 | 3.96E+00 | 2.97E-03 | 2.77E+00 | 8.18E-03 |
| 4.06E+00 | 2.58E-03 | 2.84E+00 | 8.19E-03 | 4.06E+00 | 2.52E-03 | 2.84E+00 | 8.22E-03 |
| 4.1667 | 2.22E-03 | 2.9167 | 8.24E-03 | 4.17E+00 | 2.11E-03 | 2.92E+00 | 8.26E-03 |
| 4.2708 | 5.67E-35 | 2.9896 | 8.29E-03 | 4.27E+00 | 1.72E-03 | 2.99E+00 | 8.31E-03 |
| 4.375 | 7.41E-36 | 3.0625 | 8.36E-03 | 4.38E+00 | 1.88E-03 | 3.06E+00 | 8.38E-03 |
| 4.4792 | 2.85E-36 | 3.1354 | 8.43E-03 | 4.48E+00 | 2.02E-03 | 3.14E+00 | 8.45E-03 |
| 4.5833 | 4.38E-36 | 3.2083 | 8.52E-03 | 4.58E+00 | 2.27E-03 | 3.21E+00 | 8.54E-03 |
| 4.6875 | 1.23E-35 | 3.2813 | 8.63E-03 | 4.69E+00 | 2.61E-03 | 3.28E+00 | 8.65E-03 |
| 4.7917 | 5.50E-36 | 3.3542 | 8.75E-03 | 4.79E+00 | 3.01E-03 | 3.35E+00 | 8.77E-03 |
| 4.8958 | 5.01E-36 | 3.4271 | 8.90E-03 | 4.90E+00 | 3.45E-03 | 3.43E+00 | 8.92E-03 |
| 5 | 7.17E-36 | 3.5 | 9.06E-03 | 5.00E+00 | 3.91E-03 | 3.50E+00 | 9.08E-03 |

Table B-4 Surface deflection profiles for sample N3, step 62%YS.

| **Hardened Layer** | | | | **Soft Bulk** | | | |
|---|---|---|---|---|---|---|---|
| Longitudinal | | Transverse | | Longitudinal | | Transverse | |
| Length | Stress | Length | Stress | Length | Stress | Length | Stress |
| 0.00E+00 | 3.36E-03 | 0.00E+00 | 7.98E-03 | 0.00E+00 | 3.25E-03 | 0.00E+00 | 8.02E-03 |
| 1.04E-01 | 2.97E-03 | 7.29E-02 | 7.87E-03 | 1.04E-01 | 2.85E-03 | 7.29E-02 | 7.90E-03 |
| 2.08E-01 | 2.61E-03 | 1.46E-01 | 7.76E-03 | 2.08E-01 | 2.47E-03 | 1.46E-01 | 7.79E-03 |
| 3.13E-01 | 2.29E-03 | 2.19E-01 | 7.67E-03 | 3.13E-01 | 2.13E-03 | 2.19E-01 | 7.70E-03 |
| 4.17E-01 | 2.03E-03 | 2.92E-01 | 7.59E-03 | 4.17E-01 | 1.85E-03 | 2.92E-01 | 7.63E-03 |
| 5.21E-01 | 1.85E-03 | 3.65E-01 | 7.52E-03 | 5.21E-01 | 1.66E-03 | 3.65E-01 | 7.57E-03 |
| 6.25E-01 | 1.75E-03 | 4.38E-01 | 7.47E-03 | 6.25E-01 | 1.60E-03 | 4.38E-01 | 7.51E-03 |
| 7.29E-01 | 1.70E-03 | 5.10E-01 | 7.42E-03 | 7.29E-01 | 1.61E-03 | 5.10E-01 | 7.47E-03 |
| 8.33E-01 | 2.09E-03 | 5.83E-01 | 7.39E-03 | 8.33E-01 | 1.88E-03 | 5.83E-01 | 7.43E-03 |
| 9.38E-01 | 2.46E-03 | 6.56E-01 | 7.36E-03 | 9.38E-01 | 2.28E-03 | 6.56E-01 | 7.41E-03 |
| 1.04E+00 | 2.87E-03 | 7.29E-01 | 7.33E-03 | 1.04E+00 | 2.72E-03 | 7.29E-01 | 7.38E-03 |
| 1.15E+00 | 3.29E-03 | 8.02E-01 | 7.31E-03 | 1.15E+00 | 3.17E-03 | 8.02E-01 | 7.36E-03 |
| 1.25E+00 | 3.73E-03 | 8.75E-01 | 7.30E-03 | 1.25E+00 | 3.63E-03 | 8.75E-01 | 7.35E-03 |
| 1.35E+00 | 4.17E-03 | 9.48E-01 | 7.28E-03 | 1.35E+00 | 4.09E-03 | 9.48E-01 | 7.34E-03 |
| 1.46E+00 | 4.61E-03 | 1.02E+00 | 7.27E-03 | 1.46E+00 | 4.54E-03 | 1.02E+00 | 7.33E-03 |
| 1.56E+00 | 5.04E-03 | 1.09E+00 | 7.26E-03 | 1.56E+00 | 4.99E-03 | 1.09E+00 | 7.32E-03 |
| 1.67E+00 | 5.45E-03 | 1.17E+00 | 7.26E-03 | 1.67E+00 | 5.41E-03 | 1.17E+00 | 7.31E-03 |

| | | | | | | | |
|---|---|---|---|---|---|---|---|
| 1.77E+00 | 5.84E-03 | 1.24E+00 | 7.25E-03 | 1.77E+00 | 5.82E-03 | 1.24E+00 | 7.31E-03 |
| 1.88E+00 | 6.20E-03 | 1.31E+00 | 7.25E-03 | 1.88E+00 | 6.19E-03 | 1.31E+00 | 7.30E-03 |
| 1.98E+00 | 6.51E-03 | 1.39E+00 | 7.25E-03 | 1.98E+00 | 6.52E-03 | 1.39E+00 | 7.30E-03 |
| 2.08E+00 | 6.77E-03 | 1.46E+00 | 7.24E-03 | 2.08E+00 | 6.80E-03 | 1.46E+00 | 7.30E-03 |
| 2.19E+00 | 6.97E-03 | 1.53E+00 | 7.24E-03 | 2.19E+00 | 7.01E-03 | 1.53E+00 | 7.30E-03 |
| 2.29E+00 | 7.12E-03 | 1.60E+00 | 7.24E-03 | 2.29E+00 | 7.17E-03 | 1.60E+00 | 7.30E-03 |
| 2.40E+00 | 7.21E-03 | 1.68E+00 | 7.24E-03 | 2.40E+00 | 7.27E-03 | 1.68E+00 | 7.30E-03 |
| 2.50E+00 | 7.24E-03 | 1.75E+00 | 7.24E-03 | 2.50E+00 | 7.30E-03 | 1.75E+00 | 7.30E-03 |
| 2.60E+00 | 7.21E-03 | 1.82E+00 | 7.24E-03 | 2.60E+00 | 7.27E-03 | 1.82E+00 | 7.30E-03 |
| 2.71E+00 | 7.12E-03 | 1.90E+00 | 7.24E-03 | 2.71E+00 | 7.17E-03 | 1.90E+00 | 7.30E-03 |
| 2.81E+00 | 6.97E-03 | 1.97E+00 | 7.24E-03 | 2.81E+00 | 7.01E-03 | 1.97E+00 | 7.30E-03 |
| 2.92E+00 | 6.77E-03 | 2.04E+00 | 7.24E-03 | 2.92E+00 | 6.80E-03 | 2.04E+00 | 7.30E-03 |
| 3.02E+00 | 6.51E-03 | 2.11E+00 | 7.25E-03 | 3.02E+00 | 6.53E-03 | 2.11E+00 | 7.30E-03 |
| 3.13E+00 | 6.20E-03 | 2.19E+00 | 7.25E-03 | 3.13E+00 | 6.19E-03 | 2.19E+00 | 7.30E-03 |
| 3.23E+00 | 5.84E-03 | 2.26E+00 | 7.25E-03 | 3.23E+00 | 5.82E-03 | 2.26E+00 | 7.31E-03 |
| 3.33E+00 | 5.45E-03 | 2.33E+00 | 7.26E-03 | 3.33E+00 | 5.42E-03 | 2.33E+00 | 7.31E-03 |
| 3.44E+00 | 5.04E-03 | 2.41E+00 | 7.26E-03 | 3.44E+00 | 4.99E-03 | 2.41E+00 | 7.32E-03 |
| 3.54E+00 | 4.62E-03 | 2.48E+00 | 7.27E-03 | 3.54E+00 | 4.55E-03 | 2.48E+00 | 7.33E-03 |
| 3.65E+00 | 4.18E-03 | 2.55E+00 | 7.28E-03 | 3.65E+00 | 4.10E-03 | 2.55E+00 | 7.34E-03 |
| 3.75E+00 | 3.74E-03 | 2.63E+00 | 7.30E-03 | 3.75E+00 | 3.64E-03 | 2.63E+00 | 7.35E-03 |
| 3.85E+00 | 3.30E-03 | 2.70E+00 | 7.31E-03 | 3.85E+00 | 3.18E-03 | 2.70E+00 | 7.36E-03 |
| 3.96E+00 | 2.88E-03 | 2.77E+00 | 7.33E-03 | 3.96E+00 | 2.73E-03 | 2.77E+00 | 7.38E-03 |
| 4.06E+00 | 2.47E-03 | 2.84E+00 | 7.36E-03 | 4.06E+00 | 2.29E-03 | 2.84E+00 | 7.41E-03 |
| 4.1667 | 2.11E-03 | 2.9167 | 7.39E-03 | 4.17E+00 | 1.89E-03 | 2.92E+00 | 7.43E-03 |
| 4.2708 | 1.79E-03 | 2.9896 | 7.42E-03 | 4.27E+00 | 1.63E-03 | 2.99E+00 | 7.47E-03 |
| 4.375 | 1.76E-03 | 3.0625 | 7.47E-03 | 4.38E+00 | 1.61E-03 | 3.06E+00 | 7.51E-03 |
| 4.4792 | 1.86E-03 | 3.1354 | 7.52E-03 | 4.48E+00 | 1.67E-03 | 3.14E+00 | 7.57E-03 |
| 4.5833 | 2.04E-03 | 3.2083 | 7.59E-03 | 4.58E+00 | 1.86E-03 | 3.21E+00 | 7.63E-03 |
| 4.6875 | 2.29E-03 | 3.2813 | 7.67E-03 | 4.69E+00 | 2.13E-03 | 3.28E+00 | 7.70E-03 |
| 4.7917 | 2.61E-03 | 3.3542 | 7.76E-03 | 4.79E+00 | 2.47E-03 | 3.35E+00 | 7.79E-03 |
| 4.8958 | 2.97E-03 | 3.4271 | 7.87E-03 | 4.90E+00 | 2.85E-03 | 3.43E+00 | 7.90E-03 |
| 5 | 3.36E-03 | 3.5 | 7.98E-03 | 5.00E+00 | 3.25E-03 | 3.50E+00 | 8.02E-03 |

Table B-5 Surface deflection profiles for sample N3, step 70%YS.

| **Hardened Layer** | | | | **Soft Bulk** | | | |
|---|---|---|---|---|---|---|---|
| Longitudinal | | Transverse | | Longitudinal | | Transverse | |
| Length | Stress | Length | Stress | Length | Stress | Length | Stress |
| 0.00E+00 | 4.19E-03 | 0.00E+00 | 9.90E-03 | 0.00E+00 | 4.06E-03 | 0.00E+00 | 9.95E-03 |
| 1.04E-01 | 3.70E-03 | 7.29E-02 | 9.75E-03 | 1.04E-01 | 3.55E-03 | 7.29E-02 | 9.80E-03 |
| 2.08E-01 | 3.25E-03 | 1.46E-01 | 9.61E-03 | 2.08E-01 | 3.07E-03 | 1.46E-01 | 9.66E-03 |
| 3.13E-01 | 2.84E-03 | 2.19E-01 | 9.49E-03 | 3.13E-01 | 2.64E-03 | 2.19E-01 | 9.54E-03 |

| | | | | | | | |
|---|---|---|---|---|---|---|---|
| 4.17E-01 | 2.51E-03 | 2.92E-01 | 9.39E-03 | 4.17E-01 | 2.29E-03 | 2.92E-01 | 9.44E-03 |
| 5.21E-01 | 2.28E-03 | 3.65E-01 | 9.30E-03 | 5.21E-01 | 2.05E-03 | 3.65E-01 | 9.36E-03 |
| 6.25E-01 | 2.15E-03 | 4.38E-01 | 9.23E-03 | 6.25E-01 | 1.95E-03 | 4.38E-01 | 9.29E-03 |
| 7.29E-01 | 2.06E-03 | 5.10E-01 | 9.17E-03 | 7.29E-01 | 1.96E-03 | 5.10E-01 | 9.24E-03 |
| 8.33E-01 | 2.54E-03 | 5.83E-01 | 9.13E-03 | 8.33E-01 | 2.28E-03 | 5.83E-01 | 9.19E-03 |
| 9.38E-01 | 2.99E-03 | 6.56E-01 | 9.09E-03 | 9.38E-01 | 2.77E-03 | 6.56E-01 | 9.15E-03 |
| 1.04E+00 | 3.49E-03 | 7.29E-01 | 9.06E-03 | 1.04E+00 | 3.30E-03 | 7.29E-01 | 9.13E-03 |
| 1.15E+00 | 4.01E-03 | 8.02E-01 | 9.03E-03 | 1.15E+00 | 3.86E-03 | 8.02E-01 | 9.10E-03 |
| 1.25E+00 | 4.55E-03 | 8.75E-01 | 9.01E-03 | 1.25E+00 | 4.43E-03 | 8.75E-01 | 9.08E-03 |
| 1.35E+00 | 5.10E-03 | 9.48E-01 | 9.00E-03 | 1.35E+00 | 5.00E-03 | 9.48E-01 | 9.07E-03 |
| 1.46E+00 | 5.65E-03 | 1.02E+00 | 8.98E-03 | 1.46E+00 | 5.57E-03 | 1.02E+00 | 9.06E-03 |
| 1.56E+00 | 6.18E-03 | 1.09E+00 | 8.97E-03 | 1.56E+00 | 6.12E-03 | 1.09E+00 | 9.05E-03 |
| 1.67E+00 | 6.71E-03 | 1.17E+00 | 8.97E-03 | 1.67E+00 | 6.66E-03 | 1.17E+00 | 9.04E-03 |
| 1.77E+00 | 7.20E-03 | 1.24E+00 | 8.96E-03 | 1.77E+00 | 7.17E-03 | 1.24E+00 | 9.04E-03 |
| 1.88E+00 | 7.65E-03 | 1.31E+00 | 8.96E-03 | 1.88E+00 | 7.64E-03 | 1.31E+00 | 9.03E-03 |
| 1.98E+00 | 8.04E-03 | 1.39E+00 | 8.95E-03 | 1.98E+00 | 8.05E-03 | 1.39E+00 | 9.03E-03 |
| 2.08E+00 | 8.36E-03 | 1.46E+00 | 8.95E-03 | 2.08E+00 | 8.40E-03 | 1.46E+00 | 9.03E-03 |
| 2.19E+00 | 8.61E-03 | 1.53E+00 | 8.95E-03 | 2.19E+00 | 8.67E-03 | 1.53E+00 | 9.03E-03 |
| 2.29E+00 | 8.80E-03 | 1.60E+00 | 8.95E-03 | 2.29E+00 | 8.86E-03 | 1.60E+00 | 9.02E-03 |
| 2.40E+00 | 8.91E-03 | 1.68E+00 | 8.95E-03 | 2.40E+00 | 8.98E-03 | 1.68E+00 | 9.02E-03 |
| 2.50E+00 | 8.95E-03 | 1.75E+00 | 8.95E-03 | 2.50E+00 | 9.02E-03 | 1.75E+00 | 9.02E-03 |
| 2.60E+00 | 8.91E-03 | 1.82E+00 | 8.95E-03 | 2.60E+00 | 8.98E-03 | 1.82E+00 | 9.02E-03 |
| 2.71E+00 | 8.80E-03 | 1.90E+00 | 8.95E-03 | 2.71E+00 | 8.86E-03 | 1.90E+00 | 9.02E-03 |
| 2.81E+00 | 8.61E-03 | 1.97E+00 | 8.95E-03 | 2.81E+00 | 8.67E-03 | 1.97E+00 | 9.03E-03 |
| 2.92E+00 | 8.36E-03 | 2.04E+00 | 8.95E-03 | 2.92E+00 | 8.40E-03 | 2.04E+00 | 9.03E-03 |
| 3.02E+00 | 8.04E-03 | 2.11E+00 | 8.95E-03 | 3.02E+00 | 8.06E-03 | 2.11E+00 | 9.03E-03 |
| 3.13E+00 | 7.65E-03 | 2.19E+00 | 8.95E-03 | 3.13E+00 | 7.65E-03 | 2.19E+00 | 9.03E-03 |
| 3.23E+00 | 7.21E-03 | 2.26E+00 | 8.96E-03 | 3.23E+00 | 7.18E-03 | 2.26E+00 | 9.04E-03 |
| 3.33E+00 | 6.71E-03 | 2.33E+00 | 8.97E-03 | 3.33E+00 | 6.66E-03 | 2.33E+00 | 9.04E-03 |
| 3.44E+00 | 6.19E-03 | 2.41E+00 | 8.97E-03 | 3.44E+00 | 6.13E-03 | 2.41E+00 | 9.05E-03 |
| 3.54E+00 | 5.65E-03 | 2.48E+00 | 8.98E-03 | 3.54E+00 | 5.57E-03 | 2.48E+00 | 9.06E-03 |
| 3.65E+00 | 5.11E-03 | 2.55E+00 | 9.00E-03 | 3.65E+00 | 5.01E-03 | 2.55E+00 | 9.07E-03 |
| 3.75E+00 | 4.56E-03 | 2.63E+00 | 9.01E-03 | 3.75E+00 | 4.44E-03 | 2.63E+00 | 9.08E-03 |
| 3.85E+00 | 4.02E-03 | 2.70E+00 | 9.03E-03 | 3.85E+00 | 3.87E-03 | 2.70E+00 | 9.10E-03 |
| 3.96E+00 | 3.49E-03 | 2.77E+00 | 9.06E-03 | 3.96E+00 | 3.31E-03 | 2.77E+00 | 9.12E-03 |
| 4.06E+00 | 3.00E-03 | 2.84E+00 | 9.09E-03 | 4.06E+00 | 2.78E-03 | 2.84E+00 | 9.15E-03 |
| 4.1667 | 2.55E-03 | 2.9167 | 9.13E-03 | 4.17E+00 | 2.29E-03 | 2.92E+00 | 9.19E-03 |
| 4.2708 | 2.17E-03 | 2.9896 | 9.17E-03 | 4.27E+00 | 1.98E-03 | 2.99E+00 | 9.23E-03 |
| 4.375 | 2.15E-03 | 3.0625 | 9.23E-03 | 4.38E+00 | 1.95E-03 | 3.06E+00 | 9.29E-03 |
| 4.4792 | 2.28E-03 | 3.1354 | 9.30E-03 | 4.48E+00 | 2.04E-03 | 3.14E+00 | 9.36E-03 |
| 4.5833 | 2.51E-03 | 3.2083 | 9.38E-03 | 4.58E+00 | 2.28E-03 | 3.21E+00 | 9.44E-03 |

| | | | | | | | |
|---|---|---|---|---|---|---|---|
| 4.6875 | 2.83E-03 | 3.2813 | 9.49E-03 | 4.69E+00 | 2.64E-03 | 3.28E+00 | 9.54E-03 |
| 4.7917 | 3.24E-03 | 3.3542 | 9.61E-03 | 4.79E+00 | 3.06E-03 | 3.35E+00 | 9.65E-03 |
| 4.8958 | 3.69E-03 | 3.4271 | 9.75E-03 | 4.90E+00 | 3.54E-03 | 3.43E+00 | 9.79E-03 |
| 5 | 4.18E-03 | 3.5 | 9.90E-03 | 5.00E+00 | 4.05E-03 | 3.50E+00 | 9.94E-03 |

## Sample N7

Table B-6 Surface deflection profiles for sample N7, step 44%YS.

| **Hardened Layer** | | | | **Soft Bulk** | | | |
|---|---|---|---|---|---|---|---|
| Longitudinal | | Transverse | | Longitudinal | | Transverse | |
| Length | Stress | Length | Stress | Length | Stress | Length | Stress |
| 0.00E+00 | 3.20E-03 | 0.00E+00 | 7.16E-03 | 0.00E+00 | 3.13E-03 | 0.00E+00 | 7.18E-03 |
| 1.04E-01 | 2.81E-03 | 7.29E-02 | 7.06E-03 | 1.04E-01 | 2.73E-03 | 7.29E-02 | 7.08E-03 |
| 2.08E-01 | 2.45E-03 | 1.46E-01 | 6.97E-03 | 2.08E-01 | 2.36E-03 | 1.46E-01 | 6.99E-03 |
| 3.13E-01 | 2.12E-03 | 2.19E-01 | 6.89E-03 | 3.13E-01 | 2.01E-03 | 2.19E-01 | 6.91E-03 |
| 4.17E-01 | 1.85E-03 | 2.92E-01 | 6.82E-03 | 4.17E-01 | 1.72E-03 | 2.92E-01 | 6.84E-03 |
| 5.21E-01 | 1.65E-03 | 3.65E-01 | 6.77E-03 | 5.21E-01 | 1.51E-03 | 3.65E-01 | 6.79E-03 |
| 6.25E-01 | 1.54E-03 | 4.38E-01 | 6.72E-03 | 6.25E-01 | 1.41E-03 | 4.38E-01 | 6.74E-03 |
| 7.29E-01 | 1.51E-03 | 5.10E-01 | 6.68E-03 | 7.29E-01 | 1.41E-03 | 5.10E-01 | 6.70E-03 |
| 8.33E-01 | 1.80E-03 | 5.83E-01 | 6.64E-03 | 8.33E-01 | 1.64E-03 | 5.83E-01 | 6.67E-03 |
| 9.38E-01 | 2.12E-03 | 6.56E-01 | 6.62E-03 | 9.38E-01 | 2.00E-03 | 6.56E-01 | 6.65E-03 |
| 1.04E+00 | 2.49E-03 | 7.29E-01 | 6.59E-03 | 1.04E+00 | 2.38E-03 | 7.29E-01 | 6.62E-03 |
| 1.15E+00 | 2.88E-03 | 8.02E-01 | 6.58E-03 | 1.15E+00 | 2.79E-03 | 8.02E-01 | 6.61E-03 |
| 1.25E+00 | 3.28E-03 | 8.75E-01 | 6.56E-03 | 1.25E+00 | 3.21E-03 | 8.75E-01 | 6.59E-03 |
| 1.35E+00 | 3.69E-03 | 9.48E-01 | 6.55E-03 | 1.35E+00 | 3.63E-03 | 9.48E-01 | 6.58E-03 |
| 1.46E+00 | 4.09E-03 | 1.02E+00 | 6.54E-03 | 1.46E+00 | 4.05E-03 | 1.02E+00 | 6.57E-03 |
| 1.56E+00 | 4.48E-03 | 1.09E+00 | 6.53E-03 | 1.56E+00 | 4.45E-03 | 1.09E+00 | 6.56E-03 |
| 1.67E+00 | 4.86E-03 | 1.17E+00 | 6.52E-03 | 1.67E+00 | 4.84E-03 | 1.17E+00 | 6.56E-03 |
| 1.77E+00 | 5.21E-03 | 1.24E+00 | 6.52E-03 | 1.77E+00 | 5.20E-03 | 1.24E+00 | 6.55E-03 |
| 1.88E+00 | 5.54E-03 | 1.31E+00 | 6.52E-03 | 1.88E+00 | 5.53E-03 | 1.31E+00 | 6.55E-03 |
| 1.98E+00 | 5.82E-03 | 1.39E+00 | 6.51E-03 | 1.98E+00 | 5.83E-03 | 1.39E+00 | 6.55E-03 |
| 2.08E+00 | 6.07E-03 | 1.46E+00 | 6.51E-03 | 2.08E+00 | 6.08E-03 | 1.46E+00 | 6.54E-03 |
| 2.19E+00 | 6.26E-03 | 1.53E+00 | 6.51E-03 | 2.19E+00 | 6.28E-03 | 1.53E+00 | 6.54E-03 |
| 2.29E+00 | 6.40E-03 | 1.60E+00 | 6.51E-03 | 2.29E+00 | 6.42E-03 | 1.60E+00 | 6.54E-03 |
| 2.40E+00 | 6.48E-03 | 1.68E+00 | 6.51E-03 | 2.40E+00 | 6.51E-03 | 1.68E+00 | 6.54E-03 |
| 2.50E+00 | 6.51E-03 | 1.75E+00 | 6.51E-03 | 2.50E+00 | 6.54E-03 | 1.75E+00 | 6.54E-03 |
| 2.60E+00 | 6.48E-03 | 1.82E+00 | 6.51E-03 | 2.60E+00 | 6.51E-03 | 1.82E+00 | 6.54E-03 |
| 2.71E+00 | 6.40E-03 | 1.90E+00 | 6.51E-03 | 2.71E+00 | 6.43E-03 | 1.90E+00 | 6.54E-03 |
| 2.81E+00 | 6.26E-03 | 1.97E+00 | 6.51E-03 | 2.81E+00 | 6.28E-03 | 1.97E+00 | 6.54E-03 |
| 2.92E+00 | 6.07E-03 | 2.04E+00 | 6.51E-03 | 2.92E+00 | 6.09E-03 | 2.04E+00 | 6.54E-03 |
| 3.02E+00 | 5.83E-03 | 2.11E+00 | 6.51E-03 | 3.02E+00 | 5.84E-03 | 2.11E+00 | 6.54E-03 |

| | | | | | | | |
|---|---|---|---|---|---|---|---|
| 3.13E+00 | 5.54E-03 | 2.19E+00 | 6.51E-03 | 3.13E+00 | 5.54E-03 | 2.19E+00 | 6.55E-03 |
| 3.23E+00 | 5.22E-03 | 2.26E+00 | 6.52E-03 | 3.23E+00 | 5.21E-03 | 2.26E+00 | 6.55E-03 |
| 3.33E+00 | 4.87E-03 | 2.33E+00 | 6.52E-03 | 3.33E+00 | 4.84E-03 | 2.33E+00 | 6.55E-03 |
| 3.44E+00 | 4.49E-03 | 2.41E+00 | 6.53E-03 | 3.44E+00 | 4.46E-03 | 2.41E+00 | 6.56E-03 |
| 3.54E+00 | 4.10E-03 | 2.48E+00 | 6.54E-03 | 3.54E+00 | 4.06E-03 | 2.48E+00 | 6.57E-03 |
| 3.65E+00 | 3.70E-03 | 2.55E+00 | 6.55E-03 | 3.65E+00 | 3.65E-03 | 2.55E+00 | 6.58E-03 |
| 3.75E+00 | 3.29E-03 | 2.63E+00 | 6.56E-03 | 3.75E+00 | 3.23E-03 | 2.63E+00 | 6.59E-03 |
| 3.85E+00 | 2.89E-03 | 2.70E+00 | 6.57E-03 | 3.85E+00 | 2.81E-03 | 2.70E+00 | 6.60E-03 |
| 3.96E+00 | 2.50E-03 | 2.77E+00 | 6.59E-03 | 3.96E+00 | 2.40E-03 | 2.77E+00 | 6.62E-03 |
| 4.06E+00 | 2.14E-03 | 2.84E+00 | 6.62E-03 | 4.06E+00 | 2.01E-03 | 2.84E+00 | 6.64E-03 |
| 4.1667 | 1.83E-03 | 2.9167 | 6.64E-03 | 4.17E+00 | 1.67E-03 | 2.92E+00 | 6.67E-03 |
| 4.2708 | 1.57E-03 | 2.9896 | 6.68E-03 | 4.27E+00 | 1.44E-03 | 2.99E+00 | 6.70E-03 |
| 4.375 | 1.56E-03 | 3.0625 | 6.72E-03 | 4.38E+00 | 1.43E-03 | 3.06E+00 | 6.74E-03 |
| 4.4792 | 1.67E-03 | 3.1354 | 6.76E-03 | 4.48E+00 | 1.53E-03 | 3.14E+00 | 6.79E-03 |
| 4.5833 | 1.86E-03 | 3.2083 | 6.82E-03 | 4.58E+00 | 1.73E-03 | 3.21E+00 | 6.84E-03 |
| 4.6875 | 2.13E-03 | 3.2813 | 6.89E-03 | 4.69E+00 | 2.02E-03 | 3.28E+00 | 6.91E-03 |
| 4.7917 | 2.46E-03 | 3.3542 | 6.96E-03 | 4.79E+00 | 2.36E-03 | 3.35E+00 | 6.99E-03 |
| 4.8958 | 2.82E-03 | 3.4271 | 7.06E-03 | 4.90E+00 | 2.74E-03 | 3.43E+00 | 7.08E-03 |
| 5 | 3.20E-03 | 3.5 | 7.16E-03 | 5.00E+00 | 3.13E-03 | 3.50E+00 | 7.18E-03 |

Table B-7 Surface deflection profiles for sample N7, step 52%YS.

| **Hardened Layer** | | | | **Soft Bulk** | | | |
|---|---|---|---|---|---|---|---|
| Longitudinal | | Transverse | | Longitudinal | | Transverse | |
| Length | Stress | Length | Stress | Length | Stress | Length | Stress |
| 0.00E+00 | 3.65E-03 | 0.00E+00 | 8.14E-03 | 0.00E+00 | 3.57E-03 | 0.00E+00 | 8.17E-03 |
| 1.04E-01 | 3.21E-03 | 7.29E-02 | 8.03E-03 | 1.04E-01 | 3.12E-03 | 7.29E-02 | 8.05E-03 |
| 2.08E-01 | 2.80E-03 | 1.46E-01 | 7.92E-03 | 2.08E-01 | 2.69E-03 | 1.46E-01 | 7.95E-03 |
| 3.13E-01 | 2.42E-03 | 2.19E-01 | 7.83E-03 | 3.13E-01 | 2.29E-03 | 2.19E-01 | 7.86E-03 |
| 4.17E-01 | 2.10E-03 | 2.92E-01 | 7.75E-03 | 4.17E-01 | 1.96E-03 | 2.92E-01 | 7.78E-03 |
| 5.21E-01 | 1.87E-03 | 3.65E-01 | 7.69E-03 | 5.21E-01 | 1.71E-03 | 3.65E-01 | 7.72E-03 |
| 6.25E-01 | 1.74E-03 | 4.38E-01 | 7.64E-03 | 6.25E-01 | 1.60E-03 | 4.38E-01 | 7.67E-03 |
| 7.29E-01 | 1.70E-03 | 5.10E-01 | 7.59E-03 | 7.29E-01 | 1.59E-03 | 5.10E-01 | 7.62E-03 |
| 8.33E-01 | 2.03E-03 | 5.83E-01 | 7.56E-03 | 8.33E-01 | 1.85E-03 | 5.83E-01 | 7.59E-03 |
| 9.38E-01 | 2.39E-03 | 6.56E-01 | 7.53E-03 | 9.38E-01 | 2.25E-03 | 6.56E-01 | 7.56E-03 |
| 1.04E+00 | 2.81E-03 | 7.29E-01 | 7.50E-03 | 1.04E+00 | 2.69E-03 | 7.29E-01 | 7.54E-03 |
| 1.15E+00 | 3.25E-03 | 8.02E-01 | 7.48E-03 | 1.15E+00 | 3.15E-03 | 8.02E-01 | 7.52E-03 |
| 1.25E+00 | 3.71E-03 | 8.75E-01 | 7.47E-03 | 1.25E+00 | 3.63E-03 | 8.75E-01 | 7.50E-03 |
| 1.35E+00 | 4.17E-03 | 9.48E-01 | 7.45E-03 | 1.35E+00 | 4.11E-03 | 9.48E-01 | 7.49E-03 |
| 1.46E+00 | 4.63E-03 | 1.02E+00 | 7.44E-03 | 1.46E+00 | 4.58E-03 | 1.02E+00 | 7.48E-03 |
| 1.56E+00 | 5.08E-03 | 1.09E+00 | 7.43E-03 | 1.56E+00 | 5.05E-03 | 1.09E+00 | 7.47E-03 |
| 1.67E+00 | 5.52E-03 | 1.17E+00 | 7.43E-03 | 1.67E+00 | 5.49E-03 | 1.17E+00 | 7.47E-03 |

| | | | | | | | |
|---|---|---|---|---|---|---|---|
| 1.77E+00 | 5.92E-03 | 1.24E+00 | 7.42E-03 | 1.77E+00 | 5.91E-03 | 1.24E+00 | 7.46E-03 |
| 1.88E+00 | 6.30E-03 | 1.31E+00 | 7.42E-03 | 1.88E+00 | 6.30E-03 | 1.31E+00 | 7.46E-03 |
| 1.98E+00 | 6.63E-03 | 1.39E+00 | 7.42E-03 | 1.98E+00 | 6.64E-03 | 1.39E+00 | 7.46E-03 |
| 2.08E+00 | 6.91E-03 | 1.46E+00 | 7.42E-03 | 2.08E+00 | 6.93E-03 | 1.46E+00 | 7.46E-03 |
| 2.19E+00 | 7.13E-03 | 1.53E+00 | 7.42E-03 | 2.19E+00 | 7.15E-03 | 1.53E+00 | 7.45E-03 |
| 2.29E+00 | 7.28E-03 | 1.60E+00 | 7.41E-03 | 2.29E+00 | 7.32E-03 | 1.60E+00 | 7.45E-03 |
| 2.40E+00 | 7.38E-03 | 1.68E+00 | 7.41E-03 | 2.40E+00 | 7.42E-03 | 1.68E+00 | 7.45E-03 |
| 2.50E+00 | 7.41E-03 | 1.75E+00 | 7.41E-03 | 2.50E+00 | 7.45E-03 | 1.75E+00 | 7.45E-03 |
| 2.60E+00 | 7.38E-03 | 1.82E+00 | 7.41E-03 | 2.60E+00 | 7.42E-03 | 1.82E+00 | 7.45E-03 |
| 2.71E+00 | 7.29E-03 | 1.90E+00 | 7.41E-03 | 2.71E+00 | 7.32E-03 | 1.90E+00 | 7.45E-03 |
| 2.81E+00 | 7.13E-03 | 1.97E+00 | 7.41E-03 | 2.81E+00 | 7.16E-03 | 1.97E+00 | 7.45E-03 |
| 2.92E+00 | 6.91E-03 | 2.04E+00 | 7.42E-03 | 2.92E+00 | 6.93E-03 | 2.04E+00 | 7.45E-03 |
| 3.02E+00 | 6.64E-03 | 2.11E+00 | 7.42E-03 | 3.02E+00 | 6.64E-03 | 2.11E+00 | 7.46E-03 |
| 3.13E+00 | 6.31E-03 | 2.19E+00 | 7.42E-03 | 3.13E+00 | 6.30E-03 | 2.19E+00 | 7.46E-03 |
| 3.23E+00 | 5.93E-03 | 2.26E+00 | 7.42E-03 | 3.23E+00 | 5.91E-03 | 2.26E+00 | 7.46E-03 |
| 3.33E+00 | 5.52E-03 | 2.33E+00 | 7.43E-03 | 3.33E+00 | 5.50E-03 | 2.33E+00 | 7.47E-03 |
| 3.44E+00 | 5.09E-03 | 2.41E+00 | 7.43E-03 | 3.44E+00 | 5.05E-03 | 2.41E+00 | 7.47E-03 |
| 3.54E+00 | 4.64E-03 | 2.48E+00 | 7.44E-03 | 3.54E+00 | 4.59E-03 | 2.48E+00 | 7.48E-03 |
| 3.65E+00 | 4.18E-03 | 2.55E+00 | 7.45E-03 | 3.65E+00 | 4.12E-03 | 2.55E+00 | 7.49E-03 |
| 3.75E+00 | 3.72E-03 | 2.63E+00 | 7.46E-03 | 3.75E+00 | 3.64E-03 | 2.63E+00 | 7.50E-03 |
| 3.85E+00 | 3.26E-03 | 2.70E+00 | 7.48E-03 | 3.85E+00 | 3.16E-03 | 2.70E+00 | 7.51E-03 |
| 3.96E+00 | 2.82E-03 | 2.77E+00 | 7.50E-03 | 3.96E+00 | 2.70E-03 | 2.77E+00 | 7.53E-03 |
| 4.06E+00 | 2.41E-03 | 2.84E+00 | 7.52E-03 | 4.06E+00 | 2.26E-03 | 2.84E+00 | 7.56E-03 |
| 4.1667 | 2.05E-03 | 2.9167 | 7.55E-03 | 4.17E+00 | 1.87E-03 | 2.92E+00 | 7.58E-03 |
| 4.2708 | 1.77E-03 | 2.9896 | 7.59E-03 | 4.27E+00 | 1.62E-03 | 2.99E+00 | 7.62E-03 |
| 4.375 | 1.76E-03 | 3.0625 | 7.63E-03 | 4.38E+00 | 1.61E-03 | 3.06E+00 | 7.66E-03 |
| 4.4792 | 1.88E-03 | 3.1354 | 7.69E-03 | 4.48E+00 | 1.73E-03 | 3.14E+00 | 7.71E-03 |
| 4.5833 | 2.11E-03 | 3.2083 | 7.75E-03 | 4.58E+00 | 1.97E-03 | 3.21E+00 | 7.78E-03 |
| 4.6875 | 2.43E-03 | 3.2813 | 7.83E-03 | 4.69E+00 | 2.30E-03 | 3.28E+00 | 7.85E-03 |
| 4.7917 | 2.80E-03 | 3.3542 | 7.92E-03 | 4.79E+00 | 2.69E-03 | 3.35E+00 | 7.94E-03 |
| 4.8958 | 3.21E-03 | 3.4271 | 8.02E-03 | 4.90E+00 | 3.12E-03 | 3.43E+00 | 8.05E-03 |
| 5 | 3.65E-03 | 3.5 | 8.14E-03 | 5.00E+00 | 3.57E-03 | 3.50E+00 | 8.16E-03 |

Table B-8 Surface deflection profiles for sample N7, step 59%YS.

| **Hardened Layer** | | | | **Soft Bulk** | | | |
|---|---|---|---|---|---|---|---|
| Longitudinal | | Transverse | | Longitudinal | | Transverse | |
| Length | Stress | Length | Stress | Length | Stress | Length | Stress |
| 0.00E+00 | 4.09E-03 | 0.00E+00 | 9.12E-03 | 0.00E+00 | 4.00E-03 | 0.00E+00 | 9.15E-03 |
| 1.04E-01 | 3.60E-03 | 7.29E-02 | 8.99E-03 | 1.04E-01 | 3.49E-03 | 7.29E-02 | 9.01E-03 |
| 2.08E-01 | 3.13E-03 | 1.46E-01 | 8.87E-03 | 2.08E-01 | 3.01E-03 | 1.46E-01 | 8.89E-03 |
| 3.13E-01 | 2.71E-03 | 2.19E-01 | 8.76E-03 | 3.13E-01 | 2.57E-03 | 2.19E-01 | 8.79E-03 |

| | | | | | | | |
|---|---|---|---|---|---|---|---|
| 4.17E-01 | 2.35E-03 | 2.92E-01 | 8.67E-03 | 4.17E-01 | 2.19E-03 | 2.92E-01 | 8.71E-03 |
| 5.21E-01 | 2.08E-03 | 3.65E-01 | 8.60E-03 | 5.21E-01 | 1.91E-03 | 3.65E-01 | 8.64E-03 |
| 6.25E-01 | 1.94E-03 | 4.38E-01 | 8.54E-03 | 6.25E-01 | 1.77E-03 | 4.38E-01 | 8.58E-03 |
| 7.29E-01 | 1.88E-03 | 5.10E-01 | 8.49E-03 | 7.29E-01 | 1.77E-03 | 5.10E-01 | 8.53E-03 |
| 8.33E-01 | 2.24E-03 | 5.83E-01 | 8.45E-03 | 8.33E-01 | 2.05E-03 | 5.83E-01 | 8.49E-03 |
| 9.38E-01 | 2.65E-03 | 6.56E-01 | 8.42E-03 | 9.38E-01 | 2.49E-03 | 6.56E-01 | 8.46E-03 |
| 1.04E+00 | 3.11E-03 | 7.29E-01 | 8.39E-03 | 1.04E+00 | 2.98E-03 | 7.29E-01 | 8.43E-03 |
| 1.15E+00 | 3.61E-03 | 8.02E-01 | 8.37E-03 | 1.15E+00 | 3.50E-03 | 8.02E-01 | 8.41E-03 |
| 1.25E+00 | 4.12E-03 | 8.75E-01 | 8.36E-03 | 1.25E+00 | 4.03E-03 | 8.75E-01 | 8.40E-03 |
| 1.35E+00 | 4.64E-03 | 9.48E-01 | 8.34E-03 | 1.35E+00 | 4.57E-03 | 9.48E-01 | 8.39E-03 |
| 1.46E+00 | 5.16E-03 | 1.02E+00 | 8.33E-03 | 1.46E+00 | 5.11E-03 | 1.02E+00 | 8.38E-03 |
| 1.56E+00 | 5.67E-03 | 1.09E+00 | 8.33E-03 | 1.56E+00 | 5.63E-03 | 1.09E+00 | 8.37E-03 |
| 1.67E+00 | 6.16E-03 | 1.17E+00 | 8.32E-03 | 1.67E+00 | 6.13E-03 | 1.17E+00 | 8.36E-03 |
| 1.77E+00 | 6.62E-03 | 1.24E+00 | 8.31E-03 | 1.77E+00 | 6.60E-03 | 1.24E+00 | 8.36E-03 |
| 1.88E+00 | 7.05E-03 | 1.31E+00 | 8.31E-03 | 1.88E+00 | 7.05E-03 | 1.31E+00 | 8.36E-03 |
| 1.98E+00 | 7.42E-03 | 1.39E+00 | 8.31E-03 | 1.98E+00 | 7.43E-03 | 1.39E+00 | 8.35E-03 |
| 2.08E+00 | 7.73E-03 | 1.46E+00 | 8.31E-03 | 2.08E+00 | 7.75E-03 | 1.46E+00 | 8.35E-03 |
| 2.19E+00 | 7.98E-03 | 1.53E+00 | 8.31E-03 | 2.19E+00 | 8.01E-03 | 1.53E+00 | 8.35E-03 |
| 2.29E+00 | 8.16E-03 | 1.60E+00 | 8.30E-03 | 2.29E+00 | 8.20E-03 | 1.60E+00 | 8.35E-03 |
| 2.40E+00 | 8.27E-03 | 1.68E+00 | 8.30E-03 | 2.40E+00 | 8.31E-03 | 1.68E+00 | 8.35E-03 |
| 2.50E+00 | 8.30E-03 | 1.75E+00 | 8.30E-03 | 2.50E+00 | 8.35E-03 | 1.75E+00 | 8.35E-03 |
| 2.60E+00 | 8.27E-03 | 1.82E+00 | 8.30E-03 | 2.60E+00 | 8.31E-03 | 1.82E+00 | 8.35E-03 |
| 2.71E+00 | 8.16E-03 | 1.90E+00 | 8.30E-03 | 2.71E+00 | 8.20E-03 | 1.90E+00 | 8.35E-03 |
| 2.81E+00 | 7.98E-03 | 1.97E+00 | 8.30E-03 | 2.81E+00 | 8.01E-03 | 1.97E+00 | 8.35E-03 |
| 2.92E+00 | 7.74E-03 | 2.04E+00 | 8.31E-03 | 2.92E+00 | 7.76E-03 | 2.04E+00 | 8.35E-03 |
| 3.02E+00 | 7.43E-03 | 2.11E+00 | 8.31E-03 | 3.02E+00 | 7.44E-03 | 2.11E+00 | 8.35E-03 |
| 3.13E+00 | 7.06E-03 | 2.19E+00 | 8.31E-03 | 3.13E+00 | 7.05E-03 | 2.19E+00 | 8.35E-03 |
| 3.23E+00 | 6.63E-03 | 2.26E+00 | 8.31E-03 | 3.23E+00 | 6.61E-03 | 2.26E+00 | 8.36E-03 |
| 3.33E+00 | 6.17E-03 | 2.33E+00 | 8.32E-03 | 3.33E+00 | 6.13E-03 | 2.33E+00 | 8.36E-03 |
| 3.44E+00 | 5.68E-03 | 2.41E+00 | 8.32E-03 | 3.44E+00 | 5.63E-03 | 2.41E+00 | 8.37E-03 |
| 3.54E+00 | 5.17E-03 | 2.48E+00 | 8.33E-03 | 3.54E+00 | 5.11E-03 | 2.48E+00 | 8.37E-03 |
| 3.65E+00 | 4.65E-03 | 2.55E+00 | 8.34E-03 | 3.65E+00 | 4.58E-03 | 2.55E+00 | 8.38E-03 |
| 3.75E+00 | 4.13E-03 | 2.63E+00 | 8.35E-03 | 3.75E+00 | 4.04E-03 | 2.63E+00 | 8.39E-03 |
| 3.85E+00 | 3.62E-03 | 2.70E+00 | 8.37E-03 | 3.85E+00 | 3.51E-03 | 2.70E+00 | 8.41E-03 |
| 3.96E+00 | 3.12E-03 | 2.77E+00 | 8.39E-03 | 3.96E+00 | 2.99E-03 | 2.77E+00 | 8.43E-03 |
| 4.06E+00 | 2.66E-03 | 2.84E+00 | 8.42E-03 | 4.06E+00 | 2.50E-03 | 2.84E+00 | 8.45E-03 |
| 4.1667 | 2.26E-03 | 2.9167 | 8.45E-03 | 4.17E+00 | 2.06E-03 | 2.92E+00 | 8.49E-03 |
| 4.2708 | 1.96E-03 | 2.9896 | 8.49E-03 | 4.27E+00 | 1.79E-03 | 2.99E+00 | 8.52E-03 |
| 4.375 | 1.95E-03 | 3.0625 | 8.54E-03 | 4.38E+00 | 1.79E-03 | 3.06E+00 | 8.57E-03 |
| 4.4792 | 2.10E-03 | 3.1354 | 8.60E-03 | 4.48E+00 | 1.92E-03 | 3.14E+00 | 8.63E-03 |
| 4.5833 | 2.36E-03 | 3.2083 | 8.67E-03 | 4.58E+00 | 2.20E-03 | 3.21E+00 | 8.70E-03 |

| | | | | | | | |
|---|---|---|---|---|---|---|---|
| 4.6875 | 2.71E-03 | 3.2813 | 8.76E-03 | 4.69E+00 | 2.57E-03 | 3.28E+00 | 8.79E-03 |
| 4.7917 | 3.14E-03 | 3.3542 | 8.86E-03 | 4.79E+00 | 3.01E-03 | 3.35E+00 | 8.89E-03 |
| 4.8958 | 3.60E-03 | 3.4271 | 8.98E-03 | 4.90E+00 | 3.50E-03 | 3.43E+00 | 9.01E-03 |
| 5 | 4.09E-03 | 3.5 | 9.11E-03 | 5.00E+00 | 4.00E-03 | 3.50E+00 | 9.14E-03 |

Table 0-9 Surface deflection profiles for sample N7, step 66%YS.

| **Hardened Layer** | | | | **Soft Bulk** | | | |
|---|---|---|---|---|---|---|---|
| Longitudinal | | Transverse | | Longitudinal | | Transverse | |
| Length | Stress | Length | Stress | Length | Stress | Length | Stress |
| 0.00E+00 | 4.50E-03 | 0.00E+00 | 1.00E-02 | 0.00E+00 | 4.40E-03 | 0.00E+00 | 1.01E-02 |
| 1.04E-01 | 3.96E-03 | 7.29E-02 | 9.89E-03 | 1.04E-01 | 3.84E-03 | 7.29E-02 | 9.92E-03 |
| 2.08E-01 | 3.44E-03 | 1.46E-01 | 9.75E-03 | 2.08E-01 | 3.31E-03 | 1.46E-01 | 9.78E-03 |
| 3.13E-01 | 2.97E-03 | 2.19E-01 | 9.63E-03 | 3.13E-01 | 2.82E-03 | 2.19E-01 | 9.67E-03 |
| 4.17E-01 | 2.57E-03 | 2.92E-01 | 9.54E-03 | 4.17E-01 | 2.40E-03 | 2.92E-01 | 9.57E-03 |
| 5.21E-01 | 2.28E-03 | 3.65E-01 | 9.46E-03 | 5.21E-01 | 2.09E-03 | 3.65E-01 | 9.49E-03 |
| 6.25E-01 | 2.11E-03 | 4.38E-01 | 9.39E-03 | 6.25E-01 | 1.93E-03 | 4.38E-01 | 9.43E-03 |
| 7.29E-01 | 2.05E-03 | 5.10E-01 | 9.34E-03 | 7.29E-01 | 1.92E-03 | 5.10E-01 | 9.38E-03 |
| 8.33E-01 | 2.44E-03 | 5.83E-01 | 9.29E-03 | 8.33E-01 | 2.22E-03 | 5.83E-01 | 9.33E-03 |
| 9.38E-01 | 2.88E-03 | 6.56E-01 | 9.26E-03 | 9.38E-01 | 2.70E-03 | 6.56E-01 | 9.30E-03 |
| 1.04E+00 | 3.39E-03 | 7.29E-01 | 9.23E-03 | 1.04E+00 | 3.24E-03 | 7.29E-01 | 9.27E-03 |
| 1.15E+00 | 3.93E-03 | 8.02E-01 | 9.21E-03 | 1.15E+00 | 3.82E-03 | 8.02E-01 | 9.25E-03 |
| 1.25E+00 | 4.50E-03 | 8.75E-01 | 9.19E-03 | 1.25E+00 | 4.40E-03 | 8.75E-01 | 9.24E-03 |
| 1.35E+00 | 5.08E-03 | 9.48E-01 | 9.17E-03 | 1.35E+00 | 5.00E-03 | 9.48E-01 | 9.22E-03 |
| 1.46E+00 | 5.65E-03 | 1.02E+00 | 9.16E-03 | 1.46E+00 | 5.59E-03 | 1.02E+00 | 9.21E-03 |
| 1.56E+00 | 6.21E-03 | 1.09E+00 | 9.15E-03 | 1.56E+00 | 6.16E-03 | 1.09E+00 | 9.20E-03 |
| 1.67E+00 | 6.76E-03 | 1.17E+00 | 9.15E-03 | 1.67E+00 | 6.72E-03 | 1.17E+00 | 9.20E-03 |
| 1.77E+00 | 7.27E-03 | 1.24E+00 | 9.14E-03 | 1.77E+00 | 7.25E-03 | 1.24E+00 | 9.20E-03 |
| 1.88E+00 | 7.75E-03 | 1.31E+00 | 9.14E-03 | 1.88E+00 | 7.74E-03 | 1.31E+00 | 9.19E-03 |
| 1.98E+00 | 8.16E-03 | 1.39E+00 | 9.14E-03 | 1.98E+00 | 8.17E-03 | 1.39E+00 | 9.19E-03 |
| 2.08E+00 | 8.50E-03 | 1.46E+00 | 9.14E-03 | 2.08E+00 | 8.52E-03 | 1.46E+00 | 9.19E-03 |
| 2.19E+00 | 8.77E-03 | 1.53E+00 | 9.14E-03 | 2.19E+00 | 8.81E-03 | 1.53E+00 | 9.19E-03 |
| 2.29E+00 | 8.97E-03 | 1.60E+00 | 9.13E-03 | 2.29E+00 | 9.02E-03 | 1.60E+00 | 9.19E-03 |
| 2.40E+00 | 9.09E-03 | 1.68E+00 | 9.13E-03 | 2.40E+00 | 9.14E-03 | 1.68E+00 | 9.19E-03 |
| 2.50E+00 | 9.13E-03 | 1.75E+00 | 9.13E-03 | 2.50E+00 | 9.19E-03 | 1.75E+00 | 9.19E-03 |
| 2.60E+00 | 9.09E-03 | 1.82E+00 | 9.13E-03 | 2.60E+00 | 9.14E-03 | 1.82E+00 | 9.19E-03 |
| 2.71E+00 | 8.97E-03 | 1.90E+00 | 9.13E-03 | 2.71E+00 | 9.02E-03 | 1.90E+00 | 9.19E-03 |
| 2.81E+00 | 8.77E-03 | 1.97E+00 | 9.13E-03 | 2.81E+00 | 8.81E-03 | 1.97E+00 | 9.19E-03 |
| 2.92E+00 | 8.50E-03 | 2.04E+00 | 9.13E-03 | 2.92E+00 | 8.53E-03 | 2.04E+00 | 9.19E-03 |
| 3.02E+00 | 8.16E-03 | 2.11E+00 | 9.14E-03 | 3.02E+00 | 8.17E-03 | 2.11E+00 | 9.19E-03 |
| 3.13E+00 | 7.75E-03 | 2.19E+00 | 9.14E-03 | 3.13E+00 | 7.74E-03 | 2.19E+00 | 9.19E-03 |
| 3.23E+00 | 7.28E-03 | 2.26E+00 | 9.14E-03 | 3.23E+00 | 7.25E-03 | 2.26E+00 | 9.19E-03 |

| | | | | | | | |
|---|---|---|---|---|---|---|---|
| 3.33E+00 | 6.76E-03 | 2.33E+00 | 9.15E-03 | 3.33E+00 | 6.73E-03 | 2.33E+00 | 9.20E-03 |
| 3.44E+00 | 6.22E-03 | 2.41E+00 | 9.15E-03 | 3.44E+00 | 6.17E-03 | 2.41E+00 | 9.20E-03 |
| 3.54E+00 | 5.66E-03 | 2.48E+00 | 9.16E-03 | 3.54E+00 | 5.59E-03 | 2.48E+00 | 9.21E-03 |
| 3.65E+00 | 5.09E-03 | 2.55E+00 | 9.17E-03 | 3.65E+00 | 5.01E-03 | 2.55E+00 | 9.22E-03 |
| 3.75E+00 | 4.51E-03 | 2.63E+00 | 9.18E-03 | 3.75E+00 | 4.41E-03 | 2.63E+00 | 9.23E-03 |
| 3.85E+00 | 3.94E-03 | 2.70E+00 | 9.20E-03 | 3.85E+00 | 3.82E-03 | 2.70E+00 | 9.25E-03 |
| 3.96E+00 | 3.40E-03 | 2.77E+00 | 9.22E-03 | 3.96E+00 | 3.25E-03 | 2.77E+00 | 9.27E-03 |
| 4.06E+00 | 2.89E-03 | 2.84E+00 | 9.25E-03 | 4.06E+00 | 2.72E-03 | 2.84E+00 | 9.29E-03 |
| 4.1667 | 2.45E-03 | 2.9167 | 9.28E-03 | 4.17E+00 | 2.24E-03 | 2.92E+00 | 9.33E-03 |
| 4.2708 | 2.13E-03 | 2.9896 | 9.33E-03 | 4.27E+00 | 1.94E-03 | 2.99E+00 | 9.37E-03 |
| 4.375 | 2.13E-03 | 3.0625 | 9.38E-03 | 4.38E+00 | 1.94E-03 | 3.06E+00 | 9.42E-03 |
| 4.4792 | 2.29E-03 | 3.1354 | 9.45E-03 | 4.48E+00 | 2.10E-03 | 3.14E+00 | 9.49E-03 |
| 4.5833 | 2.58E-03 | 3.2083 | 9.53E-03 | 4.58E+00 | 2.41E-03 | 3.21E+00 | 9.56E-03 |
| 4.6875 | 2.98E-03 | 3.2813 | 9.62E-03 | 4.69E+00 | 2.83E-03 | 3.28E+00 | 9.66E-03 |
| 4.7917 | 3.45E-03 | 3.3542 | 9.74E-03 | 4.79E+00 | 3.31E-03 | 3.35E+00 | 9.77E-03 |
| 4.8958 | 3.96E-03 | 3.4271 | 9.88E-03 | 4.90E+00 | 3.85E-03 | 3.43E+00 | 9.91E-03 |
| 5 | 4.50E-03 | 3.5 | 1.00E-02 | 5.00E+00 | 4.40E-03 | 3.50E+00 | 1.01E-02 |

Table B-10 Surface deflection profiles for sample N7, step 74%YS.

| **Hardened Layer** | | | | **Soft Bulk** | | | |
|---|---|---|---|---|---|---|---|
| Longitudinal | | Transverse | | Longitudinal | | Transverse | |
| Length | Stress | Length | Stress | Length | Stress | Length | Stress |
| 0.00E+00 | 4.98E-03 | 0.00E+00 | 1.10E-02 | 0.00E+00 | 4.87E-03 | 0.00E+00 | 1.11E-02 |
| 1.04E-01 | 4.38E-03 | 7.29E-02 | 1.09E-02 | 1.04E-01 | 4.25E-03 | 7.29E-02 | 1.09E-02 |
| 2.08E-01 | 3.81E-03 | 1.46E-01 | 1.07E-02 | 2.08E-01 | 3.66E-03 | 1.46E-01 | 1.08E-02 |
| 3.13E-01 | 3.29E-03 | 2.19E-01 | 1.06E-02 | 3.13E-01 | 3.12E-03 | 2.19E-01 | 1.06E-02 |
| 4.17E-01 | 2.84E-03 | 2.92E-01 | 1.05E-02 | 4.17E-01 | 2.65E-03 | 2.92E-01 | 1.05E-02 |
| 5.21E-01 | 2.51E-03 | 3.65E-01 | 1.04E-02 | 5.21E-01 | 2.30E-03 | 3.65E-01 | 1.04E-02 |
| 6.25E-01 | 2.32E-03 | 4.38E-01 | 1.03E-02 | 6.25E-01 | 2.12E-03 | 4.38E-01 | 1.04E-02 |
| 7.29E-01 | 2.25E-03 | 5.10E-01 | 1.03E-02 | 7.29E-01 | 2.10E-03 | 5.10E-01 | 1.03E-02 |
| 8.33E-01 | 2.66E-03 | 5.83E-01 | 1.02E-02 | 8.33E-01 | 2.43E-03 | 5.83E-01 | 1.03E-02 |
| 9.38E-01 | 3.15E-03 | 6.56E-01 | 1.02E-02 | 9.38E-01 | 2.95E-03 | 6.56E-01 | 1.02E-02 |
| 1.04E+00 | 3.70E-03 | 7.29E-01 | 1.02E-02 | 1.04E+00 | 3.54E-03 | 7.29E-01 | 1.02E-02 |
| 1.15E+00 | 4.30E-03 | 8.02E-01 | 1.01E-02 | 1.15E+00 | 4.17E-03 | 8.02E-01 | 1.02E-02 |
| 1.25E+00 | 4.93E-03 | 8.75E-01 | 1.01E-02 | 1.25E+00 | 4.82E-03 | 8.75E-01 | 1.02E-02 |
| 1.35E+00 | 5.56E-03 | 9.48E-01 | 1.01E-02 | 1.35E+00 | 5.47E-03 | 9.48E-01 | 1.01E-02 |
| 1.46E+00 | 6.19E-03 | 1.02E+00 | 1.01E-02 | 1.46E+00 | 6.12E-03 | 1.02E+00 | 1.01E-02 |
| 1.56E+00 | 6.82E-03 | 1.09E+00 | 1.01E-02 | 1.56E+00 | 6.76E-03 | 1.09E+00 | 1.01E-02 |
| 1.67E+00 | 7.42E-03 | 1.17E+00 | 1.01E-02 | 1.67E+00 | 7.38E-03 | 1.17E+00 | 1.01E-02 |
| 1.77E+00 | 7.99E-03 | 1.24E+00 | 1.01E-02 | 1.77E+00 | 7.97E-03 | 1.24E+00 | 1.01E-02 |
| 1.88E+00 | 8.52E-03 | 1.31E+00 | 1.01E-02 | 1.88E+00 | 8.51E-03 | 1.31E+00 | 1.01E-02 |

| | | | | | | | |
|---|---|---|---|---|---|---|---|
| 1.98E+00 | 8.97E-03 | 1.39E+00 | 1.01E-02 | 1.98E+00 | 8.98E-03 | 1.39E+00 | 1.01E-02 |
| 2.08E+00 | 9.35E-03 | 1.46E+00 | 1.01E-02 | 2.08E+00 | 9.37E-03 | 1.46E+00 | 1.01E-02 |
| 2.19E+00 | 9.65E-03 | 1.53E+00 | 1.01E-02 | 2.19E+00 | 9.69E-03 | 1.53E+00 | 1.01E-02 |
| 2.29E+00 | 9.87E-03 | 1.60E+00 | 1.01E-02 | 2.29E+00 | 9.92E-03 | 1.60E+00 | 1.01E-02 |
| 2.40E+00 | 1.00E-02 | 1.68E+00 | 1.01E-02 | 2.40E+00 | 1.01E-02 | 1.68E+00 | 1.01E-02 |
| 2.50E+00 | 1.01E-02 | 1.75E+00 | 1.01E-02 | 2.50E+00 | 1.01E-02 | 1.75E+00 | 1.01E-02 |
| 2.60E+00 | 1.00E-02 | 1.82E+00 | 1.01E-02 | 2.60E+00 | 1.01E-02 | 1.82E+00 | 1.01E-02 |
| 2.71E+00 | 9.87E-03 | 1.90E+00 | 1.01E-02 | 2.71E+00 | 9.92E-03 | 1.90E+00 | 1.01E-02 |
| 2.81E+00 | 9.65E-03 | 1.97E+00 | 1.01E-02 | 2.81E+00 | 9.69E-03 | 1.97E+00 | 1.01E-02 |
| 2.92E+00 | 9.35E-03 | 2.04E+00 | 1.01E-02 | 2.92E+00 | 9.38E-03 | 2.04E+00 | 1.01E-02 |
| 3.02E+00 | 8.97E-03 | 2.11E+00 | 1.01E-02 | 3.02E+00 | 8.98E-03 | 2.11E+00 | 1.01E-02 |
| 3.13E+00 | 8.52E-03 | 2.19E+00 | 1.01E-02 | 3.13E+00 | 8.51E-03 | 2.19E+00 | 1.01E-02 |
| 3.23E+00 | 8.00E-03 | 2.26E+00 | 1.01E-02 | 3.23E+00 | 7.97E-03 | 2.26E+00 | 1.01E-02 |
| 3.33E+00 | 7.42E-03 | 2.33E+00 | 1.01E-02 | 3.33E+00 | 7.38E-03 | 2.33E+00 | 1.01E-02 |
| 3.44E+00 | 6.82E-03 | 2.41E+00 | 1.01E-02 | 3.44E+00 | 6.77E-03 | 2.41E+00 | 1.01E-02 |
| 3.54E+00 | 6.20E-03 | 2.48E+00 | 1.01E-02 | 3.54E+00 | 6.13E-03 | 2.48E+00 | 1.01E-02 |
| 3.65E+00 | 5.57E-03 | 2.55E+00 | 1.01E-02 | 3.65E+00 | 5.48E-03 | 2.55E+00 | 1.01E-02 |
| 3.75E+00 | 4.93E-03 | 2.63E+00 | 1.01E-02 | 3.75E+00 | 4.82E-03 | 2.63E+00 | 1.02E-02 |
| 3.85E+00 | 4.31E-03 | 2.70E+00 | 1.01E-02 | 3.85E+00 | 4.18E-03 | 2.70E+00 | 1.02E-02 |
| 3.96E+00 | 3.71E-03 | 2.77E+00 | 1.01E-02 | 3.96E+00 | 3.55E-03 | 2.77E+00 | 1.02E-02 |
| 4.06E+00 | 3.16E-03 | 2.84E+00 | 1.02E-02 | 4.06E+00 | 2.96E-03 | 2.84E+00 | 1.02E-02 |
| 4.1667 | 2.68E-03 | 2.9167 | 1.02E-02 | 4.17E+00 | 2.44E-03 | 2.92E+00 | 1.03E-02 |
| 4.2708 | 2.34E-03 | 2.9896 | 1.03E-02 | 4.27E+00 | 2.12E-03 | 2.99E+00 | 1.03E-02 |
| 4.375 | 2.33E-03 | 3.0625 | 1.03E-02 | 4.38E+00 | 2.13E-03 | 3.06E+00 | 1.04E-02 |
| 4.4792 | 2.52E-03 | 3.1354 | 1.04E-02 | 4.48E+00 | 2.31E-03 | 3.14E+00 | 1.04E-02 |
| 4.5833 | 2.85E-03 | 3.2083 | 1.05E-02 | 4.58E+00 | 2.65E-03 | 3.21E+00 | 1.05E-02 |
| 4.6875 | 3.29E-03 | 3.2813 | 1.06E-02 | 4.69E+00 | 3.12E-03 | 3.28E+00 | 1.06E-02 |
| 4.7917 | 3.81E-03 | 3.3542 | 1.07E-02 | 4.79E+00 | 3.66E-03 | 3.35E+00 | 1.08E-02 |
| 4.8958 | 4.38E-03 | 3.4271 | 1.09E-02 | 4.90E+00 | 4.25E-03 | 3.43E+00 | 1.09E-02 |
| 5 | 4.98E-03 | 3.5 | 1.10E-02 | 5.00E+00 | 4.87E-03 | 3.50E+00 | 1.11E-02 |

Table 0-11 Surface deflection profiles for sample N7, step 89%YS.

| **Hardened Layer** | | | | **Soft Bulk** | | | |
|---|---|---|---|---|---|---|---|
| Longitudinal | | Transverse | | Longitudinal | | Transverse | |
| Length | Stress | Length | Stress | Length | Stress | Length | Stress |
| 0.00E+00 | 4.98E-03 | 0.00E+00 | 1.10E-02 | 0.00E+00 | 4.87E-03 | 0.00E+00 | 1.11E-02 |
| 1.04E-01 | 4.38E-03 | 7.29E-02 | 1.09E-02 | 1.04E-01 | 4.25E-03 | 7.29E-02 | 1.09E-02 |
| 2.08E-01 | 3.81E-03 | 1.46E-01 | 1.07E-02 | 2.08E-01 | 3.66E-03 | 1.46E-01 | 1.08E-02 |
| 3.13E-01 | 3.29E-03 | 2.19E-01 | 1.06E-02 | 3.13E-01 | 3.12E-03 | 2.19E-01 | 1.06E-02 |
| 4.17E-01 | 2.84E-03 | 2.92E-01 | 1.05E-02 | 4.17E-01 | 2.65E-03 | 2.92E-01 | 1.05E-02 |
| 5.21E-01 | 2.51E-03 | 3.65E-01 | 1.04E-02 | 5.21E-01 | 2.30E-03 | 3.65E-01 | 1.04E-02 |

| | | | | | | | |
|---|---|---|---|---|---|---|---|
| 6.25E-01 | 2.32E-03 | 4.38E-01 | 1.03E-02 | 6.25E-01 | 2.12E-03 | 4.38E-01 | 1.04E-02 |
| 7.29E-01 | 2.25E-03 | 5.10E-01 | 1.03E-02 | 7.29E-01 | 2.10E-03 | 5.10E-01 | 1.03E-02 |
| 8.33E-01 | 2.66E-03 | 5.83E-01 | 1.02E-02 | 8.33E-01 | 2.43E-03 | 5.83E-01 | 1.03E-02 |
| 9.38E-01 | 3.15E-03 | 6.56E-01 | 1.02E-02 | 9.38E-01 | 2.95E-03 | 6.56E-01 | 1.02E-02 |
| 1.04E+00 | 3.70E-03 | 7.29E-01 | 1.02E-02 | 1.04E+00 | 3.54E-03 | 7.29E-01 | 1.02E-02 |
| 1.15E+00 | 4.30E-03 | 8.02E-01 | 1.01E-02 | 1.15E+00 | 4.17E-03 | 8.02E-01 | 1.02E-02 |
| 1.25E+00 | 4.93E-03 | 8.75E-01 | 1.01E-02 | 1.25E+00 | 4.82E-03 | 8.75E-01 | 1.02E-02 |
| 1.35E+00 | 5.56E-03 | 9.48E-01 | 1.01E-02 | 1.35E+00 | 5.47E-03 | 9.48E-01 | 1.01E-02 |
| 1.46E+00 | 6.19E-03 | 1.02E+00 | 1.01E-02 | 1.46E+00 | 6.12E-03 | 1.02E+00 | 1.01E-02 |
| 1.56E+00 | 6.82E-03 | 1.09E+00 | 1.01E-02 | 1.56E+00 | 6.76E-03 | 1.09E+00 | 1.01E-02 |
| 1.67E+00 | 7.42E-03 | 1.17E+00 | 1.01E-02 | 1.67E+00 | 7.38E-03 | 1.17E+00 | 1.01E-02 |
| 1.77E+00 | 7.99E-03 | 1.24E+00 | 1.01E-02 | 1.77E+00 | 7.97E-03 | 1.24E+00 | 1.01E-02 |
| 1.88E+00 | 8.52E-03 | 1.31E+00 | 1.01E-02 | 1.88E+00 | 8.51E-03 | 1.31E+00 | 1.01E-02 |
| 1.98E+00 | 8.97E-03 | 1.39E+00 | 1.01E-02 | 1.98E+00 | 8.98E-03 | 1.39E+00 | 1.01E-02 |
| 2.08E+00 | 9.35E-03 | 1.46E+00 | 1.01E-02 | 2.08E+00 | 9.37E-03 | 1.46E+00 | 1.01E-02 |
| 2.19E+00 | 9.65E-03 | 1.53E+00 | 1.01E-02 | 2.19E+00 | 9.69E-03 | 1.53E+00 | 1.01E-02 |
| 2.29E+00 | 9.87E-03 | 1.60E+00 | 1.01E-02 | 2.29E+00 | 9.92E-03 | 1.60E+00 | 1.01E-02 |
| 2.40E+00 | 1.00E-02 | 1.68E+00 | 1.01E-02 | 2.40E+00 | 1.01E-02 | 1.68E+00 | 1.01E-02 |
| 2.50E+00 | 1.01E-02 | 1.75E+00 | 1.01E-02 | 2.50E+00 | 1.01E-02 | 1.75E+00 | 1.01E-02 |
| 2.60E+00 | 1.00E-02 | 1.82E+00 | 1.01E-02 | 2.60E+00 | 1.01E-02 | 1.82E+00 | 1.01E-02 |
| 2.71E+00 | 9.87E-03 | 1.90E+00 | 1.01E-02 | 2.71E+00 | 9.92E-03 | 1.90E+00 | 1.01E-02 |
| 2.81E+00 | 9.65E-03 | 1.97E+00 | 1.01E-02 | 2.81E+00 | 9.69E-03 | 1.97E+00 | 1.01E-02 |
| 2.92E+00 | 9.35E-03 | 2.04E+00 | 1.01E-02 | 2.92E+00 | 9.38E-03 | 2.04E+00 | 1.01E-02 |
| 3.02E+00 | 8.97E-03 | 2.11E+00 | 1.01E-02 | 3.02E+00 | 8.98E-03 | 2.11E+00 | 1.01E-02 |
| 3.13E+00 | 8.52E-03 | 2.19E+00 | 1.01E-02 | 3.13E+00 | 8.51E-03 | 2.19E+00 | 1.01E-02 |
| 3.23E+00 | 8.00E-03 | 2.26E+00 | 1.01E-02 | 3.23E+00 | 7.97E-03 | 2.26E+00 | 1.01E-02 |
| 3.33E+00 | 7.42E-03 | 2.33E+00 | 1.01E-02 | 3.33E+00 | 7.38E-03 | 2.33E+00 | 1.01E-02 |
| 3.44E+00 | 6.82E-03 | 2.41E+00 | 1.01E-02 | 3.44E+00 | 6.77E-03 | 2.41E+00 | 1.01E-02 |
| 3.54E+00 | 6.20E-03 | 2.48E+00 | 1.01E-02 | 3.54E+00 | 6.13E-03 | 2.48E+00 | 1.01E-02 |
| 3.65E+00 | 5.57E-03 | 2.55E+00 | 1.01E-02 | 3.65E+00 | 5.48E-03 | 2.55E+00 | 1.01E-02 |
| 3.75E+00 | 4.93E-03 | 2.63E+00 | 1.01E-02 | 3.75E+00 | 4.82E-03 | 2.63E+00 | 1.02E-02 |
| 3.85E+00 | 4.31E-03 | 2.70E+00 | 1.01E-02 | 3.85E+00 | 4.18E-03 | 2.70E+00 | 1.02E-02 |
| 3.96E+00 | 3.71E-03 | 2.77E+00 | 1.01E-02 | 3.96E+00 | 3.55E-03 | 2.77E+00 | 1.02E-02 |
| 4.06E+00 | 3.16E-03 | 2.84E+00 | 1.02E-02 | 4.06E+00 | 2.96E-03 | 2.84E+00 | 1.02E-02 |
| 4.1667 | 2.68E-03 | 2.9167 | 1.02E-02 | 4.17E+00 | 2.44E-03 | 2.92E+00 | 1.03E-02 |
| 4.2708 | 2.34E-03 | 2.9896 | 1.03E-02 | 4.27E+00 | 2.12E-03 | 2.99E+00 | 1.03E-02 |
| 4.375 | 2.33E-03 | 3.0625 | 1.03E-02 | 4.38E+00 | 2.13E-03 | 3.06E+00 | 1.04E-02 |
| 4.4792 | 2.52E-03 | 3.1354 | 1.04E-02 | 4.48E+00 | 2.31E-03 | 3.14E+00 | 1.04E-02 |
| 4.5833 | 2.85E-03 | 3.2083 | 1.05E-02 | 4.58E+00 | 2.65E-03 | 3.21E+00 | 1.05E-02 |
| 4.6875 | 3.29E-03 | 3.2813 | 1.06E-02 | 4.69E+00 | 3.12E-03 | 3.28E+00 | 1.06E-02 |
| 4.7917 | 3.81E-03 | 3.3542 | 1.07E-02 | 4.79E+00 | 3.66E-03 | 3.35E+00 | 1.08E-02 |

| | | | | | | | |
|---|---|---|---|---|---|---|---|
| 4.8958 | 4.38E-03 | 3.4271 | 1.09E-02 | 4.90E+00 | 4.25E-03 | 3.43E+00 | 1.09E-02 |
| 5 | 4.98E-03 | 3.5 | 1.10E-02 | 5.00E+00 | 4.87E-03 | 3.50E+00 | 1.11E-02 |

## Sample N10

Table 0-12 Surface deflection profiles for sample N10, step 50%YS.

| **Hardened Layer** | | | | **Soft Bulk** | | | |
|---|---|---|---|---|---|---|---|
| Longitudinal | | Transverse | | Longitudinal | | Transverse | |
| Length | Stress | Length | Stress | Length | Stress | Length | Stress |
| 0.00E+00 | 3.17E-03 | 0.00E+00 | 7.45E-03 | 0.00E+00 | 3.09E-03 | 0.00E+00 | 7.47E-03 |
| 1.04E-01 | 2.80E-03 | 7.29E-02 | 7.34E-03 | 1.04E-01 | 2.71E-03 | 7.29E-02 | 7.36E-03 |
| 2.08E-01 | 2.45E-03 | 1.46E-01 | 7.24E-03 | 2.08E-01 | 2.35E-03 | 1.46E-01 | 7.26E-03 |
| 3.13E-01 | 2.15E-03 | 2.19E-01 | 7.16E-03 | 3.13E-01 | 2.03E-03 | 2.19E-01 | 7.18E-03 |
| 4.17E-01 | 1.90E-03 | 2.92E-01 | 7.08E-03 | 4.17E-01 | 1.76E-03 | 2.92E-01 | 7.11E-03 |
| 5.21E-01 | 1.72E-03 | 3.65E-01 | 7.02E-03 | 5.21E-01 | 1.58E-03 | 3.65E-01 | 7.05E-03 |
| 6.25E-01 | 1.63E-03 | 4.38E-01 | 6.97E-03 | 6.25E-01 | 1.51E-03 | 4.38E-01 | 7.00E-03 |
| 7.29E-01 | 1.60E-03 | 5.10E-01 | 6.93E-03 | 7.29E-01 | 1.52E-03 | 5.10E-01 | 6.96E-03 |
| 8.33E-01 | 1.95E-03 | 5.83E-01 | 6.90E-03 | 8.33E-01 | 1.78E-03 | 5.83E-01 | 6.93E-03 |
| 9.38E-01 | 2.29E-03 | 6.56E-01 | 6.87E-03 | 9.38E-01 | 2.15E-03 | 6.56E-01 | 6.90E-03 |
| 1.04E+00 | 2.66E-03 | 7.29E-01 | 6.84E-03 | 1.04E+00 | 2.55E-03 | 7.29E-01 | 6.88E-03 |
| 1.15E+00 | 3.06E-03 | 8.02E-01 | 6.82E-03 | 1.15E+00 | 2.97E-03 | 8.02E-01 | 6.86E-03 |
| 1.25E+00 | 3.47E-03 | 8.75E-01 | 6.81E-03 | 1.25E+00 | 3.40E-03 | 8.75E-01 | 6.84E-03 |
| 1.35E+00 | 3.88E-03 | 9.48E-01 | 6.79E-03 | 1.35E+00 | 3.82E-03 | 9.48E-01 | 6.83E-03 |
| 1.46E+00 | 4.29E-03 | 1.02E+00 | 6.78E-03 | 1.46E+00 | 4.25E-03 | 1.02E+00 | 6.82E-03 |
| 1.56E+00 | 4.69E-03 | 1.09E+00 | 6.78E-03 | 1.56E+00 | 4.66E-03 | 1.09E+00 | 6.81E-03 |
| 1.67E+00 | 5.07E-03 | 1.17E+00 | 6.77E-03 | 1.67E+00 | 5.05E-03 | 1.17E+00 | 6.81E-03 |
| 1.77E+00 | 5.44E-03 | 1.24E+00 | 6.76E-03 | 1.77E+00 | 5.42E-03 | 1.24E+00 | 6.80E-03 |
| 1.88E+00 | 5.77E-03 | 1.31E+00 | 6.76E-03 | 1.88E+00 | 5.77E-03 | 1.31E+00 | 6.80E-03 |
| 1.98E+00 | 6.06E-03 | 1.39E+00 | 6.76E-03 | 1.98E+00 | 6.07E-03 | 1.39E+00 | 6.80E-03 |
| 2.08E+00 | 6.31E-03 | 1.46E+00 | 6.76E-03 | 2.08E+00 | 6.33E-03 | 1.46E+00 | 6.79E-03 |
| 2.19E+00 | 6.50E-03 | 1.53E+00 | 6.75E-03 | 2.19E+00 | 6.53E-03 | 1.53E+00 | 6.79E-03 |
| 2.29E+00 | 6.64E-03 | 1.60E+00 | 6.75E-03 | 2.29E+00 | 6.67E-03 | 1.60E+00 | 6.79E-03 |
| 2.40E+00 | 6.72E-03 | 1.68E+00 | 6.75E-03 | 2.40E+00 | 6.76E-03 | 1.68E+00 | 6.79E-03 |
| 2.50E+00 | 6.75E-03 | 1.75E+00 | 6.75E-03 | 2.50E+00 | 6.79E-03 | 1.75E+00 | 6.79E-03 |
| 2.60E+00 | 6.72E-03 | 1.82E+00 | 6.75E-03 | 2.60E+00 | 6.76E-03 | 1.82E+00 | 6.79E-03 |
| 2.71E+00 | 6.64E-03 | 1.90E+00 | 6.75E-03 | 2.71E+00 | 6.67E-03 | 1.90E+00 | 6.79E-03 |
| 2.81E+00 | 6.50E-03 | 1.97E+00 | 6.75E-03 | 2.81E+00 | 6.53E-03 | 1.97E+00 | 6.79E-03 |
| 2.92E+00 | 6.31E-03 | 2.04E+00 | 6.76E-03 | 2.92E+00 | 6.33E-03 | 2.04E+00 | 6.79E-03 |
| 3.02E+00 | 6.07E-03 | 2.11E+00 | 6.76E-03 | 3.02E+00 | 6.07E-03 | 2.11E+00 | 6.80E-03 |
| 3.13E+00 | 5.77E-03 | 2.19E+00 | 6.76E-03 | 3.13E+00 | 5.77E-03 | 2.19E+00 | 6.80E-03 |
| 3.23E+00 | 5.44E-03 | 2.26E+00 | 6.76E-03 | 3.23E+00 | 5.43E-03 | 2.26E+00 | 6.80E-03 |

| | | | | | | | |
|---|---|---|---|---|---|---|---|
| 3.33E+00 | 5.08E-03 | 2.33E+00 | 6.77E-03 | 3.33E+00 | 5.06E-03 | 2.33E+00 | 6.81E-03 |
| 3.44E+00 | 4.70E-03 | 2.41E+00 | 6.78E-03 | 3.44E+00 | 4.66E-03 | 2.41E+00 | 6.81E-03 |
| 3.54E+00 | 4.30E-03 | 2.48E+00 | 6.78E-03 | 3.54E+00 | 4.25E-03 | 2.48E+00 | 6.82E-03 |
| 3.65E+00 | 3.89E-03 | 2.55E+00 | 6.79E-03 | 3.65E+00 | 3.83E-03 | 2.55E+00 | 6.83E-03 |
| 3.75E+00 | 3.48E-03 | 2.63E+00 | 6.81E-03 | 3.75E+00 | 3.41E-03 | 2.63E+00 | 6.84E-03 |
| 3.85E+00 | 3.07E-03 | 2.70E+00 | 6.82E-03 | 3.85E+00 | 2.98E-03 | 2.70E+00 | 6.86E-03 |
| 3.96E+00 | 2.67E-03 | 2.77E+00 | 6.84E-03 | 3.96E+00 | 2.56E-03 | 2.77E+00 | 6.87E-03 |
| 4.06E+00 | 2.30E-03 | 2.84E+00 | 6.87E-03 | 4.06E+00 | 2.17E-03 | 2.84E+00 | 6.90E-03 |
| 4.1667 | 1.97E-03 | 2.9167 | 6.89E-03 | 4.17E+00 | 1.80E-03 | 2.92E+00 | 6.93E-03 |
| 4.2708 | 1.66E-03 | 2.9896 | 6.93E-03 | 4.27E+00 | 1.54E-03 | 2.99E+00 | 6.96E-03 |
| 4.375 | 1.65E-03 | 3.0625 | 6.97E-03 | 4.38E+00 | 1.53E-03 | 3.06E+00 | 7.00E-03 |
| 4.4792 | 1.74E-03 | 3.1354 | 7.02E-03 | 4.48E+00 | 1.60E-03 | 3.14E+00 | 7.05E-03 |
| 4.5833 | 1.91E-03 | 3.2083 | 7.08E-03 | 4.58E+00 | 1.77E-03 | 3.21E+00 | 7.11E-03 |
| 4.6875 | 2.15E-03 | 3.2813 | 7.15E-03 | 4.69E+00 | 2.03E-03 | 3.28E+00 | 7.18E-03 |
| 4.7917 | 2.46E-03 | 3.3542 | 7.24E-03 | 4.79E+00 | 2.35E-03 | 3.35E+00 | 7.26E-03 |
| 4.8958 | 2.80E-03 | 3.4271 | 7.34E-03 | 4.90E+00 | 2.71E-03 | 3.43E+00 | 7.36E-03 |
| 5 | 3.17E-03 | 3.5 | 7.45E-03 | 5.00E+00 | 3.09E-03 | 3.50E+00 | 7.47E-03 |

Table B-13 Surface deflection profiles for sample N10, step 60%YS.

| **Hardened Layer** | | | | **Soft Bulk** | | | |
|---|---|---|---|---|---|---|---|
| Longitudinal | | Transverse | | Longitudinal | | Transverse | |
| Length | Stress | Length | Stress | Length | Stress | Length | Stress |
| 0.00E+00 | 3.74E-03 | 0.00E+00 | 8.76E-03 | 0.00E+00 | 3.65E-03 | 0.00E+00 | 8.79E-03 |
| 1.04E-01 | 3.30E-03 | 7.29E-02 | 8.63E-03 | 1.04E-01 | 3.20E-03 | 7.29E-02 | 8.66E-03 |
| 2.08E-01 | 2.89E-03 | 1.46E-01 | 8.51E-03 | 2.08E-01 | 2.77E-03 | 1.46E-01 | 8.54E-03 |
| 3.13E-01 | 2.53E-03 | 2.19E-01 | 8.41E-03 | 3.13E-01 | 2.39E-03 | 2.19E-01 | 8.44E-03 |
| 4.17E-01 | 2.23E-03 | 2.92E-01 | 8.32E-03 | 4.17E-01 | 2.08E-03 | 2.92E-01 | 8.35E-03 |
| 5.21E-01 | 2.02E-03 | 3.65E-01 | 8.25E-03 | 5.21E-01 | 1.86E-03 | 3.65E-01 | 8.28E-03 |
| 6.25E-01 | 1.91E-03 | 4.38E-01 | 8.19E-03 | 6.25E-01 | 1.77E-03 | 4.38E-01 | 8.22E-03 |
| 7.29E-01 | 1.86E-03 | 5.10E-01 | 8.14E-03 | 7.29E-01 | 1.77E-03 | 5.10E-01 | 8.18E-03 |
| 8.33E-01 | 2.26E-03 | 5.83E-01 | 8.10E-03 | 8.33E-01 | 2.07E-03 | 5.83E-01 | 8.14E-03 |
| 9.38E-01 | 2.66E-03 | 6.56E-01 | 8.07E-03 | 9.38E-01 | 2.50E-03 | 6.56E-01 | 8.11E-03 |
| 1.04E+00 | 3.09E-03 | 7.29E-01 | 8.04E-03 | 1.04E+00 | 2.97E-03 | 7.29E-01 | 8.08E-03 |
| 1.15E+00 | 3.56E-03 | 8.02E-01 | 8.02E-03 | 1.15E+00 | 3.46E-03 | 8.02E-01 | 8.06E-03 |
| 1.25E+00 | 4.04E-03 | 8.75E-01 | 8.00E-03 | 1.25E+00 | 3.96E-03 | 8.75E-01 | 8.04E-03 |
| 1.35E+00 | 4.53E-03 | 9.48E-01 | 7.98E-03 | 1.35E+00 | 4.46E-03 | 9.48E-01 | 8.03E-03 |
| 1.46E+00 | 5.02E-03 | 1.02E+00 | 7.97E-03 | 1.46E+00 | 4.96E-03 | 1.02E+00 | 8.02E-03 |
| 1.56E+00 | 5.49E-03 | 1.09E+00 | 7.96E-03 | 1.56E+00 | 5.45E-03 | 1.09E+00 | 8.01E-03 |
| 1.67E+00 | 5.95E-03 | 1.17E+00 | 7.96E-03 | 1.67E+00 | 5.92E-03 | 1.17E+00 | 8.00E-03 |
| 1.77E+00 | 6.38E-03 | 1.24E+00 | 7.95E-03 | 1.77E+00 | 6.36E-03 | 1.24E+00 | 8.00E-03 |
| 1.88E+00 | 6.78E-03 | 1.31E+00 | 7.95E-03 | 1.88E+00 | 6.78E-03 | 1.31E+00 | 7.99E-03 |

| | | | | | | | |
|---|---|---|---|---|---|---|---|
| 1.98E+00 | 7.13E-03 | 1.39E+00 | 7.95E-03 | 1.98E+00 | 7.14E-03 | 1.39E+00 | 7.99E-03 |
| 2.08E+00 | 7.41E-03 | 1.46E+00 | 7.94E-03 | 2.08E+00 | 7.44E-03 | 1.46E+00 | 7.99E-03 |
| 2.19E+00 | 7.64E-03 | 1.53E+00 | 7.94E-03 | 2.19E+00 | 7.67E-03 | 1.53E+00 | 7.99E-03 |
| 2.29E+00 | 7.81E-03 | 1.60E+00 | 7.94E-03 | 2.29E+00 | 7.85E-03 | 1.60E+00 | 7.99E-03 |
| 2.40E+00 | 7.91E-03 | 1.68E+00 | 7.94E-03 | 2.40E+00 | 7.95E-03 | 1.68E+00 | 7.99E-03 |
| 2.50E+00 | 7.94E-03 | 1.75E+00 | 7.94E-03 | 2.50E+00 | 7.99E-03 | 1.75E+00 | 7.99E-03 |
| 2.60E+00 | 7.91E-03 | 1.82E+00 | 7.94E-03 | 2.60E+00 | 7.95E-03 | 1.82E+00 | 7.99E-03 |
| 2.71E+00 | 7.81E-03 | 1.90E+00 | 7.94E-03 | 2.71E+00 | 7.85E-03 | 1.90E+00 | 7.99E-03 |
| 2.81E+00 | 7.64E-03 | 1.97E+00 | 7.94E-03 | 2.81E+00 | 7.68E-03 | 1.97E+00 | 7.99E-03 |
| 2.92E+00 | 7.42E-03 | 2.04E+00 | 7.94E-03 | 2.92E+00 | 7.44E-03 | 2.04E+00 | 7.99E-03 |
| 3.02E+00 | 7.13E-03 | 2.11E+00 | 7.94E-03 | 3.02E+00 | 7.14E-03 | 2.11E+00 | 7.99E-03 |
| 3.13E+00 | 6.78E-03 | 2.19E+00 | 7.95E-03 | 3.13E+00 | 6.78E-03 | 2.19E+00 | 7.99E-03 |
| 3.23E+00 | 6.39E-03 | 2.26E+00 | 7.95E-03 | 3.23E+00 | 6.37E-03 | 2.26E+00 | 8.00E-03 |
| 3.33E+00 | 5.95E-03 | 2.33E+00 | 7.96E-03 | 3.33E+00 | 5.92E-03 | 2.33E+00 | 8.00E-03 |
| 3.44E+00 | 5.49E-03 | 2.41E+00 | 7.96E-03 | 3.44E+00 | 5.45E-03 | 2.41E+00 | 8.01E-03 |
| 3.54E+00 | 5.02E-03 | 2.48E+00 | 7.97E-03 | 3.54E+00 | 4.97E-03 | 2.48E+00 | 8.02E-03 |
| 3.65E+00 | 4.54E-03 | 2.55E+00 | 7.98E-03 | 3.65E+00 | 4.47E-03 | 2.55E+00 | 8.03E-03 |
| 3.75E+00 | 4.05E-03 | 2.63E+00 | 8.00E-03 | 3.75E+00 | 3.96E-03 | 2.63E+00 | 8.04E-03 |
| 3.85E+00 | 3.57E-03 | 2.70E+00 | 8.01E-03 | 3.85E+00 | 3.46E-03 | 2.70E+00 | 8.06E-03 |
| 3.96E+00 | 3.10E-03 | 2.77E+00 | 8.04E-03 | 3.96E+00 | 2.97E-03 | 2.77E+00 | 8.08E-03 |
| 4.06E+00 | 2.66E-03 | 2.84E+00 | 8.06E-03 | 4.06E+00 | 2.51E-03 | 2.84E+00 | 8.10E-03 |
| 4.1667 | 2.27E-03 | 2.9167 | 8.10E-03 | 4.17E+00 | 2.08E-03 | 2.92E+00 | 8.13E-03 |
| 4.2708 | 1.93E-03 | 2.9896 | 8.14E-03 | 4.27E+00 | 1.78E-03 | 2.99E+00 | 8.17E-03 |
| 4.375 | 1.91E-03 | 3.0625 | 8.19E-03 | 4.38E+00 | 1.77E-03 | 3.06E+00 | 8.22E-03 |
| 4.4792 | 2.02E-03 | 3.1354 | 8.25E-03 | 4.48E+00 | 1.86E-03 | 3.14E+00 | 8.28E-03 |
| 4.5833 | 2.23E-03 | 3.2083 | 8.32E-03 | 4.58E+00 | 2.07E-03 | 3.21E+00 | 8.35E-03 |
| 4.6875 | 2.53E-03 | 3.2813 | 8.41E-03 | 4.69E+00 | 2.39E-03 | 3.28E+00 | 8.44E-03 |
| 4.7917 | 2.89E-03 | 3.3542 | 8.51E-03 | 4.79E+00 | 2.77E-03 | 3.35E+00 | 8.54E-03 |
| 4.8958 | 3.30E-03 | 3.4271 | 8.63E-03 | 4.90E+00 | 3.19E-03 | 3.43E+00 | 8.66E-03 |
| 5 | 3.74E-03 | 3.5 | 8.76E-03 | 5.00E+00 | 3.64E-03 | 3.50E+00 | 8.79E-03 |

Table 0-14 Surface deflection profiles for sample N10, step 70%YS.

| **Hardened Layer** | | | | **Soft Bulk** | | | |
|---|---|---|---|---|---|---|---|
| Longitudinal | | Transverse | | Longitudinal | | Transverse | |
| Length | Stress | Length | Stress | Length | Stress | Length | Stress |
| 0.00E+00 | 4.27E-03 | 0.00E+00 | 9.96E-03 | 0.00E+00 | 4.16E-03 | 0.00E+00 | 1.00E-02 |
| 1.04E-01 | 3.76E-03 | 7.29E-02 | 9.81E-03 | 1.04E-01 | 3.65E-03 | 7.29E-02 | 9.85E-03 |
| 2.08E-01 | 3.30E-03 | 1.46E-01 | 9.67E-03 | 2.08E-01 | 3.16E-03 | 1.46E-01 | 9.70E-03 |
| 3.13E-01 | 2.88E-03 | 2.19E-01 | 9.55E-03 | 3.13E-01 | 2.72E-03 | 2.19E-01 | 9.59E-03 |
| 4.17E-01 | 2.53E-03 | 2.92E-01 | 9.45E-03 | 4.17E-01 | 2.36E-03 | 2.92E-01 | 9.49E-03 |
| 5.21E-01 | 2.29E-03 | 3.65E-01 | 9.36E-03 | 5.21E-01 | 2.10E-03 | 3.65E-01 | 9.40E-03 |

| | | | | | | | |
|---|---|---|---|---|---|---|---|
| 6.25E-01 | 2.15E-03 | 4.38E-01 | 9.29E-03 | 6.25E-01 | 1.99E-03 | 4.38E-01 | 9.34E-03 |
| 7.29E-01 | 2.09E-03 | 5.10E-01 | 9.24E-03 | 7.29E-01 | 1.99E-03 | 5.10E-01 | 9.28E-03 |
| 8.33E-01 | 2.53E-03 | 5.83E-01 | 9.19E-03 | 8.33E-01 | 2.33E-03 | 5.83E-01 | 9.24E-03 |
| 9.38E-01 | 2.98E-03 | 6.56E-01 | 9.15E-03 | 9.38E-01 | 2.81E-03 | 6.56E-01 | 9.20E-03 |
| 1.04E+00 | 3.48E-03 | 7.29E-01 | 9.12E-03 | 1.04E+00 | 3.34E-03 | 7.29E-01 | 9.17E-03 |
| 1.15E+00 | 4.01E-03 | 8.02E-01 | 9.10E-03 | 1.15E+00 | 3.89E-03 | 8.02E-01 | 9.15E-03 |
| 1.25E+00 | 4.56E-03 | 8.75E-01 | 9.08E-03 | 1.25E+00 | 4.46E-03 | 8.75E-01 | 9.13E-03 |
| 1.35E+00 | 5.11E-03 | 9.48E-01 | 9.06E-03 | 1.35E+00 | 5.03E-03 | 9.48E-01 | 9.11E-03 |
| 1.46E+00 | 5.67E-03 | 1.02E+00 | 9.05E-03 | 1.46E+00 | 5.60E-03 | 1.02E+00 | 9.10E-03 |
| 1.56E+00 | 6.21E-03 | 1.09E+00 | 9.04E-03 | 1.56E+00 | 6.16E-03 | 1.09E+00 | 9.09E-03 |
| 1.67E+00 | 6.74E-03 | 1.17E+00 | 9.03E-03 | 1.67E+00 | 6.70E-03 | 1.17E+00 | 9.09E-03 |
| 1.77E+00 | 7.24E-03 | 1.24E+00 | 9.03E-03 | 1.77E+00 | 7.21E-03 | 1.24E+00 | 9.08E-03 |
| 1.88E+00 | 7.69E-03 | 1.31E+00 | 9.02E-03 | 1.88E+00 | 7.69E-03 | 1.31E+00 | 9.08E-03 |
| 1.98E+00 | 8.09E-03 | 1.39E+00 | 9.02E-03 | 1.98E+00 | 8.10E-03 | 1.39E+00 | 9.07E-03 |
| 2.08E+00 | 8.41E-03 | 1.46E+00 | 9.02E-03 | 2.08E+00 | 8.44E-03 | 1.46E+00 | 9.07E-03 |
| 2.19E+00 | 8.67E-03 | 1.53E+00 | 9.01E-03 | 2.19E+00 | 8.71E-03 | 1.53E+00 | 9.07E-03 |
| 2.29E+00 | 8.86E-03 | 1.60E+00 | 9.01E-03 | 2.29E+00 | 8.91E-03 | 1.60E+00 | 9.07E-03 |
| 2.40E+00 | 8.97E-03 | 1.68E+00 | 9.01E-03 | 2.40E+00 | 9.03E-03 | 1.68E+00 | 9.07E-03 |
| 2.50E+00 | 9.01E-03 | 1.75E+00 | 9.01E-03 | 2.50E+00 | 9.07E-03 | 1.75E+00 | 9.07E-03 |
| 2.60E+00 | 8.97E-03 | 1.82E+00 | 9.01E-03 | 2.60E+00 | 9.03E-03 | 1.82E+00 | 9.07E-03 |
| 2.71E+00 | 8.86E-03 | 1.90E+00 | 9.01E-03 | 2.71E+00 | 8.91E-03 | 1.90E+00 | 9.07E-03 |
| 2.81E+00 | 8.67E-03 | 1.97E+00 | 9.01E-03 | 2.81E+00 | 8.71E-03 | 1.97E+00 | 9.07E-03 |
| 2.92E+00 | 8.41E-03 | 2.04E+00 | 9.01E-03 | 2.92E+00 | 8.44E-03 | 2.04E+00 | 9.07E-03 |
| 3.02E+00 | 8.09E-03 | 2.11E+00 | 9.02E-03 | 3.02E+00 | 8.10E-03 | 2.11E+00 | 9.07E-03 |
| 3.13E+00 | 7.70E-03 | 2.19E+00 | 9.02E-03 | 3.13E+00 | 7.69E-03 | 2.19E+00 | 9.08E-03 |
| 3.23E+00 | 7.24E-03 | 2.26E+00 | 9.02E-03 | 3.23E+00 | 7.22E-03 | 2.26E+00 | 9.08E-03 |
| 3.33E+00 | 6.74E-03 | 2.33E+00 | 9.03E-03 | 3.33E+00 | 6.70E-03 | 2.33E+00 | 9.08E-03 |
| 3.44E+00 | 6.21E-03 | 2.41E+00 | 9.04E-03 | 3.44E+00 | 6.16E-03 | 2.41E+00 | 9.09E-03 |
| 3.54E+00 | 5.67E-03 | 2.48E+00 | 9.05E-03 | 3.54E+00 | 5.61E-03 | 2.48E+00 | 9.10E-03 |
| 3.65E+00 | 5.12E-03 | 2.55E+00 | 9.06E-03 | 3.65E+00 | 5.04E-03 | 2.55E+00 | 9.11E-03 |
| 3.75E+00 | 4.56E-03 | 2.63E+00 | 9.07E-03 | 3.75E+00 | 4.46E-03 | 2.63E+00 | 9.12E-03 |
| 3.85E+00 | 4.01E-03 | 2.70E+00 | 9.09E-03 | 3.85E+00 | 3.89E-03 | 2.70E+00 | 9.14E-03 |
| 3.96E+00 | 3.48E-03 | 2.77E+00 | 9.12E-03 | 3.96E+00 | 3.34E-03 | 2.77E+00 | 9.17E-03 |
| 4.06E+00 | 2.98E-03 | 2.84E+00 | 9.15E-03 | 4.06E+00 | 2.81E-03 | 2.84E+00 | 9.19E-03 |
| 4.1667 | 2.54E-03 | 2.9167 | 9.19E-03 | 4.17E+00 | 2.33E-03 | 2.92E+00 | 9.23E-03 |
| 4.2708 | 2.17E-03 | 2.9896 | 9.23E-03 | 4.27E+00 | 2.00E-03 | 2.99E+00 | 9.28E-03 |
| 4.375 | 2.15E-03 | 3.0625 | 9.29E-03 | 4.38E+00 | 1.99E-03 | 3.06E+00 | 9.33E-03 |
| 4.4792 | 2.28E-03 | 3.1354 | 9.36E-03 | 4.48E+00 | 2.09E-03 | 3.14E+00 | 9.40E-03 |
| 4.5833 | 2.52E-03 | 3.2083 | 9.44E-03 | 4.58E+00 | 2.35E-03 | 3.21E+00 | 9.48E-03 |
| 4.6875 | 2.87E-03 | 3.2813 | 9.54E-03 | 4.69E+00 | 2.71E-03 | 3.28E+00 | 9.58E-03 |
| 4.7917 | 3.28E-03 | 3.3542 | 9.67E-03 | 4.79E+00 | 3.15E-03 | 3.35E+00 | 9.70E-03 |

| | | | | | | | |
|---|---|---|---|---|---|---|---|
| 4.8958 | 3.75E-03 | 3.4271 | 9.81E-03 | 4.90E+00 | 3.63E-03 | 3.43E+00 | 9.84E-03 |
| 5 | 4.25E-03 | 3.5 | 9.96E-03 | 5.00E+00 | 4.15E-03 | 3.50E+00 | 9.99E-03 |

## Sample L-R-1

Table B-15 Surface deflection profiles for sample L-R-1, step 50%YS.

| **Hardened Layer** | | | | **Soft Bulk** | | | |
|---|---|---|---|---|---|---|---|
| Longitudinal | | Transverse | | Longitudinal | | Transverse | |
| Length | Stress | Length | Stress | Length | Stress | Length | Stress |
| 0.00E+00 | 3.05E-03 | 0.00E+00 | 7.22E-03 | 0.00E+00 | 2.95E-03 | 0.00E+00 | 7.25E-03 |
| 1.04E-01 | 2.70E-03 | 7.29E-02 | 7.12E-03 | 1.04E-01 | 2.59E-03 | 7.29E-02 | 7.15E-03 |
| 2.08E-01 | 2.37E-03 | 1.46E-01 | 7.02E-03 | 2.08E-01 | 2.24E-03 | 1.46E-01 | 7.05E-03 |
| 3.13E-01 | 2.07E-03 | 2.19E-01 | 6.94E-03 | 3.13E-01 | 1.93E-03 | 2.19E-01 | 6.97E-03 |
| 4.17E-01 | 1.84E-03 | 2.92E-01 | 6.88E-03 | 4.17E-01 | 1.67E-03 | 2.92E-01 | 6.91E-03 |
| 5.21E-01 | 1.67E-03 | 3.65E-01 | 6.82E-03 | 5.21E-01 | 1.50E-03 | 3.65E-01 | 6.85E-03 |
| 6.25E-01 | 1.59E-03 | 4.38E-01 | 6.77E-03 | 6.25E-01 | 1.44E-03 | 4.38E-01 | 6.80E-03 |
| 7.29E-01 | 1.56E-03 | 5.10E-01 | 6.73E-03 | 7.29E-01 | 1.46E-03 | 5.10E-01 | 6.77E-03 |
| 8.33E-01 | 1.90E-03 | 5.83E-01 | 6.69E-03 | 8.33E-01 | 1.70E-03 | 5.83E-01 | 6.73E-03 |
| 9.38E-01 | 2.23E-03 | 6.56E-01 | 6.67E-03 | 9.38E-01 | 2.07E-03 | 6.56E-01 | 6.71E-03 |
| 1.04E+00 | 2.60E-03 | 7.29E-01 | 6.64E-03 | 1.04E+00 | 2.47E-03 | 7.29E-01 | 6.68E-03 |
| 1.15E+00 | 2.99E-03 | 8.02E-01 | 6.63E-03 | 1.15E+00 | 2.88E-03 | 8.02E-01 | 6.67E-03 |
| 1.25E+00 | 3.38E-03 | 8.75E-01 | 6.61E-03 | 1.25E+00 | 3.30E-03 | 8.75E-01 | 6.65E-03 |
| 1.35E+00 | 3.78E-03 | 9.48E-01 | 6.60E-03 | 1.35E+00 | 3.71E-03 | 9.48E-01 | 6.64E-03 |
| 1.46E+00 | 4.18E-03 | 1.02E+00 | 6.59E-03 | 1.46E+00 | 4.12E-03 | 1.02E+00 | 6.63E-03 |
| 1.56E+00 | 4.57E-03 | 1.09E+00 | 6.58E-03 | 1.56E+00 | 4.52E-03 | 1.09E+00 | 6.62E-03 |
| 1.67E+00 | 4.93E-03 | 1.17E+00 | 6.57E-03 | 1.67E+00 | 4.91E-03 | 1.17E+00 | 6.62E-03 |
| 1.77E+00 | 5.28E-03 | 1.24E+00 | 6.57E-03 | 1.77E+00 | 5.27E-03 | 1.24E+00 | 6.61E-03 |
| 1.88E+00 | 5.60E-03 | 1.31E+00 | 6.56E-03 | 1.88E+00 | 5.60E-03 | 1.31E+00 | 6.61E-03 |
| 1.98E+00 | 5.89E-03 | 1.39E+00 | 6.56E-03 | 1.98E+00 | 5.90E-03 | 1.39E+00 | 6.61E-03 |
| 2.08E+00 | 6.13E-03 | 1.46E+00 | 6.56E-03 | 2.08E+00 | 6.15E-03 | 1.46E+00 | 6.61E-03 |
| 2.19E+00 | 6.31E-03 | 1.53E+00 | 6.56E-03 | 2.19E+00 | 6.35E-03 | 1.53E+00 | 6.60E-03 |
| 2.29E+00 | 6.45E-03 | 1.60E+00 | 6.56E-03 | 2.29E+00 | 6.49E-03 | 1.60E+00 | 6.60E-03 |
| 2.40E+00 | 6.53E-03 | 1.68E+00 | 6.56E-03 | 2.40E+00 | 6.57E-03 | 1.68E+00 | 6.60E-03 |
| 2.50E+00 | 6.55E-03 | 1.75E+00 | 6.55E-03 | 2.50E+00 | 6.60E-03 | 1.75E+00 | 6.60E-03 |
| 2.60E+00 | 6.53E-03 | 1.82E+00 | 6.56E-03 | 2.60E+00 | 6.57E-03 | 1.82E+00 | 6.60E-03 |
| 2.71E+00 | 6.45E-03 | 1.90E+00 | 6.56E-03 | 2.71E+00 | 6.49E-03 | 1.90E+00 | 6.60E-03 |
| 2.81E+00 | 6.31E-03 | 1.97E+00 | 6.56E-03 | 2.81E+00 | 6.35E-03 | 1.97E+00 | 6.60E-03 |
| 2.92E+00 | 6.13E-03 | 2.04E+00 | 6.56E-03 | 2.92E+00 | 6.15E-03 | 2.04E+00 | 6.61E-03 |
| 3.02E+00 | 5.89E-03 | 2.11E+00 | 6.56E-03 | 3.02E+00 | 5.90E-03 | 2.11E+00 | 6.61E-03 |
| 3.13E+00 | 5.61E-03 | 2.19E+00 | 6.56E-03 | 3.13E+00 | 5.60E-03 | 2.19E+00 | 6.61E-03 |
| 3.23E+00 | 5.29E-03 | 2.26E+00 | 6.57E-03 | 3.23E+00 | 5.27E-03 | 2.26E+00 | 6.61E-03 |

| | | | | | | | |
|---|---|---|---|---|---|---|---|
| 3.33E+00 | 4.94E-03 | 2.33E+00 | 6.57E-03 | 3.33E+00 | 4.91E-03 | 2.33E+00 | 6.62E-03 |
| 3.44E+00 | 4.57E-03 | 2.41E+00 | 6.58E-03 | 3.44E+00 | 4.53E-03 | 2.41E+00 | 6.62E-03 |
| 3.54E+00 | 4.19E-03 | 2.48E+00 | 6.59E-03 | 3.54E+00 | 4.13E-03 | 2.48E+00 | 6.63E-03 |
| 3.65E+00 | 3.79E-03 | 2.55E+00 | 6.60E-03 | 3.65E+00 | 3.72E-03 | 2.55E+00 | 6.64E-03 |
| 3.75E+00 | 3.39E-03 | 2.63E+00 | 6.61E-03 | 3.75E+00 | 3.30E-03 | 2.63E+00 | 6.65E-03 |
| 3.85E+00 | 3.00E-03 | 2.70E+00 | 6.62E-03 | 3.85E+00 | 2.89E-03 | 2.70E+00 | 6.67E-03 |
| 3.96E+00 | 2.61E-03 | 2.77E+00 | 6.64E-03 | 3.96E+00 | 2.48E-03 | 2.77E+00 | 6.69E-03 |
| 4.06E+00 | 2.25E-03 | 2.84E+00 | 6.67E-03 | 4.06E+00 | 2.08E-03 | 2.84E+00 | 6.71E-03 |
| 4.1667 | 1.92E-03 | 2.9167 | 6.69E-03 | 4.17E+00 | 1.72E-03 | 2.92E+00 | 6.73E-03 |
| 4.2708 | 1.62E-03 | 2.9896 | 6.73E-03 | 4.27E+00 | 1.48E-03 | 2.99E+00 | 6.77E-03 |
| 4.375 | 1.60E-03 | 3.0625 | 6.77E-03 | 4.38E+00 | 1.46E-03 | 3.06E+00 | 6.81E-03 |
| 4.4792 | 1.69E-03 | 3.1354 | 6.82E-03 | 4.48E+00 | 1.52E-03 | 3.14E+00 | 6.85E-03 |
| 4.5833 | 1.85E-03 | 3.2083 | 6.87E-03 | 4.58E+00 | 1.68E-03 | 3.21E+00 | 6.91E-03 |
| 4.6875 | 2.08E-03 | 3.2813 | 6.94E-03 | 4.69E+00 | 1.94E-03 | 3.28E+00 | 6.98E-03 |
| 4.7917 | 2.37E-03 | 3.3542 | 7.02E-03 | 4.79E+00 | 2.24E-03 | 3.35E+00 | 7.06E-03 |
| 4.8958 | 2.70E-03 | 3.4271 | 7.12E-03 | 4.90E+00 | 2.59E-03 | 3.43E+00 | 7.15E-03 |
| 5 | 3.06E-03 | 3.5 | 7.22E-03 | 5.00E+00 | 2.96E-03 | 3.50E+00 | 7.25E-03 |

Table B-16 Surface deflection profiles for sample L-R-1, step 60%YS.

| **Hardened Layer** | | | | **Soft Bulk** | | | |
|---|---|---|---|---|---|---|---|
| Longitudinal | | Transverse | | Longitudinal | | Transverse | |
| Length | Stress | Length | Stress | Length | Stress | Length | Stress |
| 0.00E+00 | 3.59E-03 | 0.00E+00 | 8.46E-03 | 0.00E+00 | 3.48E-03 | 0.00E+00 | 8.49E-03 |
| 1.04E-01 | 3.17E-03 | 7.29E-02 | 8.34E-03 | 1.04E-01 | 3.04E-03 | 7.29E-02 | 8.37E-03 |
| 2.08E-01 | 2.78E-03 | 1.46E-01 | 8.22E-03 | 2.08E-01 | 2.63E-03 | 1.46E-01 | 8.25E-03 |
| 3.13E-01 | 2.44E-03 | 2.19E-01 | 8.12E-03 | 3.13E-01 | 2.27E-03 | 2.19E-01 | 8.16E-03 |
| 4.17E-01 | 2.15E-03 | 2.92E-01 | 8.04E-03 | 4.17E-01 | 1.96E-03 | 2.92E-01 | 8.08E-03 |
| 5.21E-01 | 1.95E-03 | 3.65E-01 | 7.97E-03 | 5.21E-01 | 1.75E-03 | 3.65E-01 | 8.01E-03 |
| 6.25E-01 | 1.85E-03 | 4.38E-01 | 7.91E-03 | 6.25E-01 | 1.68E-03 | 4.38E-01 | 7.95E-03 |
| 7.29E-01 | 1.80E-03 | 5.10E-01 | 7.86E-03 | 7.29E-01 | 1.69E-03 | 5.10E-01 | 7.91E-03 |
| 8.33E-01 | 2.20E-03 | 5.83E-01 | 7.82E-03 | 8.33E-01 | 1.97E-03 | 5.83E-01 | 7.87E-03 |
| 9.38E-01 | 2.58E-03 | 6.56E-01 | 7.79E-03 | 9.38E-01 | 2.39E-03 | 6.56E-01 | 7.84E-03 |
| 1.04E+00 | 3.01E-03 | 7.29E-01 | 7.77E-03 | 1.04E+00 | 2.85E-03 | 7.29E-01 | 7.82E-03 |
| 1.15E+00 | 3.46E-03 | 8.02E-01 | 7.74E-03 | 1.15E+00 | 3.33E-03 | 8.02E-01 | 7.80E-03 |
| 1.25E+00 | 3.92E-03 | 8.75E-01 | 7.73E-03 | 1.25E+00 | 3.82E-03 | 8.75E-01 | 7.78E-03 |
| 1.35E+00 | 4.39E-03 | 9.48E-01 | 7.71E-03 | 1.35E+00 | 4.31E-03 | 9.48E-01 | 7.77E-03 |
| 1.46E+00 | 4.86E-03 | 1.02E+00 | 7.70E-03 | 1.46E+00 | 4.79E-03 | 1.02E+00 | 7.76E-03 |
| 1.56E+00 | 5.31E-03 | 1.09E+00 | 7.69E-03 | 1.56E+00 | 5.26E-03 | 1.09E+00 | 7.75E-03 |
| 1.67E+00 | 5.75E-03 | 1.17E+00 | 7.69E-03 | 1.67E+00 | 5.72E-03 | 1.17E+00 | 7.74E-03 |
| 1.77E+00 | 6.17E-03 | 1.24E+00 | 7.68E-03 | 1.77E+00 | 6.15E-03 | 1.24E+00 | 7.74E-03 |
| 1.88E+00 | 6.55E-03 | 1.31E+00 | 7.68E-03 | 1.88E+00 | 6.55E-03 | 1.31E+00 | 7.74E-03 |

| | | | | | | | |
|---|---|---|---|---|---|---|---|
| 1.98E+00 | 6.89E-03 | 1.39E+00 | 7.67E-03 | 1.98E+00 | 6.90E-03 | 1.39E+00 | 7.73E-03 |
| 2.08E+00 | 7.16E-03 | 1.46E+00 | 7.67E-03 | 2.08E+00 | 7.19E-03 | 1.46E+00 | 7.73E-03 |
| 2.19E+00 | 7.38E-03 | 1.53E+00 | 7.67E-03 | 2.19E+00 | 7.42E-03 | 1.53E+00 | 7.73E-03 |
| 2.29E+00 | 7.54E-03 | 1.60E+00 | 7.67E-03 | 2.29E+00 | 7.59E-03 | 1.60E+00 | 7.73E-03 |
| 2.40E+00 | 7.63E-03 | 1.68E+00 | 7.67E-03 | 2.40E+00 | 7.69E-03 | 1.68E+00 | 7.73E-03 |
| 2.50E+00 | 7.67E-03 | 1.75E+00 | 7.67E-03 | 2.50E+00 | 7.73E-03 | 1.75E+00 | 7.73E-03 |
| 2.60E+00 | 7.64E-03 | 1.82E+00 | 7.67E-03 | 2.60E+00 | 7.70E-03 | 1.82E+00 | 7.73E-03 |
| 2.71E+00 | 7.54E-03 | 1.90E+00 | 7.67E-03 | 2.71E+00 | 7.59E-03 | 1.90E+00 | 7.73E-03 |
| 2.81E+00 | 7.38E-03 | 1.97E+00 | 7.67E-03 | 2.81E+00 | 7.43E-03 | 1.97E+00 | 7.73E-03 |
| 2.92E+00 | 7.17E-03 | 2.04E+00 | 7.67E-03 | 2.92E+00 | 7.20E-03 | 2.04E+00 | 7.73E-03 |
| 3.02E+00 | 6.89E-03 | 2.11E+00 | 7.67E-03 | 3.02E+00 | 6.90E-03 | 2.11E+00 | 7.73E-03 |
| 3.13E+00 | 6.56E-03 | 2.19E+00 | 7.68E-03 | 3.13E+00 | 6.55E-03 | 2.19E+00 | 7.74E-03 |
| 3.23E+00 | 6.17E-03 | 2.26E+00 | 7.68E-03 | 3.23E+00 | 6.15E-03 | 2.26E+00 | 7.74E-03 |
| 3.33E+00 | 5.76E-03 | 2.33E+00 | 7.68E-03 | 3.33E+00 | 5.72E-03 | 2.33E+00 | 7.75E-03 |
| 3.44E+00 | 5.32E-03 | 2.41E+00 | 7.69E-03 | 3.44E+00 | 5.27E-03 | 2.41E+00 | 7.75E-03 |
| 3.54E+00 | 4.86E-03 | 2.48E+00 | 7.70E-03 | 3.54E+00 | 4.80E-03 | 2.48E+00 | 7.76E-03 |
| 3.65E+00 | 4.40E-03 | 2.55E+00 | 7.71E-03 | 3.65E+00 | 4.31E-03 | 2.55E+00 | 7.77E-03 |
| 3.75E+00 | 3.93E-03 | 2.63E+00 | 7.72E-03 | 3.75E+00 | 3.82E-03 | 2.63E+00 | 7.78E-03 |
| 3.85E+00 | 3.47E-03 | 2.70E+00 | 7.74E-03 | 3.85E+00 | 3.34E-03 | 2.70E+00 | 7.80E-03 |
| 3.96E+00 | 3.01E-03 | 2.77E+00 | 7.76E-03 | 3.96E+00 | 2.86E-03 | 2.77E+00 | 7.82E-03 |
| 4.06E+00 | 2.59E-03 | 2.84E+00 | 7.79E-03 | 4.06E+00 | 2.40E-03 | 2.84E+00 | 7.84E-03 |
| 4.1667 | 2.21E-03 | 2.9167 | 7.82E-03 | 4.17E+00 | 1.98E-03 | 2.92E+00 | 7.87E-03 |
| 4.2708 | 1.88E-03 | 2.9896 | 7.86E-03 | 4.27E+00 | 1.71E-03 | 2.99E+00 | 7.91E-03 |
| 4.375 | 1.86E-03 | 3.0625 | 7.91E-03 | 4.38E+00 | 1.68E-03 | 3.06E+00 | 7.96E-03 |
| 4.4792 | 1.96E-03 | 3.1354 | 7.97E-03 | 4.48E+00 | 1.76E-03 | 3.14E+00 | 8.01E-03 |
| 4.5833 | 2.15E-03 | 3.2083 | 8.03E-03 | 4.58E+00 | 1.96E-03 | 3.21E+00 | 8.08E-03 |
| 4.6875 | 2.44E-03 | 3.2813 | 8.12E-03 | 4.69E+00 | 2.26E-03 | 3.28E+00 | 8.16E-03 |
| 4.7917 | 2.78E-03 | 3.3542 | 8.22E-03 | 4.79E+00 | 2.63E-03 | 3.35E+00 | 8.26E-03 |
| 4.8958 | 3.17E-03 | 3.4271 | 8.33E-03 | 4.90E+00 | 3.04E-03 | 3.43E+00 | 8.37E-03 |
| 5 | 3.59E-03 | 3.5 | 8.46E-03 | 5.00E+00 | 3.47E-03 | 3.50E+00 | 8.50E-03 |

Table B-17 Surface deflection profiles for sample L-R-1, step 70%YS.

| **Hardened Layer** | | | | **Soft Bulk** | | | |
|---|---|---|---|---|---|---|---|
| Longitudinal | | Transverse | | Longitudinal | | Transverse | |
| Length | Stress | Length | Stress | Length | Stress | Length | Stress |
| 0.00E+00 | 4.07E-03 | 0.00E+00 | 9.57E-03 | 0.00E+00 | 3.94E-03 | 0.00E+00 | 9.60E-03 |
| 1.04E-01 | 3.59E-03 | 7.29E-02 | 9.42E-03 | 1.04E-01 | 3.45E-03 | 7.29E-02 | 9.46E-03 |
| 2.08E-01 | 3.15E-03 | 1.46E-01 | 9.29E-03 | 2.08E-01 | 2.98E-03 | 1.46E-01 | 9.33E-03 |
| 3.13E-01 | 2.75E-03 | 2.19E-01 | 9.17E-03 | 3.13E-01 | 2.56E-03 | 2.19E-01 | 9.21E-03 |
| 4.17E-01 | 2.43E-03 | 2.92E-01 | 9.08E-03 | 4.17E-01 | 2.21E-03 | 2.92E-01 | 9.12E-03 |
| 5.21E-01 | 2.20E-03 | 3.65E-01 | 9.00E-03 | 5.21E-01 | 1.97E-03 | 3.65E-01 | 9.04E-03 |

| | | | | | | | |
|---|---|---|---|---|---|---|---|
| 6.25E-01 | 2.07E-03 | 4.38E-01 | 8.93E-03 | 6.25E-01 | 1.88E-03 | 4.38E-01 | 8.98E-03 |
| 7.29E-01 | 2.01E-03 | 5.10E-01 | 8.87E-03 | 7.29E-01 | 1.89E-03 | 5.10E-01 | 8.93E-03 |
| 8.33E-01 | 2.45E-03 | 5.83E-01 | 8.83E-03 | 8.33E-01 | 2.20E-03 | 5.83E-01 | 8.88E-03 |
| 9.38E-01 | 2.89E-03 | 6.56E-01 | 8.79E-03 | 9.38E-01 | 2.67E-03 | 6.56E-01 | 8.85E-03 |
| 1.04E+00 | 3.36E-03 | 7.29E-01 | 8.76E-03 | 1.04E+00 | 3.19E-03 | 7.29E-01 | 8.82E-03 |
| 1.15E+00 | 3.87E-03 | 8.02E-01 | 8.74E-03 | 1.15E+00 | 3.73E-03 | 8.02E-01 | 8.80E-03 |
| 1.25E+00 | 4.40E-03 | 8.75E-01 | 8.72E-03 | 1.25E+00 | 4.28E-03 | 8.75E-01 | 8.78E-03 |
| 1.35E+00 | 4.93E-03 | 9.48E-01 | 8.70E-03 | 1.35E+00 | 4.83E-03 | 9.48E-01 | 8.77E-03 |
| 1.46E+00 | 5.46E-03 | 1.02E+00 | 8.69E-03 | 1.46E+00 | 5.38E-03 | 1.02E+00 | 8.76E-03 |
| 1.56E+00 | 5.98E-03 | 1.09E+00 | 8.68E-03 | 1.56E+00 | 5.92E-03 | 1.09E+00 | 8.75E-03 |
| 1.67E+00 | 6.48E-03 | 1.17E+00 | 8.67E-03 | 1.67E+00 | 6.44E-03 | 1.17E+00 | 8.74E-03 |
| 1.77E+00 | 6.96E-03 | 1.24E+00 | 8.67E-03 | 1.77E+00 | 6.93E-03 | 1.24E+00 | 8.74E-03 |
| 1.88E+00 | 7.40E-03 | 1.31E+00 | 8.66E-03 | 1.88E+00 | 7.39E-03 | 1.31E+00 | 8.73E-03 |
| 1.98E+00 | 7.77E-03 | 1.39E+00 | 8.66E-03 | 1.98E+00 | 7.79E-03 | 1.39E+00 | 8.73E-03 |
| 2.08E+00 | 8.08E-03 | 1.46E+00 | 8.66E-03 | 2.08E+00 | 8.12E-03 | 1.46E+00 | 8.73E-03 |
| 2.19E+00 | 8.33E-03 | 1.53E+00 | 8.66E-03 | 2.19E+00 | 8.38E-03 | 1.53E+00 | 8.73E-03 |
| 2.29E+00 | 8.51E-03 | 1.60E+00 | 8.66E-03 | 2.29E+00 | 8.57E-03 | 1.60E+00 | 8.73E-03 |
| 2.40E+00 | 8.62E-03 | 1.68E+00 | 8.65E-03 | 2.40E+00 | 8.69E-03 | 1.68E+00 | 8.73E-03 |
| 2.50E+00 | 8.65E-03 | 1.75E+00 | 8.65E-03 | 2.50E+00 | 8.73E-03 | 1.75E+00 | 8.73E-03 |
| 2.60E+00 | 8.62E-03 | 1.82E+00 | 8.65E-03 | 2.60E+00 | 8.69E-03 | 1.82E+00 | 8.73E-03 |
| 2.71E+00 | 8.51E-03 | 1.90E+00 | 8.65E-03 | 2.71E+00 | 8.57E-03 | 1.90E+00 | 8.73E-03 |
| 2.81E+00 | 8.33E-03 | 1.97E+00 | 8.66E-03 | 2.81E+00 | 8.38E-03 | 1.97E+00 | 8.73E-03 |
| 2.92E+00 | 8.09E-03 | 2.04E+00 | 8.66E-03 | 2.92E+00 | 8.12E-03 | 2.04E+00 | 8.73E-03 |
| 3.02E+00 | 7.77E-03 | 2.11E+00 | 8.66E-03 | 3.02E+00 | 7.79E-03 | 2.11E+00 | 8.73E-03 |
| 3.13E+00 | 7.40E-03 | 2.19E+00 | 8.66E-03 | 3.13E+00 | 7.39E-03 | 2.19E+00 | 8.74E-03 |
| 3.23E+00 | 6.96E-03 | 2.26E+00 | 8.67E-03 | 3.23E+00 | 6.93E-03 | 2.26E+00 | 8.74E-03 |
| 3.33E+00 | 6.49E-03 | 2.33E+00 | 8.67E-03 | 3.33E+00 | 6.44E-03 | 2.33E+00 | 8.75E-03 |
| 3.44E+00 | 5.98E-03 | 2.41E+00 | 8.68E-03 | 3.44E+00 | 5.92E-03 | 2.41E+00 | 8.75E-03 |
| 3.54E+00 | 5.47E-03 | 2.48E+00 | 8.69E-03 | 3.54E+00 | 5.39E-03 | 2.48E+00 | 8.76E-03 |
| 3.65E+00 | 4.94E-03 | 2.55E+00 | 8.70E-03 | 3.65E+00 | 4.84E-03 | 2.55E+00 | 8.77E-03 |
| 3.75E+00 | 4.40E-03 | 2.63E+00 | 8.72E-03 | 3.75E+00 | 4.28E-03 | 2.63E+00 | 8.79E-03 |
| 3.85E+00 | 3.88E-03 | 2.70E+00 | 8.73E-03 | 3.85E+00 | 3.73E-03 | 2.70E+00 | 8.80E-03 |
| 3.96E+00 | 3.37E-03 | 2.77E+00 | 8.76E-03 | 3.96E+00 | 3.19E-03 | 2.77E+00 | 8.83E-03 |
| 4.06E+00 | 2.89E-03 | 2.84E+00 | 8.79E-03 | 4.06E+00 | 2.68E-03 | 2.84E+00 | 8.85E-03 |
| 4.1667 | 2.47E-03 | 2.9167 | 8.82E-03 | 4.17E+00 | 2.21E-03 | 2.92E+00 | 8.89E-03 |
| 4.2708 | 2.11E-03 | 2.9896 | 8.87E-03 | 4.27E+00 | 1.91E-03 | 2.99E+00 | 8.93E-03 |
| 4.375 | 2.08E-03 | 3.0625 | 8.92E-03 | 4.38E+00 | 1.88E-03 | 3.06E+00 | 8.98E-03 |
| 4.4792 | 2.20E-03 | 3.1354 | 8.99E-03 | 4.48E+00 | 1.97E-03 | 3.14E+00 | 9.05E-03 |
| 4.5833 | 2.42E-03 | 3.2083 | 9.07E-03 | 4.58E+00 | 2.21E-03 | 3.21E+00 | 9.13E-03 |
| 4.6875 | 2.75E-03 | 3.2813 | 9.17E-03 | 4.69E+00 | 2.55E-03 | 3.28E+00 | 9.22E-03 |
| 4.7917 | 3.14E-03 | 3.3542 | 9.28E-03 | 4.79E+00 | 2.97E-03 | 3.35E+00 | 9.33E-03 |

| | | | | | | | |
|---|---|---|---|---|---|---|---|
| 4.8958 | 3.58E-03 | 3.4271 | 9.42E-03 | 4.90E+00 | 3.44E-03 | 3.43E+00 | 9.47E-03 |
| 5 | 4.06E-03 | 3.5 | 9.56E-03 | 5.00E+00 | 3.93E-03 | 3.50E+00 | 9.61E-03 |

Table 0-18 Surface deflection profiles for sample L-R-1, step 80%YS.

| **Hardened Layer** | | | | **Soft Bulk** | | | |
|---|---|---|---|---|---|---|---|
| Longitudinal | | Transverse | | Longitudinal | | Transverse | |
| Length | Stress | Length | Stress | Length | Stress | Length | Stress |
| 0.00E+00 | 4.61E-03 | 0.00E+00 | 1.08E-02 | 0.00E+00 | 4.47E-03 | 0.00E+00 | 1.08E-02 |
| 1.04E-01 | 4.07E-03 | 7.29E-02 | 1.06E-02 | 1.04E-01 | 3.91E-03 | 7.29E-02 | 1.06E-02 |
| 2.08E-01 | 3.57E-03 | 1.46E-01 | 1.05E-02 | 2.08E-01 | 3.38E-03 | 1.46E-01 | 1.05E-02 |
| 3.13E-01 | 3.12E-03 | 2.19E-01 | 1.03E-02 | 3.13E-01 | 2.90E-03 | 2.19E-01 | 1.04E-02 |
| 4.17E-01 | 2.75E-03 | 2.92E-01 | 1.02E-02 | 4.17E-01 | 2.50E-03 | 2.92E-01 | 1.03E-02 |
| 5.21E-01 | 2.48E-03 | 3.65E-01 | 1.01E-02 | 5.21E-01 | 2.23E-03 | 3.65E-01 | 1.02E-02 |
| 6.25E-01 | 2.34E-03 | 4.38E-01 | 1.00E-02 | 6.25E-01 | 2.12E-03 | 4.38E-01 | 1.01E-02 |
| 7.29E-01 | 2.25E-03 | 5.10E-01 | 9.97E-03 | 7.29E-01 | 2.13E-03 | 5.10E-01 | 1.00E-02 |
| 8.33E-01 | 2.74E-03 | 5.83E-01 | 9.92E-03 | 8.33E-01 | 2.47E-03 | 5.83E-01 | 9.99E-03 |
| 9.38E-01 | 3.23E-03 | 6.56E-01 | 9.88E-03 | 9.38E-01 | 2.99E-03 | 6.56E-01 | 9.95E-03 |
| 1.04E+00 | 3.76E-03 | 7.29E-01 | 9.85E-03 | 1.04E+00 | 3.56E-03 | 7.29E-01 | 9.92E-03 |
| 1.15E+00 | 4.33E-03 | 8.02E-01 | 9.82E-03 | 1.15E+00 | 4.17E-03 | 8.02E-01 | 9.89E-03 |
| 1.25E+00 | 4.92E-03 | 8.75E-01 | 9.80E-03 | 1.25E+00 | 4.78E-03 | 8.75E-01 | 9.87E-03 |
| 1.35E+00 | 5.52E-03 | 9.48E-01 | 9.78E-03 | 1.35E+00 | 5.41E-03 | 9.48E-01 | 9.86E-03 |
| 1.46E+00 | 6.12E-03 | 1.02E+00 | 9.77E-03 | 1.46E+00 | 6.03E-03 | 1.02E+00 | 9.85E-03 |
| 1.56E+00 | 6.70E-03 | 1.09E+00 | 9.76E-03 | 1.56E+00 | 6.63E-03 | 1.09E+00 | 9.84E-03 |
| 1.67E+00 | 7.28E-03 | 1.17E+00 | 9.75E-03 | 1.67E+00 | 7.22E-03 | 1.17E+00 | 9.83E-03 |
| 1.77E+00 | 7.82E-03 | 1.24E+00 | 9.74E-03 | 1.77E+00 | 7.79E-03 | 1.24E+00 | 9.83E-03 |
| 1.88E+00 | 8.31E-03 | 1.31E+00 | 9.74E-03 | 1.88E+00 | 8.30E-03 | 1.31E+00 | 9.82E-03 |
| 1.98E+00 | 8.73E-03 | 1.39E+00 | 9.74E-03 | 1.98E+00 | 8.75E-03 | 1.39E+00 | 9.82E-03 |
| 2.08E+00 | 9.08E-03 | 1.46E+00 | 9.73E-03 | 2.08E+00 | 9.13E-03 | 1.46E+00 | 9.82E-03 |
| 2.19E+00 | 9.36E-03 | 1.53E+00 | 9.73E-03 | 2.19E+00 | 9.42E-03 | 1.53E+00 | 9.82E-03 |
| 2.29E+00 | 9.56E-03 | 1.60E+00 | 9.73E-03 | 2.29E+00 | 9.64E-03 | 1.60E+00 | 9.82E-03 |
| 2.40E+00 | 9.69E-03 | 1.68E+00 | 9.73E-03 | 2.40E+00 | 9.77E-03 | 1.68E+00 | 9.82E-03 |
| 2.50E+00 | 9.73E-03 | 1.75E+00 | 9.73E-03 | 2.50E+00 | 9.82E-03 | 1.75E+00 | 9.82E-03 |
| 2.60E+00 | 9.69E-03 | 1.82E+00 | 9.73E-03 | 2.60E+00 | 9.77E-03 | 1.82E+00 | 9.82E-03 |
| 2.71E+00 | 9.56E-03 | 1.90E+00 | 9.73E-03 | 2.71E+00 | 9.64E-03 | 1.90E+00 | 9.82E-03 |
| 2.81E+00 | 9.36E-03 | 1.97E+00 | 9.73E-03 | 2.81E+00 | 9.42E-03 | 1.97E+00 | 9.82E-03 |
| 2.92E+00 | 9.08E-03 | 2.04E+00 | 9.73E-03 | 2.92E+00 | 9.13E-03 | 2.04E+00 | 9.82E-03 |
| 3.02E+00 | 8.73E-03 | 2.11E+00 | 9.73E-03 | 3.02E+00 | 8.75E-03 | 2.11E+00 | 9.82E-03 |
| 3.13E+00 | 8.31E-03 | 2.19E+00 | 9.74E-03 | 3.13E+00 | 8.30E-03 | 2.19E+00 | 9.82E-03 |
| 3.23E+00 | 7.82E-03 | 2.26E+00 | 9.74E-03 | 3.23E+00 | 7.79E-03 | 2.26E+00 | 9.83E-03 |
| 3.33E+00 | 7.28E-03 | 2.33E+00 | 9.75E-03 | 3.33E+00 | 7.22E-03 | 2.33E+00 | 9.83E-03 |
| 3.44E+00 | 6.70E-03 | 2.41E+00 | 9.76E-03 | 3.44E+00 | 6.64E-03 | 2.41E+00 | 9.84E-03 |

| | | | | | | | |
|---|---|---|---|---|---|---|---|
| 3.54E+00 | 6.12E-03 | 2.48E+00 | 9.77E-03 | 3.54E+00 | 6.03E-03 | 2.48E+00 | 9.85E-03 |
| 3.65E+00 | 5.52E-03 | 2.55E+00 | 9.78E-03 | 3.65E+00 | 5.41E-03 | 2.55E+00 | 9.86E-03 |
| 3.75E+00 | 4.92E-03 | 2.63E+00 | 9.79E-03 | 3.75E+00 | 4.78E-03 | 2.63E+00 | 9.88E-03 |
| 3.85E+00 | 4.33E-03 | 2.70E+00 | 9.82E-03 | 3.85E+00 | 4.16E-03 | 2.70E+00 | 9.90E-03 |
| 3.96E+00 | 3.76E-03 | 2.77E+00 | 9.84E-03 | 3.96E+00 | 3.56E-03 | 2.77E+00 | 9.92E-03 |
| 4.06E+00 | 3.22E-03 | 2.84E+00 | 9.88E-03 | 4.06E+00 | 2.98E-03 | 2.84E+00 | 9.95E-03 |
| 4.1667 | 2.74E-03 | 2.9167 | 9.92E-03 | 4.17E+00 | 2.46E-03 | 2.92E+00 | 9.99E-03 |
| 4.2708 | 2.37E-03 | 2.9896 | 9.97E-03 | 4.27E+00 | 2.13E-03 | 2.99E+00 | 1.00E-02 |
| 4.375 | 2.33E-03 | 3.0625 | 1.00E-02 | 4.38E+00 | 2.10E-03 | 3.06E+00 | 1.01E-02 |
| 4.4792 | 2.47E-03 | 3.1354 | 1.01E-02 | 4.48E+00 | 2.21E-03 | 3.14E+00 | 1.02E-02 |
| 4.5833 | 2.72E-03 | 3.2083 | 1.02E-02 | 4.58E+00 | 2.48E-03 | 3.21E+00 | 1.03E-02 |
| 4.6875 | 3.09E-03 | 3.2813 | 1.03E-02 | 4.69E+00 | 2.88E-03 | 3.28E+00 | 1.04E-02 |
| 4.7917 | 3.55E-03 | 3.3542 | 1.04E-02 | 4.79E+00 | 3.36E-03 | 3.35E+00 | 1.05E-02 |
| 4.8958 | 4.05E-03 | 3.4271 | 1.06E-02 | 4.90E+00 | 3.89E-03 | 3.43E+00 | 1.07E-02 |
| 5 | 4.59E-03 | 3.5 | 1.08E-02 | 5.00E+00 | 4.45E-03 | 3.50E+00 | 1.08E-02 |

## Sample L-R-3

Table B-19 Surface deflection profiles for sample L-R-3, step 50%YS.

| **Hardened Layer** | | | | **Soft Bulk** | | | |
|---|---|---|---|---|---|---|---|
| Longitudinal | | Transverse | | Longitudinal | | Transverse | |
| Length | Stress | Length | Stress | Length | Stress | Length | Stress |
| 0.00E+00 | 3.01E-03 | 0.00E+00 | 7.17E-03 | 0.00E+00 | 2.91E-03 | 0.00E+00 | 7.20E-03 |
| 1.04E-01 | 2.66E-03 | 7.29E-02 | 7.07E-03 | 1.04E-01 | 2.55E-03 | 7.29E-02 | 7.10E-03 |
| 2.08E-01 | 2.34E-03 | 1.46E-01 | 6.97E-03 | 2.08E-01 | 2.21E-03 | 1.46E-01 | 7.00E-03 |
| 3.13E-01 | 2.05E-03 | 2.19E-01 | 6.89E-03 | 3.13E-01 | 1.91E-03 | 2.19E-01 | 6.92E-03 |
| 4.17E-01 | 1.82E-03 | 2.92E-01 | 6.82E-03 | 4.17E-01 | 1.66E-03 | 2.92E-01 | 6.86E-03 |
| 5.21E-01 | 1.66E-03 | 3.65E-01 | 6.77E-03 | 5.21E-01 | 1.49E-03 | 3.65E-01 | 6.80E-03 |
| 6.25E-01 | 1.58E-03 | 4.38E-01 | 6.72E-03 | 6.25E-01 | 1.43E-03 | 4.38E-01 | 6.76E-03 |
| 7.29E-01 | 1.55E-03 | 5.10E-01 | 6.68E-03 | 7.29E-01 | 1.45E-03 | 5.10E-01 | 6.72E-03 |
| 8.33E-01 | 1.89E-03 | 5.83E-01 | 6.64E-03 | 8.33E-01 | 1.70E-03 | 5.83E-01 | 6.68E-03 |
| 9.38E-01 | 2.23E-03 | 6.56E-01 | 6.62E-03 | 9.38E-01 | 2.06E-03 | 6.56E-01 | 6.66E-03 |
| 1.04E+00 | 2.59E-03 | 7.29E-01 | 6.59E-03 | 1.04E+00 | 2.46E-03 | 7.29E-01 | 6.63E-03 |
| 1.15E+00 | 2.97E-03 | 8.02E-01 | 6.57E-03 | 1.15E+00 | 2.86E-03 | 8.02E-01 | 6.62E-03 |
| 1.25E+00 | 3.36E-03 | 8.75E-01 | 6.56E-03 | 1.25E+00 | 3.28E-03 | 8.75E-01 | 6.60E-03 |
| 1.35E+00 | 3.76E-03 | 9.48E-01 | 6.55E-03 | 1.35E+00 | 3.69E-03 | 9.48E-01 | 6.59E-03 |
| 1.46E+00 | 4.15E-03 | 1.02E+00 | 6.54E-03 | 1.46E+00 | 4.10E-03 | 1.02E+00 | 6.58E-03 |
| 1.56E+00 | 4.53E-03 | 1.09E+00 | 6.53E-03 | 1.56E+00 | 4.49E-03 | 1.09E+00 | 6.57E-03 |
| 1.67E+00 | 4.90E-03 | 1.17E+00 | 6.52E-03 | 1.67E+00 | 4.87E-03 | 1.17E+00 | 6.57E-03 |
| 1.77E+00 | 5.25E-03 | 1.24E+00 | 6.52E-03 | 1.77E+00 | 5.23E-03 | 1.24E+00 | 6.56E-03 |
| 1.88E+00 | 5.56E-03 | 1.31E+00 | 6.51E-03 | 1.88E+00 | 5.56E-03 | 1.31E+00 | 6.56E-03 |

| | | | | | | | |
|---|---|---|---|---|---|---|---|
| 1.98E+00 | 5.85E-03 | 1.39E+00 | 6.51E-03 | 1.98E+00 | 5.85E-03 | 1.39E+00 | 6.56E-03 |
| 2.08E+00 | 6.08E-03 | 1.46E+00 | 6.51E-03 | 2.08E+00 | 6.10E-03 | 1.46E+00 | 6.56E-03 |
| 2.19E+00 | 6.26E-03 | 1.53E+00 | 6.51E-03 | 2.19E+00 | 6.30E-03 | 1.53E+00 | 6.55E-03 |
| 2.29E+00 | 6.40E-03 | 1.60E+00 | 6.51E-03 | 2.29E+00 | 6.44E-03 | 1.60E+00 | 6.55E-03 |
| 2.40E+00 | 6.48E-03 | 1.68E+00 | 6.50E-03 | 2.40E+00 | 6.52E-03 | 1.68E+00 | 6.55E-03 |
| 2.50E+00 | 6.50E-03 | 1.75E+00 | 6.50E-03 | 2.50E+00 | 6.55E-03 | 1.75E+00 | 6.55E-03 |
| 2.60E+00 | 6.48E-03 | 1.82E+00 | 6.50E-03 | 2.60E+00 | 6.53E-03 | 1.82E+00 | 6.55E-03 |
| 2.71E+00 | 6.40E-03 | 1.90E+00 | 6.51E-03 | 2.71E+00 | 6.44E-03 | 1.90E+00 | 6.55E-03 |
| 2.81E+00 | 6.27E-03 | 1.97E+00 | 6.51E-03 | 2.81E+00 | 6.30E-03 | 1.97E+00 | 6.55E-03 |
| 2.92E+00 | 6.08E-03 | 2.04E+00 | 6.51E-03 | 2.92E+00 | 6.11E-03 | 2.04E+00 | 6.56E-03 |
| 3.02E+00 | 5.85E-03 | 2.11E+00 | 6.51E-03 | 3.02E+00 | 5.86E-03 | 2.11E+00 | 6.56E-03 |
| 3.13E+00 | 5.57E-03 | 2.19E+00 | 6.51E-03 | 3.13E+00 | 5.56E-03 | 2.19E+00 | 6.56E-03 |
| 3.23E+00 | 5.25E-03 | 2.26E+00 | 6.52E-03 | 3.23E+00 | 5.24E-03 | 2.26E+00 | 6.56E-03 |
| 3.33E+00 | 4.91E-03 | 2.33E+00 | 6.52E-03 | 3.33E+00 | 4.88E-03 | 2.33E+00 | 6.57E-03 |
| 3.44E+00 | 4.54E-03 | 2.41E+00 | 6.53E-03 | 3.44E+00 | 4.50E-03 | 2.41E+00 | 6.57E-03 |
| 3.54E+00 | 4.16E-03 | 2.48E+00 | 6.54E-03 | 3.54E+00 | 4.11E-03 | 2.48E+00 | 6.58E-03 |
| 3.65E+00 | 3.77E-03 | 2.55E+00 | 6.55E-03 | 3.65E+00 | 3.70E-03 | 2.55E+00 | 6.59E-03 |
| 3.75E+00 | 3.37E-03 | 2.63E+00 | 6.56E-03 | 3.75E+00 | 3.29E-03 | 2.63E+00 | 6.60E-03 |
| 3.85E+00 | 2.98E-03 | 2.70E+00 | 6.57E-03 | 3.85E+00 | 2.87E-03 | 2.70E+00 | 6.62E-03 |
| 3.96E+00 | 2.60E-03 | 2.77E+00 | 6.59E-03 | 3.96E+00 | 2.47E-03 | 2.77E+00 | 6.64E-03 |
| 4.06E+00 | 2.24E-03 | 2.84E+00 | 6.62E-03 | 4.06E+00 | 2.08E-03 | 2.84E+00 | 6.66E-03 |
| 4.1667 | 1.92E-03 | 2.9167 | 6.64E-03 | 4.17E+00 | 1.71E-03 | 2.92E+00 | 6.68E-03 |
| 4.2708 | 1.61E-03 | 2.9896 | 6.68E-03 | 4.27E+00 | 1.47E-03 | 2.99E+00 | 6.72E-03 |
| 4.375 | 1.59E-03 | 3.0625 | 6.72E-03 | 4.38E+00 | 1.45E-03 | 3.06E+00 | 6.76E-03 |
| 4.4792 | 1.67E-03 | 3.1354 | 6.77E-03 | 4.48E+00 | 1.50E-03 | 3.14E+00 | 6.80E-03 |
| 4.5833 | 1.83E-03 | 3.2083 | 6.82E-03 | 4.58E+00 | 1.67E-03 | 3.21E+00 | 6.86E-03 |
| 4.6875 | 2.06E-03 | 3.2813 | 6.89E-03 | 4.69E+00 | 1.91E-03 | 3.28E+00 | 6.93E-03 |
| 4.7917 | 2.34E-03 | 3.3542 | 6.97E-03 | 4.79E+00 | 2.22E-03 | 3.35E+00 | 7.00E-03 |
| 4.8958 | 2.67E-03 | 3.4271 | 7.07E-03 | 4.90E+00 | 2.56E-03 | 3.43E+00 | 7.10E-03 |
| 5 | 3.02E-03 | 3.5 | 7.17E-03 | 5.00E+00 | 2.92E-03 | 3.50E+00 | 7.20E-03 |

Table B-20 Surface deflection profiles for sample L-R-3, step 60%YS.

| **Hardened Layer** | | | | **Soft Bulk** | | | |
|---|---|---|---|---|---|---|---|
| Longitudinal | | Transverse | | Longitudinal | | Transverse | |
| Length | Stress | Length | Stress | Length | Stress | Length | Stress |
| 0.00E+00 | 3.50E-03 | 0.00E+00 | 8.29E-03 | 0.00E+00 | 3.39E-03 | 0.00E+00 | 8.33E-03 |
| 1.04E-01 | 3.09E-03 | 7.29E-02 | 8.17E-03 | 1.04E-01 | 2.96E-03 | 7.29E-02 | 8.20E-03 |
| 2.08E-01 | 2.71E-03 | 1.46E-01 | 8.06E-03 | 2.08E-01 | 2.57E-03 | 1.46E-01 | 8.09E-03 |
| 3.13E-01 | 2.38E-03 | 2.19E-01 | 7.96E-03 | 3.13E-01 | 2.21E-03 | 2.19E-01 | 8.00E-03 |
| 4.17E-01 | 2.10E-03 | 2.92E-01 | 7.88E-03 | 4.17E-01 | 1.92E-03 | 2.92E-01 | 7.92E-03 |
| 5.21E-01 | 1.92E-03 | 3.65E-01 | 7.81E-03 | 5.21E-01 | 1.72E-03 | 3.65E-01 | 7.85E-03 |

| | | | | | | | |
|---|---|---|---|---|---|---|---|
| 6.25E-01 | 1.81E-03 | 4.38E-01 | 7.76E-03 | 6.25E-01 | 1.65E-03 | 4.38E-01 | 7.80E-03 |
| 7.29E-01 | 1.77E-03 | 5.10E-01 | 7.71E-03 | 7.29E-01 | 1.67E-03 | 5.10E-01 | 7.75E-03 |
| 8.33E-01 | 2.16E-03 | 5.83E-01 | 7.67E-03 | 8.33E-01 | 1.94E-03 | 5.83E-01 | 7.72E-03 |
| 9.38E-01 | 2.55E-03 | 6.56E-01 | 7.64E-03 | 9.38E-01 | 2.36E-03 | 6.56E-01 | 7.69E-03 |
| 1.04E+00 | 2.96E-03 | 7.29E-01 | 7.61E-03 | 1.04E+00 | 2.81E-03 | 7.29E-01 | 7.66E-03 |
| 1.15E+00 | 3.40E-03 | 8.02E-01 | 7.59E-03 | 1.15E+00 | 3.28E-03 | 8.02E-01 | 7.64E-03 |
| 1.25E+00 | 3.86E-03 | 8.75E-01 | 7.57E-03 | 1.25E+00 | 3.76E-03 | 8.75E-01 | 7.63E-03 |
| 1.35E+00 | 4.32E-03 | 9.48E-01 | 7.56E-03 | 1.35E+00 | 4.24E-03 | 9.48E-01 | 7.61E-03 |
| 1.46E+00 | 4.77E-03 | 1.02E+00 | 7.55E-03 | 1.46E+00 | 4.71E-03 | 1.02E+00 | 7.60E-03 |
| 1.56E+00 | 5.22E-03 | 1.09E+00 | 7.54E-03 | 1.56E+00 | 5.17E-03 | 1.09E+00 | 7.60E-03 |
| 1.67E+00 | 5.65E-03 | 1.17E+00 | 7.53E-03 | 1.67E+00 | 5.61E-03 | 1.17E+00 | 7.59E-03 |
| 1.77E+00 | 6.05E-03 | 1.24E+00 | 7.53E-03 | 1.77E+00 | 6.03E-03 | 1.24E+00 | 7.59E-03 |
| 1.88E+00 | 6.43E-03 | 1.31E+00 | 7.52E-03 | 1.88E+00 | 6.42E-03 | 1.31E+00 | 7.58E-03 |
| 1.98E+00 | 6.75E-03 | 1.39E+00 | 7.52E-03 | 1.98E+00 | 6.77E-03 | 1.39E+00 | 7.58E-03 |
| 2.08E+00 | 7.02E-03 | 1.46E+00 | 7.52E-03 | 2.08E+00 | 7.05E-03 | 1.46E+00 | 7.58E-03 |
| 2.19E+00 | 7.24E-03 | 1.53E+00 | 7.52E-03 | 2.19E+00 | 7.28E-03 | 1.53E+00 | 7.58E-03 |
| 2.29E+00 | 7.39E-03 | 1.60E+00 | 7.52E-03 | 2.29E+00 | 7.44E-03 | 1.60E+00 | 7.58E-03 |
| 2.40E+00 | 7.48E-03 | 1.68E+00 | 7.52E-03 | 2.40E+00 | 7.54E-03 | 1.68E+00 | 7.58E-03 |
| 2.50E+00 | 7.52E-03 | 1.75E+00 | 7.52E-03 | 2.50E+00 | 7.58E-03 | 1.75E+00 | 7.58E-03 |
| 2.60E+00 | 7.48E-03 | 1.82E+00 | 7.52E-03 | 2.60E+00 | 7.54E-03 | 1.82E+00 | 7.58E-03 |
| 2.71E+00 | 7.39E-03 | 1.90E+00 | 7.52E-03 | 2.71E+00 | 7.44E-03 | 1.90E+00 | 7.58E-03 |
| 2.81E+00 | 7.24E-03 | 1.97E+00 | 7.52E-03 | 2.81E+00 | 7.28E-03 | 1.97E+00 | 7.58E-03 |
| 2.92E+00 | 7.03E-03 | 2.04E+00 | 7.52E-03 | 2.92E+00 | 7.06E-03 | 2.04E+00 | 7.58E-03 |
| 3.02E+00 | 6.76E-03 | 2.11E+00 | 7.52E-03 | 3.02E+00 | 6.77E-03 | 2.11E+00 | 7.58E-03 |
| 3.13E+00 | 6.43E-03 | 2.19E+00 | 7.52E-03 | 3.13E+00 | 6.42E-03 | 2.19E+00 | 7.58E-03 |
| 3.23E+00 | 6.06E-03 | 2.26E+00 | 7.53E-03 | 3.23E+00 | 6.04E-03 | 2.26E+00 | 7.59E-03 |
| 3.33E+00 | 5.65E-03 | 2.33E+00 | 7.53E-03 | 3.33E+00 | 5.62E-03 | 2.33E+00 | 7.59E-03 |
| 3.44E+00 | 5.22E-03 | 2.41E+00 | 7.54E-03 | 3.44E+00 | 5.17E-03 | 2.41E+00 | 7.60E-03 |
| 3.54E+00 | 4.78E-03 | 2.48E+00 | 7.55E-03 | 3.54E+00 | 4.71E-03 | 2.48E+00 | 7.61E-03 |
| 3.65E+00 | 4.32E-03 | 2.55E+00 | 7.56E-03 | 3.65E+00 | 4.24E-03 | 2.55E+00 | 7.62E-03 |
| 3.75E+00 | 3.87E-03 | 2.63E+00 | 7.57E-03 | 3.75E+00 | 3.76E-03 | 2.63E+00 | 7.63E-03 |
| 3.85E+00 | 3.41E-03 | 2.70E+00 | 7.59E-03 | 3.85E+00 | 3.28E-03 | 2.70E+00 | 7.64E-03 |
| 3.96E+00 | 2.97E-03 | 2.77E+00 | 7.61E-03 | 3.96E+00 | 2.82E-03 | 2.77E+00 | 7.66E-03 |
| 4.06E+00 | 2.55E-03 | 2.84E+00 | 7.64E-03 | 4.06E+00 | 2.37E-03 | 2.84E+00 | 7.69E-03 |
| 4.1667 | 2.18E-03 | 2.9167 | 7.67E-03 | 4.17E+00 | 1.95E-03 | 2.92E+00 | 7.72E-03 |
| 4.2708 | 1.85E-03 | 2.9896 | 7.71E-03 | 4.27E+00 | 1.68E-03 | 2.99E+00 | 7.76E-03 |
| 4.375 | 1.82E-03 | 3.0625 | 7.75E-03 | 4.38E+00 | 1.65E-03 | 3.06E+00 | 7.80E-03 |
| 4.4792 | 1.92E-03 | 3.1354 | 7.81E-03 | 4.48E+00 | 1.72E-03 | 3.14E+00 | 7.86E-03 |
| 4.5833 | 2.11E-03 | 3.2083 | 7.88E-03 | 4.58E+00 | 1.92E-03 | 3.21E+00 | 7.92E-03 |
| 4.6875 | 2.38E-03 | 3.2813 | 7.96E-03 | 4.69E+00 | 2.21E-03 | 3.28E+00 | 8.00E-03 |
| 4.7917 | 2.71E-03 | 3.3542 | 8.06E-03 | 4.79E+00 | 2.56E-03 | 3.35E+00 | 8.10E-03 |

| | | | | | | | |
|---|---|---|---|---|---|---|---|
| 4.8958 | 3.09E-03 | 3.4271 | 8.17E-03 | 4.90E+00 | 2.96E-03 | 3.43E+00 | 8.21E-03 |
| 5 | 3.49E-03 | 3.5 | 8.29E-03 | 5.00E+00 | 3.38E-03 | 3.50E+00 | 8.33E-03 |

Table 0-21 Surface deflection profiles for sample L-R-3, step 70%YS.

| **Hardened Layer** | | | | **Soft Bulk** | | | |
|---|---|---|---|---|---|---|---|
| Longitudinal | | Transverse | | Longitudinal | | Transverse | |
| Length | Stress | Length | Stress | Length | Stress | Length | Stress |
| 0.00E+00 | 4.03E-03 | 0.00E+00 | 9.54E-03 | 0.00E+00 | 3.91E-03 | 0.00E+00 | 9.58E-03 |
| 1.04E-01 | 3.56E-03 | 7.29E-02 | 9.40E-03 | 1.04E-01 | 3.42E-03 | 7.29E-02 | 9.43E-03 |
| 2.08E-01 | 3.12E-03 | 1.46E-01 | 9.26E-03 | 2.08E-01 | 2.96E-03 | 1.46E-01 | 9.30E-03 |
| 3.13E-01 | 2.73E-03 | 2.19E-01 | 9.14E-03 | 3.13E-01 | 2.54E-03 | 2.19E-01 | 9.19E-03 |
| 4.17E-01 | 2.41E-03 | 2.92E-01 | 9.05E-03 | 4.17E-01 | 2.20E-03 | 2.92E-01 | 9.09E-03 |
| 5.21E-01 | 2.19E-03 | 3.65E-01 | 8.97E-03 | 5.21E-01 | 1.97E-03 | 3.65E-01 | 9.02E-03 |
| 6.25E-01 | 2.07E-03 | 4.38E-01 | 8.90E-03 | 6.25E-01 | 1.88E-03 | 4.38E-01 | 8.95E-03 |
| 7.29E-01 | 2.01E-03 | 5.10E-01 | 8.85E-03 | 7.29E-01 | 1.90E-03 | 5.10E-01 | 8.90E-03 |
| 8.33E-01 | 2.45E-03 | 5.83E-01 | 8.80E-03 | 8.33E-01 | 2.21E-03 | 5.83E-01 | 8.86E-03 |
| 9.38E-01 | 2.89E-03 | 6.56E-01 | 8.76E-03 | 9.38E-01 | 2.68E-03 | 6.56E-01 | 8.82E-03 |
| 1.04E+00 | 3.37E-03 | 7.29E-01 | 8.73E-03 | 1.04E+00 | 3.19E-03 | 7.29E-01 | 8.79E-03 |
| 1.15E+00 | 3.87E-03 | 8.02E-01 | 8.71E-03 | 1.15E+00 | 3.73E-03 | 8.02E-01 | 8.77E-03 |
| 1.25E+00 | 4.40E-03 | 8.75E-01 | 8.69E-03 | 1.25E+00 | 4.28E-03 | 8.75E-01 | 8.75E-03 |
| 1.35E+00 | 4.93E-03 | 9.48E-01 | 8.67E-03 | 1.35E+00 | 4.83E-03 | 9.48E-01 | 8.74E-03 |
| 1.46E+00 | 5.45E-03 | 1.02E+00 | 8.66E-03 | 1.46E+00 | 5.37E-03 | 1.02E+00 | 8.73E-03 |
| 1.56E+00 | 5.97E-03 | 1.09E+00 | 8.65E-03 | 1.56E+00 | 5.91E-03 | 1.09E+00 | 8.72E-03 |
| 1.67E+00 | 6.47E-03 | 1.17E+00 | 8.65E-03 | 1.67E+00 | 6.42E-03 | 1.17E+00 | 8.71E-03 |
| 1.77E+00 | 6.94E-03 | 1.24E+00 | 8.64E-03 | 1.77E+00 | 6.91E-03 | 1.24E+00 | 8.71E-03 |
| 1.88E+00 | 7.38E-03 | 1.31E+00 | 8.63E-03 | 1.88E+00 | 7.37E-03 | 1.31E+00 | 8.71E-03 |
| 1.98E+00 | 7.75E-03 | 1.39E+00 | 8.63E-03 | 1.98E+00 | 7.77E-03 | 1.39E+00 | 8.70E-03 |
| 2.08E+00 | 8.06E-03 | 1.46E+00 | 8.63E-03 | 2.08E+00 | 8.09E-03 | 1.46E+00 | 8.70E-03 |
| 2.19E+00 | 8.30E-03 | 1.53E+00 | 8.63E-03 | 2.19E+00 | 8.36E-03 | 1.53E+00 | 8.70E-03 |
| 2.29E+00 | 8.48E-03 | 1.60E+00 | 8.63E-03 | 2.29E+00 | 8.55E-03 | 1.60E+00 | 8.70E-03 |
| 2.40E+00 | 8.59E-03 | 1.68E+00 | 8.62E-03 | 2.40E+00 | 8.66E-03 | 1.68E+00 | 8.70E-03 |
| 2.50E+00 | 8.62E-03 | 1.75E+00 | 8.62E-03 | 2.50E+00 | 8.70E-03 | 1.75E+00 | 8.70E-03 |
| 2.60E+00 | 8.59E-03 | 1.82E+00 | 8.62E-03 | 2.60E+00 | 8.66E-03 | 1.82E+00 | 8.70E-03 |
| 2.71E+00 | 8.48E-03 | 1.90E+00 | 8.63E-03 | 2.71E+00 | 8.55E-03 | 1.90E+00 | 8.70E-03 |
| 2.81E+00 | 8.31E-03 | 1.97E+00 | 8.63E-03 | 2.81E+00 | 8.36E-03 | 1.97E+00 | 8.70E-03 |
| 2.92E+00 | 8.06E-03 | 2.04E+00 | 8.63E-03 | 2.92E+00 | 8.10E-03 | 2.04E+00 | 8.70E-03 |
| 3.02E+00 | 7.75E-03 | 2.11E+00 | 8.63E-03 | 3.02E+00 | 7.77E-03 | 2.11E+00 | 8.70E-03 |
| 3.13E+00 | 7.38E-03 | 2.19E+00 | 8.63E-03 | 3.13E+00 | 7.37E-03 | 2.19E+00 | 8.71E-03 |
| 3.23E+00 | 6.94E-03 | 2.26E+00 | 8.64E-03 | 3.23E+00 | 6.92E-03 | 2.26E+00 | 8.71E-03 |
| 3.33E+00 | 6.47E-03 | 2.33E+00 | 8.64E-03 | 3.33E+00 | 6.43E-03 | 2.33E+00 | 8.72E-03 |

| | | | | | | | |
|---|---|---|---|---|---|---|---|
| 3.44E+00 | 5.97E-03 | 2.41E+00 | 8.65E-03 | 3.44E+00 | 5.91E-03 | 2.41E+00 | 8.72E-03 |
| 3.54E+00 | 5.45E-03 | 2.48E+00 | 8.66E-03 | 3.54E+00 | 5.38E-03 | 2.48E+00 | 8.73E-03 |
| 3.65E+00 | 4.93E-03 | 2.55E+00 | 8.67E-03 | 3.65E+00 | 4.83E-03 | 2.55E+00 | 8.74E-03 |
| 3.75E+00 | 4.40E-03 | 2.63E+00 | 8.69E-03 | 3.75E+00 | 4.28E-03 | 2.63E+00 | 8.76E-03 |
| 3.85E+00 | 3.88E-03 | 2.70E+00 | 8.71E-03 | 3.85E+00 | 3.73E-03 | 2.70E+00 | 8.77E-03 |
| 3.96E+00 | 3.37E-03 | 2.77E+00 | 8.73E-03 | 3.96E+00 | 3.19E-03 | 2.77E+00 | 8.80E-03 |
| 4.06E+00 | 2.89E-03 | 2.84E+00 | 8.76E-03 | 4.06E+00 | 2.68E-03 | 2.84E+00 | 8.82E-03 |
| 4.1667 | 2.47E-03 | 2.9167 | 8.80E-03 | 4.17E+00 | 2.21E-03 | 2.92E+00 | 8.86E-03 |
| 4.2708 | 2.10E-03 | 2.9896 | 8.84E-03 | 4.27E+00 | 1.90E-03 | 2.99E+00 | 8.90E-03 |
| 4.375 | 2.07E-03 | 3.0625 | 8.90E-03 | 4.38E+00 | 1.88E-03 | 3.06E+00 | 8.96E-03 |
| 4.4792 | 2.19E-03 | 3.1354 | 8.96E-03 | 4.48E+00 | 1.96E-03 | 3.14E+00 | 9.02E-03 |
| 4.5833 | 2.41E-03 | 3.2083 | 9.04E-03 | 4.58E+00 | 2.19E-03 | 3.21E+00 | 9.10E-03 |
| 4.6875 | 2.72E-03 | 3.2813 | 9.14E-03 | 4.69E+00 | 2.53E-03 | 3.28E+00 | 9.19E-03 |
| 4.7917 | 3.11E-03 | 3.3542 | 9.25E-03 | 4.79E+00 | 2.95E-03 | 3.35E+00 | 9.30E-03 |
| 4.8958 | 3.55E-03 | 3.4271 | 9.39E-03 | 4.90E+00 | 3.41E-03 | 3.43E+00 | 9.44E-03 |
| 5 | 4.02E-03 | 3.5 | 9.53E-03 | 5.00E+00 | 3.89E-03 | 3.50E+00 | 9.58E-03 |

Table 0-22 Surface deflection profiles for sample L-R-3, step 80%YS.

| **Hardened Layer** | | | | **Soft Bulk** | | | |
|---|---|---|---|---|---|---|---|
| Longitudinal | | Transverse | | Longitudinal | | Transverse | |
| Length | Stress | Length | Stress | Length | Stress | Length | Stress |
| 0.00E+00 | 4.58E-03 | 0.00E+00 | 1.08E-02 | 0.00E+00 | 4.44E-03 | 0.00E+00 | 1.08E-02 |
| 1.04E-01 | 4.05E-03 | 7.29E-02 | 1.06E-02 | 1.04E-01 | 3.88E-03 | 7.29E-02 | 1.06E-02 |
| 2.08E-01 | 3.55E-03 | 1.46E-01 | 1.04E-02 | 2.08E-01 | 3.36E-03 | 1.46E-01 | 1.05E-02 |
| 3.13E-01 | 3.10E-03 | 2.19E-01 | 1.03E-02 | 3.13E-01 | 2.89E-03 | 2.19E-01 | 1.04E-02 |
| 4.17E-01 | 2.74E-03 | 2.92E-01 | 1.02E-02 | 4.17E-01 | 2.50E-03 | 2.92E-01 | 1.02E-02 |
| 5.21E-01 | 2.48E-03 | 3.65E-01 | 1.01E-02 | 5.21E-01 | 2.23E-03 | 3.65E-01 | 1.02E-02 |
| 6.25E-01 | 2.34E-03 | 4.38E-01 | 1.00E-02 | 6.25E-01 | 2.12E-03 | 4.38E-01 | 1.01E-02 |
| 7.29E-01 | 2.25E-03 | 5.10E-01 | 9.96E-03 | 7.29E-01 | 2.14E-03 | 5.10E-01 | 1.00E-02 |
| 8.33E-01 | 2.75E-03 | 5.83E-01 | 9.91E-03 | 8.33E-01 | 2.48E-03 | 5.83E-01 | 9.97E-03 |
| 9.38E-01 | 3.24E-03 | 6.56E-01 | 9.87E-03 | 9.38E-01 | 3.00E-03 | 6.56E-01 | 9.93E-03 |
| 1.04E+00 | 3.77E-03 | 7.29E-01 | 9.83E-03 | 1.04E+00 | 3.57E-03 | 7.29E-01 | 9.90E-03 |
| 1.15E+00 | 4.34E-03 | 8.02E-01 | 9.81E-03 | 1.15E+00 | 4.17E-03 | 8.02E-01 | 9.88E-03 |
| 1.25E+00 | 4.93E-03 | 8.75E-01 | 9.79E-03 | 1.25E+00 | 4.79E-03 | 8.75E-01 | 9.86E-03 |
| 1.35E+00 | 5.52E-03 | 9.48E-01 | 9.77E-03 | 1.35E+00 | 5.41E-03 | 9.48E-01 | 9.84E-03 |
| 1.46E+00 | 6.12E-03 | 1.02E+00 | 9.75E-03 | 1.46E+00 | 6.03E-03 | 1.02E+00 | 9.83E-03 |
| 1.56E+00 | 6.70E-03 | 1.09E+00 | 9.74E-03 | 1.56E+00 | 6.63E-03 | 1.09E+00 | 9.82E-03 |
| 1.67E+00 | 7.27E-03 | 1.17E+00 | 9.74E-03 | 1.67E+00 | 7.22E-03 | 1.17E+00 | 9.82E-03 |
| 1.77E+00 | 7.81E-03 | 1.24E+00 | 9.73E-03 | 1.77E+00 | 7.78E-03 | 1.24E+00 | 9.81E-03 |
| 1.88E+00 | 8.30E-03 | 1.31E+00 | 9.72E-03 | 1.88E+00 | 8.30E-03 | 1.31E+00 | 9.81E-03 |

| | | | | | | | |
|---|---|---|---|---|---|---|---|
| 1.98E+00 | 8.72E-03 | 1.39E+00 | 9.72E-03 | 1.98E+00 | 8.74E-03 | 1.39E+00 | 9.80E-03 |
| 2.08E+00 | 9.07E-03 | 1.46E+00 | 9.72E-03 | 2.08E+00 | 9.11E-03 | 1.46E+00 | 9.80E-03 |
| 2.19E+00 | 9.35E-03 | 1.53E+00 | 9.72E-03 | 2.19E+00 | 9.41E-03 | 1.53E+00 | 9.80E-03 |
| 2.29E+00 | 9.55E-03 | 1.60E+00 | 9.71E-03 | 2.29E+00 | 9.63E-03 | 1.60E+00 | 9.80E-03 |
| 2.40E+00 | 9.67E-03 | 1.68E+00 | 9.71E-03 | 2.40E+00 | 9.76E-03 | 1.68E+00 | 9.80E-03 |
| 2.50E+00 | 9.71E-03 | 1.75E+00 | 9.71E-03 | 2.50E+00 | 9.80E-03 | 1.75E+00 | 9.80E-03 |
| 2.60E+00 | 9.67E-03 | 1.82E+00 | 9.71E-03 | 2.60E+00 | 9.76E-03 | 1.82E+00 | 9.80E-03 |
| 2.71E+00 | 9.55E-03 | 1.90E+00 | 9.71E-03 | 2.71E+00 | 9.63E-03 | 1.90E+00 | 9.80E-03 |
| 2.81E+00 | 9.35E-03 | 1.97E+00 | 9.71E-03 | 2.81E+00 | 9.41E-03 | 1.97E+00 | 9.80E-03 |
| 2.92E+00 | 9.07E-03 | 2.04E+00 | 9.72E-03 | 2.92E+00 | 9.11E-03 | 2.04E+00 | 9.80E-03 |
| 3.02E+00 | 8.72E-03 | 2.11E+00 | 9.72E-03 | 3.02E+00 | 8.74E-03 | 2.11E+00 | 9.81E-03 |
| 3.13E+00 | 8.30E-03 | 2.19E+00 | 9.72E-03 | 3.13E+00 | 8.30E-03 | 2.19E+00 | 9.81E-03 |
| 3.23E+00 | 7.81E-03 | 2.26E+00 | 9.73E-03 | 3.23E+00 | 7.78E-03 | 2.26E+00 | 9.81E-03 |
| 3.33E+00 | 7.27E-03 | 2.33E+00 | 9.73E-03 | 3.33E+00 | 7.22E-03 | 2.33E+00 | 9.82E-03 |
| 3.44E+00 | 6.70E-03 | 2.41E+00 | 9.74E-03 | 3.44E+00 | 6.63E-03 | 2.41E+00 | 9.83E-03 |
| 3.54E+00 | 6.12E-03 | 2.48E+00 | 9.75E-03 | 3.54E+00 | 6.03E-03 | 2.48E+00 | 9.83E-03 |
| 3.65E+00 | 5.52E-03 | 2.55E+00 | 9.76E-03 | 3.65E+00 | 5.41E-03 | 2.55E+00 | 9.85E-03 |
| 3.75E+00 | 4.92E-03 | 2.63E+00 | 9.78E-03 | 3.75E+00 | 4.79E-03 | 2.63E+00 | 9.86E-03 |
| 3.85E+00 | 4.33E-03 | 2.70E+00 | 9.80E-03 | 3.85E+00 | 4.17E-03 | 2.70E+00 | 9.88E-03 |
| 3.96E+00 | 3.76E-03 | 2.77E+00 | 9.83E-03 | 3.96E+00 | 3.57E-03 | 2.77E+00 | 9.91E-03 |
| 4.06E+00 | 3.23E-03 | 2.84E+00 | 9.86E-03 | 4.06E+00 | 2.99E-03 | 2.84E+00 | 9.94E-03 |
| 4.1667 | 2.75E-03 | 2.9167 | 9.90E-03 | 4.17E+00 | 2.47E-03 | 2.92E+00 | 9.98E-03 |
| 4.2708 | 2.37E-03 | 2.9896 | 9.95E-03 | 4.27E+00 | 2.13E-03 | 2.99E+00 | 1.00E-02 |
| 4.375 | 2.32E-03 | 3.0625 | 1.00E-02 | 4.38E+00 | 2.10E-03 | 3.06E+00 | 1.01E-02 |
| 4.4792 | 2.46E-03 | 3.1354 | 1.01E-02 | 4.48E+00 | 2.20E-03 | 3.14E+00 | 1.02E-02 |
| 4.5833 | 2.71E-03 | 3.2083 | 1.02E-02 | 4.58E+00 | 2.47E-03 | 3.21E+00 | 1.03E-02 |
| 4.6875 | 3.08E-03 | 3.2813 | 1.03E-02 | 4.69E+00 | 2.86E-03 | 3.28E+00 | 1.04E-02 |
| 4.7917 | 3.52E-03 | 3.3542 | 1.04E-02 | 4.79E+00 | 3.34E-03 | 3.35E+00 | 1.05E-02 |
| 4.8958 | 4.02E-03 | 3.4271 | 1.06E-02 | 4.90E+00 | 3.86E-03 | 3.43E+00 | 1.06E-02 |
| 5 | 4.56E-03 | 3.5 | 1.08E-02 | 5.00E+00 | 4.42E-03 | 3.50E+00 | 1.08E-02 |

## Sample L-R-6

Table B-23 Surface deflection profiles for sample L-R-6, step 60%YS.

| **Hardened Layer** | | | | **Soft Bulk** | | | |
|---|---|---|---|---|---|---|---|
| Longitudinal | | Transverse | | Longitudinal | | Transverse | |
| Length | Stress | Length | Stress | Length | Stress | Length | Stress |
| 0.00E+00 | 3.60E-03 | 0.00E+00 | 8.45E-03 | 0.00E+00 | 3.48E-03 | 0.00E+00 | 8.48E-03 |
| 1.04E-01 | 3.18E-03 | 7.29E-02 | 8.32E-03 | 1.04E-01 | 3.05E-03 | 7.29E-02 | 8.36E-03 |
| 2.08E-01 | 2.79E-03 | 1.46E-01 | 8.21E-03 | 2.08E-01 | 2.64E-03 | 1.46E-01 | 8.25E-03 |
| 3.13E-01 | 2.44E-03 | 2.19E-01 | 8.11E-03 | 3.13E-01 | 2.27E-03 | 2.19E-01 | 8.15E-03 |

| | | | | | | | |
|---|---|---|---|---|---|---|---|
| 4.17E-01 | 2.15E-03 | 2.92E-01 | 8.03E-03 | 4.17E-01 | 1.96E-03 | 2.92E-01 | 8.07E-03 |
| 5.21E-01 | 1.95E-03 | 3.65E-01 | 7.96E-03 | 5.21E-01 | 1.75E-03 | 3.65E-01 | 8.00E-03 |
| 6.25E-01 | 1.84E-03 | 4.38E-01 | 7.90E-03 | 6.25E-01 | 1.67E-03 | 4.38E-01 | 7.95E-03 |
| 7.29E-01 | 1.79E-03 | 5.10E-01 | 7.86E-03 | 7.29E-01 | 1.69E-03 | 5.10E-01 | 7.90E-03 |
| 8.33E-01 | 2.18E-03 | 5.83E-01 | 7.82E-03 | 8.33E-01 | 1.96E-03 | 5.83E-01 | 7.87E-03 |
| 9.38E-01 | 2.57E-03 | 6.56E-01 | 7.79E-03 | 9.38E-01 | 2.38E-03 | 6.56E-01 | 7.84E-03 |
| 1.04E+00 | 3.00E-03 | 7.29E-01 | 7.76E-03 | 1.04E+00 | 2.84E-03 | 7.29E-01 | 7.81E-03 |
| 1.15E+00 | 3.45E-03 | 8.02E-01 | 7.74E-03 | 1.15E+00 | 3.32E-03 | 8.02E-01 | 7.79E-03 |
| 1.25E+00 | 3.92E-03 | 8.75E-01 | 7.72E-03 | 1.25E+00 | 3.81E-03 | 8.75E-01 | 7.78E-03 |
| 1.35E+00 | 4.39E-03 | 9.48E-01 | 7.71E-03 | 1.35E+00 | 4.30E-03 | 9.48E-01 | 7.77E-03 |
| 1.46E+00 | 4.85E-03 | 1.02E+00 | 7.70E-03 | 1.46E+00 | 4.79E-03 | 1.02E+00 | 7.76E-03 |
| 1.56E+00 | 5.31E-03 | 1.09E+00 | 7.69E-03 | 1.56E+00 | 5.26E-03 | 1.09E+00 | 7.75E-03 |
| 1.67E+00 | 5.75E-03 | 1.17E+00 | 7.68E-03 | 1.67E+00 | 5.71E-03 | 1.17E+00 | 7.74E-03 |
| 1.77E+00 | 6.17E-03 | 1.24E+00 | 7.68E-03 | 1.77E+00 | 6.15E-03 | 1.24E+00 | 7.74E-03 |
| 1.88E+00 | 6.55E-03 | 1.31E+00 | 7.68E-03 | 1.88E+00 | 6.54E-03 | 1.31E+00 | 7.74E-03 |
| 1.98E+00 | 6.89E-03 | 1.39E+00 | 7.67E-03 | 1.98E+00 | 6.90E-03 | 1.39E+00 | 7.73E-03 |
| 2.08E+00 | 7.16E-03 | 1.46E+00 | 7.67E-03 | 2.08E+00 | 7.19E-03 | 1.46E+00 | 7.73E-03 |
| 2.19E+00 | 7.38E-03 | 1.53E+00 | 7.67E-03 | 2.19E+00 | 7.42E-03 | 1.53E+00 | 7.73E-03 |
| 2.29E+00 | 7.54E-03 | 1.60E+00 | 7.67E-03 | 2.29E+00 | 7.59E-03 | 1.60E+00 | 7.73E-03 |
| 2.40E+00 | 7.63E-03 | 1.68E+00 | 7.67E-03 | 2.40E+00 | 7.69E-03 | 1.68E+00 | 7.73E-03 |
| 2.50E+00 | 7.67E-03 | 1.75E+00 | 7.67E-03 | 2.50E+00 | 7.73E-03 | 1.75E+00 | 7.73E-03 |
| 2.60E+00 | 7.63E-03 | 1.82E+00 | 7.67E-03 | 2.60E+00 | 7.69E-03 | 1.82E+00 | 7.73E-03 |
| 2.71E+00 | 7.54E-03 | 1.90E+00 | 7.67E-03 | 2.71E+00 | 7.59E-03 | 1.90E+00 | 7.73E-03 |
| 2.81E+00 | 7.38E-03 | 1.97E+00 | 7.67E-03 | 2.81E+00 | 7.43E-03 | 1.97E+00 | 7.73E-03 |
| 2.92E+00 | 7.17E-03 | 2.04E+00 | 7.67E-03 | 2.92E+00 | 7.19E-03 | 2.04E+00 | 7.73E-03 |
| 3.02E+00 | 6.89E-03 | 2.11E+00 | 7.67E-03 | 3.02E+00 | 6.90E-03 | 2.11E+00 | 7.73E-03 |
| 3.13E+00 | 6.56E-03 | 2.19E+00 | 7.67E-03 | 3.13E+00 | 6.55E-03 | 2.19E+00 | 7.73E-03 |
| 3.23E+00 | 6.17E-03 | 2.26E+00 | 7.68E-03 | 3.23E+00 | 6.15E-03 | 2.26E+00 | 7.74E-03 |
| 3.33E+00 | 5.76E-03 | 2.33E+00 | 7.68E-03 | 3.33E+00 | 5.72E-03 | 2.33E+00 | 7.74E-03 |
| 3.44E+00 | 5.32E-03 | 2.41E+00 | 7.69E-03 | 3.44E+00 | 5.27E-03 | 2.41E+00 | 7.75E-03 |
| 3.54E+00 | 4.86E-03 | 2.48E+00 | 7.70E-03 | 3.54E+00 | 4.80E-03 | 2.48E+00 | 7.76E-03 |
| 3.65E+00 | 4.40E-03 | 2.55E+00 | 7.71E-03 | 3.65E+00 | 4.31E-03 | 2.55E+00 | 7.77E-03 |
| 3.75E+00 | 3.93E-03 | 2.63E+00 | 7.72E-03 | 3.75E+00 | 3.82E-03 | 2.63E+00 | 7.78E-03 |
| 3.85E+00 | 3.46E-03 | 2.70E+00 | 7.74E-03 | 3.85E+00 | 3.33E-03 | 2.70E+00 | 7.79E-03 |
| 3.96E+00 | 3.01E-03 | 2.77E+00 | 7.76E-03 | 3.96E+00 | 2.86E-03 | 2.77E+00 | 7.81E-03 |
| 4.06E+00 | 2.59E-03 | 2.84E+00 | 7.79E-03 | 4.06E+00 | 2.40E-03 | 2.84E+00 | 7.84E-03 |
| 4.1667 | 2.21E-03 | 2.9167 | 7.82E-03 | 4.17E+00 | 1.98E-03 | 2.92E+00 | 7.87E-03 |
| 4.2708 | 1.88E-03 | 2.9896 | 7.86E-03 | 4.27E+00 | 1.71E-03 | 2.99E+00 | 7.90E-03 |
| 4.375 | 1.85E-03 | 3.0625 | 7.90E-03 | 4.38E+00 | 1.68E-03 | 3.06E+00 | 7.95E-03 |
| 4.4792 | 1.96E-03 | 3.1354 | 7.96E-03 | 4.48E+00 | 1.76E-03 | 3.14E+00 | 8.00E-03 |
| 4.5833 | 2.16E-03 | 3.2083 | 8.03E-03 | 4.58E+00 | 1.97E-03 | 3.21E+00 | 8.07E-03 |

| | | | | | | | |
|---|---|---|---|---|---|---|---|
| 4.6875 | 2.44E-03 | 3.2813 | 8.11E-03 | 4.69E+00 | 2.27E-03 | 3.28E+00 | 8.15E-03 |
| 4.7917 | 2.79E-03 | 3.3542 | 8.21E-03 | 4.79E+00 | 2.64E-03 | 3.35E+00 | 8.24E-03 |
| 4.8958 | 3.18E-03 | 3.4271 | 8.32E-03 | 4.90E+00 | 3.05E-03 | 3.43E+00 | 8.36E-03 |
| 5 | 3.59E-03 | 3.5 | 8.45E-03 | 5.00E+00 | 3.48E-03 | 3.50E+00 | 8.48E-03 |

Table B-24 Surface deflection profiles for sample L-R-6, step 70%YS.

| **Hardened Layer** | | | | **Soft Bulk** | | | |
|---|---|---|---|---|---|---|---|
| Longitudinal | | Transverse | | Longitudinal | | Transverse | |
| Length | Stress | Length | Stress | Length | Stress | Length | Stress |
| 0.00E+00 | 4.10E-03 | 0.00E+00 | 9.60E-03 | 0.00E+00 | 3.97E-03 | 0.00E+00 | 9.64E-03 |
| 1.04E-01 | 3.61E-03 | 7.29E-02 | 9.46E-03 | 1.04E-01 | 3.47E-03 | 7.29E-02 | 9.50E-03 |
| 2.08E-01 | 3.17E-03 | 1.46E-01 | 9.32E-03 | 2.08E-01 | 3.00E-03 | 1.46E-01 | 9.36E-03 |
| 3.13E-01 | 2.77E-03 | 2.19E-01 | 9.21E-03 | 3.13E-01 | 2.57E-03 | 2.19E-01 | 9.25E-03 |
| 4.17E-01 | 2.44E-03 | 2.92E-01 | 9.11E-03 | 4.17E-01 | 2.22E-03 | 2.92E-01 | 9.16E-03 |
| 5.21E-01 | 2.20E-03 | 3.65E-01 | 9.03E-03 | 5.21E-01 | 1.98E-03 | 3.65E-01 | 9.08E-03 |
| 6.25E-01 | 2.08E-03 | 4.38E-01 | 8.96E-03 | 6.25E-01 | 1.88E-03 | 4.38E-01 | 9.02E-03 |
| 7.29E-01 | 2.00E-03 | 5.10E-01 | 8.91E-03 | 7.29E-01 | 1.89E-03 | 5.10E-01 | 8.97E-03 |
| 8.33E-01 | 2.45E-03 | 5.83E-01 | 8.86E-03 | 8.33E-01 | 2.20E-03 | 5.83E-01 | 8.92E-03 |
| 9.38E-01 | 2.89E-03 | 6.56E-01 | 8.83E-03 | 9.38E-01 | 2.67E-03 | 6.56E-01 | 8.89E-03 |
| 1.04E+00 | 3.37E-03 | 7.29E-01 | 8.80E-03 | 1.04E+00 | 3.19E-03 | 7.29E-01 | 8.86E-03 |
| 1.15E+00 | 3.88E-03 | 8.02E-01 | 8.78E-03 | 1.15E+00 | 3.73E-03 | 8.02E-01 | 8.84E-03 |
| 1.25E+00 | 4.41E-03 | 8.75E-01 | 8.76E-03 | 1.25E+00 | 4.29E-03 | 8.75E-01 | 8.82E-03 |
| 1.35E+00 | 4.95E-03 | 9.48E-01 | 8.74E-03 | 1.35E+00 | 4.85E-03 | 9.48E-01 | 8.81E-03 |
| 1.46E+00 | 5.48E-03 | 1.02E+00 | 8.73E-03 | 1.46E+00 | 5.40E-03 | 1.02E+00 | 8.80E-03 |
| 1.56E+00 | 6.00E-03 | 1.09E+00 | 8.72E-03 | 1.56E+00 | 5.94E-03 | 1.09E+00 | 8.79E-03 |
| 1.67E+00 | 6.51E-03 | 1.17E+00 | 8.71E-03 | 1.67E+00 | 6.46E-03 | 1.17E+00 | 8.78E-03 |
| 1.77E+00 | 6.99E-03 | 1.24E+00 | 8.71E-03 | 1.77E+00 | 6.96E-03 | 1.24E+00 | 8.78E-03 |
| 1.88E+00 | 7.43E-03 | 1.31E+00 | 8.70E-03 | 1.88E+00 | 7.42E-03 | 1.31E+00 | 8.78E-03 |
| 1.98E+00 | 7.80E-03 | 1.39E+00 | 8.70E-03 | 1.98E+00 | 7.82E-03 | 1.39E+00 | 8.77E-03 |
| 2.08E+00 | 8.12E-03 | 1.46E+00 | 8.70E-03 | 2.08E+00 | 8.15E-03 | 1.46E+00 | 8.77E-03 |
| 2.19E+00 | 8.37E-03 | 1.53E+00 | 8.70E-03 | 2.19E+00 | 8.42E-03 | 1.53E+00 | 8.77E-03 |
| 2.29E+00 | 8.55E-03 | 1.60E+00 | 8.69E-03 | 2.29E+00 | 8.61E-03 | 1.60E+00 | 8.77E-03 |
| 2.40E+00 | 8.66E-03 | 1.68E+00 | 8.69E-03 | 2.40E+00 | 8.73E-03 | 1.68E+00 | 8.77E-03 |
| 2.50E+00 | 8.69E-03 | 1.75E+00 | 8.69E-03 | 2.50E+00 | 8.77E-03 | 1.75E+00 | 8.77E-03 |
| 2.60E+00 | 8.66E-03 | 1.82E+00 | 8.69E-03 | 2.60E+00 | 8.73E-03 | 1.82E+00 | 8.77E-03 |
| 2.71E+00 | 8.55E-03 | 1.90E+00 | 8.69E-03 | 2.71E+00 | 8.61E-03 | 1.90E+00 | 8.77E-03 |
| 2.81E+00 | 8.37E-03 | 1.97E+00 | 8.70E-03 | 2.81E+00 | 8.42E-03 | 1.97E+00 | 8.77E-03 |
| 2.92E+00 | 8.12E-03 | 2.04E+00 | 8.70E-03 | 2.92E+00 | 8.16E-03 | 2.04E+00 | 8.77E-03 |
| 3.02E+00 | 7.81E-03 | 2.11E+00 | 8.70E-03 | 3.02E+00 | 7.83E-03 | 2.11E+00 | 8.77E-03 |
| 3.13E+00 | 7.43E-03 | 2.19E+00 | 8.70E-03 | 3.13E+00 | 7.42E-03 | 2.19E+00 | 8.77E-03 |
| 3.23E+00 | 6.99E-03 | 2.26E+00 | 8.71E-03 | 3.23E+00 | 6.96E-03 | 2.26E+00 | 8.78E-03 |

| | | | | | | | |
|---|---|---|---|---|---|---|---|
| 3.33E+00 | 6.51E-03 | 2.33E+00 | 8.71E-03 | 3.33E+00 | 6.47E-03 | 2.33E+00 | 8.78E-03 |
| 3.44E+00 | 6.01E-03 | 2.41E+00 | 8.72E-03 | 3.44E+00 | 5.95E-03 | 2.41E+00 | 8.79E-03 |
| 3.54E+00 | 5.49E-03 | 2.48E+00 | 8.73E-03 | 3.54E+00 | 5.41E-03 | 2.48E+00 | 8.80E-03 |
| 3.65E+00 | 4.96E-03 | 2.55E+00 | 8.74E-03 | 3.65E+00 | 4.86E-03 | 2.55E+00 | 8.81E-03 |
| 3.75E+00 | 4.42E-03 | 2.63E+00 | 8.76E-03 | 3.75E+00 | 4.30E-03 | 2.63E+00 | 8.82E-03 |
| 3.85E+00 | 3.89E-03 | 2.70E+00 | 8.77E-03 | 3.85E+00 | 3.75E-03 | 2.70E+00 | 8.84E-03 |
| 3.96E+00 | 3.38E-03 | 2.77E+00 | 8.80E-03 | 3.96E+00 | 3.20E-03 | 2.77E+00 | 8.86E-03 |
| 4.06E+00 | 2.90E-03 | 2.84E+00 | 8.83E-03 | 4.06E+00 | 2.68E-03 | 2.84E+00 | 8.89E-03 |
| 4.1667 | 2.47E-03 | 2.9167 | 8.86E-03 | 4.17E+00 | 2.21E-03 | 2.92E+00 | 8.92E-03 |
| 4.2708 | 2.11E-03 | 2.9896 | 8.91E-03 | 4.27E+00 | 1.91E-03 | 2.99E+00 | 8.96E-03 |
| 4.375 | 2.09E-03 | 3.0625 | 8.96E-03 | 4.38E+00 | 1.89E-03 | 3.06E+00 | 9.02E-03 |
| 4.4792 | 2.21E-03 | 3.1354 | 9.03E-03 | 4.48E+00 | 1.98E-03 | 3.14E+00 | 9.08E-03 |
| 4.5833 | 2.44E-03 | 3.2083 | 9.11E-03 | 4.58E+00 | 2.22E-03 | 3.21E+00 | 9.16E-03 |
| 4.6875 | 2.76E-03 | 3.2813 | 9.20E-03 | 4.69E+00 | 2.57E-03 | 3.28E+00 | 9.25E-03 |
| 4.7917 | 3.16E-03 | 3.3542 | 9.32E-03 | 4.79E+00 | 2.99E-03 | 3.35E+00 | 9.36E-03 |
| 4.8958 | 3.61E-03 | 3.4271 | 9.45E-03 | 4.90E+00 | 3.46E-03 | 3.43E+00 | 9.49E-03 |
| 5 | 4.09E-03 | 3.5 | 9.60E-03 | 5.00E+00 | 3.96E-03 | 3.50E+00 | 9.64E-03 |

## B.2 B.2 Surface tensile stresses profiles

### Sample N3

Table B-25 Surface tensile stress profiles for sample N3, step 39%YS

| **Hardened Layer** | | | | **Soft Bulk** | | | |
|---|---|---|---|---|---|---|---|
| Longitudinal | | Transverse | | Longitudinal | | Transverse | |
| Length | Stress | Length | Stress | Length | Stress | Length | Stress |
| 0.00E+00 | 1.65E+00 | 0.00E+00 | 3.07E+02 | 0.00E+00 | 1.01E+00 | 0.00E+00 | 2.00E+02 |
| 1.04E-01 | 1.85E+00 | 7.29E-02 | 3.15E+02 | 1.04E-01 | 2.21E+00 | 7.29E-02 | 2.00E+02 |
| 2.08E-01 | 4.76E+00 | 1.46E-01 | 3.17E+02 | 2.08E-01 | 4.96E+00 | 1.46E-01 | 2.00E+02 |
| 3.13E-01 | 1.08E+01 | 2.19E-01 | 3.16E+02 | 3.13E-01 | 9.07E+00 | 2.19E-01 | 2.00E+02 |
| 4.17E-01 | 2.10E+01 | 2.92E-01 | 3.14E+02 | 4.17E-01 | 1.48E+01 | 2.92E-01 | 2.00E+02 |
| 5.21E-01 | 4.22E+01 | 3.65E-01 | 3.12E+02 | 5.21E-01 | 2.12E+01 | 3.65E-01 | 2.00E+02 |
| 6.25E-01 | 1.59E+02 | 4.38E-01 | 3.09E+02 | 6.25E-01 | 3.83E+01 | 4.38E-01 | 2.00E+02 |
| 7.29E-01 | 2.17E+02 | 5.10E-01 | 3.07E+02 | 7.29E-01 | 1.67E+02 | 5.10E-01 | 2.00E+02 |
| 8.33E-01 | 7.05E+01 | 5.83E-01 | 3.05E+02 | 8.33E-01 | 1.13E+02 | 5.83E-01 | 2.00E+02 |
| 9.38E-01 | 1.12E+01 | 6.56E-01 | 3.04E+02 | 9.38E-01 | 3.68E+01 | 6.56E-01 | 2.00E+02 |
| 1.04E+00 | 1.53E+01 | 7.29E-01 | 3.03E+02 | 1.04E+00 | 2.07E+01 | 7.29E-01 | 2.00E+02 |
| 1.15E+00 | 3.57E+01 | 8.02E-01 | 3.02E+02 | 1.15E+00 | 3.26E+01 | 8.02E-01 | 2.00E+02 |
| 1.25E+00 | 5.55E+01 | 8.75E-01 | 3.02E+02 | 1.25E+00 | 4.98E+01 | 8.75E-01 | 2.00E+02 |
| 1.35E+00 | 7.58E+01 | 9.48E-01 | 3.02E+02 | 1.35E+00 | 6.80E+01 | 9.48E-01 | 2.00E+02 |

| | | | | | | | |
|---|---|---|---|---|---|---|---|
| 1.46E+00 | 9.70E+01 | 1.02E+00 | 3.02E+02 | 1.46E+00 | 8.70E+01 | 1.02E+00 | 2.00E+02 |
| 1.56E+00 | 1.19E+02 | 1.09E+00 | 3.02E+02 | 1.56E+00 | 1.07E+02 | 1.09E+00 | 2.00E+02 |
| 1.67E+00 | 1.43E+02 | 1.17E+00 | 3.02E+02 | 1.67E+00 | 1.28E+02 | 1.17E+00 | 2.00E+02 |
| 1.77E+00 | 1.67E+02 | 1.24E+00 | 3.02E+02 | 1.77E+00 | 1.49E+02 | 1.24E+00 | 2.00E+02 |
| 1.88E+00 | 1.91E+02 | 1.31E+00 | 3.03E+02 | 1.88E+00 | 1.70E+02 | 1.31E+00 | 2.00E+02 |
| 1.98E+00 | 2.16E+02 | 1.39E+00 | 3.03E+02 | 1.98E+00 | 1.88E+02 | 1.39E+00 | 2.00E+02 |
| 2.08E+00 | 2.43E+02 | 1.46E+00 | 3.03E+02 | 2.08E+00 | 1.93E+02 | 1.46E+00 | 2.00E+02 |
| 2.19E+00 | 2.69E+02 | 1.53E+00 | 3.03E+02 | 2.19E+00 | 1.97E+02 | 1.53E+00 | 2.00E+02 |
| 2.29E+00 | 2.87E+02 | 1.60E+00 | 3.03E+02 | 2.29E+00 | 1.99E+02 | 1.60E+00 | 2.00E+02 |
| 2.40E+00 | 2.99E+02 | 1.68E+00 | 3.03E+02 | 2.40E+00 | 2.00E+02 | 1.68E+00 | 2.00E+02 |
| 2.50E+00 | 3.03E+02 | 1.75E+00 | 3.03E+02 | 2.50E+00 | 2.00E+02 | 1.75E+00 | 2.00E+02 |
| 2.60E+00 | 2.99E+02 | 1.82E+00 | 3.03E+02 | 2.60E+00 | 2.00E+02 | 1.82E+00 | 2.00E+02 |
| 2.71E+00 | 2.87E+02 | 1.90E+00 | 3.03E+02 | 2.71E+00 | 1.99E+02 | 1.90E+00 | 2.00E+02 |
| 2.81E+00 | 2.69E+02 | 1.97E+00 | 3.03E+02 | 2.81E+00 | 1.97E+02 | 1.97E+00 | 2.00E+02 |
| 2.92E+00 | 2.43E+02 | 2.04E+00 | 3.03E+02 | 2.92E+00 | 1.93E+02 | 2.04E+00 | 2.00E+02 |
| 3.02E+00 | 2.16E+02 | 2.11E+00 | 3.03E+02 | 3.02E+00 | 1.88E+02 | 2.11E+00 | 2.00E+02 |
| 3.13E+00 | 1.91E+02 | 2.19E+00 | 3.03E+02 | 3.13E+00 | 1.70E+02 | 2.19E+00 | 2.00E+02 |
| 3.23E+00 | 1.67E+02 | 2.26E+00 | 3.02E+02 | 3.23E+00 | 1.49E+02 | 2.26E+00 | 2.00E+02 |
| 3.33E+00 | 1.43E+02 | 2.33E+00 | 3.02E+02 | 3.33E+00 | 1.28E+02 | 2.33E+00 | 2.00E+02 |
| 3.44E+00 | 1.19E+02 | 2.41E+00 | 3.02E+02 | 3.44E+00 | 1.07E+02 | 2.41E+00 | 2.00E+02 |
| 3.54E+00 | 9.69E+01 | 2.48E+00 | 3.02E+02 | 3.54E+00 | 8.70E+01 | 2.48E+00 | 2.00E+02 |
| 3.65E+00 | 7.57E+01 | 2.55E+00 | 3.02E+02 | 3.65E+00 | 6.79E+01 | 2.55E+00 | 2.00E+02 |
| 3.75E+00 | 5.54E+01 | 2.63E+00 | 3.02E+02 | 3.75E+00 | 4.97E+01 | 2.63E+00 | 2.00E+02 |
| 3.85E+00 | 3.55E+01 | 2.70E+00 | 3.02E+02 | 3.85E+00 | 3.25E+01 | 2.70E+00 | 2.00E+02 |
| 3.96E+00 | 1.48E+01 | 2.77E+00 | 3.03E+02 | 3.96E+00 | 2.08E+01 | 2.77E+00 | 2.00E+02 |
| 4.06E+00 | 1.16E+01 | 2.84E+00 | 3.04E+02 | 4.06E+00 | 3.63E+01 | 2.84E+00 | 2.00E+02 |
| 4.1667 | 6.47E+01 | 2.9167 | 3.05E+02 | 4.17E+00 | 1.07E+02 | 2.92E+00 | 2.00E+02 |
| 4.2708 | 2.80E+02 | 2.9896 | 3.07E+02 | 4.27E+00 | 1.64E+02 | 2.99E+00 | 2.00E+02 |
| 4.375 | 1.79E+02 | 3.0625 | 3.09E+02 | 4.38E+00 | 3.73E+01 | 3.06E+00 | 2.00E+02 |
| 4.4792 | 3.91E+01 | 3.1354 | 3.12E+02 | 4.48E+00 | 2.10E+01 | 3.14E+00 | 2.00E+02 |
| 4.5833 | 2.05E+01 | 3.2083 | 3.14E+02 | 4.58E+00 | 1.49E+01 | 3.21E+00 | 2.00E+02 |
| 4.6875 | 1.08E+01 | 3.2813 | 3.16E+02 | 4.69E+00 | 9.22E+00 | 3.28E+00 | 2.00E+02 |
| 4.7917 | 4.98E+00 | 3.3542 | 3.17E+02 | 4.79E+00 | 5.12E+00 | 3.35E+00 | 2.00E+02 |
| 4.8958 | 2.24E+00 | 3.4271 | 3.15E+02 | 4.90E+00 | 2.44E+00 | 3.43E+00 | 2.00E+02 |
| 5 | 2.06E+00 | 3.5 | 3.07E+02 | 5.00E+00 | 1.38E+00 | 3.50E+00 | 2.00E+02 |

Table B-26 Surface tensile stress profiles for sample N3, step 47%YS.

| **Hardened Layer** | | **Soft Bulk** | |
|---|---|---|---|
| Longitudinal | Transverse | Longitudinal | Transverse |

| Length | Stress | Length | Stress | Length | Stress | Length | Stress |
|---|---|---|---|---|---|---|---|
| 0.00E+00 | 2.16E+00 | 0.00E+00 | 3.65E+02 | 0.00E+00 | 1.41E+00 | 0.00E+00 | 2.04E+02 |
| 1.04E-01 | 2.36E+00 | 7.29E-02 | 3.77E+02 | 1.04E-01 | 2.61E+00 | 7.29E-02 | 2.04E+02 |
| 2.08E-01 | 5.42E+00 | 1.46E-01 | 3.81E+02 | 2.08E-01 | 5.59E+00 | 1.46E-01 | 2.05E+02 |
| 3.13E-01 | 1.20E+01 | 2.19E-01 | 3.81E+02 | 3.13E-01 | 1.01E+01 | 2.19E-01 | 2.05E+02 |
| 4.17E-01 | 2.35E+01 | 2.92E-01 | 3.78E+02 | 4.17E-01 | 1.66E+01 | 2.92E-01 | 2.05E+02 |
| 5.21E-01 | 4.74E+01 | 3.65E-01 | 3.75E+02 | 5.21E-01 | 2.42E+01 | 3.65E-01 | 2.05E+02 |
| 6.25E-01 | 1.72E+02 | 4.38E-01 | 3.71E+02 | 6.25E-01 | 3.89E+01 | 4.38E-01 | 2.05E+02 |
| 7.29E-01 | 3.86E+02 | 5.10E-01 | 3.69E+02 | 7.29E-01 | 1.75E+02 | 5.10E-01 | 2.05E+02 |
| 8.33E-01 | 8.56E+01 | 5.83E-01 | 3.66E+02 | 8.33E-01 | 1.34E+02 | 5.83E-01 | 2.05E+02 |
| 9.38E-01 | 1.83E+01 | 6.56E-01 | 3.65E+02 | 9.38E-01 | 4.50E+01 | 6.56E-01 | 2.05E+02 |
| 1.04E+00 | 1.33E+01 | 7.29E-01 | 3.63E+02 | 1.04E+00 | 2.29E+01 | 7.29E-01 | 2.05E+02 |
| 1.15E+00 | 3.66E+01 | 8.02E-01 | 3.63E+02 | 1.15E+00 | 3.39E+01 | 8.02E-01 | 2.05E+02 |
| 1.25E+00 | 5.88E+01 | 8.75E-01 | 3.62E+02 | 1.25E+00 | 5.28E+01 | 8.75E-01 | 2.05E+02 |
| 1.35E+00 | 8.13E+01 | 9.48E-01 | 3.62E+02 | 1.35E+00 | 7.30E+01 | 9.48E-01 | 2.05E+02 |
| 1.46E+00 | 1.05E+02 | 1.02E+00 | 3.62E+02 | 1.46E+00 | 9.42E+01 | 1.02E+00 | 2.05E+02 |
| 1.56E+00 | 1.30E+02 | 1.09E+00 | 3.62E+02 | 1.56E+00 | 1.16E+02 | 1.09E+00 | 2.05E+02 |
| 1.67E+00 | 1.56E+02 | 1.17E+00 | 3.63E+02 | 1.67E+00 | 1.40E+02 | 1.17E+00 | 2.05E+02 |
| 1.77E+00 | 1.83E+02 | 1.24E+00 | 3.63E+02 | 1.77E+00 | 1.63E+02 | 1.24E+00 | 2.05E+02 |
| 1.88E+00 | 2.12E+02 | 1.31E+00 | 3.63E+02 | 1.88E+00 | 1.85E+02 | 1.31E+00 | 2.05E+02 |
| 1.98E+00 | 2.49E+02 | 1.39E+00 | 3.64E+02 | 1.98E+00 | 1.93E+02 | 1.39E+00 | 2.05E+02 |
| 2.08E+00 | 2.88E+02 | 1.46E+00 | 3.64E+02 | 2.08E+00 | 1.98E+02 | 1.46E+00 | 2.05E+02 |
| 2.19E+00 | 3.21E+02 | 1.53E+00 | 3.64E+02 | 2.19E+00 | 2.01E+02 | 1.53E+00 | 2.05E+02 |
| 2.29E+00 | 3.45E+02 | 1.60E+00 | 3.64E+02 | 2.29E+00 | 2.04E+02 | 1.60E+00 | 2.05E+02 |
| 2.40E+00 | 3.60E+02 | 1.68E+00 | 3.64E+02 | 2.40E+00 | 2.05E+02 | 1.68E+00 | 2.05E+02 |
| 2.50E+00 | 3.65E+02 | 1.75E+00 | 3.65E+02 | 2.50E+00 | 2.05E+02 | 1.75E+00 | 2.05E+02 |
| 2.60E+00 | 3.60E+02 | 1.82E+00 | 3.64E+02 | 2.60E+00 | 2.05E+02 | 1.82E+00 | 2.05E+02 |
| 2.71E+00 | 3.45E+02 | 1.90E+00 | 3.64E+02 | 2.71E+00 | 2.04E+02 | 1.90E+00 | 2.05E+02 |
| 2.81E+00 | 3.21E+02 | 1.97E+00 | 3.64E+02 | 2.81E+00 | 2.01E+02 | 1.97E+00 | 2.05E+02 |
| 2.92E+00 | 2.88E+02 | 2.04E+00 | 3.64E+02 | 2.92E+00 | 1.98E+02 | 2.04E+00 | 2.05E+02 |
| 3.02E+00 | 2.49E+02 | 2.11E+00 | 3.64E+02 | 3.02E+00 | 1.93E+02 | 2.11E+00 | 2.05E+02 |
| 3.13E+00 | 2.12E+02 | 2.19E+00 | 3.63E+02 | 3.13E+00 | 1.85E+02 | 2.19E+00 | 2.05E+02 |
| 3.23E+00 | 1.83E+02 | 2.26E+00 | 3.63E+02 | 3.23E+00 | 1.63E+02 | 2.26E+00 | 2.05E+02 |
| 3.33E+00 | 1.56E+02 | 2.33E+00 | 3.62E+02 | 3.33E+00 | 1.39E+02 | 2.33E+00 | 2.05E+02 |
| 3.44E+00 | 1.30E+02 | 2.41E+00 | 3.62E+02 | 3.44E+00 | 1.16E+02 | 2.41E+00 | 2.05E+02 |
| 3.54E+00 | 1.05E+02 | 2.48E+00 | 3.62E+02 | 3.54E+00 | 9.41E+01 | 2.48E+00 | 2.05E+02 |
| 3.65E+00 | 8.12E+01 | 2.55E+00 | 3.62E+02 | 3.65E+00 | 7.29E+01 | 2.55E+00 | 2.05E+02 |
| 3.75E+00 | 5.85E+01 | 2.63E+00 | 3.62E+02 | 3.75E+00 | 5.27E+01 | 2.63E+00 | 2.05E+02 |
| 3.85E+00 | 3.62E+01 | 2.70E+00 | 3.63E+02 | 3.85E+00 | 3.38E+01 | 2.70E+00 | 2.05E+02 |
| 3.96E+00 | 1.29E+01 | 2.77E+00 | 3.63E+02 | 3.96E+00 | 2.31E+01 | 2.77E+00 | 2.05E+02 |

| | | | | | | | |
|---|---|---|---|---|---|---|---|
| 4.06E+00 | 1.83E+01 | 2.84E+00 | 3.65E+02 | 4.06E+00 | 4.41E+01 | 2.84E+00 | 2.05E+02 |
| 4.1667 | 7.74E+01 | 2.9167 | 3.66E+02 | 4.17E+00 | 1.26E+02 | 2.92E+00 | 2.05E+02 |
| 4.2708 | 2.92E+02 | 2.9896 | 3.69E+02 | 4.27E+00 | 1.73E+02 | 2.99E+00 | 2.05E+02 |
| 4.375 | 1.89E+02 | 3.0625 | 3.71E+02 | 4.38E+00 | 3.86E+01 | 3.06E+00 | 2.05E+02 |
| 4.4792 | 4.37E+01 | 3.1354 | 3.75E+02 | 4.48E+00 | 2.40E+01 | 3.14E+00 | 2.05E+02 |
| 4.5833 | 2.29E+01 | 3.2083 | 3.78E+02 | 4.58E+00 | 1.68E+01 | 3.21E+00 | 2.05E+02 |
| 4.6875 | 1.21E+01 | 3.2813 | 3.80E+02 | 4.69E+00 | 1.03E+01 | 3.28E+00 | 2.05E+02 |
| 4.7917 | 5.67E+00 | 3.3542 | 3.81E+02 | 4.79E+00 | 5.78E+00 | 3.35E+00 | 2.05E+02 |
| 4.8958 | 2.80E+00 | 3.4271 | 3.77E+02 | 4.90E+00 | 2.89E+00 | 3.43E+00 | 2.04E+02 |
| 5 | 2.61E+00 | 3.5 | 3.65E+02 | 5.00E+00 | 1.81E+00 | 3.50E+00 | 2.04E+02 |

Table B-27 Surface tensile stress profiles for sample N3, step 51%YS.

| **Hardened Layer** | | | | **Soft Bulk** | | | |
|---|---|---|---|---|---|---|---|
| Longitudinal | | Transverse | | Longitudinal | | Transverse | |
| Length | Stress | Length | Stress | Length | Stress | Length | Stress |
| 0.00E+00 | 2.81E+00 | 0.00E+00 | 4.22E+02 | 0.00E+00 | 1.93E+00 | 0.00E+00 | 2.08E+02 |
| 1.04E-01 | 2.99E+00 | 7.29E-02 | 4.38E+02 | 1.04E-01 | 3.09E+00 | 7.29E-02 | 2.08E+02 |
| 2.08E-01 | 6.09E+00 | 1.46E-01 | 4.44E+02 | 2.08E-01 | 6.19E+00 | 1.46E-01 | 2.09E+02 |
| 3.13E-01 | 1.31E+01 | 2.19E-01 | 4.43E+02 | 3.13E-01 | 1.11E+01 | 2.19E-01 | 2.09E+02 |
| 4.17E-01 | 2.56E+01 | 2.92E-01 | 4.40E+02 | 4.17E-01 | 1.83E+01 | 2.92E-01 | 2.09E+02 |
| 5.21E-01 | 5.20E+01 | 3.65E-01 | 4.37E+02 | 5.21E-01 | 2.70E+01 | 3.65E-01 | 2.09E+02 |
| 6.25E-01 | 1.81E+02 | 4.38E-01 | 4.33E+02 | 6.25E-01 | 3.87E+01 | 4.38E-01 | 2.09E+02 |
| 7.29E-01 | 4.19E+02 | 5.10E-01 | 4.29E+02 | 7.29E-01 | 1.82E+02 | 5.10E-01 | 2.09E+02 |
| 8.33E-01 | 9.53E+01 | 5.83E-01 | 4.27E+02 | 8.33E-01 | 1.51E+02 | 5.83E-01 | 2.09E+02 |
| 9.38E-01 | 2.67E+01 | 6.56E-01 | 4.25E+02 | 9.38E-01 | 5.32E+01 | 6.56E-01 | 2.09E+02 |
| 1.04E+00 | 1.08E+01 | 7.29E-01 | 4.23E+02 | 1.04E+00 | 2.53E+01 | 7.29E-01 | 2.09E+02 |
| 1.15E+00 | 3.65E+01 | 8.02E-01 | 4.22E+02 | 1.15E+00 | 3.47E+01 | 8.02E-01 | 2.09E+02 |
| 1.25E+00 | 6.08E+01 | 8.75E-01 | 4.22E+02 | 1.25E+00 | 5.48E+01 | 8.75E-01 | 2.09E+02 |
| 1.35E+00 | 8.53E+01 | 9.48E-01 | 4.22E+02 | 1.35E+00 | 7.67E+01 | 9.48E-01 | 2.09E+02 |
| 1.46E+00 | 1.11E+02 | 1.02E+00 | 4.22E+02 | 1.46E+00 | 9.97E+01 | 1.02E+00 | 2.09E+02 |
| 1.56E+00 | 1.38E+02 | 1.09E+00 | 4.22E+02 | 1.56E+00 | 1.24E+02 | 1.09E+00 | 2.09E+02 |
| 1.67E+00 | 1.67E+02 | 1.17E+00 | 4.22E+02 | 1.67E+00 | 1.49E+02 | 1.17E+00 | 2.09E+02 |
| 1.77E+00 | 1.97E+02 | 1.24E+00 | 4.23E+02 | 1.77E+00 | 1.75E+02 | 1.24E+00 | 2.09E+02 |
| 1.88E+00 | 2.36E+02 | 1.31E+00 | 4.23E+02 | 1.88E+00 | 1.91E+02 | 1.31E+00 | 2.09E+02 |
| 1.98E+00 | 2.86E+02 | 1.39E+00 | 4.24E+02 | 1.98E+00 | 1.98E+02 | 1.39E+00 | 2.09E+02 |
| 2.08E+00 | 3.33E+02 | 1.46E+00 | 4.24E+02 | 2.08E+00 | 2.02E+02 | 1.46E+00 | 2.09E+02 |
| 2.19E+00 | 3.72E+02 | 1.53E+00 | 4.25E+02 | 2.19E+00 | 2.06E+02 | 1.53E+00 | 2.09E+02 |
| 2.29E+00 | 4.01E+02 | 1.60E+00 | 4.25E+02 | 2.29E+00 | 2.08E+02 | 1.60E+00 | 2.09E+02 |
| 2.40E+00 | 4.19E+02 | 1.68E+00 | 4.25E+02 | 2.40E+00 | 2.09E+02 | 1.68E+00 | 2.09E+02 |

| | | | | | | | |
|---|---|---|---|---|---|---|---|
| 2.50E+00 | 4.25E+02 | 1.75E+00 | 4.25E+02 | 2.50E+00 | 2.09E+02 | 1.75E+00 | 2.09E+02 |
| 2.60E+00 | 4.19E+02 | 1.82E+00 | 4.25E+02 | 2.60E+00 | 2.09E+02 | 1.82E+00 | 2.09E+02 |
| 2.71E+00 | 4.01E+02 | 1.90E+00 | 4.25E+02 | 2.71E+00 | 2.08E+02 | 1.90E+00 | 2.09E+02 |
| 2.81E+00 | 3.72E+02 | 1.97E+00 | 4.25E+02 | 2.81E+00 | 2.06E+02 | 1.97E+00 | 2.09E+02 |
| 2.92E+00 | 3.33E+02 | 2.04E+00 | 4.24E+02 | 2.92E+00 | 2.02E+02 | 2.04E+00 | 2.09E+02 |
| 3.02E+00 | 2.86E+02 | 2.11E+00 | 4.24E+02 | 3.02E+00 | 1.98E+02 | 2.11E+00 | 2.09E+02 |
| 3.13E+00 | 2.35E+02 | 2.19E+00 | 4.23E+02 | 3.13E+00 | 1.91E+02 | 2.19E+00 | 2.09E+02 |
| 3.23E+00 | 1.97E+02 | 2.26E+00 | 4.23E+02 | 3.23E+00 | 1.75E+02 | 2.26E+00 | 2.09E+02 |
| 3.33E+00 | 1.67E+02 | 2.33E+00 | 4.22E+02 | 3.33E+00 | 1.49E+02 | 2.33E+00 | 2.09E+02 |
| 3.44E+00 | 1.38E+02 | 2.41E+00 | 4.22E+02 | 3.44E+00 | 1.24E+02 | 2.41E+00 | 2.09E+02 |
| 3.54E+00 | 1.11E+02 | 2.48E+00 | 4.22E+02 | 3.54E+00 | 9.95E+01 | 2.48E+00 | 2.09E+02 |
| 3.65E+00 | 8.51E+01 | 2.55E+00 | 4.22E+02 | 3.65E+00 | 7.65E+01 | 2.55E+00 | 2.09E+02 |
| 3.75E+00 | 6.05E+01 | 2.63E+00 | 4.22E+02 | 3.75E+00 | 5.46E+01 | 2.63E+00 | 2.09E+02 |
| 3.85E+00 | 3.61E+01 | 2.70E+00 | 4.22E+02 | 3.85E+00 | 3.46E+01 | 2.70E+00 | 2.09E+02 |
| 3.96E+00 | 1.03E+01 | 2.77E+00 | 4.23E+02 | 3.96E+00 | 2.55E+01 | 2.77E+00 | 2.09E+02 |
| 4.06E+00 | 2.63E+01 | 2.84E+00 | 4.25E+02 | 4.06E+00 | 5.21E+01 | 2.84E+00 | 2.09E+02 |
| 4.1667 | 8.57E+01 | 2.9167 | 4.27E+02 | 4.17E+00 | 1.43E+02 | 2.92E+00 | 2.09E+02 |
| 4.2708 | 3.18E+02 | 2.9896 | 4.29E+02 | 4.27E+00 | 1.79E+02 | 2.99E+00 | 2.09E+02 |
| 4.375 | 1.95E+02 | 3.0625 | 4.33E+02 | 4.38E+00 | 3.90E+01 | 3.06E+00 | 2.09E+02 |
| 4.4792 | 4.78E+01 | 3.1354 | 4.37E+02 | 4.48E+00 | 2.67E+01 | 3.14E+00 | 2.09E+02 |
| 4.5833 | 2.49E+01 | 3.2083 | 4.40E+02 | 4.58E+00 | 1.84E+01 | 3.21E+00 | 2.09E+02 |
| 4.6875 | 1.32E+01 | 3.2813 | 4.43E+02 | 4.69E+00 | 1.13E+01 | 3.28E+00 | 2.09E+02 |
| 4.7917 | 6.39E+00 | 3.3542 | 4.44E+02 | 4.79E+00 | 6.43E+00 | 3.35E+00 | 2.09E+02 |
| 4.8958 | 3.46E+00 | 3.4271 | 4.38E+02 | 4.90E+00 | 3.42E+00 | 3.43E+00 | 2.08E+02 |
| 5 | 3.29E+00 | 3.5 | 4.22E+02 | 5.00E+00 | 2.37E+00 | 3.50E+00 | 2.08E+02 |

Table 0-28 Surface tensile stress profiles for sample N3, step 62%YS.

| **Hardened Layer** | | | | **Soft Bulk** | | | |
|---|---|---|---|---|---|---|---|
| Longitudinal | | Transverse | | Longitudinal | | Transverse | |
| Length | Stress | Length | Stress | Length | Stress | Length | Stress |
| 0.00E+00 | 3.48E+00 | 0.00E+00 | 4.75E+02 | 0.00E+00 | 2.50E+00 | 0.00E+00 | 2.10E+02 |
| 1.04E-01 | 3.64E+00 | 7.29E-02 | 4.95E+02 | 1.04E-01 | 3.59E+00 | 7.29E-02 | 2.10E+02 |
| 2.08E-01 | 6.73E+00 | 1.46E-01 | 5.02E+02 | 2.08E-01 | 6.77E+00 | 1.46E-01 | 2.11E+02 |
| 3.13E-01 | 1.41E+01 | 2.19E-01 | 5.02E+02 | 3.13E-01 | 1.20E+01 | 2.19E-01 | 2.11E+02 |
| 4.17E-01 | 2.74E+01 | 2.92E-01 | 4.99E+02 | 4.17E-01 | 1.98E+01 | 2.92E-01 | 2.11E+02 |
| 5.21E-01 | 5.60E+01 | 3.65E-01 | 4.94E+02 | 5.21E-01 | 2.97E+01 | 3.65E-01 | 2.11E+02 |
| 6.25E-01 | 1.90E+02 | 4.38E-01 | 4.90E+02 | 6.25E-01 | 3.90E+01 | 4.38E-01 | 2.11E+02 |
| 7.29E-01 | 3.99E+02 | 5.10E-01 | 4.86E+02 | 7.29E-01 | 1.87E+02 | 5.10E-01 | 2.11E+02 |
| 8.33E-01 | 1.03E+02 | 5.83E-01 | 4.83E+02 | 8.33E-01 | 1.61E+02 | 5.83E-01 | 2.11E+02 |

| | | | | | | | |
|---|---|---|---|---|---|---|---|
| 9.38E-01 | 3.59E+01 | 6.56E-01 | 4.80E+02 | 9.38E-01 | 6.11E+01 | 6.56E-01 | 2.11E+02 |
| 1.04E+00 | 7.77E+00 | 7.29E-01 | 4.78E+02 | 1.04E+00 | 2.78E+01 | 7.29E-01 | 2.11E+02 |
| 1.15E+00 | 3.54E+01 | 8.02E-01 | 4.77E+02 | 1.15E+00 | 3.47E+01 | 8.02E-01 | 2.11E+02 |
| 1.25E+00 | 6.14E+01 | 8.75E-01 | 4.77E+02 | 1.25E+00 | 5.56E+01 | 8.75E-01 | 2.11E+02 |
| 1.35E+00 | 8.76E+01 | 9.48E-01 | 4.77E+02 | 1.35E+00 | 7.88E+01 | 9.48E-01 | 2.11E+02 |
| 1.46E+00 | 1.15E+02 | 1.02E+00 | 4.77E+02 | 1.46E+00 | 1.03E+02 | 1.02E+00 | 2.11E+02 |
| 1.56E+00 | 1.44E+02 | 1.09E+00 | 4.77E+02 | 1.56E+00 | 1.29E+02 | 1.09E+00 | 2.11E+02 |
| 1.67E+00 | 1.75E+02 | 1.17E+00 | 4.78E+02 | 1.67E+00 | 1.56E+02 | 1.17E+00 | 2.11E+02 |
| 1.77E+00 | 2.09E+02 | 1.24E+00 | 4.78E+02 | 1.77E+00 | 1.82E+02 | 1.24E+00 | 2.11E+02 |
| 1.88E+00 | 2.61E+02 | 1.31E+00 | 4.79E+02 | 1.88E+00 | 1.94E+02 | 1.31E+00 | 2.11E+02 |
| 1.98E+00 | 3.20E+02 | 1.39E+00 | 4.79E+02 | 1.98E+00 | 2.01E+02 | 1.39E+00 | 2.11E+02 |
| 2.08E+00 | 3.74E+02 | 1.46E+00 | 4.80E+02 | 2.08E+00 | 2.06E+02 | 1.46E+00 | 2.11E+02 |
| 2.19E+00 | 4.19E+02 | 1.53E+00 | 4.80E+02 | 2.19E+00 | 2.09E+02 | 1.53E+00 | 2.11E+02 |
| 2.29E+00 | 4.53E+02 | 1.60E+00 | 4.80E+02 | 2.29E+00 | 2.10E+02 | 1.60E+00 | 2.11E+02 |
| 2.40E+00 | 4.74E+02 | 1.68E+00 | 4.81E+02 | 2.40E+00 | 2.11E+02 | 1.68E+00 | 2.11E+02 |
| 2.50E+00 | 4.81E+02 | 1.75E+00 | 4.81E+02 | 2.50E+00 | 2.11E+02 | 1.75E+00 | 2.11E+02 |
| 2.60E+00 | 4.74E+02 | 1.82E+00 | 4.81E+02 | 2.60E+00 | 2.11E+02 | 1.82E+00 | 2.11E+02 |
| 2.71E+00 | 4.53E+02 | 1.90E+00 | 4.80E+02 | 2.71E+00 | 2.10E+02 | 1.90E+00 | 2.11E+02 |
| 2.81E+00 | 4.19E+02 | 1.97E+00 | 4.80E+02 | 2.81E+00 | 2.09E+02 | 1.97E+00 | 2.11E+02 |
| 2.92E+00 | 3.74E+02 | 2.04E+00 | 4.80E+02 | 2.92E+00 | 2.06E+02 | 2.04E+00 | 2.11E+02 |
| 3.02E+00 | 3.20E+02 | 2.11E+00 | 4.79E+02 | 3.02E+00 | 2.01E+02 | 2.11E+00 | 2.11E+02 |
| 3.13E+00 | 2.61E+02 | 2.19E+00 | 4.79E+02 | 3.13E+00 | 1.94E+02 | 2.19E+00 | 2.11E+02 |
| 3.23E+00 | 2.09E+02 | 2.26E+00 | 4.78E+02 | 3.23E+00 | 1.82E+02 | 2.26E+00 | 2.11E+02 |
| 3.33E+00 | 1.74E+02 | 2.33E+00 | 4.78E+02 | 3.33E+00 | 1.56E+02 | 2.33E+00 | 2.11E+02 |
| 3.44E+00 | 1.44E+02 | 2.41E+00 | 4.77E+02 | 3.44E+00 | 1.29E+02 | 2.41E+00 | 2.11E+02 |
| 3.54E+00 | 1.15E+02 | 2.48E+00 | 4.77E+02 | 3.54E+00 | 1.03E+02 | 2.48E+00 | 2.11E+02 |
| 3.65E+00 | 8.73E+01 | 2.55E+00 | 4.77E+02 | 3.65E+00 | 7.85E+01 | 2.55E+00 | 2.11E+02 |
| 3.75E+00 | 6.10E+01 | 2.63E+00 | 4.77E+02 | 3.75E+00 | 5.54E+01 | 2.63E+00 | 2.11E+02 |
| 3.85E+00 | 3.49E+01 | 2.70E+00 | 4.77E+02 | 3.85E+00 | 3.46E+01 | 2.70E+00 | 2.11E+02 |
| 3.96E+00 | 7.49E+00 | 2.77E+00 | 4.78E+02 | 3.96E+00 | 2.82E+01 | 2.77E+00 | 2.11E+02 |
| 4.06E+00 | 3.49E+01 | 2.84E+00 | 4.80E+02 | 4.06E+00 | 5.99E+01 | 2.84E+00 | 2.11E+02 |
| 4.1667 | 9.08E+01 | 2.9167 | 4.82E+02 | 4.17E+00 | 1.56E+02 | 2.92E+00 | 2.11E+02 |
| 4.2708 | 3.37E+02 | 2.9896 | 4.86E+02 | 4.27E+00 | 1.84E+02 | 2.99E+00 | 2.11E+02 |
| 4.375 | 2.00E+02 | 3.0625 | 4.90E+02 | 4.38E+00 | 3.98E+01 | 3.06E+00 | 2.11E+02 |
| 4.4792 | 5.13E+01 | 3.1354 | 4.94E+02 | 4.48E+00 | 2.93E+01 | 3.14E+00 | 2.11E+02 |
| 4.5833 | 2.67E+01 | 3.2083 | 4.98E+02 | 4.58E+00 | 1.99E+01 | 3.21E+00 | 2.11E+02 |
| 4.6875 | 1.42E+01 | 3.2813 | 5.02E+02 | 4.69E+00 | 1.22E+01 | 3.28E+00 | 2.11E+02 |
| 4.7917 | 7.08E+00 | 3.3542 | 5.02E+02 | 4.79E+00 | 7.04E+00 | 3.35E+00 | 2.11E+02 |
| 4.8958 | 4.15E+00 | 3.4271 | 4.94E+02 | 4.90E+00 | 3.97E+00 | 3.43E+00 | 2.10E+02 |
| 5 | 4.02E+00 | 3.5 | 4.75E+02 | 5.00E+00 | 2.98E+00 | 3.50E+00 | 2.10E+02 |

Table B-29 Surface tensile stress profiles for sample N3, step 70%YS.

| **Hardened Layer** | | | | **Soft Bulk** | | | |
|---|---|---|---|---|---|---|---|
| Longitudinal | | Transverse | | Longitudinal | | Transverse | |
| Length | Stress | Length | Stress | Length | Stress | Length | Stress |
| 0.00E+00 | 4.47E+00 | 0.00E+00 | 5.39E+02 | 0.00E+00 | 3.38E+00 | 0.00E+00 | 2.12E+02 |
| 1.04E-01 | 4.53E+00 | 7.29E-02 | 5.62E+02 | 1.04E-01 | 4.33E+00 | 7.29E-02 | 2.12E+02 |
| 2.08E-01 | 7.56E+00 | 1.46E-01 | 5.71E+02 | 2.08E-01 | 7.52E+00 | 1.46E-01 | 2.12E+02 |
| 3.13E-01 | 1.53E+01 | 2.19E-01 | 5.72E+02 | 3.13E-01 | 1.31E+01 | 2.19E-01 | 2.12E+02 |
| 4.17E-01 | 2.96E+01 | 2.92E-01 | 5.68E+02 | 4.17E-01 | 2.16E+01 | 2.92E-01 | 2.13E+02 |
| 5.21E-01 | 6.06E+01 | 3.65E-01 | 5.63E+02 | 5.21E-01 | 3.31E+01 | 3.65E-01 | 2.13E+02 |
| 6.25E-01 | 2.02E+02 | 4.38E-01 | 5.58E+02 | 6.25E-01 | 4.02E+01 | 4.38E-01 | 2.13E+02 |
| 7.29E-01 | 4.30E+02 | 5.10E-01 | 5.54E+02 | 7.29E-01 | 1.92E+02 | 5.10E-01 | 2.13E+02 |
| 8.33E-01 | 1.09E+02 | 5.83E-01 | 5.50E+02 | 8.33E-01 | 1.73E+02 | 5.83E-01 | 2.13E+02 |
| 9.38E-01 | 4.80E+01 | 6.56E-01 | 5.47E+02 | 9.38E-01 | 7.07E+01 | 6.56E-01 | 2.13E+02 |
| 1.04E+00 | 5.11E+00 | 7.29E-01 | 5.45E+02 | 1.04E+00 | 3.13E+01 | 7.29E-01 | 2.13E+02 |
| 1.15E+00 | 3.34E+01 | 8.02E-01 | 5.44E+02 | 1.15E+00 | 3.45E+01 | 8.02E-01 | 2.13E+02 |
| 1.25E+00 | 6.14E+01 | 8.75E-01 | 5.43E+02 | 1.25E+00 | 5.59E+01 | 8.75E-01 | 2.13E+02 |
| 1.35E+00 | 8.92E+01 | 9.48E-01 | 5.43E+02 | 1.35E+00 | 8.04E+01 | 9.48E-01 | 2.13E+02 |
| 1.46E+00 | 1.18E+02 | 1.02E+00 | 5.43E+02 | 1.46E+00 | 1.06E+02 | 1.02E+00 | 2.13E+02 |
| 1.56E+00 | 1.49E+02 | 1.09E+00 | 5.43E+02 | 1.56E+00 | 1.34E+02 | 1.09E+00 | 2.13E+02 |
| 1.67E+00 | 1.83E+02 | 1.17E+00 | 5.44E+02 | 1.67E+00 | 1.63E+02 | 1.17E+00 | 2.13E+02 |
| 1.77E+00 | 2.26E+02 | 1.24E+00 | 5.44E+02 | 1.77E+00 | 1.89E+02 | 1.24E+00 | 2.13E+02 |
| 1.88E+00 | 2.93E+02 | 1.31E+00 | 5.45E+02 | 1.88E+00 | 1.97E+02 | 1.31E+00 | 2.13E+02 |
| 1.98E+00 | 3.60E+02 | 1.39E+00 | 5.46E+02 | 1.98E+00 | 2.04E+02 | 1.39E+00 | 2.13E+02 |
| 2.08E+00 | 4.22E+02 | 1.46E+00 | 5.46E+02 | 2.08E+00 | 2.09E+02 | 1.46E+00 | 2.13E+02 |
| 2.19E+00 | 4.75E+02 | 1.53E+00 | 5.47E+02 | 2.19E+00 | 2.11E+02 | 1.53E+00 | 2.13E+02 |
| 2.29E+00 | 5.15E+02 | 1.60E+00 | 5.47E+02 | 2.29E+00 | 2.12E+02 | 1.60E+00 | 2.13E+02 |
| 2.40E+00 | 5.39E+02 | 1.68E+00 | 5.47E+02 | 2.40E+00 | 2.13E+02 | 1.68E+00 | 2.13E+02 |
| 2.50E+00 | 5.47E+02 | 1.75E+00 | 5.47E+02 | 2.50E+00 | 2.13E+02 | 1.75E+00 | 2.13E+02 |
| 2.60E+00 | 5.39E+02 | 1.82E+00 | 5.47E+02 | 2.60E+00 | 2.13E+02 | 1.82E+00 | 2.13E+02 |
| 2.71E+00 | 5.15E+02 | 1.90E+00 | 5.47E+02 | 2.71E+00 | 2.12E+02 | 1.90E+00 | 2.13E+02 |
| 2.81E+00 | 4.75E+02 | 1.97E+00 | 5.47E+02 | 2.81E+00 | 2.11E+02 | 1.97E+00 | 2.13E+02 |
| 2.92E+00 | 4.22E+02 | 2.04E+00 | 5.46E+02 | 2.92E+00 | 2.09E+02 | 2.04E+00 | 2.13E+02 |
| 3.02E+00 | 3.60E+02 | 2.11E+00 | 5.46E+02 | 3.02E+00 | 2.04E+02 | 2.11E+00 | 2.13E+02 |
| 3.13E+00 | 2.93E+02 | 2.19E+00 | 5.45E+02 | 3.13E+00 | 1.97E+02 | 2.19E+00 | 2.13E+02 |
| 3.23E+00 | 2.26E+02 | 2.26E+00 | 5.44E+02 | 3.23E+00 | 1.89E+02 | 2.26E+00 | 2.13E+02 |
| 3.33E+00 | 1.82E+02 | 2.33E+00 | 5.44E+02 | 3.33E+00 | 1.63E+02 | 2.33E+00 | 2.13E+02 |
| 3.44E+00 | 1.49E+02 | 2.41E+00 | 5.43E+02 | 3.44E+00 | 1.34E+02 | 2.41E+00 | 2.13E+02 |

| | | | | | | | |
|---|---|---|---|---|---|---|---|
| 3.54E+00 | 1.18E+02 | 2.48E+00 | 5.43E+02 | 3.54E+00 | 1.06E+02 | 2.48E+00 | 2.13E+02 |
| 3.65E+00 | 8.89E+01 | 2.55E+00 | 5.43E+02 | 3.65E+00 | 8.01E+01 | 2.55E+00 | 2.13E+02 |
| 3.75E+00 | 6.09E+01 | 2.63E+00 | 5.43E+02 | 3.75E+00 | 5.56E+01 | 2.63E+00 | 2.13E+02 |
| 3.85E+00 | 3.28E+01 | 2.70E+00 | 5.44E+02 | 3.85E+00 | 3.43E+01 | 2.70E+00 | 2.13E+02 |
| 3.96E+00 | 5.63E+00 | 2.77E+00 | 5.45E+02 | 3.96E+00 | 3.18E+01 | 2.77E+00 | 2.13E+02 |
| 4.06E+00 | 4.64E+01 | 2.84E+00 | 5.47E+02 | 4.06E+00 | 6.93E+01 | 2.84E+00 | 2.13E+02 |
| 4.1667 | 9.33E+01 | 2.9167 | 5.50E+02 | 4.17E+00 | 1.68E+02 | 2.92E+00 | 2.13E+02 |
| 4.2708 | 3.59E+02 | 2.9896 | 5.54E+02 | 4.27E+00 | 1.89E+02 | 2.99E+00 | 2.13E+02 |
| 4.375 | 2.07E+02 | 3.0625 | 5.58E+02 | 4.38E+00 | 4.17E+01 | 3.06E+00 | 2.13E+02 |
| 4.4792 | 5.56E+01 | 3.1354 | 5.63E+02 | 4.48E+00 | 3.26E+01 | 3.14E+00 | 2.13E+02 |
| 4.5833 | 2.88E+01 | 3.2083 | 5.68E+02 | 4.58E+00 | 2.17E+01 | 3.21E+00 | 2.12E+02 |
| 4.6875 | 1.54E+01 | 3.2813 | 5.72E+02 | 4.69E+00 | 1.33E+01 | 3.28E+00 | 2.12E+02 |
| 4.7917 | 7.97E+00 | 3.3542 | 5.71E+02 | 4.79E+00 | 7.84E+00 | 3.35E+00 | 2.12E+02 |
| 4.8958 | 5.10E+00 | 3.4271 | 5.62E+02 | 4.90E+00 | 4.76E+00 | 3.43E+00 | 2.12E+02 |
| 5 | 5.05E+00 | 3.5 | 5.39E+02 | 5.00E+00 | 3.90E+00 | 3.50E+00 | 2.12E+02 |

## Sample N7

Table B-30 Surface tensile stress and strain profiles for sample N7, step 44%YS.

| **Hardened Layer** | | | | **Soft Bulk** | | | |
|---|---|---|---|---|---|---|---|
| Longitudinal | | Transverse | | Longitudinal | | Transverse | |
| Length | Stress | Length | Stress | Length | Stress | Length | Stress |
| 0.00E+00 | 1.20E+00 | 0.00E+00 | 3.48E+02 | 0.00E+00 | 6.95E-01 | 0.00E+00 | 1.99E+02 |
| 1.04E-01 | 1.40E+00 | 7.29E-02 | 3.58E+02 | 1.04E-01 | 1.46E+00 | 7.29E-02 | 1.99E+02 |
| 2.08E-01 | 3.42E+00 | 1.46E-01 | 3.60E+02 | 2.08E-01 | 3.54E+00 | 1.46E-01 | 1.99E+02 |
| 3.13E-01 | 7.81E+00 | 2.19E-01 | 3.59E+02 | 3.13E-01 | 6.98E+00 | 2.19E-01 | 1.99E+02 |
| 4.17E-01 | 1.55E+01 | 2.92E-01 | 3.56E+02 | 4.17E-01 | 1.23E+01 | 2.92E-01 | 1.99E+02 |
| 5.21E-01 | 3.03E+01 | 3.65E-01 | 3.53E+02 | 5.21E-01 | 1.99E+01 | 3.65E-01 | 1.99E+02 |
| 6.25E-01 | 6.63E+01 | 4.38E-01 | 3.50E+02 | 6.25E-01 | 2.28E+01 | 4.38E-01 | 1.99E+02 |
| 7.29E-01 | 1.81E+02 | 5.10E-01 | 3.47E+02 | 7.29E-01 | 1.66E+02 | 5.10E-01 | 1.99E+02 |
| 8.33E-01 | 5.94E+01 | 5.83E-01 | 3.45E+02 | 8.33E-01 | 1.03E+02 | 5.83E-01 | 1.99E+02 |
| 9.38E-01 | 6.21E+00 | 6.56E-01 | 3.43E+02 | 9.38E-01 | 2.71E+01 | 6.56E-01 | 1.99E+02 |
| 1.04E+00 | 2.00E+01 | 7.29E-01 | 3.42E+02 | 1.04E+00 | 1.99E+01 | 7.29E-01 | 1.98E+02 |
| 1.15E+00 | 4.09E+01 | 8.02E-01 | 3.41E+02 | 1.15E+00 | 3.69E+01 | 8.02E-01 | 1.98E+02 |
| 1.25E+00 | 6.16E+01 | 8.75E-01 | 3.41E+02 | 1.25E+00 | 5.59E+01 | 8.75E-01 | 1.98E+02 |
| 1.35E+00 | 8.30E+01 | 9.48E-01 | 3.41E+02 | 1.35E+00 | 7.55E+01 | 9.48E-01 | 1.98E+02 |
| 1.46E+00 | 1.05E+02 | 1.02E+00 | 3.41E+02 | 1.46E+00 | 9.60E+01 | 1.02E+00 | 1.98E+02 |
| 1.56E+00 | 1.29E+02 | 1.09E+00 | 3.41E+02 | 1.56E+00 | 1.17E+02 | 1.09E+00 | 1.98E+02 |
| 1.67E+00 | 1.54E+02 | 1.17E+00 | 3.41E+02 | 1.67E+00 | 1.40E+02 | 1.17E+00 | 1.98E+02 |
| 1.77E+00 | 1.80E+02 | 1.24E+00 | 3.42E+02 | 1.77E+00 | 1.63E+02 | 1.24E+00 | 1.98E+02 |

| | | | | | | | |
|---|---|---|---|---|---|---|---|
| 1.88E+00 | 2.07E+02 | 1.31E+00 | 3.42E+02 | 1.88E+00 | 1.86E+02 | 1.31E+00 | 1.99E+02 |
| 1.98E+00 | 2.40E+02 | 1.39E+00 | 3.42E+02 | 1.98E+00 | 1.93E+02 | 1.39E+00 | 1.99E+02 |
| 2.08E+00 | 2.76E+02 | 1.46E+00 | 3.42E+02 | 2.08E+00 | 1.98E+02 | 1.46E+00 | 1.99E+02 |
| 2.19E+00 | 3.06E+02 | 1.53E+00 | 3.43E+02 | 2.19E+00 | 2.01E+02 | 1.53E+00 | 1.99E+02 |
| 2.29E+00 | 3.27E+02 | 1.60E+00 | 3.43E+02 | 2.29E+00 | 2.02E+02 | 1.60E+00 | 1.99E+02 |
| 2.40E+00 | 3.39E+02 | 1.68E+00 | 3.43E+02 | 2.40E+00 | 2.03E+02 | 1.68E+00 | 1.99E+02 |
| 2.50E+00 | 3.43E+02 | 1.75E+00 | 3.43E+02 | 2.50E+00 | 2.04E+02 | 1.75E+00 | 1.99E+02 |
| 2.60E+00 | 3.39E+02 | 1.82E+00 | 3.43E+02 | 2.60E+00 | 2.03E+02 | 1.82E+00 | 1.99E+02 |
| 2.71E+00 | 3.27E+02 | 1.90E+00 | 3.43E+02 | 2.71E+00 | 2.02E+02 | 1.90E+00 | 1.99E+02 |
| 2.81E+00 | 3.06E+02 | 1.97E+00 | 3.43E+02 | 2.81E+00 | 2.01E+02 | 1.97E+00 | 1.99E+02 |
| 2.92E+00 | 2.76E+02 | 2.04E+00 | 3.42E+02 | 2.92E+00 | 1.98E+02 | 2.04E+00 | 1.99E+02 |
| 3.02E+00 | 2.40E+02 | 2.11E+00 | 3.42E+02 | 3.02E+00 | 1.93E+02 | 2.11E+00 | 1.99E+02 |
| 3.13E+00 | 2.07E+02 | 2.19E+00 | 3.42E+02 | 3.13E+00 | 1.86E+02 | 2.19E+00 | 1.99E+02 |
| 3.23E+00 | 1.80E+02 | 2.26E+00 | 3.42E+02 | 3.23E+00 | 1.63E+02 | 2.26E+00 | 1.98E+02 |
| 3.33E+00 | 1.54E+02 | 2.33E+00 | 3.41E+02 | 3.33E+00 | 1.40E+02 | 2.33E+00 | 1.98E+02 |
| 3.44E+00 | 1.29E+02 | 2.41E+00 | 3.41E+02 | 3.44E+00 | 1.17E+02 | 2.41E+00 | 1.98E+02 |
| 3.54E+00 | 1.05E+02 | 2.48E+00 | 3.41E+02 | 3.54E+00 | 9.59E+01 | 2.48E+00 | 1.98E+02 |
| 3.65E+00 | 8.28E+01 | 2.55E+00 | 3.41E+02 | 3.65E+00 | 7.53E+01 | 2.55E+00 | 1.98E+02 |
| 3.75E+00 | 6.14E+01 | 2.63E+00 | 3.41E+02 | 3.75E+00 | 5.57E+01 | 2.63E+00 | 1.98E+02 |
| 3.85E+00 | 4.07E+01 | 2.70E+00 | 3.41E+02 | 3.85E+00 | 3.67E+01 | 2.70E+00 | 1.98E+02 |
| 3.96E+00 | 1.96E+01 | 2.77E+00 | 3.42E+02 | 3.96E+00 | 1.99E+01 | 2.77E+00 | 1.98E+02 |
| 4.06E+00 | 6.27E+00 | 2.84E+00 | 3.43E+02 | 4.06E+00 | 2.68E+01 | 2.84E+00 | 1.99E+02 |
| 4.1667 | 5.45E+01 | 2.9167 | 3.45E+02 | 4.17E+00 | 9.67E+01 | 2.92E+00 | 1.99E+02 |
| 4.2708 | 2.49E+02 | 2.9896 | 3.47E+02 | 4.27E+00 | 1.64E+02 | 2.99E+00 | 1.99E+02 |
| 4.375 | 7.71E+01 | 3.0625 | 3.50E+02 | 4.38E+00 | 2.23E+01 | 3.06E+00 | 1.99E+02 |
| 4.4792 | 2.86E+01 | 3.1354 | 3.53E+02 | 4.48E+00 | 1.99E+01 | 3.14E+00 | 1.99E+02 |
| 4.5833 | 1.52E+01 | 3.2083 | 3.56E+02 | 4.58E+00 | 1.24E+01 | 3.21E+00 | 1.99E+02 |
| 4.6875 | 7.86E+00 | 3.2813 | 3.59E+02 | 4.69E+00 | 7.10E+00 | 3.28E+00 | 1.99E+02 |
| 4.7917 | 3.57E+00 | 3.3542 | 3.60E+02 | 4.79E+00 | 3.65E+00 | 3.35E+00 | 1.99E+02 |
| 4.8958 | 1.62E+00 | 3.4271 | 3.58E+02 | 4.90E+00 | 1.61E+00 | 3.43E+00 | 1.99E+02 |
| 5 | 1.43E+00 | 3.5 | 3.48E+02 | 5.00E+00 | 9.13E-01 | 3.50E+00 | 1.99E+02 |

Table B-31 Surface tensile stress and strain profiles for sample N7, step 52%YS.

| **Hardened Layer** | | | | **Soft Bulk** | | | |
|---|---|---|---|---|---|---|---|
| Longitudinal | | Transverse | | Longitudinal | | Transverse | |
| Length | Stress | Length | Stress | Length | Stress | Length | Stress |
| 0.00E+00 | 1.60E+00 | 0.00E+00 | 4.04E+02 | 0.00E+00 | 1.01E+00 | 0.00E+00 | 2.07E+02 |
| 1.04E-01 | 1.79E+00 | 7.29E-02 | 4.17E+02 | 1.04E-01 | 1.75E+00 | 7.29E-02 | 2.07E+02 |
| 2.08E-01 | 3.81E+00 | 1.46E-01 | 4.21E+02 | 2.08E-01 | 3.89E+00 | 1.46E-01 | 2.08E+02 |

| | | | | | | | |
|---|---|---|---|---|---|---|---|
| 3.13E-01 | 8.45E+00 | 2.19E-01 | 4.19E+02 | 3.13E-01 | 7.55E+00 | 2.19E-01 | 2.08E+02 |
| 4.17E-01 | 1.67E+01 | 2.92E-01 | 4.16E+02 | 4.17E-01 | 1.33E+01 | 2.92E-01 | 2.08E+02 |
| 5.21E-01 | 3.30E+01 | 3.65E-01 | 4.12E+02 | 5.21E-01 | 2.17E+01 | 3.65E-01 | 2.08E+02 |
| 6.25E-01 | 7.85E+01 | 4.38E-01 | 4.09E+02 | 6.25E-01 | 2.66E+01 | 4.38E-01 | 2.08E+02 |
| 7.29E-01 | 1.94E+02 | 5.10E-01 | 4.06E+02 | 7.29E-01 | 1.72E+02 | 5.10E-01 | 2.08E+02 |
| 8.33E-01 | 7.17E+01 | 5.83E-01 | 4.03E+02 | 8.33E-01 | 1.22E+02 | 5.83E-01 | 2.08E+02 |
| 9.38E-01 | 1.08E+01 | 6.56E-01 | 4.01E+02 | 9.38E-01 | 3.29E+01 | 6.56E-01 | 2.08E+02 |
| 1.04E+00 | 1.88E+01 | 7.29E-01 | 4.00E+02 | 1.04E+00 | 2.02E+01 | 7.29E-01 | 2.08E+02 |
| 1.15E+00 | 4.18E+01 | 8.02E-01 | 3.99E+02 | 1.15E+00 | 3.78E+01 | 8.02E-01 | 2.08E+02 |
| 1.25E+00 | 6.43E+01 | 8.75E-01 | 3.98E+02 | 1.25E+00 | 5.83E+01 | 8.75E-01 | 2.08E+02 |
| 1.35E+00 | 8.76E+01 | 9.48E-01 | 3.98E+02 | 1.35E+00 | 7.97E+01 | 9.48E-01 | 2.08E+02 |
| 1.46E+00 | 1.12E+02 | 1.02E+00 | 3.99E+02 | 1.46E+00 | 1.02E+02 | 1.02E+00 | 2.08E+02 |
| 1.56E+00 | 1.38E+02 | 1.09E+00 | 3.99E+02 | 1.56E+00 | 1.26E+02 | 1.09E+00 | 2.08E+02 |
| 1.67E+00 | 1.65E+02 | 1.17E+00 | 3.99E+02 | 1.67E+00 | 1.50E+02 | 1.17E+00 | 2.08E+02 |
| 1.77E+00 | 1.94E+02 | 1.24E+00 | 4.00E+02 | 1.77E+00 | 1.76E+02 | 1.24E+00 | 2.08E+02 |
| 1.88E+00 | 2.30E+02 | 1.31E+00 | 4.00E+02 | 1.88E+00 | 1.92E+02 | 1.31E+00 | 2.08E+02 |
| 1.98E+00 | 2.76E+02 | 1.39E+00 | 4.01E+02 | 1.98E+00 | 1.97E+02 | 1.39E+00 | 2.08E+02 |
| 2.08E+00 | 3.20E+02 | 1.46E+00 | 4.01E+02 | 2.08E+00 | 2.02E+02 | 1.46E+00 | 2.08E+02 |
| 2.19E+00 | 3.57E+02 | 1.53E+00 | 4.02E+02 | 2.19E+00 | 2.05E+02 | 1.53E+00 | 2.08E+02 |
| 2.29E+00 | 3.82E+02 | 1.60E+00 | 4.02E+02 | 2.29E+00 | 2.07E+02 | 1.60E+00 | 2.08E+02 |
| 2.40E+00 | 3.97E+02 | 1.68E+00 | 4.02E+02 | 2.40E+00 | 2.08E+02 | 1.68E+00 | 2.08E+02 |
| 2.50E+00 | 4.02E+02 | 1.75E+00 | 4.02E+02 | 2.50E+00 | 2.08E+02 | 1.75E+00 | 2.08E+02 |
| 2.60E+00 | 3.97E+02 | 1.82E+00 | 4.02E+02 | 2.60E+00 | 2.08E+02 | 1.82E+00 | 2.08E+02 |
| 2.71E+00 | 3.82E+02 | 1.90E+00 | 4.02E+02 | 2.71E+00 | 2.07E+02 | 1.90E+00 | 2.08E+02 |
| 2.81E+00 | 3.57E+02 | 1.97E+00 | 4.02E+02 | 2.81E+00 | 2.05E+02 | 1.97E+00 | 2.08E+02 |
| 2.92E+00 | 3.20E+02 | 2.04E+00 | 4.01E+02 | 2.92E+00 | 2.02E+02 | 2.04E+00 | 2.08E+02 |
| 3.02E+00 | 2.76E+02 | 2.11E+00 | 4.01E+02 | 3.02E+00 | 1.97E+02 | 2.11E+00 | 2.08E+02 |
| 3.13E+00 | 2.30E+02 | 2.19E+00 | 4.00E+02 | 3.13E+00 | 1.92E+02 | 2.19E+00 | 2.08E+02 |
| 3.23E+00 | 1.94E+02 | 2.26E+00 | 4.00E+02 | 3.23E+00 | 1.76E+02 | 2.26E+00 | 2.08E+02 |
| 3.33E+00 | 1.65E+02 | 2.33E+00 | 3.99E+02 | 3.33E+00 | 1.50E+02 | 2.33E+00 | 2.08E+02 |
| 3.44E+00 | 1.38E+02 | 2.41E+00 | 3.99E+02 | 3.44E+00 | 1.26E+02 | 2.41E+00 | 2.08E+02 |
| 3.54E+00 | 1.12E+02 | 2.48E+00 | 3.99E+02 | 3.54E+00 | 1.02E+02 | 2.48E+00 | 2.08E+02 |
| 3.65E+00 | 8.74E+01 | 2.55E+00 | 3.98E+02 | 3.65E+00 | 7.95E+01 | 2.55E+00 | 2.08E+02 |
| 3.75E+00 | 6.41E+01 | 2.63E+00 | 3.98E+02 | 3.75E+00 | 5.81E+01 | 2.63E+00 | 2.08E+02 |
| 3.85E+00 | 4.14E+01 | 2.70E+00 | 3.99E+02 | 3.85E+00 | 3.76E+01 | 2.70E+00 | 2.08E+02 |
| 3.96E+00 | 1.83E+01 | 2.77E+00 | 4.00E+02 | 3.96E+00 | 2.03E+01 | 2.77E+00 | 2.08E+02 |
| 4.06E+00 | 1.07E+01 | 2.84E+00 | 4.01E+02 | 4.06E+00 | 3.23E+01 | 2.84E+00 | 2.08E+02 |
| 4.1667 | 6.47E+01 | 2.9167 | 4.03E+02 | 4.17E+00 | 1.14E+02 | 2.92E+00 | 2.08E+02 |
| 4.2708 | 2.84E+02 | 2.9896 | 4.06E+02 | 4.27E+00 | 1.70E+02 | 2.99E+00 | 2.08E+02 |
| 4.375 | 8.77E+01 | 3.0625 | 4.09E+02 | 4.38E+00 | 2.58E+01 | 3.06E+00 | 2.08E+02 |

| | | | | | | | |
|---|---|---|---|---|---|---|---|
| 4.4792 | 3.12E+01 | 3.1354 | 4.12E+02 | 4.48E+00 | 2.19E+01 | 3.14E+00 | 2.08E+02 |
| 4.5833 | 1.65E+01 | 3.2083 | 4.16E+02 | 4.58E+00 | 1.36E+01 | 3.21E+00 | 2.08E+02 |
| 4.6875 | 8.59E+00 | 3.2813 | 4.19E+02 | 4.69E+00 | 7.76E+00 | 3.28E+00 | 2.08E+02 |
| 4.7917 | 4.04E+00 | 3.3542 | 4.21E+02 | 4.79E+00 | 4.07E+00 | 3.35E+00 | 2.08E+02 |
| 4.8958 | 2.09E+00 | 3.4271 | 4.17E+02 | 4.90E+00 | 1.97E+00 | 3.43E+00 | 2.07E+02 |
| 5 | 1.92E+00 | 3.5 | 4.04E+02 | 5.00E+00 | 1.32E+00 | 3.50E+00 | 2.07E+02 |

Table B-32 Surface tensile stress and strain profiles for sample N7, step 59%YS.

| **Hardened Layer** | | | | **Soft Bulk** | | | |
|---|---|---|---|---|---|---|---|
| Longitudinal | | Transverse | | Longitudinal | | Transverse | |
| Length | Stress | Length | Stress | Length | Stress | Length | Stress |
| 0.00E+00 | 2.04E+00 | 0.00E+00 | 4.59E+02 | 0.00E+00 | 1.38E+00 | 0.00E+00 | 2.10E+02 |
| 1.04E-01 | 2.22E+00 | 7.29E-02 | 4.75E+02 | 1.04E-01 | 2.08E+00 | 7.29E-02 | 2.10E+02 |
| 2.08E-01 | 4.21E+00 | 1.46E-01 | 4.80E+02 | 2.08E-01 | 4.24E+00 | 1.46E-01 | 2.10E+02 |
| 3.13E-01 | 9.06E+00 | 2.19E-01 | 4.79E+02 | 3.13E-01 | 8.11E+00 | 2.19E-01 | 2.10E+02 |
| 4.17E-01 | 1.79E+01 | 2.92E-01 | 4.75E+02 | 4.17E-01 | 1.43E+01 | 2.92E-01 | 2.10E+02 |
| 5.21E-01 | 3.56E+01 | 3.65E-01 | 4.71E+02 | 5.21E-01 | 2.37E+01 | 3.65E-01 | 2.10E+02 |
| 6.25E-01 | 8.99E+01 | 4.38E-01 | 4.66E+02 | 6.25E-01 | 3.09E+01 | 4.38E-01 | 2.10E+02 |
| 7.29E-01 | 3.65E+02 | 5.10E-01 | 4.63E+02 | 7.29E-01 | 1.77E+02 | 5.10E-01 | 2.10E+02 |
| 8.33E-01 | 8.08E+01 | 5.83E-01 | 4.59E+02 | 8.33E-01 | 1.39E+02 | 5.83E-01 | 2.10E+02 |
| 9.38E-01 | 1.70E+01 | 6.56E-01 | 4.57E+02 | 9.38E-01 | 3.94E+01 | 6.56E-01 | 2.10E+02 |
| 1.04E+00 | 1.63E+01 | 7.29E-01 | 4.56E+02 | 1.04E+00 | 2.04E+01 | 7.29E-01 | 2.10E+02 |
| 1.15E+00 | 4.14E+01 | 8.02E-01 | 4.55E+02 | 1.15E+00 | 3.77E+01 | 8.02E-01 | 2.10E+02 |
| 1.25E+00 | 6.56E+01 | 8.75E-01 | 4.55E+02 | 1.25E+00 | 5.96E+01 | 8.75E-01 | 2.10E+02 |
| 1.35E+00 | 9.06E+01 | 9.48E-01 | 4.55E+02 | 1.35E+00 | 8.24E+01 | 9.48E-01 | 2.10E+02 |
| 1.46E+00 | 1.17E+02 | 1.02E+00 | 4.55E+02 | 1.46E+00 | 1.06E+02 | 1.02E+00 | 2.10E+02 |
| 1.56E+00 | 1.45E+02 | 1.09E+00 | 4.55E+02 | 1.56E+00 | 1.32E+02 | 1.09E+00 | 2.10E+02 |
| 1.67E+00 | 1.75E+02 | 1.17E+00 | 4.56E+02 | 1.67E+00 | 1.59E+02 | 1.17E+00 | 2.10E+02 |
| 1.77E+00 | 2.07E+02 | 1.24E+00 | 4.57E+02 | 1.77E+00 | 1.86E+02 | 1.24E+00 | 2.10E+02 |
| 1.88E+00 | 2.55E+02 | 1.31E+00 | 4.57E+02 | 1.88E+00 | 1.94E+02 | 1.31E+00 | 2.11E+02 |
| 1.98E+00 | 3.12E+02 | 1.39E+00 | 4.58E+02 | 1.98E+00 | 2.01E+02 | 1.39E+00 | 2.11E+02 |
| 2.08E+00 | 3.64E+02 | 1.46E+00 | 4.59E+02 | 2.08E+00 | 2.05E+02 | 1.46E+00 | 2.11E+02 |
| 2.19E+00 | 4.06E+02 | 1.53E+00 | 4.59E+02 | 2.19E+00 | 2.09E+02 | 1.53E+00 | 2.11E+02 |
| 2.29E+00 | 4.36E+02 | 1.60E+00 | 4.59E+02 | 2.29E+00 | 2.10E+02 | 1.60E+00 | 2.11E+02 |
| 2.40E+00 | 4.54E+02 | 1.68E+00 | 4.60E+02 | 2.40E+00 | 2.10E+02 | 1.68E+00 | 2.11E+02 |
| 2.50E+00 | 4.60E+02 | 1.75E+00 | 4.60E+02 | 2.50E+00 | 2.11E+02 | 1.75E+00 | 2.11E+02 |
| 2.60E+00 | 4.54E+02 | 1.82E+00 | 4.60E+02 | 2.60E+00 | 2.10E+02 | 1.82E+00 | 2.11E+02 |
| 2.71E+00 | 4.36E+02 | 1.90E+00 | 4.59E+02 | 2.71E+00 | 2.10E+02 | 1.90E+00 | 2.11E+02 |
| 2.81E+00 | 4.05E+02 | 1.97E+00 | 4.59E+02 | 2.81E+00 | 2.09E+02 | 1.97E+00 | 2.11E+02 |

| | | | | | | | |
|---|---|---|---|---|---|---|---|
| 2.92E+00 | 3.63E+02 | 2.04E+00 | 4.59E+02 | 2.92E+00 | 2.05E+02 | 2.04E+00 | 2.11E+02 |
| 3.02E+00 | 3.12E+02 | 2.11E+00 | 4.58E+02 | 3.02E+00 | 2.01E+02 | 2.11E+00 | 2.11E+02 |
| 3.13E+00 | 2.55E+02 | 2.19E+00 | 4.57E+02 | 3.13E+00 | 1.94E+02 | 2.19E+00 | 2.11E+02 |
| 3.23E+00 | 2.07E+02 | 2.26E+00 | 4.57E+02 | 3.23E+00 | 1.86E+02 | 2.26E+00 | 2.10E+02 |
| 3.33E+00 | 1.74E+02 | 2.33E+00 | 4.56E+02 | 3.33E+00 | 1.59E+02 | 2.33E+00 | 2.10E+02 |
| 3.44E+00 | 1.45E+02 | 2.41E+00 | 4.55E+02 | 3.44E+00 | 1.32E+02 | 2.41E+00 | 2.10E+02 |
| 3.54E+00 | 1.17E+02 | 2.48E+00 | 4.55E+02 | 3.54E+00 | 1.06E+02 | 2.48E+00 | 2.10E+02 |
| 3.65E+00 | 9.04E+01 | 2.55E+00 | 4.55E+02 | 3.65E+00 | 8.22E+01 | 2.55E+00 | 2.10E+02 |
| 3.75E+00 | 6.54E+01 | 2.63E+00 | 4.55E+02 | 3.75E+00 | 5.93E+01 | 2.63E+00 | 2.10E+02 |
| 3.85E+00 | 4.10E+01 | 2.70E+00 | 4.55E+02 | 3.85E+00 | 3.74E+01 | 2.70E+00 | 2.10E+02 |
| 3.96E+00 | 1.59E+01 | 2.77E+00 | 4.56E+02 | 3.96E+00 | 2.05E+01 | 2.77E+00 | 2.10E+02 |
| 4.06E+00 | 1.64E+01 | 2.84E+00 | 4.57E+02 | 4.06E+00 | 3.84E+01 | 2.84E+00 | 2.10E+02 |
| 4.1667 | 7.33E+01 | 2.9167 | 4.60E+02 | 4.17E+00 | 1.30E+02 | 2.92E+00 | 2.10E+02 |
| 4.2708 | 2.88E+02 | 2.9896 | 4.63E+02 | 4.27E+00 | 1.75E+02 | 2.99E+00 | 2.10E+02 |
| 4.375 | 9.93E+01 | 3.0625 | 4.66E+02 | 4.38E+00 | 2.96E+01 | 3.06E+00 | 2.10E+02 |
| 4.4792 | 3.37E+01 | 3.1354 | 4.71E+02 | 4.48E+00 | 2.39E+01 | 3.14E+00 | 2.10E+02 |
| 4.5833 | 1.78E+01 | 3.2083 | 4.75E+02 | 4.58E+00 | 1.46E+01 | 3.21E+00 | 2.10E+02 |
| 4.6875 | 9.26E+00 | 3.2813 | 4.79E+02 | 4.69E+00 | 8.36E+00 | 3.28E+00 | 2.10E+02 |
| 4.7917 | 4.50E+00 | 3.3542 | 4.80E+02 | 4.79E+00 | 4.47E+00 | 3.35E+00 | 2.10E+02 |
| 4.8958 | 2.57E+00 | 3.4271 | 4.75E+02 | 4.90E+00 | 2.35E+00 | 3.43E+00 | 2.10E+02 |
| 5 | 2.42E+00 | 3.5 | 4.59E+02 | 5.00E+00 | 1.74E+00 | 3.50E+00 | 2.10E+02 |

Table B-33 Surface tensile stress and strain profiles for sample N7, step 66%YS.

| **Hardened Layer** | | | | **Soft Bulk** | | | |
|---|---|---|---|---|---|---|---|
| Longitudinal | | Transverse | | Longitudinal | | Transverse | |
| Length | Stress | Length | Stress | Length | Stress | Length | Stress |
| 0.00E+00 | 2.58E+00 | 0.00E+00 | 5.10E+02 | 0.00E+00 | 1.85E+00 | 0.00E+00 | 2.11E+02 |
| 1.04E-01 | 2.73E+00 | 7.29E-02 | 5.29E+02 | 1.04E-01 | 2.48E+00 | 7.29E-02 | 2.11E+02 |
| 2.08E-01 | 4.65E+00 | 1.46E-01 | 5.36E+02 | 2.08E-01 | 4.62E+00 | 1.46E-01 | 2.12E+02 |
| 3.13E-01 | 9.64E+00 | 2.19E-01 | 5.35E+02 | 3.13E-01 | 8.65E+00 | 2.19E-01 | 2.12E+02 |
| 4.17E-01 | 1.90E+01 | 2.92E-01 | 5.31E+02 | 4.17E-01 | 1.53E+01 | 2.92E-01 | 2.12E+02 |
| 5.21E-01 | 3.81E+01 | 3.65E-01 | 5.26E+02 | 5.21E-01 | 2.57E+01 | 3.65E-01 | 2.12E+02 |
| 6.25E-01 | 1.00E+02 | 4.38E-01 | 5.21E+02 | 6.25E-01 | 3.54E+01 | 4.38E-01 | 2.12E+02 |
| 7.29E-01 | 3.92E+02 | 5.10E-01 | 5.16E+02 | 7.29E-01 | 1.81E+02 | 5.10E-01 | 2.12E+02 |
| 8.33E-01 | 8.80E+01 | 5.83E-01 | 5.13E+02 | 8.33E-01 | 1.53E+02 | 5.83E-01 | 2.12E+02 |
| 9.38E-01 | 2.40E+01 | 6.56E-01 | 5.11E+02 | 9.38E-01 | 4.61E+01 | 6.56E-01 | 2.12E+02 |
| 1.04E+00 | 1.33E+01 | 7.29E-01 | 5.09E+02 | 1.04E+00 | 2.08E+01 | 7.29E-01 | 2.12E+02 |
| 1.15E+00 | 4.02E+01 | 8.02E-01 | 5.08E+02 | 1.15E+00 | 3.69E+01 | 8.02E-01 | 2.12E+02 |
| 1.25E+00 | 6.59E+01 | 8.75E-01 | 5.08E+02 | 1.25E+00 | 5.99E+01 | 8.75E-01 | 2.12E+02 |

| | | | | | | | |
|---|---|---|---|---|---|---|---|
| 1.35E+00 | 9.22E+01 | 9.48E-01 | 5.08E+02 | 1.35E+00 | 8.40E+01 | 9.48E-01 | 2.12E+02 |
| 1.46E+00 | 1.20E+02 | 1.02E+00 | 5.08E+02 | 1.46E+00 | 1.09E+02 | 1.02E+00 | 2.12E+02 |
| 1.56E+00 | 1.50E+02 | 1.09E+00 | 5.09E+02 | 1.56E+00 | 1.36E+02 | 1.09E+00 | 2.12E+02 |
| 1.67E+00 | 1.81E+02 | 1.17E+00 | 5.10E+02 | 1.67E+00 | 1.65E+02 | 1.17E+00 | 2.12E+02 |
| 1.77E+00 | 2.21E+02 | 1.24E+00 | 5.10E+02 | 1.77E+00 | 1.91E+02 | 1.24E+00 | 2.12E+02 |
| 1.88E+00 | 2.81E+02 | 1.31E+00 | 5.11E+02 | 1.88E+00 | 1.97E+02 | 1.31E+00 | 2.12E+02 |
| 1.98E+00 | 3.45E+02 | 1.39E+00 | 5.12E+02 | 1.98E+00 | 2.03E+02 | 1.39E+00 | 2.12E+02 |
| 2.08E+00 | 4.03E+02 | 1.46E+00 | 5.12E+02 | 2.08E+00 | 2.08E+02 | 1.46E+00 | 2.12E+02 |
| 2.19E+00 | 4.51E+02 | 1.53E+00 | 5.13E+02 | 2.19E+00 | 2.10E+02 | 1.53E+00 | 2.12E+02 |
| 2.29E+00 | 4.86E+02 | 1.60E+00 | 5.13E+02 | 2.29E+00 | 2.12E+02 | 1.60E+00 | 2.12E+02 |
| 2.40E+00 | 5.07E+02 | 1.68E+00 | 5.14E+02 | 2.40E+00 | 2.12E+02 | 1.68E+00 | 2.12E+02 |
| 2.50E+00 | 5.14E+02 | 1.75E+00 | 5.14E+02 | 2.50E+00 | 2.12E+02 | 1.75E+00 | 2.12E+02 |
| 2.60E+00 | 5.07E+02 | 1.82E+00 | 5.14E+02 | 2.60E+00 | 2.12E+02 | 1.82E+00 | 2.12E+02 |
| 2.71E+00 | 4.86E+02 | 1.90E+00 | 5.13E+02 | 2.71E+00 | 2.12E+02 | 1.90E+00 | 2.12E+02 |
| 2.81E+00 | 4.51E+02 | 1.97E+00 | 5.13E+02 | 2.81E+00 | 2.10E+02 | 1.97E+00 | 2.12E+02 |
| 2.92E+00 | 4.03E+02 | 2.04E+00 | 5.13E+02 | 2.92E+00 | 2.08E+02 | 2.04E+00 | 2.12E+02 |
| 3.02E+00 | 3.45E+02 | 2.11E+00 | 5.12E+02 | 3.02E+00 | 2.03E+02 | 2.11E+00 | 2.12E+02 |
| 3.13E+00 | 2.81E+02 | 2.19E+00 | 5.11E+02 | 3.13E+00 | 1.97E+02 | 2.19E+00 | 2.12E+02 |
| 3.23E+00 | 2.21E+02 | 2.26E+00 | 5.10E+02 | 3.23E+00 | 1.91E+02 | 2.26E+00 | 2.12E+02 |
| 3.33E+00 | 1.81E+02 | 2.33E+00 | 5.10E+02 | 3.33E+00 | 1.65E+02 | 2.33E+00 | 2.12E+02 |
| 3.44E+00 | 1.49E+02 | 2.41E+00 | 5.09E+02 | 3.44E+00 | 1.36E+02 | 2.41E+00 | 2.12E+02 |
| 3.54E+00 | 1.20E+02 | 2.48E+00 | 5.08E+02 | 3.54E+00 | 1.09E+02 | 2.48E+00 | 2.12E+02 |
| 3.65E+00 | 9.20E+01 | 2.55E+00 | 5.08E+02 | 3.65E+00 | 8.38E+01 | 2.55E+00 | 2.12E+02 |
| 3.75E+00 | 6.56E+01 | 2.63E+00 | 5.08E+02 | 3.75E+00 | 5.96E+01 | 2.63E+00 | 2.12E+02 |
| 3.85E+00 | 3.98E+01 | 2.70E+00 | 5.08E+02 | 3.85E+00 | 3.67E+01 | 2.70E+00 | 2.12E+02 |
| 3.96E+00 | 1.30E+01 | 2.77E+00 | 5.09E+02 | 3.96E+00 | 2.10E+01 | 2.77E+00 | 2.12E+02 |
| 4.06E+00 | 2.30E+01 | 2.84E+00 | 5.11E+02 | 4.06E+00 | 4.47E+01 | 2.84E+00 | 2.12E+02 |
| 4.1667 | 8.02E+01 | 2.9167 | 5.13E+02 | 4.17E+00 | 1.44E+02 | 2.92E+00 | 2.12E+02 |
| 4.2708 | 3.08E+02 | 2.9896 | 5.17E+02 | 4.27E+00 | 1.79E+02 | 2.99E+00 | 2.12E+02 |
| 4.375 | 1.10E+02 | 3.0625 | 5.21E+02 | 4.38E+00 | 3.36E+01 | 3.06E+00 | 2.12E+02 |
| 4.4792 | 3.59E+01 | 3.1354 | 5.26E+02 | 4.48E+00 | 2.58E+01 | 3.14E+00 | 2.12E+02 |
| 4.5833 | 1.89E+01 | 3.2083 | 5.31E+02 | 4.58E+00 | 1.56E+01 | 3.21E+00 | 2.12E+02 |
| 4.6875 | 9.89E+00 | 3.2813 | 5.35E+02 | 4.69E+00 | 8.94E+00 | 3.28E+00 | 2.12E+02 |
| 4.7917 | 4.98E+00 | 3.3542 | 5.36E+02 | 4.79E+00 | 4.89E+00 | 3.35E+00 | 2.12E+02 |
| 4.8958 | 3.11E+00 | 3.4271 | 5.29E+02 | 4.90E+00 | 2.79E+00 | 3.43E+00 | 2.11E+02 |
| 5 | 2.99E+00 | 3.5 | 5.11E+02 | 5.00E+00 | 2.24E+00 | 3.50E+00 | 2.11E+02 |

Table 0-34 Surface tensile stress and strain profiles for sample N7, step 74%YS.

| **Hardened Layer** | **Soft Bulk** |
|---|---|

| Longitudinal | | Transverse | | Longitudinal | | Transverse | |
|---|---|---|---|---|---|---|---|
| Length | Stress | Length | Stress | Length | Stress | Length | Stress |
| 0.00E+00 | 3.36E+00 | 0.00E+00 | 5.68E+02 | 0.00E+00 | 2.57E+00 | 0.00E+00 | 2.13E+02 |
| 1.04E-01 | 3.43E+00 | 7.29E-02 | 5.90E+02 | 1.04E-01 | 3.07E+00 | 7.29E-02 | 2.13E+02 |
| 2.08E-01 | 5.24E+00 | 1.46E-01 | 5.99E+02 | 2.08E-01 | 5.13E+00 | 1.46E-01 | 2.13E+02 |
| 3.13E-01 | 1.03E+01 | 2.19E-01 | 5.98E+02 | 3.13E-01 | 9.27E+00 | 2.19E-01 | 2.13E+02 |
| 4.17E-01 | 2.01E+01 | 2.92E-01 | 5.93E+02 | 4.17E-01 | 1.63E+01 | 2.92E-01 | 2.13E+02 |
| 5.21E-01 | 4.05E+01 | 3.65E-01 | 5.88E+02 | 5.21E-01 | 2.76E+01 | 3.65E-01 | 2.13E+02 |
| 6.25E-01 | 1.10E+02 | 4.38E-01 | 5.82E+02 | 6.25E-01 | 3.99E+01 | 4.38E-01 | 2.13E+02 |
| 7.29E-01 | 4.17E+02 | 5.10E-01 | 5.77E+02 | 7.29E-01 | 1.85E+02 | 5.10E-01 | 2.13E+02 |
| 8.33E-01 | 9.21E+01 | 5.83E-01 | 5.73E+02 | 8.33E-01 | 1.61E+02 | 5.83E-01 | 2.13E+02 |
| 9.38E-01 | 3.02E+01 | 6.56E-01 | 5.70E+02 | 9.38E-01 | 5.19E+01 | 6.56E-01 | 2.13E+02 |
| 1.04E+00 | 1.15E+01 | 7.29E-01 | 5.68E+02 | 1.04E+00 | 2.19E+01 | 7.29E-01 | 2.13E+02 |
| 1.15E+00 | 4.00E+01 | 8.02E-01 | 5.67E+02 | 1.15E+00 | 3.71E+01 | 8.02E-01 | 2.13E+02 |
| 1.25E+00 | 6.71E+01 | 8.75E-01 | 5.67E+02 | 1.25E+00 | 6.10E+01 | 8.75E-01 | 2.13E+02 |
| 1.35E+00 | 9.47E+01 | 9.48E-01 | 5.67E+02 | 1.35E+00 | 8.63E+01 | 9.48E-01 | 2.13E+02 |
| 1.46E+00 | 1.24E+02 | 1.02E+00 | 5.67E+02 | 1.46E+00 | 1.13E+02 | 1.02E+00 | 2.14E+02 |
| 1.56E+00 | 1.55E+02 | 1.09E+00 | 5.68E+02 | 1.56E+00 | 1.41E+02 | 1.09E+00 | 2.14E+02 |
| 1.67E+00 | 1.89E+02 | 1.17E+00 | 5.69E+02 | 1.67E+00 | 1.72E+02 | 1.17E+00 | 2.14E+02 |
| 1.77E+00 | 2.38E+02 | 1.24E+00 | 5.70E+02 | 1.77E+00 | 1.92E+02 | 1.24E+00 | 2.14E+02 |
| 1.88E+00 | 3.11E+02 | 1.31E+00 | 5.71E+02 | 1.88E+00 | 2.00E+02 | 1.31E+00 | 2.14E+02 |
| 1.98E+00 | 3.83E+02 | 1.39E+00 | 5.72E+02 | 1.98E+00 | 2.07E+02 | 1.39E+00 | 2.14E+02 |
| 2.08E+00 | 4.49E+02 | 1.46E+00 | 5.72E+02 | 2.08E+00 | 2.10E+02 | 1.46E+00 | 2.14E+02 |
| 2.19E+00 | 5.03E+02 | 1.53E+00 | 5.73E+02 | 2.19E+00 | 2.12E+02 | 1.53E+00 | 2.14E+02 |
| 2.29E+00 | 5.43E+02 | 1.60E+00 | 5.73E+02 | 2.29E+00 | 2.13E+02 | 1.60E+00 | 2.14E+02 |
| 2.40E+00 | 5.66E+02 | 1.68E+00 | 5.74E+02 | 2.40E+00 | 2.14E+02 | 1.68E+00 | 2.14E+02 |
| 2.50E+00 | 5.74E+02 | 1.75E+00 | 5.74E+02 | 2.50E+00 | 2.14E+02 | 1.75E+00 | 2.14E+02 |
| 2.60E+00 | 5.66E+02 | 1.82E+00 | 5.74E+02 | 2.60E+00 | 2.14E+02 | 1.82E+00 | 2.14E+02 |
| 2.71E+00 | 5.43E+02 | 1.90E+00 | 5.73E+02 | 2.71E+00 | 2.13E+02 | 1.90E+00 | 2.14E+02 |
| 2.81E+00 | 5.03E+02 | 1.97E+00 | 5.73E+02 | 2.81E+00 | 2.12E+02 | 1.97E+00 | 2.14E+02 |
| 2.92E+00 | 4.49E+02 | 2.04E+00 | 5.72E+02 | 2.92E+00 | 2.10E+02 | 2.04E+00 | 2.14E+02 |
| 3.02E+00 | 3.82E+02 | 2.11E+00 | 5.72E+02 | 3.02E+00 | 2.07E+02 | 2.11E+00 | 2.14E+02 |
| 3.13E+00 | 3.11E+02 | 2.19E+00 | 5.71E+02 | 3.13E+00 | 2.00E+02 | 2.19E+00 | 2.14E+02 |
| 3.23E+00 | 2.38E+02 | 2.26E+00 | 5.70E+02 | 3.23E+00 | 1.92E+02 | 2.26E+00 | 2.14E+02 |
| 3.33E+00 | 1.89E+02 | 2.33E+00 | 5.69E+02 | 3.33E+00 | 1.72E+02 | 2.33E+00 | 2.14E+02 |
| 3.44E+00 | 1.55E+02 | 2.41E+00 | 5.68E+02 | 3.44E+00 | 1.41E+02 | 2.41E+00 | 2.14E+02 |
| 3.54E+00 | 1.24E+02 | 2.48E+00 | 5.67E+02 | 3.54E+00 | 1.13E+02 | 2.48E+00 | 2.14E+02 |
| 3.65E+00 | 9.46E+01 | 2.55E+00 | 5.67E+02 | 3.65E+00 | 8.61E+01 | 2.55E+00 | 2.13E+02 |
| 3.75E+00 | 6.69E+01 | 2.63E+00 | 5.67E+02 | 3.75E+00 | 6.08E+01 | 2.63E+00 | 2.13E+02 |
| 3.85E+00 | 3.97E+01 | 2.70E+00 | 5.67E+02 | 3.85E+00 | 3.69E+01 | 2.70E+00 | 2.13E+02 |

| | | | | | | | |
|---|---|---|---|---|---|---|---|
| 3.96E+00 | 1.13E+01 | 2.77E+00 | 5.68E+02 | 3.96E+00 | 2.21E+01 | 2.77E+00 | 2.13E+02 |
| 4.06E+00 | 2.85E+01 | 2.84E+00 | 5.70E+02 | 4.06E+00 | 5.02E+01 | 2.84E+00 | 2.13E+02 |
| 4.1667 | 8.37E+01 | 2.9167 | 5.73E+02 | 4.17E+00 | 1.55E+02 | 2.92E+00 | 2.13E+02 |
| 4.2708 | 3.25E+02 | 2.9896 | 5.77E+02 | 4.27E+00 | 1.82E+02 | 2.99E+00 | 2.13E+02 |
| 4.375 | 1.20E+02 | 3.0625 | 5.82E+02 | 4.38E+00 | 3.75E+01 | 3.06E+00 | 2.13E+02 |
| 4.4792 | 3.79E+01 | 3.1354 | 5.88E+02 | 4.48E+00 | 2.75E+01 | 3.14E+00 | 2.13E+02 |
| 4.5833 | 1.99E+01 | 3.2083 | 5.93E+02 | 4.58E+00 | 1.65E+01 | 3.21E+00 | 2.13E+02 |
| 4.6875 | 1.06E+01 | 3.2813 | 5.98E+02 | 4.69E+00 | 9.55E+00 | 3.28E+00 | 2.13E+02 |
| 4.7917 | 5.58E+00 | 3.3542 | 5.99E+02 | 4.79E+00 | 5.40E+00 | 3.35E+00 | 2.13E+02 |
| 4.8958 | 3.80E+00 | 3.4271 | 5.90E+02 | 4.90E+00 | 3.39E+00 | 3.43E+00 | 2.13E+02 |
| 5 | 3.76E+00 | 3.5 | 5.68E+02 | 5.00E+00 | 2.94E+00 | 3.50E+00 | 2.13E+02 |

Table 0-35 Surface tensile stress and strain profiles for sample N7, step 89%YS.

| **Hardened Layer** | | | | **Soft Bulk** | | | |
|---|---|---|---|---|---|---|---|
| Longitudinal | | Transverse | | Longitudinal | | Transverse | |
| Length | Stress | Length | Stress | Length | Stress | Length | Stress |
| 0.00E+00 | 5.01E+00 | 0.00E+00 | 6.87E+02 | 0.00E+00 | 4.05E+00 | 0.00E+00 | 2.15E+02 |
| 1.04E-01 | 4.99E+00 | 7.29E-02 | 7.14E+02 | 1.04E-01 | 4.40E+00 | 7.29E-02 | 2.16E+02 |
| 2.08E-01 | 6.56E+00 | 1.46E-01 | 7.25E+02 | 2.08E-01 | 6.21E+00 | 1.46E-01 | 2.16E+02 |
| 3.13E-01 | 1.16E+01 | 2.19E-01 | 7.25E+02 | 3.13E-01 | 1.03E+01 | 2.19E-01 | 2.16E+02 |
| 4.17E-01 | 2.17E+01 | 2.92E-01 | 7.20E+02 | 4.17E-01 | 1.77E+01 | 2.92E-01 | 2.16E+02 |
| 5.21E-01 | 4.36E+01 | 3.65E-01 | 7.13E+02 | 5.21E-01 | 3.02E+01 | 3.65E-01 | 2.16E+02 |
| 6.25E-01 | 1.29E+02 | 4.38E-01 | 7.06E+02 | 6.25E-01 | 4.69E+01 | 4.38E-01 | 2.16E+02 |
| 7.29E-01 | 4.49E+02 | 5.10E-01 | 7.00E+02 | 7.29E-01 | 1.91E+02 | 5.10E-01 | 2.16E+02 |
| 8.33E-01 | 9.05E+01 | 5.83E-01 | 6.95E+02 | 8.33E-01 | 1.73E+02 | 5.83E-01 | 2.16E+02 |
| 9.38E-01 | 3.98E+01 | 6.56E-01 | 6.91E+02 | 9.38E-01 | 6.07E+01 | 6.56E-01 | 2.16E+02 |
| 1.04E+00 | 9.98E+00 | 7.29E-01 | 6.89E+02 | 1.04E+00 | 2.45E+01 | 7.29E-01 | 2.16E+02 |
| 1.15E+00 | 4.12E+01 | 8.02E-01 | 6.87E+02 | 1.15E+00 | 3.86E+01 | 8.02E-01 | 2.16E+02 |
| 1.25E+00 | 7.05E+01 | 8.75E-01 | 6.87E+02 | 1.25E+00 | 6.42E+01 | 8.75E-01 | 2.17E+02 |
| 1.35E+00 | 1.00E+02 | 9.48E-01 | 6.87E+02 | 1.35E+00 | 9.14E+01 | 9.48E-01 | 2.17E+02 |
| 1.46E+00 | 1.32E+02 | 1.02E+00 | 6.87E+02 | 1.46E+00 | 1.20E+02 | 1.02E+00 | 2.17E+02 |
| 1.56E+00 | 1.66E+02 | 1.09E+00 | 6.88E+02 | 1.56E+00 | 1.52E+02 | 1.09E+00 | 2.17E+02 |
| 1.67E+00 | 2.08E+02 | 1.17E+00 | 6.89E+02 | 1.67E+00 | 1.85E+02 | 1.17E+00 | 2.17E+02 |
| 1.77E+00 | 2.83E+02 | 1.24E+00 | 6.90E+02 | 1.77E+00 | 1.96E+02 | 1.24E+00 | 2.17E+02 |
| 1.88E+00 | 3.74E+02 | 1.31E+00 | 6.91E+02 | 1.88E+00 | 2.05E+02 | 1.31E+00 | 2.17E+02 |
| 1.98E+00 | 4.63E+02 | 1.39E+00 | 6.91E+02 | 1.98E+00 | 2.11E+02 | 1.39E+00 | 2.17E+02 |
| 2.08E+00 | 5.43E+02 | 1.46E+00 | 6.92E+02 | 2.08E+00 | 2.13E+02 | 1.46E+00 | 2.17E+02 |
| 2.19E+00 | 6.11E+02 | 1.53E+00 | 6.93E+02 | 2.19E+00 | 2.15E+02 | 1.53E+00 | 2.17E+02 |
| 2.29E+00 | 6.60E+02 | 1.60E+00 | 6.93E+02 | 2.29E+00 | 2.16E+02 | 1.60E+00 | 2.17E+02 |

| | | | | | | | |
|---|---|---|---|---|---|---|---|
| 2.40E+00 | 6.86E+02 | 1.68E+00 | 6.94E+02 | 2.40E+00 | 2.17E+02 | 1.68E+00 | 2.17E+02 |
| 2.50E+00 | 6.94E+02 | 1.75E+00 | 6.94E+02 | 2.50E+00 | 2.17E+02 | 1.75E+00 | 2.17E+02 |
| 2.60E+00 | 6.86E+02 | 1.82E+00 | 6.94E+02 | 2.60E+00 | 2.17E+02 | 1.82E+00 | 2.17E+02 |
| 2.71E+00 | 6.60E+02 | 1.90E+00 | 6.93E+02 | 2.71E+00 | 2.16E+02 | 1.90E+00 | 2.17E+02 |
| 2.81E+00 | 6.11E+02 | 1.97E+00 | 6.93E+02 | 2.81E+00 | 2.15E+02 | 1.97E+00 | 2.17E+02 |
| 2.92E+00 | 5.43E+02 | 2.04E+00 | 6.92E+02 | 2.92E+00 | 2.13E+02 | 2.04E+00 | 2.17E+02 |
| 3.02E+00 | 4.63E+02 | 2.11E+00 | 6.91E+02 | 3.02E+00 | 2.11E+02 | 2.11E+00 | 2.17E+02 |
| 3.13E+00 | 3.74E+02 | 2.19E+00 | 6.90E+02 | 3.13E+00 | 2.05E+02 | 2.19E+00 | 2.17E+02 |
| 3.23E+00 | 2.83E+02 | 2.26E+00 | 6.90E+02 | 3.23E+00 | 1.96E+02 | 2.26E+00 | 2.17E+02 |
| 3.33E+00 | 2.08E+02 | 2.33E+00 | 6.89E+02 | 3.33E+00 | 1.85E+02 | 2.33E+00 | 2.17E+02 |
| 3.44E+00 | 1.66E+02 | 2.41E+00 | 6.88E+02 | 3.44E+00 | 1.51E+02 | 2.41E+00 | 2.17E+02 |
| 3.54E+00 | 1.32E+02 | 2.48E+00 | 6.87E+02 | 3.54E+00 | 1.20E+02 | 2.48E+00 | 2.17E+02 |
| 3.65E+00 | 1.00E+02 | 2.55E+00 | 6.87E+02 | 3.65E+00 | 9.13E+01 | 2.55E+00 | 2.17E+02 |
| 3.75E+00 | 7.03E+01 | 2.63E+00 | 6.87E+02 | 3.75E+00 | 6.40E+01 | 2.63E+00 | 2.17E+02 |
| 3.85E+00 | 4.09E+01 | 2.70E+00 | 6.87E+02 | 3.85E+00 | 3.85E+01 | 2.70E+00 | 2.16E+02 |
| 3.96E+00 | 1.01E+01 | 2.77E+00 | 6.89E+02 | 3.96E+00 | 2.47E+01 | 2.77E+00 | 2.16E+02 |
| 4.06E+00 | 3.68E+01 | 2.84E+00 | 6.91E+02 | 4.06E+00 | 5.83E+01 | 2.84E+00 | 2.16E+02 |
| 4.1667 | 7.61E+01 | 2.9167 | 6.95E+02 | 4.17E+00 | 1.67E+02 | 2.92E+00 | 2.16E+02 |
| 4.2708 | 3.47E+02 | 2.9896 | 7.00E+02 | 4.27E+00 | 1.88E+02 | 2.99E+00 | 2.16E+02 |
| 4.375 | 1.36E+02 | 3.0625 | 7.06E+02 | 4.38E+00 | 4.39E+01 | 3.06E+00 | 2.16E+02 |
| 4.4792 | 4.09E+01 | 3.1354 | 7.13E+02 | 4.48E+00 | 3.01E+01 | 3.14E+00 | 2.16E+02 |
| 4.5833 | 2.15E+01 | 3.2083 | 7.20E+02 | 4.58E+00 | 1.79E+01 | 3.21E+00 | 2.16E+02 |
| 4.6875 | 1.17E+01 | 3.2813 | 7.25E+02 | 4.69E+00 | 1.06E+01 | 3.28E+00 | 2.16E+02 |
| 4.7917 | 6.81E+00 | 3.3542 | 7.25E+02 | 4.79E+00 | 6.42E+00 | 3.35E+00 | 2.16E+02 |
| 4.8958 | 5.22E+00 | 3.4271 | 7.14E+02 | 4.90E+00 | 4.60E+00 | 3.43E+00 | 2.16E+02 |
| 5 | 5.25E+00 | 3.5 | 6.87E+02 | 5.00E+00 | 4.27E+00 | 3.50E+00 | 2.15E+02 |

## Sample N10

Table B-36 Surface tensile stress and strain profiles for sample N10, step 50%YS.

| **Hardened Layer** | | | | **Soft Bulk** | | | |
|---|---|---|---|---|---|---|---|
| Longitudinal | | Transverse | | Longitudinal | | Transverse | |
| Length | Stress | Length | Stress | Length | Stress | Length | Stress |
| 0.00E+00 | 2.48E+00 | 0.00E+00 | 3.86E+02 | 0.00E+00 | 1.85E+00 | 0.00E+00 | 2.06E+02 |
| 1.04E-01 | 2.63E+00 | 7.29E-02 | 3.99E+02 | 1.04E-01 | 2.66E+00 | 7.29E-02 | 2.06E+02 |
| 2.08E-01 | 5.30E+00 | 1.46E-01 | 4.03E+02 | 2.08E-01 | 5.41E+00 | 1.46E-01 | 2.07E+02 |
| 3.13E-01 | 1.13E+01 | 2.19E-01 | 4.02E+02 | 3.13E-01 | 1.01E+01 | 2.19E-01 | 2.07E+02 |
| 4.17E-01 | 2.14E+01 | 2.92E-01 | 3.99E+02 | 4.17E-01 | 1.74E+01 | 2.92E-01 | 2.07E+02 |
| 5.21E-01 | 4.13E+01 | 3.65E-01 | 3.96E+02 | 5.21E-01 | 2.76E+01 | 3.65E-01 | 2.07E+02 |
| 6.25E-01 | 1.42E+02 | 4.38E-01 | 3.92E+02 | 6.25E-01 | 4.07E+01 | 4.38E-01 | 2.07E+02 |

| | | | | | | | |
|---|---|---|---|---|---|---|---|
| 7.29E-01 | 2.50E+02 | 5.10E-01 | 3.89E+02 | 7.29E-01 | 1.84E+02 | 5.10E-01 | 2.07E+02 |
| 8.33E-01 | 8.65E+01 | 5.83E-01 | 3.86E+02 | 8.33E-01 | 1.37E+02 | 5.83E-01 | 2.07E+02 |
| 9.38E-01 | 1.80E+01 | 6.56E-01 | 3.85E+02 | 9.38E-01 | 3.85E+01 | 6.56E-01 | 2.07E+02 |
| 1.04E+00 | 1.42E+01 | 7.29E-01 | 3.83E+02 | 1.04E+00 | 1.90E+01 | 7.29E-01 | 2.07E+02 |
| 1.15E+00 | 3.80E+01 | 8.02E-01 | 3.82E+02 | 1.15E+00 | 3.47E+01 | 8.02E-01 | 2.07E+02 |
| 1.25E+00 | 6.07E+01 | 8.75E-01 | 3.82E+02 | 1.25E+00 | 5.53E+01 | 8.75E-01 | 2.07E+02 |
| 1.35E+00 | 8.37E+01 | 9.48E-01 | 3.82E+02 | 1.35E+00 | 7.66E+01 | 9.48E-01 | 2.07E+02 |
| 1.46E+00 | 1.08E+02 | 1.02E+00 | 3.82E+02 | 1.46E+00 | 9.88E+01 | 1.02E+00 | 2.07E+02 |
| 1.56E+00 | 1.33E+02 | 1.09E+00 | 3.82E+02 | 1.56E+00 | 1.22E+02 | 1.09E+00 | 2.07E+02 |
| 1.67E+00 | 1.60E+02 | 1.17E+00 | 3.82E+02 | 1.67E+00 | 1.47E+02 | 1.17E+00 | 2.07E+02 |
| 1.77E+00 | 1.88E+02 | 1.24E+00 | 3.83E+02 | 1.77E+00 | 1.72E+02 | 1.24E+00 | 2.07E+02 |
| 1.88E+00 | 2.20E+02 | 1.31E+00 | 3.83E+02 | 1.88E+00 | 1.91E+02 | 1.31E+00 | 2.07E+02 |
| 1.98E+00 | 2.61E+02 | 1.39E+00 | 3.84E+02 | 1.98E+00 | 1.96E+02 | 1.39E+00 | 2.07E+02 |
| 2.08E+00 | 3.03E+02 | 1.46E+00 | 3.84E+02 | 2.08E+00 | 2.00E+02 | 1.46E+00 | 2.07E+02 |
| 2.19E+00 | 3.38E+02 | 1.53E+00 | 3.84E+02 | 2.19E+00 | 2.03E+02 | 1.53E+00 | 2.07E+02 |
| 2.29E+00 | 3.63E+02 | 1.60E+00 | 3.84E+02 | 2.29E+00 | 2.06E+02 | 1.60E+00 | 2.07E+02 |
| 2.40E+00 | 3.79E+02 | 1.68E+00 | 3.85E+02 | 2.40E+00 | 2.07E+02 | 1.68E+00 | 2.07E+02 |
| 2.50E+00 | 3.85E+02 | 1.75E+00 | 3.85E+02 | 2.50E+00 | 2.07E+02 | 1.75E+00 | 2.07E+02 |
| 2.60E+00 | 3.79E+02 | 1.82E+00 | 3.85E+02 | 2.60E+00 | 2.07E+02 | 1.82E+00 | 2.07E+02 |
| 2.71E+00 | 3.63E+02 | 1.90E+00 | 3.84E+02 | 2.71E+00 | 2.06E+02 | 1.90E+00 | 2.07E+02 |
| 2.81E+00 | 3.38E+02 | 1.97E+00 | 3.84E+02 | 2.81E+00 | 2.03E+02 | 1.97E+00 | 2.07E+02 |
| 2.92E+00 | 3.03E+02 | 2.04E+00 | 3.84E+02 | 2.92E+00 | 2.00E+02 | 2.04E+00 | 2.07E+02 |
| 3.02E+00 | 2.61E+02 | 2.11E+00 | 3.84E+02 | 3.02E+00 | 1.96E+02 | 2.11E+00 | 2.07E+02 |
| 3.13E+00 | 2.20E+02 | 2.19E+00 | 3.83E+02 | 3.13E+00 | 1.91E+02 | 2.19E+00 | 2.07E+02 |
| 3.23E+00 | 1.88E+02 | 2.26E+00 | 3.83E+02 | 3.23E+00 | 1.72E+02 | 2.26E+00 | 2.07E+02 |
| 3.33E+00 | 1.60E+02 | 2.33E+00 | 3.82E+02 | 3.33E+00 | 1.47E+02 | 2.33E+00 | 2.07E+02 |
| 3.44E+00 | 1.33E+02 | 2.41E+00 | 3.82E+02 | 3.44E+00 | 1.22E+02 | 2.41E+00 | 2.07E+02 |
| 3.54E+00 | 1.08E+02 | 2.48E+00 | 3.82E+02 | 3.54E+00 | 9.88E+01 | 2.48E+00 | 2.07E+02 |
| 3.65E+00 | 8.36E+01 | 2.55E+00 | 3.82E+02 | 3.65E+00 | 7.65E+01 | 2.55E+00 | 2.07E+02 |
| 3.75E+00 | 6.05E+01 | 2.63E+00 | 3.82E+02 | 3.75E+00 | 5.52E+01 | 2.63E+00 | 2.07E+02 |
| 3.85E+00 | 3.78E+01 | 2.70E+00 | 3.82E+02 | 3.85E+00 | 3.46E+01 | 2.70E+00 | 2.07E+02 |
| 3.96E+00 | 1.40E+01 | 2.77E+00 | 3.83E+02 | 3.96E+00 | 1.91E+01 | 2.77E+00 | 2.07E+02 |
| 4.06E+00 | 1.83E+01 | 2.84E+00 | 3.84E+02 | 4.06E+00 | 3.77E+01 | 2.84E+00 | 2.07E+02 |
| 4.1667 | 8.49E+01 | 2.9167 | 3.86E+02 | 4.17E+00 | 1.28E+02 | 2.92E+00 | 2.07E+02 |
| 4.2708 | 3.06E+02 | 2.9896 | 3.89E+02 | 4.27E+00 | 1.78E+02 | 2.99E+00 | 2.07E+02 |
| 4.375 | 1.45E+02 | 3.0625 | 3.92E+02 | 4.38E+00 | 3.81E+01 | 3.06E+00 | 2.07E+02 |
| 4.4792 | 3.99E+01 | 3.1354 | 3.95E+02 | 4.48E+00 | 2.71E+01 | 3.14E+00 | 2.07E+02 |
| 4.5833 | 2.10E+01 | 3.2083 | 3.99E+02 | 4.58E+00 | 1.72E+01 | 3.21E+00 | 2.07E+02 |
| 4.6875 | 1.12E+01 | 3.2813 | 4.02E+02 | 4.69E+00 | 1.01E+01 | 3.28E+00 | 2.07E+02 |
| 4.7917 | 5.35E+00 | 3.3542 | 4.03E+02 | 4.79E+00 | 5.46E+00 | 3.35E+00 | 2.07E+02 |

| | | | | | | | |
|---|---|---|---|---|---|---|---|
| 4.8958 | 2.79E+00 | 3.4271 | 3.99E+02 | 4.90E+00 | 2.77E+00 | 3.43E+00 | 2.06E+02 |
| 5 | 2.64E+00 | 3.5 | 3.86E+02 | 5.00E+00 | 1.99E+00 | 3.50E+00 | 2.06E+02 |

Table 0-37 Surface tensile stress and strain profiles for sample N10, step 60%YS.

| **Hardened Layer** | | | | **Soft Bulk** | | | |
|---|---|---|---|---|---|---|---|
| Longitudinal | | Transverse | | Longitudinal | | Transverse | |
| Length | Stress | Length | Stress | Length | Stress | Length | Stress |
| 0.00E+00 | 3.34E+00 | 0.00E+00 | 4.64E+02 | 0.00E+00 | 2.58E+00 | 0.00E+00 | 2.10E+02 |
| 1.04E-01 | 3.45E+00 | 7.29E-02 | 4.82E+02 | 1.04E-01 | 3.34E+00 | 7.29E-02 | 2.10E+02 |
| 2.08E-01 | 6.15E+00 | 1.46E-01 | 4.89E+02 | 2.08E-01 | 6.20E+00 | 1.46E-01 | 2.11E+02 |
| 3.13E-01 | 1.26E+01 | 2.19E-01 | 4.88E+02 | 3.13E-01 | 1.14E+01 | 2.19E-01 | 2.11E+02 |
| 4.17E-01 | 2.39E+01 | 2.92E-01 | 4.85E+02 | 4.17E-01 | 1.95E+01 | 2.92E-01 | 2.11E+02 |
| 5.21E-01 | 4.64E+01 | 3.65E-01 | 4.80E+02 | 5.21E-01 | 3.17E+01 | 3.65E-01 | 2.11E+02 |
| 6.25E-01 | 1.51E+02 | 4.38E-01 | 4.76E+02 | 6.25E-01 | 4.47E+01 | 4.38E-01 | 2.11E+02 |
| 7.29E-01 | 3.28E+02 | 5.10E-01 | 4.72E+02 | 7.29E-01 | 1.86E+02 | 5.10E-01 | 2.11E+02 |
| 8.33E-01 | 9.71E+01 | 5.83E-01 | 4.69E+02 | 8.33E-01 | 1.63E+02 | 5.83E-01 | 2.11E+02 |
| 9.38E-01 | 2.96E+01 | 6.56E-01 | 4.67E+02 | 9.38E-01 | 4.99E+01 | 6.56E-01 | 2.11E+02 |
| 1.04E+00 | 1.02E+01 | 7.29E-01 | 4.65E+02 | 1.04E+00 | 2.08E+01 | 7.29E-01 | 2.11E+02 |
| 1.15E+00 | 3.72E+01 | 8.02E-01 | 4.64E+02 | 1.15E+00 | 3.46E+01 | 8.02E-01 | 2.11E+02 |
| 1.25E+00 | 6.25E+01 | 8.75E-01 | 4.64E+02 | 1.25E+00 | 5.71E+01 | 8.75E-01 | 2.11E+02 |
| 1.35E+00 | 8.81E+01 | 9.48E-01 | 4.64E+02 | 1.35E+00 | 8.06E+01 | 9.48E-01 | 2.11E+02 |
| 1.46E+00 | 1.15E+02 | 1.02E+00 | 4.64E+02 | 1.46E+00 | 1.05E+02 | 1.02E+00 | 2.11E+02 |
| 1.56E+00 | 1.43E+02 | 1.09E+00 | 4.64E+02 | 1.56E+00 | 1.31E+02 | 1.09E+00 | 2.11E+02 |
| 1.67E+00 | 1.73E+02 | 1.17E+00 | 4.65E+02 | 1.67E+00 | 1.58E+02 | 1.17E+00 | 2.11E+02 |
| 1.77E+00 | 2.06E+02 | 1.24E+00 | 4.65E+02 | 1.77E+00 | 1.85E+02 | 1.24E+00 | 2.11E+02 |
| 1.88E+00 | 2.54E+02 | 1.31E+00 | 4.66E+02 | 1.88E+00 | 1.95E+02 | 1.31E+00 | 2.11E+02 |
| 1.98E+00 | 3.12E+02 | 1.39E+00 | 4.67E+02 | 1.98E+00 | 2.01E+02 | 1.39E+00 | 2.11E+02 |
| 2.08E+00 | 3.64E+02 | 1.46E+00 | 4.67E+02 | 2.08E+00 | 2.05E+02 | 1.46E+00 | 2.11E+02 |
| 2.19E+00 | 4.07E+02 | 1.53E+00 | 4.67E+02 | 2.19E+00 | 2.09E+02 | 1.53E+00 | 2.11E+02 |
| 2.29E+00 | 4.41E+02 | 1.60E+00 | 4.68E+02 | 2.29E+00 | 2.10E+02 | 1.60E+00 | 2.11E+02 |
| 2.40E+00 | 4.61E+02 | 1.68E+00 | 4.68E+02 | 2.40E+00 | 2.11E+02 | 1.68E+00 | 2.11E+02 |
| 2.50E+00 | 4.68E+02 | 1.75E+00 | 4.68E+02 | 2.50E+00 | 2.11E+02 | 1.75E+00 | 2.11E+02 |
| 2.60E+00 | 4.61E+02 | 1.82E+00 | 4.68E+02 | 2.60E+00 | 2.11E+02 | 1.82E+00 | 2.11E+02 |
| 2.71E+00 | 4.41E+02 | 1.90E+00 | 4.68E+02 | 2.71E+00 | 2.10E+02 | 1.90E+00 | 2.11E+02 |
| 2.81E+00 | 4.07E+02 | 1.97E+00 | 4.67E+02 | 2.81E+00 | 2.09E+02 | 1.97E+00 | 2.11E+02 |
| 2.92E+00 | 3.64E+02 | 2.04E+00 | 4.67E+02 | 2.92E+00 | 2.05E+02 | 2.04E+00 | 2.11E+02 |
| 3.02E+00 | 3.12E+02 | 2.11E+00 | 4.66E+02 | 3.02E+00 | 2.01E+02 | 2.11E+00 | 2.11E+02 |
| 3.13E+00 | 2.54E+02 | 2.19E+00 | 4.66E+02 | 3.13E+00 | 1.95E+02 | 2.19E+00 | 2.11E+02 |
| 3.23E+00 | 2.06E+02 | 2.26E+00 | 4.65E+02 | 3.23E+00 | 1.85E+02 | 2.26E+00 | 2.11E+02 |

| | | | | | | | |
|---|---|---|---|---|---|---|---|
| 3.33E+00 | 1.73E+02 | 2.33E+00 | 4.65E+02 | 3.33E+00 | 1.58E+02 | 2.33E+00 | 2.11E+02 |
| 3.44E+00 | 1.43E+02 | 2.41E+00 | 4.64E+02 | 3.44E+00 | 1.31E+02 | 2.41E+00 | 2.11E+02 |
| 3.54E+00 | 1.15E+02 | 2.48E+00 | 4.64E+02 | 3.54E+00 | 1.05E+02 | 2.48E+00 | 2.11E+02 |
| 3.65E+00 | 8.79E+01 | 2.55E+00 | 4.63E+02 | 3.65E+00 | 8.05E+01 | 2.55E+00 | 2.11E+02 |
| 3.75E+00 | 6.23E+01 | 2.63E+00 | 4.63E+02 | 3.75E+00 | 5.69E+01 | 2.63E+00 | 2.11E+02 |
| 3.85E+00 | 3.69E+01 | 2.70E+00 | 4.64E+02 | 3.85E+00 | 3.45E+01 | 2.70E+00 | 2.11E+02 |
| 3.96E+00 | 1.01E+01 | 2.77E+00 | 4.65E+02 | 3.96E+00 | 2.10E+01 | 2.77E+00 | 2.11E+02 |
| 4.06E+00 | 2.91E+01 | 2.84E+00 | 4.66E+02 | 4.06E+00 | 4.84E+01 | 2.84E+00 | 2.11E+02 |
| 4.1667 | 9.59E+01 | 2.9167 | 4.69E+02 | 4.17E+00 | 1.54E+02 | 2.92E+00 | 2.11E+02 |
| 4.2708 | 3.18E+02 | 2.9896 | 4.72E+02 | 4.27E+00 | 1.88E+02 | 2.99E+00 | 2.11E+02 |
| 4.375 | 1.52E+02 | 3.0625 | 4.76E+02 | 4.38E+00 | 4.22E+01 | 3.06E+00 | 2.11E+02 |
| 4.4792 | 4.42E+01 | 3.1354 | 4.80E+02 | 4.48E+00 | 3.08E+01 | 3.14E+00 | 2.11E+02 |
| 4.5833 | 2.33E+01 | 3.2083 | 4.85E+02 | 4.58E+00 | 1.93E+01 | 3.21E+00 | 2.11E+02 |
| 4.6875 | 1.25E+01 | 3.2813 | 4.88E+02 | 4.69E+00 | 1.13E+01 | 3.28E+00 | 2.11E+02 |
| 4.7917 | 6.18E+00 | 3.3542 | 4.88E+02 | 4.79E+00 | 6.23E+00 | 3.35E+00 | 2.11E+02 |
| 4.8958 | 3.59E+00 | 3.4271 | 4.82E+02 | 4.90E+00 | 3.44E+00 | 3.43E+00 | 2.10E+02 |
| 5 | 3.46E+00 | 3.5 | 4.64E+02 | 5.00E+00 | 2.69E+00 | 3.50E+00 | 2.10E+02 |

Table B-38 Surface tensile stress and strain profiles for sample N10, step 70%YS.

| **Hardened Layer** | | | | **Soft Bulk** | | | |
|---|---|---|---|---|---|---|---|
| Longitudinal | | Transverse | | Longitudinal | | Transverse | |
| Length | Stress | Length | Stress | Length | Stress | Length | Stress |
| 0.00E+00 | 4.31E+00 | 0.00E+00 | 5.36E+02 | 0.00E+00 | 3.45E+00 | 0.00E+00 | 2.12E+02 |
| 1.04E-01 | 4.35E+00 | 7.29E-02 | 5.59E+02 | 1.04E-01 | 4.11E+00 | 7.29E-02 | 2.12E+02 |
| 2.08E-01 | 6.99E+00 | 1.46E-01 | 5.67E+02 | 2.08E-01 | 6.97E+00 | 1.46E-01 | 2.12E+02 |
| 3.13E-01 | 1.38E+01 | 2.19E-01 | 5.67E+02 | 3.13E-01 | 1.25E+01 | 2.19E-01 | 2.13E+02 |
| 4.17E-01 | 2.60E+01 | 2.92E-01 | 5.64E+02 | 4.17E-01 | 2.15E+01 | 2.92E-01 | 2.13E+02 |
| 5.21E-01 | 5.08E+01 | 3.65E-01 | 5.59E+02 | 5.21E-01 | 3.54E+01 | 3.65E-01 | 2.13E+02 |
| 6.25E-01 | 1.62E+02 | 4.38E-01 | 5.53E+02 | 6.25E-01 | 4.98E+01 | 4.38E-01 | 2.13E+02 |
| 7.29E-01 | 3.89E+02 | 5.10E-01 | 5.49E+02 | 7.29E-01 | 1.81E+02 | 5.10E-01 | 2.13E+02 |
| 8.33E-01 | 1.03E+02 | 5.83E-01 | 5.45E+02 | 8.33E-01 | 1.73E+02 | 5.83E-01 | 2.13E+02 |
| 9.38E-01 | 4.19E+01 | 6.56E-01 | 5.42E+02 | 9.38E-01 | 6.09E+01 | 6.56E-01 | 2.13E+02 |
| 1.04E+00 | 6.23E+00 | 7.29E-01 | 5.40E+02 | 1.04E+00 | 2.35E+01 | 7.29E-01 | 2.13E+02 |
| 1.15E+00 | 3.53E+01 | 8.02E-01 | 5.39E+02 | 1.15E+00 | 3.36E+01 | 8.02E-01 | 2.13E+02 |
| 1.25E+00 | 6.27E+01 | 8.75E-01 | 5.39E+02 | 1.25E+00 | 5.74E+01 | 8.75E-01 | 2.13E+02 |
| 1.35E+00 | 9.02E+01 | 9.48E-01 | 5.38E+02 | 1.35E+00 | 8.26E+01 | 9.48E-01 | 2.13E+02 |
| 1.46E+00 | 1.19E+02 | 1.02E+00 | 5.39E+02 | 1.46E+00 | 1.09E+02 | 1.02E+00 | 2.13E+02 |
| 1.56E+00 | 1.50E+02 | 1.09E+00 | 5.39E+02 | 1.56E+00 | 1.37E+02 | 1.09E+00 | 2.13E+02 |
| 1.67E+00 | 1.83E+02 | 1.17E+00 | 5.40E+02 | 1.67E+00 | 1.67E+02 | 1.17E+00 | 2.13E+02 |

| | | | | | | | |
|---|---|---|---|---|---|---|---|
| 1.77E+00 | 2.25E+02 | 1.24E+00 | 5.41E+02 | 1.77E+00 | 1.90E+02 | 1.24E+00 | 2.13E+02 |
| 1.88E+00 | 2.91E+02 | 1.31E+00 | 5.41E+02 | 1.88E+00 | 1.98E+02 | 1.31E+00 | 2.13E+02 |
| 1.98E+00 | 3.57E+02 | 1.39E+00 | 5.42E+02 | 1.98E+00 | 2.05E+02 | 1.39E+00 | 2.13E+02 |
| 2.08E+00 | 4.19E+02 | 1.46E+00 | 5.42E+02 | 2.08E+00 | 2.09E+02 | 1.46E+00 | 2.13E+02 |
| 2.19E+00 | 4.71E+02 | 1.53E+00 | 5.43E+02 | 2.19E+00 | 2.11E+02 | 1.53E+00 | 2.13E+02 |
| 2.29E+00 | 5.11E+02 | 1.60E+00 | 5.43E+02 | 2.29E+00 | 2.12E+02 | 1.60E+00 | 2.13E+02 |
| 2.40E+00 | 5.35E+02 | 1.68E+00 | 5.44E+02 | 2.40E+00 | 2.13E+02 | 1.68E+00 | 2.13E+02 |
| 2.50E+00 | 5.44E+02 | 1.75E+00 | 5.44E+02 | 2.50E+00 | 2.13E+02 | 1.75E+00 | 2.13E+02 |
| 2.60E+00 | 5.35E+02 | 1.82E+00 | 5.44E+02 | 2.60E+00 | 2.13E+02 | 1.82E+00 | 2.13E+02 |
| 2.71E+00 | 5.11E+02 | 1.90E+00 | 5.43E+02 | 2.71E+00 | 2.12E+02 | 1.90E+00 | 2.13E+02 |
| 2.81E+00 | 4.71E+02 | 1.97E+00 | 5.43E+02 | 2.81E+00 | 2.11E+02 | 1.97E+00 | 2.13E+02 |
| 2.92E+00 | 4.19E+02 | 2.04E+00 | 5.42E+02 | 2.92E+00 | 2.09E+02 | 2.04E+00 | 2.13E+02 |
| 3.02E+00 | 3.57E+02 | 2.11E+00 | 5.42E+02 | 3.02E+00 | 2.05E+02 | 2.11E+00 | 2.13E+02 |
| 3.13E+00 | 2.91E+02 | 2.19E+00 | 5.41E+02 | 3.13E+00 | 1.98E+02 | 2.19E+00 | 2.13E+02 |
| 3.23E+00 | 2.25E+02 | 2.26E+00 | 5.41E+02 | 3.23E+00 | 1.90E+02 | 2.26E+00 | 2.13E+02 |
| 3.33E+00 | 1.83E+02 | 2.33E+00 | 5.40E+02 | 3.33E+00 | 1.67E+02 | 2.33E+00 | 2.13E+02 |
| 3.44E+00 | 1.49E+02 | 2.41E+00 | 5.39E+02 | 3.44E+00 | 1.37E+02 | 2.41E+00 | 2.13E+02 |
| 3.54E+00 | 1.19E+02 | 2.48E+00 | 5.39E+02 | 3.54E+00 | 1.09E+02 | 2.48E+00 | 2.13E+02 |
| 3.65E+00 | 9.00E+01 | 2.55E+00 | 5.38E+02 | 3.65E+00 | 8.24E+01 | 2.55E+00 | 2.13E+02 |
| 3.75E+00 | 6.24E+01 | 2.63E+00 | 5.38E+02 | 3.75E+00 | 5.71E+01 | 2.63E+00 | 2.13E+02 |
| 3.85E+00 | 3.48E+01 | 2.70E+00 | 5.39E+02 | 3.85E+00 | 3.35E+01 | 2.70E+00 | 2.13E+02 |
| 3.96E+00 | 6.41E+00 | 2.77E+00 | 5.40E+02 | 3.96E+00 | 2.37E+01 | 2.77E+00 | 2.13E+02 |
| 4.06E+00 | 4.06E+01 | 2.84E+00 | 5.42E+02 | 4.06E+00 | 5.88E+01 | 2.84E+00 | 2.13E+02 |
| 4.1667 | 1.00E+02 | 2.9167 | 5.45E+02 | 4.17E+00 | 1.69E+02 | 2.92E+00 | 2.13E+02 |
| 4.2708 | 3.46E+02 | 2.9896 | 5.49E+02 | 4.27E+00 | 1.95E+02 | 2.99E+00 | 2.13E+02 |
| 4.375 | 1.62E+02 | 3.0625 | 5.53E+02 | 4.38E+00 | 4.67E+01 | 3.06E+00 | 2.13E+02 |
| 4.4792 | 4.80E+01 | 3.1354 | 5.58E+02 | 4.48E+00 | 3.43E+01 | 3.14E+00 | 2.13E+02 |
| 4.5833 | 2.53E+01 | 3.2083 | 5.63E+02 | 4.58E+00 | 2.11E+01 | 3.21E+00 | 2.13E+02 |
| 4.6875 | 1.36E+01 | 3.2813 | 5.67E+02 | 4.69E+00 | 1.24E+01 | 3.28E+00 | 2.13E+02 |
| 4.7917 | 7.00E+00 | 3.3542 | 5.67E+02 | 4.79E+00 | 6.98E+00 | 3.35E+00 | 2.12E+02 |
| 4.8958 | 4.45E+00 | 3.4271 | 5.59E+02 | 4.90E+00 | 4.18E+00 | 3.43E+00 | 2.12E+02 |
| 5 | 4.39E+00 | 3.5 | 5.36E+02 | 5.00E+00 | 3.53E+00 | 3.50E+00 | 2.12E+02 |

## Sample L-R-1

Table B-39 Surface tensile stress and strain profiles for sample L-R-1, step 50%YS.

| **Hardened Layer** | | | | **Soft Bulk** | | | |
|---|---|---|---|---|---|---|---|
| Longitudinal | | Transverse | | Longitudinal | | Transverse | |
| Length | Stress | Length | Stress | Length | Stress | Length | Stress |
| 0.00E+00 | 2.34E+00 | 0.00E+00 | 3.72E+02 | 0.00E+00 | 1.55E+00 | 0.00E+00 | 2.10E+02 |

| | | | | | | | |
|---|---|---|---|---|---|---|---|
| 1.04E-01 | 2.50E+00 | 7.29E-02 | 3.84E+02 | 1.04E-01 | 2.65E+00 | 7.29E-02 | 2.11E+02 |
| 2.08E-01 | 5.33E+00 | 1.46E-01 | 3.88E+02 | 2.08E-01 | 5.51E+00 | 1.46E-01 | 2.11E+02 |
| 3.13E-01 | 1.15E+01 | 2.19E-01 | 3.87E+02 | 3.13E-01 | 9.94E+00 | 2.19E-01 | 2.11E+02 |
| 4.17E-01 | 2.18E+01 | 2.92E-01 | 3.84E+02 | 4.17E-01 | 1.63E+01 | 2.92E-01 | 2.11E+02 |
| 5.21E-01 | 4.21E+01 | 3.65E-01 | 3.81E+02 | 5.21E-01 | 2.37E+01 | 3.65E-01 | 2.11E+02 |
| 6.25E-01 | 1.56E+02 | 4.38E-01 | 3.77E+02 | 6.25E-01 | 3.63E+01 | 4.38E-01 | 2.11E+02 |
| 7.29E-01 | 2.26E+02 | 5.10E-01 | 3.74E+02 | 7.29E-01 | 1.82E+02 | 5.10E-01 | 2.11E+02 |
| 8.33E-01 | 8.91E+01 | 5.83E-01 | 3.72E+02 | 8.33E-01 | 1.33E+02 | 5.83E-01 | 2.11E+02 |
| 9.38E-01 | 1.72E+01 | 6.56E-01 | 3.70E+02 | 9.38E-01 | 4.33E+01 | 6.56E-01 | 2.11E+02 |
| 1.04E+00 | 1.45E+01 | 7.29E-01 | 3.69E+02 | 1.04E+00 | 2.32E+01 | 7.29E-01 | 2.11E+02 |
| 1.15E+00 | 3.82E+01 | 8.02E-01 | 3.68E+02 | 1.15E+00 | 3.54E+01 | 8.02E-01 | 2.11E+02 |
| 1.25E+00 | 6.08E+01 | 8.75E-01 | 3.67E+02 | 1.25E+00 | 5.46E+01 | 8.75E-01 | 2.11E+02 |
| 1.35E+00 | 8.38E+01 | 9.48E-01 | 3.67E+02 | 1.35E+00 | 7.51E+01 | 9.48E-01 | 2.11E+02 |
| 1.46E+00 | 1.08E+02 | 1.02E+00 | 3.67E+02 | 1.46E+00 | 9.67E+01 | 1.02E+00 | 2.11E+02 |
| 1.56E+00 | 1.33E+02 | 1.09E+00 | 3.67E+02 | 1.56E+00 | 1.19E+02 | 1.09E+00 | 2.11E+02 |
| 1.67E+00 | 1.60E+02 | 1.17E+00 | 3.68E+02 | 1.67E+00 | 1.43E+02 | 1.17E+00 | 2.11E+02 |
| 1.77E+00 | 1.88E+02 | 1.24E+00 | 3.68E+02 | 1.77E+00 | 1.67E+02 | 1.24E+00 | 2.11E+02 |
| 1.88E+00 | 2.16E+02 | 1.31E+00 | 3.69E+02 | 1.88E+00 | 1.90E+02 | 1.31E+00 | 2.11E+02 |
| 1.98E+00 | 2.52E+02 | 1.39E+00 | 3.69E+02 | 1.98E+00 | 1.99E+02 | 1.39E+00 | 2.11E+02 |
| 2.08E+00 | 2.92E+02 | 1.46E+00 | 3.69E+02 | 2.08E+00 | 2.05E+02 | 1.46E+00 | 2.11E+02 |
| 2.19E+00 | 3.25E+02 | 1.53E+00 | 3.69E+02 | 2.19E+00 | 2.08E+02 | 1.53E+00 | 2.11E+02 |
| 2.29E+00 | 3.50E+02 | 1.60E+00 | 3.70E+02 | 2.29E+00 | 2.10E+02 | 1.60E+00 | 2.11E+02 |
| 2.40E+00 | 3.65E+02 | 1.68E+00 | 3.70E+02 | 2.40E+00 | 2.11E+02 | 1.68E+00 | 2.11E+02 |
| 2.50E+00 | 3.70E+02 | 1.75E+00 | 3.70E+02 | 2.50E+00 | 2.11E+02 | 1.75E+00 | 2.11E+02 |
| 2.60E+00 | 3.65E+02 | 1.82E+00 | 3.70E+02 | 2.60E+00 | 2.11E+02 | 1.82E+00 | 2.11E+02 |
| 2.71E+00 | 3.50E+02 | 1.90E+00 | 3.70E+02 | 2.71E+00 | 2.10E+02 | 1.90E+00 | 2.11E+02 |
| 2.81E+00 | 3.25E+02 | 1.97E+00 | 3.69E+02 | 2.81E+00 | 2.08E+02 | 1.97E+00 | 2.11E+02 |
| 2.92E+00 | 2.92E+02 | 2.04E+00 | 3.69E+02 | 2.92E+00 | 2.05E+02 | 2.04E+00 | 2.11E+02 |
| 3.02E+00 | 2.52E+02 | 2.11E+00 | 3.69E+02 | 3.02E+00 | 1.99E+02 | 2.11E+00 | 2.11E+02 |
| 3.13E+00 | 2.16E+02 | 2.19E+00 | 3.68E+02 | 3.13E+00 | 1.90E+02 | 2.19E+00 | 2.11E+02 |
| 3.23E+00 | 1.88E+02 | 2.26E+00 | 3.68E+02 | 3.23E+00 | 1.67E+02 | 2.26E+00 | 2.11E+02 |
| 3.33E+00 | 1.60E+02 | 2.33E+00 | 3.68E+02 | 3.33E+00 | 1.43E+02 | 2.33E+00 | 2.11E+02 |
| 3.44E+00 | 1.33E+02 | 2.41E+00 | 3.67E+02 | 3.44E+00 | 1.19E+02 | 2.41E+00 | 2.11E+02 |
| 3.54E+00 | 1.08E+02 | 2.48E+00 | 3.67E+02 | 3.54E+00 | 9.66E+01 | 2.48E+00 | 2.11E+02 |
| 3.65E+00 | 8.37E+01 | 2.55E+00 | 3.67E+02 | 3.65E+00 | 7.51E+01 | 2.55E+00 | 2.11E+02 |
| 3.75E+00 | 6.07E+01 | 2.63E+00 | 3.67E+02 | 3.75E+00 | 5.45E+01 | 2.63E+00 | 2.11E+02 |
| 3.85E+00 | 3.80E+01 | 2.70E+00 | 3.68E+02 | 3.85E+00 | 3.53E+01 | 2.70E+00 | 2.11E+02 |
| 3.96E+00 | 1.44E+01 | 2.77E+00 | 3.69E+02 | 3.96E+00 | 2.33E+01 | 2.77E+00 | 2.11E+02 |
| 4.06E+00 | 1.73E+01 | 2.84E+00 | 3.70E+02 | 4.06E+00 | 4.24E+01 | 2.84E+00 | 2.11E+02 |
| 4.1667 | 8.69E+01 | 2.9167 | 3.72E+02 | 4.17E+00 | 1.24E+02 | 2.92E+00 | 2.11E+02 |

| | | | | | | | |
|---|---|---|---|---|---|---|---|
| 4.2708 | 2.86E+02 | 2.9896 | 3.74E+02 | 4.27E+00 | 1.75E+02 | 2.99E+00 | 2.11E+02 |
| 4.375 | 1.62E+02 | 3.0625 | 3.77E+02 | 4.38E+00 | 3.29E+01 | 3.06E+00 | 2.11E+02 |
| 4.4792 | 4.08E+01 | 3.1354 | 3.80E+02 | 4.48E+00 | 2.33E+01 | 3.14E+00 | 2.11E+02 |
| 4.5833 | 2.15E+01 | 3.2083 | 3.84E+02 | 4.58E+00 | 1.62E+01 | 3.21E+00 | 2.11E+02 |
| 4.6875 | 1.14E+01 | 3.2813 | 3.87E+02 | 4.69E+00 | 9.93E+00 | 3.28E+00 | 2.11E+02 |
| 4.7917 | 5.39E+00 | 3.3542 | 3.88E+02 | 4.79E+00 | 5.56E+00 | 3.35E+00 | 2.11E+02 |
| 4.8958 | 2.66E+00 | 3.4271 | 3.84E+02 | 4.90E+00 | 2.76E+00 | 3.43E+00 | 2.11E+02 |
| 5 | 2.49E+00 | 3.5 | 3.72E+02 | 5.00E+00 | 1.69E+00 | 3.50E+00 | 2.10E+02 |

Table B-40 Surface tensile stress and strain profiles for sample L-R-1, step 60%YS.

| **Hardened Layer** | | | | **Soft Bulk** | | | |
|---|---|---|---|---|---|---|---|
| Longitudinal | | Transverse | | Longitudinal | | Transverse | |
| Length | Stress | Length | Stress | Length | Stress | Length | Stress |
| 0.00E+00 | 3.22E+00 | 0.00E+00 | 4.48E+02 | 0.00E+00 | 2.29E+00 | 0.00E+00 | 2.12E+02 |
| 1.04E-01 | 3.35E+00 | 7.29E-02 | 4.64E+02 | 1.04E-01 | 3.30E+00 | 7.29E-02 | 2.12E+02 |
| 2.08E-01 | 6.17E+00 | 1.46E-01 | 4.70E+02 | 2.08E-01 | 6.25E+00 | 1.46E-01 | 2.13E+02 |
| 3.13E-01 | 1.28E+01 | 2.19E-01 | 4.70E+02 | 3.13E-01 | 1.11E+01 | 2.19E-01 | 2.13E+02 |
| 4.17E-01 | 2.41E+01 | 2.92E-01 | 4.66E+02 | 4.17E-01 | 1.82E+01 | 2.92E-01 | 2.13E+02 |
| 5.21E-01 | 4.69E+01 | 3.65E-01 | 4.62E+02 | 5.21E-01 | 2.71E+01 | 3.65E-01 | 2.13E+02 |
| 6.25E-01 | 1.64E+02 | 4.38E-01 | 4.58E+02 | 6.25E-01 | 3.66E+01 | 4.38E-01 | 2.13E+02 |
| 7.29E-01 | 3.34E+02 | 5.10E-01 | 4.54E+02 | 7.29E-01 | 1.92E+02 | 5.10E-01 | 2.13E+02 |
| 8.33E-01 | 1.00E+02 | 5.83E-01 | 4.51E+02 | 8.33E-01 | 1.56E+02 | 5.83E-01 | 2.13E+02 |
| 9.38E-01 | 2.79E+01 | 6.56E-01 | 4.49E+02 | 9.38E-01 | 5.34E+01 | 6.56E-01 | 2.13E+02 |
| 1.04E+00 | 1.09E+01 | 7.29E-01 | 4.48E+02 | 1.04E+00 | 2.59E+01 | 7.29E-01 | 2.13E+02 |
| 1.15E+00 | 3.76E+01 | 8.02E-01 | 4.47E+02 | 1.15E+00 | 3.59E+01 | 8.02E-01 | 2.13E+02 |
| 1.25E+00 | 6.27E+01 | 8.75E-01 | 4.46E+02 | 1.25E+00 | 5.65E+01 | 8.75E-01 | 2.13E+02 |
| 1.35E+00 | 8.80E+01 | 9.48E-01 | 4.46E+02 | 1.35E+00 | 7.90E+01 | 9.48E-01 | 2.13E+02 |
| 1.46E+00 | 1.14E+02 | 1.02E+00 | 4.46E+02 | 1.46E+00 | 1.03E+02 | 1.02E+00 | 2.13E+02 |
| 1.56E+00 | 1.42E+02 | 1.09E+00 | 4.47E+02 | 1.56E+00 | 1.28E+02 | 1.09E+00 | 2.13E+02 |
| 1.67E+00 | 1.72E+02 | 1.17E+00 | 4.47E+02 | 1.67E+00 | 1.54E+02 | 1.17E+00 | 2.13E+02 |
| 1.77E+00 | 2.04E+02 | 1.24E+00 | 4.48E+02 | 1.77E+00 | 1.80E+02 | 1.24E+00 | 2.13E+02 |
| 1.88E+00 | 2.46E+02 | 1.31E+00 | 4.48E+02 | 1.88E+00 | 1.94E+02 | 1.31E+00 | 2.13E+02 |
| 1.98E+00 | 3.01E+02 | 1.39E+00 | 4.49E+02 | 1.98E+00 | 2.02E+02 | 1.39E+00 | 2.13E+02 |
| 2.08E+00 | 3.51E+02 | 1.46E+00 | 4.49E+02 | 2.08E+00 | 2.07E+02 | 1.46E+00 | 2.13E+02 |
| 2.19E+00 | 3.92E+02 | 1.53E+00 | 4.50E+02 | 2.19E+00 | 2.10E+02 | 1.53E+00 | 2.13E+02 |
| 2.29E+00 | 4.23E+02 | 1.60E+00 | 4.50E+02 | 2.29E+00 | 2.12E+02 | 1.60E+00 | 2.13E+02 |
| 2.40E+00 | 4.44E+02 | 1.68E+00 | 4.50E+02 | 2.40E+00 | 2.13E+02 | 1.68E+00 | 2.13E+02 |
| 2.50E+00 | 4.50E+02 | 1.75E+00 | 4.50E+02 | 2.50E+00 | 2.13E+02 | 1.75E+00 | 2.13E+02 |
| 2.60E+00 | 4.44E+02 | 1.82E+00 | 4.50E+02 | 2.60E+00 | 2.13E+02 | 1.82E+00 | 2.13E+02 |

| | | | | | | | |
|---|---|---|---|---|---|---|---|
| 2.71E+00 | 4.23E+02 | 1.90E+00 | 4.50E+02 | 2.71E+00 | 2.12E+02 | 1.90E+00 | 2.13E+02 |
| 2.81E+00 | 3.92E+02 | 1.97E+00 | 4.50E+02 | 2.81E+00 | 2.10E+02 | 1.97E+00 | 2.13E+02 |
| 2.92E+00 | 3.51E+02 | 2.04E+00 | 4.49E+02 | 2.92E+00 | 2.07E+02 | 2.04E+00 | 2.13E+02 |
| 3.02E+00 | 3.01E+02 | 2.11E+00 | 4.49E+02 | 3.02E+00 | 2.02E+02 | 2.11E+00 | 2.13E+02 |
| 3.13E+00 | 2.46E+02 | 2.19E+00 | 4.48E+02 | 3.13E+00 | 1.94E+02 | 2.19E+00 | 2.13E+02 |
| 3.23E+00 | 2.04E+02 | 2.26E+00 | 4.48E+02 | 3.23E+00 | 1.80E+02 | 2.26E+00 | 2.13E+02 |
| 3.33E+00 | 1.72E+02 | 2.33E+00 | 4.47E+02 | 3.33E+00 | 1.54E+02 | 2.33E+00 | 2.13E+02 |
| 3.44E+00 | 1.42E+02 | 2.41E+00 | 4.47E+02 | 3.44E+00 | 1.28E+02 | 2.41E+00 | 2.13E+02 |
| 3.54E+00 | 1.14E+02 | 2.48E+00 | 4.46E+02 | 3.54E+00 | 1.03E+02 | 2.48E+00 | 2.13E+02 |
| 3.65E+00 | 8.78E+01 | 2.55E+00 | 4.46E+02 | 3.65E+00 | 7.89E+01 | 2.55E+00 | 2.13E+02 |
| 3.75E+00 | 6.25E+01 | 2.63E+00 | 4.46E+02 | 3.75E+00 | 5.64E+01 | 2.63E+00 | 2.13E+02 |
| 3.85E+00 | 3.73E+01 | 2.70E+00 | 4.47E+02 | 3.85E+00 | 3.58E+01 | 2.70E+00 | 2.13E+02 |
| 3.96E+00 | 1.08E+01 | 2.77E+00 | 4.48E+02 | 3.96E+00 | 2.60E+01 | 2.77E+00 | 2.13E+02 |
| 4.06E+00 | 2.73E+01 | 2.84E+00 | 4.49E+02 | 4.06E+00 | 5.20E+01 | 2.84E+00 | 2.13E+02 |
| 4.1667 | 9.81E+01 | 2.9167 | 4.51E+02 | 4.17E+00 | 1.47E+02 | 2.92E+00 | 2.13E+02 |
| 4.2708 | 3.15E+02 | 2.9896 | 4.54E+02 | 4.27E+00 | 1.82E+02 | 2.99E+00 | 2.13E+02 |
| 4.375 | 1.67E+02 | 3.0625 | 4.58E+02 | 4.38E+00 | 3.37E+01 | 3.06E+00 | 2.13E+02 |
| 4.4792 | 4.50E+01 | 3.1354 | 4.62E+02 | 4.48E+00 | 2.65E+01 | 3.14E+00 | 2.13E+02 |
| 4.5833 | 2.37E+01 | 3.2083 | 4.66E+02 | 4.58E+00 | 1.80E+01 | 3.21E+00 | 2.13E+02 |
| 4.6875 | 1.27E+01 | 3.2813 | 4.70E+02 | 4.69E+00 | 1.11E+01 | 3.28E+00 | 2.13E+02 |
| 4.7917 | 6.23E+00 | 3.3542 | 4.70E+02 | 4.79E+00 | 6.31E+00 | 3.35E+00 | 2.13E+02 |
| 4.8958 | 3.52E+00 | 3.4271 | 4.64E+02 | 4.90E+00 | 3.42E+00 | 3.43E+00 | 2.12E+02 |
| 5 | 3.38E+00 | 3.5 | 4.48E+02 | 5.00E+00 | 2.43E+00 | 3.50E+00 | 2.12E+02 |

Table 0-41 Surface tensile stress and strain profiles for sample L-R-1, step 70%YS.

| **Hardened Layer** | | | | **Soft Bulk** | | | |
|---|---|---|---|---|---|---|---|
| Longitudinal | | Transverse | | Longitudinal | | Transverse | |
| Length | Stress | Length | Stress | Length | Stress | Length | Stress |
| 0.00E+00 | 4.06E+00 | 0.00E+00 | 5.14E+02 | 0.00E+00 | 3.00E+00 | 0.00E+00 | 2.14E+02 |
| 1.04E-01 | 4.15E+00 | 7.29E-02 | 5.35E+02 | 1.04E-01 | 3.94E+00 | 7.29E-02 | 2.14E+02 |
| 2.08E-01 | 6.96E+00 | 1.46E-01 | 5.43E+02 | 2.08E-01 | 6.96E+00 | 1.46E-01 | 2.15E+02 |
| 3.13E-01 | 1.39E+01 | 2.19E-01 | 5.43E+02 | 3.13E-01 | 1.21E+01 | 2.19E-01 | 2.15E+02 |
| 4.17E-01 | 2.62E+01 | 2.92E-01 | 5.39E+02 | 4.17E-01 | 1.99E+01 | 2.92E-01 | 2.15E+02 |
| 5.21E-01 | 5.11E+01 | 3.65E-01 | 5.35E+02 | 5.21E-01 | 3.03E+01 | 3.65E-01 | 2.15E+02 |
| 6.25E-01 | 1.78E+02 | 4.38E-01 | 5.30E+02 | 6.25E-01 | 3.83E+01 | 4.38E-01 | 2.15E+02 |
| 7.29E-01 | 3.95E+02 | 5.10E-01 | 5.25E+02 | 7.29E-01 | 1.90E+02 | 5.10E-01 | 2.15E+02 |
| 8.33E-01 | 1.07E+02 | 5.83E-01 | 5.22E+02 | 8.33E-01 | 1.67E+02 | 5.83E-01 | 2.15E+02 |
| 9.38E-01 | 3.90E+01 | 6.56E-01 | 5.19E+02 | 9.38E-01 | 6.30E+01 | 6.56E-01 | 2.15E+02 |
| 1.04E+00 | 7.10E+00 | 7.29E-01 | 5.17E+02 | 1.04E+00 | 2.89E+01 | 7.29E-01 | 2.15E+02 |

| | | | | | | | |
|---|---|---|---|---|---|---|---|
| 1.15E+00 | 3.59E+01 | 8.02E-01 | 5.16E+02 | 1.15E+00 | 3.56E+01 | 8.02E-01 | 2.15E+02 |
| 1.25E+00 | 6.30E+01 | 8.75E-01 | 5.15E+02 | 1.25E+00 | 5.71E+01 | 8.75E-01 | 2.15E+02 |
| 1.35E+00 | 9.02E+01 | 9.48E-01 | 5.15E+02 | 1.35E+00 | 8.11E+01 | 9.48E-01 | 2.15E+02 |
| 1.46E+00 | 1.19E+02 | 1.02E+00 | 5.16E+02 | 1.46E+00 | 1.06E+02 | 1.02E+00 | 2.15E+02 |
| 1.56E+00 | 1.49E+02 | 1.09E+00 | 5.16E+02 | 1.56E+00 | 1.33E+02 | 1.09E+00 | 2.15E+02 |
| 1.67E+00 | 1.81E+02 | 1.17E+00 | 5.17E+02 | 1.67E+00 | 1.62E+02 | 1.17E+00 | 2.15E+02 |
| 1.77E+00 | 2.20E+02 | 1.24E+00 | 5.17E+02 | 1.77E+00 | 1.89E+02 | 1.24E+00 | 2.15E+02 |
| 1.88E+00 | 2.79E+02 | 1.31E+00 | 5.18E+02 | 1.88E+00 | 1.99E+02 | 1.31E+00 | 2.15E+02 |
| 1.98E+00 | 3.43E+02 | 1.39E+00 | 5.19E+02 | 1.98E+00 | 2.05E+02 | 1.39E+00 | 2.15E+02 |
| 2.08E+00 | 4.02E+02 | 1.46E+00 | 5.19E+02 | 2.08E+00 | 2.11E+02 | 1.46E+00 | 2.15E+02 |
| 2.19E+00 | 4.51E+02 | 1.53E+00 | 5.20E+02 | 2.19E+00 | 2.13E+02 | 1.53E+00 | 2.15E+02 |
| 2.29E+00 | 4.89E+02 | 1.60E+00 | 5.20E+02 | 2.29E+00 | 2.14E+02 | 1.60E+00 | 2.15E+02 |
| 2.40E+00 | 5.13E+02 | 1.68E+00 | 5.20E+02 | 2.40E+00 | 2.15E+02 | 1.68E+00 | 2.15E+02 |
| 2.50E+00 | 5.20E+02 | 1.75E+00 | 5.20E+02 | 2.50E+00 | 2.15E+02 | 1.75E+00 | 2.15E+02 |
| 2.60E+00 | 5.13E+02 | 1.82E+00 | 5.20E+02 | 2.60E+00 | 2.15E+02 | 1.82E+00 | 2.15E+02 |
| 2.71E+00 | 4.89E+02 | 1.90E+00 | 5.20E+02 | 2.71E+00 | 2.14E+02 | 1.90E+00 | 2.15E+02 |
| 2.81E+00 | 4.51E+02 | 1.97E+00 | 5.20E+02 | 2.81E+00 | 2.13E+02 | 1.97E+00 | 2.15E+02 |
| 2.92E+00 | 4.02E+02 | 2.04E+00 | 5.19E+02 | 2.92E+00 | 2.11E+02 | 2.04E+00 | 2.15E+02 |
| 3.02E+00 | 3.43E+02 | 2.11E+00 | 5.19E+02 | 3.02E+00 | 2.05E+02 | 2.11E+00 | 2.15E+02 |
| 3.13E+00 | 2.79E+02 | 2.19E+00 | 5.18E+02 | 3.13E+00 | 1.98E+02 | 2.19E+00 | 2.15E+02 |
| 3.23E+00 | 2.20E+02 | 2.26E+00 | 5.17E+02 | 3.23E+00 | 1.89E+02 | 2.26E+00 | 2.15E+02 |
| 3.33E+00 | 1.81E+02 | 2.33E+00 | 5.17E+02 | 3.33E+00 | 1.62E+02 | 2.33E+00 | 2.15E+02 |
| 3.44E+00 | 1.49E+02 | 2.41E+00 | 5.16E+02 | 3.44E+00 | 1.33E+02 | 2.41E+00 | 2.15E+02 |
| 3.54E+00 | 1.19E+02 | 2.48E+00 | 5.16E+02 | 3.54E+00 | 1.06E+02 | 2.48E+00 | 2.15E+02 |
| 3.65E+00 | 9.00E+01 | 2.55E+00 | 5.15E+02 | 3.65E+00 | 8.09E+01 | 2.55E+00 | 2.15E+02 |
| 3.75E+00 | 6.27E+01 | 2.63E+00 | 5.15E+02 | 3.75E+00 | 5.69E+01 | 2.63E+00 | 2.15E+02 |
| 3.85E+00 | 3.55E+01 | 2.70E+00 | 5.16E+02 | 3.85E+00 | 3.55E+01 | 2.70E+00 | 2.15E+02 |
| 3.96E+00 | 7.24E+00 | 2.77E+00 | 5.17E+02 | 3.96E+00 | 2.91E+01 | 2.77E+00 | 2.15E+02 |
| 4.06E+00 | 3.78E+01 | 2.84E+00 | 5.19E+02 | 4.06E+00 | 6.12E+01 | 2.84E+00 | 2.15E+02 |
| 4.1667 | 1.03E+02 | 2.9167 | 5.22E+02 | 4.17E+00 | 1.63E+02 | 2.92E+00 | 2.15E+02 |
| 4.2708 | 3.40E+02 | 2.9896 | 5.25E+02 | 4.27E+00 | 1.88E+02 | 2.99E+00 | 2.15E+02 |
| 4.375 | 1.77E+02 | 3.0625 | 5.29E+02 | 4.38E+00 | 3.56E+01 | 3.06E+00 | 2.15E+02 |
| 4.4792 | 4.86E+01 | 3.1354 | 5.34E+02 | 4.48E+00 | 2.94E+01 | 3.14E+00 | 2.15E+02 |
| 4.5833 | 2.56E+01 | 3.2083 | 5.39E+02 | 4.58E+00 | 1.97E+01 | 3.21E+00 | 2.15E+02 |
| 4.6875 | 1.38E+01 | 3.2813 | 5.43E+02 | 4.69E+00 | 1.21E+01 | 3.28E+00 | 2.15E+02 |
| 4.7917 | 7.01E+00 | 3.3542 | 5.43E+02 | 4.79E+00 | 7.00E+00 | 3.35E+00 | 2.15E+02 |
| 4.8958 | 4.31E+00 | 3.4271 | 5.35E+02 | 4.90E+00 | 4.06E+00 | 3.43E+00 | 2.14E+02 |
| 5 | 4.21E+00 | 3.5 | 5.14E+02 | 5.00E+00 | 3.14E+00 | 3.50E+00 | 2.14E+02 |

Table B-42 Surface tensile stress and strain profiles for sample L-R-1, step 80%YS.

| **Hardened Layer** | | | | **Soft Bulk** | | | |
|---|---|---|---|---|---|---|---|
| Longitudinal | | Transverse | | Longitudinal | | Transverse | |
| Length | Stress | Length | Stress | Length | Stress | Length | Stress |
| 0.00E+00 | 5.20E+00 | 0.00E+00 | 5.86E+02 | 0.00E+00 | 4.02E+00 | 0.00E+00 | 2.16E+02 |
| 1.04E-01 | 5.19E+00 | 7.29E-02 | 6.11E+02 | 1.04E-01 | 4.80E+00 | 7.29E-02 | 2.16E+02 |
| 2.08E-01 | 7.89E+00 | 1.46E-01 | 6.22E+02 | 2.08E-01 | 7.77E+00 | 1.46E-01 | 2.16E+02 |
| 3.13E-01 | 1.51E+01 | 2.19E-01 | 6.22E+02 | 3.13E-01 | 1.32E+01 | 2.19E-01 | 2.17E+02 |
| 4.17E-01 | 2.82E+01 | 2.92E-01 | 6.19E+02 | 4.17E-01 | 2.16E+01 | 2.92E-01 | 2.17E+02 |
| 5.21E-01 | 5.50E+01 | 3.65E-01 | 6.13E+02 | 5.21E-01 | 3.34E+01 | 3.65E-01 | 2.17E+02 |
| 6.25E-01 | 1.90E+02 | 4.38E-01 | 6.08E+02 | 6.25E-01 | 4.00E+01 | 4.38E-01 | 2.17E+02 |
| 7.29E-01 | 3.84E+02 | 5.10E-01 | 6.02E+02 | 7.29E-01 | 1.85E+02 | 5.10E-01 | 2.17E+02 |
| 8.33E-01 | 1.10E+02 | 5.83E-01 | 5.98E+02 | 8.33E-01 | 1.77E+02 | 5.83E-01 | 2.17E+02 |
| 9.38E-01 | 4.91E+01 | 6.56E-01 | 5.95E+02 | 9.38E-01 | 7.13E+01 | 6.56E-01 | 2.17E+02 |
| 1.04E+00 | 5.66E+00 | 7.29E-01 | 5.93E+02 | 1.04E+00 | 3.21E+01 | 7.29E-01 | 2.17E+02 |
| 1.15E+00 | 3.52E+01 | 8.02E-01 | 5.92E+02 | 1.15E+00 | 3.62E+01 | 8.02E-01 | 2.17E+02 |
| 1.25E+00 | 6.41E+01 | 8.75E-01 | 5.91E+02 | 1.25E+00 | 5.84E+01 | 8.75E-01 | 2.17E+02 |
| 1.35E+00 | 9.30E+01 | 9.48E-01 | 5.91E+02 | 1.35E+00 | 8.38E+01 | 9.48E-01 | 2.17E+02 |
| 1.46E+00 | 1.23E+02 | 1.02E+00 | 5.91E+02 | 1.46E+00 | 1.11E+02 | 1.02E+00 | 2.17E+02 |
| 1.56E+00 | 1.56E+02 | 1.09E+00 | 5.91E+02 | 1.56E+00 | 1.39E+02 | 1.09E+00 | 2.17E+02 |
| 1.67E+00 | 1.91E+02 | 1.17E+00 | 5.92E+02 | 1.67E+00 | 1.70E+02 | 1.17E+00 | 2.17E+02 |
| 1.77E+00 | 2.41E+02 | 1.24E+00 | 5.93E+02 | 1.77E+00 | 1.93E+02 | 1.24E+00 | 2.17E+02 |
| 1.88E+00 | 3.16E+02 | 1.31E+00 | 5.93E+02 | 1.88E+00 | 2.02E+02 | 1.31E+00 | 2.17E+02 |
| 1.98E+00 | 3.90E+02 | 1.39E+00 | 5.94E+02 | 1.98E+00 | 2.09E+02 | 1.39E+00 | 2.17E+02 |
| 2.08E+00 | 4.59E+02 | 1.46E+00 | 5.95E+02 | 2.08E+00 | 2.13E+02 | 1.46E+00 | 2.17E+02 |
| 2.19E+00 | 5.17E+02 | 1.53E+00 | 5.95E+02 | 2.19E+00 | 2.15E+02 | 1.53E+00 | 2.17E+02 |
| 2.29E+00 | 5.60E+02 | 1.60E+00 | 5.96E+02 | 2.29E+00 | 2.16E+02 | 1.60E+00 | 2.17E+02 |
| 2.40E+00 | 5.87E+02 | 1.68E+00 | 5.96E+02 | 2.40E+00 | 2.17E+02 | 1.68E+00 | 2.17E+02 |
| 2.50E+00 | 5.96E+02 | 1.75E+00 | 5.96E+02 | 2.50E+00 | 2.17E+02 | 1.75E+00 | 2.17E+02 |
| 2.60E+00 | 5.87E+02 | 1.82E+00 | 5.96E+02 | 2.60E+00 | 2.17E+02 | 1.82E+00 | 2.17E+02 |
| 2.71E+00 | 5.60E+02 | 1.90E+00 | 5.96E+02 | 2.71E+00 | 2.16E+02 | 1.90E+00 | 2.17E+02 |
| 2.81E+00 | 5.17E+02 | 1.97E+00 | 5.95E+02 | 2.81E+00 | 2.15E+02 | 1.97E+00 | 2.17E+02 |
| 2.92E+00 | 4.59E+02 | 2.04E+00 | 5.95E+02 | 2.92E+00 | 2.13E+02 | 2.04E+00 | 2.17E+02 |
| 3.02E+00 | 3.90E+02 | 2.11E+00 | 5.94E+02 | 3.02E+00 | 2.09E+02 | 2.11E+00 | 2.17E+02 |
| 3.13E+00 | 3.16E+02 | 2.19E+00 | 5.93E+02 | 3.13E+00 | 2.02E+02 | 2.19E+00 | 2.17E+02 |
| 3.23E+00 | 2.41E+02 | 2.26E+00 | 5.93E+02 | 3.23E+00 | 1.93E+02 | 2.26E+00 | 2.17E+02 |
| 3.33E+00 | 1.91E+02 | 2.33E+00 | 5.92E+02 | 3.33E+00 | 1.70E+02 | 2.33E+00 | 2.17E+02 |
| 3.44E+00 | 1.56E+02 | 2.41E+00 | 5.91E+02 | 3.44E+00 | 1.39E+02 | 2.41E+00 | 2.17E+02 |

| | | | | | | | |
|---|---|---|---|---|---|---|---|
| 3.54E+00 | 1.23E+02 | 2.48E+00 | 5.91E+02 | 3.54E+00 | 1.11E+02 | 2.48E+00 | 2.17E+02 |
| 3.65E+00 | 9.29E+01 | 2.55E+00 | 5.90E+02 | 3.65E+00 | 8.36E+01 | 2.55E+00 | 2.17E+02 |
| 3.75E+00 | 6.38E+01 | 2.63E+00 | 5.91E+02 | 3.75E+00 | 5.82E+01 | 2.63E+00 | 2.17E+02 |
| 3.85E+00 | 3.47E+01 | 2.70E+00 | 5.91E+02 | 3.85E+00 | 3.61E+01 | 2.70E+00 | 2.17E+02 |
| 3.96E+00 | 6.15E+00 | 2.77E+00 | 5.93E+02 | 3.96E+00 | 3.24E+01 | 2.77E+00 | 2.17E+02 |
| 4.06E+00 | 4.70E+01 | 2.84E+00 | 5.95E+02 | 4.06E+00 | 6.93E+01 | 2.84E+00 | 2.17E+02 |
| 4.1667 | 9.70E+01 | 2.9167 | 5.98E+02 | 4.17E+00 | 1.71E+02 | 2.92E+00 | 2.17E+02 |
| 4.2708 | 3.62E+02 | 2.9896 | 6.02E+02 | 4.27E+00 | 1.93E+02 | 2.99E+00 | 2.17E+02 |
| 4.375 | 1.85E+02 | 3.0625 | 6.07E+02 | 4.38E+00 | 3.74E+01 | 3.06E+00 | 2.17E+02 |
| 4.4792 | 5.20E+01 | 3.1354 | 6.13E+02 | 4.48E+00 | 3.23E+01 | 3.14E+00 | 2.17E+02 |
| 4.5833 | 2.74E+01 | 3.2083 | 6.18E+02 | 4.58E+00 | 2.13E+01 | 3.21E+00 | 2.17E+02 |
| 4.6875 | 1.49E+01 | 3.2813 | 6.22E+02 | 4.69E+00 | 1.31E+01 | 3.28E+00 | 2.17E+02 |
| 4.7917 | 7.91E+00 | 3.3542 | 6.21E+02 | 4.79E+00 | 7.78E+00 | 3.35E+00 | 2.16E+02 |
| 4.8958 | 5.29E+00 | 3.4271 | 6.11E+02 | 4.90E+00 | 4.87E+00 | 3.43E+00 | 2.16E+02 |
| 5 | 5.28E+00 | 3.5 | 5.86E+02 | 5.00E+00 | 4.09E+00 | 3.50E+00 | 2.16E+02 |

## Sample L-R-3

Table 0-43 Surface tensile stress and strain profiles for sample L-R-3, step 50%YS.

| **Hardened Layer** | | | | **Soft Bulk** | | | |
|---|---|---|---|---|---|---|---|
| Longitudinal | | Transverse | | Longitudinal | | Transverse | |
| Length | Stress | Length | Stress | Length | Stress | Length | Stress |
| 0.00E+00 | 2.41E+00 | 0.00E+00 | 3.71E+02 | 0.00E+00 | 1.63E+00 | 0.00E+00 | 2.07E+02 |
| 1.04E-01 | 2.58E+00 | 7.29E-02 | 3.84E+02 | 1.04E-01 | 2.73E+00 | 7.29E-02 | 2.08E+02 |
| 2.08E-01 | 5.44E+00 | 1.46E-01 | 3.87E+02 | 2.08E-01 | 5.62E+00 | 1.46E-01 | 2.08E+02 |
| 3.13E-01 | 1.17E+01 | 2.19E-01 | 3.86E+02 | 3.13E-01 | 1.01E+01 | 2.19E-01 | 2.08E+02 |
| 4.17E-01 | 2.21E+01 | 2.92E-01 | 3.84E+02 | 4.17E-01 | 1.65E+01 | 2.92E-01 | 2.08E+02 |
| 5.21E-01 | 4.28E+01 | 3.65E-01 | 3.80E+02 | 5.21E-01 | 2.40E+01 | 3.65E-01 | 2.08E+02 |
| 6.25E-01 | 1.64E+02 | 4.38E-01 | 3.77E+02 | 6.25E-01 | 3.84E+01 | 4.38E-01 | 2.08E+02 |
| 7.29E-01 | 2.26E+02 | 5.10E-01 | 3.74E+02 | 7.29E-01 | 1.80E+02 | 5.10E-01 | 2.08E+02 |
| 8.33E-01 | 8.86E+01 | 5.83E-01 | 3.72E+02 | 8.33E-01 | 1.33E+02 | 5.83E-01 | 2.08E+02 |
| 9.38E-01 | 1.79E+01 | 6.56E-01 | 3.70E+02 | 9.38E-01 | 4.36E+01 | 6.56E-01 | 2.08E+02 |
| 1.04E+00 | 1.40E+01 | 7.29E-01 | 3.68E+02 | 1.04E+00 | 2.31E+01 | 7.29E-01 | 2.08E+02 |
| 1.15E+00 | 3.75E+01 | 8.02E-01 | 3.68E+02 | 1.15E+00 | 3.48E+01 | 8.02E-01 | 2.08E+02 |
| 1.25E+00 | 6.00E+01 | 8.75E-01 | 3.67E+02 | 1.25E+00 | 5.39E+01 | 8.75E-01 | 2.08E+02 |
| 1.35E+00 | 8.28E+01 | 9.48E-01 | 3.67E+02 | 1.35E+00 | 7.43E+01 | 9.48E-01 | 2.08E+02 |
| 1.46E+00 | 1.07E+02 | 1.02E+00 | 3.67E+02 | 1.46E+00 | 9.57E+01 | 1.02E+00 | 2.08E+02 |
| 1.56E+00 | 1.32E+02 | 1.09E+00 | 3.67E+02 | 1.56E+00 | 1.18E+02 | 1.09E+00 | 2.08E+02 |
| 1.67E+00 | 1.58E+02 | 1.17E+00 | 3.67E+02 | 1.67E+00 | 1.42E+02 | 1.17E+00 | 2.08E+02 |
| 1.77E+00 | 1.86E+02 | 1.24E+00 | 3.68E+02 | 1.77E+00 | 1.66E+02 | 1.24E+00 | 2.08E+02 |

| | | | | | | | |
|---|---|---|---|---|---|---|---|
| 1.88E+00 | 2.15E+02 | 1.31E+00 | 3.68E+02 | 1.88E+00 | 1.88E+02 | 1.31E+00 | 2.08E+02 |
| 1.98E+00 | 2.52E+02 | 1.39E+00 | 3.68E+02 | 1.98E+00 | 1.96E+02 | 1.39E+00 | 2.08E+02 |
| 2.08E+00 | 2.91E+02 | 1.46E+00 | 3.69E+02 | 2.08E+00 | 2.02E+02 | 1.46E+00 | 2.08E+02 |
| 2.19E+00 | 3.25E+02 | 1.53E+00 | 3.69E+02 | 2.19E+00 | 2.05E+02 | 1.53E+00 | 2.08E+02 |
| 2.29E+00 | 3.49E+02 | 1.60E+00 | 3.69E+02 | 2.29E+00 | 2.07E+02 | 1.60E+00 | 2.08E+02 |
| 2.40E+00 | 3.64E+02 | 1.68E+00 | 3.69E+02 | 2.40E+00 | 2.08E+02 | 1.68E+00 | 2.08E+02 |
| 2.50E+00 | 3.69E+02 | 1.75E+00 | 3.69E+02 | 2.50E+00 | 2.09E+02 | 1.75E+00 | 2.09E+02 |
| 2.60E+00 | 3.64E+02 | 1.82E+00 | 3.69E+02 | 2.60E+00 | 2.08E+02 | 1.82E+00 | 2.08E+02 |
| 2.71E+00 | 3.49E+02 | 1.90E+00 | 3.69E+02 | 2.71E+00 | 2.07E+02 | 1.90E+00 | 2.08E+02 |
| 2.81E+00 | 3.25E+02 | 1.97E+00 | 3.69E+02 | 2.81E+00 | 2.05E+02 | 1.97E+00 | 2.08E+02 |
| 2.92E+00 | 2.91E+02 | 2.04E+00 | 3.69E+02 | 2.92E+00 | 2.02E+02 | 2.04E+00 | 2.08E+02 |
| 3.02E+00 | 2.52E+02 | 2.11E+00 | 3.68E+02 | 3.02E+00 | 1.96E+02 | 2.11E+00 | 2.08E+02 |
| 3.13E+00 | 2.15E+02 | 2.19E+00 | 3.68E+02 | 3.13E+00 | 1.88E+02 | 2.19E+00 | 2.08E+02 |
| 3.23E+00 | 1.86E+02 | 2.26E+00 | 3.68E+02 | 3.23E+00 | 1.66E+02 | 2.26E+00 | 2.08E+02 |
| 3.33E+00 | 1.58E+02 | 2.33E+00 | 3.67E+02 | 3.33E+00 | 1.42E+02 | 2.33E+00 | 2.08E+02 |
| 3.44E+00 | 1.32E+02 | 2.41E+00 | 3.67E+02 | 3.44E+00 | 1.18E+02 | 2.41E+00 | 2.08E+02 |
| 3.54E+00 | 1.07E+02 | 2.48E+00 | 3.67E+02 | 3.54E+00 | 9.56E+01 | 2.48E+00 | 2.08E+02 |
| 3.65E+00 | 8.28E+01 | 2.55E+00 | 3.67E+02 | 3.65E+00 | 7.43E+01 | 2.55E+00 | 2.08E+02 |
| 3.75E+00 | 5.99E+01 | 2.63E+00 | 3.67E+02 | 3.75E+00 | 5.38E+01 | 2.63E+00 | 2.08E+02 |
| 3.85E+00 | 3.73E+01 | 2.70E+00 | 3.67E+02 | 3.85E+00 | 3.48E+01 | 2.70E+00 | 2.08E+02 |
| 3.96E+00 | 1.38E+01 | 2.77E+00 | 3.68E+02 | 3.96E+00 | 2.32E+01 | 2.77E+00 | 2.08E+02 |
| 4.06E+00 | 1.81E+01 | 2.84E+00 | 3.70E+02 | 4.06E+00 | 4.27E+01 | 2.84E+00 | 2.08E+02 |
| 4.1667 | 8.75E+01 | 2.9167 | 3.71E+02 | 4.17E+00 | 1.25E+02 | 2.92E+00 | 2.08E+02 |
| 4.2708 | 2.86E+02 | 2.9896 | 3.74E+02 | 4.27E+00 | 1.74E+02 | 2.99E+00 | 2.08E+02 |
| 4.375 | 1.76E+02 | 3.0625 | 3.77E+02 | 4.38E+00 | 3.53E+01 | 3.06E+00 | 2.08E+02 |
| 4.4792 | 4.17E+01 | 3.1354 | 3.80E+02 | 4.48E+00 | 2.36E+01 | 3.14E+00 | 2.08E+02 |
| 4.5833 | 2.19E+01 | 3.2083 | 3.83E+02 | 4.58E+00 | 1.64E+01 | 3.21E+00 | 2.08E+02 |
| 4.6875 | 1.17E+01 | 3.2813 | 3.86E+02 | 4.69E+00 | 1.01E+01 | 3.28E+00 | 2.08E+02 |
| 4.7917 | 5.50E+00 | 3.3542 | 3.87E+02 | 4.79E+00 | 5.66E+00 | 3.35E+00 | 2.08E+02 |
| 4.8958 | 2.74E+00 | 3.4271 | 3.83E+02 | 4.90E+00 | 2.83E+00 | 3.43E+00 | 2.08E+02 |
| 5 | 2.57E+00 | 3.5 | 3.71E+02 | 5.00E+00 | 1.77E+00 | 3.50E+00 | 2.07E+02 |

Table 0-44 Surface tensile stress and strain profiles for sample L-R-3, step 60%YS

| **Hardened Layer** | | | | **Soft Bulk** | | | |
|---|---|---|---|---|---|---|---|
| Longitudinal | | Transverse | | Longitudinal | | Transverse | |
| Length | Stress | Length | Stress | Length | Stress | Length | Stress |
| 0.00E+00 | 3.20E+00 | 0.00E+00 | 4.39E+02 | 0.00E+00 | 2.28E+00 | 0.00E+00 | 2.12E+02 |
| 1.04E-01 | 3.34E+00 | 7.29E-02 | 4.55E+02 | 1.04E-01 | 3.32E+00 | 7.29E-02 | 2.12E+02 |
| 2.08E-01 | 6.24E+00 | 1.46E-01 | 4.61E+02 | 2.08E-01 | 6.34E+00 | 1.46E-01 | 2.12E+02 |

| | | | | | | | |
|---|---|---|---|---|---|---|---|
| 3.13E-01 | 1.30E+01 | 2.19E-01 | 4.60E+02 | 3.13E-01 | 1.12E+01 | 2.19E-01 | 2.12E+02 |
| 4.17E-01 | 2.45E+01 | 2.92E-01 | 4.57E+02 | 4.17E-01 | 1.84E+01 | 2.92E-01 | 2.12E+02 |
| 5.21E-01 | 4.76E+01 | 3.65E-01 | 4.53E+02 | 5.21E-01 | 2.73E+01 | 3.65E-01 | 2.12E+02 |
| 6.25E-01 | 1.75E+02 | 4.38E-01 | 4.49E+02 | 6.25E-01 | 3.95E+01 | 4.38E-01 | 2.12E+02 |
| 7.29E-01 | 3.31E+02 | 5.10E-01 | 4.45E+02 | 7.29E-01 | 1.92E+02 | 5.10E-01 | 2.12E+02 |
| 8.33E-01 | 1.00E+02 | 5.83E-01 | 4.43E+02 | 8.33E-01 | 1.55E+02 | 5.83E-01 | 2.12E+02 |
| 9.38E-01 | 2.75E+01 | 6.56E-01 | 4.40E+02 | 9.38E-01 | 5.30E+01 | 6.56E-01 | 2.12E+02 |
| 1.04E+00 | 1.09E+01 | 7.29E-01 | 4.39E+02 | 1.04E+00 | 2.57E+01 | 7.29E-01 | 2.12E+02 |
| 1.15E+00 | 3.73E+01 | 8.02E-01 | 4.38E+02 | 1.15E+00 | 3.56E+01 | 8.02E-01 | 2.12E+02 |
| 1.25E+00 | 6.22E+01 | 8.75E-01 | 4.37E+02 | 1.25E+00 | 5.61E+01 | 8.75E-01 | 2.12E+02 |
| 1.35E+00 | 8.73E+01 | 9.48E-01 | 4.37E+02 | 1.35E+00 | 7.84E+01 | 9.48E-01 | 2.12E+02 |
| 1.46E+00 | 1.14E+02 | 1.02E+00 | 4.37E+02 | 1.46E+00 | 1.02E+02 | 1.02E+00 | 2.12E+02 |
| 1.56E+00 | 1.41E+02 | 1.09E+00 | 4.38E+02 | 1.56E+00 | 1.27E+02 | 1.09E+00 | 2.13E+02 |
| 1.67E+00 | 1.71E+02 | 1.17E+00 | 4.38E+02 | 1.67E+00 | 1.52E+02 | 1.17E+00 | 2.13E+02 |
| 1.77E+00 | 2.02E+02 | 1.24E+00 | 4.39E+02 | 1.77E+00 | 1.79E+02 | 1.24E+00 | 2.13E+02 |
| 1.88E+00 | 2.42E+02 | 1.31E+00 | 4.39E+02 | 1.88E+00 | 1.94E+02 | 1.31E+00 | 2.13E+02 |
| 1.98E+00 | 2.95E+02 | 1.39E+00 | 4.40E+02 | 1.98E+00 | 2.02E+02 | 1.39E+00 | 2.13E+02 |
| 2.08E+00 | 3.44E+02 | 1.46E+00 | 4.40E+02 | 2.08E+00 | 2.06E+02 | 1.46E+00 | 2.13E+02 |
| 2.19E+00 | 3.85E+02 | 1.53E+00 | 4.41E+02 | 2.19E+00 | 2.10E+02 | 1.53E+00 | 2.13E+02 |
| 2.29E+00 | 4.15E+02 | 1.60E+00 | 4.41E+02 | 2.29E+00 | 2.12E+02 | 1.60E+00 | 2.13E+02 |
| 2.40E+00 | 4.35E+02 | 1.68E+00 | 4.41E+02 | 2.40E+00 | 2.13E+02 | 1.68E+00 | 2.13E+02 |
| 2.50E+00 | 4.41E+02 | 1.75E+00 | 4.41E+02 | 2.50E+00 | 2.13E+02 | 1.75E+00 | 2.13E+02 |
| 2.60E+00 | 4.35E+02 | 1.82E+00 | 4.41E+02 | 2.60E+00 | 2.13E+02 | 1.82E+00 | 2.13E+02 |
| 2.71E+00 | 4.15E+02 | 1.90E+00 | 4.41E+02 | 2.71E+00 | 2.12E+02 | 1.90E+00 | 2.13E+02 |
| 2.81E+00 | 3.85E+02 | 1.97E+00 | 4.41E+02 | 2.81E+00 | 2.10E+02 | 1.97E+00 | 2.13E+02 |
| 2.92E+00 | 3.44E+02 | 2.04E+00 | 4.40E+02 | 2.92E+00 | 2.06E+02 | 2.04E+00 | 2.13E+02 |
| 3.02E+00 | 2.95E+02 | 2.11E+00 | 4.40E+02 | 3.02E+00 | 2.02E+02 | 2.11E+00 | 2.13E+02 |
| 3.13E+00 | 2.42E+02 | 2.19E+00 | 4.39E+02 | 3.13E+00 | 1.94E+02 | 2.19E+00 | 2.13E+02 |
| 3.23E+00 | 2.02E+02 | 2.26E+00 | 4.39E+02 | 3.23E+00 | 1.79E+02 | 2.26E+00 | 2.13E+02 |
| 3.33E+00 | 1.71E+02 | 2.33E+00 | 4.38E+02 | 3.33E+00 | 1.52E+02 | 2.33E+00 | 2.13E+02 |
| 3.44E+00 | 1.41E+02 | 2.41E+00 | 4.38E+02 | 3.44E+00 | 1.27E+02 | 2.41E+00 | 2.13E+02 |
| 3.54E+00 | 1.13E+02 | 2.48E+00 | 4.37E+02 | 3.54E+00 | 1.02E+02 | 2.48E+00 | 2.12E+02 |
| 3.65E+00 | 8.72E+01 | 2.55E+00 | 4.37E+02 | 3.65E+00 | 7.83E+01 | 2.55E+00 | 2.12E+02 |
| 3.75E+00 | 6.20E+01 | 2.63E+00 | 4.37E+02 | 3.75E+00 | 5.60E+01 | 2.63E+00 | 2.12E+02 |
| 3.85E+00 | 3.71E+01 | 2.70E+00 | 4.38E+02 | 3.85E+00 | 3.55E+01 | 2.70E+00 | 2.12E+02 |
| 3.96E+00 | 1.08E+01 | 2.77E+00 | 4.39E+02 | 3.96E+00 | 2.58E+01 | 2.77E+00 | 2.12E+02 |
| 4.06E+00 | 2.70E+01 | 2.84E+00 | 4.40E+02 | 4.06E+00 | 5.16E+01 | 2.84E+00 | 2.12E+02 |
| 4.1667 | 9.85E+01 | 2.9167 | 4.42E+02 | 4.17E+00 | 1.46E+02 | 2.92E+00 | 2.12E+02 |
| 4.2708 | 3.13E+02 | 2.9896 | 4.45E+02 | 4.27E+00 | 1.82E+02 | 2.99E+00 | 2.12E+02 |
| 4.375 | 1.84E+02 | 3.0625 | 4.49E+02 | 4.38E+00 | 3.68E+01 | 3.06E+00 | 2.12E+02 |

| | | | | | | | |
|---|---|---|---|---|---|---|---|
| 4.4792 | 4.59E+01 | 3.1354 | 4.53E+02 | 4.48E+00 | 2.67E+01 | 3.14E+00 | 2.12E+02 |
| 4.5833 | 2.41E+01 | 3.2083 | 4.57E+02 | 4.58E+00 | 1.82E+01 | 3.21E+00 | 2.12E+02 |
| 4.6875 | 1.29E+01 | 3.2813 | 4.60E+02 | 4.69E+00 | 1.12E+01 | 3.28E+00 | 2.12E+02 |
| 4.7917 | 6.31E+00 | 3.3542 | 4.61E+02 | 4.79E+00 | 6.40E+00 | 3.35E+00 | 2.12E+02 |
| 4.8958 | 3.51E+00 | 3.4271 | 4.55E+02 | 4.90E+00 | 3.44E+00 | 3.43E+00 | 2.12E+02 |
| 5 | 3.37E+00 | 3.5 | 4.39E+02 | 5.00E+00 | 2.43E+00 | 3.50E+00 | 2.12E+02 |

Table B-45 Surface tensile stress and strain profiles for sample L-R-3, step 70%YS.

| **Hardened Layer** | | | | **Soft Bulk** | | | |
|---|---|---|---|---|---|---|---|
| Longitudinal | | Transverse | | Longitudinal | | Transverse | |
| Length | Stress | Length | Stress | Length | Stress | Length | Stress |
| 0.00E+00 | 4.18E+00 | 0.00E+00 | 5.14E+02 | 0.00E+00 | 3.11E+00 | 0.00E+00 | 2.14E+02 |
| 1.04E-01 | 4.26E+00 | 7.29E-02 | 5.35E+02 | 1.04E-01 | 4.06E+00 | 7.29E-02 | 2.14E+02 |
| 2.08E-01 | 7.15E+00 | 1.46E-01 | 5.43E+02 | 2.08E-01 | 7.16E+00 | 1.46E-01 | 2.15E+02 |
| 3.13E-01 | 1.43E+01 | 2.19E-01 | 5.43E+02 | 3.13E-01 | 1.25E+01 | 2.19E-01 | 2.15E+02 |
| 4.17E-01 | 2.70E+01 | 2.92E-01 | 5.40E+02 | 4.17E-01 | 2.04E+01 | 2.92E-01 | 2.15E+02 |
| 5.21E-01 | 5.26E+01 | 3.65E-01 | 5.35E+02 | 5.21E-01 | 3.10E+01 | 3.65E-01 | 2.15E+02 |
| 6.25E-01 | 1.91E+02 | 4.38E-01 | 5.30E+02 | 6.25E-01 | 4.14E+01 | 4.38E-01 | 2.15E+02 |
| 7.29E-01 | 3.99E+02 | 5.10E-01 | 5.26E+02 | 7.29E-01 | 1.90E+02 | 5.10E-01 | 2.15E+02 |
| 8.33E-01 | 1.08E+02 | 5.83E-01 | 5.22E+02 | 8.33E-01 | 1.68E+02 | 5.83E-01 | 2.15E+02 |
| 9.38E-01 | 4.00E+01 | 6.56E-01 | 5.19E+02 | 9.38E-01 | 6.39E+01 | 6.56E-01 | 2.15E+02 |
| 1.04E+00 | 6.72E+00 | 7.29E-01 | 5.17E+02 | 1.04E+00 | 2.91E+01 | 7.29E-01 | 2.15E+02 |
| 1.15E+00 | 3.55E+01 | 8.02E-01 | 5.16E+02 | 1.15E+00 | 3.54E+01 | 8.02E-01 | 2.15E+02 |
| 1.25E+00 | 6.27E+01 | 8.75E-01 | 5.16E+02 | 1.25E+00 | 5.69E+01 | 8.75E-01 | 2.15E+02 |
| 1.35E+00 | 9.00E+01 | 9.48E-01 | 5.15E+02 | 1.35E+00 | 8.09E+01 | 9.48E-01 | 2.15E+02 |
| 1.46E+00 | 1.18E+02 | 1.02E+00 | 5.16E+02 | 1.46E+00 | 1.06E+02 | 1.02E+00 | 2.15E+02 |
| 1.56E+00 | 1.49E+02 | 1.09E+00 | 5.16E+02 | 1.56E+00 | 1.33E+02 | 1.09E+00 | 2.15E+02 |
| 1.67E+00 | 1.81E+02 | 1.17E+00 | 5.17E+02 | 1.67E+00 | 1.62E+02 | 1.17E+00 | 2.15E+02 |
| 1.77E+00 | 2.20E+02 | 1.24E+00 | 5.17E+02 | 1.77E+00 | 1.89E+02 | 1.24E+00 | 2.15E+02 |
| 1.88E+00 | 2.78E+02 | 1.31E+00 | 5.18E+02 | 1.88E+00 | 1.98E+02 | 1.31E+00 | 2.15E+02 |
| 1.98E+00 | 3.43E+02 | 1.39E+00 | 5.19E+02 | 1.98E+00 | 2.05E+02 | 1.39E+00 | 2.15E+02 |
| 2.08E+00 | 4.02E+02 | 1.46E+00 | 5.19E+02 | 2.08E+00 | 2.11E+02 | 1.46E+00 | 2.15E+02 |
| 2.19E+00 | 4.51E+02 | 1.53E+00 | 5.20E+02 | 2.19E+00 | 2.13E+02 | 1.53E+00 | 2.15E+02 |
| 2.29E+00 | 4.89E+02 | 1.60E+00 | 5.20E+02 | 2.29E+00 | 2.14E+02 | 1.60E+00 | 2.15E+02 |
| 2.40E+00 | 5.12E+02 | 1.68E+00 | 5.20E+02 | 2.40E+00 | 2.15E+02 | 1.68E+00 | 2.15E+02 |
| 2.50E+00 | 5.20E+02 | 1.75E+00 | 5.20E+02 | 2.50E+00 | 2.15E+02 | 1.75E+00 | 2.15E+02 |
| 2.60E+00 | 5.12E+02 | 1.82E+00 | 5.20E+02 | 2.60E+00 | 2.15E+02 | 1.82E+00 | 2.15E+02 |
| 2.71E+00 | 4.89E+02 | 1.90E+00 | 5.20E+02 | 2.71E+00 | 2.14E+02 | 1.90E+00 | 2.15E+02 |
| 2.81E+00 | 4.51E+02 | 1.97E+00 | 5.20E+02 | 2.81E+00 | 2.13E+02 | 1.97E+00 | 2.15E+02 |

| | | | | | | | |
|---|---|---|---|---|---|---|---|
| 2.92E+00 | 4.02E+02 | 2.04E+00 | 5.19E+02 | 2.92E+00 | 2.11E+02 | 2.04E+00 | 2.15E+02 |
| 3.02E+00 | 3.43E+02 | 2.11E+00 | 5.19E+02 | 3.02E+00 | 2.05E+02 | 2.11E+00 | 2.15E+02 |
| 3.13E+00 | 2.78E+02 | 2.19E+00 | 5.18E+02 | 3.13E+00 | 1.98E+02 | 2.19E+00 | 2.15E+02 |
| 3.23E+00 | 2.20E+02 | 2.26E+00 | 5.17E+02 | 3.23E+00 | 1.89E+02 | 2.26E+00 | 2.15E+02 |
| 3.33E+00 | 1.81E+02 | 2.33E+00 | 5.17E+02 | 3.33E+00 | 1.62E+02 | 2.33E+00 | 2.15E+02 |
| 3.44E+00 | 1.49E+02 | 2.41E+00 | 5.16E+02 | 3.44E+00 | 1.33E+02 | 2.41E+00 | 2.15E+02 |
| 3.54E+00 | 1.18E+02 | 2.48E+00 | 5.16E+02 | 3.54E+00 | 1.06E+02 | 2.48E+00 | 2.15E+02 |
| 3.65E+00 | 8.98E+01 | 2.55E+00 | 5.15E+02 | 3.65E+00 | 8.08E+01 | 2.55E+00 | 2.15E+02 |
| 3.75E+00 | 6.24E+01 | 2.63E+00 | 5.15E+02 | 3.75E+00 | 5.67E+01 | 2.63E+00 | 2.15E+02 |
| 3.85E+00 | 3.51E+01 | 2.70E+00 | 5.16E+02 | 3.85E+00 | 3.53E+01 | 2.70E+00 | 2.15E+02 |
| 3.96E+00 | 6.94E+00 | 2.77E+00 | 5.17E+02 | 3.96E+00 | 2.93E+01 | 2.77E+00 | 2.15E+02 |
| 4.06E+00 | 3.88E+01 | 2.84E+00 | 5.19E+02 | 4.06E+00 | 6.21E+01 | 2.84E+00 | 2.15E+02 |
| 4.1667 | 1.05E+02 | 2.9167 | 5.22E+02 | 4.17E+00 | 1.64E+02 | 2.92E+00 | 2.15E+02 |
| 4.2708 | 3.41E+02 | 2.9896 | 5.25E+02 | 4.27E+00 | 1.88E+02 | 2.99E+00 | 2.15E+02 |
| 4.375 | 1.94E+02 | 3.0625 | 5.30E+02 | 4.38E+00 | 3.90E+01 | 3.06E+00 | 2.15E+02 |
| 4.4792 | 5.03E+01 | 3.1354 | 5.35E+02 | 4.48E+00 | 3.01E+01 | 3.14E+00 | 2.15E+02 |
| 4.5833 | 2.64E+01 | 3.2083 | 5.40E+02 | 4.58E+00 | 2.02E+01 | 3.21E+00 | 2.15E+02 |
| 4.6875 | 1.42E+01 | 3.2813 | 5.43E+02 | 4.69E+00 | 1.24E+01 | 3.28E+00 | 2.15E+02 |
| 4.7917 | 7.24E+00 | 3.3542 | 5.43E+02 | 4.79E+00 | 7.23E+00 | 3.35E+00 | 2.15E+02 |
| 4.8958 | 4.46E+00 | 3.4271 | 5.35E+02 | 4.90E+00 | 4.21E+00 | 3.43E+00 | 2.14E+02 |
| 5 | 4.36E+00 | 3.5 | 5.14E+02 | 5.00E+00 | 3.28E+00 | 3.50E+00 | 2.14E+02 |

Table 0-46 Surface tensile stress and strain profiles for sample L-R-3, step 80%YS.

| **Hardened Layer** | | | | **Soft Bulk** | | | |
|---|---|---|---|---|---|---|---|
| Longitudinal | | Transverse | | Longitudinal | | Transverse | |
| Length | Stress | Length | Stress | Length | Stress | Length | Stress |
| 0.00E+00 | 5.33E+00 | 0.00E+00 | 5.88E+02 | 0.00E+00 | 4.14E+00 | 0.00E+00 | 2.16E+02 |
| 1.04E-01 | 5.32E+00 | 7.29E-02 | 6.13E+02 | 1.04E-01 | 4.94E+00 | 7.29E-02 | 2.16E+02 |
| 2.08E-01 | 8.12E+00 | 1.46E-01 | 6.23E+02 | 2.08E-01 | 8.00E+00 | 1.46E-01 | 2.16E+02 |
| 3.13E-01 | 1.56E+01 | 2.19E-01 | 6.24E+02 | 3.13E-01 | 1.36E+01 | 2.19E-01 | 2.17E+02 |
| 4.17E-01 | 2.90E+01 | 2.92E-01 | 6.20E+02 | 4.17E-01 | 2.22E+01 | 2.92E-01 | 2.17E+02 |
| 5.21E-01 | 5.68E+01 | 3.65E-01 | 6.15E+02 | 5.21E-01 | 3.42E+01 | 3.65E-01 | 2.17E+02 |
| 6.25E-01 | 2.04E+02 | 4.38E-01 | 6.09E+02 | 6.25E-01 | 4.29E+01 | 4.38E-01 | 2.17E+02 |
| 7.29E-01 | 3.86E+02 | 5.10E-01 | 6.04E+02 | 7.29E-01 | 1.86E+02 | 5.10E-01 | 2.17E+02 |
| 8.33E-01 | 1.10E+02 | 5.83E-01 | 6.00E+02 | 8.33E-01 | 1.78E+02 | 5.83E-01 | 2.17E+02 |
| 9.38E-01 | 5.03E+01 | 6.56E-01 | 5.97E+02 | 9.38E-01 | 7.22E+01 | 6.56E-01 | 2.17E+02 |
| 1.04E+00 | 5.63E+00 | 7.29E-01 | 5.95E+02 | 1.04E+00 | 3.24E+01 | 7.29E-01 | 2.17E+02 |
| 1.15E+00 | 3.49E+01 | 8.02E-01 | 5.93E+02 | 1.15E+00 | 3.61E+01 | 8.02E-01 | 2.17E+02 |
| 1.25E+00 | 6.40E+01 | 8.75E-01 | 5.92E+02 | 1.25E+00 | 5.83E+01 | 8.75E-01 | 2.17E+02 |

| | | | | | | | |
|---|---|---|---|---|---|---|---|
| 1.35E+00 | 9.30E+01 | 9.48E-01 | 5.92E+02 | 1.35E+00 | 8.37E+01 | 9.48E-01 | 2.17E+02 |
| 1.46E+00 | 1.23E+02 | 1.02E+00 | 5.92E+02 | 1.46E+00 | 1.11E+02 | 1.02E+00 | 2.17E+02 |
| 1.56E+00 | 1.56E+02 | 1.09E+00 | 5.93E+02 | 1.56E+00 | 1.40E+02 | 1.09E+00 | 2.17E+02 |
| 1.67E+00 | 1.91E+02 | 1.17E+00 | 5.93E+02 | 1.67E+00 | 1.70E+02 | 1.17E+00 | 2.17E+02 |
| 1.77E+00 | 2.42E+02 | 1.24E+00 | 5.94E+02 | 1.77E+00 | 1.93E+02 | 1.24E+00 | 2.17E+02 |
| 1.88E+00 | 3.17E+02 | 1.31E+00 | 5.95E+02 | 1.88E+00 | 2.02E+02 | 1.31E+00 | 2.17E+02 |
| 1.98E+00 | 3.90E+02 | 1.39E+00 | 5.96E+02 | 1.98E+00 | 2.09E+02 | 1.39E+00 | 2.17E+02 |
| 2.08E+00 | 4.60E+02 | 1.46E+00 | 5.96E+02 | 2.08E+00 | 2.13E+02 | 1.46E+00 | 2.17E+02 |
| 2.19E+00 | 5.18E+02 | 1.53E+00 | 5.97E+02 | 2.19E+00 | 2.15E+02 | 1.53E+00 | 2.17E+02 |
| 2.29E+00 | 5.62E+02 | 1.60E+00 | 5.97E+02 | 2.29E+00 | 2.16E+02 | 1.60E+00 | 2.17E+02 |
| 2.40E+00 | 5.88E+02 | 1.68E+00 | 5.97E+02 | 2.40E+00 | 2.17E+02 | 1.68E+00 | 2.17E+02 |
| 2.50E+00 | 5.97E+02 | 1.75E+00 | 5.97E+02 | 2.50E+00 | 2.17E+02 | 1.75E+00 | 2.17E+02 |
| 2.60E+00 | 5.88E+02 | 1.82E+00 | 5.97E+02 | 2.60E+00 | 2.17E+02 | 1.82E+00 | 2.17E+02 |
| 2.71E+00 | 5.62E+02 | 1.90E+00 | 5.97E+02 | 2.71E+00 | 2.16E+02 | 1.90E+00 | 2.17E+02 |
| 2.81E+00 | 5.18E+02 | 1.97E+00 | 5.97E+02 | 2.81E+00 | 2.15E+02 | 1.97E+00 | 2.17E+02 |
| 2.92E+00 | 4.60E+02 | 2.04E+00 | 5.96E+02 | 2.92E+00 | 2.13E+02 | 2.04E+00 | 2.17E+02 |
| 3.02E+00 | 3.90E+02 | 2.11E+00 | 5.95E+02 | 3.02E+00 | 2.09E+02 | 2.11E+00 | 2.17E+02 |
| 3.13E+00 | 3.17E+02 | 2.19E+00 | 5.95E+02 | 3.13E+00 | 2.02E+02 | 2.19E+00 | 2.17E+02 |
| 3.23E+00 | 2.42E+02 | 2.26E+00 | 5.94E+02 | 3.23E+00 | 1.93E+02 | 2.26E+00 | 2.17E+02 |
| 3.33E+00 | 1.91E+02 | 2.33E+00 | 5.93E+02 | 3.33E+00 | 1.70E+02 | 2.33E+00 | 2.17E+02 |
| 3.44E+00 | 1.56E+02 | 2.41E+00 | 5.93E+02 | 3.44E+00 | 1.39E+02 | 2.41E+00 | 2.17E+02 |
| 3.54E+00 | 1.23E+02 | 2.48E+00 | 5.92E+02 | 3.54E+00 | 1.11E+02 | 2.48E+00 | 2.17E+02 |
| 3.65E+00 | 9.28E+01 | 2.55E+00 | 5.92E+02 | 3.65E+00 | 8.36E+01 | 2.55E+00 | 2.17E+02 |
| 3.75E+00 | 6.37E+01 | 2.63E+00 | 5.92E+02 | 3.75E+00 | 5.81E+01 | 2.63E+00 | 2.17E+02 |
| 3.85E+00 | 3.45E+01 | 2.70E+00 | 5.93E+02 | 3.85E+00 | 3.60E+01 | 2.70E+00 | 2.17E+02 |
| 3.96E+00 | 6.24E+00 | 2.77E+00 | 5.94E+02 | 3.96E+00 | 3.27E+01 | 2.77E+00 | 2.17E+02 |
| 4.06E+00 | 4.80E+01 | 2.84E+00 | 5.97E+02 | 4.06E+00 | 7.01E+01 | 2.84E+00 | 2.17E+02 |
| 4.1667 | 9.78E+01 | 2.9167 | 6.00E+02 | 4.17E+00 | 1.72E+02 | 2.92E+00 | 2.17E+02 |
| 4.2708 | 3.63E+02 | 2.9896 | 6.04E+02 | 4.27E+00 | 1.93E+02 | 2.99E+00 | 2.17E+02 |
| 4.375 | 2.02E+02 | 3.0625 | 6.09E+02 | 4.38E+00 | 4.06E+01 | 3.06E+00 | 2.17E+02 |
| 4.4792 | 5.38E+01 | 3.1354 | 6.15E+02 | 4.48E+00 | 3.31E+01 | 3.14E+00 | 2.17E+02 |
| 4.5833 | 2.83E+01 | 3.2083 | 6.20E+02 | 4.58E+00 | 2.19E+01 | 3.21E+00 | 2.17E+02 |
| 4.6875 | 1.54E+01 | 3.2813 | 6.24E+02 | 4.69E+00 | 1.35E+01 | 3.28E+00 | 2.17E+02 |
| 4.7917 | 8.19E+00 | 3.3542 | 6.23E+02 | 4.79E+00 | 8.05E+00 | 3.35E+00 | 2.16E+02 |
| 4.8958 | 5.48E+00 | 3.4271 | 6.13E+02 | 4.90E+00 | 5.07E+00 | 3.43E+00 | 2.16E+02 |
| 5 | 5.48E+00 | 3.5 | 5.87E+02 | 5.00E+00 | 4.27E+00 | 3.50E+00 | 2.16E+02 |

Sample L-R-6

Table 0-47 Surface tensile stress and strain profiles for sample L-R-6, step 60%YS.

| **Hardened Layer** | | | | **Soft Bulk** | | | |
|---|---|---|---|---|---|---|---|
| Longitudinal | | Transverse | | Longitudinal | | Transverse | |
| Length | Stress | Length | Stress | Length | Stress | Length | Stress |
| 0.00E+00 | 2.86E+00 | 0.00E+00 | 4.45E+02 | 0.00E+00 | 1.95E+00 | 0.00E+00 | 2.12E+02 |
| 1.04E-01 | 3.03E+00 | 7.29E-02 | 4.62E+02 | 1.04E-01 | 3.05E+00 | 7.29E-02 | 2.12E+02 |
| 2.08E-01 | 5.98E+00 | 1.46E-01 | 4.67E+02 | 2.08E-01 | 6.05E+00 | 1.46E-01 | 2.12E+02 |
| 3.13E-01 | 1.28E+01 | 2.19E-01 | 4.67E+02 | 3.13E-01 | 1.09E+01 | 2.19E-01 | 2.13E+02 |
| 4.17E-01 | 2.50E+01 | 2.92E-01 | 4.64E+02 | 4.17E-01 | 1.80E+01 | 2.92E-01 | 2.13E+02 |
| 5.21E-01 | 5.06E+01 | 3.65E-01 | 4.60E+02 | 5.21E-01 | 2.69E+01 | 3.65E-01 | 2.13E+02 |
| 6.25E-01 | 1.63E+02 | 4.38E-01 | 4.56E+02 | 6.25E-01 | 3.42E+01 | 4.38E-01 | 2.13E+02 |
| 7.29E-01 | 3.79E+02 | 5.10E-01 | 4.52E+02 | 7.29E-01 | 1.85E+02 | 5.10E-01 | 2.13E+02 |
| 8.33E-01 | 9.96E+01 | 5.83E-01 | 4.49E+02 | 8.33E-01 | 1.54E+02 | 5.83E-01 | 2.13E+02 |
| 9.38E-01 | 2.73E+01 | 6.56E-01 | 4.47E+02 | 9.38E-01 | 5.42E+01 | 6.56E-01 | 2.13E+02 |
| 1.04E+00 | 1.11E+01 | 7.29E-01 | 4.46E+02 | 1.04E+00 | 2.59E+01 | 7.29E-01 | 2.13E+02 |
| 1.15E+00 | 3.75E+01 | 8.02E-01 | 4.45E+02 | 1.15E+00 | 3.57E+01 | 8.02E-01 | 2.13E+02 |
| 1.25E+00 | 6.25E+01 | 8.75E-01 | 4.44E+02 | 1.25E+00 | 5.63E+01 | 8.75E-01 | 2.13E+02 |
| 1.35E+00 | 8.79E+01 | 9.48E-01 | 4.44E+02 | 1.35E+00 | 7.88E+01 | 9.48E-01 | 2.13E+02 |
| 1.46E+00 | 1.14E+02 | 1.02E+00 | 4.44E+02 | 1.46E+00 | 1.03E+02 | 1.02E+00 | 2.13E+02 |
| 1.56E+00 | 1.42E+02 | 1.09E+00 | 4.45E+02 | 1.56E+00 | 1.27E+02 | 1.09E+00 | 2.13E+02 |
| 1.67E+00 | 1.72E+02 | 1.17E+00 | 4.45E+02 | 1.67E+00 | 1.54E+02 | 1.17E+00 | 2.13E+02 |
| 1.77E+00 | 2.04E+02 | 1.24E+00 | 4.46E+02 | 1.77E+00 | 1.80E+02 | 1.24E+00 | 2.13E+02 |
| 1.88E+00 | 2.47E+02 | 1.31E+00 | 4.46E+02 | 1.88E+00 | 1.95E+02 | 1.31E+00 | 2.13E+02 |
| 1.98E+00 | 3.01E+02 | 1.39E+00 | 4.47E+02 | 1.98E+00 | 2.02E+02 | 1.39E+00 | 2.13E+02 |
| 2.08E+00 | 3.51E+02 | 1.46E+00 | 4.47E+02 | 2.08E+00 | 2.07E+02 | 1.46E+00 | 2.13E+02 |
| 2.19E+00 | 3.92E+02 | 1.53E+00 | 4.48E+02 | 2.19E+00 | 2.10E+02 | 1.53E+00 | 2.13E+02 |
| 2.29E+00 | 4.22E+02 | 1.60E+00 | 4.48E+02 | 2.29E+00 | 2.12E+02 | 1.60E+00 | 2.13E+02 |
| 2.40E+00 | 4.42E+02 | 1.68E+00 | 4.48E+02 | 2.40E+00 | 2.13E+02 | 1.68E+00 | 2.13E+02 |
| 2.50E+00 | 4.48E+02 | 1.75E+00 | 4.48E+02 | 2.50E+00 | 2.13E+02 | 1.75E+00 | 2.13E+02 |
| 2.60E+00 | 4.42E+02 | 1.82E+00 | 4.48E+02 | 2.60E+00 | 2.13E+02 | 1.82E+00 | 2.13E+02 |
| 2.71E+00 | 4.22E+02 | 1.90E+00 | 4.48E+02 | 2.71E+00 | 2.12E+02 | 1.90E+00 | 2.13E+02 |
| 2.81E+00 | 3.92E+02 | 1.97E+00 | 4.48E+02 | 2.81E+00 | 2.10E+02 | 1.97E+00 | 2.13E+02 |
| 2.92E+00 | 3.51E+02 | 2.04E+00 | 4.47E+02 | 2.92E+00 | 2.07E+02 | 2.04E+00 | 2.13E+02 |
| 3.02E+00 | 3.01E+02 | 2.11E+00 | 4.47E+02 | 3.02E+00 | 2.02E+02 | 2.11E+00 | 2.13E+02 |
| 3.13E+00 | 2.46E+02 | 2.19E+00 | 4.46E+02 | 3.13E+00 | 1.94E+02 | 2.19E+00 | 2.13E+02 |
| 3.23E+00 | 2.04E+02 | 2.26E+00 | 4.46E+02 | 3.23E+00 | 1.80E+02 | 2.26E+00 | 2.13E+02 |
| 3.33E+00 | 1.72E+02 | 2.33E+00 | 4.45E+02 | 3.33E+00 | 1.54E+02 | 2.33E+00 | 2.13E+02 |
| 3.44E+00 | 1.42E+02 | 2.41E+00 | 4.45E+02 | 3.44E+00 | 1.27E+02 | 2.41E+00 | 2.13E+02 |
| 3.54E+00 | 1.14E+02 | 2.48E+00 | 4.44E+02 | 3.54E+00 | 1.02E+02 | 2.48E+00 | 2.13E+02 |
| 3.65E+00 | 8.76E+01 | 2.55E+00 | 4.44E+02 | 3.65E+00 | 7.86E+01 | 2.55E+00 | 2.13E+02 |

| | | | | | | | |
|---|---|---|---|---|---|---|---|
| 3.75E+00 | 6.22E+01 | 2.63E+00 | 4.44E+02 | 3.75E+00 | 5.61E+01 | 2.63E+00 | 2.13E+02 |
| 3.85E+00 | 3.71E+01 | 2.70E+00 | 4.45E+02 | 3.85E+00 | 3.55E+01 | 2.70E+00 | 2.13E+02 |
| 3.96E+00 | 1.07E+01 | 2.77E+00 | 4.46E+02 | 3.96E+00 | 2.62E+01 | 2.77E+00 | 2.13E+02 |
| 4.06E+00 | 2.65E+01 | 2.84E+00 | 4.47E+02 | 4.06E+00 | 5.31E+01 | 2.84E+00 | 2.13E+02 |
| 4.1667 | 8.77E+01 | 2.9167 | 4.49E+02 | 4.17E+00 | 1.46E+02 | 2.92E+00 | 2.13E+02 |
| 4.2708 | 3.20E+02 | 2.9896 | 4.52E+02 | 4.27E+00 | 1.81E+02 | 2.99E+00 | 2.13E+02 |
| 4.375 | 1.71E+02 | 3.0625 | 4.56E+02 | 4.38E+00 | 3.38E+01 | 3.06E+00 | 2.13E+02 |
| 4.4792 | 4.61E+01 | 3.1354 | 4.60E+02 | 4.48E+00 | 2.64E+01 | 3.14E+00 | 2.13E+02 |
| 4.5833 | 2.42E+01 | 3.2083 | 4.64E+02 | 4.58E+00 | 1.80E+01 | 3.21E+00 | 2.13E+02 |
| 4.6875 | 1.29E+01 | 3.2813 | 4.67E+02 | 4.69E+00 | 1.11E+01 | 3.28E+00 | 2.13E+02 |
| 4.7917 | 6.30E+00 | 3.3542 | 4.67E+02 | 4.79E+00 | 6.30E+00 | 3.35E+00 | 2.12E+02 |
| 4.8958 | 3.55E+00 | 3.4271 | 4.62E+02 | 4.90E+00 | 3.42E+00 | 3.43E+00 | 2.12E+02 |
| 5 | 3.38E+00 | 3.5 | 4.45E+02 | 5.00E+00 | 2.43E+00 | 3.50E+00 | 2.12E+02 |

Table B-48 Surface tensile stress and strain profiles for sample L-R-6, step 70%YS.

| **Hardened Layer** | | | | **Soft Bulk** | | | |
|---|---|---|---|---|---|---|---|
| Longitudinal | | Transverse | | Longitudinal | | Transverse | |
| Length | Stress | Length | Stress | Length | Stress | Length | Stress |
| 0.00E+00 | 3.78E+00 | 0.00E+00 | 5.14E+02 | 0.00E+00 | 2.74E+00 | 0.00E+00 | 2.14E+02 |
| 1.04E-01 | 3.91E+00 | 7.29E-02 | 5.35E+02 | 1.04E-01 | 3.73E+00 | 7.29E-02 | 2.14E+02 |
| 2.08E-01 | 6.80E+00 | 1.46E-01 | 5.43E+02 | 2.08E-01 | 6.78E+00 | 1.46E-01 | 2.15E+02 |
| 3.13E-01 | 1.40E+01 | 2.19E-01 | 5.43E+02 | 3.13E-01 | 1.19E+01 | 2.19E-01 | 2.15E+02 |
| 4.17E-01 | 2.72E+01 | 2.92E-01 | 5.40E+02 | 4.17E-01 | 1.98E+01 | 2.92E-01 | 2.15E+02 |
| 5.21E-01 | 5.51E+01 | 3.65E-01 | 5.35E+02 | 5.21E-01 | 3.02E+01 | 3.65E-01 | 2.15E+02 |
| 6.25E-01 | 1.75E+02 | 4.38E-01 | 5.30E+02 | 6.25E-01 | 3.52E+01 | 4.38E-01 | 2.15E+02 |
| 7.29E-01 | 4.13E+02 | 5.10E-01 | 5.26E+02 | 7.29E-01 | 1.90E+02 | 5.10E-01 | 2.15E+02 |
| 8.33E-01 | 1.10E+02 | 5.83E-01 | 5.22E+02 | 8.33E-01 | 1.67E+02 | 5.83E-01 | 2.15E+02 |
| 9.38E-01 | 3.94E+01 | 6.56E-01 | 5.19E+02 | 9.38E-01 | 6.44E+01 | 6.56E-01 | 2.15E+02 |
| 1.04E+00 | 7.08E+00 | 7.29E-01 | 5.18E+02 | 1.04E+00 | 2.91E+01 | 7.29E-01 | 2.15E+02 |
| 1.15E+00 | 3.57E+01 | 8.02E-01 | 5.17E+02 | 1.15E+00 | 3.54E+01 | 8.02E-01 | 2.15E+02 |
| 1.25E+00 | 6.28E+01 | 8.75E-01 | 5.16E+02 | 1.25E+00 | 5.69E+01 | 8.75E-01 | 2.15E+02 |
| 1.35E+00 | 9.01E+01 | 9.48E-01 | 5.16E+02 | 1.35E+00 | 8.10E+01 | 9.48E-01 | 2.15E+02 |
| 1.46E+00 | 1.19E+02 | 1.02E+00 | 5.16E+02 | 1.46E+00 | 1.06E+02 | 1.02E+00 | 2.15E+02 |
| 1.56E+00 | 1.49E+02 | 1.09E+00 | 5.17E+02 | 1.56E+00 | 1.33E+02 | 1.09E+00 | 2.15E+02 |
| 1.67E+00 | 1.81E+02 | 1.17E+00 | 5.17E+02 | 1.67E+00 | 1.62E+02 | 1.17E+00 | 2.15E+02 |
| 1.77E+00 | 2.21E+02 | 1.24E+00 | 5.18E+02 | 1.77E+00 | 1.89E+02 | 1.24E+00 | 2.15E+02 |
| 1.88E+00 | 2.80E+02 | 1.31E+00 | 5.19E+02 | 1.88E+00 | 1.99E+02 | 1.31E+00 | 2.15E+02 |
| 1.98E+00 | 3.45E+02 | 1.39E+00 | 5.19E+02 | 1.98E+00 | 2.06E+02 | 1.39E+00 | 2.15E+02 |
| 2.08E+00 | 4.04E+02 | 1.46E+00 | 5.20E+02 | 2.08E+00 | 2.11E+02 | 1.46E+00 | 2.15E+02 |

| | | | | | | | |
|---|---|---|---|---|---|---|---|
| 2.19E+00 | 4.53E+02 | 1.53E+00 | 5.20E+02 | 2.19E+00 | 2.13E+02 | 1.53E+00 | 2.15E+02 |
| 2.29E+00 | 4.91E+02 | 1.60E+00 | 5.21E+02 | 2.29E+00 | 2.14E+02 | 1.60E+00 | 2.15E+02 |
| 2.40E+00 | 5.13E+02 | 1.68E+00 | 5.21E+02 | 2.40E+00 | 2.15E+02 | 1.68E+00 | 2.15E+02 |
| 2.50E+00 | 5.21E+02 | 1.75E+00 | 5.21E+02 | 2.50E+00 | 2.15E+02 | 1.75E+00 | 2.15E+02 |
| 2.60E+00 | 5.13E+02 | 1.82E+00 | 5.21E+02 | 2.60E+00 | 2.15E+02 | 1.82E+00 | 2.15E+02 |
| 2.71E+00 | 4.91E+02 | 1.90E+00 | 5.21E+02 | 2.71E+00 | 2.14E+02 | 1.90E+00 | 2.15E+02 |
| 2.81E+00 | 4.53E+02 | 1.97E+00 | 5.20E+02 | 2.81E+00 | 2.13E+02 | 1.97E+00 | 2.15E+02 |
| 2.92E+00 | 4.04E+02 | 2.04E+00 | 5.20E+02 | 2.92E+00 | 2.11E+02 | 2.04E+00 | 2.15E+02 |
| 3.02E+00 | 3.45E+02 | 2.11E+00 | 5.19E+02 | 3.02E+00 | 2.06E+02 | 2.11E+00 | 2.15E+02 |
| 3.13E+00 | 2.80E+02 | 2.19E+00 | 5.18E+02 | 3.13E+00 | 1.99E+02 | 2.19E+00 | 2.15E+02 |
| 3.23E+00 | 2.21E+02 | 2.26E+00 | 5.18E+02 | 3.23E+00 | 1.89E+02 | 2.26E+00 | 2.15E+02 |
| 3.33E+00 | 1.81E+02 | 2.33E+00 | 5.17E+02 | 3.33E+00 | 1.62E+02 | 2.33E+00 | 2.15E+02 |
| 3.44E+00 | 1.49E+02 | 2.41E+00 | 5.17E+02 | 3.44E+00 | 1.33E+02 | 2.41E+00 | 2.15E+02 |
| 3.54E+00 | 1.18E+02 | 2.48E+00 | 5.16E+02 | 3.54E+00 | 1.06E+02 | 2.48E+00 | 2.15E+02 |
| 3.65E+00 | 8.98E+01 | 2.55E+00 | 5.16E+02 | 3.65E+00 | 8.07E+01 | 2.55E+00 | 2.15E+02 |
| 3.75E+00 | 6.24E+01 | 2.63E+00 | 5.16E+02 | 3.75E+00 | 5.66E+01 | 2.63E+00 | 2.15E+02 |
| 3.85E+00 | 3.51E+01 | 2.70E+00 | 5.16E+02 | 3.85E+00 | 3.52E+01 | 2.70E+00 | 2.15E+02 |
| 3.96E+00 | 6.89E+00 | 2.77E+00 | 5.18E+02 | 3.96E+00 | 2.95E+01 | 2.77E+00 | 2.15E+02 |
| 4.06E+00 | 3.79E+01 | 2.84E+00 | 5.19E+02 | 4.06E+00 | 6.31E+01 | 2.84E+00 | 2.15E+02 |
| 4.1667 | 9.38E+01 | 2.9167 | 5.22E+02 | 4.17E+00 | 1.61E+02 | 2.92E+00 | 2.15E+02 |
| 4.2708 | 3.44E+02 | 2.9896 | 5.26E+02 | 4.27E+00 | 1.86E+02 | 2.99E+00 | 2.15E+02 |
| 4.375 | 1.80E+02 | 3.0625 | 5.30E+02 | 4.38E+00 | 3.52E+01 | 3.06E+00 | 2.15E+02 |
| 4.4792 | 5.01E+01 | 3.1354 | 5.35E+02 | 4.48E+00 | 2.96E+01 | 3.14E+00 | 2.15E+02 |
| 4.5833 | 2.63E+01 | 3.2083 | 5.39E+02 | 4.58E+00 | 1.98E+01 | 3.21E+00 | 2.15E+02 |
| 4.6875 | 1.41E+01 | 3.2813 | 5.43E+02 | 4.69E+00 | 1.21E+01 | 3.28E+00 | 2.15E+02 |
| 4.7917 | 7.15E+00 | 3.3542 | 5.43E+02 | 4.79E+00 | 7.06E+00 | 3.35E+00 | 2.15E+02 |
| 4.8958 | 4.43E+00 | 3.4271 | 5.35E+02 | 4.90E+00 | 4.13E+00 | 3.43E+00 | 2.14E+02 |
| 5 | 4.32E+00 | 3.5 | 5.14E+02 | 5.00E+00 | 3.22E+00 | 3.50E+00 | 2.14E+02 |

## B.3 Surface tensile strain profiles

### Sample N3

Table B-49 Surface tensile strain profiles for sample N3, step 39%YS.

| **Hardened Layer** | | | | **Soft Bulk** | | | |
|---|---|---|---|---|---|---|---|
| Longitudinal | | Transverse | | Longitudinal | | Transverse | |
| Length | Strain | Length | Strain | Length | Strain | Length | Strain |
| 0.00E+00 | 9.61E-06 | 0.00E+00 | 1.78E-03 | 0.00E+00 | 6.14E-06 | 0.00E+00 | 1.53E-03 |
| 1.04E-01 | 1.09E-05 | 7.29E-02 | 1.83E-03 | 1.04E-01 | 1.41E-05 | 7.29E-02 | 1.55E-03 |
| 2.08E-01 | 2.78E-05 | 1.46E-01 | 1.84E-03 | 2.08E-01 | 3.09E-05 | 1.46E-01 | 1.57E-03 |
| 3.13E-01 | 6.31E-05 | 2.19E-01 | 1.84E-03 | 3.13E-01 | 5.64E-05 | 2.19E-01 | 1.57E-03 |

| | | | | | | | |
|---|---|---|---|---|---|---|---|
| 4.17E-01 | 1.25E-04 | 2.92E-01 | 1.83E-03 | 4.17E-01 | 9.23E-05 | 2.92E-01 | 1.57E-03 |
| 5.21E-01 | 2.71E-04 | 3.65E-01 | 1.81E-03 | 5.21E-01 | 1.35E-04 | 3.65E-01 | 1.56E-03 |
| 6.25E-01 | 1.65E-03 | 4.38E-01 | 1.80E-03 | 6.25E-01 | 2.76E-04 | 4.38E-01 | 1.55E-03 |
| 7.29E-01 | 7.40E-03 | 5.10E-01 | 1.79E-03 | 7.29E-01 | 1.62E-03 | 5.10E-01 | 1.55E-03 |
| 8.33E-01 | 9.36E-04 | 5.83E-01 | 1.78E-03 | 8.33E-01 | 7.15E-04 | 5.83E-01 | 1.54E-03 |
| 9.38E-01 | 1.89E-04 | 6.56E-01 | 1.77E-03 | 9.38E-01 | 2.25E-04 | 6.56E-01 | 1.54E-03 |
| 1.04E+00 | 9.75E-05 | 7.29E-01 | 1.76E-03 | 1.04E+00 | 1.28E-04 | 7.29E-01 | 1.53E-03 |
| 1.15E+00 | 2.08E-04 | 8.02E-01 | 1.76E-03 | 1.15E+00 | 2.01E-04 | 8.02E-01 | 1.53E-03 |
| 1.25E+00 | 3.23E-04 | 8.75E-01 | 1.76E-03 | 1.25E+00 | 2.98E-04 | 8.75E-01 | 1.53E-03 |
| 1.35E+00 | 4.41E-04 | 9.48E-01 | 1.76E-03 | 1.35E+00 | 4.02E-04 | 9.48E-01 | 1.54E-03 |
| 1.46E+00 | 5.64E-04 | 1.02E+00 | 1.76E-03 | 1.46E+00 | 5.11E-04 | 1.02E+00 | 1.54E-03 |
| 1.56E+00 | 6.93E-04 | 1.09E+00 | 1.76E-03 | 1.56E+00 | 6.26E-04 | 1.09E+00 | 1.54E-03 |
| 1.67E+00 | 8.29E-04 | 1.17E+00 | 1.76E-03 | 1.67E+00 | 7.46E-04 | 1.17E+00 | 1.54E-03 |
| 1.77E+00 | 9.70E-04 | 1.24E+00 | 1.76E-03 | 1.77E+00 | 8.69E-04 | 1.24E+00 | 1.55E-03 |
| 1.88E+00 | 1.11E-03 | 1.31E+00 | 1.76E-03 | 1.88E+00 | 9.90E-04 | 1.31E+00 | 1.55E-03 |
| 1.98E+00 | 1.25E-03 | 1.39E+00 | 1.76E-03 | 1.98E+00 | 1.10E-03 | 1.39E+00 | 1.55E-03 |
| 2.08E+00 | 1.41E-03 | 1.46E+00 | 1.76E-03 | 2.08E+00 | 1.21E-03 | 1.46E+00 | 1.55E-03 |
| 2.19E+00 | 1.56E-03 | 1.53E+00 | 1.76E-03 | 2.19E+00 | 1.35E-03 | 1.53E+00 | 1.55E-03 |
| 2.29E+00 | 1.67E-03 | 1.60E+00 | 1.76E-03 | 2.29E+00 | 1.47E-03 | 1.60E+00 | 1.55E-03 |
| 2.40E+00 | 1.74E-03 | 1.68E+00 | 1.76E-03 | 2.40E+00 | 1.54E-03 | 1.68E+00 | 1.56E-03 |
| 2.50E+00 | 1.76E-03 | 1.75E+00 | 1.76E-03 | 2.50E+00 | 1.56E-03 | 1.75E+00 | 1.56E-03 |
| 2.60E+00 | 1.74E-03 | 1.82E+00 | 1.76E-03 | 2.60E+00 | 1.54E-03 | 1.82E+00 | 1.56E-03 |
| 2.71E+00 | 1.67E-03 | 1.90E+00 | 1.76E-03 | 2.71E+00 | 1.47E-03 | 1.90E+00 | 1.55E-03 |
| 2.81E+00 | 1.56E-03 | 1.97E+00 | 1.76E-03 | 2.81E+00 | 1.35E-03 | 1.97E+00 | 1.55E-03 |
| 2.92E+00 | 1.41E-03 | 2.04E+00 | 1.76E-03 | 2.92E+00 | 1.21E-03 | 2.04E+00 | 1.55E-03 |
| 3.02E+00 | 1.25E-03 | 2.11E+00 | 1.76E-03 | 3.02E+00 | 1.10E-03 | 2.11E+00 | 1.55E-03 |
| 3.13E+00 | 1.11E-03 | 2.19E+00 | 1.76E-03 | 3.13E+00 | 9.90E-04 | 2.19E+00 | 1.55E-03 |
| 3.23E+00 | 9.70E-04 | 2.26E+00 | 1.76E-03 | 3.23E+00 | 8.69E-04 | 2.26E+00 | 1.55E-03 |
| 3.33E+00 | 8.29E-04 | 2.33E+00 | 1.76E-03 | 3.33E+00 | 7.46E-04 | 2.33E+00 | 1.54E-03 |
| 3.44E+00 | 6.93E-04 | 2.41E+00 | 1.76E-03 | 3.44E+00 | 6.26E-04 | 2.41E+00 | 1.54E-03 |
| 3.54E+00 | 5.63E-04 | 2.48E+00 | 1.76E-03 | 3.54E+00 | 5.11E-04 | 2.48E+00 | 1.54E-03 |
| 3.65E+00 | 4.40E-04 | 2.55E+00 | 1.76E-03 | 3.65E+00 | 4.01E-04 | 2.55E+00 | 1.54E-03 |
| 3.75E+00 | 3.22E-04 | 2.63E+00 | 1.76E-03 | 3.75E+00 | 2.97E-04 | 2.63E+00 | 1.53E-03 |
| 3.85E+00 | 2.06E-04 | 2.70E+00 | 1.76E-03 | 3.85E+00 | 2.01E-04 | 2.70E+00 | 1.53E-03 |
| 3.96E+00 | 8.62E-05 | 2.77E+00 | 1.76E-03 | 3.96E+00 | 1.29E-04 | 2.77E+00 | 1.53E-03 |
| 4.06E+00 | 7.18E-05 | 2.84E+00 | 1.77E-03 | 4.06E+00 | 2.22E-04 | 2.84E+00 | 1.54E-03 |
| 4.1667 | 5.34E-04 | 2.9167 | 1.78E-03 | 4.17E+00 | 6.78E-04 | 2.92E+00 | 1.54E-03 |
| 4.2708 | 7.00E-03 | 2.9896 | 1.79E-03 | 4.27E+00 | 1.44E-03 | 2.99E+00 | 1.55E-03 |
| 4.375 | 1.48E-03 | 3.0625 | 1.80E-03 | 4.38E+00 | 2.69E-04 | 3.06E+00 | 1.55E-03 |
| 4.4792 | 2.65E-04 | 3.1354 | 1.81E-03 | 4.48E+00 | 1.34E-04 | 3.14E+00 | 1.56E-03 |
| 4.5833 | 1.23E-04 | 3.2083 | 1.83E-03 | 4.58E+00 | 9.30E-05 | 3.21E+00 | 1.57E-03 |

| | | | | | | | |
|---|---|---|---|---|---|---|---|
| 4.6875 | 6.34E-05 | 3.2813 | 1.84E-03 | 4.69E+00 | 5.73E-05 | 3.28E+00 | 1.57E-03 |
| 4.7917 | 2.91E-05 | 3.3542 | 1.84E-03 | 4.79E+00 | 3.19E-05 | 3.35E+00 | 1.57E-03 |
| 4.8958 | 1.31E-05 | 3.4271 | 1.83E-03 | 4.90E+00 | 1.55E-05 | 3.43E+00 | 1.55E-03 |
| 5 | 1.20E-05 | 3.5 | 1.78E-03 | 5.00E+00 | 8.18E-06 | 3.50E+00 | 1.52E-03 |

Table B-50 Surface tensile strain profiles for sample N3, step 47%YS.

| **Hardened Layer** | | | | **Soft Bulk** | | | |
|---|---|---|---|---|---|---|---|
| Longitudinal | | Transverse | | Longitudinal | | Transverse | |
| Length | Strain | Length | Strain | Length | Strain | Length | Strain |
| 0.00E+00 | 1.26E-05 | 0.00E+00 | 2.12E-03 | 0.00E+00 | 8.37E-06 | 0.00E+00 | 1.83E-03 |
| 1.04E-01 | 1.38E-05 | 7.29E-02 | 2.19E-03 | 1.04E-01 | 1.66E-05 | 7.29E-02 | 1.86E-03 |
| 2.08E-01 | 3.17E-05 | 1.46E-01 | 2.22E-03 | 2.08E-01 | 3.48E-05 | 1.46E-01 | 1.89E-03 |
| 3.13E-01 | 7.04E-05 | 2.19E-01 | 2.21E-03 | 3.13E-01 | 6.30E-05 | 2.19E-01 | 1.89E-03 |
| 4.17E-01 | 1.40E-04 | 2.92E-01 | 2.20E-03 | 4.17E-01 | 1.04E-04 | 2.92E-01 | 1.89E-03 |
| 5.21E-01 | 3.09E-04 | 3.65E-01 | 2.18E-03 | 5.21E-01 | 1.55E-04 | 3.65E-01 | 1.89E-03 |
| 6.25E-01 | 1.78E-03 | 4.38E-01 | 2.16E-03 | 6.25E-01 | 2.98E-04 | 4.38E-01 | 1.88E-03 |
| 7.29E-01 | 6.43E-03 | 5.10E-01 | 2.14E-03 | 7.29E-01 | 1.95E-03 | 5.10E-01 | 1.88E-03 |
| 8.33E-01 | 1.21E-03 | 5.83E-01 | 2.13E-03 | 8.33E-01 | 8.61E-04 | 5.83E-01 | 1.87E-03 |
| 9.38E-01 | 2.55E-04 | 6.56E-01 | 2.12E-03 | 9.38E-01 | 2.77E-04 | 6.56E-01 | 1.87E-03 |
| 1.04E+00 | 9.44E-05 | 7.29E-01 | 2.11E-03 | 1.04E+00 | 1.39E-04 | 7.29E-01 | 1.87E-03 |
| 1.15E+00 | 2.13E-04 | 8.02E-01 | 2.11E-03 | 1.15E+00 | 2.11E-04 | 8.02E-01 | 1.87E-03 |
| 1.25E+00 | 3.42E-04 | 8.75E-01 | 2.11E-03 | 1.25E+00 | 3.17E-04 | 8.75E-01 | 1.87E-03 |
| 1.35E+00 | 4.73E-04 | 9.48E-01 | 2.10E-03 | 1.35E+00 | 4.32E-04 | 9.48E-01 | 1.88E-03 |
| 1.46E+00 | 6.10E-04 | 1.02E+00 | 2.10E-03 | 1.46E+00 | 5.54E-04 | 1.02E+00 | 1.88E-03 |
| 1.56E+00 | 7.55E-04 | 1.09E+00 | 2.11E-03 | 1.56E+00 | 6.82E-04 | 1.09E+00 | 1.89E-03 |
| 1.67E+00 | 9.07E-04 | 1.17E+00 | 2.11E-03 | 1.67E+00 | 8.16E-04 | 1.17E+00 | 1.89E-03 |
| 1.77E+00 | 1.06E-03 | 1.24E+00 | 2.11E-03 | 1.77E+00 | 9.53E-04 | 1.24E+00 | 1.90E-03 |
| 1.88E+00 | 1.23E-03 | 1.31E+00 | 2.11E-03 | 1.88E+00 | 1.08E-03 | 1.31E+00 | 1.90E-03 |
| 1.98E+00 | 1.45E-03 | 1.39E+00 | 2.11E-03 | 1.98E+00 | 1.22E-03 | 1.39E+00 | 1.91E-03 |
| 2.08E+00 | 1.67E-03 | 1.46E+00 | 2.12E-03 | 2.08E+00 | 1.44E-03 | 1.46E+00 | 1.91E-03 |
| 2.19E+00 | 1.86E-03 | 1.53E+00 | 2.12E-03 | 2.19E+00 | 1.65E-03 | 1.53E+00 | 1.91E-03 |
| 2.29E+00 | 2.01E-03 | 1.60E+00 | 2.12E-03 | 2.29E+00 | 1.80E-03 | 1.60E+00 | 1.92E-03 |
| 2.40E+00 | 2.09E-03 | 1.68E+00 | 2.12E-03 | 2.40E+00 | 1.89E-03 | 1.68E+00 | 1.92E-03 |
| 2.50E+00 | 2.12E-03 | 1.75E+00 | 2.12E-03 | 2.50E+00 | 1.92E-03 | 1.75E+00 | 1.92E-03 |
| 2.60E+00 | 2.09E-03 | 1.82E+00 | 2.12E-03 | 2.60E+00 | 1.89E-03 | 1.82E+00 | 1.92E-03 |
| 2.71E+00 | 2.01E-03 | 1.90E+00 | 2.12E-03 | 2.71E+00 | 1.80E-03 | 1.90E+00 | 1.92E-03 |
| 2.81E+00 | 1.86E-03 | 1.97E+00 | 2.12E-03 | 2.81E+00 | 1.65E-03 | 1.97E+00 | 1.91E-03 |
| 2.92E+00 | 1.67E-03 | 2.04E+00 | 2.12E-03 | 2.92E+00 | 1.44E-03 | 2.04E+00 | 1.91E-03 |
| 3.02E+00 | 1.45E-03 | 2.11E+00 | 2.11E-03 | 3.02E+00 | 1.22E-03 | 2.11E+00 | 1.91E-03 |
| 3.13E+00 | 1.23E-03 | 2.19E+00 | 2.11E-03 | 3.13E+00 | 1.08E-03 | 2.19E+00 | 1.90E-03 |

| | | | | | | | |
|---|---|---|---|---|---|---|---|
| 3.23E+00 | 1.06E-03 | 2.26E+00 | 2.11E-03 | 3.23E+00 | 9.53E-04 | 2.26E+00 | 1.90E-03 |
| 3.33E+00 | 9.07E-04 | 2.33E+00 | 2.11E-03 | 3.33E+00 | 8.16E-04 | 2.33E+00 | 1.89E-03 |
| 3.44E+00 | 7.54E-04 | 2.41E+00 | 2.11E-03 | 3.44E+00 | 6.82E-04 | 2.41E+00 | 1.89E-03 |
| 3.54E+00 | 6.09E-04 | 2.48E+00 | 2.10E-03 | 3.54E+00 | 5.53E-04 | 2.48E+00 | 1.88E-03 |
| 3.65E+00 | 4.72E-04 | 2.55E+00 | 2.10E-03 | 3.65E+00 | 4.31E-04 | 2.55E+00 | 1.88E-03 |
| 3.75E+00 | 3.40E-04 | 2.63E+00 | 2.11E-03 | 3.75E+00 | 3.16E-04 | 2.63E+00 | 1.87E-03 |
| 3.85E+00 | 2.11E-04 | 2.70E+00 | 2.11E-03 | 3.85E+00 | 2.10E-04 | 2.70E+00 | 1.87E-03 |
| 3.96E+00 | 7.59E-05 | 2.77E+00 | 2.11E-03 | 3.96E+00 | 1.40E-04 | 2.77E+00 | 1.87E-03 |
| 4.06E+00 | 1.18E-04 | 2.84E+00 | 2.12E-03 | 4.06E+00 | 2.71E-04 | 2.84E+00 | 1.87E-03 |
| 4.1667 | 6.69E-04 | 2.9167 | 2.13E-03 | 4.17E+00 | 8.04E-04 | 2.92E+00 | 1.87E-03 |
| 4.2708 | 8.49E-03 | 2.9896 | 2.14E-03 | 4.27E+00 | 1.69E-03 | 2.99E+00 | 1.88E-03 |
| 4.375 | 1.51E-03 | 3.0625 | 2.16E-03 | 4.38E+00 | 2.90E-04 | 3.06E+00 | 1.88E-03 |
| 4.4792 | 2.87E-04 | 3.1354 | 2.18E-03 | 4.48E+00 | 1.53E-04 | 3.14E+00 | 1.89E-03 |
| 4.5833 | 1.36E-04 | 3.2083 | 2.20E-03 | 4.58E+00 | 1.04E-04 | 3.21E+00 | 1.89E-03 |
| 4.6875 | 7.06E-05 | 3.2813 | 2.21E-03 | 4.69E+00 | 6.40E-05 | 3.28E+00 | 1.89E-03 |
| 4.7917 | 3.31E-05 | 3.3542 | 2.22E-03 | 4.79E+00 | 3.60E-05 | 3.35E+00 | 1.89E-03 |
| 4.8958 | 1.63E-05 | 3.4271 | 2.19E-03 | 4.90E+00 | 1.82E-05 | 3.43E+00 | 1.86E-03 |
| 5 | 1.52E-05 | 3.5 | 2.12E-03 | 5.00E+00 | 1.07E-05 | 3.50E+00 | 1.83E-03 |

Table B-51 Surface tensile strain profiles for sample N3, step 51%YS.

| **Hardened Layer** | | | | **Soft Bulk** | | | |
|---|---|---|---|---|---|---|---|
| Longitudinal | | Transverse | | Longitudinal | | Transverse | |
| Length | Strain | Length | Strain | Length | Strain | Length | Strain |
| 0.00E+00 | 1.63E-05 | 0.00E+00 | 2.46E-03 | 0.00E+00 | 1.14E-05 | 0.00E+00 | 2.12E-03 |
| 1.04E-01 | 1.75E-05 | 7.29E-02 | 2.55E-03 | 1.04E-01 | 1.95E-05 | 7.29E-02 | 2.16E-03 |
| 2.08E-01 | 3.56E-05 | 1.46E-01 | 2.58E-03 | 2.08E-01 | 3.85E-05 | 1.46E-01 | 2.20E-03 |
| 3.13E-01 | 7.70E-05 | 2.19E-01 | 2.58E-03 | 3.13E-01 | 6.90E-05 | 2.19E-01 | 2.21E-03 |
| 4.17E-01 | 1.53E-04 | 2.92E-01 | 2.56E-03 | 4.17E-01 | 1.14E-04 | 2.92E-01 | 2.21E-03 |
| 5.21E-01 | 3.41E-04 | 3.65E-01 | 2.54E-03 | 5.21E-01 | 1.74E-04 | 3.65E-01 | 2.21E-03 |
| 6.25E-01 | 1.84E-03 | 4.38E-01 | 2.52E-03 | 6.25E-01 | 3.18E-04 | 4.38E-01 | 2.20E-03 |
| 7.29E-01 | 7.65E-03 | 5.10E-01 | 2.50E-03 | 7.29E-01 | 2.25E-03 | 5.10E-01 | 2.20E-03 |
| 8.33E-01 | 1.44E-03 | 5.83E-01 | 2.48E-03 | 8.33E-01 | 1.05E-03 | 5.83E-01 | 2.20E-03 |
| 9.38E-01 | 3.16E-04 | 6.56E-01 | 2.47E-03 | 9.38E-01 | 3.28E-04 | 6.56E-01 | 2.20E-03 |
| 1.04E+00 | 9.08E-05 | 7.29E-01 | 2.46E-03 | 1.04E+00 | 1.51E-04 | 7.29E-01 | 2.20E-03 |
| 1.15E+00 | 2.13E-04 | 8.02E-01 | 2.45E-03 | 1.15E+00 | 2.16E-04 | 8.02E-01 | 2.20E-03 |
| 1.25E+00 | 3.53E-04 | 8.75E-01 | 2.45E-03 | 1.25E+00 | 3.30E-04 | 8.75E-01 | 2.21E-03 |
| 1.35E+00 | 4.96E-04 | 9.48E-01 | 2.45E-03 | 1.35E+00 | 4.54E-04 | 9.48E-01 | 2.21E-03 |
| 1.46E+00 | 6.45E-04 | 1.02E+00 | 2.45E-03 | 1.46E+00 | 5.86E-04 | 1.02E+00 | 2.22E-03 |
| 1.56E+00 | 8.03E-04 | 1.09E+00 | 2.45E-03 | 1.56E+00 | 7.26E-04 | 1.09E+00 | 2.23E-03 |
| 1.67E+00 | 9.69E-04 | 1.17E+00 | 2.46E-03 | 1.67E+00 | 8.72E-04 | 1.17E+00 | 2.24E-03 |
| 1.77E+00 | 1.14E-03 | 1.24E+00 | 2.46E-03 | 1.77E+00 | 1.02E-03 | 1.24E+00 | 2.24E-03 |

| | | | | | | | |
|---|---|---|---|---|---|---|---|
| 1.88E+00 | 1.37E-03 | 1.31E+00 | 2.46E-03 | 1.88E+00 | 1.16E-03 | 1.31E+00 | 2.25E-03 |
| 1.98E+00 | 1.67E-03 | 1.39E+00 | 2.46E-03 | 1.98E+00 | 1.40E-03 | 1.39E+00 | 2.26E-03 |
| 2.08E+00 | 1.94E-03 | 1.46E+00 | 2.47E-03 | 2.08E+00 | 1.71E-03 | 1.46E+00 | 2.26E-03 |
| 2.19E+00 | 2.16E-03 | 1.53E+00 | 2.47E-03 | 2.19E+00 | 1.95E-03 | 1.53E+00 | 2.26E-03 |
| 2.29E+00 | 2.33E-03 | 1.60E+00 | 2.47E-03 | 2.29E+00 | 2.13E-03 | 1.60E+00 | 2.27E-03 |
| 2.40E+00 | 2.44E-03 | 1.68E+00 | 2.47E-03 | 2.40E+00 | 2.23E-03 | 1.68E+00 | 2.27E-03 |
| 2.50E+00 | 2.47E-03 | 1.75E+00 | 2.47E-03 | 2.50E+00 | 2.27E-03 | 1.75E+00 | 2.27E-03 |
| 2.60E+00 | 2.44E-03 | 1.82E+00 | 2.47E-03 | 2.60E+00 | 2.23E-03 | 1.82E+00 | 2.27E-03 |
| 2.71E+00 | 2.33E-03 | 1.90E+00 | 2.47E-03 | 2.71E+00 | 2.13E-03 | 1.90E+00 | 2.27E-03 |
| 2.81E+00 | 2.16E-03 | 1.97E+00 | 2.47E-03 | 2.81E+00 | 1.95E-03 | 1.97E+00 | 2.26E-03 |
| 2.92E+00 | 1.94E-03 | 2.04E+00 | 2.47E-03 | 2.92E+00 | 1.71E-03 | 2.04E+00 | 2.26E-03 |
| 3.02E+00 | 1.66E-03 | 2.11E+00 | 2.46E-03 | 3.02E+00 | 1.40E-03 | 2.11E+00 | 2.26E-03 |
| 3.13E+00 | 1.37E-03 | 2.19E+00 | 2.46E-03 | 3.13E+00 | 1.16E-03 | 2.19E+00 | 2.25E-03 |
| 3.23E+00 | 1.14E-03 | 2.26E+00 | 2.46E-03 | 3.23E+00 | 1.02E-03 | 2.26E+00 | 2.24E-03 |
| 3.33E+00 | 9.69E-04 | 2.33E+00 | 2.46E-03 | 3.33E+00 | 8.72E-04 | 2.33E+00 | 2.24E-03 |
| 3.44E+00 | 8.02E-04 | 2.41E+00 | 2.45E-03 | 3.44E+00 | 7.25E-04 | 2.41E+00 | 2.23E-03 |
| 3.54E+00 | 6.45E-04 | 2.48E+00 | 2.45E-03 | 3.54E+00 | 5.86E-04 | 2.48E+00 | 2.22E-03 |
| 3.65E+00 | 4.95E-04 | 2.55E+00 | 2.45E-03 | 3.65E+00 | 4.53E-04 | 2.55E+00 | 2.21E-03 |
| 3.75E+00 | 3.52E-04 | 2.63E+00 | 2.45E-03 | 3.75E+00 | 3.28E-04 | 2.63E+00 | 2.21E-03 |
| 3.85E+00 | 2.10E-04 | 2.70E+00 | 2.45E-03 | 3.85E+00 | 2.15E-04 | 2.70E+00 | 2.20E-03 |
| 3.96E+00 | 6.39E-05 | 2.77E+00 | 2.46E-03 | 3.96E+00 | 1.52E-04 | 2.77E+00 | 2.20E-03 |
| 4.06E+00 | 1.74E-04 | 2.84E+00 | 2.47E-03 | 4.06E+00 | 3.21E-04 | 2.84E+00 | 2.20E-03 |
| 4.1667 | 8.10E-04 | 2.9167 | 2.48E-03 | 4.17E+00 | 9.59E-04 | 2.92E+00 | 2.20E-03 |
| 4.2708 | 1.05E-02 | 2.9896 | 2.50E-03 | 4.27E+00 | 1.95E-03 | 2.99E+00 | 2.20E-03 |
| 4.375 | 1.52E-03 | 3.0625 | 2.52E-03 | 4.38E+00 | 3.10E-04 | 3.06E+00 | 2.20E-03 |
| 4.4792 | 3.06E-04 | 3.1354 | 2.54E-03 | 4.48E+00 | 1.71E-04 | 3.14E+00 | 2.21E-03 |
| 4.5833 | 1.48E-04 | 3.2083 | 2.56E-03 | 4.58E+00 | 1.15E-04 | 3.21E+00 | 2.21E-03 |
| 4.6875 | 7.71E-05 | 3.2813 | 2.58E-03 | 4.69E+00 | 7.01E-05 | 3.28E+00 | 2.21E-03 |
| 4.7917 | 3.73E-05 | 3.3542 | 2.58E-03 | 4.79E+00 | 3.99E-05 | 3.35E+00 | 2.20E-03 |
| 4.8958 | 2.02E-05 | 3.4271 | 2.55E-03 | 4.90E+00 | 2.14E-05 | 3.43E+00 | 2.16E-03 |
| 5 | 1.92E-05 | 3.5 | 2.46E-03 | 5.00E+00 | 1.39E-05 | 3.50E+00 | 2.12E-03 |

Table 0-52 Surface tensile strain profiles for sample N3, step 62%YS.

| **Hardened Layer** | | | | **Soft Bulk** | | | |
|---|---|---|---|---|---|---|---|
| Longitudinal | | Transverse | | Longitudinal | | Transverse | |
| Length | Strain | Length | Strain | Length | Strain | Length | Strain |
| 0.00E+00 | 2.02E-05 | 0.00E+00 | 2.76E-03 | 0.00E+00 | 1.46E-05 | 0.00E+00 | 2.39E-03 |
| 1.04E-01 | 2.12E-05 | 7.29E-02 | 2.88E-03 | 1.04E-01 | 2.25E-05 | 7.29E-02 | 2.44E-03 |
| 2.08E-01 | 3.93E-05 | 1.46E-01 | 2.92E-03 | 2.08E-01 | 4.20E-05 | 1.46E-01 | 2.48E-03 |
| 3.13E-01 | 8.28E-05 | 2.19E-01 | 2.92E-03 | 3.13E-01 | 7.44E-05 | 2.19E-01 | 2.50E-03 |
| 4.17E-01 | 1.65E-04 | 2.92E-01 | 2.90E-03 | 4.17E-01 | 1.23E-04 | 2.92E-01 | 2.51E-03 |

| | | | | | | | |
|---|---|---|---|---|---|---|---|
| 5.21E-01 | 3.66E-04 | 3.65E-01 | 2.87E-03 | 5.21E-01 | 1.92E-04 | 3.65E-01 | 2.51E-03 |
| 6.25E-01 | 1.86E-03 | 4.38E-01 | 2.85E-03 | 6.25E-01 | 3.40E-04 | 4.38E-01 | 2.51E-03 |
| 7.29E-01 | 8.70E-03 | 5.10E-01 | 2.82E-03 | 7.29E-01 | 2.51E-03 | 5.10E-01 | 2.50E-03 |
| 8.33E-01 | 1.66E-03 | 5.83E-01 | 2.81E-03 | 8.33E-01 | 1.19E-03 | 5.83E-01 | 2.50E-03 |
| 9.38E-01 | 3.79E-04 | 6.56E-01 | 2.79E-03 | 9.38E-01 | 3.77E-04 | 6.56E-01 | 2.50E-03 |
| 1.04E+00 | 9.05E-05 | 7.29E-01 | 2.78E-03 | 1.04E+00 | 1.65E-04 | 7.29E-01 | 2.51E-03 |
| 1.15E+00 | 2.07E-04 | 8.02E-01 | 2.78E-03 | 1.15E+00 | 2.17E-04 | 8.02E-01 | 2.51E-03 |
| 1.25E+00 | 3.57E-04 | 8.75E-01 | 2.77E-03 | 1.25E+00 | 3.35E-04 | 8.75E-01 | 2.52E-03 |
| 1.35E+00 | 5.09E-04 | 9.48E-01 | 2.77E-03 | 1.35E+00 | 4.67E-04 | 9.48E-01 | 2.53E-03 |
| 1.46E+00 | 6.68E-04 | 1.02E+00 | 2.77E-03 | 1.46E+00 | 6.07E-04 | 1.02E+00 | 2.54E-03 |
| 1.56E+00 | 8.36E-04 | 1.09E+00 | 2.77E-03 | 1.56E+00 | 7.56E-04 | 1.09E+00 | 2.55E-03 |
| 1.67E+00 | 1.01E-03 | 1.17E+00 | 2.78E-03 | 1.67E+00 | 9.13E-04 | 1.17E+00 | 2.56E-03 |
| 1.77E+00 | 1.22E-03 | 1.24E+00 | 2.78E-03 | 1.77E+00 | 1.06E-03 | 1.24E+00 | 2.57E-03 |
| 1.88E+00 | 1.52E-03 | 1.31E+00 | 2.78E-03 | 1.88E+00 | 1.25E-03 | 1.31E+00 | 2.58E-03 |
| 1.98E+00 | 1.86E-03 | 1.39E+00 | 2.79E-03 | 1.98E+00 | 1.59E-03 | 1.39E+00 | 2.58E-03 |
| 2.08E+00 | 2.17E-03 | 1.46E+00 | 2.79E-03 | 2.08E+00 | 1.95E-03 | 1.46E+00 | 2.59E-03 |
| 2.19E+00 | 2.43E-03 | 1.53E+00 | 2.79E-03 | 2.19E+00 | 2.23E-03 | 1.53E+00 | 2.59E-03 |
| 2.29E+00 | 2.64E-03 | 1.60E+00 | 2.79E-03 | 2.29E+00 | 2.44E-03 | 1.60E+00 | 2.60E-03 |
| 2.40E+00 | 2.76E-03 | 1.68E+00 | 2.79E-03 | 2.40E+00 | 2.56E-03 | 1.68E+00 | 2.60E-03 |
| 2.50E+00 | 2.79E-03 | 1.75E+00 | 2.79E-03 | 2.50E+00 | 2.60E-03 | 1.75E+00 | 2.60E-03 |
| 2.60E+00 | 2.76E-03 | 1.82E+00 | 2.79E-03 | 2.60E+00 | 2.56E-03 | 1.82E+00 | 2.60E-03 |
| 2.71E+00 | 2.64E-03 | 1.90E+00 | 2.79E-03 | 2.71E+00 | 2.44E-03 | 1.90E+00 | 2.60E-03 |
| 2.81E+00 | 2.43E-03 | 1.97E+00 | 2.79E-03 | 2.81E+00 | 2.23E-03 | 1.97E+00 | 2.59E-03 |
| 2.92E+00 | 2.17E-03 | 2.04E+00 | 2.79E-03 | 2.92E+00 | 1.95E-03 | 2.04E+00 | 2.59E-03 |
| 3.02E+00 | 1.86E-03 | 2.11E+00 | 2.79E-03 | 3.02E+00 | 1.59E-03 | 2.11E+00 | 2.58E-03 |
| 3.13E+00 | 1.52E-03 | 2.19E+00 | 2.78E-03 | 3.13E+00 | 1.25E-03 | 2.19E+00 | 2.58E-03 |
| 3.23E+00 | 1.22E-03 | 2.26E+00 | 2.78E-03 | 3.23E+00 | 1.06E-03 | 2.26E+00 | 2.57E-03 |
| 3.33E+00 | 1.01E-03 | 2.33E+00 | 2.78E-03 | 3.33E+00 | 9.13E-04 | 2.33E+00 | 2.56E-03 |
| 3.44E+00 | 8.35E-04 | 2.41E+00 | 2.77E-03 | 3.44E+00 | 7.56E-04 | 2.41E+00 | 2.55E-03 |
| 3.54E+00 | 6.67E-04 | 2.48E+00 | 2.77E-03 | 3.54E+00 | 6.07E-04 | 2.48E+00 | 2.54E-03 |
| 3.65E+00 | 5.08E-04 | 2.55E+00 | 2.77E-03 | 3.65E+00 | 4.66E-04 | 2.55E+00 | 2.53E-03 |
| 3.75E+00 | 3.55E-04 | 2.63E+00 | 2.77E-03 | 3.75E+00 | 3.34E-04 | 2.63E+00 | 2.52E-03 |
| 3.85E+00 | 2.03E-04 | 2.70E+00 | 2.77E-03 | 3.85E+00 | 2.16E-04 | 2.70E+00 | 2.51E-03 |
| 3.96E+00 | 5.41E-05 | 2.77E+00 | 2.78E-03 | 3.96E+00 | 1.67E-04 | 2.77E+00 | 2.51E-03 |
| 4.06E+00 | 2.34E-04 | 2.84E+00 | 2.79E-03 | 4.06E+00 | 3.70E-04 | 2.84E+00 | 2.50E-03 |
| 4.1667 | 9.63E-04 | 2.9167 | 2.81E-03 | 4.17E+00 | 1.11E-03 | 2.92E+00 | 2.50E-03 |
| 4.2708 | 1.26E-02 | 2.9896 | 2.82E-03 | 4.27E+00 | 2.16E-03 | 2.99E+00 | 2.50E-03 |
| 4.375 | 1.55E-03 | 3.0625 | 2.85E-03 | 4.38E+00 | 3.30E-04 | 3.06E+00 | 2.51E-03 |
| 4.4792 | 3.27E-04 | 3.1354 | 2.87E-03 | 4.48E+00 | 1.89E-04 | 3.14E+00 | 2.51E-03 |
| 4.5833 | 1.58E-04 | 3.2083 | 2.90E-03 | 4.58E+00 | 1.24E-04 | 3.21E+00 | 2.51E-03 |
| 4.6875 | 8.30E-05 | 3.2813 | 2.92E-03 | 4.69E+00 | 7.57E-05 | 3.28E+00 | 2.50E-03 |

| | | | | | | | |
|---|---|---|---|---|---|---|---|
| 4.7917 | 4.13E-05 | 3.3542 | 2.92E-03 | 4.79E+00 | 4.36E-05 | 3.35E+00 | 2.48E-03 |
| 4.8958 | 2.42E-05 | 3.4271 | 2.87E-03 | 4.90E+00 | 2.47E-05 | 3.43E+00 | 2.44E-03 |
| 5 | 2.33E-05 | 3.5 | 2.76E-03 | 5.00E+00 | 1.74E-05 | 3.50E+00 | 2.39E-03 |

Table B-53 Surface tensile strain profiles for sample N3, step 70%YS.

| **Hardened Layer** | | | | **Soft Bulk** | | | |
|---|---|---|---|---|---|---|---|
| Longitudinal | | Transverse | | Longitudinal | | Transverse | |
| Length | Strain | Length | Strain | Length | Strain | Length | Strain |
| 0.00E+00 | 2.60E-05 | 0.00E+00 | 3.13E-03 | 0.00E+00 | 1.98E-05 | 0.00E+00 | 2.71E-03 |
| 1.04E-01 | 2.64E-05 | 7.29E-02 | 3.27E-03 | 1.04E-01 | 2.68E-05 | 7.29E-02 | 2.77E-03 |
| 2.08E-01 | 4.42E-05 | 1.46E-01 | 3.32E-03 | 2.08E-01 | 4.66E-05 | 1.46E-01 | 2.83E-03 |
| 3.13E-01 | 8.97E-05 | 2.19E-01 | 3.32E-03 | 3.13E-01 | 8.10E-05 | 2.19E-01 | 2.86E-03 |
| 4.17E-01 | 1.77E-04 | 2.92E-01 | 3.30E-03 | 4.17E-01 | 1.35E-04 | 2.92E-01 | 2.87E-03 |
| 5.21E-01 | 3.91E-04 | 3.65E-01 | 3.28E-03 | 5.21E-01 | 2.15E-04 | 3.65E-01 | 2.87E-03 |
| 6.25E-01 | 1.86E-03 | 4.38E-01 | 3.25E-03 | 6.25E-01 | 3.70E-04 | 4.38E-01 | 2.87E-03 |
| 7.29E-01 | 1.09E-02 | 5.10E-01 | 3.22E-03 | 7.29E-01 | 2.79E-03 | 5.10E-01 | 2.87E-03 |
| 8.33E-01 | 1.93E-03 | 5.83E-01 | 3.20E-03 | 8.33E-01 | 1.44E-03 | 5.83E-01 | 2.87E-03 |
| 9.38E-01 | 4.58E-04 | 6.56E-01 | 3.18E-03 | 9.38E-01 | 4.38E-04 | 6.56E-01 | 2.88E-03 |
| 1.04E+00 | 9.71E-05 | 7.29E-01 | 3.17E-03 | 1.04E+00 | 1.86E-04 | 7.29E-01 | 2.88E-03 |
| 1.15E+00 | 1.96E-04 | 8.02E-01 | 3.16E-03 | 1.15E+00 | 2.16E-04 | 8.02E-01 | 2.89E-03 |
| 1.25E+00 | 3.57E-04 | 8.75E-01 | 3.16E-03 | 1.25E+00 | 3.38E-04 | 8.75E-01 | 2.90E-03 |
| 1.35E+00 | 5.19E-04 | 9.48E-01 | 3.16E-03 | 1.35E+00 | 4.77E-04 | 9.48E-01 | 2.91E-03 |
| 1.46E+00 | 6.88E-04 | 1.02E+00 | 3.16E-03 | 1.46E+00 | 6.27E-04 | 1.02E+00 | 2.93E-03 |
| 1.56E+00 | 8.68E-04 | 1.09E+00 | 3.16E-03 | 1.56E+00 | 7.86E-04 | 1.09E+00 | 2.94E-03 |
| 1.67E+00 | 1.06E-03 | 1.17E+00 | 3.16E-03 | 1.67E+00 | 9.54E-04 | 1.17E+00 | 2.95E-03 |
| 1.77E+00 | 1.32E-03 | 1.24E+00 | 3.17E-03 | 1.77E+00 | 1.11E-03 | 1.24E+00 | 2.96E-03 |
| 1.88E+00 | 1.70E-03 | 1.31E+00 | 3.17E-03 | 1.88E+00 | 1.39E-03 | 1.31E+00 | 2.97E-03 |
| 1.98E+00 | 2.09E-03 | 1.39E+00 | 3.17E-03 | 1.98E+00 | 1.84E-03 | 1.39E+00 | 2.98E-03 |
| 2.08E+00 | 2.46E-03 | 1.46E+00 | 3.18E-03 | 2.08E+00 | 2.23E-03 | 1.46E+00 | 2.99E-03 |
| 2.19E+00 | 2.76E-03 | 1.53E+00 | 3.18E-03 | 2.19E+00 | 2.56E-03 | 1.53E+00 | 2.99E-03 |
| 2.29E+00 | 2.99E-03 | 1.60E+00 | 3.18E-03 | 2.29E+00 | 2.80E-03 | 1.60E+00 | 3.00E-03 |
| 2.40E+00 | 3.13E-03 | 1.68E+00 | 3.18E-03 | 2.40E+00 | 2.95E-03 | 1.68E+00 | 3.00E-03 |
| 2.50E+00 | 3.18E-03 | 1.75E+00 | 3.18E-03 | 2.50E+00 | 3.00E-03 | 1.75E+00 | 3.00E-03 |
| 2.60E+00 | 3.13E-03 | 1.82E+00 | 3.18E-03 | 2.60E+00 | 2.95E-03 | 1.82E+00 | 3.00E-03 |
| 2.71E+00 | 2.99E-03 | 1.90E+00 | 3.18E-03 | 2.71E+00 | 2.80E-03 | 1.90E+00 | 3.00E-03 |
| 2.81E+00 | 2.76E-03 | 1.97E+00 | 3.18E-03 | 2.81E+00 | 2.56E-03 | 1.97E+00 | 2.99E-03 |
| 2.92E+00 | 2.45E-03 | 2.04E+00 | 3.18E-03 | 2.92E+00 | 2.23E-03 | 2.04E+00 | 2.99E-03 |
| 3.02E+00 | 2.09E-03 | 2.11E+00 | 3.17E-03 | 3.02E+00 | 1.83E-03 | 2.11E+00 | 2.98E-03 |
| 3.13E+00 | 1.70E-03 | 2.19E+00 | 3.17E-03 | 3.13E+00 | 1.39E-03 | 2.19E+00 | 2.97E-03 |
| 3.23E+00 | 1.32E-03 | 2.26E+00 | 3.16E-03 | 3.23E+00 | 1.11E-03 | 2.26E+00 | 2.96E-03 |
| 3.33E+00 | 1.06E-03 | 2.33E+00 | 3.16E-03 | 3.33E+00 | 9.53E-04 | 2.33E+00 | 2.95E-03 |

| | | | | | | | |
|---|---|---|---|---|---|---|---|
| 3.44E+00 | 8.67E-04 | 2.41E+00 | 3.16E-03 | 3.44E+00 | 7.85E-04 | 2.41E+00 | 2.94E-03 |
| 3.54E+00 | 6.87E-04 | 2.48E+00 | 3.16E-03 | 3.54E+00 | 6.25E-04 | 2.48E+00 | 2.93E-03 |
| 3.65E+00 | 5.17E-04 | 2.55E+00 | 3.16E-03 | 3.65E+00 | 4.76E-04 | 2.55E+00 | 2.91E-03 |
| 3.75E+00 | 3.54E-04 | 2.63E+00 | 3.16E-03 | 3.75E+00 | 3.37E-04 | 2.63E+00 | 2.90E-03 |
| 3.85E+00 | 1.91E-04 | 2.70E+00 | 3.16E-03 | 3.85E+00 | 2.15E-04 | 2.70E+00 | 2.89E-03 |
| 3.96E+00 | 5.70E-05 | 2.77E+00 | 3.17E-03 | 3.96E+00 | 1.89E-04 | 2.77E+00 | 2.88E-03 |
| 4.06E+00 | 3.15E-04 | 2.84E+00 | 3.18E-03 | 4.06E+00 | 4.29E-04 | 2.84E+00 | 2.88E-03 |
| 4.1667 | 1.16E-03 | 2.9167 | 3.20E-03 | 4.17E+00 | 1.31E-03 | 2.92E+00 | 2.87E-03 |
| 4.2708 | 1.54E-02 | 2.9896 | 3.22E-03 | 4.27E+00 | 2.39E-03 | 2.99E+00 | 2.87E-03 |
| 4.375 | 1.60E-03 | 3.0625 | 3.24E-03 | 4.38E+00 | 3.58E-04 | 3.06E+00 | 2.87E-03 |
| 4.4792 | 3.51E-04 | 3.1354 | 3.27E-03 | 4.48E+00 | 2.10E-04 | 3.14E+00 | 2.87E-03 |
| 4.5833 | 1.70E-04 | 3.2083 | 3.30E-03 | 4.58E+00 | 1.35E-04 | 3.21E+00 | 2.87E-03 |
| 4.6875 | 9.00E-05 | 3.2813 | 3.32E-03 | 4.69E+00 | 8.24E-05 | 3.28E+00 | 2.86E-03 |
| 4.7917 | 4.65E-05 | 3.3542 | 3.32E-03 | 4.79E+00 | 4.84E-05 | 3.35E+00 | 2.83E-03 |
| 4.8958 | 2.97E-05 | 3.4271 | 3.27E-03 | 4.90E+00 | 2.92E-05 | 3.43E+00 | 2.77E-03 |
| 5 | 2.94E-05 | 3.5 | 3.13E-03 | 5.00E+00 | 2.28E-05 | 3.50E+00 | 2.71E-03 |

## Sample N7

Table B-54 Surface tensile strain profiles for sample N7, step 44%YS.

| **Hardened Layer** | | | | **Soft Bulk** | | | |
|---|---|---|---|---|---|---|---|
| Longitudinal | | Transverse | | Longitudinal | | Transverse | |
| Length | Strain | Length | Strain | Length | Strain | Length | Strain |
| 0.00E+00 | 6.97E-06 | 0.00E+00 | 2.02E-03 | 0.00E+00 | 4.27E-06 | 0.00E+00 | 1.76E-03 |
| 1.04E-01 | 8.20E-06 | 7.29E-02 | 2.08E-03 | 1.04E-01 | 9.20E-06 | 7.29E-02 | 1.78E-03 |
| 2.08E-01 | 2.00E-05 | 1.46E-01 | 2.09E-03 | 2.08E-01 | 2.16E-05 | 1.46E-01 | 1.80E-03 |
| 3.13E-01 | 4.55E-05 | 2.19E-01 | 2.09E-03 | 3.13E-01 | 4.22E-05 | 2.19E-01 | 1.80E-03 |
| 4.17E-01 | 9.06E-05 | 2.92E-01 | 2.07E-03 | 4.17E-01 | 7.43E-05 | 2.92E-01 | 1.80E-03 |
| 5.21E-01 | 1.82E-04 | 3.65E-01 | 2.05E-03 | 5.21E-01 | 1.20E-04 | 3.65E-01 | 1.79E-03 |
| 6.25E-01 | 4.43E-04 | 4.38E-01 | 2.03E-03 | 6.25E-01 | 1.73E-04 | 4.38E-01 | 1.78E-03 |
| 7.29E-01 | 6.82E-03 | 5.10E-01 | 2.02E-03 | 7.29E-01 | 1.59E-03 | 5.10E-01 | 1.78E-03 |
| 8.33E-01 | 7.92E-04 | 5.83E-01 | 2.01E-03 | 8.33E-01 | 6.37E-04 | 5.83E-01 | 1.77E-03 |
| 9.38E-01 | 1.55E-04 | 6.56E-01 | 2.00E-03 | 9.38E-01 | 1.64E-04 | 6.56E-01 | 1.77E-03 |
| 1.04E+00 | 1.21E-04 | 7.29E-01 | 1.99E-03 | 1.04E+00 | 1.23E-04 | 7.29E-01 | 1.77E-03 |
| 1.15E+00 | 2.38E-04 | 8.02E-01 | 1.98E-03 | 1.15E+00 | 2.21E-04 | 8.02E-01 | 1.77E-03 |
| 1.25E+00 | 3.58E-04 | 8.75E-01 | 1.98E-03 | 1.25E+00 | 3.29E-04 | 8.75E-01 | 1.77E-03 |
| 1.35E+00 | 4.82E-04 | 9.48E-01 | 1.98E-03 | 1.35E+00 | 4.43E-04 | 9.48E-01 | 1.77E-03 |
| 1.46E+00 | 6.12E-04 | 1.02E+00 | 1.98E-03 | 1.46E+00 | 5.61E-04 | 1.02E+00 | 1.77E-03 |
| 1.56E+00 | 7.50E-04 | 1.09E+00 | 1.98E-03 | 1.56E+00 | 6.86E-04 | 1.09E+00 | 1.78E-03 |
| 1.67E+00 | 8.95E-04 | 1.17E+00 | 1.98E-03 | 1.67E+00 | 8.17E-04 | 1.17E+00 | 1.78E-03 |
| 1.77E+00 | 1.05E-03 | 1.24E+00 | 1.99E-03 | 1.77E+00 | 9.52E-04 | 1.24E+00 | 1.79E-03 |

| | | | | | | | |
|---|---|---|---|---|---|---|---|
| 1.88E+00 | 1.20E-03 | 1.31E+00 | 1.99E-03 | 1.88E+00 | 1.08E-03 | 1.31E+00 | 1.79E-03 |
| 1.98E+00 | 1.39E-03 | 1.39E+00 | 1.99E-03 | 1.98E+00 | 1.20E-03 | 1.39E+00 | 1.79E-03 |
| 2.08E+00 | 1.60E-03 | 1.46E+00 | 1.99E-03 | 2.08E+00 | 1.40E-03 | 1.46E+00 | 1.80E-03 |
| 2.19E+00 | 1.78E-03 | 1.53E+00 | 1.99E-03 | 2.19E+00 | 1.59E-03 | 1.53E+00 | 1.80E-03 |
| 2.29E+00 | 1.90E-03 | 1.60E+00 | 1.99E-03 | 2.29E+00 | 1.71E-03 | 1.60E+00 | 1.80E-03 |
| 2.40E+00 | 1.97E-03 | 1.68E+00 | 1.99E-03 | 2.40E+00 | 1.78E-03 | 1.68E+00 | 1.80E-03 |
| 2.50E+00 | 1.99E-03 | 1.75E+00 | 1.99E-03 | 2.50E+00 | 1.80E-03 | 1.75E+00 | 1.80E-03 |
| 2.60E+00 | 1.97E-03 | 1.82E+00 | 1.99E-03 | 2.60E+00 | 1.78E-03 | 1.82E+00 | 1.80E-03 |
| 2.71E+00 | 1.90E-03 | 1.90E+00 | 1.99E-03 | 2.71E+00 | 1.71E-03 | 1.90E+00 | 1.80E-03 |
| 2.81E+00 | 1.78E-03 | 1.97E+00 | 1.99E-03 | 2.81E+00 | 1.59E-03 | 1.97E+00 | 1.80E-03 |
| 2.92E+00 | 1.60E-03 | 2.04E+00 | 1.99E-03 | 2.92E+00 | 1.40E-03 | 2.04E+00 | 1.80E-03 |
| 3.02E+00 | 1.39E-03 | 2.11E+00 | 1.99E-03 | 3.02E+00 | 1.20E-03 | 2.11E+00 | 1.79E-03 |
| 3.13E+00 | 1.20E-03 | 2.19E+00 | 1.99E-03 | 3.13E+00 | 1.08E-03 | 2.19E+00 | 1.79E-03 |
| 3.23E+00 | 1.05E-03 | 2.26E+00 | 1.99E-03 | 3.23E+00 | 9.52E-04 | 2.26E+00 | 1.79E-03 |
| 3.33E+00 | 8.95E-04 | 2.33E+00 | 1.98E-03 | 3.33E+00 | 8.16E-04 | 2.33E+00 | 1.78E-03 |
| 3.44E+00 | 7.49E-04 | 2.41E+00 | 1.98E-03 | 3.44E+00 | 6.85E-04 | 2.41E+00 | 1.78E-03 |
| 3.54E+00 | 6.12E-04 | 2.48E+00 | 1.98E-03 | 3.54E+00 | 5.60E-04 | 2.48E+00 | 1.77E-03 |
| 3.65E+00 | 4.81E-04 | 2.55E+00 | 1.98E-03 | 3.65E+00 | 4.42E-04 | 2.55E+00 | 1.77E-03 |
| 3.75E+00 | 3.57E-04 | 2.63E+00 | 1.98E-03 | 3.75E+00 | 3.28E-04 | 2.63E+00 | 1.77E-03 |
| 3.85E+00 | 2.36E-04 | 2.70E+00 | 1.98E-03 | 3.85E+00 | 2.20E-04 | 2.70E+00 | 1.77E-03 |
| 3.96E+00 | 1.14E-04 | 2.77E+00 | 1.99E-03 | 3.96E+00 | 1.23E-04 | 2.77E+00 | 1.77E-03 |
| 4.06E+00 | 5.38E-05 | 2.84E+00 | 2.00E-03 | 4.06E+00 | 1.62E-04 | 2.84E+00 | 1.77E-03 |
| 4.1667 | 4.59E-04 | 2.9167 | 2.01E-03 | 4.17E+00 | 6.02E-04 | 2.92E+00 | 1.77E-03 |
| 4.2708 | 6.64E-03 | 2.9896 | 2.02E-03 | 4.27E+00 | 1.41E-03 | 2.99E+00 | 1.78E-03 |
| 4.375 | 8.87E-04 | 3.0625 | 2.03E-03 | 4.38E+00 | 1.68E-04 | 3.06E+00 | 1.78E-03 |
| 4.4792 | 1.98E-04 | 3.1354 | 2.05E-03 | 4.48E+00 | 1.21E-04 | 3.14E+00 | 1.79E-03 |
| 4.5833 | 9.16E-05 | 3.2083 | 2.07E-03 | 4.58E+00 | 7.50E-05 | 3.21E+00 | 1.80E-03 |
| 4.6875 | 4.61E-05 | 3.2813 | 2.09E-03 | 4.69E+00 | 4.29E-05 | 3.28E+00 | 1.80E-03 |
| 4.7917 | 2.09E-05 | 3.3542 | 2.09E-03 | 4.79E+00 | 2.22E-05 | 3.35E+00 | 1.80E-03 |
| 4.8958 | 9.50E-06 | 3.4271 | 2.08E-03 | 4.90E+00 | 1.01E-05 | 3.43E+00 | 1.78E-03 |
| 5 | 8.33E-06 | 3.5 | 2.02E-03 | 5.00E+00 | 5.41E-06 | 3.50E+00 | 1.76E-03 |

Table B-55 Surface tensile strain profiles for sample N7, step 52%YS.

| **Hardened Layer** | | | | **Soft Bulk** | | | |
|---|---|---|---|---|---|---|---|
| Longitudinal | | Transverse | | Longitudinal | | Transverse | |
| Length | Strain | Length | Strain | Length | Strain | Length | Strain |
| 0.00E+00 | 9.27E-06 | 0.00E+00 | 2.35E-03 | 0.00E+00 | 6.00E-06 | 0.00E+00 | 2.04E-03 |
| 1.04E-01 | 1.05E-05 | 7.29E-02 | 2.42E-03 | 1.04E-01 | 1.09E-05 | 7.29E-02 | 2.07E-03 |
| 2.08E-01 | 2.22E-05 | 1.46E-01 | 2.45E-03 | 2.08E-01 | 2.37E-05 | 1.46E-01 | 2.10E-03 |
| 3.13E-01 | 4.93E-05 | 2.19E-01 | 2.44E-03 | 3.13E-01 | 4.57E-05 | 2.19E-01 | 2.11E-03 |
| 4.17E-01 | 9.85E-05 | 2.92E-01 | 2.42E-03 | 4.17E-01 | 8.04E-05 | 2.92E-01 | 2.11E-03 |

| | | | | | | | |
|---|---|---|---|---|---|---|---|
| 5.21E-01 | 2.03E-04 | 3.65E-01 | 2.40E-03 | 5.21E-01 | 1.32E-04 | 3.65E-01 | 2.10E-03 |
| 6.25E-01 | 5.67E-04 | 4.38E-01 | 2.38E-03 | 6.25E-01 | 2.01E-04 | 4.38E-01 | 2.09E-03 |
| 7.29E-01 | 7.81E-03 | 5.10E-01 | 2.36E-03 | 7.29E-01 | 1.84E-03 | 5.10E-01 | 2.09E-03 |
| 8.33E-01 | 9.88E-04 | 5.83E-01 | 2.34E-03 | 8.33E-01 | 7.52E-04 | 5.83E-01 | 2.08E-03 |
| 9.38E-01 | 1.99E-04 | 6.56E-01 | 2.33E-03 | 9.38E-01 | 1.99E-04 | 6.56E-01 | 2.08E-03 |
| 1.04E+00 | 1.17E-04 | 7.29E-01 | 2.32E-03 | 1.04E+00 | 1.25E-04 | 7.29E-01 | 2.08E-03 |
| 1.15E+00 | 2.43E-04 | 8.02E-01 | 2.32E-03 | 1.15E+00 | 2.27E-04 | 8.02E-01 | 2.08E-03 |
| 1.25E+00 | 3.74E-04 | 8.75E-01 | 2.32E-03 | 1.25E+00 | 3.45E-04 | 8.75E-01 | 2.09E-03 |
| 1.35E+00 | 5.09E-04 | 9.48E-01 | 2.32E-03 | 1.35E+00 | 4.68E-04 | 9.48E-01 | 2.09E-03 |
| 1.46E+00 | 6.51E-04 | 1.02E+00 | 2.32E-03 | 1.46E+00 | 5.97E-04 | 1.02E+00 | 2.10E-03 |
| 1.56E+00 | 8.02E-04 | 1.09E+00 | 2.32E-03 | 1.56E+00 | 7.34E-04 | 1.09E+00 | 2.11E-03 |
| 1.67E+00 | 9.62E-04 | 1.17E+00 | 2.32E-03 | 1.67E+00 | 8.77E-04 | 1.17E+00 | 2.11E-03 |
| 1.77E+00 | 1.13E-03 | 1.24E+00 | 2.33E-03 | 1.77E+00 | 1.03E-03 | 1.24E+00 | 2.12E-03 |
| 1.88E+00 | 1.33E-03 | 1.31E+00 | 2.33E-03 | 1.88E+00 | 1.15E-03 | 1.31E+00 | 2.13E-03 |
| 1.98E+00 | 1.61E-03 | 1.39E+00 | 2.33E-03 | 1.98E+00 | 1.38E-03 | 1.39E+00 | 2.13E-03 |
| 2.08E+00 | 1.86E-03 | 1.46E+00 | 2.33E-03 | 2.08E+00 | 1.66E-03 | 1.46E+00 | 2.14E-03 |
| 2.19E+00 | 2.07E-03 | 1.53E+00 | 2.34E-03 | 2.19E+00 | 1.89E-03 | 1.53E+00 | 2.14E-03 |
| 2.29E+00 | 2.22E-03 | 1.60E+00 | 2.34E-03 | 2.29E+00 | 2.04E-03 | 1.60E+00 | 2.14E-03 |
| 2.40E+00 | 2.31E-03 | 1.68E+00 | 2.34E-03 | 2.40E+00 | 2.12E-03 | 1.68E+00 | 2.14E-03 |
| 2.50E+00 | 2.34E-03 | 1.75E+00 | 2.34E-03 | 2.50E+00 | 2.14E-03 | 1.75E+00 | 2.14E-03 |
| 2.60E+00 | 2.31E-03 | 1.82E+00 | 2.34E-03 | 2.60E+00 | 2.12E-03 | 1.82E+00 | 2.14E-03 |
| 2.71E+00 | 2.22E-03 | 1.90E+00 | 2.34E-03 | 2.71E+00 | 2.03E-03 | 1.90E+00 | 2.14E-03 |
| 2.81E+00 | 2.07E-03 | 1.97E+00 | 2.34E-03 | 2.81E+00 | 1.89E-03 | 1.97E+00 | 2.14E-03 |
| 2.92E+00 | 1.86E-03 | 2.04E+00 | 2.33E-03 | 2.92E+00 | 1.66E-03 | 2.04E+00 | 2.14E-03 |
| 3.02E+00 | 1.61E-03 | 2.11E+00 | 2.33E-03 | 3.02E+00 | 1.38E-03 | 2.11E+00 | 2.13E-03 |
| 3.13E+00 | 1.33E-03 | 2.19E+00 | 2.33E-03 | 3.13E+00 | 1.15E-03 | 2.19E+00 | 2.13E-03 |
| 3.23E+00 | 1.13E-03 | 2.26E+00 | 2.33E-03 | 3.23E+00 | 1.03E-03 | 2.26E+00 | 2.12E-03 |
| 3.33E+00 | 9.61E-04 | 2.33E+00 | 2.32E-03 | 3.33E+00 | 8.77E-04 | 2.33E+00 | 2.11E-03 |
| 3.44E+00 | 8.01E-04 | 2.41E+00 | 2.32E-03 | 3.44E+00 | 7.33E-04 | 2.41E+00 | 2.11E-03 |
| 3.54E+00 | 6.50E-04 | 2.48E+00 | 2.32E-03 | 3.54E+00 | 5.96E-04 | 2.48E+00 | 2.10E-03 |
| 3.65E+00 | 5.08E-04 | 2.55E+00 | 2.32E-03 | 3.65E+00 | 4.67E-04 | 2.55E+00 | 2.09E-03 |
| 3.75E+00 | 3.73E-04 | 2.63E+00 | 2.32E-03 | 3.75E+00 | 3.43E-04 | 2.63E+00 | 2.09E-03 |
| 3.85E+00 | 2.41E-04 | 2.70E+00 | 2.32E-03 | 3.85E+00 | 2.26E-04 | 2.70E+00 | 2.08E-03 |
| 3.96E+00 | 1.07E-04 | 2.77E+00 | 2.32E-03 | 3.96E+00 | 1.25E-04 | 2.77E+00 | 2.08E-03 |
| 4.06E+00 | 8.74E-05 | 2.84E+00 | 2.33E-03 | 4.06E+00 | 1.96E-04 | 2.84E+00 | 2.08E-03 |
| 4.1667 | 5.61E-04 | 2.9167 | 2.34E-03 | 4.17E+00 | 7.05E-04 | 2.92E+00 | 2.08E-03 |
| 4.2708 | 7.96E-03 | 2.9896 | 2.36E-03 | 4.27E+00 | 1.60E-03 | 2.99E+00 | 2.09E-03 |
| 4.375 | 9.52E-04 | 3.0625 | 2.38E-03 | 4.38E+00 | 1.93E-04 | 3.06E+00 | 2.09E-03 |
| 4.4792 | 2.11E-04 | 3.1354 | 2.40E-03 | 4.48E+00 | 1.33E-04 | 3.14E+00 | 2.10E-03 |
| 4.5833 | 9.90E-05 | 3.2083 | 2.42E-03 | 4.58E+00 | 8.19E-05 | 3.21E+00 | 2.11E-03 |
| 4.6875 | 5.03E-05 | 3.2813 | 2.44E-03 | 4.69E+00 | 4.69E-05 | 3.28E+00 | 2.11E-03 |

| | | | | | | | |
|---|---|---|---|---|---|---|---|
| 4.7917 | 2.36E-05 | 3.3542 | 2.45E-03 | 4.79E+00 | 2.48E-05 | 3.35E+00 | 2.10E-03 |
| 4.8958 | 1.22E-05 | 3.4271 | 2.42E-03 | 4.90E+00 | 1.22E-05 | 3.43E+00 | 2.07E-03 |
| 5 | 1.12E-05 | 3.5 | 2.35E-03 | 5.00E+00 | 7.73E-06 | 3.50E+00 | 2.04E-03 |

Table B-56 Surface tensile strain profiles for sample N7, step 59%YS.

| **Hardened Layer** | | | | **Soft Bulk** | | | |
|---|---|---|---|---|---|---|---|
| Longitudinal | | Transverse | | Longitudinal | | Transverse | |
| Length | Strain | Length | Strain | Length | Strain | Length | Strain |
| 0.00E+00 | 1.19E-05 | 0.00E+00 | 2.67E-03 | 0.00E+00 | 8.09E-06 | 0.00E+00 | 2.32E-03 |
| 1.04E-01 | 1.30E-05 | 7.29E-02 | 2.76E-03 | 1.04E-01 | 1.29E-05 | 7.29E-02 | 2.36E-03 |
| 2.08E-01 | 2.46E-05 | 1.46E-01 | 2.79E-03 | 2.08E-01 | 2.59E-05 | 1.46E-01 | 2.40E-03 |
| 3.13E-01 | 5.29E-05 | 2.19E-01 | 2.78E-03 | 3.13E-01 | 4.91E-05 | 2.19E-01 | 2.41E-03 |
| 4.17E-01 | 1.06E-04 | 2.92E-01 | 2.76E-03 | 4.17E-01 | 8.65E-05 | 2.92E-01 | 2.41E-03 |
| 5.21E-01 | 2.22E-04 | 3.65E-01 | 2.74E-03 | 5.21E-01 | 1.44E-04 | 3.65E-01 | 2.40E-03 |
| 6.25E-01 | 6.63E-04 | 4.38E-01 | 2.71E-03 | 6.25E-01 | 2.32E-04 | 4.38E-01 | 2.40E-03 |
| 7.29E-01 | 6.22E-03 | 5.10E-01 | 2.69E-03 | 7.29E-01 | 2.07E-03 | 5.10E-01 | 2.39E-03 |
| 8.33E-01 | 1.15E-03 | 5.83E-01 | 2.67E-03 | 8.33E-01 | 8.83E-04 | 5.83E-01 | 2.39E-03 |
| 9.38E-01 | 2.41E-04 | 6.56E-01 | 2.66E-03 | 9.38E-01 | 2.39E-04 | 6.56E-01 | 2.39E-03 |
| 1.04E+00 | 1.07E-04 | 7.29E-01 | 2.65E-03 | 1.04E+00 | 1.24E-04 | 7.29E-01 | 2.39E-03 |
| 1.15E+00 | 2.41E-04 | 8.02E-01 | 2.64E-03 | 1.15E+00 | 2.27E-04 | 8.02E-01 | 2.40E-03 |
| 1.25E+00 | 3.82E-04 | 8.75E-01 | 2.64E-03 | 1.25E+00 | 3.52E-04 | 8.75E-01 | 2.41E-03 |
| 1.35E+00 | 5.26E-04 | 9.48E-01 | 2.64E-03 | 1.35E+00 | 4.84E-04 | 9.48E-01 | 2.42E-03 |
| 1.46E+00 | 6.79E-04 | 1.02E+00 | 2.64E-03 | 1.46E+00 | 6.23E-04 | 1.02E+00 | 2.43E-03 |
| 1.56E+00 | 8.41E-04 | 1.09E+00 | 2.65E-03 | 1.56E+00 | 7.70E-04 | 1.09E+00 | 2.44E-03 |
| 1.67E+00 | 1.01E-03 | 1.17E+00 | 2.65E-03 | 1.67E+00 | 9.26E-04 | 1.17E+00 | 2.44E-03 |
| 1.77E+00 | 1.21E-03 | 1.24E+00 | 2.66E-03 | 1.77E+00 | 1.08E-03 | 1.24E+00 | 2.45E-03 |
| 1.88E+00 | 1.48E-03 | 1.31E+00 | 2.66E-03 | 1.88E+00 | 1.25E-03 | 1.31E+00 | 2.46E-03 |
| 1.98E+00 | 1.82E-03 | 1.39E+00 | 2.66E-03 | 1.98E+00 | 1.58E-03 | 1.39E+00 | 2.47E-03 |
| 2.08E+00 | 2.11E-03 | 1.46E+00 | 2.67E-03 | 2.08E+00 | 1.92E-03 | 1.46E+00 | 2.48E-03 |
| 2.19E+00 | 2.36E-03 | 1.53E+00 | 2.67E-03 | 2.19E+00 | 2.17E-03 | 1.53E+00 | 2.48E-03 |
| 2.29E+00 | 2.53E-03 | 1.60E+00 | 2.67E-03 | 2.29E+00 | 2.36E-03 | 1.60E+00 | 2.49E-03 |
| 2.40E+00 | 2.64E-03 | 1.68E+00 | 2.67E-03 | 2.40E+00 | 2.45E-03 | 1.68E+00 | 2.49E-03 |
| 2.50E+00 | 2.67E-03 | 1.75E+00 | 2.67E-03 | 2.50E+00 | 2.49E-03 | 1.75E+00 | 2.49E-03 |
| 2.60E+00 | 2.64E-03 | 1.82E+00 | 2.67E-03 | 2.60E+00 | 2.45E-03 | 1.82E+00 | 2.49E-03 |
| 2.71E+00 | 2.53E-03 | 1.90E+00 | 2.67E-03 | 2.71E+00 | 2.36E-03 | 1.90E+00 | 2.49E-03 |
| 2.81E+00 | 2.36E-03 | 1.97E+00 | 2.67E-03 | 2.81E+00 | 2.17E-03 | 1.97E+00 | 2.48E-03 |
| 2.92E+00 | 2.11E-03 | 2.04E+00 | 2.67E-03 | 2.92E+00 | 1.92E-03 | 2.04E+00 | 2.48E-03 |
| 3.02E+00 | 1.82E-03 | 2.11E+00 | 2.66E-03 | 3.02E+00 | 1.58E-03 | 2.11E+00 | 2.47E-03 |
| 3.13E+00 | 1.48E-03 | 2.19E+00 | 2.66E-03 | 3.13E+00 | 1.25E-03 | 2.19E+00 | 2.46E-03 |
| 3.23E+00 | 1.21E-03 | 2.26E+00 | 2.66E-03 | 3.23E+00 | 1.08E-03 | 2.26E+00 | 2.45E-03 |
| 3.33E+00 | 1.01E-03 | 2.33E+00 | 2.65E-03 | 3.33E+00 | 9.25E-04 | 2.33E+00 | 2.44E-03 |

| | | | | | | | |
|---|---|---|---|---|---|---|---|
| 3.44E+00 | 8.41E-04 | 2.41E+00 | 2.65E-03 | 3.44E+00 | 7.69E-04 | 2.41E+00 | 2.44E-03 |
| 3.54E+00 | 6.78E-04 | 2.48E+00 | 2.64E-03 | 3.54E+00 | 6.22E-04 | 2.48E+00 | 2.43E-03 |
| 3.65E+00 | 5.25E-04 | 2.55E+00 | 2.64E-03 | 3.65E+00 | 4.83E-04 | 2.55E+00 | 2.42E-03 |
| 3.75E+00 | 3.80E-04 | 2.63E+00 | 2.64E-03 | 3.75E+00 | 3.51E-04 | 2.63E+00 | 2.41E-03 |
| 3.85E+00 | 2.39E-04 | 2.70E+00 | 2.64E-03 | 3.85E+00 | 2.26E-04 | 2.70E+00 | 2.40E-03 |
| 3.96E+00 | 9.47E-05 | 2.77E+00 | 2.65E-03 | 3.96E+00 | 1.25E-04 | 2.77E+00 | 2.39E-03 |
| 4.06E+00 | 1.27E-04 | 2.84E+00 | 2.66E-03 | 4.06E+00 | 2.33E-04 | 2.84E+00 | 2.39E-03 |
| 4.1667 | 6.72E-04 | 2.9167 | 2.67E-03 | 4.17E+00 | 8.07E-04 | 2.92E+00 | 2.39E-03 |
| 4.2708 | 8.31E-03 | 2.9896 | 2.69E-03 | 4.27E+00 | 1.77E-03 | 2.99E+00 | 2.39E-03 |
| 4.375 | 1.02E-03 | 3.0625 | 2.71E-03 | 4.38E+00 | 2.19E-04 | 3.06E+00 | 2.40E-03 |
| 4.4792 | 2.22E-04 | 3.1354 | 2.74E-03 | 4.48E+00 | 1.45E-04 | 3.14E+00 | 2.40E-03 |
| 4.5833 | 1.06E-04 | 3.2083 | 2.76E-03 | 4.58E+00 | 8.83E-05 | 3.21E+00 | 2.41E-03 |
| 4.6875 | 5.42E-05 | 3.2813 | 2.78E-03 | 4.69E+00 | 5.06E-05 | 3.28E+00 | 2.41E-03 |
| 4.7917 | 2.63E-05 | 3.3542 | 2.79E-03 | 4.79E+00 | 2.72E-05 | 3.35E+00 | 2.40E-03 |
| 4.8958 | 1.50E-05 | 3.4271 | 2.76E-03 | 4.90E+00 | 1.44E-05 | 3.43E+00 | 2.36E-03 |
| 5 | 1.41E-05 | 3.5 | 2.67E-03 | 5.00E+00 | 1.01E-05 | 3.50E+00 | 2.32E-03 |

Table 0-57 Surface tensile strain profiles for sample N7, step 66%YS.

| **Hardened Layer** | | | | **Soft Bulk** | | | |
|---|---|---|---|---|---|---|---|
| Longitudinal | | Transverse | | Longitudinal | | Transverse | |
| Length | Strain | Length | Strain | Length | Strain | Length | Strain |
| 0.00E+00 | 1.50E-05 | 0.00E+00 | 2.97E-03 | 0.00E+00 | 1.08E-05 | 0.00E+00 | 2.59E-03 |
| 1.04E-01 | 1.59E-05 | 7.29E-02 | 3.08E-03 | 1.04E-01 | 1.52E-05 | 7.29E-02 | 2.63E-03 |
| 2.08E-01 | 2.72E-05 | 1.46E-01 | 3.11E-03 | 2.08E-01 | 2.81E-05 | 1.46E-01 | 2.67E-03 |
| 3.13E-01 | 5.64E-05 | 2.19E-01 | 3.11E-03 | 3.13E-01 | 5.24E-05 | 2.19E-01 | 2.69E-03 |
| 4.17E-01 | 1.13E-04 | 2.92E-01 | 3.09E-03 | 4.17E-01 | 9.23E-05 | 2.92E-01 | 2.69E-03 |
| 5.21E-01 | 2.40E-04 | 3.65E-01 | 3.06E-03 | 5.21E-01 | 1.57E-04 | 3.65E-01 | 2.69E-03 |
| 6.25E-01 | 7.41E-04 | 4.38E-01 | 3.03E-03 | 6.25E-01 | 2.63E-04 | 4.38E-01 | 2.69E-03 |
| 7.29E-01 | 7.04E-03 | 5.10E-01 | 3.00E-03 | 7.29E-01 | 2.28E-03 | 5.10E-01 | 2.68E-03 |
| 8.33E-01 | 1.31E-03 | 5.83E-01 | 2.98E-03 | 8.33E-01 | 1.04E-03 | 5.83E-01 | 2.68E-03 |
| 9.38E-01 | 2.85E-04 | 6.56E-01 | 2.97E-03 | 9.38E-01 | 2.80E-04 | 6.56E-01 | 2.68E-03 |
| 1.04E+00 | 9.68E-05 | 7.29E-01 | 2.96E-03 | 1.04E+00 | 1.25E-04 | 7.29E-01 | 2.69E-03 |
| 1.15E+00 | 2.34E-04 | 8.02E-01 | 2.95E-03 | 1.15E+00 | 2.24E-04 | 8.02E-01 | 2.70E-03 |
| 1.25E+00 | 3.83E-04 | 8.75E-01 | 2.95E-03 | 1.25E+00 | 3.55E-04 | 8.75E-01 | 2.71E-03 |
| 1.35E+00 | 5.36E-04 | 9.48E-01 | 2.95E-03 | 1.35E+00 | 4.93E-04 | 9.48E-01 | 2.72E-03 |
| 1.46E+00 | 6.97E-04 | 1.02E+00 | 2.95E-03 | 1.46E+00 | 6.40E-04 | 1.02E+00 | 2.73E-03 |
| 1.56E+00 | 8.70E-04 | 1.09E+00 | 2.96E-03 | 1.56E+00 | 7.96E-04 | 1.09E+00 | 2.74E-03 |
| 1.67E+00 | 1.06E-03 | 1.17E+00 | 2.96E-03 | 1.67E+00 | 9.62E-04 | 1.17E+00 | 2.76E-03 |
| 1.77E+00 | 1.29E-03 | 1.24E+00 | 2.97E-03 | 1.77E+00 | 1.11E-03 | 1.24E+00 | 2.77E-03 |
| 1.88E+00 | 1.63E-03 | 1.31E+00 | 2.97E-03 | 1.88E+00 | 1.37E-03 | 1.31E+00 | 2.78E-03 |
| 1.98E+00 | 2.01E-03 | 1.39E+00 | 2.98E-03 | 1.98E+00 | 1.78E-03 | 1.39E+00 | 2.78E-03 |

| | | | | | | | |
|---|---|---|---|---|---|---|---|
| 2.08E+00 | 2.34E-03 | 1.46E+00 | 2.98E-03 | 2.08E+00 | 2.15E-03 | 1.46E+00 | 2.79E-03 |
| 2.19E+00 | 2.62E-03 | 1.53E+00 | 2.98E-03 | 2.19E+00 | 2.45E-03 | 1.53E+00 | 2.80E-03 |
| 2.29E+00 | 2.83E-03 | 1.60E+00 | 2.98E-03 | 2.29E+00 | 2.65E-03 | 1.60E+00 | 2.80E-03 |
| 2.40E+00 | 2.95E-03 | 1.68E+00 | 2.99E-03 | 2.40E+00 | 2.77E-03 | 1.68E+00 | 2.80E-03 |
| 2.50E+00 | 2.99E-03 | 1.75E+00 | 2.99E-03 | 2.50E+00 | 2.81E-03 | 1.75E+00 | 2.81E-03 |
| 2.60E+00 | 2.95E-03 | 1.82E+00 | 2.99E-03 | 2.60E+00 | 2.77E-03 | 1.82E+00 | 2.80E-03 |
| 2.71E+00 | 2.83E-03 | 1.90E+00 | 2.99E-03 | 2.71E+00 | 2.65E-03 | 1.90E+00 | 2.80E-03 |
| 2.81E+00 | 2.62E-03 | 1.97E+00 | 2.98E-03 | 2.81E+00 | 2.45E-03 | 1.97E+00 | 2.80E-03 |
| 2.92E+00 | 2.34E-03 | 2.04E+00 | 2.98E-03 | 2.92E+00 | 2.15E-03 | 2.04E+00 | 2.79E-03 |
| 3.02E+00 | 2.01E-03 | 2.11E+00 | 2.98E-03 | 3.02E+00 | 1.78E-03 | 2.11E+00 | 2.78E-03 |
| 3.13E+00 | 1.63E-03 | 2.19E+00 | 2.97E-03 | 3.13E+00 | 1.37E-03 | 2.19E+00 | 2.78E-03 |
| 3.23E+00 | 1.29E-03 | 2.26E+00 | 2.97E-03 | 3.23E+00 | 1.11E-03 | 2.26E+00 | 2.77E-03 |
| 3.33E+00 | 1.05E-03 | 2.33E+00 | 2.96E-03 | 3.33E+00 | 9.62E-04 | 2.33E+00 | 2.76E-03 |
| 3.44E+00 | 8.69E-04 | 2.41E+00 | 2.96E-03 | 3.44E+00 | 7.95E-04 | 2.41E+00 | 2.74E-03 |
| 3.54E+00 | 6.96E-04 | 2.48E+00 | 2.95E-03 | 3.54E+00 | 6.39E-04 | 2.48E+00 | 2.73E-03 |
| 3.65E+00 | 5.35E-04 | 2.55E+00 | 2.95E-03 | 3.65E+00 | 4.92E-04 | 2.55E+00 | 2.72E-03 |
| 3.75E+00 | 3.81E-04 | 2.63E+00 | 2.95E-03 | 3.75E+00 | 3.53E-04 | 2.63E+00 | 2.71E-03 |
| 3.85E+00 | 2.32E-04 | 2.70E+00 | 2.95E-03 | 3.85E+00 | 2.23E-04 | 2.70E+00 | 2.70E-03 |
| 3.96E+00 | 8.00E-05 | 2.77E+00 | 2.96E-03 | 3.96E+00 | 1.26E-04 | 2.77E+00 | 2.69E-03 |
| 4.06E+00 | 1.71E-04 | 2.84E+00 | 2.97E-03 | 4.06E+00 | 2.71E-04 | 2.84E+00 | 2.68E-03 |
| 4.1667 | 7.81E-04 | 2.9167 | 2.98E-03 | 4.17E+00 | 9.36E-04 | 2.92E+00 | 2.68E-03 |
| 4.2708 | 9.63E-03 | 2.9896 | 3.00E-03 | 4.27E+00 | 1.93E-03 | 2.99E+00 | 2.68E-03 |
| 4.375 | 1.08E-03 | 3.0625 | 3.03E-03 | 4.38E+00 | 2.45E-04 | 3.06E+00 | 2.69E-03 |
| 4.4792 | 2.33E-04 | 3.1354 | 3.06E-03 | 4.48E+00 | 1.57E-04 | 3.14E+00 | 2.69E-03 |
| 4.5833 | 1.12E-04 | 3.2083 | 3.09E-03 | 4.58E+00 | 9.43E-05 | 3.21E+00 | 2.69E-03 |
| 4.6875 | 5.78E-05 | 3.2813 | 3.11E-03 | 4.69E+00 | 5.41E-05 | 3.28E+00 | 2.69E-03 |
| 4.7917 | 2.91E-05 | 3.3542 | 3.12E-03 | 4.79E+00 | 2.97E-05 | 3.35E+00 | 2.67E-03 |
| 4.8958 | 1.81E-05 | 3.4271 | 3.08E-03 | 4.90E+00 | 1.70E-05 | 3.43E+00 | 2.63E-03 |
| 5 | 1.74E-05 | 3.5 | 2.97E-03 | 5.00E+00 | 1.30E-05 | 3.50E+00 | 2.59E-03 |

Table B-58 Surface tensile strain profiles for sample N7, step 74%YS.

| **Hardened Layer** | | | | **Soft Bulk** | | | |
|---|---|---|---|---|---|---|---|
| Longitudinal | | Transverse | | Longitudinal | | Transverse | |
| Length | Strain | Length | Strain | Length | Strain | Length | Strain |
| 0.00E+00 | 1.95E-05 | 0.00E+00 | 3.30E-03 | 0.00E+00 | 1.50E-05 | 0.00E+00 | 2.89E-03 |
| 1.04E-01 | 2.00E-05 | 7.29E-02 | 3.43E-03 | 1.04E-01 | 1.86E-05 | 7.29E-02 | 2.94E-03 |
| 2.08E-01 | 3.07E-05 | 1.46E-01 | 3.48E-03 | 2.08E-01 | 3.11E-05 | 1.46E-01 | 2.99E-03 |
| 3.13E-01 | 6.05E-05 | 2.19E-01 | 3.48E-03 | 3.13E-01 | 5.60E-05 | 2.19E-01 | 3.01E-03 |
| 4.17E-01 | 1.20E-04 | 2.92E-01 | 3.45E-03 | 4.17E-01 | 9.83E-05 | 2.92E-01 | 3.02E-03 |
| 5.21E-01 | 2.56E-04 | 3.65E-01 | 3.42E-03 | 5.21E-01 | 1.68E-04 | 3.65E-01 | 3.02E-03 |
| 6.25E-01 | 8.10E-04 | 4.38E-01 | 3.38E-03 | 6.25E-01 | 2.94E-04 | 4.38E-01 | 3.02E-03 |

| | | | | | | | |
|---|---|---|---|---|---|---|---|
| 7.29E-01 | 8.00E-03 | 5.10E-01 | 3.36E-03 | 7.29E-01 | 2.48E-03 | 5.10E-01 | 3.01E-03 |
| 8.33E-01 | 1.45E-03 | 5.83E-01 | 3.33E-03 | 8.33E-01 | 1.15E-03 | 5.83E-01 | 3.02E-03 |
| 9.38E-01 | 3.26E-04 | 6.56E-01 | 3.32E-03 | 9.38E-01 | 3.15E-04 | 6.56E-01 | 3.02E-03 |
| 1.04E+00 | 9.35E-05 | 7.29E-01 | 3.30E-03 | 1.04E+00 | 1.31E-04 | 7.29E-01 | 3.03E-03 |
| 1.15E+00 | 2.33E-04 | 8.02E-01 | 3.30E-03 | 1.15E+00 | 2.25E-04 | 8.02E-01 | 3.04E-03 |
| 1.25E+00 | 3.90E-04 | 8.75E-01 | 3.30E-03 | 1.25E+00 | 3.62E-04 | 8.75E-01 | 3.05E-03 |
| 1.35E+00 | 5.51E-04 | 9.48E-01 | 3.30E-03 | 1.35E+00 | 5.07E-04 | 9.48E-01 | 3.07E-03 |
| 1.46E+00 | 7.20E-04 | 1.02E+00 | 3.30E-03 | 1.46E+00 | 6.61E-04 | 1.02E+00 | 3.08E-03 |
| 1.56E+00 | 9.02E-04 | 1.09E+00 | 3.30E-03 | 1.56E+00 | 8.26E-04 | 1.09E+00 | 3.10E-03 |
| 1.67E+00 | 1.10E-03 | 1.17E+00 | 3.31E-03 | 1.67E+00 | 1.00E-03 | 1.17E+00 | 3.11E-03 |
| 1.77E+00 | 1.38E-03 | 1.24E+00 | 3.31E-03 | 1.77E+00 | 1.16E-03 | 1.24E+00 | 3.12E-03 |
| 1.88E+00 | 1.81E-03 | 1.31E+00 | 3.32E-03 | 1.88E+00 | 1.53E-03 | 1.31E+00 | 3.14E-03 |
| 1.98E+00 | 2.22E-03 | 1.39E+00 | 3.32E-03 | 1.98E+00 | 2.01E-03 | 1.39E+00 | 3.15E-03 |
| 2.08E+00 | 2.61E-03 | 1.46E+00 | 3.33E-03 | 2.08E+00 | 2.42E-03 | 1.46E+00 | 3.16E-03 |
| 2.19E+00 | 2.92E-03 | 1.53E+00 | 3.33E-03 | 2.19E+00 | 2.76E-03 | 1.53E+00 | 3.16E-03 |
| 2.29E+00 | 3.16E-03 | 1.60E+00 | 3.33E-03 | 2.29E+00 | 2.99E-03 | 1.60E+00 | 3.17E-03 |
| 2.40E+00 | 3.29E-03 | 1.68E+00 | 3.33E-03 | 2.40E+00 | 3.13E-03 | 1.68E+00 | 3.17E-03 |
| 2.50E+00 | 3.34E-03 | 1.75E+00 | 3.34E-03 | 2.50E+00 | 3.17E-03 | 1.75E+00 | 3.17E-03 |
| 2.60E+00 | 3.29E-03 | 1.82E+00 | 3.33E-03 | 2.60E+00 | 3.13E-03 | 1.82E+00 | 3.17E-03 |
| 2.71E+00 | 3.16E-03 | 1.90E+00 | 3.33E-03 | 2.71E+00 | 2.99E-03 | 1.90E+00 | 3.17E-03 |
| 2.81E+00 | 2.92E-03 | 1.97E+00 | 3.33E-03 | 2.81E+00 | 2.76E-03 | 1.97E+00 | 3.16E-03 |
| 2.92E+00 | 2.61E-03 | 2.04E+00 | 3.33E-03 | 2.92E+00 | 2.42E-03 | 2.04E+00 | 3.16E-03 |
| 3.02E+00 | 2.22E-03 | 2.11E+00 | 3.32E-03 | 3.02E+00 | 2.01E-03 | 2.11E+00 | 3.15E-03 |
| 3.13E+00 | 1.81E-03 | 2.19E+00 | 3.32E-03 | 3.13E+00 | 1.53E-03 | 2.19E+00 | 3.14E-03 |
| 3.23E+00 | 1.38E-03 | 2.26E+00 | 3.31E-03 | 3.23E+00 | 1.16E-03 | 2.26E+00 | 3.12E-03 |
| 3.33E+00 | 1.10E-03 | 2.33E+00 | 3.31E-03 | 3.33E+00 | 1.00E-03 | 2.33E+00 | 3.11E-03 |
| 3.44E+00 | 9.01E-04 | 2.41E+00 | 3.30E-03 | 3.44E+00 | 8.25E-04 | 2.41E+00 | 3.10E-03 |
| 3.54E+00 | 7.19E-04 | 2.48E+00 | 3.30E-03 | 3.54E+00 | 6.60E-04 | 2.48E+00 | 3.08E-03 |
| 3.65E+00 | 5.50E-04 | 2.55E+00 | 3.30E-03 | 3.65E+00 | 5.06E-04 | 2.55E+00 | 3.07E-03 |
| 3.75E+00 | 3.89E-04 | 2.63E+00 | 3.30E-03 | 3.75E+00 | 3.61E-04 | 2.63E+00 | 3.06E-03 |
| 3.85E+00 | 2.31E-04 | 2.70E+00 | 3.30E-03 | 3.85E+00 | 2.24E-04 | 2.70E+00 | 3.04E-03 |
| 3.96E+00 | 7.33E-05 | 2.77E+00 | 3.30E-03 | 3.96E+00 | 1.32E-04 | 2.77E+00 | 3.03E-03 |
| 4.06E+00 | 2.11E-04 | 2.84E+00 | 3.32E-03 | 4.06E+00 | 3.05E-04 | 2.84E+00 | 3.02E-03 |
| 4.1667 | 8.84E-04 | 2.9167 | 3.33E-03 | 4.17E+00 | 1.05E-03 | 2.92E+00 | 3.02E-03 |
| 4.2708 | 1.10E-02 | 2.9896 | 3.36E-03 | 4.27E+00 | 2.09E-03 | 2.99E+00 | 3.02E-03 |
| 4.375 | 1.14E-03 | 3.0625 | 3.38E-03 | 4.38E+00 | 2.72E-04 | 3.06E+00 | 3.02E-03 |
| 4.4792 | 2.42E-04 | 3.1354 | 3.42E-03 | 4.48E+00 | 1.68E-04 | 3.14E+00 | 3.02E-03 |
| 4.5833 | 1.18E-04 | 3.2083 | 3.45E-03 | 4.58E+00 | 9.99E-05 | 3.21E+00 | 3.02E-03 |
| 4.6875 | 6.17E-05 | 3.2813 | 3.48E-03 | 4.69E+00 | 5.77E-05 | 3.28E+00 | 3.01E-03 |
| 4.7917 | 3.26E-05 | 3.3542 | 3.48E-03 | 4.79E+00 | 3.27E-05 | 3.35E+00 | 2.99E-03 |
| 4.8958 | 2.22E-05 | 3.4271 | 3.43E-03 | 4.90E+00 | 2.04E-05 | 3.43E+00 | 2.94E-03 |

| | | | | | | | |
|---|---|---|---|---|---|---|---|
| 5 | 2.19E-05 | 3.5 | 3.30E-03 | 5.00E+00 | 1.71E-05 | 3.50E+00 | 2.89E-03 |

Table B-59 Surface tensile strain profiles for sample N7, step 89%YS.

| **Hardened Layer** | | | | **Soft Bulk** | | | |
|---|---|---|---|---|---|---|---|
| Longitudinal | | Transverse | | Longitudinal | | Transverse | |
| Length | Strain | Length | Strain | Length | Strain | Length | Strain |
| 0.00E+00 | 2.91E-05 | 0.00E+00 | 3.99E-03 | 0.00E+00 | 2.35E-05 | 0.00E+00 | 3.49E-03 |
| 1.04E-01 | 2.90E-05 | 7.29E-02 | 4.15E-03 | 1.04E-01 | 2.62E-05 | 7.29E-02 | 3.56E-03 |
| 2.08E-01 | 3.83E-05 | 1.46E-01 | 4.22E-03 | 2.08E-01 | 3.74E-05 | 1.46E-01 | 3.62E-03 |
| 3.13E-01 | 6.76E-05 | 2.19E-01 | 4.21E-03 | 3.13E-01 | 6.23E-05 | 2.19E-01 | 3.65E-03 |
| 4.17E-01 | 1.29E-04 | 2.92E-01 | 4.19E-03 | 4.17E-01 | 1.07E-04 | 2.92E-01 | 3.67E-03 |
| 5.21E-01 | 2.75E-04 | 3.65E-01 | 4.15E-03 | 5.21E-01 | 1.84E-04 | 3.65E-01 | 3.67E-03 |
| 6.25E-01 | 9.10E-04 | 4.38E-01 | 4.11E-03 | 6.25E-01 | 3.43E-04 | 4.38E-01 | 3.67E-03 |
| 7.29E-01 | 1.02E-02 | 5.10E-01 | 4.07E-03 | 7.29E-01 | 2.83E-03 | 5.10E-01 | 3.68E-03 |
| 8.33E-01 | 1.75E-03 | 5.83E-01 | 4.04E-03 | 8.33E-01 | 1.43E-03 | 5.83E-01 | 3.68E-03 |
| 9.38E-01 | 4.06E-04 | 6.56E-01 | 4.02E-03 | 9.38E-01 | 3.69E-04 | 6.56E-01 | 3.69E-03 |
| 1.04E+00 | 1.01E-04 | 7.29E-01 | 4.01E-03 | 1.04E+00 | 1.46E-04 | 7.29E-01 | 3.71E-03 |
| 1.15E+00 | 2.40E-04 | 8.02E-01 | 4.00E-03 | 1.15E+00 | 2.35E-04 | 8.02E-01 | 3.72E-03 |
| 1.25E+00 | 4.10E-04 | 8.75E-01 | 3.99E-03 | 1.25E+00 | 3.81E-04 | 8.75E-01 | 3.74E-03 |
| 1.35E+00 | 5.83E-04 | 9.48E-01 | 3.99E-03 | 1.35E+00 | 5.38E-04 | 9.48E-01 | 3.76E-03 |
| 1.46E+00 | 7.67E-04 | 1.02E+00 | 3.99E-03 | 1.46E+00 | 7.05E-04 | 1.02E+00 | 3.78E-03 |
| 1.56E+00 | 9.67E-04 | 1.09E+00 | 4.00E-03 | 1.56E+00 | 8.86E-04 | 1.09E+00 | 3.80E-03 |
| 1.67E+00 | 1.21E-03 | 1.17E+00 | 4.00E-03 | 1.67E+00 | 1.08E-03 | 1.17E+00 | 3.82E-03 |
| 1.77E+00 | 1.65E-03 | 1.24E+00 | 4.01E-03 | 1.77E+00 | 1.34E-03 | 1.24E+00 | 3.83E-03 |
| 1.88E+00 | 2.17E-03 | 1.31E+00 | 4.01E-03 | 1.88E+00 | 1.92E-03 | 1.31E+00 | 3.85E-03 |
| 1.98E+00 | 2.69E-03 | 1.39E+00 | 4.02E-03 | 1.98E+00 | 2.50E-03 | 1.39E+00 | 3.86E-03 |
| 2.08E+00 | 3.16E-03 | 1.46E+00 | 4.02E-03 | 2.08E+00 | 3.02E-03 | 1.46E+00 | 3.87E-03 |
| 2.19E+00 | 3.55E-03 | 1.53E+00 | 4.03E-03 | 2.19E+00 | 3.42E-03 | 1.53E+00 | 3.88E-03 |
| 2.29E+00 | 3.84E-03 | 1.60E+00 | 4.03E-03 | 2.29E+00 | 3.69E-03 | 1.60E+00 | 3.88E-03 |
| 2.40E+00 | 3.99E-03 | 1.68E+00 | 4.03E-03 | 2.40E+00 | 3.84E-03 | 1.68E+00 | 3.89E-03 |
| 2.50E+00 | 4.03E-03 | 1.75E+00 | 4.03E-03 | 2.50E+00 | 3.89E-03 | 1.75E+00 | 3.89E-03 |
| 2.60E+00 | 3.99E-03 | 1.82E+00 | 4.03E-03 | 2.60E+00 | 3.84E-03 | 1.82E+00 | 3.89E-03 |
| 2.71E+00 | 3.84E-03 | 1.90E+00 | 4.03E-03 | 2.71E+00 | 3.69E-03 | 1.90E+00 | 3.88E-03 |
| 2.81E+00 | 3.55E-03 | 1.97E+00 | 4.03E-03 | 2.81E+00 | 3.42E-03 | 1.97E+00 | 3.88E-03 |
| 2.92E+00 | 3.16E-03 | 2.04E+00 | 4.02E-03 | 2.92E+00 | 3.02E-03 | 2.04E+00 | 3.87E-03 |
| 3.02E+00 | 2.69E-03 | 2.11E+00 | 4.02E-03 | 3.02E+00 | 2.49E-03 | 2.11E+00 | 3.86E-03 |
| 3.13E+00 | 2.17E-03 | 2.19E+00 | 4.01E-03 | 3.13E+00 | 1.92E-03 | 2.19E+00 | 3.85E-03 |
| 3.23E+00 | 1.65E-03 | 2.26E+00 | 4.01E-03 | 3.23E+00 | 1.34E-03 | 2.26E+00 | 3.83E-03 |
| 3.33E+00 | 1.21E-03 | 2.33E+00 | 4.00E-03 | 3.33E+00 | 1.08E-03 | 2.33E+00 | 3.82E-03 |
| 3.44E+00 | 9.67E-04 | 2.41E+00 | 4.00E-03 | 3.44E+00 | 8.86E-04 | 2.41E+00 | 3.80E-03 |
| 3.54E+00 | 7.66E-04 | 2.48E+00 | 3.99E-03 | 3.54E+00 | 7.04E-04 | 2.48E+00 | 3.78E-03 |

| | | | | | | | |
|---|---|---|---|---|---|---|---|
| 3.65E+00 | 5.82E-04 | 2.55E+00 | 3.99E-03 | 3.65E+00 | 5.37E-04 | 2.55E+00 | 3.76E-03 |
| 3.75E+00 | 4.09E-04 | 2.63E+00 | 3.99E-03 | 3.75E+00 | 3.80E-04 | 2.63E+00 | 3.74E-03 |
| 3.85E+00 | 2.38E-04 | 2.70E+00 | 4.00E-03 | 3.85E+00 | 2.34E-04 | 2.70E+00 | 3.72E-03 |
| 3.96E+00 | 7.81E-05 | 2.77E+00 | 4.00E-03 | 3.96E+00 | 1.47E-04 | 2.77E+00 | 3.71E-03 |
| 4.06E+00 | 2.95E-04 | 2.84E+00 | 4.02E-03 | 4.06E+00 | 3.54E-04 | 2.84E+00 | 3.69E-03 |
| 4.1667 | 1.18E-03 | 2.9167 | 4.04E-03 | 4.17E+00 | 1.28E-03 | 2.92E+00 | 3.68E-03 |
| 4.2708 | 1.37E-02 | 2.9896 | 4.07E-03 | 4.27E+00 | 2.38E-03 | 2.99E+00 | 3.68E-03 |
| 4.375 | 1.26E-03 | 3.0625 | 4.10E-03 | 4.38E+00 | 3.17E-04 | 3.06E+00 | 3.67E-03 |
| 4.4792 | 2.55E-04 | 3.1354 | 4.14E-03 | 4.48E+00 | 1.84E-04 | 3.14E+00 | 3.67E-03 |
| 4.5833 | 1.27E-04 | 3.2083 | 4.18E-03 | 4.58E+00 | 1.08E-04 | 3.21E+00 | 3.67E-03 |
| 4.6875 | 6.85E-05 | 3.2813 | 4.21E-03 | 4.69E+00 | 6.38E-05 | 3.28E+00 | 3.65E-03 |
| 4.7917 | 3.98E-05 | 3.3542 | 4.22E-03 | 4.79E+00 | 3.86E-05 | 3.35E+00 | 3.62E-03 |
| 4.8958 | 3.04E-05 | 3.4271 | 4.15E-03 | 4.90E+00 | 2.74E-05 | 3.43E+00 | 3.56E-03 |
| 5 | 3.05E-05 | 3.5 | 3.99E-03 | 5.00E+00 | 2.48E-05 | 3.50E+00 | 3.49E-03 |

## Sample L-R-1

Table 0-60 Surface tensile strain profiles for sample L-R-1, step 50%YS.

| **Hardened Layer** | | | | **Soft Bulk** | | | |
|---|---|---|---|---|---|---|---|
| Longitudinal | | Transverse | | Longitudinal | | Transverse | |
| Length | Strain | Length | Strain | Length | Strain | Length | Strain |
| 0.00E+00 | 2.16E-03 | 0.00E+00 | 2.16E-03 | 0.00E+00 | 9.18E-06 | 0.00E+00 | 1.86E-03 |
| 1.04E-01 | 2.23E-03 | 7.29E-02 | 2.23E-03 | 1.04E-01 | 1.68E-05 | 7.29E-02 | 1.89E-03 |
| 2.08E-01 | 2.25E-03 | 1.46E-01 | 2.25E-03 | 2.08E-01 | 3.43E-05 | 1.46E-01 | 1.92E-03 |
| 3.13E-01 | 2.25E-03 | 2.19E-01 | 2.25E-03 | 3.13E-01 | 6.18E-05 | 2.19E-01 | 1.92E-03 |
| 4.17E-01 | 2.23E-03 | 2.92E-01 | 2.23E-03 | 4.17E-01 | 1.01E-04 | 2.92E-01 | 1.92E-03 |
| 5.21E-01 | 2.21E-03 | 3.65E-01 | 2.21E-03 | 5.21E-01 | 1.51E-04 | 3.65E-01 | 1.91E-03 |
| 6.25E-01 | 2.19E-03 | 4.38E-01 | 2.19E-03 | 6.25E-01 | 2.92E-04 | 4.38E-01 | 1.91E-03 |
| 7.29E-01 | 2.18E-03 | 5.10E-01 | 2.18E-03 | 7.29E-01 | 1.79E-03 | 5.10E-01 | 1.90E-03 |
| 8.33E-01 | 2.16E-03 | 5.83E-01 | 2.16E-03 | 8.33E-01 | 8.39E-04 | 5.83E-01 | 1.90E-03 |
| 9.38E-01 | 2.15E-03 | 6.56E-01 | 2.15E-03 | 9.38E-01 | 2.65E-04 | 6.56E-01 | 1.89E-03 |
| 1.04E+00 | 2.14E-03 | 7.29E-01 | 2.14E-03 | 1.04E+00 | 1.42E-04 | 7.29E-01 | 1.89E-03 |
| 1.15E+00 | 2.14E-03 | 8.02E-01 | 2.14E-03 | 1.15E+00 | 2.19E-04 | 8.02E-01 | 1.89E-03 |
| 1.25E+00 | 2.14E-03 | 8.75E-01 | 2.14E-03 | 1.25E+00 | 3.27E-04 | 8.75E-01 | 1.90E-03 |
| 1.35E+00 | 2.14E-03 | 9.48E-01 | 2.14E-03 | 1.35E+00 | 4.44E-04 | 9.48E-01 | 1.90E-03 |
| 1.46E+00 | 2.14E-03 | 1.02E+00 | 2.14E-03 | 1.46E+00 | 5.68E-04 | 1.02E+00 | 1.90E-03 |
| 1.56E+00 | 2.14E-03 | 1.09E+00 | 2.14E-03 | 1.56E+00 | 6.99E-04 | 1.09E+00 | 1.91E-03 |
| 1.67E+00 | 2.14E-03 | 1.17E+00 | 2.14E-03 | 1.67E+00 | 8.35E-04 | 1.17E+00 | 1.91E-03 |
| 1.77E+00 | 2.14E-03 | 1.24E+00 | 2.14E-03 | 1.77E+00 | 9.76E-04 | 1.24E+00 | 1.92E-03 |
| 1.88E+00 | 2.14E-03 | 1.31E+00 | 2.14E-03 | 1.88E+00 | 1.11E-03 | 1.31E+00 | 1.92E-03 |
| 1.98E+00 | 2.14E-03 | 1.39E+00 | 2.14E-03 | 1.98E+00 | 1.24E-03 | 1.39E+00 | 1.93E-03 |

| | | | | | | | |
|---|---|---|---|---|---|---|---|
| 2.08E+00 | 2.15E-03 | 1.46E+00 | 2.15E-03 | 2.08E+00 | 1.45E-03 | 1.46E+00 | 1.93E-03 |
| 2.19E+00 | 2.15E-03 | 1.53E+00 | 2.15E-03 | 2.19E+00 | 1.67E-03 | 1.53E+00 | 1.93E-03 |
| 2.29E+00 | 2.15E-03 | 1.60E+00 | 2.15E-03 | 2.29E+00 | 1.82E-03 | 1.60E+00 | 1.94E-03 |
| 2.40E+00 | 2.15E-03 | 1.68E+00 | 2.15E-03 | 2.40E+00 | 1.91E-03 | 1.68E+00 | 1.94E-03 |
| 2.50E+00 | 2.15E-03 | 1.75E+00 | 2.15E-03 | 2.50E+00 | 1.94E-03 | 1.75E+00 | 1.94E-03 |
| 2.60E+00 | 2.15E-03 | 1.82E+00 | 2.15E-03 | 2.60E+00 | 1.91E-03 | 1.82E+00 | 1.94E-03 |
| 2.71E+00 | 2.15E-03 | 1.90E+00 | 2.15E-03 | 2.71E+00 | 1.82E-03 | 1.90E+00 | 1.94E-03 |
| 2.81E+00 | 2.15E-03 | 1.97E+00 | 2.15E-03 | 2.81E+00 | 1.67E-03 | 1.97E+00 | 1.93E-03 |
| 2.92E+00 | 2.15E-03 | 2.04E+00 | 2.15E-03 | 2.92E+00 | 1.45E-03 | 2.04E+00 | 1.93E-03 |
| 3.02E+00 | 2.14E-03 | 2.11E+00 | 2.14E-03 | 3.02E+00 | 1.24E-03 | 2.11E+00 | 1.93E-03 |
| 3.13E+00 | 2.14E-03 | 2.19E+00 | 2.14E-03 | 3.13E+00 | 1.11E-03 | 2.19E+00 | 1.92E-03 |
| 3.23E+00 | 2.14E-03 | 2.26E+00 | 2.14E-03 | 3.23E+00 | 9.75E-04 | 2.26E+00 | 1.92E-03 |
| 3.33E+00 | 2.14E-03 | 2.33E+00 | 2.14E-03 | 3.33E+00 | 8.35E-04 | 2.33E+00 | 1.91E-03 |
| 3.44E+00 | 2.14E-03 | 2.41E+00 | 2.14E-03 | 3.44E+00 | 6.99E-04 | 2.41E+00 | 1.91E-03 |
| 3.54E+00 | 2.14E-03 | 2.48E+00 | 2.14E-03 | 3.54E+00 | 5.68E-04 | 2.48E+00 | 1.90E-03 |
| 3.65E+00 | 2.13E-03 | 2.55E+00 | 2.13E-03 | 3.65E+00 | 4.44E-04 | 2.55E+00 | 1.90E-03 |
| 3.75E+00 | 2.14E-03 | 2.63E+00 | 2.14E-03 | 3.75E+00 | 3.26E-04 | 2.63E+00 | 1.90E-03 |
| 3.85E+00 | 2.14E-03 | 2.70E+00 | 2.14E-03 | 3.85E+00 | 2.19E-04 | 2.70E+00 | 1.89E-03 |
| 3.96E+00 | 2.14E-03 | 2.77E+00 | 2.14E-03 | 3.96E+00 | 1.43E-04 | 2.77E+00 | 1.89E-03 |
| 4.06E+00 | 2.15E-03 | 2.84E+00 | 2.15E-03 | 4.06E+00 | 2.59E-04 | 2.84E+00 | 1.89E-03 |
| 4.1667 | 2.16E-03 | 2.9167 | 2.16E-03 | 4.17E+00 | 7.85E-04 | 2.92E+00 | 1.90E-03 |
| 4.2708 | 2.18E-03 | 2.9896 | 2.18E-03 | 4.27E+00 | 1.55E-03 | 2.99E+00 | 1.90E-03 |
| 4.375 | 2.19E-03 | 3.0625 | 2.19E-03 | 4.38E+00 | 2.68E-04 | 3.06E+00 | 1.91E-03 |
| 4.4792 | 2.21E-03 | 3.1354 | 2.21E-03 | 4.48E+00 | 1.48E-04 | 3.14E+00 | 1.92E-03 |
| 4.5833 | 2.23E-03 | 3.2083 | 2.23E-03 | 4.58E+00 | 1.01E-04 | 3.21E+00 | 1.92E-03 |
| 4.6875 | 2.25E-03 | 3.2813 | 2.25E-03 | 4.69E+00 | 6.17E-05 | 3.28E+00 | 1.92E-03 |
| 4.7917 | 2.25E-03 | 3.3542 | 2.25E-03 | 4.79E+00 | 3.46E-05 | 3.35E+00 | 1.92E-03 |
| 4.8958 | 2.23E-03 | 3.4271 | 2.23E-03 | 4.90E+00 | 1.74E-05 | 3.43E+00 | 1.89E-03 |
| 5 | 2.16E-03 | 3.5 | 2.16E-03 | 5.00E+00 | 9.95E-06 | 3.50E+00 | 1.86E-03 |

Table 0-61 Surface tensile strain profiles for sample L-R-1, step 60%YS.

| **Hardened Layer** | | | | **Soft Bulk** | | | |
|---|---|---|---|---|---|---|---|
| Longitudinal | | Transverse | | Longitudinal | | Transverse | |
| Length | Strain | Length | Strain | Length | Strain | Length | Strain |
| 0.00E+00 | 1.87E-05 | 0.00E+00 | 2.60E-03 | 0.00E+00 | 1.34E-05 | 0.00E+00 | 2.24E-03 |
| 1.04E-01 | 1.96E-05 | 7.29E-02 | 2.70E-03 | 1.04E-01 | 2.07E-05 | 7.29E-02 | 2.29E-03 |
| 2.08E-01 | 3.63E-05 | 1.46E-01 | 2.73E-03 | 2.08E-01 | 3.88E-05 | 1.46E-01 | 2.32E-03 |
| 3.13E-01 | 7.63E-05 | 2.19E-01 | 2.73E-03 | 3.13E-01 | 6.87E-05 | 2.19E-01 | 2.34E-03 |
| 4.17E-01 | 1.56E-04 | 2.92E-01 | 2.71E-03 | 4.17E-01 | 1.13E-04 | 2.92E-01 | 2.34E-03 |
| 5.21E-01 | 4.04E-04 | 3.65E-01 | 2.69E-03 | 5.21E-01 | 1.73E-04 | 3.65E-01 | 2.34E-03 |
| 6.25E-01 | 2.10E-03 | 4.38E-01 | 2.66E-03 | 6.25E-01 | 3.18E-04 | 4.38E-01 | 2.33E-03 |

| | | | | | | | |
|---|---|---|---|---|---|---|---|
| 7.29E-01 | 7.18E-03 | 5.10E-01 | 2.64E-03 | 7.29E-01 | 2.17E-03 | 5.10E-01 | 2.33E-03 |
| 8.33E-01 | 7.20E-04 | 5.83E-01 | 2.62E-03 | 8.33E-01 | 1.05E-03 | 5.83E-01 | 2.33E-03 |
| 9.38E-01 | 1.71E-04 | 6.56E-01 | 2.61E-03 | 9.38E-01 | 3.28E-04 | 6.56E-01 | 2.33E-03 |
| 1.04E+00 | 6.64E-05 | 7.29E-01 | 2.60E-03 | 1.04E+00 | 1.54E-04 | 7.29E-01 | 2.33E-03 |
| 1.15E+00 | 2.19E-04 | 8.02E-01 | 2.60E-03 | 1.15E+00 | 2.23E-04 | 8.02E-01 | 2.33E-03 |
| 1.25E+00 | 3.64E-04 | 8.75E-01 | 2.59E-03 | 1.25E+00 | 3.40E-04 | 8.75E-01 | 2.34E-03 |
| 1.35E+00 | 5.12E-04 | 9.48E-01 | 2.59E-03 | 1.35E+00 | 4.68E-04 | 9.48E-01 | 2.35E-03 |
| 1.46E+00 | 6.65E-04 | 1.02E+00 | 2.60E-03 | 1.46E+00 | 6.04E-04 | 1.02E+00 | 2.36E-03 |
| 1.56E+00 | 8.28E-04 | 1.09E+00 | 2.60E-03 | 1.56E+00 | 7.48E-04 | 1.09E+00 | 2.36E-03 |
| 1.67E+00 | 1.00E-03 | 1.17E+00 | 2.60E-03 | 1.67E+00 | 8.99E-04 | 1.17E+00 | 2.37E-03 |
| 1.77E+00 | 1.18E-03 | 1.24E+00 | 2.60E-03 | 1.77E+00 | 1.05E-03 | 1.24E+00 | 2.38E-03 |
| 1.88E+00 | 1.43E-03 | 1.31E+00 | 2.61E-03 | 1.88E+00 | 1.20E-03 | 1.31E+00 | 2.39E-03 |
| 1.98E+00 | 1.75E-03 | 1.39E+00 | 2.61E-03 | 1.98E+00 | 1.48E-03 | 1.39E+00 | 2.40E-03 |
| 2.08E+00 | 2.04E-03 | 1.46E+00 | 2.61E-03 | 2.08E+00 | 1.80E-03 | 1.46E+00 | 2.40E-03 |
| 2.19E+00 | 2.28E-03 | 1.53E+00 | 2.61E-03 | 2.19E+00 | 2.06E-03 | 1.53E+00 | 2.41E-03 |
| 2.29E+00 | 2.46E-03 | 1.60E+00 | 2.62E-03 | 2.29E+00 | 2.26E-03 | 1.60E+00 | 2.41E-03 |
| 2.40E+00 | 2.58E-03 | 1.68E+00 | 2.62E-03 | 2.40E+00 | 2.37E-03 | 1.68E+00 | 2.41E-03 |
| 2.50E+00 | 2.62E-03 | 1.75E+00 | 2.62E-03 | 2.50E+00 | 2.41E-03 | 1.75E+00 | 2.41E-03 |
| 2.60E+00 | 2.58E-03 | 1.82E+00 | 2.62E-03 | 2.60E+00 | 2.37E-03 | 1.82E+00 | 2.41E-03 |
| 2.71E+00 | 2.46E-03 | 1.90E+00 | 2.62E-03 | 2.71E+00 | 2.26E-03 | 1.90E+00 | 2.41E-03 |
| 2.81E+00 | 2.28E-03 | 1.97E+00 | 2.61E-03 | 2.81E+00 | 2.06E-03 | 1.97E+00 | 2.41E-03 |
| 2.92E+00 | 2.04E-03 | 2.04E+00 | 2.61E-03 | 2.92E+00 | 1.80E-03 | 2.04E+00 | 2.40E-03 |
| 3.02E+00 | 1.75E-03 | 2.11E+00 | 2.61E-03 | 3.02E+00 | 1.47E-03 | 2.11E+00 | 2.40E-03 |
| 3.13E+00 | 1.43E-03 | 2.19E+00 | 2.61E-03 | 3.13E+00 | 1.20E-03 | 2.19E+00 | 2.39E-03 |
| 3.23E+00 | 1.18E-03 | 2.26E+00 | 2.60E-03 | 3.23E+00 | 1.05E-03 | 2.26E+00 | 2.38E-03 |
| 3.33E+00 | 1.00E-03 | 2.33E+00 | 2.60E-03 | 3.33E+00 | 8.99E-04 | 2.33E+00 | 2.37E-03 |
| 3.44E+00 | 8.28E-04 | 2.41E+00 | 2.60E-03 | 3.44E+00 | 7.48E-04 | 2.41E+00 | 2.36E-03 |
| 3.54E+00 | 6.65E-04 | 2.48E+00 | 2.59E-03 | 3.54E+00 | 6.03E-04 | 2.48E+00 | 2.36E-03 |
| 3.65E+00 | 5.11E-04 | 2.55E+00 | 2.59E-03 | 3.65E+00 | 4.67E-04 | 2.55E+00 | 2.35E-03 |
| 3.75E+00 | 3.63E-04 | 2.63E+00 | 2.59E-03 | 3.75E+00 | 3.39E-04 | 2.63E+00 | 2.34E-03 |
| 3.85E+00 | 2.17E-04 | 2.70E+00 | 2.60E-03 | 3.85E+00 | 2.23E-04 | 2.70E+00 | 2.33E-03 |
| 3.96E+00 | 6.70E-05 | 2.77E+00 | 2.60E-03 | 3.96E+00 | 1.55E-04 | 2.77E+00 | 2.33E-03 |
| 4.06E+00 | 1.70E-04 | 2.84E+00 | 2.61E-03 | 4.06E+00 | 3.20E-04 | 2.84E+00 | 2.33E-03 |
| 4.1667 | 9.65E-04 | 2.9167 | 2.62E-03 | 4.17E+00 | 9.40E-04 | 2.92E+00 | 2.33E-03 |
| 4.2708 | 9.74E-03 | 2.9896 | 2.64E-03 | 4.27E+00 | 1.82E-03 | 2.99E+00 | 2.33E-03 |
| 4.375 | 2.35E-03 | 3.0625 | 2.66E-03 | 4.38E+00 | 2.91E-04 | 3.06E+00 | 2.33E-03 |
| 4.4792 | 4.47E-04 | 3.1354 | 2.69E-03 | 4.48E+00 | 1.69E-04 | 3.14E+00 | 2.34E-03 |
| 4.5833 | 1.62E-04 | 3.2083 | 2.71E-03 | 4.58E+00 | 1.12E-04 | 3.21E+00 | 2.34E-03 |
| 4.6875 | 7.69E-05 | 3.2813 | 2.73E-03 | 4.69E+00 | 6.86E-05 | 3.28E+00 | 2.34E-03 |
| 4.7917 | 3.68E-05 | 3.3542 | 2.73E-03 | 4.79E+00 | 3.91E-05 | 3.35E+00 | 2.32E-03 |
| 4.8958 | 2.06E-05 | 3.4271 | 2.70E-03 | 4.90E+00 | 2.13E-05 | 3.43E+00 | 2.29E-03 |

| | | | | | | | |
|---|---|---|---|---|---|---|---|
| 5 | 1.96E-05 | 3.5 | 2.60E-03 | 5.00E+00 | 1.42E-05 | 3.50E+00 | 2.24E-03 |

Table 0-62 Surface tensile strain profiles for sample L-R-1, step 70%YS.

| **Hardened Layer** | | | | **Soft Bulk** | | | |
|---|---|---|---|---|---|---|---|
| Longitudinal | | Transverse | | Longitudinal | | Transverse | |
| Length | Strain | Length | Strain | Length | Strain | Length | Strain |
| 0.00E+00 | 2.36E-05 | 0.00E+00 | 2.99E-03 | 0.00E+00 | 1.76E-05 | 0.00E+00 | 2.58E-03 |
| 1.04E-01 | 2.43E-05 | 7.29E-02 | 3.11E-03 | 1.04E-01 | 2.45E-05 | 7.29E-02 | 2.64E-03 |
| 2.08E-01 | 4.09E-05 | 1.46E-01 | 3.16E-03 | 2.08E-01 | 4.31E-05 | 1.46E-01 | 2.69E-03 |
| 3.13E-01 | 8.33E-05 | 2.19E-01 | 3.16E-03 | 3.13E-01 | 7.51E-05 | 2.19E-01 | 2.71E-03 |
| 4.17E-01 | 1.70E-04 | 2.92E-01 | 3.14E-03 | 4.17E-01 | 1.24E-04 | 2.92E-01 | 2.72E-03 |
| 5.21E-01 | 4.42E-04 | 3.65E-01 | 3.11E-03 | 5.21E-01 | 1.95E-04 | 3.65E-01 | 2.72E-03 |
| 6.25E-01 | 2.24E-03 | 4.38E-01 | 3.08E-03 | 6.25E-01 | 3.47E-04 | 4.38E-01 | 2.72E-03 |
| 7.29E-01 | 9.48E-03 | 5.10E-01 | 3.05E-03 | 7.29E-01 | 2.39E-03 | 5.10E-01 | 2.71E-03 |
| 8.33E-01 | 9.21E-04 | 5.83E-01 | 3.03E-03 | 8.33E-01 | 1.21E-03 | 5.83E-01 | 2.72E-03 |
| 9.38E-01 | 2.46E-04 | 6.56E-01 | 3.02E-03 | 9.38E-01 | 3.89E-04 | 6.56E-01 | 2.72E-03 |
| 1.04E+00 | 5.15E-05 | 7.29E-01 | 3.01E-03 | 1.04E+00 | 1.70E-04 | 7.29E-01 | 2.72E-03 |
| 1.15E+00 | 2.09E-04 | 8.02E-01 | 3.00E-03 | 1.15E+00 | 2.23E-04 | 8.02E-01 | 2.73E-03 |
| 1.25E+00 | 3.66E-04 | 8.75E-01 | 3.00E-03 | 1.25E+00 | 3.44E-04 | 8.75E-01 | 2.74E-03 |
| 1.35E+00 | 5.25E-04 | 9.48E-01 | 3.00E-03 | 1.35E+00 | 4.81E-04 | 9.48E-01 | 2.75E-03 |
| 1.46E+00 | 6.90E-04 | 1.02E+00 | 3.00E-03 | 1.46E+00 | 6.27E-04 | 1.02E+00 | 2.77E-03 |
| 1.56E+00 | 8.66E-04 | 1.09E+00 | 3.00E-03 | 1.56E+00 | 7.82E-04 | 1.09E+00 | 2.78E-03 |
| 1.67E+00 | 1.05E-03 | 1.17E+00 | 3.00E-03 | 1.67E+00 | 9.46E-04 | 1.17E+00 | 2.79E-03 |
| 1.77E+00 | 1.28E-03 | 1.24E+00 | 3.01E-03 | 1.77E+00 | 1.10E-03 | 1.24E+00 | 2.80E-03 |
| 1.88E+00 | 1.62E-03 | 1.31E+00 | 3.01E-03 | 1.88E+00 | 1.32E-03 | 1.31E+00 | 2.81E-03 |
| 1.98E+00 | 1.99E-03 | 1.39E+00 | 3.02E-03 | 1.98E+00 | 1.72E-03 | 1.39E+00 | 2.82E-03 |
| 2.08E+00 | 2.34E-03 | 1.46E+00 | 3.02E-03 | 2.08E+00 | 2.10E-03 | 1.46E+00 | 2.82E-03 |
| 2.19E+00 | 2.62E-03 | 1.53E+00 | 3.02E-03 | 2.19E+00 | 2.41E-03 | 1.53E+00 | 2.83E-03 |
| 2.29E+00 | 2.84E-03 | 1.60E+00 | 3.02E-03 | 2.29E+00 | 2.64E-03 | 1.60E+00 | 2.83E-03 |
| 2.40E+00 | 2.98E-03 | 1.68E+00 | 3.02E-03 | 2.40E+00 | 2.78E-03 | 1.68E+00 | 2.84E-03 |
| 2.50E+00 | 3.03E-03 | 1.75E+00 | 3.03E-03 | 2.50E+00 | 2.84E-03 | 1.75E+00 | 2.84E-03 |
| 2.60E+00 | 2.98E-03 | 1.82E+00 | 3.02E-03 | 2.60E+00 | 2.78E-03 | 1.82E+00 | 2.84E-03 |
| 2.71E+00 | 2.84E-03 | 1.90E+00 | 3.02E-03 | 2.71E+00 | 2.64E-03 | 1.90E+00 | 2.83E-03 |
| 2.81E+00 | 2.62E-03 | 1.97E+00 | 3.02E-03 | 2.81E+00 | 2.41E-03 | 1.97E+00 | 2.83E-03 |
| 2.92E+00 | 2.34E-03 | 2.04E+00 | 3.02E-03 | 2.92E+00 | 2.10E-03 | 2.04E+00 | 2.82E-03 |
| 3.02E+00 | 1.99E-03 | 2.11E+00 | 3.02E-03 | 3.02E+00 | 1.72E-03 | 2.11E+00 | 2.82E-03 |
| 3.13E+00 | 1.62E-03 | 2.19E+00 | 3.01E-03 | 3.13E+00 | 1.32E-03 | 2.19E+00 | 2.81E-03 |
| 3.23E+00 | 1.28E-03 | 2.26E+00 | 3.01E-03 | 3.23E+00 | 1.10E-03 | 2.26E+00 | 2.80E-03 |
| 3.33E+00 | 1.05E-03 | 2.33E+00 | 3.00E-03 | 3.33E+00 | 9.46E-04 | 2.33E+00 | 2.79E-03 |
| 3.44E+00 | 8.65E-04 | 2.41E+00 | 3.00E-03 | 3.44E+00 | 7.82E-04 | 2.41E+00 | 2.78E-03 |
| 3.54E+00 | 6.89E-04 | 2.48E+00 | 3.00E-03 | 3.54E+00 | 6.26E-04 | 2.48E+00 | 2.77E-03 |

| | | | | | | | |
|---|---|---|---|---|---|---|---|
| 3.65E+00 | 5.23E-04 | 2.55E+00 | 3.00E-03 | 3.65E+00 | 4.80E-04 | 2.55E+00 | 2.75E-03 |
| 3.75E+00 | 3.65E-04 | 2.63E+00 | 3.00E-03 | 3.75E+00 | 3.43E-04 | 2.63E+00 | 2.74E-03 |
| 3.85E+00 | 2.07E-04 | 2.70E+00 | 3.00E-03 | 3.85E+00 | 2.22E-04 | 2.70E+00 | 2.73E-03 |
| 3.96E+00 | 4.86E-05 | 2.77E+00 | 3.01E-03 | 3.96E+00 | 1.72E-04 | 2.77E+00 | 2.73E-03 |
| 4.06E+00 | 2.25E-04 | 2.84E+00 | 3.02E-03 | 4.06E+00 | 3.78E-04 | 2.84E+00 | 2.72E-03 |
| 4.1667 | 1.10E-03 | 2.9167 | 3.03E-03 | 4.17E+00 | 1.14E-03 | 2.92E+00 | 2.72E-03 |
| 4.2708 | 1.25E-02 | 2.9896 | 3.05E-03 | 4.27E+00 | 2.02E-03 | 2.99E+00 | 2.72E-03 |
| 4.375 | 2.53E-03 | 3.0625 | 3.08E-03 | 4.38E+00 | 3.14E-04 | 3.06E+00 | 2.72E-03 |
| 4.4792 | 4.90E-04 | 3.1354 | 3.11E-03 | 4.48E+00 | 1.89E-04 | 3.14E+00 | 2.72E-03 |
| 4.5833 | 1.76E-04 | 3.2083 | 3.14E-03 | 4.58E+00 | 1.23E-04 | 3.21E+00 | 2.72E-03 |
| 4.6875 | 8.38E-05 | 3.2813 | 3.16E-03 | 4.69E+00 | 7.48E-05 | 3.28E+00 | 2.71E-03 |
| 4.7917 | 4.14E-05 | 3.3542 | 3.16E-03 | 4.79E+00 | 4.33E-05 | 3.35E+00 | 2.69E-03 |
| 4.8958 | 2.52E-05 | 3.4271 | 3.11E-03 | 4.90E+00 | 2.51E-05 | 3.43E+00 | 2.64E-03 |
| 5 | 2.45E-05 | 3.5 | 2.99E-03 | 5.00E+00 | 1.83E-05 | 3.50E+00 | 2.58E-03 |

Table B-63 Surface tensile strain profiles for sample L-R-1, step 80%YS.

| **Hardened Layer** | | | | **Soft Bulk** | | | |
|---|---|---|---|---|---|---|---|
| Longitudinal | | Transverse | | Longitudinal | | Transverse | |
| Length | Strain | Length | Strain | Length | Strain | Length | Strain |
| 0.00E+00 | 3.03E-05 | 0.00E+00 | 3.41E-03 | 0.00E+00 | 2.35E-05 | 0.00E+00 | 2.95E-03 |
| 1.04E-01 | 3.03E-05 | 7.29E-02 | 3.56E-03 | 1.04E-01 | 2.94E-05 | 7.29E-02 | 3.01E-03 |
| 2.08E-01 | 4.64E-05 | 1.46E-01 | 3.62E-03 | 2.08E-01 | 4.79E-05 | 1.46E-01 | 3.07E-03 |
| 3.13E-01 | 9.03E-05 | 2.19E-01 | 3.62E-03 | 3.13E-01 | 8.16E-05 | 2.19E-01 | 3.11E-03 |
| 4.17E-01 | 1.83E-04 | 2.92E-01 | 3.60E-03 | 4.17E-01 | 1.35E-04 | 2.92E-01 | 3.12E-03 |
| 5.21E-01 | 4.78E-04 | 3.65E-01 | 3.56E-03 | 5.21E-01 | 2.15E-04 | 3.65E-01 | 3.12E-03 |
| 6.25E-01 | 2.37E-03 | 4.38E-01 | 3.53E-03 | 6.25E-01 | 3.76E-04 | 4.38E-01 | 3.12E-03 |
| 7.29E-01 | 1.19E-02 | 5.10E-01 | 3.50E-03 | 7.29E-01 | 2.58E-03 | 5.10E-01 | 3.12E-03 |
| 8.33E-01 | 1.19E-03 | 5.83E-01 | 3.48E-03 | 8.33E-01 | 1.45E-03 | 5.83E-01 | 3.13E-03 |
| 9.38E-01 | 3.23E-04 | 6.56E-01 | 3.46E-03 | 9.38E-01 | 4.40E-04 | 6.56E-01 | 3.13E-03 |
| 1.04E+00 | 5.39E-05 | 7.29E-01 | 3.45E-03 | 1.04E+00 | 1.89E-04 | 7.29E-01 | 3.14E-03 |
| 1.15E+00 | 2.05E-04 | 8.02E-01 | 3.44E-03 | 1.15E+00 | 2.27E-04 | 8.02E-01 | 3.15E-03 |
| 1.25E+00 | 3.73E-04 | 8.75E-01 | 3.44E-03 | 1.25E+00 | 3.53E-04 | 8.75E-01 | 3.17E-03 |
| 1.35E+00 | 5.41E-04 | 9.48E-01 | 3.43E-03 | 1.35E+00 | 4.97E-04 | 9.48E-01 | 3.18E-03 |
| 1.46E+00 | 7.17E-04 | 1.02E+00 | 3.44E-03 | 1.46E+00 | 6.52E-04 | 1.02E+00 | 3.19E-03 |
| 1.56E+00 | 9.05E-04 | 1.09E+00 | 3.44E-03 | 1.56E+00 | 8.18E-04 | 1.09E+00 | 3.21E-03 |
| 1.67E+00 | 1.11E-03 | 1.17E+00 | 3.44E-03 | 1.67E+00 | 9.94E-04 | 1.17E+00 | 3.22E-03 |
| 1.77E+00 | 1.40E-03 | 1.24E+00 | 3.45E-03 | 1.77E+00 | 1.16E-03 | 1.24E+00 | 3.23E-03 |
| 1.88E+00 | 1.84E-03 | 1.31E+00 | 3.45E-03 | 1.88E+00 | 1.51E-03 | 1.31E+00 | 3.24E-03 |
| 1.98E+00 | 2.27E-03 | 1.39E+00 | 3.45E-03 | 1.98E+00 | 2.00E-03 | 1.39E+00 | 3.25E-03 |
| 2.08E+00 | 2.67E-03 | 1.46E+00 | 3.46E-03 | 2.08E+00 | 2.43E-03 | 1.46E+00 | 3.26E-03 |
| 2.19E+00 | 3.01E-03 | 1.53E+00 | 3.46E-03 | 2.19E+00 | 2.81E-03 | 1.53E+00 | 3.27E-03 |

| | | | | | | | |
|---|---|---|---|---|---|---|---|
| 2.29E+00 | 3.26E-03 | 1.60E+00 | 3.46E-03 | 2.29E+00 | 3.08E-03 | 1.60E+00 | 3.27E-03 |
| 2.40E+00 | 3.41E-03 | 1.68E+00 | 3.46E-03 | 2.40E+00 | 3.24E-03 | 1.68E+00 | 3.27E-03 |
| 2.50E+00 | 3.46E-03 | 1.75E+00 | 3.46E-03 | 2.50E+00 | 3.28E-03 | 1.75E+00 | 3.28E-03 |
| 2.60E+00 | 3.41E-03 | 1.82E+00 | 3.46E-03 | 2.60E+00 | 3.24E-03 | 1.82E+00 | 3.27E-03 |
| 2.71E+00 | 3.26E-03 | 1.90E+00 | 3.46E-03 | 2.71E+00 | 3.08E-03 | 1.90E+00 | 3.27E-03 |
| 2.81E+00 | 3.01E-03 | 1.97E+00 | 3.46E-03 | 2.81E+00 | 2.81E-03 | 1.97E+00 | 3.27E-03 |
| 2.92E+00 | 2.67E-03 | 2.04E+00 | 3.46E-03 | 2.92E+00 | 2.43E-03 | 2.04E+00 | 3.26E-03 |
| 3.02E+00 | 2.27E-03 | 2.11E+00 | 3.45E-03 | 3.02E+00 | 2.00E-03 | 2.11E+00 | 3.25E-03 |
| 3.13E+00 | 1.84E-03 | 2.19E+00 | 3.45E-03 | 3.13E+00 | 1.51E-03 | 2.19E+00 | 3.24E-03 |
| 3.23E+00 | 1.40E-03 | 2.26E+00 | 3.45E-03 | 3.23E+00 | 1.16E-03 | 2.26E+00 | 3.23E-03 |
| 3.33E+00 | 1.11E-03 | 2.33E+00 | 3.44E-03 | 3.33E+00 | 9.94E-04 | 2.33E+00 | 3.22E-03 |
| 3.44E+00 | 9.04E-04 | 2.41E+00 | 3.44E-03 | 3.44E+00 | 8.18E-04 | 2.41E+00 | 3.21E-03 |
| 3.54E+00 | 7.16E-04 | 2.48E+00 | 3.43E-03 | 3.54E+00 | 6.52E-04 | 2.48E+00 | 3.19E-03 |
| 3.65E+00 | 5.40E-04 | 2.55E+00 | 3.43E-03 | 3.65E+00 | 4.96E-04 | 2.55E+00 | 3.18E-03 |
| 3.75E+00 | 3.71E-04 | 2.63E+00 | 3.43E-03 | 3.75E+00 | 3.52E-04 | 2.63E+00 | 3.17E-03 |
| 3.85E+00 | 2.02E-04 | 2.70E+00 | 3.44E-03 | 3.85E+00 | 2.26E-04 | 2.70E+00 | 3.15E-03 |
| 3.96E+00 | 4.13E-05 | 2.77E+00 | 3.45E-03 | 3.96E+00 | 1.91E-04 | 2.77E+00 | 3.14E-03 |
| 4.06E+00 | 2.74E-04 | 2.84E+00 | 3.46E-03 | 4.06E+00 | 4.28E-04 | 2.84E+00 | 3.14E-03 |
| 4.1667 | 1.11E-03 | 2.9167 | 3.48E-03 | 4.17E+00 | 1.27E-03 | 2.92E+00 | 3.13E-03 |
| 4.2708 | 1.59E-02 | 2.9896 | 3.50E-03 | 4.27E+00 | 2.20E-03 | 2.99E+00 | 3.13E-03 |
| 4.375 | 2.72E-03 | 3.0625 | 3.53E-03 | 4.38E+00 | 3.38E-04 | 3.06E+00 | 3.13E-03 |
| 4.4792 | 5.35E-04 | 3.1354 | 3.56E-03 | 4.48E+00 | 2.08E-04 | 3.14E+00 | 3.12E-03 |
| 4.5833 | 1.90E-04 | 3.2083 | 3.59E-03 | 4.58E+00 | 1.33E-04 | 3.21E+00 | 3.12E-03 |
| 4.6875 | 9.07E-05 | 3.2813 | 3.62E-03 | 4.69E+00 | 8.10E-05 | 3.28E+00 | 3.11E-03 |
| 4.7917 | 4.67E-05 | 3.3542 | 3.61E-03 | 4.79E+00 | 4.80E-05 | 3.35E+00 | 3.08E-03 |
| 4.8958 | 3.09E-05 | 3.4271 | 3.55E-03 | 4.90E+00 | 2.98E-05 | 3.43E+00 | 3.02E-03 |
| 5 | 3.07E-05 | 3.5 | 3.41E-03 | 5.00E+00 | 2.38E-05 | 3.50E+00 | 2.95E-03 |

## Sample L-R-3

Table B-64 Surface tensile strain profiles for sample L-R-3, step 50%YS.

| **Hardened Layer** | | | | **Soft Bulk** | | | |
|---|---|---|---|---|---|---|---|
| Longitudinal | | Transverse | | Longitudinal | | Transverse | |
| Length | Strain | Length | Strain | Length | Strain | Length | Strain |
| 0.00E+00 | 1.40E-05 | 0.00E+00 | 2.16E-03 | 0.00E+00 | 9.60E-06 | 0.00E+00 | 1.86E-03 |
| 1.04E-01 | 1.51E-05 | 7.29E-02 | 2.23E-03 | 1.04E-01 | 1.73E-05 | 7.29E-02 | 1.89E-03 |
| 2.08E-01 | 3.20E-05 | 1.46E-01 | 2.25E-03 | 2.08E-01 | 3.50E-05 | 1.46E-01 | 1.91E-03 |
| 3.13E-01 | 7.00E-05 | 2.19E-01 | 2.25E-03 | 3.13E-01 | 6.27E-05 | 2.19E-01 | 1.92E-03 |
| 4.17E-01 | 1.44E-04 | 2.92E-01 | 2.23E-03 | 4.17E-01 | 1.03E-04 | 2.92E-01 | 1.92E-03 |
| 5.21E-01 | 3.77E-04 | 3.65E-01 | 2.21E-03 | 5.21E-01 | 1.53E-04 | 3.65E-01 | 1.91E-03 |
| 6.25E-01 | 2.12E-03 | 4.38E-01 | 2.19E-03 | 6.25E-01 | 3.04E-04 | 4.38E-01 | 1.91E-03 |

| | | | | | | | |
|---|---|---|---|---|---|---|---|
| 7.29E-01 | 7.29E-03 | 5.10E-01 | 2.17E-03 | 7.29E-01 | 1.80E-03 | 5.10E-01 | 1.90E-03 |
| 8.33E-01 | 5.57E-04 | 5.83E-01 | 2.16E-03 | 8.33E-01 | 8.40E-04 | 5.83E-01 | 1.90E-03 |
| 9.38E-01 | 1.05E-04 | 6.56E-01 | 2.15E-03 | 9.38E-01 | 2.67E-04 | 6.56E-01 | 1.89E-03 |
| 1.04E+00 | 8.14E-05 | 7.29E-01 | 2.14E-03 | 1.04E+00 | 1.41E-04 | 7.29E-01 | 1.89E-03 |
| 1.15E+00 | 2.18E-04 | 8.02E-01 | 2.14E-03 | 1.15E+00 | 2.16E-04 | 8.02E-01 | 1.89E-03 |
| 1.25E+00 | 3.49E-04 | 8.75E-01 | 2.13E-03 | 1.25E+00 | 3.23E-04 | 8.75E-01 | 1.90E-03 |
| 1.35E+00 | 4.82E-04 | 9.48E-01 | 2.13E-03 | 1.35E+00 | 4.39E-04 | 9.48E-01 | 1.90E-03 |
| 1.46E+00 | 6.20E-04 | 1.02E+00 | 2.13E-03 | 1.46E+00 | 5.62E-04 | 1.02E+00 | 1.91E-03 |
| 1.56E+00 | 7.67E-04 | 1.09E+00 | 2.13E-03 | 1.56E+00 | 6.92E-04 | 1.09E+00 | 1.91E-03 |
| 1.67E+00 | 9.21E-04 | 1.17E+00 | 2.14E-03 | 1.67E+00 | 8.28E-04 | 1.17E+00 | 1.92E-03 |
| 1.77E+00 | 1.08E-03 | 1.24E+00 | 2.14E-03 | 1.77E+00 | 9.67E-04 | 1.24E+00 | 1.92E-03 |
| 1.88E+00 | 1.25E-03 | 1.31E+00 | 2.14E-03 | 1.88E+00 | 1.10E-03 | 1.31E+00 | 1.93E-03 |
| 1.98E+00 | 1.46E-03 | 1.39E+00 | 2.14E-03 | 1.98E+00 | 1.24E-03 | 1.39E+00 | 1.93E-03 |
| 2.08E+00 | 1.69E-03 | 1.46E+00 | 2.14E-03 | 2.08E+00 | 1.45E-03 | 1.46E+00 | 1.93E-03 |
| 2.19E+00 | 1.89E-03 | 1.53E+00 | 2.15E-03 | 2.19E+00 | 1.67E-03 | 1.53E+00 | 1.94E-03 |
| 2.29E+00 | 2.03E-03 | 1.60E+00 | 2.15E-03 | 2.29E+00 | 1.82E-03 | 1.60E+00 | 1.94E-03 |
| 2.40E+00 | 2.12E-03 | 1.68E+00 | 2.15E-03 | 2.40E+00 | 1.91E-03 | 1.68E+00 | 1.94E-03 |
| 2.50E+00 | 2.15E-03 | 1.75E+00 | 2.15E-03 | 2.50E+00 | 1.94E-03 | 1.75E+00 | 1.94E-03 |
| 2.60E+00 | 2.12E-03 | 1.82E+00 | 2.15E-03 | 2.60E+00 | 1.91E-03 | 1.82E+00 | 1.94E-03 |
| 2.71E+00 | 2.03E-03 | 1.90E+00 | 2.15E-03 | 2.71E+00 | 1.82E-03 | 1.90E+00 | 1.94E-03 |
| 2.81E+00 | 1.89E-03 | 1.97E+00 | 2.15E-03 | 2.81E+00 | 1.67E-03 | 1.97E+00 | 1.94E-03 |
| 2.92E+00 | 1.69E-03 | 2.04E+00 | 2.14E-03 | 2.92E+00 | 1.45E-03 | 2.04E+00 | 1.93E-03 |
| 3.02E+00 | 1.46E-03 | 2.11E+00 | 2.14E-03 | 3.02E+00 | 1.24E-03 | 2.11E+00 | 1.93E-03 |
| 3.13E+00 | 1.25E-03 | 2.19E+00 | 2.14E-03 | 3.13E+00 | 1.10E-03 | 2.19E+00 | 1.93E-03 |
| 3.23E+00 | 1.08E-03 | 2.26E+00 | 2.14E-03 | 3.23E+00 | 9.67E-04 | 2.26E+00 | 1.92E-03 |
| 3.33E+00 | 9.21E-04 | 2.33E+00 | 2.14E-03 | 3.33E+00 | 8.28E-04 | 2.33E+00 | 1.92E-03 |
| 3.44E+00 | 7.66E-04 | 2.41E+00 | 2.13E-03 | 3.44E+00 | 6.92E-04 | 2.41E+00 | 1.91E-03 |
| 3.54E+00 | 6.20E-04 | 2.48E+00 | 2.13E-03 | 3.54E+00 | 5.62E-04 | 2.48E+00 | 1.91E-03 |
| 3.65E+00 | 4.81E-04 | 2.55E+00 | 2.13E-03 | 3.65E+00 | 4.39E-04 | 2.55E+00 | 1.90E-03 |
| 3.75E+00 | 3.48E-04 | 2.63E+00 | 2.13E-03 | 3.75E+00 | 3.22E-04 | 2.63E+00 | 1.90E-03 |
| 3.85E+00 | 2.17E-04 | 2.70E+00 | 2.14E-03 | 3.85E+00 | 2.16E-04 | 2.70E+00 | 1.90E-03 |
| 3.96E+00 | 8.40E-05 | 2.77E+00 | 2.14E-03 | 3.96E+00 | 1.41E-04 | 2.77E+00 | 1.89E-03 |
| 4.06E+00 | 1.33E-04 | 2.84E+00 | 2.15E-03 | 4.06E+00 | 2.61E-04 | 2.84E+00 | 1.89E-03 |
| 4.1667 | 8.33E-04 | 2.9167 | 2.16E-03 | 4.17E+00 | 7.88E-04 | 2.92E+00 | 1.90E-03 |
| 4.2708 | 7.31E-03 | 2.9896 | 2.17E-03 | 4.27E+00 | 1.56E-03 | 2.99E+00 | 1.90E-03 |
| 4.375 | 2.32E-03 | 3.0625 | 2.19E-03 | 4.38E+00 | 2.82E-04 | 3.06E+00 | 1.91E-03 |
| 4.4792 | 4.13E-04 | 3.1354 | 2.21E-03 | 4.48E+00 | 1.50E-04 | 3.14E+00 | 1.92E-03 |
| 4.5833 | 1.49E-04 | 3.2083 | 2.23E-03 | 4.58E+00 | 1.02E-04 | 3.21E+00 | 1.92E-03 |
| 4.6875 | 7.06E-05 | 3.2813 | 2.25E-03 | 4.69E+00 | 6.27E-05 | 3.28E+00 | 1.92E-03 |
| 4.7917 | 3.25E-05 | 3.3542 | 2.25E-03 | 4.79E+00 | 3.52E-05 | 3.35E+00 | 1.91E-03 |
| 4.8958 | 1.61E-05 | 3.4271 | 2.23E-03 | 4.90E+00 | 1.79E-05 | 3.43E+00 | 1.89E-03 |

| | | | | | | | |
|---|---|---|---|---|---|---|---|
| 5 | 1.49E-05 | 3.5 | 2.16E-03 | 5.00E+00 | 1.04E-05 | 3.50E+00 | 1.86E-03 |

Table B-65 Surface tensile strain profiles for sample L-R-3, step 60%YS.

| **Hardened Layer** | | | | **Soft Bulk** | | | |
|---|---|---|---|---|---|---|---|
| Longitudinal | | Transverse | | Longitudinal | | Transverse | |
| Length | Strain | Length | Strain | Length | Strain | Length | Strain |
| 0.00E+00 | 1.86E-05 | 0.00E+00 | 2.55E-03 | 0.00E+00 | 1.34E-05 | 0.00E+00 | 2.20E-03 |
| 1.04E-01 | 1.95E-05 | 7.29E-02 | 2.65E-03 | 1.04E-01 | 2.08E-05 | 7.29E-02 | 2.24E-03 |
| 2.08E-01 | 3.67E-05 | 1.46E-01 | 2.68E-03 | 2.08E-01 | 3.94E-05 | 1.46E-01 | 2.28E-03 |
| 3.13E-01 | 7.75E-05 | 2.19E-01 | 2.68E-03 | 3.13E-01 | 6.97E-05 | 2.19E-01 | 2.29E-03 |
| 4.17E-01 | 1.58E-04 | 2.92E-01 | 2.66E-03 | 4.17E-01 | 1.15E-04 | 2.92E-01 | 2.30E-03 |
| 5.21E-01 | 4.10E-04 | 3.65E-01 | 2.63E-03 | 5.21E-01 | 1.75E-04 | 3.65E-01 | 2.29E-03 |
| 6.25E-01 | 2.21E-03 | 4.38E-01 | 2.61E-03 | 6.25E-01 | 3.31E-04 | 4.38E-01 | 2.29E-03 |
| 7.29E-01 | 7.05E-03 | 5.10E-01 | 2.59E-03 | 7.29E-01 | 2.14E-03 | 5.10E-01 | 2.28E-03 |
| 8.33E-01 | 7.00E-04 | 5.83E-01 | 2.57E-03 | 8.33E-01 | 1.03E-03 | 5.83E-01 | 2.28E-03 |
| 9.38E-01 | 1.67E-04 | 6.56E-01 | 2.56E-03 | 9.38E-01 | 3.26E-04 | 6.56E-01 | 2.28E-03 |
| 1.04E+00 | 6.57E-05 | 7.29E-01 | 2.55E-03 | 1.04E+00 | 1.53E-04 | 7.29E-01 | 2.28E-03 |
| 1.15E+00 | 2.17E-04 | 8.02E-01 | 2.55E-03 | 1.15E+00 | 2.22E-04 | 8.02E-01 | 2.29E-03 |
| 1.25E+00 | 3.62E-04 | 8.75E-01 | 2.54E-03 | 1.25E+00 | 3.37E-04 | 8.75E-01 | 2.29E-03 |
| 1.35E+00 | 5.08E-04 | 9.48E-01 | 2.54E-03 | 1.35E+00 | 4.64E-04 | 9.48E-01 | 2.30E-03 |
| 1.46E+00 | 6.60E-04 | 1.02E+00 | 2.54E-03 | 1.46E+00 | 5.99E-04 | 1.02E+00 | 2.31E-03 |
| 1.56E+00 | 8.21E-04 | 1.09E+00 | 2.55E-03 | 1.56E+00 | 7.42E-04 | 1.09E+00 | 2.32E-03 |
| 1.67E+00 | 9.92E-04 | 1.17E+00 | 2.55E-03 | 1.67E+00 | 8.92E-04 | 1.17E+00 | 2.32E-03 |
| 1.77E+00 | 1.17E-03 | 1.24E+00 | 2.55E-03 | 1.77E+00 | 1.04E-03 | 1.24E+00 | 2.33E-03 |
| 1.88E+00 | 1.41E-03 | 1.31E+00 | 2.55E-03 | 1.88E+00 | 1.18E-03 | 1.31E+00 | 2.34E-03 |
| 1.98E+00 | 1.71E-03 | 1.39E+00 | 2.56E-03 | 1.98E+00 | 1.44E-03 | 1.39E+00 | 2.34E-03 |
| 2.08E+00 | 2.00E-03 | 1.46E+00 | 2.56E-03 | 2.08E+00 | 1.76E-03 | 1.46E+00 | 2.35E-03 |
| 2.19E+00 | 2.24E-03 | 1.53E+00 | 2.56E-03 | 2.19E+00 | 2.02E-03 | 1.53E+00 | 2.35E-03 |
| 2.29E+00 | 2.41E-03 | 1.60E+00 | 2.56E-03 | 2.29E+00 | 2.21E-03 | 1.60E+00 | 2.36E-03 |
| 2.40E+00 | 2.53E-03 | 1.68E+00 | 2.56E-03 | 2.40E+00 | 2.32E-03 | 1.68E+00 | 2.36E-03 |
| 2.50E+00 | 2.56E-03 | 1.75E+00 | 2.56E-03 | 2.50E+00 | 2.36E-03 | 1.75E+00 | 2.36E-03 |
| 2.60E+00 | 2.53E-03 | 1.82E+00 | 2.56E-03 | 2.60E+00 | 2.32E-03 | 1.82E+00 | 2.36E-03 |
| 2.71E+00 | 2.41E-03 | 1.90E+00 | 2.56E-03 | 2.71E+00 | 2.21E-03 | 1.90E+00 | 2.36E-03 |
| 2.81E+00 | 2.24E-03 | 1.97E+00 | 2.56E-03 | 2.81E+00 | 2.02E-03 | 1.97E+00 | 2.35E-03 |
| 2.92E+00 | 2.00E-03 | 2.04E+00 | 2.56E-03 | 2.92E+00 | 1.76E-03 | 2.04E+00 | 2.35E-03 |
| 3.02E+00 | 1.71E-03 | 2.11E+00 | 2.56E-03 | 3.02E+00 | 1.44E-03 | 2.11E+00 | 2.34E-03 |
| 3.13E+00 | 1.41E-03 | 2.19E+00 | 2.55E-03 | 3.13E+00 | 1.18E-03 | 2.19E+00 | 2.34E-03 |
| 3.23E+00 | 1.17E-03 | 2.26E+00 | 2.55E-03 | 3.23E+00 | 1.04E-03 | 2.26E+00 | 2.33E-03 |
| 3.33E+00 | 9.92E-04 | 2.33E+00 | 2.55E-03 | 3.33E+00 | 8.92E-04 | 2.33E+00 | 2.32E-03 |
| 3.44E+00 | 8.21E-04 | 2.41E+00 | 2.55E-03 | 3.44E+00 | 7.42E-04 | 2.41E+00 | 2.32E-03 |
| 3.54E+00 | 6.60E-04 | 2.48E+00 | 2.54E-03 | 3.54E+00 | 5.99E-04 | 2.48E+00 | 2.31E-03 |

| | | | | | | | |
|---|---|---|---|---|---|---|---|
| 3.65E+00 | 5.07E-04 | 2.55E+00 | 2.54E-03 | 3.65E+00 | 4.64E-04 | 2.55E+00 | 2.30E-03 |
| 3.75E+00 | 3.61E-04 | 2.63E+00 | 2.54E-03 | 3.75E+00 | 3.36E-04 | 2.63E+00 | 2.29E-03 |
| 3.85E+00 | 2.16E-04 | 2.70E+00 | 2.55E-03 | 3.85E+00 | 2.21E-04 | 2.70E+00 | 2.29E-03 |
| 3.96E+00 | 6.74E-05 | 2.77E+00 | 2.55E-03 | 3.96E+00 | 1.54E-04 | 2.77E+00 | 2.28E-03 |
| 4.06E+00 | 1.71E-04 | 2.84E+00 | 2.56E-03 | 4.06E+00 | 3.17E-04 | 2.84E+00 | 2.28E-03 |
| 4.1667 | 9.62E-04 | 2.9167 | 2.57E-03 | 4.17E+00 | 9.28E-04 | 2.92E+00 | 2.28E-03 |
| 4.2708 | 9.56E-03 | 2.9896 | 2.59E-03 | 4.27E+00 | 1.80E-03 | 2.99E+00 | 2.28E-03 |
| 4.375 | 2.47E-03 | 3.0625 | 2.61E-03 | 4.38E+00 | 3.05E-04 | 3.06E+00 | 2.29E-03 |
| 4.4792 | 4.55E-04 | 3.1354 | 2.63E-03 | 4.48E+00 | 1.71E-04 | 3.14E+00 | 2.29E-03 |
| 4.5833 | 1.64E-04 | 3.2083 | 2.66E-03 | 4.58E+00 | 1.14E-04 | 3.21E+00 | 2.30E-03 |
| 4.6875 | 7.82E-05 | 3.2813 | 2.68E-03 | 4.69E+00 | 6.96E-05 | 3.28E+00 | 2.29E-03 |
| 4.7917 | 3.73E-05 | 3.3542 | 2.68E-03 | 4.79E+00 | 3.97E-05 | 3.35E+00 | 2.28E-03 |
| 4.8958 | 2.06E-05 | 3.4271 | 2.65E-03 | 4.90E+00 | 2.15E-05 | 3.43E+00 | 2.24E-03 |
| 5 | 1.96E-05 | 3.5 | 2.55E-03 | 5.00E+00 | 1.42E-05 | 3.50E+00 | 2.20E-03 |

Table B-66 Surface tensile strain profiles for sample L-R-3, step 70%YS.

| **Hardened Layer** | | | | **Soft Bulk** | | | |
|---|---|---|---|---|---|---|---|
| Longitudinal | | Transverse | | Longitudinal | | Transverse | |
| Length | Strain | Length | Strain | Length | Strain | Length | Strain |
| 0.00E+00 | 2.43E-05 | 0.00E+00 | 2.99E-03 | 0.00E+00 | 1.82E-05 | 0.00E+00 | 2.58E-03 |
| 1.04E-01 | 2.49E-05 | 7.29E-02 | 3.11E-03 | 1.04E-01 | 2.52E-05 | 7.29E-02 | 2.64E-03 |
| 2.08E-01 | 4.21E-05 | 1.46E-01 | 3.16E-03 | 2.08E-01 | 4.43E-05 | 1.46E-01 | 2.69E-03 |
| 3.13E-01 | 8.56E-05 | 2.19E-01 | 3.16E-03 | 3.13E-01 | 7.72E-05 | 2.19E-01 | 2.71E-03 |
| 4.17E-01 | 1.74E-04 | 2.92E-01 | 3.14E-03 | 4.17E-01 | 1.28E-04 | 2.92E-01 | 2.72E-03 |
| 5.21E-01 | 4.53E-04 | 3.65E-01 | 3.11E-03 | 5.21E-01 | 1.99E-04 | 3.65E-01 | 2.72E-03 |
| 6.25E-01 | 2.36E-03 | 4.38E-01 | 3.08E-03 | 6.25E-01 | 3.64E-04 | 4.38E-01 | 2.72E-03 |
| 7.29E-01 | 9.61E-03 | 5.10E-01 | 3.06E-03 | 7.29E-01 | 2.40E-03 | 5.10E-01 | 2.72E-03 |
| 8.33E-01 | 9.20E-04 | 5.83E-01 | 3.03E-03 | 8.33E-01 | 1.23E-03 | 5.83E-01 | 2.72E-03 |
| 9.38E-01 | 2.51E-04 | 6.56E-01 | 3.02E-03 | 9.38E-01 | 3.94E-04 | 6.56E-01 | 2.72E-03 |
| 1.04E+00 | 4.97E-05 | 7.29E-01 | 3.01E-03 | 1.04E+00 | 1.72E-04 | 7.29E-01 | 2.73E-03 |
| 1.15E+00 | 2.07E-04 | 8.02E-01 | 3.00E-03 | 1.15E+00 | 2.22E-04 | 8.02E-01 | 2.74E-03 |
| 1.25E+00 | 3.65E-04 | 8.75E-01 | 3.00E-03 | 1.25E+00 | 3.43E-04 | 8.75E-01 | 2.75E-03 |
| 1.35E+00 | 5.23E-04 | 9.48E-01 | 3.00E-03 | 1.35E+00 | 4.80E-04 | 9.48E-01 | 2.76E-03 |
| 1.46E+00 | 6.89E-04 | 1.02E+00 | 3.00E-03 | 1.46E+00 | 6.26E-04 | 1.02E+00 | 2.77E-03 |
| 1.56E+00 | 8.65E-04 | 1.09E+00 | 3.00E-03 | 1.56E+00 | 7.82E-04 | 1.09E+00 | 2.78E-03 |
| 1.67E+00 | 1.05E-03 | 1.17E+00 | 3.00E-03 | 1.67E+00 | 9.46E-04 | 1.17E+00 | 2.79E-03 |
| 1.77E+00 | 1.28E-03 | 1.24E+00 | 3.01E-03 | 1.77E+00 | 1.10E-03 | 1.24E+00 | 2.80E-03 |
| 1.88E+00 | 1.62E-03 | 1.31E+00 | 3.01E-03 | 1.88E+00 | 1.32E-03 | 1.31E+00 | 2.81E-03 |
| 1.98E+00 | 1.99E-03 | 1.39E+00 | 3.02E-03 | 1.98E+00 | 1.72E-03 | 1.39E+00 | 2.82E-03 |
| 2.08E+00 | 2.34E-03 | 1.46E+00 | 3.02E-03 | 2.08E+00 | 2.10E-03 | 1.46E+00 | 2.83E-03 |
| 2.19E+00 | 2.62E-03 | 1.53E+00 | 3.02E-03 | 2.19E+00 | 2.41E-03 | 1.53E+00 | 2.83E-03 |

| | | | | | | | |
|---|---|---|---|---|---|---|---|
| 2.29E+00 | 2.84E-03 | 1.60E+00 | 3.02E-03 | 2.29E+00 | 2.65E-03 | 1.60E+00 | 2.84E-03 |
| 2.40E+00 | 2.98E-03 | 1.68E+00 | 3.02E-03 | 2.40E+00 | 2.79E-03 | 1.68E+00 | 2.84E-03 |
| 2.50E+00 | 3.02E-03 | 1.75E+00 | 3.02E-03 | 2.50E+00 | 2.84E-03 | 1.75E+00 | 2.84E-03 |
| 2.60E+00 | 2.98E-03 | 1.82E+00 | 3.02E-03 | 2.60E+00 | 2.79E-03 | 1.82E+00 | 2.84E-03 |
| 2.71E+00 | 2.84E-03 | 1.90E+00 | 3.02E-03 | 2.71E+00 | 2.65E-03 | 1.90E+00 | 2.84E-03 |
| 2.81E+00 | 2.62E-03 | 1.97E+00 | 3.02E-03 | 2.81E+00 | 2.41E-03 | 1.97E+00 | 2.83E-03 |
| 2.92E+00 | 2.34E-03 | 2.04E+00 | 3.02E-03 | 2.92E+00 | 2.10E-03 | 2.04E+00 | 2.83E-03 |
| 3.02E+00 | 1.99E-03 | 2.11E+00 | 3.02E-03 | 3.02E+00 | 1.72E-03 | 2.11E+00 | 2.82E-03 |
| 3.13E+00 | 1.62E-03 | 2.19E+00 | 3.01E-03 | 3.13E+00 | 1.32E-03 | 2.19E+00 | 2.81E-03 |
| 3.23E+00 | 1.28E-03 | 2.26E+00 | 3.01E-03 | 3.23E+00 | 1.10E-03 | 2.26E+00 | 2.80E-03 |
| 3.33E+00 | 1.05E-03 | 2.33E+00 | 3.00E-03 | 3.33E+00 | 9.46E-04 | 2.33E+00 | 2.79E-03 |
| 3.44E+00 | 8.64E-04 | 2.41E+00 | 3.00E-03 | 3.44E+00 | 7.81E-04 | 2.41E+00 | 2.78E-03 |
| 3.54E+00 | 6.88E-04 | 2.48E+00 | 3.00E-03 | 3.54E+00 | 6.26E-04 | 2.48E+00 | 2.77E-03 |
| 3.65E+00 | 5.22E-04 | 2.55E+00 | 3.00E-03 | 3.65E+00 | 4.79E-04 | 2.55E+00 | 2.76E-03 |
| 3.75E+00 | 3.63E-04 | 2.63E+00 | 3.00E-03 | 3.75E+00 | 3.42E-04 | 2.63E+00 | 2.75E-03 |
| 3.85E+00 | 2.04E-04 | 2.70E+00 | 3.00E-03 | 3.85E+00 | 2.21E-04 | 2.70E+00 | 2.74E-03 |
| 3.96E+00 | 4.75E-05 | 2.77E+00 | 3.01E-03 | 3.96E+00 | 1.73E-04 | 2.77E+00 | 2.73E-03 |
| 4.06E+00 | 2.32E-04 | 2.84E+00 | 3.02E-03 | 4.06E+00 | 3.83E-04 | 2.84E+00 | 2.72E-03 |
| 4.1667 | 1.12E-03 | 2.9167 | 3.03E-03 | 4.17E+00 | 1.15E-03 | 2.92E+00 | 2.72E-03 |
| 4.2708 | 1.27E-02 | 2.9896 | 3.05E-03 | 4.27E+00 | 2.03E-03 | 2.99E+00 | 2.72E-03 |
| 4.375 | 2.67E-03 | 3.0625 | 3.08E-03 | 4.38E+00 | 3.31E-04 | 3.06E+00 | 2.72E-03 |
| 4.4792 | 5.05E-04 | 3.1354 | 3.11E-03 | 4.48E+00 | 1.93E-04 | 3.14E+00 | 2.72E-03 |
| 4.5833 | 1.81E-04 | 3.2083 | 3.14E-03 | 4.58E+00 | 1.26E-04 | 3.21E+00 | 2.72E-03 |
| 4.6875 | 8.64E-05 | 3.2813 | 3.16E-03 | 4.69E+00 | 7.71E-05 | 3.28E+00 | 2.71E-03 |
| 4.7917 | 4.28E-05 | 3.3542 | 3.16E-03 | 4.79E+00 | 4.47E-05 | 3.35E+00 | 2.69E-03 |
| 4.8958 | 2.61E-05 | 3.4271 | 3.11E-03 | 4.90E+00 | 2.60E-05 | 3.43E+00 | 2.64E-03 |
| 5 | 2.54E-05 | 3.5 | 2.99E-03 | 5.00E+00 | 1.91E-05 | 3.50E+00 | 2.58E-03 |

Table B-67 Surface tensile strain profiles for sample L-R-3, step 80%YS.

| **Hardened Layer** | | | | **Soft Bulk** | | | |
|---|---|---|---|---|---|---|---|
| Longitudinal | | Transverse | | Longitudinal | | Transverse | |
| Length | Strain | Length | Strain | Length | Strain | Length | Strain |
| 0.00E+00 | 3.10E-05 | 0.00E+00 | 3.42E-03 | 0.00E+00 | 2.42E-05 | 0.00E+00 | 2.95E-03 |
| 1.04E-01 | 3.10E-05 | 7.29E-02 | 3.56E-03 | 1.04E-01 | 3.03E-05 | 7.29E-02 | 3.02E-03 |
| 2.08E-01 | 4.77E-05 | 1.46E-01 | 3.62E-03 | 2.08E-01 | 4.93E-05 | 1.46E-01 | 3.08E-03 |
| 3.13E-01 | 9.30E-05 | 2.19E-01 | 3.63E-03 | 3.13E-01 | 8.39E-05 | 2.19E-01 | 3.12E-03 |
| 4.17E-01 | 1.88E-04 | 2.92E-01 | 3.61E-03 | 4.17E-01 | 1.39E-04 | 2.92E-01 | 3.13E-03 |
| 5.21E-01 | 4.89E-04 | 3.65E-01 | 3.58E-03 | 5.21E-01 | 2.20E-04 | 3.65E-01 | 3.13E-03 |
| 6.25E-01 | 2.48E-03 | 4.38E-01 | 3.54E-03 | 6.25E-01 | 3.92E-04 | 4.38E-01 | 3.14E-03 |
| 7.29E-01 | 1.21E-02 | 5.10E-01 | 3.51E-03 | 7.29E-01 | 2.61E-03 | 5.10E-01 | 3.14E-03 |
| 8.33E-01 | 1.19E-03 | 5.83E-01 | 3.49E-03 | 8.33E-01 | 1.47E-03 | 5.83E-01 | 3.14E-03 |

| | | | | | | | |
|---|---|---|---|---|---|---|---|
| 9.38E-01 | 3.29E-04 | 6.56E-01 | 3.47E-03 | 9.38E-01 | 4.46E-04 | 6.56E-01 | 3.15E-03 |
| 1.04E+00 | 5.37E-05 | 7.29E-01 | 3.46E-03 | 1.04E+00 | 1.92E-04 | 7.29E-01 | 3.15E-03 |
| 1.15E+00 | 2.03E-04 | 8.02E-01 | 3.45E-03 | 1.15E+00 | 2.26E-04 | 8.02E-01 | 3.17E-03 |
| 1.25E+00 | 3.72E-04 | 8.75E-01 | 3.44E-03 | 1.25E+00 | 3.53E-04 | 8.75E-01 | 3.18E-03 |
| 1.35E+00 | 5.40E-04 | 9.48E-01 | 3.44E-03 | 1.35E+00 | 4.97E-04 | 9.48E-01 | 3.19E-03 |
| 1.46E+00 | 7.17E-04 | 1.02E+00 | 3.44E-03 | 1.46E+00 | 6.52E-04 | 1.02E+00 | 3.20E-03 |
| 1.56E+00 | 9.05E-04 | 1.09E+00 | 3.45E-03 | 1.56E+00 | 8.19E-04 | 1.09E+00 | 3.22E-03 |
| 1.67E+00 | 1.11E-03 | 1.17E+00 | 3.45E-03 | 1.67E+00 | 9.96E-04 | 1.17E+00 | 3.23E-03 |
| 1.77E+00 | 1.41E-03 | 1.24E+00 | 3.45E-03 | 1.77E+00 | 1.16E-03 | 1.24E+00 | 3.24E-03 |
| 1.88E+00 | 1.84E-03 | 1.31E+00 | 3.46E-03 | 1.88E+00 | 1.51E-03 | 1.31E+00 | 3.25E-03 |
| 1.98E+00 | 2.27E-03 | 1.39E+00 | 3.46E-03 | 1.98E+00 | 2.01E-03 | 1.39E+00 | 3.26E-03 |
| 2.08E+00 | 2.67E-03 | 1.46E+00 | 3.47E-03 | 2.08E+00 | 2.44E-03 | 1.46E+00 | 3.27E-03 |
| 2.19E+00 | 3.01E-03 | 1.53E+00 | 3.47E-03 | 2.19E+00 | 2.81E-03 | 1.53E+00 | 3.28E-03 |
| 2.29E+00 | 3.27E-03 | 1.60E+00 | 3.47E-03 | 2.29E+00 | 3.09E-03 | 1.60E+00 | 3.28E-03 |
| 2.40E+00 | 3.42E-03 | 1.68E+00 | 3.47E-03 | 2.40E+00 | 3.25E-03 | 1.68E+00 | 3.29E-03 |
| 2.50E+00 | 3.47E-03 | 1.75E+00 | 3.47E-03 | 2.50E+00 | 3.29E-03 | 1.75E+00 | 3.29E-03 |
| 2.60E+00 | 3.42E-03 | 1.82E+00 | 3.47E-03 | 2.60E+00 | 3.25E-03 | 1.82E+00 | 3.29E-03 |
| 2.71E+00 | 3.27E-03 | 1.90E+00 | 3.47E-03 | 2.71E+00 | 3.09E-03 | 1.90E+00 | 3.28E-03 |
| 2.81E+00 | 3.01E-03 | 1.97E+00 | 3.47E-03 | 2.81E+00 | 2.81E-03 | 1.97E+00 | 3.28E-03 |
| 2.92E+00 | 2.67E-03 | 2.04E+00 | 3.47E-03 | 2.92E+00 | 2.44E-03 | 2.04E+00 | 3.27E-03 |
| 3.02E+00 | 2.27E-03 | 2.11E+00 | 3.46E-03 | 3.02E+00 | 2.01E-03 | 2.11E+00 | 3.26E-03 |
| 3.13E+00 | 1.84E-03 | 2.19E+00 | 3.46E-03 | 3.13E+00 | 1.51E-03 | 2.19E+00 | 3.25E-03 |
| 3.23E+00 | 1.41E-03 | 2.26E+00 | 3.45E-03 | 3.23E+00 | 1.16E-03 | 2.26E+00 | 3.24E-03 |
| 3.33E+00 | 1.11E-03 | 2.33E+00 | 3.45E-03 | 3.33E+00 | 9.95E-04 | 2.33E+00 | 3.23E-03 |
| 3.44E+00 | 9.05E-04 | 2.41E+00 | 3.45E-03 | 3.44E+00 | 8.19E-04 | 2.41E+00 | 3.22E-03 |
| 3.54E+00 | 7.16E-04 | 2.48E+00 | 3.44E-03 | 3.54E+00 | 6.52E-04 | 2.48E+00 | 3.21E-03 |
| 3.65E+00 | 5.39E-04 | 2.55E+00 | 3.44E-03 | 3.65E+00 | 4.96E-04 | 2.55E+00 | 3.19E-03 |
| 3.75E+00 | 3.70E-04 | 2.63E+00 | 3.44E-03 | 3.75E+00 | 3.52E-04 | 2.63E+00 | 3.18E-03 |
| 3.85E+00 | 2.00E-04 | 2.70E+00 | 3.45E-03 | 3.85E+00 | 2.26E-04 | 2.70E+00 | 3.17E-03 |
| 3.96E+00 | 4.17E-05 | 2.77E+00 | 3.46E-03 | 3.96E+00 | 1.93E-04 | 2.77E+00 | 3.16E-03 |
| 4.06E+00 | 2.81E-04 | 2.84E+00 | 3.47E-03 | 4.06E+00 | 4.33E-04 | 2.84E+00 | 3.15E-03 |
| 4.1667 | 1.12E-03 | 2.9167 | 3.49E-03 | 4.17E+00 | 1.28E-03 | 2.92E+00 | 3.14E-03 |
| 4.2708 | 1.62E-02 | 2.9896 | 3.51E-03 | 4.27E+00 | 2.21E-03 | 2.99E+00 | 3.14E-03 |
| 4.375 | 2.85E-03 | 3.0625 | 3.54E-03 | 4.38E+00 | 3.54E-04 | 3.06E+00 | 3.14E-03 |
| 4.4792 | 5.51E-04 | 3.1354 | 3.57E-03 | 4.48E+00 | 2.13E-04 | 3.14E+00 | 3.14E-03 |
| 4.5833 | 1.95E-04 | 3.2083 | 3.60E-03 | 4.58E+00 | 1.37E-04 | 3.21E+00 | 3.13E-03 |
| 4.6875 | 9.37E-05 | 3.2813 | 3.63E-03 | 4.69E+00 | 8.35E-05 | 3.28E+00 | 3.12E-03 |
| 4.7917 | 4.84E-05 | 3.3542 | 3.62E-03 | 4.79E+00 | 4.96E-05 | 3.35E+00 | 3.09E-03 |
| 4.8958 | 3.20E-05 | 3.4271 | 3.56E-03 | 4.90E+00 | 3.10E-05 | 3.43E+00 | 3.02E-03 |
| 5 | 3.19E-05 | 3.5 | 3.41E-03 | 5.00E+00 | 2.49E-05 | 3.50E+00 | 2.96E-03 |

Sample L-R-6

Table 0-68 Surface tensile strain profiles for sample L-R-6, step 60%YS.

| Hardened Layer | | | | Soft Bulk | | | |
|---|---|---|---|---|---|---|---|
| Longitudinal | | Transverse | | Longitudinal | | Transverse | |
| Length | Strain | Length | Strain | Length | Strain | Length | Strain |
| 0.00E+00 | 1.66E-05 | 0.00E+00 | 2.59E-03 | 0.00E+00 | 1.15E-05 | 0.00E+00 | 2.23E-03 |
| 1.04E-01 | 1.77E-05 | 7.29E-02 | 2.68E-03 | 1.04E-01 | 1.92E-05 | 7.29E-02 | 2.27E-03 |
| 2.08E-01 | 3.49E-05 | 1.46E-01 | 2.72E-03 | 2.08E-01 | 3.76E-05 | 1.46E-01 | 2.31E-03 |
| 3.13E-01 | 7.50E-05 | 2.19E-01 | 2.71E-03 | 3.13E-01 | 6.75E-05 | 2.19E-01 | 2.32E-03 |
| 4.17E-01 | 1.49E-04 | 2.92E-01 | 2.70E-03 | 4.17E-01 | 1.12E-04 | 2.92E-01 | 2.33E-03 |
| 5.21E-01 | 3.27E-04 | 3.65E-01 | 2.67E-03 | 5.21E-01 | 1.73E-04 | 3.65E-01 | 2.32E-03 |
| 6.25E-01 | 1.56E-03 | 4.38E-01 | 2.65E-03 | 6.25E-01 | 3.00E-04 | 4.38E-01 | 2.32E-03 |
| 7.29E-01 | 8.38E-03 | 5.10E-01 | 2.63E-03 | 7.29E-01 | 2.27E-03 | 5.10E-01 | 2.32E-03 |
| 8.33E-01 | 1.55E-03 | 5.83E-01 | 2.61E-03 | 8.33E-01 | 1.07E-03 | 5.83E-01 | 2.31E-03 |
| 9.38E-01 | 3.36E-04 | 6.56E-01 | 2.60E-03 | 9.38E-01 | 3.34E-04 | 6.56E-01 | 2.31E-03 |
| 1.04E+00 | 9.56E-05 | 7.29E-01 | 2.59E-03 | 1.04E+00 | 1.54E-04 | 7.29E-01 | 2.32E-03 |
| 1.15E+00 | 2.19E-04 | 8.02E-01 | 2.59E-03 | 1.15E+00 | 2.22E-04 | 8.02E-01 | 2.32E-03 |
| 1.25E+00 | 3.64E-04 | 8.75E-01 | 2.58E-03 | 1.25E+00 | 3.39E-04 | 8.75E-01 | 2.33E-03 |
| 1.35E+00 | 5.11E-04 | 9.48E-01 | 2.58E-03 | 1.35E+00 | 4.67E-04 | 9.48E-01 | 2.33E-03 |
| 1.46E+00 | 6.65E-04 | 1.02E+00 | 2.58E-03 | 1.46E+00 | 6.03E-04 | 1.02E+00 | 2.34E-03 |
| 1.56E+00 | 8.28E-04 | 1.09E+00 | 2.59E-03 | 1.56E+00 | 7.47E-04 | 1.09E+00 | 2.35E-03 |
| 1.67E+00 | 1.00E-03 | 1.17E+00 | 2.59E-03 | 1.67E+00 | 8.99E-04 | 1.17E+00 | 2.36E-03 |
| 1.77E+00 | 1.18E-03 | 1.24E+00 | 2.59E-03 | 1.77E+00 | 1.05E-03 | 1.24E+00 | 2.37E-03 |
| 1.88E+00 | 1.43E-03 | 1.31E+00 | 2.60E-03 | 1.88E+00 | 1.20E-03 | 1.31E+00 | 2.37E-03 |
| 1.98E+00 | 1.75E-03 | 1.39E+00 | 2.60E-03 | 1.98E+00 | 1.48E-03 | 1.39E+00 | 2.38E-03 |
| 2.08E+00 | 2.04E-03 | 1.46E+00 | 2.60E-03 | 2.08E+00 | 1.81E-03 | 1.46E+00 | 2.39E-03 |
| 2.19E+00 | 2.28E-03 | 1.53E+00 | 2.60E-03 | 2.19E+00 | 2.06E-03 | 1.53E+00 | 2.39E-03 |
| 2.29E+00 | 2.46E-03 | 1.60E+00 | 2.60E-03 | 2.29E+00 | 2.25E-03 | 1.60E+00 | 2.39E-03 |
| 2.40E+00 | 2.57E-03 | 1.68E+00 | 2.61E-03 | 2.40E+00 | 2.36E-03 | 1.68E+00 | 2.40E-03 |
| 2.50E+00 | 2.61E-03 | 1.75E+00 | 2.61E-03 | 2.50E+00 | 2.40E-03 | 1.75E+00 | 2.40E-03 |
| 2.60E+00 | 2.57E-03 | 1.82E+00 | 2.61E-03 | 2.60E+00 | 2.36E-03 | 1.82E+00 | 2.40E-03 |
| 2.71E+00 | 2.46E-03 | 1.90E+00 | 2.60E-03 | 2.71E+00 | 2.25E-03 | 1.90E+00 | 2.39E-03 |
| 2.81E+00 | 2.28E-03 | 1.97E+00 | 2.60E-03 | 2.81E+00 | 2.06E-03 | 1.97E+00 | 2.39E-03 |
| 2.92E+00 | 2.04E-03 | 2.04E+00 | 2.60E-03 | 2.92E+00 | 1.81E-03 | 2.04E+00 | 2.39E-03 |
| 3.02E+00 | 1.75E-03 | 2.11E+00 | 2.60E-03 | 3.02E+00 | 1.48E-03 | 2.11E+00 | 2.38E-03 |
| 3.13E+00 | 1.43E-03 | 2.19E+00 | 2.60E-03 | 3.13E+00 | 1.20E-03 | 2.19E+00 | 2.37E-03 |
| 3.23E+00 | 1.18E-03 | 2.26E+00 | 2.59E-03 | 3.23E+00 | 1.05E-03 | 2.26E+00 | 2.37E-03 |
| 3.33E+00 | 1.00E-03 | 2.33E+00 | 2.59E-03 | 3.33E+00 | 8.98E-04 | 2.33E+00 | 2.36E-03 |
| 3.44E+00 | 8.27E-04 | 2.41E+00 | 2.59E-03 | 3.44E+00 | 7.47E-04 | 2.41E+00 | 2.35E-03 |
| 3.54E+00 | 6.64E-04 | 2.48E+00 | 2.58E-03 | 3.54E+00 | 6.02E-04 | 2.48E+00 | 2.34E-03 |
| 3.65E+00 | 5.09E-04 | 2.55E+00 | 2.58E-03 | 3.65E+00 | 4.66E-04 | 2.55E+00 | 2.33E-03 |
| 3.75E+00 | 3.62E-04 | 2.63E+00 | 2.58E-03 | 3.75E+00 | 3.37E-04 | 2.63E+00 | 2.33E-03 |

| | | | | | | | |
|---|---|---|---|---|---|---|---|
| 3.85E+00 | 2.16E-04 | 2.70E+00 | 2.59E-03 | 3.85E+00 | 2.21E-04 | 2.70E+00 | 2.32E-03 |
| 3.96E+00 | 6.75E-05 | 2.77E+00 | 2.59E-03 | 3.96E+00 | 1.56E-04 | 2.77E+00 | 2.32E-03 |
| 4.06E+00 | 1.86E-04 | 2.84E+00 | 2.60E-03 | 4.06E+00 | 3.27E-04 | 2.84E+00 | 2.31E-03 |
| 4.1667 | 9.14E-04 | 2.9167 | 2.61E-03 | 4.17E+00 | 9.78E-04 | 2.92E+00 | 2.31E-03 |
| 4.2708 | 1.20E-02 | 2.9896 | 2.63E-03 | 4.27E+00 | 1.93E-03 | 2.99E+00 | 2.32E-03 |
| 4.375 | 1.39E-03 | 3.0625 | 2.65E-03 | 4.38E+00 | 2.85E-04 | 3.06E+00 | 2.32E-03 |
| 4.4792 | 3.01E-04 | 3.1354 | 2.67E-03 | 4.48E+00 | 1.69E-04 | 3.14E+00 | 2.32E-03 |
| 4.5833 | 1.44E-04 | 3.2083 | 2.70E-03 | 4.58E+00 | 1.12E-04 | 3.21E+00 | 2.33E-03 |
| 4.6875 | 7.52E-05 | 3.2813 | 2.71E-03 | 4.69E+00 | 6.85E-05 | 3.28E+00 | 2.32E-03 |
| 4.7917 | 3.68E-05 | 3.3542 | 2.72E-03 | 4.79E+00 | 3.91E-05 | 3.35E+00 | 2.31E-03 |
| 4.8958 | 2.07E-05 | 3.4271 | 2.68E-03 | 4.90E+00 | 2.13E-05 | 3.43E+00 | 2.27E-03 |
| 5 | 1.97E-05 | 3.5 | 2.59E-03 | 5.00E+00 | 1.42E-05 | 3.50E+00 | 2.23E-03 |

Table B-69 Surface tensile strain profiles for sample L-R-6, step 70%YS.

| **Hardened Layer** | | | | **Soft Bulk** | | | |
|---|---|---|---|---|---|---|---|
| Longitudinal | | Transverse | | Longitudinal | | Transverse | |
| Length | Strain | Length | Strain | Length | Strain | Length | Strain |
| 0.00E+00 | 2.20E-05 | 0.00E+00 | 2.99E-03 | 0.00E+00 | 1.60E-05 | 0.00E+00 | 2.58E-03 |
| 1.04E-01 | 2.28E-05 | 7.29E-02 | 3.11E-03 | 1.04E-01 | 2.33E-05 | 7.29E-02 | 2.64E-03 |
| 2.08E-01 | 3.97E-05 | 1.46E-01 | 3.16E-03 | 2.08E-01 | 4.20E-05 | 1.46E-01 | 2.68E-03 |
| 3.13E-01 | 8.18E-05 | 2.19E-01 | 3.16E-03 | 3.13E-01 | 7.41E-05 | 2.19E-01 | 2.71E-03 |
| 4.17E-01 | 1.61E-04 | 2.92E-01 | 3.14E-03 | 4.17E-01 | 1.24E-04 | 2.92E-01 | 2.72E-03 |
| 5.21E-01 | 3.50E-04 | 3.65E-01 | 3.11E-03 | 5.21E-01 | 1.95E-04 | 3.65E-01 | 2.72E-03 |
| 6.25E-01 | 1.55E-03 | 4.38E-01 | 3.08E-03 | 6.25E-01 | 3.30E-04 | 4.38E-01 | 2.72E-03 |
| 7.29E-01 | 1.10E-02 | 5.10E-01 | 3.06E-03 | 7.29E-01 | 2.56E-03 | 5.10E-01 | 2.72E-03 |
| 8.33E-01 | 1.87E-03 | 5.83E-01 | 3.04E-03 | 8.33E-01 | 1.27E-03 | 5.83E-01 | 2.72E-03 |
| 9.38E-01 | 4.21E-04 | 6.56E-01 | 3.02E-03 | 9.38E-01 | 3.98E-04 | 6.56E-01 | 2.72E-03 |
| 1.04E+00 | 9.65E-05 | 7.29E-01 | 3.01E-03 | 1.04E+00 | 1.72E-04 | 7.29E-01 | 2.72E-03 |
| 1.15E+00 | 2.09E-04 | 8.02E-01 | 3.00E-03 | 1.15E+00 | 2.21E-04 | 8.02E-01 | 2.73E-03 |
| 1.25E+00 | 3.65E-04 | 8.75E-01 | 3.00E-03 | 1.25E+00 | 3.43E-04 | 8.75E-01 | 2.74E-03 |
| 1.35E+00 | 5.24E-04 | 9.48E-01 | 3.00E-03 | 1.35E+00 | 4.80E-04 | 9.48E-01 | 2.75E-03 |
| 1.46E+00 | 6.90E-04 | 1.02E+00 | 3.00E-03 | 1.46E+00 | 6.27E-04 | 1.02E+00 | 2.76E-03 |
| 1.56E+00 | 8.66E-04 | 1.09E+00 | 3.00E-03 | 1.56E+00 | 7.82E-04 | 1.09E+00 | 2.78E-03 |
| 1.67E+00 | 1.05E-03 | 1.17E+00 | 3.01E-03 | 1.67E+00 | 9.47E-04 | 1.17E+00 | 2.79E-03 |
| 1.77E+00 | 1.28E-03 | 1.24E+00 | 3.01E-03 | 1.77E+00 | 1.10E-03 | 1.24E+00 | 2.80E-03 |
| 1.88E+00 | 1.63E-03 | 1.31E+00 | 3.01E-03 | 1.88E+00 | 1.33E-03 | 1.31E+00 | 2.81E-03 |
| 1.98E+00 | 2.01E-03 | 1.39E+00 | 3.02E-03 | 1.98E+00 | 1.73E-03 | 1.39E+00 | 2.81E-03 |
| 2.08E+00 | 2.35E-03 | 1.46E+00 | 3.02E-03 | 2.08E+00 | 2.11E-03 | 1.46E+00 | 2.82E-03 |
| 2.19E+00 | 2.64E-03 | 1.53E+00 | 3.02E-03 | 2.19E+00 | 2.42E-03 | 1.53E+00 | 2.83E-03 |
| 2.29E+00 | 2.85E-03 | 1.60E+00 | 3.03E-03 | 2.29E+00 | 2.65E-03 | 1.60E+00 | 2.83E-03 |
| 2.40E+00 | 2.98E-03 | 1.68E+00 | 3.03E-03 | 2.40E+00 | 2.79E-03 | 1.68E+00 | 2.83E-03 |

| | | | | | | | |
|---|---|---|---|---|---|---|---|
| 2.50E+00 | 3.03E-03 | 1.75E+00 | 3.03E-03 | 2.50E+00 | 2.83E-03 | 1.75E+00 | 2.83E-03 |
| 2.60E+00 | 2.98E-03 | 1.82E+00 | 3.03E-03 | 2.60E+00 | 2.79E-03 | 1.82E+00 | 2.83E-03 |
| 2.71E+00 | 2.85E-03 | 1.90E+00 | 3.03E-03 | 2.71E+00 | 2.65E-03 | 1.90E+00 | 2.83E-03 |
| 2.81E+00 | 2.64E-03 | 1.97E+00 | 3.02E-03 | 2.81E+00 | 2.42E-03 | 1.97E+00 | 2.83E-03 |
| 2.92E+00 | 2.35E-03 | 2.04E+00 | 3.02E-03 | 2.92E+00 | 2.11E-03 | 2.04E+00 | 2.82E-03 |
| 3.02E+00 | 2.00E-03 | 2.11E+00 | 3.02E-03 | 3.02E+00 | 1.73E-03 | 2.11E+00 | 2.81E-03 |
| 3.13E+00 | 1.63E-03 | 2.19E+00 | 3.01E-03 | 3.13E+00 | 1.33E-03 | 2.19E+00 | 2.81E-03 |
| 3.23E+00 | 1.28E-03 | 2.26E+00 | 3.01E-03 | 3.23E+00 | 1.10E-03 | 2.26E+00 | 2.80E-03 |
| 3.33E+00 | 1.05E-03 | 2.33E+00 | 3.01E-03 | 3.33E+00 | 9.47E-04 | 2.33E+00 | 2.79E-03 |
| 3.44E+00 | 8.65E-04 | 2.41E+00 | 3.00E-03 | 3.44E+00 | 7.82E-04 | 2.41E+00 | 2.78E-03 |
| 3.54E+00 | 6.89E-04 | 2.48E+00 | 3.00E-03 | 3.54E+00 | 6.25E-04 | 2.48E+00 | 2.76E-03 |
| 3.65E+00 | 5.22E-04 | 2.55E+00 | 3.00E-03 | 3.65E+00 | 4.79E-04 | 2.55E+00 | 2.75E-03 |
| 3.75E+00 | 3.63E-04 | 2.63E+00 | 3.00E-03 | 3.75E+00 | 3.42E-04 | 2.63E+00 | 2.74E-03 |
| 3.85E+00 | 2.04E-04 | 2.70E+00 | 3.00E-03 | 3.85E+00 | 2.20E-04 | 2.70E+00 | 2.73E-03 |
| 3.96E+00 | 5.77E-05 | 2.77E+00 | 3.01E-03 | 3.96E+00 | 1.75E-04 | 2.77E+00 | 2.72E-03 |
| 4.06E+00 | 2.69E-04 | 2.84E+00 | 3.02E-03 | 4.06E+00 | 3.90E-04 | 2.84E+00 | 2.72E-03 |
| 4.1667 | 1.13E-03 | 2.9167 | 3.04E-03 | 4.17E+00 | 1.15E-03 | 2.92E+00 | 2.72E-03 |
| 4.2708 | 1.53E-02 | 2.9896 | 3.06E-03 | 4.27E+00 | 2.18E-03 | 2.99E+00 | 2.71E-03 |
| 4.375 | 1.47E-03 | 3.0625 | 3.08E-03 | 4.38E+00 | 3.12E-04 | 3.06E+00 | 2.72E-03 |
| 4.4792 | 3.26E-04 | 3.1354 | 3.11E-03 | 4.48E+00 | 1.90E-04 | 3.14E+00 | 2.72E-03 |
| 4.5833 | 1.56E-04 | 3.2083 | 3.14E-03 | 4.58E+00 | 1.24E-04 | 3.21E+00 | 2.72E-03 |
| 4.6875 | 8.22E-05 | 3.2813 | 3.16E-03 | 4.69E+00 | 7.52E-05 | 3.28E+00 | 2.71E-03 |
| 4.7917 | 4.18E-05 | 3.3542 | 3.16E-03 | 4.79E+00 | 4.36E-05 | 3.35E+00 | 2.68E-03 |
| 4.8958 | 2.58E-05 | 3.4271 | 3.11E-03 | 4.90E+00 | 2.55E-05 | 3.43E+00 | 2.64E-03 |
| 5 | 2.51E-05 | 3.5 | 2.99E-03 | 5.00E+00 | 1.88E-05 | 3.50E+00 | 2.58E-03 |

## B.4 Stress and strain profiles across the sample thickness

Sample N3

Table B-70 Stress and strain profiles across sample thickness for sample N3, step 39%YS.

| Normal Stress | | Equivalent Stress | | Normal Strain | | Equivalent Strain | |
|---|---|---|---|---|---|---|---|
| Length | Stress | Length | Stress | Length | Stress | Length | Stress |
| 0.00E+00 | -2.23E+02 | 0.00E+00 | 1.99E+02 | 0.00E+00 | -1.18E-03 | 0.00E+00 | 1.16E-03 |
| 1.88E-02 | -2.23E+02 | 1.88E-02 | 1.99E+02 | 1.88E-02 | -1.18E-03 | 1.88E-02 | 1.16E-03 |
| 3.75E-02 | -2.22E+02 | 3.75E-02 | 1.99E+02 | 3.75E-02 | -1.18E-03 | 3.75E-02 | 1.16E-03 |
| 5.63E-02 | -2.22E+02 | 5.63E-02 | 1.99E+02 | 5.63E-02 | -1.18E-03 | 5.63E-02 | 1.16E-03 |
| 7.50E-02 | -2.22E+02 | 7.50E-02 | 1.98E+02 | 7.50E-02 | -1.18E-03 | 7.50E-02 | 1.15E-03 |
| 9.38E-02 | -2.22E+02 | 9.38E-02 | 1.98E+02 | 9.38E-02 | -1.18E-03 | 9.38E-02 | 1.15E-03 |

| | | | | | | | |
|---|---|---|---|---|---|---|---|
| 1.13E-01 | -2.22E+02 | 1.13E-01 | 1.98E+02 | 1.13E-01 | -1.18E-03 | 1.13E-01 | 1.15E-03 |
| 1.31E-01 | -2.22E+02 | 1.31E-01 | 1.97E+02 | 1.31E-01 | -1.18E-03 | 1.31E-01 | 1.15E-03 |
| 1.50E-01 | -2.23E+02 | 1.50E-01 | 1.96E+02 | 1.50E-01 | -1.18E-03 | 1.50E-01 | 1.14E-03 |
| 1.69E-01 | -2.23E+02 | 1.69E-01 | 1.95E+02 | 1.69E-01 | -1.18E-03 | 1.69E-01 | 1.14E-03 |
| 1.88E-01 | -2.24E+02 | 1.88E-01 | 1.95E+02 | 1.88E-01 | -1.18E-03 | 1.88E-01 | 1.13E-03 |
| 2.06E-01 | -2.21E+02 | 2.06E-01 | 1.90E+02 | 2.06E-01 | -1.16E-03 | 2.06E-01 | 1.11E-03 |
| 2.25E-01 | -2.05E+02 | 2.25E-01 | 1.73E+02 | 2.25E-01 | -1.07E-03 | 2.25E-01 | 1.01E-03 |
| 2.44E-01 | -1.90E+02 | 2.44E-01 | 1.57E+02 | 2.44E-01 | -9.77E-04 | 2.44E-01 | 9.12E-04 |
| 2.63E-01 | -1.75E+02 | 2.63E-01 | 1.40E+02 | 2.63E-01 | -8.86E-04 | 2.63E-01 | 8.15E-04 |
| 2.81E-01 | -1.59E+02 | 2.81E-01 | 1.25E+02 | 2.81E-01 | -7.98E-04 | 2.81E-01 | 7.25E-04 |
| 3.00E-01 | -1.44E+02 | 3.00E-01 | 1.10E+02 | 3.00E-01 | -7.12E-04 | 3.00E-01 | 6.40E-04 |
| 3.19E-01 | -1.28E+02 | 3.19E-01 | 9.51E+01 | 3.19E-01 | -6.26E-04 | 3.19E-01 | 5.54E-04 |
| 3.38E-01 | -1.13E+02 | 3.38E-01 | 8.07E+01 | 3.38E-01 | -5.40E-04 | 3.38E-01 | 4.69E-04 |
| 3.56E-01 | -9.79E+01 | 3.56E-01 | 6.79E+01 | 3.56E-01 | -4.61E-04 | 3.56E-01 | 3.98E-04 |
| 3.75E-01 | -8.30E+01 | 3.75E-01 | 5.54E+01 | 3.75E-01 | -3.81E-04 | 3.75E-01 | 3.27E-04 |
| 3.94E-01 | -6.82E+01 | 3.94E-01 | 4.34E+01 | 3.94E-01 | -3.02E-04 | 3.94E-01 | 2.55E-04 |
| 4.13E-01 | -5.35E+01 | 4.13E-01 | 3.27E+01 | 4.13E-01 | -2.25E-04 | 4.13E-01 | 2.06E-04 |
| 4.31E-01 | -3.92E+01 | 4.31E-01 | 2.43E+01 | 4.31E-01 | -1.51E-04 | 4.31E-01 | 1.83E-04 |
| 4.50E-01 | -2.48E+01 | 4.50E-01 | 2.00E+01 | 4.50E-01 | -7.66E-05 | 4.50E-01 | 1.61E-04 |
| 4.69E-01 | -1.05E+01 | 4.69E-01 | 2.24E+01 | 4.69E-01 | -2.47E-06 | 4.69E-01 | 1.38E-04 |
| 4.88E-01 | 3.59E+00 | 4.88E-01 | 2.92E+01 | 4.88E-01 | 6.92E-05 | 4.88E-01 | 1.81E-04 |
| 5.06E-01 | 1.77E+01 | 5.06E-01 | 3.83E+01 | 5.06E-01 | 1.40E-04 | 5.06E-01 | 2.34E-04 |
| 5.25E-01 | 3.17E+01 | 5.25E-01 | 4.83E+01 | 5.25E-01 | 2.12E-04 | 5.25E-01 | 2.87E-04 |
| 5.44E-01 | 4.58E+01 | 5.44E-01 | 5.87E+01 | 5.44E-01 | 2.83E-04 | 5.44E-01 | 3.42E-04 |
| 5.63E-01 | 6.00E+01 | 5.63E-01 | 6.94E+01 | 5.63E-01 | 3.54E-04 | 5.63E-01 | 4.05E-04 |
| 5.81E-01 | 7.41E+01 | 5.81E-01 | 8.03E+01 | 5.81E-01 | 4.26E-04 | 5.81E-01 | 4.68E-04 |
| 6.00E-01 | 8.83E+01 | 6.00E-01 | 9.12E+01 | 6.00E-01 | 4.97E-04 | 6.00E-01 | 5.31E-04 |

| | | | | | | | |
|---|---|---|---|---|---|---|---|
| 6.19E-01 | 1.03E+02 | 6.19E-01 | 1.03E+02 | 6.19E-01 | 5.70E-04 | 6.19E-01 | 5.97E-04 |
| 6.38E-01 | 1.17E+02 | 6.38E-01 | 1.14E+02 | 6.38E-01 | 6.44E-04 | 6.38E-01 | 6.65E-04 |
| 6.56E-01 | 1.32E+02 | 6.56E-01 | 1.26E+02 | 6.56E-01 | 7.18E-04 | 6.56E-01 | 7.32E-04 |
| 6.75E-01 | 1.47E+02 | 6.75E-01 | 1.38E+02 | 6.75E-01 | 7.94E-04 | 6.75E-01 | 8.01E-04 |
| 6.94E-01 | 1.64E+02 | 6.94E-01 | 1.52E+02 | 6.94E-01 | 8.83E-04 | 6.94E-01 | 8.85E-04 |
| 7.13E-01 | 1.82E+02 | 7.13E-01 | 1.67E+02 | 7.13E-01 | 9.72E-04 | 7.13E-01 | 9.68E-04 |
| 7.31E-01 | 1.99E+02 | 7.31E-01 | 1.81E+02 | 7.31E-01 | 1.06E-03 | 7.31E-01 | 1.05E-03 |
| 0.75 | 2.10E+02 | 0.75 | 1.89E+02 | 7.50E-01 | 1.11E-03 | 7.50E-01 | 1.10E-03 |
| 0.76875 | 2.14E+02 | 0.76875 | 1.92E+02 | 7.69E-01 | 1.13E-03 | 7.69E-01 | 1.12E-03 |
| 0.7875 | 2.18E+02 | 0.7875 | 1.95E+02 | 7.88E-01 | 1.15E-03 | 7.88E-01 | 1.13E-03 |
| 0.80625 | 2.22E+02 | 0.80625 | 1.97E+02 | 8.06E-01 | 1.16E-03 | 8.06E-01 | 1.15E-03 |
| 0.825 | 2.24E+02 | 0.825 | 1.98E+02 | 8.25E-01 | 1.17E-03 | 8.25E-01 | 1.15E-03 |
| 0.84375 | 2.25E+02 | 0.84375 | 1.99E+02 | 8.44E-01 | 1.17E-03 | 8.44E-01 | 1.16E-03 |
| 0.8625 | 2.27E+02 | 0.8625 | 2.00E+02 | 8.63E-01 | 1.18E-03 | 8.63E-01 | 1.17E-03 |
| 0.88125 | 3.24E+02 | 0.88125 | 2.89E+02 | 8.81E-01 | 1.71E-03 | 8.81E-01 | 1.68E-03 |
| 0.9 | 3.41E+02 | 0.9 | 3.03E+02 | 9.00E-01 | 1.80E-03 | 9.00E-01 | 1.76E-03 |

Table B-71 Stress and strain profiles across sample thickness for sample N3, step 47%YS.

| **Normal Stress** | | **Equivalent Stress** | | **Normal Strain** | | **Equivalent Strain** | |
|---|---|---|---|---|---|---|---|
| Length | Stress | Length | Stress | Length | Stress | Length | Stress |
| 0.00E+00 | -2.30E+02 | 0.00E+00 | 2.03E+02 | 0.00E+00 | -1.20E-03 | 0.00E+00 | 1.18E-03 |
| 1.88E-02 | -2.30E+02 | 1.88E-02 | 2.03E+02 | 1.88E-02 | -1.20E-03 | 1.88E-02 | 1.18E-03 |
| 3.75E-02 | -2.30E+02 | 3.75E-02 | 2.04E+02 | 3.75E-02 | -1.20E-03 | 3.75E-02 | 1.18E-03 |
| 5.63E-02 | -2.30E+02 | 5.63E-02 | 2.04E+02 | 5.63E-02 | -1.20E-03 | 5.63E-02 | 1.19E-03 |
| 7.50E-02 | -2.30E+02 | 7.50E-02 | 2.04E+02 | 7.50E-02 | -1.21E-03 | 7.50E-02 | 1.19E-03 |
| 9.38E-02 | -2.31E+02 | 9.38E-02 | 2.04E+02 | 9.38E-02 | -1.21E-03 | 9.38E-02 | 1.19E-03 |
| 1.13E-01 | -2.32E+02 | 1.13E-01 | 2.04E+02 | 1.13E-01 | -1.21E-03 | 1.13E-01 | 1.18E-03 |
| 1.31E-01 | -2.33E+02 | 1.31E-01 | 2.04E+02 | 1.31E-01 | -1.21E-03 | 1.31E-01 | 1.18E-03 |

| | | | | | | | |
|---|---|---|---|---|---|---|---|
| 1.50E-01 | -2.34E+02 | 1.50E-01 | 2.03E+02 | 1.50E-01 | -1.21E-03 | 1.50E-01 | 1.18E-03 |
| 1.69E-01 | -2.35E+02 | 1.69E-01 | 2.01E+02 | 1.69E-01 | -1.21E-03 | 1.69E-01 | 1.17E-03 |
| 1.88E-01 | -2.37E+02 | 1.88E-01 | 2.00E+02 | 1.88E-01 | -1.22E-03 | 1.88E-01 | 1.17E-03 |
| 2.06E-01 | -2.37E+02 | 2.06E-01 | 1.98E+02 | 2.06E-01 | -1.21E-03 | 2.06E-01 | 1.15E-03 |
| 2.25E-01 | -2.33E+02 | 2.25E-01 | 1.92E+02 | 2.25E-01 | -1.19E-03 | 2.25E-01 | 1.12E-03 |
| 2.44E-01 | -2.29E+02 | 2.44E-01 | 1.86E+02 | 2.44E-01 | -1.17E-03 | 2.44E-01 | 1.09E-03 |
| 2.63E-01 | -2.25E+02 | 2.63E-01 | 1.81E+02 | 2.63E-01 | -1.14E-03 | 2.63E-01 | 1.05E-03 |
| 2.81E-01 | -2.09E+02 | 2.81E-01 | 1.65E+02 | 2.81E-01 | -1.05E-03 | 2.81E-01 | 9.60E-04 |
| 3.00E-01 | -1.86E+02 | 3.00E-01 | 1.43E+02 | 3.00E-01 | -9.23E-04 | 3.00E-01 | 8.33E-04 |
| 3.19E-01 | -1.63E+02 | 3.19E-01 | 1.21E+02 | 3.19E-01 | -7.95E-04 | 3.19E-01 | 7.06E-04 |
| 3.38E-01 | -1.40E+02 | 3.38E-01 | 9.99E+01 | 3.38E-01 | -6.69E-04 | 3.38E-01 | 5.81E-04 |
| 3.56E-01 | -1.22E+02 | 3.56E-01 | 8.46E+01 | 3.56E-01 | -5.73E-04 | 3.56E-01 | 4.95E-04 |
| 3.75E-01 | -1.03E+02 | 3.75E-01 | 6.94E+01 | 3.75E-01 | -4.77E-04 | 3.75E-01 | 4.08E-04 |
| 3.94E-01 | -8.52E+01 | 3.94E-01 | 5.48E+01 | 3.94E-01 | -3.82E-04 | 3.94E-01 | 3.21E-04 |
| 4.13E-01 | -6.73E+01 | 4.13E-01 | 4.15E+01 | 4.13E-01 | -2.89E-04 | 4.13E-01 | 2.58E-04 |
| 4.31E-01 | -4.98E+01 | 4.31E-01 | 3.03E+01 | 4.31E-01 | -1.99E-04 | 4.31E-01 | 2.22E-04 |
| 4.50E-01 | -3.23E+01 | 4.50E-01 | 2.32E+01 | 4.50E-01 | -1.10E-04 | 4.50E-01 | 1.85E-04 |
| 4.69E-01 | -1.48E+01 | 4.69E-01 | 2.39E+01 | 4.69E-01 | -2.01E-05 | 4.69E-01 | 1.49E-04 |
| 4.88E-01 | 2.47E+00 | 4.88E-01 | 3.15E+01 | 4.88E-01 | 6.73E-05 | 4.88E-01 | 1.99E-04 |
| 5.06E-01 | 1.97E+01 | 5.06E-01 | 4.23E+01 | 5.06E-01 | 1.54E-04 | 5.06E-01 | 2.62E-04 |
| 5.25E-01 | 3.70E+01 | 5.25E-01 | 5.45E+01 | 5.25E-01 | 2.41E-04 | 5.25E-01 | 3.25E-04 |
| 5.44E-01 | 5.43E+01 | 5.44E-01 | 6.74E+01 | 5.44E-01 | 3.29E-04 | 5.44E-01 | 3.93E-04 |
| 5.63E-01 | 7.19E+01 | 5.63E-01 | 8.08E+01 | 5.63E-01 | 4.18E-04 | 5.63E-01 | 4.71E-04 |
| 5.81E-01 | 8.95E+01 | 5.81E-01 | 9.44E+01 | 5.81E-01 | 5.06E-04 | 5.81E-01 | 5.50E-04 |
| 6.00E-01 | 1.07E+02 | 6.00E-01 | 1.08E+02 | 6.00E-01 | 5.95E-04 | 6.00E-01 | 6.29E-04 |
| 6.19E-01 | 1.27E+02 | 6.19E-01 | 1.24E+02 | 6.19E-01 | 6.95E-04 | 6.19E-01 | 7.21E-04 |
| 6.38E-01 | 1.48E+02 | 6.38E-01 | 1.41E+02 | 6.38E-01 | 8.01E-04 | 6.38E-01 | 8.19E-04 |

| | | | | | | | |
|---|---|---|---|---|---|---|---|
| 6.56E-01 | 1.68E+02 | 6.56E-01 | 1.58E+02 | 6.56E-01 | 9.07E-04 | 6.56E-01 | 9.17E-04 |
| 6.75E-01 | 1.88E+02 | 6.75E-01 | 1.74E+02 | 6.75E-01 | 1.01E-03 | 6.75E-01 | 1.01E-03 |
| 6.94E-01 | 1.97E+02 | 6.94E-01 | 1.80E+02 | 6.94E-01 | 1.05E-03 | 6.94E-01 | 1.05E-03 |
| 7.13E-01 | 2.05E+02 | 7.13E-01 | 1.87E+02 | 7.13E-01 | 1.09E-03 | 7.13E-01 | 1.09E-03 |
| 7.31E-01 | 2.14E+02 | 7.31E-01 | 1.94E+02 | 7.31E-01 | 1.13E-03 | 7.31E-01 | 1.13E-03 |
| 0.75 | 2.20E+02 | 0.75 | 1.98E+02 | 7.50E-01 | 1.15E-03 | 7.50E-01 | 1.15E-03 |
| 0.76875 | 2.22E+02 | 0.76875 | 1.99E+02 | 7.69E-01 | 1.16E-03 | 7.69E-01 | 1.16E-03 |
| 0.7875 | 2.25E+02 | 0.7875 | 2.01E+02 | 7.88E-01 | 1.17E-03 | 7.88E-01 | 1.17E-03 |
| 0.80625 | 2.28E+02 | 0.80625 | 2.02E+02 | 8.06E-01 | 1.18E-03 | 8.06E-01 | 1.18E-03 |
| 0.825 | 2.30E+02 | 0.825 | 2.03E+02 | 8.25E-01 | 1.19E-03 | 8.25E-01 | 1.18E-03 |
| 0.84375 | 2.32E+02 | 0.84375 | 2.05E+02 | 8.44E-01 | 1.20E-03 | 8.44E-01 | 1.19E-03 |
| 0.8625 | 2.34E+02 | 0.8625 | 2.06E+02 | 8.63E-01 | 1.20E-03 | 8.63E-01 | 1.20E-03 |
| 0.88125 | 3.91E+02 | 0.88125 | 3.48E+02 | 8.81E-01 | 2.06E-03 | 8.81E-01 | 2.02E-03 |
| 0.9 | 4.10E+02 | 0.9 | 3.65E+02 | 9.00E-01 | 2.16E-03 | 9.00E-01 | 2.12E-03 |

Table 0-72 Stress and strain profiles across sample thickness for sample N3, step 51%YS.

| **Normal Stress** | | **Equivalent Stress** | | **Normal Strain** | | **Equivalent Strain** | |
|---|---|---|---|---|---|---|---|
| Length | Stress | Length | Stress | Length | Stress | Length | Stress |
| 0.00E+00 | -2.35E+02 | 0.00E+00 | 2.07E+02 | 0.00E+00 | -1.22E-03 | 0.00E+00 | 1.20E-03 |
| 1.88E-02 | -2.35E+02 | 1.88E-02 | 2.07E+02 | 1.88E-02 | -1.22E-03 | 1.88E-02 | 1.21E-03 |
| 3.75E-02 | -2.36E+02 | 3.75E-02 | 2.08E+02 | 3.75E-02 | -1.23E-03 | 3.75E-02 | 1.21E-03 |
| 5.63E-02 | -2.37E+02 | 5.63E-02 | 2.08E+02 | 5.63E-02 | -1.23E-03 | 5.63E-02 | 1.21E-03 |
| 7.50E-02 | -2.37E+02 | 7.50E-02 | 2.09E+02 | 7.50E-02 | -1.23E-03 | 7.50E-02 | 1.21E-03 |
| 9.38E-02 | -2.39E+02 | 9.38E-02 | 2.09E+02 | 9.38E-02 | -1.23E-03 | 9.38E-02 | 1.22E-03 |
| 1.13E-01 | -2.40E+02 | 1.13E-01 | 2.09E+02 | 1.13E-01 | -1.23E-03 | 1.13E-01 | 1.22E-03 |
| 1.31E-01 | -2.41E+02 | 1.31E-01 | 2.10E+02 | 1.31E-01 | -1.24E-03 | 1.31E-01 | 1.22E-03 |
| 1.50E-01 | -2.43E+02 | 1.50E-01 | 2.09E+02 | 1.50E-01 | -1.24E-03 | 1.50E-01 | 1.21E-03 |
| 1.69E-01 | -2.46E+02 | 1.69E-01 | 2.08E+02 | 1.69E-01 | -1.25E-03 | 1.69E-01 | 1.21E-03 |

| | | | | | | | |
|---|---|---|---|---|---|---|---|
| 1.88E-01 | -2.48E+02 | 1.88E-01 | 2.07E+02 | 1.88E-01 | -1.25E-03 | 1.88E-01 | 1.20E-03 |
| 2.06E-01 | -2.50E+02 | 2.06E-01 | 2.06E+02 | 2.06E-01 | -1.26E-03 | 2.06E-01 | 1.20E-03 |
| 2.25E-01 | -2.52E+02 | 2.25E-01 | 2.04E+02 | 2.25E-01 | -1.26E-03 | 2.25E-01 | 1.19E-03 |
| 2.44E-01 | -2.54E+02 | 2.44E-01 | 2.03E+02 | 2.44E-01 | -1.27E-03 | 2.44E-01 | 1.18E-03 |
| 2.63E-01 | -2.56E+02 | 2.63E-01 | 2.02E+02 | 2.63E-01 | -1.28E-03 | 2.63E-01 | 1.18E-03 |
| 2.81E-01 | -2.42E+02 | 2.81E-01 | 1.88E+02 | 2.81E-01 | -1.20E-03 | 2.81E-01 | 1.10E-03 |
| 3.00E-01 | -2.19E+02 | 3.00E-01 | 1.67E+02 | 3.00E-01 | -1.08E-03 | 3.00E-01 | 9.73E-04 |
| 3.19E-01 | -1.97E+02 | 3.19E-01 | 1.46E+02 | 3.19E-01 | -9.58E-04 | 3.19E-01 | 8.50E-04 |
| 3.38E-01 | -1.74E+02 | 3.38E-01 | 1.25E+02 | 3.38E-01 | -8.35E-04 | 3.38E-01 | 7.27E-04 |
| 3.56E-01 | -1.51E+02 | 3.56E-01 | 1.05E+02 | 3.56E-01 | -7.13E-04 | 3.56E-01 | 6.16E-04 |
| 3.75E-01 | -1.27E+02 | 3.75E-01 | 8.60E+01 | 3.75E-01 | -5.90E-04 | 3.75E-01 | 5.04E-04 |
| 3.94E-01 | -1.03E+02 | 3.94E-01 | 6.71E+01 | 3.94E-01 | -4.67E-04 | 3.94E-01 | 3.93E-04 |
| 4.13E-01 | -8.11E+01 | 4.13E-01 | 5.04E+01 | 4.13E-01 | -3.52E-04 | 4.13E-01 | 3.10E-04 |
| 4.31E-01 | -6.03E+01 | 4.31E-01 | 3.66E+01 | 4.31E-01 | -2.47E-04 | 4.31E-01 | 2.61E-04 |
| 4.50E-01 | -3.95E+01 | 4.50E-01 | 2.67E+01 | 4.50E-01 | -1.41E-04 | 4.50E-01 | 2.11E-04 |
| 4.69E-01 | -1.87E+01 | 4.69E-01 | 2.57E+01 | 4.69E-01 | -3.57E-05 | 4.69E-01 | 1.61E-04 |
| 4.88E-01 | 1.91E+00 | 4.88E-01 | 3.40E+01 | 4.88E-01 | 6.83E-05 | 4.88E-01 | 2.20E-04 |
| 5.06E-01 | 2.25E+01 | 5.06E-01 | 4.68E+01 | 5.06E-01 | 1.72E-04 | 5.06E-01 | 2.94E-04 |
| 5.25E-01 | 4.31E+01 | 5.25E-01 | 6.14E+01 | 5.25E-01 | 2.76E-04 | 5.25E-01 | 3.68E-04 |
| 5.44E-01 | 6.39E+01 | 5.44E-01 | 7.70E+01 | 5.44E-01 | 3.81E-04 | 5.44E-01 | 4.49E-04 |
| 5.63E-01 | 8.51E+01 | 5.63E-01 | 9.34E+01 | 5.63E-01 | 4.88E-04 | 5.63E-01 | 5.45E-04 |
| 5.81E-01 | 1.06E+02 | 5.81E-01 | 1.10E+02 | 5.81E-01 | 5.95E-04 | 5.81E-01 | 6.41E-04 |
| 6.00E-01 | 1.28E+02 | 6.00E-01 | 1.27E+02 | 6.00E-01 | 7.02E-04 | 6.00E-01 | 7.38E-04 |
| 6.19E-01 | 1.50E+02 | 6.19E-01 | 1.45E+02 | 6.19E-01 | 8.14E-04 | 6.19E-01 | 8.41E-04 |
| 6.38E-01 | 1.72E+02 | 6.38E-01 | 1.63E+02 | 6.38E-01 | 9.27E-04 | 6.38E-01 | 9.47E-04 |
| 6.56E-01 | 1.94E+02 | 6.56E-01 | 1.81E+02 | 6.56E-01 | 1.04E-03 | 6.56E-01 | 1.05E-03 |
| 6.75E-01 | 2.14E+02 | 6.75E-01 | 1.97E+02 | 6.75E-01 | 1.14E-03 | 6.75E-01 | 1.15E-03 |

| | | | | | | | |
|---|---|---|---|---|---|---|---|
| 6.94E-01 | 2.17E+02 | 6.94E-01 | 1.98E+02 | 6.94E-01 | 1.15E-03 | 6.94E-01 | 1.15E-03 |
| 7.13E-01 | 2.19E+02 | 7.13E-01 | 1.99E+02 | 7.13E-01 | 1.16E-03 | 7.13E-01 | 1.16E-03 |
| 7.31E-01 | 2.22E+02 | 7.31E-01 | 2.00E+02 | 7.31E-01 | 1.16E-03 | 7.31E-01 | 1.16E-03 |
| 0.75 | 2.25E+02 | 0.75 | 2.02E+02 | 7.50E-01 | 1.17E-03 | 7.50E-01 | 1.17E-03 |
| 0.76875 | 2.28E+02 | 0.76875 | 2.03E+02 | 7.69E-01 | 1.18E-03 | 7.69E-01 | 1.18E-03 |
| 0.7875 | 2.31E+02 | 0.7875 | 2.05E+02 | 7.88E-01 | 1.19E-03 | 7.88E-01 | 1.19E-03 |
| 0.80625 | 2.34E+02 | 0.80625 | 2.07E+02 | 8.06E-01 | 1.20E-03 | 8.06E-01 | 1.20E-03 |
| 0.825 | 2.36E+02 | 0.825 | 2.08E+02 | 8.25E-01 | 1.21E-03 | 8.25E-01 | 1.21E-03 |
| 0.84375 | 2.38E+02 | 0.84375 | 2.09E+02 | 8.44E-01 | 1.21E-03 | 8.44E-01 | 1.21E-03 |
| 0.8625 | 2.39E+02 | 0.8625 | 2.10E+02 | 8.63E-01 | 1.22E-03 | 8.63E-01 | 1.22E-03 |
| 0.88125 | 4.56E+02 | 0.88125 | 4.06E+02 | 8.81E-01 | 2.41E-03 | 8.81E-01 | 2.36E-03 |
| 0.9 | 4.78E+02 | 0.9 | 4.25E+02 | 9.00E-01 | 2.52E-03 | 9.00E-01 | 2.47E-03 |

Table B-73 Stress and strain profiles across sample thickness for sample N3, step 62%YS.

| **Normal Stress** | | **Equivalent Stress** | | **Normal Strain** | | **Equivalent Strain** | |
|---|---|---|---|---|---|---|---|
| Length | Stress | Length | Stress | Length | Stress | Length | Stress |
| 0.00E+00 | -2.38E+02 | 0.00E+00 | 2.10E+02 | 0.00E+00 | -1.24E-03 | 0.00E+00 | 1.22E-03 |
| 1.88E-02 | -2.39E+02 | 1.88E-02 | 2.10E+02 | 1.88E-02 | -1.24E-03 | 1.88E-02 | 1.22E-03 |
| 3.75E-02 | -2.39E+02 | 3.75E-02 | 2.10E+02 | 3.75E-02 | -1.24E-03 | 3.75E-02 | 1.22E-03 |
| 5.63E-02 | -2.40E+02 | 5.63E-02 | 2.11E+02 | 5.63E-02 | -1.23E-03 | 5.63E-02 | 1.22E-03 |
| 7.50E-02 | -2.41E+02 | 7.50E-02 | 2.11E+02 | 7.50E-02 | -1.24E-03 | 7.50E-02 | 1.23E-03 |
| 9.38E-02 | -2.42E+02 | 9.38E-02 | 2.11E+02 | 9.38E-02 | -1.24E-03 | 9.38E-02 | 1.23E-03 |
| 1.13E-01 | -2.43E+02 | 1.13E-01 | 2.11E+02 | 1.13E-01 | -1.24E-03 | 1.13E-01 | 1.23E-03 |
| 1.31E-01 | -2.45E+02 | 1.31E-01 | 2.12E+02 | 1.31E-01 | -1.24E-03 | 1.31E-01 | 1.23E-03 |
| 1.50E-01 | -2.48E+02 | 1.50E-01 | 2.11E+02 | 1.50E-01 | -1.25E-03 | 1.50E-01 | 1.23E-03 |
| 1.69E-01 | -2.52E+02 | 1.69E-01 | 2.11E+02 | 1.69E-01 | -1.26E-03 | 1.69E-01 | 1.23E-03 |
| 1.88E-01 | -2.56E+02 | 1.88E-01 | 2.11E+02 | 1.88E-01 | -1.27E-03 | 1.88E-01 | 1.23E-03 |
| 2.06E-01 | -2.60E+02 | 2.06E-01 | 2.10E+02 | 2.06E-01 | -1.28E-03 | 2.06E-01 | 1.22E-03 |

| | | | | | | | |
|---|---|---|---|---|---|---|---|
| 2.25E-01 | -2.62E+02 | 2.25E-01 | 2.07E+02 | 2.25E-01 | -1.28E-03 | 2.25E-01 | 1.21E-03 |
| 2.44E-01 | -2.63E+02 | 2.44E-01 | 2.04E+02 | 2.44E-01 | -1.29E-03 | 2.44E-01 | 1.19E-03 |
| 2.63E-01 | -2.65E+02 | 2.63E-01 | 2.02E+02 | 2.63E-01 | -1.29E-03 | 2.63E-01 | 1.18E-03 |
| 2.81E-01 | -2.57E+02 | 2.81E-01 | 1.93E+02 | 2.81E-01 | -1.25E-03 | 2.81E-01 | 1.13E-03 |
| 3.00E-01 | -2.44E+02 | 3.00E-01 | 1.81E+02 | 3.00E-01 | -1.18E-03 | 3.00E-01 | 1.06E-03 |
| 3.19E-01 | -2.32E+02 | 3.19E-01 | 1.69E+02 | 3.19E-01 | -1.12E-03 | 3.19E-01 | 9.88E-04 |
| 3.38E-01 | -2.18E+02 | 3.38E-01 | 1.57E+02 | 3.38E-01 | -1.05E-03 | 3.38E-01 | 9.15E-04 |
| 3.56E-01 | -1.86E+02 | 3.56E-01 | 1.31E+02 | 3.56E-01 | -8.84E-04 | 3.56E-01 | 7.66E-04 |
| 3.75E-01 | -1.55E+02 | 3.75E-01 | 1.05E+02 | 3.75E-01 | -7.21E-04 | 3.75E-01 | 6.18E-04 |
| 3.94E-01 | -1.23E+02 | 3.94E-01 | 8.00E+01 | 3.94E-01 | -5.58E-04 | 3.94E-01 | 4.69E-04 |
| 4.13E-01 | -9.52E+01 | 4.13E-01 | 5.89E+01 | 4.13E-01 | -4.14E-04 | 4.13E-01 | 3.61E-04 |
| 4.31E-01 | -7.10E+01 | 4.31E-01 | 4.28E+01 | 4.31E-01 | -2.93E-04 | 4.31E-01 | 3.00E-04 |
| 4.50E-01 | -4.68E+01 | 4.50E-01 | 3.06E+01 | 4.50E-01 | -1.72E-04 | 4.50E-01 | 2.38E-04 |
| 4.69E-01 | -2.26E+01 | 4.69E-01 | 2.80E+01 | 4.69E-01 | -5.02E-05 | 4.69E-01 | 1.76E-04 |
| 4.88E-01 | 1.38E+00 | 4.88E-01 | 3.69E+01 | 4.88E-01 | 7.02E-05 | 4.88E-01 | 2.43E-04 |
| 5.06E-01 | 2.54E+01 | 5.06E-01 | 5.16E+01 | 5.06E-01 | 1.90E-04 | 5.06E-01 | 3.27E-04 |
| 5.25E-01 | 4.93E+01 | 5.25E-01 | 6.85E+01 | 5.25E-01 | 3.11E-04 | 5.25E-01 | 4.12E-04 |
| 5.44E-01 | 7.44E+01 | 5.44E-01 | 8.73E+01 | 5.44E-01 | 4.37E-04 | 5.44E-01 | 5.09E-04 |
| 5.63E-01 | 1.02E+02 | 5.63E-01 | 1.09E+02 | 5.63E-01 | 5.78E-04 | 5.63E-01 | 6.38E-04 |
| 5.81E-01 | 1.30E+02 | 5.81E-01 | 1.31E+02 | 5.81E-01 | 7.19E-04 | 5.81E-01 | 7.66E-04 |
| 6.00E-01 | 1.58E+02 | 6.00E-01 | 1.54E+02 | 6.00E-01 | 8.61E-04 | 6.00E-01 | 8.94E-04 |
| 6.19E-01 | 1.76E+02 | 6.19E-01 | 1.68E+02 | 6.19E-01 | 9.48E-04 | 6.19E-01 | 9.75E-04 |
| 6.38E-01 | 1.89E+02 | 6.38E-01 | 1.78E+02 | 6.38E-01 | 1.01E-03 | 6.38E-01 | 1.03E-03 |
| 6.56E-01 | 2.02E+02 | 6.56E-01 | 1.88E+02 | 6.56E-01 | 1.08E-03 | 6.56E-01 | 1.09E-03 |
| 6.75E-01 | 2.14E+02 | 6.75E-01 | 1.98E+02 | 6.75E-01 | 1.13E-03 | 6.75E-01 | 1.15E-03 |
| 6.94E-01 | 2.18E+02 | 6.94E-01 | 2.00E+02 | 6.94E-01 | 1.15E-03 | 6.94E-01 | 1.16E-03 |
| 7.13E-01 | 2.22E+02 | 7.13E-01 | 2.02E+02 | 7.13E-01 | 1.16E-03 | 7.13E-01 | 1.17E-03 |

| | | | | | | | |
|---|---|---|---|---|---|---|---|
| 7.31E-01 | 2.26E+02 | 7.31E-01 | 2.04E+02 | 7.31E-01 | 1.17E-03 | 7.31E-01 | 1.18E-03 |
| 0.75 | 2.29E+02 | 0.75 | 2.05E+02 | 7.50E-01 | 1.18E-03 | 7.50E-01 | 1.19E-03 |
| 0.76875 | 2.32E+02 | 0.76875 | 2.07E+02 | 7.69E-01 | 1.19E-03 | 7.69E-01 | 1.20E-03 |
| 0.7875 | 2.35E+02 | 0.7875 | 2.08E+02 | 7.88E-01 | 1.20E-03 | 7.88E-01 | 1.21E-03 |
| 0.80625 | 2.38E+02 | 0.80625 | 2.10E+02 | 8.06E-01 | 1.21E-03 | 8.06E-01 | 1.22E-03 |
| 0.825 | 2.39E+02 | 0.825 | 2.11E+02 | 8.25E-01 | 1.22E-03 | 8.25E-01 | 1.22E-03 |
| 0.84375 | 2.41E+02 | 0.84375 | 2.11E+02 | 8.44E-01 | 1.22E-03 | 8.44E-01 | 1.23E-03 |
| 0.8625 | 2.42E+02 | 0.8625 | 2.11E+02 | 8.63E-01 | 1.22E-03 | 8.63E-01 | 1.23E-03 |
| 0.88125 | 5.16E+02 | 0.88125 | 4.59E+02 | 8.81E-01 | 2.72E-03 | 8.81E-01 | 2.67E-03 |
| 0.9 | 5.41E+02 | 0.9 | 4.81E+02 | 9.00E-01 | 2.85E-03 | 9.00E-01 | 2.79E-03 |

Table B-74 Stress and strain profiles across sample thickness for sample N3, step 70%YS.

| **Normal Stress** | | **Equivalent Stress** | | **Normal Strain** | | **Equivalent Strain** | |
|---|---|---|---|---|---|---|---|
| Length | Stress | Length | Stress | Length | Stress | Length | Stress |
| 0.00E+00 | -2.40E+02 | 0.00E+00 | 2.11E+02 | 0.00E+00 | -1.24E-03 | 0.00E+00 | 1.22E-03 |
| 1.88E-02 | -2.41E+02 | 1.88E-02 | 2.11E+02 | 1.88E-02 | -1.24E-03 | 1.88E-02 | 1.23E-03 |
| 3.75E-02 | -2.42E+02 | 3.75E-02 | 2.12E+02 | 3.75E-02 | -1.24E-03 | 3.75E-02 | 1.23E-03 |
| 5.63E-02 | -2.42E+02 | 5.63E-02 | 2.12E+02 | 5.63E-02 | -1.24E-03 | 5.63E-02 | 1.23E-03 |
| 7.50E-02 | -2.44E+02 | 7.50E-02 | 2.13E+02 | 7.50E-02 | -1.24E-03 | 7.50E-02 | 1.24E-03 |
| 9.38E-02 | -2.45E+02 | 9.38E-02 | 2.13E+02 | 9.38E-02 | -1.25E-03 | 9.38E-02 | 1.24E-03 |
| 1.13E-01 | -2.47E+02 | 1.13E-01 | 2.14E+02 | 1.13E-01 | -1.25E-03 | 1.13E-01 | 1.24E-03 |
| 1.31E-01 | -2.49E+02 | 1.31E-01 | 2.14E+02 | 1.31E-01 | -1.25E-03 | 1.31E-01 | 1.25E-03 |
| 1.50E-01 | -2.53E+02 | 1.50E-01 | 2.14E+02 | 1.50E-01 | -1.26E-03 | 1.50E-01 | 1.25E-03 |
| 1.69E-01 | -2.58E+02 | 1.69E-01 | 2.14E+02 | 1.69E-01 | -1.27E-03 | 1.69E-01 | 1.24E-03 |
| 1.88E-01 | -2.62E+02 | 1.88E-01 | 2.14E+02 | 1.88E-01 | -1.28E-03 | 1.88E-01 | 1.24E-03 |
| 2.06E-01 | -2.67E+02 | 2.06E-01 | 2.13E+02 | 2.06E-01 | -1.29E-03 | 2.06E-01 | 1.24E-03 |
| 2.25E-01 | -2.71E+02 | 2.25E-01 | 2.11E+02 | 2.25E-01 | -1.30E-03 | 2.25E-01 | 1.23E-03 |
| 2.44E-01 | -2.75E+02 | 2.44E-01 | 2.09E+02 | 2.44E-01 | -1.31E-03 | 2.44E-01 | 1.22E-03 |

| | | | | | | | |
|---|---|---|---|---|---|---|---|
| 2.63E-01 | -2.79E+02 | 2.63E-01 | 2.07E+02 | 2.63E-01 | -1.33E-03 | 2.63E-01 | 1.21E-03 |
| 2.81E-01 | -2.77E+02 | 2.81E-01 | 2.03E+02 | 2.81E-01 | -1.32E-03 | 2.81E-01 | 1.18E-03 |
| 3.00E-01 | -2.72E+02 | 3.00E-01 | 1.97E+02 | 3.00E-01 | -1.29E-03 | 3.00E-01 | 1.15E-03 |
| 3.19E-01 | -2.66E+02 | 3.19E-01 | 1.92E+02 | 3.19E-01 | -1.27E-03 | 3.19E-01 | 1.12E-03 |
| 3.38E-01 | -2.59E+02 | 3.38E-01 | 1.87E+02 | 3.38E-01 | -1.24E-03 | 3.38E-01 | 1.09E-03 |
| 3.56E-01 | -2.22E+02 | 3.56E-01 | 1.55E+02 | 3.56E-01 | -1.05E-03 | 3.56E-01 | 9.09E-04 |
| 3.75E-01 | -1.84E+02 | 3.75E-01 | 1.24E+02 | 3.75E-01 | -8.55E-04 | 3.75E-01 | 7.32E-04 |
| 3.94E-01 | -1.46E+02 | 3.94E-01 | 9.44E+01 | 3.94E-01 | -6.61E-04 | 3.94E-01 | 5.55E-04 |
| 4.13E-01 | -1.13E+02 | 4.13E-01 | 6.95E+01 | 4.13E-01 | -4.92E-04 | 4.13E-01 | 4.25E-04 |
| 4.31E-01 | -8.44E+01 | 4.31E-01 | 5.05E+01 | 4.31E-01 | -3.50E-04 | 4.31E-01 | 3.49E-04 |
| 4.50E-01 | -5.60E+01 | 4.50E-01 | 3.56E+01 | 4.50E-01 | -2.09E-04 | 4.50E-01 | 2.73E-04 |
| 4.69E-01 | -2.76E+01 | 4.69E-01 | 3.11E+01 | 4.69E-01 | -6.77E-05 | 4.69E-01 | 1.97E-04 |
| 4.88E-01 | 4.68E-01 | 4.88E-01 | 4.07E+01 | 4.88E-01 | 7.24E-05 | 4.88E-01 | 2.72E-04 |
| 5.06E-01 | 2.85E+01 | 5.06E-01 | 5.77E+01 | 5.06E-01 | 2.12E-04 | 5.06E-01 | 3.70E-04 |
| 5.25E-01 | 5.65E+01 | 5.25E-01 | 7.73E+01 | 5.25E-01 | 3.52E-04 | 5.25E-01 | 4.67E-04 |
| 5.44E-01 | 8.58E+01 | 5.44E-01 | 9.93E+01 | 5.44E-01 | 4.99E-04 | 5.44E-01 | 5.79E-04 |
| 5.63E-01 | 1.18E+02 | 5.63E-01 | 1.25E+02 | 5.63E-01 | 6.64E-04 | 5.63E-01 | 7.29E-04 |
| 5.81E-01 | 1.51E+02 | 5.81E-01 | 1.51E+02 | 5.81E-01 | 8.29E-04 | 5.81E-01 | 8.80E-04 |
| 6.00E-01 | 1.83E+02 | 6.00E-01 | 1.77E+02 | 6.00E-01 | 9.94E-04 | 6.00E-01 | 1.03E-03 |
| 6.19E-01 | 1.98E+02 | 6.19E-01 | 1.88E+02 | 6.19E-01 | 1.06E-03 | 6.19E-01 | 1.09E-03 |
| 6.38E-01 | 2.05E+02 | 6.38E-01 | 1.92E+02 | 6.38E-01 | 1.09E-03 | 6.38E-01 | 1.12E-03 |
| 6.56E-01 | 2.11E+02 | 6.56E-01 | 1.97E+02 | 6.56E-01 | 1.12E-03 | 6.56E-01 | 1.14E-03 |
| 6.75E-01 | 2.18E+02 | 6.75E-01 | 2.01E+02 | 6.75E-01 | 1.15E-03 | 6.75E-01 | 1.17E-03 |
| 6.94E-01 | 2.22E+02 | 6.94E-01 | 2.03E+02 | 6.94E-01 | 1.16E-03 | 6.94E-01 | 1.18E-03 |
| 7.13E-01 | 2.26E+02 | 7.13E-01 | 2.05E+02 | 7.13E-01 | 1.17E-03 | 7.13E-01 | 1.19E-03 |
| 7.31E-01 | 2.30E+02 | 7.31E-01 | 2.07E+02 | 7.31E-01 | 1.19E-03 | 7.31E-01 | 1.21E-03 |
| 0.75 | 2.33E+02 | 0.75 | 2.09E+02 | 7.50E-01 | 1.20E-03 | 7.50E-01 | 1.22E-03 |

| | | | | | | | |
|---|---|---|---|---|---|---|---|
| 0.76875 | 2.35E+02 | 0.76875 | 2.10E+02 | 7.69E-01 | 1.20E-03 | 7.69E-01 | 1.22E-03 |
| 0.7875 | 2.37E+02 | 0.7875 | 2.11E+02 | 7.88E-01 | 1.21E-03 | 7.88E-01 | 1.23E-03 |
| 0.80625 | 2.40E+02 | 0.80625 | 2.12E+02 | 8.06E-01 | 1.21E-03 | 8.06E-01 | 1.23E-03 |
| 0.825 | 2.41E+02 | 0.825 | 2.12E+02 | 8.25E-01 | 1.22E-03 | 8.25E-01 | 1.23E-03 |
| 0.84375 | 2.43E+02 | 0.84375 | 2.13E+02 | 8.44E-01 | 1.22E-03 | 8.44E-01 | 1.24E-03 |
| 0.8625 | 2.44E+02 | 0.8625 | 2.13E+02 | 8.63E-01 | 1.23E-03 | 8.63E-01 | 1.24E-03 |
| 0.88125 | 5.88E+02 | 0.88125 | 5.23E+02 | 8.81E-01 | 3.10E-03 | 8.81E-01 | 3.04E-03 |
| 0.9 | 6.16E+02 | 0.9 | 5.47E+02 | 9.00E-01 | 3.25E-03 | 9.00E-01 | 3.18E-03 |

## Sample N7

Table 0-75 Stress and strain profiles across sample thickness for sample N7, step 44%YS.

| **Normal Stress** | | **Equivalent Stress** | | **Normal Strain** | | **Equivalent Strain** | |
|---|---|---|---|---|---|---|---|
| Length | Stress | Length | Stress | Length | Stress | Length | Stress |
| 0.00E+00 | -2.30E+02 | 0.00E+00 | 2.03E+02 | 0.00E+00 | -1.20E-03 | 0.00E+00 | 1.18E-03 |
| 1.68E-02 | -2.30E+02 | 1.68E-02 | 2.03E+02 | 1.68E-02 | -1.20E-03 | 1.68E-02 | 1.18E-03 |
| 3.37E-02 | -2.29E+02 | 3.37E-02 | 2.02E+02 | 3.37E-02 | -1.20E-03 | 3.37E-02 | 1.18E-03 |
| 5.05E-02 | -2.28E+02 | 5.05E-02 | 2.02E+02 | 5.05E-02 | -1.19E-03 | 5.05E-02 | 1.17E-03 |
| 6.73E-02 | -2.27E+02 | 6.73E-02 | 2.01E+02 | 6.73E-02 | -1.19E-03 | 6.73E-02 | 1.17E-03 |
| 8.42E-02 | -2.26E+02 | 8.42E-02 | 2.01E+02 | 8.42E-02 | -1.19E-03 | 8.42E-02 | 1.17E-03 |
| 1.01E-01 | -2.24E+02 | 1.01E-01 | 2.00E+02 | 1.01E-01 | -1.18E-03 | 1.01E-01 | 1.16E-03 |
| 1.18E-01 | -2.23E+02 | 1.18E-01 | 1.99E+02 | 1.18E-01 | -1.18E-03 | 1.18E-01 | 1.16E-03 |
| 1.35E-01 | -2.22E+02 | 1.35E-01 | 1.99E+02 | 1.35E-01 | -1.18E-03 | 1.35E-01 | 1.16E-03 |
| 1.52E-01 | -2.22E+02 | 1.52E-01 | 1.98E+02 | 1.52E-01 | -1.18E-03 | 1.52E-01 | 1.15E-03 |
| 1.68E-01 | -2.22E+02 | 1.68E-01 | 1.97E+02 | 1.68E-01 | -1.17E-03 | 1.68E-01 | 1.14E-03 |
| 1.85E-01 | -2.21E+02 | 1.85E-01 | 1.96E+02 | 1.85E-01 | -1.17E-03 | 1.85E-01 | 1.14E-03 |
| 2.02E-01 | -2.17E+02 | 2.02E-01 | 1.91E+02 | 2.02E-01 | -1.15E-03 | 2.02E-01 | 1.11E-03 |
| 2.19E-01 | -2.07E+02 | 2.19E-01 | 1.80E+02 | 2.19E-01 | -1.09E-03 | 2.19E-01 | 1.05E-03 |
| 2.36E-01 | -1.96E+02 | 2.36E-01 | 1.69E+02 | 2.36E-01 | -1.03E-03 | 2.36E-01 | 9.81E-04 |

| | | | | | | | |
|---|---|---|---|---|---|---|---|
| 2.53E-01 | -1.85E+02 | 2.53E-01 | 1.57E+02 | 2.53E-01 | -9.66E-04 | 2.53E-01 | 9.16E-04 |
| 2.69E-01 | -1.71E+02 | 2.69E-01 | 1.43E+02 | 2.69E-01 | -8.84E-04 | 2.69E-01 | 8.31E-04 |
| 2.86E-01 | -1.52E+02 | 2.86E-01 | 1.24E+02 | 2.86E-01 | -7.78E-04 | 2.86E-01 | 7.25E-04 |
| 3.03E-01 | -1.33E+02 | 3.03E-01 | 1.06E+02 | 3.03E-01 | -6.72E-04 | 3.03E-01 | 6.19E-04 |
| 3.20E-01 | -1.13E+02 | 3.20E-01 | 8.81E+01 | 3.20E-01 | -5.67E-04 | 3.20E-01 | 5.13E-04 |
| 3.37E-01 | -9.58E+01 | 3.37E-01 | 7.21E+01 | 3.37E-01 | -4.71E-04 | 3.37E-01 | 4.22E-04 |
| 3.54E-01 | -7.90E+01 | 3.54E-01 | 5.76E+01 | 3.54E-01 | -3.82E-04 | 3.54E-01 | 3.39E-04 |
| 3.70E-01 | -6.23E+01 | 3.70E-01 | 4.33E+01 | 3.70E-01 | -2.93E-04 | 3.70E-01 | 2.57E-04 |
| 3.87E-01 | -4.55E+01 | 3.87E-01 | 2.97E+01 | 3.87E-01 | -2.04E-04 | 3.87E-01 | 1.75E-04 |
| 4.04E-01 | -2.90E+01 | 4.04E-01 | 1.86E+01 | 4.04E-01 | -1.17E-04 | 4.04E-01 | 1.64E-04 |
| 4.21E-01 | -1.25E+01 | 4.21E-01 | 1.48E+01 | 4.21E-01 | -3.17E-05 | 4.21E-01 | 1.78E-04 |
| 4.38E-01 | 3.92E+00 | 4.38E-01 | 2.20E+01 | 4.38E-01 | 5.40E-05 | 4.38E-01 | 1.91E-04 |
| 4.55E-01 | 2.04E+01 | 4.55E-01 | 3.38E+01 | 4.55E-01 | 1.40E-04 | 4.55E-01 | 2.05E-04 |
| 4.71E-01 | 3.69E+01 | 4.71E-01 | 4.66E+01 | 4.71E-01 | 2.24E-04 | 4.71E-01 | 2.73E-04 |
| 4.88E-01 | 5.33E+01 | 4.88E-01 | 5.98E+01 | 4.88E-01 | 3.09E-04 | 4.88E-01 | 3.50E-04 |
| 5.05E-01 | 6.98E+01 | 5.05E-01 | 7.32E+01 | 5.05E-01 | 3.94E-04 | 5.05E-01 | 4.27E-04 |
| 5.22E-01 | 8.63E+01 | 5.22E-01 | 8.67E+01 | 5.22E-01 | 4.79E-04 | 5.22E-01 | 5.04E-04 |
| 5.39E-01 | 1.03E+02 | 5.39E-01 | 1.01E+02 | 5.39E-01 | 5.66E-04 | 5.39E-01 | 5.86E-04 |
| 5.56E-01 | 1.20E+02 | 5.56E-01 | 1.15E+02 | 5.56E-01 | 6.53E-04 | 5.56E-01 | 6.67E-04 |
| 5.72E-01 | 1.37E+02 | 5.72E-01 | 1.29E+02 | 5.72E-01 | 7.40E-04 | 5.72E-01 | 7.49E-04 |
| 5.89E-01 | 1.54E+02 | 5.89E-01 | 1.43E+02 | 5.89E-01 | 8.27E-04 | 5.89E-01 | 8.31E-04 |
| 6.06E-01 | 1.71E+02 | 6.06E-01 | 1.57E+02 | 6.06E-01 | 9.16E-04 | 6.06E-01 | 9.16E-04 |
| 6.23E-01 | 1.89E+02 | 6.23E-01 | 1.72E+02 | 6.23E-01 | 1.00E-03 | 6.23E-01 | 1.00E-03 |
| 6.40E-01 | 2.06E+02 | 6.40E-01 | 1.87E+02 | 6.40E-01 | 1.09E-03 | 6.40E-01 | 1.09E-03 |
| 6.57E-01 | 2.20E+02 | 6.57E-01 | 1.98E+02 | 6.57E-01 | 1.16E-03 | 6.57E-01 | 1.15E-03 |
| 0.67333 | 2.21E+02 | 0.67333 | 1.98E+02 | 6.73E-01 | 1.17E-03 | 6.73E-01 | 1.15E-03 |
| 0.69017 | 2.23E+02 | 0.69017 | 1.99E+02 | 6.90E-01 | 1.17E-03 | 6.90E-01 | 1.16E-03 |

| | | | | | | | |
|---|---|---|---|---|---|---|---|
| 0.707 | 2.25E+02 | 0.707 | 2.00E+02 | 7.07E-01 | 1.17E-03 | 7.07E-01 | 1.16E-03 |
| 0.72383 | 2.26E+02 | 0.72383 | 2.00E+02 | 7.24E-01 | 1.18E-03 | 7.24E-01 | 1.17E-03 |
| 0.74067 | 2.28E+02 | 0.74067 | 2.01E+02 | 7.41E-01 | 1.18E-03 | 7.41E-01 | 1.17E-03 |
| 0.7575 | 2.30E+02 | 0.7575 | 2.03E+02 | 7.58E-01 | 1.19E-03 | 7.58E-01 | 1.18E-03 |
| 0.77433 | 2.32E+02 | 0.77433 | 2.04E+02 | 7.74E-01 | 1.19E-03 | 7.74E-01 | 1.18E-03 |
| 0.79117 | 3.67E+02 | 0.79117 | 3.27E+02 | 7.91E-01 | 1.94E-03 | 7.91E-01 | 1.90E-03 |
| 0.808 | 3.86E+02 | 0.808 | 3.43E+02 | 8.08E-01 | 2.04E-03 | 8.08E-01 | 1.99E-03 |

Table B-76 Stress and strain profiles across sample thickness for sample N7, step 52%YS.

| **Normal Stress** | | **Equivalent Stress** | | **Normal Strain** | | **Equivalent Strain** | |
|---|---|---|---|---|---|---|---|
| Length | Stress | Length | Stress | Length | Stress | Length | Stress |
| 0.00E+00 | -2.37E+02 | 0.00E+00 | 2.08E+02 | 0.00E+00 | -1.22E-03 | 0.00E+00 | 1.21E-03 |
| 1.68E-02 | -2.36E+02 | 1.68E-02 | 2.07E+02 | 1.68E-02 | -1.22E-03 | 1.68E-02 | 1.21E-03 |
| 3.37E-02 | -2.35E+02 | 3.37E-02 | 2.07E+02 | 3.37E-02 | -1.22E-03 | 3.37E-02 | 1.20E-03 |
| 5.05E-02 | -2.35E+02 | 5.05E-02 | 2.07E+02 | 5.05E-02 | -1.22E-03 | 5.05E-02 | 1.20E-03 |
| 6.73E-02 | -2.34E+02 | 6.73E-02 | 2.07E+02 | 6.73E-02 | -1.21E-03 | 6.73E-02 | 1.20E-03 |
| 8.42E-02 | -2.33E+02 | 8.42E-02 | 2.06E+02 | 8.42E-02 | -1.21E-03 | 8.42E-02 | 1.20E-03 |
| 1.01E-01 | -2.33E+02 | 1.01E-01 | 2.06E+02 | 1.01E-01 | -1.21E-03 | 1.01E-01 | 1.20E-03 |
| 1.18E-01 | -2.32E+02 | 1.18E-01 | 2.05E+02 | 1.18E-01 | -1.21E-03 | 1.18E-01 | 1.19E-03 |
| 1.35E-01 | -2.31E+02 | 1.35E-01 | 2.05E+02 | 1.35E-01 | -1.20E-03 | 1.35E-01 | 1.19E-03 |
| 1.52E-01 | -2.31E+02 | 1.52E-01 | 2.03E+02 | 1.52E-01 | -1.20E-03 | 1.52E-01 | 1.18E-03 |
| 1.68E-01 | -2.31E+02 | 1.68E-01 | 2.02E+02 | 1.68E-01 | -1.20E-03 | 1.68E-01 | 1.18E-03 |
| 1.85E-01 | -2.31E+02 | 1.85E-01 | 2.01E+02 | 1.85E-01 | -1.20E-03 | 1.85E-01 | 1.17E-03 |
| 2.02E-01 | -2.30E+02 | 2.02E-01 | 1.99E+02 | 2.02E-01 | -1.19E-03 | 2.02E-01 | 1.16E-03 |
| 2.19E-01 | -2.28E+02 | 2.19E-01 | 1.96E+02 | 2.19E-01 | -1.18E-03 | 2.19E-01 | 1.14E-03 |
| 2.36E-01 | -2.26E+02 | 2.36E-01 | 1.92E+02 | 2.36E-01 | -1.17E-03 | 2.36E-01 | 1.12E-03 |
| 2.53E-01 | -2.25E+02 | 2.53E-01 | 1.89E+02 | 2.53E-01 | -1.16E-03 | 2.53E-01 | 1.10E-03 |
| 2.69E-01 | -2.11E+02 | 2.69E-01 | 1.76E+02 | 2.69E-01 | -1.09E-03 | 2.69E-01 | 1.02E-03 |

| | | | | | | | |
|---|---|---|---|---|---|---|---|
| 2.86E-01 | -1.87E+02 | 2.86E-01 | 1.52E+02 | 2.86E-01 | -9.54E-04 | 2.86E-01 | 8.88E-04 |
| 3.03E-01 | -1.62E+02 | 3.03E-01 | 1.29E+02 | 3.03E-01 | -8.19E-04 | 3.03E-01 | 7.53E-04 |
| 3.20E-01 | -1.38E+02 | 3.20E-01 | 1.06E+02 | 3.20E-01 | -6.84E-04 | 3.20E-01 | 6.18E-04 |
| 3.37E-01 | -1.16E+02 | 3.37E-01 | 8.67E+01 | 3.37E-01 | -5.68E-04 | 3.37E-01 | 5.06E-04 |
| 3.54E-01 | -9.58E+01 | 3.54E-01 | 6.95E+01 | 3.54E-01 | -4.62E-04 | 3.54E-01 | 4.09E-04 |
| 3.70E-01 | -7.58E+01 | 3.70E-01 | 5.27E+01 | 3.70E-01 | -3.57E-04 | 3.70E-01 | 3.12E-04 |
| 3.87E-01 | -5.57E+01 | 3.87E-01 | 3.65E+01 | 3.87E-01 | -2.51E-04 | 3.87E-01 | 2.15E-04 |
| 4.04E-01 | -3.59E+01 | 4.04E-01 | 2.28E+01 | 4.04E-01 | -1.48E-04 | 4.04E-01 | 1.98E-04 |
| 4.21E-01 | -1.62E+01 | 4.21E-01 | 1.66E+01 | 4.21E-01 | -4.66E-05 | 4.21E-01 | 2.09E-04 |
| 4.38E-01 | 3.53E+00 | 4.38E-01 | 2.42E+01 | 4.38E-01 | 5.52E-05 | 4.38E-01 | 2.21E-04 |
| 4.55E-01 | 2.32E+01 | 4.55E-01 | 3.81E+01 | 4.55E-01 | 1.57E-04 | 4.55E-01 | 2.32E-04 |
| 4.71E-01 | 4.30E+01 | 4.71E-01 | 5.34E+01 | 4.71E-01 | 2.59E-04 | 4.71E-01 | 3.14E-04 |
| 4.88E-01 | 6.28E+01 | 4.88E-01 | 6.93E+01 | 4.88E-01 | 3.60E-04 | 4.88E-01 | 4.06E-04 |
| 5.05E-01 | 8.26E+01 | 5.05E-01 | 8.54E+01 | 5.05E-01 | 4.62E-04 | 5.05E-01 | 4.99E-04 |
| 5.22E-01 | 1.02E+02 | 5.22E-01 | 1.02E+02 | 5.22E-01 | 5.63E-04 | 5.22E-01 | 5.91E-04 |
| 5.39E-01 | 1.25E+02 | 5.39E-01 | 1.21E+02 | 5.39E-01 | 6.80E-04 | 5.39E-01 | 7.01E-04 |
| 5.56E-01 | 1.48E+02 | 5.56E-01 | 1.40E+02 | 5.56E-01 | 7.97E-04 | 5.56E-01 | 8.12E-04 |
| 5.72E-01 | 1.70E+02 | 5.72E-01 | 1.59E+02 | 5.72E-01 | 9.14E-04 | 5.72E-01 | 9.22E-04 |
| 5.89E-01 | 1.91E+02 | 5.89E-01 | 1.76E+02 | 5.89E-01 | 1.02E-03 | 5.89E-01 | 1.02E-03 |
| 6.06E-01 | 1.99E+02 | 6.06E-01 | 1.82E+02 | 6.06E-01 | 1.06E-03 | 6.06E-01 | 1.06E-03 |
| 6.23E-01 | 2.07E+02 | 6.23E-01 | 1.88E+02 | 6.23E-01 | 1.09E-03 | 6.23E-01 | 1.09E-03 |
| 6.40E-01 | 2.14E+02 | 6.40E-01 | 1.94E+02 | 6.40E-01 | 1.13E-03 | 6.40E-01 | 1.13E-03 |
| 6.57E-01 | 2.21E+02 | 6.57E-01 | 1.98E+02 | 6.57E-01 | 1.16E-03 | 6.57E-01 | 1.15E-03 |
| 0.67333 | 2.24E+02 | 0.67333 | 2.00E+02 | 6.73E-01 | 1.17E-03 | 6.73E-01 | 1.16E-03 |
| 0.69017 | 2.27E+02 | 0.69017 | 2.02E+02 | 6.90E-01 | 1.18E-03 | 6.90E-01 | 1.17E-03 |
| 0.707 | 2.29E+02 | 0.707 | 2.03E+02 | 7.07E-01 | 1.18E-03 | 7.07E-01 | 1.18E-03 |
| 0.72383 | 2.32E+02 | 0.72383 | 2.05E+02 | 7.24E-01 | 1.19E-03 | 7.24E-01 | 1.19E-03 |

| | | | | | | | |
|---|---|---|---|---|---|---|---|
| 0.74067 | 2.34E+02 | 0.74067 | 2.06E+02 | 7.41E-01 | 1.20E-03 | 7.41E-01 | 1.20E-03 |
| 0.7575 | 2.36E+02 | 0.7575 | 2.07E+02 | 7.58E-01 | 1.21E-03 | 7.58E-01 | 1.21E-03 |
| 0.77433 | 2.38E+02 | 0.77433 | 2.09E+02 | 7.74E-01 | 1.21E-03 | 7.74E-01 | 1.21E-03 |
| 0.79117 | 4.31E+02 | 0.79117 | 3.83E+02 | 7.91E-01 | 2.27E-03 | 7.91E-01 | 2.23E-03 |
| 0.808 | 4.53E+02 | 0.808 | 4.02E+02 | 8.08E-01 | 2.39E-03 | 8.08E-01 | 2.34E-03 |

Table 0-77 Stress and strain profiles across sample thickness for sample N7, step 59%YS.

| **Normal Stress** | | **Equivalent Stress** | | **Normal Strain** | | **Equivalent Strain** | |
|---|---|---|---|---|---|---|---|
| Length | Stress | Length | Stress | Length | Stress | Length | Stress |
| 0.00E+00 | -2.41E+02 | 0.00E+00 | 2.10E+02 | 0.00E+00 | -1.23E-03 | 0.00E+00 | 1.22E-03 |
| 1.68E-02 | -2.40E+02 | 1.68E-02 | 2.10E+02 | 1.68E-02 | -1.23E-03 | 1.68E-02 | 1.22E-03 |
| 3.37E-02 | -2.40E+02 | 3.37E-02 | 2.10E+02 | 3.37E-02 | -1.23E-03 | 3.37E-02 | 1.22E-03 |
| 5.05E-02 | -2.40E+02 | 5.05E-02 | 2.10E+02 | 5.05E-02 | -1.23E-03 | 5.05E-02 | 1.22E-03 |
| 6.73E-02 | -2.39E+02 | 6.73E-02 | 2.10E+02 | 6.73E-02 | -1.23E-03 | 6.73E-02 | 1.22E-03 |
| 8.42E-02 | -2.39E+02 | 8.42E-02 | 2.10E+02 | 8.42E-02 | -1.23E-03 | 8.42E-02 | 1.22E-03 |
| 1.01E-01 | -2.39E+02 | 1.01E-01 | 2.10E+02 | 1.01E-01 | -1.23E-03 | 1.01E-01 | 1.22E-03 |
| 1.18E-01 | -2.38E+02 | 1.18E-01 | 2.10E+02 | 1.18E-01 | -1.23E-03 | 1.18E-01 | 1.22E-03 |
| 1.35E-01 | -2.38E+02 | 1.35E-01 | 2.10E+02 | 1.35E-01 | -1.23E-03 | 1.35E-01 | 1.22E-03 |
| 1.52E-01 | -2.39E+02 | 1.52E-01 | 2.09E+02 | 1.52E-01 | -1.23E-03 | 1.52E-01 | 1.21E-03 |
| 1.68E-01 | -2.39E+02 | 1.68E-01 | 2.08E+02 | 1.68E-01 | -1.23E-03 | 1.68E-01 | 1.21E-03 |
| 1.85E-01 | -2.40E+02 | 1.85E-01 | 2.07E+02 | 1.85E-01 | -1.23E-03 | 1.85E-01 | 1.20E-03 |
| 2.02E-01 | -2.40E+02 | 2.02E-01 | 2.05E+02 | 2.02E-01 | -1.23E-03 | 2.02E-01 | 1.20E-03 |
| 2.19E-01 | -2.40E+02 | 2.19E-01 | 2.03E+02 | 2.19E-01 | -1.22E-03 | 2.19E-01 | 1.18E-03 |
| 2.36E-01 | -2.40E+02 | 2.36E-01 | 2.00E+02 | 2.36E-01 | -1.22E-03 | 2.36E-01 | 1.17E-03 |
| 2.53E-01 | -2.40E+02 | 2.53E-01 | 1.98E+02 | 2.53E-01 | -1.22E-03 | 2.53E-01 | 1.15E-03 |
| 2.69E-01 | -2.30E+02 | 2.69E-01 | 1.88E+02 | 2.69E-01 | -1.17E-03 | 2.69E-01 | 1.09E-03 |
| 2.86E-01 | -2.12E+02 | 2.86E-01 | 1.70E+02 | 2.86E-01 | -1.07E-03 | 2.86E-01 | 9.89E-04 |
| 3.03E-01 | -1.93E+02 | 3.03E-01 | 1.52E+02 | 3.03E-01 | -9.64E-04 | 3.03E-01 | 8.85E-04 |

| | | | | | | | |
|---|---|---|---|---|---|---|---|
| 3.20E-01 | -1.74E+02 | 3.20E-01 | 1.34E+02 | 3.20E-01 | -8.63E-04 | 3.20E-01 | 7.80E-04 |
| 3.37E-01 | -1.50E+02 | 3.37E-01 | 1.13E+02 | 3.37E-01 | -7.35E-04 | 3.37E-01 | 6.58E-04 |
| 3.54E-01 | -1.22E+02 | 3.54E-01 | 8.95E+01 | 3.54E-01 | -5.92E-04 | 3.54E-01 | 5.26E-04 |
| 3.70E-01 | -9.50E+01 | 3.70E-01 | 6.65E+01 | 3.70E-01 | -4.49E-04 | 3.70E-01 | 3.93E-04 |
| 3.87E-01 | -6.77E+01 | 3.87E-01 | 4.44E+01 | 3.87E-01 | -3.06E-04 | 3.87E-01 | 2.61E-04 |
| 4.04E-01 | -4.35E+01 | 4.04E-01 | 2.74E+01 | 4.04E-01 | -1.82E-04 | 4.04E-01 | 2.33E-04 |
| 4.21E-01 | -2.05E+01 | 4.21E-01 | 1.89E+01 | 4.21E-01 | -6.37E-05 | 4.21E-01 | 2.42E-04 |
| 4.38E-01 | 2.55E+00 | 4.38E-01 | 2.65E+01 | 4.38E-01 | 5.45E-05 | 4.38E-01 | 2.50E-04 |
| 4.55E-01 | 2.56E+01 | 4.55E-01 | 4.23E+01 | 4.55E-01 | 1.73E-04 | 4.55E-01 | 2.59E-04 |
| 4.71E-01 | 4.87E+01 | 4.71E-01 | 6.02E+01 | 4.71E-01 | 2.91E-04 | 4.71E-01 | 3.54E-04 |
| 4.88E-01 | 7.19E+01 | 4.88E-01 | 7.88E+01 | 4.88E-01 | 4.10E-04 | 4.88E-01 | 4.62E-04 |
| 5.05E-01 | 9.51E+01 | 5.05E-01 | 9.76E+01 | 5.05E-01 | 5.29E-04 | 5.05E-01 | 5.70E-04 |
| 5.22E-01 | 1.18E+02 | 5.22E-01 | 1.17E+02 | 5.22E-01 | 6.48E-04 | 5.22E-01 | 6.78E-04 |
| 5.39E-01 | 1.42E+02 | 5.39E-01 | 1.37E+02 | 5.39E-01 | 7.72E-04 | 5.39E-01 | 7.96E-04 |
| 5.56E-01 | 1.67E+02 | 5.56E-01 | 1.57E+02 | 5.56E-01 | 8.96E-04 | 5.56E-01 | 9.13E-04 |
| 5.72E-01 | 1.91E+02 | 5.72E-01 | 1.77E+02 | 5.72E-01 | 1.02E-03 | 5.72E-01 | 1.03E-03 |
| 5.89E-01 | 2.13E+02 | 5.89E-01 | 1.95E+02 | 5.89E-01 | 1.13E-03 | 5.89E-01 | 1.14E-03 |
| 6.06E-01 | 2.16E+02 | 6.06E-01 | 1.97E+02 | 6.06E-01 | 1.14E-03 | 6.06E-01 | 1.15E-03 |
| 6.23E-01 | 2.19E+02 | 6.23E-01 | 1.99E+02 | 6.23E-01 | 1.15E-03 | 6.23E-01 | 1.15E-03 |
| 6.40E-01 | 2.22E+02 | 6.40E-01 | 2.00E+02 | 6.40E-01 | 1.16E-03 | 6.40E-01 | 1.16E-03 |
| 6.57E-01 | 2.25E+02 | 6.57E-01 | 2.02E+02 | 6.57E-01 | 1.17E-03 | 6.57E-01 | 1.17E-03 |
| 0.67333 | 2.28E+02 | 0.67333 | 2.04E+02 | 6.73E-01 | 1.18E-03 | 6.73E-01 | 1.18E-03 |
| 0.69017 | 2.31E+02 | 0.69017 | 2.05E+02 | 6.90E-01 | 1.19E-03 | 6.90E-01 | 1.19E-03 |
| 0.707 | 2.34E+02 | 0.707 | 2.07E+02 | 7.07E-01 | 1.20E-03 | 7.07E-01 | 1.21E-03 |
| 0.72383 | 2.37E+02 | 0.72383 | 2.09E+02 | 7.24E-01 | 1.21E-03 | 7.24E-01 | 1.21E-03 |
| 0.74067 | 2.38E+02 | 0.74067 | 2.09E+02 | 7.41E-01 | 1.21E-03 | 7.41E-01 | 1.22E-03 |
| 0.7575 | 2.40E+02 | 0.7575 | 2.10E+02 | 7.58E-01 | 1.22E-03 | 7.58E-01 | 1.22E-03 |

| | | | | | | | |
|---|---|---|---|---|---|---|---|
| 0.77433 | 2.41E+02 | 0.77433 | 2.11E+02 | 7.74E-01 | 1.22E-03 | 7.74E-01 | 1.23E-03 |
| 0.79117 | 4.94E+02 | 0.79117 | 4.39E+02 | 7.91E-01 | 2.60E-03 | 7.91E-01 | 2.55E-03 |
| 0.808 | 5.18E+02 | 0.808 | 4.60E+02 | 8.08E-01 | 2.73E-03 | 8.08E-01 | 2.67E-03 |

Table B-78 Stress and strain profiles across sample thickness for sample N7, step 66%YS.

| **Normal Stress** | | **Equivalent Stress** | | **Normal Strain** | | **Equivalent Strain** | |
|---|---|---|---|---|---|---|---|
| Length | Stress | Length | Stress | Length | Stress | Length | Stress |
| 0.00E+00 | -2.43E+02 | 0.00E+00 | 2.12E+02 | 0.00E+00 | -1.24E-03 | 0.00E+00 | 1.23E-03 |
| 1.68E-02 | -2.43E+02 | 1.68E-02 | 2.12E+02 | 1.68E-02 | -1.24E-03 | 1.68E-02 | 1.23E-03 |
| 3.37E-02 | -2.42E+02 | 3.37E-02 | 2.12E+02 | 3.37E-02 | -1.24E-03 | 3.37E-02 | 1.23E-03 |
| 5.05E-02 | -2.42E+02 | 5.05E-02 | 2.12E+02 | 5.05E-02 | -1.23E-03 | 5.05E-02 | 1.23E-03 |
| 6.73E-02 | -2.42E+02 | 6.73E-02 | 2.12E+02 | 6.73E-02 | -1.23E-03 | 6.73E-02 | 1.23E-03 |
| 8.42E-02 | -2.42E+02 | 8.42E-02 | 2.12E+02 | 8.42E-02 | -1.23E-03 | 8.42E-02 | 1.23E-03 |
| 1.01E-01 | -2.42E+02 | 1.01E-01 | 2.12E+02 | 1.01E-01 | -1.23E-03 | 1.01E-01 | 1.23E-03 |
| 1.18E-01 | -2.42E+02 | 1.18E-01 | 2.12E+02 | 1.18E-01 | -1.23E-03 | 1.18E-01 | 1.23E-03 |
| 1.35E-01 | -2.42E+02 | 1.35E-01 | 2.12E+02 | 1.35E-01 | -1.23E-03 | 1.35E-01 | 1.23E-03 |
| 1.52E-01 | -2.44E+02 | 1.52E-01 | 2.11E+02 | 1.52E-01 | -1.24E-03 | 1.52E-01 | 1.23E-03 |
| 1.68E-01 | -2.46E+02 | 1.68E-01 | 2.11E+02 | 1.68E-01 | -1.24E-03 | 1.68E-01 | 1.23E-03 |
| 1.85E-01 | -2.47E+02 | 1.85E-01 | 2.11E+02 | 1.85E-01 | -1.25E-03 | 1.85E-01 | 1.23E-03 |
| 2.02E-01 | -2.49E+02 | 2.02E-01 | 2.09E+02 | 2.02E-01 | -1.25E-03 | 2.02E-01 | 1.22E-03 |
| 2.19E-01 | -2.49E+02 | 2.19E-01 | 2.07E+02 | 2.19E-01 | -1.25E-03 | 2.19E-01 | 1.21E-03 |
| 2.36E-01 | -2.50E+02 | 2.36E-01 | 2.05E+02 | 2.36E-01 | -1.25E-03 | 2.36E-01 | 1.19E-03 |
| 2.53E-01 | -2.51E+02 | 2.53E-01 | 2.02E+02 | 2.53E-01 | -1.25E-03 | 2.53E-01 | 1.18E-03 |
| 2.69E-01 | -2.45E+02 | 2.69E-01 | 1.95E+02 | 2.69E-01 | -1.22E-03 | 2.69E-01 | 1.14E-03 |
| 2.86E-01 | -2.32E+02 | 2.86E-01 | 1.82E+02 | 2.86E-01 | -1.15E-03 | 2.86E-01 | 1.06E-03 |
| 3.03E-01 | -2.18E+02 | 3.03E-01 | 1.69E+02 | 3.03E-01 | -1.08E-03 | 3.03E-01 | 9.88E-04 |
| 3.20E-01 | -2.05E+02 | 3.20E-01 | 1.57E+02 | 3.20E-01 | -1.01E-03 | 3.20E-01 | 9.14E-04 |
| 3.37E-01 | -1.80E+02 | 3.37E-01 | 1.35E+02 | 3.37E-01 | -8.80E-04 | 3.37E-01 | 7.87E-04 |

| | | | | | | | |
|---|---|---|---|---|---|---|---|
| 3.54E-01 | -1.47E+02 | 3.54E-01 | 1.07E+02 | 3.54E-01 | -7.07E-04 | 3.54E-01 | 6.27E-04 |
| 3.70E-01 | -1.13E+02 | 3.70E-01 | 7.88E+01 | 3.70E-01 | -5.34E-04 | 3.70E-01 | 4.67E-04 |
| 3.87E-01 | -8.02E+01 | 3.87E-01 | 5.20E+01 | 3.87E-01 | -3.61E-04 | 3.87E-01 | 3.07E-04 |
| 4.04E-01 | -5.20E+01 | 4.04E-01 | 3.22E+01 | 4.04E-01 | -2.17E-04 | 4.04E-01 | 2.69E-04 |
| 4.21E-01 | -2.56E+01 | 4.21E-01 | 2.16E+01 | 4.21E-01 | -8.29E-05 | 4.21E-01 | 2.75E-04 |
| 4.38E-01 | 8.06E-01 | 4.38E-01 | 2.90E+01 | 4.38E-01 | 5.15E-05 | 4.38E-01 | 2.80E-04 |
| 4.55E-01 | 2.72E+01 | 4.55E-01 | 4.64E+01 | 4.55E-01 | 1.86E-04 | 4.55E-01 | 2.85E-04 |
| 4.71E-01 | 5.63E+01 | 4.71E-01 | 6.88E+01 | 4.71E-01 | 3.35E-04 | 4.71E-01 | 4.05E-04 |
| 4.88E-01 | 8.59E+01 | 4.88E-01 | 9.25E+01 | 4.88E-01 | 4.86E-04 | 4.88E-01 | 5.43E-04 |
| 5.05E-01 | 1.15E+02 | 5.05E-01 | 1.16E+02 | 5.05E-01 | 6.37E-04 | 5.05E-01 | 6.81E-04 |
| 5.22E-01 | 1.45E+02 | 5.22E-01 | 1.41E+02 | 5.22E-01 | 7.88E-04 | 5.22E-01 | 8.19E-04 |
| 5.39E-01 | 1.63E+02 | 5.39E-01 | 1.55E+02 | 5.39E-01 | 8.76E-04 | 5.39E-01 | 9.02E-04 |
| 5.56E-01 | 1.80E+02 | 5.56E-01 | 1.69E+02 | 5.56E-01 | 9.64E-04 | 5.56E-01 | 9.86E-04 |
| 5.72E-01 | 1.98E+02 | 5.72E-01 | 1.84E+02 | 5.72E-01 | 1.05E-03 | 5.72E-01 | 1.07E-03 |
| 5.89E-01 | 2.14E+02 | 5.89E-01 | 1.97E+02 | 5.89E-01 | 1.13E-03 | 5.89E-01 | 1.14E-03 |
| 6.06E-01 | 2.18E+02 | 6.06E-01 | 1.99E+02 | 6.06E-01 | 1.14E-03 | 6.06E-01 | 1.16E-03 |
| 6.23E-01 | 2.21E+02 | 6.23E-01 | 2.01E+02 | 6.23E-01 | 1.16E-03 | 6.23E-01 | 1.17E-03 |
| 6.40E-01 | 2.25E+02 | 6.40E-01 | 2.03E+02 | 6.40E-01 | 1.17E-03 | 6.40E-01 | 1.18E-03 |
| 6.57E-01 | 2.29E+02 | 6.57E-01 | 2.05E+02 | 6.57E-01 | 1.18E-03 | 6.57E-01 | 1.19E-03 |
| 0.67333 | 2.32E+02 | 0.67333 | 2.07E+02 | 6.73E-01 | 1.19E-03 | 6.73E-01 | 1.20E-03 |
| 0.69017 | 2.34E+02 | 0.69017 | 2.08E+02 | 6.90E-01 | 1.20E-03 | 6.90E-01 | 1.21E-03 |
| 0.707 | 2.37E+02 | 0.707 | 2.10E+02 | 7.07E-01 | 1.21E-03 | 7.07E-01 | 1.22E-03 |
| 0.72383 | 2.40E+02 | 0.72383 | 2.11E+02 | 7.24E-01 | 1.21E-03 | 7.24E-01 | 1.23E-03 |
| 0.74067 | 2.41E+02 | 0.74067 | 2.11E+02 | 7.41E-01 | 1.22E-03 | 7.41E-01 | 1.23E-03 |
| 0.7575 | 2.42E+02 | 0.7575 | 2.12E+02 | 7.58E-01 | 1.22E-03 | 7.58E-01 | 1.23E-03 |
| 0.77433 | 2.43E+02 | 0.77433 | 2.12E+02 | 7.74E-01 | 1.22E-03 | 7.74E-01 | 1.23E-03 |
| 0.79117 | 5.52E+02 | 0.79117 | 4.90E+02 | 7.91E-01 | 2.90E-03 | 7.91E-01 | 2.85E-03 |

| | | | | | | | |
|---|---|---|---|---|---|---|---|
| 0.808 | 5.79E+02 | 0.808 | 5.14E+02 | 8.08E-01 | 3.05E-03 | 8.08E-01 | 2.99E-03 |

Table 0-79 Stress and strain profiles across sample thickness for sample N7, step 74%YS.

| Normal Stress | | Equivalent Stress | | Normal Strain | | Equivalent Strain | |
|---|---|---|---|---|---|---|---|
| Length | Stress | Length | Stress | Length | Stress | Length | Stress |
| 0.00E+00 | -2.45E+02 | 0.00E+00 | 2.13E+02 | 0.00E+00 | -1.24E-03 | 0.00E+00 | 1.24E-03 |
| 1.68E-02 | -2.45E+02 | 1.68E-02 | 2.13E+02 | 1.68E-02 | -1.24E-03 | 1.68E-02 | 1.24E-03 |
| 3.37E-02 | -2.45E+02 | 3.37E-02 | 2.13E+02 | 3.37E-02 | -1.24E-03 | 3.37E-02 | 1.24E-03 |
| 5.05E-02 | -2.45E+02 | 5.05E-02 | 2.13E+02 | 5.05E-02 | -1.24E-03 | 5.05E-02 | 1.24E-03 |
| 6.73E-02 | -2.45E+02 | 6.73E-02 | 2.14E+02 | 6.73E-02 | -1.24E-03 | 6.73E-02 | 1.24E-03 |
| 8.42E-02 | -2.45E+02 | 8.42E-02 | 2.14E+02 | 8.42E-02 | -1.24E-03 | 8.42E-02 | 1.24E-03 |
| 1.01E-01 | -2.45E+02 | 1.01E-01 | 2.14E+02 | 1.01E-01 | -1.24E-03 | 1.01E-01 | 1.24E-03 |
| 1.18E-01 | -2.45E+02 | 1.18E-01 | 2.14E+02 | 1.18E-01 | -1.24E-03 | 1.18E-01 | 1.24E-03 |
| 1.35E-01 | -2.46E+02 | 1.35E-01 | 2.14E+02 | 1.35E-01 | -1.24E-03 | 1.35E-01 | 1.24E-03 |
| 1.52E-01 | -2.48E+02 | 1.52E-01 | 2.14E+02 | 1.52E-01 | -1.25E-03 | 1.52E-01 | 1.24E-03 |
| 1.68E-01 | -2.50E+02 | 1.68E-01 | 2.13E+02 | 1.68E-01 | -1.25E-03 | 1.68E-01 | 1.24E-03 |
| 1.85E-01 | -2.52E+02 | 1.85E-01 | 2.13E+02 | 1.85E-01 | -1.26E-03 | 1.85E-01 | 1.24E-03 |
| 2.02E-01 | -2.54E+02 | 2.02E-01 | 2.12E+02 | 2.02E-01 | -1.26E-03 | 2.02E-01 | 1.23E-03 |
| 2.19E-01 | -2.56E+02 | 2.19E-01 | 2.10E+02 | 2.19E-01 | -1.27E-03 | 2.19E-01 | 1.22E-03 |
| 2.36E-01 | -2.58E+02 | 2.36E-01 | 2.08E+02 | 2.36E-01 | -1.27E-03 | 2.36E-01 | 1.21E-03 |
| 2.53E-01 | -2.60E+02 | 2.53E-01 | 2.07E+02 | 2.53E-01 | -1.28E-03 | 2.53E-01 | 1.20E-03 |
| 2.69E-01 | -2.58E+02 | 2.69E-01 | 2.02E+02 | 2.69E-01 | -1.26E-03 | 2.69E-01 | 1.18E-03 |
| 2.86E-01 | -2.50E+02 | 2.86E-01 | 1.94E+02 | 2.86E-01 | -1.23E-03 | 2.86E-01 | 1.14E-03 |
| 3.03E-01 | -2.43E+02 | 3.03E-01 | 1.87E+02 | 3.03E-01 | -1.20E-03 | 3.03E-01 | 1.09E-03 |
| 3.20E-01 | -2.36E+02 | 3.20E-01 | 1.81E+02 | 3.20E-01 | -1.16E-03 | 3.20E-01 | 1.05E-03 |
| 3.37E-01 | -2.09E+02 | 3.37E-01 | 1.58E+02 | 3.37E-01 | -1.03E-03 | 3.37E-01 | 9.20E-04 |
| 3.54E-01 | -1.70E+02 | 3.54E-01 | 1.24E+02 | 3.54E-01 | -8.24E-04 | 3.54E-01 | 7.31E-04 |
| 3.70E-01 | -1.32E+02 | 3.70E-01 | 9.17E+01 | 3.70E-01 | -6.21E-04 | 3.70E-01 | 5.43E-04 |

| | | | | | | | |
|---|---|---|---|---|---|---|---|
| 3.87E-01 | -9.28E+01 | 3.87E-01 | 6.01E+01 | 3.87E-01 | -4.19E-04 | 3.87E-01 | 3.55E-04 |
| 4.04E-01 | -6.02E+01 | 4.04E-01 | 3.70E+01 | 4.04E-01 | -2.52E-04 | 4.04E-01 | 3.09E-04 |
| 4.21E-01 | -2.98E+01 | 4.21E-01 | 2.42E+01 | 4.21E-01 | -9.81E-05 | 4.21E-01 | 3.14E-04 |
| 4.38E-01 | 5.97E-01 | 4.38E-01 | 3.23E+01 | 4.38E-01 | 5.61E-05 | 4.38E-01 | 3.18E-04 |
| 4.55E-01 | 3.10E+01 | 4.55E-01 | 5.23E+01 | 4.55E-01 | 2.10E-04 | 4.55E-01 | 3.22E-04 |
| 4.71E-01 | 6.44E+01 | 4.71E-01 | 7.80E+01 | 4.71E-01 | 3.81E-04 | 4.71E-01 | 4.59E-04 |
| 4.88E-01 | 9.82E+01 | 4.88E-01 | 1.05E+02 | 4.88E-01 | 5.53E-04 | 4.88E-01 | 6.17E-04 |
| 5.05E-01 | 1.32E+02 | 5.05E-01 | 1.33E+02 | 5.05E-01 | 7.26E-04 | 5.05E-01 | 7.74E-04 |
| 5.22E-01 | 1.66E+02 | 5.22E-01 | 1.60E+02 | 5.22E-01 | 9.00E-04 | 5.22E-01 | 9.33E-04 |
| 5.39E-01 | 1.79E+02 | 5.39E-01 | 1.70E+02 | 5.39E-01 | 9.61E-04 | 5.39E-01 | 9.91E-04 |
| 5.56E-01 | 1.92E+02 | 5.56E-01 | 1.80E+02 | 5.56E-01 | 1.02E-03 | 5.56E-01 | 1.05E-03 |
| 5.72E-01 | 2.05E+02 | 5.72E-01 | 1.90E+02 | 5.72E-01 | 1.08E-03 | 5.72E-01 | 1.11E-03 |
| 5.89E-01 | 2.17E+02 | 5.89E-01 | 2.00E+02 | 5.89E-01 | 1.14E-03 | 5.89E-01 | 1.16E-03 |
| 6.06E-01 | 2.21E+02 | 6.06E-01 | 2.02E+02 | 6.06E-01 | 1.15E-03 | 6.06E-01 | 1.17E-03 |
| 6.23E-01 | 2.25E+02 | 6.23E-01 | 2.04E+02 | 6.23E-01 | 1.17E-03 | 6.23E-01 | 1.19E-03 |
| 6.40E-01 | 2.29E+02 | 6.40E-01 | 2.06E+02 | 6.40E-01 | 1.18E-03 | 6.40E-01 | 1.20E-03 |
| 6.57E-01 | 2.32E+02 | 6.57E-01 | 2.08E+02 | 6.57E-01 | 1.19E-03 | 6.57E-01 | 1.21E-03 |
| 0.67333 | 2.35E+02 | 0.67333 | 2.09E+02 | 6.73E-01 | 1.20E-03 | 6.73E-01 | 1.22E-03 |
| 0.69017 | 2.37E+02 | 0.69017 | 2.10E+02 | 6.90E-01 | 1.20E-03 | 6.90E-01 | 1.22E-03 |
| 0.707 | 2.39E+02 | 0.707 | 2.11E+02 | 7.07E-01 | 1.21E-03 | 7.07E-01 | 1.23E-03 |
| 0.72383 | 2.41E+02 | 0.72383 | 2.12E+02 | 7.24E-01 | 1.22E-03 | 7.24E-01 | 1.23E-03 |
| 0.74067 | 2.43E+02 | 0.74067 | 2.13E+02 | 7.41E-01 | 1.22E-03 | 7.41E-01 | 1.24E-03 |
| 0.7575 | 2.44E+02 | 0.7575 | 2.13E+02 | 7.58E-01 | 1.22E-03 | 7.58E-01 | 1.24E-03 |
| 0.77433 | 2.45E+02 | 0.77433 | 2.14E+02 | 7.74E-01 | 1.23E-03 | 7.74E-01 | 1.24E-03 |
| 0.79117 | 6.17E+02 | 0.79117 | 5.48E+02 | 7.91E-01 | 3.25E-03 | 7.91E-01 | 3.18E-03 |
| 0.808 | 6.47E+02 | 0.808 | 5.74E+02 | 8.08E-01 | 3.40E-03 | 8.08E-01 | 3.34E-03 |

Table 0-80 Stress and strain profiles across sample thickness for sample N7, step 89%YS.

| Normal Stress | | Equivalent Stress | | Normal Strain | | Equivalent Strain | |
|---|---|---|---|---|---|---|---|
| Length | Stress | Length | Stress | Length | Stress | Length | Stress |
| 0.00E+00 | -2.48E+02 | 0.00E+00 | 2.15E+02 | 0.00E+00 | -1.25E-03 | 0.00E+00 | 1.25E-03 |
| 1.68E-02 | -2.48E+02 | 1.68E-02 | 2.16E+02 | 1.68E-02 | -1.25E-03 | 1.68E-02 | 1.25E-03 |
| 3.37E-02 | -2.48E+02 | 3.37E-02 | 2.16E+02 | 3.37E-02 | -1.25E-03 | 3.37E-02 | 1.26E-03 |
| 5.05E-02 | -2.48E+02 | 5.05E-02 | 2.16E+02 | 5.05E-02 | -1.25E-03 | 5.05E-02 | 1.26E-03 |
| 6.73E-02 | -2.49E+02 | 6.73E-02 | 2.17E+02 | 6.73E-02 | -1.25E-03 | 6.73E-02 | 1.26E-03 |
| 8.42E-02 | -2.49E+02 | 8.42E-02 | 2.17E+02 | 8.42E-02 | -1.25E-03 | 8.42E-02 | 1.26E-03 |
| 1.01E-01 | -2.50E+02 | 1.01E-01 | 2.18E+02 | 1.01E-01 | -1.25E-03 | 1.01E-01 | 1.27E-03 |
| 1.18E-01 | -2.51E+02 | 1.18E-01 | 2.18E+02 | 1.18E-01 | -1.26E-03 | 1.18E-01 | 1.27E-03 |
| 1.35E-01 | -2.52E+02 | 1.35E-01 | 2.18E+02 | 1.35E-01 | -1.26E-03 | 1.35E-01 | 1.27E-03 |
| 1.52E-01 | -2.55E+02 | 1.52E-01 | 2.18E+02 | 1.52E-01 | -1.26E-03 | 1.52E-01 | 1.27E-03 |
| 1.68E-01 | -2.57E+02 | 1.68E-01 | 2.18E+02 | 1.68E-01 | -1.27E-03 | 1.68E-01 | 1.27E-03 |
| 1.85E-01 | -2.60E+02 | 1.85E-01 | 2.18E+02 | 1.85E-01 | -1.28E-03 | 1.85E-01 | 1.27E-03 |
| 2.02E-01 | -2.63E+02 | 2.02E-01 | 2.17E+02 | 2.02E-01 | -1.28E-03 | 2.02E-01 | 1.26E-03 |
| 2.19E-01 | -2.67E+02 | 2.19E-01 | 2.15E+02 | 2.19E-01 | -1.29E-03 | 2.19E-01 | 1.25E-03 |
| 2.36E-01 | -2.71E+02 | 2.36E-01 | 2.14E+02 | 2.36E-01 | -1.30E-03 | 2.36E-01 | 1.25E-03 |
| 2.53E-01 | -2.74E+02 | 2.53E-01 | 2.12E+02 | 2.53E-01 | -1.31E-03 | 2.53E-01 | 1.24E-03 |
| 2.69E-01 | -2.77E+02 | 2.69E-01 | 2.11E+02 | 2.69E-01 | -1.32E-03 | 2.69E-01 | 1.23E-03 |
| 2.86E-01 | -2.79E+02 | 2.86E-01 | 2.11E+02 | 2.86E-01 | -1.34E-03 | 2.86E-01 | 1.23E-03 |
| 3.03E-01 | -2.81E+02 | 3.03E-01 | 2.11E+02 | 3.03E-01 | -1.35E-03 | 3.03E-01 | 1.23E-03 |
| 3.20E-01 | -2.82E+02 | 3.20E-01 | 2.12E+02 | 3.20E-01 | -1.37E-03 | 3.20E-01 | 1.23E-03 |
| 3.37E-01 | -2.56E+02 | 3.37E-01 | 1.89E+02 | 3.37E-01 | -1.23E-03 | 3.37E-01 | 1.10E-03 |
| 3.54E-01 | -2.11E+02 | 3.54E-01 | 1.51E+02 | 3.54E-01 | -1.01E-03 | 3.54E-01 | 8.89E-04 |
| 3.70E-01 | -1.67E+02 | 3.70E-01 | 1.14E+02 | 3.70E-01 | -7.78E-04 | 3.70E-01 | 6.76E-04 |
| 3.87E-01 | -1.22E+02 | 3.87E-01 | 7.84E+01 | 3.87E-01 | -5.50E-04 | 3.87E-01 | 4.63E-04 |

| | | | | | | | |
|---|---|---|---|---|---|---|---|
| 4.04E-01 | -8.14E+01 | 4.04E-01 | 4.93E+01 | 4.04E-01 | -3.45E-04 | 4.04E-01 | 4.04E-04 |
| 4.21E-01 | -4.21E+01 | 4.21E-01 | 3.00E+01 | 4.21E-01 | -1.47E-04 | 4.21E-01 | 3.99E-04 |
| 4.38E-01 | -2.82E+00 | 4.38E-01 | 3.73E+01 | 4.38E-01 | 5.09E-05 | 4.38E-01 | 3.93E-04 |
| 4.55E-01 | 3.65E+01 | 4.55E-01 | 6.25E+01 | 4.55E-01 | 2.49E-04 | 4.55E-01 | 3.88E-04 |
| 4.71E-01 | 7.70E+01 | 4.71E-01 | 9.35E+01 | 4.71E-01 | 4.54E-04 | 4.71E-01 | 5.51E-04 |
| 4.88E-01 | 1.18E+02 | 4.88E-01 | 1.26E+02 | 4.88E-01 | 6.61E-04 | 4.88E-01 | 7.39E-04 |
| 5.05E-01 | 1.59E+02 | 5.05E-01 | 1.59E+02 | 5.05E-01 | 8.68E-04 | 5.05E-01 | 9.28E-04 |
| 5.22E-01 | 2.00E+02 | 5.22E-01 | 1.92E+02 | 5.22E-01 | 1.08E-03 | 5.22E-01 | 1.12E-03 |
| 5.39E-01 | 2.05E+02 | 5.39E-01 | 1.96E+02 | 5.39E-01 | 1.10E-03 | 5.39E-01 | 1.14E-03 |
| 5.56E-01 | 2.11E+02 | 5.56E-01 | 1.99E+02 | 5.56E-01 | 1.12E-03 | 5.56E-01 | 1.16E-03 |
| 5.72E-01 | 2.17E+02 | 5.72E-01 | 2.02E+02 | 5.72E-01 | 1.14E-03 | 5.72E-01 | 1.18E-03 |
| 5.89E-01 | 2.22E+02 | 5.89E-01 | 2.05E+02 | 5.89E-01 | 1.16E-03 | 5.89E-01 | 1.19E-03 |
| 6.06E-01 | 2.26E+02 | 6.06E-01 | 2.07E+02 | 6.06E-01 | 1.17E-03 | 6.06E-01 | 1.20E-03 |
| 6.23E-01 | 2.29E+02 | 6.23E-01 | 2.09E+02 | 6.23E-01 | 1.18E-03 | 6.23E-01 | 1.21E-03 |
| 6.40E-01 | 2.33E+02 | 6.40E-01 | 2.10E+02 | 6.40E-01 | 1.19E-03 | 6.40E-01 | 1.22E-03 |
| 6.57E-01 | 2.36E+02 | 6.57E-01 | 2.12E+02 | 6.57E-01 | 1.20E-03 | 6.57E-01 | 1.23E-03 |
| 0.67333 | 2.38E+02 | 0.67333 | 2.13E+02 | 6.73E-01 | 1.21E-03 | 6.73E-01 | 1.24E-03 |
| 0.69017 | 2.40E+02 | 0.69017 | 2.14E+02 | 6.90E-01 | 1.21E-03 | 6.90E-01 | 1.24E-03 |
| 0.707 | 2.43E+02 | 0.707 | 2.14E+02 | 7.07E-01 | 1.22E-03 | 7.07E-01 | 1.25E-03 |
| 0.72383 | 2.45E+02 | 0.72383 | 2.15E+02 | 7.24E-01 | 1.22E-03 | 7.24E-01 | 1.25E-03 |
| 0.74067 | 2.46E+02 | 0.74067 | 2.16E+02 | 7.41E-01 | 1.23E-03 | 7.41E-01 | 1.26E-03 |
| 0.7575 | 2.48E+02 | 0.7575 | 2.17E+02 | 7.58E-01 | 1.23E-03 | 7.58E-01 | 1.26E-03 |
| 0.77433 | 2.49E+02 | 0.77433 | 2.17E+02 | 7.74E-01 | 1.24E-03 | 7.74E-01 | 1.26E-03 |
| 0.79117 | 7.46E+02 | 0.79117 | 6.62E+02 | 7.91E-01 | 3.92E-03 | 7.91E-01 | 3.85E-03 |
| 0.808 | 7.83E+02 | 0.808 | 6.94E+02 | 8.08E-01 | 4.11E-03 | 8.08E-01 | 4.03E-03 |

Sample N10

Table 0-81 Stress and strain profiles across sample thickness for sample N10, step 50%YS.

| Normal Stress | | Equivalent Stress | | Normal Strain | | Equivalent Strain | |
|---|---|---|---|---|---|---|---|
| Length | Stress | Length | Stress | Length | Stress | Length | Stress |
| 0.00E+00 | -2.32E+02 | 0.00E+00 | 2.05E+02 | 0.00E+00 | -1.21E-03 | 0.00E+00 | 1.19E-03 |
| 1.83E-02 | -2.32E+02 | 1.83E-02 | 2.05E+02 | 1.83E-02 | -1.21E-03 | 1.83E-02 | 1.19E-03 |
| 3.67E-02 | -2.32E+02 | 3.67E-02 | 2.05E+02 | 3.67E-02 | -1.21E-03 | 3.67E-02 | 1.19E-03 |
| 5.50E-02 | -2.32E+02 | 5.50E-02 | 2.05E+02 | 5.50E-02 | -1.21E-03 | 5.50E-02 | 1.19E-03 |
| 7.33E-02 | -2.32E+02 | 7.33E-02 | 2.05E+02 | 7.33E-02 | -1.21E-03 | 7.33E-02 | 1.19E-03 |
| 9.17E-02 | -2.32E+02 | 9.17E-02 | 2.05E+02 | 9.17E-02 | -1.21E-03 | 9.17E-02 | 1.19E-03 |
| 1.10E-01 | -2.32E+02 | 1.10E-01 | 2.05E+02 | 1.10E-01 | -1.21E-03 | 1.10E-01 | 1.19E-03 |
| 1.28E-01 | -2.32E+02 | 1.28E-01 | 2.05E+02 | 1.28E-01 | -1.21E-03 | 1.28E-01 | 1.19E-03 |
| 1.47E-01 | -2.33E+02 | 1.47E-01 | 2.05E+02 | 1.47E-01 | -1.21E-03 | 1.47E-01 | 1.19E-03 |
| 1.65E-01 | -2.34E+02 | 1.65E-01 | 2.04E+02 | 1.65E-01 | -1.21E-03 | 1.65E-01 | 1.19E-03 |
| 1.83E-01 | -2.35E+02 | 1.83E-01 | 2.03E+02 | 1.83E-01 | -1.22E-03 | 1.83E-01 | 1.18E-03 |
| 2.02E-01 | -2.36E+02 | 2.02E-01 | 2.02E+02 | 2.02E-01 | -1.22E-03 | 2.02E-01 | 1.18E-03 |
| 2.20E-01 | -2.38E+02 | 2.20E-01 | 2.00E+02 | 2.20E-01 | -1.22E-03 | 2.20E-01 | 1.17E-03 |
| 2.38E-01 | -2.39E+02 | 2.38E-01 | 1.99E+02 | 2.38E-01 | -1.22E-03 | 2.38E-01 | 1.16E-03 |
| 2.57E-01 | -2.40E+02 | 2.57E-01 | 1.97E+02 | 2.57E-01 | -1.22E-03 | 2.57E-01 | 1.15E-03 |
| 2.75E-01 | -2.35E+02 | 2.75E-01 | 1.91E+02 | 2.75E-01 | -1.20E-03 | 2.75E-01 | 1.11E-03 |
| 2.93E-01 | -2.11E+02 | 2.93E-01 | 1.68E+02 | 2.93E-01 | -1.06E-03 | 2.93E-01 | 9.76E-04 |
| 3.12E-01 | -1.87E+02 | 3.12E-01 | 1.45E+02 | 3.12E-01 | -9.32E-04 | 3.12E-01 | 8.43E-04 |
| 3.30E-01 | -1.64E+02 | 3.30E-01 | 1.22E+02 | 3.30E-01 | -7.99E-04 | 3.30E-01 | 7.09E-04 |
| 3.48E-01 | -1.42E+02 | 3.48E-01 | 1.03E+02 | 3.48E-01 | -6.84E-04 | 3.48E-01 | 5.98E-04 |
| 3.67E-01 | -1.23E+02 | 3.67E-01 | 8.65E+01 | 3.67E-01 | -5.84E-04 | 3.67E-01 | 5.06E-04 |
| 3.85E-01 | -1.04E+02 | 3.85E-01 | 7.07E+01 | 3.85E-01 | -4.84E-04 | 3.85E-01 | 4.14E-04 |
| 4.03E-01 | -8.50E+01 | 4.03E-01 | 5.54E+01 | 4.03E-01 | -3.83E-04 | 4.03E-01 | 3.23E-04 |
| 4.22E-01 | -6.66E+01 | 4.22E-01 | 4.18E+01 | 4.22E-01 | -2.89E-04 | 4.22E-01 | 2.70E-04 |
| 4.40E-01 | -4.83E+01 | 4.40E-01 | 3.02E+01 | 4.40E-01 | -1.95E-04 | 4.40E-01 | 2.24E-04 |

| | | | | | | | |
|---|---|---|---|---|---|---|---|
| 4.58E-01 | -3.00E+01 | 4.58E-01 | 2.31E+01 | 4.58E-01 | -1.01E-04 | 4.58E-01 | 1.78E-04 |
| 4.77E-01 | -1.18E+01 | 4.77E-01 | 2.48E+01 | 4.77E-01 | -7.81E-06 | 4.77E-01 | 1.49E-04 |
| 4.95E-01 | 6.11E+00 | 4.95E-01 | 3.33E+01 | 4.95E-01 | 8.31E-05 | 4.95E-01 | 2.14E-04 |
| 5.13E-01 | 2.40E+01 | 5.13E-01 | 4.50E+01 | 5.13E-01 | 1.74E-04 | 5.13E-01 | 2.79E-04 |
| 5.32E-01 | 4.20E+01 | 5.32E-01 | 5.80E+01 | 5.32E-01 | 2.65E-04 | 5.32E-01 | 3.45E-04 |
| 5.50E-01 | 6.01E+01 | 5.50E-01 | 7.17E+01 | 5.50E-01 | 3.56E-04 | 5.50E-01 | 4.18E-04 |
| 5.68E-01 | 7.83E+01 | 5.68E-01 | 8.58E+01 | 5.68E-01 | 4.49E-04 | 5.68E-01 | 5.01E-04 |
| 5.87E-01 | 9.66E+01 | 5.87E-01 | 1.00E+02 | 5.87E-01 | 5.41E-04 | 5.87E-01 | 5.84E-04 |
| 6.05E-01 | 1.15E+02 | 6.05E-01 | 1.15E+02 | 6.05E-01 | 6.34E-04 | 6.05E-01 | 6.67E-04 |
| 6.23E-01 | 1.36E+02 | 6.23E-01 | 1.31E+02 | 6.23E-01 | 7.39E-04 | 6.23E-01 | 7.64E-04 |
| 6.42E-01 | 1.57E+02 | 6.42E-01 | 1.49E+02 | 6.42E-01 | 8.49E-04 | 6.42E-01 | 8.66E-04 |
| 6.60E-01 | 1.78E+02 | 6.60E-01 | 1.66E+02 | 6.60E-01 | 9.58E-04 | 6.60E-01 | 9.68E-04 |
| 6.78E-01 | 1.98E+02 | 6.78E-01 | 1.83E+02 | 6.78E-01 | 1.06E-03 | 6.78E-01 | 1.06E-03 |
| 6.97E-01 | 2.04E+02 | 6.97E-01 | 1.87E+02 | 6.97E-01 | 1.09E-03 | 6.97E-01 | 1.09E-03 |
| 7.15E-01 | 2.10E+02 | 7.15E-01 | 1.91E+02 | 7.15E-01 | 1.11E-03 | 7.15E-01 | 1.11E-03 |
| 0.73333 | 2.16E+02 | 0.73333 | 1.96E+02 | 7.33E-01 | 1.14E-03 | 7.33E-01 | 1.14E-03 |
| 0.75167 | 2.21E+02 | 0.75167 | 1.99E+02 | 7.52E-01 | 1.16E-03 | 7.52E-01 | 1.16E-03 |
| 0.77 | 2.24E+02 | 0.77 | 2.00E+02 | 7.70E-01 | 1.17E-03 | 7.70E-01 | 1.16E-03 |
| 0.78833 | 2.27E+02 | 0.78833 | 2.02E+02 | 7.88E-01 | 1.18E-03 | 7.88E-01 | 1.17E-03 |
| 0.80667 | 2.29E+02 | 0.80667 | 2.03E+02 | 8.07E-01 | 1.18E-03 | 8.07E-01 | 1.18E-03 |
| 0.825 | 2.32E+02 | 0.825 | 2.05E+02 | 8.25E-01 | 1.19E-03 | 8.25E-01 | 1.19E-03 |
| 0.84333 | 2.34E+02 | 0.84333 | 2.06E+02 | 8.43E-01 | 1.20E-03 | 8.43E-01 | 1.20E-03 |
| 0.86167 | 2.36E+02 | 0.86167 | 2.07E+02 | 8.62E-01 | 1.21E-03 | 8.62E-01 | 1.20E-03 |
| 0.88 | 4.05E+02 | 0.88 | 3.60E+02 | 8.80E-01 | 2.14E-03 | 8.80E-01 | 2.09E-03 |

Table 0-82 Stress and strain profiles across sample thickness for sample N10, step 60%YS.

| **Normal Stress** | | **Equivalent Stress** | | **Normal Strain** | | **Equivalent Strain** | |
|---|---|---|---|---|---|---|---|
| Length | Stress | Length | Stress | Length | Stress | Length | Stress |

| | | | | | | | |
|---|---|---|---|---|---|---|---|
| 0.00E+00 | -2.39E+02 | 0.00E+00 | 2.10E+02 | 0.00E+00 | -1.23E-03 | 0.00E+00 | 1.22E-03 |
| 1.83E-02 | -2.39E+02 | 1.83E-02 | 2.10E+02 | 1.83E-02 | -1.23E-03 | 1.83E-02 | 1.22E-03 |
| 3.67E-02 | -2.39E+02 | 3.67E-02 | 2.10E+02 | 3.67E-02 | -1.23E-03 | 3.67E-02 | 1.22E-03 |
| 5.50E-02 | -2.39E+02 | 5.50E-02 | 2.10E+02 | 5.50E-02 | -1.23E-03 | 5.50E-02 | 1.22E-03 |
| 7.33E-02 | -2.39E+02 | 7.33E-02 | 2.10E+02 | 7.33E-02 | -1.23E-03 | 7.33E-02 | 1.22E-03 |
| 9.17E-02 | -2.40E+02 | 9.17E-02 | 2.11E+02 | 9.17E-02 | -1.23E-03 | 9.17E-02 | 1.22E-03 |
| 1.10E-01 | -2.40E+02 | 1.10E-01 | 2.11E+02 | 1.10E-01 | -1.23E-03 | 1.10E-01 | 1.23E-03 |
| 1.28E-01 | -2.41E+02 | 1.28E-01 | 2.11E+02 | 1.28E-01 | -1.23E-03 | 1.28E-01 | 1.23E-03 |
| 1.47E-01 | -2.43E+02 | 1.47E-01 | 2.11E+02 | 1.47E-01 | -1.24E-03 | 1.47E-01 | 1.23E-03 |
| 1.65E-01 | -2.47E+02 | 1.65E-01 | 2.11E+02 | 1.65E-01 | -1.25E-03 | 1.65E-01 | 1.23E-03 |
| 1.83E-01 | -2.50E+02 | 1.83E-01 | 2.11E+02 | 1.83E-01 | -1.26E-03 | 1.83E-01 | 1.22E-03 |
| 2.02E-01 | -2.53E+02 | 2.02E-01 | 2.10E+02 | 2.02E-01 | -1.26E-03 | 2.02E-01 | 1.22E-03 |
| 2.20E-01 | -2.55E+02 | 2.20E-01 | 2.07E+02 | 2.20E-01 | -1.27E-03 | 2.20E-01 | 1.21E-03 |
| 2.38E-01 | -2.57E+02 | 2.38E-01 | 2.04E+02 | 2.38E-01 | -1.27E-03 | 2.38E-01 | 1.19E-03 |
| 2.57E-01 | -2.59E+02 | 2.57E-01 | 2.02E+02 | 2.57E-01 | -1.27E-03 | 2.57E-01 | 1.18E-03 |
| 2.75E-01 | -2.52E+02 | 2.75E-01 | 1.93E+02 | 2.75E-01 | -1.23E-03 | 2.75E-01 | 1.13E-03 |
| 2.93E-01 | -2.40E+02 | 2.93E-01 | 1.81E+02 | 2.93E-01 | -1.17E-03 | 2.93E-01 | 1.06E-03 |
| 3.12E-01 | -2.28E+02 | 3.12E-01 | 1.69E+02 | 3.12E-01 | -1.11E-03 | 3.12E-01 | 9.88E-04 |
| 3.30E-01 | -2.14E+02 | 3.30E-01 | 1.57E+02 | 3.30E-01 | -1.04E-03 | 3.30E-01 | 9.14E-04 |
| 3.48E-01 | -1.83E+02 | 3.48E-01 | 1.31E+02 | 3.48E-01 | -8.75E-04 | 3.48E-01 | 7.64E-04 |
| 3.67E-01 | -1.52E+02 | 3.67E-01 | 1.05E+02 | 3.67E-01 | -7.13E-04 | 3.67E-01 | 6.15E-04 |
| 3.85E-01 | -1.21E+02 | 3.85E-01 | 7.94E+01 | 3.85E-01 | -5.51E-04 | 3.85E-01 | 4.65E-04 |
| 4.03E-01 | -9.31E+01 | 4.03E-01 | 5.83E+01 | 4.03E-01 | -4.09E-04 | 4.03E-01 | 3.56E-04 |
| 4.22E-01 | -6.95E+01 | 4.22E-01 | 4.23E+01 | 4.22E-01 | -2.90E-04 | 4.22E-01 | 2.93E-04 |
| 4.40E-01 | -4.58E+01 | 4.40E-01 | 2.99E+01 | 4.40E-01 | -1.71E-04 | 4.40E-01 | 2.29E-04 |
| 4.58E-01 | -2.21E+01 | 4.58E-01 | 2.68E+01 | 4.58E-01 | -5.13E-05 | 4.58E-01 | 1.66E-04 |
| 4.77E-01 | 1.25E+00 | 4.77E-01 | 3.53E+01 | 4.77E-01 | 6.61E-05 | 4.77E-01 | 2.32E-04 |

| | | | | | | | |
|---|---|---|---|---|---|---|---|
| 4.95E-01 | 2.46E+01 | 4.95E-01 | 4.97E+01 | 4.95E-01 | 1.83E-04 | 4.95E-01 | 3.15E-04 |
| 5.13E-01 | 4.79E+01 | 5.13E-01 | 6.62E+01 | 5.13E-01 | 3.01E-04 | 5.13E-01 | 3.98E-04 |
| 5.32E-01 | 7.23E+01 | 5.32E-01 | 8.46E+01 | 5.32E-01 | 4.24E-04 | 5.32E-01 | 4.93E-04 |
| 5.50E-01 | 9.92E+01 | 5.50E-01 | 1.06E+02 | 5.50E-01 | 5.60E-04 | 5.50E-01 | 6.17E-04 |
| 5.68E-01 | 1.26E+02 | 5.68E-01 | 1.27E+02 | 5.68E-01 | 6.97E-04 | 5.68E-01 | 7.42E-04 |
| 5.87E-01 | 1.53E+02 | 5.87E-01 | 1.49E+02 | 5.87E-01 | 8.34E-04 | 5.87E-01 | 8.66E-04 |
| 6.05E-01 | 1.71E+02 | 6.05E-01 | 1.63E+02 | 6.05E-01 | 9.24E-04 | 6.05E-01 | 9.50E-04 |
| 6.23E-01 | 1.86E+02 | 6.23E-01 | 1.75E+02 | 6.23E-01 | 9.96E-04 | 6.23E-01 | 1.02E-03 |
| 6.42E-01 | 2.00E+02 | 6.42E-01 | 1.87E+02 | 6.42E-01 | 1.07E-03 | 6.42E-01 | 1.08E-03 |
| 6.60E-01 | 2.14E+02 | 6.60E-01 | 1.97E+02 | 6.60E-01 | 1.13E-03 | 6.60E-01 | 1.15E-03 |
| 6.78E-01 | 2.17E+02 | 6.78E-01 | 1.99E+02 | 6.78E-01 | 1.15E-03 | 6.78E-01 | 1.16E-03 |
| 6.97E-01 | 2.21E+02 | 6.97E-01 | 2.01E+02 | 6.97E-01 | 1.16E-03 | 6.97E-01 | 1.17E-03 |
| 7.15E-01 | 2.25E+02 | 7.15E-01 | 2.03E+02 | 7.15E-01 | 1.17E-03 | 7.15E-01 | 1.18E-03 |
| 0.73333 | 2.28E+02 | 0.73333 | 2.04E+02 | 7.33E-01 | 1.18E-03 | 7.33E-01 | 1.19E-03 |
| 0.75167 | 2.31E+02 | 0.75167 | 2.06E+02 | 7.52E-01 | 1.19E-03 | 7.52E-01 | 1.20E-03 |
| 0.77 | 2.34E+02 | 0.77 | 2.08E+02 | 7.70E-01 | 1.20E-03 | 7.70E-01 | 1.21E-03 |
| 0.78833 | 2.37E+02 | 0.78833 | 2.09E+02 | 7.88E-01 | 1.21E-03 | 7.88E-01 | 1.22E-03 |
| 0.80667 | 2.39E+02 | 0.80667 | 2.10E+02 | 8.07E-01 | 1.21E-03 | 8.07E-01 | 1.22E-03 |
| 0.825 | 2.40E+02 | 0.825 | 2.11E+02 | 8.25E-01 | 1.22E-03 | 8.25E-01 | 1.22E-03 |
| 0.84333 | 2.41E+02 | 0.84333 | 2.11E+02 | 8.43E-01 | 1.22E-03 | 8.43E-01 | 1.23E-03 |
| 0.86167 | 5.02E+02 | 0.86167 | 4.46E+02 | 8.62E-01 | 2.65E-03 | 8.62E-01 | 2.60E-03 |
| 0.88 | 5.27E+02 | 0.88 | 4.68E+02 | 8.80E-01 | 2.78E-03 | 8.80E-01 | 2.72E-03 |

Table 0-83 Stress and strain profiles across sample thickness for sample N10, step 70%YS.

| **Normal Stress** | | **Equivalent Stress** | | **Normal Strain** | | **Equivalent Strain** | |
|---|---|---|---|---|---|---|---|
| Length | Stress | Length | Stress | Length | Stress | Length | Stress |
| 0.00E+00 | -2.41E+02 | 0.00E+00 | 2.11E+02 | 0.00E+00 | -1.24E-03 | 0.00E+00 | 1.23E-03 |
| 1.83E-02 | -2.42E+02 | 1.83E-02 | 2.11E+02 | 1.83E-02 | -1.24E-03 | 1.83E-02 | 1.23E-03 |

| | | | | | | | |
|---|---|---|---|---|---|---|---|
| 3.67E-02 | -2.42E+02 | 3.67E-02 | 2.12E+02 | 3.67E-02 | -1.24E-03 | 3.67E-02 | 1.23E-03 |
| 5.50E-02 | -2.42E+02 | 5.50E-02 | 2.12E+02 | 5.50E-02 | -1.24E-03 | 5.50E-02 | 1.23E-03 |
| 7.33E-02 | -2.43E+02 | 7.33E-02 | 2.12E+02 | 7.33E-02 | -1.24E-03 | 7.33E-02 | 1.24E-03 |
| 9.17E-02 | -2.44E+02 | 9.17E-02 | 2.13E+02 | 9.17E-02 | -1.24E-03 | 9.17E-02 | 1.24E-03 |
| 1.10E-01 | -2.45E+02 | 1.10E-01 | 2.13E+02 | 1.10E-01 | -1.24E-03 | 1.10E-01 | 1.24E-03 |
| 1.28E-01 | -2.46E+02 | 1.28E-01 | 2.14E+02 | 1.28E-01 | -1.24E-03 | 1.28E-01 | 1.24E-03 |
| 1.47E-01 | -2.49E+02 | 1.47E-01 | 2.14E+02 | 1.47E-01 | -1.25E-03 | 1.47E-01 | 1.24E-03 |
| 1.65E-01 | -2.53E+02 | 1.65E-01 | 2.14E+02 | 1.65E-01 | -1.26E-03 | 1.65E-01 | 1.24E-03 |
| 1.83E-01 | -2.57E+02 | 1.83E-01 | 2.14E+02 | 1.83E-01 | -1.27E-03 | 1.83E-01 | 1.24E-03 |
| 2.02E-01 | -2.61E+02 | 2.02E-01 | 2.13E+02 | 2.02E-01 | -1.28E-03 | 2.02E-01 | 1.24E-03 |
| 2.20E-01 | -2.66E+02 | 2.20E-01 | 2.11E+02 | 2.20E-01 | -1.29E-03 | 2.20E-01 | 1.23E-03 |
| 2.38E-01 | -2.70E+02 | 2.38E-01 | 2.10E+02 | 2.38E-01 | -1.30E-03 | 2.38E-01 | 1.22E-03 |
| 2.57E-01 | -2.74E+02 | 2.57E-01 | 2.08E+02 | 2.57E-01 | -1.32E-03 | 2.57E-01 | 1.21E-03 |
| 2.75E-01 | -2.74E+02 | 2.75E-01 | 2.04E+02 | 2.75E-01 | -1.31E-03 | 2.75E-01 | 1.19E-03 |
| 2.93E-01 | -2.70E+02 | 2.93E-01 | 1.99E+02 | 2.93E-01 | -1.29E-03 | 2.93E-01 | 1.17E-03 |
| 3.12E-01 | -2.66E+02 | 3.12E-01 | 1.95E+02 | 3.12E-01 | -1.28E-03 | 3.12E-01 | 1.14E-03 |
| 3.30E-01 | -2.60E+02 | 3.30E-01 | 1.90E+02 | 3.30E-01 | -1.25E-03 | 3.30E-01 | 1.10E-03 |
| 3.48E-01 | -2.22E+02 | 3.48E-01 | 1.58E+02 | 3.48E-01 | -1.06E-03 | 3.48E-01 | 9.23E-04 |
| 3.67E-01 | -1.85E+02 | 3.67E-01 | 1.26E+02 | 3.67E-01 | -8.63E-04 | 3.67E-01 | 7.43E-04 |
| 3.85E-01 | -1.47E+02 | 3.85E-01 | 9.58E+01 | 3.85E-01 | -6.68E-04 | 3.85E-01 | 5.62E-04 |
| 4.03E-01 | -1.13E+02 | 4.03E-01 | 7.05E+01 | 4.03E-01 | -4.98E-04 | 4.03E-01 | 4.29E-04 |
| 4.22E-01 | -8.48E+01 | 4.22E-01 | 5.11E+01 | 4.22E-01 | -3.55E-04 | 4.22E-01 | 3.49E-04 |
| 4.40E-01 | -5.62E+01 | 4.40E-01 | 3.54E+01 | 4.40E-01 | -2.13E-04 | 4.40E-01 | 2.68E-04 |
| 4.58E-01 | -2.76E+01 | 4.58E-01 | 3.03E+01 | 4.58E-01 | -7.03E-05 | 4.58E-01 | 1.88E-04 |
| 4.77E-01 | 4.61E-01 | 4.77E-01 | 3.98E+01 | 4.77E-01 | 7.01E-05 | 4.77E-01 | 2.66E-04 |
| 4.95E-01 | 2.85E+01 | 4.95E-01 | 5.69E+01 | 4.95E-01 | 2.10E-04 | 4.95E-01 | 3.64E-04 |
| 5.13E-01 | 5.64E+01 | 5.13E-01 | 7.66E+01 | 5.13E-01 | 3.50E-04 | 5.13E-01 | 4.61E-04 |

| | | | | | | | |
|---|---|---|---|---|---|---|---|
| 5.32E-01 | 8.57E+01 | 5.32E-01 | 9.87E+01 | 5.32E-01 | 4.97E-04 | 5.32E-01 | 5.75E-04 |
| 5.50E-01 | 1.18E+02 | 5.50E-01 | 1.24E+02 | 5.50E-01 | 6.61E-04 | 5.50E-01 | 7.25E-04 |
| 5.68E-01 | 1.50E+02 | 5.68E-01 | 1.50E+02 | 5.68E-01 | 8.25E-04 | 5.68E-01 | 8.75E-04 |
| 5.87E-01 | 1.83E+02 | 5.87E-01 | 1.76E+02 | 5.87E-01 | 9.89E-04 | 5.87E-01 | 1.02E-03 |
| 6.05E-01 | 1.97E+02 | 6.05E-01 | 1.87E+02 | 6.05E-01 | 1.06E-03 | 6.05E-01 | 1.09E-03 |
| 6.23E-01 | 2.04E+02 | 6.23E-01 | 1.92E+02 | 6.23E-01 | 1.09E-03 | 6.23E-01 | 1.11E-03 |
| 6.42E-01 | 2.11E+02 | 6.42E-01 | 1.96E+02 | 6.42E-01 | 1.12E-03 | 6.42E-01 | 1.14E-03 |
| 6.60E-01 | 2.18E+02 | 6.60E-01 | 2.01E+02 | 6.60E-01 | 1.14E-03 | 6.60E-01 | 1.17E-03 |
| 6.78E-01 | 2.22E+02 | 6.78E-01 | 2.03E+02 | 6.78E-01 | 1.16E-03 | 6.78E-01 | 1.18E-03 |
| 6.97E-01 | 2.26E+02 | 6.97E-01 | 2.05E+02 | 6.97E-01 | 1.17E-03 | 6.97E-01 | 1.19E-03 |
| 7.15E-01 | 2.30E+02 | 7.15E-01 | 2.07E+02 | 7.15E-01 | 1.19E-03 | 7.15E-01 | 1.21E-03 |
| 0.73333 | 2.33E+02 | 0.73333 | 2.09E+02 | 7.33E-01 | 1.20E-03 | 7.33E-01 | 1.21E-03 |
| 0.75167 | 2.35E+02 | 0.75167 | 2.10E+02 | 7.52E-01 | 1.20E-03 | 7.52E-01 | 1.22E-03 |
| 0.77 | 2.37E+02 | 0.77 | 2.11E+02 | 7.70E-01 | 1.21E-03 | 7.70E-01 | 1.23E-03 |
| 0.78833 | 2.40E+02 | 0.78833 | 2.12E+02 | 7.88E-01 | 1.21E-03 | 7.88E-01 | 1.23E-03 |
| 0.80667 | 2.41E+02 | 0.80667 | 2.12E+02 | 8.07E-01 | 1.22E-03 | 8.07E-01 | 1.23E-03 |
| 0.825 | 2.43E+02 | 0.825 | 2.13E+02 | 8.25E-01 | 1.22E-03 | 8.25E-01 | 1.24E-03 |
| 0.84333 | 2.44E+02 | 0.84333 | 2.13E+02 | 8.43E-01 | 1.22E-03 | 8.43E-01 | 1.24E-03 |
| 0.86167 | 5.84E+02 | 0.86167 | 5.19E+02 | 8.62E-01 | 3.08E-03 | 8.62E-01 | 3.02E-03 |
| 0.88 | 6.12E+02 | 0.88 | 5.44E+02 | 8.80E-01 | 3.22E-03 | 8.80E-01 | 3.16E-03 |

## Sample L-R-1

Table 0-84 Stress and strain profiles across sample thickness for sample L-R-1, step 50%YS.

| Normal Stress | | Equivalent Stress | | Normal Strain | | Equivalent Strain | |
|---|---|---|---|---|---|---|---|
| Length | Stress | Length | Stress | Length | Stress | Length | Stress |
| 0.00E+00 | -2.37E+02 | 0.00E+00 | 2.10E+02 | 0.00E+00 | -1.24E-03 | 0.00E+00 | 1.22E-03 |
| 1.95E-02 | -2.37E+02 | 1.95E-02 | 2.10E+02 | 1.95E-02 | -1.24E-03 | 1.95E-02 | 1.22E-03 |
| 3.90E-02 | -2.37E+02 | 3.90E-02 | 2.10E+02 | 3.90E-02 | -1.24E-03 | 3.90E-02 | 1.22E-03 |

| | | | | | | | |
|---|---|---|---|---|---|---|---|
| 5.86E-02 | -2.36E+02 | 5.86E-02 | 2.10E+02 | 5.86E-02 | -1.24E-03 | 5.86E-02 | 1.22E-03 |
| 7.81E-02 | -2.36E+02 | 7.81E-02 | 2.10E+02 | 7.81E-02 | -1.24E-03 | 7.81E-02 | 1.22E-03 |
| 9.76E-02 | -2.36E+02 | 9.76E-02 | 2.10E+02 | 9.76E-02 | -1.24E-03 | 9.76E-02 | 1.22E-03 |
| 1.17E-01 | -2.36E+02 | 1.17E-01 | 2.10E+02 | 1.17E-01 | -1.24E-03 | 1.17E-01 | 1.22E-03 |
| 1.37E-01 | -2.36E+02 | 1.37E-01 | 2.09E+02 | 1.37E-01 | -1.24E-03 | 1.37E-01 | 1.22E-03 |
| 1.56E-01 | -2.37E+02 | 1.56E-01 | 2.09E+02 | 1.56E-01 | -1.24E-03 | 1.56E-01 | 1.21E-03 |
| 1.76E-01 | -2.39E+02 | 1.76E-01 | 2.08E+02 | 1.76E-01 | -1.24E-03 | 1.76E-01 | 1.21E-03 |
| 1.95E-01 | -2.40E+02 | 1.95E-01 | 2.07E+02 | 1.95E-01 | -1.25E-03 | 1.95E-01 | 1.20E-03 |
| 2.15E-01 | -2.40E+02 | 2.15E-01 | 2.05E+02 | 2.15E-01 | -1.24E-03 | 2.15E-01 | 1.19E-03 |
| 2.34E-01 | -2.37E+02 | 2.34E-01 | 2.00E+02 | 2.34E-01 | -1.22E-03 | 2.34E-01 | 1.16E-03 |
| 2.54E-01 | -2.34E+02 | 2.54E-01 | 1.94E+02 | 2.54E-01 | -1.20E-03 | 2.54E-01 | 1.13E-03 |
| 2.73E-01 | -2.31E+02 | 2.73E-01 | 1.89E+02 | 2.73E-01 | -1.18E-03 | 2.73E-01 | 1.10E-03 |
| 2.93E-01 | -2.14E+02 | 2.93E-01 | 1.72E+02 | 2.93E-01 | -1.09E-03 | 2.93E-01 | 1.00E-03 |
| 3.12E-01 | -1.91E+02 | 3.12E-01 | 1.49E+02 | 3.12E-01 | -9.56E-04 | 3.12E-01 | 8.70E-04 |
| 3.32E-01 | -1.67E+02 | 3.32E-01 | 1.27E+02 | 3.32E-01 | -8.24E-04 | 3.32E-01 | 7.38E-04 |
| 3.51E-01 | -1.44E+02 | 3.51E-01 | 1.04E+02 | 3.51E-01 | -6.94E-04 | 3.51E-01 | 6.07E-04 |
| 3.71E-01 | -1.25E+02 | 3.71E-01 | 8.84E+01 | 3.71E-01 | -5.95E-04 | 3.71E-01 | 5.17E-04 |
| 3.90E-01 | -1.06E+02 | 3.90E-01 | 7.27E+01 | 3.90E-01 | -4.96E-04 | 3.90E-01 | 4.26E-04 |
| 4.10E-01 | -8.74E+01 | 4.10E-01 | 5.74E+01 | 4.10E-01 | -3.97E-04 | 4.10E-01 | 3.36E-04 |
| 4.29E-01 | -6.91E+01 | 4.29E-01 | 4.34E+01 | 4.29E-01 | -3.01E-04 | 4.29E-01 | 2.69E-04 |
| 4.49E-01 | -5.13E+01 | 4.49E-01 | 3.17E+01 | 4.49E-01 | -2.09E-04 | 4.49E-01 | 2.28E-04 |
| 4.69E-01 | -3.34E+01 | 4.69E-01 | 2.37E+01 | 4.69E-01 | -1.17E-04 | 4.69E-01 | 1.87E-04 |
| 4.88E-01 | -1.55E+01 | 4.88E-01 | 2.37E+01 | 4.88E-01 | -2.53E-05 | 4.88E-01 | 1.46E-04 |
| 5.08E-01 | 2.09E+00 | 5.08E-01 | 3.11E+01 | 5.08E-01 | 6.40E-05 | 5.08E-01 | 1.98E-04 |
| 5.27E-01 | 1.97E+01 | 5.27E-01 | 4.21E+01 | 5.27E-01 | 1.53E-04 | 5.27E-01 | 2.62E-04 |
| 5.47E-01 | 3.72E+01 | 5.47E-01 | 5.46E+01 | 5.47E-01 | 2.42E-04 | 5.47E-01 | 3.26E-04 |
| 5.66E-01 | 5.49E+01 | 5.66E-01 | 6.78E+01 | 5.66E-01 | 3.31E-04 | 5.66E-01 | 3.95E-04 |

| | | | | | | | |
|---|---|---|---|---|---|---|---|
| 5.86E-01 | 7.28E+01 | 5.86E-01 | 8.14E+01 | 5.86E-01 | 4.21E-04 | 5.86E-01 | 4.75E-04 |
| 6.05E-01 | 9.06E+01 | 6.05E-01 | 9.53E+01 | 6.05E-01 | 5.11E-04 | 6.05E-01 | 5.55E-04 |
| 6.25E-01 | 1.08E+02 | 6.25E-01 | 1.09E+02 | 6.25E-01 | 6.02E-04 | 6.25E-01 | 6.36E-04 |
| 6.44E-01 | 1.29E+02 | 6.44E-01 | 1.25E+02 | 6.44E-01 | 7.04E-04 | 6.44E-01 | 7.29E-04 |
| 6.64E-01 | 1.50E+02 | 6.64E-01 | 1.43E+02 | 6.64E-01 | 8.11E-04 | 6.64E-01 | 8.29E-04 |
| 6.83E-01 | 1.71E+02 | 6.83E-01 | 1.60E+02 | 6.83E-01 | 9.18E-04 | 6.83E-01 | 9.28E-04 |
| 7.03E-01 | 1.90E+02 | 7.03E-01 | 1.76E+02 | 7.03E-01 | 1.02E-03 | 7.03E-01 | 1.02E-03 |
| 7.22E-01 | 2.00E+02 | 7.22E-01 | 1.84E+02 | 7.22E-01 | 1.07E-03 | 7.22E-01 | 1.07E-03 |
| 7.42E-01 | 2.11E+02 | 7.42E-01 | 1.92E+02 | 7.42E-01 | 1.12E-03 | 7.42E-01 | 1.11E-03 |
| 7.61E-01 | 2.21E+02 | 7.61E-01 | 2.00E+02 | 7.61E-01 | 1.17E-03 | 7.61E-01 | 1.16E-03 |
| 0.78083 | 2.27E+02 | 0.78083 | 2.04E+02 | 7.81E-01 | 1.19E-03 | 7.81E-01 | 1.19E-03 |
| 0.80035 | 2.30E+02 | 0.80035 | 2.06E+02 | 8.00E-01 | 1.20E-03 | 8.00E-01 | 1.20E-03 |
| 0.81988 | 2.33E+02 | 0.81988 | 2.07E+02 | 8.20E-01 | 1.21E-03 | 8.20E-01 | 1.20E-03 |
| 0.8394 | 2.35E+02 | 0.8394 | 2.09E+02 | 8.39E-01 | 1.22E-03 | 8.39E-01 | 1.21E-03 |
| 0.85892 | 2.38E+02 | 0.85892 | 2.10E+02 | 8.59E-01 | 1.23E-03 | 8.59E-01 | 1.22E-03 |
| 0.87844 | 2.40E+02 | 0.87844 | 2.11E+02 | 8.78E-01 | 1.23E-03 | 8.78E-01 | 1.23E-03 |
| 0.89796 | 2.42E+02 | 0.89796 | 2.12E+02 | 8.98E-01 | 1.24E-03 | 8.98E-01 | 1.23E-03 |
| 0.91748 | 3.97E+02 | 0.91748 | 3.53E+02 | 9.17E-01 | 2.09E-03 | 9.17E-01 | 2.05E-03 |
| 0.937 | 4.16E+02 | 0.937 | 3.70E+02 | 9.37E-01 | 2.19E-03 | 9.37E-01 | 2.15E-03 |

Table B-85 Stress and strain profiles across sample thickness for sample L-R-1, step 60%YS.

| **Normal Stress** | | **Equivalent Stress** | | **Normal Strain** | | **Equivalent Strain** | |
|---|---|---|---|---|---|---|---|
| Length | Stress | Length | Stress | Length | Stress | Length | Stress |
| 0.00E+00 | -2.41E+02 | 0.00E+00 | 2.12E+02 | 0.00E+00 | 1.23E-03 | 0.00E+00 | 1.23E-03 |
| 1.95E-02 | -2.41E+02 | 1.95E-02 | 2.12E+02 | 1.95E-02 | 1.23E-03 | 1.95E-02 | 1.23E-03 |
| 3.90E-02 | -2.41E+02 | 3.90E-02 | 2.12E+02 | 3.90E-02 | 1.23E-03 | 3.90E-02 | 1.23E-03 |
| 5.86E-02 | -2.41E+02 | 5.86E-02 | 2.13E+02 | 5.86E-02 | 1.24E-03 | 5.86E-02 | 1.24E-03 |
| 7.81E-02 | -2.41E+02 | 7.81E-02 | 2.13E+02 | 7.81E-02 | 1.24E-03 | 7.81E-02 | 1.24E-03 |

| | | | | | | | |
|---|---|---|---|---|---|---|---|
| 9.76E-02 | -2.42E+02 | 9.76E-02 | 2.13E+02 | 9.76E-02 | 1.24E-03 | 9.76E-02 | 1.24E-03 |
| 1.17E-01 | -2.42E+02 | 1.17E-01 | 2.13E+02 | 1.17E-01 | 1.24E-03 | 1.17E-01 | 1.24E-03 |
| 1.37E-01 | -2.43E+02 | 1.37E-01 | 2.13E+02 | 1.37E-01 | 1.24E-03 | 1.37E-01 | 1.24E-03 |
| 1.56E-01 | -2.45E+02 | 1.56E-01 | 2.13E+02 | 1.56E-01 | 1.24E-03 | 1.56E-01 | 1.24E-03 |
| 1.76E-01 | -2.48E+02 | 1.76E-01 | 2.13E+02 | 1.76E-01 | 1.24E-03 | 1.76E-01 | 1.24E-03 |
| 1.95E-01 | -2.51E+02 | 1.95E-01 | 2.12E+02 | 1.95E-01 | 1.23E-03 | 1.95E-01 | 1.23E-03 |
| 2.15E-01 | -2.54E+02 | 2.15E-01 | 2.11E+02 | 2.15E-01 | 1.23E-03 | 2.15E-01 | 1.23E-03 |
| 2.34E-01 | -2.56E+02 | 2.34E-01 | 2.08E+02 | 2.34E-01 | 1.21E-03 | 2.34E-01 | 1.21E-03 |
| 2.54E-01 | -2.58E+02 | 2.54E-01 | 2.06E+02 | 2.54E-01 | 1.20E-03 | 2.54E-01 | 1.20E-03 |
| 2.73E-01 | -2.59E+02 | 2.73E-01 | 2.03E+02 | 2.73E-01 | 1.18E-03 | 2.73E-01 | 1.18E-03 |
| 2.93E-01 | -2.49E+02 | 2.93E-01 | 1.92E+02 | 2.93E-01 | 1.12E-03 | 2.93E-01 | 1.12E-03 |
| 3.12E-01 | -2.33E+02 | 3.12E-01 | 1.76E+02 | 3.12E-01 | 1.03E-03 | 3.12E-01 | 1.03E-03 |
| 3.32E-01 | -2.17E+02 | 3.32E-01 | 1.61E+02 | 3.32E-01 | 9.38E-04 | 3.32E-01 | 9.38E-04 |
| 3.51E-01 | -2.00E+02 | 3.51E-01 | 1.45E+02 | 3.51E-01 | 8.45E-04 | 3.51E-01 | 8.45E-04 |
| 3.71E-01 | -1.71E+02 | 3.71E-01 | 1.21E+02 | 3.71E-01 | 7.08E-04 | 3.71E-01 | 7.08E-04 |
| 3.90E-01 | -1.43E+02 | 3.90E-01 | 9.75E+01 | 3.90E-01 | 5.72E-04 | 3.90E-01 | 5.72E-04 |
| 4.10E-01 | -1.14E+02 | 4.10E-01 | 7.44E+01 | 4.10E-01 | 4.36E-04 | 4.10E-01 | 4.36E-04 |
| 4.29E-01 | -8.82E+01 | 4.29E-01 | 5.50E+01 | 4.29E-01 | 3.37E-04 | 4.29E-01 | 3.37E-04 |
| 4.49E-01 | -6.58E+01 | 4.49E-01 | 4.00E+01 | 4.49E-01 | 2.80E-04 | 4.49E-01 | 2.80E-04 |
| 4.69E-01 | -4.33E+01 | 4.69E-01 | 2.89E+01 | 4.69E-01 | 2.23E-04 | 4.69E-01 | 2.23E-04 |
| 4.88E-01 | -2.09E+01 | 4.88E-01 | 2.69E+01 | 4.88E-01 | 1.66E-04 | 4.88E-01 | 1.66E-04 |
| 5.08E-01 | 1.23E+00 | 5.08E-01 | 3.53E+01 | 5.08E-01 | 2.29E-04 | 5.08E-01 | 2.29E-04 |
| 5.27E-01 | 2.33E+01 | 5.27E-01 | 4.89E+01 | 5.27E-01 | 3.08E-04 | 5.27E-01 | 3.08E-04 |
| 5.47E-01 | 4.54E+01 | 5.47E-01 | 6.45E+01 | 5.47E-01 | 3.87E-04 | 5.47E-01 | 3.87E-04 |
| 5.66E-01 | 6.77E+01 | 5.66E-01 | 8.11E+01 | 5.66E-01 | 4.73E-04 | 5.66E-01 | 4.73E-04 |
| 5.86E-01 | 9.04E+01 | 5.86E-01 | 9.87E+01 | 5.86E-01 | 5.76E-04 | 5.86E-01 | 5.76E-04 |
| 6.05E-01 | 1.13E+02 | 6.05E-01 | 1.17E+02 | 6.05E-01 | 6.79E-04 | 6.05E-01 | 6.79E-04 |

| | | | | | | | |
|---|---|---|---|---|---|---|---|
| 6.25E-01 | 1.36E+02 | 6.25E-01 | 1.35E+02 | 6.25E-01 | 7.83E-04 | 6.25E-01 | 7.83E-04 |
| 6.44E-01 | 1.58E+02 | 6.44E-01 | 1.53E+02 | 6.44E-01 | 8.89E-04 | 6.44E-01 | 8.89E-04 |
| 6.64E-01 | 1.81E+02 | 6.64E-01 | 1.71E+02 | 6.64E-01 | 9.95E-04 | 6.64E-01 | 9.95E-04 |
| 6.83E-01 | 2.04E+02 | 6.83E-01 | 1.90E+02 | 6.83E-01 | 1.10E-03 | 6.83E-01 | 1.10E-03 |
| 7.03E-01 | 2.24E+02 | 7.03E-01 | 2.06E+02 | 7.03E-01 | 1.20E-03 | 7.03E-01 | 1.20E-03 |
| 7.22E-01 | 2.25E+02 | 7.22E-01 | 2.06E+02 | 7.22E-01 | 1.20E-03 | 7.22E-01 | 1.20E-03 |
| 7.42E-01 | 2.26E+02 | 7.42E-01 | 2.05E+02 | 7.42E-01 | 1.19E-03 | 7.42E-01 | 1.19E-03 |
| 7.61E-01 | 2.28E+02 | 7.61E-01 | 2.05E+02 | 7.61E-01 | 1.19E-03 | 7.61E-01 | 1.19E-03 |
| 0.78083 | 2.30E+02 | 0.78083 | 2.06E+02 | 7.81E-01 | 1.20E-03 | 7.81E-01 | 1.20E-03 |
| 0.80035 | 2.33E+02 | 0.80035 | 2.08E+02 | 8.00E-01 | 1.21E-03 | 8.00E-01 | 1.21E-03 |
| 0.81988 | 2.36E+02 | 0.81988 | 2.10E+02 | 8.20E-01 | 1.22E-03 | 8.20E-01 | 1.22E-03 |
| 0.8394 | 2.39E+02 | 0.8394 | 2.11E+02 | 8.39E-01 | 1.23E-03 | 8.39E-01 | 1.23E-03 |
| 0.85892 | 2.41E+02 | 0.85892 | 2.12E+02 | 8.59E-01 | 1.23E-03 | 8.59E-01 | 1.23E-03 |
| 0.87844 | 2.43E+02 | 0.87844 | 2.13E+02 | 8.78E-01 | 1.24E-03 | 8.78E-01 | 1.24E-03 |
| 0.89796 | 2.44E+02 | 0.89796 | 2.13E+02 | 8.98E-01 | 1.24E-03 | 8.98E-01 | 1.24E-03 |
| 0.91748 | 4.84E+02 | 0.91748 | 4.30E+02 | 9.17E-01 | 2.50E-03 | 9.17E-01 | 2.50E-03 |
| 0.937 | 5.07E+02 | 0.937 | 4.50E+02 | 9.37E-01 | 2.62E-03 | 9.37E-01 | 2.62E-03 |

Table 0-86 Stress and strain profiles across sample thickness for sample L-R-1, step 70%YS.

| **Normal Stress** | | **Equivalent Stress** | | **Normal Strain** | | **Equivalent Strain** | |
|---|---|---|---|---|---|---|---|
| Length | Stress | Length | Stress | Length | Stress | Length | Stress |
| 0.00E+00 | -2.44E+02 | 0.00E+00 | 2.14E+02 | 0.00E+00 | -1.26E-03 | 0.00E+00 | 1.24E-03 |
| 1.95E-02 | -2.44E+02 | 1.95E-02 | 2.14E+02 | 1.95E-02 | -1.26E-03 | 1.95E-02 | 1.24E-03 |
| 3.90E-02 | -2.44E+02 | 3.90E-02 | 2.14E+02 | 3.90E-02 | -1.26E-03 | 3.90E-02 | 1.25E-03 |
| 5.86E-02 | -2.45E+02 | 5.86E-02 | 2.14E+02 | 5.86E-02 | -1.25E-03 | 5.86E-02 | 1.25E-03 |
| 7.81E-02 | -2.45E+02 | 7.81E-02 | 2.15E+02 | 7.81E-02 | -1.26E-03 | 7.81E-02 | 1.25E-03 |
| 9.76E-02 | -2.46E+02 | 9.76E-02 | 2.15E+02 | 9.76E-02 | -1.26E-03 | 9.76E-02 | 1.25E-03 |
| 1.17E-01 | -2.47E+02 | 1.17E-01 | 2.15E+02 | 1.17E-01 | -1.26E-03 | 1.17E-01 | 1.25E-03 |

| | | | | | | | |
|---|---|---|---|---|---|---|---|
| 1.37E-01 | -2.48E+02 | 1.37E-01 | 2.16E+02 | 1.37E-01 | -1.26E-03 | 1.37E-01 | 1.25E-03 |
| 1.56E-01 | -2.51E+02 | 1.56E-01 | 2.16E+02 | 1.56E-01 | -1.27E-03 | 1.56E-01 | 1.25E-03 |
| 1.76E-01 | -2.55E+02 | 1.76E-01 | 2.16E+02 | 1.76E-01 | -1.28E-03 | 1.76E-01 | 1.25E-03 |
| 1.95E-01 | -2.59E+02 | 1.95E-01 | 2.16E+02 | 1.95E-01 | -1.29E-03 | 1.95E-01 | 1.25E-03 |
| 2.15E-01 | -2.63E+02 | 2.15E-01 | 2.15E+02 | 2.15E-01 | -1.30E-03 | 2.15E-01 | 1.25E-03 |
| 2.34E-01 | -2.67E+02 | 2.34E-01 | 2.13E+02 | 2.34E-01 | -1.31E-03 | 2.34E-01 | 1.24E-03 |
| 2.54E-01 | -2.71E+02 | 2.54E-01 | 2.11E+02 | 2.54E-01 | -1.32E-03 | 2.54E-01 | 1.23E-03 |
| 2.73E-01 | -2.74E+02 | 2.73E-01 | 2.09E+02 | 2.73E-01 | -1.33E-03 | 2.73E-01 | 1.22E-03 |
| 2.93E-01 | -2.71E+02 | 2.93E-01 | 2.03E+02 | 2.93E-01 | -1.31E-03 | 2.93E-01 | 1.19E-03 |
| 3.12E-01 | -2.64E+02 | 3.12E-01 | 1.96E+02 | 3.12E-01 | -1.27E-03 | 3.12E-01 | 1.15E-03 |
| 3.32E-01 | -2.56E+02 | 3.32E-01 | 1.89E+02 | 3.32E-01 | -1.24E-03 | 3.32E-01 | 1.10E-03 |
| 3.51E-01 | -2.47E+02 | 3.51E-01 | 1.81E+02 | 3.51E-01 | -1.20E-03 | 3.51E-01 | 1.05E-03 |
| 3.71E-01 | -2.11E+02 | 3.71E-01 | 1.50E+02 | 3.71E-01 | -1.01E-03 | 3.71E-01 | 8.79E-04 |
| 3.90E-01 | -1.75E+02 | 3.90E-01 | 1.20E+02 | 3.90E-01 | -8.19E-04 | 3.90E-01 | 7.05E-04 |
| 4.10E-01 | -1.38E+02 | 4.10E-01 | 9.05E+01 | 4.10E-01 | -6.30E-04 | 4.10E-01 | 5.31E-04 |
| 4.29E-01 | -1.06E+02 | 4.29E-01 | 6.63E+01 | 4.29E-01 | -4.67E-04 | 4.29E-01 | 4.04E-04 |
| 4.49E-01 | -7.95E+01 | 4.49E-01 | 4.81E+01 | 4.49E-01 | -3.32E-04 | 4.49E-01 | 3.31E-04 |
| 4.69E-01 | -5.26E+01 | 4.69E-01 | 3.38E+01 | 4.69E-01 | -1.97E-04 | 4.69E-01 | 2.57E-04 |
| 4.88E-01 | -2.57E+01 | 4.88E-01 | 2.97E+01 | 4.88E-01 | -6.28E-05 | 4.88E-01 | 1.84E-04 |
| 5.08E-01 | 7.90E-01 | 5.08E-01 | 3.89E+01 | 5.08E-01 | 7.01E-05 | 5.08E-01 | 2.58E-04 |
| 5.27E-01 | 2.73E+01 | 5.27E-01 | 5.51E+01 | 5.27E-01 | 2.03E-04 | 5.27E-01 | 3.50E-04 |
| 5.47E-01 | 5.37E+01 | 5.47E-01 | 7.37E+01 | 5.47E-01 | 3.35E-04 | 5.47E-01 | 4.43E-04 |
| 5.66E-01 | 8.14E+01 | 5.66E-01 | 9.46E+01 | 5.66E-01 | 4.75E-04 | 5.66E-01 | 5.51E-04 |
| 5.86E-01 | 1.12E+02 | 5.86E-01 | 1.19E+02 | 5.86E-01 | 6.30E-04 | 5.86E-01 | 6.93E-04 |
| 6.05E-01 | 1.43E+02 | 6.05E-01 | 1.43E+02 | 6.05E-01 | 7.86E-04 | 6.05E-01 | 8.34E-04 |
| 6.25E-01 | 1.73E+02 | 6.25E-01 | 1.68E+02 | 6.25E-01 | 9.41E-04 | 6.25E-01 | 9.76E-04 |
| 6.44E-01 | 1.90E+02 | 6.44E-01 | 1.80E+02 | 6.44E-01 | 1.02E-03 | 6.44E-01 | 1.05E-03 |

| | | | | | | | |
|---|---|---|---|---|---|---|---|
| 6.64E-01 | 2.00E+02 | 6.64E-01 | 1.88E+02 | 6.64E-01 | 1.07E-03 | 6.64E-01 | 1.09E-03 |
| 6.83E-01 | 2.10E+02 | 6.83E-01 | 1.96E+02 | 6.83E-01 | 1.12E-03 | 6.83E-01 | 1.14E-03 |
| 7.03E-01 | 2.20E+02 | 7.03E-01 | 2.03E+02 | 7.03E-01 | 1.16E-03 | 7.03E-01 | 1.18E-03 |
| 7.22E-01 | 2.24E+02 | 7.22E-01 | 2.05E+02 | 7.22E-01 | 1.17E-03 | 7.22E-01 | 1.19E-03 |
| 7.42E-01 | 2.28E+02 | 7.42E-01 | 2.07E+02 | 7.42E-01 | 1.19E-03 | 7.42E-01 | 1.20E-03 |
| 7.61E-01 | 2.32E+02 | 7.61E-01 | 2.09E+02 | 7.61E-01 | 1.20E-03 | 7.61E-01 | 1.22E-03 |
| 0.78083 | 2.35E+02 | 0.78083 | 2.11E+02 | 7.81E-01 | 1.21E-03 | 7.81E-01 | 1.22E-03 |
| 0.80035 | 2.37E+02 | 0.80035 | 2.12E+02 | 8.00E-01 | 1.22E-03 | 8.00E-01 | 1.23E-03 |
| 0.81988 | 2.40E+02 | 0.81988 | 2.13E+02 | 8.20E-01 | 1.22E-03 | 8.20E-01 | 1.24E-03 |
| 0.8394 | 2.42E+02 | 0.8394 | 2.14E+02 | 8.39E-01 | 1.23E-03 | 8.39E-01 | 1.24E-03 |
| 0.85892 | 2.44E+02 | 0.85892 | 2.15E+02 | 8.59E-01 | 1.23E-03 | 8.59E-01 | 1.25E-03 |
| 0.87844 | 2.45E+02 | 0.87844 | 2.15E+02 | 8.78E-01 | 1.24E-03 | 8.78E-01 | 1.25E-03 |
| 0.89796 | 2.47E+02 | 0.89796 | 2.16E+02 | 8.98E-01 | 1.24E-03 | 8.98E-01 | 1.25E-03 |
| 0.91748 | 5.60E+02 | 0.91748 | 4.97E+02 | 9.17E-01 | 2.95E-03 | 9.17E-01 | 2.89E-03 |
| 0.937 | 5.86E+02 | 0.937 | 5.20E+02 | 9.37E-01 | 3.09E-03 | 9.37E-01 | 3.03E-03 |

Table B-87 Stress and strain profiles across sample thickness for sample L-R-1, step 80%YS.

| **Normal Stress** | | **Equivalent Stress** | | **Normal Strain** | | **Equivalent Strain** | |
|---|---|---|---|---|---|---|---|
| Length | Stress | Length | Stress | Length | Stress | Length | Stress |
| 0.00E+00 | -2.45E+02 | 0.00E+00 | 2.15E+02 | 0.00E+00 | -1.26E-03 | 0.00E+00 | 1.25E-03 |
| 1.95E-02 | -2.46E+02 | 1.95E-02 | 2.15E+02 | 1.95E-02 | -1.26E-03 | 1.95E-02 | 1.25E-03 |
| 3.90E-02 | -2.47E+02 | 3.90E-02 | 2.16E+02 | 3.90E-02 | -1.26E-03 | 3.90E-02 | 1.25E-03 |
| 5.86E-02 | -2.47E+02 | 5.86E-02 | 2.16E+02 | 5.86E-02 | -1.26E-03 | 5.86E-02 | 1.26E-03 |
| 7.81E-02 | -2.48E+02 | 7.81E-02 | 2.17E+02 | 7.81E-02 | -1.26E-03 | 7.81E-02 | 1.26E-03 |
| 9.76E-02 | -2.49E+02 | 9.76E-02 | 2.17E+02 | 9.76E-02 | -1.26E-03 | 9.76E-02 | 1.26E-03 |
| 1.17E-01 | -2.51E+02 | 1.17E-01 | 2.18E+02 | 1.17E-01 | -1.27E-03 | 1.17E-01 | 1.27E-03 |
| 1.37E-01 | -2.52E+02 | 1.37E-01 | 2.18E+02 | 1.37E-01 | -1.27E-03 | 1.37E-01 | 1.27E-03 |
| 1.56E-01 | -2.56E+02 | 1.56E-01 | 2.18E+02 | 1.56E-01 | -1.28E-03 | 1.56E-01 | 1.27E-03 |
| 1.76E-01 | -2.61E+02 | 1.76E-01 | 2.19E+02 | 1.76E-01 | -1.29E-03 | 1.76E-01 | 1.27E-03 |
| 1.95E-01 | -2.65E+02 | 1.95E-01 | 2.19E+02 | 1.95E-01 | -1.30E-03 | 1.95E-01 | 1.27E-03 |
| 2.15E-01 | -2.70E+02 | 2.15E-01 | 2.18E+02 | 2.15E-01 | -1.31E-03 | 2.15E-01 | 1.27E-03 |
| 2.34E-01 | -2.76E+02 | 2.34E-01 | 2.17E+02 | 2.34E-01 | -1.33E-03 | 2.34E-01 | 1.26E-03 |
| 2.54E-01 | -2.82E+02 | 2.54E-01 | 2.15E+02 | 2.54E-01 | -1.34E-03 | 2.54E-01 | 1.25E-03 |

| | | | | | | | |
|---|---|---|---|---|---|---|---|
| 2.73E-01 | -2.87E+02 | 2.73E-01 | 2.14E+02 | 2.73E-01 | -1.36E-03 | 2.73E-01 | 1.25E-03 |
| 2.93E-01 | -2.89E+02 | 2.93E-01 | 2.12E+02 | 2.93E-01 | -1.36E-03 | 2.93E-01 | 1.24E-03 |
| 3.12E-01 | -2.88E+02 | 3.12E-01 | 2.09E+02 | 3.12E-01 | -1.37E-03 | 3.12E-01 | 1.23E-03 |
| 3.32E-01 | -2.88E+02 | 3.32E-01 | 2.08E+02 | 3.32E-01 | -1.37E-03 | 3.32E-01 | 1.22E-03 |
| 3.51E-01 | -2.85E+02 | 3.51E-01 | 2.05E+02 | 3.51E-01 | -1.36E-03 | 3.51E-01 | 1.19E-03 |
| 3.71E-01 | -2.45E+02 | 3.71E-01 | 1.72E+02 | 3.71E-01 | -1.16E-03 | 3.71E-01 | 1.00E-03 |
| 3.90E-01 | -2.04E+02 | 3.90E-01 | 1.39E+02 | 3.90E-01 | -9.51E-04 | 3.90E-01 | 8.15E-04 |
| 4.10E-01 | -1.64E+02 | 4.10E-01 | 1.06E+02 | 4.10E-01 | -7.45E-04 | 4.10E-01 | 6.25E-04 |
| 4.29E-01 | -1.28E+02 | 4.29E-01 | 7.92E+01 | 4.29E-01 | -5.61E-04 | 4.29E-01 | 4.81E-04 |
| 4.49E-01 | -9.53E+01 | 4.49E-01 | 5.72E+01 | 4.49E-01 | -4.00E-04 | 4.49E-01 | 3.89E-04 |
| 4.69E-01 | -6.29E+01 | 4.69E-01 | 3.92E+01 | 4.69E-01 | -2.39E-04 | 4.69E-01 | 2.97E-04 |
| 4.88E-01 | -3.05E+01 | 4.88E-01 | 3.30E+01 | 4.88E-01 | -7.87E-05 | 4.88E-01 | 2.05E-04 |
| 5.08E-01 | 1.05E+00 | 5.08E-01 | 4.36E+01 | 5.08E-01 | 7.85E-05 | 5.08E-01 | 2.91E-04 |
| 5.27E-01 | 3.25E+01 | 5.27E-01 | 6.27E+01 | 5.27E-01 | 2.35E-04 | 5.27E-01 | 4.01E-04 |
| 5.47E-01 | 6.39E+01 | 5.47E-01 | 8.48E+01 | 5.47E-01 | 3.92E-04 | 5.47E-01 | 5.11E-04 |
| 5.66E-01 | 9.61E+01 | 5.66E-01 | 1.09E+02 | 5.66E-01 | 5.53E-04 | 5.66E-01 | 6.35E-04 |
| 5.86E-01 | 1.30E+02 | 5.86E-01 | 1.36E+02 | 5.86E-01 | 7.24E-04 | 5.86E-01 | 7.92E-04 |
| 6.05E-01 | 1.64E+02 | 6.05E-01 | 1.63E+02 | 6.05E-01 | 8.96E-04 | 6.05E-01 | 9.49E-04 |
| 6.25E-01 | 1.98E+02 | 6.25E-01 | 1.90E+02 | 6.25E-01 | 1.07E-03 | 6.25E-01 | 1.11E-03 |
| 6.44E-01 | 2.11E+02 | 6.44E-01 | 2.00E+02 | 6.44E-01 | 1.13E-03 | 6.44E-01 | 1.16E-03 |
| 6.64E-01 | 2.15E+02 | 6.64E-01 | 2.02E+02 | 6.64E-01 | 1.14E-03 | 6.64E-01 | 1.18E-03 |
| 6.83E-01 | 2.20E+02 | 6.83E-01 | 2.05E+02 | 6.83E-01 | 1.16E-03 | 6.83E-01 | 1.19E-03 |
| 7.03E-01 | 2.24E+02 | 7.03E-01 | 2.07E+02 | 7.03E-01 | 1.17E-03 | 7.03E-01 | 1.20E-03 |
| 7.22E-01 | 2.28E+02 | 7.22E-01 | 2.09E+02 | 7.22E-01 | 1.19E-03 | 7.22E-01 | 1.21E-03 |
| 7.42E-01 | 2.32E+02 | 7.42E-01 | 2.11E+02 | 7.42E-01 | 1.20E-03 | 7.42E-01 | 1.22E-03 |
| 7.61E-01 | 2.35E+02 | 7.61E-01 | 2.12E+02 | 7.61E-01 | 1.21E-03 | 7.61E-01 | 1.24E-03 |
| 0.78083 | 2.38E+02 | 0.78083 | 2.14E+02 | 7.81E-01 | 1.22E-03 | 7.81E-01 | 1.24E-03 |
| 0.80035 | 2.40E+02 | 0.80035 | 2.14E+02 | 8.00E-01 | 1.22E-03 | 8.00E-01 | 1.25E-03 |
| 0.81988 | 2.43E+02 | 0.81988 | 2.15E+02 | 8.20E-01 | 1.23E-03 | 8.20E-01 | 1.25E-03 |
| 0.8394 | 2.45E+02 | 0.8394 | 2.16E+02 | 8.39E-01 | 1.23E-03 | 8.39E-01 | 1.26E-03 |
| 0.85892 | 2.46E+02 | 0.85892 | 2.16E+02 | 8.59E-01 | 1.24E-03 | 8.59E-01 | 1.26E-03 |
| 0.87844 | 2.48E+02 | 0.87844 | 2.17E+02 | 8.78E-01 | 1.24E-03 | 8.78E-01 | 1.26E-03 |
| 0.89796 | 2.49E+02 | 0.89796 | 2.18E+02 | 8.98E-01 | 1.25E-03 | 8.98E-01 | 1.26E-03 |
| 0.91748 | 6.40E+02 | 0.91748 | 5.69E+02 | 9.17E-01 | 3.37E-03 | 9.17E-01 | 3.31E-03 |
| 0.937 | 6.71E+02 | 0.937 | 5.96E+02 | 9.37E-01 | 3.53E-03 | 9.37E-01 | 3.46E-03 |

## Sample L-R-3

Table 0-88 Stress and strain profiles across sample thickness for sample L-R-3, step 50%YS.

| **Normal Stress** | | **Equivalent Stress** | | **Normal Strain** | | **Equivalent Strain** | |
|---|---|---|---|---|---|---|---|
| Length | Stress | Length | Stress | Length | Stress | Length | Stress |

| | | | | | | | |
|---|---|---|---|---|---|---|---|
| 0.00E+00 | -2.34E+02 | 0.00E+00 | 2.07E+02 | 0.00E+00 | -1.22E-03 | 0.00E+00 | 1.20E-03 |
| 1.88E-02 | -2.33E+02 | 1.88E-02 | 2.07E+02 | 1.88E-02 | -1.22E-03 | 1.88E-02 | 1.20E-03 |
| 3.75E-02 | -2.33E+02 | 3.75E-02 | 2.07E+02 | 3.75E-02 | -1.22E-03 | 3.75E-02 | 1.20E-03 |
| 5.63E-02 | -2.33E+02 | 5.63E-02 | 2.07E+02 | 5.63E-02 | -1.22E-03 | 5.63E-02 | 1.20E-03 |
| 7.50E-02 | -2.33E+02 | 7.50E-02 | 2.07E+02 | 7.50E-02 | -1.22E-03 | 7.50E-02 | 1.20E-03 |
| 9.38E-02 | -2.33E+02 | 9.38E-02 | 2.07E+02 | 9.38E-02 | -1.22E-03 | 9.38E-02 | 1.20E-03 |
| 1.13E-01 | -2.34E+02 | 1.13E-01 | 2.07E+02 | 1.13E-01 | -1.22E-03 | 1.13E-01 | 1.20E-03 |
| 1.31E-01 | -2.34E+02 | 1.31E-01 | 2.07E+02 | 1.31E-01 | -1.22E-03 | 1.31E-01 | 1.20E-03 |
| 1.50E-01 | -2.35E+02 | 1.50E-01 | 2.06E+02 | 1.50E-01 | -1.23E-03 | 1.50E-01 | 1.20E-03 |
| 1.69E-01 | -2.36E+02 | 1.69E-01 | 2.05E+02 | 1.69E-01 | -1.23E-03 | 1.69E-01 | 1.19E-03 |
| 1.88E-01 | -2.38E+02 | 1.88E-01 | 2.04E+02 | 1.88E-01 | -1.23E-03 | 1.88E-01 | 1.19E-03 |
| 2.06E-01 | -2.38E+02 | 2.06E-01 | 2.02E+02 | 2.06E-01 | -1.23E-03 | 2.06E-01 | 1.18E-03 |
| 2.25E-01 | -2.36E+02 | 2.25E-01 | 1.98E+02 | 2.25E-01 | -1.21E-03 | 2.25E-01 | 1.15E-03 |
| 2.44E-01 | -2.34E+02 | 2.44E-01 | 1.93E+02 | 2.44E-01 | -1.20E-03 | 2.44E-01 | 1.12E-03 |
| 2.63E-01 | -2.31E+02 | 2.63E-01 | 1.89E+02 | 2.63E-01 | -1.18E-03 | 2.63E-01 | 1.10E-03 |
| 2.81E-01 | -2.15E+02 | 2.81E-01 | 1.72E+02 | 2.81E-01 | -1.09E-03 | 2.81E-01 | 1.00E-03 |
| 3.00E-01 | -1.91E+02 | 3.00E-01 | 1.49E+02 | 3.00E-01 | -9.57E-04 | 3.00E-01 | 8.69E-04 |
| 3.19E-01 | -1.67E+02 | 3.19E-01 | 1.26E+02 | 3.19E-01 | -8.23E-04 | 3.19E-01 | 7.35E-04 |
| 3.38E-01 | -1.44E+02 | 3.38E-01 | 1.04E+02 | 3.38E-01 | -6.91E-04 | 3.38E-01 | 6.04E-04 |
| 3.56E-01 | -1.25E+02 | 3.56E-01 | 8.79E+01 | 3.56E-01 | -5.93E-04 | 3.56E-01 | 5.14E-04 |
| 3.75E-01 | -1.06E+02 | 3.75E-01 | 7.22E+01 | 3.75E-01 | -4.94E-04 | 3.75E-01 | 4.24E-04 |
| 3.94E-01 | -8.74E+01 | 3.94E-01 | 5.70E+01 | 3.94E-01 | -3.95E-04 | 3.94E-01 | 3.34E-04 |
| 4.13E-01 | -6.91E+01 | 4.13E-01 | 4.32E+01 | 4.13E-01 | -2.99E-04 | 4.13E-01 | 2.68E-04 |
| 4.31E-01 | -5.13E+01 | 4.31E-01 | 3.17E+01 | 4.31E-01 | -2.08E-04 | 4.31E-01 | 2.28E-04 |
| 4.50E-01 | -3.34E+01 | 4.50E-01 | 2.39E+01 | 4.50E-01 | -1.16E-04 | 4.50E-01 | 1.89E-04 |
| 4.69E-01 | -1.56E+01 | 4.69E-01 | 2.41E+01 | 4.69E-01 | -2.47E-05 | 4.69E-01 | 1.49E-04 |
| 4.88E-01 | 2.02E+00 | 4.88E-01 | 3.15E+01 | 4.88E-01 | 6.43E-05 | 4.88E-01 | 2.00E-04 |

| | | | | | | | |
|---|---|---|---|---|---|---|---|
| 5.06E-01 | 1.96E+01 | 5.06E-01 | 4.24E+01 | 5.06E-01 | 1.53E-04 | 5.06E-01 | 2.63E-04 |
| 5.25E-01 | 3.71E+01 | 5.25E-01 | 5.48E+01 | 5.25E-01 | 2.42E-04 | 5.25E-01 | 3.27E-04 |
| 5.44E-01 | 5.48E+01 | 5.44E-01 | 6.79E+01 | 5.44E-01 | 3.31E-04 | 5.44E-01 | 3.95E-04 |
| 5.63E-01 | 7.26E+01 | 5.63E-01 | 8.15E+01 | 5.63E-01 | 4.21E-04 | 5.63E-01 | 4.75E-04 |
| 5.81E-01 | 9.05E+01 | 5.81E-01 | 9.53E+01 | 5.81E-01 | 5.11E-04 | 5.81E-01 | 5.56E-04 |
| 6.00E-01 | 1.08E+02 | 6.00E-01 | 1.09E+02 | 6.00E-01 | 6.01E-04 | 6.00E-01 | 6.36E-04 |
| 6.19E-01 | 1.28E+02 | 6.19E-01 | 1.25E+02 | 6.19E-01 | 7.03E-04 | 6.19E-01 | 7.29E-04 |
| 6.38E-01 | 1.49E+02 | 6.38E-01 | 1.43E+02 | 6.38E-01 | 8.11E-04 | 6.38E-01 | 8.29E-04 |
| 6.56E-01 | 1.71E+02 | 6.56E-01 | 1.60E+02 | 6.56E-01 | 9.18E-04 | 6.56E-01 | 9.29E-04 |
| 6.75E-01 | 1.90E+02 | 6.75E-01 | 1.76E+02 | 6.75E-01 | 1.02E-03 | 6.75E-01 | 1.02E-03 |
| 6.94E-01 | 1.99E+02 | 6.94E-01 | 1.83E+02 | 6.94E-01 | 1.06E-03 | 6.94E-01 | 1.06E-03 |
| 7.13E-01 | 2.08E+02 | 7.13E-01 | 1.90E+02 | 7.13E-01 | 1.11E-03 | 7.13E-01 | 1.10E-03 |
| 7.31E-01 | 2.18E+02 | 7.31E-01 | 1.97E+02 | 7.31E-01 | 1.15E-03 | 7.31E-01 | 1.15E-03 |
| 0.75 | 2.23E+02 | 0.75 | 2.01E+02 | 7.50E-01 | 1.17E-03 | 7.50E-01 | 1.17E-03 |
| 0.76875 | 2.26E+02 | 0.76875 | 2.03E+02 | 7.69E-01 | 1.18E-03 | 7.69E-01 | 1.18E-03 |
| 0.7875 | 2.29E+02 | 0.7875 | 2.04E+02 | 7.88E-01 | 1.19E-03 | 7.88E-01 | 1.19E-03 |
| 0.80625 | 2.32E+02 | 0.80625 | 2.06E+02 | 8.06E-01 | 1.20E-03 | 8.06E-01 | 1.20E-03 |
| 0.825 | 2.34E+02 | 0.825 | 2.07E+02 | 8.25E-01 | 1.21E-03 | 8.25E-01 | 1.20E-03 |
| 0.84375 | 2.36E+02 | 0.84375 | 2.08E+02 | 8.44E-01 | 1.21E-03 | 8.44E-01 | 1.21E-03 |
| 0.8625 | 2.38E+02 | 0.8625 | 2.09E+02 | 8.63E-01 | 1.22E-03 | 8.63E-01 | 1.22E-03 |
| 0.88125 | 3.96E+02 | 0.88125 | 3.52E+02 | 8.81E-01 | 2.09E-03 | 8.81E-01 | 2.05E-03 |
| 0.9 | 4.15E+02 | 0.9 | 3.69E+02 | 9.00E-01 | 2.19E-03 | 9.00E-01 | 2.15E-03 |

Table B-89 Stress and strain profiles across sample thickness for sample L-R-3, step 60%YS.

| **Normal Stress** | | **Equivalent Stress** | | **Normal Strain** | | **Equivalent Strain** | |
|---|---|---|---|---|---|---|---|
| Length | Stress | Length | Stress | Length | Stress | Length | Stress |
| 0.00E+00 | -2.40E+02 | 0.00E+00 | 2.11E+02 | 0.00E+00 | -1.25E-03 | 0.00E+00 | 1.23E-03 |
| 1.88E-02 | -2.40E+02 | 1.88E-02 | 2.12E+02 | 1.88E-02 | -1.25E-03 | 1.88E-02 | 1.23E-03 |

| | | | | | | | |
|---|---|---|---|---|---|---|---|
| 3.75E-02 | -2.40E+02 | 3.75E-02 | 2.12E+02 | 3.75E-02 | -1.25E-03 | 3.75E-02 | 1.23E-03 |
| 5.63E-02 | -2.41E+02 | 5.63E-02 | 2.12E+02 | 5.63E-02 | -1.25E-03 | 5.63E-02 | 1.23E-03 |
| 7.50E-02 | -2.41E+02 | 7.50E-02 | 2.13E+02 | 7.50E-02 | -1.25E-03 | 7.50E-02 | 1.24E-03 |
| 9.38E-02 | -2.42E+02 | 9.38E-02 | 2.13E+02 | 9.38E-02 | -1.25E-03 | 9.38E-02 | 1.24E-03 |
| 1.13E-01 | -2.42E+02 | 1.13E-01 | 2.13E+02 | 1.13E-01 | -1.25E-03 | 1.13E-01 | 1.24E-03 |
| 1.31E-01 | -2.43E+02 | 1.31E-01 | 2.13E+02 | 1.31E-01 | -1.25E-03 | 1.31E-01 | 1.24E-03 |
| 1.50E-01 | -2.45E+02 | 1.50E-01 | 2.13E+02 | 1.50E-01 | -1.26E-03 | 1.50E-01 | 1.24E-03 |
| 1.69E-01 | -2.48E+02 | 1.69E-01 | 2.12E+02 | 1.69E-01 | -1.26E-03 | 1.69E-01 | 1.23E-03 |
| 1.88E-01 | -2.51E+02 | 1.88E-01 | 2.12E+02 | 1.88E-01 | -1.27E-03 | 1.88E-01 | 1.23E-03 |
| 2.06E-01 | -2.54E+02 | 2.06E-01 | 2.11E+02 | 2.06E-01 | -1.28E-03 | 2.06E-01 | 1.23E-03 |
| 2.25E-01 | -2.55E+02 | 2.25E-01 | 2.08E+02 | 2.25E-01 | -1.28E-03 | 2.25E-01 | 1.21E-03 |
| 2.44E-01 | -2.57E+02 | 2.44E-01 | 2.05E+02 | 2.44E-01 | -1.28E-03 | 2.44E-01 | 1.19E-03 |
| 2.63E-01 | -2.58E+02 | 2.63E-01 | 2.02E+02 | 2.63E-01 | -1.28E-03 | 2.63E-01 | 1.18E-03 |
| 2.81E-01 | -2.47E+02 | 2.81E-01 | 1.90E+02 | 2.81E-01 | -1.22E-03 | 2.81E-01 | 1.11E-03 |
| 3.00E-01 | -2.29E+02 | 3.00E-01 | 1.73E+02 | 3.00E-01 | -1.12E-03 | 3.00E-01 | 1.01E-03 |
| 3.19E-01 | -2.12E+02 | 3.19E-01 | 1.56E+02 | 3.19E-01 | -1.03E-03 | 3.19E-01 | 9.13E-04 |
| 3.38E-01 | -1.93E+02 | 3.38E-01 | 1.40E+02 | 3.38E-01 | -9.30E-04 | 3.38E-01 | 8.13E-04 |
| 3.56E-01 | -1.66E+02 | 3.56E-01 | 1.17E+02 | 3.56E-01 | -7.87E-04 | 3.56E-01 | 6.83E-04 |
| 3.75E-01 | -1.38E+02 | 3.75E-01 | 9.42E+01 | 3.75E-01 | -6.45E-04 | 3.75E-01 | 5.53E-04 |
| 3.94E-01 | -1.11E+02 | 3.94E-01 | 7.21E+01 | 3.94E-01 | -5.02E-04 | 3.94E-01 | 4.23E-04 |
| 4.13E-01 | -8.60E+01 | 4.13E-01 | 5.35E+01 | 4.13E-01 | -3.74E-04 | 4.13E-01 | 3.28E-04 |
| 4.31E-01 | -6.41E+01 | 4.31E-01 | 3.91E+01 | 4.31E-01 | -2.63E-04 | 4.31E-01 | 2.75E-04 |
| 4.50E-01 | -4.22E+01 | 4.50E-01 | 2.86E+01 | 4.50E-01 | -1.53E-04 | 4.50E-01 | 2.21E-04 |
| 4.69E-01 | -2.04E+01 | 4.69E-01 | 2.70E+01 | 4.69E-01 | -4.19E-05 | 4.69E-01 | 1.67E-04 |
| 4.88E-01 | 1.23E+00 | 4.88E-01 | 3.53E+01 | 4.88E-01 | 6.68E-05 | 4.88E-01 | 2.28E-04 |
| 5.06E-01 | 2.28E+01 | 5.06E-01 | 4.85E+01 | 5.06E-01 | 1.75E-04 | 5.06E-01 | 3.04E-04 |
| 5.25E-01 | 4.43E+01 | 5.25E-01 | 6.36E+01 | 5.25E-01 | 2.84E-04 | 5.25E-01 | 3.81E-04 |

| | | | | | | | |
|---|---|---|---|---|---|---|---|
| 5.44E-01 | 6.61E+01 | 5.44E-01 | 7.98E+01 | 5.44E-01 | 3.93E-04 | 5.44E-01 | 4.65E-04 |
| 5.63E-01 | 8.82E+01 | 5.63E-01 | 9.69E+01 | 5.63E-01 | 5.05E-04 | 5.63E-01 | 5.65E-04 |
| 5.81E-01 | 1.10E+02 | 5.81E-01 | 1.14E+02 | 5.81E-01 | 6.17E-04 | 5.81E-01 | 6.66E-04 |
| 6.00E-01 | 1.33E+02 | 6.00E-01 | 1.32E+02 | 6.00E-01 | 7.29E-04 | 6.00E-01 | 7.66E-04 |
| 6.19E-01 | 1.55E+02 | 6.19E-01 | 1.50E+02 | 6.19E-01 | 8.43E-04 | 6.19E-01 | 8.72E-04 |
| 6.38E-01 | 1.78E+02 | 6.38E-01 | 1.68E+02 | 6.38E-01 | 9.58E-04 | 6.38E-01 | 9.79E-04 |
| 6.56E-01 | 2.00E+02 | 6.56E-01 | 1.87E+02 | 6.56E-01 | 1.07E-03 | 6.56E-01 | 1.09E-03 |
| 6.75E-01 | 2.21E+02 | 6.75E-01 | 2.03E+02 | 6.75E-01 | 1.18E-03 | 6.75E-01 | 1.18E-03 |
| 6.94E-01 | 2.23E+02 | 6.94E-01 | 2.04E+02 | 6.94E-01 | 1.18E-03 | 6.94E-01 | 1.18E-03 |
| 7.13E-01 | 2.25E+02 | 7.13E-01 | 2.04E+02 | 7.13E-01 | 1.18E-03 | 7.13E-01 | 1.19E-03 |
| 7.31E-01 | 2.27E+02 | 7.31E-01 | 2.05E+02 | 7.31E-01 | 1.18E-03 | 7.31E-01 | 1.19E-03 |
| 0.75 | 2.29E+02 | 0.75 | 2.06E+02 | 7.50E-01 | 1.19E-03 | 7.50E-01 | 1.20E-03 |
| 0.76875 | 2.32E+02 | 0.76875 | 2.07E+02 | 7.69E-01 | 1.20E-03 | 7.69E-01 | 1.21E-03 |
| 0.7875 | 2.36E+02 | 0.7875 | 2.09E+02 | 7.88E-01 | 1.21E-03 | 7.88E-01 | 1.22E-03 |
| 0.80625 | 2.39E+02 | 0.80625 | 2.11E+02 | 8.06E-01 | 1.22E-03 | 8.06E-01 | 1.23E-03 |
| 0.825 | 2.40E+02 | 0.825 | 2.12E+02 | 8.25E-01 | 1.23E-03 | 8.25E-01 | 1.23E-03 |
| 0.84375 | 2.42E+02 | 0.84375 | 2.12E+02 | 8.44E-01 | 1.23E-03 | 8.44E-01 | 1.24E-03 |
| 0.8625 | 2.44E+02 | 0.8625 | 2.13E+02 | 8.63E-01 | 1.24E-03 | 8.63E-01 | 1.24E-03 |
| 0.88125 | 4.74E+02 | 0.88125 | 4.21E+02 | 8.81E-01 | 2.50E-03 | 8.81E-01 | 2.45E-03 |
| 0.9 | 4.97E+02 | 0.9 | 4.41E+02 | 9.00E-01 | 2.62E-03 | 9.00E-01 | 2.56E-03 |

Table 0-90 Stress and strain profiles across sample thickness for sample L-R-3, step 70%YS.

| **Normal Stress** | | **Equivalent Stress** | | **Normal Strain** | | **Equivalent Strain** | |
|---|---|---|---|---|---|---|---|
| Length | Stress | Length | Stress | Length | Stress | Length | Stress |
| 0.00E+00 | -2.43E+02 | 0.00E+00 | 2.13E+02 | 0.00E+00 | 1.24E-03 | 0.00E+00 | -1.26E-03 |
| 1.88E-02 | -2.44E+02 | 1.88E-02 | 2.14E+02 | 1.88E-02 | 1.24E-03 | 1.88E-02 | -1.26E-03 |
| 3.75E-02 | -2.44E+02 | 3.75E-02 | 2.14E+02 | 3.75E-02 | 1.24E-03 | 3.75E-02 | -1.26E-03 |
| 5.63E-02 | -2.45E+02 | 5.63E-02 | 2.14E+02 | 5.63E-02 | 1.25E-03 | 5.63E-02 | -1.26E-03 |

| | | | | | | | |
|---|---|---|---|---|---|---|---|
| 7.50E-02 | -2.45E+02 | 7.50E-02 | 2.15E+02 | 7.50E-02 | 1.25E-03 | 7.50E-02 | -1.26E-03 |
| 9.38E-02 | -2.46E+02 | 9.38E-02 | 2.15E+02 | 9.38E-02 | 1.25E-03 | 9.38E-02 | -1.26E-03 |
| 1.13E-01 | -2.47E+02 | 1.13E-01 | 2.15E+02 | 1.13E-01 | 1.25E-03 | 1.13E-01 | -1.26E-03 |
| 1.31E-01 | -2.48E+02 | 1.31E-01 | 2.16E+02 | 1.31E-01 | 1.25E-03 | 1.31E-01 | -1.26E-03 |
| 1.50E-01 | -2.52E+02 | 1.50E-01 | 2.16E+02 | 1.50E-01 | 1.26E-03 | 1.50E-01 | -1.27E-03 |
| 1.69E-01 | -2.56E+02 | 1.69E-01 | 2.16E+02 | 1.69E-01 | 1.26E-03 | 1.69E-01 | -1.28E-03 |
| 1.88E-01 | -2.60E+02 | 1.88E-01 | 2.16E+02 | 1.88E-01 | 1.25E-03 | 1.88E-01 | -1.29E-03 |
| 2.06E-01 | -2.65E+02 | 2.06E-01 | 2.15E+02 | 2.06E-01 | 1.25E-03 | 2.06E-01 | -1.30E-03 |
| 2.25E-01 | -2.68E+02 | 2.25E-01 | 2.13E+02 | 2.25E-01 | 1.24E-03 | 2.25E-01 | -1.31E-03 |
| 2.44E-01 | -2.72E+02 | 2.44E-01 | 2.11E+02 | 2.44E-01 | 1.23E-03 | 2.44E-01 | -1.32E-03 |
| 2.63E-01 | -2.76E+02 | 2.63E-01 | 2.09E+02 | 2.63E-01 | 1.22E-03 | 2.63E-01 | -1.33E-03 |
| 2.81E-01 | -2.72E+02 | 2.81E-01 | 2.03E+02 | 2.81E-01 | 1.19E-03 | 2.81E-01 | -1.31E-03 |
| 3.00E-01 | -2.64E+02 | 3.00E-01 | 1.95E+02 | 3.00E-01 | 1.14E-03 | 3.00E-01 | -1.27E-03 |
| 3.19E-01 | -2.56E+02 | 3.19E-01 | 1.88E+02 | 3.19E-01 | 1.10E-03 | 3.19E-01 | -1.24E-03 |
| 3.38E-01 | -2.47E+02 | 3.38E-01 | 1.80E+02 | 3.38E-01 | 1.05E-03 | 3.38E-01 | -1.19E-03 |
| 3.56E-01 | -2.11E+02 | 3.56E-01 | 1.50E+02 | 3.56E-01 | 8.74E-04 | 3.56E-01 | -1.00E-03 |
| 3.75E-01 | -1.75E+02 | 3.75E-01 | 1.20E+02 | 3.75E-01 | 7.01E-04 | 3.75E-01 | -8.16E-04 |
| 3.94E-01 | -1.38E+02 | 3.94E-01 | 9.01E+01 | 3.94E-01 | 5.28E-04 | 3.94E-01 | -6.28E-04 |
| 4.13E-01 | -1.07E+02 | 4.13E-01 | 6.60E+01 | 4.13E-01 | 4.03E-04 | 4.13E-01 | -4.65E-04 |
| 4.31E-01 | -7.96E+01 | 4.31E-01 | 4.80E+01 | 4.31E-01 | 3.31E-04 | 4.31E-01 | -3.31E-04 |
| 4.50E-01 | -5.27E+01 | 4.50E-01 | 3.40E+01 | 4.50E-01 | 2.60E-04 | 4.50E-01 | -1.96E-04 |
| 4.69E-01 | -2.58E+01 | 4.69E-01 | 3.03E+01 | 4.69E-01 | 1.88E-04 | 4.69E-01 | -6.16E-05 |
| 4.88E-01 | 7.23E-01 | 4.88E-01 | 3.95E+01 | 4.88E-01 | 2.60E-04 | 4.88E-01 | 7.10E-05 |
| 5.06E-01 | 2.72E+01 | 5.06E-01 | 5.55E+01 | 5.06E-01 | 3.53E-04 | 5.06E-01 | 2.03E-04 |
| 5.25E-01 | 5.36E+01 | 5.25E-01 | 7.41E+01 | 5.25E-01 | 4.45E-04 | 5.25E-01 | 3.35E-04 |
| 5.44E-01 | 8.12E+01 | 5.44E-01 | 9.48E+01 | 5.44E-01 | 5.52E-04 | 5.44E-01 | 4.74E-04 |
| 5.63E-01 | 1.12E+02 | 5.63E-01 | 1.19E+02 | 5.63E-01 | 6.94E-04 | 5.63E-01 | 6.30E-04 |

| | | | | | | | |
|---|---|---|---|---|---|---|---|
| 5.81E-01 | 1.43E+02 | 5.81E-01 | 1.43E+02 | 5.81E-01 | 8.35E-04 | 5.81E-01 | 7.86E-04 |
| 6.00E-01 | 1.73E+02 | 6.00E-01 | 1.68E+02 | 6.00E-01 | 9.77E-04 | 6.00E-01 | 9.41E-04 |
| 6.19E-01 | 1.90E+02 | 6.19E-01 | 1.81E+02 | 6.19E-01 | 1.05E-03 | 6.19E-01 | 1.02E-03 |
| 6.38E-01 | 2.00E+02 | 6.38E-01 | 1.88E+02 | 6.38E-01 | 1.09E-03 | 6.38E-01 | 1.07E-03 |
| 6.56E-01 | 2.10E+02 | 6.56E-01 | 1.96E+02 | 6.56E-01 | 1.14E-03 | 6.56E-01 | 1.12E-03 |
| 6.75E-01 | 2.20E+02 | 6.75E-01 | 2.03E+02 | 6.75E-01 | 1.18E-03 | 6.75E-01 | 1.16E-03 |
| 6.94E-01 | 2.24E+02 | 6.94E-01 | 2.05E+02 | 6.94E-01 | 1.19E-03 | 6.94E-01 | 1.17E-03 |
| 7.13E-01 | 2.28E+02 | 7.13E-01 | 2.07E+02 | 7.13E-01 | 1.20E-03 | 7.13E-01 | 1.19E-03 |
| 7.31E-01 | 2.32E+02 | 7.31E-01 | 2.09E+02 | 7.31E-01 | 1.22E-03 | 7.31E-01 | 1.20E-03 |
| 0.75 | 2.35E+02 | 0.75 | 2.11E+02 | 7.50E-01 | 1.22E-03 | 7.50E-01 | 1.21E-03 |
| 0.76875 | 2.37E+02 | 0.76875 | 2.12E+02 | 7.69E-01 | 1.23E-03 | 7.69E-01 | 1.22E-03 |
| 0.7875 | 2.40E+02 | 0.7875 | 2.13E+02 | 7.88E-01 | 1.24E-03 | 7.88E-01 | 1.22E-03 |
| 0.80625 | 2.42E+02 | 0.80625 | 2.14E+02 | 8.06E-01 | 1.24E-03 | 8.06E-01 | 1.23E-03 |
| 0.825 | 2.44E+02 | 0.825 | 2.15E+02 | 8.25E-01 | 1.25E-03 | 8.25E-01 | 1.23E-03 |
| 0.84375 | 2.45E+02 | 0.84375 | 2.15E+02 | 8.44E-01 | 1.25E-03 | 8.44E-01 | 1.24E-03 |
| 0.8625 | 2.47E+02 | 0.8625 | 2.16E+02 | 8.63E-01 | 1.25E-03 | 8.63E-01 | 1.24E-03 |
| 0.88125 | 5.60E+02 | 0.88125 | 4.97E+02 | 8.81E-01 | 2.89E-03 | 8.81E-01 | 2.95E-03 |
| 0.9 | 5.86E+02 | 0.9 | 5.20E+02 | 9.00E-01 | 3.02E-03 | 9.00E-01 | 3.09E-03 |

Table B-91 Stress and strain profiles across sample thickness for sample L-R-3, step 80%YS.

| **Normal Stress** | | **Equivalent Stress** | | **Normal Strain** | | **Equivalent Strain** | |
|---|---|---|---|---|---|---|---|
| Length | Stress | Length | Stress | Length | Stress | Length | Stress |
| 0.00E+00 | -2.45E+02 | 0.00E+00 | 2.14E+02 | 0.00E+00 | -1.26E-03 | 0.00E+00 | 1.25E-03 |
| 1.86E-02 | -2.46E+02 | 1.86E-02 | 2.15E+02 | 1.86E-02 | -1.26E-03 | 1.86E-02 | 1.25E-03 |
| 3.72E-02 | -2.46E+02 | 3.72E-02 | 2.16E+02 | 3.72E-02 | -1.26E-03 | 3.72E-02 | 1.25E-03 |
| 5.58E-02 | -2.47E+02 | 5.58E-02 | 2.16E+02 | 5.58E-02 | -1.26E-03 | 5.58E-02 | 1.26E-03 |
| 7.44E-02 | -2.48E+02 | 7.44E-02 | 2.17E+02 | 7.44E-02 | -1.26E-03 | 7.44E-02 | 1.26E-03 |
| 9.30E-02 | -2.49E+02 | 9.30E-02 | 2.17E+02 | 9.30E-02 | -1.26E-03 | 9.30E-02 | 1.26E-03 |

| | | | | | | | |
|---|---|---|---|---|---|---|---|
| 1.12E-01 | -2.51E+02 | 1.12E-01 | 2.18E+02 | 1.12E-01 | -1.27E-03 | 1.12E-01 | 1.27E-03 |
| 1.30E-01 | -2.52E+02 | 1.30E-01 | 2.18E+02 | 1.30E-01 | -1.27E-03 | 1.30E-01 | 1.27E-03 |
| 1.49E-01 | -2.57E+02 | 1.49E-01 | 2.19E+02 | 1.49E-01 | -1.28E-03 | 1.49E-01 | 1.27E-03 |
| 1.67E-01 | -2.62E+02 | 1.67E-01 | 2.19E+02 | 1.67E-01 | -1.29E-03 | 1.67E-01 | 1.27E-03 |
| 1.86E-01 | -2.67E+02 | 1.86E-01 | 2.19E+02 | 1.86E-01 | -1.30E-03 | 1.86E-01 | 1.27E-03 |
| 2.05E-01 | -2.72E+02 | 2.05E-01 | 2.19E+02 | 2.05E-01 | -1.31E-03 | 2.05E-01 | 1.27E-03 |
| 2.23E-01 | -2.77E+02 | 2.23E-01 | 2.17E+02 | 2.23E-01 | -1.33E-03 | 2.23E-01 | 1.26E-03 |
| 2.42E-01 | -2.83E+02 | 2.42E-01 | 2.15E+02 | 2.42E-01 | -1.35E-03 | 2.42E-01 | 1.25E-03 |
| 2.60E-01 | -2.89E+02 | 2.60E-01 | 2.14E+02 | 2.60E-01 | -1.36E-03 | 2.60E-01 | 1.25E-03 |
| 2.79E-01 | -2.90E+02 | 2.79E-01 | 2.12E+02 | 2.79E-01 | -1.37E-03 | 2.79E-01 | 1.24E-03 |
| 2.98E-01 | -2.90E+02 | 2.98E-01 | 2.09E+02 | 2.98E-01 | -1.37E-03 | 2.98E-01 | 1.22E-03 |
| 3.16E-01 | -2.89E+02 | 3.16E-01 | 2.07E+02 | 3.16E-01 | -1.37E-03 | 3.16E-01 | 1.21E-03 |
| 3.35E-01 | -2.86E+02 | 3.35E-01 | 2.05E+02 | 3.35E-01 | -1.36E-03 | 3.35E-01 | 1.19E-03 |
| 3.53E-01 | -2.45E+02 | 3.53E-01 | 1.71E+02 | 3.53E-01 | -1.16E-03 | 3.53E-01 | 1.00E-03 |
| 3.72E-01 | -2.05E+02 | 3.72E-01 | 1.38E+02 | 3.72E-01 | -9.50E-04 | 3.72E-01 | 8.12E-04 |
| 3.91E-01 | -1.64E+02 | 3.91E-01 | 1.06E+02 | 3.91E-01 | -7.44E-04 | 3.91E-01 | 6.22E-04 |
| 4.09E-01 | -1.28E+02 | 4.09E-01 | 7.88E+01 | 4.09E-01 | -5.59E-04 | 4.09E-01 | 4.79E-04 |
| 4.28E-01 | -9.52E+01 | 4.28E-01 | 5.70E+01 | 4.28E-01 | -3.98E-04 | 4.28E-01 | 3.89E-04 |
| 4.47E-01 | -6.28E+01 | 4.47E-01 | 3.94E+01 | 4.47E-01 | -2.38E-04 | 4.47E-01 | 2.99E-04 |
| 4.65E-01 | -3.04E+01 | 4.65E-01 | 3.36E+01 | 4.65E-01 | -7.69E-05 | 4.65E-01 | 2.10E-04 |
| 4.84E-01 | 1.19E+00 | 4.84E-01 | 4.43E+01 | 4.84E-01 | 8.05E-05 | 4.84E-01 | 2.95E-04 |
| 5.02E-01 | 3.27E+01 | 5.02E-01 | 6.34E+01 | 5.02E-01 | 2.37E-04 | 5.02E-01 | 4.05E-04 |
| 5.21E-01 | 6.42E+01 | 5.21E-01 | 8.55E+01 | 5.21E-01 | 3.94E-04 | 5.21E-01 | 5.15E-04 |
| 5.40E-01 | 9.64E+01 | 5.40E-01 | 1.10E+02 | 5.40E-01 | 5.55E-04 | 5.40E-01 | 6.38E-04 |
| 5.58E-01 | 1.30E+02 | 5.58E-01 | 1.36E+02 | 5.58E-01 | 7.27E-04 | 5.58E-01 | 7.95E-04 |
| 5.77E-01 | 1.64E+02 | 5.77E-01 | 1.63E+02 | 5.77E-01 | 8.98E-04 | 5.77E-01 | 9.52E-04 |
| 5.95E-01 | 1.98E+02 | 5.95E-01 | 1.91E+02 | 5.95E-01 | 1.07E-03 | 5.95E-01 | 1.11E-03 |

| | | | | | | | |
|---|---|---|---|---|---|---|---|
| 6.14E-01 | 2.11E+02 | 6.14E-01 | 2.00E+02 | 6.14E-01 | 1.13E-03 | 6.14E-01 | 1.17E-03 |
| 6.33E-01 | 2.16E+02 | 6.33E-01 | 2.03E+02 | 6.33E-01 | 1.15E-03 | 6.33E-01 | 1.18E-03 |
| 6.51E-01 | 2.20E+02 | 6.51E-01 | 2.05E+02 | 6.51E-01 | 1.16E-03 | 6.51E-01 | 1.19E-03 |
| 6.70E-01 | 2.24E+02 | 6.70E-01 | 2.07E+02 | 6.70E-01 | 1.17E-03 | 6.70E-01 | 1.20E-03 |
| 6.88E-01 | 2.28E+02 | 6.88E-01 | 2.09E+02 | 6.88E-01 | 1.19E-03 | 6.88E-01 | 1.21E-03 |
| 7.07E-01 | 2.32E+02 | 7.07E-01 | 2.11E+02 | 7.07E-01 | 1.20E-03 | 7.07E-01 | 1.22E-03 |
| 7.26E-01 | 2.35E+02 | 7.26E-01 | 2.13E+02 | 7.26E-01 | 1.21E-03 | 7.26E-01 | 1.24E-03 |
| 0.74417 | 2.38E+02 | 0.74417 | 2.14E+02 | 7.44E-01 | 1.22E-03 | 7.44E-01 | 1.24E-03 |
| 0.76277 | 2.40E+02 | 0.76277 | 2.15E+02 | 7.63E-01 | 1.22E-03 | 7.63E-01 | 1.25E-03 |
| 0.78137 | 2.43E+02 | 0.78137 | 2.15E+02 | 7.81E-01 | 1.23E-03 | 7.81E-01 | 1.25E-03 |
| 0.79998 | 2.45E+02 | 0.79998 | 2.16E+02 | 8.00E-01 | 1.23E-03 | 8.00E-01 | 1.26E-03 |
| 0.81858 | 2.46E+02 | 0.81858 | 2.17E+02 | 8.19E-01 | 1.24E-03 | 8.19E-01 | 1.26E-03 |
| 0.83719 | 2.48E+02 | 0.83719 | 2.17E+02 | 8.37E-01 | 1.24E-03 | 8.37E-01 | 1.26E-03 |
| 0.85579 | 2.49E+02 | 0.85579 | 2.18E+02 | 8.56E-01 | 1.25E-03 | 8.56E-01 | 1.27E-03 |
| 0.8744 | 6.42E+02 | 0.8744 | 5.70E+02 | 8.74E-01 | 3.38E-03 | 8.74E-01 | 3.31E-03 |
| 0.893 | 6.73E+02 | 0.893 | 5.97E+02 | 8.93E-01 | 3.54E-03 | 8.93E-01 | 3.47E-03 |

## Sample L-R-6

Table B-92 Stress and strain profiles across sample thickness for sample L-R-6, step 60%YS.

| **Normal Stress** | | **Equivalent Stress** | | **Normal Strain** | | **Equivalent Strain** | |
|---|---|---|---|---|---|---|---|
| Length | Stress | Length | Stress | Length | Stress | Length | Stress |
| 0.00E+00 | -2.40E+02 | 0.00E+00 | 2.11E+02 | 0.00E+00 | -1.25E-03 | 0.00E+00 | 1.23E-03 |
| 1.84E-02 | -2.41E+02 | 1.84E-02 | 2.12E+02 | 1.84E-02 | -1.25E-03 | 1.84E-02 | 1.23E-03 |
| 3.68E-02 | -2.41E+02 | 3.68E-02 | 2.12E+02 | 3.68E-02 | -1.25E-03 | 3.68E-02 | 1.23E-03 |
| 5.53E-02 | -2.42E+02 | 5.53E-02 | 2.13E+02 | 5.53E-02 | -1.25E-03 | 5.53E-02 | 1.24E-03 |
| 7.37E-02 | -2.42E+02 | 7.37E-02 | 2.13E+02 | 7.37E-02 | -1.25E-03 | 7.37E-02 | 1.24E-03 |
| 9.21E-02 | -2.43E+02 | 9.21E-02 | 2.13E+02 | 9.21E-02 | -1.25E-03 | 9.21E-02 | 1.24E-03 |
| 1.11E-01 | -2.44E+02 | 1.11E-01 | 2.13E+02 | 1.11E-01 | -1.25E-03 | 1.11E-01 | 1.24E-03 |

| | | | | | | | |
|---|---|---|---|---|---|---|---|
| 1.29E-01 | -2.45E+02 | 1.29E-01 | 2.13E+02 | 1.29E-01 | -1.25E-03 | 1.29E-01 | 1.24E-03 |
| 1.47E-01 | -2.47E+02 | 1.47E-01 | 2.13E+02 | 1.47E-01 | -1.26E-03 | 1.47E-01 | 1.24E-03 |
| 1.66E-01 | -2.50E+02 | 1.66E-01 | 2.12E+02 | 1.66E-01 | -1.27E-03 | 1.66E-01 | 1.23E-03 |
| 1.84E-01 | -2.52E+02 | 1.84E-01 | 2.11E+02 | 1.84E-01 | -1.27E-03 | 1.84E-01 | 1.23E-03 |
| 2.03E-01 | -2.55E+02 | 2.03E-01 | 2.10E+02 | 2.03E-01 | -1.28E-03 | 2.03E-01 | 1.22E-03 |
| 2.21E-01 | -2.55E+02 | 2.21E-01 | 2.07E+02 | 2.21E-01 | -1.28E-03 | 2.21E-01 | 1.21E-03 |
| 2.39E-01 | -2.56E+02 | 2.39E-01 | 2.04E+02 | 2.39E-01 | -1.28E-03 | 2.39E-01 | 1.19E-03 |
| 2.58E-01 | -2.57E+02 | 2.58E-01 | 2.02E+02 | 2.58E-01 | -1.28E-03 | 2.58E-01 | 1.18E-03 |
| 2.76E-01 | -2.46E+02 | 2.76E-01 | 1.90E+02 | 2.76E-01 | -1.22E-03 | 2.76E-01 | 1.11E-03 |
| 2.95E-01 | -2.29E+02 | 2.95E-01 | 1.74E+02 | 2.95E-01 | -1.12E-03 | 2.95E-01 | 1.02E-03 |
| 3.13E-01 | -2.12E+02 | 3.13E-01 | 1.58E+02 | 3.13E-01 | -1.03E-03 | 3.13E-01 | 9.22E-04 |
| 3.32E-01 | -1.94E+02 | 3.32E-01 | 1.42E+02 | 3.32E-01 | -9.39E-04 | 3.32E-01 | 8.25E-04 |
| 3.50E-01 | -1.66E+02 | 3.50E-01 | 1.19E+02 | 3.50E-01 | -7.96E-04 | 3.50E-01 | 6.94E-04 |
| 3.68E-01 | -1.39E+02 | 3.68E-01 | 9.59E+01 | 3.68E-01 | -6.53E-04 | 3.68E-01 | 5.62E-04 |
| 3.87E-01 | -1.12E+02 | 3.87E-01 | 7.36E+01 | 3.87E-01 | -5.10E-04 | 3.87E-01 | 4.31E-04 |
| 4.05E-01 | -8.66E+01 | 4.05E-01 | 5.44E+01 | 4.05E-01 | -3.81E-04 | 4.05E-01 | 3.34E-04 |
| 4.24E-01 | -6.45E+01 | 4.24E-01 | 3.92E+01 | 4.24E-01 | -2.69E-04 | 4.24E-01 | 2.75E-04 |
| 4.42E-01 | -4.23E+01 | 4.42E-01 | 2.76E+01 | 4.42E-01 | -1.56E-04 | 4.42E-01 | 2.17E-04 |
| 4.60E-01 | -2.01E+01 | 4.60E-01 | 2.52E+01 | 4.60E-01 | -4.40E-05 | 4.60E-01 | 1.58E-04 |
| 4.79E-01 | 1.81E+00 | 4.79E-01 | 3.38E+01 | 4.79E-01 | 6.68E-05 | 4.79E-01 | 2.22E-04 |
| 4.97E-01 | 2.37E+01 | 4.97E-01 | 4.76E+01 | 4.97E-01 | 1.77E-04 | 4.97E-01 | 3.01E-04 |
| 5.16E-01 | 4.57E+01 | 5.16E-01 | 6.34E+01 | 5.16E-01 | 2.88E-04 | 5.16E-01 | 3.80E-04 |
| 5.34E-01 | 6.78E+01 | 5.34E-01 | 8.01E+01 | 5.34E-01 | 4.00E-04 | 5.34E-01 | 4.67E-04 |
| 5.53E-01 | 9.03E+01 | 5.53E-01 | 9.77E+01 | 5.53E-01 | 5.14E-04 | 5.53E-01 | 5.70E-04 |
| 5.71E-01 | 1.13E+02 | 5.71E-01 | 1.16E+02 | 5.71E-01 | 6.28E-04 | 5.71E-01 | 6.74E-04 |
| 5.89E-01 | 1.35E+02 | 5.89E-01 | 1.34E+02 | 5.89E-01 | 7.43E-04 | 5.89E-01 | 7.77E-04 |
| 6.08E-01 | 1.58E+02 | 6.08E-01 | 1.52E+02 | 6.08E-01 | 8.57E-04 | 6.08E-01 | 8.83E-04 |

| | | | | | | | |
|---|---|---|---|---|---|---|---|
| 6.26E-01 | 1.80E+02 | 6.26E-01 | 1.70E+02 | 6.26E-01 | 9.71E-04 | 6.26E-01 | 9.90E-04 |
| 6.45E-01 | 2.03E+02 | 6.45E-01 | 1.89E+02 | 6.45E-01 | 1.09E-03 | 6.45E-01 | 1.10E-03 |
| 6.63E-01 | 2.23E+02 | 6.63E-01 | 2.05E+02 | 6.63E-01 | 1.19E-03 | 6.63E-01 | 1.19E-03 |
| 6.81E-01 | 2.24E+02 | 6.81E-01 | 2.05E+02 | 6.81E-01 | 1.19E-03 | 6.81E-01 | 1.19E-03 |
| 7.00E-01 | 2.26E+02 | 7.00E-01 | 2.05E+02 | 7.00E-01 | 1.19E-03 | 7.00E-01 | 1.19E-03 |
| 7.18E-01 | 2.27E+02 | 7.18E-01 | 2.05E+02 | 7.18E-01 | 1.19E-03 | 7.18E-01 | 1.19E-03 |
| 0.73667 | 2.30E+02 | 0.73667 | 2.06E+02 | 7.37E-01 | 1.19E-03 | 7.37E-01 | 1.20E-03 |
| 0.75508 | 2.33E+02 | 0.75508 | 2.08E+02 | 7.55E-01 | 1.20E-03 | 7.55E-01 | 1.21E-03 |
| 0.7735 | 2.36E+02 | 0.7735 | 2.10E+02 | 7.74E-01 | 1.21E-03 | 7.74E-01 | 1.22E-03 |
| 0.79192 | 2.39E+02 | 0.79192 | 2.11E+02 | 7.92E-01 | 1.23E-03 | 7.92E-01 | 1.23E-03 |
| 0.81033 | 2.41E+02 | 0.81033 | 2.12E+02 | 8.10E-01 | 1.23E-03 | 8.10E-01 | 1.23E-03 |
| 0.82875 | 2.42E+02 | 0.82875 | 2.13E+02 | 8.29E-01 | 1.23E-03 | 8.29E-01 | 1.24E-03 |
| 0.84717 | 2.44E+02 | 0.84717 | 2.13E+02 | 8.47E-01 | 1.24E-03 | 8.47E-01 | 1.24E-03 |
| 0.86558 | 4.81E+02 | 0.86558 | 4.28E+02 | 8.66E-01 | 2.54E-03 | 8.66E-01 | 2.49E-03 |
| 0.884 | 5.04E+02 | 0.884 | 4.48E+02 | 8.84E-01 | 2.66E-03 | 8.84E-01 | 2.61E-03 |

Table 0-93 Stress and strain profiles across sample thickness for sample L-R-6, step 70%YS.

| **Normal Stress** | | **Equivalent Stress** | | **Normal Strain** | | **Equivalent Strain** | |
|---|---|---|---|---|---|---|---|
| Length | Stress | Length | Stress | Length | Stress | Length | Stress |
| 0.00E+00 | -2.44E+02 | 0.00E+00 | 2.14E+02 | 0.00E+00 | 1.24E-03 | 0.00E+00 | 1.24E-03 |
| 1.84E-02 | -2.44E+02 | 1.84E-02 | 2.14E+02 | 1.84E-02 | 1.24E-03 | 1.84E-02 | 1.24E-03 |
| 3.68E-02 | -2.44E+02 | 3.68E-02 | 2.14E+02 | 3.68E-02 | 1.25E-03 | 3.68E-02 | 1.25E-03 |
| 5.53E-02 | -2.45E+02 | 5.53E-02 | 2.14E+02 | 5.53E-02 | 1.25E-03 | 5.53E-02 | 1.25E-03 |
| 7.37E-02 | -2.46E+02 | 7.37E-02 | 2.15E+02 | 7.37E-02 | 1.25E-03 | 7.37E-02 | 1.25E-03 |
| 9.21E-02 | -2.47E+02 | 9.21E-02 | 2.15E+02 | 9.21E-02 | 1.25E-03 | 9.21E-02 | 1.25E-03 |
| 1.11E-01 | -2.48E+02 | 1.11E-01 | 2.16E+02 | 1.11E-01 | 1.25E-03 | 1.11E-01 | 1.25E-03 |
| 1.29E-01 | -2.49E+02 | 1.29E-01 | 2.16E+02 | 1.29E-01 | 1.26E-03 | 1.29E-01 | 1.26E-03 |
| 1.47E-01 | -2.53E+02 | 1.47E-01 | 2.16E+02 | 1.47E-01 | 1.25E-03 | 1.47E-01 | 1.25E-03 |

| | | | | | | | |
|---|---|---|---|---|---|---|---|
| 1.66E-01 | -2.57E+02 | 1.66E-01 | 2.15E+02 | 1.66E-01 | 1.25E-03 | 1.66E-01 | 1.25E-03 |
| 1.84E-01 | -2.61E+02 | 1.84E-01 | 2.15E+02 | 1.84E-01 | 1.25E-03 | 1.84E-01 | 1.25E-03 |
| 2.03E-01 | -2.64E+02 | 2.03E-01 | 2.14E+02 | 2.03E-01 | 1.25E-03 | 2.03E-01 | 1.25E-03 |
| 2.21E-01 | -2.67E+02 | 2.21E-01 | 2.12E+02 | 2.21E-01 | 1.24E-03 | 2.21E-01 | 1.24E-03 |
| 2.39E-01 | -2.70E+02 | 2.39E-01 | 2.10E+02 | 2.39E-01 | 1.23E-03 | 2.39E-01 | 1.23E-03 |
| 2.58E-01 | -2.73E+02 | 2.58E-01 | 2.08E+02 | 2.58E-01 | 1.21E-03 | 2.58E-01 | 1.21E-03 |
| 2.76E-01 | -2.69E+02 | 2.76E-01 | 2.02E+02 | 2.76E-01 | 1.18E-03 | 2.76E-01 | 1.18E-03 |
| 2.95E-01 | -2.61E+02 | 2.95E-01 | 1.94E+02 | 2.95E-01 | 1.14E-03 | 2.95E-01 | 1.14E-03 |
| 3.13E-01 | -2.53E+02 | 3.13E-01 | 1.87E+02 | 3.13E-01 | 1.09E-03 | 3.13E-01 | 1.09E-03 |
| 3.32E-01 | -2.43E+02 | 3.32E-01 | 1.79E+02 | 3.32E-01 | 1.04E-03 | 3.32E-01 | 1.04E-03 |
| 3.50E-01 | -2.08E+02 | 3.50E-01 | 1.49E+02 | 3.50E-01 | 8.72E-04 | 3.50E-01 | 8.72E-04 |
| 3.68E-01 | -1.72E+02 | 3.68E-01 | 1.20E+02 | 3.68E-01 | 7.02E-04 | 3.68E-01 | 7.02E-04 |
| 3.87E-01 | -1.37E+02 | 3.87E-01 | 9.06E+01 | 3.87E-01 | 5.31E-04 | 3.87E-01 | 5.31E-04 |
| 4.05E-01 | -1.06E+02 | 4.05E-01 | 6.65E+01 | 4.05E-01 | 4.06E-04 | 4.05E-01 | 4.06E-04 |
| 4.24E-01 | -7.90E+01 | 4.24E-01 | 4.79E+01 | 4.24E-01 | 3.30E-04 | 4.24E-01 | 3.30E-04 |
| 4.42E-01 | -5.22E+01 | 4.42E-01 | 3.30E+01 | 4.42E-01 | 2.54E-04 | 4.42E-01 | 2.54E-04 |
| 4.60E-01 | -2.54E+01 | 4.60E-01 | 2.82E+01 | 4.60E-01 | 1.78E-04 | 4.60E-01 | 1.78E-04 |
| 4.79E-01 | 1.06E+00 | 4.79E-01 | 3.75E+01 | 4.79E-01 | 2.52E-04 | 4.79E-01 | 2.52E-04 |
| 4.97E-01 | 2.75E+01 | 4.97E-01 | 5.39E+01 | 4.97E-01 | 3.45E-04 | 4.97E-01 | 3.45E-04 |
| 5.16E-01 | 5.39E+01 | 5.16E-01 | 7.27E+01 | 5.16E-01 | 4.39E-04 | 5.16E-01 | 4.39E-04 |
| 5.34E-01 | 8.15E+01 | 5.34E-01 | 9.37E+01 | 5.34E-01 | 5.47E-04 | 5.34E-01 | 5.47E-04 |
| 5.53E-01 | 1.12E+02 | 5.53E-01 | 1.18E+02 | 5.53E-01 | 6.89E-04 | 5.53E-01 | 6.89E-04 |
| 5.71E-01 | 1.43E+02 | 5.71E-01 | 1.43E+02 | 5.71E-01 | 8.31E-04 | 5.71E-01 | 8.31E-04 |
| 5.89E-01 | 1.73E+02 | 5.89E-01 | 1.67E+02 | 5.89E-01 | 9.73E-04 | 5.89E-01 | 9.73E-04 |
| 6.08E-01 | 1.89E+02 | 6.08E-01 | 1.80E+02 | 6.08E-01 | 1.05E-03 | 6.08E-01 | 1.05E-03 |
| 6.26E-01 | 2.00E+02 | 6.26E-01 | 1.88E+02 | 6.26E-01 | 1.09E-03 | 6.26E-01 | 1.09E-03 |
| 6.45E-01 | 2.10E+02 | 6.45E-01 | 1.96E+02 | 6.45E-01 | 1.14E-03 | 6.45E-01 | 1.14E-03 |

| | | | | | | | |
|---|---|---|---|---|---|---|---|
| 6.63E-01 | 2.20E+02 | 6.63E-01 | 2.03E+02 | 6.63E-01 | 1.18E-03 | 6.63E-01 | 1.18E-03 |
| 6.81E-01 | 2.24E+02 | 6.81E-01 | 2.05E+02 | 6.81E-01 | 1.19E-03 | 6.81E-01 | 1.19E-03 |
| 7.00E-01 | 2.28E+02 | 7.00E-01 | 2.07E+02 | 7.00E-01 | 1.20E-03 | 7.00E-01 | 1.20E-03 |
| 7.18E-01 | 2.32E+02 | 7.18E-01 | 2.09E+02 | 7.18E-01 | 1.21E-03 | 7.18E-01 | 1.21E-03 |
| 0.73667 | 2.35E+02 | 0.73667 | 2.11E+02 | 7.37E-01 | 1.22E-03 | 7.37E-01 | 1.22E-03 |
| 0.75508 | 2.37E+02 | 0.75508 | 2.12E+02 | 7.55E-01 | 1.23E-03 | 7.55E-01 | 1.23E-03 |
| 0.7735 | 2.40E+02 | 0.7735 | 2.13E+02 | 7.74E-01 | 1.24E-03 | 7.74E-01 | 1.24E-03 |
| 0.79192 | 2.43E+02 | 0.79192 | 2.14E+02 | 7.92E-01 | 1.24E-03 | 7.92E-01 | 1.24E-03 |
| 0.81033 | 2.44E+02 | 0.81033 | 2.15E+02 | 8.10E-01 | 1.25E-03 | 8.10E-01 | 1.25E-03 |
| 0.82875 | 2.45E+02 | 0.82875 | 2.15E+02 | 8.29E-01 | 1.25E-03 | 8.29E-01 | 1.25E-03 |
| 0.84717 | 2.47E+02 | 0.84717 | 2.16E+02 | 8.47E-01 | 1.25E-03 | 8.47E-01 | 1.25E-03 |
| 0.86558 | 5.60E+02 | 0.86558 | 4.98E+02 | 8.66E-01 | 2.89E-03 | 8.66E-01 | 2.89E-03 |
| 0.884 | 5.86E+02 | 0.884 | 5.21E+02 | 8.84E-01 | 3.03E-03 | 8.84E-01 | 3.03E-03 |

## B.5 FEA sensitivity analysis

### SS 304LN

Table B-94 Surface stress profiles for reference.

| **Hardened Layer** | | | | **Soft Bulk** | | | |
|---|---|---|---|---|---|---|---|
| Longitudinal | | Transverse | | Longitudinal | | Transverse | |
| Length | Stress | Length | Stress | Length | Stress | Length | Stress |
| 0.00E+00 | 2.47E+00 | 0.00E+00 | 3.94E+02 | 0.00E+00 | 1.65E+00 | 0.00E+00 | 2.06E+02 |
| 1.04E-01 | 2.66E+00 | 7.29E-02 | 4.08E+02 | 1.04E-01 | 2.84E+00 | 7.29E-02 | 2.06E+02 |
| 2.08E-01 | 5.75E+00 | 1.46E-01 | 4.12E+02 | 2.08E-01 | 5.89E+00 | 1.46E-01 | 2.07E+02 |
| 3.13E-01 | 1.26E+01 | 2.19E-01 | 4.12E+02 | 3.13E-01 | 1.06E+01 | 2.19E-01 | 2.07E+02 |
| 4.17E-01 | 2.45E+01 | 2.92E-01 | 4.09E+02 | 4.17E-01 | 1.74E+01 | 2.92E-01 | 2.07E+02 |
| 5.21E-01 | 4.97E+01 | 3.65E-01 | 4.06E+02 | 5.21E-01 | 2.56E+01 | 3.65E-01 | 2.07E+02 |
| 6.25E-01 | 1.76E+02 | 4.38E-01 | 4.02E+02 | 6.25E-01 | 3.89E+01 | 4.38E-01 | 2.07E+02 |
| 7.29E-01 | 4.02E+02 | 5.10E-01 | 3.99E+02 | 7.29E-01 | 1.79E+02 | 5.10E-01 | 2.07E+02 |
| 8.33E-01 | 9.09E+01 | 5.83E-01 | 3.97E+02 | 8.33E-01 | 1.42E+02 | 5.83E-01 | 2.07E+02 |
| 9.38E-01 | 2.22E+01 | 6.56E-01 | 3.95E+02 | 9.38E-01 | 4.90E+01 | 6.56E-01 | 2.07E+02 |
| 1.04E+00 | 1.22E+01 | 7.29E-01 | 3.93E+02 | 1.04E+00 | 2.41E+01 | 7.29E-01 | 2.07E+02 |
| 1.15E+00 | 3.67E+01 | 8.02E-01 | 3.93E+02 | 1.15E+00 | 3.45E+01 | 8.02E-01 | 2.07E+02 |

| | | | | | | | |
|---|---|---|---|---|---|---|---|
| 1.25E+00 | 6.00E+01 | 8.75E-01 | 3.92E+02 | 1.25E+00 | 5.40E+01 | 8.75E-01 | 2.07E+02 |
| 1.35E+00 | 8.36E+01 | 9.48E-01 | 3.92E+02 | 1.35E+00 | 7.51E+01 | 9.48E-01 | 2.07E+02 |
| 1.46E+00 | 1.08E+02 | 1.02E+00 | 3.92E+02 | 1.46E+00 | 9.72E+01 | 1.02E+00 | 2.07E+02 |
| 1.56E+00 | 1.34E+02 | 1.09E+00 | 3.92E+02 | 1.56E+00 | 1.20E+02 | 1.09E+00 | 2.07E+02 |
| 1.67E+00 | 1.62E+02 | 1.17E+00 | 3.93E+02 | 1.67E+00 | 1.45E+02 | 1.17E+00 | 2.07E+02 |
| 1.77E+00 | 1.90E+02 | 1.24E+00 | 3.93E+02 | 1.77E+00 | 1.69E+02 | 1.24E+00 | 2.07E+02 |
| 1.88E+00 | 2.23E+02 | 1.31E+00 | 3.94E+02 | 1.88E+00 | 1.88E+02 | 1.31E+00 | 2.07E+02 |
| 1.98E+00 | 2.68E+02 | 1.39E+00 | 3.94E+02 | 1.98E+00 | 1.96E+02 | 1.39E+00 | 2.07E+02 |
| 2.08E+00 | 3.11E+02 | 1.46E+00 | 3.94E+02 | 2.08E+00 | 2.00E+02 | 1.46E+00 | 2.08E+02 |
| 2.19E+00 | 3.47E+02 | 1.53E+00 | 3.95E+02 | 2.19E+00 | 2.04E+02 | 1.53E+00 | 2.08E+02 |
| 2.29E+00 | 3.73E+02 | 1.60E+00 | 3.95E+02 | 2.29E+00 | 2.06E+02 | 1.60E+00 | 2.08E+02 |
| 2.40E+00 | 3.89E+02 | 1.68E+00 | 3.95E+02 | 2.40E+00 | 2.07E+02 | 1.68E+00 | 2.08E+02 |
| 2.50E+00 | 3.95E+02 | 1.75E+00 | 3.95E+02 | 2.50E+00 | 2.08E+02 | 1.75E+00 | 2.08E+02 |
| 2.60E+00 | 3.89E+02 | 1.82E+00 | 3.95E+02 | 2.60E+00 | 2.07E+02 | 1.82E+00 | 2.08E+02 |
| 2.71E+00 | 3.73E+02 | 1.90E+00 | 3.95E+02 | 2.71E+00 | 2.06E+02 | 1.90E+00 | 2.08E+02 |
| 2.81E+00 | 3.47E+02 | 1.97E+00 | 3.95E+02 | 2.81E+00 | 2.04E+02 | 1.97E+00 | 2.08E+02 |
| 2.92E+00 | 3.11E+02 | 2.04E+00 | 3.94E+02 | 2.92E+00 | 2.00E+02 | 2.04E+00 | 2.08E+02 |
| 3.02E+00 | 2.68E+02 | 2.11E+00 | 3.94E+02 | 3.02E+00 | 1.96E+02 | 2.11E+00 | 2.07E+02 |
| 3.13E+00 | 2.23E+02 | 2.19E+00 | 3.94E+02 | 3.13E+00 | 1.88E+02 | 2.19E+00 | 2.07E+02 |
| 3.23E+00 | 1.90E+02 | 2.26E+00 | 3.93E+02 | 3.23E+00 | 1.69E+02 | 2.26E+00 | 2.07E+02 |
| 3.33E+00 | 1.62E+02 | 2.33E+00 | 3.93E+02 | 3.33E+00 | 1.45E+02 | 2.33E+00 | 2.07E+02 |
| 3.44E+00 | 1.34E+02 | 2.41E+00 | 3.92E+02 | 3.44E+00 | 1.20E+02 | 2.41E+00 | 2.07E+02 |
| 3.54E+00 | 1.08E+02 | 2.48E+00 | 3.92E+02 | 3.54E+00 | 9.71E+01 | 2.48E+00 | 2.07E+02 |
| 3.65E+00 | 8.34E+01 | 2.55E+00 | 3.92E+02 | 3.65E+00 | 7.49E+01 | 2.55E+00 | 2.07E+02 |
| 3.75E+00 | 5.97E+01 | 2.63E+00 | 3.92E+02 | 3.75E+00 | 5.38E+01 | 2.63E+00 | 2.07E+02 |
| 3.85E+00 | 3.63E+01 | 2.70E+00 | 3.93E+02 | 3.85E+00 | 3.43E+01 | 2.70E+00 | 2.07E+02 |
| 3.96E+00 | 1.18E+01 | 2.77E+00 | 3.93E+02 | 3.96E+00 | 2.43E+01 | 2.77E+00 | 2.07E+02 |
| 4.06E+00 | 2.20E+01 | 2.84E+00 | 3.95E+02 | 4.06E+00 | 4.80E+01 | 2.84E+00 | 2.07E+02 |
| 4.1667 | 8.17E+01 | 2.9167 | 3.97E+02 | 4.17E+00 | 1.35E+02 | 2.92E+00 | 2.07E+02 |
| 4.2708 | 3.05E+02 | 2.9896 | 3.99E+02 | 4.27E+00 | 1.76E+02 | 2.99E+00 | 2.07E+02 |
| 4.375 | 1.93E+02 | 3.0625 | 4.02E+02 | 4.38E+00 | 3.88E+01 | 3.06E+00 | 2.07E+02 |
| 4.4792 | 4.58E+01 | 3.1354 | 4.05E+02 | 4.48E+00 | 2.53E+01 | 3.14E+00 | 2.07E+02 |
| 4.5833 | 2.39E+01 | 3.2083 | 4.09E+02 | 4.58E+00 | 1.76E+01 | 3.21E+00 | 2.07E+02 |
| 4.6875 | 1.26E+01 | 3.2813 | 4.12E+02 | 4.69E+00 | 1.08E+01 | 3.28E+00 | 2.07E+02 |
| 4.7917 | 6.02E+00 | 3.3542 | 4.12E+02 | 4.79E+00 | 6.10E+00 | 3.35E+00 | 2.07E+02 |
| 4.8958 | 3.11E+00 | 3.4271 | 4.08E+02 | 4.90E+00 | 3.14E+00 | 3.43E+00 | 2.06E+02 |
| 5 | 2.93E+00 | 3.5 | 3.94E+02 | 5.00E+00 | 2.07E+00 | 3.50E+00 | 2.06E+02 |

Table 0-95 Surface stress profiles for applied loading sensitivity.

| **Hardened Layer** | | **Soft Bulk** | |
|---|---|---|---|
| Longitudinal | Transverse | Longitudinal | Transverse |

| Length | Stress | Length | Stress | Length | Stress | Length | Stress |
|---|---|---|---|---|---|---|---|
| 0.00E+00 | 2.48E+00 | 0.00E+00 | 3.95E+02 | 0.00E+00 | 1.82E+00 | 0.00E+00 | 2.07E+02 |
| 1.04E-01 | 2.67E+00 | 7.29E-02 | 4.09E+02 | 1.04E-01 | 2.78E+00 | 7.29E-02 | 2.07E+02 |
| 2.08E-01 | 5.76E+00 | 1.46E-01 | 4.13E+02 | 2.08E-01 | 5.86E+00 | 1.46E-01 | 2.08E+02 |
| 3.13E-01 | 1.26E+01 | 2.19E-01 | 4.13E+02 | 3.13E-01 | 1.11E+01 | 2.19E-01 | 2.08E+02 |
| 4.17E-01 | 2.46E+01 | 2.92E-01 | 4.10E+02 | 4.17E-01 | 1.90E+01 | 2.92E-01 | 2.08E+02 |
| 5.21E-01 | 4.98E+01 | 3.65E-01 | 4.06E+02 | 5.21E-01 | 3.02E+01 | 3.65E-01 | 2.08E+02 |
| 6.25E-01 | 1.77E+02 | 4.38E-01 | 4.03E+02 | 6.25E-01 | 4.62E+01 | 4.38E-01 | 2.08E+02 |
| 7.29E-01 | 4.02E+02 | 5.10E-01 | 4.00E+02 | 7.29E-01 | 1.81E+02 | 5.10E-01 | 2.08E+02 |
| 8.33E-01 | 9.10E+01 | 5.83E-01 | 3.97E+02 | 8.33E-01 | 1.47E+02 | 5.83E-01 | 2.08E+02 |
| 9.38E-01 | 2.24E+01 | 6.56E-01 | 3.96E+02 | 9.38E-01 | 4.44E+01 | 6.56E-01 | 2.08E+02 |
| 1.04E+00 | 1.22E+01 | 7.29E-01 | 3.94E+02 | 1.04E+00 | 1.92E+01 | 7.29E-01 | 2.08E+02 |
| 1.15E+00 | 3.67E+01 | 8.02E-01 | 3.93E+02 | 1.15E+00 | 3.36E+01 | 8.02E-01 | 2.08E+02 |
| 1.25E+00 | 6.00E+01 | 8.75E-01 | 3.93E+02 | 1.25E+00 | 5.47E+01 | 8.75E-01 | 2.08E+02 |
| 1.35E+00 | 8.36E+01 | 9.48E-01 | 3.93E+02 | 1.35E+00 | 7.66E+01 | 9.48E-01 | 2.08E+02 |
| 1.46E+00 | 1.08E+02 | 1.02E+00 | 3.93E+02 | 1.46E+00 | 9.95E+01 | 1.02E+00 | 2.08E+02 |
| 1.56E+00 | 1.34E+02 | 1.09E+00 | 3.93E+02 | 1.56E+00 | 1.23E+02 | 1.09E+00 | 2.08E+02 |
| 1.67E+00 | 1.62E+02 | 1.17E+00 | 3.94E+02 | 1.67E+00 | 1.48E+02 | 1.17E+00 | 2.08E+02 |
| 1.77E+00 | 1.90E+02 | 1.24E+00 | 3.94E+02 | 1.77E+00 | 1.74E+02 | 1.24E+00 | 2.08E+02 |
| 1.88E+00 | 2.24E+02 | 1.31E+00 | 3.94E+02 | 1.88E+00 | 1.91E+02 | 1.31E+00 | 2.08E+02 |
| 1.98E+00 | 2.68E+02 | 1.39E+00 | 3.95E+02 | 1.98E+00 | 1.97E+02 | 1.39E+00 | 2.08E+02 |
| 2.08E+00 | 3.11E+02 | 1.46E+00 | 3.95E+02 | 2.08E+00 | 2.01E+02 | 1.46E+00 | 2.08E+02 |
| 2.19E+00 | 3.47E+02 | 1.53E+00 | 3.95E+02 | 2.19E+00 | 2.04E+02 | 1.53E+00 | 2.08E+02 |
| 2.29E+00 | 3.73E+02 | 1.60E+00 | 3.96E+02 | 2.29E+00 | 2.07E+02 | 1.60E+00 | 2.08E+02 |
| 2.40E+00 | 3.90E+02 | 1.68E+00 | 3.96E+02 | 2.40E+00 | 2.08E+02 | 1.68E+00 | 2.08E+02 |
| 2.50E+00 | 3.96E+02 | 1.75E+00 | 3.96E+02 | 2.50E+00 | 2.08E+02 | 1.75E+00 | 2.08E+02 |
| 2.60E+00 | 3.90E+02 | 1.82E+00 | 3.96E+02 | 2.60E+00 | 2.08E+02 | 1.82E+00 | 2.08E+02 |
| 2.71E+00 | 3.73E+02 | 1.90E+00 | 3.96E+02 | 2.71E+00 | 2.07E+02 | 1.90E+00 | 2.08E+02 |
| 2.81E+00 | 3.47E+02 | 1.97E+00 | 3.95E+02 | 2.81E+00 | 2.04E+02 | 1.97E+00 | 2.08E+02 |
| 2.92E+00 | 3.11E+02 | 2.04E+00 | 3.95E+02 | 2.92E+00 | 2.01E+02 | 2.04E+00 | 2.08E+02 |
| 3.02E+00 | 2.68E+02 | 2.11E+00 | 3.95E+02 | 3.02E+00 | 1.97E+02 | 2.11E+00 | 2.08E+02 |
| 3.13E+00 | 2.24E+02 | 2.19E+00 | 3.94E+02 | 3.13E+00 | 1.91E+02 | 2.19E+00 | 2.08E+02 |
| 3.23E+00 | 1.90E+02 | 2.26E+00 | 3.94E+02 | 3.23E+00 | 1.74E+02 | 2.26E+00 | 2.08E+02 |
| 3.33E+00 | 1.62E+02 | 2.33E+00 | 3.94E+02 | 3.33E+00 | 1.48E+02 | 2.33E+00 | 2.08E+02 |
| 3.44E+00 | 1.34E+02 | 2.41E+00 | 3.93E+02 | 3.44E+00 | 1.23E+02 | 2.41E+00 | 2.08E+02 |
| 3.54E+00 | 1.08E+02 | 2.48E+00 | 3.93E+02 | 3.54E+00 | 9.93E+01 | 2.48E+00 | 2.08E+02 |
| 3.65E+00 | 8.35E+01 | 2.55E+00 | 3.93E+02 | 3.65E+00 | 7.65E+01 | 2.55E+00 | 2.08E+02 |
| 3.75E+00 | 5.97E+01 | 2.63E+00 | 3.93E+02 | 3.75E+00 | 5.45E+01 | 2.63E+00 | 2.08E+02 |
| 3.85E+00 | 3.63E+01 | 2.70E+00 | 3.93E+02 | 3.85E+00 | 3.35E+01 | 2.70E+00 | 2.08E+02 |
| 3.96E+00 | 1.17E+01 | 2.77E+00 | 3.94E+02 | 3.96E+00 | 1.94E+01 | 2.77E+00 | 2.08E+02 |
| 4.06E+00 | 2.21E+01 | 2.84E+00 | 3.95E+02 | 4.06E+00 | 4.33E+01 | 2.84E+00 | 2.08E+02 |

| | | | | | | | |
|---|---|---|---|---|---|---|---|
| 4.1667 | 8.19E+01 | 2.9167 | 3.97E+02 | 4.17E+00 | 1.39E+02 | 2.92E+00 | 2.08E+02 |
| 4.2708 | 3.06E+02 | 2.9896 | 4.00E+02 | 4.27E+00 | 1.79E+02 | 2.99E+00 | 2.08E+02 |
| 4.375 | 1.93E+02 | 3.0625 | 4.03E+02 | 4.38E+00 | 4.67E+01 | 3.06E+00 | 2.08E+02 |
| 4.4792 | 4.58E+01 | 3.1354 | 4.06E+02 | 4.48E+00 | 2.99E+01 | 3.14E+00 | 2.08E+02 |
| 4.5833 | 2.39E+01 | 3.2083 | 4.10E+02 | 4.58E+00 | 1.91E+01 | 3.21E+00 | 2.08E+02 |
| 4.6875 | 1.27E+01 | 3.2813 | 4.13E+02 | 4.69E+00 | 1.13E+01 | 3.28E+00 | 2.08E+02 |
| 4.7917 | 6.03E+00 | 3.3542 | 4.13E+02 | 4.79E+00 | 6.10E+00 | 3.35E+00 | 2.08E+02 |
| 4.8958 | 3.12E+00 | 3.4271 | 4.09E+02 | 4.90E+00 | 3.12E+00 | 3.43E+00 | 2.07E+02 |
| 5 | 2.94E+00 | 3.5 | 3.95E+02 | 5.00E+00 | 2.25E+00 | 3.50E+00 | 2.07E+02 |

Table 0-96 Surface stress profiles for unirradiated bulk yield strength sensitivity.

| **Hardened Layer** | | | | **Soft Bulk** | | | |
|---|---|---|---|---|---|---|---|
| Longitudinal | | Transverse | | Longitudinal | | Transverse | |
| Length | Stress | Length | Stress | Length | Stress | Length | Stress |
| 0.00E+00 | 2.46E+00 | 0.00E+00 | 3.94E+02 | 0.00E+00 | 1.81E+00 | 0.00E+00 | 2.07E+02 |
| 1.04E-01 | 2.65E+00 | 7.29E-02 | 4.07E+02 | 1.04E-01 | 2.76E+00 | 7.29E-02 | 2.07E+02 |
| 2.08E-01 | 5.74E+00 | 1.46E-01 | 4.12E+02 | 2.08E-01 | 5.85E+00 | 1.46E-01 | 2.08E+02 |
| 3.13E-01 | 1.26E+01 | 2.19E-01 | 4.11E+02 | 3.13E-01 | 1.10E+01 | 2.19E-01 | 2.08E+02 |
| 4.17E-01 | 2.45E+01 | 2.92E-01 | 4.09E+02 | 4.17E-01 | 1.90E+01 | 2.92E-01 | 2.08E+02 |
| 5.21E-01 | 4.97E+01 | 3.65E-01 | 4.05E+02 | 5.21E-01 | 3.02E+01 | 3.65E-01 | 2.08E+02 |
| 6.25E-01 | 1.77E+02 | 4.38E-01 | 4.02E+02 | 6.25E-01 | 4.61E+01 | 4.38E-01 | 2.08E+02 |
| 7.29E-01 | 4.02E+02 | 5.10E-01 | 3.99E+02 | 7.29E-01 | 1.81E+02 | 5.10E-01 | 2.08E+02 |
| 8.33E-01 | 9.09E+01 | 5.83E-01 | 3.96E+02 | 8.33E-01 | 1.47E+02 | 5.83E-01 | 2.08E+02 |
| 9.38E-01 | 2.22E+01 | 6.56E-01 | 3.94E+02 | 9.38E-01 | 4.42E+01 | 6.56E-01 | 2.08E+02 |
| 1.04E+00 | 1.23E+01 | 7.29E-01 | 3.93E+02 | 1.04E+00 | 1.92E+01 | 7.29E-01 | 2.08E+02 |
| 1.15E+00 | 3.67E+01 | 8.02E-01 | 3.92E+02 | 1.15E+00 | 3.36E+01 | 8.02E-01 | 2.08E+02 |
| 1.25E+00 | 6.00E+01 | 8.75E-01 | 3.92E+02 | 1.25E+00 | 5.47E+01 | 8.75E-01 | 2.08E+02 |
| 1.35E+00 | 8.36E+01 | 9.48E-01 | 3.92E+02 | 1.35E+00 | 7.66E+01 | 9.48E-01 | 2.08E+02 |
| 1.46E+00 | 1.08E+02 | 1.02E+00 | 3.92E+02 | 1.46E+00 | 9.94E+01 | 1.02E+00 | 2.08E+02 |
| 1.56E+00 | 1.34E+02 | 1.09E+00 | 3.92E+02 | 1.56E+00 | 1.23E+02 | 1.09E+00 | 2.08E+02 |
| 1.67E+00 | 1.62E+02 | 1.17E+00 | 3.92E+02 | 1.67E+00 | 1.48E+02 | 1.17E+00 | 2.08E+02 |
| 1.77E+00 | 1.90E+02 | 1.24E+00 | 3.93E+02 | 1.77E+00 | 1.74E+02 | 1.24E+00 | 2.08E+02 |
| 1.88E+00 | 2.23E+02 | 1.31E+00 | 3.93E+02 | 1.88E+00 | 1.91E+02 | 1.31E+00 | 2.08E+02 |
| 1.98E+00 | 2.67E+02 | 1.39E+00 | 3.94E+02 | 1.98E+00 | 1.97E+02 | 1.39E+00 | 2.08E+02 |
| 2.08E+00 | 3.10E+02 | 1.46E+00 | 3.94E+02 | 2.08E+00 | 2.01E+02 | 1.46E+00 | 2.08E+02 |
| 2.19E+00 | 3.46E+02 | 1.53E+00 | 3.94E+02 | 2.19E+00 | 2.04E+02 | 1.53E+00 | 2.08E+02 |
| 2.29E+00 | 3.72E+02 | 1.60E+00 | 3.94E+02 | 2.29E+00 | 2.07E+02 | 1.60E+00 | 2.08E+02 |
| 2.40E+00 | 3.89E+02 | 1.68E+00 | 3.95E+02 | 2.40E+00 | 2.08E+02 | 1.68E+00 | 2.08E+02 |
| 2.50E+00 | 3.95E+02 | 1.75E+00 | 3.95E+02 | 2.50E+00 | 2.08E+02 | 1.75E+00 | 2.08E+02 |
| 2.60E+00 | 3.89E+02 | 1.82E+00 | 3.95E+02 | 2.60E+00 | 2.08E+02 | 1.82E+00 | 2.08E+02 |
| 2.71E+00 | 3.72E+02 | 1.90E+00 | 3.94E+02 | 2.71E+00 | 2.07E+02 | 1.90E+00 | 2.08E+02 |

| | | | | | | | |
|---|---|---|---|---|---|---|---|
| 2.81E+00 | 3.46E+02 | 1.97E+00 | 3.94E+02 | 2.81E+00 | 2.04E+02 | 1.97E+00 | 2.08E+02 |
| 2.92E+00 | 3.10E+02 | 2.04E+00 | 3.94E+02 | 2.92E+00 | 2.01E+02 | 2.04E+00 | 2.08E+02 |
| 3.02E+00 | 2.67E+02 | 2.11E+00 | 3.94E+02 | 3.02E+00 | 1.97E+02 | 2.11E+00 | 2.08E+02 |
| 3.13E+00 | 2.23E+02 | 2.19E+00 | 3.93E+02 | 3.13E+00 | 1.91E+02 | 2.19E+00 | 2.08E+02 |
| 3.23E+00 | 1.90E+02 | 2.26E+00 | 3.93E+02 | 3.23E+00 | 1.74E+02 | 2.26E+00 | 2.08E+02 |
| 3.33E+00 | 1.62E+02 | 2.33E+00 | 3.92E+02 | 3.33E+00 | 1.48E+02 | 2.33E+00 | 2.08E+02 |
| 3.44E+00 | 1.34E+02 | 2.41E+00 | 3.92E+02 | 3.44E+00 | 1.23E+02 | 2.41E+00 | 2.08E+02 |
| 3.54E+00 | 1.08E+02 | 2.48E+00 | 3.92E+02 | 3.54E+00 | 9.93E+01 | 2.48E+00 | 2.08E+02 |
| 3.65E+00 | 8.34E+01 | 2.55E+00 | 3.92E+02 | 3.65E+00 | 7.64E+01 | 2.55E+00 | 2.08E+02 |
| 3.75E+00 | 5.97E+01 | 2.63E+00 | 3.92E+02 | 3.75E+00 | 5.45E+01 | 2.63E+00 | 2.08E+02 |
| 3.85E+00 | 3.64E+01 | 2.70E+00 | 3.92E+02 | 3.85E+00 | 3.35E+01 | 2.70E+00 | 2.08E+02 |
| 3.96E+00 | 1.18E+01 | 2.77E+00 | 3.93E+02 | 3.96E+00 | 1.94E+01 | 2.77E+00 | 2.08E+02 |
| 4.06E+00 | 2.19E+01 | 2.84E+00 | 3.94E+02 | 4.06E+00 | 4.31E+01 | 2.84E+00 | 2.08E+02 |
| 4.1667 | 8.17E+01 | 2.9167 | 3.96E+02 | 4.17E+00 | 1.39E+02 | 2.92E+00 | 2.08E+02 |
| 4.2708 | 3.05E+02 | 2.9896 | 3.99E+02 | 4.27E+00 | 1.79E+02 | 2.99E+00 | 2.08E+02 |
| 4.375 | 1.93E+02 | 3.0625 | 4.02E+02 | 4.38E+00 | 4.67E+01 | 3.06E+00 | 2.08E+02 |
| 4.4792 | 4.57E+01 | 3.1354 | 4.05E+02 | 4.48E+00 | 2.98E+01 | 3.14E+00 | 2.08E+02 |
| 4.5833 | 2.39E+01 | 3.2083 | 4.09E+02 | 4.58E+00 | 1.91E+01 | 3.21E+00 | 2.08E+02 |
| 4.6875 | 1.26E+01 | 3.2813 | 4.11E+02 | 4.69E+00 | 1.12E+01 | 3.28E+00 | 2.08E+02 |
| 4.7917 | 6.02E+00 | 3.3542 | 4.12E+02 | 4.79E+00 | 6.09E+00 | 3.35E+00 | 2.08E+02 |
| 4.8958 | 3.10E+00 | 3.4271 | 4.07E+02 | 4.90E+00 | 3.10E+00 | 3.43E+00 | 2.07E+02 |
| 5 | 2.92E+00 | 3.5 | 3.94E+02 | 5.00E+00 | 2.23E+00 | 3.50E+00 | 2.07E+02 |

Table 0-97 Surface stress profiles for irradiated layer yield strength sensitivity.

| **Hardened Layer** | | | | **Soft Bulk** | | | |
|---|---|---|---|---|---|---|---|
| Longitudinal | | Transverse | | Longitudinal | | Transverse | |
| Length | Stress | Length | Stress | Length | Stress | Length | Stress |
| 0.00E+00 | 2.47E+00 | 0.00E+00 | 3.94E+02 | 0.00E+00 | 1.81E+00 | 0.00E+00 | 2.07E+02 |
| 1.04E-01 | 2.66E+00 | 7.29E-02 | 4.08E+02 | 1.04E-01 | 2.77E+00 | 7.29E-02 | 2.07E+02 |
| 2.08E-01 | 5.75E+00 | 1.46E-01 | 4.12E+02 | 2.08E-01 | 5.86E+00 | 1.46E-01 | 2.08E+02 |
| 3.13E-01 | 1.26E+01 | 2.19E-01 | 4.12E+02 | 3.13E-01 | 1.11E+01 | 2.19E-01 | 2.08E+02 |
| 4.17E-01 | 2.45E+01 | 2.92E-01 | 4.09E+02 | 4.17E-01 | 1.90E+01 | 2.92E-01 | 2.08E+02 |
| 5.21E-01 | 4.97E+01 | 3.65E-01 | 4.06E+02 | 5.21E-01 | 3.02E+01 | 3.65E-01 | 2.08E+02 |
| 6.25E-01 | 1.76E+02 | 4.38E-01 | 4.02E+02 | 6.25E-01 | 4.61E+01 | 4.38E-01 | 2.08E+02 |
| 7.29E-01 | 4.02E+02 | 5.10E-01 | 3.99E+02 | 7.29E-01 | 1.81E+02 | 5.10E-01 | 2.08E+02 |
| 8.33E-01 | 9.09E+01 | 5.83E-01 | 3.97E+02 | 8.33E-01 | 1.47E+02 | 5.83E-01 | 2.07E+02 |
| 9.38E-01 | 2.22E+01 | 6.56E-01 | 3.95E+02 | 9.38E-01 | 4.43E+01 | 6.56E-01 | 2.07E+02 |
| 1.04E+00 | 1.22E+01 | 7.29E-01 | 3.93E+02 | 1.04E+00 | 1.92E+01 | 7.29E-01 | 2.07E+02 |
| 1.15E+00 | 3.67E+01 | 8.02E-01 | 3.93E+02 | 1.15E+00 | 3.36E+01 | 8.02E-01 | 2.08E+02 |
| 1.25E+00 | 6.00E+01 | 8.75E-01 | 3.92E+02 | 1.25E+00 | 5.47E+01 | 8.75E-01 | 2.08E+02 |
| 1.35E+00 | 8.36E+01 | 9.48E-01 | 3.92E+02 | 1.35E+00 | 7.66E+01 | 9.48E-01 | 2.08E+02 |

| | | | | | | | |
|---|---|---|---|---|---|---|---|
| 1.46E+00 | 1.08E+02 | 1.02E+00 | 3.92E+02 | 1.46E+00 | 9.94E+01 | 1.02E+00 | 2.08E+02 |
| 1.56E+00 | 1.34E+02 | 1.09E+00 | 3.92E+02 | 1.56E+00 | 1.23E+02 | 1.09E+00 | 2.08E+02 |
| 1.67E+00 | 1.62E+02 | 1.17E+00 | 3.93E+02 | 1.67E+00 | 1.48E+02 | 1.17E+00 | 2.08E+02 |
| 1.77E+00 | 1.90E+02 | 1.24E+00 | 3.93E+02 | 1.77E+00 | 1.74E+02 | 1.24E+00 | 2.08E+02 |
| 1.88E+00 | 2.23E+02 | 1.31E+00 | 3.94E+02 | 1.88E+00 | 1.91E+02 | 1.31E+00 | 2.08E+02 |
| 1.98E+00 | 2.68E+02 | 1.39E+00 | 3.94E+02 | 1.98E+00 | 1.97E+02 | 1.39E+00 | 2.08E+02 |
| 2.08E+00 | 3.11E+02 | 1.46E+00 | 3.94E+02 | 2.08E+00 | 2.01E+02 | 1.46E+00 | 2.08E+02 |
| 2.19E+00 | 3.47E+02 | 1.53E+00 | 3.95E+02 | 2.19E+00 | 2.04E+02 | 1.53E+00 | 2.08E+02 |
| 2.29E+00 | 3.73E+02 | 1.60E+00 | 3.95E+02 | 2.29E+00 | 2.06E+02 | 1.60E+00 | 2.08E+02 |
| 2.40E+00 | 3.89E+02 | 1.68E+00 | 3.95E+02 | 2.40E+00 | 2.08E+02 | 1.68E+00 | 2.08E+02 |
| 2.50E+00 | 3.95E+02 | 1.75E+00 | 3.95E+02 | 2.50E+00 | 2.08E+02 | 1.75E+00 | 2.08E+02 |
| 2.60E+00 | 3.89E+02 | 1.82E+00 | 3.95E+02 | 2.60E+00 | 2.08E+02 | 1.82E+00 | 2.08E+02 |
| 2.71E+00 | 3.73E+02 | 1.90E+00 | 3.95E+02 | 2.71E+00 | 2.06E+02 | 1.90E+00 | 2.08E+02 |
| 2.81E+00 | 3.47E+02 | 1.97E+00 | 3.95E+02 | 2.81E+00 | 2.04E+02 | 1.97E+00 | 2.08E+02 |
| 2.92E+00 | 3.11E+02 | 2.04E+00 | 3.94E+02 | 2.92E+00 | 2.01E+02 | 2.04E+00 | 2.08E+02 |
| 3.02E+00 | 2.68E+02 | 2.11E+00 | 3.94E+02 | 3.02E+00 | 1.97E+02 | 2.11E+00 | 2.08E+02 |
| 3.13E+00 | 2.23E+02 | 2.19E+00 | 3.94E+02 | 3.13E+00 | 1.91E+02 | 2.19E+00 | 2.08E+02 |
| 3.23E+00 | 1.90E+02 | 2.26E+00 | 3.93E+02 | 3.23E+00 | 1.74E+02 | 2.26E+00 | 2.08E+02 |
| 3.33E+00 | 1.62E+02 | 2.33E+00 | 3.93E+02 | 3.33E+00 | 1.48E+02 | 2.33E+00 | 2.08E+02 |
| 3.44E+00 | 1.34E+02 | 2.41E+00 | 3.92E+02 | 3.44E+00 | 1.23E+02 | 2.41E+00 | 2.08E+02 |
| 3.54E+00 | 1.08E+02 | 2.48E+00 | 3.92E+02 | 3.54E+00 | 9.93E+01 | 2.48E+00 | 2.08E+02 |
| 3.65E+00 | 8.34E+01 | 2.55E+00 | 3.92E+02 | 3.65E+00 | 7.64E+01 | 2.55E+00 | 2.08E+02 |
| 3.75E+00 | 5.97E+01 | 2.63E+00 | 3.92E+02 | 3.75E+00 | 5.45E+01 | 2.63E+00 | 2.08E+02 |
| 3.85E+00 | 3.63E+01 | 2.70E+00 | 3.93E+02 | 3.85E+00 | 3.35E+01 | 2.70E+00 | 2.08E+02 |
| 3.96E+00 | 1.18E+01 | 2.77E+00 | 3.93E+02 | 3.96E+00 | 1.94E+01 | 2.77E+00 | 2.07E+02 |
| 4.06E+00 | 2.20E+01 | 2.84E+00 | 3.95E+02 | 4.06E+00 | 4.32E+01 | 2.84E+00 | 2.07E+02 |
| 4.1667 | 8.17E+01 | 2.9167 | 3.97E+02 | 4.17E+00 | 1.39E+02 | 2.92E+00 | 2.07E+02 |
| 4.2708 | 3.05E+02 | 2.9896 | 3.99E+02 | 4.27E+00 | 1.79E+02 | 2.99E+00 | 2.07E+02 |
| 4.375 | 1.93E+02 | 3.0625 | 4.02E+02 | 4.38E+00 | 4.67E+01 | 3.06E+00 | 2.08E+02 |
| 4.4792 | 4.58E+01 | 3.1354 | 4.05E+02 | 4.48E+00 | 2.98E+01 | 3.14E+00 | 2.08E+02 |
| 4.5833 | 2.39E+01 | 3.2083 | 4.09E+02 | 4.58E+00 | 1.91E+01 | 3.21E+00 | 2.08E+02 |
| 4.6875 | 1.26E+01 | 3.2813 | 4.12E+02 | 4.69E+00 | 1.12E+01 | 3.28E+00 | 2.08E+02 |
| 4.7917 | 6.02E+00 | 3.3542 | 4.12E+02 | 4.79E+00 | 6.09E+00 | 3.35E+00 | 2.08E+02 |
| 4.8958 | 3.11E+00 | 3.4271 | 4.08E+02 | 4.90E+00 | 3.11E+00 | 3.43E+00 | 2.07E+02 |
| 5 | 2.93E+00 | 3.5 | 3.94E+02 | 5.00E+00 | 2.24E+00 | 3.50E+00 | 2.07E+02 |

Table 0-98 Surface stress profiles for the sample thickness sensitivity.

| **Hardened Layer** | | | | **Soft Bulk** | | | |
|---|---|---|---|---|---|---|---|
| Longitudinal | | Transverse | | Longitudinal | | Transverse | |
| Length | Stress | Length | Stress | Length | Stress | Length | Stress |
| 0.00E+00 | 2.74E+00 | 0.00E+00 | 3.94E+02 | 0.00E+00 | 1.91E+00 | 0.00E+00 | 2.06E+02 |

| | | | | | | | |
|---|---|---|---|---|---|---|---|
| 1.04E-01 | 2.90E+00 | 7.29E-02 | 4.07E+02 | 1.04E-01 | 3.02E+00 | 7.29E-02 | 2.06E+02 |
| 2.08E-01 | 5.83E+00 | 1.46E-01 | 4.12E+02 | 2.08E-01 | 6.00E+00 | 1.46E-01 | 2.07E+02 |
| 3.13E-01 | 1.24E+01 | 2.19E-01 | 4.11E+02 | 3.13E-01 | 1.07E+01 | 2.19E-01 | 2.07E+02 |
| 4.17E-01 | 2.33E+01 | 2.92E-01 | 4.08E+02 | 4.17E-01 | 1.73E+01 | 2.92E-01 | 2.07E+02 |
| 5.21E-01 | 4.49E+01 | 3.65E-01 | 4.05E+02 | 5.21E-01 | 2.51E+01 | 3.65E-01 | 2.07E+02 |
| 6.25E-01 | 1.59E+02 | 4.38E-01 | 4.01E+02 | 6.25E-01 | 3.92E+01 | 4.38E-01 | 2.07E+02 |
| 7.29E-01 | 2.35E+02 | 5.10E-01 | 3.98E+02 | 7.29E-01 | 1.84E+02 | 5.10E-01 | 2.07E+02 |
| 8.33E-01 | 9.22E+01 | 5.83E-01 | 3.96E+02 | 8.33E-01 | 1.43E+02 | 5.83E-01 | 2.07E+02 |
| 9.38E-01 | 2.28E+01 | 6.56E-01 | 3.94E+02 | 9.38E-01 | 4.82E+01 | 6.56E-01 | 2.07E+02 |
| 1.04E+00 | 1.20E+01 | 7.29E-01 | 3.92E+02 | 1.04E+00 | 2.44E+01 | 7.29E-01 | 2.07E+02 |
| 1.15E+00 | 3.66E+01 | 8.02E-01 | 3.91E+02 | 1.15E+00 | 3.47E+01 | 8.02E-01 | 2.07E+02 |
| 1.25E+00 | 5.99E+01 | 8.75E-01 | 3.91E+02 | 1.25E+00 | 5.41E+01 | 8.75E-01 | 2.07E+02 |
| 1.35E+00 | 8.34E+01 | 9.48E-01 | 3.91E+02 | 1.35E+00 | 7.50E+01 | 9.48E-01 | 2.07E+02 |
| 1.46E+00 | 1.08E+02 | 1.02E+00 | 3.91E+02 | 1.46E+00 | 9.69E+01 | 1.02E+00 | 2.07E+02 |
| 1.56E+00 | 1.34E+02 | 1.09E+00 | 3.91E+02 | 1.56E+00 | 1.20E+02 | 1.09E+00 | 2.07E+02 |
| 1.67E+00 | 1.61E+02 | 1.17E+00 | 3.91E+02 | 1.67E+00 | 1.44E+02 | 1.17E+00 | 2.07E+02 |
| 1.77E+00 | 1.89E+02 | 1.24E+00 | 3.92E+02 | 1.77E+00 | 1.69E+02 | 1.24E+00 | 2.07E+02 |
| 1.88E+00 | 2.22E+02 | 1.31E+00 | 3.92E+02 | 1.88E+00 | 1.88E+02 | 1.31E+00 | 2.07E+02 |
| 1.98E+00 | 2.66E+02 | 1.39E+00 | 3.93E+02 | 1.98E+00 | 1.96E+02 | 1.39E+00 | 2.07E+02 |
| 2.08E+00 | 3.08E+02 | 1.46E+00 | 3.93E+02 | 2.08E+00 | 2.00E+02 | 1.46E+00 | 2.07E+02 |
| 2.19E+00 | 3.44E+02 | 1.53E+00 | 3.93E+02 | 2.19E+00 | 2.03E+02 | 1.53E+00 | 2.08E+02 |
| 2.29E+00 | 3.71E+02 | 1.60E+00 | 3.94E+02 | 2.29E+00 | 2.06E+02 | 1.60E+00 | 2.08E+02 |
| 2.40E+00 | 3.87E+02 | 1.68E+00 | 3.94E+02 | 2.40E+00 | 2.07E+02 | 1.68E+00 | 2.08E+02 |
| 2.50E+00 | 3.94E+02 | 1.75E+00 | 3.94E+02 | 2.50E+00 | 2.08E+02 | 1.75E+00 | 2.08E+02 |
| 2.60E+00 | 3.87E+02 | 1.82E+00 | 3.94E+02 | 2.60E+00 | 2.07E+02 | 1.82E+00 | 2.08E+02 |
| 2.71E+00 | 3.71E+02 | 1.90E+00 | 3.94E+02 | 2.71E+00 | 2.06E+02 | 1.90E+00 | 2.08E+02 |
| 2.81E+00 | 3.44E+02 | 1.97E+00 | 3.93E+02 | 2.81E+00 | 2.03E+02 | 1.97E+00 | 2.08E+02 |
| 2.92E+00 | 3.08E+02 | 2.04E+00 | 3.93E+02 | 2.92E+00 | 2.00E+02 | 2.04E+00 | 2.07E+02 |
| 3.02E+00 | 2.66E+02 | 2.11E+00 | 3.93E+02 | 3.02E+00 | 1.96E+02 | 2.11E+00 | 2.07E+02 |
| 3.13E+00 | 2.22E+02 | 2.19E+00 | 3.92E+02 | 3.13E+00 | 1.88E+02 | 2.19E+00 | 2.07E+02 |
| 3.23E+00 | 1.89E+02 | 2.26E+00 | 3.92E+02 | 3.23E+00 | 1.69E+02 | 2.26E+00 | 2.07E+02 |
| 3.33E+00 | 1.61E+02 | 2.33E+00 | 3.91E+02 | 3.33E+00 | 1.44E+02 | 2.33E+00 | 2.07E+02 |
| 3.44E+00 | 1.34E+02 | 2.41E+00 | 3.91E+02 | 3.44E+00 | 1.20E+02 | 2.41E+00 | 2.07E+02 |
| 3.54E+00 | 1.08E+02 | 2.48E+00 | 3.91E+02 | 3.54E+00 | 9.69E+01 | 2.48E+00 | 2.07E+02 |
| 3.65E+00 | 8.33E+01 | 2.55E+00 | 3.91E+02 | 3.65E+00 | 7.49E+01 | 2.55E+00 | 2.07E+02 |
| 3.75E+00 | 5.98E+01 | 2.63E+00 | 3.91E+02 | 3.75E+00 | 5.40E+01 | 2.63E+00 | 2.07E+02 |
| 3.85E+00 | 3.65E+01 | 2.70E+00 | 3.91E+02 | 3.85E+00 | 3.47E+01 | 2.70E+00 | 2.07E+02 |
| 3.96E+00 | 1.18E+01 | 2.77E+00 | 3.92E+02 | 3.96E+00 | 2.45E+01 | 2.77E+00 | 2.07E+02 |
| 4.06E+00 | 2.26E+01 | 2.84E+00 | 3.94E+02 | 4.06E+00 | 4.72E+01 | 2.84E+00 | 2.07E+02 |
| 4.1667 | 9.06E+01 | 2.9167 | 3.95E+02 | 4.17E+00 | 1.34E+02 | 2.92E+00 | 2.07E+02 |
| 4.2708 | 2.92E+02 | 2.9896 | 3.98E+02 | 4.27E+00 | 1.77E+02 | 2.99E+00 | 2.07E+02 |

| | | | | | | | |
|---|---|---|---|---|---|---|---|
| 4.375 | 1.70E+02 | 3.0625 | 4.01E+02 | 4.38E+00 | 3.63E+01 | 3.06E+00 | 2.07E+02 |
| 4.4792 | 4.36E+01 | 3.1354 | 4.05E+02 | 4.48E+00 | 2.47E+01 | 3.14E+00 | 2.07E+02 |
| 4.5833 | 2.30E+01 | 3.2083 | 4.08E+02 | 4.58E+00 | 1.72E+01 | 3.21E+00 | 2.07E+02 |
| 4.6875 | 1.23E+01 | 3.2813 | 4.11E+02 | 4.69E+00 | 1.07E+01 | 3.28E+00 | 2.07E+02 |
| 4.7917 | 5.89E+00 | 3.3542 | 4.12E+02 | 4.79E+00 | 6.04E+00 | 3.35E+00 | 2.07E+02 |
| 4.8958 | 3.05E+00 | 3.4271 | 4.07E+02 | 4.90E+00 | 3.11E+00 | 3.43E+00 | 2.06E+02 |
| 5 | 2.88E+00 | 3.5 | 3.93E+02 | 5.00E+00 | 2.03E+00 | 3.50E+00 | 2.06E+02 |

## SS 304L-R

Table B-99 Surface stress profiles for reference.

| **Hardened Layer** | | | | **Soft Bulk** | | | |
|---|---|---|---|---|---|---|---|
| Longitudinal | | Transverse | | Longitudinal | | Transverse | |
| Length | Stress | Length | Stress | Length | Stress | Length | Stress |
| 0.00E+00 | 4.22E+00 | 0.00E+00 | 4.91E+02 | 0.00E+00 | 3.21E+00 | 0.00E+00 | 1.83E+02 |
| 1.04E-01 | 4.30E+00 | 7.29E-02 | 5.11E+02 | 1.04E-01 | 4.00E+00 | 7.29E-02 | 1.83E+02 |
| 2.08E-01 | 6.82E+00 | 1.46E-01 | 5.20E+02 | 2.08E-01 | 6.67E+00 | 1.46E-01 | 1.83E+02 |
| 3.13E-01 | 1.34E+01 | 2.19E-01 | 5.21E+02 | 3.13E-01 | 1.14E+01 | 2.19E-01 | 1.84E+02 |
| 4.17E-01 | 2.57E+01 | 2.92E-01 | 5.18E+02 | 4.17E-01 | 1.87E+01 | 2.92E-01 | 1.84E+02 |
| 5.21E-01 | 5.26E+01 | 3.65E-01 | 5.13E+02 | 5.21E-01 | 2.86E+01 | 3.65E-01 | 1.84E+02 |
| 6.25E-01 | 1.69E+02 | 4.38E-01 | 5.09E+02 | 6.25E-01 | 3.27E+01 | 4.38E-01 | 1.84E+02 |
| 7.29E-01 | 3.69E+02 | 5.10E-01 | 5.04E+02 | 7.29E-01 | 1.64E+02 | 5.10E-01 | 1.84E+02 |
| 8.33E-01 | 8.78E+01 | 5.83E-01 | 5.01E+02 | 8.33E-01 | 1.47E+02 | 5.83E-01 | 1.84E+02 |
| 9.38E-01 | 4.00E+01 | 6.56E-01 | 4.98E+02 | 9.38E-01 | 5.98E+01 | 6.56E-01 | 1.84E+02 |
| 1.04E+00 | 5.55E+00 | 7.29E-01 | 4.96E+02 | 1.04E+00 | 2.70E+01 | 7.29E-01 | 1.84E+02 |
| 1.15E+00 | 3.10E+01 | 8.02E-01 | 4.95E+02 | 1.15E+00 | 3.14E+01 | 8.02E-01 | 1.84E+02 |
| 1.25E+00 | 5.53E+01 | 8.75E-01 | 4.94E+02 | 1.25E+00 | 5.03E+01 | 8.75E-01 | 1.84E+02 |
| 1.35E+00 | 7.96E+01 | 9.48E-01 | 4.93E+02 | 1.35E+00 | 7.17E+01 | 9.48E-01 | 1.84E+02 |
| 1.46E+00 | 1.05E+02 | 1.02E+00 | 4.93E+02 | 1.46E+00 | 9.44E+01 | 1.02E+00 | 1.84E+02 |
| 1.56E+00 | 1.32E+02 | 1.09E+00 | 4.94E+02 | 1.56E+00 | 1.19E+02 | 1.09E+00 | 1.84E+02 |
| 1.67E+00 | 1.63E+02 | 1.17E+00 | 4.94E+02 | 1.67E+00 | 1.44E+02 | 1.17E+00 | 1.84E+02 |
| 1.77E+00 | 2.11E+02 | 1.24E+00 | 4.95E+02 | 1.77E+00 | 1.58E+02 | 1.24E+00 | 1.84E+02 |
| 1.88E+00 | 2.74E+02 | 1.31E+00 | 4.95E+02 | 1.88E+00 | 1.68E+02 | 1.31E+00 | 1.84E+02 |
| 1.98E+00 | 3.33E+02 | 1.39E+00 | 4.96E+02 | 1.98E+00 | 1.75E+02 | 1.39E+00 | 1.84E+02 |
| 2.08E+00 | 3.87E+02 | 1.46E+00 | 4.96E+02 | 2.08E+00 | 1.80E+02 | 1.46E+00 | 1.84E+02 |
| 2.19E+00 | 4.35E+02 | 1.53E+00 | 4.96E+02 | 2.19E+00 | 1.82E+02 | 1.53E+00 | 1.84E+02 |
| 2.29E+00 | 4.69E+02 | 1.60E+00 | 4.97E+02 | 2.29E+00 | 1.84E+02 | 1.60E+00 | 1.84E+02 |
| 2.40E+00 | 4.90E+02 | 1.68E+00 | 4.97E+02 | 2.40E+00 | 1.84E+02 | 1.68E+00 | 1.84E+02 |
| 2.50E+00 | 4.97E+02 | 1.75E+00 | 4.97E+02 | 2.50E+00 | 1.84E+02 | 1.75E+00 | 1.84E+02 |
| 2.60E+00 | 4.90E+02 | 1.82E+00 | 4.97E+02 | 2.60E+00 | 1.84E+02 | 1.82E+00 | 1.84E+02 |
| 2.71E+00 | 4.69E+02 | 1.90E+00 | 4.97E+02 | 2.71E+00 | 1.84E+02 | 1.90E+00 | 1.84E+02 |

| | | | | | | | |
|---|---|---|---|---|---|---|---|
| 2.81E+00 | 4.35E+02 | 1.97E+00 | 4.96E+02 | 2.81E+00 | 1.82E+02 | 1.97E+00 | 1.84E+02 |
| 2.92E+00 | 3.87E+02 | 2.04E+00 | 4.96E+02 | 2.92E+00 | 1.80E+02 | 2.04E+00 | 1.84E+02 |
| 3.02E+00 | 3.33E+02 | 2.11E+00 | 4.96E+02 | 3.02E+00 | 1.75E+02 | 2.11E+00 | 1.84E+02 |
| 3.13E+00 | 2.74E+02 | 2.19E+00 | 4.95E+02 | 3.13E+00 | 1.68E+02 | 2.19E+00 | 1.84E+02 |
| 3.23E+00 | 2.11E+02 | 2.26E+00 | 4.95E+02 | 3.23E+00 | 1.58E+02 | 2.26E+00 | 1.84E+02 |
| 3.33E+00 | 1.63E+02 | 2.33E+00 | 4.94E+02 | 3.33E+00 | 1.44E+02 | 2.33E+00 | 1.84E+02 |
| 3.44E+00 | 1.32E+02 | 2.41E+00 | 4.94E+02 | 3.44E+00 | 1.18E+02 | 2.41E+00 | 1.84E+02 |
| 3.54E+00 | 1.05E+02 | 2.48E+00 | 4.93E+02 | 3.54E+00 | 9.42E+01 | 2.48E+00 | 1.84E+02 |
| 3.65E+00 | 7.93E+01 | 2.55E+00 | 4.93E+02 | 3.65E+00 | 7.15E+01 | 2.55E+00 | 1.84E+02 |
| 3.75E+00 | 5.49E+01 | 2.63E+00 | 4.94E+02 | 3.75E+00 | 5.01E+01 | 2.63E+00 | 1.84E+02 |
| 3.85E+00 | 3.04E+01 | 2.70E+00 | 4.95E+02 | 3.85E+00 | 3.12E+01 | 2.70E+00 | 1.84E+02 |
| 3.96E+00 | 5.81E+00 | 2.77E+00 | 4.96E+02 | 3.96E+00 | 2.74E+01 | 2.77E+00 | 1.84E+02 |
| 4.06E+00 | 3.90E+01 | 2.84E+00 | 4.98E+02 | 4.06E+00 | 5.88E+01 | 2.84E+00 | 1.84E+02 |
| 4.1667 | 7.50E+01 | 2.9167 | 5.01E+02 | 4.17E+00 | 1.42E+02 | 2.92E+00 | 1.84E+02 |
| 4.2708 | 3.12E+02 | 2.9896 | 5.04E+02 | 4.27E+00 | 1.65E+02 | 2.99E+00 | 1.84E+02 |
| 4.375 | 1.71E+02 | 3.0625 | 5.08E+02 | 4.38E+00 | 3.34E+01 | 3.06E+00 | 1.84E+02 |
| 4.4792 | 4.81E+01 | 3.1354 | 5.13E+02 | 4.48E+00 | 2.82E+01 | 3.14E+00 | 1.84E+02 |
| 4.5833 | 2.49E+01 | 3.2083 | 5.17E+02 | 4.58E+00 | 1.87E+01 | 3.21E+00 | 1.84E+02 |
| 4.6875 | 1.35E+01 | 3.2813 | 5.20E+02 | 4.69E+00 | 1.16E+01 | 3.28E+00 | 1.84E+02 |
| 4.7917 | 7.16E+00 | 3.3542 | 5.20E+02 | 4.79E+00 | 6.94E+00 | 3.35E+00 | 1.83E+02 |
| 4.8958 | 4.77E+00 | 3.4271 | 5.11E+02 | 4.90E+00 | 4.38E+00 | 3.43E+00 | 1.83E+02 |
| 5 | 4.70E+00 | 3.5 | 4.90E+02 | 5.00E+00 | 3.65E+00 | 3.50E+00 | 1.83E+02 |

Table 0-100 Surface stress profiles for applied loading sensitivity.

| **Hardened Layer** | | | | **Soft Bulk** | | | |
|---|---|---|---|---|---|---|---|
| Longitudinal | | Transverse | | Longitudinal | | Transverse | |
| Length | Stress | Length | Stress | Length | Stress | Length | Stress |
| 0.00E+00 | 4.24E+00 | 0.00E+00 | 4.92E+02 | 0.00E+00 | 3.23E+00 | 0.00E+00 | 1.83E+02 |
| 1.04E-01 | 4.31E+00 | 7.29E-02 | 5.12E+02 | 1.04E-01 | 4.02E+00 | 7.29E-02 | 1.83E+02 |
| 2.08E-01 | 6.83E+00 | 1.46E-01 | 5.21E+02 | 2.08E-01 | 6.68E+00 | 1.46E-01 | 1.84E+02 |
| 3.13E-01 | 1.34E+01 | 2.19E-01 | 5.22E+02 | 3.13E-01 | 1.14E+01 | 2.19E-01 | 1.84E+02 |
| 4.17E-01 | 2.57E+01 | 2.92E-01 | 5.19E+02 | 4.17E-01 | 1.87E+01 | 2.92E-01 | 1.84E+02 |
| 5.21E-01 | 5.26E+01 | 3.65E-01 | 5.14E+02 | 5.21E-01 | 2.87E+01 | 3.65E-01 | 1.84E+02 |
| 6.25E-01 | 1.69E+02 | 4.38E-01 | 5.10E+02 | 6.25E-01 | 3.28E+01 | 4.38E-01 | 1.84E+02 |
| 7.29E-01 | 3.69E+02 | 5.10E-01 | 5.06E+02 | 7.29E-01 | 1.64E+02 | 5.10E-01 | 1.84E+02 |
| 8.33E-01 | 8.79E+01 | 5.83E-01 | 5.02E+02 | 8.33E-01 | 1.47E+02 | 5.83E-01 | 1.84E+02 |
| 9.38E-01 | 4.02E+01 | 6.56E-01 | 4.99E+02 | 9.38E-01 | 6.00E+01 | 6.56E-01 | 1.84E+02 |
| 1.04E+00 | 5.51E+00 | 7.29E-01 | 4.97E+02 | 1.04E+00 | 2.71E+01 | 7.29E-01 | 1.84E+02 |
| 1.15E+00 | 3.09E+01 | 8.02E-01 | 4.96E+02 | 1.15E+00 | 3.14E+01 | 8.02E-01 | 1.84E+02 |
| 1.25E+00 | 5.53E+01 | 8.75E-01 | 4.95E+02 | 1.25E+00 | 5.03E+01 | 8.75E-01 | 1.84E+02 |
| 1.35E+00 | 7.96E+01 | 9.48E-01 | 4.95E+02 | 1.35E+00 | 7.17E+01 | 9.48E-01 | 1.84E+02 |

| | | | | | | | |
|---|---|---|---|---|---|---|---|
| 1.46E+00 | 1.05E+02 | 1.02E+00 | 4.95E+02 | 1.46E+00 | 9.44E+01 | 1.02E+00 | 1.84E+02 |
| 1.56E+00 | 1.32E+02 | 1.09E+00 | 4.95E+02 | 1.56E+00 | 1.19E+02 | 1.09E+00 | 1.84E+02 |
| 1.67E+00 | 1.63E+02 | 1.17E+00 | 4.95E+02 | 1.67E+00 | 1.44E+02 | 1.17E+00 | 1.84E+02 |
| 1.77E+00 | 2.12E+02 | 1.24E+00 | 4.96E+02 | 1.77E+00 | 1.58E+02 | 1.24E+00 | 1.84E+02 |
| 1.88E+00 | 2.75E+02 | 1.31E+00 | 4.96E+02 | 1.88E+00 | 1.68E+02 | 1.31E+00 | 1.84E+02 |
| 1.98E+00 | 3.34E+02 | 1.39E+00 | 4.97E+02 | 1.98E+00 | 1.75E+02 | 1.39E+00 | 1.84E+02 |
| 2.08E+00 | 3.88E+02 | 1.46E+00 | 4.97E+02 | 2.08E+00 | 1.80E+02 | 1.46E+00 | 1.84E+02 |
| 2.19E+00 | 4.36E+02 | 1.53E+00 | 4.98E+02 | 2.19E+00 | 1.82E+02 | 1.53E+00 | 1.84E+02 |
| 2.29E+00 | 4.71E+02 | 1.60E+00 | 4.98E+02 | 2.29E+00 | 1.84E+02 | 1.60E+00 | 1.84E+02 |
| 2.40E+00 | 4.92E+02 | 1.68E+00 | 4.98E+02 | 2.40E+00 | 1.84E+02 | 1.68E+00 | 1.84E+02 |
| 2.50E+00 | 4.98E+02 | 1.75E+00 | 4.98E+02 | 2.50E+00 | 1.84E+02 | 1.75E+00 | 1.84E+02 |
| 2.60E+00 | 4.92E+02 | 1.82E+00 | 4.98E+02 | 2.60E+00 | 1.84E+02 | 1.82E+00 | 1.84E+02 |
| 2.71E+00 | 4.71E+02 | 1.90E+00 | 4.98E+02 | 2.71E+00 | 1.84E+02 | 1.90E+00 | 1.84E+02 |
| 2.81E+00 | 4.36E+02 | 1.97E+00 | 4.98E+02 | 2.81E+00 | 1.82E+02 | 1.97E+00 | 1.84E+02 |
| 2.92E+00 | 3.88E+02 | 2.04E+00 | 4.97E+02 | 2.92E+00 | 1.80E+02 | 2.04E+00 | 1.84E+02 |
| 3.02E+00 | 3.34E+02 | 2.11E+00 | 4.97E+02 | 3.02E+00 | 1.75E+02 | 2.11E+00 | 1.84E+02 |
| 3.13E+00 | 2.75E+02 | 2.19E+00 | 4.96E+02 | 3.13E+00 | 1.68E+02 | 2.19E+00 | 1.84E+02 |
| 3.23E+00 | 2.11E+02 | 2.26E+00 | 4.96E+02 | 3.23E+00 | 1.58E+02 | 2.26E+00 | 1.84E+02 |
| 3.33E+00 | 1.63E+02 | 2.33E+00 | 4.95E+02 | 3.33E+00 | 1.44E+02 | 2.33E+00 | 1.84E+02 |
| 3.44E+00 | 1.32E+02 | 2.41E+00 | 4.95E+02 | 3.44E+00 | 1.18E+02 | 2.41E+00 | 1.84E+02 |
| 3.54E+00 | 1.05E+02 | 2.48E+00 | 4.95E+02 | 3.54E+00 | 9.43E+01 | 2.48E+00 | 1.84E+02 |
| 3.65E+00 | 7.93E+01 | 2.55E+00 | 4.95E+02 | 3.65E+00 | 7.15E+01 | 2.55E+00 | 1.84E+02 |
| 3.75E+00 | 5.49E+01 | 2.63E+00 | 4.95E+02 | 3.75E+00 | 5.01E+01 | 2.63E+00 | 1.84E+02 |
| 3.85E+00 | 3.04E+01 | 2.70E+00 | 4.96E+02 | 3.85E+00 | 3.12E+01 | 2.70E+00 | 1.84E+02 |
| 3.96E+00 | 5.79E+00 | 2.77E+00 | 4.97E+02 | 3.96E+00 | 2.75E+01 | 2.77E+00 | 1.84E+02 |
| 4.06E+00 | 3.92E+01 | 2.84E+00 | 4.99E+02 | 4.06E+00 | 5.89E+01 | 2.84E+00 | 1.84E+02 |
| 4.1667 | 7.50E+01 | 2.9167 | 5.02E+02 | 4.17E+00 | 1.42E+02 | 2.92E+00 | 1.84E+02 |
| 4.2708 | 3.13E+02 | 2.9896 | 5.05E+02 | 4.27E+00 | 1.65E+02 | 2.99E+00 | 1.84E+02 |
| 4.375 | 1.72E+02 | 3.0625 | 5.10E+02 | 4.38E+00 | 3.34E+01 | 3.06E+00 | 1.84E+02 |
| 4.4792 | 4.82E+01 | 3.1354 | 5.14E+02 | 4.48E+00 | 2.82E+01 | 3.14E+00 | 1.84E+02 |
| 4.5833 | 2.50E+01 | 3.2083 | 5.19E+02 | 4.58E+00 | 1.87E+01 | 3.21E+00 | 1.84E+02 |
| 4.6875 | 1.35E+01 | 3.2813 | 5.22E+02 | 4.69E+00 | 1.16E+01 | 3.28E+00 | 1.84E+02 |
| 4.7917 | 7.18E+00 | 3.3542 | 5.21E+02 | 4.79E+00 | 6.95E+00 | 3.35E+00 | 1.84E+02 |
| 4.8958 | 4.79E+00 | 3.4271 | 5.12E+02 | 4.90E+00 | 4.39E+00 | 3.43E+00 | 1.83E+02 |
| 5 | 4.72E+00 | 3.5 | 4.92E+02 | 5.00E+00 | 3.66E+00 | 3.50E+00 | 1.83E+02 |

Table 0-101 Surface stress profiles for unirradiated bulk yield strength sensitivity.

| **Hardened Layer** | | | | **Soft Bulk** | | | |
|---|---|---|---|---|---|---|---|
| Longitudinal | | Transverse | | Longitudinal | | Transverse | |
| Length | Stress | Length | Stress | Length | Stress | Length | Stress |
| 0.00E+00 | 4.21E+00 | 0.00E+00 | 4.90E+02 | 0.00E+00 | 3.21E+00 | 0.00E+00 | 1.83E+02 |

| | | | | | | | |
|---|---|---|---|---|---|---|---|
| 1.04E-01 | 4.29E+00 | 7.29E-02 | 5.11E+02 | 1.04E-01 | 4.00E+00 | 7.29E-02 | 1.83E+02 |
| 2.08E-01 | 6.81E+00 | 1.46E-01 | 5.19E+02 | 2.08E-01 | 6.66E+00 | 1.46E-01 | 1.84E+02 |
| 3.13E-01 | 1.34E+01 | 2.19E-01 | 5.20E+02 | 3.13E-01 | 1.14E+01 | 2.19E-01 | 1.84E+02 |
| 4.17E-01 | 2.57E+01 | 2.92E-01 | 5.17E+02 | 4.17E-01 | 1.87E+01 | 2.92E-01 | 1.84E+02 |
| 5.21E-01 | 5.25E+01 | 3.65E-01 | 5.13E+02 | 5.21E-01 | 2.86E+01 | 3.65E-01 | 1.84E+02 |
| 6.25E-01 | 1.69E+02 | 4.38E-01 | 5.08E+02 | 6.25E-01 | 3.27E+01 | 4.38E-01 | 1.84E+02 |
| 7.29E-01 | 3.69E+02 | 5.10E-01 | 5.04E+02 | 7.29E-01 | 1.64E+02 | 5.10E-01 | 1.84E+02 |
| 8.33E-01 | 8.79E+01 | 5.83E-01 | 5.00E+02 | 8.33E-01 | 1.47E+02 | 5.83E-01 | 1.84E+02 |
| 9.38E-01 | 3.98E+01 | 6.56E-01 | 4.97E+02 | 9.38E-01 | 5.98E+01 | 6.56E-01 | 1.84E+02 |
| 1.04E+00 | 5.58E+00 | 7.29E-01 | 4.95E+02 | 1.04E+00 | 2.70E+01 | 7.29E-01 | 1.84E+02 |
| 1.15E+00 | 3.10E+01 | 8.02E-01 | 4.94E+02 | 1.15E+00 | 3.14E+01 | 8.02E-01 | 1.84E+02 |
| 1.25E+00 | 5.53E+01 | 8.75E-01 | 4.93E+02 | 1.25E+00 | 5.04E+01 | 8.75E-01 | 1.84E+02 |
| 1.35E+00 | 7.96E+01 | 9.48E-01 | 4.93E+02 | 1.35E+00 | 7.17E+01 | 9.48E-01 | 1.84E+02 |
| 1.46E+00 | 1.05E+02 | 1.02E+00 | 4.93E+02 | 1.46E+00 | 9.44E+01 | 1.02E+00 | 1.84E+02 |
| 1.56E+00 | 1.32E+02 | 1.09E+00 | 4.93E+02 | 1.56E+00 | 1.19E+02 | 1.09E+00 | 1.84E+02 |
| 1.67E+00 | 1.63E+02 | 1.17E+00 | 4.93E+02 | 1.67E+00 | 1.44E+02 | 1.17E+00 | 1.84E+02 |
| 1.77E+00 | 2.11E+02 | 1.24E+00 | 4.94E+02 | 1.77E+00 | 1.58E+02 | 1.24E+00 | 1.84E+02 |
| 1.88E+00 | 2.74E+02 | 1.31E+00 | 4.94E+02 | 1.88E+00 | 1.68E+02 | 1.31E+00 | 1.84E+02 |
| 1.98E+00 | 3.33E+02 | 1.39E+00 | 4.95E+02 | 1.98E+00 | 1.75E+02 | 1.39E+00 | 1.84E+02 |
| 2.08E+00 | 3.87E+02 | 1.46E+00 | 4.95E+02 | 2.08E+00 | 1.80E+02 | 1.46E+00 | 1.84E+02 |
| 2.19E+00 | 4.34E+02 | 1.53E+00 | 4.96E+02 | 2.19E+00 | 1.82E+02 | 1.53E+00 | 1.84E+02 |
| 2.29E+00 | 4.69E+02 | 1.60E+00 | 4.96E+02 | 2.29E+00 | 1.84E+02 | 1.60E+00 | 1.85E+02 |
| 2.40E+00 | 4.90E+02 | 1.68E+00 | 4.96E+02 | 2.40E+00 | 1.84E+02 | 1.68E+00 | 1.85E+02 |
| 2.50E+00 | 4.96E+02 | 1.75E+00 | 4.96E+02 | 2.50E+00 | 1.85E+02 | 1.75E+00 | 1.85E+02 |
| 2.60E+00 | 4.90E+02 | 1.82E+00 | 4.96E+02 | 2.60E+00 | 1.84E+02 | 1.82E+00 | 1.85E+02 |
| 2.71E+00 | 4.69E+02 | 1.90E+00 | 4.96E+02 | 2.71E+00 | 1.84E+02 | 1.90E+00 | 1.85E+02 |
| 2.81E+00 | 4.34E+02 | 1.97E+00 | 4.96E+02 | 2.81E+00 | 1.82E+02 | 1.97E+00 | 1.84E+02 |
| 2.92E+00 | 3.87E+02 | 2.04E+00 | 4.95E+02 | 2.92E+00 | 1.80E+02 | 2.04E+00 | 1.84E+02 |
| 3.02E+00 | 3.32E+02 | 2.11E+00 | 4.95E+02 | 3.02E+00 | 1.75E+02 | 2.11E+00 | 1.84E+02 |
| 3.13E+00 | 2.74E+02 | 2.19E+00 | 4.94E+02 | 3.13E+00 | 1.68E+02 | 2.19E+00 | 1.84E+02 |
| 3.23E+00 | 2.11E+02 | 2.26E+00 | 4.94E+02 | 3.23E+00 | 1.58E+02 | 2.26E+00 | 1.84E+02 |
| 3.33E+00 | 1.63E+02 | 2.33E+00 | 4.93E+02 | 3.33E+00 | 1.44E+02 | 2.33E+00 | 1.84E+02 |
| 3.44E+00 | 1.32E+02 | 2.41E+00 | 4.93E+02 | 3.44E+00 | 1.18E+02 | 2.41E+00 | 1.84E+02 |
| 3.54E+00 | 1.05E+02 | 2.48E+00 | 4.93E+02 | 3.54E+00 | 9.42E+01 | 2.48E+00 | 1.84E+02 |
| 3.65E+00 | 7.94E+01 | 2.55E+00 | 4.93E+02 | 3.65E+00 | 7.15E+01 | 2.55E+00 | 1.84E+02 |
| 3.75E+00 | 5.49E+01 | 2.63E+00 | 4.93E+02 | 3.75E+00 | 5.01E+01 | 2.63E+00 | 1.84E+02 |
| 3.85E+00 | 3.05E+01 | 2.70E+00 | 4.94E+02 | 3.85E+00 | 3.13E+01 | 2.70E+00 | 1.84E+02 |
| 3.96E+00 | 5.83E+00 | 2.77E+00 | 4.95E+02 | 3.96E+00 | 2.74E+01 | 2.77E+00 | 1.84E+02 |
| 4.06E+00 | 3.89E+01 | 2.84E+00 | 4.97E+02 | 4.06E+00 | 5.87E+01 | 2.84E+00 | 1.84E+02 |
| 4.1667 | 7.51E+01 | 2.9167 | 5.00E+02 | 4.17E+00 | 1.42E+02 | 2.92E+00 | 1.84E+02 |
| 4.2708 | 3.12E+02 | 2.9896 | 5.04E+02 | 4.27E+00 | 1.65E+02 | 2.99E+00 | 1.84E+02 |

| | | | | | | | |
|---|---|---|---|---|---|---|---|
| 4.375 | 1.72E+02 | 3.0625 | 5.08E+02 | 4.38E+00 | 3.34E+01 | 3.06E+00 | 1.84E+02 |
| 4.4792 | 4.81E+01 | 3.1354 | 5.12E+02 | 4.48E+00 | 2.81E+01 | 3.14E+00 | 1.84E+02 |
| 4.5833 | 2.49E+01 | 3.2083 | 5.17E+02 | 4.58E+00 | 1.87E+01 | 3.21E+00 | 1.84E+02 |
| 4.6875 | 1.35E+01 | 3.2813 | 5.20E+02 | 4.69E+00 | 1.16E+01 | 3.28E+00 | 1.84E+02 |
| 4.7917 | 7.15E+00 | 3.3542 | 5.19E+02 | 4.79E+00 | 6.93E+00 | 3.35E+00 | 1.84E+02 |
| 4.8958 | 4.76E+00 | 3.4271 | 5.11E+02 | 4.90E+00 | 4.37E+00 | 3.43E+00 | 1.83E+02 |
| 5 | 4.69E+00 | 3.5 | 4.90E+02 | 5.00E+00 | 3.64E+00 | 3.50E+00 | 1.83E+02 |

Table B-102 Surface stress profiles for irradiated layer yield strength sensitivity.

| **Hardened Layer** | | | | **Soft Bulk** | | | |
|---|---|---|---|---|---|---|---|
| Longitudinal | | Transverse | | Longitudinal | | Transverse | |
| Length | Stress | Length | Stress | Length | Stress | Length | Stress |
| 0.00E+00 | 4.22E+00 | 0.00E+00 | 4.91E+02 | 0.00E+00 | 3.21E+00 | 0.00E+00 | 1.83E+02 |
| 1.04E-01 | 4.30E+00 | 7.29E-02 | 5.11E+02 | 1.04E-01 | 4.00E+00 | 7.29E-02 | 1.83E+02 |
| 2.08E-01 | 6.82E+00 | 1.46E-01 | 5.20E+02 | 2.08E-01 | 6.67E+00 | 1.46E-01 | 1.83E+02 |
| 3.13E-01 | 1.34E+01 | 2.19E-01 | 5.21E+02 | 3.13E-01 | 1.14E+01 | 2.19E-01 | 1.84E+02 |
| 4.17E-01 | 2.57E+01 | 2.92E-01 | 5.18E+02 | 4.17E-01 | 1.87E+01 | 2.92E-01 | 1.84E+02 |
| 5.21E-01 | 5.26E+01 | 3.65E-01 | 5.13E+02 | 5.21E-01 | 2.86E+01 | 3.65E-01 | 1.84E+02 |
| 6.25E-01 | 1.69E+02 | 4.38E-01 | 5.09E+02 | 6.25E-01 | 3.27E+01 | 4.38E-01 | 1.84E+02 |
| 7.29E-01 | 3.69E+02 | 5.10E-01 | 5.04E+02 | 7.29E-01 | 1.64E+02 | 5.10E-01 | 1.84E+02 |
| 8.33E-01 | 8.78E+01 | 5.83E-01 | 5.01E+02 | 8.33E-01 | 1.47E+02 | 5.83E-01 | 1.84E+02 |
| 9.38E-01 | 4.00E+01 | 6.56E-01 | 4.98E+02 | 9.38E-01 | 5.98E+01 | 6.56E-01 | 1.84E+02 |
| 1.04E+00 | 5.55E+00 | 7.29E-01 | 4.96E+02 | 1.04E+00 | 2.70E+01 | 7.29E-01 | 1.84E+02 |
| 1.15E+00 | 3.10E+01 | 8.02E-01 | 4.95E+02 | 1.15E+00 | 3.14E+01 | 8.02E-01 | 1.84E+02 |
| 1.25E+00 | 5.53E+01 | 8.75E-01 | 4.94E+02 | 1.25E+00 | 5.03E+01 | 8.75E-01 | 1.84E+02 |
| 1.35E+00 | 7.96E+01 | 9.48E-01 | 4.93E+02 | 1.35E+00 | 7.17E+01 | 9.48E-01 | 1.84E+02 |
| 1.46E+00 | 1.05E+02 | 1.02E+00 | 4.93E+02 | 1.46E+00 | 9.44E+01 | 1.02E+00 | 1.84E+02 |
| 1.56E+00 | 1.32E+02 | 1.09E+00 | 4.94E+02 | 1.56E+00 | 1.19E+02 | 1.09E+00 | 1.84E+02 |
| 1.67E+00 | 1.63E+02 | 1.17E+00 | 4.94E+02 | 1.67E+00 | 1.44E+02 | 1.17E+00 | 1.84E+02 |
| 1.77E+00 | 2.11E+02 | 1.24E+00 | 4.95E+02 | 1.77E+00 | 1.58E+02 | 1.24E+00 | 1.84E+02 |
| 1.88E+00 | 2.74E+02 | 1.31E+00 | 4.95E+02 | 1.88E+00 | 1.68E+02 | 1.31E+00 | 1.84E+02 |
| 1.98E+00 | 3.33E+02 | 1.39E+00 | 4.96E+02 | 1.98E+00 | 1.75E+02 | 1.39E+00 | 1.84E+02 |
| 2.08E+00 | 3.87E+02 | 1.46E+00 | 4.96E+02 | 2.08E+00 | 1.80E+02 | 1.46E+00 | 1.84E+02 |
| 2.19E+00 | 4.35E+02 | 1.53E+00 | 4.96E+02 | 2.19E+00 | 1.82E+02 | 1.53E+00 | 1.84E+02 |
| 2.29E+00 | 4.69E+02 | 1.60E+00 | 4.97E+02 | 2.29E+00 | 1.84E+02 | 1.60E+00 | 1.84E+02 |
| 2.40E+00 | 4.90E+02 | 1.68E+00 | 4.97E+02 | 2.40E+00 | 1.84E+02 | 1.68E+00 | 1.84E+02 |
| 2.50E+00 | 4.97E+02 | 1.75E+00 | 4.97E+02 | 2.50E+00 | 1.84E+02 | 1.75E+00 | 1.84E+02 |
| 2.60E+00 | 4.90E+02 | 1.82E+00 | 4.97E+02 | 2.60E+00 | 1.84E+02 | 1.82E+00 | 1.84E+02 |
| 2.71E+00 | 4.69E+02 | 1.90E+00 | 4.97E+02 | 2.71E+00 | 1.84E+02 | 1.90E+00 | 1.84E+02 |
| 2.81E+00 | 4.35E+02 | 1.97E+00 | 4.96E+02 | 2.81E+00 | 1.82E+02 | 1.97E+00 | 1.84E+02 |
| 2.92E+00 | 3.87E+02 | 2.04E+00 | 4.96E+02 | 2.92E+00 | 1.80E+02 | 2.04E+00 | 1.84E+02 |

| | | | | | | | |
|---|---|---|---|---|---|---|---|
| 3.02E+00 | 3.33E+02 | 2.11E+00 | 4.96E+02 | 3.02E+00 | 1.75E+02 | 2.11E+00 | 1.84E+02 |
| 3.13E+00 | 2.74E+02 | 2.19E+00 | 4.95E+02 | 3.13E+00 | 1.68E+02 | 2.19E+00 | 1.84E+02 |
| 3.23E+00 | 2.11E+02 | 2.26E+00 | 4.95E+02 | 3.23E+00 | 1.58E+02 | 2.26E+00 | 1.84E+02 |
| 3.33E+00 | 1.63E+02 | 2.33E+00 | 4.94E+02 | 3.33E+00 | 1.44E+02 | 2.33E+00 | 1.84E+02 |
| 3.44E+00 | 1.32E+02 | 2.41E+00 | 4.94E+02 | 3.44E+00 | 1.18E+02 | 2.41E+00 | 1.84E+02 |
| 3.54E+00 | 1.05E+02 | 2.48E+00 | 4.93E+02 | 3.54E+00 | 9.42E+01 | 2.48E+00 | 1.84E+02 |
| 3.65E+00 | 7.93E+01 | 2.55E+00 | 4.93E+02 | 3.65E+00 | 7.15E+01 | 2.55E+00 | 1.84E+02 |
| 3.75E+00 | 5.49E+01 | 2.63E+00 | 4.94E+02 | 3.75E+00 | 5.01E+01 | 2.63E+00 | 1.84E+02 |
| 3.85E+00 | 3.04E+01 | 2.70E+00 | 4.94E+02 | 3.85E+00 | 3.12E+01 | 2.70E+00 | 1.84E+02 |
| 3.96E+00 | 5.81E+00 | 2.77E+00 | 4.96E+02 | 3.96E+00 | 2.74E+01 | 2.77E+00 | 1.84E+02 |
| 4.06E+00 | 3.90E+01 | 2.84E+00 | 4.98E+02 | 4.06E+00 | 5.88E+01 | 2.84E+00 | 1.84E+02 |
| 4.1667 | 7.50E+01 | 2.9167 | 5.01E+02 | 4.17E+00 | 1.42E+02 | 2.92E+00 | 1.84E+02 |
| 4.2708 | 3.12E+02 | 2.9896 | 5.04E+02 | 4.27E+00 | 1.65E+02 | 2.99E+00 | 1.84E+02 |
| 4.375 | 1.71E+02 | 3.0625 | 5.08E+02 | 4.38E+00 | 3.34E+01 | 3.06E+00 | 1.84E+02 |
| 4.4792 | 4.81E+01 | 3.1354 | 5.13E+02 | 4.48E+00 | 2.82E+01 | 3.14E+00 | 1.84E+02 |
| 4.5833 | 2.49E+01 | 3.2083 | 5.17E+02 | 4.58E+00 | 1.87E+01 | 3.21E+00 | 1.84E+02 |
| 4.6875 | 1.35E+01 | 3.2813 | 5.20E+02 | 4.69E+00 | 1.16E+01 | 3.28E+00 | 1.84E+02 |
| 4.7917 | 7.16E+00 | 3.3542 | 5.20E+02 | 4.79E+00 | 6.94E+00 | 3.35E+00 | 1.83E+02 |
| 4.8958 | 4.77E+00 | 3.4271 | 5.11E+02 | 4.90E+00 | 4.38E+00 | 3.43E+00 | 1.83E+02 |
| 5 | 4.70E+00 | 3.5 | 4.90E+02 | 5.00E+00 | 3.64E+00 | 3.50E+00 | 1.83E+02 |

Table 0-103 Surface stress profiles for the sample thickness sensitivity.

| **Hardened Layer** | | | | **Soft Bulk** | | | |
|---|---|---|---|---|---|---|---|
| Longitudinal | | Transverse | | Longitudinal | | Transverse | |
| Length | Stress | Length | Stress | Length | Stress | Length | Stress |
| 0.00E+00 | 4.42E+00 | 0.00E+00 | 4.89E+02 | 0.00E+00 | 3.40E+00 | 0.00E+00 | 1.83E+02 |
| 1.04E-01 | 4.46E+00 | 7.29E-02 | 5.10E+02 | 1.04E-01 | 4.16E+00 | 7.29E-02 | 1.83E+02 |
| 2.08E-01 | 6.90E+00 | 1.46E-01 | 5.19E+02 | 2.08E-01 | 6.78E+00 | 1.46E-01 | 1.83E+02 |
| 3.13E-01 | 1.32E+01 | 2.19E-01 | 5.19E+02 | 3.13E-01 | 1.14E+01 | 2.19E-01 | 1.84E+02 |
| 4.17E-01 | 2.46E+01 | 2.92E-01 | 5.16E+02 | 4.17E-01 | 1.86E+01 | 2.92E-01 | 1.84E+02 |
| 5.21E-01 | 4.80E+01 | 3.65E-01 | 5.12E+02 | 5.21E-01 | 2.81E+01 | 3.65E-01 | 1.84E+02 |
| 6.25E-01 | 1.51E+02 | 4.38E-01 | 5.07E+02 | 6.25E-01 | 3.38E+01 | 4.38E-01 | 1.84E+02 |
| 7.29E-01 | 3.20E+02 | 5.10E-01 | 5.03E+02 | 7.29E-01 | 1.56E+02 | 5.10E-01 | 1.84E+02 |
| 8.33E-01 | 8.24E+01 | 5.83E-01 | 4.99E+02 | 8.33E-01 | 1.45E+02 | 5.83E-01 | 1.84E+02 |
| 9.38E-01 | 4.00E+01 | 6.56E-01 | 4.96E+02 | 9.38E-01 | 5.87E+01 | 6.56E-01 | 1.84E+02 |
| 1.04E+00 | 5.66E+00 | 7.29E-01 | 4.94E+02 | 1.04E+00 | 2.72E+01 | 7.29E-01 | 1.84E+02 |
| 1.15E+00 | 3.11E+01 | 8.02E-01 | 4.93E+02 | 1.15E+00 | 3.18E+01 | 8.02E-01 | 1.84E+02 |
| 1.25E+00 | 5.54E+01 | 8.75E-01 | 4.92E+02 | 1.25E+00 | 5.06E+01 | 8.75E-01 | 1.84E+02 |
| 1.35E+00 | 7.96E+01 | 9.48E-01 | 4.92E+02 | 1.35E+00 | 7.18E+01 | 9.48E-01 | 1.84E+02 |
| 1.46E+00 | 1.05E+02 | 1.02E+00 | 4.92E+02 | 1.46E+00 | 9.43E+01 | 1.02E+00 | 1.84E+02 |
| 1.56E+00 | 1.32E+02 | 1.09E+00 | 4.92E+02 | 1.56E+00 | 1.18E+02 | 1.09E+00 | 1.84E+02 |

| | | | | | | | |
|---|---|---|---|---|---|---|---|
| 1.67E+00 | 1.62E+02 | 1.17E+00 | 4.92E+02 | 1.67E+00 | 1.43E+02 | 1.17E+00 | 1.84E+02 |
| 1.77E+00 | 2.10E+02 | 1.24E+00 | 4.93E+02 | 1.77E+00 | 1.58E+02 | 1.24E+00 | 1.84E+02 |
| 1.88E+00 | 2.72E+02 | 1.31E+00 | 4.93E+02 | 1.88E+00 | 1.67E+02 | 1.31E+00 | 1.84E+02 |
| 1.98E+00 | 3.31E+02 | 1.39E+00 | 4.94E+02 | 1.98E+00 | 1.75E+02 | 1.39E+00 | 1.84E+02 |
| 2.08E+00 | 3.85E+02 | 1.46E+00 | 4.94E+02 | 2.08E+00 | 1.80E+02 | 1.46E+00 | 1.84E+02 |
| 2.19E+00 | 4.32E+02 | 1.53E+00 | 4.95E+02 | 2.19E+00 | 1.82E+02 | 1.53E+00 | 1.84E+02 |
| 2.29E+00 | 4.67E+02 | 1.60E+00 | 4.95E+02 | 2.29E+00 | 1.83E+02 | 1.60E+00 | 1.84E+02 |
| 2.40E+00 | 4.89E+02 | 1.68E+00 | 4.95E+02 | 2.40E+00 | 1.84E+02 | 1.68E+00 | 1.84E+02 |
| 2.50E+00 | 4.95E+02 | 1.75E+00 | 4.95E+02 | 2.50E+00 | 1.84E+02 | 1.75E+00 | 1.84E+02 |
| 2.60E+00 | 4.89E+02 | 1.82E+00 | 4.95E+02 | 2.60E+00 | 1.84E+02 | 1.82E+00 | 1.84E+02 |
| 2.71E+00 | 4.67E+02 | 1.90E+00 | 4.95E+02 | 2.71E+00 | 1.83E+02 | 1.90E+00 | 1.84E+02 |
| 2.81E+00 | 4.32E+02 | 1.97E+00 | 4.95E+02 | 2.81E+00 | 1.82E+02 | 1.97E+00 | 1.84E+02 |
| 2.92E+00 | 3.85E+02 | 2.04E+00 | 4.94E+02 | 2.92E+00 | 1.80E+02 | 2.04E+00 | 1.84E+02 |
| 3.02E+00 | 3.31E+02 | 2.11E+00 | 4.94E+02 | 3.02E+00 | 1.75E+02 | 2.11E+00 | 1.84E+02 |
| 3.13E+00 | 2.72E+02 | 2.19E+00 | 4.93E+02 | 3.13E+00 | 1.67E+02 | 2.19E+00 | 1.84E+02 |
| 3.23E+00 | 2.10E+02 | 2.26E+00 | 4.93E+02 | 3.23E+00 | 1.58E+02 | 2.26E+00 | 1.84E+02 |
| 3.33E+00 | 1.62E+02 | 2.33E+00 | 4.92E+02 | 3.33E+00 | 1.43E+02 | 2.33E+00 | 1.84E+02 |
| 3.44E+00 | 1.32E+02 | 2.41E+00 | 4.92E+02 | 3.44E+00 | 1.18E+02 | 2.41E+00 | 1.84E+02 |
| 3.54E+00 | 1.05E+02 | 2.48E+00 | 4.92E+02 | 3.54E+00 | 9.42E+01 | 2.48E+00 | 1.84E+02 |
| 3.65E+00 | 7.94E+01 | 2.55E+00 | 4.92E+02 | 3.65E+00 | 7.17E+01 | 2.55E+00 | 1.84E+02 |
| 3.75E+00 | 5.51E+01 | 2.63E+00 | 4.92E+02 | 3.75E+00 | 5.04E+01 | 2.63E+00 | 1.84E+02 |
| 3.85E+00 | 3.07E+01 | 2.70E+00 | 4.93E+02 | 3.85E+00 | 3.17E+01 | 2.70E+00 | 1.84E+02 |
| 3.96E+00 | 6.02E+00 | 2.77E+00 | 4.94E+02 | 3.96E+00 | 2.74E+01 | 2.77E+00 | 1.84E+02 |
| 4.06E+00 | 3.86E+01 | 2.84E+00 | 4.96E+02 | 4.06E+00 | 5.73E+01 | 2.84E+00 | 1.84E+02 |
| 4.1667 | 8.29E+01 | 2.9167 | 4.99E+02 | 4.17E+00 | 1.41E+02 | 2.92E+00 | 1.84E+02 |
| 4.2708 | 2.99E+02 | 2.9896 | 5.03E+02 | 4.27E+00 | 1.53E+02 | 2.99E+00 | 1.84E+02 |
| 4.375 | 1.50E+02 | 3.0625 | 5.07E+02 | 4.38E+00 | 3.22E+01 | 3.06E+00 | 1.84E+02 |
| 4.4792 | 4.57E+01 | 3.1354 | 5.12E+02 | 4.48E+00 | 2.74E+01 | 3.14E+00 | 1.84E+02 |
| 4.5833 | 2.40E+01 | 3.2083 | 5.16E+02 | 4.58E+00 | 1.83E+01 | 3.21E+00 | 1.84E+02 |
| 4.6875 | 1.31E+01 | 3.2813 | 5.19E+02 | 4.69E+00 | 1.14E+01 | 3.28E+00 | 1.84E+02 |
| 4.7917 | 6.98E+00 | 3.3542 | 5.19E+02 | 4.79E+00 | 6.84E+00 | 3.35E+00 | 1.83E+02 |
| 4.8958 | 4.64E+00 | 3.4271 | 5.10E+02 | 4.90E+00 | 4.29E+00 | 3.43E+00 | 1.83E+02 |
| 5 | 4.58E+00 | 3.5 | 4.89E+02 | 5.00E+00 | 3.54E+00 | 3.50E+00 | 1.83E+02 |

## Appendix C: Surface Cracks Morphology

### C.1 Surface cracks

Sample N3

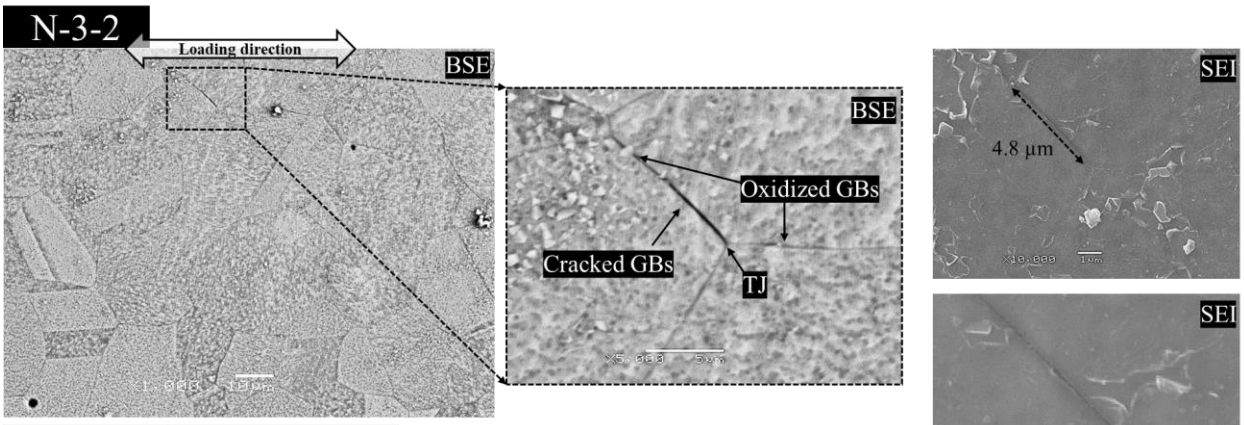


| | |
|---|---|
| Crack ID | N-3-2 |
| Crack Length | 4.8 µm |
| GB Angle | 135º |
| Initiation feature | Triple Junction |

Figure C-1 Surface morphology of crack N-3-2

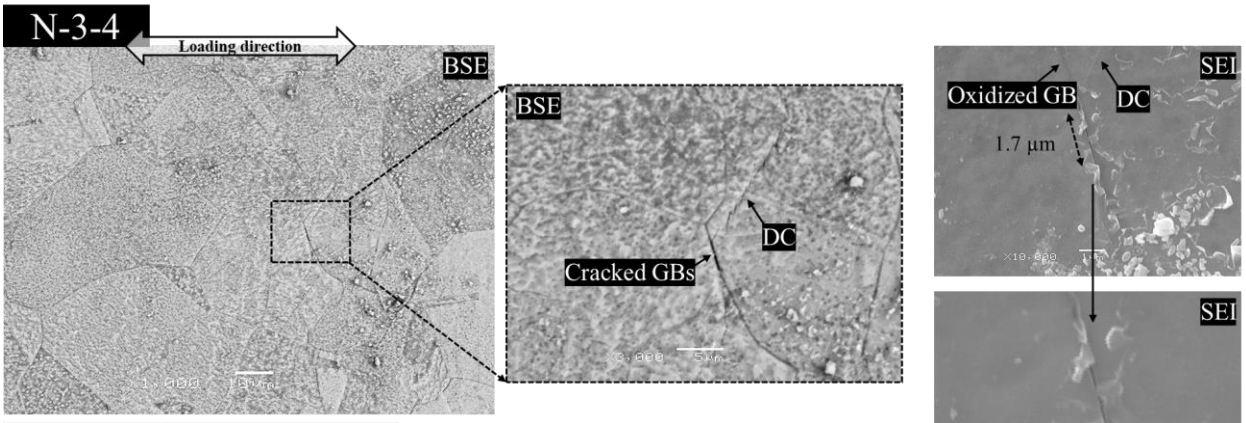


| | |
|---|---|
| Crack ID | N-3-4 |
| Crack Length | 1.7 µm |
| GB Angle | 105º |
| Initiation feature | Dislocation channel |

Figure C-2 Surface morphology of crack N-3-4

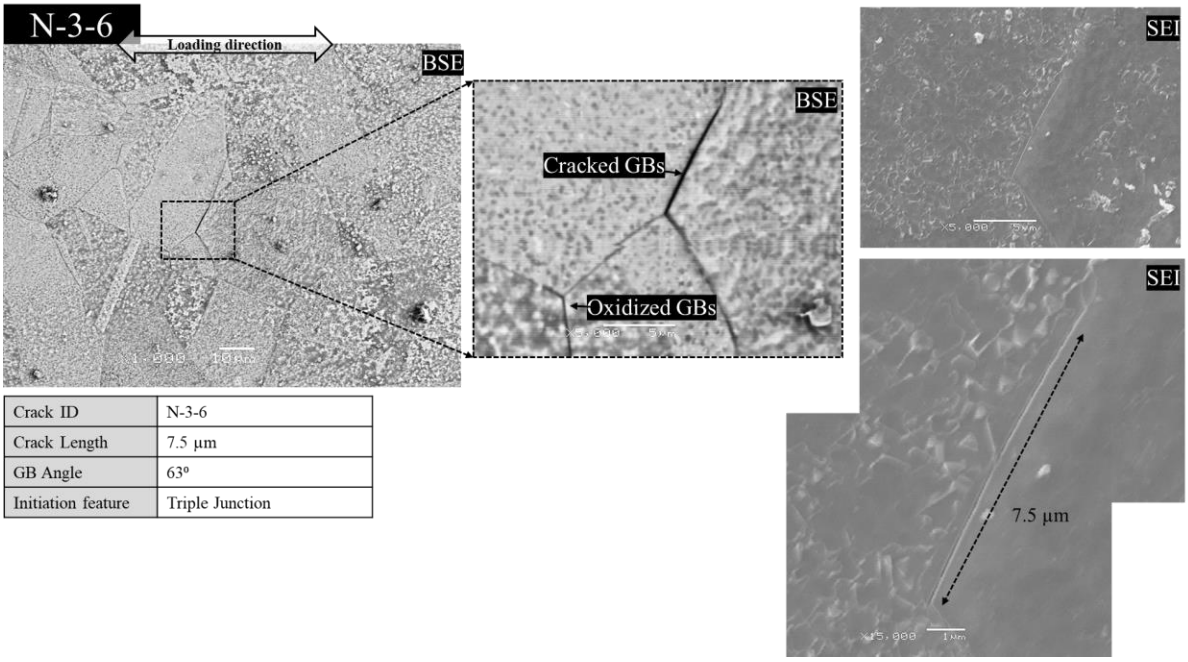


| | |
|---|---|
| Crack ID | N-3-6 |
| Crack Length | 7.5 µm |
| GB Angle | 63º |
| Initiation feature | Triple Junction |

Figure 0-3 Surface morphology of crack N-3-6.

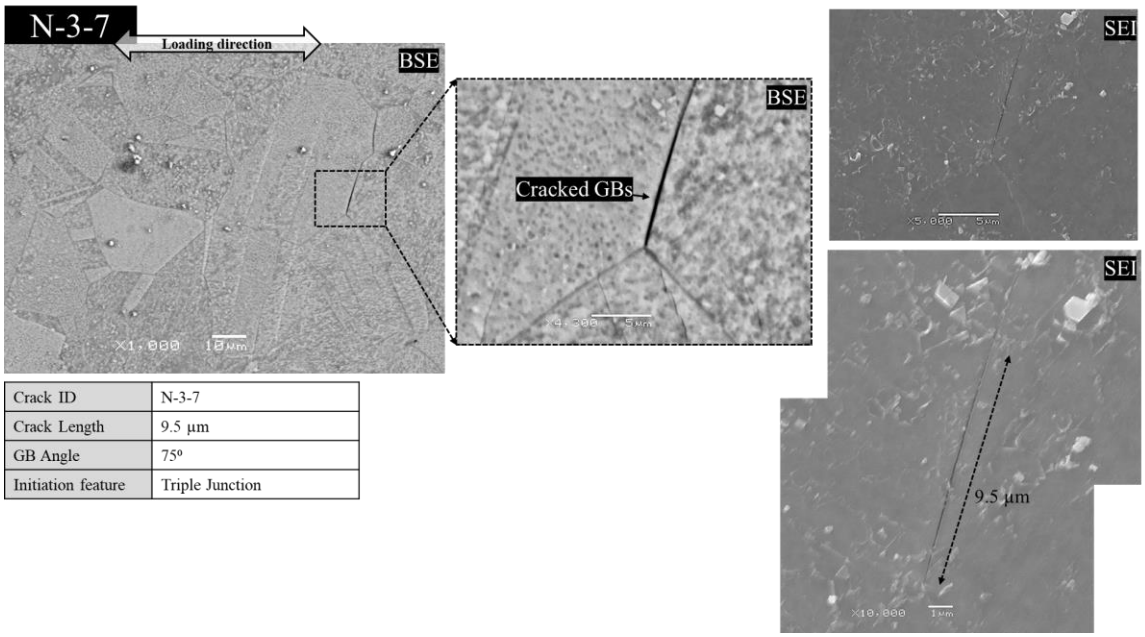


| | |
|---|---|
| Crack ID | N-3-7 |
| Crack Length | 9.5 µm |
| GB Angle | 75º |
| Initiation feature | Triple Junction |

Figure 0-4 Surface morphology of crack N-3-7.

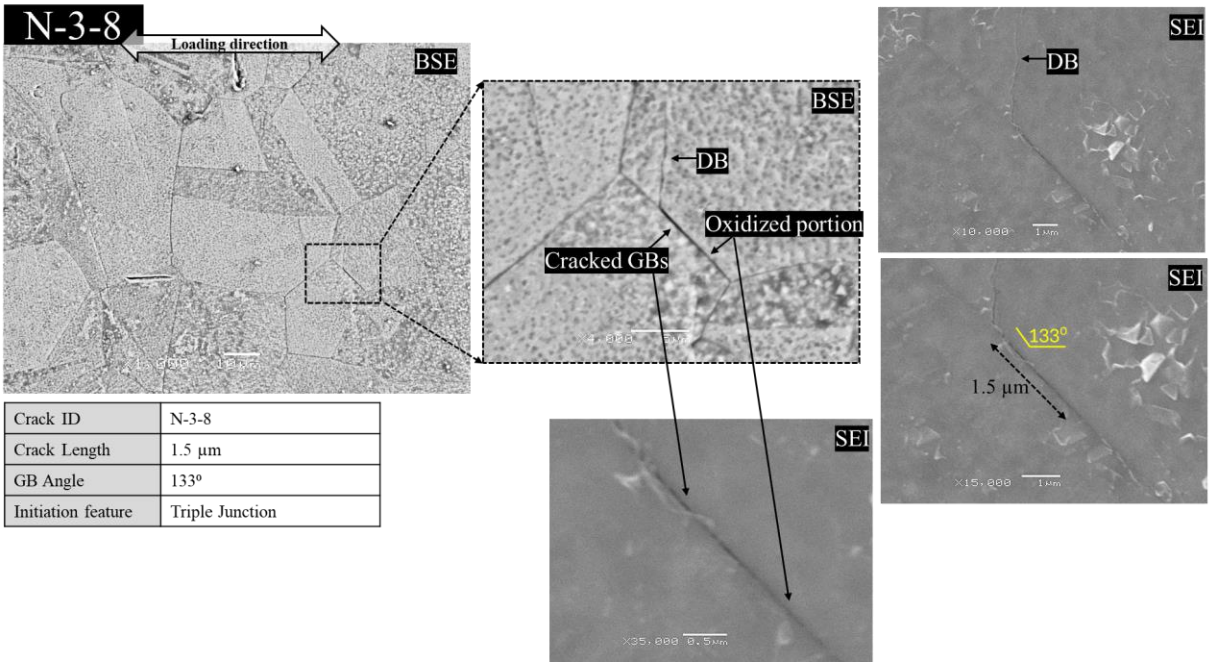


| | |
|---|---|
| Crack ID | N-3-8 |
| Crack Length | 1.5 µm |
| GB Angle | 133º |
| Initiation feature | Triple Junction |

Figure C-5 Surface morphology of crack N-3-8.

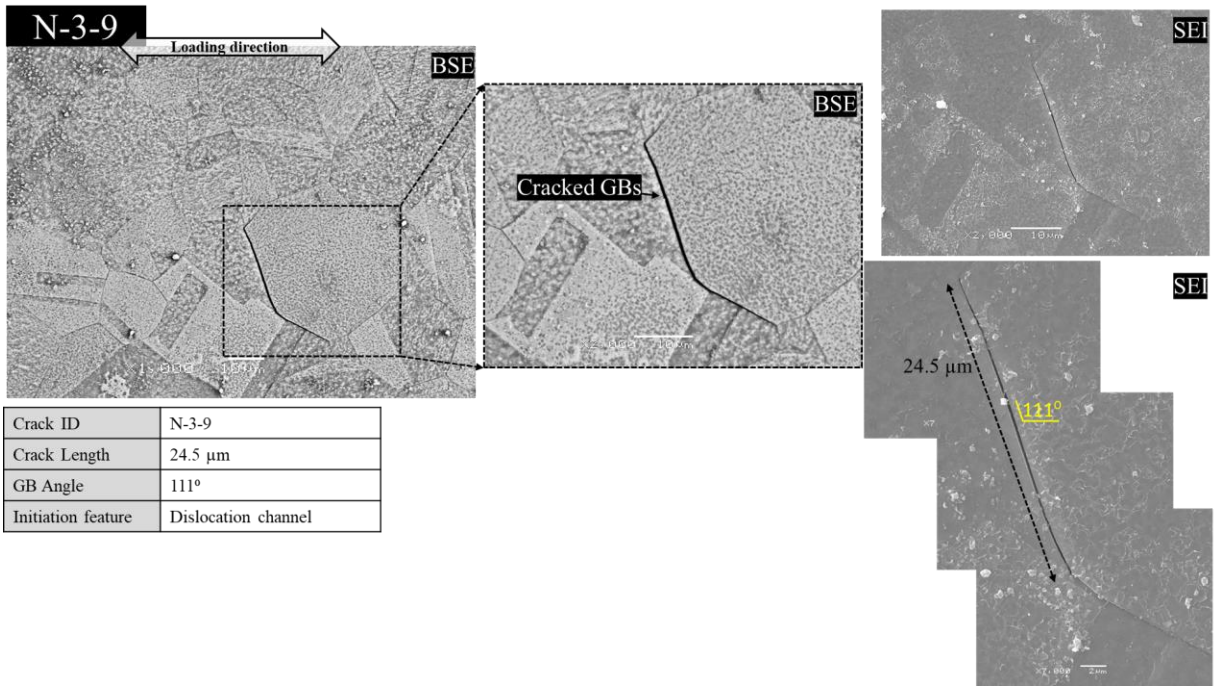


| | |
|---|---|
| Crack ID | N-3-9 |
| Crack Length | 24.5 µm |
| GB Angle | 111° |
| Initiation feature | Dislocation channel |

Figure 0-6 Surface morphology of crack N-3-9.

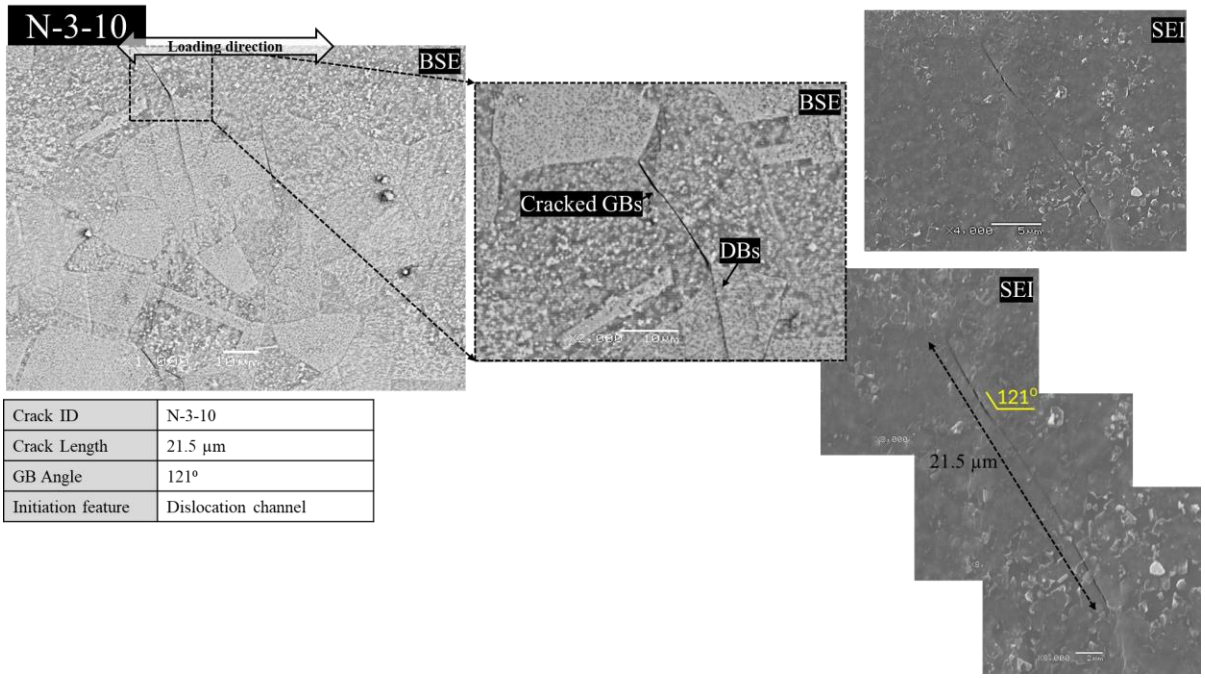


| | |
|---|---|
| Crack ID | N-3-10 |
| Crack Length | 21.5 µm |
| GB Angle | 121° |
| Initiation feature | Dislocation channel |

Figure C-7 Surface morphology of crack N-3-10.

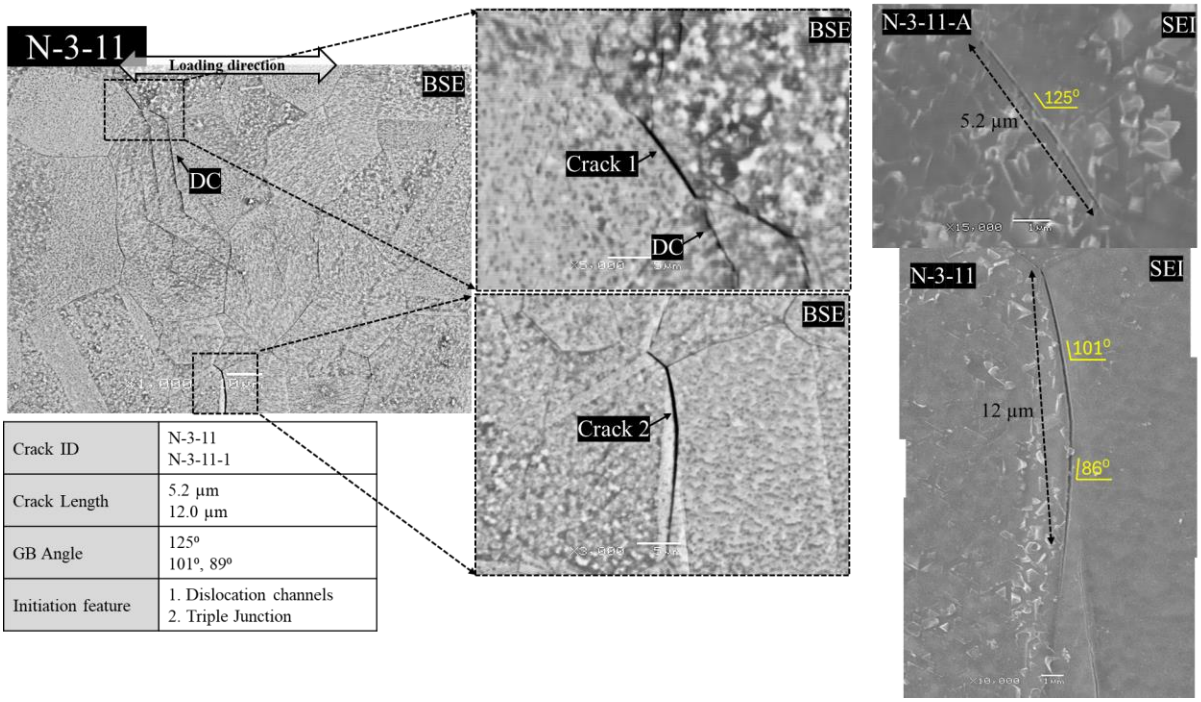


| Crack ID | N-3-11<br>N-3-11-1 |
|---|---|
| Crack Length | 5.2 µm<br>12.0 µm |
| GB Angle | 125°<br>101°, 89° |
| Initiation feature | 1. Dislocation channels<br>2. Triple Junction |

Figure C-8 Surface morphology of crack N-3-11.

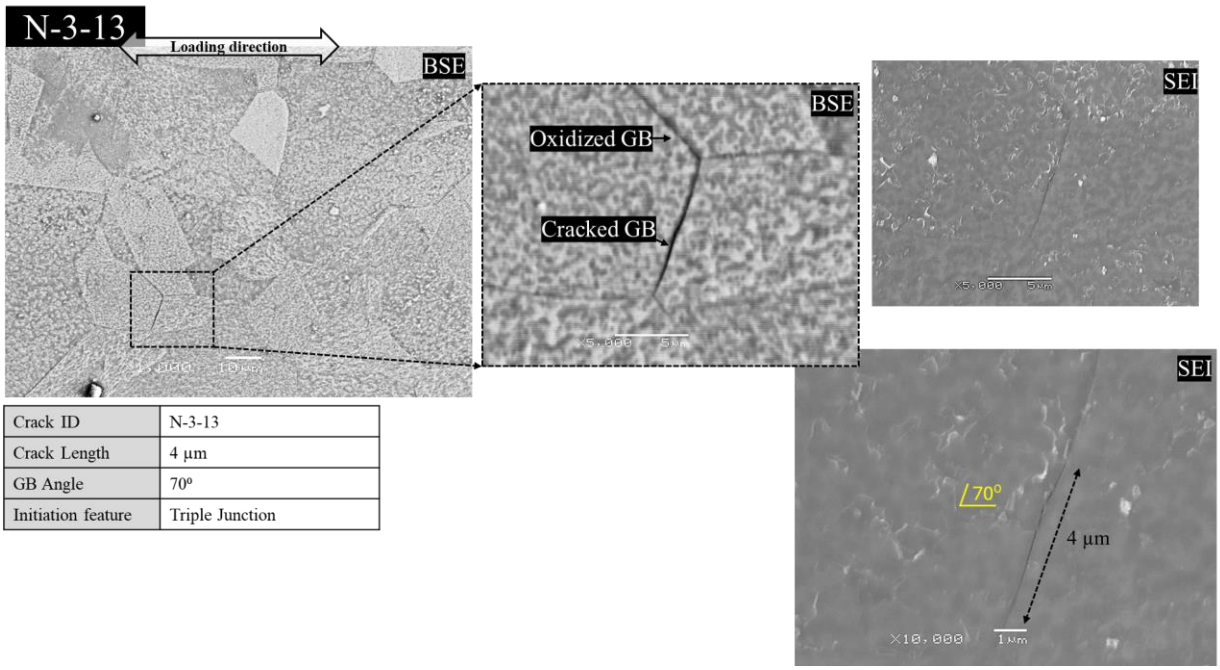


| Crack ID | N-3-13 |
|---|---|
| Crack Length | 4 µm |
| GB Angle | 70° |
| Initiation feature | Triple Junction |

Figure 0-9 Surface morphology of crack N-3-13.

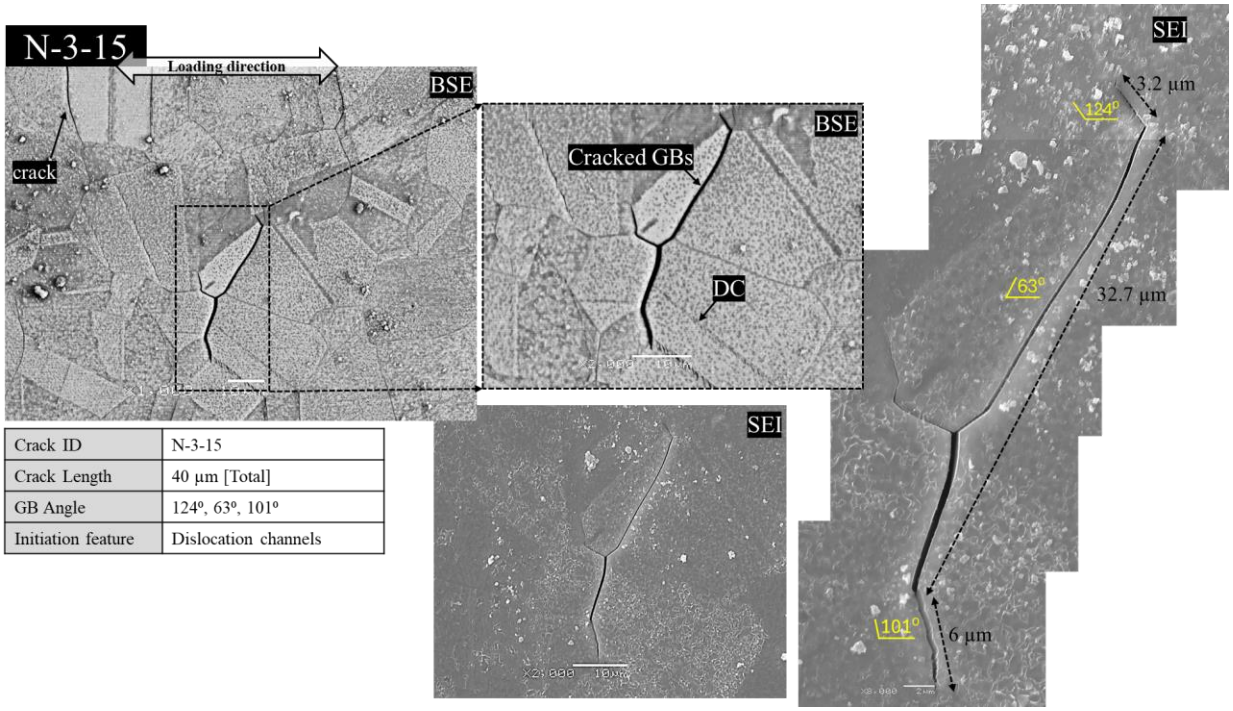


| Crack ID | N-3-15 |
|---|---|
| Crack Length | 40 µm [Total] |
| GB Angle | 124°, 63°, 101° |
| Initiation feature | Dislocation channels |

Figure C-10 Surface morphology of crack N-3-15.

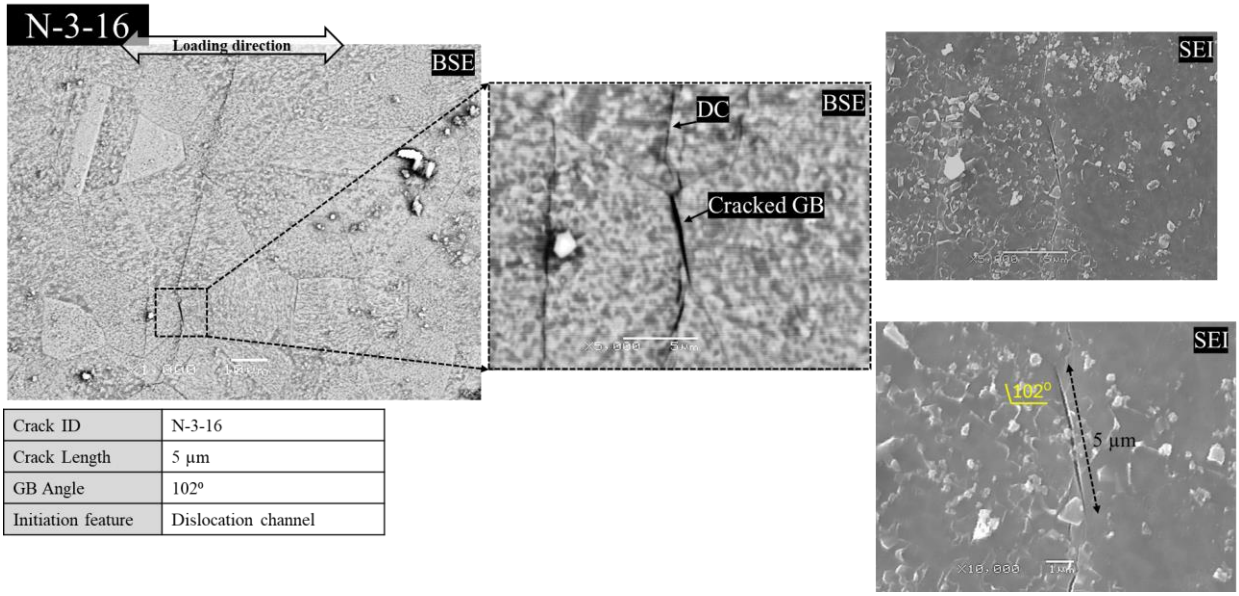


| Crack ID | N-3-16 |
|---|---|
| Crack Length | 5 µm |
| GB Angle | 102° |
| Initiation feature | Dislocation channel |

Figure C-11 Surface morphology of crack N-3-16.

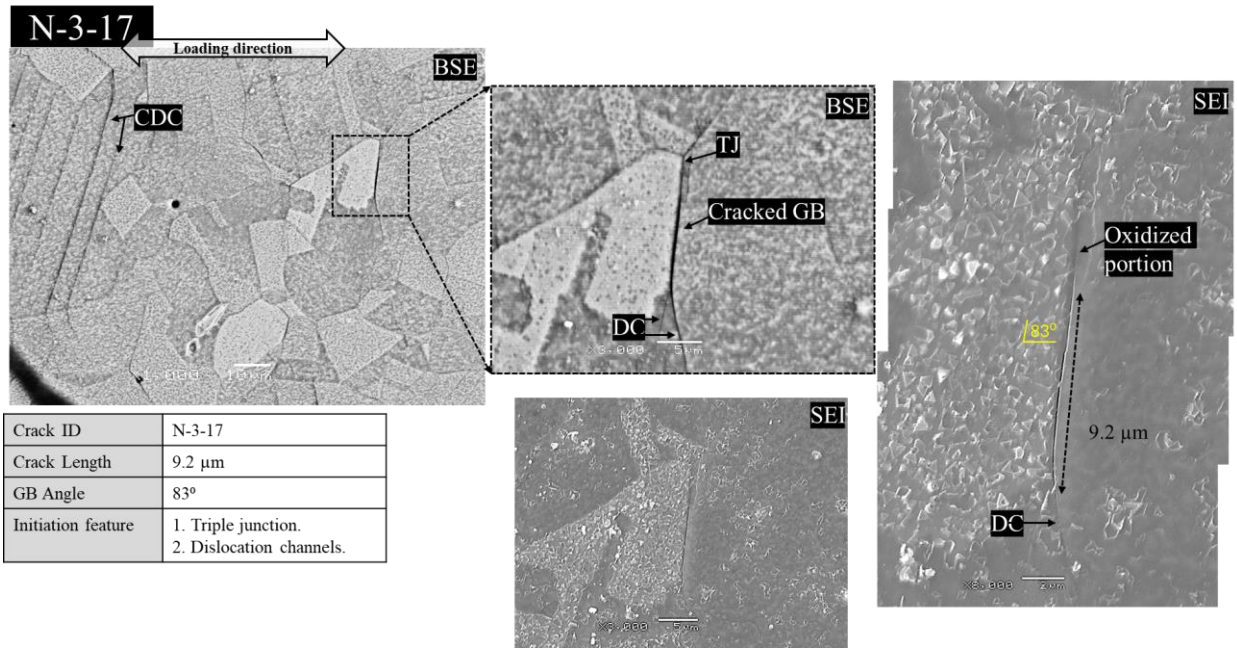


| | |
|---|---|
| Crack ID | N-3-17 |
| Crack Length | 9.2 µm |
| GB Angle | 83° |
| Initiation feature | 1. Triple junction.<br>2. Dislocation channels. |

Figure 0-12 Surface morphology of crack N-3-17.

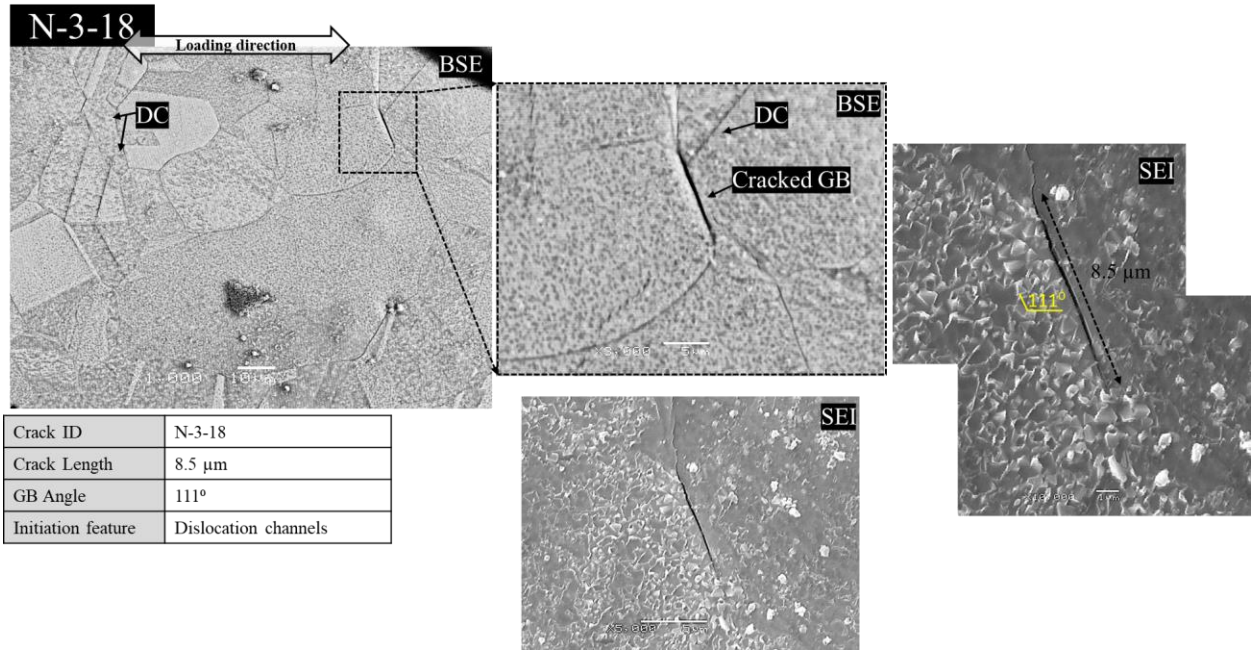


| | |
|---|---|
| Crack ID | N-3-18 |
| Crack Length | 8.5 µm |
| GB Angle | 111° |
| Initiation feature | Dislocation channels |

Figure 0-13 Surface morphology of crack N-3-18.

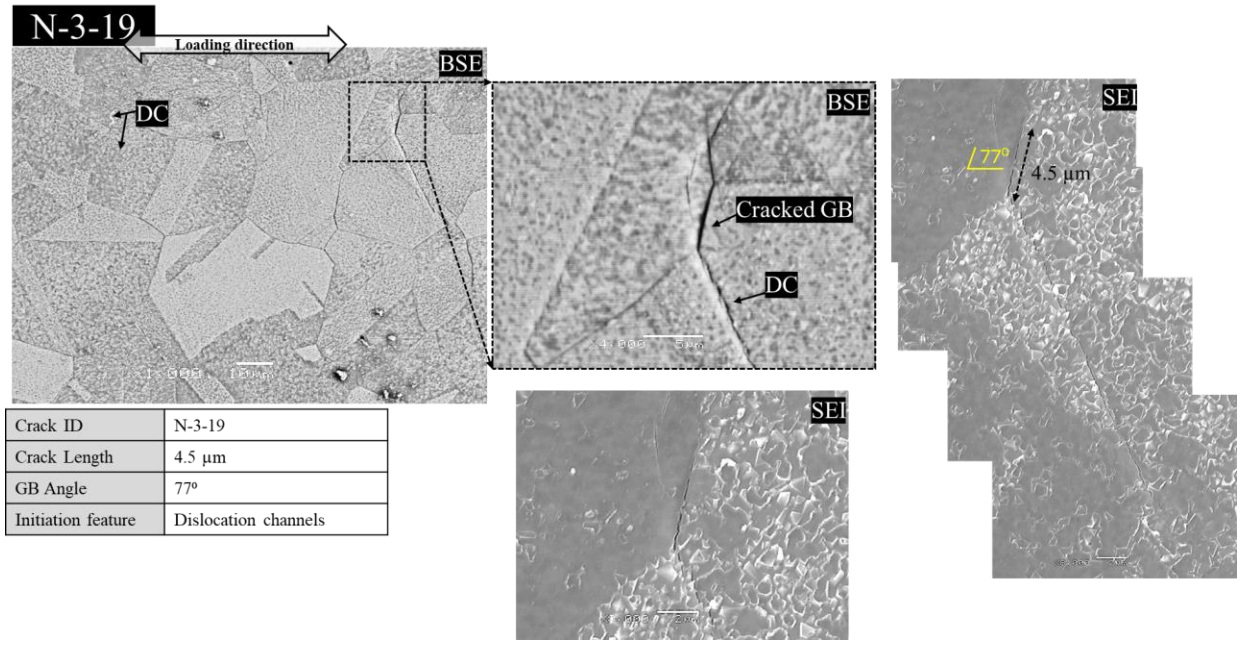


| | |
|---|---|
| Crack ID | N-3-19 |
| Crack Length | 4.5 µm |
| GB Angle | 77º |
| Initiation feature | Dislocation channels |

Figure C-14 Surface morphology of crack N-3-19

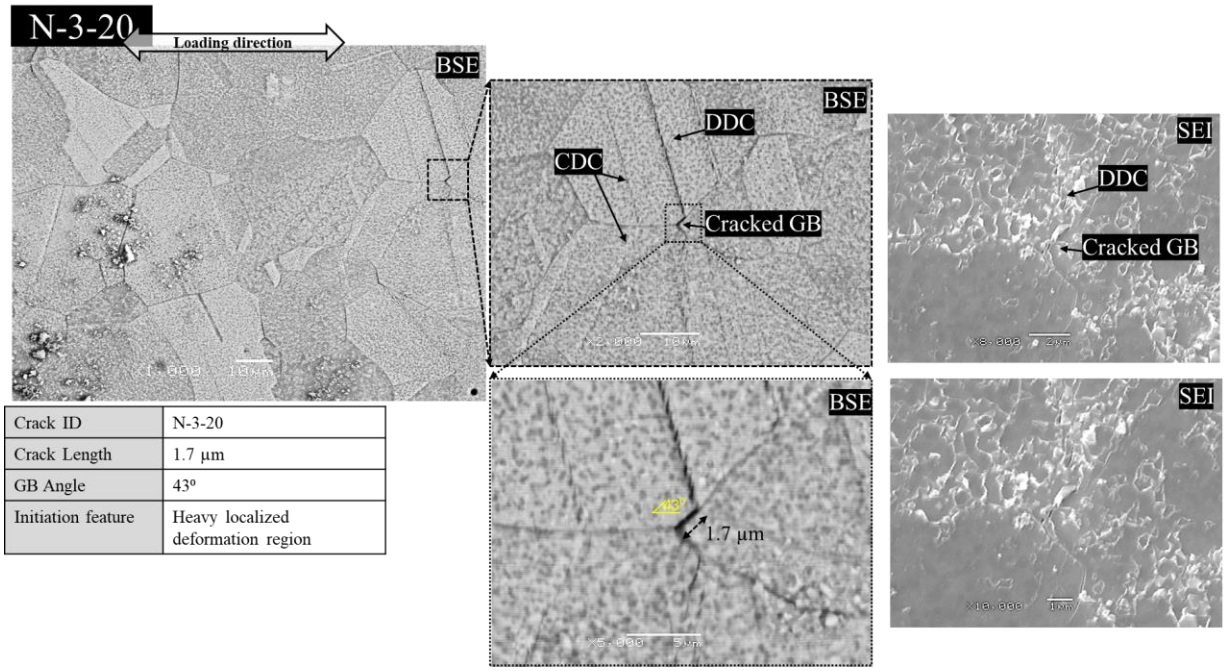


| | |
|---|---|
| Crack ID | N-3-20 |
| Crack Length | 1.7 µm |
| GB Angle | 43º |
| Initiation feature | Heavy localized deformation region |

Figure 0-15 Surface morphology of crack N-3-20.

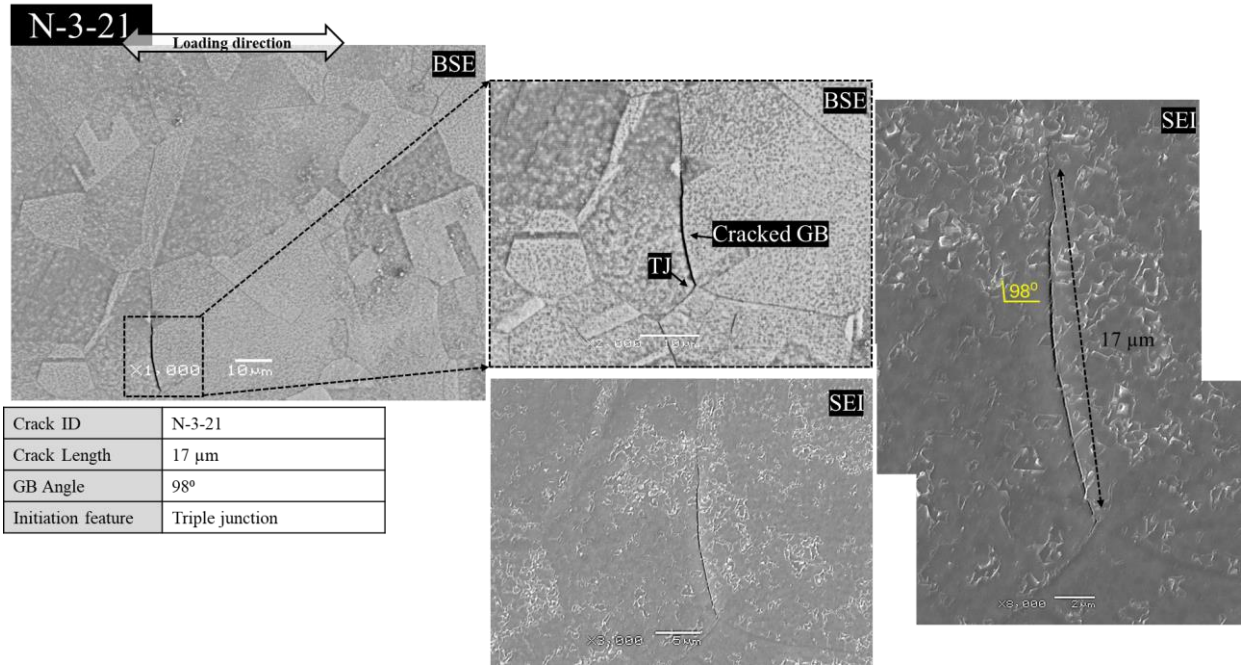


| | |
|---|---|
| Crack ID | N-3-21 |
| Crack Length | 17 µm |
| GB Angle | 98º |
| Initiation feature | Triple junction |

Figure 0-16 Surface morphology of crack N-3-21.

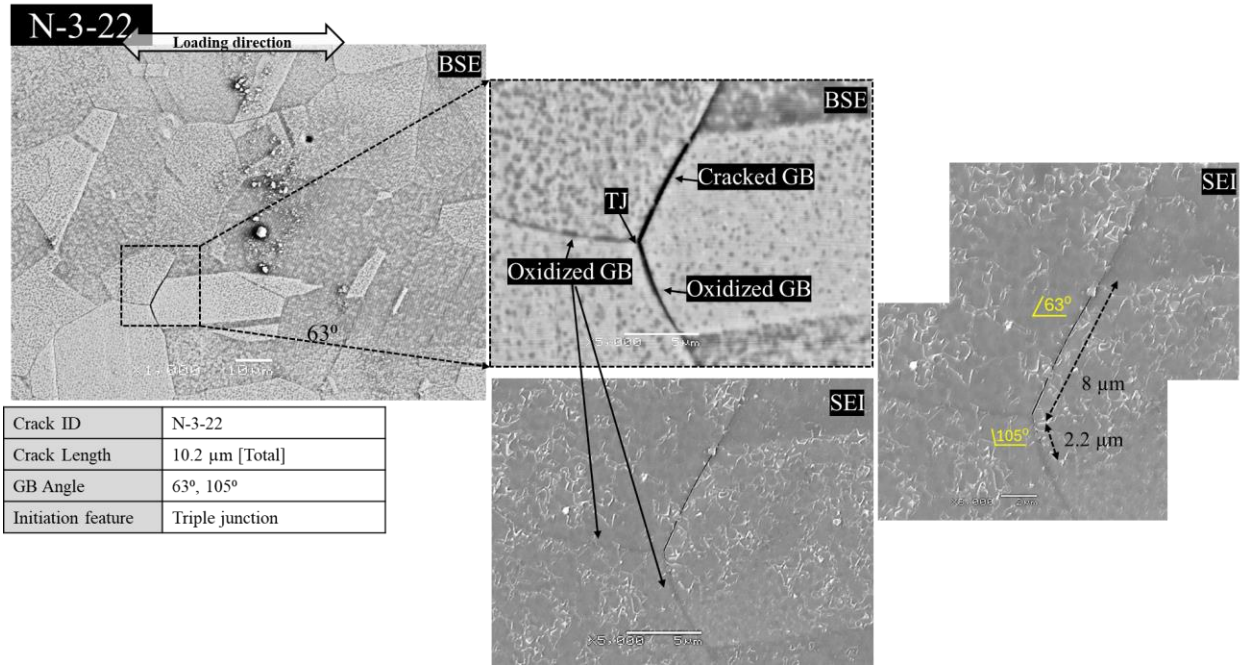


| | |
|---|---|
| Crack ID | N-3-22 |
| Crack Length | 10.2 µm [Total] |
| GB Angle | 63º, 105º |
| Initiation feature | Triple junction |

Figure C-17 Surface morphology of crack N-3-22.

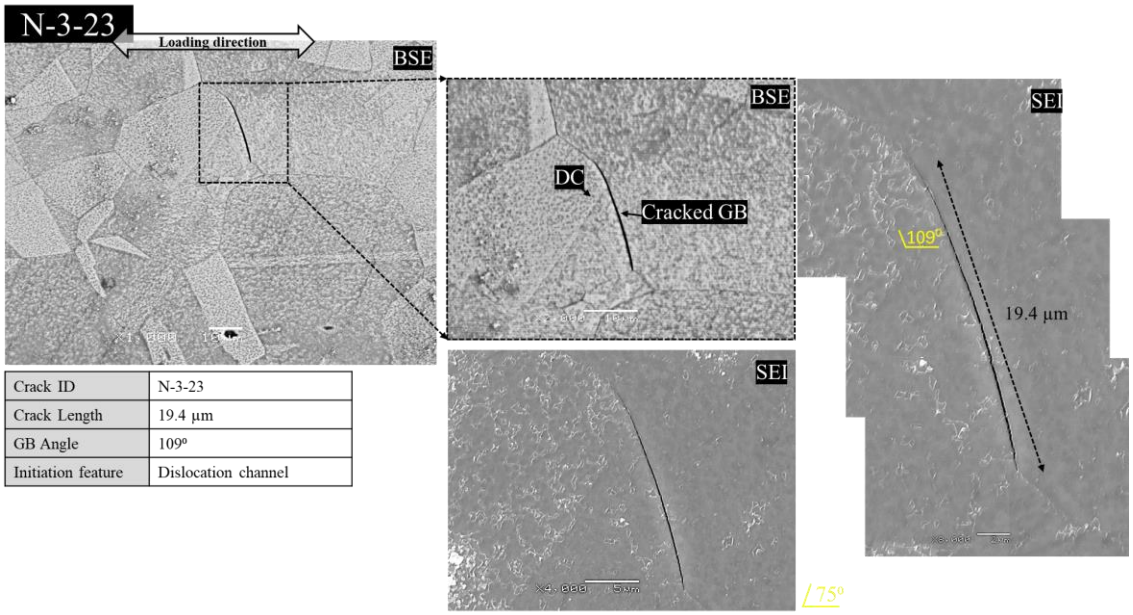


| | |
|---|---|
| Crack ID | N-3-23 |
| Crack Length | 19.4 µm |
| GB Angle | 109º |
| Initiation feature | Dislocation channel |

Figure 0-18 Surface morphology of crack N-3-23.

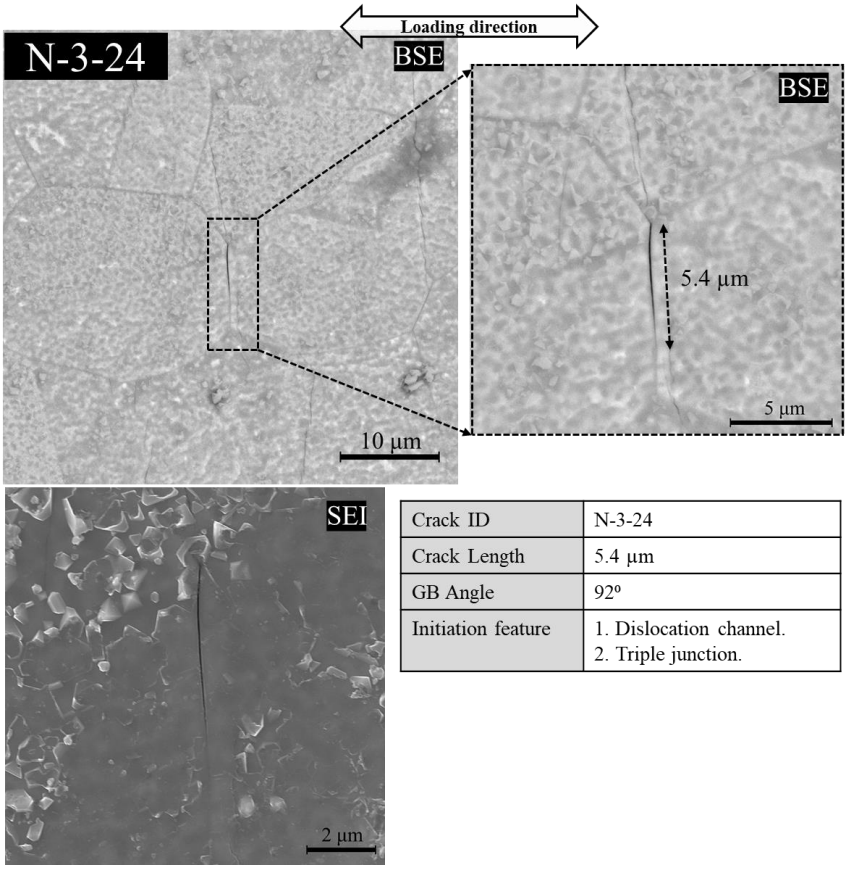


| | |
|---|---|
| Crack ID | N-3-24 |
| Crack Length | 5.4 µm |
| GB Angle | 92º |
| Initiation feature | 1. Dislocation channel.<br>2. Triple junction. |

Figure C-19 Surface morphology of crack N-3-24.

Sample N7

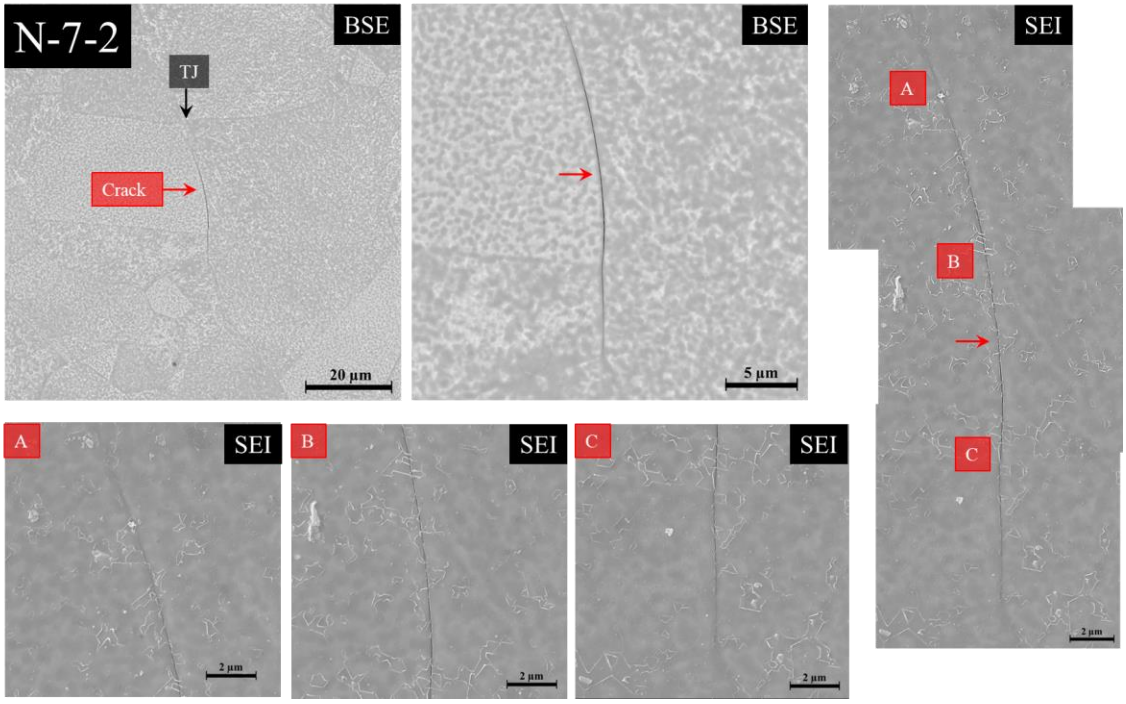


Figure C-20 Surface morphology of crack N-7-2.

Sample N10

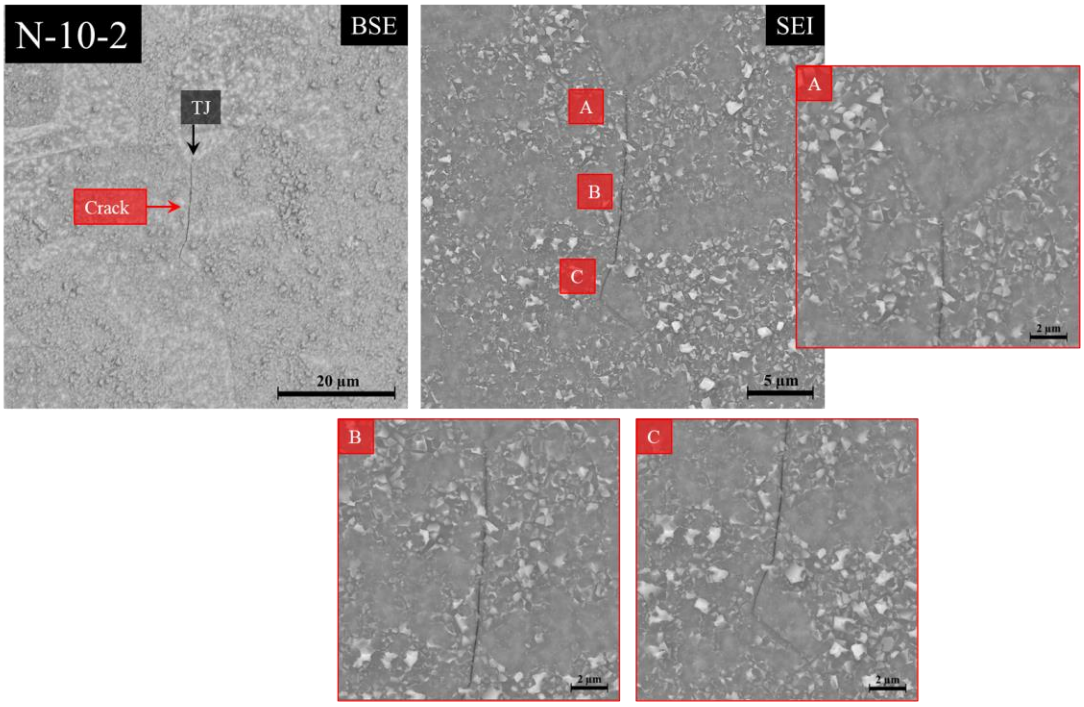


Figure C-21 Surface morphology of crack N-10-2.

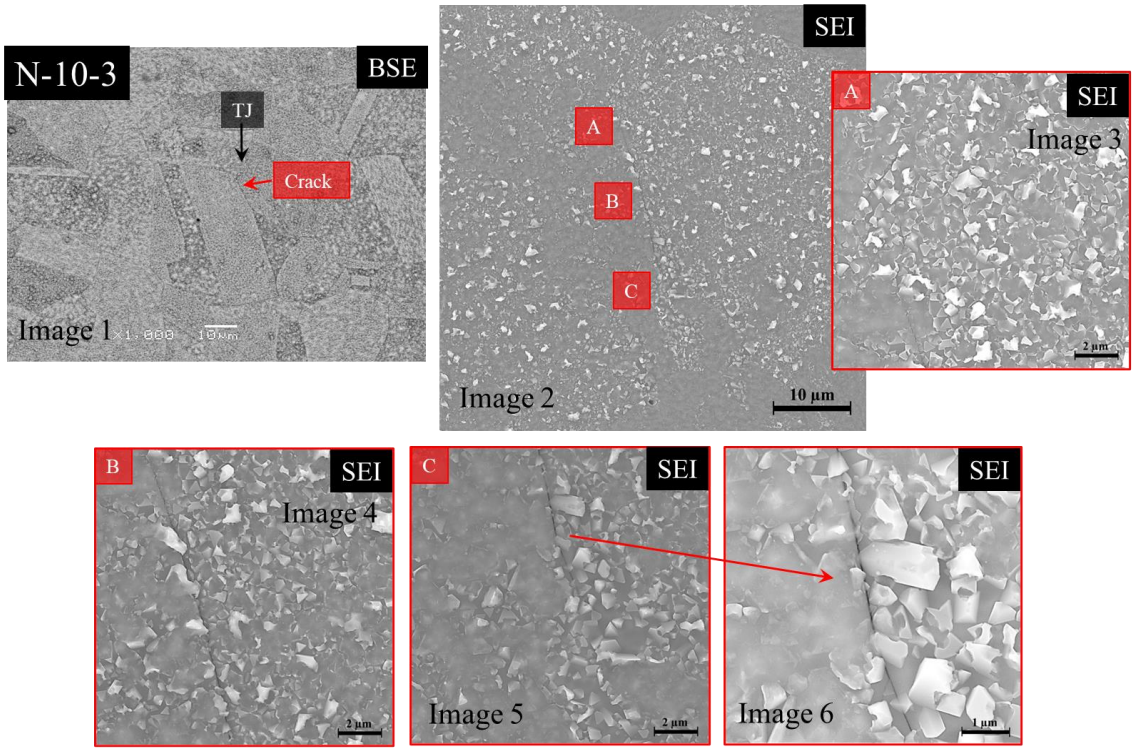


Figure 0-22 Surface morphology of crack N-10-3.

Sample L-R-1

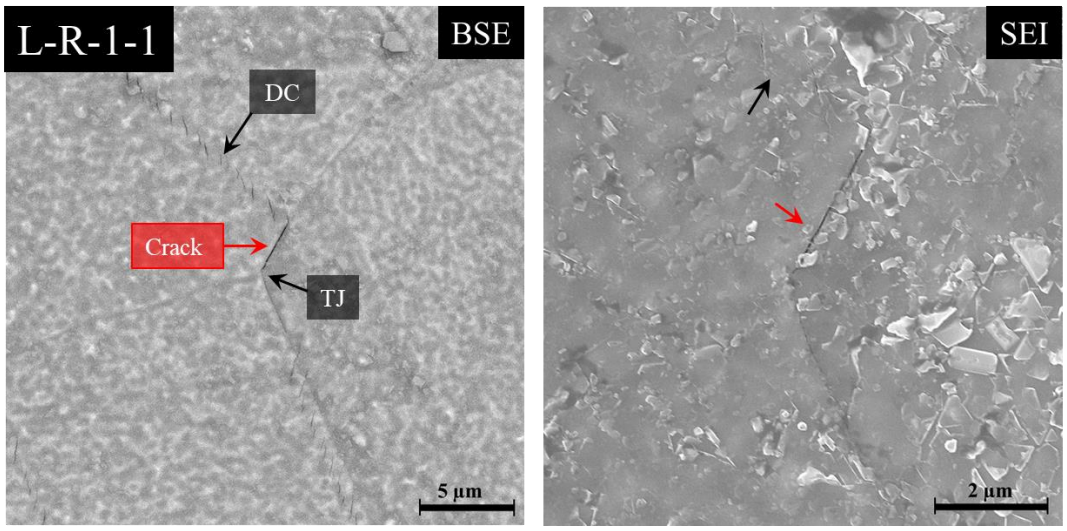


Figure 0-23 Surface morphology of crack L-R-1-1.

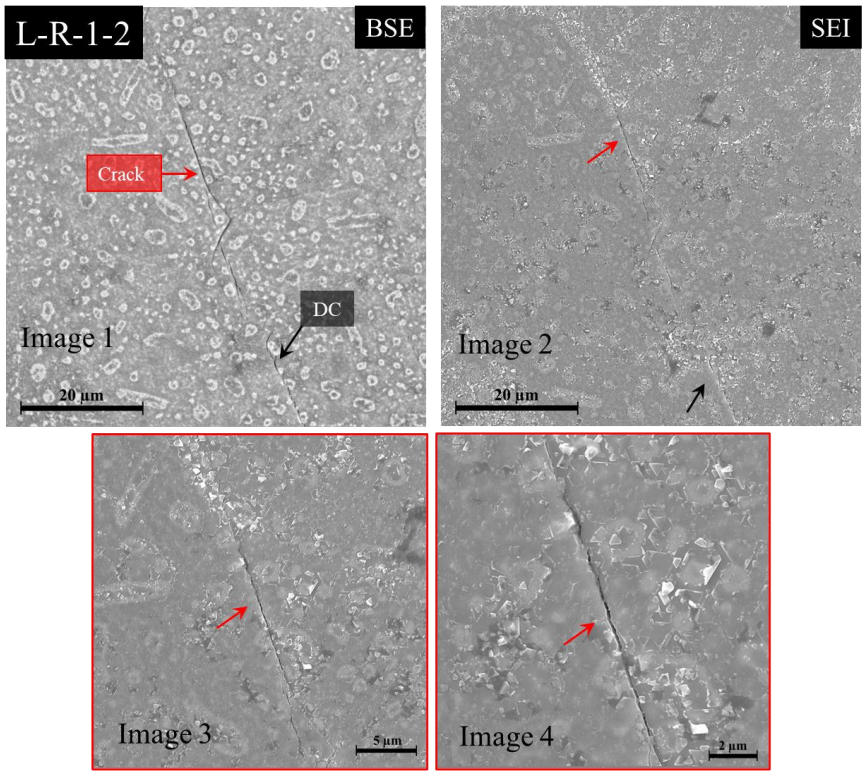


Figure C-24 Surface morphology of crack L-R-1-2.

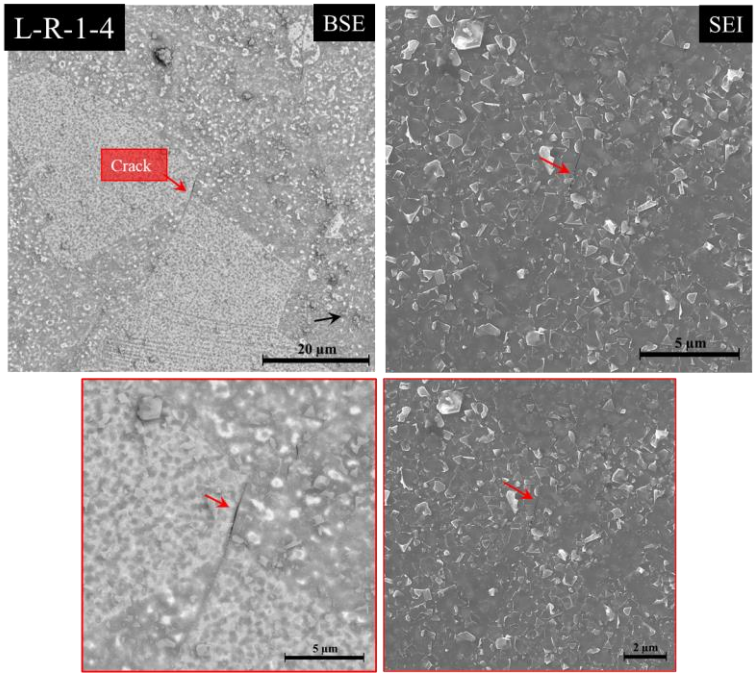


Figure C-25 Surface morphology of crack L-R-1-4.

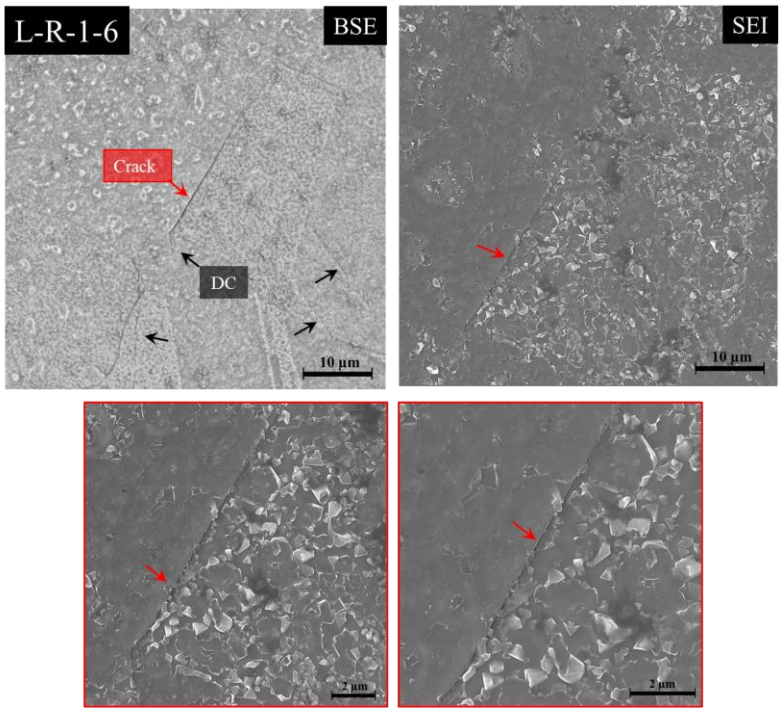


Figure 0-26 Surface morphology of crack L-R-1-6.

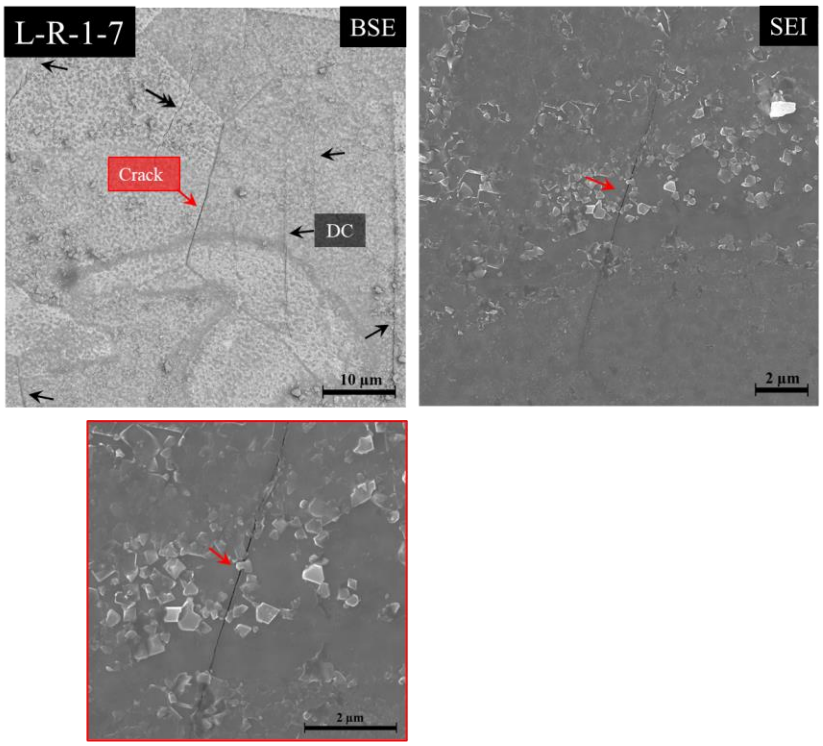


Figure C-27 Surface morphology of crack L-R-1-7.

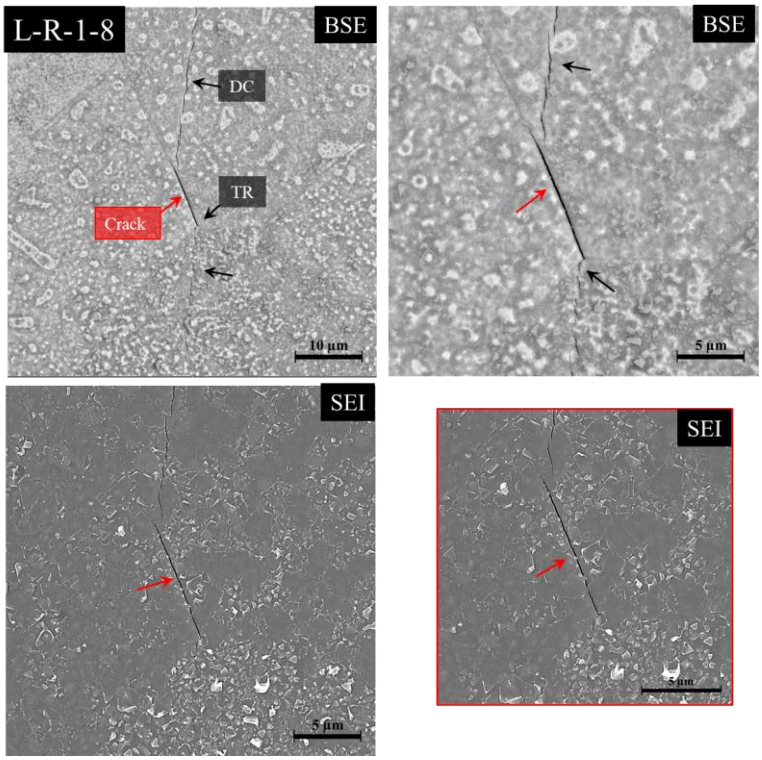


Figure C-28 Surface morphology of crack L-R-1-8.

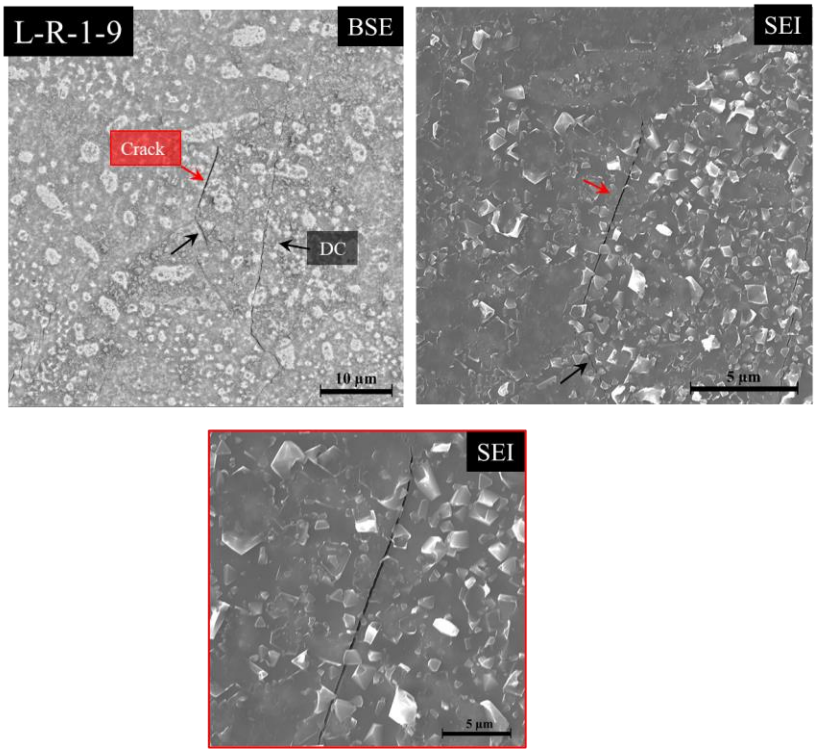


Figure C-29 Surface morphology of crack L-R-1-9.

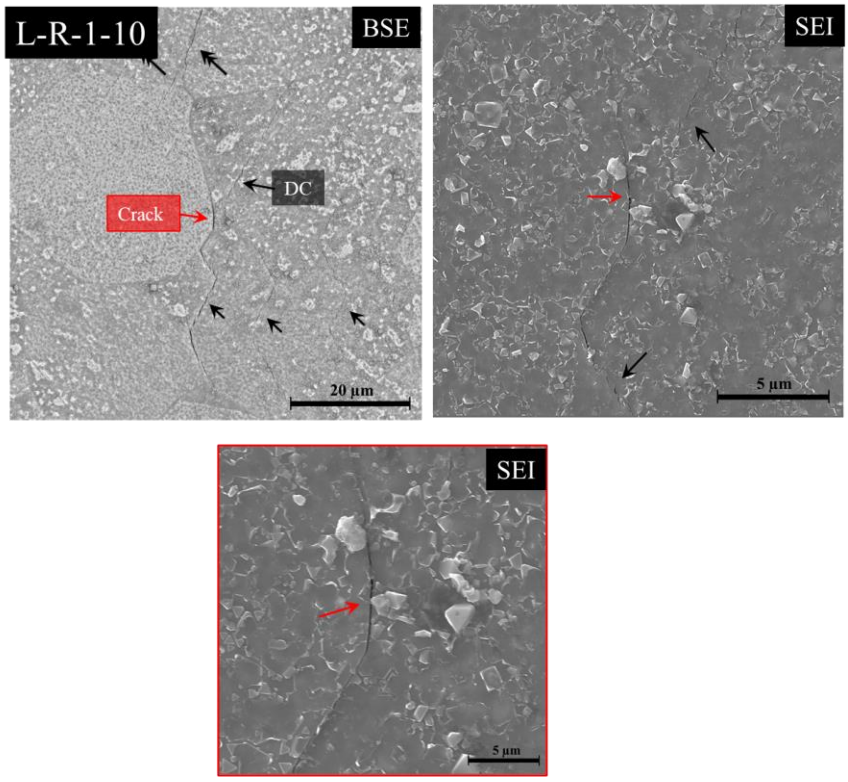


Figure C-30 Surface morphology of crack L-R-1-10.

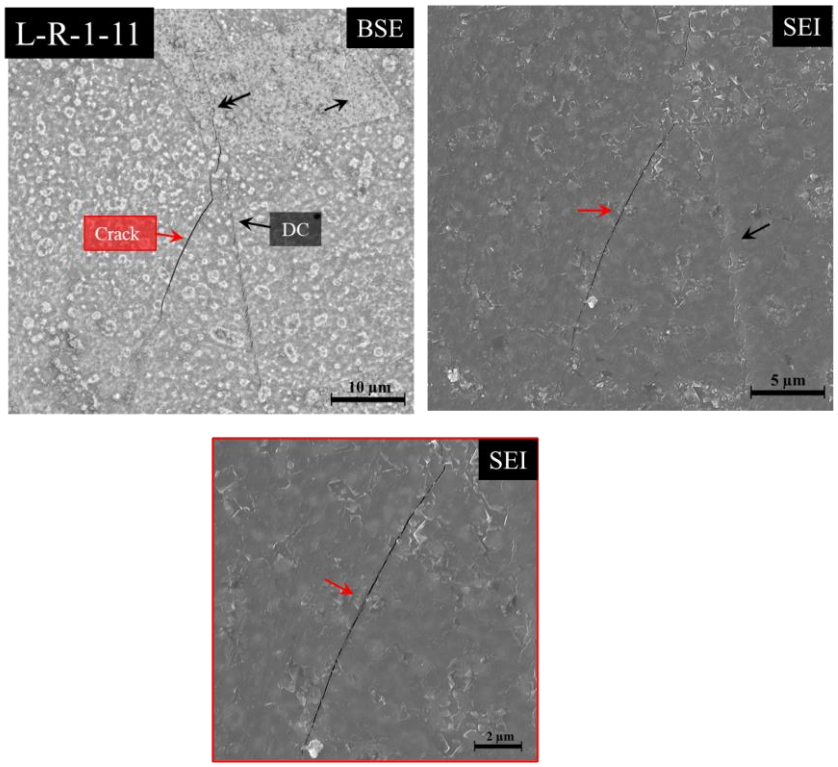


Figure 0-31 Surface morphology of crack L-R-1-11.

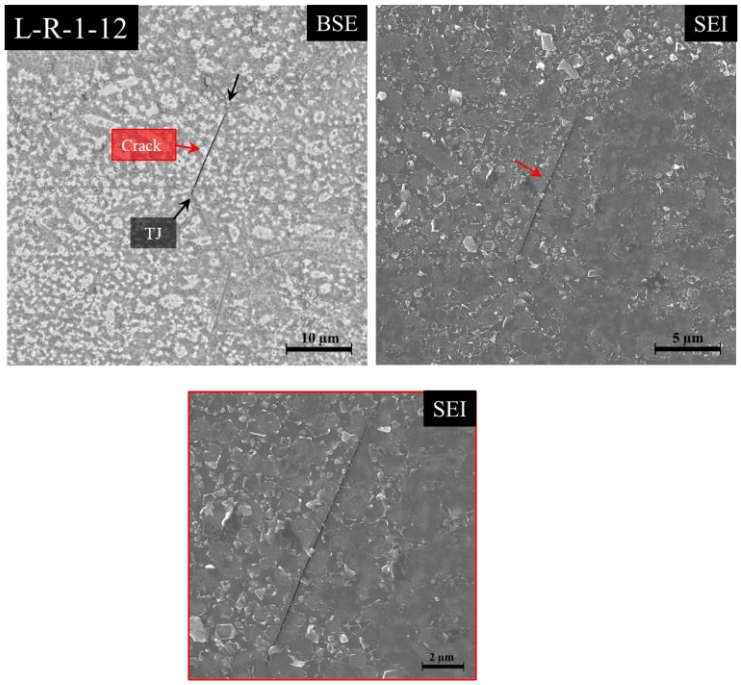


Figure C-32 Surface morphology of crack L-R-1-12.

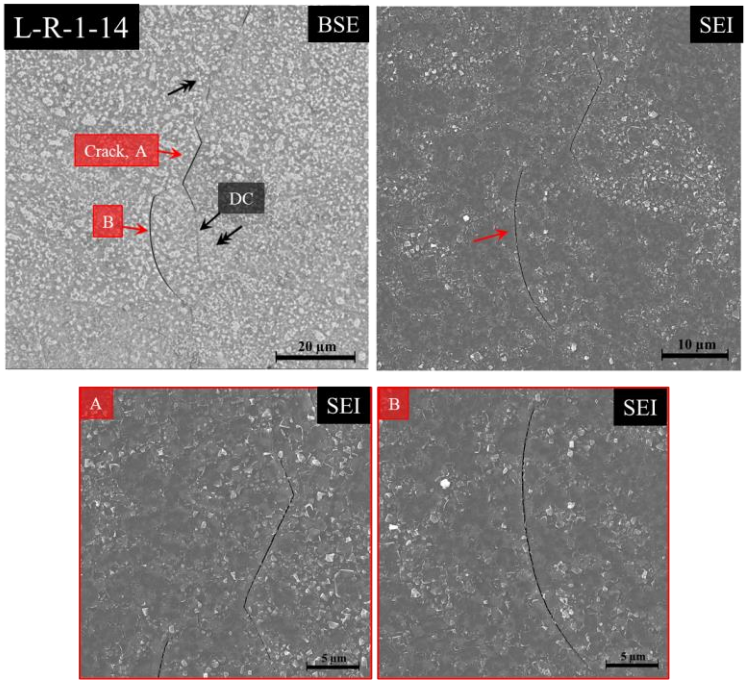


Figure 0-33 Surface morphology of crack L-R-1-14.

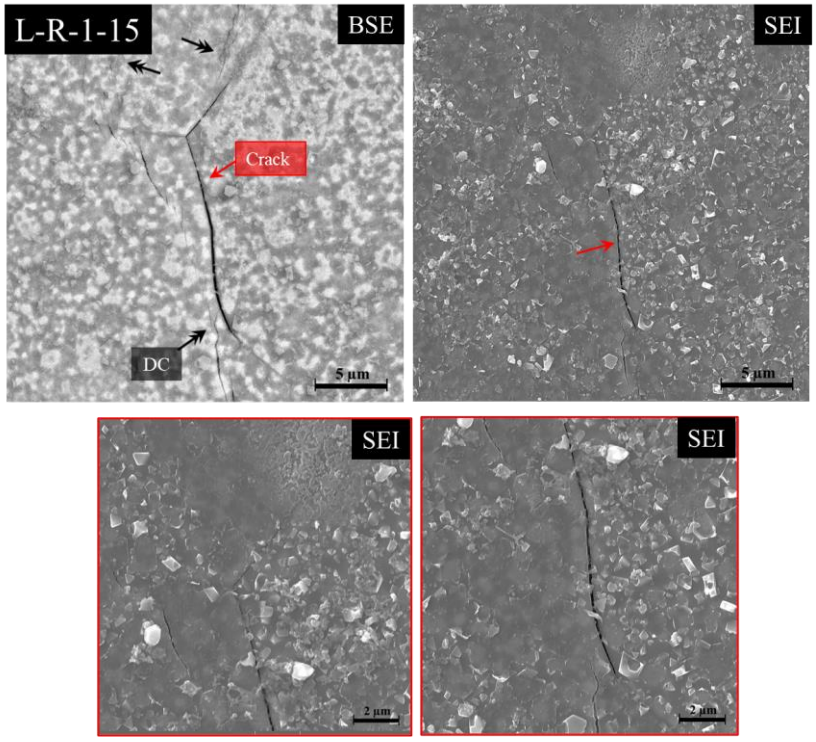


Figure C-34 Surface morphology of crack L-R-1-15.

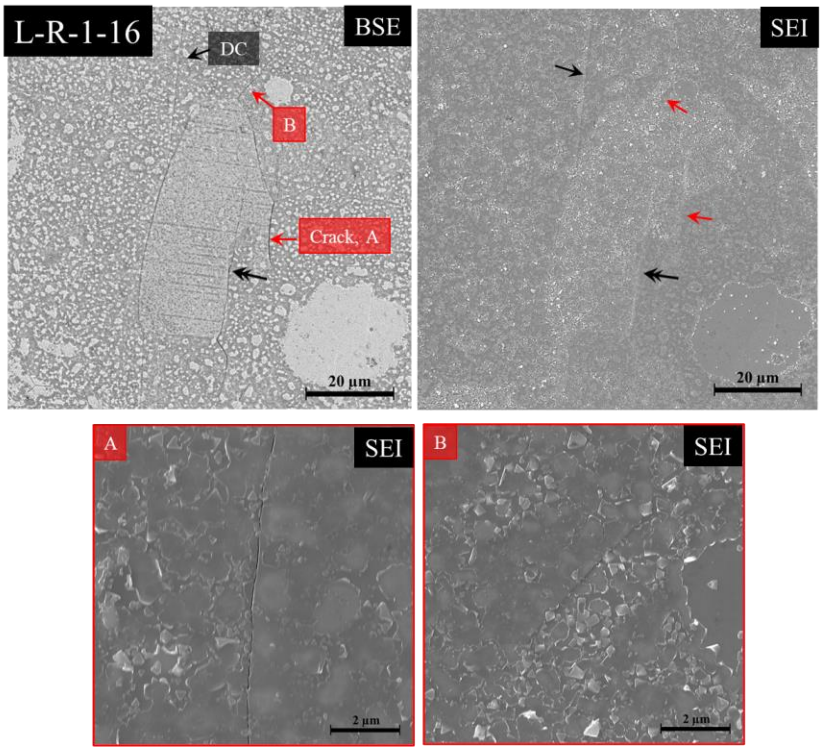


Figure 0-35 Surface morphology of crack L-R-1-16.

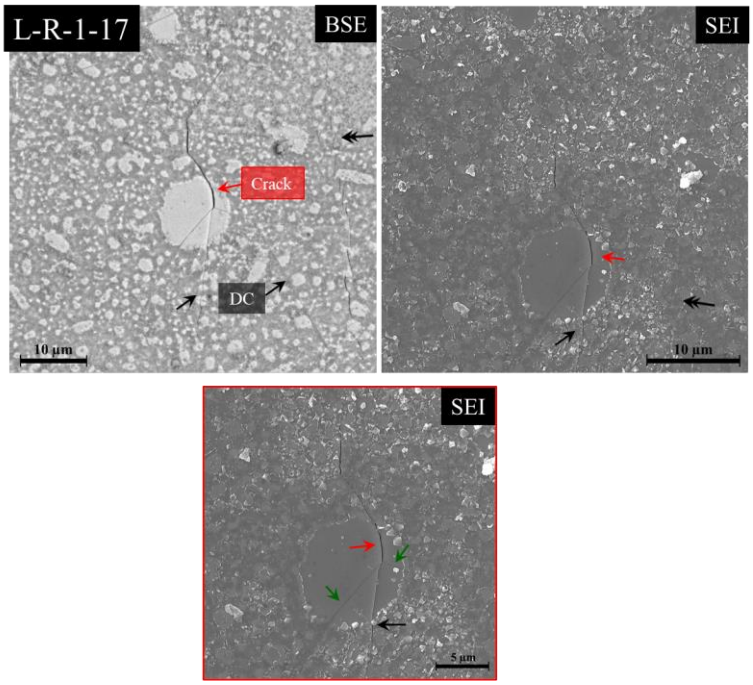


Figure 0-36 Surface morphology of crack L-R-1-17.

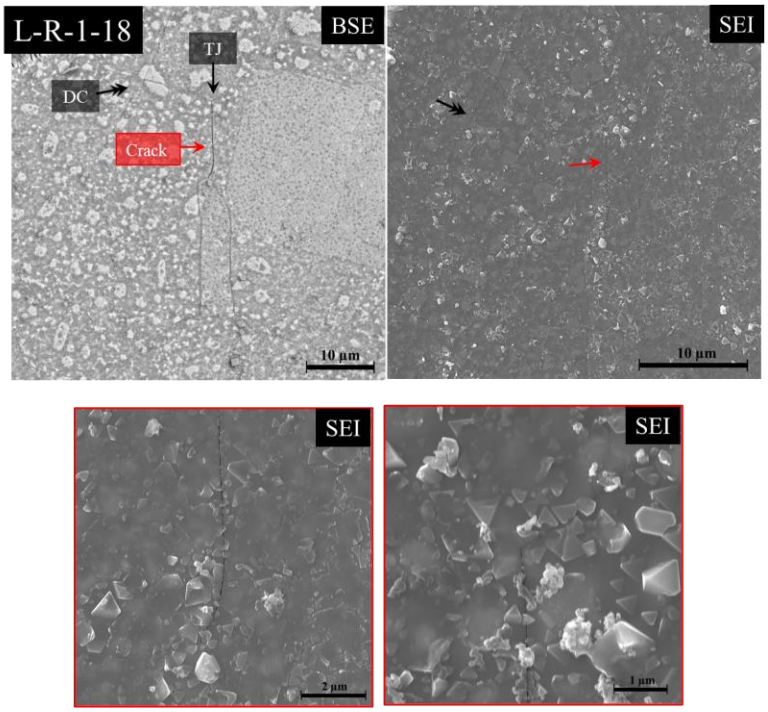


Figure C-37 Surface morphology of crack L-R-1-18.

Sample L-R-3

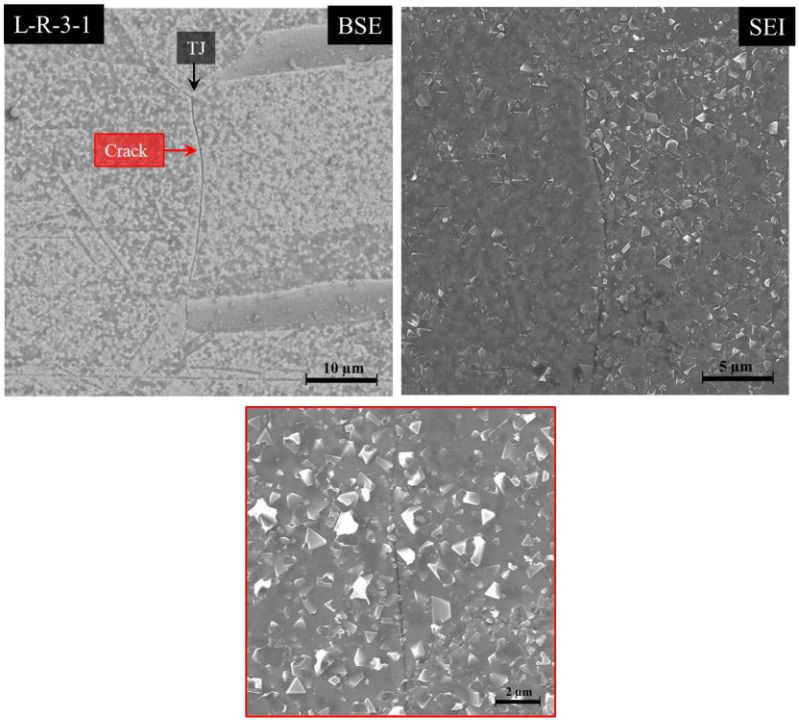


Figure C-38 Surface morphology of crack L-R-3-1.

Sample L-R-6

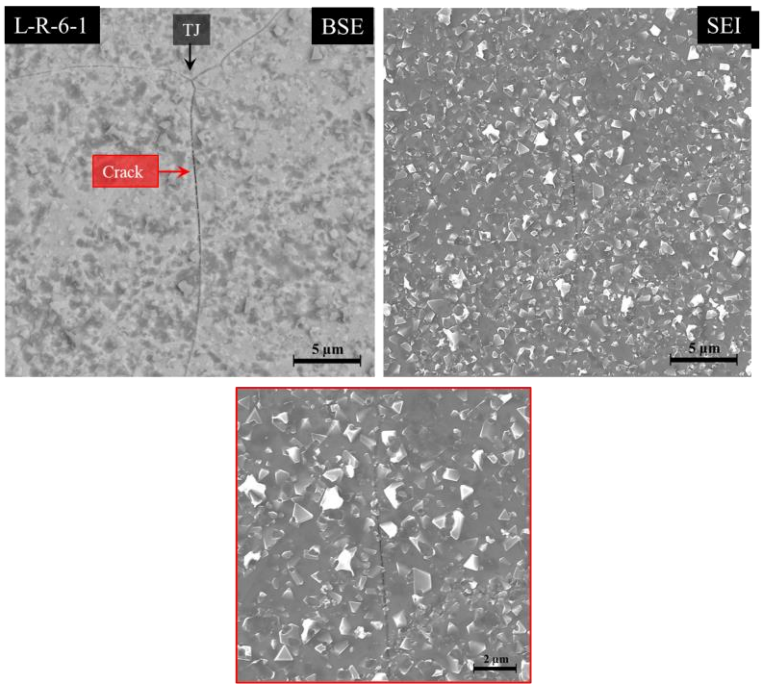


Figure C-39 Surface morphology of crack L-R-6-1.

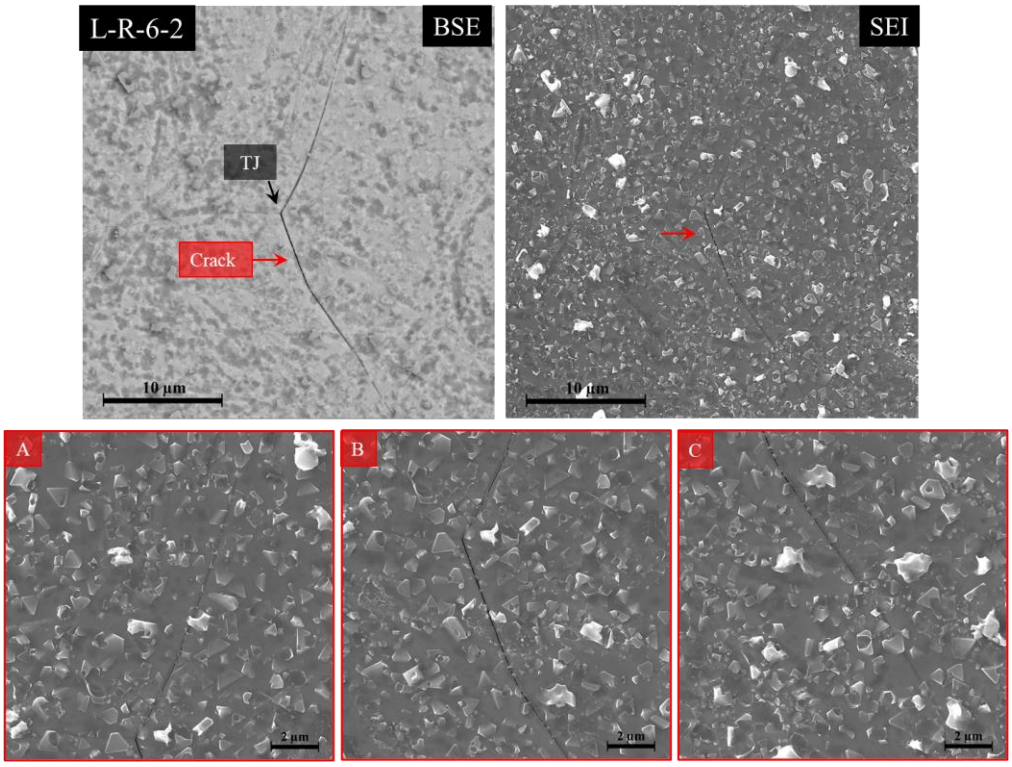


Figure C-40 Surface morphology of crack L-R-6-2.

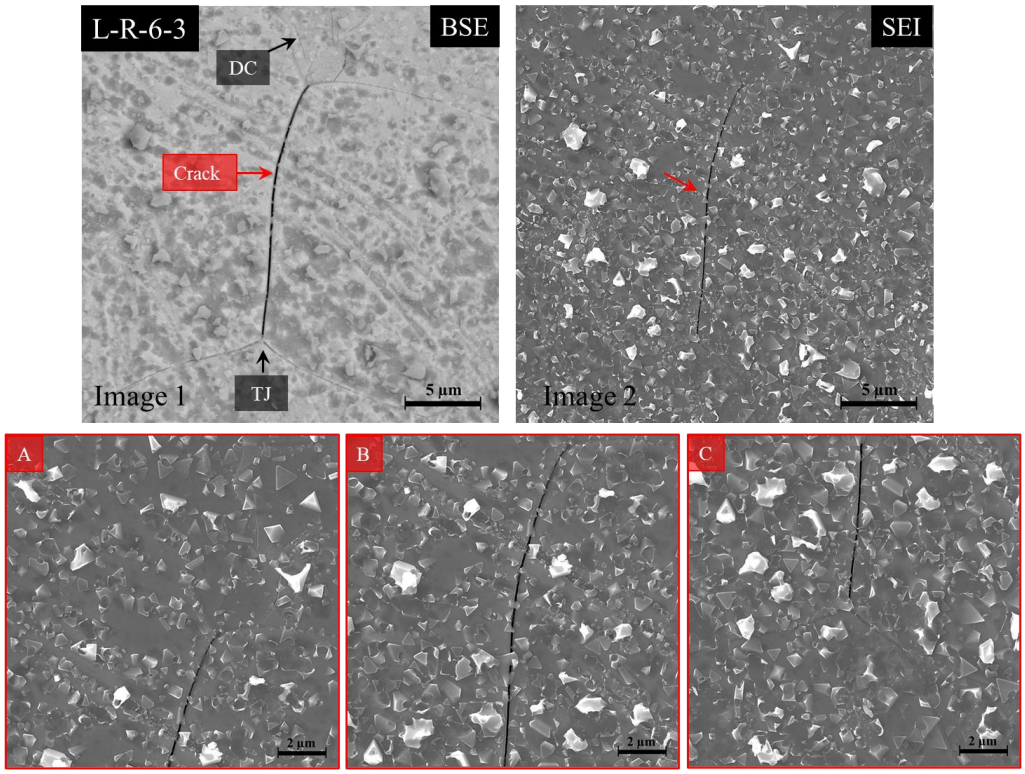


Figure C-41 Surface morphology of crack L-R-6-3.

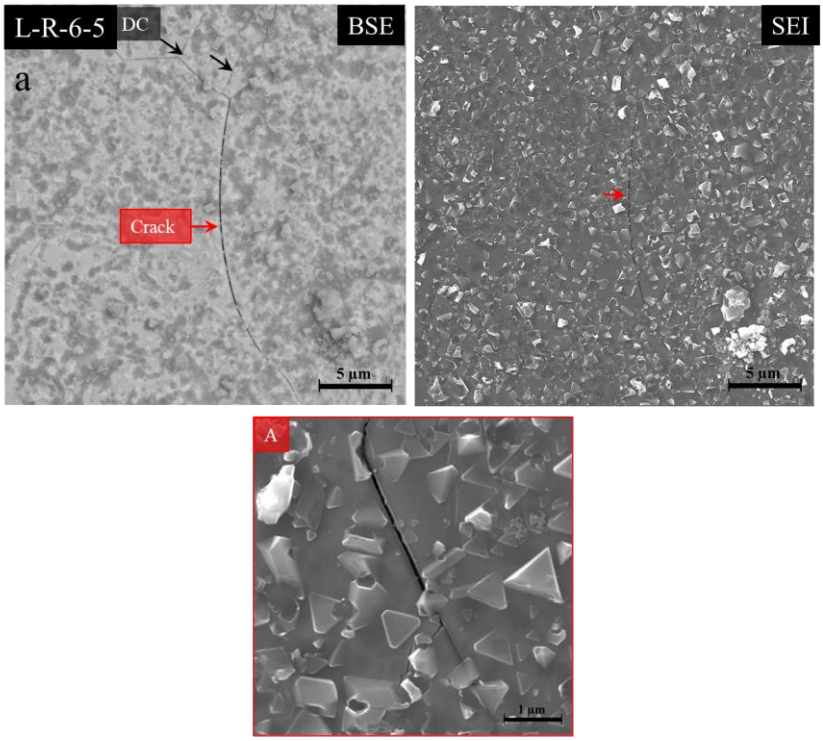


Figure C-42 Surface morphology of crack L-R-6-5.

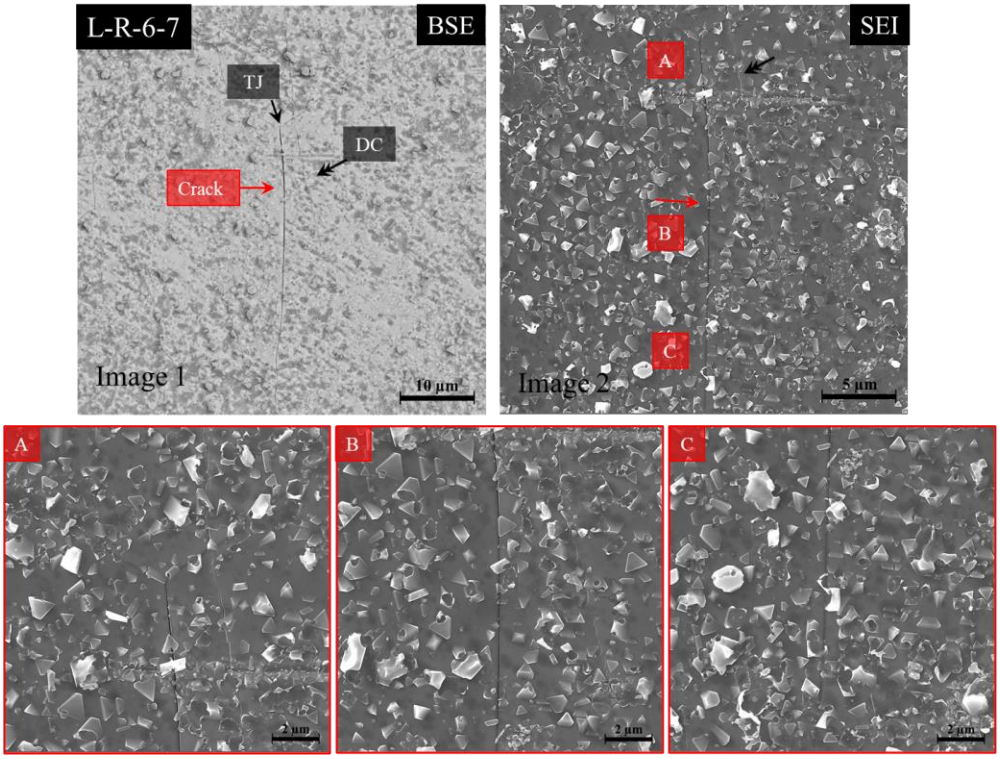


Figure C-43 Surface morphology of crack L-R-6-7.

## Bibliography


[1] "Nuclear Energy of a Net Zero World," International Atomic Energy Agency (IAEA), 2021.

[2] "The Ultimate Fast Facts Guide To Nuclear Energy, DOE/NE-0150,," US Department of Energy, 2021.

[3] "Safely And Responsibility Expanding U.S. Nuclear Energy: Deployment Targets and A Framework For Action," The White House,, Novermber 2024.

[4] G. S. Was, Y. Ashida and P. L. Andresen, "Irradiation-assisted stress corrosion cracking," *Corrosion Review,* vol. 29, pp. 7-49, 2011.

[5] M. Jeong and J. . S. You, "Estimating the economic costs of nuclear power plant outages in a regulated market using a latent factor model," *Renewable and Sustainable Energy Reviews,* vol. 166, p. 112582, 2022.

[6] D. Mandelli, S. W. S. Germain, E. Chen, C. Otani, J. T. Boyce, J. N. Mapes, A. Y. Al Rashdan, C. Wang and S. Lawrence, "Tools And Methods to Analyze Plant Outage Schedule and Assist Schedulers in Improving Outage Resilience, INL/RPT-24-80380-Revision-0,," Idaho National Laboratory, , 2024.

[7] M. D. McMutrey, B. Cui, I. Robertson, D. Farkas and G. S. Was, "Mechanism of dislocation channel-induced irradiation assisted stress corrosion crack initiation in

austenitic stainless steel," *Current Opinion in Solid State and Materials Science,* vol. 19, pp. 305-314, 2015.

[8] Z. Jiao and G. S. Was, "Localized deformation and IASCC initiation in austenitic stainless steels," *Journal of Nuclear Materials,* vol. 382, pp. 203-209, 2008.

[9] Z. Jiao and G. S. Was, " Impact of localized deformation on IASCC in austenitic stainless steels," *Journal of Nuclear Materials,* vol. 408, pp. 246-256, 2011.

[10] K. Fukuya, H. Nishioka, K. Fujii and T. Miura, "An EBSD examination of SUS316 stainless steel irradiated to 73 dpa and deformed at 593 K," *Journal of Nuclear Materials,* vol. 417, pp. 958-962, 2011.

[11] P. L. Andresen, F. P. Ford, G. Gott, P. M. Scott, T. Shoji, R. W. Staehle and R. L. Tapping, "Expert Panel Report on Proactive Materials Degradation Assessment, NUREG/CR-6923," US.NRC, 2007.

[12] J. . T. Busby, "Overview of Structural Materials in Water-Cooled Fission Reactors," in *Structural Alloys for Nuclear Energy Applications*, Elsevier, 2019, pp. 1-22.

[13] S. J. Zinkle and J. T. Busby, "Structural materials for fission and fusion energy," *Materials Today,* vol. 12, no. 11, pp. 12-19, 2009.

[14] F. A. Garner, M. B. Toloczko and B. H. Sencer, "Comparison of swelling and irradiation creep behavior of fcc-austenitic and bcc-ferritic/martensitic alloys at high neutron exposure," *Journal of Nuclear Materials,* vol. 276, no. 1-3, pp. 123-142, 2000.

[15] A. Todd, J. Busby, M. Meyer and D. Petti, "Materials challenges for nuclear systems," *Materials Today,* vol. 13, no. 12, pp. 14-23, 2010.

[16] J. T. Busby, R. K. Nanstad, R. E. Stoller, Z. Feng and D. J. Naus, "Materials Degradation in Light Water Reactors: Life After 60, ORNL White Paper on Materials for LWRSP," [Online]. Available: https://www.energy.gov/ne/articles/materials-degradation-light-water-reactors-life-after-60. [Accessed 13 08 2025].

[17] J. C. Danko, "Corrosion in the nuclear power industry," in *Gulf Publishing Company*, 1987, pp. p. 927–984.

[18] G. S. Was and P. L. Andresen, "Irradiation assisted corrosion and stress corrosion cracking (IAC/IASCC) in nuclear reactor systems and components," in *Nuclear corrosion science and engineering*, Oxford, Woodhead Publishing Ltd, 2012, p. 131.

[19] G. S. Was, Y. Ashida and P. L. Andresen, "Irradiation-assisted stress corrosion cracking," *Corrosion Reviews,* vol. 29, pp. 7-49, 2011.

[20] G. S. Was, C. -B. Bahn, J. Busby, B. Cui, D. Farkas, M. Gussev, M. Rigen He, J. Hesterberg, Z. Jiao, D. Johnson, W. Kuang, M. McMurtrey, I. Robertson, A. Sinjlawi, M. Song, K. Stephenson, K. Sun, S. Swaminathan, M. Wang and E. West, "How irradiation promotes intergranular stress," *Progress in Materials Science,* vol. 143, p. 101255, 2024.

[21] J. R. Davis, ASM Speciality Handbook – Stainless Steels, ASM International, 1999.

[22] W. F. Hosford, Iron and Steel, Cambridge University Press, 2012.

[23] A. L. Shaeffler, "Welding dissimilar metals with stainless electrodes," *Iron Age,* vol. 72, 1948.

[24] J. R. Davis, Metals Handbook Desk Edition, ASM International, 1998.

[25] D. H. Philip, Engineering Properties of Steel, ASM International, 1982.

[26] G. George and H. Shaikh, "Introduction to Austenitic Stainless Steels," in *Corrosion of Austenitic Stainless Steels: Mechanism, Mitigation and Monitoring*, Woodhead Publishing, 2002, pp. 1-36.

[27] P. Lacombe, B. Baroux and G. Beranger, "Stainless Steels," in *Austenitic Stainless Steels*, ASM International, 1993.

[28] V. G. Gavriljuk and S. P. Jephimenko, "Distribution of Nitrogen Atoms, their Interaction with Dislocations and Properties of High-Nitrogen Austenite," in *The 2nd international conference on high nitrogen steel (HNS-90)*, Aachen, 1990.

[29] P. R. Swann, "Dislocation Substructure vs Transgranular Stress Corrosion Susceptibility Of Single Phase Alloys," *Corrosion,* pp. 102t-104t, 1963.

[30] J. G. Sassen, A. J. Garratt-Reed and W. S. Owen, "Electron microscopy of austenitic Fe-Ni-Cr alloys containing N," in *HNS 88, The Institute of Metals*, Lille, 1989.

[31] M. FUJIKURA, K. TAKADA and K. ISHIDA, "Effect of Manganese and Nitrogen on the Mechanical Properties of Fe-18%Cr-1O%Ni Stainless Steels," *Transactions of the Iron and Steel Institute of Japan,* vol. 15, no. 9, pp. 464-469, 1975.

[32] S. Kibey, J. B. Liu, M. J. Curtis, D. D. Johnson and H. Sehitoglu, "Effect of nitrogen on generalized stacking fault energy and stacking fault widths in high nitrogen steels," *Acta Materialia,* vol. 54, no. 11, pp. 2991-3001, 2006.

[33] L. Mosecker and A. Saeed-Akbari, "Nitrogen in chromium–manganese stainless steels: a review on the evaluation of stacking fault energy by computational thermodynamics," *Science and Technology of Advanced Materials,* vol. 14, p. 033001, 2013.

[34] J.-Y. Lee, Y. M. Koo, S. Lu, L. Vitos and S. K. Kwon, "The behavior of stacking fault energy upon interstitial alloying," *Scientific Reports,* p. 11074, 2017.

[35] T.-H. Lee, E. Shin, C.-S. Oh, H.-Y. Ha and S.-J. Kim, "Correlation between stacking fault energy and deformation microstructure in high-interstitial-alloyed austenitic steels," *Acta Materialia,* vol. 58, pp. 3173-3186, 2010.

[36] A. H. Cottrell and B. A. Bilby, "Dislocation Theory of Yielding and Strain Ageing of Iron," *Proceedings of the Physical Society A,* vol. 62, pp. 49-62, 1949.

[37] P. Mullner, C. Solenthaler, P. Uggowitzer and M. O. Speidel, "On the effect of nitrogen on the dislocation structure of austenitic stainless steel," *Materials Science and Engineering: A,* vol. 164, no. 1-2, pp. 164-169., 1993.

[38] M. L. Byrnes, M. Grujicic and W. S. Owen, "Nitrogen strengthening of a stable austenitic stainless steel," *Acta Materialia,* vol. 35, pp. 1853-1862, 1987.

[39] K. Dae Whan, "Influence of nitrogen-induced grain refinement on mechanical properties of nitrogen alloyed type 316LN stainless steel," *Journal of Nuclear Materials,* vol. 420, pp. 473-478, 2012.

[40] J. Rawers and M. Grujicic, "Effects of metal composition and temperature on the yield strength of nitrogen strengthened stainless steels," *Materials Science and Engineering: A,* vol. 207, no. 2, pp. 188-194, 1996.

[41] E. Werner, M. Grujicic and W. S. Owen, "Solid solution and grain size hardening of nitrogen-alloyed austenitic steels," *Materials Science and Engineerin A,* vol. 101, pp. 93-98, 1988.

[42] L. -Å. Norström, M. Grujicic and W. S. Owen, "The influence of nitrogen and grain size on yield strength in Type AISI 316L austenitic stainless steel," *Metal Science,* Vols. 208-212, no. 6, p. 11, 1977.

[43] O. Bouaziz, H. Zurob, B. Chehab, J. D. Embury, S. Allain and M. Huang, "Effect of chemical composition on work hardening of Fe-Mn-C TWIP steels," *Materials Science and Technology,* vol. 27, no. 3, pp. 707-709, 2011.

[44] É. V. Kozlov, L. A. Teplyakova, N. A. Koneva, V. G. Gavrilyuk, N. A. Popova, L. N. Ignatenko, G. . L. Fedoseeva, S. Y. Smuk, A. V. Paul and V. . P. Podkovka, "Role of solid-solution strengthening and interactions in the dislocation ensemble in the formation of flow stress in austenitic nitrogen steel," *Russian Physics Journal ,* vol. 39, pp. 211-229, 1996.

[45] K. Ishio and H. Nakajima, "Effects of Nitrogen on the Mechanical Properties of 316LN Stainless steels," *Testu-to-Hagane,* vol. 92, pp. 38-44, 2006.

[46] P. R. Okamoto and L. E. Rehn, "Radiation-induced segregation in binary and ternary alloys," *Journal of Nuclear Materials,* vol. 83, pp. 2-23, 1979.

[47] R. D. Carter, D. L. Damcott, M. Atzmon and E. A. Kenik, "Effects of proton irradiation on the microstructure and microchemistry of type 304L stainless steel," *Journal of Nuclear Materials,* vol. 205, pp. 361-373, 1993.

[48] T. Miura, K. Fujii and Y. Ito, "Characterization of deformation structure in ion-irradiated stainless steels," *Journal of Nuclear Materials ,* Vols. 386-388, pp. 210-213, 2009.

[49] S. J. Zinkle and G. S. Was, "Materials challenges in nuclear energy," *Acta Materialia,* vol. 61, pp. 735-758, 2013.

[50] G. S. Was and J. T. Busby, "Role of irradiated microstructure and microchemistry in irradiation-assisted stress corrosion cracking," *Philosophical Magazine,* vol. 85, pp. 443-465, 2005.

[51] S. J. Zinkle and J. T. Busby, "Structural materials for fission & fusion energy," *Materials Today,* vol. 12, pp. 12-19, 2009.

[52] B. N. Singh and C. H. Woo, "Consequences of intra-cascade clustering on defect accumulation and materials performance," *Radiation Effects and Defects in Solids,* vol. 144, no. 1-4, pp. 119-143, 1998.

[53] G. S. Was, B. Alexandreanu and J. Busby, "Localized Deformation Induced IGSCC and IASCC of Austenitic Alloys in High Temperature Water," *Key Engineering Materials,* Vols. 261-263, pp. 885-902, 2004.

[54] D. J. Edwards, E. P. Simonen and S. M. Bruemmer, "Evolution of fine-scale defects in stainless steels neutron-irradiated at 275 °C," *Journal of Nuclear Materials,* vol. 317, pp. 13-31, 2003.

[55] G. S. Was and P. L. Andresen, "Mechanisms behind irradiation-assisted stress corrosion cracking," in *Nuclear Corrosion: Research, Progress, and Challenges*, Woodhead Publishing, 2020, pp. 47-88.

[56] A. Etienne, M. Hernández-Mayoral, C. Genevois, B. Radiguet and P. Pareige, "Dislocation loop evolution under ion irradiation in austenitic stainless steels," *Journal of Nuclear Materials,* vol. 400, pp. 56-63, 2010.

[57] S. J. Zinkle, P. J. Maziasz and R. E. Stoller, "Dose dependence of the microstructural evolution in neutron-irradiated austenitic stainless steel," *Journal of Nuclear Materials,* vol. 206, no. 2-3, pp. 266-286, 1993.

[58] L. K. Mansur, "Theory and experimental background on dimensional changes in irradiated alloys☆," *Journal of Nuclear Materials,* vol. 216, pp. 97-123, 1994.

[59] D. J. Bacon, F. Gao and Y. N. Osetsky, "The primary damage state in fcc, bcc and hcp metals as seen in molecular dynamics simulations," *Journal of Nuclear Materials,* vol. 276, no. 1-3, pp. 1-12, 2000.

[60] M. Horiki and M. Kiritani, "Microstructural evolution in low-dose neutron-irradiated Fe-16Ni-15Cr alloy," *Journal of Nuclear Materials,* Vols. 212-215, pp. 246-251, 1994.

[61] C. Pokor, Y. Brechet, P. Dubuisson, J. -P. Massoud and A. Barbu, "Irradiation damage in 304 and 316 stainless steels: experimental investigation and modeling. Part I: Evolution of the microstructure," *Journal of Nuclear Materials,* vol. 326, pp. 19-29, 2004.

[62] Z. Jiao and G. S. Was, "Segregation behavior in proton- and heavy-ion-irradiated ferritic–martensitic alloys," *Acta Materialia,* vol. 59, pp. 4467-4481, 2011.

[63] Z. Jiao and G. S. Was, "Novel features of radiation-induced segregation and radiation-induced precipitation in austenitic stainless steels," *Acta Materialia,* vol. 59, no. 3, pp. 1220-1238, 2011.

[64] Z. Ma, G. Ra, X. Qiu, Y. Li, Y. Ding, R. Zhang, Y. Zhang and X. Huang, "In-situ TEM investigation of dislocation loop evolution in Al-forming austenitic stainless steels during Fe+ irradiation: Effects of irradiation dose and pre-existing dislocations," *Journal of Nuclear Materials,* vol. 563, p. 153654, 2022.

[65] S. M. Bruemmer, D. J. Edwards, V. Y. Gertsman and E. P. Simonen, "Grain Boundary Modification during Neutron Irradiation at Intermediate Temperatures," in *Microstructural Processes in Irradiated Materials - 2000*, Boston, 2000.

[66] H. Wiedersich, "On the Theory of Void Formation During Irradiation," *Radiation Effects,* vol. 12, pp. 111-125, 1972.

[67] F. A. Garner, "Void swelling and irradiation creep in light water reactor (LWR) environments," in *Understanding and Mitigating Ageing in Nuclear Power Plants*, Woodhead Publishing Series in Energy, 2010, pp. 308-356.

[68] H. M. Chung, "Assessment of Voids Swelling in Austenitic Stainless Steel Core Internals," US.NRC, Argonne, IL, 2006.

[69] F. A. Garner, E. P. Simonen, B. M. Oliver, L. R. Greenwood, M. L. Grossbeck, W. G. Wolfer and P. M. Scott, "Retention of hydrogen in fcc metals irradiated at temperatures leading to high densities of bubbles or voids," *Journal of Nuclear Materials,* vol. 356, pp. 122-135, 2006.

[70] A. S. Sinjlawi, L. Dong, M. Ickes, K. Sun and G. S. Was, "Irradiation assisted stress corrosion cracking of 347 stainless steel in simulated PWR primary water containing lithium hydroxide or potassium hydroxide," *Journal of Nuclear Materials,* vol. 586, p. 154676, 2023.

[71] Y. Chen, Y. Yang, Y. Huang, T. Allen, B. Alexandreanu and K. Natesan, "oid Swelling and Microstructure of Austenitic Stainless Steels Irradiated in the BOR-60 Reactor," US.NRC, 2012.

[72] G. M. Bond, B. H. Sencer, F. A. Garner, M. L. Hamilton, T. R. Allen and D. L. Porter, "Void Swelling of Annealed 304 Stainless steel at 370-385 ºC and PWR-Relevant Displacement Rates," in *Ninth International Symposium on Environmental Degradation of Materials in Nuclear Power Systems—Water Reactors Radiation Effects on Deformation and Swelling*, 1999.

[73] Z. Jiao, J. T. Busby and G. S. Was, "Deformation microstructure of proton-irradiated stainless steels," *Journal of Nuclear Materials,* vol. 361, pp. 218-227, 2007.

[74] H. T. Vo, D. Frazer, A. A. Kohnert, S. Teysseyre, S. Fensin and P. Hosemann, "Role of low-level void swelling on plasticity and failure in a 33 dpa neutron-irradiated 304 stainless steel," *International Journal of Plasticity,* vol. 164, p. 103577, 2023.

[75] A. Ustrzycka, F. J. Dominguez-Gutierrez and W. Chromiński, "Atomistic analysis of the mechanisms underlying irradiation-hardening in Fe–Ni–Cr alloys," *International Journal of Plasticity,* vol. 182, p. 104118, 2024.

[76] P. R. Okamoto and L. E. Rehn, "Radiation-induced segregation in binary and ternary alloys," *Journal of Nuclear Materials,* vol. 83, pp. 2-23, 1979.

[77] E. O. Kirkendall and A. D. Smigelskas, "Zinc diffusion in alpha brass," *AIME Transactions,* vol. 171, p. 130, 1947.

[78] I. Olefjrod, "The Passive State of Stainless Steels," *Materials Science and Engineering,* vol. 42, pp. 161-171, 1980.

[79] P. L. Andresen, F. P. Ford, S. M. Murphy and J. M. Perks, "State of Knowledge of Radiation Effects on Environmental Cracking in Light Water Reactor Core Materials," in

*Proc. 4th Int. Symp. on Environmental Degradation of Materials in Nuclear Power Systems – Water Reactors, NACE*, 1990.

[80] G. W. Was and P. L. Andresen, "Stress Corrosion Cracking Behavior of Alloys in Aggressive Nuclear Reactor Core Environments, Corrosion 63 (2007) 19-45.," *Corrosion,* vol. 63, pp. 19-45, 2007.

[81] P. L. Andresen and G. S. Was, "Irradiation Assisted Stress Corrosion Cracking," *Comprehensive Nuclear Materials,* vol. 5, pp. 177-205, 2012.

[82] W. Shengkai , Z. Shihao , X. Jiayu , S. Miao and . K. Wenjun, "The time dependence of proton irradiation effect on the intergranular oxidation of 316 L stainless steel in high-temperature hydrogenated water," *Acta Materialia,* vol. 260, p. 119340, 2023.

[83] G. S. Was, Fundamentals of Radiation Materials Science: Metals and Alloys, New York: Springer New York, 2017.

[84] L. E. Rehn, P. R. Okamoto and R. S. Averback, "Relative efficiencies of different ions for producing freely migrating defects," *Physics Review B,* vol. 30, p. 3073, 1984.

[85] Z. Jiao and G. S. Was, "Novel features of radiation-induced segregation and radiation-induced precipitation in austenitic stainless steels," *Acta Materialia,* vol. 59, pp. 1220-1238, 2011.

[86] E. A. Kenik, "Radiation-induced segregation in irradiated type-304 stainless-steels," *Journal of Nuclear Materials,* vol. 187, pp. 239-246, 1992.

[87] A. Etienne, B. Radiguet, N. J. Cunningham, G. R. Odette and P. Pareige, "Atomic scale investigation of radiation-induced segregation in austenitic stainless steels," *Journal of Nuclear Materials,* vol. 406, pp. 244-250, 2010.

[88] T. Toyama, . Y. Nozawa, W. Van Renterghem, Y. Matsukawa, M. Hatakeyama, Y. Nagai, A. Al Mazouzi and S. Van Dyck, "Irradiation-induced precipitates in a neutron irradiated 304 stainless steel studied by three-dimensional atom probe," *Journal of Nuclear Materials,* vol. 418, pp. 62-68, 2011.

[89] Y. Chen, P. H. Chou and E. A. Marquis, "Quantitative atom probe tomography characterization of microstructures in a proton irradiated 304 stainless steel," *Journal of Nuclear Materials,* vol. 451, pp. 130-136, 2014.

[90] M. Hatakeyama, . S. Tamura and I. Yamagata, "Direct observation of solute-dislocation interaction on screw dislocation in a neutron irradiated modified 316 stainless steel," *Materials letters,* vol. 122, pp. 301-305, 2014.

[91] M. Hatakeyama, I. Yamagata, Y. Matsukawa and S. Tamura, "Direct observation of solute–dislocation interaction on extended edge dislocation in irradiated austenitic stainless steel," *Philosophical Magazine Letters,* vol. 94, pp. 18-24, 2014.

[92] M. Tomozawa, Y. Miyahara and K. Kako, "Solute segregation on Σ3 and random grain boundaries in type 316L stainless steel," *Materials Sciencei and Engineering A,* vol. 578, pp. 167-173, 2013.

[93] A. J. Ardell and P. Bellon, "Radiation-induced solute segregation in metallic alloys," *Current Opinion in Solid State and Materials Science,* vol. 20, pp. 115-139, 2016.

[94] J. T. Busby, G. S. Was, S. M. Bruemmer, D. J. Edwards and E. A. Kenik, "Influence of initial grain boundary composition on the evolution of radiation-induced segregation profiles," in *Symposium on Microstructural Processes in Irradiated Materials, Fall MRS Meeting,*, 1998.

[95] C. C. Goodwin, R. G. Faulkner and S. B. Fisher, "The Modelling of Combined radiation-induced and Thermal Non-equilibrium Segregation of Chromium in Neutron-irradiated Austenitic Stainless Steels. Effects of Radiation on Materials," in *18th International Symposium, ASTM STP 1325*, 1999.

[96] A. Kashinath, A. Misra and M. J. Demkowicz, "Stable storage of helium in nanoscale platelets at semicoherent interfaces," *Physical Review Letters,* vol. 110, p. 086101, 2013.

[97] T. R. Allen, J. I. Cole, E. A. Kenik and G. S. Was, " Analyzing the effect of displacement rate on radiation-induced segregation in 304 and 316 stainless steels by examining irradiated EBR-II components and samples irradiated with protons," *Journal of Nuclear Materials,* vol. 376, pp. 169-173, 2008.

[98] T. R. Allen, D. Kaoumi, J. P. Wharry, Z. Jiao, C. Topbasi, A. Kohnert, L. Barnard, A. Certain, K. G. Field and G. S. Was, "Characterization of microstructure and property evolution in advanced cladding and duct: materials exposed to high dose and elevated temperature," *Journal of Materials Research,* vol. 30, pp. 1246-1274, 2015.

[99] F. Kano, K. Fukuya, . S. Hamada and Y. Miwa, "Effect of carbon and nitrogen on grain boundary segregation in irradiated stainless steels," *Journal of Nuclear Materials,* vol. 258, pp. 1713-1717, 1998.

[100] E. H. Lee, P. J. Maziasz and A. F. Rowcliffe, "The Metallurgical Society of AIME," in *AFRJR Holland*, Warrendale, PA, 1981.

[101] P. J. Maziasz and C. J. McHargue, "Microstructural evolution in annealed austenitic stainless steels during neutron irradiation," *International Materials Reviews,* vol. 32, p. 190, 1987.

[102] A. K. Edward and J. T. Busby, "Radiation-induced degradation of stainless steel light water reactor internals," *Materials Science and Engineering: R: Reports,* vol. 73, pp. 67-83, 2012.

[103] K. Fujii and K. Fukuya, "Irradiation-induced microchemical changes in highly irradiated 316 stainless steel," *Journal of Nuclear Materials,* vol. 469, pp. 82-88, 2016.

[104] L. Tan and J. T. Busby, "Alloying effect of Ni and Cr on irradiated microstructural evolution of type 304 stainless steels," *Journal of Nuclear Materials,* vol. 443, pp. 351-358, 2013.

[105] D. J. Edwards, E. P. Simonen, F. A. Garner, L. R. Greenwood, B. M. Oliver and S. M. Bruemmer, "Influence of irradiation temperature and dose gradients on the microstructural evolution in neutron-irradiated 316SS," *Journal of Nuclear Materials,* vol. 317, pp. 32-45, 2003.

[106] K. Fukuya, . Fujii, H. Nishioka and Y. Kitsunai, "Evolution of microstructure and microchemistry in cold-worked 316 stainless steels under PWR irradiation," *Journal of Nuclear Science and Technology,* vol. 43, pp. 159-173, 2006.

[107] D. J. Edwards, . F. A. Garner, . S. M. Bruemmer and P. Efsing, "Nano-cavities observed in a 316SS PWR flux thimble tube irradiated to 33 and 70 dpa," *Journal of Nuclear Materials,* vol. 384, pp. 249-255, 2009.

[108] K. Fujimoto, "Effect of the accelerated irradiation and hydrogen/helium gas on IASCC characteristics for highly irradiated austenitic stainless steels," in *Proc. 12th Int. Conf. On Environmental Degradation of Materials in Nuclear Power Systems-Water Reactors, TMS*, 2005.

[109] S. M. Levine, C. Pareige, Z. Jiao, P. D. Edmondson, G. S. Was, S. J. Zinkle and A. Bhattacharya, "Phase instabilities in austenitic steels during particle bombardment at high and low dose rates," *Materials & Design ,* vol. 217, p. 110588, 2022.

[110] S. M. Samara M. Levine, C. Pareige, Z. Jiao, P. . D. Edmondson, G. S. Was, S. . J. Zinkle and A. Bhattacharya, "Data on Cu- and Ni-Si-Mn-rich solute clustering in a neutron irradiated austenitic stainless steel," *Data in Brief,* vol. 42, p. 108263, 2022.

[111] Z. Jiao, J. Hesterberg, and G. S. Was, "Effect of post-irradiation annealing on the irradiated microstructure of neutron-irradiated 304L stainless steel," *Journal of Nuclear Materials,* vol. 500, pp. 220-234, 2018.

[112] Z. Jiao and G. S. Was, "recipitate behavior in self-ion irradiated stainless steels at high doses," *Journal of Nuclear Materials,* vol. 449, pp. 200-206, 2014.

[113] . O. K. Chopra and A. S. Rao, "A review of irradiation effects on LWR core internal materials – IASCC susceptibility and crack growth rates of austenitic stainless steels," *Journal of Nuclear Materials,* vol. 409, pp. 235-256, 2011.

[114] J. A. Venables and C. J. Harland, "Electron back-scattering patterns—A new technique for obtaining crystallographic information in the scanning electron microscope," *The Philosophical Magazine: A Journal of Theoretical Experimental and Applied Physics,* vol. 27, pp. 1193-1200, 1973.

[115] A. Seeger, "On the theory of radiation damage and radiation hardening," in *Proceedings of the Second United Nations International Conference on The Peaceful Uses of Atomic Energy*, Geneva, 1958.

[116] F. A. Garner, M. L. Hamilton, N. F. Panayotou and G. D. Johnson, "The microstructural origins of yield strength changes in aisi 316 during fission or fusion irradiation," *Journal of Nuclear Materials,* Vols. 103-104, pp. 803-808, 1981.

[117] G. S. Was and P. L. Andresen, "Effect of irradiation and corrosion on SCC in LWRs," in *Corrosion in the Nuclear Power Industry*, Ohio, American Society for Metals, 2007.

[118] J. T. Busby, M. C. Hash and G. S. Was, "The relationship between hardness and yield stress in irradiated austenitic and ferritic steels," *Journal of Nuclear Materials,* vol. 336, pp. 267-278, 2005.

[119] J. E. Pawel, A. F. Rowcliffe, G. E. Lucas and . S. J. Zinkle, "Irradiation performance of stainless steels for ITER application," *Journal of Nuclear Materials,* vol. 239, pp. 126-131, 1996.

[120] F. A. Garner, " Radiation-Induced Damage in Austenitic Structural Steels Used in Nuclear Reactors," in *Comprehensive Nuclear Materials, 2nd Ed.*, Elsevier, 2020, pp. 57-168.

[121] D. J. Dingley, "On-line determination of crystal orientation and texture determination in an SEM," in *Proceedings of the Royal Microscopical Society*, 1984.

[122] A. Seeger, . J. Dieh, S. Mader and . H. Rebstock, "Work-hardening and work-softening of face-centred cubic metal crystals," *The Philosophical Magazine,* vol. 2, pp. 323-350, 1952.

[123] S. J. Zinkle and Y. Matsukawa, "Observation and analysis of defect cluster production and interactions with dislocations," *Journal of Nuclear Materials,* Vols. 329-333, pp. 88-96, 2004.

[124] P. Zhu, . Y.-R. Lin, S. Agarwal, V. Pauly, S. Taller and S. J. Zinkle, "Comparison of hardening and microstructures of ferritic/martensitic steels irradiated with fast neutrons and dual ions," *Journal of Nuclear Materials,* vol. 599, p. 155211, 2024.

[125] L. Tan and . J. T. Busby, "Formulating the strength factor α for improved predictability of radiation hardening," *Journal of Nuclear Materials,* vol. 465, pp. 724-730, 2015.

[126] D. Hull and D. J. Bacon, Introdcution to Dislocations, Oxford: Butterworth-Heinemann, 2011.

[127] H. M. Ledbetter, "Manganese contributions to the elastic constants of face centred cubic Fe-Cr-Ni stainless steel," *Journal of Materials Science,* vol. 20, pp. 2923-2929, 1985.

[128] Austenitic Chromium-nickel Stainless Steels – Engineering Properties at Elevated Temperatures, Nickel Institute, 2021.

[129] G. Miyamoto, A. Shibata, . T. Maki and T. Furuhara, "Precise measurement of strain accommodation in austenite matrix surrounding martensite in ferrous alloys by electron backscatter diffraction analysis," *Acta Materialia,* vol. 57, pp. 1120-1131, 2009.

[130] A. J. Wilkinson , . E. E. Clarke, T. B. Britton , P. Littlewood and P. S. Karamched , "High-resolution electron backscatter diffraction: An emerging tool for studying local deformation," *The Journal of Strain Analysis for Engineering Design,* vol. 45, pp. 365-376, 2009.

[131] T. . B. Britton and A. J. Wilkinson, "Stress fields and geometrically necessary dislocation density distributions near the head of a blocked slip band," *Acta Materialia,* vol. 60, pp. 5773-5782, 2012.

[132] D. J. Dingley and . V. Randle, "Microtexture determination by electron back-scatter diffraction," *Journal of Materials Science,* vol. 27, pp. 4545-4566, 1992.

[133] K. Z. Baba-Kishi and D. . J. Dingley, "Backscatter Kikuchi diffraction in the SEM for identification of crystallographic point groups," *Journal of Scanning Microscopies,* vol. 11, pp. 305-312, 1989.

[134] Z. Jiao and G. S. Was, "The role of irradiated microstructure in the localized deformation of austenitic stainless steels," *Journal of Nuclear Materials,* vol. 407, pp. 34-43, 2010.

[135] E. A. West, M. D. McMurtrey, Z. Jiao and G. S. Was, "Role of Localized Deformation in Irradiation-Assisted Stress Corrosion Cracking Initiation," *Metallurgical and Materials Transactions A ,* vol. 43, pp. 136-146, 2012.

[136] G. S. Was , Z. Jiao and J. T. Busby, in *Proceedings of the 16th European conference of fracture*, Berlin, 2006.

[137] K. J. Stephenson and G. S. Was, "The role of dislocation channeling in IASCC initiation of neutron irradiated stainless steel," *Journal of Nuclear Materials,* vol. 481, pp. 214-225, 2016.

[138] M. D. McMurtrey, B. Cui, I. Robertson, D. Farkas and G. S. Was, "Mechanism of dislocation channel-induced irradiation assisted stress corrosion crack initiation in austenitic stainless steel," *Current Opinion in Solid State and Materials Science,* vol. 19, pp. 305-314, 2015.

[139] G. S. Was, D. Farkas and I. M. Robertson, "Micromechanics of dislocation channeling in intergranular stress corrosion crack nucleation," *Current Opinion in Solid State and Materials Science,* vol. 16, pp. 134-142, 2012.

[140] D. C. Johnson, . B. Kuhr, D. Farkas and G. S. Was, "Quantitative analysis of localized stresses in irradiated stainless steels using high resolution electron backscatter diffraction and molecular dynamics modeling," *Scripta Materialia,* vol. 116, p. 87, 2016.

[141] H. M. Chung, . W. E. Ruther, J. E. Sanecki, A. Hins, N. J. Zaluzec and . T. F. Kassner, "Irradiation-assisted stress corrosion cracking of austenitic stainless steels: recent progress and new approaches," *Journal of Nuclear Materials,* vol. 239, pp. 61-79, 1996.

[142] M. Kodama, . J. Morisawa, S. Nishimura, . K. Asano, S. Shima and T. K. Nakata, "Stress corrosion cracking and intergranular corrosion of austenitic stainless steels irradiated at 323 K," *Journal of Nuclear Materials,* Vols. 212-215, pp. 1509-1514, 1994.

[143] P. Zhu, Y. Zhao, Y.-R. Lin, J. Henry and S. . J. Zinkle, "Defect-specific strength factors and superposition model for predicting strengthening of ion irradiated Fe18Cr alloy," *Journal of Nuclear Materials,* vol. 588, p. 154823, 2024.

[144] W. Y. Chen, Y. Miao, J. Gan, M. A. Okuniewski, S. A. Maloy and . J. F. Stubbins, "Neutron irradiation effects in Fe and Fe-Cr at 300°C," *Acta Materialia,* vol. 111, pp. 407-406, 2016.

[145] D. Cubicciotti, "Pourbaix Diagrams for Mixed Metal Oxides — Chemistry of Copper in BWR Water," *Corrosion,* vol. 44, pp. 875-880, 1988.

[146] D. Cubicciotti, "Potential-pH diagrams for alloy-water systems under LWR conditions," *Journal of Nuclear Materials,* vol. 201, pp. 176-183, 1993.

[147] D. Feron, E. Herms and B. Tanguy, "Behavior of stainless steels in pressurized water reactor primary circuits," *Journal of Nuclear Material,* vol. 427, pp. 364-377, 2012.

[148] F. P. Ford and P. L. Andresen, "Corrosion in nuclear systems: environmentally assisted cracking in light water reactors," in *Corrosion Mechanisms*, New York, 1994.

[149] F. P. Ford and P. L. Andresen, "Development and use of a predictive model of crack propagation in 304/316L, A533B/A508 and Inconel 600/182 in 288C water," in *Proc. 3rd Int'l Symp. on Environmental Degradation of Materials in Nuclear Power Systems—Water Reactors*, New York, 1988.

[150] F. P. Ford, B. Gordon and R. M. Horn, "Corrosion in boiling water reactors," in *ASM handbook, in: Corrosion: Environments and Industries*, Ohio, 2006.

[151] R. W. Staehle, "Historical views on stress corrosion cracking of nickel-based alloys: The Coriou effect," in *Stress Corrosion Cracking of Nickel Based Alloys in Water-cooled Nuclear Reactors*, WoodHead Publishing, 2016, pp. 3-131.

[152] L. E. Murr, "Microstructural changes associated with yielding and plastic flow in fcc metals and alloys," *Res Mechanica,* vol. 9, pp. 159-187, 1983.

[153] J. W. Simmon, "Overview: high-nitrogen alloying of stainless steels," *Materials Science and Engineering A,* vol. 207, pp. 159-169, 1996.

[154] J. J. Eckenrod and C. W. Kovach, "Effect of nitrogen on the sensitization, corrosion and mechanical properties of 18Cr-8Ni stainless steel," *ASTM Special Techology ,* vol. 679, p. 17, 1979.

[155] J. F. Eckel and T. . B. Cox, "Some Effects of Nitrogen Content on the Stress Corrosion Susceptibility of AIS1 Type 304 Austenitic Stainless Steel," *Corrosion,* vol. 24, pp. 218-222, 1968.

[156] J. F. Eckel and G. S. Clevinger, " Aging of AISI Type 304 Austenitic Stainless Steel Containing Nitrogen and Its Influence on Stress Corrosion Cracking," *Corrosion,* vol. 26, pp. 351-355, 1970.

[157] Z. Lu, T. Shoji, F. Meng, Y. Qiu, . T. Dan and H. Xue, "Effects of water chemistry and loading conditions on stress corrosion cracking of cold-rolled 316NG stainless steel in high temperature water," *Corrosion Science,* vol. 53, pp. 247-262, 2011.

[158] S. C. Bali, . V. Kain and V. S. Raja, "Effect of low temperature sensitization on IGSCC behavior of austenitic stainless steels in simulated boiling water reactor environment," *Corrosion,* vol. 65, pp. 726-740, 2009.

[159] R. L. Jones, "Prevention of stress corrosion cracking in boiling water reactors," *Corrosion,* pp. 1-17, 1990.

[160] K. W. , M. Ivanchenko, U. Ehrnsren, Y. Yagodzinskyy and H. Hanninen, "Microstructural manifestation of dynamic strain aging in AISI 316 stainless steel," *Journal Nuclear Materials,* vol. 395, pp. 156-161, 2009.

[161] S. Roychwodhury, V. Kain, M. Gupta and R. C. Prasad, "IGSCC crack growth in simulated BWR environment – Effect of nitrogen content in non-sensitised and warm rolled austenitic stainless steel," *Corrosion Science,* vol. 53, pp. 1120-1129, 2011.

[162] R.-W. Bosch, W. Van Renterghem, S. Van Dyck, R. Chaouadi, . R. Gérard and F. Somville, "Microstructure, mechanical properties and IASCC susceptibility of stainless steel baffle bolts after 30 years of operation in a PWR,," *Journal of Nuclear Materials,* vol. 543, p. 152615, 2015.

[163] T. R. Anthony, "Solute segregation in vacancy gradients generated by sintering and temperature changes," *Acta Materialia,* vol. 17, pp. 603-609, 1696.

[164] P. L. Andresen and G. S. Was, "A historical perspective on understanding IASCC," *Journal Nuclear Materials,* vol. 517, pp. 380-392, 2019.

[165] T. G. Lach, M. . N. Gussev and X. (. Chen, "In-Service Oxidation And IASCC In High Fluence Baffle-Former Bolts Retrieved From a Westinghouse PWR," Oak Ridge National Laboratory, Oak Ridge, TN, 2024.

[166] A. G. Penders, M. J. Konstantinovic, W. Van Renterghem, R.-W. Bosch, . D. Schryvers and F. Somville, "Characterization of IASCC crack tips extracted from neutron-irradiated flux thimble tube specimens in view of a probabilistic fracture model," *Journal of Nuclear Materials,* vol. 571, p. 154015, 2022.

[167] "Materials Reliability Program: Characterizations of Type 316 Cold Worked Stainless Steel Highly Irradiated Under PWR Operating Conditions (International IASCC Advisory Committee Phase 3 Program Interim Report) (MRP-202) Technical Report," Electric Power Research Institute, Palo Alto, CA, 2006.

[168] R. Bosch, M. Vankeerberghen, R. Gérard and F. Somville, "Crack initiation testing of thimble tube material under PWR conditions to determine a stress threshold for IASCC," *Journal of Nuclear Materials,* vol. 461, pp. 112-121, 2015.

[169] A. G. Penders, M. J. Konstantinović, T. Yang, R.-W. Bosch and D. Schryvers, "Microstructural investigation of IASCC crack tips extracted from thimble tube O-ring specimens," *Journal of Nuclear Materials,* vol. 565, p. 153727, 2022.

[170] D. Du, K. Sun and G. S. Was, " Crack initiation of neutron-irradiated 304 L stainless steel in PWR primary water," *Corrosion Science,* vol. 193, p. 109902, 2021.

[171] S. Swaminathan, . K. Sun and G. S. Was, "Decoupling the roles of grain boundary oxidation and stress in IASCC of neutron-irradiated 304L stainless steel," *Journal of Nuclear Materials,* vol. 585, p. 154604, 2023.

[172] D. F. Falaakh, . P. Myers, J. P. Park, G. . S. Was and C. B. Bahn, "Statistical determination of stress threshold and survival analysis on IASCC initiation data of stainless steels in pressurized water reactor conditions," *Journal of Nuclear Materials,* vol. 583, p. 154549, 2023.

[173] B. N. Singh, A. J. Foreman and . H. Trinkaus, "Radiation hardening revisited: role of intracascade clustering," *Journal of Nuclear Materials,* vol. 249, pp. 103-115, 1997.

[174] . S. M. Bruemmer, J. I. Cole, J. L. Brimhall, R. D. Carter and G. S. Was, "'Radiation hardening effects on localized deformation and stress corrosion cracking of stainless steels," in *Sixth International Symposium on Environmental Degradation of Materials in Nuclear Power Systems - Water Reactors*, 1993.

[175] G. E. Lucas, "The evolution of mechanical property change in irradiated austenitic stainless steels," *Journal of Nuclear Materials,* vol. 206, pp. 287-305, 1993.

[176] S. Fyfitch , S. Davidsaver and K. Amberge , "Irradiation-Assisted Stress Corrosion Cracking Initiation Screening Criteria for Stainless Steels in PWR Systems," in *Proceedings of the 18th International Conference on Environmental Degradation of Materials in Nuclear Power Systems – Water Reactors*, 2018.

[177] S. M. Bruemmer, E. P. Simonen, P. M. Scott, P. L. Andresen, G. S. Was and J. L. Nelson, " Radiation-induced material changes and susceptibility to intergranular failure of light-water-reactor core internals," *Journal of Nuclear Materials,* vol. 274, pp. 299-314, 1999.

[178] . M. O. Speidel and R. Magdowski , "Stress corrosion cracking of stabilized austenitic stainless steels in various types of nuclear power plants," in *Proc. 9th International Symposium on Environmental Degradation of Materials in Nuclear Power Systems – Water Reactors*, 1999.

[179] W. Shengkai , Z. Shihao , X. Jiayu , S. Miao and K. Wenjun , "The time dependence of proton irradiation effect on the intergranular oxidation of 316 L stainless steel in high-temperature hydrogenated water," *Acta Materialia,* vol. 260, p. 119340, 2023.

[180] J. T. Busby, G. S. Was and E. A. Kenik, "Isolating the effect of radiation-induced segregation in irradiation-assisted stress corrosion cracking of austenitic stainless steels," *Journal of Nuclear Materials,* vol. 302, pp. 20-40, 2002.

[181] P. L. Andresen and M. M. Morra, "Effect of Si on SCC of irradiated and unirradiated stainless steels and nickel alloys," in *Proc. 12th International Symposium on Environmental Degradation of Materials in Nuclear Power Systems – Water Reactors*, 2005.

[182] F. Li, Y. Kaneshima and T. Shoji, "A high-resolution characterization of irradiation-assisted stress corrosion cracking of proton-irradiated 316L stainless steel in simulated pressurized water reactor primary water," *Corrosion,* vol. 56, pp. 460-469, 2000.

[183] W. Kuang, X. Feng, D. Du, M. Song, M. Wang and G. . S. Was, "A high-resolution characterization of irradiation-assisted stress corrosion cracking of proton-irradiated 316L

stainless steel in simulated pressurized water reactor primary water," *Corrosion Science,* vol. 199, p. 110187, 2022.

[184] . E. P. Simonen, R. H. Jones and S. M. Bruemmer, "Radiation effects on grain boundary chemistry relevant to stress corrosion cracking of stainless steels," *Journal of Nuclear Materials,* Vols. 191-194, pp. 1002-1006, 1992.

[185] Y. Miwa, T. Tsukada, S. Jitsukawa, S. Kita, S. Hamada, Y. Matsui and M. Shindo, "Effect of minor elements on irradiation assisted stress corrosion cracking of model austenitic stainless steels," *Journal of Nuclear Materials,* Vols. 233-237, pp. 1393-1396, 1996.

[186] R. L. Tapping, R. D. Davidson, E. McAlpine and D. H. Lister, "The composition and morphology of oxide films formed on type 304 stainless steel in lithiated high temperature water," *Corrosion Science,* vol. 26, pp. 563-576, 1986.

[187] B. Stellwag, "The mechanism of oxide film formation on austenitic stainless steels in high temperature water," *Corrosion Science,* vol. 40, pp. 337-370, 1998.

[188] J. Robertson, "The mechanism of high temperature aqueous corrosion of stainless steels," *Corrosion Science,* vol. 32, pp. 443-465, 1991.

[189] S. Zhang, S. Wang, X. Feng, Z. Ning, J. Hou and W. Kuang, "Insights into the stress corrosion cracking resistance of a selective laser melted 304L stainless steel in high-temperature hydrogenated water," *Acta Materialia,* vol. 244, p. 118561, 2023.

[190] K. Fujii and . K. Fukuya, "Development of Micro Tensile Testing Method in an FIB System for Evaluating Grain Boundary Strength," *Materials Transactions,* vol. 52, pp. 20-24, 2011.

[191] K. Fujii, T. Miura, H. Nishioka and K. Fukuya, "Degredation of Grain Boundary Strength by Oxidation in Alloy 600," in *15th International Conference on Environmental Degradation, The Minerals, Metals, & Materials Society (TMS)*, 2011.

[192] H. Dugdale, . D. E. Armstrong, E. Tarleton, S. G. Roberts and S. Lozano-Perez, "How oxidized grain boundaries fail," *Acta Materialia,* vol. 61, pp. 4707-4713, 2013.

[193] T. Fukumura, K. Fukuya, K. Fujii, T. Miura and Y. Ktisunai, "Grain Boundary Oxidation of Neutron Irradiated Stainless Steels in Simulated PWR water," in *Proceedings of the 18 International Conference on Environmental Degradation of Materials in Nuclear Power Systems - Water Reactors, The Minerals, Metals & Materials Series*, 2018.

[194] D. Du, K. Sun and G. . S. Was, "IASCC of neutron irradiated 316 stainless steel to 125 dpa," *Materials Characterization ,* vol. 173, p. 110897, 2021.

[195] "Standard Test Methods for Determination of Carbon, Sulfur, Nitrogen, and Oxygen in Steel, Iron, Nickel, and Cobalt Alloys by Various Combustion and Inert Gas Fusion Techniques," ASTM International.

[196] "Standard Guide for Determination of Various Elements by Direct Current Plasma Atomic Emission Spectrometry," ASTM International.

[197] "Standard Test Methods for Determining Average Grain Size," ASTM International.

[198] "Standard Test Method for Microindentation Hardness of Materials," ASTM International.

[199] J. F. Ziegler, M. D. Ziegler and J. P. Biersack, "SRIM - The stopping and range of ions in matter," 2013.

[200] "Standard Practice for Investigating the Effects of Neutron Radiation Damage Using Charged-Particle Irradiation," ASTM International.

[201] D. J. Edwards, . F. A. Garner, E. P. Simonen and S. M. Bruemmer, "Characterization of neutron-irradiated 300-series stainless steels to assess mechanisms of irradiation-assisted stress corrosion cracking," Electric Power Research Institute (EPRI), 2001.

[202] D. M. Himmelblau, " Solubilities of Inert Gases in Water," *Journal of Chemical and Engineering Data,* vol. 5, pp. 10-15, 1960.

[203] J. Bonet and R. D. Wood, Nonlinear Continuum Mechanics for Finite Element Analysis, Cambridge University Press, 1997.

[204] C. Earls, "Nonlinear Finite Element Analysis: Structures," Cornell University NLFEA notes, 2016.

[205] N. E. Dowling, Mechanical Behavior of Materials, Pearson, 2013.

[206] "CIR II Program: Crack Growth Testing of Fast Reactor Irradiated Type 304L Stainless Steel in BWR Environments," Electric Power Research Institute (EPRI), Palo Alto, CA, 2006.

[207] G. . S. Was and J. . T. Busby, "Use of Proton Irradiation to Determine IASCC Mechanisms in Light Water Reactors: Phase 2: Commercial Alloys," Electric Power Reserach Institute (EPRI), 2004.

[208] Y. Chen, A. S. Rao, . B. Alexandreanu and K. Natesan, "Slow strain rate tensile tests on irradiated austenitic stainless steels in simulated light water reactor environments," *Nuclear Materials and Engineering Design,* vol. 269, pp. 38-44, 2014.

[209] Y. Chen, W. Soppet, . B. Alexandreanu and K. Natesan, "Technical Letter Report of Slow-Strain-Rate Tensile Tests on Irradiated Stainless Steels in a PWR Environment," Argonne National Laboratory, 2012.

[210] S. A. Maloy, M. R. James, W. R. Johnson, T. S. Byun, K. Farrell and M. B. Toloczko, "Comparison of fission neutron and proton/spallation neutron irradiation effects on the tensile behavior of type 316 and 304 stainless steel," *Journal of Nuclear Materials,* vol. 318, pp. 283-291, 2003.

[211] "Materials Reliability Program: Crack Initiation Testing and Slow Strain Rate Tensile (SSRT) Testing of Boris-60 Irradiated Materials, and Effect of Hydrogen on IASCC Susceptibility (MRP-159)," Electric Power Research Institute (EPRI), Palo Alto, 2005.

[212] "Irradiation Assisted Stress Corrosion Cracking of Highly Irradiated 300-Series Stainless Steels in PWR Primary Water Environment," Electric Power Research Institute (EPRI), Palo Alto, CA, 2021.

[213] "Characterization of Neutron-Irradiated 300-Series Stainless Steels," Electric Power Research Institute (EPRI), Palo Alto, CA, 2006.

[214] Y. Takeuti, S. Komori, N. Noda and H. Nyuko, "Thermal-Stress Problems In Industry. 3: Temperature Dependency Of Elastic Moduli For Several Metals At Temperatures From -196 TO 1000° C," *Journal of Thermal Stresses,* vol. 2, pp. 233-250, 1979.

[215] T. Kayaba and A. Iwabuchi, "The Fretting Wear of 0.45% C Steel and Austenitic Stainless Steel From 20 to 650 C in Air," *Wear,* vol. 74, pp. 229-245, 1981-1982.

[216] A. F. Smith, "The friction and sliding wear of unlubricated 316 stainless steel at room temperature in air," *Wear,* vol. 96, pp. 301-318, 1984.

[217] N. L. Parthasarathi, U. Borah and S. K. Albert, "Correlation Between Coefficient Of Friction And Surface Roughness In Dry Sliding Wear Of Aisi 316 L (N) Stainless Steel At Elevated Temperatures," *Computer Modelling and New Technologies,* vol. 17, pp. 51-63, 2013.

[218] "The Engineering ToolBox (2004). Metals and Alloys - Young's Modulus of Elasticity.," [Online]. Available: https://www.engineeringtoolbox.com/young-modulus-d_773.html. [Accessed 31 05 2025].

[219] T. S. Byun, N. Hashimoto and . K. Farrell, "Temperature dependence of strain hardening and plastic instability behaviors in austenitic stainless steels," *Acta Materialia,* vol. 52, pp. 3889-3899, 2004.

[220] "Elevated Temperature Physical Properties of Stainless Steels," British Stainless-Steel Association (BSSA), [Online]. Available: https://bssa.org.uk/bssa_articles/elevated-temperature-physical-properties-of-stainless-steels/. [Accessed 31 05 2025].

[221] P.-Y. Cheng, Influence of Residual Stress and Heat Affected Zone on Fatigue Failure of Welded Piping Joints, North Carolina State University, 2009.

[222] "Proceedings of the 2nd International Topical Meeting on Nuclear Applications of Accelerator Technology," La Grange Park, 1998.

[223] J. M. Cookson, R. D. Carter, D. L. Damcott, M. Atzmon and G. S. Was, "Irradiation assisted stress corrosion cracking of controlled purity 304L stainless steels," *Journal of Nuclear Materials,* vol. 202, pp. 104-121, 1993.

[224] Z. Jiao, . J. Michalicka and G. S. Was, "Self-ion emulation of high dose neutron irradiated," *Journal of Nuclear Materials,* vol. 501, pp. 312-318, 2018.

[225] E. E. Bloom, J. O. Stiegler and C. J. McHargue, "Radiation Damage in Annealed Type 304 Stainless Steel," *Radiation Effects,* vol. 14, pp. 231-243, 1972.

[226] J. Gan and G. S. Was, "Microstructure evolution in austenitic Fe-Cr-Ni alloys irradiated with rotons: comparison with neutron-irradiated microstructure," *Journal of Nuclear Materials,* vol. 297, pp. 161-175, 2001.

[227] L. Tan, R. E. Stoller, K. G. Field, Y. Yang, H. Nam, D. Morgan, B. D. Wirth, M. N. Gussev and J. T. Busby, "Microstructural Evolution of Type 304 and 316 Stainless Steels Under Neutron Irradiation at LWR Relevant Conditions," *Journal of Nuclear Materials,* vol. 68, pp. 517-529, 2016.

[228] M. Shreevalli , B. S. Dash, D. Ramachandran, . C. Padmaprabu and V. Karthik , "Defects analysis in low displacement damage neutron-irradiated austenitic stainless steels," *Journal of Nuclear Materials,* vol. 599, p. 155234, 2024.

[229] M. Song, K. G. Field, K. Sun and G. S. Was, "Extending damage accumulation of commercial reactor irradiated 316 stainless steel with ion irradiation," *Journal of Nuclear Materials,* vol. 593, p. 154989, 2024.

[230] F. A. Garner and D. L. Porter, "Irradiation creep and swelling of AISI 316 to exposures of 130 dpa at 385-400°C," *Journal of Nuclear Materials,* Vols. 155-157, pp. 1006-1013, 1988.

[231] B. H. Sencer, G. M. Bond, M. L. Hamilton, F. A. Garner, S. A. Maloy and W. . F. Sommer, "Microstructural origins of radiation-induced changes in mechanical properties of 316 L and 304 L austenitic stainless steels irradiated with mixed spectra of high-energy

protons and spallation neutrons," *Journal of Nuclear Materials,* vol. 296, pp. 112-118, 2001.

[232] A. Etienne, B. Radiguet, P. Pareige, J. -P. Massoud and C. Pokor, "Tomographic atom probe characterization of the microstructure of a cold worked 316 austenitic stainless steel after neutron irradiation," *Journal of Nuclear Materials,* vol. 382, pp. 64-69, 2008.

[233] O. P. Maksimkin, K. V. Tsai, L. G. Turubarova, T. Doronina and F. A. Garner, "Characterization of 08Cr16Ni11Mo3 stainless steel irradiated in the BN-350 reactor," *Journal of Nuclear Materials,* Vols. 329-333, pp. 625-629, 2004.

[234] J. F. Williams, T. R. Mager, P. Spellward, K. Koyama, I. Suzuki, J. Walmsley and H. Mimaki, in *Proceedings of 8th International Sympsium on Environmental Degradation of Materials in Nuclear PowerSystems—Water Reactors*, Amelia Island, FL, 1997.

[235] K. Asano, K. Fukuya, K. Nakata and M. Kodama, in *Proceedings of 5th Inernational Symposium on Environmental Degradation of Materials in NuclearPower Systems—Water Reactors,*, 1991.

[236] M. Kodama, R. Katsura, J. Morisawa, S. Nishimura, S. Suzuki, K. Asano, K. Fukuya and K. Nakata, in *Proceedings of 6th International Symposium on En-vironmental Degradation of Materials in Nuclear Power Systems—Water Reactors*, 1993.

[237] K. . G. Field, Y. Yang, T. R. Allen and . J. T. Busby, "Defect sink characteristics of specific grain boundary types in 304 stainless steels under high dose neutron environments,," *Acta Materialia,* vol. 89, pp. 438-449, 2015.

[238] G. S. Was, J. T. Busby, T. Allen, E. A. Kenik, A. Jensson, S. M. Bruemmer, J. Gan, A. D. Edwards, P. M. Scott and P. L. Andresen, " Emulation of neutron irradiation effects with

protons: validation of principle," *Journal of Nuclear Materials,* vol. 300, pp. 198-216, 2002.

[239] "Materials Reliability Program A Review of Radiation Embrittlement for Stainless Steels (MRP-79)," 2004.

[240] V. G. Gavriljuk and H. Berns, High Nitrogen Steels Structure: Properties, Manufacture, Applications, Germany: Springer, 1999.

[241] S. V. Astafurov, . G. G. Maier, . E. V. Melinkov, M. Y. Panchenko and E. G. Astafurova, " The Strain-rate dependence pf the Hall-Petch effect in two austenitic stainless steels with different stacking fault energies," *Materials Science and Engineerin A,* vol. 756, pp. 365-372, 2019.

[242] É. . V. Kozlov, L. A. Teplyakova, N. A. Koneva, V. G. Gavrilyuk, N. A. Popova, L. . N. Ignatenko, G. . L. Fedoseeva, . Y. Smuk, A. V. Paul and V. P. Podkovka, "Role of solid-solution strengthening and interactions in the dislocation ensemble in the formation of flow stress in austenitic nitrogen steel," *Russian Physics Journal ,* vol. 39, pp. 211-229, 1996.

[243] O. Bouaziz, H. Zurob, B. Chehab, J. D. Embury, S. Allain and M. Huang, "Effect of chemical composition on work hardening of Fe-Mn-C TWIP steels," *Materials Science and Technology,* vol. 27, pp. 707-709, 2011.

[244] G. S. Was, Z. Jiao and . J. T. Busby, in *In: Gdoutos EE (ed) Proceedings of the 16th European*, 2006 .

[245] H. Nishioka, K. Fukuya, K. Fuji and T. Torimaru, "IASCC Initiation in Highly Irradiated Stainless Steels under Uniaxial Constant Load Conditions," *Journal of Nuclear Science and Technology ,* vol. 45, no. 10, pp. 1072-1077, 2008.

[246] K. Takakura, K. Nakata, M. Ando, K. Fujimoto and E. Wachi, "Lifetime evaluation for IASCC initiation of cold worked 316 stainless steels BFB," in *PWR Primary Water, in: Proceedings of the 13th International Conference on Environmental Degradation of Materials in Nuclear Power System – Water Reactors*, Whistler, B.C., Canada, 2007.

[247] C. Pokor, A. Toivonen, M. Wintergerst, U. Ehrnsten, W. Karlsen and J. P. Massoud, "Determination of the time to failure curve as a function of stress for a highly irradiated AISI 304 stainless steel after constant load tests in simulated PWR water environment," in *Fontevraud 7 Symposium – Contribution of Materials Investigations to Improve the Safety and Performance of LWRs*, Avignon, France, 2010.

[248] B. Tanguy, C. Pokor, . A. Stern and P. Bossis, "Initiation Stress Threshold Irradiation Assisted Stress Corrosion Cracking Criterion Assessment for Core Internals in PWR Environment," in *Pressure Vessels and Piping Conference*, Baltimore, Maryland, USA, 2011.

[249] Y. Bao, X. Yang, F. Meng, Y. Yang, Q. Chu , M. Wang and A. Jenssen, "Effects of irradiation and stress on crack initiation behavior of 316SS flux thimble tubes in PWR environment," *Corrosion Communications,* vol. 16, pp. 1-13, 2024.

[250] "Materials Reliability Program: Characterization of Type 316 Cold Worked Stainless Steel Highly Irradiated Under PWR Operating Condit ions (International IASCC

Advisory Committee Phase 3 Program Final Report) (MRP-214)," EPRI, Palo Alto, CA and the International IASCC Advisory Committee: 2007. 1015332, 2007.

[251] K. Fuji, "Effects of Dissolved Hydrogen on IASCC Behavior," in *Fontevraud 7*, Avignon, France, 2010.

[252] J. Conermann, R. Shogan, K. Fujimoto, T. Yonezawa and Y. Yamaguchi, "Irradiation effects in a highly irradiated cold worked stainless steel removed from a commercial PWR," in *Proceedings of the 12th International Conference on Environmental Degradation of Materials in Nuclear Power System – Water Reactors*, 2005.

[253] "EPRI Letter MRP 2016-008, Biennial Report of MRP-227-A Reactor Internals Inspection Results".

[254] S. Wang, S. Zhang, J. Xie, X. Feng, M. Song, G. . S. Was and W. Kuang, "Clarifying the mitigation effect of proton irradiation on the intergranular oxidation of 316L stainless steel in high temperature water," vol. 241, p. 118408, Acta Materialia.

[255] S. Zhang, S. Wang, X. Feng, Z. Ning, J. Hou and W. Kuang, "Insights into the stress corrosion cracking resistance of a selective laser melted 304L stainless steel in high-temperature hydrogenated water," *Acta Materialia,* vol. 244, p. 118561, 2023.

[256] M. R. Ickes, G. S. Was, K. Sun, A. Sinjlawi and L. Dong, "Irradiation-assisted Stress Corrosion Cracking of PWRirradiated Type 347 Stainless Steel (NSUF CINR 19-16567)," Idaho National Laboratory (INL), Idaho Falls, ID , 2023.

[257] T. Fukumura, K. Fukuya, K. Fujii, T. Miur and Y. Kitsunai, "Grain Boundary Oxidation of Neutron Irradiated Stainless Steels in Simulated PWR Water," in *Proceedings of the*

*18th International Conference on Environmental Degradation of Materials in Nuclear Power Systems – Water Reactors,*, 2017.

[258] H. M. Chung and W. J. Shack, "Irradiation-assisted Stress Corrosion Cracking Behavior of Austenitic Stainless Steels Applicable to LWR Core Internals," Argonne National Laboratory, Argonne, IL, 2006.

[259] K. Fukuya, S. Shima, H. Kayano and M. Narui, "Stress corrosion cracking and intergranular corrosion of neutron irradiated austenitic stainless steels," *Journal of Nuclear Materials,* Vols. 191-194, pp. 1007-1011, 1992.

[260] J. Nakano, Y. Miwa, T. Kohya and T. Tsukada, "Effects of silicon, carbon and molybdenum additions on IASCC of neutron irradiated austenitic stainless steels," *Journal of Nuclear Materials,* Vols. 329-333, pp. 643-647, 2004.

[261] K. . J. Stephenson and G. S. Was, "Comparison of the microstructure, deformation and crack initiation behavior of austenitic stainless steel irradiated in-reactor or with protons," *Journal of Nuclear Materials,* vol. 456, pp. 85-98, 2015.